SOLASE - A Conceptual Laser Fusion Reactor Design

R.W. Conn, S.I. Abdel-Khalik, G.A. Moses, F. Beranek, E.T. Cheng, G.W. Cooper, R.B. Droll, T. Henderson, J. Howard, T.O. Hunter, E.M. Larsen, G.L. Kulcinski, E.G. Lovell, G.R. Magelssen, C.W. Maynard, K.R. Okula, M. Ortman, M. Ragheb, W.B. Rensel, D. Solomon, R. Spencer, I.N. Sviatoslavsky, W.F. Vogelsang, R.D. Watson, and W.G. Wolfer

December 1977

UWFDM-220

FUSION TECHNOLOGY INSTITUTE

UNIVERSITY OF WISCONSIN

MADISON WISCONSIN

SOLASE - A Conceptual Laser Fusion Reactor Design

R.W. Conn, S.I. Abdel-Khalik, G.A. Moses, F. Beranek, E.T. Cheng, G.W. Cooper, R.B. Droll, T. Henderson, J. Howard, T.O. Hunter, E.M. Larsen, G.L. Kulcinski, E.G. Lovell, G.R. Magelssen, C.W. Maynard, K.R. Okula, M. Ortman, M. Ragheb, W.B. Rensel, D. Solomon, R. Spencer, I.N. Sviatoslavsky, W.F. Vogelsang, R.D. Watson, and W.G. Wolfer

Fusion Technology Institute
University of Wisconsin
1500 Engineering Drive
Madison, WI 53706

http://fti.neep.wisc.edu

December 1977

UWFDM-220

SOLASE

A CONCEPTUAL LASER FUSION REACTOR DESIGN

R.W. Conn
S.I. Abdel-Khalik
G.A. Moses
F. Beranek
E.T. Cheng
G.W. Cooper
R.B. Droll
T. Henderson*
J. Howard
T.O. Hunter
E.M. Larsen
G.L. Kulcinski
E.G. Lovell
G.R. Magelssen
C.W. Maynard
K.R. Okula
M. Ortman
M.M.H. Ragheb
W.B. Rensel*
D. Solomon*
R.L. Spencer
I.N. Sviatoslavsky
W.F. Vogelsang
R.D. Watson
W.G. Wolfer

UWFDM-220

Fusion Research Program
Nuclear Engineering Department
The University of Wisconsin
Madison, Wisconsin 53706

December 1977

*KMS Fusion Inc., Ann Arbor, Michigan

"LEGAL NOTICE"

"This work was prepared by the University of Wisconsin as an account of work sponsored by the Electric Power Research Institute, Inc. ("EPRI"). Neither EPRI, members of EPRI, the University of Wisconsin, nor any person acting on behalf of either:

"a. Makes any warranty or representation, express or implied, with respect to the accuracy, completeness, or usefulness of the information contained in this report, or that the use of any information, apparatus, method, or process disclosed in this report may not infringe privately owned rights; or

"b. Assumes any liabilities with respect to the use of, or for damages resulting from the use of, any information, apparatus, method or process disclosed in this report."

Acknowledgment

Any effort as substantial as a conceptual fusion reactor design inevitably involves more people than those who appear on the title page. It is a pleasure to acknowledge the Electric Power Research Institute for its financial support of this research under contract RF-237-3. Dr. Noel Amherd of EPRI monitored this work and his efforts in organizing review meetings so that we could receive early feedback from others in the field is greatly appreciated. We also appreciate the encouragement of our University which contributed to this work both financially and by providing an environment supportive of research. This is of course a long standing tradition at Madison but it is important to note that this tradition remains in a healthy state.

Finally, we gratefully acknowledge the help of our secretarial staff -- Mrs. Connie Linehan, Ms. Gail Herrington, Mrs. Bonnie Smart, and Mrs. Linda Kraft -- and our support staff, particularly Mr. Dennis Bruggink -- who together were responsible for the typing, reproduction, and distribution of this report.

Preface

Inertial confinement fusion is a rapidly growing part of the search to achieve commercial power applications from the fusion process. Experiments are planned over the next five years with enough energy and power on target to determine if the targets designed can produce the gains required for reactor applications. With this perspective, it is auspicious to consider the technological aspects of ICF reactors. We have found that a conceptual reactor study is an ideal way of exploring such a problem and the SOLASE system is the product of such an effort. We hope that the results, analysis, and analytical methods described here will be helpful to others in the field and to those who must make policy regarding a broadly based program aimed at ICF reactor development.

Abstract

The SOLASE conceptual laser fusion reactor has been designed to elucidate the technological problems posed by inertial confinement fusion reactors. This report contains a detailed description of all aspects of the study including the physics of pellet implosion and burn, optics and target illumination, last mirror design, laser system analysis, cavity design, pellet fabrication and delivery, vacuum system requirements, blanket design, thermal hydraulics, tritium analysis, neutronics calculations, radiation effects, stress analysis, shield design, reactor and plant building layout, maintenance procedures, and power cycle design. The reactor is designed as a 1000 MW_e unit for central station electric power generation. This should be typical of central station power plants produced by a mature (rather than a developing) technology. The net plant efficiency is 30% and the recirculating power fraction is 25%. The laser energy on target is 1 MJ and 20 targets are exploded per second, each with a gain of 150. The gas phase laser relies on multipassing to achieve an efficiency of 6.7%. No particular laser wavelength is specified. A buffer gas of neon or xenon is used to prevent particle debris and X-rays from directly impacting the cavity first wall. The reactor cavity is spherical with a radius of 6 m and is constructed of graphite designed to guide the flow of lithium oxide (Li_2O) which serves as both the tritium breeding and heat transport medium. The neutron wall loading is 5 MW/m^2 and the tritium breeding ratio is 1.33. The overall radioactivity levels of the blanket are very low and the activity at 50 years after shutdown is just 3 Ci. The target is illuminated from two sides by 12 beams, 6 on each side, and the last mirrors are copper diamond turned on an aluminum backstructure. The mirrors are cooled to 50°C to minimize neutron radiation effects. The reactor system itself is highly accessible and a detailed but relatively simple procedure is outlined for blanket replacement. The 16 blanket segments making up the sphere are so inexpensive that replacement rather than maintenance of the blanket modules has been the design philosophy.

The major technological conclusions developed from this study include the following: 1. An energy gain on target of 100-200 or higher is difficult to achieve with a 1 MJ laser. High gain targets have been reported and their performance must be verified by experiment. 2. A laser driver with an efficiency of about 5% and matching all other requirements including those of the pellet must be developed. The requirement is that the product of laser efficiency and pellet gain, $\eta_L G$, exceed about 10. However values of η_L less than 1-2% will imply high laser costs because of power supplies regardless of target gain. 3. Power supplies and switches with lifetimes of 10^8-10^9 shots are needed. 4. A basic manufacturing procedure is needed for the mass production of targets. 5. Target delivery can be by pneumatic guns but accuracy, trajectory determination, and coordination with the laser firing is required. 6. Automatic methods for maintaining alignment in the entire optical train will be necessary. 7. The gas protection method is an attractive approach to cavity design that can be verified in principle on current and near term experiments. 8. Permeation filling of targets will imply that the tritium inventory will be dominated by the time to fill targets. In SOLASE, the inventory can vary from 10 kg to 25 kg of tritium depending on the encapsulating material. 9. The performance of the graphite blanket design requires verification and data is needed on radiation effects at temperatures above 1400°C. 10. The design and protection of the last mirror poses no insuperable problems unless dielectric coatings (required if

$\lambda_L \lesssim 8000$ Å) are used. Color center formation at low neutron fluences can so increase light absorption that visible lasers may not be usable. Much more work is required here. 11. Vacuum requirements are modest if set by wall erosion. 12. An unprotected dry wall cavity designed with conventional structural metals will not survive a microexplosion at economically reasonable wall loadings (neutron wall loading greater than 1 MW/m^2). 13. The blanket tritium inventory using Li_2O can be low (~ 1 kg) and tritium release rates through the steam generators and reheaters is low enough that no intermediate loop in the power cycle appears necessary. 14. Accessibility of the reactor cavity is very good simplifying blanket maintenance or replacement methods.

The issues outlined here and others discussed in the report are those one would have to pursue vigorously to allow the employment of laser fusion reactors beginning in the early part of the next century. Results from experiments carried out over the next five to seven years with ever increasing energy and power on target, taken together with results from reactor studies such as SOLASE, should provide the basis to determine if an ambitious engineering-oriented program aimed at reactor development is justified.

TABLE OF CONTENTS

	Page
I. Overview of SOLASE	
I-A. Introduction	I-A-1
I-B. Initial Questions	I-B-1
I-C. Description of SOLASE	I-C-1
I-C-1. Pellet performance in SOLASE	I-C-8
I-C-2. Targets for laser fusion	I-C-27
I-C-3. Injection of targets	I-C-33
I-C-4. Optics, target illumination, and mirror mechanical design	I-C-37
I-C-5. The laser system	I-C-43
I-C-6. Laser gas handling,power supplies,beam layout	I-C-51
I-C-7. Reactor cavity & blanket design	I-C-56
I-C-8. Radiation damage	I-C-67
I-C-8-a. Radiation effects to graphite	I-C-67
I-C-8-b. Stress & failure analysis for the blanket-determination of blanket lifetime	I-C-71
I-C-8-c. Radiation effects to dielectric coatings on mirrors	I-C-83
I-C-9. Vacuum system & mechanical design	I-C-94
I-C-10. The fuel cycle & tritium processing	I-C-98
I-C-11. Power flows in SOLASE	I-C-108
References for Chapter I	I-C-115
II. Summary & Conclusions	
II-A. Brief Summary of SOLASE & General Conclusions	II-A-1
II-B. Summaries of Specific Topics & Conclusions by Subject Area	
II-B-1. Laser pellet physics & pellet design	II-B-1
II-B-2. Lasers for laser fusion & for SOLASE	II-B-6
II-B-3. Illumination & optics design	II-B-9
II-B-4. Pellets for laser fusion reactor applications	II-B-11
II-B-5. Cavity design & first wall protection	II-B-13
II-B-6. Blanket design	II-B-16
II-B-7. Radiation effects to materials	II-B-17
II-B-7-a. The blanket	II-B-17
II-B-7-b. The lithium oxide	II-B-19
II-B-7-c. Radiation effects to dielectric coatings on mirrors	II-B-19
II-B-8. Tritium	II-B-20
II-B-9. Mechanical design & blanket replacement	II-B-21
II-B-10. Neutronics	II-B-21
II-B-11. The power cycle	II-B-22
II-B-12. General	II-B-23
References for Chapter II	II-B-27
III. Laser Fusion Physics	
III-A. Introduction to General Ideas of Inertial Confinement	III-A-1
III-A-1. Laser requirements for laser fusion	III-A-3
III-A-2. Implosion scenario	III-A-5
References for Section III-A	III-A-8
III-B. Efficiencies & Pellet Gain Requirements for Laser Fusion Reactors	III-B-1
III-C. Laser Plasma Modelling	III-C-1
III-C-1. Hydrodynamics	III-C-1
III-C-1-a. Introduction	III-C-1

TABLE OF CONTENTS (contd)

	Page
III-C-1-b. One fluid - 2 temperature model	III-C-2
III-C-1-c. Equation of state	III-C-5
III-C-1-d. Transport coefficients	III-C-6
References for Section III-C-1	III-C-9
III-C-2. Burn dynamics	III-C-10
III-C-2-a. Reaction rates	III-C-10
III-C-2-b. Charged particle transport	III-C-12
References for Section III-C-2	III-C-16
III-C-3. Laser light absorbtion	III-C-17
III-C-3-a. Introduction	III-C-17
III-C-3-b. Classical absorption	III-C-20
III-C-3-c. Absorption at oblique incidence	III-C-27
III-C-3-c-i Slab geometry	III-C-27
III-C-3-d. Total power absorbed at oblique incidence	III-C-37
III-C-3-e. Effect of expanding critical radius	III-C-44
III-C-3-f. Resonance absorption & density profile steepening	III-C-54
References for Section III-C-3	III-C-56
III-C-4. Radiation	III-C-57
III-C-4-a. Introduction	III-C-57
III-C-4-b. The radiation transport equation	III-C-57
III-C-4-c. Radiation processes in a laser fusion plasma	III-C-59
III-C-4-c-i Introduction	III-C-59
III-C-4-c-ii Description of atomic states of a plasma	III-C-61
III-C-4-c-iii The distribution of ion states	III-C-62
III-C-4-c-iv A mean ion representation for computing radiative properties	III-C-66
III-C-4-c-v Emission processes	III-C-67
References for Section III-C-4	III-C-74
III-C-5. Hydrodynamic stability	III-C-76
References for Section III-C-5	III-C-78
III-C-6. Hot Electrons	III-C-79
III-C-6-a. Introduction	III-C-79
III-C-6-b. Creation	III-C-79
III-C-6-c. Propagation	III-C-80
References for Section III-C-6	III-C-83
III-D. Numerical Modelling	III-D-1
References for Section III-D	III-D-3
III-E. Comparison of PHD-IV Results With Other Published Results	III-E-1
III-E-1. Thermonuclear burn - A comparision with other published results	III-E-1
III-E-2. Radiation transport	III-E-9
References for Section III-E	III-E-14
III-F. Advanced Fuels	III-F-1
III-F-1. Introduction	III-F-1
III-F-2. Deuterium	III-F-1
III-F-3. Proton-Boron-11	III-F-10
References for Section III-F	III-F-15
III-G. Prospects for High Gain Pellets	III-G-1

TABLE OF CONTENTS (contd)

	Page
IV. Pellet Design for SOLASE	
IV-A. Basic Pellet Physics	IV-A-1
References for Section IV-A	IV-A-8
IV-B. Thermonuclear burn	IV-B-1
IV-B-1. Bare core pellet burn calculations	IV-B-7
IV-B-2. Tamped pellet core burn calculations	IV-B-28
References for Section IV-B	IV-B-41
IV-C. Pellet Implosion	IV-C-1
IV-C-1. An example pellet implosion	IV-C-1
IV-C-2. Sphere vs. shell targets	IV-C-16
IV-C-3. Exploding pusher targets	IV-C-17
IV-C-4. Multishelled targets	IV-C-20
References for Section IV-C	IV-C-22
IV-D. Pellet Material Considerations	IV-D-1
IV-E. Model Pellet for SOLASE	IV-E-1
IV-F. Feasibility of Achieving Reactor Pellet Performance	IV-F-1
References for Section IV-F	IV-F-4
V. Optics and Illumination Studies	
V-A. Laser Fusion Optics	V-A-1
V-A-1. Introduction	V-A-1
V-A-2. Mirrors Yes, Lenses No	V-A-4
V-A-3. Surface Damage Thresholds and Aperture Size	V-A-5
V-A-4. Self-Focusing	V-A-8
V-A-5. The Case Against Uniform Illumination	V-A-13
V-A-6. Thermal Distortion	V-A-14
V-A-7. Location and Protection of Final Mirrors	V-A-17
V-A-8. Diffraction at an Annular Aperture	V-A-19
V-A-9. Pointing Errors	V-A-24
V-A-10. Consequences of Laser Wavelength Choice	V-A-25
V-A-10-a. Laser-Plasma Coupling	V-A-25
V-A-10-b. Corona-Core Coupling	V-A-25
V-A-10-c. Rayleigh-Taylor Instability	V-A-25
V-A-10-d. Self-Focusing	V-A-26
V-A-10-e. Gas Breakdown Threshold	V-A-26
V-A-10-f. Diffraction	V-A-26
V-A-10-g. Optical Surface Requirements	V-A-26
V-A-10-h. Mirror Surface Damage Thresholds	V-A-26
V-A-11. Mirror Mechanical Design Considerations	V-A-27
References for Section V-A	V-A-32

TABLE OF CONTENTS (contd)

	Page
V-B. Optimal Illumination Studies	V-B-1
V-B-1. Introduction	V-B-1
V-B-2. The platonic solids	V-B-2
V-B-3. Irradiance profiles	V-B-6
V-B-4. Calculating beam overlap	V-B-12
V-B-4-a. Octahedron	V-B-13
V-B-4-b. Dodecahedron	V-B-16
V-B-4-c. Icosahedron	V-B-16
V-B-4-d. Minimum value of θ_{max} for total coverage	V-B-18
V-B-5. Numerical results	V-B-23
V-B-5-a. Optimization	V-B-23
V-B-5-b. Solid angle-limited designs	V-B-38
V-B-6. Discussion	V-B-41
Appendix: Theorem on Uniformity	V-B-43
References for Section V-B	V-B-45
V-C. Imaging Properties of Off Axis Paraboloidal Mirrors	V-C-1
V-C-1. Introduction	V-C-1
V-C-2. Image distortion	V-C-5
V-C-3. Two-dimensional irradiance profiles	V-C-13
V-C-4. Mirror positioning & pointing errors	V-C-26
V-C-4-a. Translational positioning errors	V-C-26
V-C-4-b. Rotational positioning errors	V-C-26
V-C-4-a-i. Rotation about the y-axis ($\delta\phi$)	V-C-27
V-C-4-a-ii. Rotation about the z-axis ($\delta\theta$)	V-C-29
V-C-4-a-iii. Rotation about the x-axis ($\delta\eta$)	V-C-30
V-C-5. Perturbed Irradiances	V-C-33
V-C-5-a. Translation of the target in the z-direction	V-C-35
V-C-5-b. Target irradiance under the rotation $\delta\phi$	V-C-38
V-C-6. Discussion	V-C-43
Appendix A: General Method for Calculating Perturbed Rays	V-C-44
Appendix B: Caustics for Tilted Paraboloid	V-C-45
References for Section V-C	V-C-50
VI. Optics and Beam Transport for SOLASE	
VI-A. The Beam Transport System	VI-A-1
VI-A-1. Introduction	VI-A-1
VI-A-2. Multipassing considerations	VI-A-1
VI-A-3. Beam combining	VI-A-2
VI-A-4. The optical delay lines	VI-A-5
VI-A-5. The last mirror placement	VI-A-6
VI-A-6. Additional considerations	VI-A-12
VI-A-7. Summary of the beam transport system	VI-A-21
References for Section VI-A	VI-A-21

TABLE OF CONTENTS (contd)

	Page
VI-B. Final Mirror Design for SOLASE	VI-B-1
VI-B-1. Fabrication	VI-B-1
VI-B-2. Thermal response to radiation	VI-B-5
VI-B-2-a. Laser light	VI-B-5
VI-B-2-b. X-rays	VI-B-6
VI-B-2-c. Neutrons and secondary γ-rays	VI-B-8
References for Section VI-B	VI-B-12
VII. Lasers for Laser Fusion	
VII-A. Introduction	VII-A-1
VII-B. Survey of Lasers for Laser Fusion	VII-B-1
VII-B-1. The iodine laser	VII-B-1
VII-B-2. Advantages of iodine lasers	VII-B-3
VII-B-3. Disadvantages of the iodine laser	VII-B-3
VII-B-4. Possible improvements	VII-B-4
VII-B-5. Summary of iodine lasers	VII-B-5
VII-B-6. The HF chemical laser	VII-B-6
VII-B-7. Advantages of the HF laser	VII-B-8
VII-B-8. Disadvantages of the HF laser	VII-B-8
VII-B-9. Possible improvements	VII-B-10
VII-B-10. Summary of the HF laser	VII-B-12
VII-B-11. The CO_2 laser	VII-B-14
VII-B-12. Advantages of the CO_2 laser	VII-B-16
VII-B-13. Disadvantages of the CO_2 laser	VII-B-16
VII-B-14. Possible improvements	VII-B-18
VII-B-15. Summary of the CO_2 laser	VII-B-19
VII-B-16. Brand X lasers	VII-B-19
VII-C. A Summary of the Laser Survey	VII-C-1
VII-D. Design Study System	VII-D-1
References for Chapter VII	VII-D-3
VIII. Laser & Power Supplies for SOLASE	
VIII-A. Introduction	VIII-A-1
VIII-B. The Laser Design	VIII-B-1
VIII-B-1. General description of CO_2 laser	VIII-B-1
VIII-B-2. Laser mixture & discharge parameters	VIII-B-4
VIII-B-3. Engineering extraction from an amplifier	VIII-B-8
VIII-B-4. Multipass extraction	VIII-B-12
VIII-B-5. Laser master oscillator and preamplifiers	VIII-B-19

TABLE OF CONTENTS (contd)

	Page
VIII-B-6. Efficiency of the SOLASE laser	VIII-B-27
VIII-B-7. The gas handling system	VIII-B-30
VIII-B-8. Additional problem areas	VIII-B-32
VIII-B-9. The SOLASE laser as a generic laser	VIII-B-43
VIII-B-10. Conclusions of laser design	VIII-B-48
References for Section VIII-B	VIII-B-51
VIII-C. Power Supplies for Laser Fusion Reactors	VIII-C-1
VIII-C-1. Introduction	VIII-C-1
VIII-C-2. General supply design considerations	VIII-C-3
VIII-C-3. The capacitor bank	VIII-C-4
VIII-C-4. Switching	VIII-C-12
VIII-C-4-a. Spark gaps	VIII-C-13
VIII-C-4-b. Semiconductor switches	VIII-C-18
VIII-C-5. General design of the laser power supplies	VIII-C-22
VIII-C-6. Final amplifiers design	VIII-C-24
VIII-C-7. Power supply conclusions	VIII-C-29
References for Section VIII-C	VIII-C-31
Appendix - Beam Extraction from a Multipassed Annular Amplifier	VIII-1
IX. Target Fabrication & Delivery Considerations	
IX-A. Present Inertial Confinement Target Requirements	IX-A-1
IX-A-1. Glass Microshell$_{TM}$ Pellets	IX-A-4
IX-A-1-a. Fabrication procedures	IX-A-4
IX-A-1-b. Shell quantities & sizes	IX-A-8
IX-A-1-c. DT permeation & storage	IX-A-9
IX-A-2. Polymeric Microshell$_{TM}$ Pellets	IX-A-13
IX-A-2-a. Fabrication procedures	IX-A-13
IX-A-2-b. Permeation fueling, storage & shelf life	IX-A-15
IX-A-3. Cryogenic Targets	IX-A-16
IX-A-3-a. Present status	IX-A-17
IX-A-3-b. Cryogenic reactor pellet considerations	IX-A-19
IX-B. Reactor Pellet Requirements	IX-B-1
IX-B-1. Representative reactor pellets	IX-B-2
IX-B-2. Fabrication & processing of reactor pellets	IX-B-4
IX-B-2-a. Fabrication techniques	IX-B-4
IX-B-2-b. Storage requirements	IX-B-6
IX-B-2-c. Pellet cost estimates	IX-B-9
IX-C. Pellet Injection	IX-C-1
IX-C-1. Electrostatic injection & deflection	IX-C-1
IX-C-2. Pneumatic Injection	IX-C-2
References for Chapter IX	IX-C-6

TABLE OF CONTENTS (contd)

	Page
X. Cavity Design Concepts	
X-A. Pedagogy	X-A-1
X-A-1. Wall protection -- problem definition	X-A-2
References for Section X-A	X-A-15
X-B. Wall Protection Concepts	X-B-1
X-B-1. The wetted wall concept	X-B-2
X-B-2. The liquid Li "waterfall" concept	X-B-4
X-B-3. Magnetic protection	X-B-7
X-B-3-a. Diffusion of the magnetic field into the conducting wall	X-B-9
X-B-3-b. Diffusion of the magnetic field in the plasma	X-B-10
X-B-3-c. Time of flight spreading of the particles	X-B-11
References for Section X-B	X-B-18
X-C. Thermal & Mechanical Response of ICTR First Walls	X-C-1
X-C-1. Thermal response to photon irradiation without buffer gas	X-C-1
X-C-1-a. Temperature rise produced by the reflected laser light	X-C-6
X-C-1-b. Temperature rise produced by the X-rays	X-C-10
X-C-2. Thermal response to pulsed ion sources with no buffer gas	X-C-15
X-C-3. Effect of residual chamber gas on wall thermal response	X-C-24
X-C-4. Surface evaporation rate	X-C-36
X-C-5. Stress analysis for ICTR walls	X-C-42
X-C-5-a. Impulsive heat deposition in a semi-infinite medium	X-C-42
X-C-5-b. Energy deposition in a finite elastic layer	X-C-43
X-C-5-b-i. Series solutions	X-C-43
X-C-5-b-ii. Wave solutions	X-C-47
X-C-5-b-iii. Stress wave results	X-C-49
X-C-6. Structural design considerations for the first wall	X-C-52
References for Section X-C	X-C-60
XI. Cavity Design for SOLASE	
XI-A. General Description of the SOLASE Cavity	XI-A-1
XI-B. Analyses of the Gas Protection Concept	XI-B-1
XI-B-1. Charged particle attenuation	XI-B-2
XI-B-2. X-ray attenuation	XI-B-7
XI-B-3. Pressure impulse at the first wall	XI-B-12
XI-B-4. Gas cooling -- energy transfer to the wall	XI-B-19

TABLE OF CONTENTS (contd)

	Page
XI-B-5. Laser induced gas breakdown	XI-B-32
XI-B-5-a. Introduction	XI-B-35
XI-B-5-b. Theory of Hacker, Cohn & Lax	XI-B-37
XI-B-5-c. Classical microwave breakdown theory	XI-B-39
XI-B-5-c-i. Breakdown threshold for He	XI-B-42
XI-B-5-c-ii. Breakdown threshold for Ne	XI-B-44
XI-B-5-c-iii. Low collision frequency limit	XI-B-46
XI-B-5-c-iv. The diffusion limit	XI-B-47
XI-B-5-d. Multiphoton absorption	XI-B-47
XI-B-5-e. Target intensity for SOLASE	XI-B-49
XI-B-5-f. Breakdown thresholds for SOLASE	XI-B-52
XI-B-5-g. Consequences of breakdown	XI-B-54
XI-B-5-h. Conclusions	XI-B-55
XI-B-6. Postscript: Xe as a buffer gas	XI-B-56
XI-B-6-a. Ion stopping power	XI-B-56
XI-B-6-b. X-ray attenuation	XI-B-59
XI-B-6-c. Pressure Impulse to the First Wall	XI-B-61
XI-B-6-d. Gas Cooling & Reradiation to First Wall	XI-B-61
XI-B-6-e. Disadvantages of Using Xenon	XI-B-62
References for Section XI-B	XI-B-63
XI-C. Summary: First Wall Protection in SOLASE	XI-C-1
XII. Blanket Design and Analysis	
XII-A. Introduction	XII-A-1
References for Section XII-A	XII-A-2
XII-B. Blanket Design for SOLASE	XII-B-1
XII-B-1. The Li_2O/Graphite Blanket Concept	XII-B-1
References for Section XII-B-1	XII-B-10
XII-B-2. Thermal-Hydraulic Design of the SOLASE Blanket	XII-B-11
References for Section XII-B-2	XII-B-20
XII-B-3. Closure	XII-B-26
XIII. Blanket Neutronics Analyses and Shield Design for SOLASE	
XIII-A. Introduction	XIII-A-1
XIII-B. Time-Integrated (Steady State) Neutronics Studies	XIII-B-1
XIII-B-1. Calculational Method	XIII-B-1
XIII-B-2. Blanket Model and Survey Calculations	XIII-B-2
XIII-B-3. Final Blanket Model and Nuclear Analysis	XIII-B-9
XIII-B-3-a. Tritium Breeding	XIII-B-11
XIII-B-3-b. Nuclear Heating	XIII-B-11
XIII-B-3-c. Gas Production and DPA	XIII-B-11
XIII-B-3-d. Neutron Scalar Fluxes & Leakages	XIII-B-16
References for Section XIII-B	XIII-B-21
XIII-C. Time Dependent Neutronics	XIII-C-1
XIII-C-1. Neutron Source	XIII-C-2
XIII-C-2. Computational Techniques	XIII-C-7
XIII-C-2-a. Energy Dependent Quadrature	XIII-C-7
XIII-C-2-b. Discrete Cross Section Expansion	XIII-C-8
XIII-C-3. SOLASE Calculation	XIII-C-15
References for Section XIII-C	XIII-C-25

TABLE OF CONTENTS (contd)

		Page
XIII-D.	Shield Design	XIII-D-1
	XIII-D-1. Concrete Shield Design	XIII-D-1
	XIII-D-2. Lead Acetate Shield	XIII-D-3
XIII-E.	Radioactivity	XIII-E-1
	XIII-E-1. Calculational Methods	XIII-E-1
	XIII-E-2. System Geometry and Material Composition	XIII-E-5
	XIII-E-3. Induced Activity in Blanket and Shield	XIII-E-10
	XIII-E-4. After Shutdown Gamma Dose Rates	XIII-E-25
	XIII-E-5. Conclusions Concerning Radioactivity in the Laser Fusion System	XIII-E-34
	References for Section XIII-E	XIII-E-36
XIII-F.	Calculated Neutron and γ Irradiation Response of Candidate Laser Mirror Materials	XIII-F-1
	XIII-F-1. Introduction	XIII-F-1
	XIII-F-2. Calculational Model	XIII-F-3
	XIII-F-3. Results of Calculations and Discussion	XIII-F-5
	XIII-F-4. Summary	XIII-F-12
	References for Section XIII-F	XIII-F-14
XIV.	Mechanical Design, Assembly and Disassembly of SOLASE	
	XIV-A. General Description	XIV-A-1
	XIV-B. Graphite Blanket and Back Structure	XIV-B-1
	XIV-C. Shield	XIV-C-1
	XIV-D. Assembly and Disassembly	XIV-D-1
XV.	Radiation Damage and Materials Considerations	
	XV-A. Radiation Effects in Graphite	XV-A-1
	XV-A-1. Behavior of Point Defects in Graphite	XV-A-1
	XV-A-2. Dimensional Changes of Polycrystalline Graphites	XV-A-3
	XV-A-3. Irradiation Creep of Graphite	XV-A-15
	XV-A-4. Changes of Elastic Properties and Strength	XV-A-21
	XV-A-5. Fatigue Strength of Graphite	XV-A-25
	XV-B. Stress and Failure Analysis of the Blanket	XV-B-1
	XV-B-1. Procedure for Lifetime Analysis	XV-B-1
	XV-B-2. Inelastic Stress Analysis	XV-B-4
	XV-B-3. Results of the Stress Analysis	XV-B-11
	XV-B-4. Discussion of the Results	XV-B-30
	XV-C. Effects of Radiation on Lithium Oxide	XV-C-1
	XV-C-1. An Assessment of Radiation-Enhanced Densification	XV-C-1
	XV-C-2. The Densification Model	XV-C-1
	References for Chapter XV	XV-C-5

TABLE OF CONTENTS (contd)

		Page
XVI.	The Fuel Cycle and Tritium Processing	
	XVI-A. Introduction	XVI-A-1
	XVI-B. Reactor Fueling Cycle	XVI-B-1
	XVI-B-1. Compatibility of Wall and Pellet	XVI-B-1
	XVI-B-1-a. General Description and Pellet Composition	XVI-B-1
	XVI-B-1-b. Exhaust Gas Compositions	XVI-B-1
	XVI-B-2. Vacuum System Design and Requirement	XVI-B-11
	XVI-B-2-a. General Description	XVI-B-11
	XVI-B-2-b. Pump Selection	XVI-B-14
	XVI-B-2-c. System Conductance and Pump Capacity	XVI-B-17
	XVI-C. Reactor Exhaust and Fuel Logistics	XVI-C-1
	XVI-C-1. Separation and Recycling of Reactor Exhaust	XVI-C-1
	XVI-C-1-a. Neon Cleanup Scheme	XVI-C-3
	XVI-C-1-b. Hydrogen Isotope Recovery	XVI-C-7
	XVI-C-2. Fuel Supply Logistics	XVI-C-8
	XVI-D. Tritium Breeding and Extraction	XVI-D-1
	XVI-D-1. The Lithium Oxide Blanket	XVI-D-1
	XVI-D-2. Extraction of Bred Tritium	XVI-D-1
	XVI-D-3. Lithium Oxide - Wall Interactions	XVI-D-7
	XVI-E. Tritium Control System	XVI-E-1
	XVI-E-1. Primary and Secondary Containments	XVI-E-1
	XVI-E-1-a. Fueling, Exhaust and Extraction Systems	XVI-E-1
	XVI-E-1-b. Steam Generators and Steam Reheaters	XVI-E-5
	XVI-E-2. Tertiary Containment	XVI-E-9
	XVI-F. Conclusions	XVI-F-1
	References for Chapter XVI	XVI-F-2
XVII.	Power Conversion System for SOLASE	
	XVII-A. Steam Generator and Reheater Design	XVII-A-2
	XVII-B. Particle Transport System	XVII-B-1
	References for Chapter XVII	XVII-B-5

I. Overview of SOLASE

I-A. Introduction

Research on inertial confinement fusion has expanded dramatically in recent years. Experimental results on compression and neutron yields from laser[1-4] and electron beam[5-6] illuminated targets are measures of this rapid progress. The theory that suggested achieving high gains by illuminating small spherical deuterium-tritium targets[7-8] has also matured rapidly. The progress is such that several energy breakeven experiments are planned for the not too distant future. Given both this progress and the level of research effort, it is worthwhile at this time to determine the requirements for inertial confinement fusion reactors and the technological problems such systems might pose. In turn, such work can provide the basis for more substantial efforts on the most important reactor technology problems.

Laser initiated thermonuclear fusion is presently the most widely studied inertial confinement area. To examine laser fusion technology problems, we have developed a conceptual laser fusion power reactor, SOLASE[a], for electric power production. This research should help lay a foundation to make a more realistic assessment of the ultimate potential of laser fusion reactors. We describe in this overview the major features of the SOLASE design. In the next chapter, we present a summary and list our major conclusions. Greater detail on all topics can be found in subsequent chapters. Review chapters have been included in the report for pedagogical purposes and we trust these will be useful to groups desiring an introduction to the field.

---

[a] SOLASE, as in "their solase in dorckaness, and splattering together joyously the plaps of their tappyhands as, with one cry of genuine distress, so prettl prattly pollylogue, they viewed him, the just one, their darling, away". J. Joyce, Finnegans Wake, The Viking Press, New York (1939), p. 470.

I-B. Initial Questions

The questions which present themselves early in a laser fusion study can be classified as follows:

1. Laser Pellet Studies: What range of pellet gain is required? What yield should one choose? What value of laser energy is appropriate? What are the spectra associated with various forms of pellet debris? What degree of target illumination uniformity is required and how many laser beams are needed? What do targets cost, how are they fabricated, and how are they delivered to a spot inside the chamber?

2. Laser Studies: What is the range of viable wavelengths? What is the laser energy? What is the laser pulse shape? How are beam lines designed and what are the problems with the last mirror? What repetition rate is required and how does this influence laser design, power supplies, and component lifetimes?

3. Optical Beam Train: How many last mirrors are there and how are they designed? How is the beam train integrated with the laser system? Do we combine beams? What is the shape and location of the last mirrors? How does the wavelength influence optics system design?

4. Cavity and Blanket Design: Is a protective liner for the first wall required? How does the liner or first wall respond to X-rays, ions, and reflected laser light? How does this response vary as the spectra and fraction of energy in each category change? How will we design the first wall? How will the blanket be designed to remove the heat and breed tritium?

5. Materials and Neutron Radiation Damage: Are there special rate effects in inertial confinement reactor systems? How does the damage vary with temperature? What structural material should one choose? What should one choose for the neutron wall loading? What are the dynamic stress problems and how should they be treated?

6. Tritium Systems and Power Cycle: What does the complete tritium cycle look like? How do we breed and recover tritium? How do we minimize leakage effects? How do we integrate the various forms of heat flow into an optimum power cycle? Is an intermediate loop needed?

It is clear that developing the tools to analyze the problems and questions outlined above provides one with the basis necessary to carry out an integrated reactor study. We have developed the requisite analytical tools and carried out many parametric studies in all areas in the course of doing this research. From these studies, we have developed the SOLASE design.

I-C. Description of SOLASE

The main parameters characterizing the SOLASE conceptual laser fusion power reactor are listed in Tables I-C-1 and I-C-2. A top view of the entire SOLASE power plant is given in Fig. I-C-1 and a more detailed view of the reactor cavity is shown in Fig. I-C-2. The system has a pellet gain of 150 and the laser energy on target is 1 MJ. The cavity is spherical with a radius of 6 m and the average neutron wall loading is 5 MW/m^2. The blanket design is based on the use of lithium oxide (Li_2O) ceramic microspheres (50-100 μm radii) flowing under gravity through a structure made from chopped fiber graphite composite. The temperature of the graphite and lithium oxide can be effectively decoupled in this design, an important feature in avoiding excessive radiation damage. There are twelve final mirrors of diamond-turned Cu on Al which illuminate the target from two sides. The cavity first wall and last mirror are protected from charged particle pellet debris by a low density (0.5 torr at 300°K) neon buffer gas. Neon was chosen initially because it has the highest breakdown threshold. Xenon is an alternate choice having the advantage of simultaneously stopping the X-rays as well as ions. Only experiments will allow a clear choice. It appears gas breakdown can

Table I-C-1

Parameters for the SOLASE Laser Fusion Reactor

CAVITY SHAPE	SPHERICAL
CAVITY RADIUS	6 m
14 MeV NEUTRON WALL LOADING	5 MW/m^2
THERMAL POWER	3340 MW
GROSS ELECTRICAL POWER	1334 MW
NET ELECTRICAL POWER	1000 MW
RECIRCULATING POWER FRACTION	28%
NET PLANT THERMAL EFFICIENCY	30%
LASER TYPE	GAS PHASE
LASER ENERGY ON TARGET	1 MJ
LASER EFFICIENCY (WITH MULTIPASSING)	6.7%
NUMBER OF FINAL AMPLIFIERS	6
NUMBER OF FINAL BEAMS	12
ENERGY OUTPUT/AMPLIFIER PASS	45.8 kJ
PULSE WIDTH	1 ns
PULSE REPETITION RATE	20 Hz
PELLET YIELD AND GAIN	150 MJ
FRACTIONAL BURNUP OF FUEL	45%
INITIAL FUEL MASS	1 mg
GENERIC TARGET DESIGN	MULTILAYERED-CRYOGENIC

Table I-C-2

Parameters for the SOLASE Laser Fusion Reactor

TARGET ILLUMINATION	TWO SIDED
NUMBER OF FINAL MIRRORS	12
F/No. OF FINAL MIRROR	7.5
DISTANCE FROM LAST MIRROR TO PELLET	15 m
DIAMETER OF LAST MIRROR	3.5 m
COMPOSITION OF LAST MIRROR	Cu on Al
MANUFACTURING PROCEDURE	DIAMOND TURNING
FIRST WALL PROTECTION METHOD	Ne or Xe BUFFER GAS
BLANKET STRUCTURE	GRAPHITE COMPOSITE
BLANKET BREEDING AND HEAT TRANSPORT MEDIUM	LITHIUM OXIDE (Li_2O)
TRITIUM BREEDING RATIO	1.33
TOTAL ENERGY PER FUSION EVENT	18.6 MeV
TOTAL Li_2O FLOW RATE	3.12×10^7 kg/hr
AVERAGE Li_2O FLOW VELOCITY	0.7 m/s
Li_2O INLET TEMPERATURE	400°C
Li_2O OUTLET TEMPERATURE	600°C
TRITIUM INVENTORY	
GLASS ENCAPSULATION OF TARGET	24.7 kg
POLYMER ENCAPSULATION OF TARGET	10.9 kg
TOTAL REACTOR RADIOACTIVITY LEVEL 50 YEARS AFTER SHUTDOWN	3 Ci

TOP VIEW OF SOLASE

A CONCEPTUAL LASER FUSION REACTOR POWER PLANT

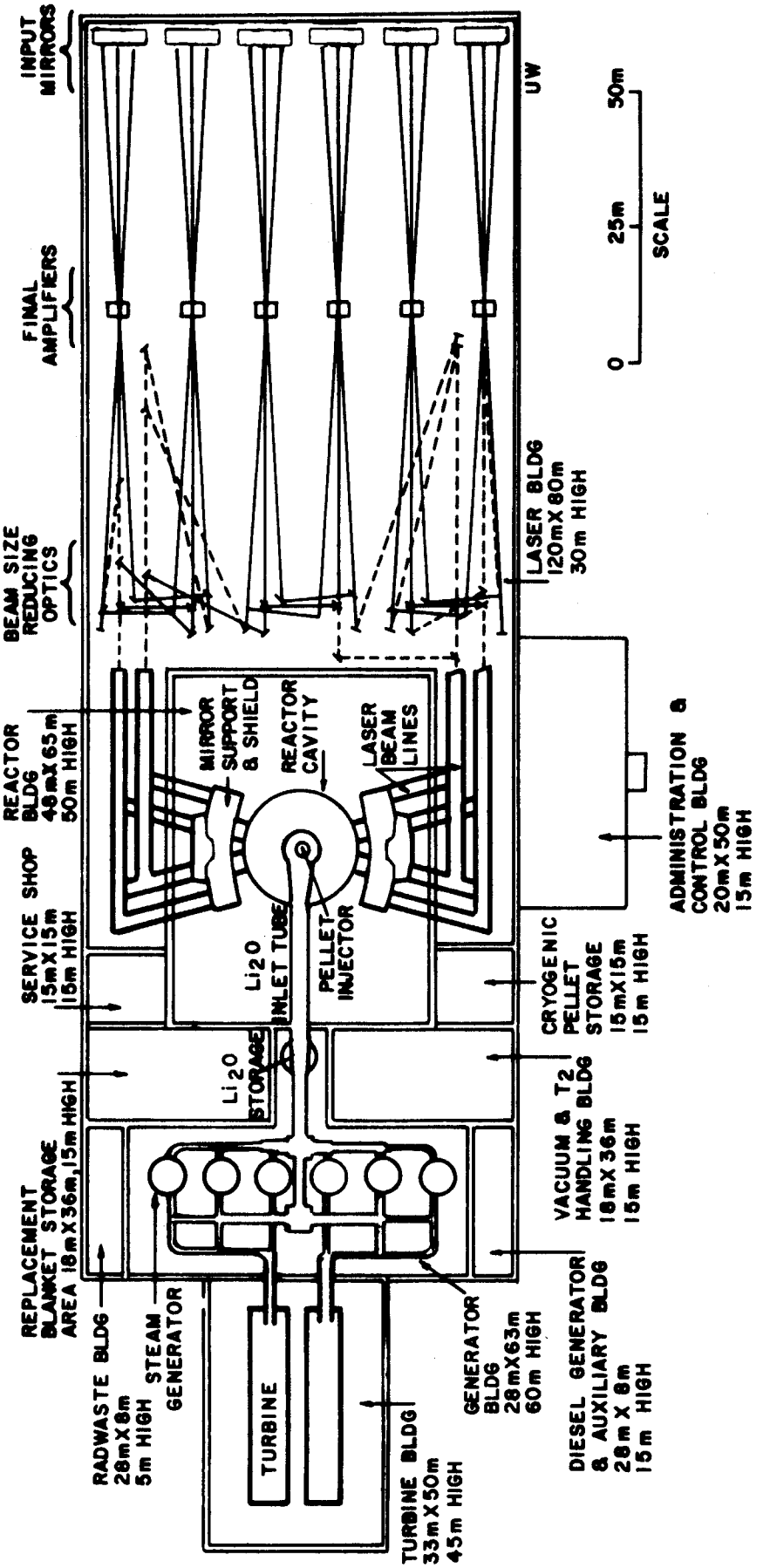

Fig. I-C-1

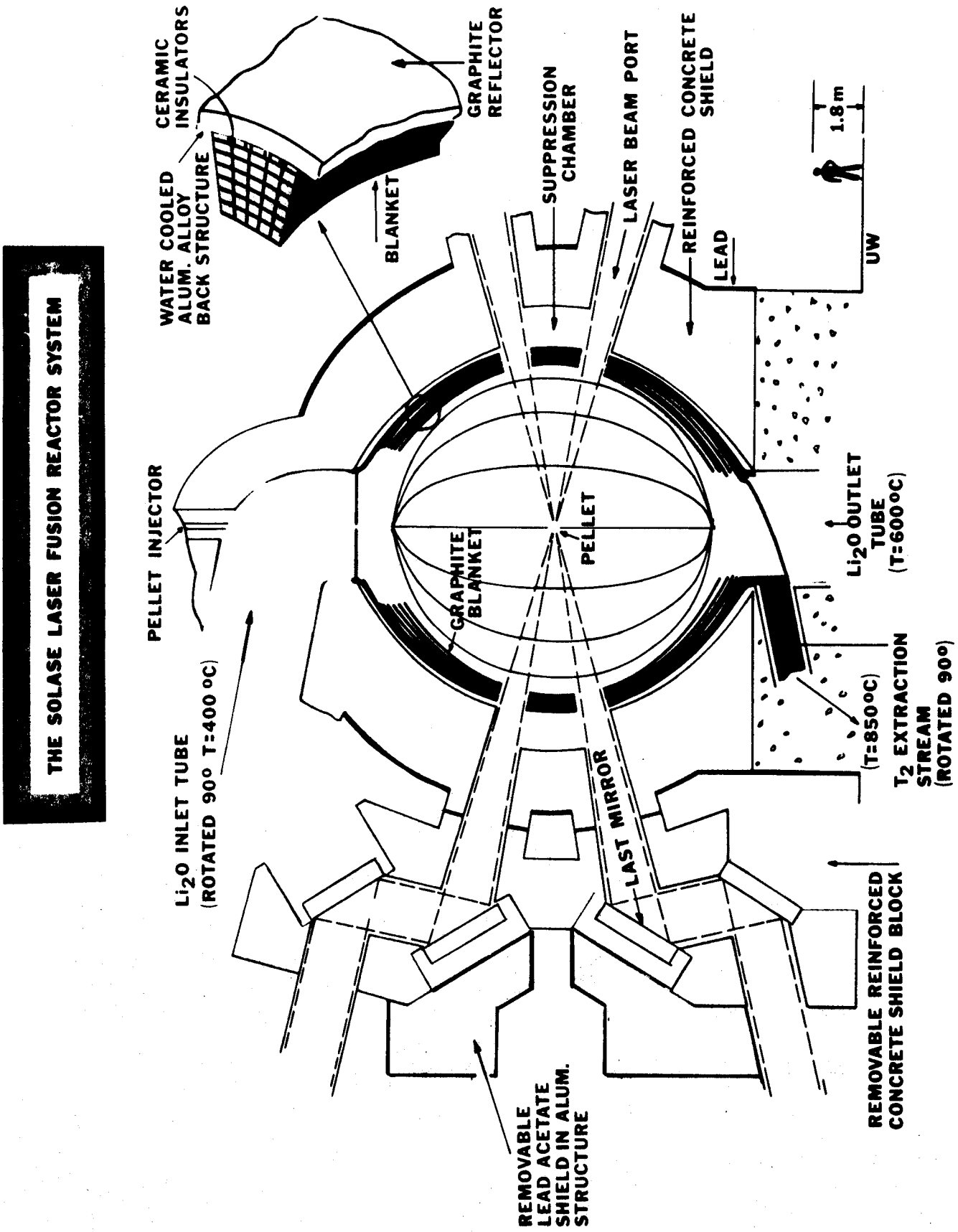
THE SOLASE LASER FUSION REACTOR SYSTEM
CERAMIC INSULATORS
GRAPHITE REFLECTOR
WATER COOLED ALUM. ALLOY BACK STRUCTURE
BLANKET
SUPPRESSION CHAMBER
LASER BEAM PORT
REINFORCED CONCRETE SHIELD
LEAD
1.8m
UW
PELLET INJECTOR
Li_2O INLET TUBE (ROTATED 90° T=400 °C)
GRAPHITE BLANKET
PELLET
Li_2O OUTLET TUBE (T=600°C)
(T=850°C)
T_2 EXTRACTION STREAM (ROTATED 90°)
LAST MIRROR
REMOVABLE LEAD ACETATE SHIELD IN ALUM. STRUCTURE
REMOVABLE REINFORCED CONCRETE SHIELD BLOCK

occur but its effect may be minimal for shorter laser wavelengths and reactor size pellets where the focal spot size can exceed 2 mm.

The laser system is designed as generically as possible but is modeled after the CO_2 laser where specificity is required. This is not necessarily ideal from a target point of view and this choice is not a specific endorsement of CO_2. Rather, it is a recognition that the CO_2 laser has many of the characteristics of the desirable laser for laser fusion. With multipassing as described in Chapter VII, the estimated overall efficiency is 6.7% and the maximum final amplifier energy is 45.8 kJ. There are 6 final amplifiers and the 24 beams are subsequently recombined to 12 final beams.

The system power cycle outlined in Fig. I-C-3 shows that the Li_2O transports heat directly to steam generators which then drive turbines producing 1334 MW_e gross. The laser recirculating power requirement is 300 MW_e and other internal plant power requirements lead to a net plant electrical output of 1000 MW_e and a net thermal efficiency of 30%. The large recirculating laser power fraction appears typical of laser fusion systems unless gains much larger than 150 or laser efficiencies much greater than 5-10% can be achieved. The following analysis demonstrates this point.

The pellet gain is defined as the ratio of thermonuclear energy produced (Y) to the laser energy incident on the pellet (E_L). For breakeven the gain must equal unity, but for power plant applications the necessary gain is determined by the laser efficiency and plant thermal efficiency. The relation between these quantities is given by the expression

$$G = \left[\frac{1}{\eta_L\,(\eta_{th}-\eta_p)}\right] - 1 \quad , \qquad (1)$$

where η_L = laser efficiency

η_{th} = gross plant thermal efficiency

η_p = net plant thermal efficiency

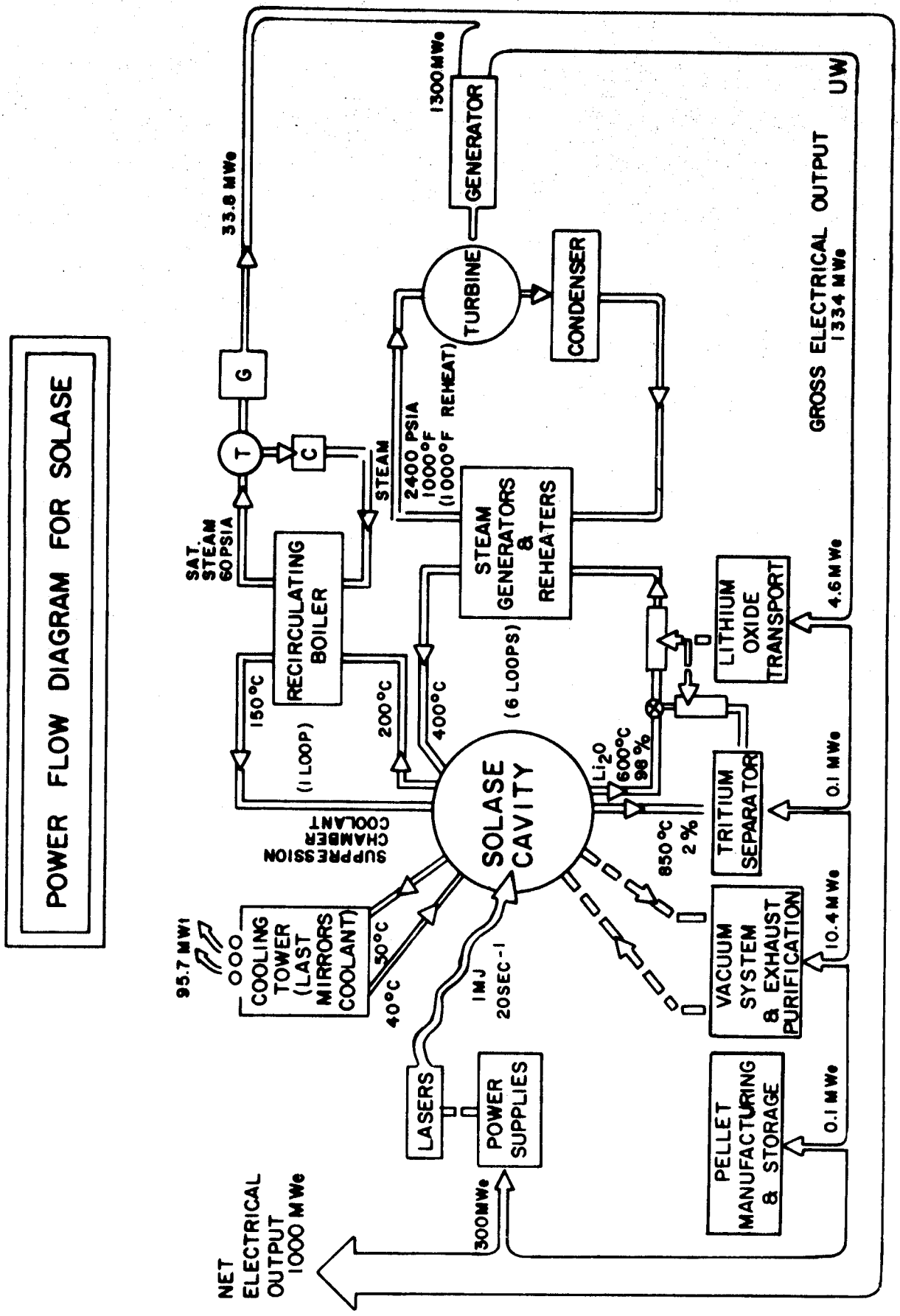
POWER FLOW DIAGRAM FOR SOLASE
NET ELECTRICAL OUTPUT 1000 MWe
300MWe
LASERS
POWER SUPPLIES
IMJ 20SEC-1
95.7 MWt
COOLING TOWER (LAST MIRRORS COOLANT)
40°C
50°C
SUPPRESSION CHAMBER COOLANT
SOLASE CAVITY
(6 LOOPS)
(1 LOOP)
150°C
200°C
400°C
RECIRCULATING BOILER
SAT. STEAM 60PSIA
T
C
G
33.6 MWe
STEAM
2400 PSIA 1000°F (1000°F REHEAT)
STEAM GENERATORS & REHEATERS
TURBINE
CONDENSER
1300MWe
GENERATOR
GROSS ELECTRICAL OUTPUT 1334 MWe
UW
4.6 MWe
LITHIUM OXIDE TRANSPORT
Li_2O 600°C 90%
850°C 2%
TRITIUM SEPARATOR
0.1 MWe
VACUUM SYSTEM & EXHAUST PURIFICATION
10.4 MWe
PELLET MANUFACTURING & STORAGE
0.1 MWe

Fig. I-C-3

In Fig. I-C-4 the gain is plotted as a function of the difference between η_{th} and η_p for different η_L. If we make the reasonable assumptions that (1) the gross thermal efficiency is about 40%, (2) that the net plant efficiency must be at least 30% from economic and environmental considerations, and (3) that the laser efficiency is about 10%, then the pellet gain must be 100. For a laser efficiency of 5% the pellet gain must be 200. Therefore realistic gross and net plant efficiencies and optimistic values of laser efficiency indicate that a pellet gain of 100 to 200 is necessary for reactor applications. The SOLASE design requires a pellet gain of 150 because the laser design with multi-passed amplifiers has an efficiency of 6.7%. For a 1 MJ laser, this gain implies a pellet yield of 150 MJ.

I-C-1. Pellet Performance in SOLASE

To determine whether such pellet performance is consistent with the physics of pellet dynamics, the details of this dynamical process have been investigated. The pellet behavior has been separated into two parts with the first part being the laser light absorption and implosion of the DT fuel. This part ends at the time of ignition when there is a hot central microcore surrounded by cool isentropically compressed DT and possibly a high Z tamper material. Once ignition occurs, the second part of the dynamics, thermonuclear burn propagation, begins with the propagation of a temperature front out through the initially cold DT fuel. The first part of the dynamics can be simply characterized by the hydrodynamic efficiency with which laser light energy is transferred into the DT fuel. This efficiency is defined as

$$\eta_H = E_c/E_L \quad , \qquad (2)$$

where E_c is the internal energy of the compressed DT fuel material (or core) at the time of ignition. The second part of the dynamics is characterized

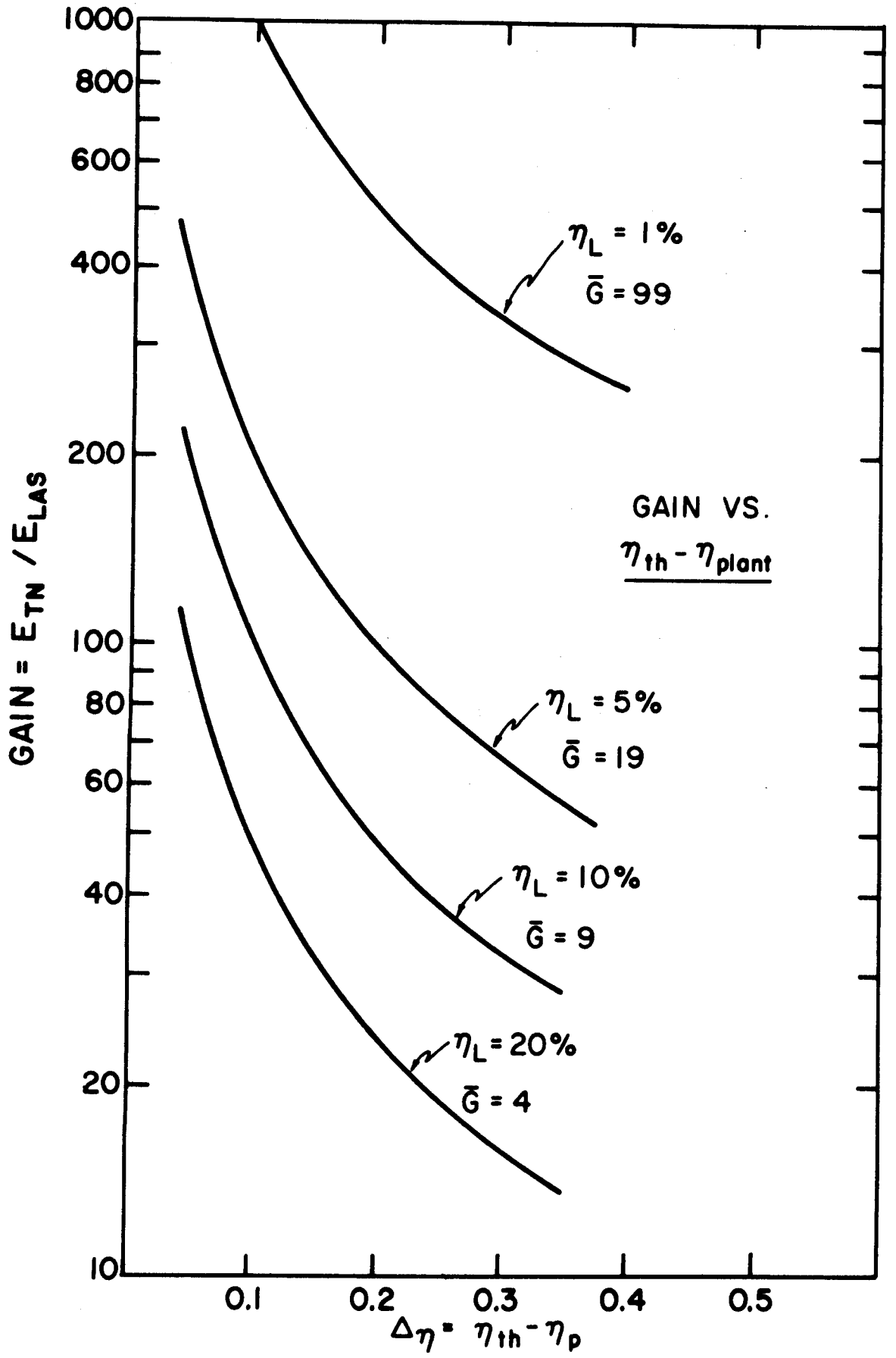
1000
800
600
400
200
100
80
60
40
20
10
GAIN = E_{TN} / E_{LAS}
η_L = 1%
$\bar{G}$ = 99
GAIN VS.
$\eta_{th} - \eta_{plant}$
η_L = 5%
$\bar{G}$ = 19
η_L = 10%
$\bar{G}$ = 9
η_L = 20%
$\bar{G}$ = 4
0.1
0.2
0.3
0.4
0.5
$\Delta\eta = \eta_{th} - \eta_p$

Fig. I-C-4

by the energy gain of the compressed DT fuel, or gain-on-core, given by

$$G_c = Y/E_c \ . \tag{3}$$

The total pellet gain is

$$G = \eta_H \, G_c \ . \tag{4}$$

Pellet performance can now be estimated by studying the dependence of the two factors (η_H and G_c) on specific pellet designs. For SOLASE this is done in a parametric fashion using the PHD-IV computer code and simplified analytic scaling laws both described in chapters III and IV. A generic analysis is usually attempted because specific pellet designs are beyond the scope of this study. However, these generic analyses do indicate the necessary magnitudes of G_c and η_H for reactor pellet performance and comparison of these performance characteristics with current laser fusion experiments is a valuable measure of ultimate feasibility. We find that values of G_c on the order of 4000 and η_H on the order of 10% are required for reactor applications. The optimum G_c occurs at a core ρR value of about 3 g/cm^2.

To study the thermonuclear burn process the pellet core is modelled as shown in Fig. I-C-5. The density is assumed to be uniform but the temperature profile consists of a hot microcore characterized by ρR_μ and T_μ and a cold surrounding plasma at temperature T. The total pellet core is characterized by its ρR value. The temperature of the cold compressed fuel is computed from the formula

$$T = T_0(\rho/\rho_0)^{2/3} \tag{5}$$

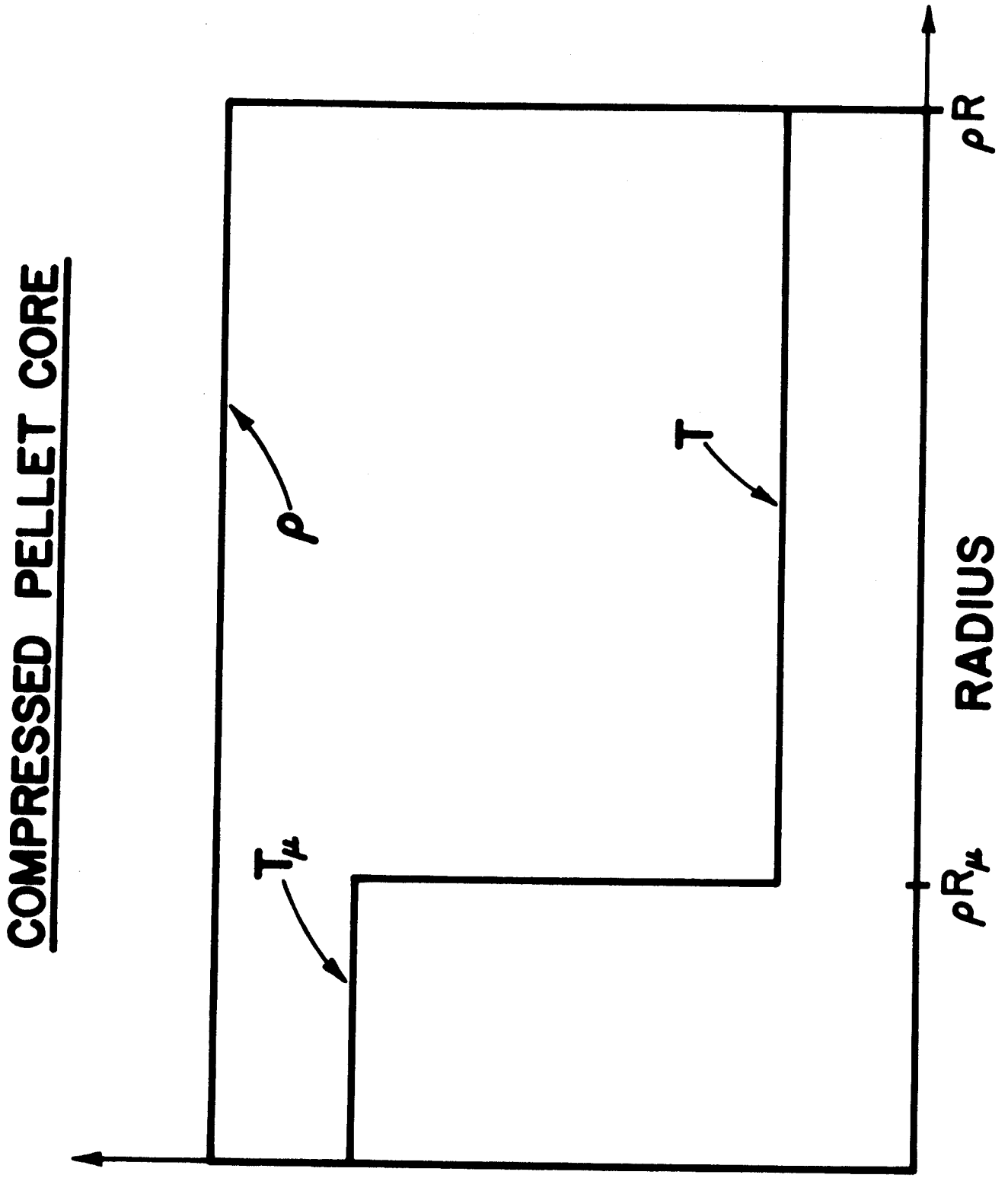

Fig. I-C-5

which is the temperature along an isentrope corresponding to a fuel compression of ρ/ρ_0. The initial temperature and density (T_0 and ρ_0) are taken as 1 eV and 0.213 g/cm^3. These calculations assume that the ablated part of the pellet that surrounds the core does not play any role in the burn dynamics. The PHD-IV hydrodynamics-thermonuclear burn computer code developed at Wisconsin is used to study the behavior of this model pellet core for the following ranges of parameters:

$$\begin{aligned} &0.1 \text{ mg} \leq \text{mass} \leq 1. \text{ mg} \\ &1 \text{ g/cm}^2 \leq \rho R \leq 7 \text{ g/cm}^2 \\ &0.1 \text{ g/cm}^2 \leq \rho R_\mu \leq 0.7 \text{ g/cm}^2 \\ &T_\mu = 10 \text{ keV}. \end{aligned} \tag{6}$$

The results of this study are given in Table I-C-3 and the dependence of yield on ρR is shown in Fig. I-C-6. It is seen that for this range of masses the separation of yield dependence on core mass and ρR is justified. The yield is a linear function of mass and a strong function of ρR for values less than 3 g/cm^2. For ρR values greater than 3 g/cm^2 the yield does not improve very much. This dependence on ρR can be explained by looking at the details of the burn and hydrodynamic disassembly process. At ρR = 3 g/cm^2 the pellet disassembly and fuel depletion due to burn have about an equal effect on quenching the burn. For $\rho R < 3$ g/cm^2 the pellet core disassembly is the dominant mechanism affecting the fractional burn up while for $\rho R > 3$ g/cm^2 the pellet inertial confinement time is great enough to allow fuel depletion to quench the burn. The dependence of yield on the ρR value

Table I-C-3

Summary of Burn Parameter Study

MASS	ρR	$(\rho R_{\mu}) = .3$	$(\rho R_{\mu}) = .4$	$(\rho R_{\mu}) = .5$	$(\rho R_{\mu}) = .7$
.1	1	3.41-2*	.32	1.54	2.8
		7.99	37.4	99	68.8
				0	
.1	2			7.4	
				1804	
.1	3	2.27-3	7.7	10.22	10.2
		.626	2034	2525	2048
.1	5	1.18-3	12.8	13	13
		.2	2155	2168	2103
.1	7	3.55-2	14.5	14.6	14.6
		4.3	1756	1764	1749
.316	1	.109	.971	5.03	
		8.93	38.1	106	
.316	2	.019	.763	23.2	
		3.2	99	2220	
.316	3	.009	27.2	32.0	
		1.21	3369	3602	
.316	5	.012	40.55	40.83	
		.278	3313	3289	
.316	7	2.5-3	45.8	46.4	
		.147	2702	2649	
1.	1	.344	3.3	16.5	30
		9.5	41.3	110	74.8
1.	2			76.3	
				2649	
1.	3	2.2-2	83.6	104	101
		1.3	4292	4786	3415
1.	5	8.4-3	129	130	131
		.306	4641	4597	4303
1.	7	5.6-3	146	148	148
		.147	3795	3836	3754

*First number is yield in mega joules. Second number is the gain on core assuming perfect adiabatic compression from 1 ev.

Microcore temperature = 10 keV.

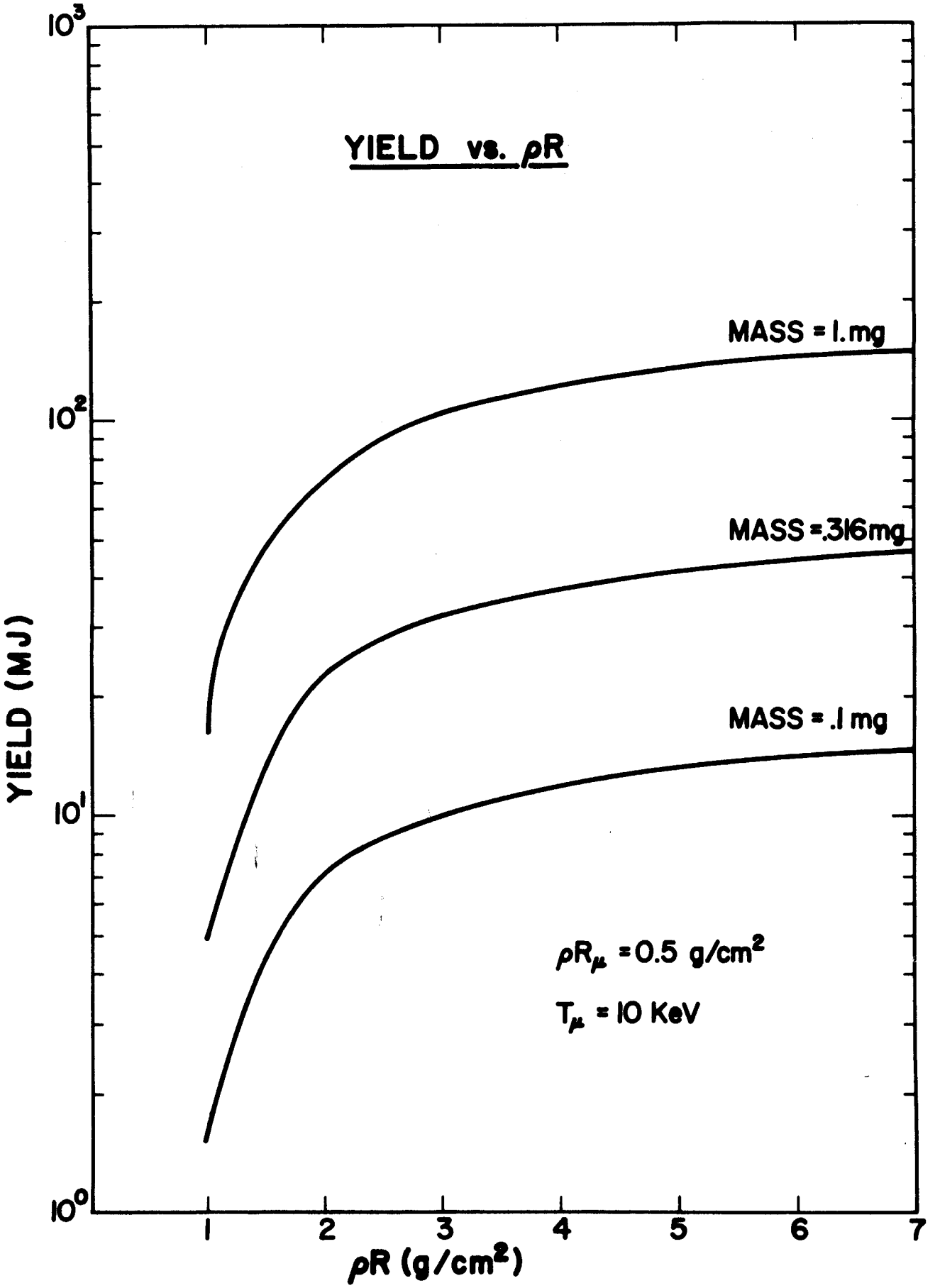
YIELD vs. ρR
MASS = 1. mg
MASS = .316mg
MASS = .1 mg
ρR_μ = 0.5 g/cm²
T_μ = 10 KeV
YIELD (MJ)
ρR (g/cm²)
10³
10²
10¹
10⁰
1
2
3
4
5
6
7

Fig. I-C-6

of the 10 keV microcore is shown in Fig. I-C-7. This dependence is of a threshold nature with almost constant yield for $\rho R_\mu > 0.38$ g/cm^2. Analytic expressions can be fit to the simulation results for use in the simple theory of pellet gain on core described in Chapter IV, Section B. The yield and fractional burnup are given by

$$Y = 10^3 mH(\rho R_\mu - 0.38) \begin{cases} [16 + 60\ (\rho R-1)^{.585}] & 1 < \rho R < 3 \\ [71 + 11\ \rho R] & 3 < \rho R < 7 \end{cases} \quad (7)$$

and

$$f_B = mH(\rho R_\mu - 0.38) \begin{cases} [0.047 + 0.178\ (\rho R-1)^{.585}] & 1 < \rho R < 3 \\ [0.211 + 0.033\ \rho R] & 3 < \rho R < 7 \end{cases} \quad (8)$$

where Y is the yield in MJ, m is the core mass in grams, ρR and ρR_μ are in g/cm^2, and H is a step function. Using these analytic formulas, iso-yield contours can be plotted for mass and ρR. These contours are shown in Fig. I-C-8 for 100, 150 and 500 MJ yields. The gain on core for each of these mass-ρR pairs is plotted in Fig. I-C-9. The gain on core is maximized for $\rho R = 3$ g/cm^2. For 100 MJ the optimum mass is 1 mg and for 150 MJ the optimum mass is 1.5 mg. The maximum gain on core for 150 MJ yield is 5495. This, however, assumes a perfect isentropic compression from an initial temperature of 1 eV. Such a perfect compression is quite unlikely unless the laser pulse can be very accurately shaped in time. This large value of G_c is of course the result of thermonuclear burn propagation.

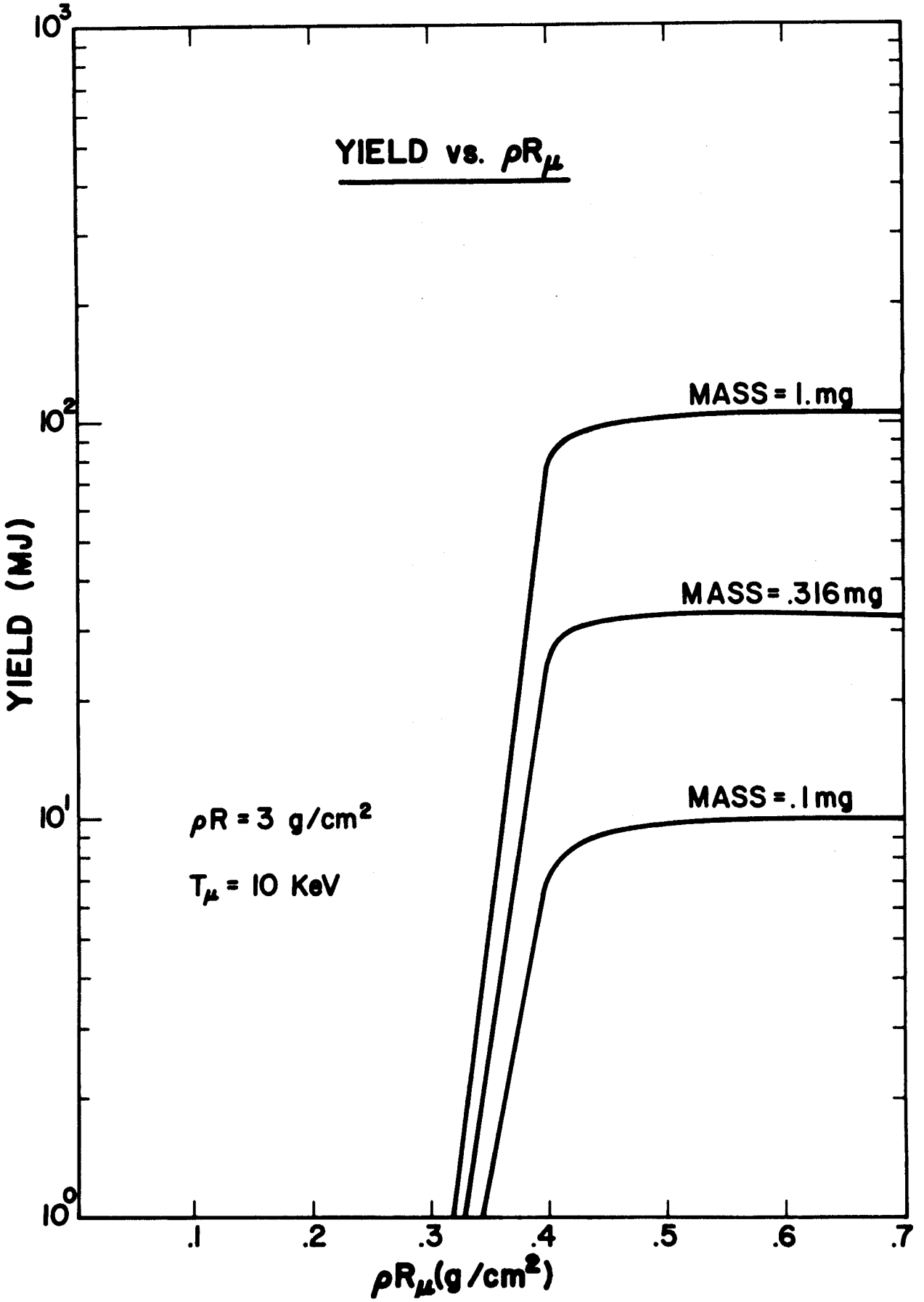
YIELD vs. ρR_μ
MASS = 1. mg
MASS = .316 mg
MASS = .1 mg
ρR = 3 g/cm^2
T_μ = 10 KeV
YIELD (MJ)
10^3
10^2
10^1
10^0
.1
.2
.3
.4
.5
.6
.7
ρR_μ(g/cm^2)

Fig. I-C-7

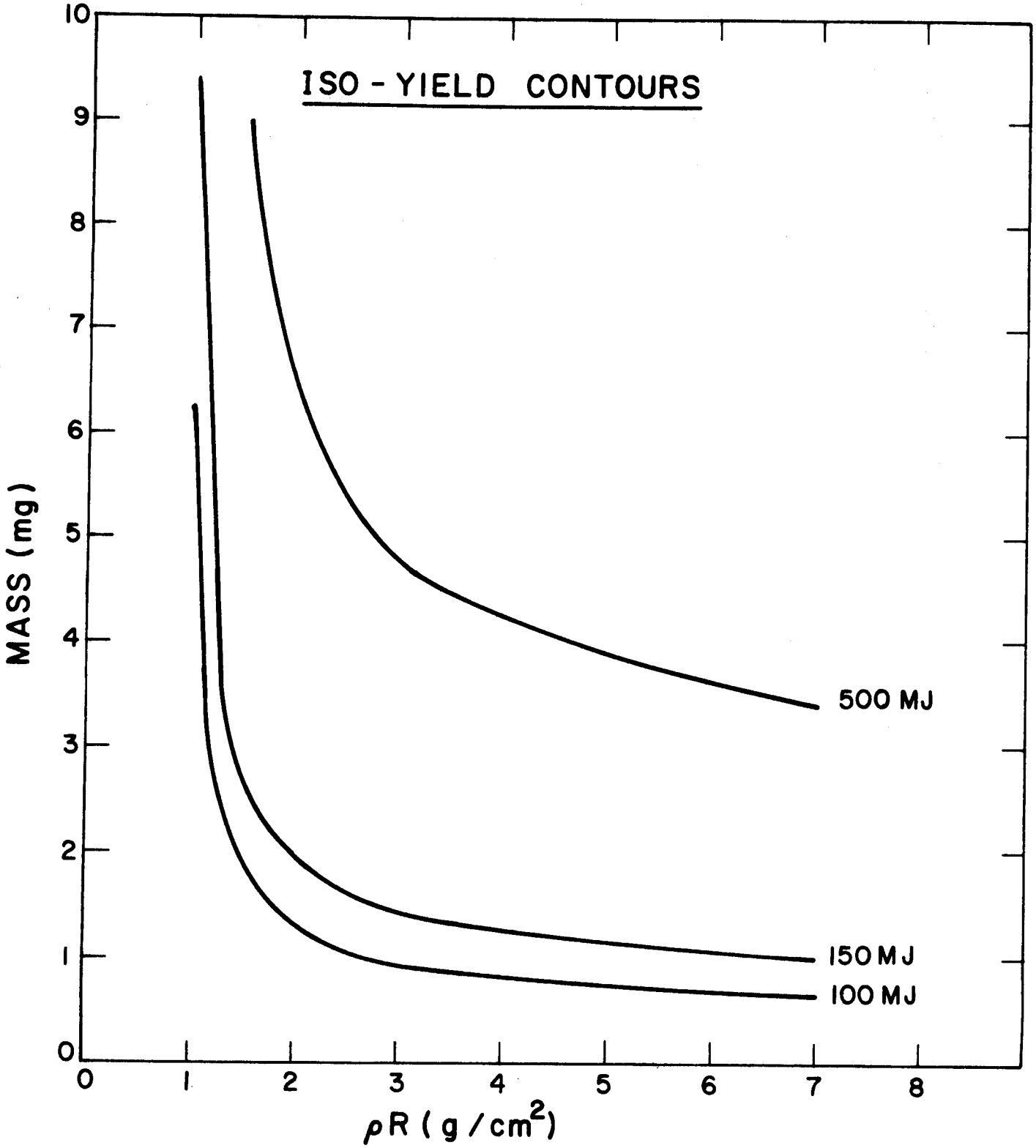
ISO - YIELD CONTOURS
MASS (mg)
ρR (g / cm²)
500 MJ
150 MJ
100 MJ
0
1
2
3
4
5
6
7
8
9
10

Fig. I-C-8

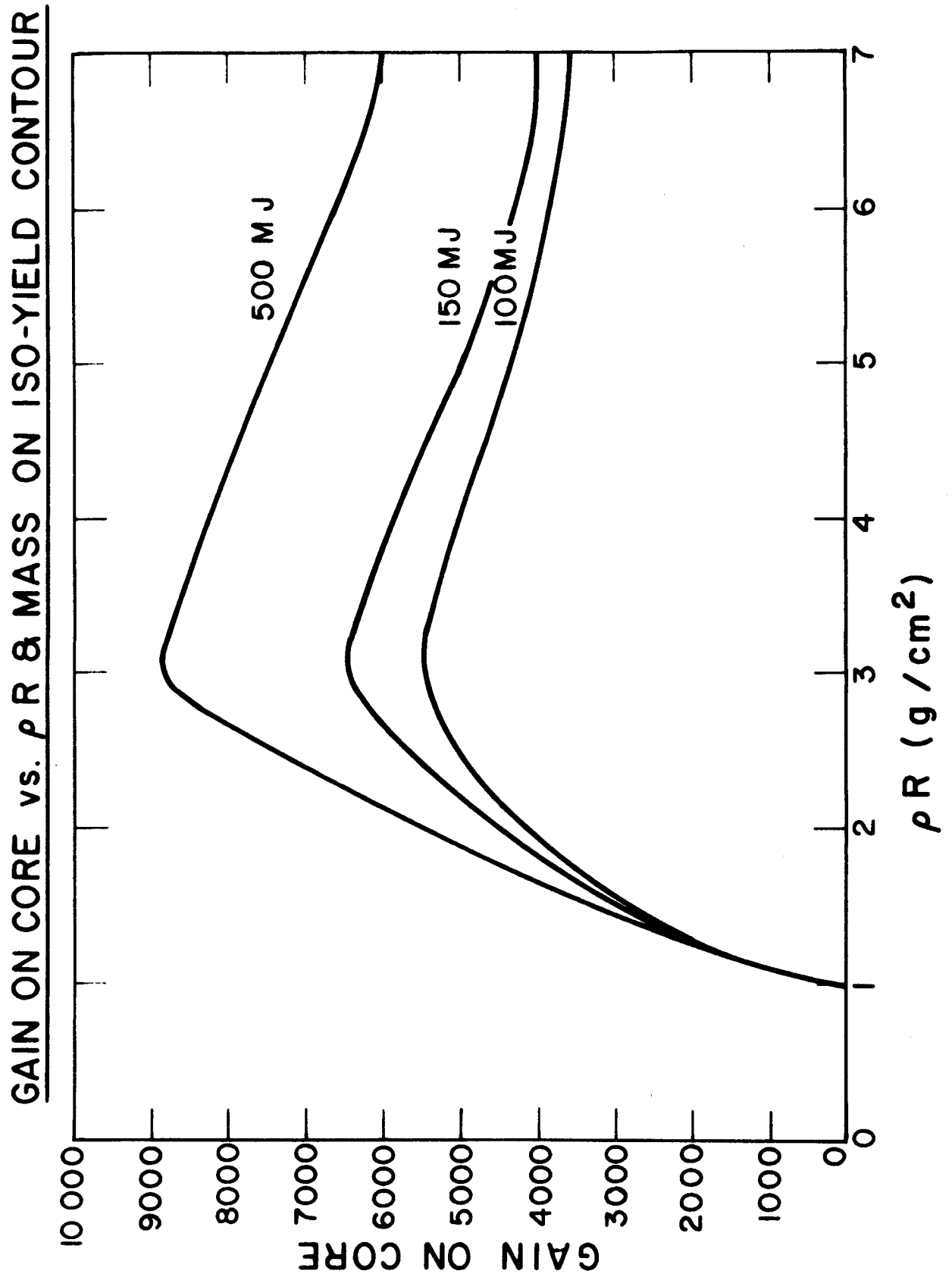
GAIN ON CORE vs. ρR & MASS ON ISO-YIELD CONTOUR
500 MJ
150 MJ
100 MJ
GAIN ON CORE
10 000
9000
8000
7000
6000
5000
4000
3000
2000
1000
0
0
1
2
3
4
5
6
7
ρR (g/cm²)

Fig. I-C-9

Energy from the pellet comes in three forms: neutrons, charged particles, and X-rays. For the bare DT pellet cores discussed thus far, 80% of the yield is assumed to be in the form of 14.1 MeV neutrons and 19% and 1% are computed as escaping charged particle and X-ray energy. The charged particle energy is in two forms: nonthermal DT and DD reaction products that escape the pellet core before thermalizing and the blow-off plasma that results from the hydrodynamic disassembly of the pellet core. For the 3 g/cm^2, 1 mg pellet core, 33% of the reactor product charged particles escape carrying 19% of the total charged particle energy. The time integrated spectra of the $_2He^4$, $_2He^3$, T^3, and $_1p^1$ reaction products are plotted in Figs. I-C-10 and 11. The average alpha particle energy is 1.84 MeV in the laboratory frame of reference. The average energy per ion in the disassembling plasma is computed by allowing the PHD-IV simulation to run until the fluid velocity reaches a free streaming limit. This average velocity is 8×10^8 cm/sec. This corresponds to 668 keV deuterons, 1000 keV tritons, and 1330 keV alphas. The X-ray spectrum for the bare core is plotted in Fig. I-C-12. It is quite hard and nonthermal, but it can be approximated as an 8 keV black body/spectrum.

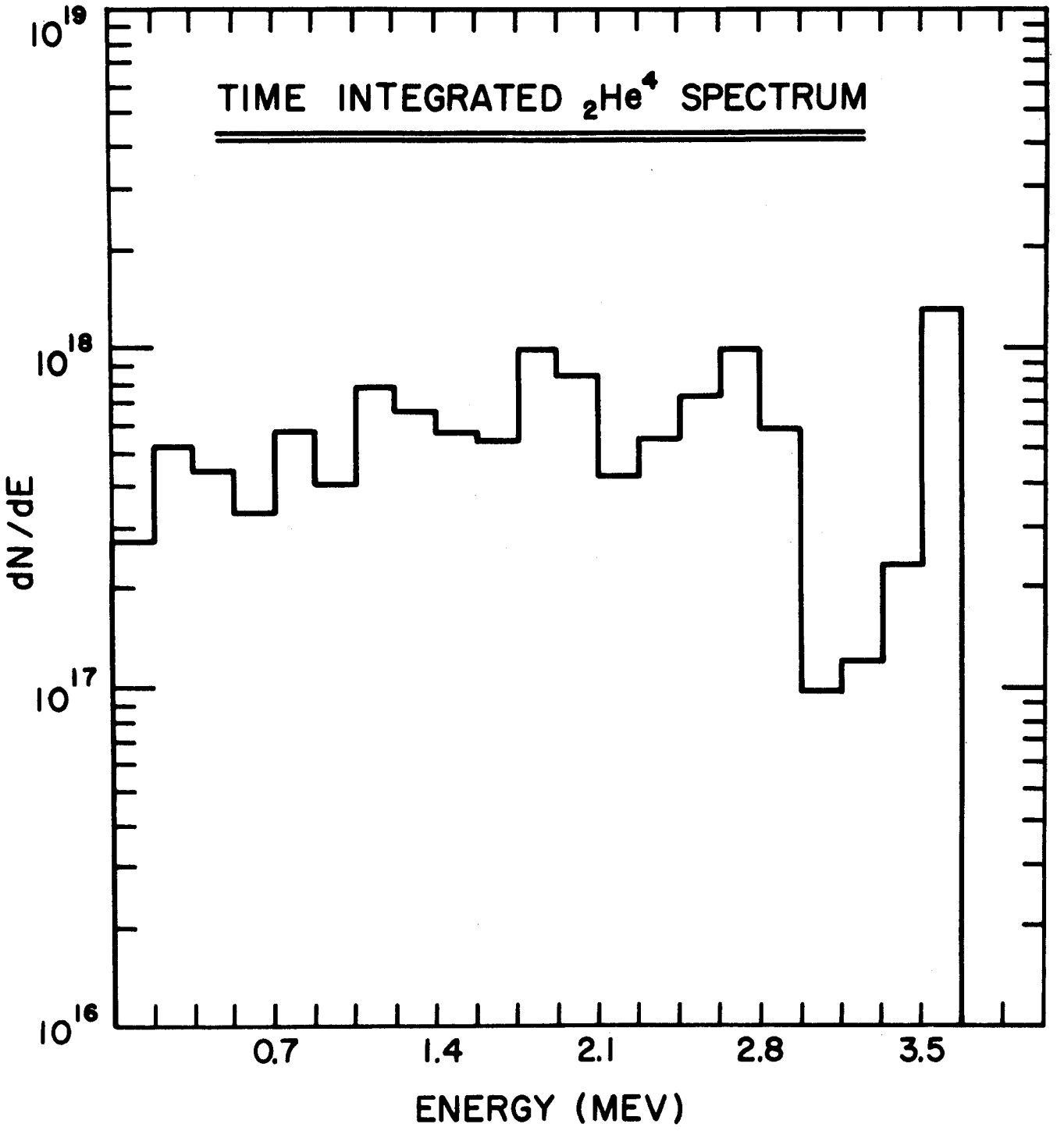
TIME INTEGRATED $_2He^4$ SPECTRUM
10^{19}
10^{18}
10^{17}
10^{16}
dN/dE
0.7
1.4
2.1
2.8
3.5
ENERGY (MEV)

Fig. I-C-10

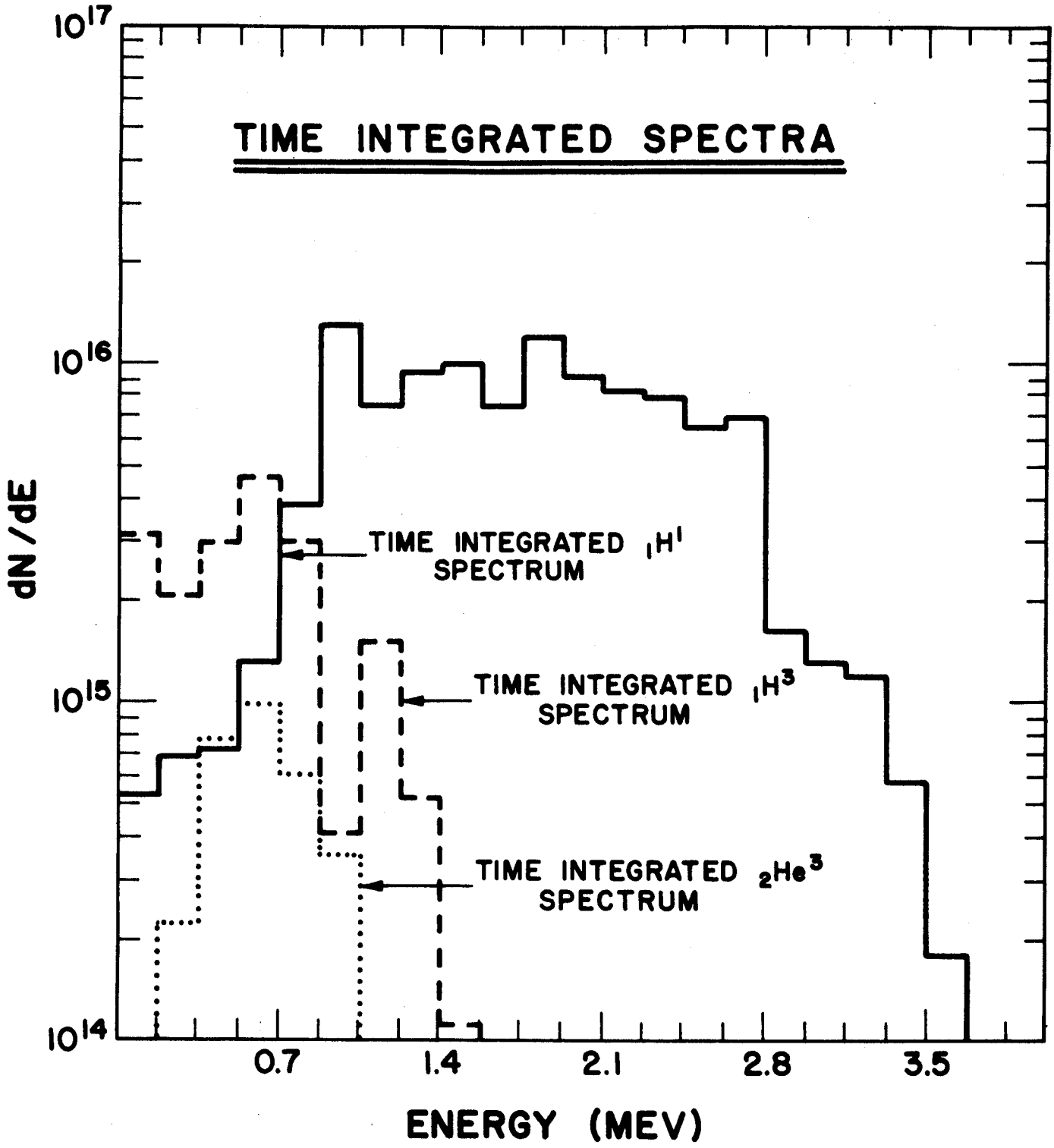
TIME INTEGRATED SPECTRA
10^{17}
10^{16}
10^{15}
10^{14}
dN/dE
TIME INTEGRATED $_1H^1$ SPECTRUM
TIME INTEGRATED $_1H^3$ SPECTRUM
TIME INTEGRATED $_2He^3$ SPECTRUM
0.7
1.4
2.1
2.8
3.5
ENERGY (MEV)

Fig. I-C-11

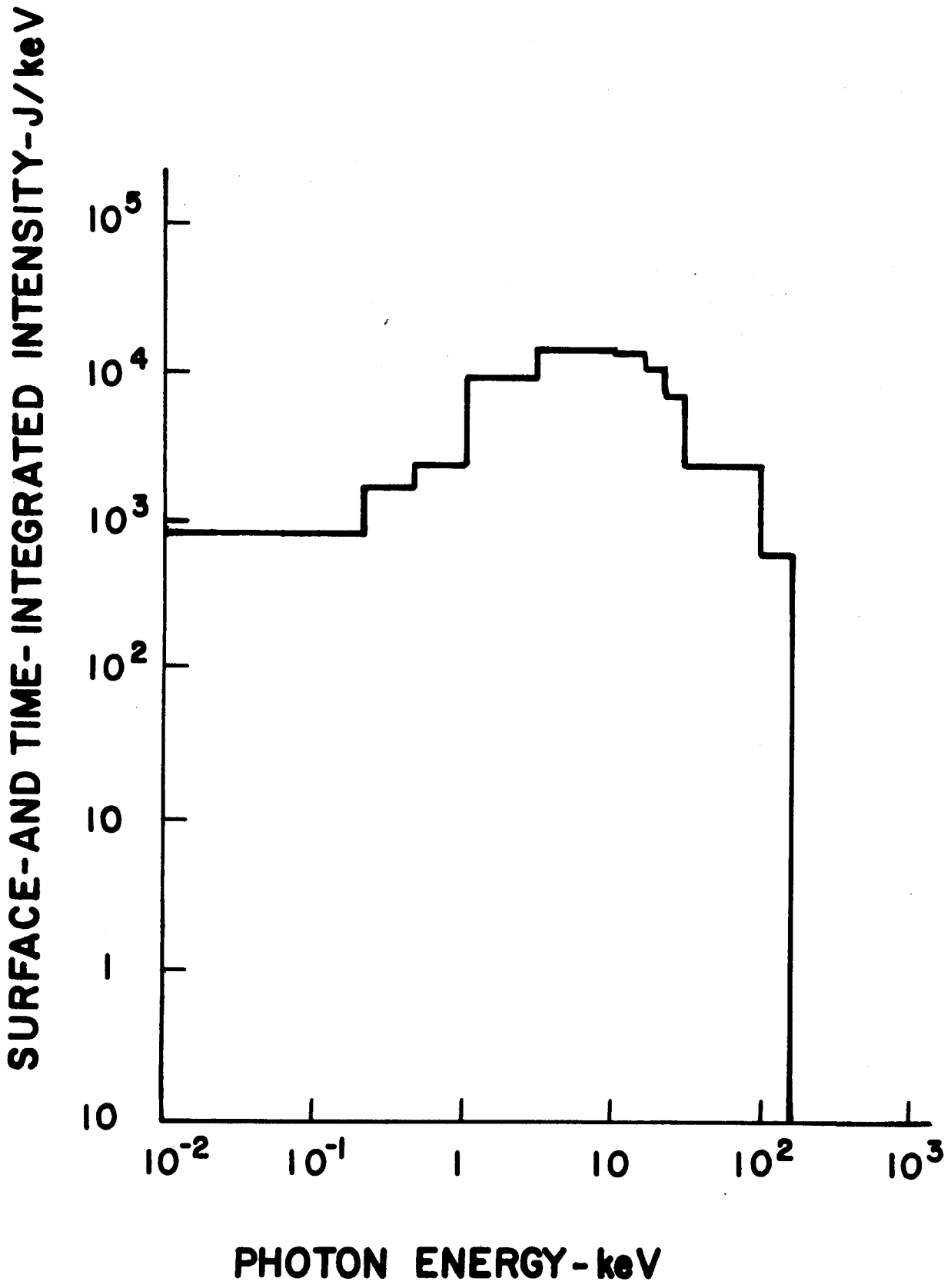

RADIATION SPECTRUM FOR BARE DT PELLET. (10 FREQUENCY GROUPS)

Fig. I-C-12

None of these spectra account for transport through the ablated pellet surrounding the compressed core. If the remainder of the pellet is specified, these spectra can be used as source distributions for the transport of X-rays and charged particles to the first wall. We have also carried out parametric studies of pellet output spectra from tamped pellets since bare DT pellet cores are not a realistic model of reactor-type laser fusion pellets. A multi-frequency radiation transport package based on the variable Eddington technique has been written and incorporated into PhD-IV. Results analogous to those given here for bare DT pellets are given for tamped cores in Chapter IV, Section IV-B-2.

The compatibility of pellet materials with the first wall and last mirror is a consideration that is important to all conceptual laser fusion reactor designs. At the high operating temperatures of laser fusion reactors there are many troublesome chemical reactions. For instance, in the case of SOLASE with a graphite first wall, the production of hydrocarbons from hydrogenic species in the pellet dictates the cavity pumping rate. These problems are important to the pellet design for they place limits on the types and amounts of materials that are allowed in the target.

To achieve a yield of 150 MJ, the SOLASE pellet design uses a 45% burn-up of 1 mg of DT fuel. The remaining unburned deuterium and tritium represents hydrogen that is available to react with the first wall. Clearly, for SOLASE it is desirable to limit the amount of hydrogen in the pellet to only the DT fuel. This poses some contradiction to current pellet designs that contain CH_2 or other plastic low Z ablators. To ease the hydrogen isotope separation problem, any hydrogen in the pellet other than the fuel should be deuterium rather than protium.

The most likely approach to reactor-type pellet designs will be substitution of acceptable materials for experimentally convenient materials. For instance, a thin layer of gold is often used as a high-Z fast electron shield in current pellet designs. The mass of this gold is most often at least ten times the mass of the DT fuel. Extrapolated to reactor size pellets, when the DT mass is 1 mg, this represents a consumption of 720 grams of gold per hour. Such quantities of gold are available and affordable but the efficiency of the recovery process will determine the fraction of gold that is unrecoverable. Should this fraction be too high, or should the cost of the equipment necessary to recover an acceptable fraction be too high, then the use of a substitute material such as mercury or lead must be considered. In the SOLASE design, low temperature condensates such as lead or gold should be avoided and thus mercury is an obvious choice. A more exotic material that might serve the same purpose is xenon. Xenon can be diffused into the glass or plastic shell along with the 1 mg of DT. When the pellet is cooled to cryogenic temperatures the xenon will freeze onto the inside surface of the shell before the DT thereby providing a high-Z layer surrounding the solid DT. However, the Z-value of Xe is only 54 compared to 80 for Hg and 79 for Au.

Hence, its acceptability as a pusher-tamper-hot electron shield must yet be verified. If Xe is acceptable then its use reduces the first wall chemical erosion due to carbide formation. Problems still exist in separating the three noble gas constituents of the exhaust: Ne, He, and Xe. For SOLASE, such structural materials as iron and nickel must be avoided because they will plate out on the first wall. When high-Z or intermediate-Z material must play a structural role in the pellet design, it might be replaced by a thin glass shell coated with a high-Z material like mercury. Substitutions such as these must be verified using pellet design computer codes and ultimately by experiment.

Table I-C-4 shows the ratio of pellet mass devoted to non-fuel materials to the fuel mass for several different generations of laser fusion pellets. The general trend is clearly toward more non-fuel pellet material to alleviate such problems as hydrodynamic instabilities, hot electron and hard X-ray preheat, and fuel tamping. Extrapolated to reactor grade pellets with 1 mg of fuel, this trend implies 10-1000 mg of non-fuel materials. Such large quantities per pellet imply that the handling and recovery equipment for non-fuel materials will be an important consideration in the overall fuel cycle. To minimize the complexity of the fuel cycle, it is desirable to have as few different materials in the pellet as possible. In addition, the mass of non-fuel materials should be minimized to reduce the magnitude of the materials handling equipment. The interaction of non-fuel materials with the first wall and exhaust gas processing equipment is a problem unique to inertial confinement fusion and may prove as troublesome as the plasma impurity problem in magnetic confinement approaches. Greater emphasis should be given to this problem once pellet designers begin to place more confidence in specific pellet designs that can be analyzed in detail.

Table I-C-4

Mass of DT and Other Materials in Laser Fusion Pellet

I. Ball and Shell Target*

DT - 0.0388 μg
SiO_2 - 117.3 μg
Au - 10.46 μg
CH - 5.33 μg
H_2 - 0.1 μg

$$\frac{\text{OTHER mass}}{\text{DT mass}} = 3432$$

II. Vacuum Insulation Target**

DT - 0.83 μg
Au - 36 μg
CH - 154 μg
Ni - 2022 μg

$$\frac{\text{OTHER mass}}{\text{DT mass}} = 2659$$

III. Glass Microballoon Target***

DT - 1 ng
SiO_2 - 30 mg

$$\frac{\text{OTHER mass}}{\text{DT mass}} = 30$$

*"Laser Program Annual Report," UCRL-50021-75, p.

**R. Perkins, "The Laser-Fusion Program at LASL," LA-UR-77-174.

***G. Charatis et. al., Glass Microballoon Experiments, IAEA Tokyo Meeting, 1974.

I-C-2. Targets for Laser Fusion

Targets used in present laser and e-beam fusion experiments can be classified by the type of material used to retain the high pressure D-T fuel mixture. In the majority of neutron-producing laser-induced implosions, the fuel container material has been glass. More recently, polymeric materials, e.g., polyvinyl alcohol (PVA), have been used either as the primary container or as a low-Z coating on the exterior of glass-shell or metal-shell containers.

Shell diameters, shell wall thicknesses, fill pressures, etc. are dictated by the characteristics of available lasers and in particular by available laser power. Primarily because of the latter consideration, total target mass is still less than 2 μg. With this limitation, the glass targets of interest, i.e. those suitable for producing thermonuclear neutrons, have diameters in the range of 50 μm to 300 μm with walls ranging from 0.5 μm to 5 μm in thickness.

Although many present day targets are noncryogenic, multilayered cryogenic pellets are of great interest at this stage in the laser-fusion program. Interest stems not only from the expected enhancement of neutron yields from such targets but also from the awareness that reactor-type pellets may well be cryogenic. The development of this technology should begin as early as possible. Within the last year, cryogenic targets in which the fuel is condensed as a liquid film on the interior surface of glass microshells have been irradiated and an enhancement in neutron yield has been observed.

The present state-of-the-art in target production has been reviewed and an examination made of a generic target that is likely to be typical of targets for laser fusion reactor applications. The generic

target is a spherical shell that contains a 50:50 deuterium-tritium fuel mixture and may be coated with one or more layers of various materials. The fuel gases are condensed uniformly on the inner surface of the shell. The primary functions of the coatings or layers are to increase laser coupling and/or decrease fuel preheating.

Reactor-pellet requirements can be stated only in general terms since presently available data are insufficient to define the optimum pellet design. However, the generic pellet consists of 4 layers as shown in Fig. I-C-13. The first, or innermost layer, is the condensed fuel mixture, which has a total mass of 1 mg. The second layer is usually the structural capsule which serves to contain the fuel during processing and injection. If PVA capsules are used, a layer of Xe condensed between the DT and the PVA is probably required to protect the capsule from radiation damage. Xe condenses before DT so that producing such a target appears feasible. Storing the pellet at a temperature below 164 °K, the triple point temperature of xenon, and continually removing the energy due to β-heating (1.8×10^{-4} W per pellet) should significantly increase the shelf life of the polymer shells. The dimensions of this capsule are determined primarily by its material and mechanical properties rather than by the physics of laser-pellet interactions. The third layer is made of high Z material (e.g., Hg) with a mass of perhaps 10 mg and is needed only when the Z of the structural shell is not sufficiently high to protect the fuel from preheat. The outermost layer is chosen to be a low-Z, low-density ablator.

The reactor pellets can be conveniently classified according to the material out of which the capsule or structural shell is composed. The

LASER FUSION PELLETS

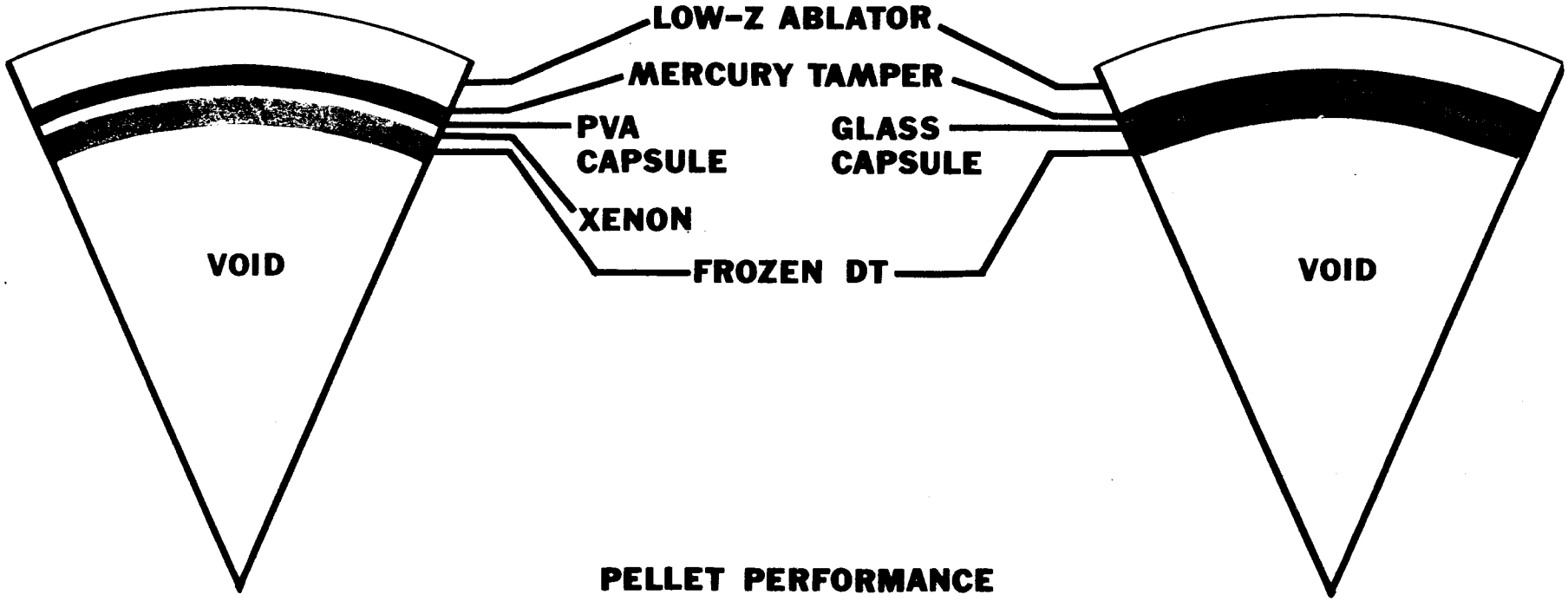

PELLET PERFORMANCE

PELLET GAIN = (YIELD/CORE ENERGY) X (CORE ENERGY/LASER ENERGY)

= (GAIN ON CORE) X (IMPLOSION EFFICIENCY)

UW

Fig. I-C-13

two most probable classes of container materials are glasses and polymers. Of these, based on present technology, the silicate glasses and polyvinyl alcohol (PVA) are the most promising candidates. Possible alternatives to glass and polymeric containers are iron and beryllium.

Numbering the shells or layers from inside out and starting with the material in contact with the fuel layer, Table I-C-5 contains a list of the materials which satisfy the pellet requirements and have the highest probability of being fabricable into small uniform shells. It is worth noting that another particularly interesting class of reactor pellets is that in which the container is fabricated from a high-Z material. The significant factor is that only one coating material is required which reduces the number of fabrication steps.

From the reactor point of view, the ideal pellet materials would contain no oxygen and would produce only volatile non-reactive agents. The configuration coming closest to this is a DT-filled, deuterated polystyrene, polyethylene or parylene shell with xenon deposited on the inner and perhaps on the outer surface of the shell. The outermost layer would be a low density foam, again of a polymer containing no oxygen.

Three steps appear in all candidate pellet-processing schemes; (a) permeation (fuel) filling, (b) final cryogenic processing (immediately prior to injection), and (c) deposition technology (for low-Z ablators, high-Z layers). These processes will of course require modifications, but the basic techniques, e.g. radiographic inspection, cleaning, and floatation are well established procedures. The technology to perform all the fabrication operations for any of the representative pellets is already in existence.

Table I-C-2

REACTOR PELLET MATERIALS

CONTAINER MATERIAL (pertinent properties)	SHELL (LAYER) MATERIAL LAYER NUMBER* 1	2	3
GLASS (strength, H_2-permeability)	High Z[1] Materials	Glass	Low ρ, low Z[2] Materials
POLYMER (heavy atom-permeability)	Xe and High Z[1] Materials	PVA	Low ρ, low Z[2] Materials
HIGH Z CONTAINER	---	W-25 Re[3] 50 Mo-50 Re	Low ρ, low Z[2] Materials

(1) High Z coating materials - Ta, W, Pb, Hg, Pt, Au, Pd

(2) Low density, low Z layers - CH_2, $LiBH_4$ (foams); Be, B, B_4C, LiH or LiD (open structures)
H_2, D_2 (low density frost)

(3) Candidate high Z materials - tensile strengths > 2×10^5 psi
shell fabricability - unknown

*The layers are numbered in sequence starting with the innermost layer, which is next to the DT fuel layer

High-volume processing for power-plant reactors will require only limited extensions and modifications of well-established techniques.

Storage requirements for reactor fuel pellets are derived primarily from considerations of: (1) safety, (2) shelf life and material properties of fabricated pellets, and (3) energy costs for pellet fabrication and storage. The main safety concern is with the large tritium inventory resulting from storing large quantities of pellets. The pellet usage rate is 1.728×10^6 pellets per day. At 1 mg of fuel per pellet, this corresponds to a tritium consumption of 9.95 MCi per day. Avoiding interruptions in power plant operation caused by lack of reactor pellets requires a stockpile of fuel pellets. The number of pellets stockpiled is determined by the number of days required to bring the tritium fueling operations back on line. In SOLASE, a one week store of pellets is employed. The total tritium inventory in the plant will also depend on the pellet fill time. The tritium inventory with PVA capsules is about 10 kg compared with about 25 kg for glass encapsulation. The difference is due to the high diffusion rate of DT through PVA and the consequent shorter pellet fueling time. This large difference strongly suggests PVA encapsulation and further work to perfect this approach. Nevertheless, such an extensive inventory combined with the low permissible tritium concentrations implies strict control and prevention of tritium release to the environment.

Several storage techniques are feasible but cryogenic storage appears the most attractive. The outpermeation of the fuel through any of the shell materials may be reduced to a negligible level by storing the DT-charged pellets at low temperatures; pressure-induced stresses and radiation damage are also reduced.

An estimate of the manufacturing cost of reactor pellets has been made with the objective of bounding the costs. The results are shown in Table I-C-6. Assumptions about technological advances are necessary to develop any cost estimate. It is estimated that with automation no more than one man-year will be required to process a billion-pellet batch of reactor pellets. One man-year of labor (2000 hours) at $20,000 plus an overhead rate of 200% would give a total of approximately $60,000 per billion pellet batch, or a labor content of 6×10^{-5} cents per pellet. An error of an order of magnitude here makes little difference in the pellet cost. Appropriate automation techniques are well within the scope of present technology.

It is assumed that pellets will be manufactured by batch processes where a batch size is of the order of billions of pellets. This second assumption allows amortization of expendable tooling over a sufficiently large number of pellets that tooling costs per pellet appear to be acceptable. In a 1000 MW_e unit the capital costs associated with the pellet factory can be as high as $100,000,000. The cost of materials is found to be very low.

I-C-3. Injection of Targets

Injection of laser fusion targets into the reactor chamber is inherently different from the static mounting procedures followed today. Electrostatic and pneumatic injection are the two injection modes which have been given the most attention. The state of the art for both techniques is highly advanced and their application to the reactor appears potentially straightforward. Electrostatic injection also appears desirable because of the possibility of correcting the trajectory of pellets while in flight. The

TABLE I-C-6

Direct Materials Costs[a]

Material	Total Weight (kg/yr)	Material Unit Cost ($/kg)	Total Material Cost/Year ($/year)	Cost per Net Pellet ($/pellet)	Weight per Pellet (mg)[d]
Deuterium[c]	1.11×10^2	1000.0	1.11×10^5	0.00022	0.40
Glass[b]	9.7×10^4	7.63	7.39×10^5	0.00146	2.52
Mercury[b]	1.54×10^4	66.0	1.016×10^6	0.00201	10.0
Plastic[b]	1.05×10^4	1.10	1.155×10^4	0.00002	10.65
TOTAL			1.877×10^6	0.00371	23.57

(a) 20 pellets/sec, 80% plant factor $\Rightarrow 5.046 \times 10^8$ pellets/year

(b) No recovery in manufacturing

(c) Assumes 45% fractional burnup of deuterium in the pellet and 100% recovery of unburned deuterium

(d) The total weight per year is not equal to the total weight of one years' worth of pellets because of manufacturing inefficiency.

TABLE I-C-6, cont.

Estimated Pellet Cost

Effect of Increasing Developmental Costs

Materials (a)	$ 4,480,000	$ 4,480,000	$ 4,480,000
Labor	7,000,000	3,500,000	1,750,000
Capital Charges (b)	18,000,000	9,000,000(d)	4,500,000(e)
Total	$29,480,000	$16,980,000	$10,730,000
Cost Per Pellet (c)	4.67¢	2.69¢	1.70¢

(a) all materials, supplies and utilities

(b) @ 18% of investment in plant

(c) plant factor 0.9 assumed

(d) assumes a $50,000,000 investment in plant

(e) assumes a $25,000,000 investment in plant

method consists in depositing an electrical charge on the pellet and accelerating the pellet in an electric field to the desired velocity. While the pellet is in flight, one can in principle make position and velocity measurements electronically, evaluate these data and use them for in-flight trajectory correction by fields between sets of deflector plates.

An analysis of this scheme in the framework of the reactor radiation and temperature environment reveals some severe shortcomings. During both acceleration and deflection, the resultant velocity and trajectory correction depend on the charge-to-mass ratio of each individual pellet. Control of this charge-to-mass ratio is not possible in the reactor environment particularly if an ablator is used to preserve the cryogenic DT fuel. Trajectory corrector plates would have to establish the electrical deflection fields inside the high temperature region of the reactor. There is no known reliable way to accomplish this. In addition, the system requires velocity and position measuring schemes that would function reliably in an environment of at least 2000°C.

The scheme of pellet injection which appears the most feasible employs a pneumatically operated launching device which injects the pellet along a vertical trajectory. In this configuration, the pellet traverses a distance of about 12 m to the cavity center at a speed compatible with the timing requirements inherent in the laser injector synchronization and the maximum lifetime of a pellet in the 2000°C environment of the reactor chamber. With presently available high-precision air guns, projectiles can be delivered into an area of radius less than ~0.7 mm at a distance of 12 m with a generally horizontal trajectory. This is still a slightly greater circle of uncertainty than that required for the delivery

of fuel pellets into the laser focal volume of future laser fusion reactors. For a vertical trajectory, improvement in this accuracy or a decrease in the spread of projectile impact points can be expected. Further increases in accuracy may require delivery from shorter distances, e.g., insertion of the barrel into the cavity. A major advantage of a pneumatic injection system is its relative ruggedness and insensitivity to ionizing radiation. It is also worth noting that the accelerating gas can be the same as that used in the cavity, neon or xenon. During operation approximately 100 torr-ltr/sec of gas is introduced into the cavity. This additional gas load can be easily handled with the proposed chamber pumping speed of 5×10^5 torr-ltr/sec.

The system is, however, sensitive to high temperatures and to temperature changes. The pneumatic injection system must be kept at a constant temperature both to maintain mechanical dimensions and to protect the fuel pellets from heating during loading and acceleration. A combination of cooling the injector, synchronized rotating shutter and a gently curved barrel can meet these requirements.

Trajectory correction can only be done by correcting the gun's aim and predicting or obtaining coincidence between the laser firing and the pellet arrival in the focal volume is likely to be very difficult. The measurements required, i.e. measurements of pellet position as a function of time, cannot easily be accomplished

with either optical or electrical methods because of the high temperature of the cavity (which results in an unacceptably high radiation background) and the requirement that the pellet be located within 100 μm of the target position.

For a delivery rate of 20 sec^{-1} and a flight time of 1.40 sec the velocity of the pellet will be approximately 480 m/sec, which means it will remain within the target volume (as defined by the requirement for 100-μm positioning accuracy) for 0.42 μsec. Since laser jitter is expected to be less than 0.1 μsec, it appears feasible, once the trajectory is established, to trigger the laser to fire at the instant the epllet arrives at the focal volume.

I-C-4. Optics, Target Illumination, and Mirror Mechanical Design

The illumination of the target by the laser beam will typically require a carefully designed beam train and last optical element. To analyze this part of the system, one must first decide whether the target can or must be illuminated uniformly. The required degree of uniformity is determined chiefly by its effect on growth of the Rayleigh-Taylor instability while the angles of incidence must be held down in order to maximize absorption and minimize refraction in the blowoff layer.

It is found that uniform illumination is not truly compatible with reactor requirements. In SOLASE, for example, at least 20 beams would be required, the allowed solid angle devoted to beams being 10%. With the last mirror located at 15 m, the diameter of the last optical element at f/2.74 is 5.5 m. This is clearly very large. One can locate the mirrors closer to the target to reduce their size but this in turn increases the difficulty of protecting the mirrors and complicates cavity design by

reducing accessiblity. We have therefore used non-uniform illumination with six beams on each side to give effectively two-sided illumination. If future pellet designs cannot accommodate this, laser fusion reactors will be much more difficult to realize.

The last mirror is diamond turned copper on an aluminum backing and structure. The shape of the mirror is an off-axis paraboloid as depicted in Fig. I-C-14. It is found that neutron induced damage is not a serious problem. Neutron damage in the Cu on Al substrate mirror at 15 m from a 150 MJ yield pellet at the rate of 20 Hz is moderate, about 10^{-7} dpa/sec, and the neutron heating is less than 10 W/cm^3. This provides little incentive to move the mirror farther than 15 meters from the target. In addition, pointing errors grow increasingly greater as the mirrors are moved far from the target. In the limit of very large distances (50 to 100 meters) the size of the primary containment building becomes an important issue if the last mirror must still reside within it. The neutronics analysis of course does not demand that mirrors be placed at these distances.

Surface damage to the mirror by X-rays and pellet debris is a much more significant problem. Large quantities of pellet debris on the mirror surface cannot be tolerated. Physical, and more importantly, chemical reactions at the mirror surface will degrade the optical quality. This is another reason to choose chemically compatible pellet and mirror materials. A method to protect the mirrors from the pellet debris is to flow a gas, such as xenon or neon, in front of the mirror surface. This is shown schematically in Fig. I-C-15. All six laser beam lines pass through a suppression chamber on the outside. As the pellet debris

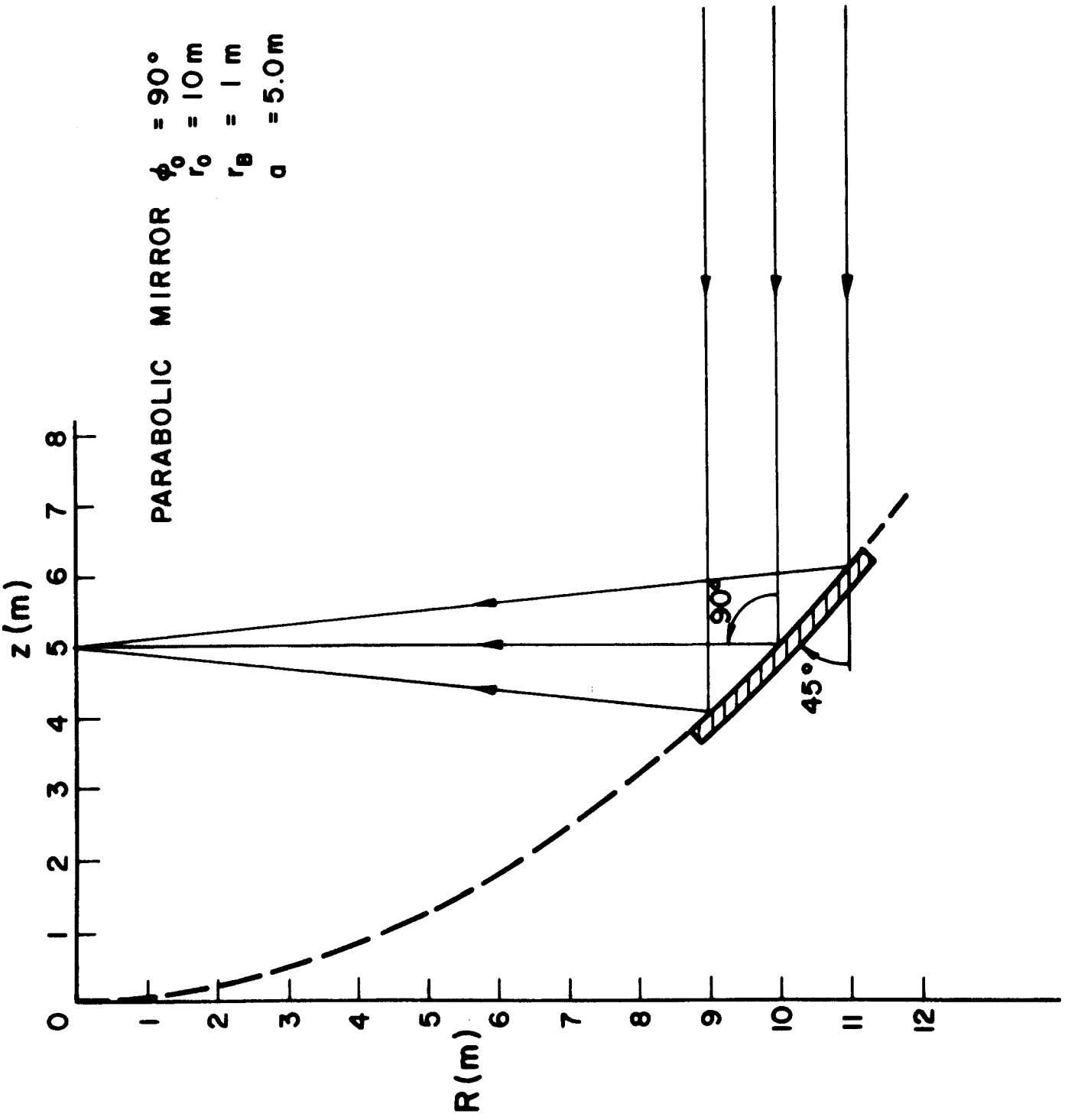
PARABOLIC MIRROR ϕ_o = 90°
r_o = 10 m
r_B = 1 m
a = 5.0 m
z(m)
R(m)
90°
45°
0
1
2
3
4
5
6
7
8
9
10
11
12

Fig. I-C-14

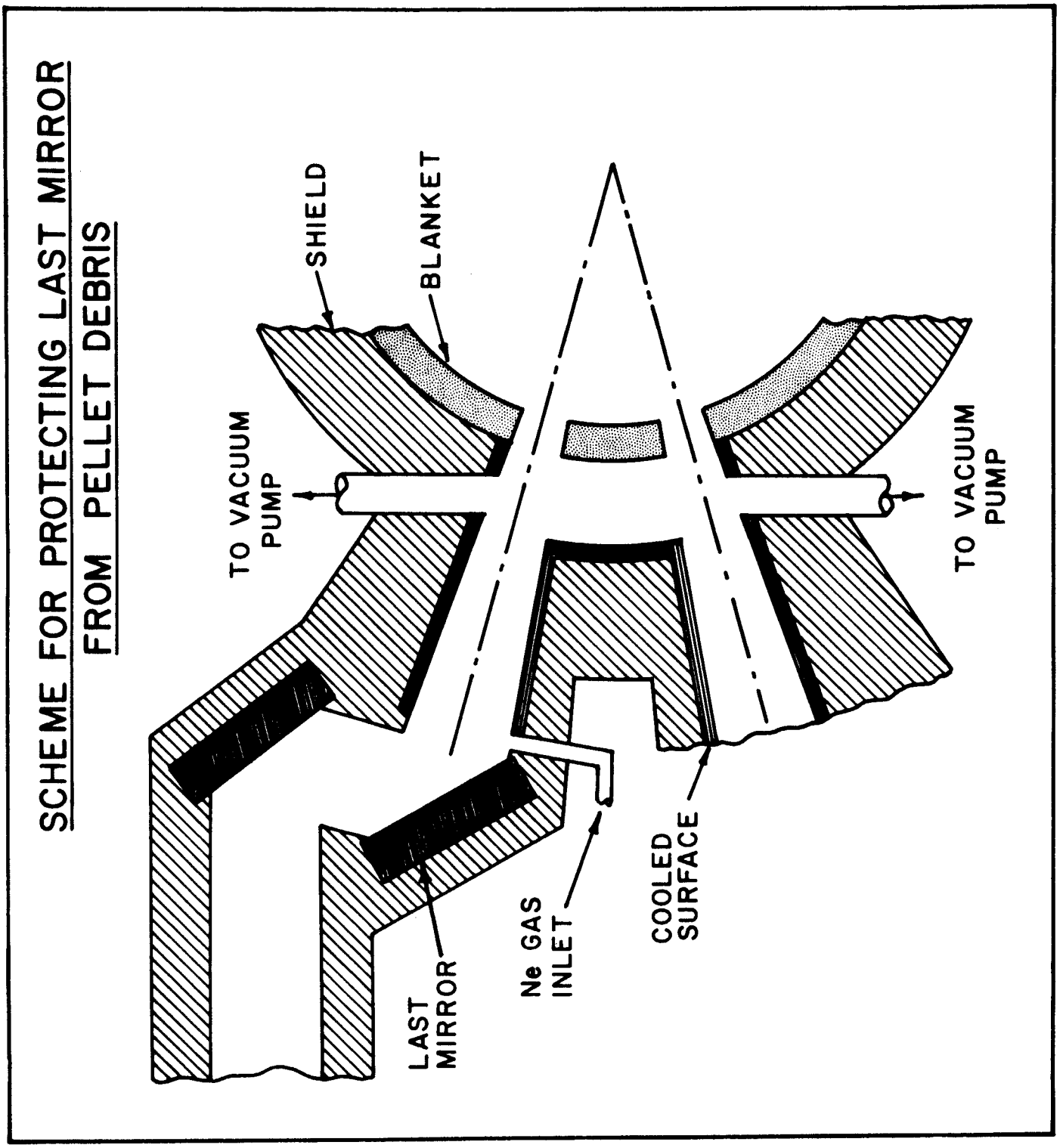
SCHEME FOR PROTECTING LAST MIRROR FROM PELLET DEBRIS
SHIELD
BLANKET
TO VACUUM PUMP
TO VACUUM PUMP
LAST MIRROR
Ne GAS INLET
COOLED SURFACE

flows out through the blanket beam ports, it expands in this chamber. This reduces the shock strength while the chamber's actively-cooled walls cool the debris before it reaches the vacuum pumps. The walls of the beam lines from the chamber to the last mirror are also actively cooled and neon or xenon gas is flowed at low pressure from near the mirror surface toward the suppression chamber. Hot debris diffusing in this beam line is cooled by convection to a diffusion rate sufficiently low such that the flowing gas will convect it away from the mirror surface. Such a scheme has been used on a small scale to protect windows from hot expanding plasmas in laser-plasma experiments and appears suitable for laser fusion reactor applications.

To control pellet irradiance, four independent quantities are at our disposal: N, the number of beams; δ, the shift of the beam focus relative to the pellet center; F, the f/no. of the focused beam; and the beam profile $I_o(r)$, where r is the beam radius of the last optical element. The beam profile may depend on two or three parameters so it would seem there is a formidable parameter space to deal with. In practice, however, only a few values of N are considered and F is being determined by the maximum solid angle allotted to optics. Of course, the optics must be sufficiently distant from the target so that the beam aperture is adequate to handle the energy and power per beam as well as the radiation and debris from the target. The total aperture area is determined in practice by material damage constraints on the beam energy rather than self-focusing constraints on the beam power. We have used a maximum value of 5 J/cm^2.

Illuminating a 2 mm radius target from a distance of 15 m with a large off-axis paraboloid and keeping it on target is a formidable technical task. Six degrees of freedom must be controlled in an explosive environment.

Disturbances arise from firing the laser and shocks in the buffer gas, as well as the usual environmental sources. Pointing, centering and focusing are controlled very accurately in current experiments. For example, the pointing error $\delta\phi$ is less than 1 μrad in SHIVA while $\delta\phi < 10$ μrad is anticipated for ANTARES. As shown in Sec. V-C, the requisite $\delta\phi$ depends on focal length and target size. Our studies on caustic formation from parabolic mirrors suggest that $\delta\phi < 10$ μrad is more than adequate for SOLASE and most laser fusion reactor designs, except for very long focal length systems. SHIVA's 1 μrad tolerance was intended to accommodate uniform illumination (now defunct) and would be much more costly than a 10 μrad system.

Further, it is not clear how alignment control can be accomplished without a stationary surrogate target, or how often corrections would have to be made. Current large scale experiments allow hours between shots for alignment, as compared to perhaps 50 msec between pulses in a reactor. While their sheer inertia would prevent appreciable motion of the large SOLASE mirrors on this time scale, the problem remains of rapic corrections of any secular drift.

One of the important structural characteristics for the mirrors is the ratio of flexural stiffness to weight. One wants this ratio to be high in order to minimize transverse deflections and slope changes. Solid mirrors with the necessary stiffness would be prohibitively massive. Rib-stiffening would lead to a more efficient overall design but local deflections could be unacceptable. The best configuration for achieving high stiffness and low weight without local effects is a sandwich construction - essentially two face plates separated by a light core such as aluminum foil honeycomb. An additional advantage of the honeycomb is that it can also be designed to accommodate appropriate cooling for the unit.

Transverse deflections and slope changes of a sandwich mirror do not depend upon the thickness of the face plates since both the flexural stiffness and the gravitational loading are proportional to this parameter. Thus, the faces can be kept relatively thin with the stiffness and therefore deflections governed by the core dimension.

A continuous uniform support condition is advantageous for symmetric surface deflections. Statically indeterminate supports would generally reduce deflections but lead to additional design complications of the substructure to which such members would be attached. A ring support is one possible scheme for consideration. The largest deflections and rotations are produced when the support is located at the outer edge. Reducing the support to a center post results in deflections and slopes approximately half of the largest values of the preceding case. Overall plate deflections can be kept to a relative minimum if the support is located such that deflections of the edge and center are equal. Any change in the radial position of the support from this will increase one or the other. This particular support location corresponds to approximately 67.3% of the outer radius. With this criterion, maximum deflections and rotations have been determined as shown in Fig. I-C-16. It is seen that reasonable core thicknesses can be used to keep these deflections within design limits.

I-C-5. The Laser System

The laser is obviously a key item in a laser fusion reactor and from the requirements listed in Table I-C-7, one can infer a number of properties that would be exhibited by the ideal laser. First, the wavelength range of 3000-6000 Å implies an electronic transition. This wavelength range is desirable to efficiently couple laser energy into the pellet. The lower cutoff at 3000 Å is dictated by two-photon absorption damage suffered by optical components at shorter wavelengths and the lack of efficient reflectors.

Today, there is no laser known which will obviously meet the requirements for laser fusion reactors. The optimum laser will depend on the ultimate wavelength, efficiency, and power requirements imposed by the physics of the laser-pellet interaction as well as developments in the lasers themselves. We have used the CO_2 laser to give a concrete basis to a generic design. The basic requirements for a laser fusion laser (a flowing gas system, 1 MJ total energy out, and energy densities dictated by the optics and not

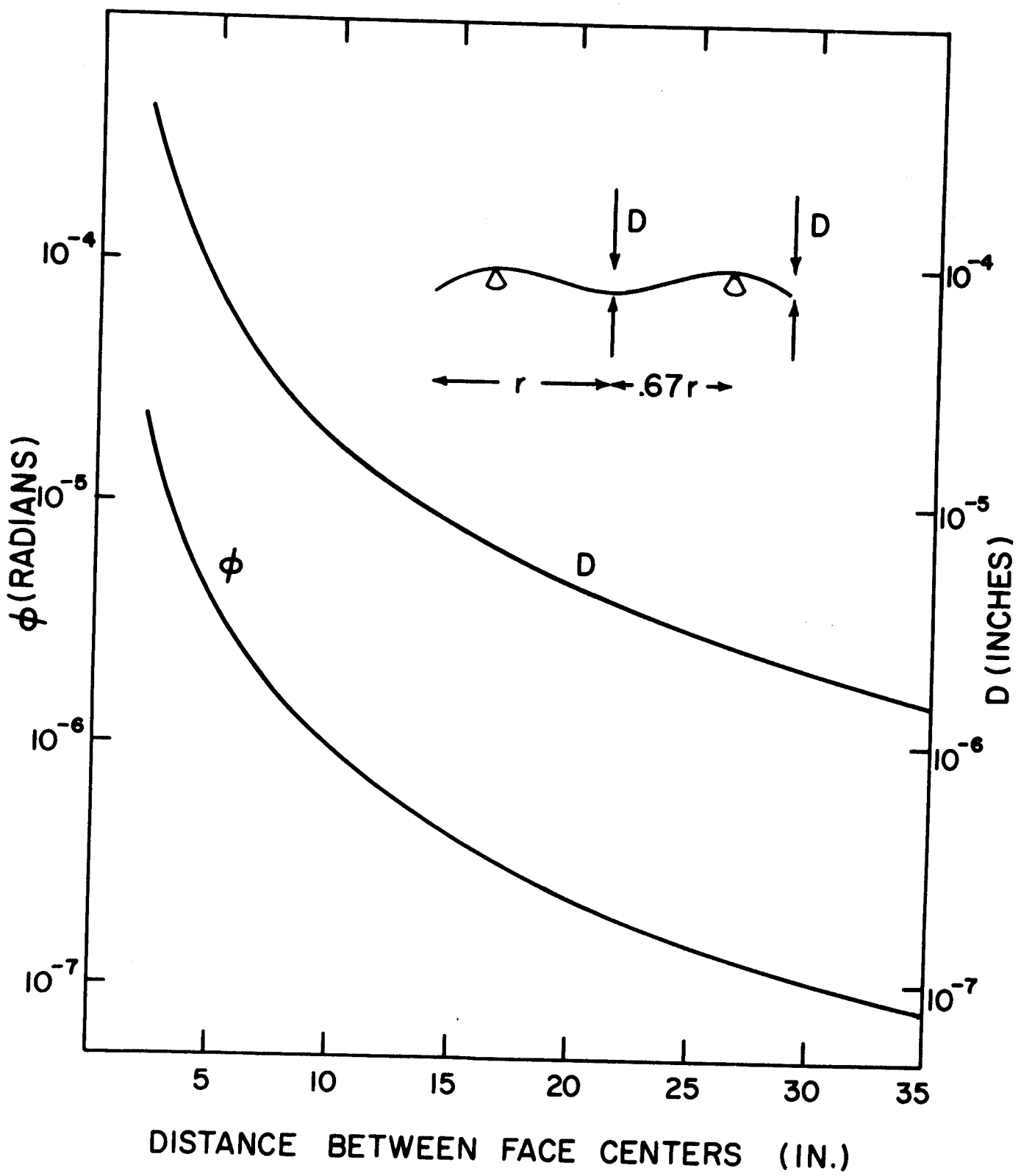
D
D
r
.67r
10^{-4}
10^{-5}
10^{-6}
10^{-7}
ϕ (RADIANS)
D (INCHES)
ϕ
D
5
10
15
20
25
30
35
DISTANCE BETWEEN FACE CENTERS (IN.)

FIG. I – C – 16

Table I-C-7

Requirements of the Laser for Laser Fusion

	Performance Requirements
Energy	$\sim 10^6$ MJ
Peak Power	~100 - 1000 TW
Pulse Width	~ 1 ns
Wavelength	0.3 - 10.6 μm*
Pulse Shape	$P(t) \sim \frac{P_o}{(1 - t/t_o)^2}$

	Practical Considerations
Efficiency	> 1%
Pulse Repetition Rate	1 - 50 sec^{-1}
Small Signal Gain	0.001 - .01 cm^{-1}
Stored Energy Density	10^2 - 10^3 J/liter
Stimulated Emission Cross Section	10^{-19} - 10^{-20} cm^2

Low Capital Costs and Low Maintenance Requirements

*In general, shorter wavelengths are preferable from the target interaction viewpoint but the issue is still open.

the laser medium) regarding the electrical, mechanical and optical parameters should not be dramatically different from those of the CO_2 design. Of course, each laser will have its own particular requirements for such things as optical components, possible chemical reprocessing and flash as opposed to discharge pumping. This will not be specifically considered in our design. However, the total design should be quite similar and specific modifications readily made. (For example, flash pumped systems such as I*, O*, or Nd^{+3} will likely use electron-beam generated fluorescence to improve efficiencies and, thus, utilize the electron beam technology development for CO_2).

The SOLASE laser design is based on the more conservative estimates given in Table I-C-7. For example, the laser system must deliver 1 MJ of energy to the pellet. It is assumed that approximately 10% of the energy is lost in transport so the total laser output is 1.1 MJ. In addition, the SOLASE laser must have a peak power of ~ 1000 TW and a pulse shape that closely approximates the ideal shape. The wavelengths thought necessary are still subject to considerable debate and no choice of wavelength has been made for SOLASE.

For the particular operating parameters chosen for the SOLASE reactor, the laser must have an efficiency of at least 7%. This efficiency includes all plant recirculating power costs so that the laser itself must have a higher operating efficiency. Another parameter that has been chosen is a laser pulse repetition rate of 20 per second.

Prevention of damage to the various optical components in the system will limit the damage energy density threshold for nanosecond pulses to about 1 to 10 J/cm^2. For purposes of our generic design a value of 3 J/cm^2 has been chosen. An important consequence is that the damage threshold combined with the total energy requirement determines the minimum total aperture of the laser.

The number of final amplifiers chosen depends on two principal criteria: the largest size of a single amplifier and the number of beams required to illuminate the target. For SOLASE we have chosen 12 beams as a compromise between the ability to illuminate the target uniformly and the desire to minimize the complexity of the beam transport system and to maximize the accessibility of the reactor. The total energy output requirement for each amplifier is reduced by multi-passing the last two amplifiers and combining the beams in pairs. This limits the output of each amplifier to less than 50 kJ per pass, a realistic value for the average laser system.

Although CO_2 has the potential of being extremely efficient, on nanosecond time scales the advantageous collisional processes have insufficient time to contribute to the pumping process. Thus, only energy stored directly in the upper laser level contributes to the energy output for a nanosecond pulse. Consequently, for short pulse extraction one should lase on as many transitions as possible to obtain maximum efficiency. However, even with multi-line and multi-band extraction the efficiency will be limited to a few percent. This efficiency could be improved by utilizing a multi-passing technique which allows time for the collisional repopulation

of the upper laser level. This can be accomplished by either a single beam making multiple passes or multiple beams making single passes through an amplifier as illustrated in Fig. I-C-17. In this manner, energy which has been stored in the laser system but is unavailable for short laser pulses can be extracted.

From the total energy output and the output energy density, the aperture required is $3.67 \times 10^7 cm^2$. In the SOLASE design, there are six final amplifiers and from each amplifier four successive beams are extracted. Thus, the aperture per beam is about 1.527 m^2. The total input energy required to drive an amplifier is 4720J per amplifier per pass. Since the total energy output per amplifier per pass is 45.8 kJ, the input energy will comprise over 10% of the total output energy. It is therefore desirable to multi-pass the next to last stage of the amplifier chain to improve its efficiency as well as that of the last stage. Assuming the same basic parameters as for the final amplifier, the next to last amplifier will require an aperture of 0.1573 m^2 and an input driving energy at 486J.

For successful operation of a four beam, multi-pass amplifier, the passage of each beam through the amplifier must be separated by sufficient time to allow the upper laser level to repopulate. At 1800 torr, this time is approximately 0.1 μs. After passing through the amplifiers each beam must be delayed the appropriate amount in order that all beams reach the target simultaneously.

The layout of the beam lines is schematically shown in Fig. I-C-18. One attempts to pass each successive beam through the last two amplifiers at as small an angle as possible to make maximum use of the amplifying medium. However, the smaller the angle between successive beam passages, the larger is the

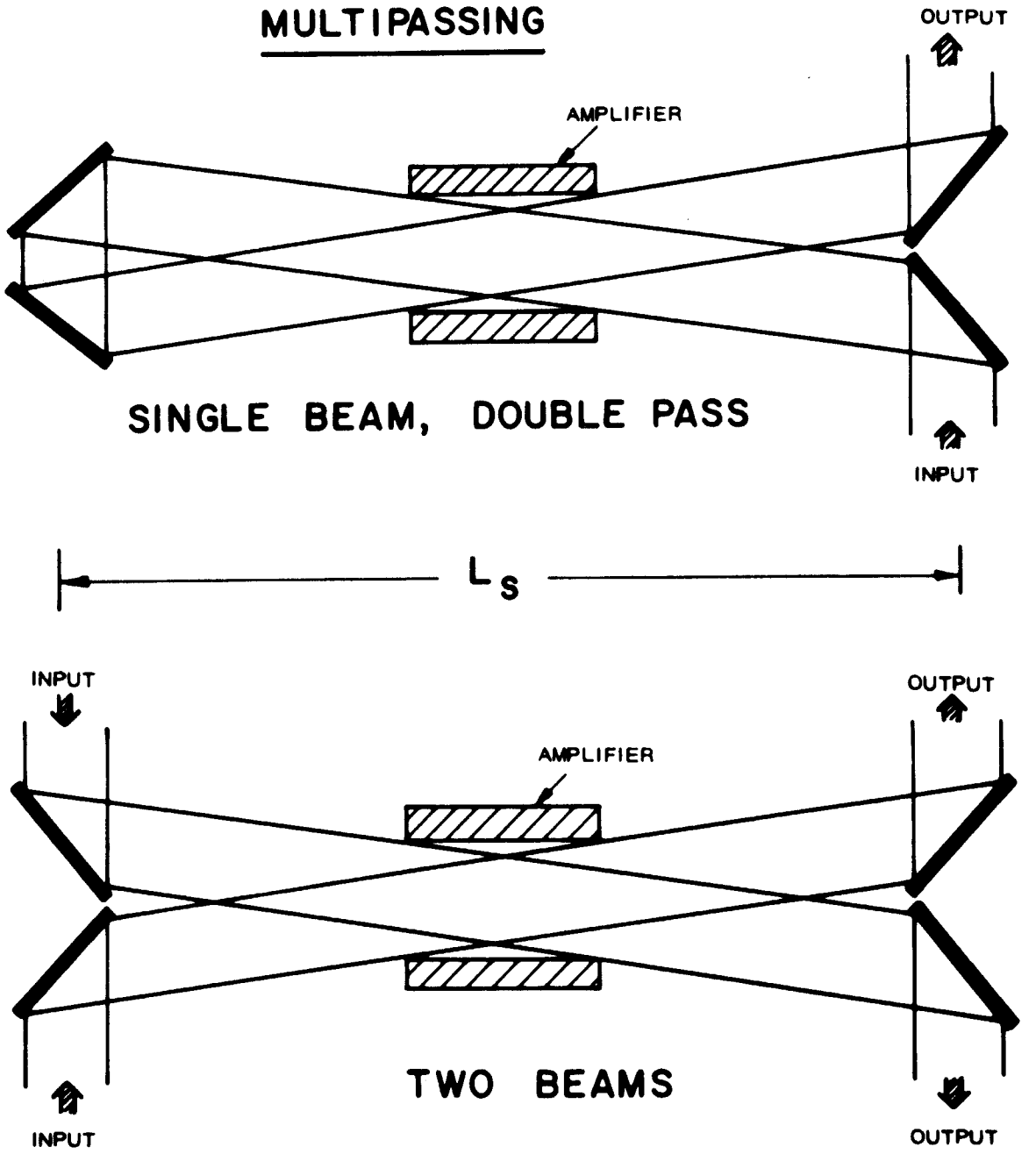
MULTIPASSING
OUTPUT
AMPLIFIER
SINGLE BEAM, DOUBLE PASS
INPUT
L_s
INPUT
OUTPUT
AMPLIFIER
TWO BEAMS
INPUT
OUTPUT

Fig. I-C-17

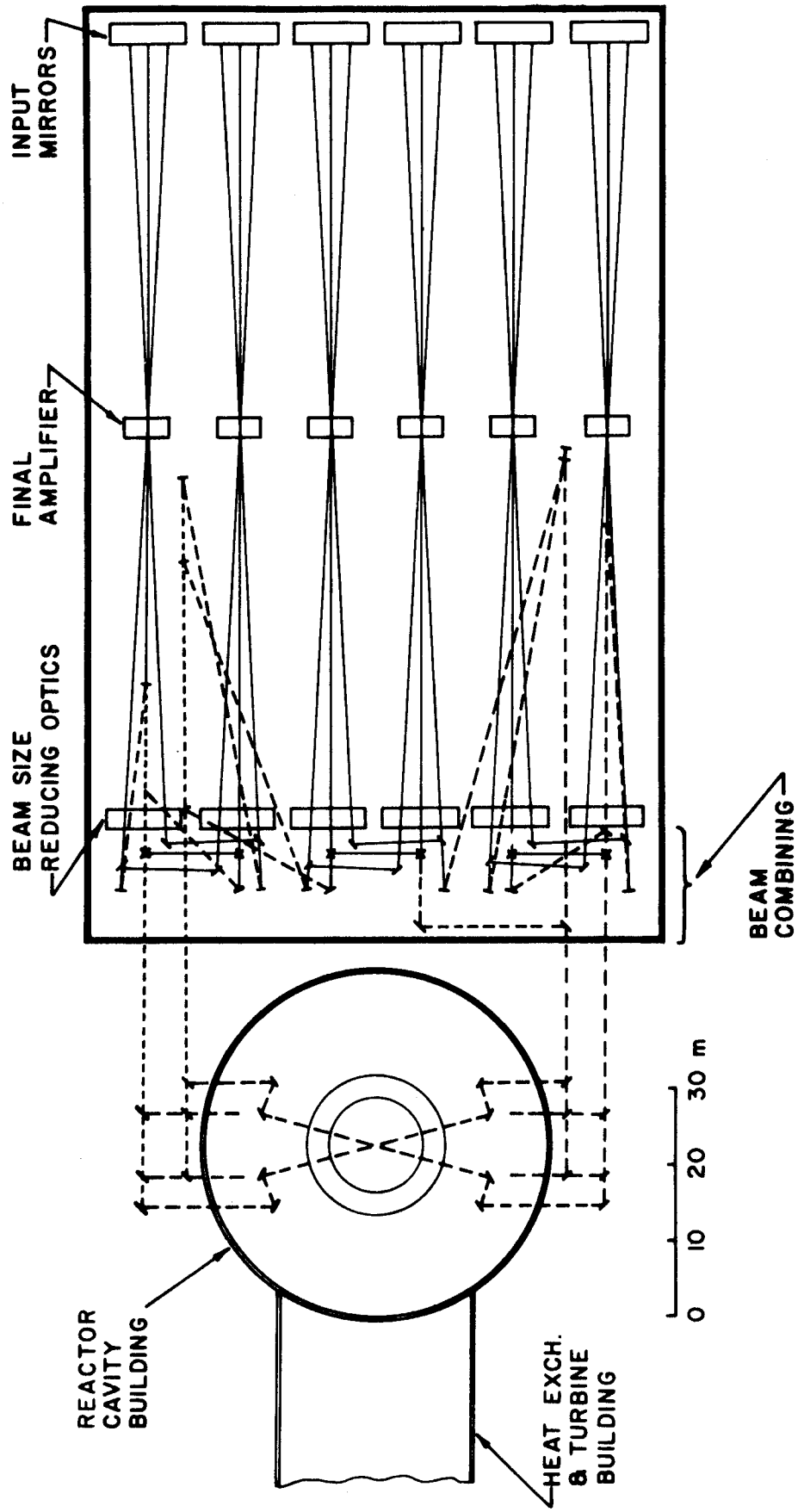
INPUT MIRRORS
FINAL AMPLIFIER
BEAM SIZE REDUCING OPTICS
BEAM COMBINING
REACTOR CAVITY BUILDING
HEAT EXCH. & TURBINE BUILDING
0
10
20
30 m

Fig. I-C-18

distance away one must go before the beams are separated. The distances shown on Fig. I-C-18 represent a reasonable, although not fully optimized, compromise. Note that the distance from the amplifier to the turning mirrors where the multi-passed beams are physically separated exceeds the distances required for delay lines. Therefore, the delay lines are not critical to determining the laser building size.

In summary, the SOLASE multi-pass laser has the following design parameters: the amplifier will have a length of 2.5 m and a small signal gain of 0.04/cm. The amplifier will be a segmented annulus with inner and outer diameters of the pumping volume being 298 and 372 cm respectively. There will be twenty-four, 34 × 37 cm segments spaced 5 cm apart at the inner radius. The laser beam itself will be annular with inner and outer diameters of 313 and 357 cm respectively. The distance between input and output mirrors is 100 m. The angle the beams make with respect to the center axis of the amplifier is 60 mrad. With these values of the parameters, 59% of the volume can be extracted per pass. This corresponds to an aperture area of 1.775 m^2. Since only 1.527 m^2 are required for a uniform plane wave of 3J/cm^2 to yield the required output, this design allows for an 86% geometric utilization factor (a quantity that accounts for the fact that the entire aperture does not contribute equally to the energy extracted).

I-C-6. Laser Gas Handling, Power Supplies, and Beam Layout

A gas handling system will be essential in gas lasers because the gas flow is necessary to remove heat. Pumps to flow the gas and heat exchangers to remove the heat will be needed. In SOLASE this system must handle ~ 10^6 ℓ/sec.

The laser power supply system represents one of the most critical components of the entire laser fusion reactor system. State-of-the-art power supply systems cannot meet the requirements that will be imposed by a laser fusion reactor. Major advances must be made in several areas before a practical, economic system can be developed.

The power supply system will consist of three primary components—a D.C. power supply, an energy storage unit, and switches to transfer the energy from the store to the load. The D.C. power supply simply charges the main energy storage unit. The energy storage unit will generally be a large capacitor bank for laser applications. The switches serve to prevent transfer of energy from the capacitor bank to the load until desired and then pass this energy as efficiently as possible.

The most efficient method of pumping a CO_2 laser is by an electron-beam-sustained discharge because the electronic cross sections for the pumping of CO_2 peak at values of E/N (electric field/gas number density) that can only be obtained by providing a source of ionization external to the discharge. The electron beam provides this source. By carefully controlling the e-beam current, the E/N can be adjusted to maximize the pumping efficiency. Further, energy deposited during the rise and fall times of the pulse does not contribute significantly to the laser pumping but is instead deposited as heat. To minimize detrimental effects, the rise and fall times of the discharge pulse should be as short as possible.

The main energy store for the primary discharge supply could be either a capacitive run-down circuit or a pulse-forming network (PFN). A PFN is generally more efficient, requiring much less energy storage capacity. Also the shape of the discharge pulse can be controlled about as accurately as desired with a PFN but at the expense of increasing circuit complexity.

The power supplies must be designed so that either on-line repairs can be made or so that the entire faulty unit can be replaced by a new unit without shutting down the reactor. The desirability of such a design depends on the ability and practicality of operating the reactor at reduced capacity until the fault is repaired. The ability to operate at reduced capacity will depend primarily on the physics of the laser-pellet interaction.

The design of the capacitor bank incorporates stress reducing features and the capacitors for each PFN will be placed in a bath of oil which will be flowed for cooling. Assuming semi-conductor switches with satisfactory rise times are developed, laser triggered semi-conductor switches are used because of their potential for long lifetimes (in excess of 10^7 shots).

The electrical output requirements for both the PFN's and the e-beams of the SOLASE final amplifiers are given in Table I-C-8. The requirements are given on both a per amplifier and per segment basis. Similarly Table I-C-9 gives the power supply requirements for the next to last stage of the amplifier chain.

Table I-C-8

Power Supply Parameters for the Final Amplifier

Discharge Supply Parameters	Per Segment	Total Amplifier
Electric Field	18 kV/cm	18 kV/cm
Total Applied Voltage	666 kV	666 kV
Current Density	15 A/cm^2	15 A/cm^2
Total Current	0.128 MA	3.06 MA
Pumping Time	2/3 μs	2/3 μs
Total Energy Deposited	56.6 kJ	1.36 MJ
Electron Beam Parameters		
Beam Energy	~ 700 keV	~ 700 keV
Current Density	~ 0.144 A/cm^2	~ 0.144 A/cm^2
Total Current	~ 1.22 kA	~ 19.38 kA
Pulse Width	3 μs	3 μs
Total Energy Deposited	~ 2.52 kJ	~ 60.38 kJ

Table I-C-9

Power Supply Parameters for the Next-to-Last Amplifying Stage

Discharge Supply Parameters	Per Segment	Total Per Amplifier
Electric Field	18 kV/cm	18 kV/cm
Total Applied Voltage	234 kV	234 kV
Current Density	15 A/cm^2	15 A/cm^2
Total Current	45 kA	1.08 MA
Pumping Time	2/3 μs	2/3 μs
Total Energy Deposited	7.02 kJ	168 kJ
Electron Beam Parameters	**Per Segment**	**Total Per Amplifier**
Beam Energy	~ 250 keV	~ 250 keV
Current Density	~ 0.144 A/cm^2	~ 0.144 A/cm^2
Total Current	~ 0.43 kA	~ 10.6 kA
Pulse Width	3 μs	3 μs
Total Energy Deposited	~ 0.34 kJ	~ 8.1 kJ

I-C-7. Reactor Cavity and Blanket Design

The reactor cavity in the SOLASE design is filled with neon gas at less than 1 torr pressure, sufficient to protect the front wall from the ions and soft X-rays produced by the microexplosion. The energy deposited in the gas is radiated to the front wall over a relatively long time period (>1 ms) so that surface heating and thermal ablation of the wall become insignificant. Since a complete pellet design is unavailable now, parametric studies have been carried out using the PHD-IV pellet burn code to provide input information on the possible variability of output spectra.

The range in neon of the different particles found in the pellet at energies that appear to be a maximum for the given particle are summarized in Table I-C-10. The calculations are based on Lindhard stopping theory which is most accurate for the heavy ions. Since only enough gas is placed in the chamber to prevent particles from hitting the wall, these particles deposit their energy in the gas over a large volume. As such, strong shock theory is not applicable and we have developed a Lax-Wendroff fluid dynamics code for the problem. Shocks are observed to develop but they are weak because of the rather weak initial condition. The peak values for the kinetic energy fraction and the total momentum in the shock are about half that predicted by strong shock theory. The peak pressure at the wall is about 90 torr and is spread over about 5×10^{-4} seconds. The momentum transferred to the wall, obtained by integrating the pressure

Table I-C-10

Ranges In Neon ($1.5 \times 10^{16} cm^{-3}$) For Different Particles Found In The Pellet.
(The Energies Given Are The Maximum Values For Each Particle.)

Particle	Energy	Mean Range (m)	RMS Deviation
D	20 keV	2.3	0.1
T	30 keV	3.4	0.2
^4He	90 keV	3.6	0.2
Hg	4.2 MeV	4.9	0.8

profile over time, is about 2 x 10^8 g cm/sec, a hundred times larger than that estimated for the mercury alone.

Hard X-rays deposit their energy directly in the front graphite wall of the blanket but produce a relatively small surface temperature rise because they have a sufficiently long range in carbon. This protection scheme is generic inasmuch as it can accommodate a wide range of spectra and ion and X-ray energy fractions for the 150 MJ pellet yields considered. Maps showing the ranges of pellet output parameters over which this protection scheme will operate successfully have been generated.

The pulsed surface heat flux radiated by the gas is rectified in the front wall of the blanket and directly convected and radiated to the flowing lithium oxide. The combined heat transfer coefficient is low (~0.2 W/cm^2-°C) so that the front wall temperature is significantly higher than that for the Li_2O stream. As shown in Fig. I-C-19, the lithium oxide particles enter the blanket at 400°C and leave at 600°C except for the outermost zone where the exit temperatur is 850°C. (The hot stream contains ~2% of the total flow rate and is used for tritium extraction). The back surface of the front wall will operate at ~1400°C with the front surface temperature reaching ~1800°C after each microexplosion. These temperatures are sufficiently high that excessive swelling of the graphite should not be a problem. Also, at these temperatures the vapor pressure of carbon remains low so that thermal ablation of the graphite is insignificant.

The blanket is constructed primarily with graphite and either nuclear grade graphite or chopped-fiber type graphite composite can be used. Lithium oxide particles, 100-200 μm in diameter, flow under gravity through the blanket and serve the dual purpose of tritium breeding and heat trans-

SCHEMATIC OF GRAPHITE BLANKET SEGMENT FOR SOLASE

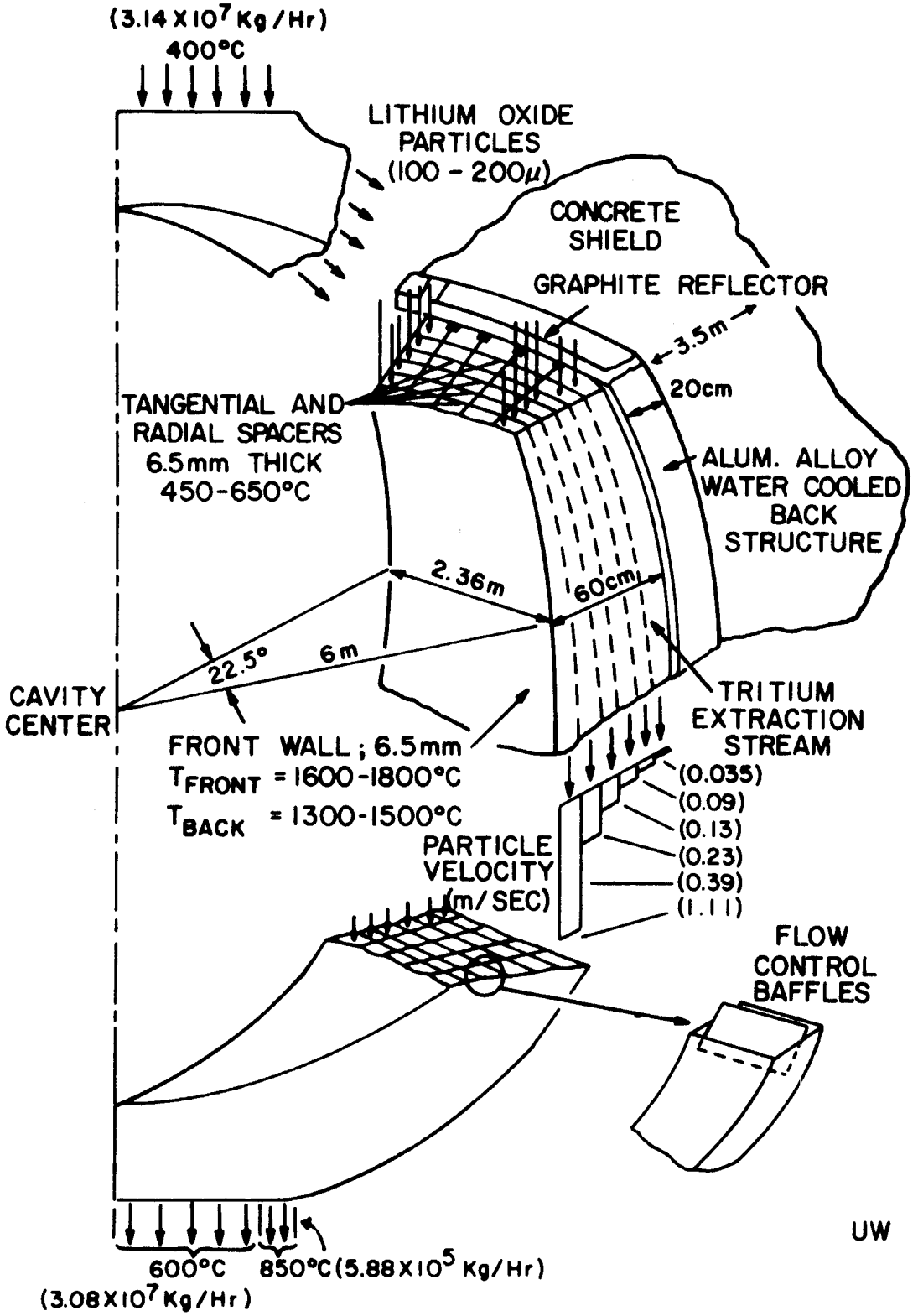

Fig. I-C-19

port. The spherical cavity is divided along longitudes into sixteen blanket segments each with a honeycomb type construction (Fig. I-C-19). The tangential spacers parallel to the front wall allow the velocity distribution of the Li_2O particles to be tailored to match the radial heat deposition curve. The radial supports provide structural rigidity and allow impulse loadings on the front wall to be transmitted to the support structure behind the blanket. This design eliminates the need for metallic first walls and liners since the front wall of the blanket can readily accommodate the microexplosion both thermally and mechanically.

The tangential spacers parallel to the front wall will operate at nearly 650°C since the amount of heat generated within them is low. At 650°C, volume changes in the graphite upon irradiation are also low. This means that the graphite temperatures in the blanket are either above or below the temperature region (~850-1150°C) where excessive swelling limits graphite performance. The temperature gradient between the front wall and the first tangential spacer is accommodated by high density graphite. The estimated lifetime of the blanket structure at 5 MW/m^2 wall loading is approximately 1 year (~30 dpa). Given the relative ease with which blanket replacement can be accomplished here (based on accessibility and the fact that graphite blanket segments will simply be replaced, not refurbished) this lifetime should be adequate.

A special feature of the Li_2O/graphite blanket is the very low levels of induced radioactivity and the adequate breeding ratio. Detailed neutronic calculations give a breeding ratio of 1.33. Typical results showing the blanket radioactivity as a function of time after shutdown are given in Fig. I-C-20. These results show that the activity level of such a blanket

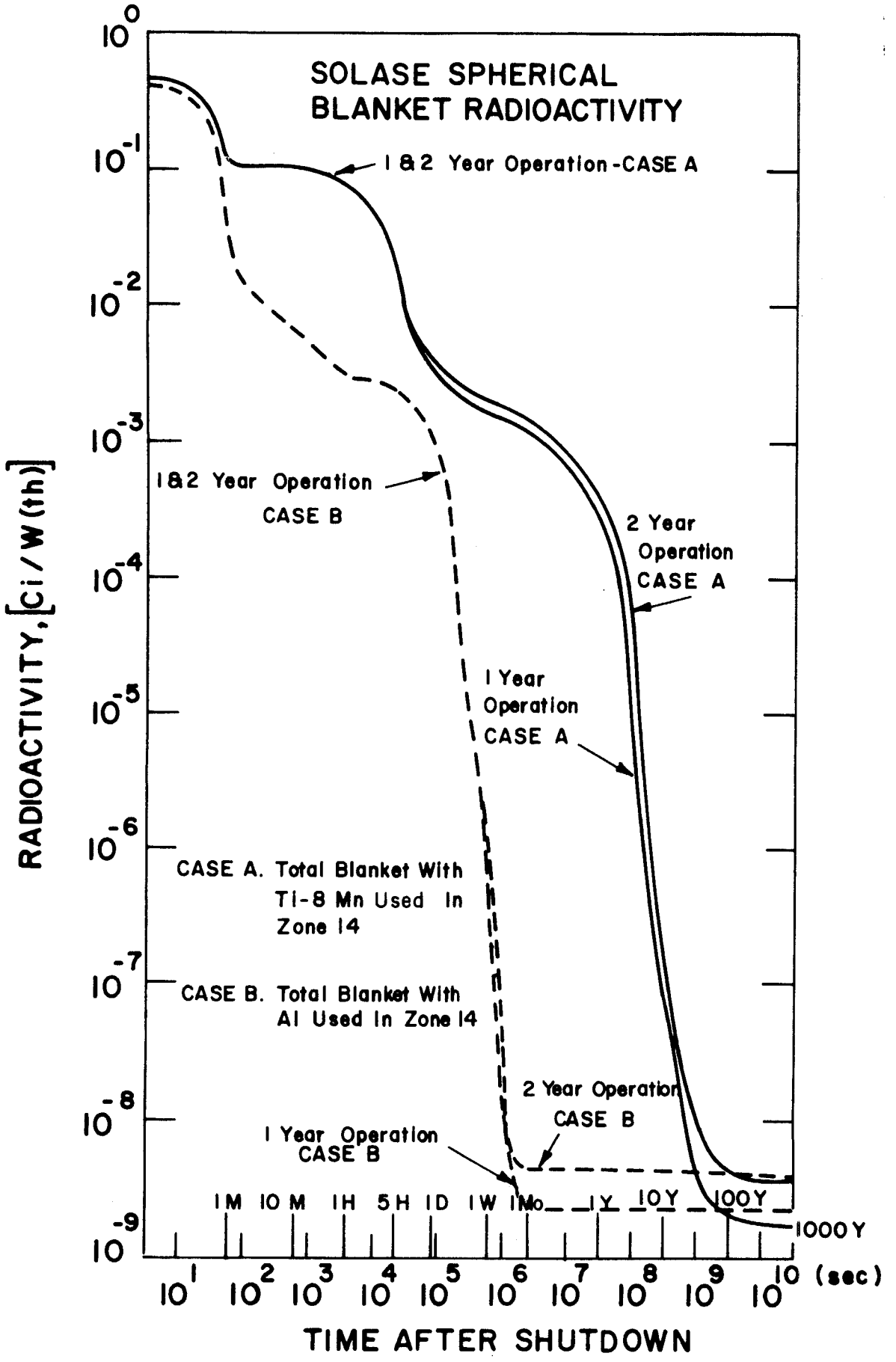
SOLASE SPHERICAL
BLANKET RADIOACTIVITY
1 & 2 Year Operation - CASE A
1 & 2 Year Operation
CASE B
2 Year
Operation
CASE A
1 Year
Operation
CASE A
CASE A. Total Blanket With
Ti-8 Mn Used In
Zone 14
CASE B. Total Blanket With
Al Used In Zone 14
2 Year Operation
CASE B
1 Year Operation
CASE B
1M 10 M 1H 5H 1D 1W 1Mo 1Y 10Y 100Y
1000 Y
RADIOACTIVITY, [Ci / W (th)]
TIME AFTER SHUTDOWN
(sec)

Fig. I-C-20

is very low. The graphite shells are supported on an aluminum alloy structure so that the entire blanket radioactivity drops substantially after a short period. Hence, limited hands-on maintenance appears feasible which should greatly simplify blanket replacement. Assembly and disassembly procedures for this modular blanket design have been developed. The blanket segments can be readily removed by opening the sphere in quadrants after halting the Li_2O flow as shown schematically in Fig. I-C-21. The estimated annual downtime for blanket segment replacement is two weeks.

Possible chemical reactions between the blanket's front wall and pellet materials have been investigated. The reaction rates between the unburned hydrogen isotopes and the graphite front wall have been estimated at the front wall temperature of interest (~1800°C) and acetylene will be formed. For pellet designs of interest, the erosion rate can be limited to ~2 mm/yr and the corresponding pumping power required is less than 10 MW. Special attention has also been given to possible non-hydrogenic pellet constituents and their separation from the reactor exhaust gases. Several pellet compositions containing glass, organic polymers, and high-Z materials have been considered. Xenon appears to be an ideal high-Z component although the use of lead or mercury in the pellet does not pose significant problems since they do not form stable carbides.

The volumetric heat generation profile in the different blanket zones is shown in Fig. I-C-22. The Li_2O particle velocity distribution is tailored to match the radial heat deposition curve. Faster flow is provided near the front wall in order to remove the surface heat flux. The shaping of the velocity profile is provided by adjustable baffles at the exit of the six radial zones. The required velocities (Fig. I-C-19)

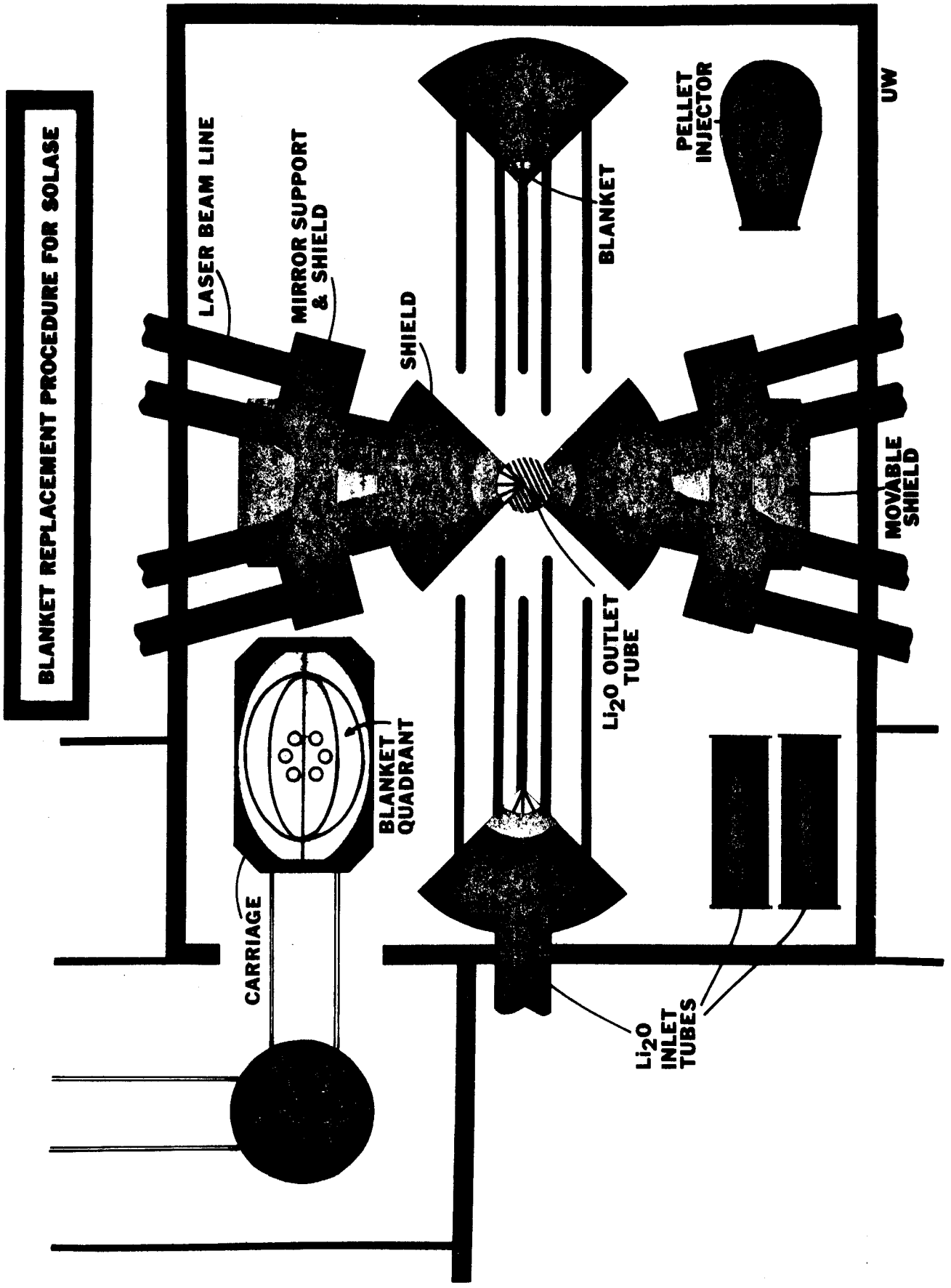
BLANKET REPLACEMENT PROCEDURE FOR SOLASE
LASER BEAM LINE
MIRROR SUPPORT & SHIELD
SHIELD
BLANKET
PELLET INJECTOR
UW
MOVABLE SHIELD
Li_2O OUTLET TUBE
BLANKET QUADRANT
CARRIAGE
Li_2O INLET TUBES

Fig. I-C-21

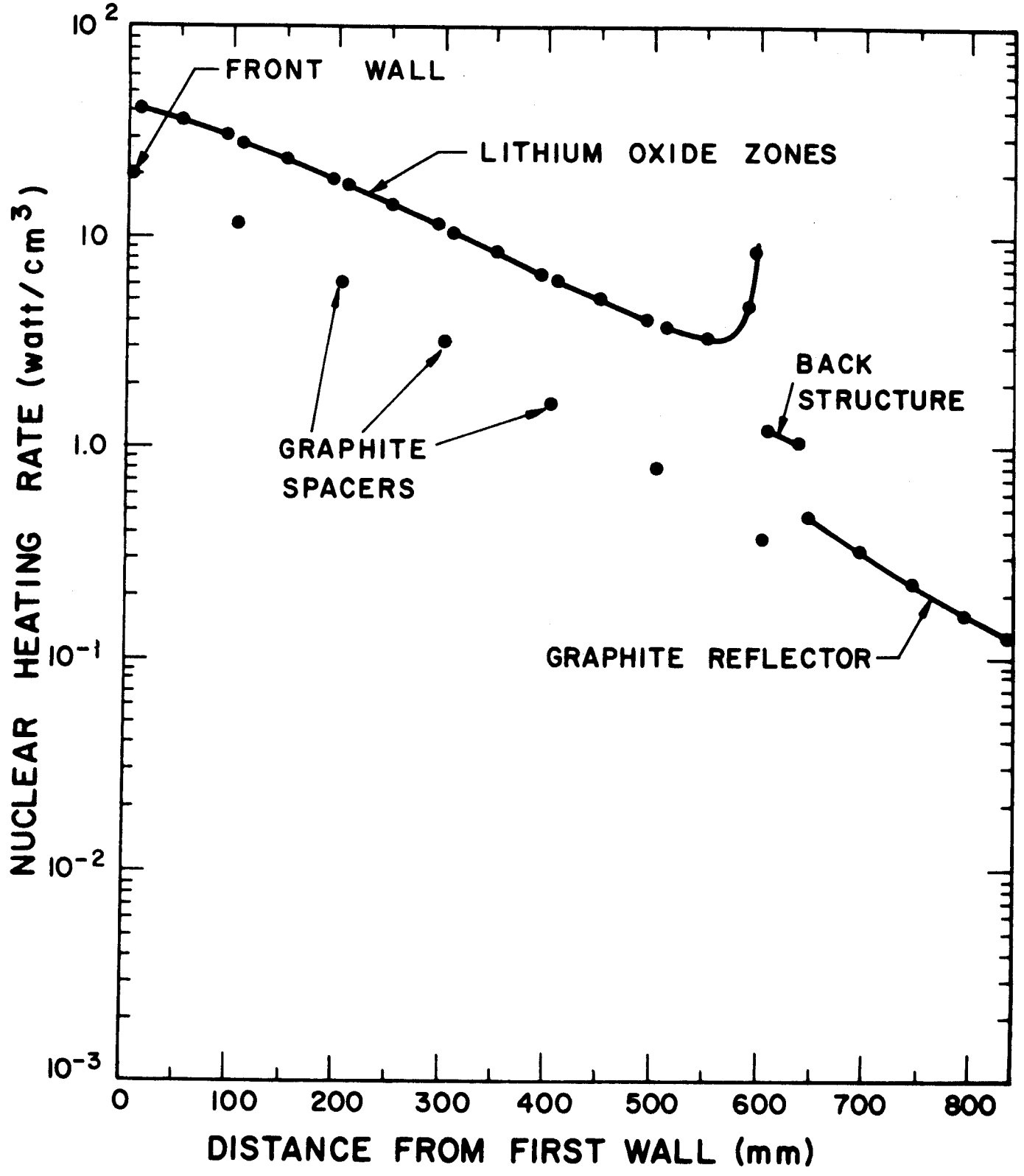
FRONT WALL
LITHIUM OXIDE ZONES
BACK STRUCTURE
GRAPHITE SPACERS
GRAPHITE REFLECTOR
NUCLEAR HEATING RATE (watt/cm³)
DISTANCE FROM FIRST WALL (mm)
10²
10
1.0
10⁻¹
10⁻²
10⁻³
0
100
200
300
400
500
600
700
800

Fig. I-C-22

are low so that structural erosion does not appear to be a problem. The aluminum alloy back structure on which the blanket is supported is water-cooled and is maintained at 150°C. The power removed at such a low temperature is small and is added to the steam cycle through a feed water heater.

The blanket design used in SOLASE offers many advantages, including low cost, low weight, low induced radioactivity levels, the potential for hands-on maintenance, modular construction, low pressure, adequate breeding, low tritium inventory and leakage, and sufficiently long life. It is particularly suitable for ICTRs since the vacuum requirements are not stringent and it is superior to blankets with metallic first walls and protective liners inasmuch as the neutron wall loading in such designs is limited by the ability to radiate the ion and photon energy deposited in the liner to the cold first wall. These designs, however, may be more suitable for magnetic confinement systems. While the Li_2O particles act as a good heat transport medium to remove the heat generated within the blanket (high ρC_p/circulating power), the heat transfer coefficient between the first wall and the particle stream is quite low. This makes it possible to operate the front wall at temperatures significantly different from those of the blanket coolant. The latter are dictated by power cycle efficiency requirements while the former can be selected on the basis of radiation damage considerations. For our graphite blanket, the front wall temperature is sufficiently high to avoid runaway swelling. On the other hand, for blankets with metallic first walls and protective liners, the first wall can be maintained at temperatures well below those of the Li_2O stream without having an adverse effect on the overall thermal efficiency of the

plant.[9] In such systems, the first wall can be separately cooled and maintained at ~300°C which would significantly reduce swelling and increase wall life. Hence, the use of lithium oxide as a coolant and breeder in fusion systems (both inertial and magnetic confinement) allows greater flexibility in system design.

Shielding of the reactor cavity does not pose special problems because of the simple geometries involved. A free-standing concrete shield approximately 3.5 m thick with a 10 cm thick outside layer of lead (to stop the gammas) is used. The concrete is reinforced with aluminum alloy to minimize long-term radioactivity. It is divided in quadrants with two mobile sections to allow access to the blanket during replacement. The two other quadrants contain the laser beam ports and suppression chambers. The cost of shield materials is less than $\$5 \times 10^6$ and the anticipated dose rates outside the shield during reactor operation are sufficiently low (~1 mrem/hr).

The possibility of using a water-soluble lead compound (e.g. lead acetate) enclosed in aluminum alloy containers as a shield has also been investigated. Drainage of the solution into shielded (underground) containers during blanket replacement allows easy access. The required shield thickness in this case will be somewhat less than concrete shields. This shielding concept is attractive and requires further attention to determine its cost effectiveness.

I-C-8. Radiation Damage

I-C-8-a. Radiation Effects to Graphite

Polycrystalline graphites exhibit large dimensional changes after irradiation. These dimensional changes depend strongly on the raw material and the fabrication process used. They are characterized by an initial densification followed by an expansion at higher radiation doses and the behavior can be explained by the dimensional changes of the graphite crystallites that make up the graphite particles and by the closure and expansion of pores and microcracks. There are three different types of pores and the crystallites themselves contain micropores which contribute the volume ΔV_{p_1} to the total porosity. Many crystallites are contained in a single graphite particle and transgranular microcracks between the crystallites occupy a volume ΔV_{p_2}. In turn, the particles are held together by a binder, such as coal-tar pitch, and they may enclose intergranular microcracks which take up the volume ΔV_{p_3}.

During irradiation the individual crystallites expand in the c-direction, i.e. perpendicular to the basal planes, but contract parallel to the basal planes (or in the a-direction). As a result, the different pore volumina change with time. Initially the dimensional changes are produced by a partial closure of all three pore types, but as the crystallites continue to expand in the c-directions, new and old microcracks open up causing ΔV_{p_2} and ΔV_{p_3} to increase.

A phenomenological equation describing the porosity change as a function of fluence is

$$P - P_o = \frac{\Delta V}{V} = \frac{A\,F^{n+1}}{BP+F^n} - P_o\,[1 - \exp\,(-CF)]\,, \qquad (9)$$

where F is the radiation dose, P_o is the initial porosity, P is the porosity, and A, B, C and n are material parameters which must be determined by fitting this equation to the experimental data. The particular dose dependence chosen for the first term is based on the assumption that the volumetric expansion will eventually become linear with dose. At present, there are no data at high doses available that either contradict or confirm this conjecture. However, it appears reasonable to assume that the expansion of the crystallites along their c-axis must eventually be linear with dose. No attempt was made to fit Eq. (9) to any particular graphite but rather we strived for a description that is generic rather than specific. By inspection of available data and various equations of the form of Eq. (9), it was determined that the Eqn. (10) is most compatible with the entire body of data utilized.

$$P - P_o = \frac{\Delta V}{V} = \frac{AF^3}{P_o/C+F^2} - P_o\,[1 - \exp\,(-CF)]\,. \qquad (10)$$

This equation contains only two parameters, A and C, which must be determined from experimental data. The most convenient way to accomplish this is to compare the initial shrinkage rate and the final growth rate with the data. This was done for both low and high growth graphites. For the low growth graphites, we find

$$A = \left.\frac{dP}{dF}\right|_{F\to\infty} = \{(\frac{800}{T})^2 + (\frac{T}{1250})^{12}\}^{-1}\ \{\frac{\Delta V}{V}\ (\%/\text{dpa})\} \qquad (11)$$

and

$$C = -\frac{1}{P_o}\frac{dP}{dF}\Big|_{F=0} = 0.01\ (\frac{T-700}{170})^2 + 0.02 \qquad (12)$$

where T is the temperature in ^oC.

Concurrent with the dimensional changes, graphite also exhibits radiation-enhanced creep when subject to either external loads or self-generated stresses due to non-uniform dimensional changes. The creep rate $d\varepsilon/dF$ of graphite under irradiation is a linear function of the stress σ, i.e.

$$\frac{d\varepsilon}{dF} = K\sigma \qquad (13)$$

where K is the creep coefficient. Available data can be correlated with the expression

$$KE_o = \frac{f(T)}{\dot{F}} + g(T) \qquad (14)$$

where E_o is Young's modulus and f(T) and g(T) are linear functions of the temperature given by

$$f(T) = (1.775 + 0.0185*T) \times 10^{-8}\ sec^{-1} \qquad (12)$$

and

$$g(T) = (-0.544 + 0.00403*T)\ dpa^{-1}\ . \qquad (13)$$

Fast neutron irradiation also produces changes in both the elastic modulus and the ultimate strength of the graphite. In our analysis, we have used the results of Christensen, who gives as a lower bound for the shear modulus, G, the expression

$$\frac{G}{G^*} = \{1 + \frac{15(1-\nu)(7+5\nu)(p^{7/3}-1)p^{1/3}}{(7-5\nu)(7+5\nu)(1-p)(p^{7/3}-1)+126p(1-p^{2/3})^2}\}^{-1} \qquad (14)$$

where ν is Poisson's ratio, G* the shear modulus of the theoretically dense material, and p is the volume fraction of the pores, i.e. p = P/100. In order to compute a lower bound for E/E*, it would be necessary to utilize the lower bound for the ratio K/K* for the bulk modulus. However, since G is much more affected by the porosity than K, we use the approximation $E/E^* \sim G/G^*$.

Finally when graphite is subjected to alternating loads, fatigue fracture occurs at stress levels below the static strength of the material. In general the lower the stress amplitude produced by the alternating load, the greater is the number of load cycles the material can endure before fracture. Examination of fatigue data shows that a long fatigue life can be obtained if the stress amplitude does not exceed 65% of the static strength. We find it necessary to modify this rule somewhat since the fatigue life depends also on the mean stress. It appears prudent to adopt the conservative rule that the tensile stress level for fatigue loading should not exceed one-half of the static tensile strength. This rule has been employed in the stress analysis of the blanket structure as a design criterion to determine lifetime.

I-C-8-b. Stress and Failure Analysis for the Blanket--Determination of Blanket Lifetime

A lifetime analysis of the blanket structure is carried out according to the following guidelines illustrated by the flow-diagram in Fig. I-C-23. The central criterion for determining the lifetime was that the stress at any location in the blanket structure must be lower than one-half of the tensile strength at that location. This must be true for the stress distribution during reactor operation as well as during a shutdown. To implement this procedure, it is necessary to first specify the boundary conditions and the distribution of temperature and atomic displacement rates. Next the thermal stress distribution is computed and a test is performed to determine if the strength is exceeded. Then for a short time step, the change of the porosity, elastic modulus, and static strength is calculated. In addition the irradiation creep strains are computed for this time interval and the new stress distributions for on and off power are evaluated. Comparison between stresses and strength is made again. This cycle is repeated until the failure criterion is satisfied at some location in the blanket structure. This procedure represents a general, self-consistent approach to the determination of the lifetime of fusion reactor components. However to carry this procedure out in detail would have required an inelastic finite-element analysis which was judged to be beyond the scope of this design study. Therefore we selected a part of the blanket structure for the analysis which is subject to the largest temperature and neutron flux gradients. Clearly this part is one of the radial dividers in a blanket module. To further simplify the

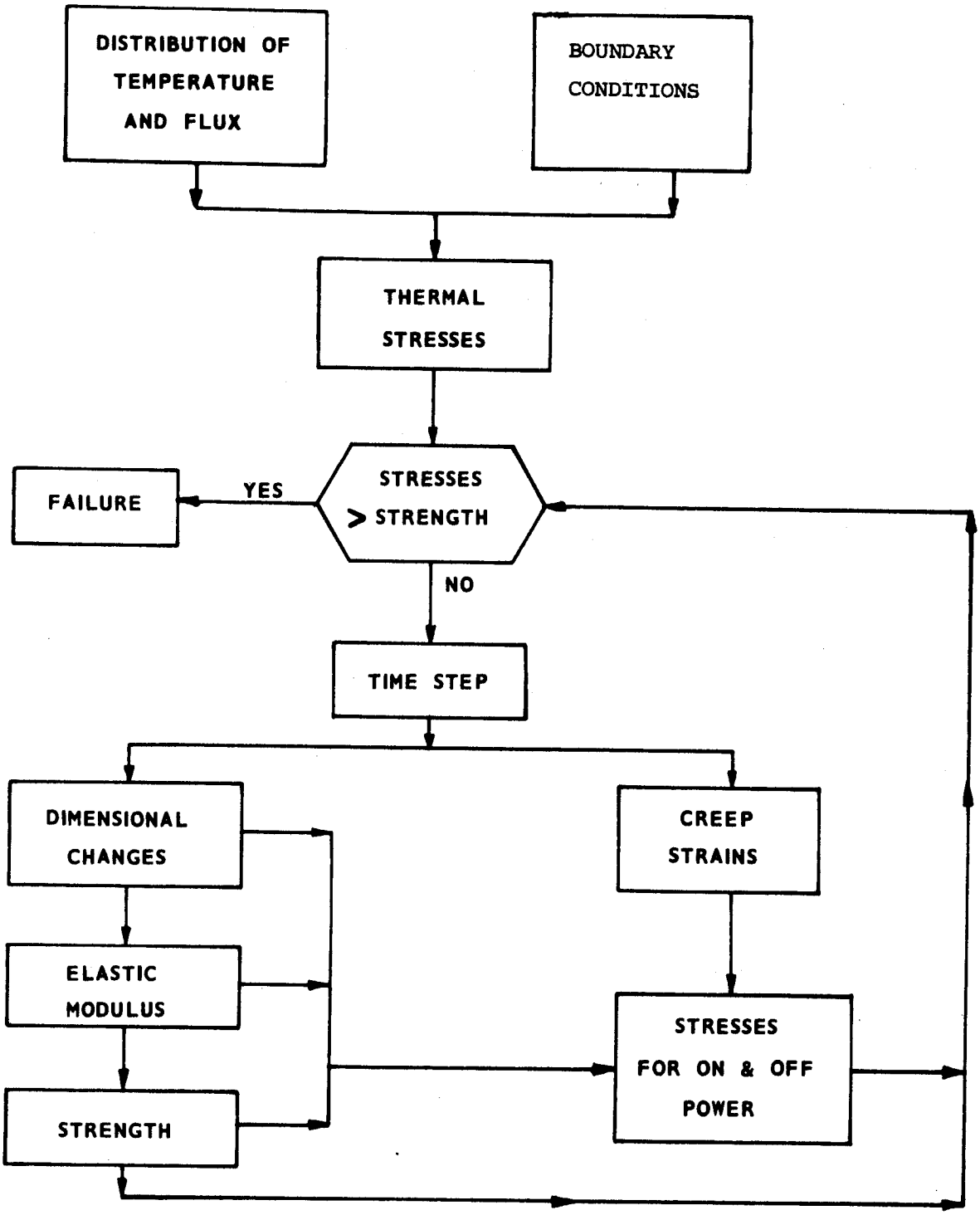

Fig. I-C-23 Flow Diagram for the Lifetime Analysis Code

analysis the radial divider was modelled as a thin, annular disk to simulate in an approximate fashion the circumferential constraints imposed on the blanket sections when they are connected to form the entire reactor cavity.

The sequence of Figs. I-C-24a to 24i shows the radial distribution of the hoop stress σ_θ for on and off power together with the distribution of one-half of the tensile strength for a graphite with 5% initial porosity. One can see from Figs. I-C-24b and 24c that the thermal stresses relax rapidly as a result of irradiation creep. After about a month of operation, densification of the graphite commences where the temperature and neutron flux is high. This gives rise to a small tensile stress on power at the inside of the disk, as seen in Fig. I-C-24d. Further irradiation leads then to expansion, particularly at the radial location $r \cong 6.01$ m where the temperature is around $1000^{o}C$, the range of maximum expansion. At this location compressive stresses build up as seen in Fig. I-C-24e.

The increase in porosity at this location is reflected in the reduction of the strength. This degradation of the strength becomes more pronounced with irradiation as illustrated by Figs. I-C-24f to 24i. It is seen that after about <u>one year</u> of operation the hoop stress for the off-power case approaches the value of 1/2 of the tensile strength near the inner boundary. It is important to emphasize that the analysis summarized here shows that the stresses during shutdown are the controlling factor rather than the stresses during operation.

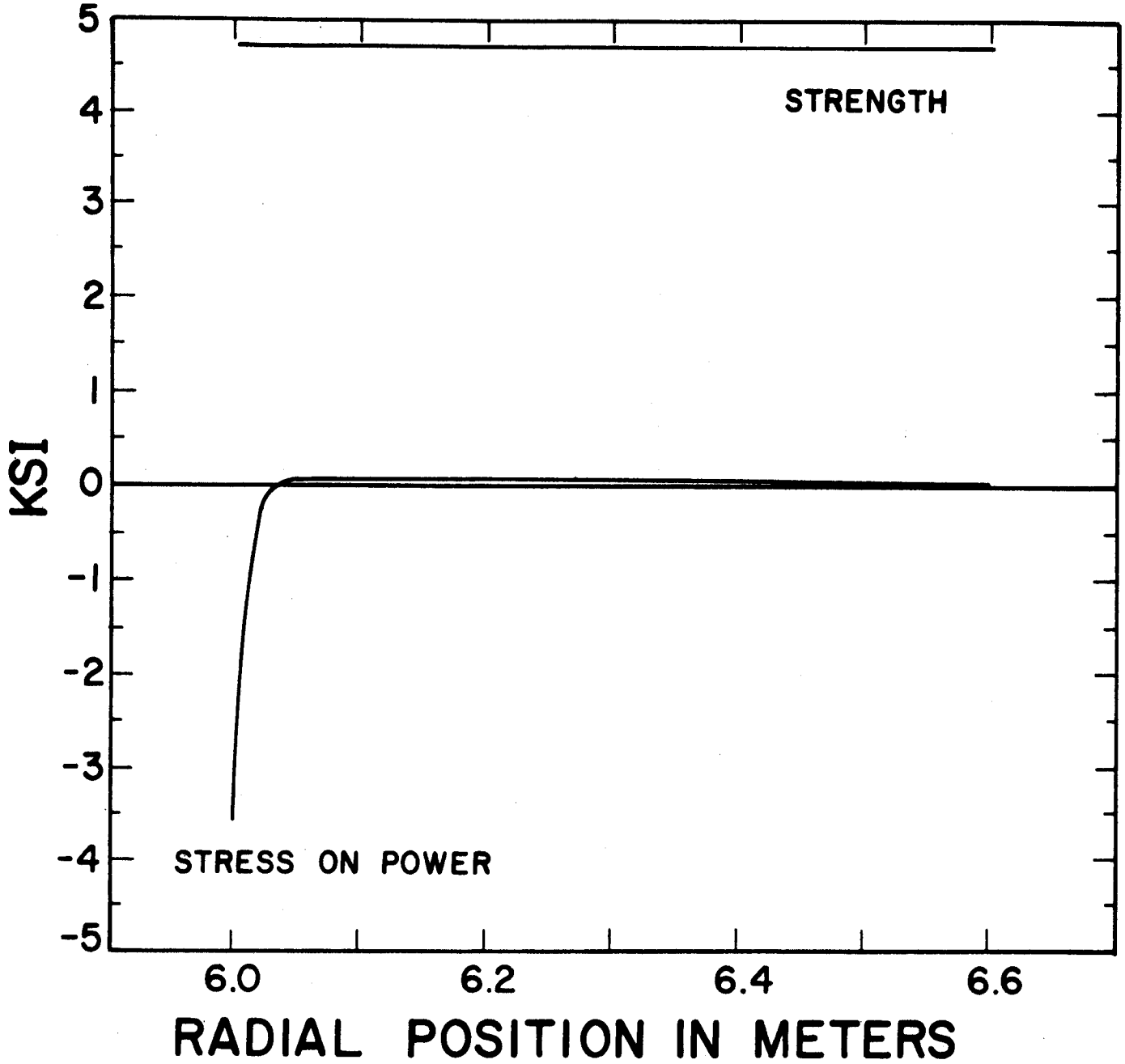

Fig. I-C-24a Hoop Stress and Tensile Strength Distribution in the Radial Divider made of Low-Growth Graphite with 5% Initial Porosity; After Start-up

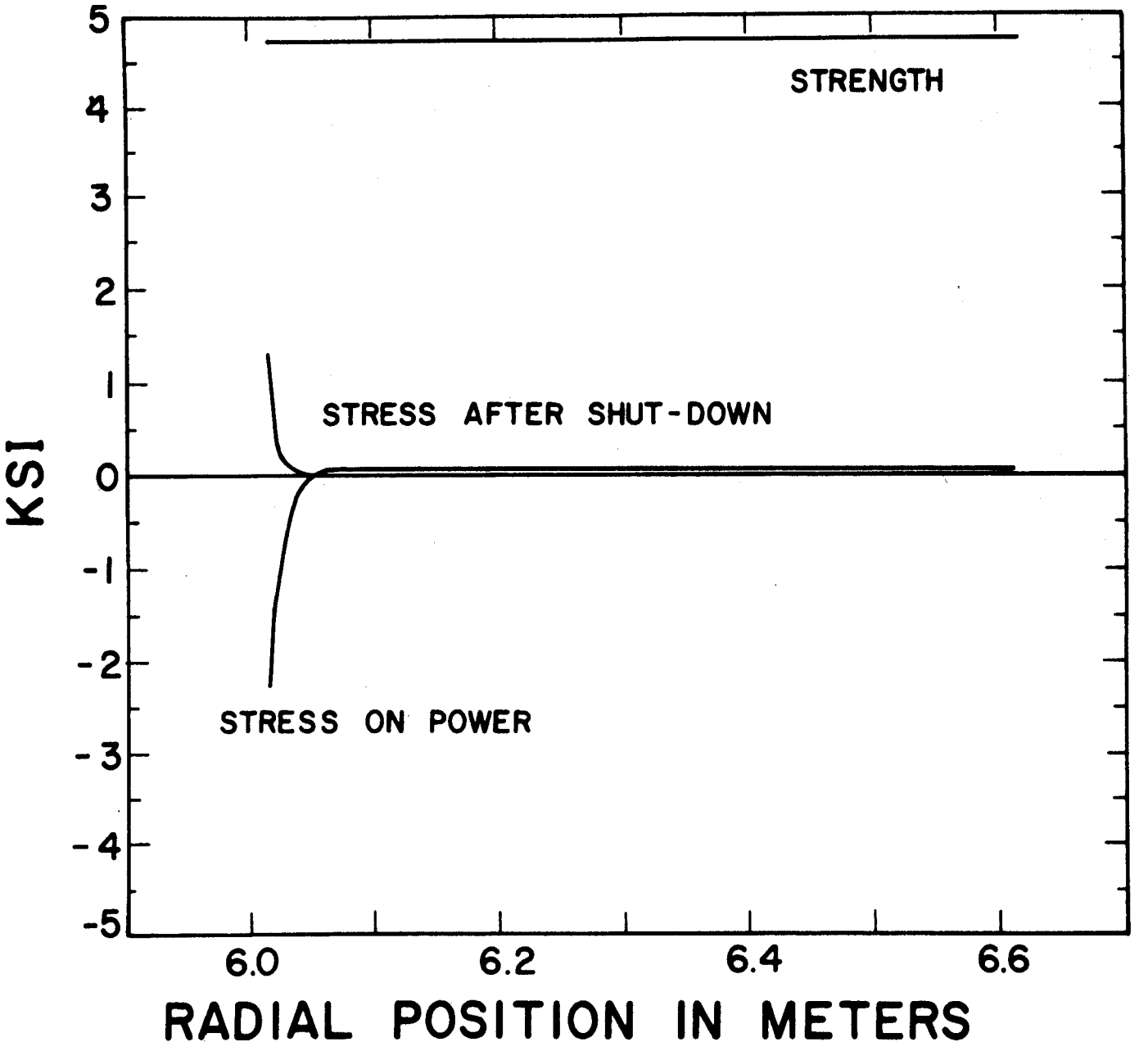

Fig. I-C-24b After 17.5 Hours of Irradiation

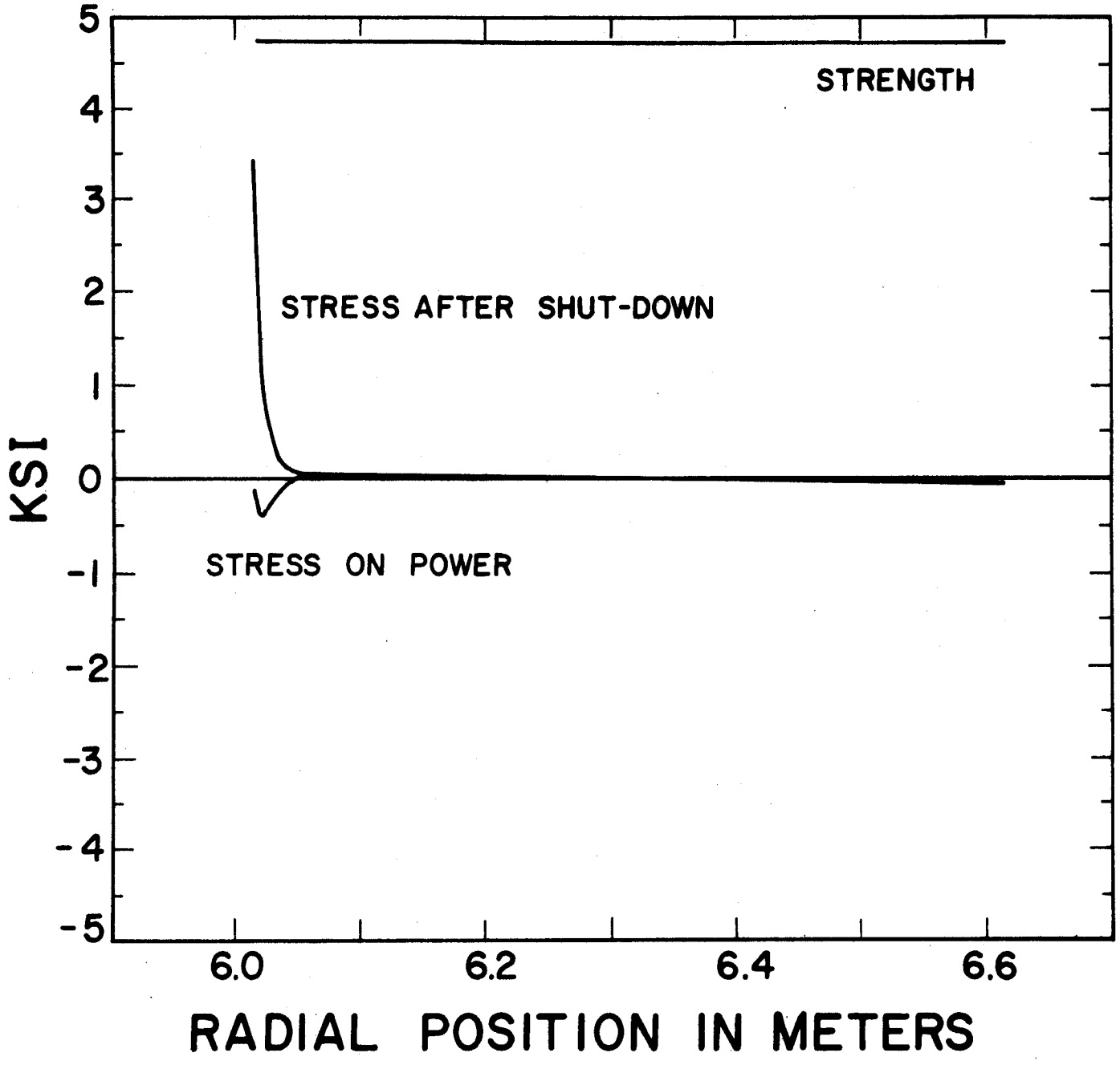

Fig. I-C-24c After 3.6 Days of Irradiation

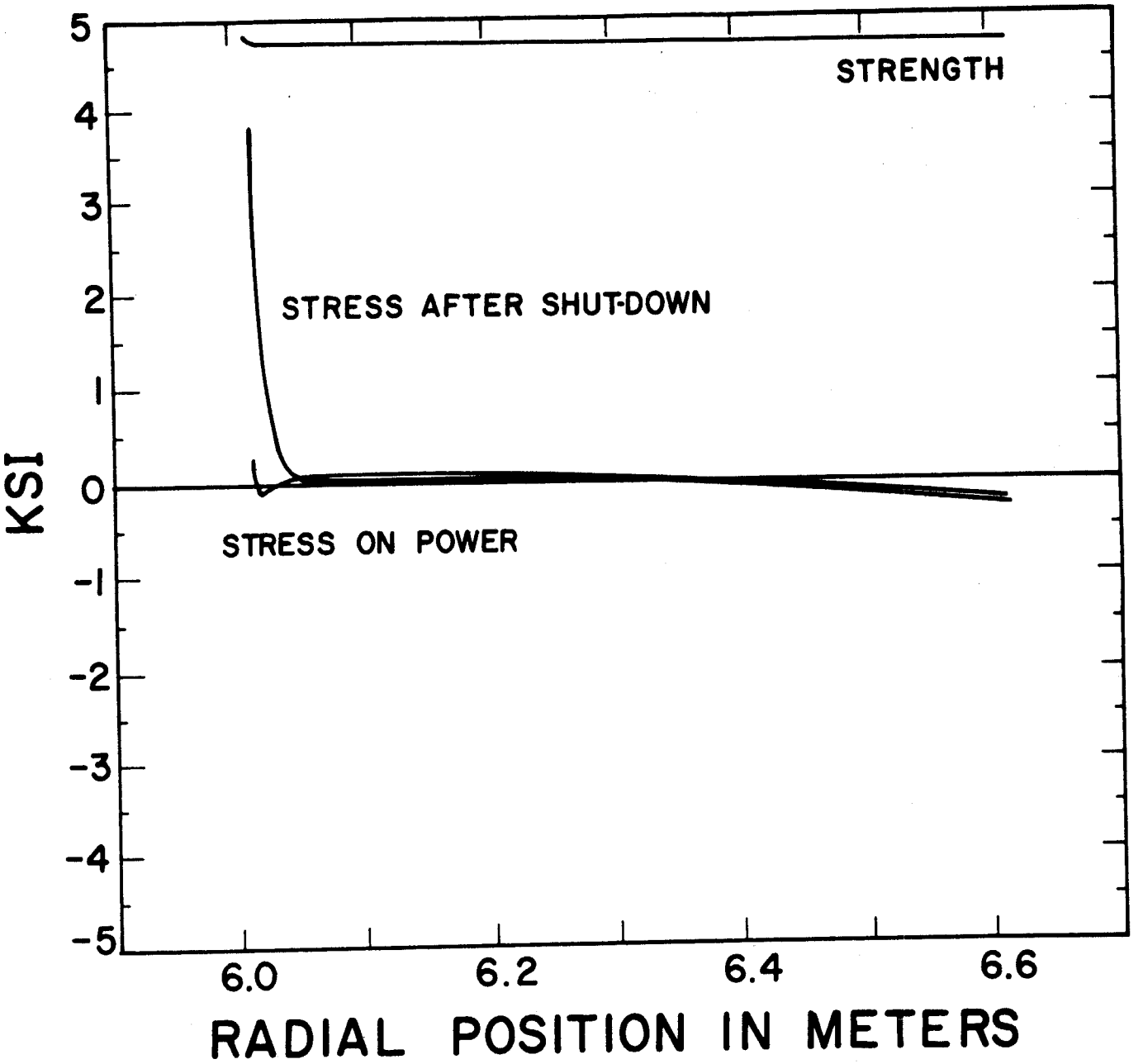

Fig. I-C-24d After 36.5 Days of Irradiation

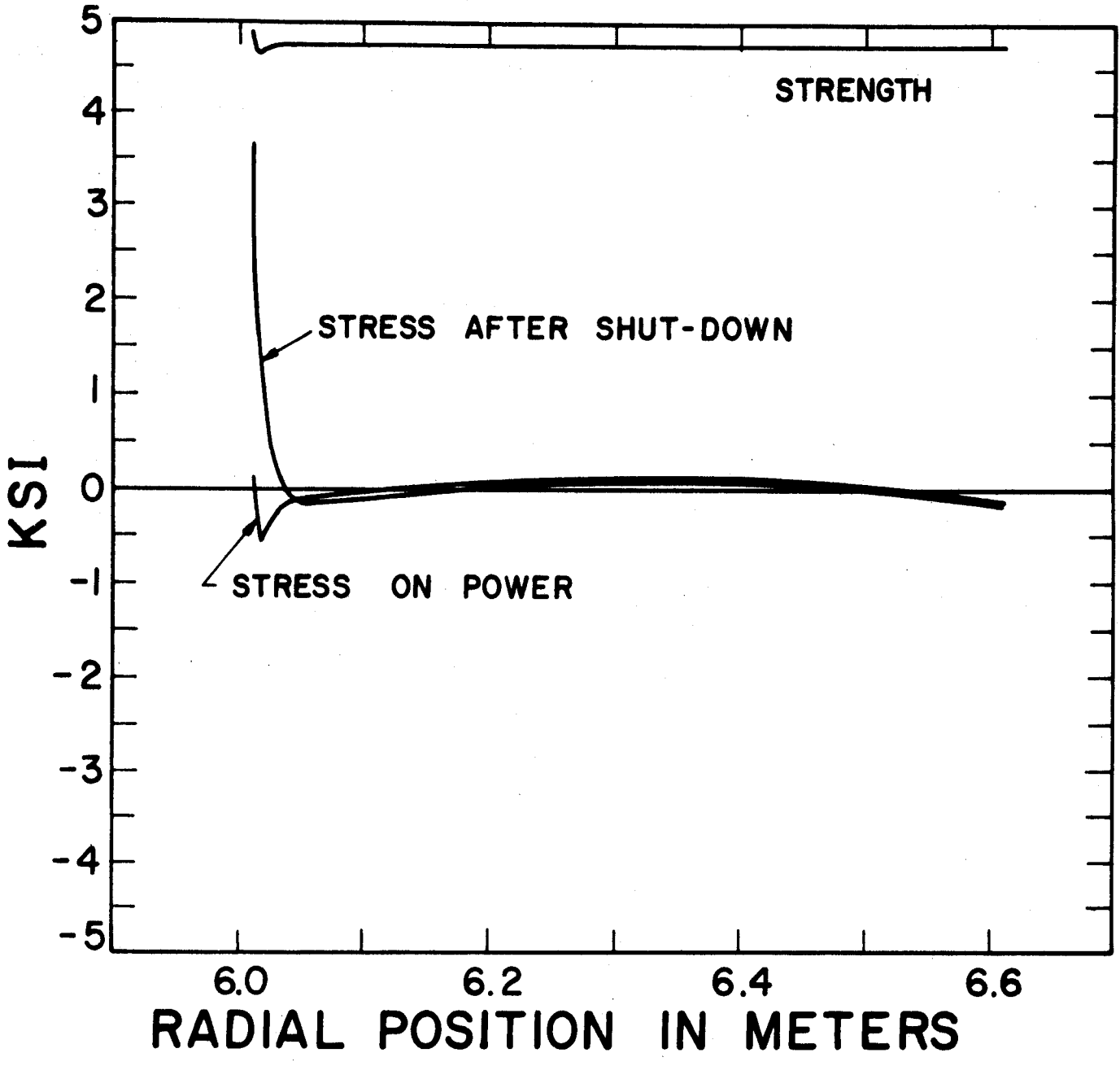

Fig. I-C-24e After 0.2 Years of Irradiation

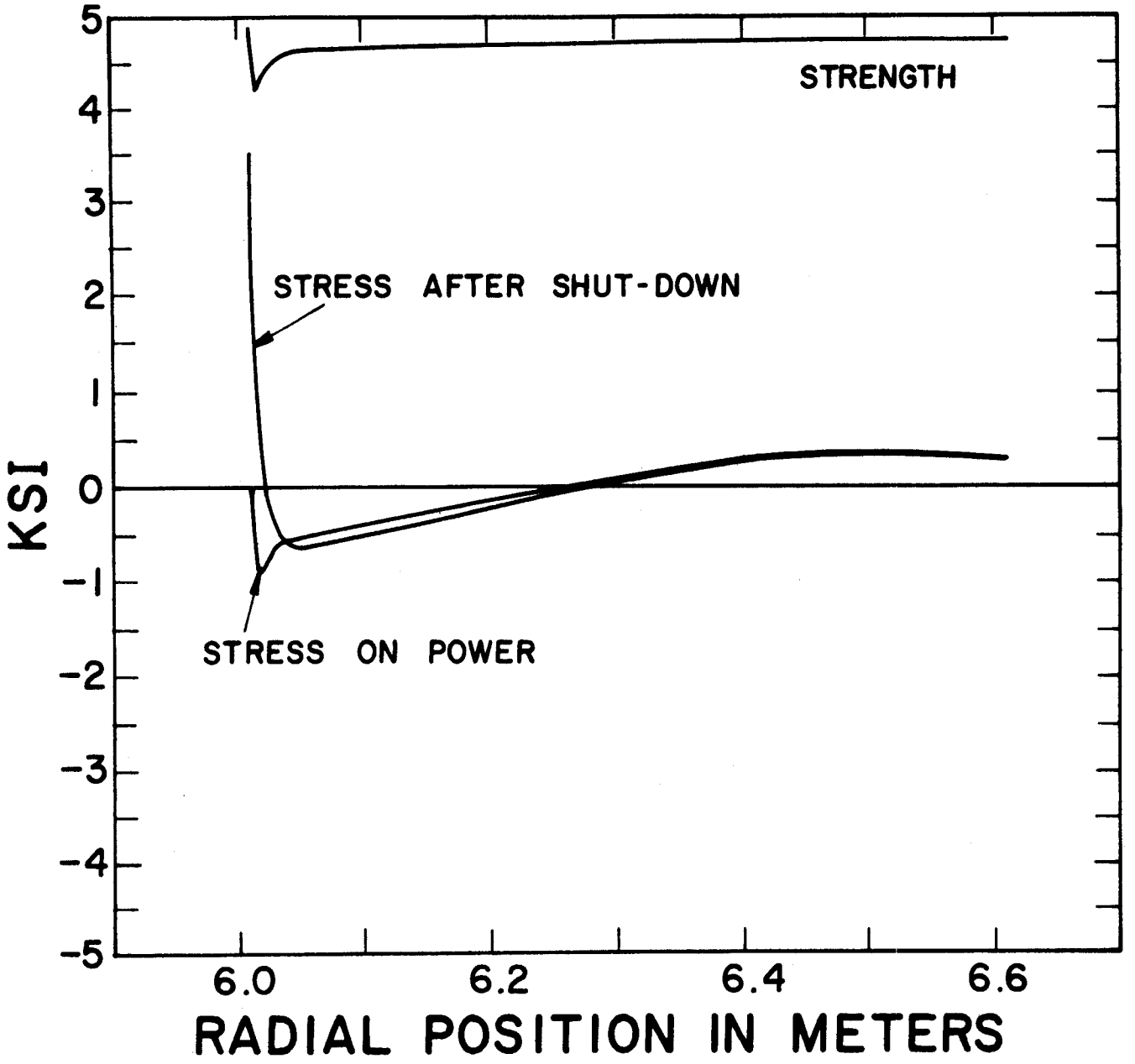

Fig. I-C-24f After 0.4 Years of Irradiation

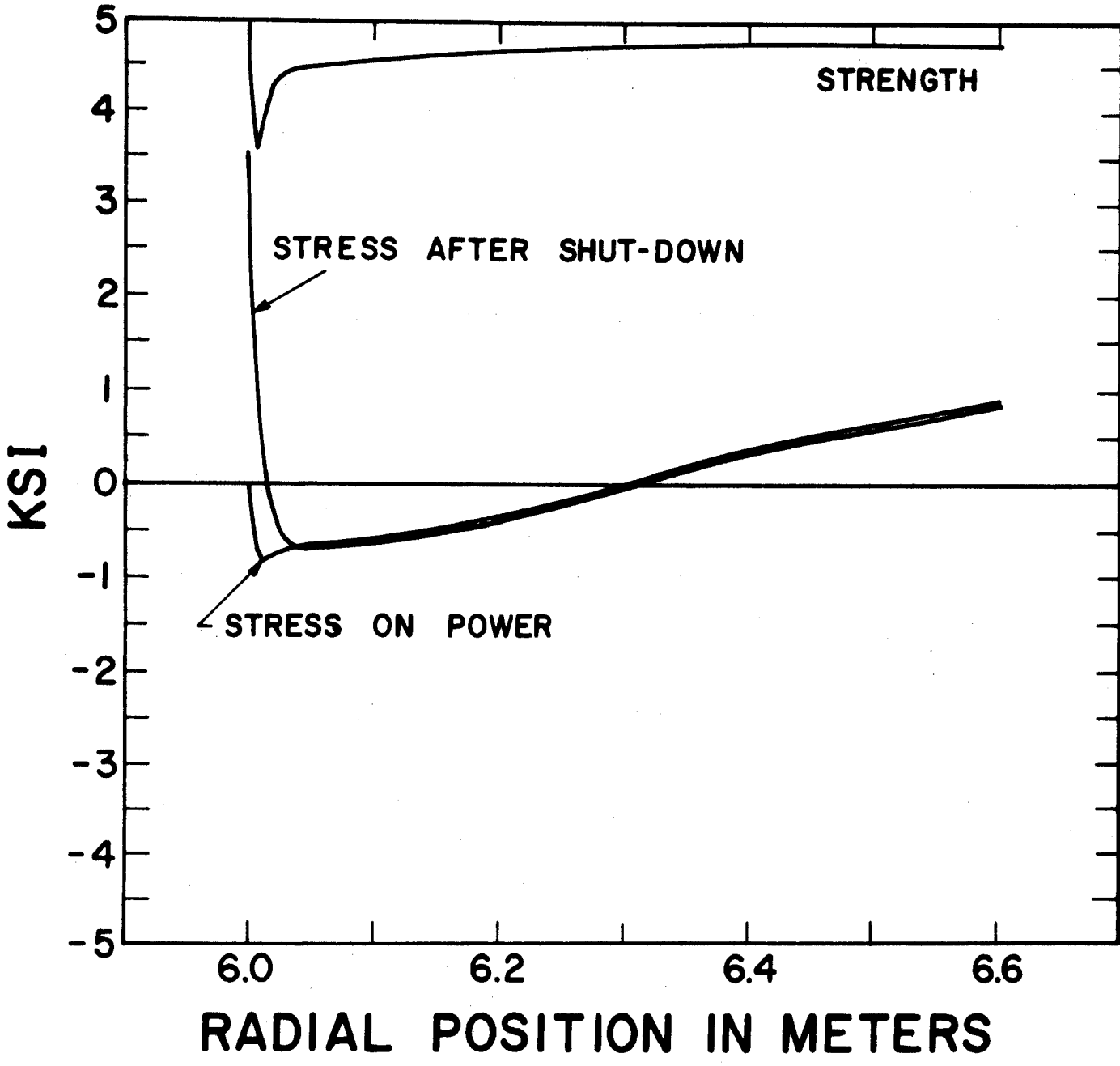

Fig. I-C-24g After 0.6 Years of Irradiation

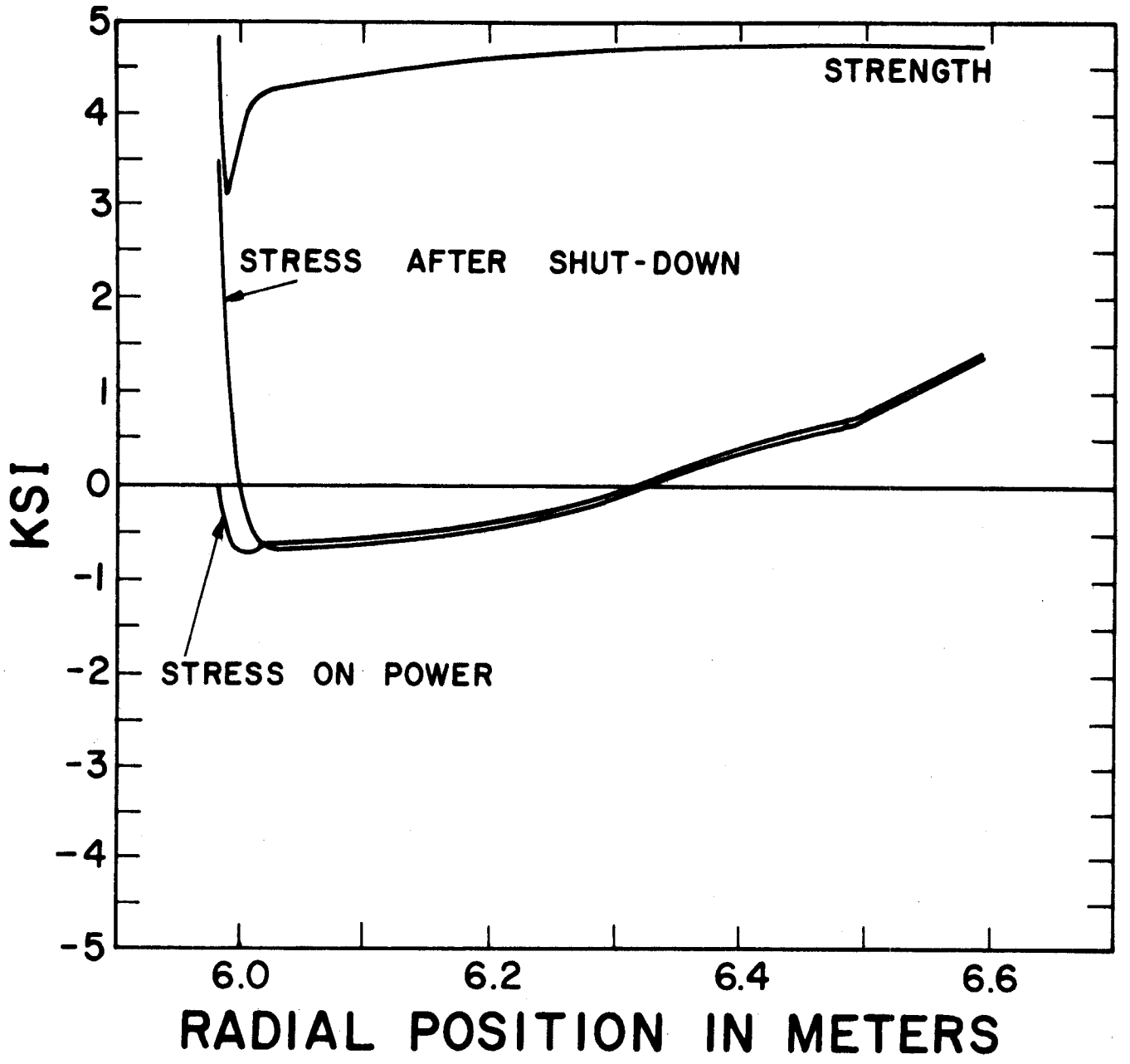

Fig. I-C-24h After 0.8 Years of Irradiation

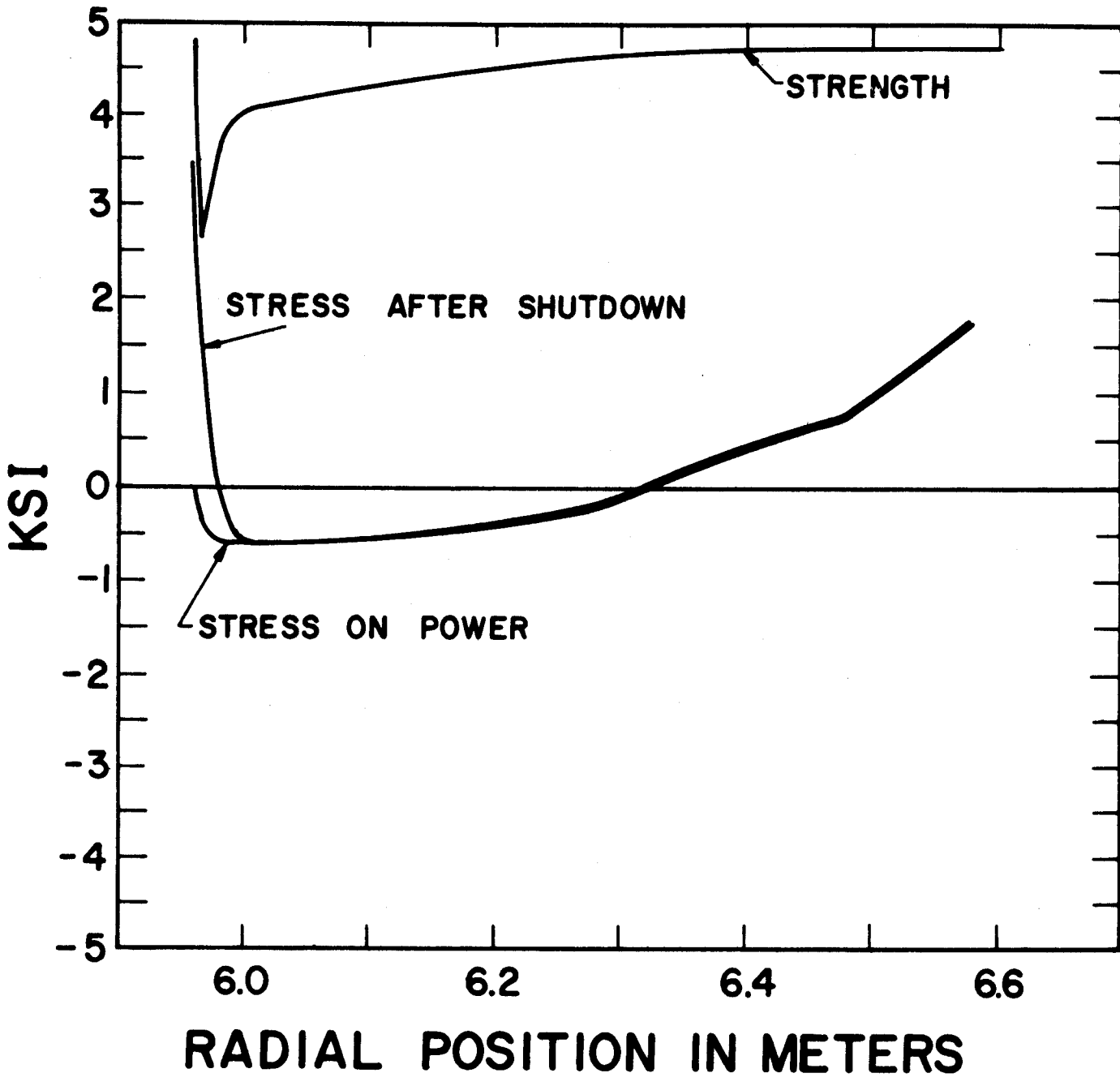

Fig. I-C-24i After 1.0 Year of Irradiation

The case illustrated by the Figs. I-C-24a to 24i is for a rather dense graphite with only 5% initial porosity. Present-day nuclear graphites have typically an initial porosity of 20%. For such a graphite material, the stress-distribution upon shutdown exceeds one-half of the strength after a short irradiation period of only 3.6 days. The reason for this situation is that thermal stress relaxation and densification have produced a tensile hoop stress on the inner radius of the disk in excess of the safe limit. This problem persists up to an irradiation time of 36.5 days. After this time, further irradiation removes the problem and after about one year, the hoop stress near the inner boundary of the disk approaches again the value of 1/2 of the tensile strength.

I-C-8-c. Radiation Effects to Dielectric Coatings on Mirrors

The use of copper as the reflecting surface is acceptable so long as the laser wavelength is greater than about 8000 $\mathring{A}$. We have found radiation damage to the Cu not to be a serious problem. However many of the more promising target designs call for a laser wavelength in the range 2000-5000 $\mathring{A}$. At such short wavelengths, bare metal mirrors become absorbing as shown by the plot of reflectivity versus wavelength in Fig. I-C-25. Instead dielectric mirrors must be used. A dielectric mirror consists of a stack of many layers of alternating high and low index material on a substrate such as glass. Typically each layer has a thickness equal to one-quarter of the laser wavelength.

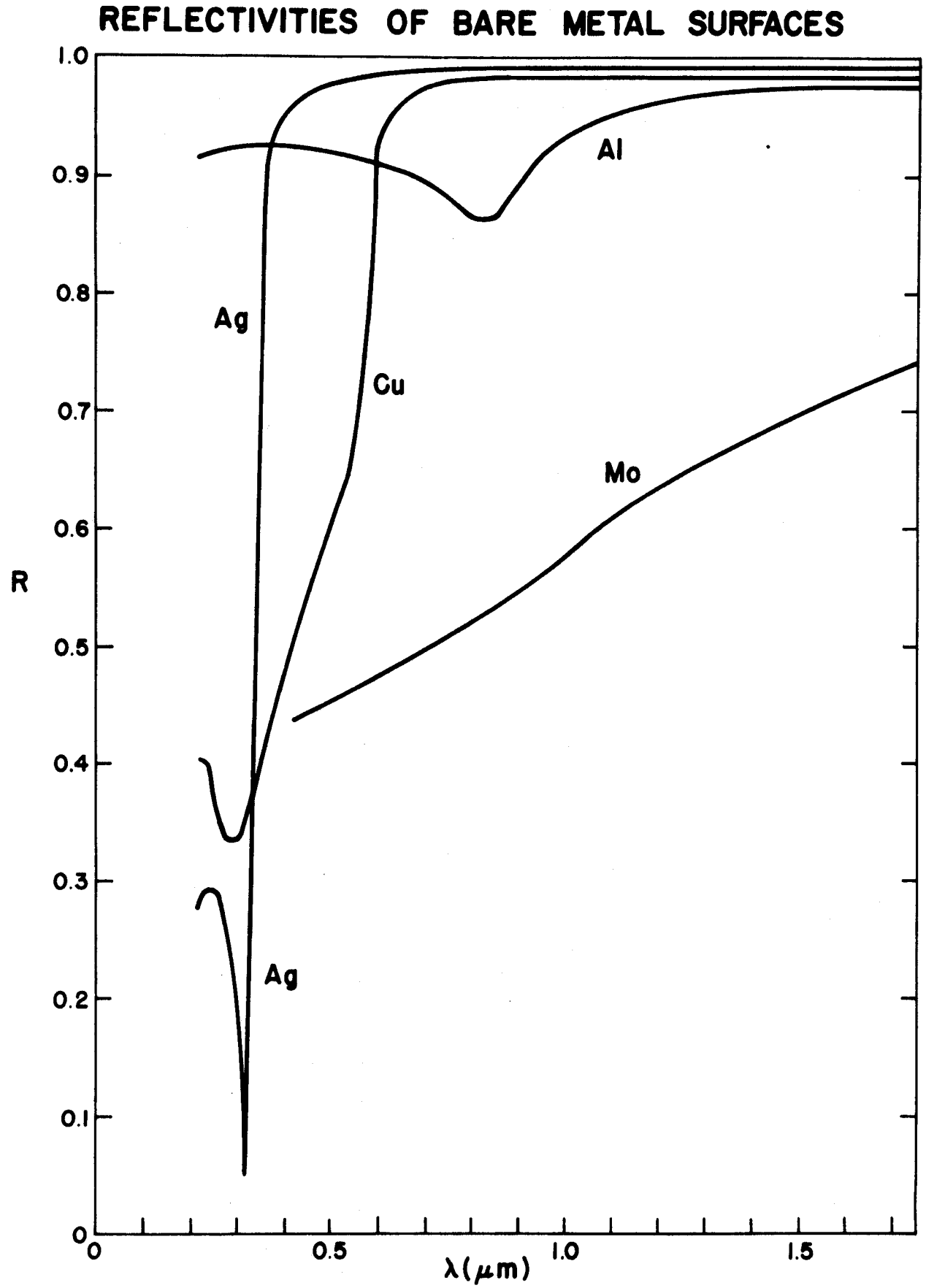
REFLECTIVITIES OF BARE METAL SURFACES
1.0
0.9
0.8
0.7
0.6
0.5
0.4
0.3
0.2
0.1
0
R
Al
Ag
Cu
Mo
Ag
0
0.5
1.0
1.5
λ(μm)

Fig. I-C-25

As the list of candidate materials (Table I-C-11) for dielectric coating materials shows they are either ionic crystals or covalently bound insulators. Both groups, in particular the first one, are highly susceptible to color center formation under neutron, ion, and X-ray irradiation. Each color center is associated with a particular lattice defect which introduces additional electronic energy levels within the band gap of the perfect crystal. These levels can be excited by photo excitation and ionization so that each type of color center produces a characteristic optical absorption band. The great variety of color centers essentially cover the photon energy gap between IR and UV that is normally transparent to light. The associations of absorption bands to color centers in relatively pure alkali halides are given in Table I-C-12. Not listed in this table are the V_k and the H centers, both of which will anneal out at temperatures below room temperature. The H center is the equivalent of the interstitial defect in metals. The wavelength of the various absorption peaks in alkali halides are listed in Table I-C-13. The locations of some of these peaks can be related to the lattice parameter of the crystal. This correlation, the Mollwo-Ivey law, is shown in Fig. I-C-26. It can provide a tool to predict absorption peaks in other alkali halide crystals for which no data exist. For other ionic crystals the Mollwo-Ivey law can also be used, but with less accuracy.

Crystals with constituents of multiply charged ions contain additional types of color centers. For example, in the alkaline earth oxides the anion vacancy center can be in either the singly or doubly charged state, and one has both "one-trapped" (F^+-center) or "two-trapped" (F-center) color centers. Their absorption bands are listed in Table I-C-14.

Table I-C-11

Candidate UV Coating Materials

	High Index	Low Index
2500 Å	•ThO_2 (2.05)	BeF_2 (1.33)
	CsI (2.00) (76% ionic)	•NaF (1.35)
	RbCl (1.87) (ionic)	KF (1.38) (80% ionic)
	•MgO (1.85)	LiF (1.4) (90% ionic)
	KI (1.82) (75% ionic)	•MgF_2 (1.41) (rutile ionic structure)
	Al_2O_3 (1.72-1.80)	$3NaF \cdot AlF_3$ (1.4) (ionic)
	•ThF_4 (1.75)	SiO_2 (1.5)
	LaF_3	
	NdF_3	
3500 Å	All of Above	All of Above
	•ZrO_2 (2.10) (fluorite ionic structure)	
	•HfO_2 (2.05) (fluorite ionic structure)	
	Sb_2O_3	
	PbF_2 (1.85) (fluorite ionic structure)	
	C (diamond) (2.1)	

Table I-C-12

Absorption Band and Defect in Pure Alkali Halides

α band (F^+)	A halogen ion vacancy which modifies electronic transitions of the lattice.
β band	A lattice excitation near an F centre.
F band (F)	A halogen ion vacancy that has trapped an electron.
K, L_1, L_2, L_3 bands	Absorption produced by transitions of the F centre to higher states.
F_A, F_B bands	(Sometimes labelled A and B) - absorption bands which arise from impurity alkali ions at one of the six neighbouring metal ions sites of an F centre. (There are two bands because of the reduced symmetry of the centre, and the dipole may lie along the axis through, or perpendicular to, the impurity ion).
F' band (F^-)	A halogen ion vacancy that has trapped two electrons.
M band (F_2)	A pair of adjacent F centres.
R bands (F_3)	A triangular array of three F centres. Although possible arrangements are a linear chain of three vacancies, an L-shaped set in the (100) plane or a triangular set in the (111) plane, the model currently believed is the latter (111) arrangement.
N bands (F_4)	Four F centres linked together. Two possible configurations are a parallelogram of vacancies in the (111) plane which may produce the N_1 absorption and a tetrahedron of vacancies which may give the N_2 absorption.
M', R', N' bands (F_2^-, F_3^-, F_4^-)	By analogy with the F centre the M, R or N centres may trap an additional electron. Some absorption bands have been associated with these defect models and are discussed in the review article of F aggregate centres by Compton and Rabin.

Table I-C-13

Wavelengths of the Absorption Peaks Arising From Various Trapped-Electron and Trapped-Hole Centers in the Alkali Halides*(mμ)

Center	L_3	L_2	L_1	K	F	F'	F'	R_1	R_2	M	α	β	H	V_1	V_K	V_2	V_3	V_4
Temperature of Observation (^{0}K)	93	93	93	93	300	140	170	300	300	300	~90	~90	4	77	77	300	300	90
LiF					250			313	380	444					348			
LiCl					385				580	650								
NaF					341				415	505	131	127						
NaCl					458	510		545	596	725	174	168	330	345		223	210	
NaBr					540						199							
NaI					588													
KF					455				570									
KCl	251	288	344	457	556		750	658	727	825	177	166	335	356	365	230	212	~254
KBr	276	316	374	525	625		700	735	790	918	201	192	380	410	385	265	231	275
KI	326	382	447	585	689						238	226			404			
RbCl	279	335	402	523	609													
RbBr	300	362	435	593	694			805	859	957	205	196						
RbI	338	413	506	646	756						240	229						
CsCl					605													
CsBr					680													

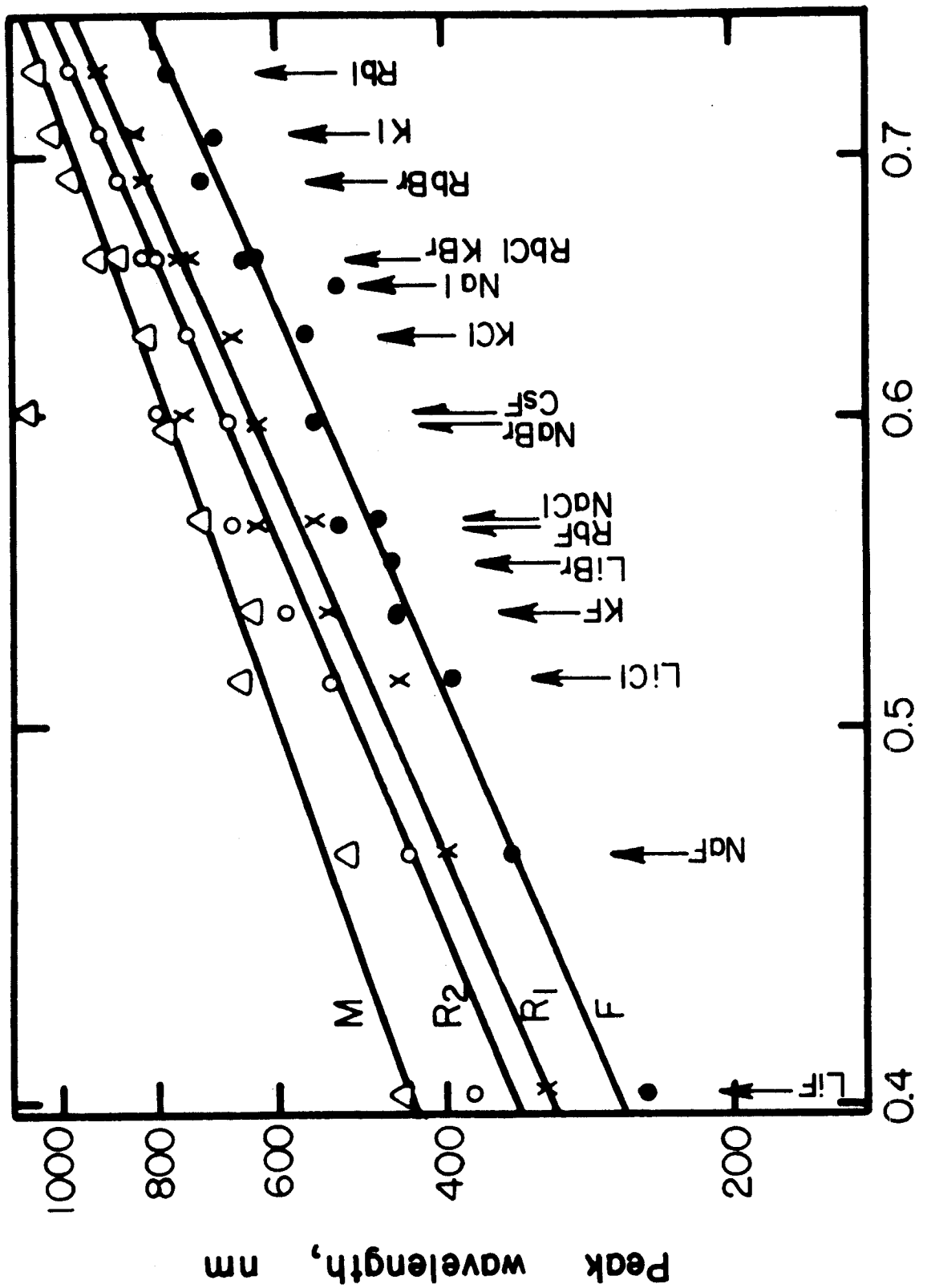

Fig. I-C-26. Mollwo-Ivey law for F, R_1, R_2, and M centers in the f.c.c. alkali halides

Table I-C-14

	Peak Position, nm		
	Two $e^-(F)$	One $e^-(F^+)$	Lattice Constant d
MgO	247	251	0.4203 nm
CaO	400	345	0.4797 nm
SrO	497	400	0.5144 nm
BaO	620	620 or 485	0.5523 nm

The production of color centers in alkali halides is not only possible with neutrons but also with X-rays. The latter mode of production is quite efficient. It should be noted that X-rays do not produce displacements in metals and that color centers can also be produced in quartz and silica. In a fusion environment additional color centers will be produced because of the generation or presence of hydrogen. These centers have been labelled U centers. Irradiation also causes dimensional changes in dielectric materials as well as the formation of optical absorption bands. In alkali halides the density change can be correlated with the concentration of F-centers.

Neutron irradiation of glass and quartz can produce density changes after very low fluences and an example is shown on Fig. I-C-27. In addition, X-ray and γ-ray irradiation produces density changes as well. The production of hydrogen and helium in silica provides an additional source for density changes. These density changes not only influence stress build-up and fracture of the coatings but they also induce changes in the refractive index which in turn can result in a reduction of the reflectivity of the mirror, i.e., an increase in the absorption.

Finally, there are effects due to the collision cascade. It may well be that the crucial mechanism for damage in dielectric coatings must be sought in the production of collision cascades. The spacial extent of these cascades produced by 14 MeV neutrons is of the order of a few hundred angstroms. Since the coatings are only one-quarter wavelength thick, the cascades extend almost through the entire thickness of one layer.

Fig. I-C-27. Change in density of vitreous silica on irragiation.

The local refractive index in the region of the cascade is certainly very different from the intact material. Hence laser light absorption at the damaged location will further damage the underlying material and more light will be absorbed in the substrate which will lead to local heating. It is very conceivable that this could result in a catalytic damage mechanism for the dielectric coating. Considered together, all the above problems may very well eliminate dielectric coatings for application in reactors. This has profound implications for the use of lasers in the 2000-6000 Å range and further work is clearly required.

I-C-9. Vacuum System and Mechanical Design

The vacuum system for the reactor cavity removes the products of the fusion reaction and the general pellet debris. It also maintains the cavity at a prescribed pressure and delivers the effluent to a processing center for fuel recovery. In SOLASE, the reactor cavity is filled with neon gas in order to protect the front wall from the ions and soft X-rays produced by the microexplosion. The neon gas throughput depends on the type of pellets used and the allowable chemical erosion rate of the graphite blanket.

The reactor cavity is evacuated through the laser beam ports and the two suppression chambers which act as vacuum plenums. The surfaces of the suppression chambers are cooled so that the low-melting materials leaving the reactor cavity will condense out preventing them from contaminating the last mirrors or from being ingested into the vacuum pumps.

There are two pumping stations on each suppression chamber. The stations are connected to the suppression chamber by tubes leading out of the reactor cavity building. Roots blowers are selected as the primary vacuum pumps. They provide very high pumping speeds in a relatively compact design and their efficiency peaks at the desired pressure range (0.1-1.0 torr). Such pumps are relatively contamination-free, are rugged enough for continuous operation and require little maintenance. The primary blowers are backed by secondary blowers of about one-sixth capacity. In turn, these are backed up by dry sealed mechanical compressors. The resulting

effluent is delivered at about atmospheric pressure to the tritium extraction and fuel processing system. Table I-C-15 gives the vacuum pumping requirements for two pellet designs.

Reactor disassembly is schematically outlined in Fig. I-C-21. The philosophy is to quickly replace damaged blanket segments rather than repair or maintain them. The reactor cavity is spherical with an inside diameter of 12 m surrounded by a 60 cm thick graphite blanket which has Li_2O microspheres flowing through it. As shown in Figs. I-C-2 and I-C-19, the Li_2O breeding material enters the blanket at the top and flows by gravity to a return duct at the bottom. It is then mechanically lifted to the steam generator where it again flows by gravity and is subsequently returned to the reactor by another mechanical lift. A small fraction of the breeding material (2%) is made to flow at a lower velocity through the blanket thus reaching a higher temperature. This stream is diverted to a tritium extraction system.

The graphite blanket consists of 16 segments attached to a back structure made of aluminum alloy (see Fig. I-C-19). The segments resemble wedges made by equally spaced vertical planes going through the center of a thick walled hollow sphere. The spherical back structure is divided into four quadrants, each supporting four blanket segments. It is attached to the shield which is also divided into four segments. The shield is a free standing thick walled hollow sphere which can be opened by moving quadrants radially away from the cavity. It is made of alluminum alloy

Table I-C-15

Vacuum Pumping Requirements for Pellets I & II*

Pellet I

	Graphite Erosion Rate		
	1 mm/yr	2 mm/yr	3 mm/yr
Effective pump capacity, liters/sec	1.81×10^6	6.47×10^5	2.57×10^5
Actual pump capacity, liters/sec	2.24×10^6	6.94×10^5	2.64×10^5
Number of primary Roots blowers	132	40	16
Capacity of each primary R.b., liters/sec	18,000	18,000	18,000
Number of secondary Roots blowers	28	8	4
Capacity of each secondary R.b.,liters/sec	18,000	15,000	12,000
Total power consumption, MW	23.8	7.37	2.8
Total cooling water consumption, liters/min	4,700	1,460	560

Pellet II

Effective pump capacity, liters/sec	2.2×10^6	8.47×10^5	3.92×10^5
Actual pump capacity, liters/sec	2.86×10^6	9.3×10^5	4.09×10^5
Number of primary Roots blowers	168	56	24
Capacity of each primary R.b., liters/sec	18,000	18,000	18,000
Number of secondary Roots blowers	28	12	4
Capacity of each secondary R.b., liters/sec	18,000	15,000	18,000
Total power consumption, MW	30.4	9.9	4.35
Total cooling water consumption, liters/min	6000	1960	860

*Pellet I - Glass encapsulation

Pellet II - PVA encapsulation

reinforced concrete with an overall thickness of 3.75 m. Suppression chambers are built into the shields at the beam port locations as a protection scheme for the last mirrors.

The blanket segments weighing 3.3 tonnes each are made of chopped graphite fibers compressed together at elevated temperature and pressure to make panels. These panels are then shaped and joined together to form the blanket structure. Ceramic insulators and spacers are used between the graphite blanket segments and the cooled back structure for thermal isolation. Lugs are used to engage the back side of the blanket segments to the aluminum back structure.

Four of the blanket segments will have beam ports built into them. Each port will have a graphite liner cemented to the blanket segment and sealed to the back structure. A flange on the back structure surrounding all six beam ports will mate with a similar flange on the suppression chamber and a soft aluminum wire between the flanges will constitute the seal.

The shield quadrants having beam ports will remain stationary. All others can be moved out radially from the cavity. Replacement of the blanket segments will be accomplished by opening the shield, removing back structure quadrants with the attached blanket segments, and replacing them with a new back structure and blanket segments. In this way, the time consuming labor of attaching the blanket segments to the back structure is avoided.

Removable shield segments will be used above the reactor cavity to shield the Li_2O inlet tube. It is assumed that a 50 tonne overhead crane will be available in the reactor building. In Table I-C-16 we give the masses of materials used in the reactor cavity.

I-C-10. The Fuel Cycle and Tritium Processing

The tritium flow pathways identified for SOLASE are shown in Fig. I-C-28. For the reactor cavity, a key issue is the compatibility of the first wall (graphite) with materials making up the pellet. The pellets have either glass or polymers as the fuel containers, xenon, lead, or mercury as the high Z material, and an outer layer of a polymeric hydrocarbon ablator. Any hydrogenic species present in either the unburned fuel or pellet material has the potential at the temperature of the front wall to chemically erode the graphite by acetylene formation. An acceptable wall erosion rate ($\lesssim$ 2 mm/yr) is predicted when the total pressure provided by the "fill" gas (neon or xenon) is 0.7 torr (1800°C) and the pumping speed is about 6-23 x 10^4 torr-ℓ/sec (at 300°K). The pumping power required is less than 10 MW so this condition can be met. Somewhat higher pumping speed is required with plastic encapsulation because of the higher hydrogen content. However, the use of plastic capsules helps avoid the problem of metal carbide formation. Optimally, the plastic and pellet would not contain oxygen to avoid further chemical erosion of the wall by carbon monoxide formation. Xenon is the preferred high Z material from a cavity-pellet compatibility viewpoint but this will ultimately depend on pellet design.

Table I-C-16

Masses of Blanket & Shield	Tonnes
Weight of blanket segment	3.34
Total weight of blanket	53.4
Weight of back structure quadrant	14.4
Total weight of back structure	57.5
Weight of a shield quadrant	2200
Weight of Li_2O inlet tube shield	800
Total weight of shield	9580
Weight of removable section of Li_2O tube	15.0
Mass of graphite in shield	163
Mass of concrete in shield	6920
Mass of aluminum alloy in shield	950
Mass of lead in shield	1550

TRITIUM PATHWAYS IN SOLASE

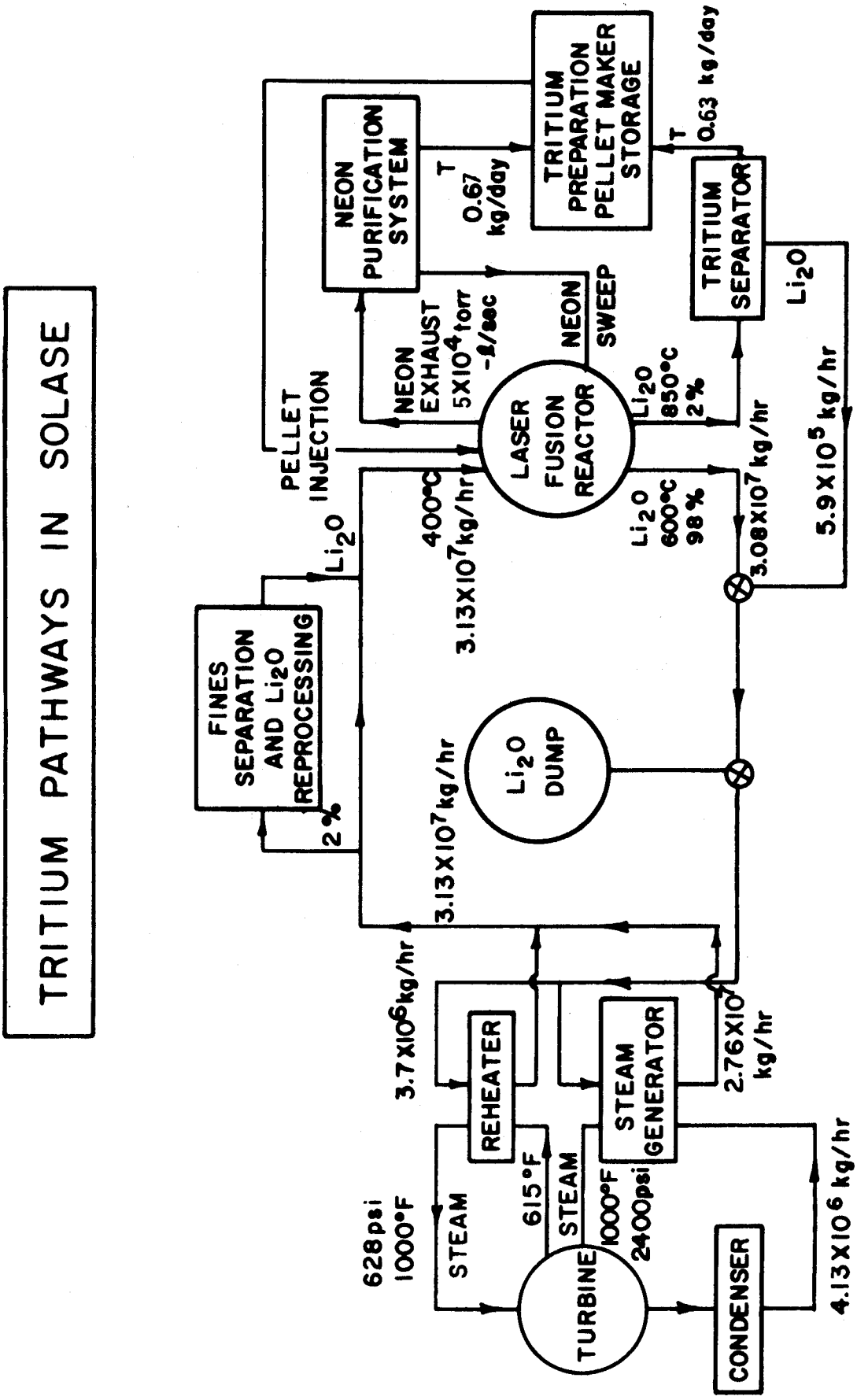

Two schemes for separation and recycling of reactor exhaust materials have been developed. For the pellet with glass, the reactor exhaust will be greater than 99% of the fill gas material (neon or xenon) and will contain, in order of decreasing quantity, carbon monoxide, acetylene, carbon, silicon carbide, hydrogen isotopes, helium, boron carbide, sodium oxide, aluminum oxide and xenon (unknown quantity). For a plastic (polyvinyl alcohol) pellet the exhaust will be greater than 99% neon (or xenon) fill gas and contain, in decreasing amounts, carbon, acetylene, hydrogen isotopes, carbon monoxide, helium and xenon (if neon is the fill gas). After the high temperature condensables have been removed, one processing procedure consists of oxidizing the hydrogenic species acetylene and carbon monoxide and then removing the water and carbon dioxide from the noble gas mixture. A second procedure would achieve separation solely through sequential absorption on molecular sieves.

The total reactor system tritium inventory is summarized in Table I-C-17. Importantly, the inventory depends on the choice of encapsulating material. The estimated tritium inventory is 26 kg for the glass pellet case and 11 kg in the plastic pellet case. The difference is due to the shorter fill time (1 day) for the plastic pellets compared to the glass pellets (5 days). The largest portion of the tritium inventory is in the pellet fabrication and storage facility. (To reduce pellet failure, especially for the plastic pellets, storage at 5 ^{o}K will probably be necessary).

Table I-C-17

Total Tritium Inventory

(Steady State Quantities)

Location		Quantity (kg)	
		glass pellet	PVA pellet
Reactor, Scrubber Oxidizer, CO_2 absorber		2×10^{-5}	2×10^{-5}
H-isotope fractionator		0.03	0.03
Electrolysis equipment		0.1	0.1
Molecular sieves		0.67	0.67
Lithium oxide		1.0	1.0
Pellet maker and storage		23.9	9.4
	TOTAL	25.7	11.2

The breeding process results in the loss of one lithium atom for each tritium bred, as expressed by the following equation:

$$LiO^{6}_{3}Li + {}^{1}_{0}n \rightarrow LiO^{3}_{1}T + {}^{4}_{2}He \ .$$

Approximately 0.63 kg of T are bred each day in the SOLASE blanket. (Daily consumption = 0.47 kg T/day, and breeding ratio = 1.33). The bred tritium is present in the Li_2O as LiOT. Approximately 1×10^6 kg of Li_2O are used in the primary loop so that the tritium recovery process must be based on the separation of low concentrations of LiOT from a large quantity of Li_2O.

A reasonable approach would be to allow the total tritium inventory to grow to a significant concentration; a small side stream (~2%) is then diverted to the extraction system to separate the gas phase containing tritium mainly as T_2O. A 1 ppm level can be attained in about 2 days. While this approach seems reasonable, a straightforward calculation quickly shows that the total gas volume available and the equilibrium vapor pressure for T_2O at any reasonable temperature make the total amount of tritium in the gas phase considerably smaller than the daily requirement. This is true even at a 10 ppm tritium concentration in the Li_2O and even if a small amount of water is added to the lithium oxide so that the vapor phase H_2O would act as a carrier for tritium species. (In fact, it is very difficult to completely dehydrate lithium oxide so that some water will always

be present). When water is added, HTO will be the most important tritium species in the gas phase. For Li_2O with 0.1% of water by weight and 1 ppm of T in the solid phase, the vapor pressure of HTO at 850°C is only 9×10^{-5} torr. This means that less than 0.1 moles/day of HTO will be available in the gas accompanying the 2% Li_2O side stream. This is an insignificant fraction of the required amount.

It is clear, therefore, that there is no way to extract the daily tritium demand from the Li_2O without considering diffusion of the tritium species in the solid phase and allowing some residence time in the extractor. The residence time, and the corresponding extractor size, required to recover the bred tritium from the 2% side stream can be easily determined. We assume that the tritium species diffusing out of the solid particles will be instantaneously condensed on a cold surface so that the tritium concentration at the surface of the particles remains zero during their transit through the extractor. The tritium concentration in the Li_2O will be kept at 1 ppm so that the total tritium inventory in the lithium oxide is only 1 kg. We shall also retain the 0.1% by weight of water in the Li_2O. A simple mass balance can be used to determine the tritium concentration in the particles leaving the extractor. Using Fick's law of diffusion, the time required for the concentration to drop to the exit value can be obtained. For an effective diffusion path length of 0.1 μ and a diffusivity of 1×10^{-15} cm^2/sec, the required residence time in the extractor is 300 sec. This corresponds to an

extractor volume of 40 m^3. The effective diffusion length used in these calculations is much smaller than the particle radius since the particles are expected to be quite porous. Lithium oxide can be prepared by thermal decomposition of the peroxide, carbonate or hydroxide with the evolution of a gas and a diffusion length of 0.1 μ should be attainable. Diffusivity data for T_2O through Li_2O are unavailable. The 1×10^{-15} cm^2/sec value used in the above estimates corresponds to diffusion of T_2O through BeO at 850°C which should be representative. Diffusivity data are clearly required to firmly establish the feasibility of this scheme.

The actual extractor volume may be somewhat larger than the 40 m^3 estimated above on the basis of zero tritium concentration at the surface of the particles. The required residence time and extractor volume can, however, be decreased by allowing a higher tritium concentration in the Li_2O. For a 10 ppm concentration (i.e., 10 kg T inventory in the Li_2O), the extractor volume would be 4 m^3. In either case, the apparatus must be constructed in such a way that the gas phase is separated from the solid phase by a membrane with a pore size of less than 100 microns so the Li_2O solid is not transported into the gas phase. The condensables in the gas phase are cold trapped and the carrier gas recycled.

The condensables, consisting of H_2O, HTO, T_2O, LiOH and LiOT are merged with the D_2O, DTO, and T_2O from the reactor exhaust and electrolyzed to produce tritium, deuterium and protium gaseous species which are in

turn sent to the isotope separation facility and then returned to the fueling cycle. Problems related to the high β activity of tritium in the condensate have not been considered.

The lithium oxide particles flowing through the blanket will come in direct contact with the graphite structure. The average inside surface temperature of the blanket's front wall is ~1350°C. This high temperature makes it necessary to consider the chemical and physical compatibility of lithium oxide and the graphite front wall. The remaining blanket structure will operate at a relatively low temperature (~650°C). The average flow velocity of the particles near the front wall is 1.1 m/sec. This is relatively slow so that a Li_2O particle coming in contact with the hot graphite will have a long residence time. The spherical geometry of the reactor and the nature of the flow will lead to many such collisions. Three potential problems then become apparent: (1) reaction of the vapor species with the graphite, (2) diffusion of these species through the front wall to the reactor cavity, and (3) particle integrity.

At elevated temperatures, LiOH and Li_2O undergo several reactions with graphite:

Reaction	ΔG (kcal) 1300°C	1500°C
$LiOH_{(g)} + 2C_{(s)} \rightarrow 1/2Li_2C_{2(s)} + 1/2H_{2(g)} + CO_{(g)}$	-4.8	-9.2
$LiOH_{(g)} + 1/2C_{(s)} \rightarrow 1/2Li_2O_{(s)} + 1/2H_{2(g)} + 1/2CO_{(g)}$	+1.3	-2.2
$1/2Li_2O_{(g)} + 1/2C_{(s)} \rightarrow Li_{(g)} + 1/2CO_{(g)}$	-1.8	-5.8
$1/2Li_2O_{(g)} + 3/2C_{(s)} \rightarrow 1/2Li_2C_{2(s)} + 1/2CO_{(g)}$	-5.9	-7.1
$1/2Li_2O_{(g)} + 1/6C_{(s)} \rightarrow 1/6Li_2CO_{3(\ell)} + 2/3Li_{(g)}$	-3.8	-3.6

The products of these reactions must be dealt with in the system, though Li_2C_2 has been found to decompose above 800°C.

Diffusion of the vapor species (HTO, H_2O, T_2O) through the graphite wall would be undesirable because it would erode the carbon due to the gas-water reaction,

$$H_2O_{(g)} + C_{(s)} \rightarrow H_{2(g)} + CO_{(g)} ,$$

and introduce protium into the cavity.

The third problem concerns the integrity of the Li_2O particles. The melting point of Li_2O is variously given as 1427°C, 1570°C, 1700°C and 1723°C in different references. The presence of LiOH in the pellet should lower the melting point, but the extent of the reduction is unclear from available data. This problem is further complicated by the presence of graphite since the formation of some quantity of Li_2CO_3 seems highly probable. Li_2CO_3-Li_2O-LiOH appear to form an eutectic at 410°C in the Li_2O rich region, although other authors attribute this low melting phase to a 13% Li_2CO_3, 87% Li_2O binary eutectic. The Li_2CO_3-LiOH binary eutectic melts at 419°C. While the available data is quantitatively inconclusive and somewhat contradictory, it is clear that the possibility of sintering and/or melting of the Li_2O particles which come in contact with the hot graphite wall should be considered. If sintering occurs, tritium diffusion out of the particles will be slowed. Melting would prove particularly detrimental since the presence of a liquid phase would cause particle agglomeration resulting in flow impedance or blockage.

Tritium circulates through the plant system in SOLASE because the lithium oxide is transported from the reactor to the steam generator. Secondary containment is achieved largely by enclosing small primary containment items in glove boxes and by enclosing primary containment rooms within larger rooms. The space between the walls is swept with an inert gas. All tritium bearing pipes will contain an annular space through which an inert gas flows. Whenever any particular inert atmosphere has a tritium content exceeding 2 ppm, the gas will be diverted to a tritium effluent removal system. The permeation rate of tritium through the walls of the reheaters and steam generators is 4-6 Ci/day or 40-60 nCi/ℓ of water when the blanket tritium concentration is 1 ppm. This concentration is within the RCG limits. Tertiary containment must handle 60.1 x 10^4 m^3 of building space and the air flow through those buildings will be approximately 12 x 10^4 m^3/day. These numbers could be reduced by 48% if the laser building can be designed to exclude any possible contact with tritium.

I-C-11. Power Flows in SOLASE

The power flows in the SOLASE reactor are summarized in Fig. I-C-3. The main distinguishing features are: (1) lithium oxide is the primary heat transport medium requiring special steam generator and reheater design as well as a particle-transport system, (2) an intermediate coolant loop is not required because of the expected low tritium leakage rate,

and (3) heat sources at different temperature are available, viz. the blanket coolant (Li_2O), the suppression chamber cooling water, and the cooling water for the last mirrors.

Most of the reactor thermal power is contained in the lithium oxide stream which enters the blanket at 400°C and leaves at 600°C. This power is utilized in a high temperature reheat steam cycle with an overall thermal efficiency of 42.9%. A small fraction (~5%) of the reactor thermal power is removed by the suppression chamber cooling water at a relatively low temperature (~ 200°C). The amount of power removed at this low temperature depends on many factors including the ion and X-ray energy fractions and spectra, chamber fill gas pressure, pellet composition, and vacuum pumping throughput. This power is utilized in a saturated 60 psia steam cycle with a thermal efficiency of 21.1%.

Approximately 3% of the energy produced by the microexplosion is deposited in the structure and cooling water of the last mirror. This energy is removed at a very low temperature (~50°C) to prevent swelling of the aluminum-alloy mirror structure. This low-grade heat is discharged to the atmosphere via a dry cooling tower.

The steam generators, reheaters, and particle transport system for the Li_2O cycle have been designed in conjunction with the Babcock and Wilcox Company. Multi-stage Archimedes lift pumps are used to transport the lithium oxide particles around the primary heat transport loops. Archimedes pumps offer many desirable features including: (1) low particle attrition

comparable to that obtained with mass lift or bucket elevators, (2) low power requirements (~ 10 MW), (3) continuous flow as compared to batch type operation of the mass lift technique, (4) ability to operate at sub-atmospheric pressures consistent with blanket pressure, (5) reduced particle inventory through elimination of pressurizing and receiving tanks of mass lift, and (6) reduced system complexity through elimination of the tanks, gas filters, cyclones, etc. needed for mass lift systems. The ability to operate under vacuum conditions is important to avoid excessive gas leakage into the cavity through the graphite front wall.

A once-through steam generator with an appropriate steam cycle has also been designed based upon analyses by Babcock and Wilcox for a similar system[10]. steam generator design does not pose special problems. The lithium oxide particles flow by gravity through the steam generator and the steam tubes are designed to allow thorough mixing of the microspheres as they pass over the heating surface. The heating surface required is ~ 0.05 m^2/kWe which is comparable to that found in large fossil fuel fired utility steam power plants. The steam cycle is a standard 2400 psi, 1000^{o}F with 1000^{o}F reheat giving an overall gross cycle efficiency, including the low efficiency suppression chamber cycle, of 41.8%. A summary of power cycle system parameters is given in Tables I-C-18 to I-C-20.

Table I-C-18

Power Cycle Parameters for SOLASE

I. Li_2O/Steam Cycle	
Thermal Power (MWt)	3030
Number of Loops	6
Gross Electrical Output (MWe)	1300
Thermal Efficiency	42.9%
Steam Pressure (psia)	2400
Steam Temperatures (^{o}F)	1000/1000 Reheat
II. Suppression Chamber Coolant Cycle	
Thermal Power (MWt)	160
Number of Loops	1
Gross Electrical Output (MWe)	33.8
Overall Thermal Efficiency	21.1%
Steam Pressure (psia)	60
Steam Temperature (^{o}F)	293
III. Overall Plant Parameters	
Thermal Power (MWt)	3190
Gross Electrical Output	1334
Overall Gross Thermal Efficiency	41.8%
Recirculating Power Fraction	0.284
Overall Net Thermal Efficiency	30%

Table I-C-19

Steam Generator Parameters

Heat load per unit (MWt)	449
Steam flow rate (kg/hr per loop)	6.89×10^5
Li_2O flow rate (kg/hr per loop)	4.59×10^6
Li_2O inlet/outlet temperature (^oC)	600/400
Feed water temperature at full power (^oC)	243
Steam exit temperature (^oC)	538
Steam pressure at outlet header (psia)	2410
Total heating surface per unit (m^2)	5690
Total number of tubes per unit	1.02×10^4
Tube material	Croloy

Thermal Design Parameters:

	Economizer	Boiler	Superheater
Li_2O inlet temperature (^oF)	847	984	1112
Li_2O exit temperature (^oF)	752	847	984
H_2O inlet temperature (^oF)	470	662	662
H_2O exit temperature	662	662	1000
LMTD (^oF)	230	247	199
Effectiveness	0.51	0.43	0.75
NTU (-)	0.42	0.55	0.65
Li_2O conductance (Btu/hr-ft^2 ^oF)	150	150	150
Wall conductance (Btu/hr-ft^2 ^oF)	1790	1790	1790
H_2O conductance (Btu/hr-ft^2 ^oF)	906	10,400	332
Required heated length (ft)	5.6	6.6	10.8

Table I-C-20

Principal Design Parameters for Steam Reheaters

Heat load per unit (MWt)	59.6
Steam flow rate (kg/hr per loop)	5.99×10^5
Li_2O flow rate (kg/hr per loop)	6.10×10^5
Li_2O inlet/outlet temperature (^oC)	600/400
Steam inlet pressure (psia)	628
Steam inlet temperature (^oC)	324
Steam exit temperature (^oC)	538
Total heating surface per unit (m^2)	2170
Total number of tubes per unit	4580
Design Parameters for Archimedes Lift Pumps	
Total tube length (m)	21.5
Outside diameter (m)	3.2
Li_2O flow rate/loop (m^3/sec)	1.20
Pump speed (RPM)	25
Screw pitch angle	14^o
Inclination	60^o
Pumping power per pump (kw)	364
Total pumping power (MW)	4.6

Stage #	OD (m)	ID (m)	Max. Sliding Speed (ft/sec)	Friction H.P.
1	3.00	2.40	20.0	269
2	2.35	1.88	15.7	129
3	1.83	1.46	12.2	61.8
4	1.41	1.13	9.4	27.8

An intermediate heat exchanger does not appear to be required since tritium diffusion through the primary system is sufficiently low. A Li_2O/water reaction caused by a leak in the steam generator is non-explosive. Elimination of the intermediate loop should have a significant impact on system economics since it allows for better steam conditions and hence a higher overall thermal efficiency. The net plant efficiency of just 30% reflects the high recirculating power fraction characteristic of a system where the product of laser efficiency and pellet gain (η_L G) is the order of 10. The 28% recirculating power fraction can be expected to strongly influence economics since one must buy generating and power handling equipment for the gross electrical output of 1334 MW_e.

References for Chapter I

1. G. Charatis, et al., in Plasma Physics and Controlled Nuclear Fusion Research 1974 (Proc. Int. Conf., Tokyo, 1974), IAEA, Vienna (1975), Vol. II, 317.

2. J. Holtzrichter, et al., in IEEE Second International Conference on Plasma Science, IEEE, Ann Arbor (1975), p. 85.

3. E. K. Storm, et al., "Laser Fusion Experiments at 2 TW," presented at the 10th Eur. Conf. on Laser Interactions with Matter, Talaiseau, France (Oct. 18-22, 1976).

4. D. Giovanelli, et al., "Laser Fusion Target Interaction Studies at 10.6 μm," in Proceedings of Conference on Laser Engineering and Applications, Washington, D.C. (June 1-3, 1977).

5. S. L. Bogolyubskij, et al., in Plasma Physics and Controlled Nuclear Fusion Research 1976 (Proc. Int. Conf., Berchtesgaden, 1976), IAEA, Vienna (1977), Vol. I, 177.

6. J. Chang, et al., "Neutron Production from Advanced REB Fusion Targets," Sandia Laboratory Report, SAND-77-2017 (March 1977).

7. J. Nucholls, L. Wood, A. Thiessen, and G. Zimmerman, Nature 239, 139 (1972).

8. K. Brueckner and S. Jorna, Rev. Mod. Phys. 46, 325 (1974).

9. R. W. Conn, et al., "Studies of the Technological Problems of Laser Driven Fusion Reactors", Fusion Research Program Report, UWFDM-190 (University of Wisconsin, 1977).

10. D.C. Schluderberg, "Li_2O Microsphere Fabrication", Progress Report COO-4262-4, Babcock and Wilcox (September 1977).

II. Summary and Conclusions

II-A. Brief Summary of SOLASE and General Conclusions

A laser fusion conceptual reactor, SOLASE, has been designed for the production of electric power. The purpose of this study is the self-consistent examination of problems, both in physics and technology, likely to be important to the future development of this particular approach to fusion power. The SOLASE reactor is designed to produce 1000 MW_e at a net efficiency of 30% from laser ignited fusion pellets that have a gain of 150. The laser energy on target is 1 MJ and 20 targets are exploded per second. The net laser efficiency is 6.7% including multipassing of the next-to-last and last laser amplifier. The laser is designed, generically where possible, as a gas phase laser modelled after the CO_2 system but no laser wavelength is specified. The optimistic laser efficiency of 6.7% still implies relatively large power supply needs and the recirculating power fraction is 28%. These facts will have important but detrimental consequences for reactor economics. Thermonuclear burn-dynamics calculations have been performed to determine pellet debris spectra for cavity design analysis. A buffer gas of neon at 0.5 to 1 torr pressure is used to stop the ions. Multilayered cryogenic targets produced in a batch process appear to have acceptable costs because tooling costs can be amortized over the lifetime of the plant and materials costs are negligible. Target delivery is by pneumatic guns although trajectory diagnostic and correction techniques must be developed. The last mirrors are diamond turned copper on an aluminum structure located 15 m from the reactor cavity center with f/no. = 7.5. Heating of the mirror surface is minor so long as the debris ions are stopped in the buffer gas.

The reactor cavity itself is a spherical 6 m in radius. It is constructed from graphite designed to guide the gravitational flow of lithium oxide (Li_2O) serving as both the tritium breeding and heat transport medium. The breeding ratio is 1.33 and the maximum Li_2O flow velocity is only about 1 m/s. The neutron wall loading is 5 MW/m^2 so that SOLASE represents a reasonably compact system given the net power produced. The blanket back structure is made from an aluminum alloy and the shield can be either concrete or lead acetate solution. Thus, the overall levels of neutron induced activity decay very rapidly following shutdown. It appears that limited hands-on maintenance is possible after just one week.

This spherical system is highly accessible from the outside provided that two-sided target illumination (six beams on each side) is acceptable. A procedure has been developed for annual blanket replacement that is simple and fast. We expect down-time periods to replace graphite blanket segments to be on the order of two weeks. The philosophy is that blanket maintenance per se will be avoided; after draining the Li_2O, the graphite will be simply discarded. Such a simple procedure is critical if a high system availability is to be achieved.

Overall, the SOLASE laser fusion reactor concept is an interesting fusion system. It has a relatively simple and accessible reactor chamber design with a blanket system that has very low levels of long term induced radioactivity. The flowing lithium oxide system permits low pressure operation in the blanket while the modest chamber vacuum requirements make the use of graphite or graphite composities for the blanket structure more feasible. The recirculating power fraction of 25% will strongly influence economics but the replacement, rather than the maintenance, of

reactor modules of low activity should permit short down times, improving overall system reliability. Last mirror protection, initially considered a critically difficult problem, appears to be manageable by a simple design solution. The reactor is pulsed twenty times a second but is effectively steady state from a power production viewpoint such that a thermal energy store to smooth the power to the turbines is not required. The system is of moderate size for the power produced and the laser building, although quite large, need not be primary containment.

One of the goals of our study is to determine the major technical issues associated with laser fusion reactors. We present first a general list of major issues in rough priority order and then give more detailed conclusions according to specific subject areas.

1. An energy gain on target of 100 to 200 or higher is difficult to achieve with a 1 MJ laser and although high gain target designs have been reported[1] they still must be verified by experiment. The basic question is whether the laser energy can be coupled into the target efficiently enough to make the target work. Physics analysis performed as part of this study shows that inertial confinement systems will have much better energy economics (higher pellet gain and yield) if larger laser (or other driver) input energy can be used. We have also found that small deviations from the perfect pulse shape required to achieve isentropic compression can sharply reduce pellet performance. The experiments planned in the next several years should bring us much closer to an answer on these matters. Clearly the next 1 to 5 years will be critical for physics developments in the field.

2. The assumption that a laser design with multipassing of the last two amplifiers can have an efficiency of about 7% must be verified.

In particular a laser with this efficiency and with the appropriate wavelength and pulse shaping characteristics is required. (If very large gains are possible, e.g., $G = E_{TN}/E_L > 500$, then low efficiency lasers can be considered. However, if the incident laser energy remains at 1 MJ or more, the very large pellet yield will pose unique cavity design problems and low laser efficiency, even offset by high pellet gain, could prove uneconomical due to high power supply costs.)[a] At present there is no laser that clearly meets all the requirements for laser fusion but several lasers have potential efficiencies exceeding 1%. If the pulse width can be longer than 1 ns (e.g., 5-20 ns), then the design of a laser would become easier and in some cases the efficiency would improve.

3. The development of power supplies and very short pulsed switches (1 μs or so) that can operate reliably for 10^8-10^9 shots and are of modest costs are clearly critical.

4. The gas protection method analyzed for SOLASE using either neon or xenon at 0.1-1 torr pressure to prevent charged particle debris (and X-rays in the case of xenon) from reaching the first wall and last mirror requires verification. At the laser intensity level required ($> 10^{15}$ W/cm^2) on target gas breakdown will occur, but for reactor size targets with radii on the order of 2 mm, this may not be serious. The viability of this concept can be tested in both present and near term laser facilities.

---

[a] In the results reported by Lindl,[1] 4 MJ of energy were absorbed by the target and the calculations gave a yield of about 4000 MJ. Assuming 100% target absorption efficiency, the gain, $G = E_{TN}/E_L$, is about 1000. Thus, if the laser is 1-2% efficient, the laser power supplies are for 200-400 MJ. The cost of such power supplies may dominate reactor economics except for units of very large (> 1000 MW$_e$) power output.

5. A key issue is the development of a basic manufacturing procedure for the mass production of targets at an acceptable investment of capital. The delivery of targets into the reactor chamber appears feasible but trajectory correction in flight will be very difficult. A major issue for reactors (both near and long term) will be the maintenance of proper alignment in the laser optical train and the possible tracking of targets.

6. The tritium inventory in such reactors may be dominated by the tritium associated with the filling and storage of targets. For SOLASE a one week inventory is employed to allow operation during a malfunction in any part of the tritium cycle external to the reactor. There is also an inventory associated with pellets being fabricated and with other reactor subsystems such as the vacuum pumps and the reactor blanket. However the inventory is dominated by the pellet inventory and particularly by the time to fill a target with DT fuel when permeation filling is used.

In general, cryogenic targets consist of multiple layers. Working out from the center of a sphere, these layers include a central void, the DT fuel, a capsule, a high Z tamper layer, and a low Z, low density ablative layer. The capsule layer may be glass or a polymer such as polyvinyl alcohol (PVA). The diffusion rates of DT through glass are much lower than the rates through PVA so that the estimated total plant tritium inventory is approximately 10 kg with PVA encapsulation and 25 kg with glass capsules. There is therefore a strong incentive to use polymer encapsulation. This is incidentally just one of many instances where pellet design has a significant impact on reactor analysis.

7. The performance of graphite composite blanket segments under reactor irradiation must be verified particularly at temperatures above 1200°C. The temperature decoupling of the graphite and Li_2O offers the possibility of operating the graphite at optimal temperatures but the reversal of thermal stresses on reactor shutdown could limit the blanket lifetime. The concept is extremely attractive from other viewpoints (e.g., very low induced radioactivity) and therefore deserves serious study in the future.

8. The design and protection of the last mirror poses no insuperable difficulties unless dielectric coatings are required. Such coatings are essential for lasers in the optimum 3000-6000 Å range in order to obtain adequately high mirror reflectivity (> 99%). Yet neutron damage to such coatings through the formation of color centers can occur at very low fluence levels. Unless overcome, this problem may prohibit the use of visible or UV lasers.

9. The vacuum requirements of laser fusion reactors may be modest if the pumping speed is set by wall erosion limits. However the key issues relate to the nature of the pellet debris, to the influence of materials remaining in the gas on laser beam transport and gas breakdown, and to the energy content of the gas flowing from the chamber. Separation techniques required to handle the radioactive chamber effluent, the unburnt tritium, and other materials that are recycled to the pellet factory. A definitive answer to vacuum requirements must await the availability of the final target design for reactor applications.

10. The use of multiple cavities rather than a single cavity was briefly investigated. The primary motivation was to increase the potential availability time of the reactor. On the contrary, we have found that the most reliability-sensitive subsystem is the laser, rather than the reactor chamber. Multiple lasers and power supplies, while not economically attractive, would be preferable to multiple cavities. Further, the use of multiple cavities increases the complexity of the beam line system and reduces accessiblity. Multiple cavities may however be the only solution if methods to re-establish the required chamber environment take too long.

11. The success and choice of a cavity design will strongly depend on pellet materials and output characteristics. At this time little information is available on this subject. It is likely that a generic reactor design independent of the pellet output spectra will not be optimum and may not make laser fusion appear as attractive as it ultimately might be.

12. An unprotected dry wall cavity design made from any reasonable material will not survive a microexplosion at "economically reasonable" wall loadings ($\gtrsim$ 1 MW/m^2) for the following reasons:

(a) Excessive Thermal Ablation: Both graphite and metallic first walls (Mo, Ta, SS) will experience large surface temperature excursions since the ions and soft X-rays deposit their energy in a thin surface layer. Excessive ablation (> 1 cm/y) will take place.

(b) Sputtering: Sputtering will be significant (> 1 cm/y) since damage occurs at elevated temperatures. (Sputtering yields increase sharply as the surface approaches the melting temperature).

Spallation does not appear to be a problem since there will be no thermoelastic stress wave from ion energy deposition (because of the spread in arrival time). Also, if the X-ray spectrum is harder than about a 1 keV black body, only small amplitude transient stresses will be generated.

13. The blanket tritium inventory in SOLASE can be on the order of 1 kg but the exact method of tritium recovery will depend on the purity of the Li_2O, the value of the tritium diffusivity (presently unknown), and the porosity of the Li_2O microspheres. Tritium release rates from the plant through the steam generators and reheaters appears to be acceptably low. This rate is 4-6 Ci/day or 40-60 nCi/l of water so that the Li_2O blanket concept appears to be compatible with a power cycle that does not have an intermediate loop.

The tritium reprocessing system for the pellet debris is strongly dependent on both pellet and cavity design. Chemical reactivity with the cavity wall as well as the potential variety of materials that might be used in the target complicate the problem. While we have analyzed the issue for several pellet designs in SOLASE, more information on pellet composition will be required before a firm assessment of the difficulties can be made.

14. A general advantage of laser fusion reactors is that the reactor cavity and blanket are not surrounded by complex magnet systems. This greatly improves accessibility. However, if uniform illumination of the target is required, this advantage tends to be offset by a complex beam delivery system with mirrors that must be closer to the target.

15. An important issue specific to inertial confinement has to do with commercialization of this technology, nuclear proliferation, and security classification. There are many facets to this question because fusion produces more neutrons per unit of energy than fission and the fuel cycle involves tritium. However perhaps the most important issue is the relationship of ICF to technical ideas and information related to thermonuclear weapons. Such a connection, if any, could be protected by classification but this would surely impede the commercialization process. The problem of safeguards could thus be further complicated by the desire to protect ideas as well as materials. The introduction of commercial laser fusion would seem to require declassification of relevant information to avoid social, institutional and political problems. Otherwise, licensing and public participation would be restricted and there would be a significant extra burden placed on local utilities. Further examination of this issue by an appropriate panel that includes government representatives is clearly desirable.

II-B. Summaries of Specific Topics and Conclusions by Subject Area

II-B-1. Laser Pellet Physics and Pellet Design

The task of pellet design for SOLASE has been performed in a parametric fashion and no specific total pellet design is proposed. However, generic relationships that should guide the pellet design are developed. To study pellet physics, a plasma hydrodynamics-thermonuclear burn-radiative transfer computer code (PHD-IV) has been developed. This code represents the most sophisticated pellet modelling code available to the general scientific community. With this tool, thermonuclear burn propagation in bare compressed DT pellet cores has been studied by ignoring the compression phase of the process and beginning with the compressed core as an initial condition. The burn dynamics of compressed DT cores tamped with a compressed high Z material has also been examined. Charged particle and X-ray spectra resulting from the burn and explosion of these cores have been computed.

In addition to these results, the development of this code provided the opportunity to gain first hand experience in the detailed problems of laser fusion pellet modelling and we have used it to model the implosion of DT shells to thermonuclear conditions. The results were used to "normalize"

a simple analytic description of the "energy economics" of pellet implosion and burn to determine the feasibility of laser fusion for reactor applications. The conditions necessary to burn advanced fuels has also been examined.

The main conclusions from these studies are as follows:

1. The pellet performance required for SOLASE (i.e., $G = E_{TN}/E_L = 150$ with input energy of 1 MJ) is possible but difficult to achieve. Laser light absorption (50%) and hydrodynamic implosion (5%) efficiencies are too low for gains of 100-200. Recently reported pellet designs[1] offer the possibility of achieving gains of 150 (or even much more) if they prove to be successful. These pellets are really two single shell pellets, one inside the other. The DT fuel is located in two different parts of the pellet. The massive outer shell is imploded at a velocity less than that necessary for ignition and compresses the low density gas between the inner and outer pellet. This compressed gas acts as a spring and subsequently implodes the inner pellet at a higher velocity. The inner pellet implodes, ignites, and burns with a gain of about 50. The exploding inner pellet delivers 10 MJ of X-ray and ion debris onto the inner surface of the outer pellet, thereby igniting it. Burn then propagates through the more massive outer shell providing a total gain of possibly 500. Hence the inner pellet gain of 50 can be multiplied by 10 by "propagating" the burn into the outer

pellet where ρR is achieved by more DT mass rather than high compression. This is in fact an implementation of the ideas for high gain pellets given in Section III-G and first reported in the preliminary SOLASE design.[2]

Should such pellet design concepts be only marginally successful they may offer the possibility of achieving gains of at least 150, (i.e., that which is needed for the SOLASE concept). Should they be highly successful, their high gain would reduce the laser demands considerably, both in pulse repetition rate and efficiency.

2. The maximum gain-on-core is achieved for a fuel ρR value of 3 g/cm^2 and a hot central microcore with ρR = 0.4 g/cm^2. For 1 mg of DT fuel, the gain on core is 4800.

3. The fractional burn-up of the fuel at 3 g/cm^2 is 31%, implying a specific yield of 100 MJ per milligram of DT compressed to 3 g/cm^2.

4. The maximum gain-on-core scales as $(M_{DT})^{1/3}$ for DT masses greater than 1 mg.

5. Conclusions (2), (3), and (4) imply that inertial confinement systems will offer much better energy economics if a larger laser (or other) driver) input energy and pellet yields can be used. For instance, an input energy of 10 MJ, rather than 1 MJ, will greatly increase the likelihood of achieving a gain of 150. Conversely, if a gain of 150 is achievable with 1 MJ of input energy, then the equivalently optimistic gain at 10 MJ is 279. This gain reduces the recirculating energy fraction for a 6.7% laser from 25 to 13%.

6. The burn dynamics of bare and tamped pellet cores is significantly different. In the case of a bare core the DT becomes transparent and the radiation escapes. For tamped cores, radiation is trapped, thereby raising the temperature and pressure inside the core until it explodes.

7. Both tamped and untamped cores explode with a high fluid velocity ($> 10^8$ cm/sec) that corresponds to hundred's of keV per ion.

8. The X-ray spectra for tamped cores varies as a function of the ratio of tamper to fuel mass. For ratios between 1 and 10 the spectrum actually becomes harder because the fuel is burning at a higher temperature. For higher ratios the spectrum becomes softer due to down conversion in the high Z material. A large fraction of the X-ray energy is in photons with energies greater than 1 keV even for tamper to fuel mass ratios of 100.

9. The fraction of total energy in X-rays is between 1 and 10% and peaks for mass ratios of about 10. The bare DT core has 1% of its yield in X-rays. For mass ratios greater than 10 the fraction again decreases.

10. The charged particle and X-ray energy fractions and spectra depend upon the fuel and tamper density profiles at ignition. Since implosion calculations of tamped fuel were not done, this situation is studied parametrically.

11. Implosion calculations of DT shells using the perfect pulse shape to achieve isentropic compression indicate that small deviations from the perfect pulse have catastrophic consequences. The most sensitive parameter is the initial intensity of the energy input because this determines the adiabat along which the implosion will take place. Differences in initial plasma temperature as little as 1 eV produce pellet yields differing by 2 to 3.

12. Burning D-D in inertial confinement systems appears to be very difficult because of the high values of ρR needed to support burn propagation. Input energies of 100 MJ appear to be necessary. However, recycling of unburned tritium (a DD reaction product) into the pellets could reduce these requirements considerably. Burning p-^{11}B requires even greater values of ρR (500 g/cm^2) and a very high ignition temperature (300 keV). To achieve such ρR values requires unrealistic compressions or fuel masses that imply unrealistically large input energies and yields. Hydrodynamic implosions cannot generate the necessary ignition temperature. Some other method must be developed.

13. The success of laser driven implosions depends sensitively on many non-linear coupled processes. To achieve isentropic compressions requires that each process (laser absorption, thermal conduction, fluid dynamics) is accurately modelled to within a few percent. This is complicated by the existence of non-thermal particles (electrons and photons) with long

characteristic mean free paths. These must also be modelled properly. The current understanding of these processes is inadequate to formulate such models. Recent experiments have generated considerable information but the degree of detail in even the best pellet modelling codes is inadequate. This inadequacy is due in large part to the extremely large computing times needed to simulate such processes in sufficient detail. (This is true for even the fastest computers available today). Future pellet designs must exhibit a reduced sensitivity to the detailed laser absorption, thermal conduction, hot electron generation and transport and fluid instabilities to have a reasonable success probability for fusion reactor applications.

II-B-2. Lasers for Laser Fusion and for SOLASE

The current estimates of the laser requirements for laser fusion were given in chapter I. We have performed a survey of three "proven" lasers, I, HF, and CO_2 giving characteristics, advantages, disadvantages and possible improvements for each. A survey of potential laser candidates is also given including various excimers, group VI lasers, and mercury-mono-halides. On the basis of this work, a decision was made to use the parameters of the CO_2 laser as the basis for a generic design of a laser for SOLASE. From our general analysis, the conclusions are:

1. No laser presently known will obviously meet the requirements for laser fusion but several lasers can probably be scaled to meet minimum requirements for energy (1-4 MJ), power (100-1000 TW) and pulse width (1-10 ns).

2. There are few lasers that have the potential to achieve an efficiency greater than 1 or 2%. If a power plant can be designed to operate with a laser of this efficiency then the number of potential laser candidates increases substantially and the chance of finding a suitable laser should also improve. Lasers with 1-2% efficiency demand pellet gain in the 500-1000 range in order that the plant have acceptable thermal efficiency and large power supplies.

3. If the pulse width can be longer than 1 nsec, the design of a laser would become easier and in some cases efficiency would improve.

4. The laser wavelength can be converted to more optimum ranges for pellet implosion but usually at a significant cost in net efficiency. Thus the broader the range of allowable wavelengths, the greater will be the probability of finding a suitable laser.

The laser for SOLASE is designed as a generic gas phase laser wherever possible and is modeled after the CO_2 system when a more specific design is required. The SOLASE design requirements are that the laser be 6.7% efficient, fire at the rate of $20s^{-1}$, have an output energy of 1.1 MJ (1 MJ on target) with an optical beam energy density of 5 J/cm^2 maximum. The final amplifiers, the master oscillator, the gas handling system, and the power supplies have been studied in detail. In addition, questions of component lifetime and reliability have been considered including topics such as redundancy, modularization, on-line repairs, and rapid fault detection. The conclusions from the specific study of a laser for SOLASE include:

1. The laser design for SOLASE is generally representative of a "typical" laser for laser fusion applications.

2. Areas that will present difficulties in scaling up include optical isolation, beam quality, and pulse shaping.

3. Solutions to above problems tend to be specific to a given laser so that no absolute statements can be made about the ability to develop a laser fusion laser. However, ignoring power supply and beam transport problems, there appear to be lasers such as CO_2 and I that can be scaled to meet energy (1 MJ), power (1000 TW) and pulse width (1 nsec) requirements. On the other hand, no conclusion is possible on whether a laser

can be developed to meet the wavelength, efficiency, and pulse shaping requirements, particularly because the wavelength and pulse shape requirements remain ill-defined.

4. The state-of-the-art lifetimes for power supply components such as capacitors and switches are presently inadequate for laser fusion applications.

5. Capacitor failure generally results from breakdown of materials due to electrical and thermal stresses. It appears that the lifetime can be improved by improving materials and reducing stresses by redesigning foil placement and foil-terminal connections, by decreasing the energy density and using active cooling.

6. Switches must stand-off high voltages, carry large currents, have low inductance and resistance, close on command, and operate repetitively. Currently only spark gaps and semiconductor switches approach these requirements.

7. Spark gaps fail because of electrode erosion, degradation of the dielectric, cracking of the housing, and failure to stand-off voltages. These areas can be improved by developing better materials, decreasing the erosion rate, reducing the power loading, flowing the dielectric, using active cooling and cleaning.

8. Semiconductor switches have relatively low current and voltage capabilities and must be laser triggered for rapid enough risetimes. They fail because of damage to materials caused, for example, by carrying too high a current density. For laser fusion applications, they must operate in large parallel and series arrays. Adequate lifetimes have been demonstrated for slow risetime switches. This must be verified when the risetime is short, as required for laser fusion applications. These switches appear to be the most promising.

9. A sophisticated fault detection system will be required for the laser.

10. The exact lifetime requirements for all laser and power supply components must be about 10^9 shots. This is several orders of magnitude beyond the present state of the art but the question of lifetime has rarely been important in experiments and substantial improvements should be possible given the R and D effort.

II-B-3. Illumination and Optics Design

A study of the requirements to provide greater than 90% uniform illumination has been done. The methodology for the study is to vary the number of beams, N, the focal shift or beam overlap angle, the f/no. of the last mirror, and the laser beam profile. Given N, the f/no. is determined by the total solid angle allotted to optics, typically taken as 10%. Minimum aperture area is determined by damage threshold to last mirrors and 5 J/cm^2 is used. The focal distance is determined by the chamber size.

1. The results show that 20 beams are only slightly better than 12 beams in uniformly illuminating the target but that 8 beams will not work. More generically, we find that the requirements for uniform illumination are not consistent with the reactor requirements for accessibility, small solid angle devoted to beams, reasonable last mirror size (mirror diameter less than 3.5 m), and mirror protection from pellet debris. It appears that pellets requiring uniform illumination will not be feasible for reactor applications.

The final design for SOLASE is based on 12 beam, two sided illumination. The final mirrors are to have the shape of off-axis paraboloids. These can

presently be rapidly and inexpensively produced with the diamond-turning method. However, the literature on paraboloids is sparse. The classical theory of aberrations does not apply to far off-axis rays and most packaged ray-tracing codes provide no insight. Using geometric optics, we have calculated analytically the image shape of a circular beam, the target intensity, and the effective f/no. Tilt error criteria for roll, pitch and yaw rotations are developed and the perturbed target intensity under a pitch tilt (in medium plane) is calculated based on a new expression for the caustic curve.

2. Results of the study are that the image is very nearly circular for moderate f/no. and that the optical axis is shifted from the centroid of the reflected beam. The effective f/no. is nearly independent of turning angle while tilt errors depend only weakly on this parameter. The perturbed intensity is less severe for smaller turning angles.

3. The last mirror can be diamond turned Cu on an Al substrate. Such mirrors can be constructed with present day technology. An analysis of the mechanical design shows the important characteristic to be a high ratio of flexural stiffness to weight in order to minimize transverse deflections and slope changes. Solid mirrors would be prohibitively massive and a rib-stiffened design could have unacceptable local deflections. The best configuration, as used in SOLASE, is to use a sandwich construction where essentially two face plates are separated by a light core such as an aluminum honeycomb.

4. The last mirror at 15 m from a target yielding 150 MJ per shot and ignited 20 times per second will not be affected by neutron bombardment or hard X-rays. The largest temperature change on the mirror face, using the

pellet spectra from PHD-IV, is about 20°C. The major issue is protection of the last mirror from the charged particle debris.

5. Feasible methods exist to protect the last mirror from charged particle bombardment. A specific design is used in SOLASE. Thus, it appears that a solid last mirror is feasible for use in laser fusion reactors. A major unresolved issue is maintaining proper alignment of the optical beam train in a way that is properly coupled to the target injection system.

6. The formation of color centers in dielectric coatings under relatively low neutron fluences may increase the absorption on mirrors to such a degree that they become unusable in short times. Such coatings are required if the laser wavelength is less than 0.8-1.0 μm and may therefore have a serious limiting influence on the acceptability of lasers in the 3000-6000 Å for use in a reactor environment.

II-B-4. Pellets for Laser Fusion Reactor Applications

As noted previously, a specific pellet design for SOLASE has not been developed but a generic target as described in Chapters I and IX has been studied. This target consists of frozen DT encapsulated by a glass or polyvinyl alcohol (PVA) shell. This shell is then surrounded by a high Z layer and there is a final low Z, low density ablative zone. We have reviewed the present status of laser fusion target fabrication and discussed the reactor aspects of pellet manufacture, storage, and delivery. The conclusions are:

1. Pellet costs appear to be dominated by tooling costs which can be amortized over the life of the plant. These costs appear reasonable for the generic target studied in SOLASE but the conclusion can be strongly affected by target design.

2. High volume processing of generic targets requires only limited extensions and modifications of well-established techniques.

3. The lifetime of cryogenic targets during delivery is a generic problem for all ICTR's.

4. Compatibility of pellet materials with cavity walls is critical and pellet designers should avoid the use of reactive materials. Oxygen should be eliminated if possible and the hydrogen content should be held to a minimum.

5. Fabrication of targets involves three main processes: permeation filling, cryogenic processing, and deposition techniques; all these techniques are used today.

6. The use of PVA capsules requires a protective layer between the frozen DT and the shell to prevent degradation due to radiation damage from β-particles. Xenon is particularly attractive for this purpose.

7. The total plant tritium inventory is highly sensitive to the DT filling time of the capsules. This in turn depends on the capsule material and PVA is much more advantageous than glass in this respect.

8. Storage of pellets is required because the manufacturing process is a batch process and because a store is needed to allow plant operation in the event of a failure. The storage is likely to be at cryogenic temperatures to minimize the out diffusion of the fuel. In addition, active cooling will be required to remove the β-decay heat.

9. Target injection and flight determination as well as coordination with the firing of the laser is sensitively dependent on conditions in the chamber. A complete analysis remains to be done.

II-B-5. Cavity Design and First Wall Protection

1. The cavity design for SOLASE is based on the use of neon or xenon as a buffer gas to prevent the charged particle debris from striking the first wall unimpeded. The neon pressure required is between 0.5 and 1 torr at 300°K. The momentum transferred to the wall is less than half the value one would calculate from simple strong shock theory, i.e., assuming all the energy becomes kinetic energy. The maximum overpressure at the first wall in SOLASE is thus only 90 torr. The energy deposited in the gas is transferred to the first wall by radiation and the characteristic time exceeds 1 ms. However, an exact time has not been evaluated because it requires a full radiation transport calculation. An experiment on this topic would be highly valuable.

The feasibility of the neon gas approach also depends on the pellet output X-ray spectrum. The K-edge in neon is at about 900 eV and there is a window in the absorption spectrum between about 100 eV and the K-edge.

The use of xenon removes this difficulty and acceptable X-ray absorption is found using 0.25 torr xenon regardless of the X-ray spectrum.

Laser induced gas breakdown is an important aspect in the feasibility of the buffer gas approach. Breakdown proceeds in the pressure range of interest by multiphoton absorption and data on this topic are sparse and conflicting. The result of our analysis is that breakdown will occur but that the consequences appear manageable for reactor size targets. Breakdown is sensitive to the type of gas, the laser wavelength, and the laser intensity. Targets that can operate with a peak intensity of 100 TW would produce no gas breakdown problems.

2. The use of multiple cavities, rather than a single cavity, was briefly investigated. The primary motivation is to increase the potential availability of the reactor. On the contrary, we have found the most reliability-sensitive subsystem is the laser rather than the reactor chamber. Multiple lasers and power supplies, while not economically attractive, would be preferrable to multiple cavities. The use of multiple cavities may however be necessary if the appropriate reactor chamber conditions for pellet injection take too long to re-establish.

3. The success and choice of a cavity design will strongly depend on pellet materials and output characteristics. At this time, little information is available on this subject. It is likely that a generic reactor design independent of the pellet output spectra may not be optimum and will not make laser fusion appear as attractive as it might ultimately be.

4. The vacuum requirements of laser fusion reactors are modest and can be met with existing technology.

5. Unprotected dry walls will not survive the microexplosion at "economically reasonable" wall loadings ($\gtrsim$ 1 MW/m^2) for the following reasons:

(a) Excessive Thermal Ablation: Both graphite and metallic first walls (Mo, Ta, S.S.) will experience large surface temperature excursions since the ions and soft X-rays deposit their energy in a thin surface layer. Excessive ablation (> 1 cm/y) will take place.

(b) Sputtering: Sputtering will be significant (> 1 cm/y) since damage occurs at elevated temperatures. (Sputtering yields increase sharply as the surface approaches the melting temperature).

6. Spallation does not appear to be a problem since there will be no thermoelastic stress wave from ion energy deposition (because of the spread in arrival time). Also, if the X-ray spectrum is harder than ~ 1 keV only small amplitude transient stresses will be generated.

7. Hard X-rays produce a small surface temperature rise in the first wall. For example, with no residual gas, the SOLASE cavity can withstand about 7% of the energy yield in 1 keV black body radiation; the fraction increases to ~ 20% for 2 keV radiation.

8. The first wall temperature rise produced by the neutrons is insignificant (~ 2°C for SOLASE) because of the long neutron mean free path.

9. For short wavelength lasers with short pulses and high pellet reflectivity, the reflected laser light will cause excessive surface heating of the wall. For example, for a pulse width of 0.1 ns, the maximum tolerable pellet reflectivities for iodine (λ = 1.3 μ) and CO_2 (λ = 10.6 μ) lasers are ~ 7 and 18% respectively. These values increase to ~ 16 and 32% for a pulse width of 1 ns.

10. Ion bombardment of unprotected dry walls will cause excessive surface heating, evaporation, and sputtering. Without gas protection, the ions from a 150 MJ bare DT pellet would produce a surface temperature rise in the SOLASE front wall of ~ 2500°C; for a structured pellet with 10 mg Hg, the temperature rise is 2200°C.

II-B-6. Blanket Design

The blanket design in SOLASE is unique in many respects and attempts to take advantage of the unique aspects of laser fusion. It is not an adaptation of fission reactor design. The use of graphite is especially notable since the vacuum requirements are quite modest. Such an approach would be more difficult to apply to magnetic confinement reactors. Specifically, our conclusions are:

1. A flowing lithium oxide/graphite composite blanket allows the Li_2O temperature to be decoupled from that of the graphite. This permits the choice of an optimum operating temperature from the viewpoints of maximum lifetime, acceptable particle temperatures, and tritium recovery.

2. Tritium breeding is adequate in Li_2O without the need for a neutron multiplier.

3. The blanket can operate at low pressures, low stress levels, and moderate lithium oxide flow velocity.

4. The lithium oxide acts as a heat transport medium (rather than as a coolant) and is efficient in this regard.

5. The induced radioactivity levels of the blanket are very low at long times after shutdown. A comparison of biological hazard potential between the SOLASE blanket and decaying spent fuel from an LMFBR show the levels in SOLASE to be 10^{-8} of the radioactivity levels from LMFBR spent

fuel at 50 years after shutdown. This includes reprocessing of the LMFBR fuel after one year.

6. The stress levels in graphite produced by differential swelling are adequately relieved by irradiation creep. The blanket lifetime appears to be about 1 year at 5 MW/m^2 wall loading but blanket replacement does not appear difficult in the open geometry of a laser fusion system. The most severe stresses in the blanket structure arise during reactor shutdown and are due to the reversal of thermal stresses.

7. The general attractiveness of the blanket design approach developed here suggests that further experimental investigation of the concept be explored. In particular, one must examine the fabrication of sufficiently pure Li_2O microspheres, the temperature decoupling concept, and the flow characteristics of a circulating Li_2O system.

II-B-7. Radiation Effects to Materials

II-B-7-a. The Blanket

For the purpose of structural analysis of the blanket and its lifetime determination, models have been developed for the radiation-induced dimensional changes of graphite, for the change in the elastic properties, and for the change in the tensile strength. It is found that the porosity P of graphite can be described by the equation

$$P - P_o = \frac{AF^3}{P_o/C+F^2} - P_o\,[1 - \exp(-CF)]$$

where P_o is the original porosity, F the displacement damage, and A and C are temperature-dependent functions. The graphite strength can be related to the elastic modulus and the change in this modulus can be computed from the porosity P.

A self-consistent inelastic analysis has been performed on the blanket structure which follows the distribution of the stresses (during on and off power) and the distribution of the tensile strength as a function of time. The lifetime criterion is that the stresses should not exceed 50% of the tensile strength at any time.

The major results of the inelastic analysis on a graphite structure in SOLASE can be summarized as follows:

1. The structure must not be rigidly restrained at its boundaries in order to avoid excessive thermal and swelling stresses.
2. Stresses generated internally by differential shrinkage and growth are sufficiently relieved during operation.
3. However, stresses on shutdown, mainly due to the reversal of thermal stresses, are life limiting.
4. The safe limit of the tensile strength reduces with increasing growth of the graphite porosity. This represents the other life-limiting factor.
5. Low-density graphite develops tensile stresses due to excessive shrinkage which when added to the reversed thermal stresses exceed the allowable tensile strength very early in life.

From these results we can draw a number of important conclusions. The graphite structure must either be manufactured from a high-density material ($\sim$ 5% initial porosity) or, possibly, a tailored density distribution must be achieved so that the dense graphite is in the high-flux

and medium temperature region (~ 1000°C). The mechanical connections between the blanket structure and its surrounding support structure must be flexible. These two basic requirements are well within the range of present-day technology. Nevertheless, the behavior of graphite under irradiation was based on models which need further experimental verification in particular with regard to irradiations at high temperatures (> 1200°C) and high fluences (> 10 dpa). Since the extrapolation of graphite behavior under irradiation is rather modest in this study, the results indicate that graphite is a suitable structural material for the blanket of fusion reactors and lifetimes of about one year or more are realistic.

II-B-7-b. The Lithium Oxide

For the assessment of this problem, the same model was used that describes successfully the densification of uranium oxide fuel in LWRs. Our analysis shows that radiation-enhanced densification in Li_2O will not occur because the stopping power of the recoiling atoms is too small to result in localized melting.

II-B-7-c. Radiation Effects to Dielectric Coatings on Mirrors

A preliminary survey has shown that dielectric materials are much more susceptible to radiation damage than metals. Color centers of many kinds and with different absorption bands are readily produced by the neutrons, by transmutation products, and even by X-rays. The presence of color centers drastically reduces the transparency of dielectric coatings.

Irradiation also leads to substantial density changes. This will result in the generation of stresses in the coatings and in a change in their refractive indices. The latter may again induce enhanced absorption by laser light.

The collision cascades produced by 14 MeV neutrons have dimensions similar to the coating thickness. Localized absorption of light may lead to further damage and the process may then spread continuously with every laser pulse.

In sumary, it appears that radiation damage to the dielectric coatings may pose a severe problem when short wavelength lasers (λ_L < 8000 Å) are used in inertially confined fusion reactors.

II-B-8. Tritium

1. The tritium inventory in laser fusion reactors strongly depends on target design. For the generic targets with glass or polymer encapsulation we have discussed, the inventory is determined by the fill time of the targets. In this respect, when permeation filling is used, the use of glass encapsulation can more than double the plant tritium inventory. A more definitive analysis of this problem must await clarification of the target design.

2. The blanket tritium inventory in SOLASE can be on the order of 1 kg. The exact method of tritium recovery will depend on the purity of the Li_2O, the value of the tritium diffusivity, and the porosity of the Li_2O microspheres.

3. Tritium release rates from the plant through the steam generators and reheaters appears to be acceptably low. This rate is 4-6 Ci/day or 40-60 nCi/l of water. Thus it appears the Li_2O blanket concept is compatible with a power cycle that does not have an intermediate loop.

4. The tritium reprocessing system for the pellet debris is strongly dependent on both pellet and cavity design. Chemical reactivity with the cavity wall as well as the potential variety of materials that might be used in the target complicate the problem. While we have analyzed the issue for several pellet designs in SOLASE, more information on pellet composition will be required before a firm assessment of the difficulties here can be made.

II-B-9. Mechanical Design and Blanket Replacement

1. A general advantage of laser fusion reactors is that the reactor cavity and blanket are not surrounded by complex magnet systems greatly improving access. However, if uniform illumination of the target is required, this advantage tends to be offset by a complex beam delivery system with mirrors that must be closer to the target.

2. A procedure is proposed for blanket replacement which is within present day technology because of the ready access to the chamber, the simplicity of the blanket design and the fact that entire blanket segments of graphite are simply replaced rather than maintained. In addition, the low levels of radioactivity after shutdown can allow limited hands-on work about one week after shutdown.

3. The down time to replace blanket sections can be short and the graphite itself is inexpensive. The method proposed to fabricate the graphite composite blanket segments must be verified.

II-B-10. Neutronics

1. The time dependence of the radiation damage can be important in determining materials behavior. The normal procedure for calculating this

information leads to negative angular and scalar fluxes when the source is highly anisotropic. Procedures have been developed to correct this problem and a correct computation predicts a peak atom displacement rate in graphite that is 6 m from a 150 MJ microexplosion of 1.65 dpa/s.

2. Steady state neutron transport calculations, adequate to predict integral parameters, shows that breeding is no problem in a graphite/Li_2O system. For SOLASE, the total energy per fusion event is 18.83 MeV.

II-B-11. The Power Cycle

1. The high Li_2O blanket exit temperature (600°C) allows the use of a high temperature reheat steam cycle with an overall thermal efficiency of 42.9%. Operation at this high temperature should be possible in view of the high melting temperature for Li_2O. The presence of low melting impurities in the Li_2O may necessitate lower-temperature operation to avoid particle agglomeration and flow maldistribution.

2. The energy deposited by the hot gas leaving the chamber into the suppression chamber coolant is utilized in a low pressure saturated steam cycle with a thermal efficiency of 21.1% which reduces the overall plant thermal efficiency to 41.8%.

3. Steam generator design is within present technology but experimental verification of heat transfer data from gravitational flow of particles is needed.

4. The use of Archimedes pumps to transport the Li_2O particles offers many advantages including low particle attrition, low power requirements, compatibility with blanket pressure, and simplicity. Design of these pumps is within present technology but again experimental verification is required to allow scale up.

5. The use of lithium oxide as a primary coolant may eliminate the need for an intermediate heat exchanger. Tritium leakage from the Li_2O to the steam side is well below release limits. The use of double-walled steam generator tubes with continuous monitoring of a He gap allows detection of tube failures or leaks to prevent Li_2O/water reactions.

6. The relatively large recirculating power fraction (28% in SOLASE) is characteristic of inertial confinement fusion systems where the driver is inefficient and the produce of driver efficiency and target gain is about 10. Of course, inefficient lasers can be countered with very high gain targets (G > 500) but if the laser energy required to permit such targets to work is 1 MJ or greater, the very large target yield will pose unique cavity design problems and the low laser efficiency will imply large power supply requirements and thus high laser costs.

II-B-12. General

Experimental results on compression and neutron yield from laser and electron beam illuminated targets summarized in Table II-B-1 are a measure of the rapid progress being made in this field. The progress is such that several energy breakeven experiments as listed in Table II-B-2 are planned for the not too distant future. The predicted performance for these experimental facilities, if realized, will mean that substantial advances will have been achieved in the physics of laser and e-beam pellet implosions. If a gain on target of 100 is achieved, as is predicted for the NOVA facility, then the physics basis for targets applicable to reactors will have been demonstrated. At that point, the key technical issues will be many of those outlined in this chapter. Results from the next five years of physics

Table II-B-1

NEUTRON PRODUCTION MILESTONES IN INERTIAL CONFINEMENT FUSION RESEARCH

LABORATORY	DRIVER	POWER (TW)	NEUTRON YIELD	DATE
KMS[1]	Nd: GLASS	0.2	$\sim 10^7$ (DT FUEL)	1974
LLL	Nd: GLASS (JANUS I)	0.2	10^6 (DT FUEL)	1974
LLL[2]	Nd: GLASS (JANUS II)	0.4	10^7 (DT FUEL)	1975
LLL[3]	Nd: GLASS (ARGUS)	4.6	10^9 (DT FUEL)	1976
KURCHATOV[5]	e-BEAM (TRITON)	0.06	10^6 (D_2 FUEL)	1976
LASL[4]	CO_2	0.4	10^6 (DT FUEL)	1977
SLA[6]	e-BEAM (HYDRA)	0.1	10^6 (D_2 FUEL)	1977

Table II-B-2

NEAR TERM EXPERIMENTAL DRIVERS FOR

INERTIAL CONFINEMENT FUSION EXPERIMENTS

LABORATORY	DRIVER	POWER, TW	COMPLETION DATE	ANTICIPATED EXPERIMENTAL RESULTS
SANDIA-A	e-BEAM (PROTO-II)	7	1977	10^7 - 10^9 NEUTRONS
LLL	Nd: GLASS LASER (SHIVA)	10-40	1977	~10^{13} NEUTRONS
LASL	8-BEAM CO_2 LASER	10-20	1978	10^{10} - 10^{12} NEUTRONS
LLE-UR	Nd: GLASS LASER (OMEGA-10)	3-30	1979-80	USER FACILITY
SANDIA-A	e-BEAM (EBFA-I)	30 (1 MJ, 40 ns)	1980	10^{10} - 10^{13} NEUTRONS
KURCHATOV	e-BEAM (ANGARA V)	80 (5 MJ, 85 ns)	1982	G ~ 100
LLL	Nd: GLASS LASER (NOVA)	100-300	1983	10^{16} - 10^{19} NEUTRONS G ~ 1 - 100
LASL	CO_2 LASER (ANTARES)	100-200	1983	10^{16} - 10^{17} NEUTRONS G ~ 1 - 10
SANDIA-A	e-BEAM (EBFA-II)	60-80	1983-85	10^{15} - 10^{17} NEUTRONS G ~ 0.1 - 10

experiments carried out with ever increasing driver energy and power on target, taken together with the results of reactor studies like SOLASE, should establish whether an ambitious engineering-oriented program aimed at reactor development is justified.

References for Chapter II

1. J. Lindl, "High Gain Targets for Advanced Laser System", Bull. Amer. Phys. Soc. 22, 1078 (1977). Also, J. Lindl, "Low Aspect Ratio Double Shells for High Density and High Gain", Topical Meeting on Inertial Confinement (to be published, Optical Society of America, Feb. 1978).

2. R. W. Conn, et al., "Studies of the Technological Problems of Laser Driven Fusion Reactors -- Annual Report", Fusion Research Program Report UWFDM-190, Nuclear Eng. Dept., The University of Wisconsin (Dec. 1976).

III. Laser Fusion Physics

III-A. Introduction to General Ideas of Inertial Confinement

The laser driven fusion concept of CTR[1-3] involves the implosion of spheres or shells of fusion fuel to densities of 10^3 to 10^4 times normal solid density. At these high densities the inertial confinement time, dictated by the disassembly time of the fuel pellet, is greater than the thermonuclear reaction time and net energy gain from the pellet is predicted. This implosion to high densities is driven by laser heating of the pellet surface which in turn ablates and drives the interior of the pellet inward due to the so-called rocket effect, Fig. III-A-1.

The most meaningful figure of merit for inertially confined plasmas is the product of fuel density and radius, ρR, rather than the customary density-energy confinement time product, $n\tau$. The density-radius product can be interpreted in several equivalent ways. If the thermonuclear burn efficiency of a fuel pellet is expressed as the ratio of characteristic disassembly time to thermonuclear burn time, then this ratio is proportional to ρR, namely

$$\tau_d = R/C_s$$

$$\tau_b = \frac{1}{(\overline{\sigma v})\ \rho/m_i}$$

$$\tau_d/\tau_b = \rho R\ \overline{\sigma v}/C_s m_i .$$

For deuterium-tritium fuel (the most reactive fusion fuel) at 20 keV $\overline{\sigma v}/C_s m_i \approx 1$, hence the ρR product should exceed 1 to provide good efficiency. To sustain the burn, the fuel temperature must be maintained at 20 keV or greate by redeposition of energy from the thermonuclear reaction products. In the case

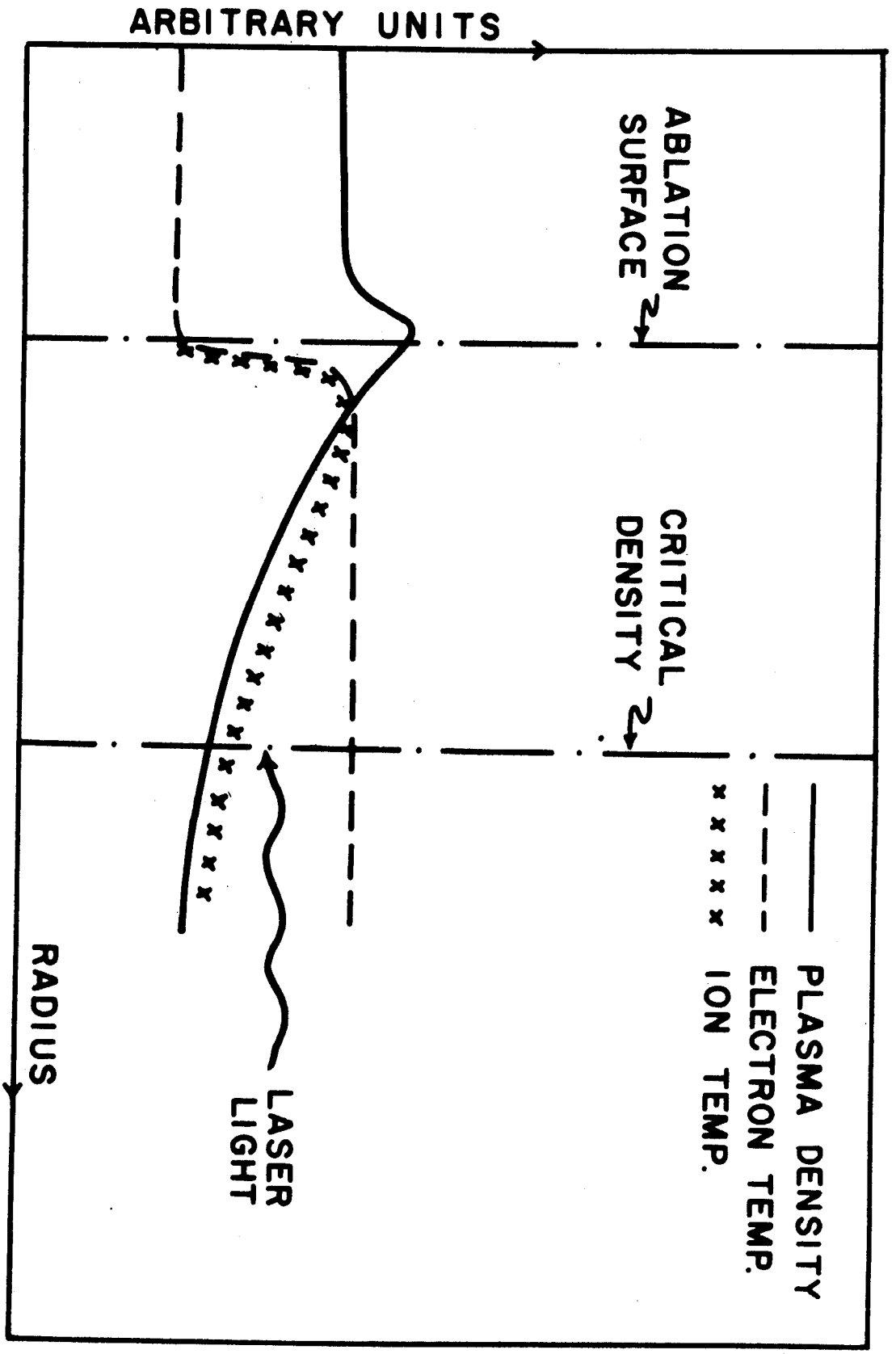

LASER-PELLET INTERACTION SCENARIO

Fig. III-A-1

of DT fuel this is a 3.5 MeV alpha particle. Thus, the fuel must be characterize by a "size" that is in excess of the range of a 3.5 MeV alpha particle.[4] The density independent range of a 3.5 MeV alpha particle in a 20 KeV DT plasma is about 0.5 gram/cm^2. Hence the ρR value of the fuel must exceed 0.5 g/cm^2 and computer calculations show that $\rho R = 3$ g/cm^2 is the optimum value for the fusion fuel.

The density-radius product can be related to the fuel mass and radius by

$$\rho R = \frac{M}{\frac{4}{3}\pi R^3} R = \frac{3}{4\pi} \frac{M}{R^2} .$$

III-A-1. Laser Requirements for Laser Fusion

The necessary conditions to promote efficient thermonuclear burning have been established and now the energy necessary to achieve these conditions must be determined and related to the thermonuclear energy yield to determine under what conditions inertial confinement fusion becomes attractive from an energy gain point of view. This can be done by relating the input (laser) energy to the plasma thermal energy via an efficiency ε and by also relating the thermonuclear yield energy to the plasma thermal energy by a multiplication factor β that accounts for thermonuclear burn propagation.[5] Define

$$G_p \equiv E_{fusion}/E_{laser}$$

$$\varepsilon \equiv E_{plasma}/E_{laser}$$

$$E_{fusion} = \beta \frac{4}{3}\pi R^3 n^2 \overline{\sigma v} \tau_d$$

$$\tau_d = R/C_s$$

n = plasma density

C_s = isothermal sound speed

R = plasma radius

$\overline{\sigma v}$ = fusion reaction rate

Combining these terms gives an expression for the laser energy as a function of pellet gain energy, coupling efficiencies and the volumetric compression of the fuel.[3,5]

$$E_{laser} = \frac{G_p^3}{(\varepsilon\beta)^4} \frac{1}{\eta^2} (x)\ 1.6\ MJ$$

$$\eta = n/n_{solid} \text{ - compression factor}$$

To reach energy breakeven ($G_p = 1$) at solid DT density ($\eta = 1$) assuming $\varepsilon\beta = 1$ requires a laser energy of 1.6 MJ. For reactor applications the gain must be about 100 to compensate for power plant inefficiencies. Thus for this case, $E_{laser} = 1.6 \times 10^6$ MJ. This laser energy is far in excess of any conceivable laser system. If, however, the pellet can be compressed to ten thousand times solid density ($\eta = 10^4$) then the necessary laser energy for a reactor is 16 KJ

$$E_{laser} = \frac{(100)^3}{(1)^4} \frac{1}{(10^4)^2} \times 1.6\ MJ = 16\ KJ\ .$$

This laser energy is within reach of lasers in the planning stage today. However, more detailed analysis will show that this simple argument is too optimistic by probably an order of magnitude or more because η and ε are in fact not independent parameters. Two observations should be made about this formula:

(i) Increasing the value of η has implicitly reduced the amount of mass being compressed. In other words, the same ρR value is achieved by compressing a small amount of fuel. Hence, with the gain held fixed at 100 the lower laser energy requirement really is the result of less fuel mass.

(ii) The laser-plasma coupling efficiency is typically 5% with the remaining 95% of the laser energy used to compress the fuel pellet. The multiplication factor (β) accounting for thermonuclear burn propagation must then be 20 to give $\varepsilon\beta = 1$. Such multiplication is only feasible for fuel masses greater than or equal to one milligram.

These additional constraints must be satisfied when defining fuel pellet requirements for power plant applications. This will be done in section III-B.

III-A-2. Implosion Scenario

The next step is to identify how laser beams can, in fact, compress and heat a pellet of fusion fuel by following through an implosion scenario

A small (one millimeter), spherical drop of liquid deuterium-tritium fusion fuel is irradiated uniformly over its surface with light from a high power laser source. The outer surface of the droplet heats, ionizes and ablates outward. The electrons in this cloud of plasma continue to absorb more laser radiation via inverse bremsstrahlung. The laser radiation is only able to penetrate into the plasma up to the "critical density" where the electron plasma frequency is equal to the incident laser frequency. The transport of energy from the critical density inward occurs via the mechanisms of thermal conduction and hydrodynamic motion. As the plasma surface is heated and ablates outward (blow-off) a shock front is formed that converges (implodes) inward toward the center, pushing cold D-T fuel ahead of it to higher and higher densities along a Fermi degenerate adiabat (Fig. III-A-1). Fig. III-A-1 distinguishes three regions in the plasma during the implosion process.

Beyond the critical density (Region III) the underdense plasma absorbs the laser energy and expands outward. Between the shock front and the critical density (Region II), electron thermal conduction is the dominant mechanism transporting energy from Region III in to the ablation surface. Inside the ablation surface (Region I) the D-T fuel is compressed along a low adiabat (~1 ev) to very high densities. When the shock fronts finally converge together at the center of the pellet, the central part of the dense pellet is shock-heated to thermonuclear temperatures (Fig. III-A-2). This central hot spot or microcore must have a density-radius product of 0.4 g/cm^2 to initiate bootstrap heating and the entire core must have ρR = 3 g/cm^2 to provide significant yield and gain. The microcore will then self-heat to 20 keV or more and the alpha particle reaction products will heat the next thin layer of surrounding plasma, raising its temperature to thermonuclear values. As this process continues, a burn wave will propagate outward, consuming the dense pellet core. The idea is thus to adiabatically compress the D-T fuel to ρR = 3 g/cm^2 and then ignite the central microcore. Detailed calculations indicate that such a scenario might be possible, utilizing a very precisely programmed laser pulse. The simple theory of homogeneous isentropic compression[6,7] shows that the laser pulse should take the general form

$$P_L(t) = P_L(o)\,[1 - t/t_o]^{-m}$$

where t_o is approximately the collapse time of the shock front and $m \simeq 2$. The detailed calculations show that this pulse is in fact nearly the ideal form.[8] The laser pulse must deliver energy to the plasma at the proper rate to preserve

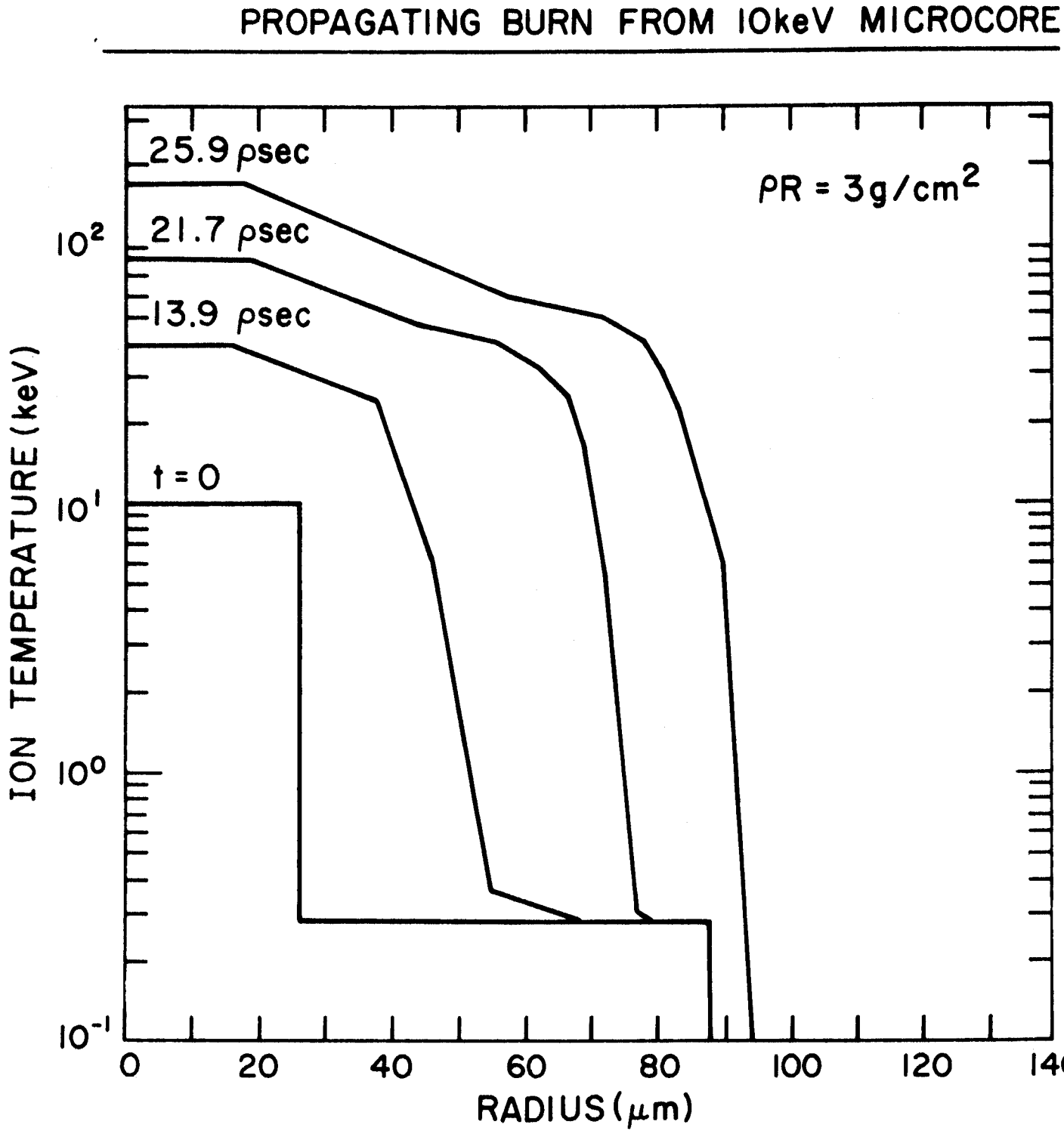
PROPAGATING BURN FROM 10keV MICROCORE
25.9 ρsec
21.7 ρsec
13.9 ρsec
t = 0
ρR = 3g/cm²
ION TEMPERATURE (keV)
10²
10¹
10⁰
10⁻¹
0
20
40
60
80
100
120
140
RADIUS (μm)

Fig. III-A-2

the delicate relation between the electron temperature front and the converging shock front. The temperature front must propagate inward at the proper speed to drive the shock front ahead of it. Should energy be added too quickly the electron temperature front will race ahead of the shock, preheat the core, and degrade or destroy the implosion. Should energy not be delivered at a high enough rate the shock front will not have sufficient strength to compress the plasma to high densities.

The proper laser pulse shape is thus very dependent on plasma properties such as thermal conductivity, laser light absorption, and equation of state. The physical models used to describe the laser-pellet implosion and burn will be discussed in section III-C.

References for Section III-A

1. J. Nuckolls, L. Wood, A. Thiessen, and G. Zimmerman, Nature 239, 139 (1972).
2. J. Clarke, H. Fisher, and R. Mason, Phys. Rev. Lett. 30, 89 (1973).
3. K. Brueckner and S. Jorna, Rev. Mod. Phys. 46, 325 (1974).
4. G. Fraley, E. Linnebur, R. Mason, and R. Morse, Phys. Fl. 17, 474 (1974).
5. R. Kidder, in Fundamental and Applied Laser Physics, (Wiley, New York, 1973).
6. R. Kidder, Nuc. Fus. 14, 797 (1974).
7. R. Kidder, Nucl Fus. 16, 3 (1976).
8. A. Thiessen, G. Zimmerman, T. Weaver, J. Emmett, J. Nuckolls, and L. Wood, Lawrence Livermore Laboratory Report UCRL-74802 (1973).

III-B. Efficiencies and Pellet Gain Requirements for Laser Fusion Reactors

The relationship between target gain and system efficiency is an important one when there are several subsystems with low efficiency. In laser-driven fusion, the laser itself is a key subsystem which has a low anticipated efficiency. To determine the level of target gain required, we proceed by defining the gain of a fusion target by

$$G = \frac{E_F}{E_{LAS}} , \qquad (1)$$

where E_F is the total thermonuclear energy produced and E_{LAS} is the incident energy onto the target. The energy absorbed by the target, E_A, is related to E_{LAS} by

$$E_A = \eta_c \, E_{LAS} \qquad (2)$$

where η_c is the coupling efficiency, i.e., the fraction of incident laser light absorbed by the pellet. Let us define three additional efficiencies:

η_L = laser efficiency

n_{th} = gross plant thermal efficiency

n_p = net plant thermal efficiency

Then the gain is given by

$$G = \left[\frac{1}{\eta_L \, (n_{th} - n_p)} \right] - 1 , \qquad (3)$$

while the net plant efficiency is given by

$$n_p = n_{th} - \frac{1}{\eta_L \, (G+1)} . \qquad (4)$$

Thus, we can determine the pellet gain required to achieve a certain net plant efficiency, η_p, for a system with a laser efficiency, η_L, and a gross power cycle efficiency η_{th}. (This assumes the laser energy dominates the recycle power requirements).

The fraction of gross electrical power recycled to keep the laser operating is

$$F_R = \frac{1}{\eta_L \eta_{th} (G + 1)} \quad . \tag{5}$$

An engineering breakeven condition can be defined as the value of gain, denoted $\bar{G}$, for which $F_R = 1$. $\bar{G}$ is given by

$$\bar{G} = \left(\frac{1 - \eta_L}{\eta_L} \right) \quad .$$

Scientific breakeven, on the other hand, is defined as $G \equiv G_S = 1$. Clearly, $\bar{G}$ can be substantially greater than G_S.

The gain required to achieve a given value of $(\eta_{th} - \eta_p)$ for various values of η_L is shown in Fig. III-B-1. Typically, $\eta_{th} - \eta_p$ is no larger than 0.3 since at this value, η_{th} must be 60% to allow a net plant efficiency of only 30%. In general, η_{th} is between 35 and 50% so that we would consider $(\eta_{th} - \eta_p)$ values of 0.1 to 0.15 interesting with larger values quite difficult to achieve. The analysis shows clearly that for values of η_L like 10%, the gain required for engineering breakeven is 9 and the gain required to achieve $(\eta_{th} - \eta_p)$ of 0.1 to 0.15 is between 65 and 100. Close examination of these simple relationships shows that for most cases of practical interest, pellet gain values in the range of 75-100 and higher will be required. Such gains have been reported in the literature (Fig. III-B-2). We see that in general the gain increases with higher yield and that a gain of 75-100 is associated with yields of about

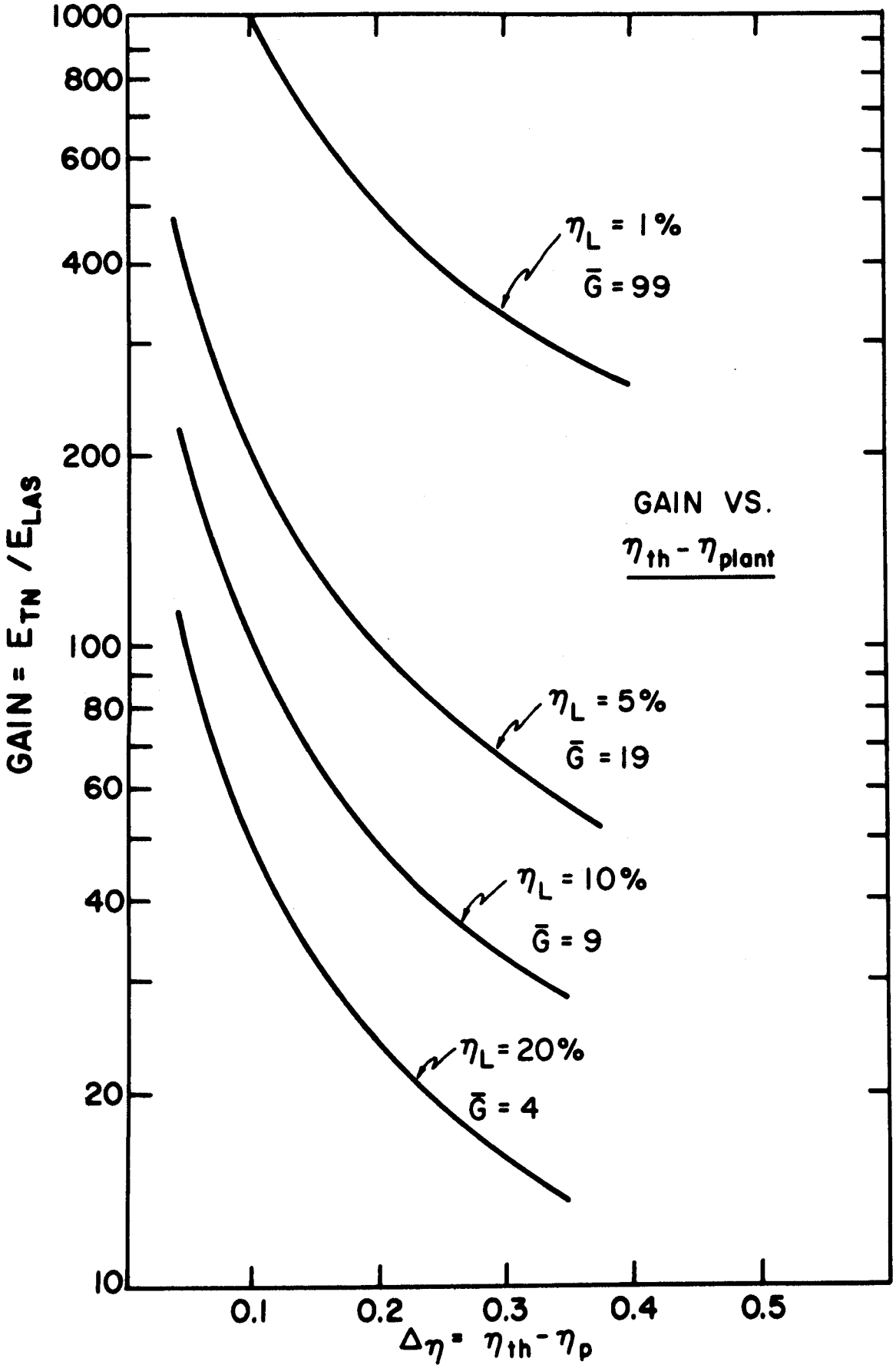
1000
800
600
400
200
100
80
60
40
20
10
GAIN = E_{TN} / E_{LAS}
η_L = 1%
$\bar{G}$ = 99
GAIN VS.
$\eta_{th} - \eta_{plant}$
η_L = 5%
$\bar{G}$ = 19
η_L = 10%
$\bar{G}$ = 9
η_L = 20%
$\bar{G}$ = 4
0.1
0.2
0.3
0.4
0.5
$\Delta\eta = \eta_{th} - \eta_p$

Fig. III-B-1

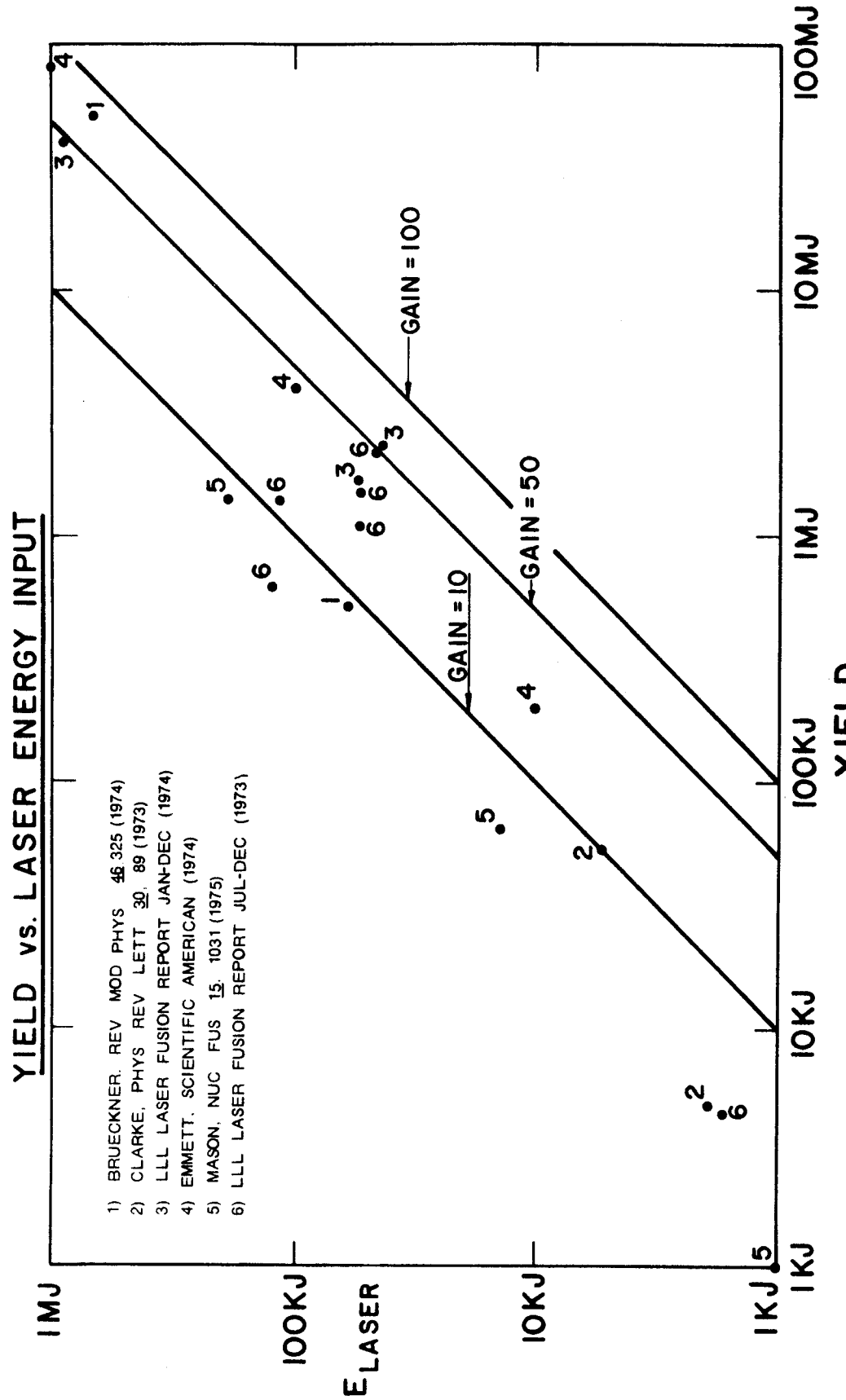
YIELD vs. LASER ENERGY INPUT
1) BRUECKNER, REV MOD PHYS 46 325 (1974)
2) CLARKE, PHYS REV LETT 30, 89 (1973)
3) LLL LASER FUSION REPORT JAN-DEC (1974)
4) EMMETT, SCIENTIFIC AMERICAN (1974)
5) MASON, NUC FUS 15, 1031 (1975)
6) LLL LASER FUSION REPORT JUL-DEC (1973)
GAIN = 100
GAIN = 50
GAIN = 10
1MJ
100KJ
10KJ
1KJ
E LASER
100MJ
10MJ
1MJ
100KJ
10KJ
1KJ
YIELD

Fig. III-B-2

100 MJ, which is in the necessary range. However, some of these more optimistic results have been obtained from high aspect ratio shell targets and serious doubts have been raised about the hydrodynamic stability of these shells.

From the viewpoint of reactor design, a pellet gain of 150 is necessary to make a pure laser fusion reactor feasible with a laser efficiency of 7%. Also a yield of 150 MJ is consistent with a full scale reactor power system. The 150 MJ yield will determine the amount of fuel in the pellet (i.e. the mass of the compressed core) and the gain of 150 implies that this fuel must reach thermonuclear conditions using a 1 MJ laser.

The mass of fuel is calculated by assuming the DT fusion reaction Q value is 17.6 MeV. Then a mass of 0.4455 milligrams (mg) of DT must react to produce 150 MJ of energy. The total number of reactions, N, is

$$N = \frac{Y(MJ)}{Q(MeV)(1.6 \times 10^{-19}\ MJ/MeV)} = 5.325 \times 10^{19}\ \text{reactions}$$

Each reaction requires one deuterium and one tritium nucleus so that

$$M_b = N^*[M_D + M_T]$$

$$= 0.4455\ \text{mg}.$$

To determine the necessary total mass of the core, the fractional burn-up must be determined. For $\rho R = 3\ g/cm^2$ and a T = 10 KeV microcore of $0.5\ g/cm^2$, the fractional burnup is $f_B = 0.31$. This gives the total core mass as 1.437 mg. This mass of DT compressed to $\rho R = 3\ g/cm^2$ implies a compression of $\eta = 1314$ So for $\varepsilon\beta = 3.1$, the necessary laser energy is found to be 1 MJ.

$$E_L = \frac{(150)^3}{(3.1)^4} \frac{1.6\ \text{MJ}}{(1314)^2} = 1\ \text{MJ}$$

Therefore, the yield and gain found necessary for a pure laser fusion power plant derived from purely electrical output and plant efficiency arguments fall close to those values considered achieveable from only pellet physics arguments.

III-C. Laser Plasma Modelling

III-C-1. Hydrodynamics

III-C-1-a. Introduction

In this section we present a rather pragmatic discussion of the physics used to model laser produced plasmas. The emphasis is on what is currently used rather than what should be used.

To understand in detail the dynamics and interaction of laser light heating, heat transfer, ablation-implosion, and thermonuclear burn, the laser fusion plasma is typically modeled using the hydrodynamic description along with laser-plasma interaction physics and rate equations to predict thermonuclear yield.[1] Solution of the hydrodynamics equations generally requires that the plasma be in local thermodynamic equilibrium (LTE) where equations of state and transport coefficients can be defined to close the set of equations.[2] This is generally valid for the collision dominated dense plasma, although there are important exceptions that can strongly alter the results given by the purely hydrodynamic description. These effects are treated through corrections to the transport coefficients.

Non-thermal particles such as thermonuclear reaction product charged particles, photons and non-thermal electrons are treated as particle species separate from the "thermal background plasma" described by the hydrodynamic treatment. These non-thermal particles have mean free paths much longer than

the hydrodynamic scale lengths and must be treated using kinetic theory. These will be described in later sections. This section will deal with the purely hydrodynamic description.

III-C-1-b. One Fluid-Two Temperature Model

For the purposes of modeling pellet implosions as well as interpreting current experiments, the one fluid-two temperature plasma hydrodynamic model is typically used. In this model, the electrons and ions are assumed to move together as a single fluid (with the same velocity $\underline{U}$ ($\underline{r}$,t)) implying charge neutrality over lengths of hydrodynamic interest. This approximation is verified by comparing the plasma Debye length with the hydrodynamic scale of about one micron over the temperature and density range relevant to laser fusion plasmas.

Table III-C-1.

Debye Length (cm)

Temp (eV) \ Density (cm^{-3})	10^{18}	10^{20}	10^{22}	10^{24}
10	2.35×10^{-6}	2.35×10^{-7}	2.35×10^{-8}	2.35×10^{-9}
10^2	7.43×10^{-6}	7.43×10^{-7}	7.43×10^{-8}	7.43×10^{-9}
10^3	2.35×10^{-5}	2.35×10^{-6}	2.35×10^{-7}	2.35×10^{-8}
10^4	7.43×10^{-5}	7.43×10^{-6}	7.43×10^{-7}	7.43×10^{-8}

For purposes of energy transfer, the electrons and ions are treated as separate species, each in local thermodynamic equilibrium at different temperatures, $T_e(\underline{r}, t)$ and $T_i(\underline{r}, t)$. A two temperature model is suggested by comparison of the electron-electron, ion-ion, and electron-ion energy equilibration times in Table III-C-2.

Table III-C-2.

Electron-Electron, Ion-Ion, Electron-Ion Collision Times

Density (cm^{-3})

Temperature (ev)	10^{19}			10^{21}			10^{23}		
	t_{ee}	t_{ii}	t_{ei}	t_{ee}	t_{ii}	t_{ei}	t_{ee}	t_{ii}	t_{ei}
10	10^{-13}	7×10^{-12}	2×10^{-10}	10^{-15}	7×10^{-12}	2×10^{-12}	10^{-17}	7×10^{-16}	2×10^{-14}
100	10^{-12}	2×10^{-10}	6×10^{-9}	10^{-14}	2×10^{-12}	6×10^{-11}	10^{-16}	2×10^{-14}	6×10^{-13}
1000	10^{-10}	7×10^{-9}	2×10^{-7}	10^{-12}	7×10^{-11}	2×10^{-9}	10^{-14}	7×10^{-13}	2×10^{-11}
10000	10^{-9}	2×10^{-7}	6×10^{-6}	10^{-11}	2×10^{-9}	6×10^{-8}	10^{-13}	2×10^{-11}	6×10^{-10}

t (seconds)

Since typical time scales in an implosion are less than 10^{-9} seconds, it is likely that energy will diffuse through electron and ion populations before the electrons and ions can equilibrate.

Momentarily treating the plasma as an inviscid fluid, the one fluid-two temperature hydrodynamics equations can be written:

$$\frac{\partial \rho}{\partial t} + \nabla \cdot (\rho \underline{u}) = 0 \qquad \text{(Continuity)}$$

$$\rho[\frac{\partial u}{\partial t} + \underline{u} \cdot \nabla \underline{u}] = - \nabla(P_e + P_i) \qquad \text{(Momentum)}$$

$$\rho C_{v_e}[\frac{\partial T_e}{\partial t} + \underline{u} \cdot \nabla T_e] = \nabla \cdot K_e \nabla T_e - P_e(\nabla \cdot \underline{u}) - \omega_{ei}(T_e - T_i) + S_e \qquad \text{(Energy)}$$

$$\rho C_{v_i}[\frac{\partial T_i}{\partial t} + \underline{u} \cdot \nabla T_i] = \nabla \cdot K_i \nabla T_i - P_i(\nabla \cdot \underline{u}) + \omega_{ei}(T_e - T_i) + S_i$$

$$\rho = n_e m_e + n_i m_i$$

One must have equations of state to close this set of equations.

$$P_e = P_e(n_e, T_e) \quad ; P_i = P_i(n_i, T_i)$$

$$C_{v_e} = C_{v_e}(n_e, T_e) \quad ; C_{v_i} = C_{v_i}(n_i, T_i)$$

The transport law for the heat fluxes $\underline{q}_e$ and $\underline{q}_i$ has already been specified in the form of Fourier's Law:

$$\underline{q}_e = - K_e \nabla T_e \ \& \ \underline{q}_i = - K_i \nabla T_i \ ,$$

so that expressions must also be supplied for the transport coefficients:

K_e - electron thermal conductivity

K_i - ion thermal conductivity

ω_{ei} - electron-ion temperature equilibration coefficient.

The exact forms of these terms will be discussed in the next two sections. Along with the convection, conduction, work and equilibration terms, each temperature equation has an external source term. The electron source term will account for temporal and spatial electron energy gain and loss with the non thermal radiation field; energy gain from the absorption of laser light; and gain from the redeposition of energy by non-thermal thermonuclear reaction products. The ion source must account for gain from thermonuclear reaction product energy redeposition.

With the annihilation of ions by fusion reactions and the treatment of the resultant reaction products as separate non-hydrodynamic species, the right hand side of the continuity equation must strictly be replaced by annihilation and creation terms to account for fusion reactions and rethermalization of the reaction products.

III-C-1-c. Equation of State

The equations of state for a relatively hot, fully ionized plasma can be adequately approximated by the ideal gas laws.

$$P_e = n_e k_B T_e , \quad P_i = n_i k_B T_i$$

$$C_{v_e} = \frac{3}{2} k_B Z/m_i , \quad C_{v_i} = \frac{3}{2} k_B/m_i \quad .$$

Unfortunately, the cold, highly compressed DT plasma ahead of the converging shock fronts during implosion does not obey this law. The electrons are Fermions and strictly obey Fermi-Dirac rather than Boltzmann statistics. In their highly compressed, cold state they begin to fill all the available low energy states and equations of state must be derived from the Fermi-Dirac distribution function[3]. In addition, the energy associated with different solid phases, the liquid phase, and dissociation and ionization of real materials must be treated in order to correctly predict the electron pressure[4]. For

higher Z materials the differing ionization states must also be treated, even at high temperatures, through models such as Saha equilibrium or by solving the non-equilibrium ionization rate equations. These complications require different theories and approximations for each temperature and density range and for every different material. A great amount of theoretical and experimental work has been invested in accurate equations of state in support of the nuclear weapons program, and more recently directly in support of the needs of the laser fusion effort. Equations of state for purposes of computation are usually in the form of tables of pressure values or tables of fitting parameters that are evaluated to obtain pressure values as functions of density or compressibility and temperature.

Equations of state are most important in correctly predicting the adiabatic compression of the dense pellet core.

III-C-1-d. Transport Coefficients

Whereas the accuracy of equation of state values is most important in the cold, dense pellet core, the transport coefficients are dominant in the hot, ablating pellet corona. Classical (Spitzer) values for the transport coefficients are[5]

$$K_e = 20\left(\frac{2}{\pi}\right)^{3/2} \frac{k_B (k_B T_e)^{5/2}}{m_e^{1/2} e^4 Z \ln\Lambda_{ei}}$$

$$K_i = 20\left(\frac{2}{\pi}\right)^{3/2} \frac{k_B (k_B T_i)^{5/2}}{m_i^{1/2} e^4 Z^4 \ln\Lambda_{ii}}$$

$$\omega_{ei} = \frac{8(2\pi)^{1/2} n_e Z^2 e^4 \ln\Lambda_{ei}}{3 m_e m_i k_B^{3/2}} \left(\frac{T_e}{m_e} + \frac{T_i}{m_i}\right)^{-3/2}$$

The coefficients all depend strongly on T_e or T_i, making the electron and ion temperature diffusion equations highly non-linear. If non-parallel temperature and density gradients exist, (due to a nonsymmetric implosion), self-generated magnetic fields arise, and the transport coefficients must be corrected for conduction perpendicular to the B-field[6], i.e.

$$K_e \rightarrow \frac{K_e}{1 + \omega_c^2 \tau^2}$$

In addition to these purely magnetohydrodynamic effects, the electron heat flux is often poorly described by a Fourier transport law. Because the laser heats the electrons, the electron heat flux can be very strong, resulting in very steep temperature gradients that apparently violate the hydrodynamic criteria

$$T_e/\nabla T_e < \lambda_e$$

where λ_e is the electron mean free path.

The result of this breakdown of the transport law is an electron thermal wave propagation speed far in excess of the electron thermal velocity; a clearly nonphysical result. To alleviate this troublesome problem, (and in effect to model nonhydrodynamic behavior with hydrodynamic equations) an electron thermal flux limiter is often added to the temperature equations[7]

$$q_e = - K_e \nabla T_e \rightarrow \frac{K_e \nabla T_e}{1 + \left| \frac{K_e \nabla T_e}{q_{MAX}} \right|}$$

where q_{MAX} is an upper limit on the physically achievable heat flux which is usually dependent on local electron density and temperature. Just as for the pressure, these transport coefficients must be derived using Fermi-Dirac statistics for the dense cold pellet core plasma[8,9].

Comparison of calculational hydrodynamic models with results of current experiments indicate that the classical values of these transport coefficients may be in error by a significant amount[10,11]. They generally overestimate thermal conductivity by as much as a factor of ten! Explanations of this reduced thermal conduction include: the effect of self generated magnetic fields and effective enhancement of the electron collision frequency by plasma turbulence[11].

In all of the previous discussion, the other major transport coefficient, viscosity, has been ignored. Laser fusion plasmas are generally treated as an inviscid fluid although the equation of motion for such a fluid becomes purely hyperbolic and admits discontinuous solutions such as shocks. Such discontinuitie are very difficult to treat numerically so an artificial viscosity[12] is empirically introduced into the hydrodynamics equations in the form of an additional ion pressure

$$P_i \rightarrow P_i + q$$

that is zero everywhere except in the vicinity of a shock, where it adds dissipation. Its form is necessarily such that the jump conditions (Heugoniot relations) across the shock are preserved. This clever "fudge" greatly facilitates the numerical solution of the coupled, non-linear, partial differential equations of hydrodynamics.

References for Section III-C-1

1. K. Brueckner and S. Jorna, Rev. Mod. Phys. 46, 325 (1974).

2. S. Chapman and T. Cowling, The Mathematical Theory of Non-uniform Gases, (Cambridge University Press, Cambridge, 1953).

3. Landau and Liftsitz, Statistical Physics, 2nd Ed., (Addison-Wesley, Reading, Mass., 1969).

4. S. G. Brush, in Progress in High Temperature Physics and Chemistry, Vol. I, Ed. C. A. Rouse (Pergamon Press, London, 1967).

5. L. Spitzer, Physics of Fully Ionized Gases, (Wiley, New York, 1965).

6. S. I. Braginskii, in Review of Plasma Physics, Vol. I, (Consultants Bureau, New York, 1965).

7. J. Shearer, Lawrence Livermore Laboratory Report, UCID-15745 (1970).

8. H. Brysk, P. Campbell, and P. Hammerling, Plasma Phys. 17, 473 (1975).

9. H. Brysk, Plasma Phys. 16, 927 (1974).

10. R. Malone, R. Mc Crory, and R. Morse, Phys. Rev. Lett. 34, 721 (1975).

11. Mount Lassen Conference on Transport Processes in Laser Produced Plasmas (1976).

12. J. Von Neumann, J. Appl. Phys. 21, 232 (1950).

III-C-2. Burn Dynamics

III-C-2-a. Reaction Rates

The basic goal of laser driven fusion is of course to produce a net energy gain via fusion reactions. We first consider the most reactive fusion fuel, a 50-50 atomic percent mixture of deuterium and tritium, the two heavy isotopes of hydrogen. They fuse to form a helium nucleus (alpha particle) and a neutron.

$$ {}_1D^2 + {}_1T^3 \rightarrow {}_2He^4\ (3.5\ \text{MeV}) + {}_0n^1\ (14.1\ \text{MeV}) $$

The energy released in this reaction (Q-value) is approximately 17.6 MeV with 3.5 MeV going to the charged alpha particle. The reaction rate for thermonuclear D-T fusion $(\overline{\sigma v})_{DT}$ is plotted in Fig. III-C-1. Note that it has a broad maximum between ion temperatures of 20 KeV and 80 KeV. The next most probable reaction is between two deuterium nuclei.

$$ {}_1D^2 + {}_1D^2 \xrightarrow{50\%} {}_2He^3\ (0.82\ \text{MeV}) + {}_0n^1\ (2.45\ \text{MeV}) $$

$$ \xrightarrow{50\%} {}_1T^3\ (1.01\ \text{MeV}) + {}_1p^1\ (3.02\ \text{MeV}) $$

The average Q-value is 3.15 MeV while the average energy going into charged particles is 1.925 MeV. The D-D fusion reaction rate $(\overline{\sigma v})_{DD}$ is also plotted in Fig. III-C-1. The D-T reaction is favored over the D-D reaction by about two orders of magnitude. The rate equations for thermal deuterium and tritium concentrations are

$$ \frac{dn_D}{dt} = - n_D n_T (\overline{\sigma v})_{DT} - n_D^2 (\overline{\sigma v})_{DD} $$

$$ \frac{dn_T}{dt} = - n_D n_T (\overline{\sigma v})_{DT} \cdot $$

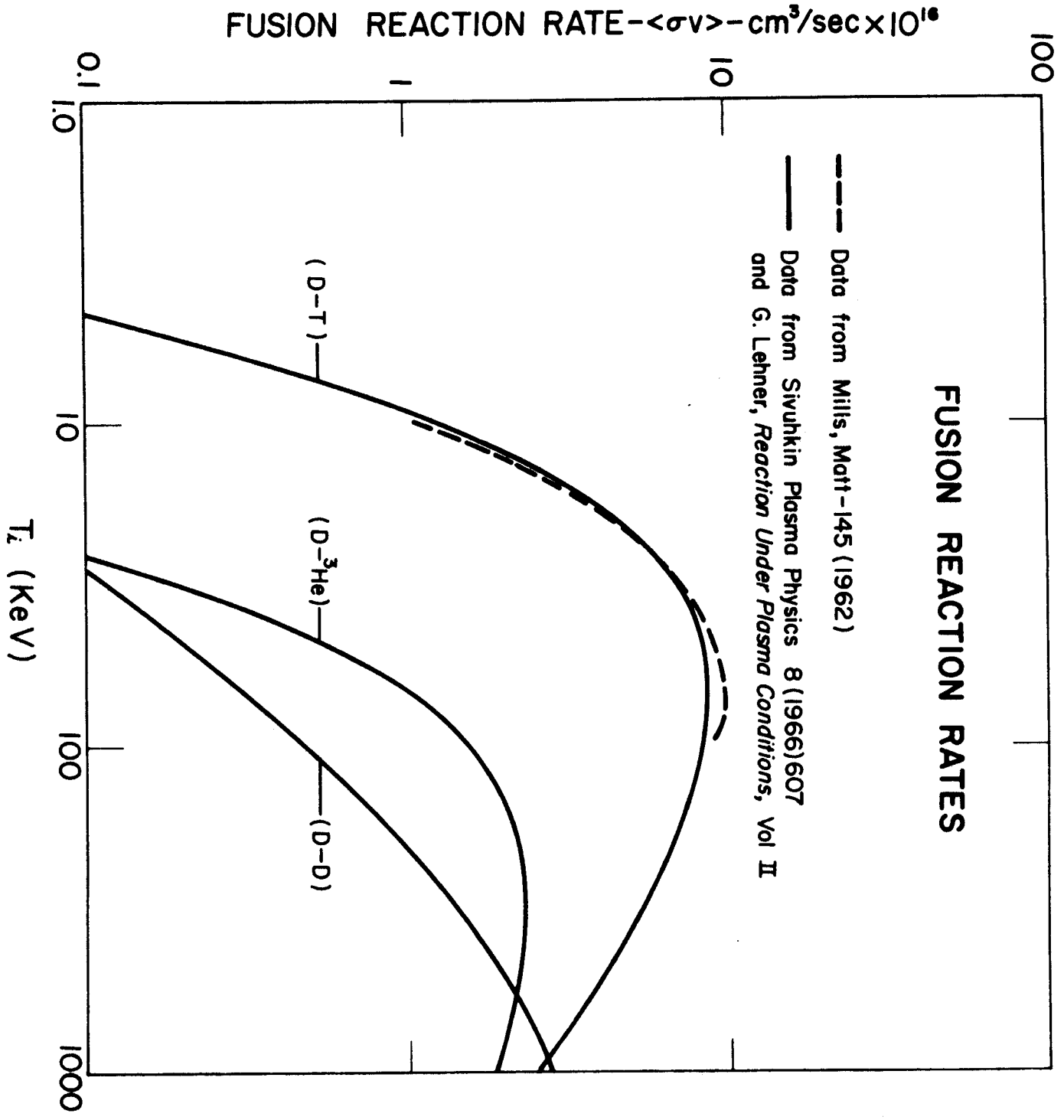
FUSION REACTION RATE-<σv>-cm³/sec×10¹⁶
0.1
1.0
10
100
FUSION REACTION RATES
Data from Mills, Matt-145 (1962)
Data from Sivukhin Plasma Physics 8 (1966)607
and G. Lehner, Reaction Under Plasma Conditions, Vol II
(D-T)
(D-³He)
(D-D)
10
100
1000
Tᵢ (KeV)

Fig. III-C-1

Since the D-D reaction produces a tritium ion for every two fusions it would seem that the equation for n_T should contain a positive term proportional to $n_D^2 (\overline{\sigma v})_{DD}$. The tritium ion reaction product is not thermal however and must be treated separately since its "beam plasma" reaction rate will be much greater than the Maxwellian averaged thermal reaction rate.

III-C-2-b. Charged Particle Transport

Particular attention has been drawn to the energy of the charged particle reaction products. The requirement for efficient thermonuclear burning is that the range of the charged particle reaction products is a small fraction of the radius of the dense pellet core. If this is true then the reaction products will slow down and further heat the core. In this way, only a small central hot spot (microcore) need be heated to an ignition temperature, 4-10 keV. Once burning starts, the reaction product energy redeposition will quickly "bootstrap", heating the microcore to greater than 20 keV where the D-T reaction rate is greatest. As the hot microcore becomes transparent to the reaction products they stream out and are rapidly thermalized in the surrounding colder plasma. In this way a thermonuclear detonation wave propagates outward from the microcore, Fig. III-C-2. To accurately describe this process one must not only solve the rate equations but must treat the transport and thermalization of the reaction products. To do this the Fokker-Planck equation is solved for a fast test particle in a thermal background plasma to obtain a range-energy relation.[1]

$$\frac{dv}{ds} = - 4\pi r_o^2 m_e^2 n_i Z_i^2 Z^2 \ell n\Lambda_i / m_i m v^3 - 4(2\pi)^{1/2} r_o^2 m_e^{5/2} n_e Z^2 \ell n\Lambda_e / 3m(k_B T_e)^{3/2}$$

where r_o is the classical electron radius, and the unsubscripted variables apply to the fast charged particle. The two terms for slowing down in

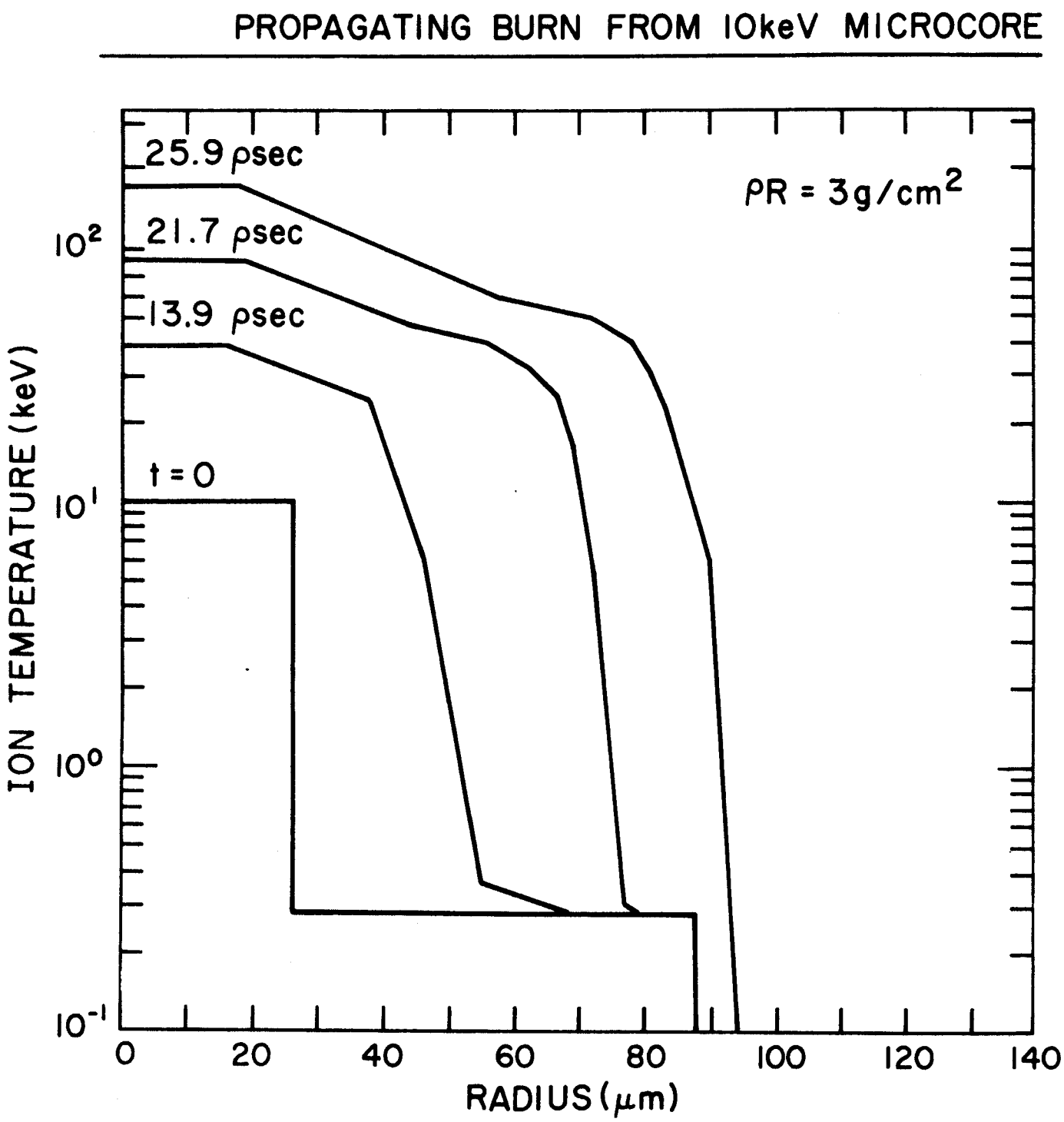
PROPAGATING BURN FROM 10keV MICROCORE
25.9 ρsec
21.7 ρsec
13.9 ρsec
t = 0
ρR = 3g/cm²
ION TEMPERATURE (keV)
10²
10¹
10⁰
10⁻¹
0
20
40
60
80
100
120
140
RADIUS (μm)

Fig. III-C-2

electrons and ions are plotted in Fig. III-C-3. The energy loss rate to electrons is independent of the fast particle velocity; however, the energy loss rate to ions increases as the fast particle velocity decreases. Thus the particles lose most of their energy to electrons along the first part of their path and to the ions near the end of their flight. Fast ions lose half of their energy to electrons and half to ions at an electron temperature of about 30 KeV. Actual transport of the charged particles can be modelled to varying degrees of accuracy by any of the standard linear transport techniques (discrete ordinates S_N,[2] flux limited diffusion,[3] time dependent particle tracking,[4] no transport-local energy deposition[5]).

The range-energy equation implies that the density independent range of a 3.5 MeV alpha particle in a 10 KeV D-T plasma is about 0.3-0.4 g/cm^2. This, therefore, defines the minimum size of the microcore (it must have a density-radius product of at least 0.4 g/cm^2). The charged particles slowing down in the background plasma act as a source of both energy and momentum and as such they affect the hydrodynamic behavior of the plasma. The hydrodynamics in turn affects the temperature and density so that the hydrodynamics and burn dynamics must be treated as coupled processes.

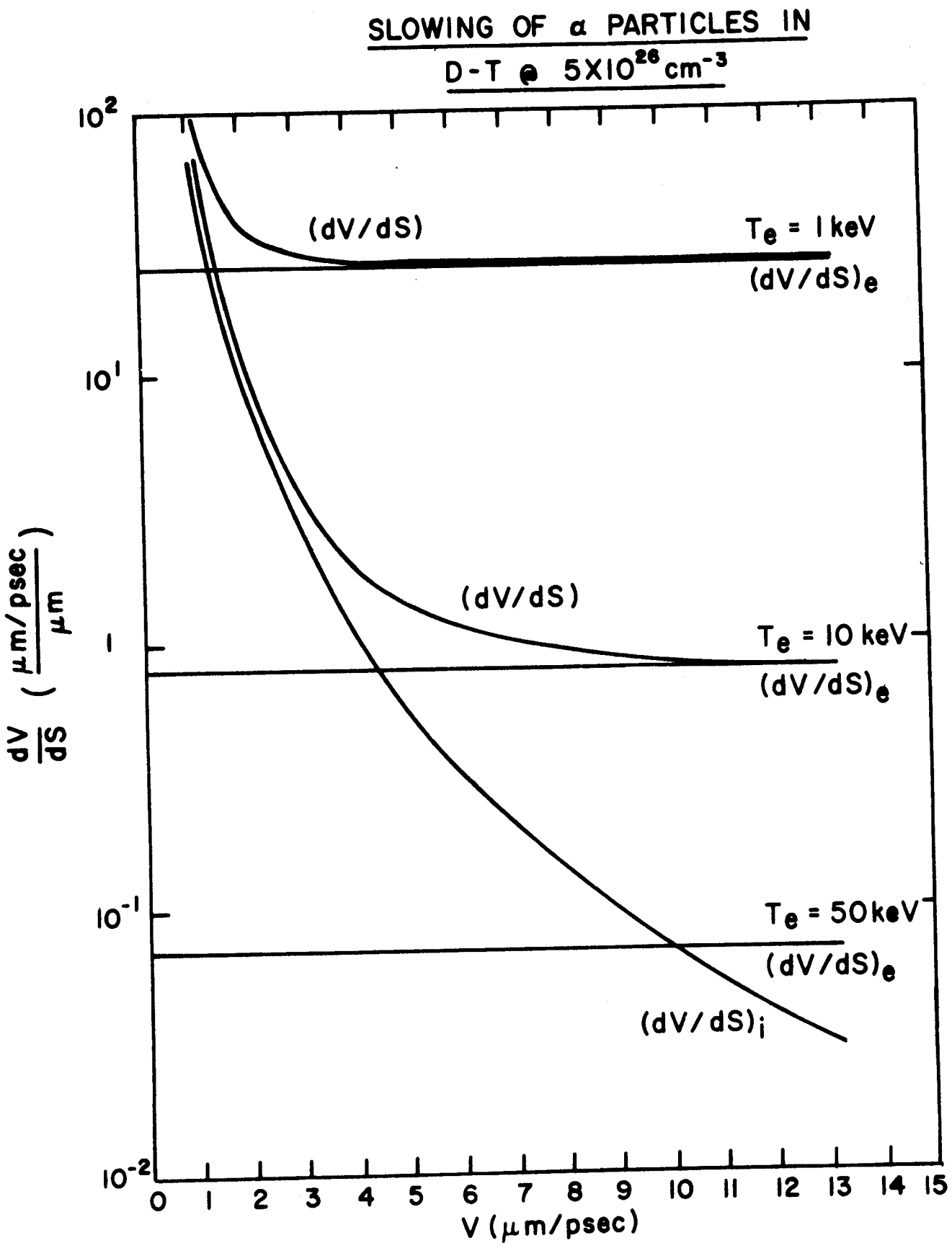
SLOWING OF α PARTICLES IN
D-T @ 5X10^26 cm^-3
10^2
10^1
1
10^-1
10^-2
dV/dS (μm/psec / μm)
(dV/dS)
Te = 1 keV
(dV/dS)e
(dV/dS)
Te = 10 keV
(dV/dS)e
Te = 50keV
(dV/dS)e
(dV/dS)i
0 1 2 3 4 5 6 7 8 9 10 11 12 13 14 15
V (μm/psec)

Fig. III-C-3

References for Section III-C-2

1. K. Brueckner and H. Brysk, J. Plasma Phys. 10, 141 (1973).

2. M. Antal and C. Lee, Los Alamos Scientific Laboratory Report LA-UR-75-726 (1975).

3. Corman, Nuc. Fus. 15, 377 (1975).

4. G. Moses, Nucl. Sci. and Eng. 64, 49 (1977).

5. R. Kidder and Barnes, Lawrence Livermore Laboratory Report UCRL-50583 (1969).

III-C-3. Laser Light Absorption

III-C-3-a. Introduction

Economic operation of a laser fusion reactor depends critically on the amount of laser energy absorbed by the target material. It is well known that collisional absorption decreases rapidly with increasing electron temperature and therefore some additional process, probably resonance absorption[1], is needed to account for the amount of absorption observed experimentally[2,3]. Nevertheless, in many cases a substantial fraction of the total absorption may still be attributed to inverse bremsstrahlung and must be included in numerical simulations of resonance absorption[4].

In this section we shall study linear collisional absorption by means of geometrical optics, which applies whenever the refractive index of the plasma does not change appreciably in a distance of one wavelength. Even at normal incidence, when the ray penetrates to the critical surface, it can be shown that geometric optics gives the correct absorption to within a few percent, except for long laser wavelengths and high-Z materials.[5] For spherically symmetric isothermal plasmas the absorption integral along a ray path can be reduced to a simple radial integral depending only on the density scale height and angle of incidence. This integral is performed in closed form in slab geometry, and asymptotically for small scale heights and angles of incidence in the spherical case.

Besides reducing the total absorption, refraction at oblique incidence also affects the distribution of energy within the corona[6]. Thus, an optical system designed to give uniform illumination at the critical radius (where the bulk of absorption occurs) may have to take into consideration the varying refraction of individual rays. Handy formulas are derived for ray displacements in terms of the density scale height

and angle of incidence in plane geometry, which approximates the sensitive initial phase in illuminating spherical targets. The reason for this sensitivity is the Rayleigh-Taylor instability .

Both theoretical studies[7] and numerical simulations[8] indicate that if catastrophic growth of the Rayleigh-Taylor instability is to be avoided, about 90% optical uniformity must be maintained at early times. Optimal illumination studies[10] show that better uniformity usually means larger angles of incidence as beams are overlapped. Thus, a certain amount of uniformity must be sacrificed in favor of smaller angles of incidence, to avoid excessive refractive loss of energy. In order to quantify this trade-off we have calculated the net absorption for an ideal illumination system, integrated over a spatial beam profile based on the aforementioned optimal illumination studies. The results show an encouraging insensitivity to the maximum angle of incidence, due to the concentration of energy near the beam axis. However, the effective (weighted average) angle of incidence turns out to exceed the range where resonance absorption is expected to be strongest.

A possible mechanism for reducing the effective angle of incidence is the expansion of the critical surface as laser energy is absorbed. Numerical simulations of pellet implosions over a wide variety of pulse shapes and pellet sizes[11] predict an increase of 50-100% in critical radius by the time the maximum laser power arrives. This expansion is modelled and effective angles of incidence calculated for a realistic beam profile. The results are encouraging for small or moderate size pellets. Unfortunately, it appears to be difficult to achieve the requisite conditions for resonance absorption in reactor-size pellets, even allowing for the expansion of the critical radius.

It should be noted that most of today's theory is motivated by the need to interpret current experiments using small targets. Reactor-grade pellets are much more massive, with the consequence that corona temperatures will be highly non-isothermal. Most present-day analyses of parametric instabilities ignore temperature gradients. For example, back-reflection due to stimulated Brillouin scattering[12], a small effect in current experiments, may well be more pronounced in more massive targets.

Another important question is the dependence of absorption on laser wavelength. First, since collisional absorption $\sim \lambda^{-2}$, shorter wavelengths are favored. Further, the critical density $\sim \lambda^{-2}$, with the result that shorter wavelength light will be absorbed closer to the ablation front, reducing the conduction length. Thus, shorter wavelengths (3000-5000 Å) are favored for increased pellet gain. Until recently, experimental evidence indicated that, at flux densities of 10^{14} W/cm^2, most of the incident energy at 10.6 μm would be lost to fast ion motion. However a recent experiment[9] finds that 1.06 μm and 10.6 μm radiation both yield about the same supra-thermal electron energy at flux densities of 10^{15} W/cm^2. Whether or not this surprising result is borne out by further experiments is of vital importance to the laser fusion program. As will be seen in Section V, longer wavelengths are much easier to deal with in designing a beam transport system.

III-C-3-b. Classical Absorption

In the classical picture, individual electrons gain energy by absorbing photons in the coulomb field on a nearby ion. For this reason, inverse bremsstrahlung is often referred to as "collisional", or "free-free" absorption. At low intensities, the classical and quantum-mechanical results are comparable, in which case the latter treatment might be termed "semiclassical" Both, however, are linear. The important nonlinear effects that come into play at intensities greater than about 10^{13} W/cm^2 will be discussed later.

Consider laser radiation obliquely incident on a spherically symmetric plasma, as illustrated in Fig. III-C-4. The intensity along a ray path is given by

$$\Phi = \Phi_{IN} \exp\left(-\int_0^{\ell} \kappa(\ell) d\ell\right) \text{ W/cm}^2, \qquad (1)$$

where Φ_{IN} is the flux incident on the pellet and ℓ is distance measured along a ray. The quantum mechanical free-free absorption coefficient, corrected for spontaneous emission, can be written[13]

$$\kappa = \frac{4}{3}\left(\frac{2}{\pi m}\right)^{1/2} \left(\frac{e^6}{mc^3}\right)\lambda_L^2 \frac{Z_{eff}\, n_e^2}{N\theta_e^{3/2}} f(x) \text{ cm}^{-1} \qquad (2)$$

where, for a multi-species plasma,

$$Z_{eff} \equiv \frac{\langle Z^2 \rangle}{\langle Z \rangle}, \qquad (3)$$

$\theta_e = k\, T_e$, λ_L is the vacuum laser wavelength, N is the refractive index, and

$$f(x) \equiv \frac{\sinh x}{x} K_o(x), \qquad (4)$$

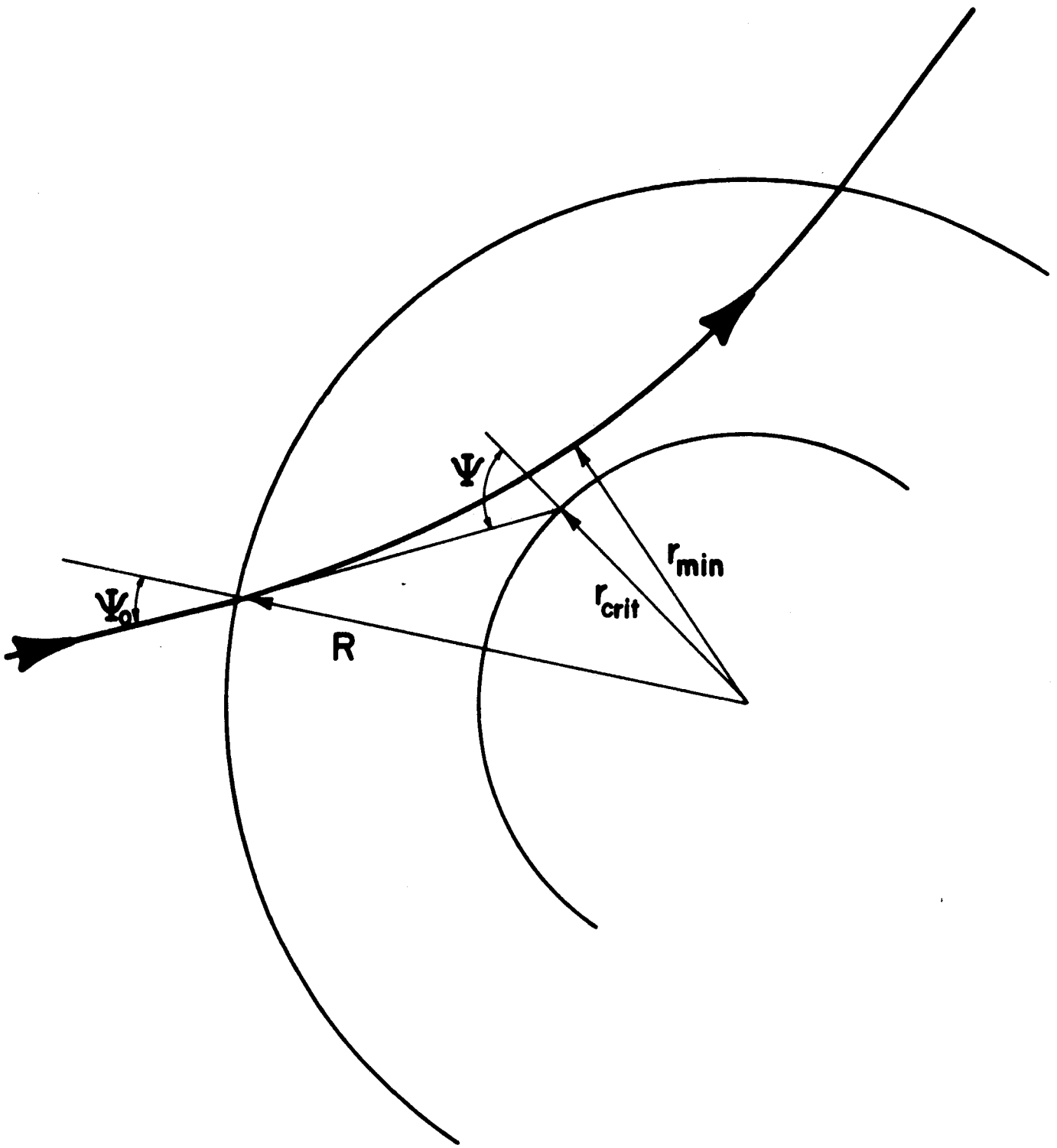

Fig. III-C-4.

where $K_o(x)$ is the modified Bessel function of the second kind, and

$$x \equiv \frac{h\nu}{2\theta_e} . \tag{5}$$

Typically λ_L = 1 μm and θ_e = 1 keV, so that we may take $x << 1$ in Eq. (4) and write

$$\lim_{x \to o} f(x) = \ell n \frac{2}{x} - .5772 = \ell n\ (2.25\ \theta_e/h\nu). \tag{6}$$

In a purely classical treatment of collisional absorption, f(x) is replaced by $\ell n\Lambda$. The present discussion would more appropriately be labelled "linear" absorption.

When the electron-ion collision frequency $\nu_{ei} << \omega$, the refractive index of the underdense plasma is simply

$$N = \sqrt{1 - \omega_p^2/\omega^2} = \sqrt{1 - n_e/n_c}, \quad \omega_p < \omega \tag{7}$$

Thus, inverse bremsstrahlung absorption is most effective for high Z materials at relatively low electron temperatures. Restricting our attention to an isothermal plasma, let us write

$$\kappa = \kappa_o(\theta_e)\ \frac{n_e^2}{N}. \tag{8}$$

The total absorption suffered by a ray as it passes in and out of the corona is then given by

$$\Phi_{ABS} = \Phi_{IN}\ (1 - e^{-\kappa_o A}). \tag{9}$$

The quantity $p = \kappa_o A/2$ is the optical thickness.

We shall refer to

$$A = 2 \int_0^\infty \frac{n_e^2}{N} \, d\ell \tag{10}$$

as the absorption integral.

The phase and group velocities are given by

$$v_p = \frac{c}{\sqrt{1 - \omega_p^2/\omega^2}} \tag{11}$$

$$v_G = c^2/v_p = c\sqrt{1 - \omega_p^2/\omega^2} \, , \tag{12}$$

showing clearly that the laser energy spends most of its time near the critical surface where the bulk of the absorption takes place. A relevant quantity of interest is the energy transit time (in and out):

$$t_T = 2 \int \frac{d\ell}{v_G} = \frac{2}{c} \int \frac{d\ell}{\sqrt{1 - \omega_p^2/\omega^2}} \, . \tag{13}$$

In order for ray tracing studies to make sense, t_T must be much less than the laser pulse length. Even more restrictedly, there must not be significant changes in the intensity in a time t_T. To evaluate the transit time integral (13), let us assume an exponential density profile

$$n_e = n_c e^{-x/L}, \tag{14}$$

where x is distance measured from the critical surface and L is the scale height. This profile is fairly accurate for isothermal atmospheres at relatively low laser intensities.[14] Then, at normal incidence,

$$t_T = \frac{2}{c} \int_0^X \frac{dx}{\sqrt{1 - e^{-x/L}}} \quad , \tag{15}$$

where X is chosen where the plasma density becomes negligibly tenuous. Carrying out the integral, we find

$$t_T = \frac{2X}{c} + \frac{4L}{c} \ln \left(1+\sqrt{1 - e^{-X/L}}\right). \tag{16}$$

Let us choose X large enough that $e^{-X/L} \ll 1$. Then

$$t_T \approx \frac{2X}{c} + (4\ln 2) \frac{L}{c}. \tag{17}$$

Since 2X/c is just the vacuum travel time, we see that the energy lag time is simply

$$\Delta t_T \approx 4\ln 2 \frac{L}{c} = 2.773 \frac{L}{c} . \tag{18}$$

For small pellets, L ≈ 100 μm, so that $\Delta t_T \approx 0.9$ psec. If X = 300 μm, the total transit time through the plasma is about 3.0 psec, still a very short time, even for 40 psec pulses. For very steeply rising pulses there is the possibility of some pulse shape distortion by the time the laser energy reaches the critical surface, due to the time dependence of L.

Another approximation made in deriving the linear absorption coefficient is the transparency condition,

$$\nu_c/\omega_L \ll 1, \tag{19}$$

where ν_c is the electron-ion collision frequency. The full classical absorption coefficient may be written

$$\kappa = \frac{2\omega_L}{c} \left[- \frac{\beta}{2} + \frac{1}{2} \sqrt{\beta^2 + (1 - \beta)^2 (\nu_c/\omega_L)^2} \right]^{1/2} , \tag{20}$$

where

$$\beta \equiv 1 - \frac{\omega_p^2}{\omega_L^2 + \nu_c^2} \tag{21}$$

When (19) is satisfied this simplifies to

$$\kappa^{(o)} = \left(\frac{\omega_p}{\omega_L}\right)^2 \left(\frac{\nu_c}{v_G}\right) . \tag{22}$$

As a sufficient condition for transparency let us evaluate (22) at the critical surface where the absorption is strongest:

$$v_G \kappa_c^{(o)} = \nu_c << \omega_L . \tag{23}$$

Kidder [5] shows that, for $\lambda_L = 1.06$ μm,

$$v_G \kappa_c^{(o)} = \frac{3 \ell n\Lambda \; c Z_{eff}}{\theta_e^{3/2}} \text{ cm}^{-1}, \tag{24}$$

with θ_e in KeV. Using (24) in (23) then gives the result,

$$\frac{Z_{eff} \ell n\Lambda}{\theta_e^{3/2}} << 2 \times 10^4 . \tag{25}$$

Since $\ell n\Lambda$ lies in the range 5-10 for kilovolt temperatures, we see that the transparency condition is well met for DT or glass, but might be violated for higher Z materials.

The classical absorption coefficient (2) is subject to several restrictions. First of all, at normal incidence, when the ray penetrates to the critical surface, the geometrical optics approximation breaks down. Dawson, Kaw and Green [15] show that consideration of the full wave equation gives an increase in absorption over that predicted by (2).

A veritable host of pronounced nonlinear effects come into play at higher laser intensities, perhaps the most important being density profile modification due to pondermotive forces[16] and resonance absorption[1]. Other effects include self-focusing in the plasma itself[16], stimulated Brillouin and Raman scattering[12], and parametric instabilities[16]. For reactors, one might consider 1 MJ of 5000 Å laser radiation with a peak power of 1000 TW incident on pure DT shells of radius 1 mm. These parameters imply intensities of about 10^{16} W/cm^2 and electron temperatures in the 10 KeV range. Thus, relatively small collisional absorption in highly non-isothermal atmospheres, strong density steepening, and (hopefully) enhanced resonance absorption can be expected.

With these caveats, let us as a first step evaluate the absorption integral (10) under the very simplified conditions of an isothermal exponential density profile.

III-C-3-c. Absorption at Oblique Incidence

In a previous report[10] we found that at least 12 and probably 20 beams would be required to yield acceptably uniform irradiance over the pellet surface. However, a price must be paid for such high uniformity in the form of non-normal incidence and consequent refractive losses. The primary aim of this section is to estimate the magnitude of these losses in a conceptual laser fusion reactor.

Generally we find that for physically realistic spatial beam profiles, the integrated absorption does not depend strongly on the maximum angle of incidence, due to the concentration of beam power near the optical axis. However, the weighted average ("effective") angle of incidence usually turns out to exceed the range where resonance absorption is expected to be strongest. It should be emphasized that the present work takes no account of such non-linear effects as self-steepening[16] of the density profile, due to the substantial pondermotive forces generated at high laser intensities.

III-C-3-c-i. Slab Geometry

Consider a ray incident at angle Ψ on an infinite isothermal slab of plasma, as illustrated in Fig. III-C-5. Assuming the density profile (17)

$$n_e = \begin{cases} n_c e^{-x/L} & x < X \\ 0 & x > X \end{cases} \qquad (26)$$

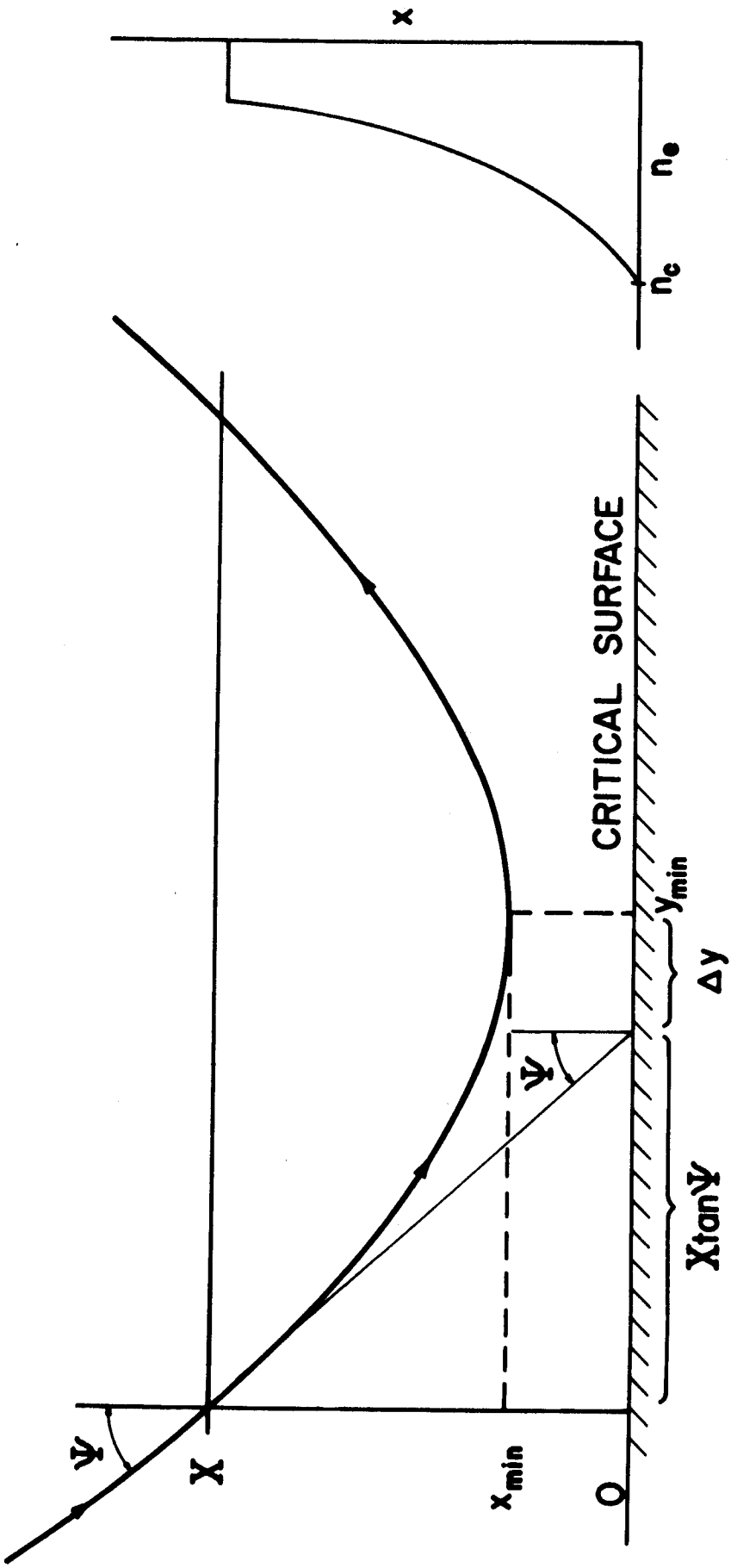

Fig. III-C-5.

we can find the ray path in the x-y plane as follows. From the invariant

$$N(x)\,\sin\theta = \sin\Psi\ , \tag{27}$$

where θ is the angle between the normal and the local tangent, we find

$$N(x_{min}) = \sin\Psi \tag{28}$$

$$y_{min} = \sin\Psi \int_{x_m}^{X} \frac{dx}{\sqrt{N^2 - \sin^2\Psi}}\ . \tag{29}$$

Since

$$N = \sqrt{1 - e^{-x/L}} \tag{30}$$

we have

$$x_{min} = 2L\ \ell n\ \sec\Psi \tag{31}$$

and

$$y_{min} = X\tan\Psi + 2L\tan\Psi\ \ell n\ (\cos\Psi + \sqrt{\cos^2\Psi - e^{-X/L}}\ )\ . \tag{32}$$

A quantity useful for computing the uniformity of energy deposited near the critical surface is the <u>net displacement</u>

$$\Delta y = y_{min} - X\tan\Psi \tag{33}$$

or

$$\Delta y = 2L\tan\Psi\ \ell n\ (\cos\Psi + \sqrt{\cos^2\Psi - e^{-X/L}}\ )\ . \tag{34}$$

When Ψ is small, this reduces to

$$\Delta y \approx 2L\ \Psi\ \ell n\ (1 + \sqrt{1 - e^{-X/L}}\ )\ , \tag{35}$$

and when $X >> L$, Eq. (34) becomes

$$\Delta y \approx 2L\tan\Psi\ \ell n\ (2\cos\Psi)\ . \tag{36}$$

Note that Δy reaches a maximum for some value of Ψ, as Fig. III-C-6 shows for th case $X >> L$.

The absorption integral (10) becomes

$$A = 2 \int_{x_m}^{X} \frac{n_e^2}{N} \frac{d\ell}{dx} dx = 2 \int_{x_m}^{X} \frac{n_e^2 \, dx}{\sqrt{1 - n_e/n_c} \cos\theta} \quad . \tag{37}$$

For the exponential profile (26), this may be written

$$A = 4L \int_{\sin\Psi}^{N_1} \frac{N (1 - N^2) \, dN}{\sqrt{N^2 - \sin^2\Psi}} \quad , \tag{38}$$

where $N_1^2 = 1 - e^{-X/L}$. Thus,

$$A = \frac{8L}{3} \sqrt{\cos^2\Psi - e^{-X/L}} \; (\cos^2\Psi + \frac{1}{2} e^{-X/L}) \quad . \tag{39}$$

When $X >> L$,

$$A = \frac{8L}{3} \cos^3\Psi \quad . \tag{40}$$

This formula is widely used in estimating the effect of oblique incidence on absorption. In the next section, we shall derive the analogue in spherical geometry as an asymptotic series in L. A case of interest is $\Psi << 1$, but $e^{-X/L}$ not small. We find

$$A = \frac{8L}{3} (1 + \frac{1}{2}\gamma) \sqrt{1 - \gamma} \left[1 - \frac{3 (2 - \gamma)}{2 (1 - \gamma) (2 + \gamma)} \Psi^2\right] , \tag{41}$$

where $\gamma \equiv e^{-X/L}$. Equations (36) and (40) have been previously derived by Brueckner[18]. Shearer[19] obtains a $\cos^5\Psi$ law for linear density profiles.

III-C-3-c-ii. Spherical Geometry

Figure III-C-4 shows a ray impinging on a spherically symmetric isothermal plasma. Note that in this case the projected angle of incidence at

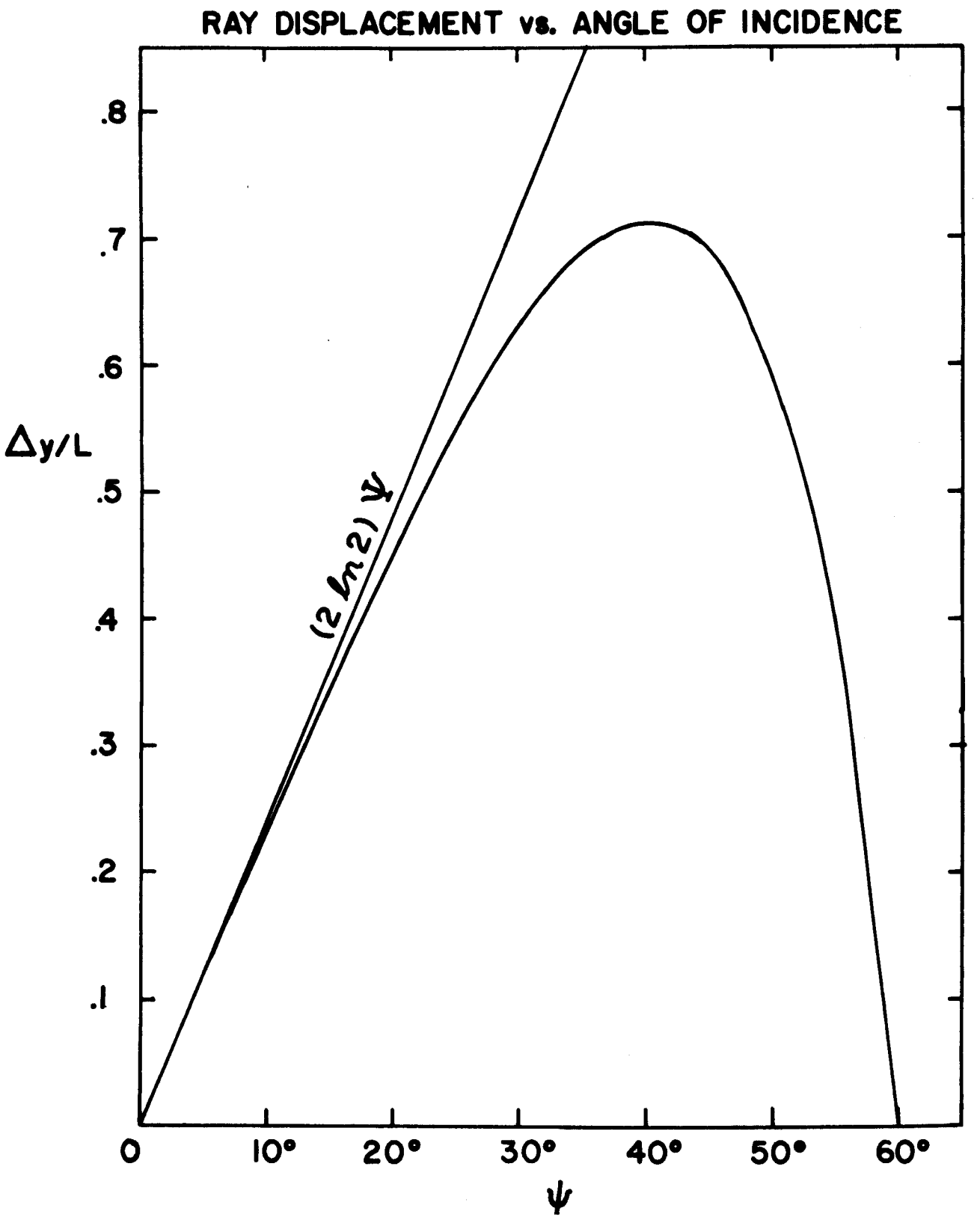
RAY DISPLACEMENT vs. ANGLE OF INCIDENCE
.8
.7
.6
Δy/L
.5
.4
.3
.2
.1
(2 ln 2) Ψ
0
10°
20°
30°
40°
50°
60°
Ψ

Fig. III-C-6.

r_{crit}, Ψ, differs from the exterior angle Ψ_o. When $N = N(r)$, an invariant exists, known as Bouger's Law[20],

$$rN(r)\sin\theta = r_c \sin\Psi = r_m N(r_m) = R\sin\Psi_o. \tag{42}$$

For small Ψ, (42) yields

$$r_{min} \approx r_c + \frac{n_c}{|n_c'|}\sin^2\Psi . \tag{43}$$

For larger Ψ, this is a good starting point for an iterative solution of (42). For an exponential density profile,

$$r_m \approx r_c + L\sin^2\Psi . \tag{44}$$

While the angular displacement θ_{min} is readily calculated, we shall omit it here, since for multibeam systems, uniformity is of interest only at early times, when the scale height is short enough for the slab result (34) to apply. The absorption is

$$A = 2\int_{r_m}^{\infty} \frac{n_e^2}{N}\frac{d\ell}{dr}\,dr , \tag{45}$$

where we have taken $r \to \infty$ for simplicity. From Fig. III-C-4,

$$d\ell = dr\sec\theta . \tag{46}$$

Thus,

$$A(\Psi,L) = 2\int_{r_m}^{\infty} \frac{rn_e^2 dr}{\sqrt{r^2N^2 - \sin^2\Psi}} , \tag{47}$$

where r_c has been scaled out. Note that A depends on Ψ and L through the lower limit of integration as well as the integrand itself. Numerical evaluation of (47) is complicated by the singularity at r_m, even though N(r) doesn't vanish for $\Psi \neq 0$. At normal incidence, (47) reduces to

$$A_\perp = 2 \int_{r_c}^{\infty} \frac{n_e^2 \, dr}{\sqrt{1 - n_e/n_c}} \quad . \tag{48}$$

In this case the integrand is singular at r_c because N = 0. For the exponential density profile we again obtain

$$A_\perp = \frac{8L}{3} \quad . \tag{49}$$

At oblique incidence, closed form expressions for A do not seem to exist. However, two limiting cases may be treated analytically; (a) small incident angles, for arbitrary L; and (b) small L, for which the slab geometry results apply.

Before proceeding to these special cases, let us ask whether L can be predicted <u>a priori</u>. In slab geometry, the "isothermal blowoff model" gives[17]

$$L = v_s t \tag{50}$$

where

$$v_s = \left(\frac{n_i \theta_i + n_e \theta_e}{m_i} \right)^{1/2} \approx \left(\frac{n_e \theta_e}{m_i} \right)^{1/2} \tag{51}$$

is the isothermal sound speed.

In spherical geometry, numerical studies and experiments suggest that a better model may be

$$n_e = n_c \left(\frac{r_c}{r} \right)^2 e^{-(r - r_c)/L} \quad . \tag{52}$$

The effective scale height at r_c is therefore

$$L_{true} = -\frac{n_c}{n_c'} = \frac{L}{1 + 2L/r_c} \quad . \tag{53}$$

At early times the slab result is recovered, but at later times,

$$L_{true} \to r_c/2 \quad . \tag{54}$$

In most cases of interest we may let $R \to \infty$ in the absorption integrals, the expansion front typically extending to about three scale heights or so. Figure III-C-7 shows the normalized absorption integral $A/A_\perp$ as a function of for various scale heights for the exponential density profile (26). As one would expect, the slab result,

$$A/A_\perp = \cos^3\Psi \tag{55}$$

is recovered as $L \to 0$. In fact, because the curves cross near $\Psi = 30^o$, eq. (55) fits to within 5% for $L < 1$, $\Psi \leq 30^o$. Thus, curvature <u>decreases</u> absorption slightly at small angles of incidence, but substantially <u>increases</u> absorption at larger Ψ due to the increased path length in the plasma.

An asymptotic expansion of $A(\Psi,L)$ for $\Psi << 1$ may be carried out as follows. Taking

$$z^2 = N^2 - \frac{\sin^2\Psi}{r^2} \tag{56}$$

eq. (47) may be manipulated into the (exact) form

$$A/A_\perp = 1 - \frac{3}{2}(I_1 + I_2)\sin^2\Psi, \tag{57}$$

where

$$I_1 = \int_0^1 \frac{dz}{r^2} \tag{58}$$

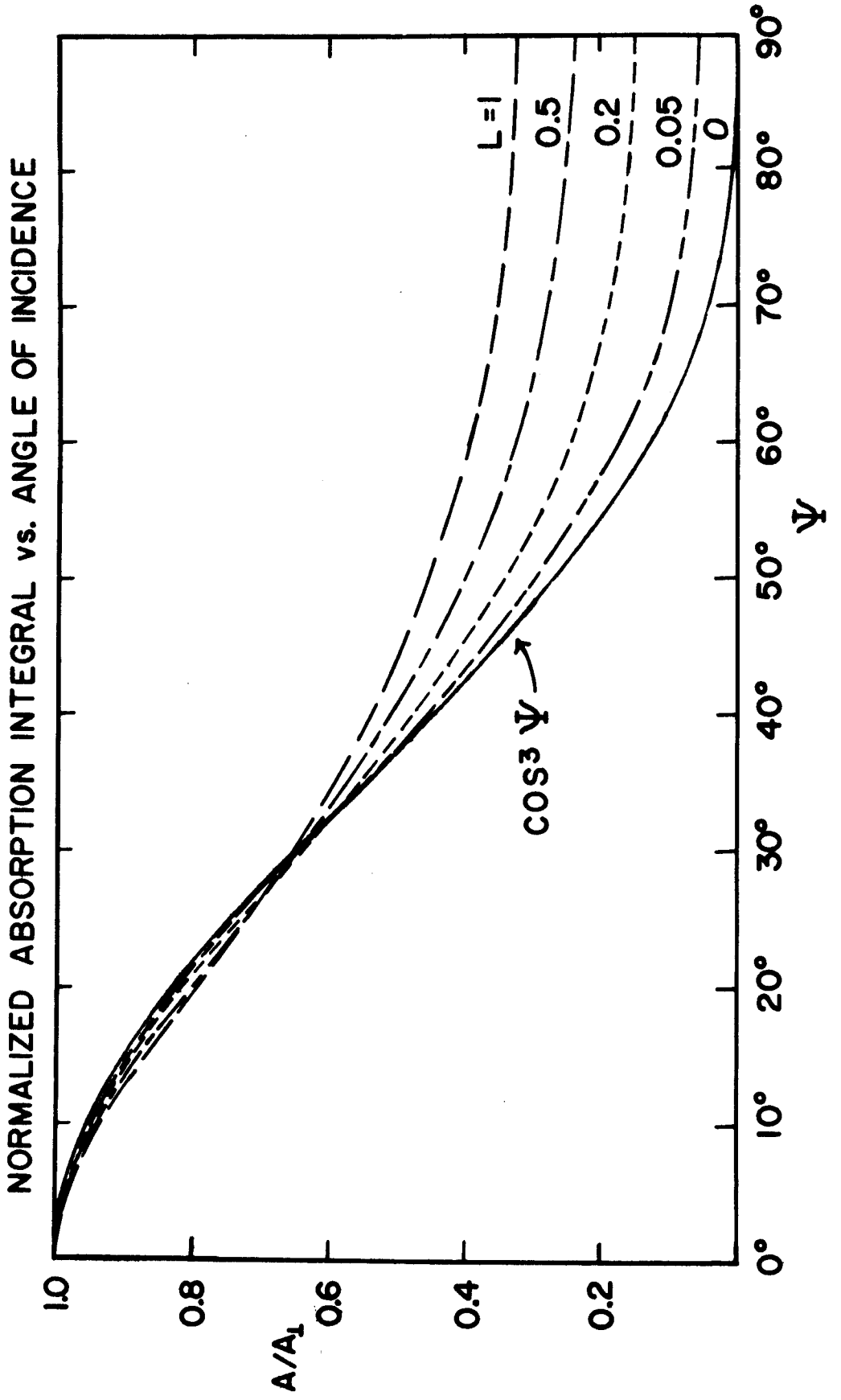
NORMALIZED ABSORPTION INTEGRAL vs. ANGLE OF INCIDENCE
A/A1
1.0
0.8
0.6
0.4
0.2
0°
10°
20°
30°
40°
50°
60°
70°
80°
90°
Ψ
L=1
0.5
0.2
0.05
0
COS3 Ψ

Fig. III-C-7.

$$I_2 = \int_{r_m}^{\infty} \frac{e^{-x/L}}{r^3 z}\, dr \,, \tag{59}$$

where $x = r-1$, all distances being measured in units of r_c. For small Ψ,

$$I_1' = \tilde{I}_1 + I_1' \sin^2\psi \tag{60}$$

$$I_2 = \tilde{I}_2 + I_2' \sin^2\psi, \tag{61}$$

where

$$\tilde{I}_1 = 2\int_0^{\infty} \frac{\sqrt{1 - e^{-x/L}}}{(1+x)^3}\, dx \sim 1 - 1.227L + 6.522L^2 - \ldots \tag{62}$$

$$\tilde{I}_2 = 6L\int_0^{\infty} \frac{\sqrt{1 - e^{-x/L}}}{(1+x)^4}\, dx \sim 2L - 3.681L^2 + 13.04L^3 - \ldots \tag{63}$$

and

$$I_1' = -\int_0^{\infty} \frac{dx}{(1+x)^5 \sqrt{1 - e^{-x/L}}} \tag{64}$$

$$I_2' = -5L\int_0^{\infty} \frac{dx}{(1+x)^6 \sqrt{1 - e^{-x/L}}} \tag{65}$$

This gives the desired expansion

$$A/A_{\perp} \sim 1 - \frac{3}{2}(\tilde{I}_1 + \tilde{I}_2)\sin^2\psi + \frac{3}{2}(I_1' + I_2')\sin^4\psi \,, \tag{66}$$

from which

$$\lim_{\psi \to 0} A/A_{\perp} = 1 - \frac{3}{2}(\tilde{I}_1 + \tilde{I}_2)\psi^2 \,. \tag{67}$$

This formula is very accurate for $L \leq 1$ and $\psi < 10^{\circ}$. From the asymptotic expansions (62) and (63) we see

$$\lim_{\substack{\Psi \to 0 \\ L \to 0}} A/A_{\perp} = 1 - \frac{3}{2}\Psi^2 (1 + 0.773\, L) \quad . \tag{68}$$

in agreement with the slab result as $L \to 0$ and accurate to 0.1% for $L < .2$, $\Psi < 10^{o}$.

In general, our attempts to improve on the $\cos^3\Psi$ approximation to $A/A_{\perp}$ were disappointing, only modest improvements resulting for $L < 0.2$, $\Psi < 40^{o}$ or for $L < 1.0$, $\Psi < 10^{o}$.

III-C-3-d. Total Power Absorbed at Oblique Incidence

In estimating the total laser power absorbed by a pellet we must take into account the distribution of angles of incident due to

(1) The specific optical element (lens or mirror) employed

(2) The spatial beam profile incident on that element

Consider then an annular flux tube incident on a spherical target whose center is located a distance Δx inside the focus f, as depicted in Fig. III-C-8 (assuming lenses for concreteness). The plasma corona is assumed to extend to an outer radius R, outside of which negligible absorption and refraction occur. The projected angle of incidence Ψ and lens angle ξ are related by

$$\sin\Psi = \frac{\Delta x}{r_c} \sin\xi \quad , \tag{69}$$

where

$$\tan\xi = \frac{r_L}{f} \tag{70}$$

Recall that the f/no. is

$$F = f/2R_L \quad . \tag{71}$$

In eq. (69) we assume that the critical radius remains near the original pellet radius, so that Ψ is a known function of the lens radius r_L. In reality r_c usually expands by about 50%, which enhances absorption, as will be seen in the next section.

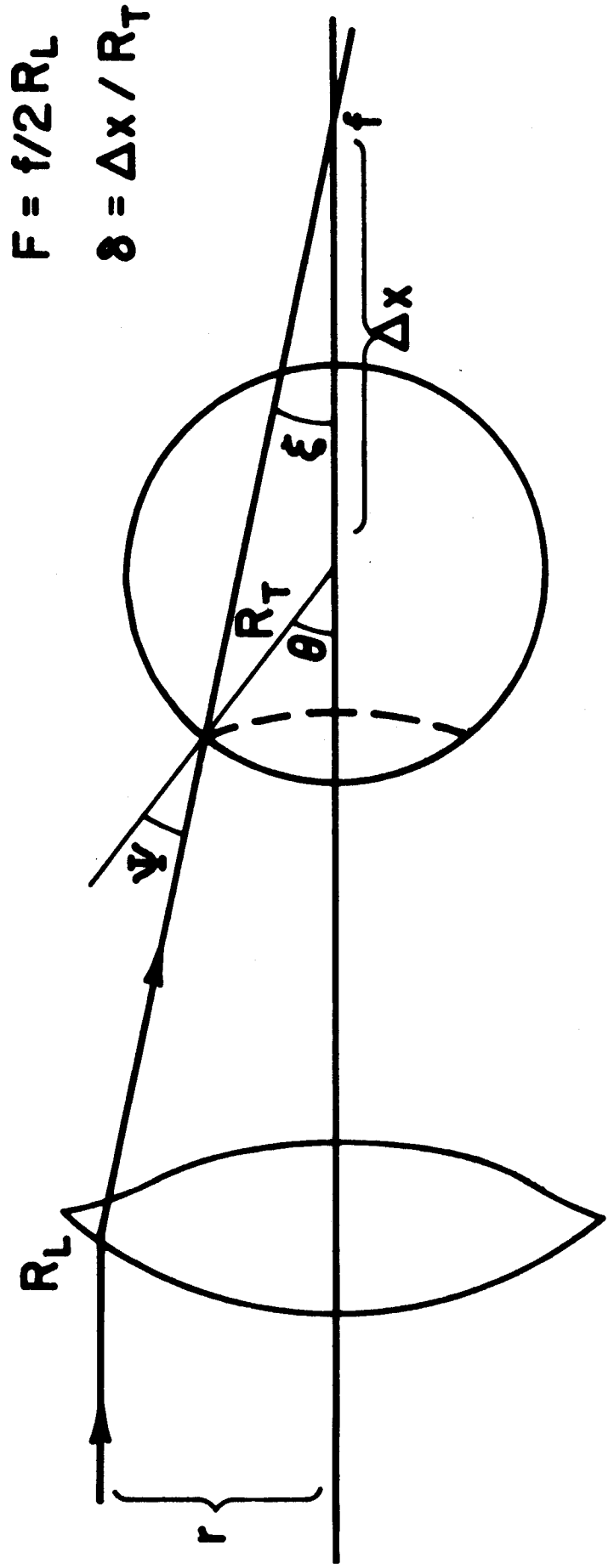

Fig. III-C-8.

The flux Φ_{in} (W/cm^2) incident on the pellet at r = R is related to the flux on the lens $\Phi_L(r_L)$ by

$$\Phi_L \, dA_L = \Phi_{in} \, dA_{in} \, , \tag{72}$$

which yields an expression for the target irradiance

$$\Phi_{in} = \Phi_L(r_L) \left(\frac{f}{R}\right)^2 \frac{1 + \frac{\Delta x}{R} \cos\theta}{(\cos\theta + \frac{\Delta x}{R})^3} \, . \tag{73}$$

To calculate the total absorption, we first observe that in the presence of focusing, the exponential law, eq. (1) must be replaced by

$$\frac{\partial \Phi}{\partial \ell} = -\kappa\Phi + \left(\frac{\partial \Phi}{\partial \ell}\right)_{foc} \, . \tag{74}$$

An infinitesimal flux tube of cross sectional area δa encloses a power

$$\delta P = \Phi \delta a. \tag{75}$$

Along this flux tube,

$$\left(\frac{\partial \Phi}{\partial \ell}\right)_{foc} = - \frac{\Phi}{\delta a} \frac{\partial}{\partial \ell} \delta a. \tag{76}$$

Using this expression in eq. (74) and integrating then yields

$$\delta P_{out} = \delta P_{in} e^{-\int_0^{\ell} \kappa d\ell} \, . \tag{77}$$

Thus, it is <u>power</u>, not flux, that obeys an exponential absorption law.

To apply eq. (77) to the problem at hand, let us integrate over all flux tubes incident on the pellet

$$P_{out} = \int e^{-\int \kappa d\ell} \, dP_{in} = \int e^{-\int \kappa d\ell} \, dP_L. \tag{78}$$

The total power incident on the lens is

$$P_{in} = P_L = \int \Phi_L(r_L) dA_L. \tag{79}$$

The fractional absorption is therefore

$$\eta_{AB} = 1 - \frac{P_{out}}{P_L} = 1 - \frac{\int_0^{R_L} \Phi_L \, e^{-\kappa_o A_\perp \cos^3 \Psi} \, r_L dr_L}{\int_0^{R_L} \Phi_L r_L dr_L} \, , \tag{80}$$

where $\Psi(r)$ is given by (69) and (70). Finally we may define an "effective angle of incidence" by

$$P_{out} = P_L \, e^{-\kappa_o A_\perp \cos^3 \Psi_{eff}} \quad . \tag{81}$$

As a specific example let us take

$$\Phi_L(r_L) = \Phi_o \, e^{-(r_L/a)^3} \quad , \tag{82}$$

with a = 0.70. This beam profile, depicted in Fig. III-C-9, gives good uniformity[10] for 20 f/1.5 lenses and a beam overlap $\theta_{max} \gtrsim 50°$. To complete the necessary algebra we have, from Fig. III-C-8,

$$\delta = \Delta x / r_c = 2F \sin\theta_{max} - \cos\theta_{max} \tag{83}$$

$$\sin\theta_{max} = \frac{2F\delta + \sqrt{1 + 4F^2 - \delta^2}}{1 + 4F^2} \quad . \tag{84}$$

The integrated absorption and Ψ_{eff} are shown in Figs. III-C-10 and 11 for several values of $\kappa_o L$, with L in cm and, for $\lambda_L = 1.06$ μm,

$$\kappa_o = \frac{3 \, \ell n \Lambda \, Z_{eff}}{\theta_e^{3/2}} \ \text{cm}^{-1} \quad .$$

Thus, if $\theta_e = 1$ keV and $Z_{eff} = 1$, $L = 10^{-2}$ cm, $\kappa_o L = 0.25$ and $\eta_{ab} \simeq 45\%$. η_{ab} reaches a maximum and Ψ_{eff} vanishes at $\theta_{max} = \xi = 18.4^o$, as they should. Due to the concentration of energy near the beam axis, the refractive loss at oblique incidence is quite moderate, amounting to only a few percent at $\theta_{max} = 50^o$.

For reference, Fig. III-C-11 also shows the maximum angle of incidence, assuming f/1.5 lenses. Thus, at $\theta_{max} = 50^o$ most of the beam energy is

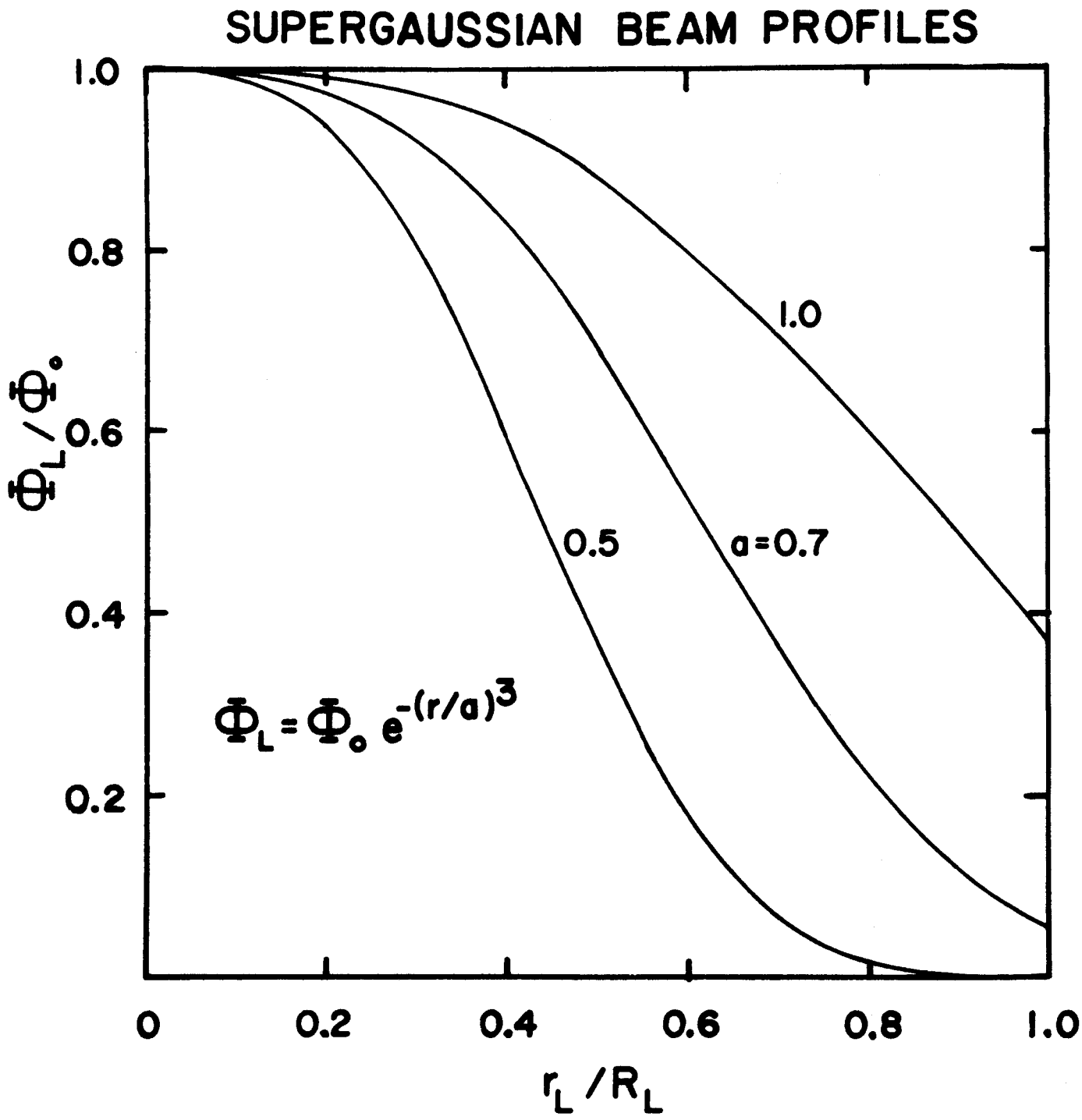
SUPERGAUSSIAN BEAM PROFILES
1.0
0.8
0.6
0.4
0.2
0
0.2
0.4
0.6
0.8
1.0
Φ_L / Φ_o
r_L / R_L
$\Phi_L = \Phi_o e^{-(r/a)^3}$
1.0
0.5
a=0.7

Fig. III-C-9.

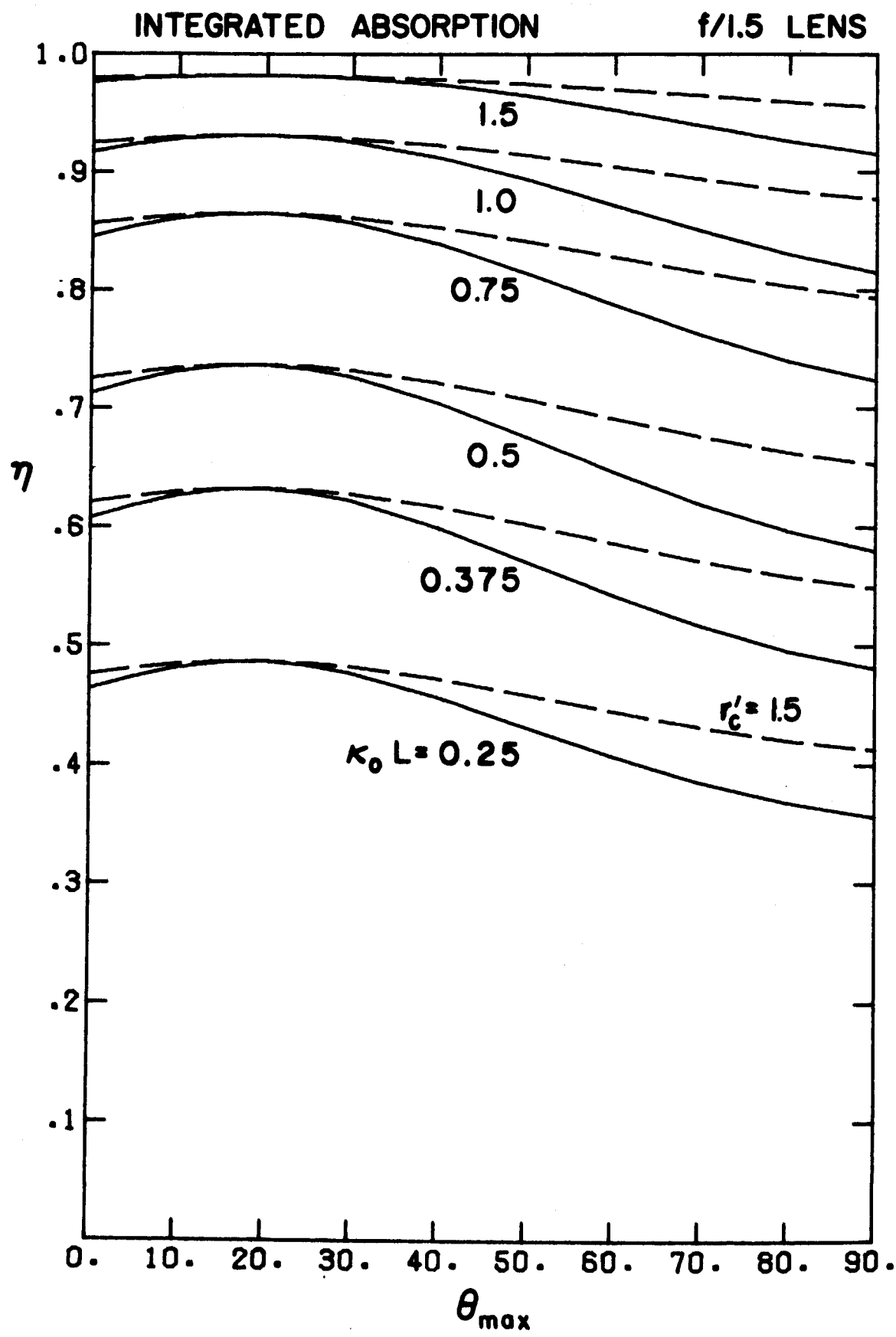
INTEGRATED ABSORPTION
f/1.5 LENS
1.0
.9
.8
.7
.6
.5
.4
.3
.2
.1
η
1.5
1.0
0.75
0.5
0.375
$r_c' = 1.5$
$\kappa_0 L = 0.25$
0.
10.
20.
30.
40.
50.
60.
70.
80.
90.
θ_{max}

Fig. III-C-10

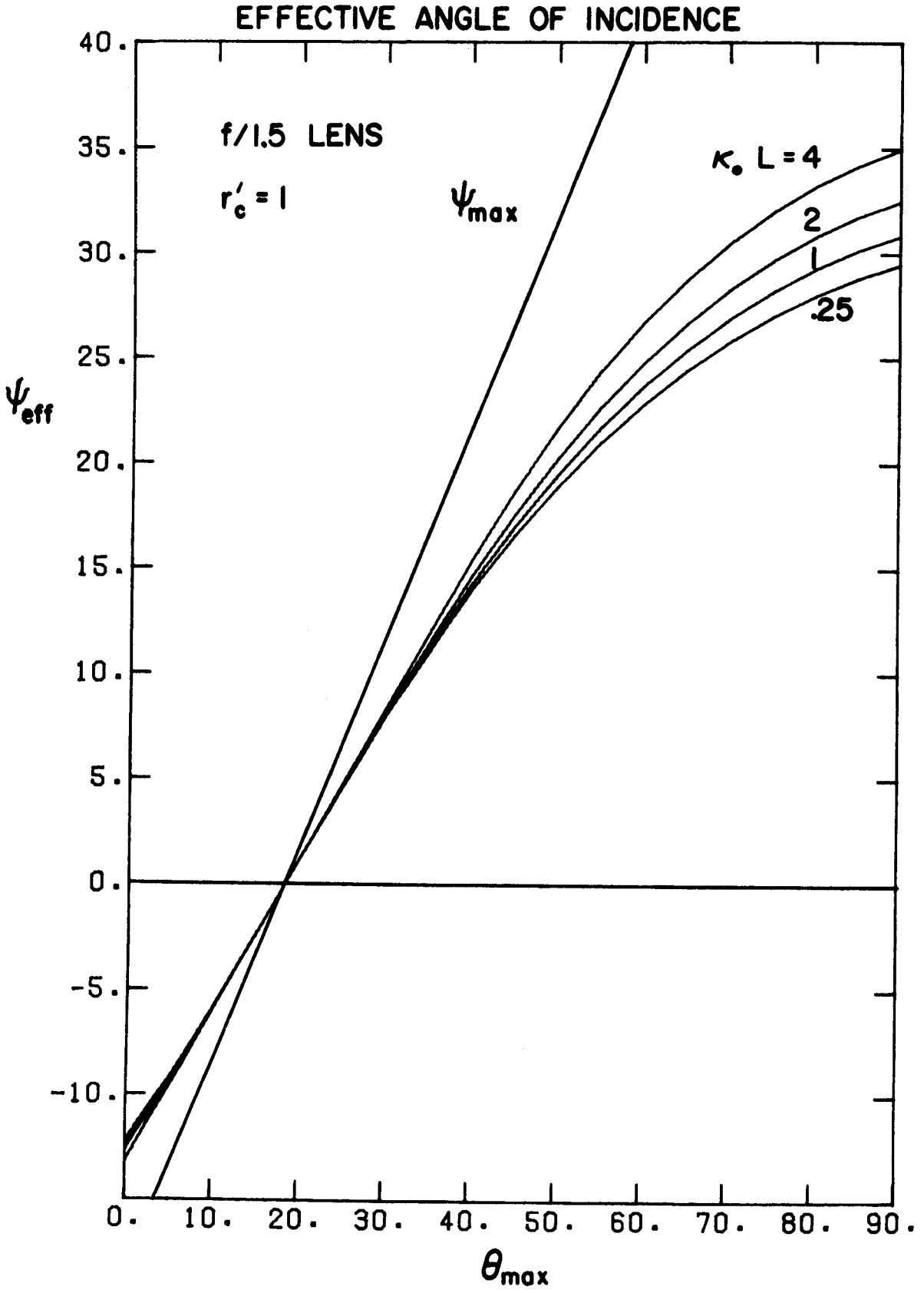
EFFECTIVE ANGLE OF INCIDENCE
f/1.5 LENS
$r_c' = 1$
ψ_{max}
$\kappa_o L = 4$
2
1
.25
ψ_{eff}
40.
35.
30.
25.
20.
15.
10.
5.
0.
-5.
-10.
0.
10.
20.
30.
40.
50.
60.
70.
80.
90.
θ_{max}

Fig. III-C-11.

incident near $\Psi_{eff} \simeq 20^o$, considerably less than $\Psi_{max} = 31.5^o$, but still above the range for effective resonant absorption.

III-C-3-e. Effect of Expanding Critical Radius

When r_c increases in time, the projected angle of incidence Ψ decreases, enhancing absorption. Suppose that r_c has moved out to a position r_c'; then, as Fig. III-C-12 shows, the angle of incidence is reduced

$$\sin\Psi' = \frac{r_c}{r_c'} \sin\Psi \ . \tag{85}$$

Thus

$$\sin\Psi'(r_L) = \frac{r_L \left(\frac{r_c}{r_c'}\right) \delta}{\sqrt{r_L^2 + 4F^2}} \ . \tag{86}$$

Using (86) in (80) and (81) we readily define a new absorption η_{ab}' and effective angle of incidence Ψ_{eff}'.

Since $\theta' < \theta$, the effective spot size is also reduced as r_c increases. The resulting degraded uniformity of illumination is of no consequence at later times, where a substantial hot corona has been established. While it is straightforward to calculate θ'_{max}, we shall plot η_{ab}' and Ψ_{eff}' vs. θ_{max}, as this is our reference value. The integrated absorption is shown as the dashed curves in Fig. III-C-10 for $r_c' = 1.5\ r_c$ and in Fig. III-C-13 f $r_c' = 2.0\ r_c$. Clearly, the effect of these (quite typical) expansions is to reduce refractive losses due to nonnormal illumination to entirely negligible levels. The burden then falls on resonant absorption to absorb the remaining energy. As Figs. III-C-14 and 15 show, the expansion

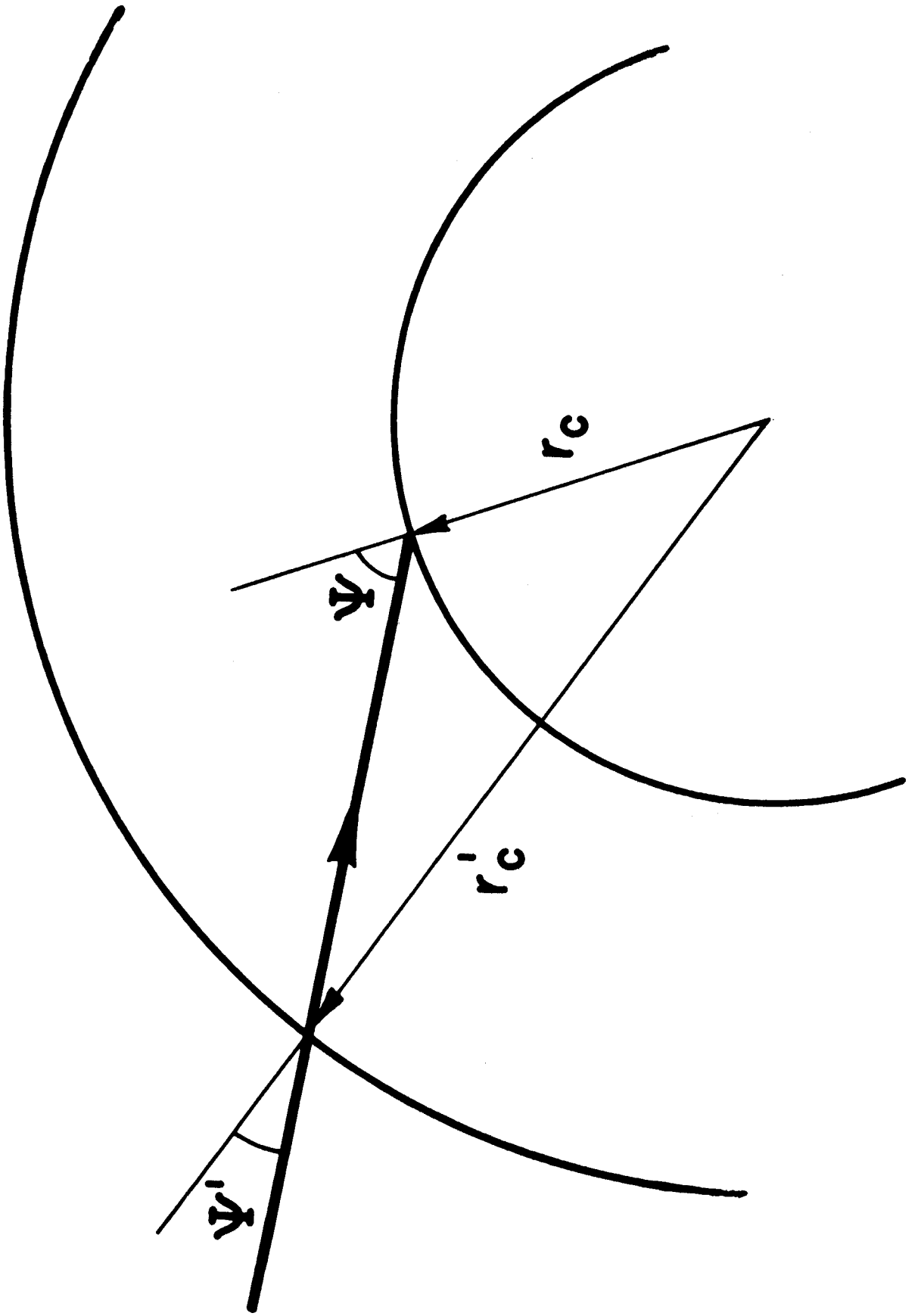

Fig. III-C-12

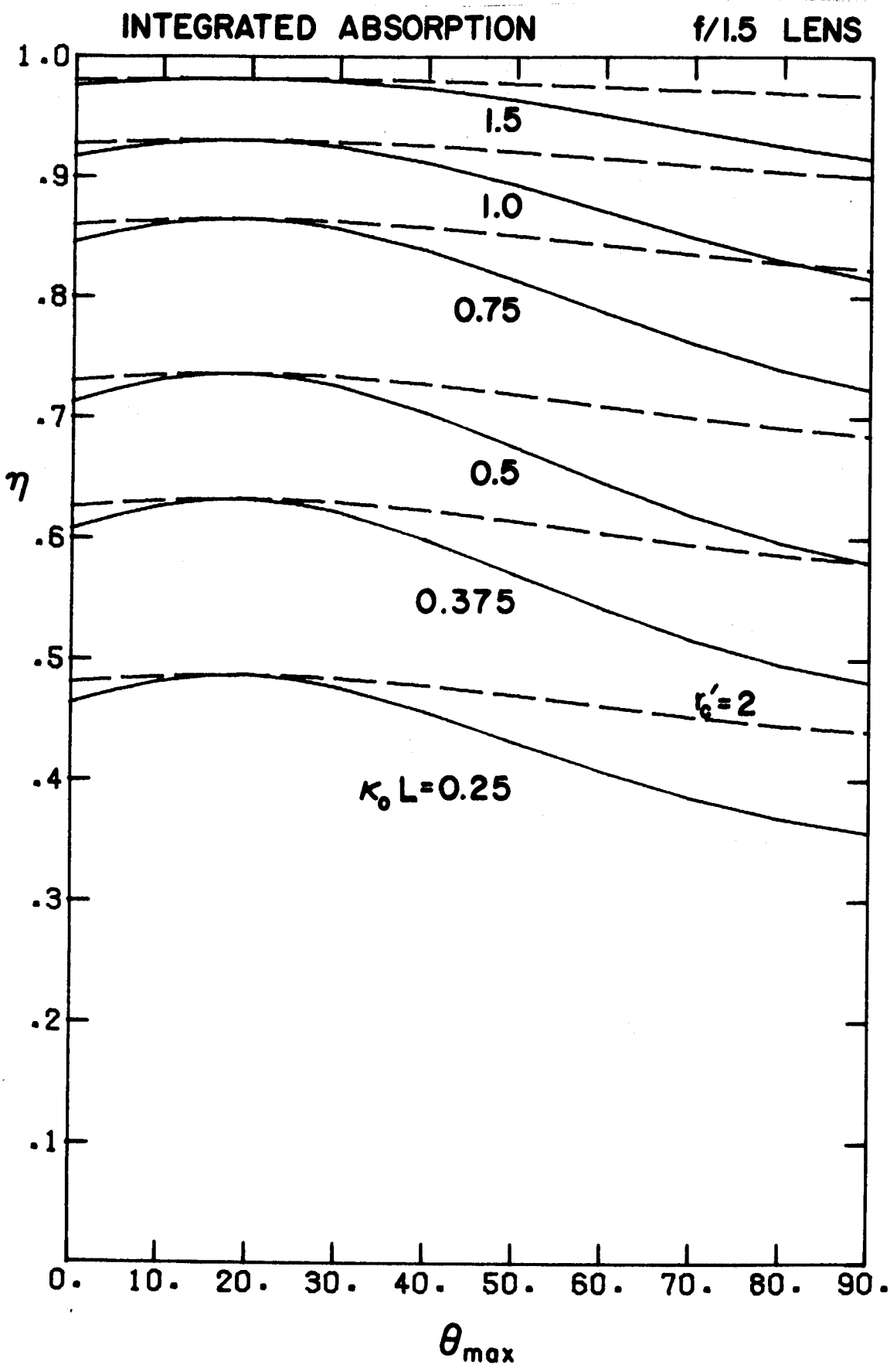
INTEGRATED ABSORPTION
f/1.5 LENS
1.0
.9
.8
.7
.6
.5
.4
.3
.2
.1
η
1.5
1.0
0.75
0.5
0.375
$r_0' = 2$
$\kappa_0 L = 0.25$
0.
10.
20.
30.
40.
50.
60.
70.
80.
90.
θ_{max}

Fig. III-C-13.

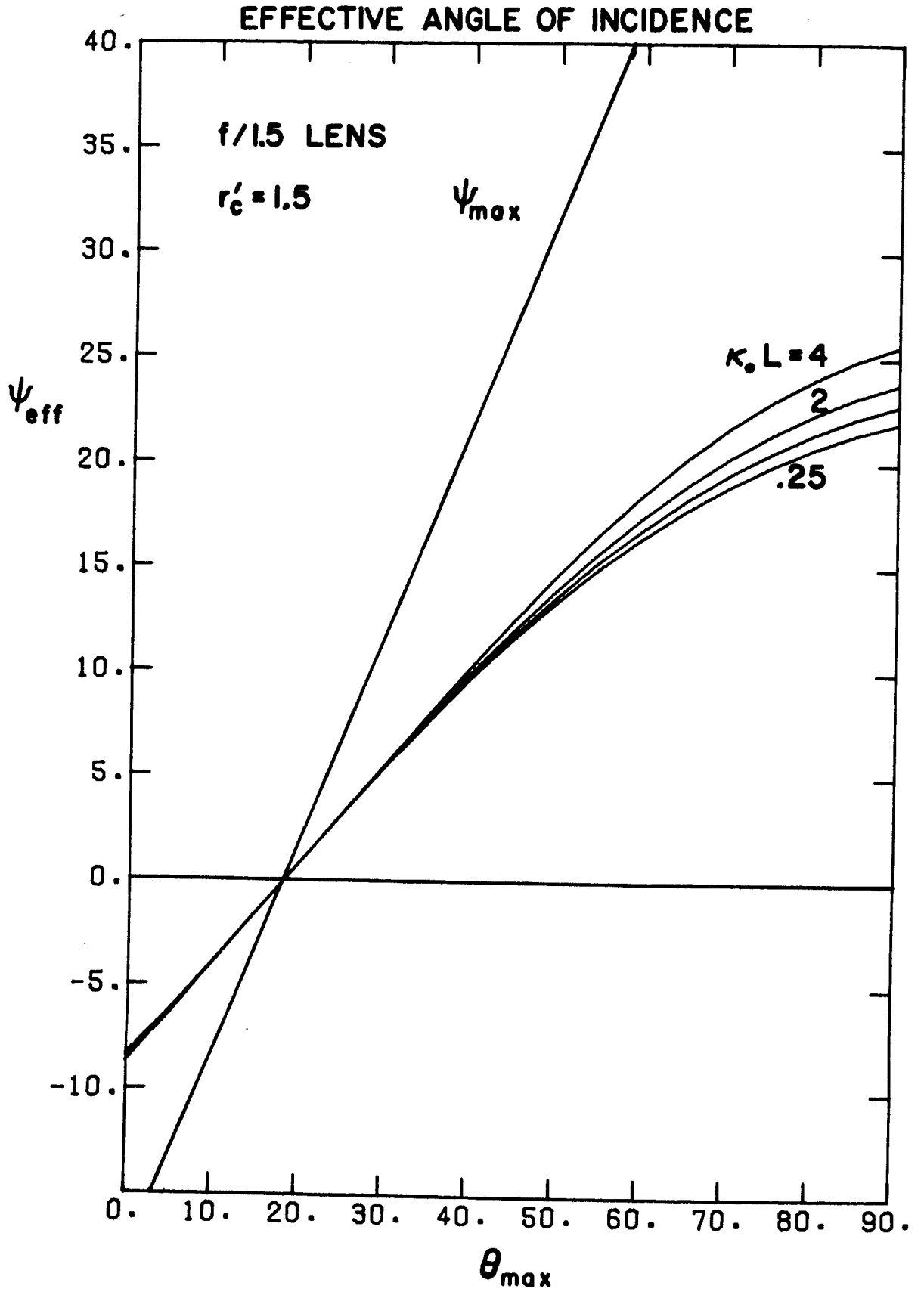
EFFECTIVE ANGLE OF INCIDENCE
f/1.5 LENS
$r_c' = 1.5$
ψ_{max}
$\kappa_o L = 4$
2
.25
ψ_{eff}
θ_{max}
40.
35.
30.
25.
20.
15.
10.
5.
0.
-5.
-10.
0. 10. 20. 30. 40. 50. 60. 70. 80. 90.

Fig. III-C-14

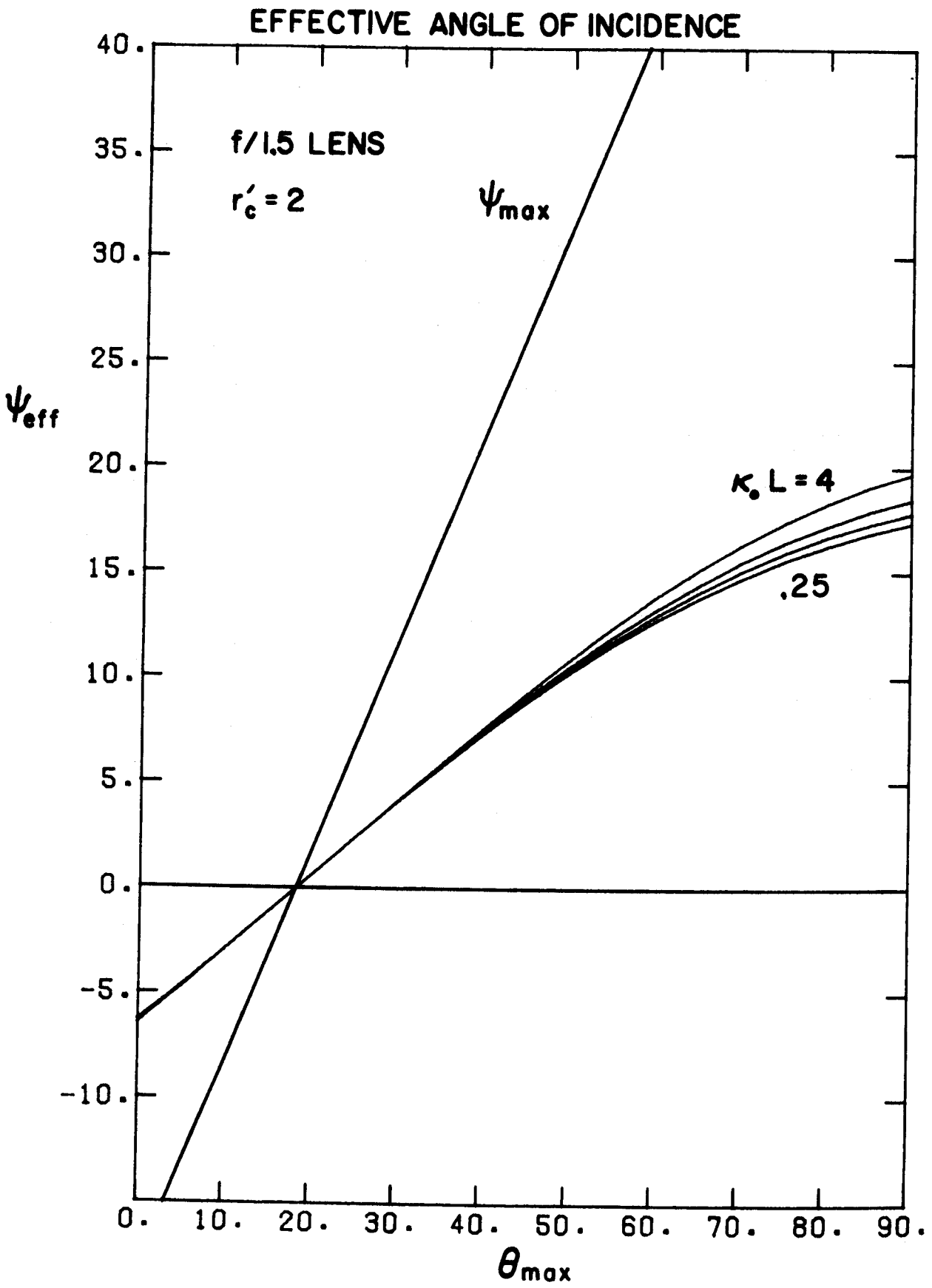
EFFECTIVE ANGLE OF INCIDENCE
f/1.5 LENS
$r_c' = 2$
ψ_{max}
$\kappa_o L = 4$
.25
ψ_{eff}
θ_{max}
40.
35.
30.
25.
20.
15.
10.
5.
0.
-5.
-10.
0.
10.
20.
30.
40.
50.
60.
70.
80.
90.

Fig. III-C-15

of r_c can dramatically reduce Ψ_{eff}. For example, if $\theta_{max} = 50^o$, $\Psi_{eff} = 14^o$ for $r_c' = 1.5\ r_c$, and $\Psi_{eff} \simeq 10^o$ for $r_c' = 2.0\ r_c$.

We have also calculated η_{ab} and Ψ_{eff} for f/3.5 lenses. An illumination system composed of 20 f/3.5 lenses takes up only 10% of the target solid angle as opposed to 50% for 20 f/1.5 lenses. As Figure III-C-16 indicates, the absorption again does not depart significantly from that at normal incidence, the net absorption at $\theta_{max} = 50^o$ being only slightly inferior to that using f/1.5 lenses. On the other hand, the effective angles of incidence are significantly larger using f/3.5 lenses, as shown in Figs. III-C-17-19. This time the values at $r_c' = 1$, 1.5 and 2.0 are about 25^o, 17.5^o and 12.5^o, resp., all at $\theta_{max} = 50^o$. Since resonant absorption is expected to be strongest for $\Psi = 7\text{-}10^o$, it is apparent that f/3.5 optics exceed this range, even for large expansions of r_c, while f/1.5 optics are marginal, and then only if r_c doubles by the time the bulk of the laser pulse arrives.

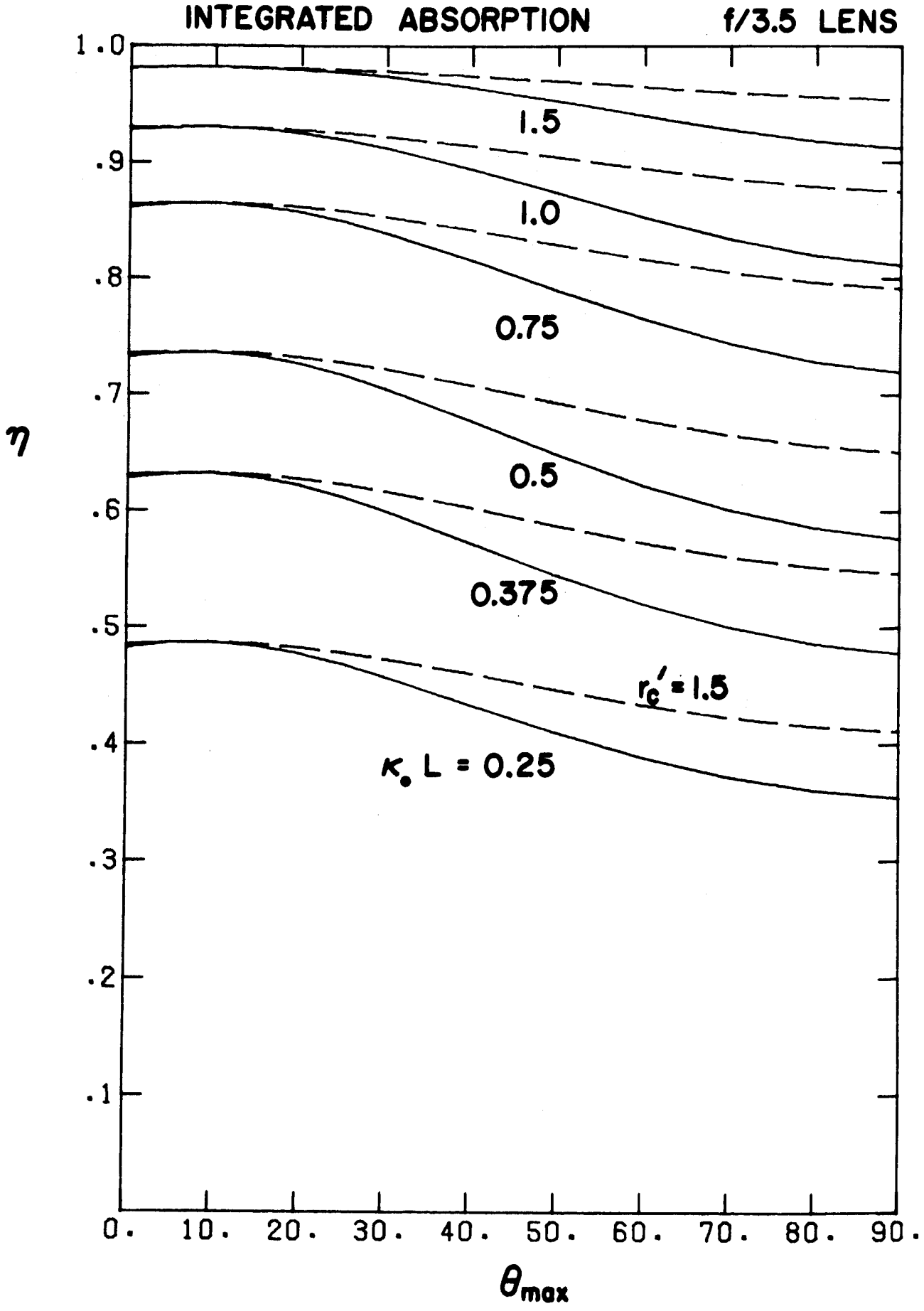
INTEGRATED ABSORPTION
f/3.5 LENS
1.0
.9
.8
.7
.6
.5
.4
.3
.2
.1
η
1.5
1.0
0.75
0.5
0.375
$r_c' = 1.5$
$\kappa_o L = 0.25$
0.
10.
20.
30.
40.
50.
60.
70.
80.
90.
θ_{max}

Fig. III-C-16.

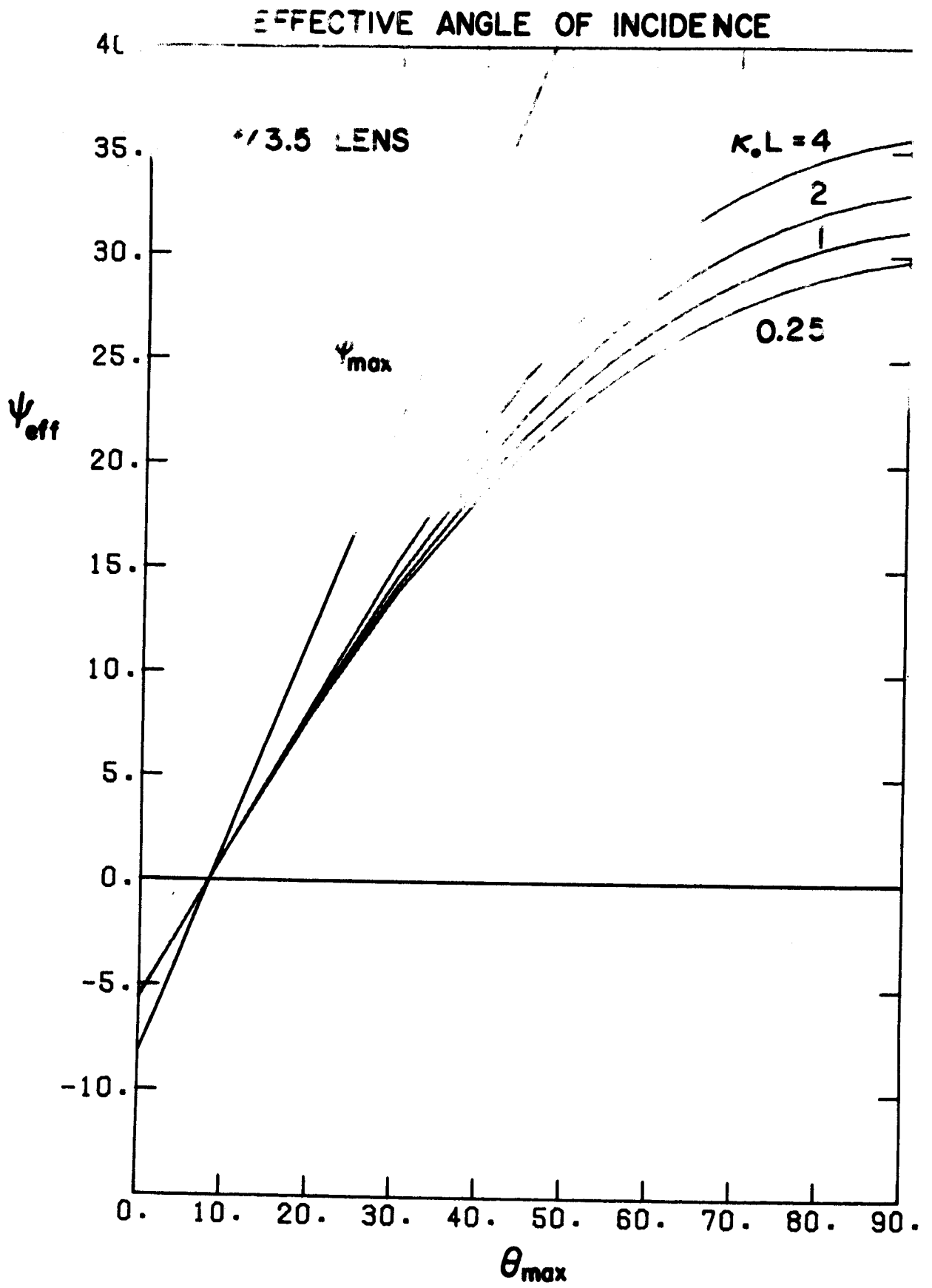
EFFECTIVE ANGLE OF INCIDENCE
40
35.
f/3.5 LENS
$K_0L = 4$
2
1
0.25
30.
25.
ψ_{max}
ψ_{eff}
20.
15.
10.
5.
0.
-5.
-10.
0. 10. 20. 30. 40. 50. 60. 70. 80. 90.
θ_{max}

Fig. III-C-17.

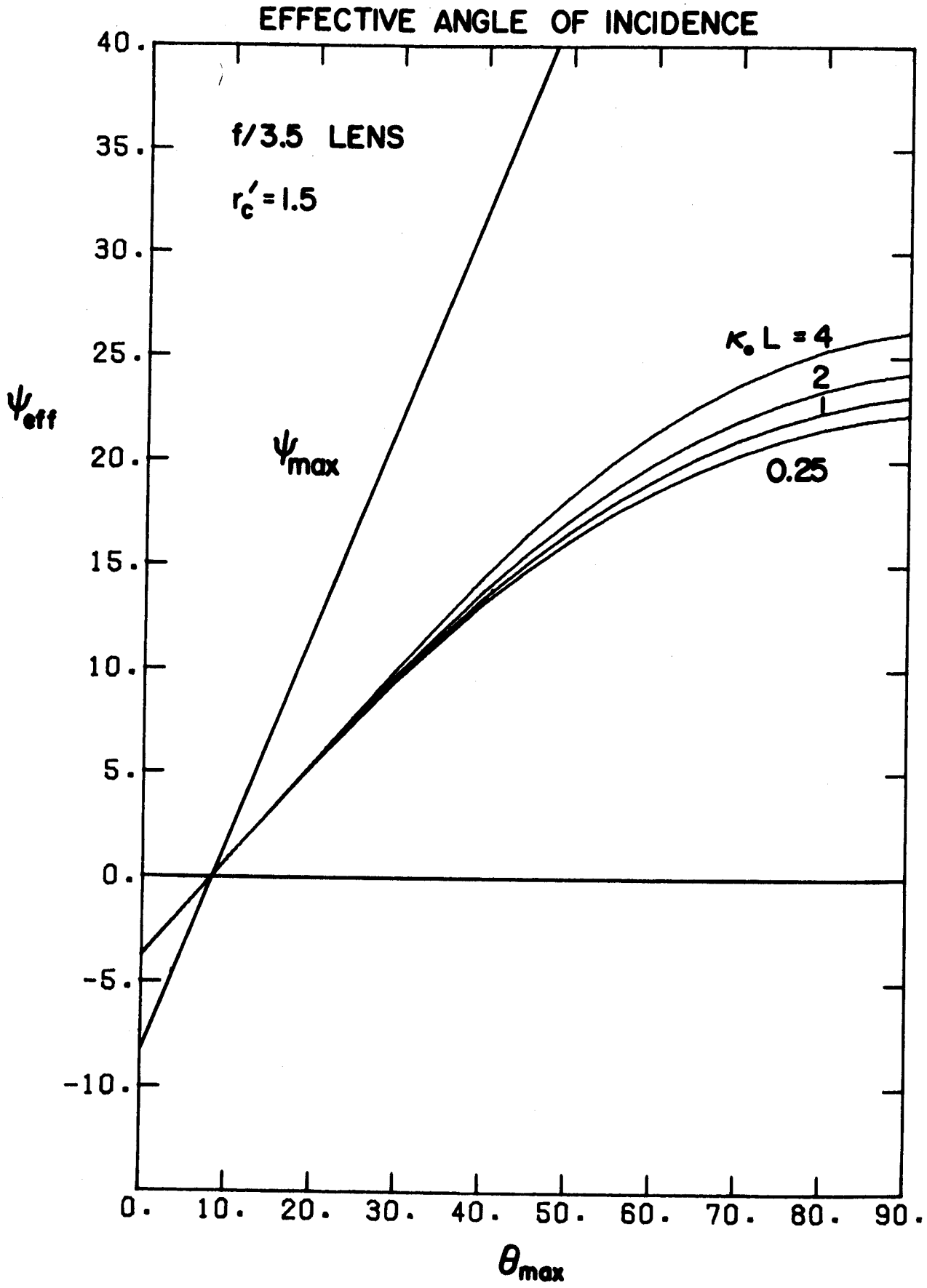
EFFECTIVE ANGLE OF INCIDENCE
f/3.5 LENS
$r_c' = 1.5$
ψ_{max}
$\kappa_o L = 4$
2
1
0.25
ψ_{eff}
θ_{max}
40.
35.
30.
25.
20.
15.
10.
5.
0.
-5.
-10.
0. 10. 20. 30. 40. 50. 60. 70. 80. 90.

Fig. III-C-18

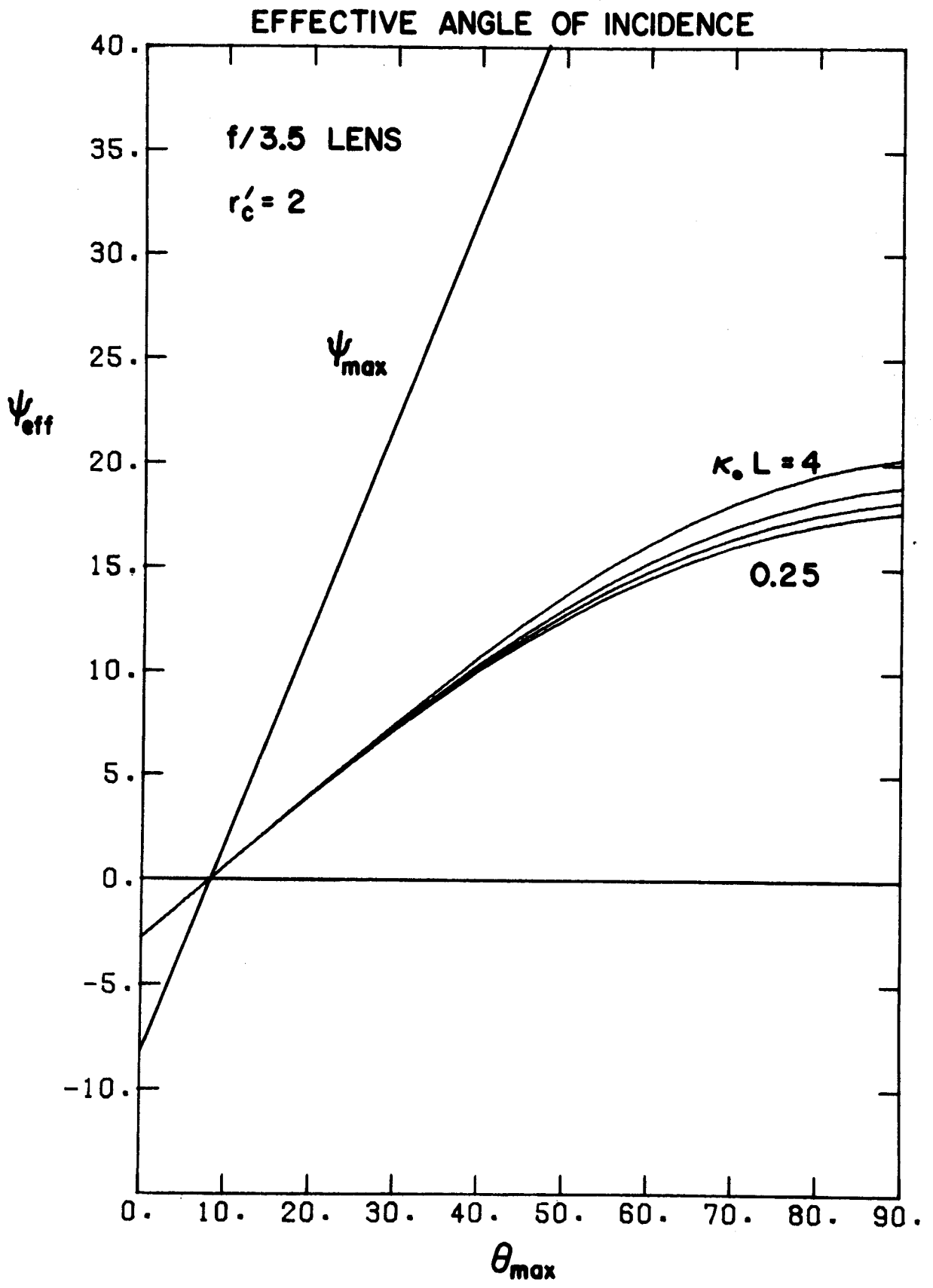
EFFECTIVE ANGLE OF INCIDENCE
f/3.5 LENS
$r_c' = 2$
ψ_{max}
$\kappa_o L = 4$
0.25
ψ_{eff}
θ_{max}
40.
35.
30.
25.
20.
15.
10.
5.
0.
-5.
-10.
0.
10.
20.
30.
40.
50.
60.
70.
80.
90.

Fig. III-C-19.

III-C-3-f. Resonance Absorption and Density Profile Steepening

It is generally acknowledged that nonclassical processes must be invoked to explain the amount of absorption experimentally observed and required for projected reactor-grade implosions. The prevailing view is that resonance absorption[1] plays a dominant role, the p-polarized component of $\vec{E}$ driving plasma oscillations at the critical surface. A total absorption of over 50% may be obtained in this way.

Resonance absorption is maximized when

$$L\sin^3\theta_o = \lambda/10.6, \tag{87}$$

where θ_o is the angle of incidence (our Ψ) and L is the scale height at the critical surface. In the absence of any density profile steepening, strong absorption is confined to a rather narrow range of θ_o. Typical values are 30-50% absorption. Fig. III-C-20 shows L as a function of θ_o for λ = 0.53 μm, 1.06μm and 10.6μm. For current experiments on small targets (L = 50-100μm) with λ = 1.06μm, the optimal angle of incidence is seen to be 6-7°, but reactor-grade pellets (L ≅ 1000μm) would require $\theta_o \simeq 3°$. It is difficult to see how such small angles of incidence could be produced under conditions of uniform illumination.

Fortunately, density profile steepening due to radiation pressure, as well as by the resonance absorption process itself[16], broadens the effective range of incident angles. Extensive numerical studies have been carried out for small pellets, for which scale heights as small as 1μm have been measured[21]. Further numerical simulation is needed to estimate the degree of self-steepening and resonance absorption in the larger pellets envisioned for use in a laser fusion reactor such as SOLASE.

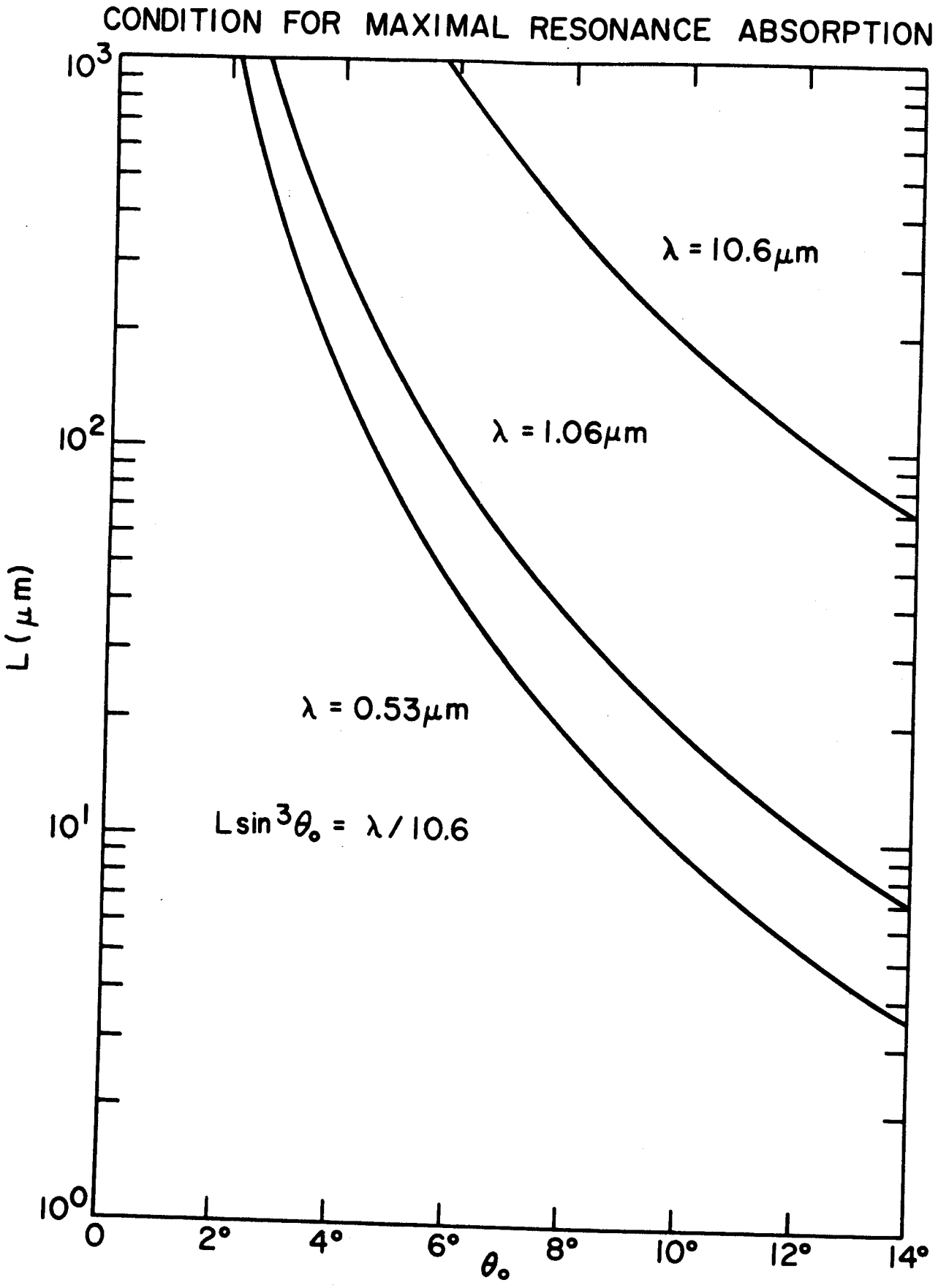
CONDITION FOR MAXIMAL RESONANCE ABSORPTION
10^3
10^2
10^1
10^0
L (μm)
λ = 10.6μm
λ = 1.06μm
λ = 0.53μm
$L\sin^3\theta_o = \lambda / 10.6$
0
2°
4°
6°
8°
10°
12°
14°
θ_o

Fig. III-C-20.

References for Section III-C-3

1. J. P. Freidberg, R. W. Mitchell, R. L. Morse and L. I. Rudsinski, Phys. Rev. Lett. 28,795 (1972).
2. H. G. Ahstrom, et. al., Bull. Am. Phys. Soc. 21,1046 (1976).
3. LLL Laser Program Annual Report-1975, UCRL 50021-75, p.307.
4. I. Pelah, E. B. Goldman and B. Yaakobi, Phys. Rev. Lett. 37,829 (1976).
5. R. E. Kidder, Proc. Int. School of Physics (Enrico Fermi) Course 45 (1971).
6. J. E. Howard, R. A. Cover and S. Jorna, Bull. Am. Phys. Soc. 18,1346 (1973).
7. J. N. Shiau, E. B. Goldman and C. I. Weng, Phys. Rev. Lett. 32,352 (1974).
   S. E. Bodner, Phys. Rev. Lett. 33, 761 (1974).
   R. E. Kidder, Nucl. Fusion 16, 3 (1976).
8. J. D. Lindl and W. C. Mead, Phys. Rev. Lett. 34, 1273 (1975).
9. D. V. Giovanielli, Bull. Am. Phys. Soc. 21, 1047 (1976).
10. J. E. Howard, Univ. of Wisconsin Nuclear Engineering Department Report UWFDM-172, 1976.
11. G. Moses, private communication.
    P. Hammerling, private communication.
12. D. W. Forslund, J. M. Kindel and E. L. Lindman, Phys. Fluids 18,1002 (1975).
    LLL Laser Program Annual Report-1975, UCRL 50021-75, p. 311.
13. J. W. Shearer and W. S. Barnes, in Laser Interaction and Related Phenomena, Ed. H. Hora and H. Schwartz, Plenum Press, (New York) 1971.
14. K. A. Brueckner and S. Jorna, Rev. Mod. Phys. 46,325 (1974).
15. J. Dawson, P. Kaw and B. Green, Phys. Fluids 12, 875 (1969).
16. K. G. Estabrook, E. J. Valeo and W.L. Kruer, Phys. Fluids 18,1151 (1975).
17. E. Cojacaru and P. Mulser, Plasma Phys. 17,393 (1975).
18. K. A. Brueckner, private communication.
19. J. W. Shearer, Phys. Fluids 14,183 (1971).
20. M. Born and E. Wolf, Principles of Optics, 2nd ed. Pergamon Press (Oxford) 1964, p. 123.
21. D. W. Phillion and R. L. Lerche, Bull. Am. Phys. Soc. 21,1046 (1976).

III-C-4. Radiation

III-C-4-a. Introduction

Radiative processes and transport can play an important role in the compression and heating of the pellet and in the design of the laser fusion reactor. In order to achieve densities high enough for efficient thermonuclear burn, the fusion pellet must be compressed along a low adiabat.(1) This will not be possible if the compressed region of the pellet is significantly preheated by X-rays originating in the hot outer regions.(2) In addition, radiation flow and energy loss during implosion and burn can effect the ion and electron fluid motion and energy and, therefore, the implosion and burn process. Because reactor wall damage may depend upon the X-ray spectra and energy leaving the pellet, radiation could also play a significant role in the design of the laser fusion reactor. The X-ray spectra and energy escaping a pellet will depend upon its design. For example, the X-ray spectra leaving the pellet, the transit time to the wall and the energy content will change with the design of the pellet. A satisfactory model of compression and thermonuclear burn should, therefore, include a comprehensive treatment of radiation and radiation transport.

III-C-4-b. The Radiation Transport Equation

To solve the radiation transport problem the relationship between radiative specific intensity and other physically meaningful quantities needs to be determined. In terms of the specific intensity the energy density at a given frequency is

$$E(\underline{r},\nu,t) = 1/c \int_{4\pi} d\underline{\Omega}\, I(\underline{r},\nu,\underline{\Omega},t) \qquad (1)$$

the i-th component of the radiative flux vector is

$$F_i(\underline{r},\nu,t) = \int_{4\pi} d\underline{\Omega}\, \Omega_i\, I(\underline{r},\nu,\underline{\Omega},t) \qquad (2)$$

and the ij-th component of the radiative pressure tensor is

$$P_{ij}(\underline{r},\nu,t) = \int_{4\pi} d\underline{\Omega}\ \Omega_i\Omega_j\ I(\underline{r},\nu,\Omega,t) \tag{3}$$

These are the variables we will use in our radiation transport model.

After making certain assumptions about the radiation and its interaction with matter, the radiative specific intensity can be shown to satisfy a continuity equation of the form[3]

$$\begin{aligned} 1/c\ \frac{\partial}{\partial t}\ I(\nu,\underline{\Omega}) &= -\underline{\Omega}\cdot\underline{\nabla}\ I(\nu,\underline{\Omega}) \\ &- \sigma_a(\nu)\ I(\nu,\Omega) + J(\nu)(1 + c^2 I(\nu,\underline{\Omega})/2h\nu^3) \\ &- \int\int d\nu'\ d\underline{\Omega}'\ \sigma_s(\nu\to\nu',\ \underline{\Omega}\cdot\underline{\Omega}')\ I(\nu,\underline{\Omega})\left(1 + \frac{c^2 I(\nu',\underline{\Omega}')}{ch\nu'^3}\right) \\ &+ \int\int d\nu'\ d\underline{\Omega}'\ \sigma_s(\nu'\to\nu,\ \underline{\Omega}\cdot\underline{\Omega}')\ \frac{\nu}{\nu'}\ I(\nu',\underline{\Omega}')\left(1 + \frac{c^2 I(\nu,\underline{\Omega})}{2h\nu^3}\right) \end{aligned} \tag{4}$$

where the first term on the right hand side of the equation is due to photon streaming, the second to photon absorption, the third to photon emission, the fourth to photon outscattering ($\nu \to \nu'$ and $\underline{\Omega} \to \underline{\Omega}'$) and the last to photon inscattering ($\nu \to \nu'$ and $\Omega' \to \Omega$).

A discussion of the variable Eddington method, the method used to solve the transport equation, is given in UWFDM-194. This method is based on the expansion of the angular moments $\int I\mu^k d\mu$ for one dimensional planar or spherical symmetric problems. The expansion is truncated after the second moment and a semiempirical expression is used to determine the pressure tensor.

III-C-4-c. Radiation Processes in a Laser-Fusion Plasma

III-C-4-c-i. Introduction

Figure III-C-21 illustrates a typical plasma configuration which results when a target pellet consisting of a relatively high density spherical shell containing DT fuel in gaseous form is compressed by an intense laser pulse.[2] Region I is the compressed fuel. Region II is the compressed inner layer of the tamper shell, and region III and region IV are the expanding outer layers of the tamper shell. The laser energy is deposited in region IV, just outside the critical density surface.

Each of the last three regions represents a different atomic modeling problem. Since region II is relatively cold and highly compressed, it is opaque to most of the X-ray radiation and can be described by an LTE equation of state. Conversely, regions III and IV are transparent to most of the radiation. Region III can, in general, be represented by a steady state coronal equation of state, but the coronal model breaks down in region IV and must be replaced by a time-dependent solution to the rate equations.

Bremsstrahlung radiation in the region of the critical density surface, region IV, must be corrected for forced oscillations of the electrons in the laser electric field. Suprathermal electrons created by plasma instabilities in region IV radiate a hard bremsstrahlung spectrum when they undergo scattering as they propagate inward toward region II.

This section is concerned with developing an atomic plasma model and the corresponding radiation emission and absorption coefficients, including nonthermal processes.

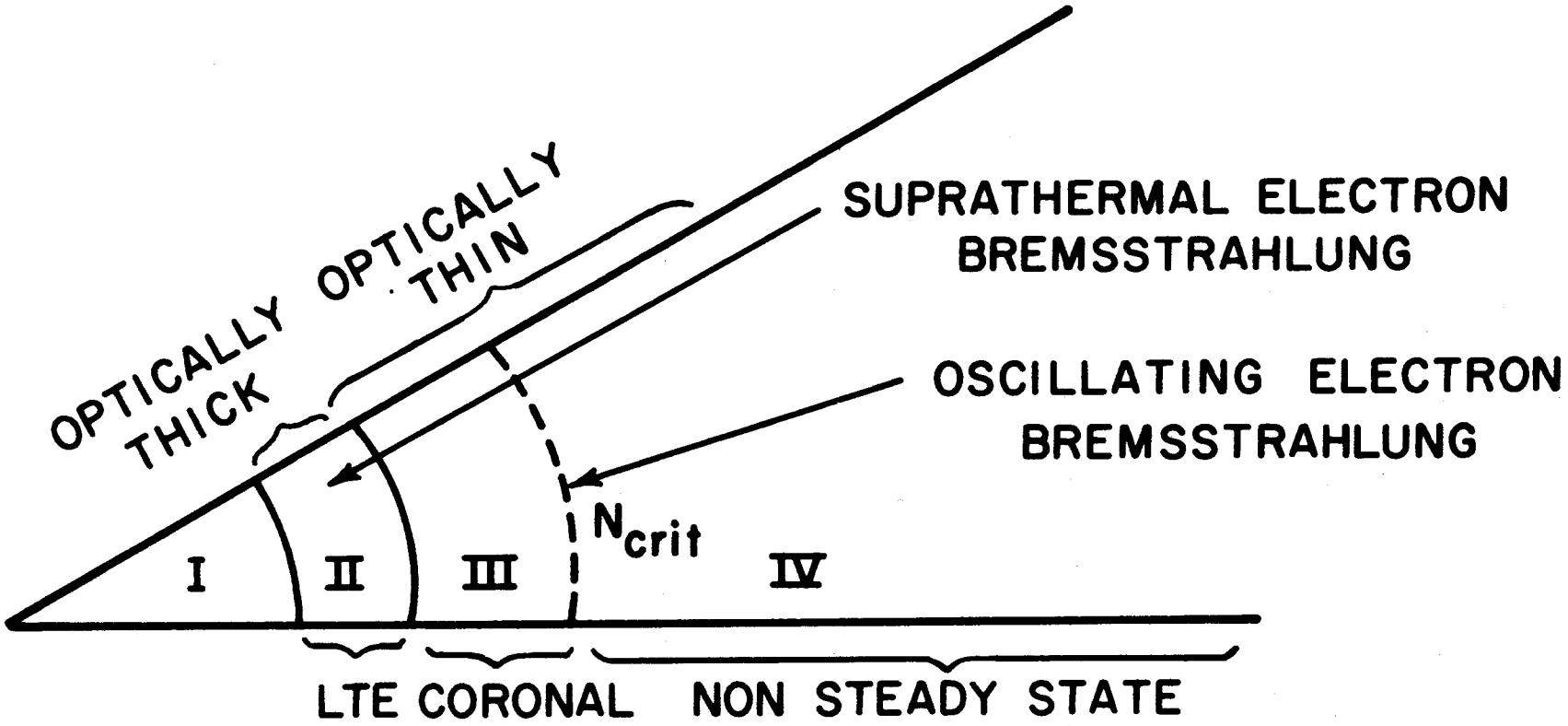

TYPICAL PLASMA CONFIGURATION OCCURRING IN LASER HEATED FUSION TARGETS SHOWING THE DIFFERENT REGIONS PERTINENT TO THE RADIATION TRANSPORT PROBLEM.

III-C-4-c-ii. Description of the Atomic State of a Plasma

To describe radiative processes occurring in a laser-fusion plasma, a model of the atomic state of a partially ionized mixture of chemical elements is needed. The model should be able to calculate the charge state and the electron configuration state of any ion in the plasma.

Let the concentration of atoms of atomic number Z be specified by C_Z. The number density of atoms of type Z is

$$N_Z = C_Z N_i ,$$

where N_i is the number density of atoms of all types given by

$$N_i = \rho \frac{N_o}{\bar{A}}$$

In the above expression, N_o is Avogadro's number, ρ is the density and $\bar{A} = \Sigma C_Z A_Z$, where A_Z is the atomic weight of element Z. An atom of atomic number Z can exist in various ionic charge states. The fraction of atoms of element Z that exist in charge state S is defined as $f_{Z,S}$; therefore, the population of ions in a chemical mixture at any time is given by C_Z and $f_{Z,S}$. The electron configuration of an ion is specified by the occupation numbers for each energy level. The number of bound electrons in level j of an ion of element Z in charge state S is defined as $n_{Z,S,j}$. When $f_{Z,S}$ and $n_{Z,S,j}$ are known, the radiation emission and absorption coefficients for the plasma can be obtained. In the model presented, a mean ion configuration is first obtained from $f_{Z,S}$ for each element and the radiation properties are then determined for a mixture of mean ions of concentration C_Z.

III-C-4-c-iii. The Distribution of Ion States

Local Thermal Equilibrium (LTE)

In general, both collisional and radiative transition rates determine the distribution of electrons among the various energy states. In high density plasmas dominated by collisional processes, the ion population is said to be in local thermal equilibrium (LTE) at the material temperature T. In LTE the distribution of energy states can be obtained from the law of equipartition without requiring a specific knowledge of transition rates.

Three-body recombination is a radiationless interaction involving one ion and two electrons in which one electron is captured by the ion and the other is scattered away while conserving energy and momentum. The processes of ionization by two-body electron-ion collisions and three-body recombination are statistical inverses of one another, and LTE is a condition of statistical equilibrium. Thus, for LTE plasmas, ionization states can be determined by equations (the Saha equations) which result from a balance between collisional ionization by two-body electron-ion collisions and three-body recombination.

The state of a LTE plasma is described by the following equations which are given for Fermi-Dirac statistics in order to be applicable for any degree of degeneracy. The density of free electrons in the velocity range $dv = dp/m$ is[2]

$$N_e(p)dp = \frac{8\pi}{h^3} \frac{p^2 dp}{e^{-n + p^2/2mkT} + 1} \qquad (5)$$

where p is the electron momentum, m the electron mass and n is the degeneracy parameter. The degeneracy parameter is obtained in terms of the density and temperature by normalization,

$$N_e = \frac{4\pi}{h^3} (2mkT)^{3/2} F_{1/2}(\eta) \qquad (6)$$

where $F_{1/2}(\eta)$ is the Fermi-Dirac integral of order 1/2. The distribution of ions of element Z in the ground state is given by the Saha equation

$$\frac{f_{Z,S+1}}{f_{Z,S}} = \frac{w_{S+1}}{w_S} e^{-\eta - X_{Z,S}/kT} \qquad (7)$$

where w_S is the statistical weight and $X_{Z,S}$ is the ionization energy of state S. If each ion is assumed to exist in the ground state only, the Saha equation for small degeneracy becomes[4]

$$\frac{f_{Z,S+1}}{f_{Z,S}} = \frac{2}{N_e} \left(\frac{2\pi mkT}{h^2}\right)^{3/2} e^{-X_{Z,S}/kT} \qquad (8)$$

Steady State Coronal Region

In an optically thin plasma, the photon emission process is not balanced by its inverse process. As a result, the population distribution departs from that of equipartition and LTE ceases to be valid.

At moderately low densities, the ion population can exist in a quasi-steady state where collisional ionization is balanced by radiative recombination. A plasma in this condition is described by the steady state coronal model. In this model the ion population is given by the expression[4]

$$\frac{f_{Z,S+1}}{f_{Z,S}} = 3.3 \times 10^{-16} \frac{\Delta_{Z,S}}{1+d} \frac{(kT)^{3/4}}{X_{Z,S}^{11/4}} e^{-X_{Z,S}/kT} \quad \text{cgs units} \qquad (9)$$

where $\Delta_{Z,S}$ is the number of electrons in the last occupied shell of the ion S, and d is the correction for dielectric recombination. Dielectric recombination is a process whereby a free electron is captured by an ion which is left in a doubly excited state.[5] The doubly excited ion subsequently decays to a singly excited state with the emission of a photon. Consequently, this process requires detailed knowledge of the excited states.

Nonsteady State Region

So far it has been assumed that atomic processes occur quickly enough that the population densities adjust almost instantaneously to external changes in the plasma. Because transition rates are density dependent, the quasi-steady state assumption will break down at sufficiently low density. For a coronal model plasma, the atomic relaxation time τ is almost independent of temperature and given approximately by[4] $\tau = 10^{12} N_e^{-1}$. Atomic relaxation times for different electron densities are given in Table III-C-3[2]. When hydrodynamic wor or thermal conduction rates are comparable to those represented by Table III-C-3, the quasi-steady state model breaks down and rate equations must be solved to obtain the ionic populations.

Table III-C-3

Atomic Relaxation Times for Corona Model Plasmas

N_e	10^{21}	10^{22}	10^{23}	10^{24}
τ(sec)	10^{-9}	10^{-10}	10^{-11}	10^{-12}

Occupation Numbers for Ions - Ground State Model

Each ion will be assumed to exist in the ground state only. Occupation numbers for ions in the ground state are obtained as follows.[2] Let the maximum number of bound electrons per shell be $A_j = 2j^2$ and let the cumulative number of bound electrons out to and including shell j be

$$B_j = \sum_{k=1}^{j} 2k^2 .$$

Define j' as the quantum number at the last full shell j, i.e. $B_{j'} \leq Z-S$, where $Z - S = n_{BE}$ is the total number of bound electrons. The occupation number of each level j for the ionic state S of element Z is given by:

if $n_{BE} \leq 2$, $j' = 0$ and $n_{Z,S,1} = n_{BE}$

$$n_{Z,S,j} = 0, \quad j > j'$$

if $n_{BE} > 2$, $j' > 0$ and $n_{Z,S,j} = A_j$, $j = 1,2 \ldots, j'$

$$n_{Z,S,j'+1} = n_{BE} - B_{j'}$$

$$n_{Z,S,j} = 0, \quad j > j' + 1$$

A Model for the LTE and Steady State Coronal Regions of the Plasma

The model presented here is based on the idea that collisional ionization is balanced by three-body recombination at high densities and by radiative recombination at low densities.(2) Thus, the model assumes that radiative excitation is negligible compared with collisional excitation in determining populations of energy states. The steady state model is determined by

$$R_{CI} = R_{RR} + R_{CR} \tag{10}$$

where the collisional ionization rate neglecting degeneracy, R_{CI}, is given by(4)

$$R_{CI} = f_{Z,S} N_e S_s ,$$

$$S_s = 4.9 \cdot 10^{-24} \frac{\Delta_{Z,S} (kT)^{1/4}}{X_{Z,S}^{7/4}} e^{-X_{Z,S}/kT} \tag{11}$$

the radiative recombination rate, R_{RR}, is given by(4)

$$R_{RR} = f_{Z,S+1} N_e \alpha_{S+1} \tag{12}$$

$$\alpha_{S+1} = 1.5 \cdot 10^{-8}(1 + d) \frac{w_{Z,S}}{(kT)^{1/2}}$$

and the collisional recombination rate, R_{CR}, is given by[6]

$$R_{CR} = f_{Z,S+1} N_e^2 B_{S+1} ,$$

$$B_{S+1} = 1.6 \cdot 10^{-63} \frac{\Delta_{Z,S}}{\chi_{Z,S}^{7/4}(kT)^{5/4}} \qquad (13)$$

The balance of rates, equation (10) then gives for the ratio of ion fraction

$$\frac{f_{Z,S+1}}{f_{Z,S}} = \frac{S_s}{\alpha_{S+1} + N_e B_{S+1}} \qquad (14)$$

which in regions of high density, $\alpha >> N_e B$, reduces to the Saha equation (8) and in regions of low density, $\alpha << N_e B$, reduces to the coronal equation (9).

III-C-4-c-iv. A Mean Ion Representation for Computing Radiative Properti

Once the ionization energies are known, the ion distribution can be obtained for a wide range of temperatures and densities from equation (14). Ionization energies can be computed using the Mayer method.[7,8] Because the number of possible charge states and energy levels for mixtures of several moderately high Z elements is large, the model used to calculate these levels and states needs to be computationally inexpensive. Ion distributions are usually clustered rather closely about the mean. This special behavior is used by defining a mean ion configuration for each element in the plasma. These mean values are then used to calculate radiation emission and absorption.[9] The mean ion configuration is defined in terms of the distribution of ionic states,[2]

$$n_{Z,j} = \Sigma f_{Z,S} n_{Z,S,j} \qquad (15)$$

The mean ion defined by (15) will have a charge given by

$$Z' = Z - \sum_j n_{Z,j} \tag{16}$$

Once the occupation numbers of the mean ion are known, the screened nuclear charge can be determined by

$$Z^*_{Z,j} = Z - \sum_{k \neq j} n_{Z,K}\, \sigma_{jK} - n_{Z,j}(1 - 1/d_j)\sigma_{jj} \ , \tag{17}$$

where σ_{jK} are the Slater screening constants and where

$$d_j = \min[2_j^2,\ n_{BE} - \sum_{k=1}^{j-1} n_{Z,K}]$$

The mean ion ionization energy in electron volts can be written as

$$X_{Z,j} = 13.6\left(\frac{Z^*_{Z,j}}{j}\right)^2 - \frac{Z'e^2}{2a_{Z'}}\left[3 - \frac{\langle r^2_{Z,j}\rangle}{a^2_{Z'}}\right] - E_o \tag{18}$$

where

$$E_o = 13.6 \cdot \frac{3}{5} \cdot \frac{N_i}{N_e} \sum_Z C_Z \sum_S f_{Z,S}\, S^2 \left(\frac{a_o}{a_s}\right) \ ,$$

$$a_{Z'} = \left(\frac{3}{4\pi}\frac{Z'}{N_e}\right)^{1/3} \ ,$$

$$\langle r^2_{Z,j}\rangle = a_o^2 \frac{2j^4}{(Z^*_{Z,j})^2}\left[1 + \frac{1}{2j^2}\right] \ ,$$

and a_o is the Bohr radius.

III-C-4-c-v. Emission Processes

Thermal Bremsstrahlung Emission

The bremsstrahlung emission into 4π steradians is given by[10]

$$J_{ff}^{\nu}\, d\nu = 8.05 \cdot 10^{-46} \frac{N_e N_i}{\sqrt{kT}} \sum C_Z Z'^2 e^{-\frac{h\nu}{kT}}\, \bar{g}_{ff}\, d\nu \tag{19}$$

ergs/cm^3-sec

where C_Z is the concentration of atomic element Z, Z' is the mean ion charge of element Z, N_e and N_i are the electron and ion number densities and $\bar{g}_{ff}$ is the Gaunt factor averaged over a Maxwellian velocity distribution. In the Born approximation, the Gaunt factor is written[11]

$$\bar{g}_{ff} = \frac{\sqrt{3}}{\pi} K_o(x) e^x$$

$$x = \frac{1}{2} \frac{h\nu}{kT}$$

where $K_o(x)$ is given in terms of the modified Bessel function of imaginary argument

$$K_o(x) = \pi/2 \; [i \; H_o(ix)]$$

When the electrons are degenerate, the Gaunt factor must be averaged over a Fermi distribution and must include a factor which limits the availability of free states in the continuum. These corrections can be expressed in terms of an average Gaunt factor,

$$\frac{8\pi mkT}{h^3} \bar{g}_o \; \ln \; (1 + e^n)$$

when $\bar{g}_o$ contains the limitation on the availability of states and has been tabulated by Greene.[12]

Recombination Emission

The recombination emission into 4π steradians is given by[10]

$$J_{fb} \, d\nu = 1.75 \cdot 10^{-56} \; \frac{N_e N_i}{(kT)^{3/2}} \; \sum_Z C_Z \sum_j \Delta_j \cdot$$

$$\frac{Z^{*4}}{j^5} \; \bar{g}_j \; H(h\nu - X_j) \; e^{-(h\nu - X_j)/kT} d\nu \qquad (20)$$

$$\text{ergs/cm}^3\text{-sec}$$

where Δ_j gives the number of vacancies in level j of the mean ion of element Z, X_j is the ionization energy of level j of the mean ion, and g_j is the Gaunt factor. The recombination spectrum into the state j does not extend to energies smaller than X_j, a property which is insured by the step function H(x), where

$$H(x) = 0, \quad x < 0$$

$$H(x) = 1, \quad x > 0$$

The Gaunt corrections are taken only in the vicinity of the edge and are averages obtained from Karzas and Latter.[13] The correction for the availability of free states in the continuum under degenerate conditions is handled in a way similar to that for bremsstrahlung where the probability of finding an electron in a free state which will recombine to the level j with the emission of a photon of energy $h\nu$ is

$$q_j = \frac{1}{e^{n-(h\nu-X_j)/kT} + 1}$$

Degeneracy corrections can, therefore, be included by means of a modified Gaunt factor for each level.

Line Emission

The treatment of line emission divides itself naturally into LTE and non-LTE regions. In the high density region there are many ion states, each with a different distribution of energy levels creating a large number of lines, the positions of which shift with changes in the temperature and density.

The model described here does not provide a detailed treatment of excited states and populations. The lines are assumed to be completely smeared together from the position of each edge X_j to the position of the transition to the nearest level $(X_j - X_{j+1})$.[8]

This approximation probably yields an overestimate of the line emission, but in regions which are opaque to the radiation the method is not critical.[2] The criterion for the validity of the smearing approximation is that the wing-spreads of the lines should be on the order of the separation between the lines. This is often the case in high density regions where collisional broadening dominates.

In the LTE region, the line emission into 4π steradians in the smearing approximation can be written[14]

$$J_{bb}\, d\nu = \frac{8\pi^2 e^2}{mh^2 c^3}\, N_i \sum_Z C_Z \sum_j f_j\, \frac{n_{Z,j}}{\Delta X_{Z,j}} \cdot$$
$$[H(h\nu - X_{Z,j} + \Delta X_{Z,j}) - H(h\nu - X_{Z,j})] \cdot$$
$$e^{-h\nu/kT}\, (h\nu)^3\, d(h\nu) \qquad \text{ergs/cm}^3\text{-sec} \qquad (21)$$

where $n_{Z,j}$ is the occupation number for level j, f_j is the sum of the oscillator strengths corresponding to transitions from level j to all higher levels averaged over all possible angular momenta and $\Delta X_{Z,j} = A_{Z,j} - (X_{Z,j} - X_{Z,j+1})$ is the width of the region of smeared lines. The f numbers can be obtained from tables.[7]

In the non-LTE region, an expression for line emission given by Griem is used which is derived for electron impact ionization and radiation decay.[15] The total line radiation into 4π steradians from transitions to the ground state from all excited states is

$$J_{bb} d\nu = 4.35 \cdot 10^{-24}\, \frac{N_e N_i}{\sqrt{kT}} \sum C_s\, \frac{1}{\Delta X_{Z,1}}\, e^{-\Delta E_Z/kT}$$

$$[H(h\nu - X_{Z,i} + \Delta X_{Z,i}) - H(h\nu - X_{Z,i})]\, d(h\nu) \qquad (22)$$

$$\text{ergs/cm}^3\text{-sec}$$

where $\Delta E_Z = X_{Z,1} - X_{Z,2}$ is the excitation energy of the resonance line, and the emission is assumed to be smeared over the energy range $\Delta X_{Z,i}$ as previously described.

Nonthermal Emission

Two additional radiation processes should be included in the laser-heated plasma problem. Both processes are associated with nonthermal electron distributions resulting from the electric field of the laser beam.

The first process results from forced electron oscillations created by the laser electric field near the critical density surface.[16] The inclusion of this forced oscillation into the Maxwellian distribution results in a bremsstrahlung spectrum which is harder than the purely thermal spectrum. The velocity distribution can be assumed to be a Maxwellian displaced by the instantaneous oscillation velocity

$$f(\underline{v}) = \left(\frac{m}{2\pi kT}\right)^{3/2} e^{-\frac{m}{2kT}(\underline{v} - \underline{v}_{osc})^2} \qquad (23)$$

where

$$v_{osc} = \frac{e\varepsilon}{m\omega_L} \cos\ell$$

$$\ell = \omega_L t$$

In these expressions, ε is the peak electric field strength, and ω_L is the angular frequency of the laser light. Equation (23) is only valid if the electron-ion collision time is greater than the laser oscillation time in the region of the critical density. This will be the case for 1.06 μm laser radiation.

The bremsstrahlung emission into 4π steradians is given by

$$J\, d\nu = 4\pi N_e N_i \int d\sigma(\nu)\, v\, f(\underline{v})\, d^3\underline{v} \qquad (24)$$

where the differential cross section is[17]

$$d\sigma(\nu) = 8/3\, Z^2\, \frac{e^6}{m^2c^3}\, \ln \Lambda\, v^{-2}\, d\nu\ .$$

The $\ln\Lambda$ factor is approximately 0 for $v < v_o = \sqrt{2h\nu/m}$ and $\ln\Lambda_o$ for $\underline{v} \geq v_o$. The time average of the instantaneous emission rate is

$$J_{oe}\, d\nu = \frac{16\sqrt{2}}{3}\, \frac{e^6 \ln\Lambda_o}{(mc^2)^{3/2}}\, \Sigma\, C_Z\, Z'^2\, \frac{N_e N_i}{\sqrt{kT}}\ \cdot$$

$$\int_o^{\pi/2} \frac{\mathrm{erfc}(\rho_\nu - \varepsilon\cos\ell) - \mathrm{erfc}(\rho_\nu + \varepsilon\cos\ell)}{\varepsilon\cos\ell}\, d\ell\, d\nu \qquad (25)$$

$$\text{ergs/cm}^3\text{-sec}$$

where $\rho\nu = \sqrt{\frac{h\nu}{kT}}$

$$\varepsilon = \sqrt{\frac{m}{2kT}}\, \frac{e\varepsilon}{m\omega_L}$$

The second nonthermal radiation process is bremsstrahlung emission caused by suprathermal electrons which are thought to be created by plasma instabilities near the region of the critical density surface. If a suprathermal electron distribution of the form[18]

$$f_{st}(v) = \frac{2\pi}{3}\, \left(\frac{m}{2\pi\alpha kT}\right)^{5/2}\, v^2\, e^{-\frac{mv^2}{2\alpha kT}} \qquad (26)$$

is assumed which is normalized to unity and where α is a free parameter, the bremsstrahlung emission into 4π steradians is given by

$$J_{st}\, d\nu = \frac{64}{9}\, \left(\frac{e^6}{hm^2c^4}\right)\, \Sigma\, C_Z Z'^2\, N_{st} N_i\ (x)$$

$$\sqrt{2\pi \frac{mc^2}{\alpha kT}}\ \ln\Lambda_o\ (1 + \frac{h\nu}{\alpha kT})\ e^{-h\nu/\alpha kT}\ d(h\nu) \qquad (27)$$

$$\text{ergs/cm}^3\text{-sec}$$

Matches to recent experimental data indicate values of α in the range from 4 to 6.[18] The suprathermal electron density N_{St} must be determined by an electron transport calculation.

III-C-4-c-vi. Absorption Coefficients

In the LTE region absorption coefficients corrected for induced emission are obtained from the emission functions by Kirchhoff's law,

$$\sigma(\nu) = \frac{J(\nu)}{B(\nu)} = \frac{(hc)^2}{2}\ \frac{J(\nu)}{(h\nu)^3}\ (e^{\frac{h\nu}{kT}} - 1) \qquad (28)$$

where $J(\nu) = J_{ff} + J_{fb} + J_{bb}$.

In the non-LTE regions, Kirchhoff's law is not valid, but since the plasma is always transparent there, the form of the absorption coefficient is immaterial.

References for Section III-C-4

1. J. Nuckolls, et al., "Laser Compression of Matter to Super-High Densities: Thermonuclear Applications," Nature 239, 139-142 (1972).

2. P. M. Campbell, et al., "Radiation Processes in a Laser-Fusion Plasma", KMSF-U457 (1976).

3. G. C. Pomraning, Radiation Hydrodynamics, Pergamon Press, Oxford (1973).

4. R. McWhirter, Spectral Intensities, Ed. R. H. Huddlestone and S. L. Leonard, Academic Press (1965).

5. A Burgess, "Dielectric Recombination and the Temperature of the Solar Corona", Astrophys. J. 139, 776-780 (1964).

6. P. J. Mallozzi, et al., "X-Ray Emission from Laser Generated Plasmas", Battelle Columbus Laboratories, Final Report on Contract DAAH01-71-C-0550 (1972).

7. H. M. Mayer, "Methods of Opacity Calculations", Los Alamos Scientific Laboratory Report, LA-647 (1947).

8. B. Kivel and H. Mayer, "Opacity of Highly Ionized Air", J. Quant. Spectr. and Radiation Transfer 5, 13-38 (1965).

9. A. N. Cox, Stellar Absorption Coefficients and Opacities, Ed. D. McLaughlin, University of Chicago Press (1965).

10. T. F. Stratton, X-Ray Spectroscopy, Ed. R. H. Huddlestone and S. L. Leonard, Academic Press (1965).

11. J. Shearer and W. Barnes, "Numerical Calculations of Plasma Heating by Means of Sub-Nanosecond Laser Pulses", in Laser Interaction and Related Phenomena, Ed. H. Hora and H. Schwartz, Plenum Press (1971).

12. J. M. Greene, "Fermi-Dirac Averages of the Free-Free Hydrogenic Gaunt Factor", Rand Corp. Report RM-2580-AEC (1960).

13. W. Karzas and R. Latter, "Radiation Transitions in a Coulomb Field", Astrophys. J. Suppl. 6, 167-212 (1961).

14. R. Woolley and S. Stibbs, The Outer Layers of a Star, Oxford University Press (1953).

15. H. R. Griem, Plasma Spectroscopy, McGraw Hill (1964).

16. D. Mitrovich, K. Brueckner and S. Segall, "Bremsstrahlung Radiation from Forced Oscillation of Thermal Electrons in a Laser Electric Field", KMS Document KMSF-U361 (1975).

References (cont.)

17. J. D. Jackson, Classical Electrodynamics, John Wiley and Sons (1962).

18. J. Nuckolls, "Laser Fusion", Chapter 6 in Laser Fusion Program Semiannual Report - July-December 1973, Lawrence Livermore Laboratory Report UCRL-50021-73-2 (1974).

III-C-5. Hydrodynamic Stability

The hydrodynamic stability of spherical laser driven implosions is one of the most important unanswered experimental questions facing laser fusion feasibility. The ablation front in the implosion process as described in section III-A-2 experiences an acceleration characteristic of the classical Rayleigh-Taylor instability.[1,2] The situation is not exactly analogous however because there are a strong temperature gradient and ablative effects in the laser driven implosion. Early arguments[3] claimed that the ablation process would convect instabilities away from the ablation surface before they could grow to large amplitudes. This thinking was further re-enforced by the results of numerical three dimensional perturbation calculations[4] where the fluid variables were expanded in spherical harmonics. Another early study[5] using a similar numerical treatment showed, however, that the instability was not stabilized and in fact low mode numbers grew at a rate greater than the classic Rayleigh-Taylor rate. This discrepancy was resolved[6,7] with the discovery that one must distinguish between truly ablatively driven, isentropic implosions and the very fast non isentropic, "exploding pusher" implosion, characteristic of the computer calculations in Ref. 4 and also characteristic of the glass microballoon targets used in laser fusion experiments today.[11] In these implosions the shell target is heated isothermally very quickly. It then explodes, both inward and outward. This different nonisentropic implosion mechanism explains the absence of instabilities in target implosions to date and in the Ref. 4 calculations. The major laser fusion experimental groups today generally agree that the results of full two dimensional hydrodynamic simulations,[7] the perturbation approach,[6] and analytic estimates[8] indicate isentropic implosion of thin shells (high aspect ratio $R/\Delta R=8$) will be impossible because

of the excessive Rayleigh-Taylor growth rates. Thin shells quickly break up when the perturbation amplitude becomes comparable to the shell thickness. Since the implosion of a thin shell is over a much longer distance, the perturbation has more chance to grow. This is a very serious problem because thin shells offer the opportunity to reduce the laser power and wavelength requirements over those for a solid DT ball.[9] Less power is required because a smaller force is acting through a longer distance and the wavelength requirement is reduced because the scale heights at large radii in a shell implosion are greater than in an equivalent sphere implosion. The pulse shape is also not as critical. With aspect ratios limited to less than 8, the advantages of shells over spheres is reduced. Two dimensional simulations of a 400 μm sphere with a carefully shaped 50 KJ laser pulse indicates that a good implosion can be achieved with ± 10% variation in the laser uniformity provided that a low density atmosphere is initially created with a pre-pulse and that long wavelength light (2um) is used in the first part of the pulse.[10] This rather ideal case seems at this point to be unattainable for laser fusion power plant applications because of the exacting laser parameters that are required (spatial profile, pulse shape, variable wavelength, excessive power).

The conclusion at this point must be that theoretical estimates of Rayleigh-Taylor instability growth during the implosion of shells will limit the aspect ratio to less than 8. This gives these thick shells very little advantage over solid balls which require enormous laser powers and very exacting pulse shapes to achieve isentropic compression to the density and temperature requisite for yields and gains of 150 MJ and 150 respectively.

References for Section III-C-5

1. Lord Rayleigh, Scientific Papers, II, p 200-207, Cambridge, England (1900).
2. G. Taylor, Proc. Roy. Soc. A 201, 192 (1950).
3. J. Nuckolls, L. Wood, A. Thiessen, and G. Zimmerman, Nature 239, 193 (1972).
4. D. Henderson, and R. Morse, Phys. Rev. Lett. 32, 355 (1974).
5. J. Shiau, E. Goldman, and C. Weng, Phys. Rev. Lett. 32, 352 (1974).
6. G. Fraley, W. Gula, D. Henderson, R. McCrory, R. Malone, R. Mason, and R. Morse, IAEA Conf. on Plasma Physics and Controlled Nuclear Fusion Research (1974), paper IAEA-CN - 33/F 505.
7. J. Lindl and W. Mead, Phys. Rev. Lett. 34, 1273 (1975).
8. R. Kidder, Nuc. Fus. 16, 3 (1976).
9. J. Nuckolls, J. Lindl, W. Mead, A. Thiessen, L. Wood and G. Zimmerman, IAEA Conf. on Plasma Physics and Controlled Nuclear Fusion Research (1974), paper IAEA-CN - 33/F 5-4.
10. LLL Laser Fusion Annual Report UCRL-50021-74, 392 (1974).
11. G. Charatis, et al, IAEA Conf. on Plasma Physics and Controlled Nuclear Fusion Research (1974), paper IAEA-CN - 33/F 1.

III-C-6. Hot Electrons

III-C-6-a. Introduction

Efficient thermonuclear burn requires compression along a low adiabat.[1] If nearly adiabatic compression is to be achieved, there must be strong coupling, in the form of thermal conduction, between the electrons heated by the laser and electrons inside the critical radius. One possible coupling problem is the formation of high energy tails on the electron distribution function due to resonance absorption of the laser light near the critical density surface.[2-4] Numerous experiments and simulations have detected these hot electrons;[5-10] i.e., they are evidenced by hard X-ray spectra in experimental studies. Very energetic electrons might deposit their energy deep inside the pellet ahead of the ablation front and this energy deposition would result in a continually rising adiabat. A higher abiabat means that a higher driving pressure would be required to achieve a given compression.[11] In addition, suprathermal electrons could give rise to a lower ablation pressure for a given laser power. This would occur if the energy coupling rate between hot and cold electrons decreased as the energy of the hot electrons increased. Clearly, a comprehensive model of hot electron creation and propagation is necessary if current and future laser-plasma experiments are to be understood.

III-C-6-b. Creation

Several theories have been proposed to explain the creation of a suprathermal electron tail caused by the laser-plasma interaction. These theories fall into two broad categories, the incoherent[12-14] production of energetic electrons by a broad wave spectrum, and the coherent[15] production of energetic electrons by a single wave. The fundamental assumption of these theories is that one can calculate the rate at which the source of free

energy, the laser light, couples energy and momentum into a plasma fluctuation.[15] For example, in Raman backscatter, the incident and backscattered waves exert a ponderomotive force on the electrons and, thereby, produce an electron current. Since this current is in phase with the electric field of an electron plasma oscillation, one has an energy input into the plasma. The energy dissipation mechanism is another question. If the plasma wave has small amplitude, one can show that the laser light momentum and energy are fed into the plasma wave causing it to grow exponentially at a linear growth rate.[15] When the wave reaches a sufficient amplitude, the energy input is dissipated nonlinearly, for instance, by trapping or by mode coupling and diffusion through wave number space. If the plasma wave grows to sufficient amplitude to trap electrons, the energy is dissipated by pulling electrons into an energetic nonthermal tail of the distribution function. If mode coupling occurs, diffusion through wave number space results in dissipation through Landau damping on the electrons. This damping also generates an energetic tail.

III-C-6-c. Propagation

The theory of hot electron transport is just beginning to be developed. Lawrence Livermore Laboratory uses a multigroup flux-limited diffusion model.[11] In this model the electrons lose energy to radiation by bremsstrahlung and to the background electrons by Coulomb collisions. In addition, relative to the ions, the net current of all electrons is assumed to be zero and the electric field required to enforce this condition is calculated. The ohmic work done by the electrons against this electric field is transferred between electron groups and provides an additional coupling between thermal and suprathermal electrons.

The role of magnetic fields, turbulence, electrostatic sheaths, and collisions on hot electron transport will all have to be understood before a comprehensive theory is developed. We list some of the processes which may need to be considered in developing such a theory and describe some of the possible consequences of the transport.

A spatially localized high energy electron tail can become two stream unstable as the electrons propagate inward toward the pellet center.[16] As a result they may lose considerable energy to Langmuir turbulence. This streaming behavior will also induce a background electron return current which may create ion-acoustic turbulence. If a magnetic field is present, the field could slow the transport to the pellet interior and increase the possibility of collisional energy loss. Electron energy loss resulting from electron impact ionization should also be considered.

All these processes will decrease the hot electron energy deposited in the pellet interior. Also, ion-acoustic turbulence and laser generated magnetic fields will reduce thermal conduction.[17-19] A reduced thermal conduction will result in slower transport of heat from the laser-absorbing region into the interior of the pellet and, therefore, may decouple the temperature of the pellet surface and the interior. Furthermore, additional hot electron energy loss and surface-interior decoupling will greatly increase the pellet surface energy.

This higher surface energy poses at least two problems. Higher electron temperatures will mean larger radiation losses and a greater

likelihood of core preheat by radiation. It also means that relatively few ions, those which initially lay close to the pellet surface, will carry off a relatively larger fraction of the absorbed laser energy as they expand into the vacuum than if the thermal conduction was classical.[20] The general result of this hot ion creation is that for a given laser power, one achieves a lower ablation pressure than the classical result would suggest.

Besides the processes discussed above one would need to understand the effects of the electrostatic sheath[20] which forms as a result of electron-ion charge separation when hot electrons move toward the vacuum.

References for Section III-C-6

1. J. Nuckolls, L. Wood, R. Thiessen and G. Zimmerman, Nature 239, 139 (1972).

2. J. S. DeGroot and J. E. Tull, Phys. Fluids 18, 672 (1975).

3. K. G. Estrabrook, E. J. Valeo and L. Kruer, Phys. Fluids 18, 1151 (1975).

4. J. P. Freidberg, R. W. Mitchell, R. L. Morse and L. I. Rudsinski, Phys. Rev. Lett. 28, 795 (1972).

5. J. W. Shearer, S. W. Mead, J. Petruzzi, F. Rainer, J. E. Swain and C. E. Violet, Phys. Rev. A6, 764 (1972).

6. H. Dreicer, D. B. Henderson and J. C. Ingraham, Phys. Rev. Lett. 26, 1616 (1971).

7. H. Dreicer, D. B. Henderson and J. C. Ingraham, Phys. Rev. Lett. 31 426 (1973).

8. D. Forslund, J. Kindel and E. Lindman, Phys. Rev. Lett. 30, 739 (1973).

9. J. S. DeGroot and J. I. Katz, Phys. Fluids 16, 401 (1973).

10. W. L. Kruer and J. M. Dawson, Phys. Fluids 15, 446 (1972).

11. J. D. Lindl, Nuclear Fusion 14, 511 (1974).

12. J. I. Katz, J. Weinstock, W. L. Kruer, J. S. DeGroot, and R. J. Faehl, Phys. Fluids 12, 1951 (1973).

13. J. J. Thompson, R. J. Faehl and W. L. Kruer, Phys. Rev. Lett. 31, 918 (1973).

14. M. Z. Caponi and R. C. Davidson, Phys. Rev. Lett. 31, 86 (1973).

15. W. M. Manheimer and H. H. Klein, Phys. Fluids 17, 1889 (1974).

16. G. Magelssen, N.C.A.R. Cooperative Thesis No. 37 (1976).

17. D. W. Forslund, J. Geophys. Res. 75, 17 (1970).

18. R. J. Bickerton, Nuclear Fusion 13, 457 (1973).

19. K. G. Estrabrook, "Plasma Physics", Chapter 6 in Laser Fusion Program Annual Report - January - December 1975, Lawrence Livermore Laboratory Report UCRL-50021-75.

20. F. Skoberne, Los Alamos Scientific Laboratory Report LA-5739-PR (1974).

III-D. Numerical Modelling

Laser driven fusion feasibility has only been demonstrated through the results of hydrodynamic simulation computer codes. Such codes first indicated that sufficient pellet gain might be possible to make laser driven fusion a candidate for power plant applications[1,2]. Currently these codes are being used to study and unfold the results of laser-plasma interaction experiments and the compression of D-T fuel by laser driven implosion.

A survey of laser fusion computer codes is given with all information taken from the literature. It is understood that such codes are under constant development so in fact this survey may not include all aspects of each code.

The most notable of the laser fusion hydrodynamics codes is LASNEX[3], which was developed at Lawrence Livermore Lab (LLL) but is currently also used at Los Alamos Scientific Laboratory (LASL). LASNEX is described as a laser fusion target design code. It is a two dimensional (r,z), one fluid, two temperature Lagrangian hydrodynamics code, that treats the nonthermal radiation field and nonthermal electrons using multi-group flux limited diffusion theory. It solves for the magnetic field in cases where self-generated fields arise and uses Braginskii's, B-field corrected, transport coefficients. It contains a ray trace option to follow the paths of laser light rays in the environment of complex electron density gradients, and by virtue of its home it has available sophisticated tables of equation of state and radiation opacity values. This sophistication allows LASNEX to simulate the experiments performed currently and to analyze the diagnostics (mostly X-rays) that come from these experiments. Such experiments may be fundamentally two dimensional, such as ball on disk targets, or the fluid motion may develop into two dimensional flow, such as a laser focussed to a small spot on a slab, and these require a two dimensional

computer simulation to correctly predict the effects of self-generated magnetic fields and laser light refraction. The nonthermal X-ray spectrum measured in the laboratory must be analyzed by accounting for the numerous bound-bound and free-bound transitions of high Z materials as well as the free-free bremsstrahlung radiation from thermal and non-thermal electrons. This radiation must be transported in a multi-group calculation to reproduce the measured X-ray spectrum. LASNEX uses multi-group flux limited diffusion to describe the transport of DT and DD reaction products.

Another two dimensional laser plasma hydrodynamics code has been developed at the Naval Research Laboratory (NRL). This code is a two dimensional (r,z) one fluid, two temperature Eulerian code with sophisticated treatments of the self generated magnetic field equations and radiative processes. It uses Braginskii transport coefficients but does not contain any treatment of thermonuclear burn.

KMS Fusion, Incorporated uses a rather sophisticated one dimensional hydrodynamics code called TRYHD[5] that has one-fluid, two temperature hydrodynamics with a multi-frequency variable Eddington treatment of radiation transport and a particle tracking method of calculating charged particle reaction product transport. The burn dynamics capability of this code suffers from the time independent approximation for the transport which deviates somewhat from a time dependent calculation as will be seen in a later section.

The University of Rochester has developed a one dimensional, one fluid two temperature code called SUPER[6]. This code uses a very simple local deposition approximation of burn dynamics.

A sophisticated thermonuclear burn code is the one dimensional, one fluid, three temperature code used at LASL[7]. Again it has elaborate equations of state and opacity tables. This code uses the S_N discrete ordinates transport approximation to transport both charged particle and neutron reaction products in the laser fusion pellet.

None of the computer codes described above are available for distribution due to either proprietary of security classification reasons. Only two laser fusion hydrodynamics codes are available to the general scientific community and neither of these has good thermonuclear burn, equation of state or radiation transport capability[8,9].

For the purposes of studying laser fusion power plant feasibility the ability to estimate pellet yield, fractional burn up, and gain is essential. Also, since many of these estimates rely on physical parameters whose values are not well known it is important to test the sensitivity of yield, fractional burnup, and gain to uncertainties in these parameters. This requires a hydrodynamic-thermonuclear burn-radiative transfer modeling code. Such a code, PHD-IV, has been developed at the University of Wisconsin for general distribution, and is described in UWFDM-194.

References for Section III-D

1. J. Nuckolls, L. Wood, A. Thiessen, and G. Zimmerman, Nature 239, 139 (1972).
2. J. Clarke, H. Fisher, and R. Mason, Phys. Rev. Lett. 30, 89 (1973).
3. G. Zimmerman, in Comments on Modern Physics, Part E, Vol. II, No. 2 (1975).
4. D. Colombant, K. Whitney, D. Tidman, N. Winsor, and J. Davis, Phys. Fl. 18, 1687 (1975).
5. K. Brueckner and S. Jorna, Rev. Mod. Phys. 46, 325 (1974).
6. E. Goldman, Univ. of Rochester Lab. for Laser Energetics Report #16, 1973.
7. G. Fraley, E. Linnebur, R. Mason, and R. Morse, Phys. Fl. 17, 474 (1974).
8. J. Christiansen, D. Ashby, and K. Roberts, Comp. Phys. Comm. 7, 271 (1974).
9. G. Moses and J. Duderstadt, Transactions of the ANS Meeting, Toronto, p. 50 (1976).

III-E. Comparison of PHD-IV Results with Other Published Results

III-E-1. Thermonuclear Burn - A Comparison with Other Published Results

With little experimental data available on alpha particle slowing down in dense plasmas, the best test of our calculations comes from comparison with the results of others. Favorable comparison of our results with other results derived from a similar transport and slowing down model coupled to a hydrodynamics calculation indicates that we are correctly treating the problem within the restrictions of our model. Favorable comparison with a more exact Monte Carlo collisional slowing down calculation indicates that our time dependent particle tracking model is in fact quite accurate within the restrictions of collisional slowing down theory. By arbitrarily scaling the slowing down terms in our model we simulate the possible effect of enhanced slowing down from collective interactions with the plasma.

Our first comparison is with a propagating burn calculation published by Fraley, et al.,[1] where a 10 μg DT pellet compressed to a density of 6000 g/cm^3 (ρR = 4.4 g/cm^2) with the inner 10% of the pellet mass raised to 20 KeV is allowed to burn and disassemble. Temperature and density "snap shots" of the Fraley calculation and the PHD calculation are shown in Fig. III-E-1. Notice that the absolute magnitudes of the temperature and density are often different but that the general nature of the hydrodynamics is very similar. The temperature of the center zone is too large in the PHD results because the μ = -1 inward direction of the alpha particles from each zone pass through the center zone along its diameter. This is an inaccurate average path length through the center zone, the average will of

TEMPERATURE AND DENSITY SNAPSHOTS

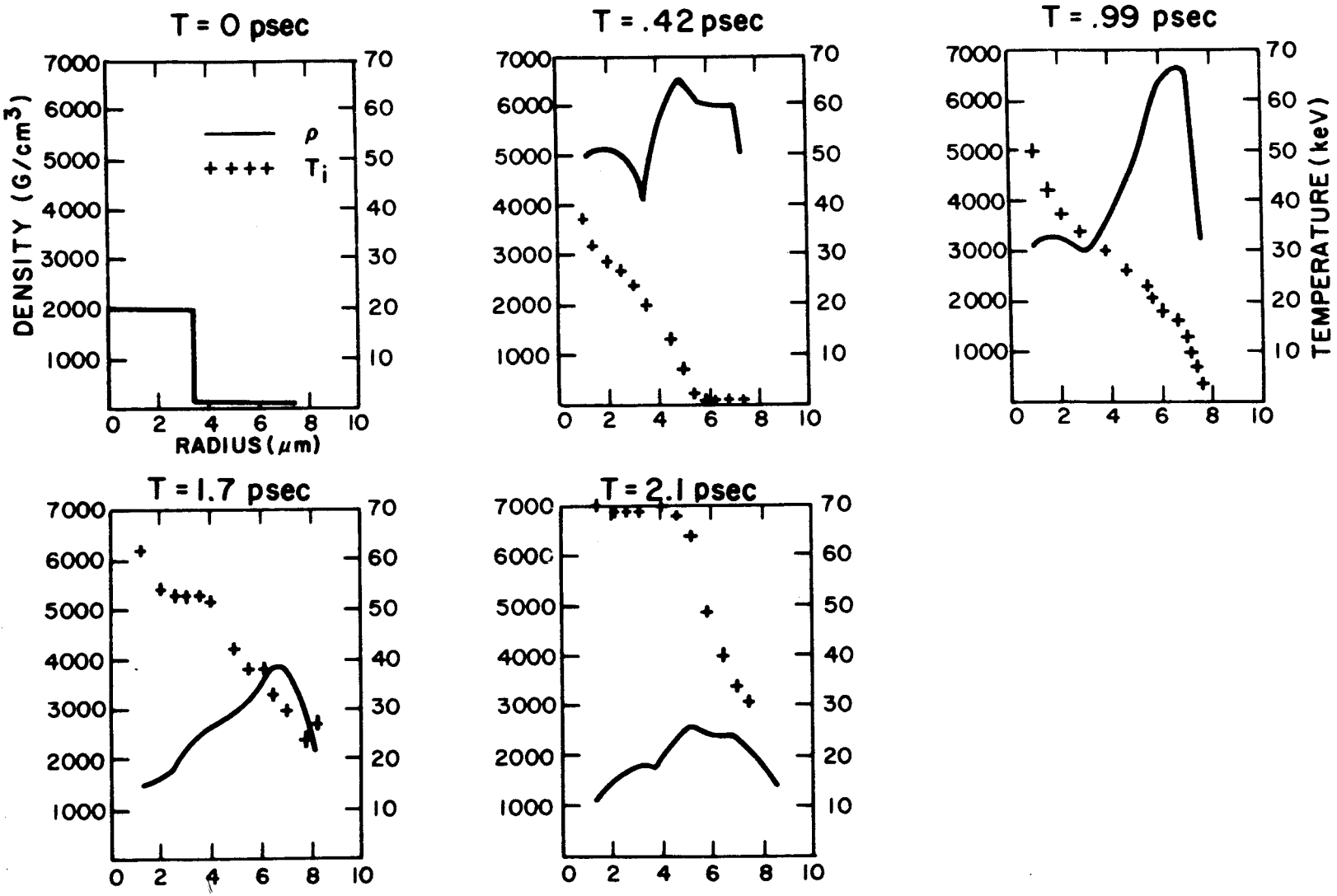

Fig. III-E-1.

Temperature and Density Snapshots

(from: G. Fraley, et. al., Phys. Fluids 17, 474 (1974))

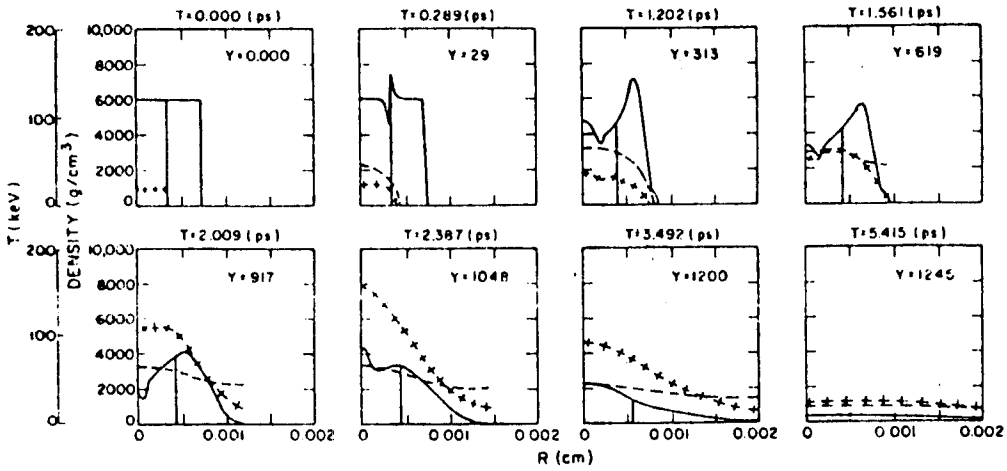

FIG. 6. Propagating burn in a 10-μg sphere; free outer boundary. Inner 10% of the mass T = 20 keV; remaining mass T = 1 keV.

Fig. III-E-1 (cont.)

course always be less than this. Methods for correcting this without going to a larger number of directions is being investigated. For the strongly burning pellets that we are currently investigating this is not a serious problem. Due to the broad peak in the DT reaction rate, the thermonuclear energy output vs. time for the two calculations shown in Fig. III-E-2 is similar, with the final yield differing by 18%. Such results should be considered as acceptable agreement considering that no attempt was made to normalize our calculations to this or any other similar hydrodynamics calculations.

The Fraley, et al. model uses one dimensional, one fluid, 3 temperature Langrangian hydrodynamics coupled to an S_N transport treatment of the alpha particles using the slowing down formulation of Longmire.[4] The PHD model, as explained in UWFDM-194, uses one dimensional, one fluid, two temperature Langrangian hydrodynamics coupled to a time dependent particle tracking transport collisional slowing down model. As such, we must consider our relatively good agreement with the results of the LASL calculations as confirmation of the correctness of the PHD computer program, within the approximation of the transport technique. In the case of alpha particle transport where most of the energy loss is through small angle scattering, the time dependent tracking technique and S_N transport are quite similar.

In the next test we compare the particle tracking technique (with straight line trajectories) to the more accurate Monte Carlo calculation of Corman, et al.[3] In Fig. III-E-3, we look in detail at the fractional energy redeposition into the electrons and ions vs. the distance from the

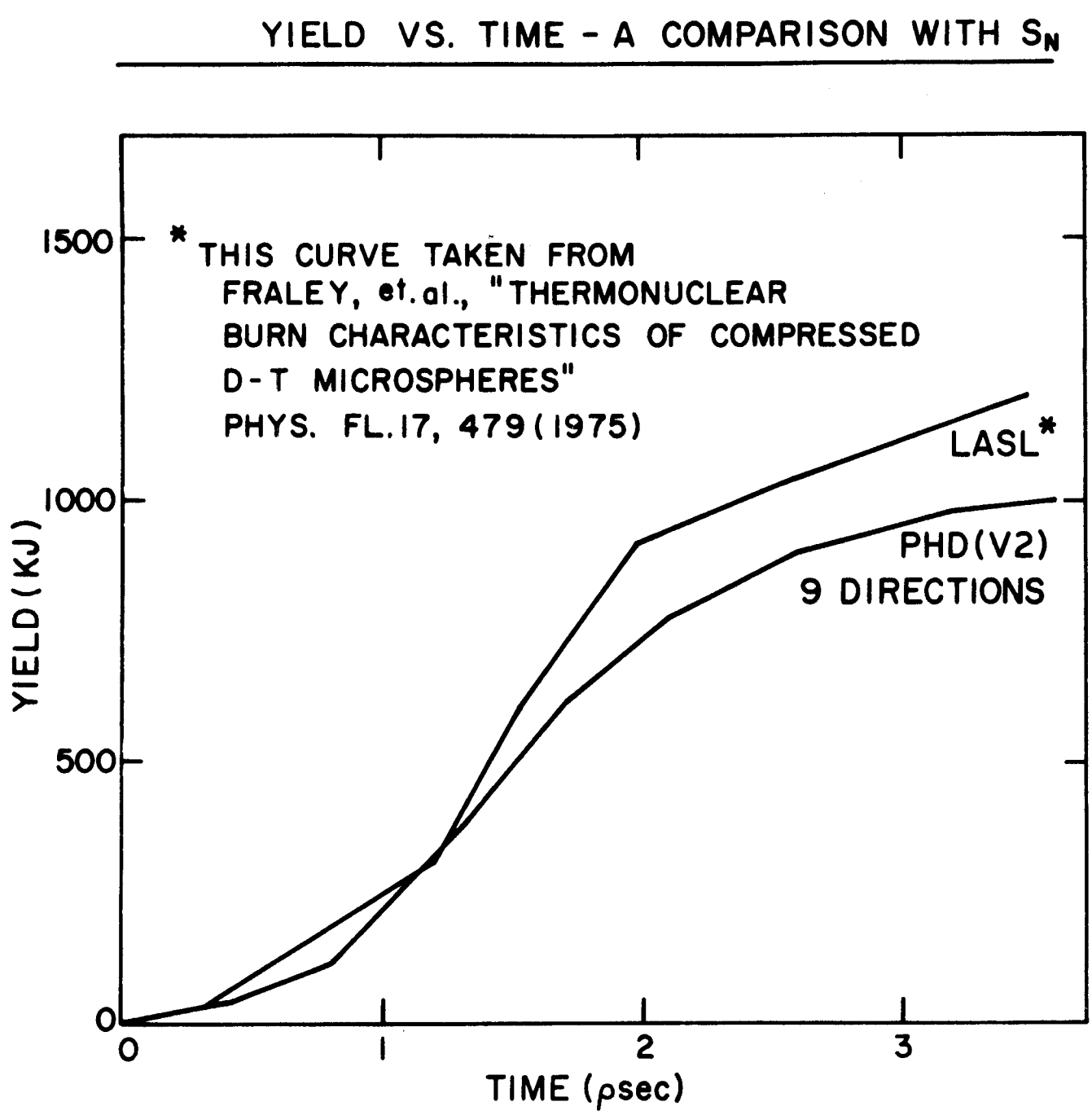
YIELD VS. TIME - A COMPARISON WITH S_N
* THIS CURVE TAKEN FROM FRALEY, et.al., "THERMONUCLEAR BURN CHARACTERISTICS OF COMPRESSED D-T MICROSPHERES" PHYS. FL.17, 479(1975)
LASL*
PHD(V2) 9 DIRECTIONS
YIELD (KJ)
1500
1000
500
0
0
1
2
3
TIME (psec)

Fig. III-E-2.

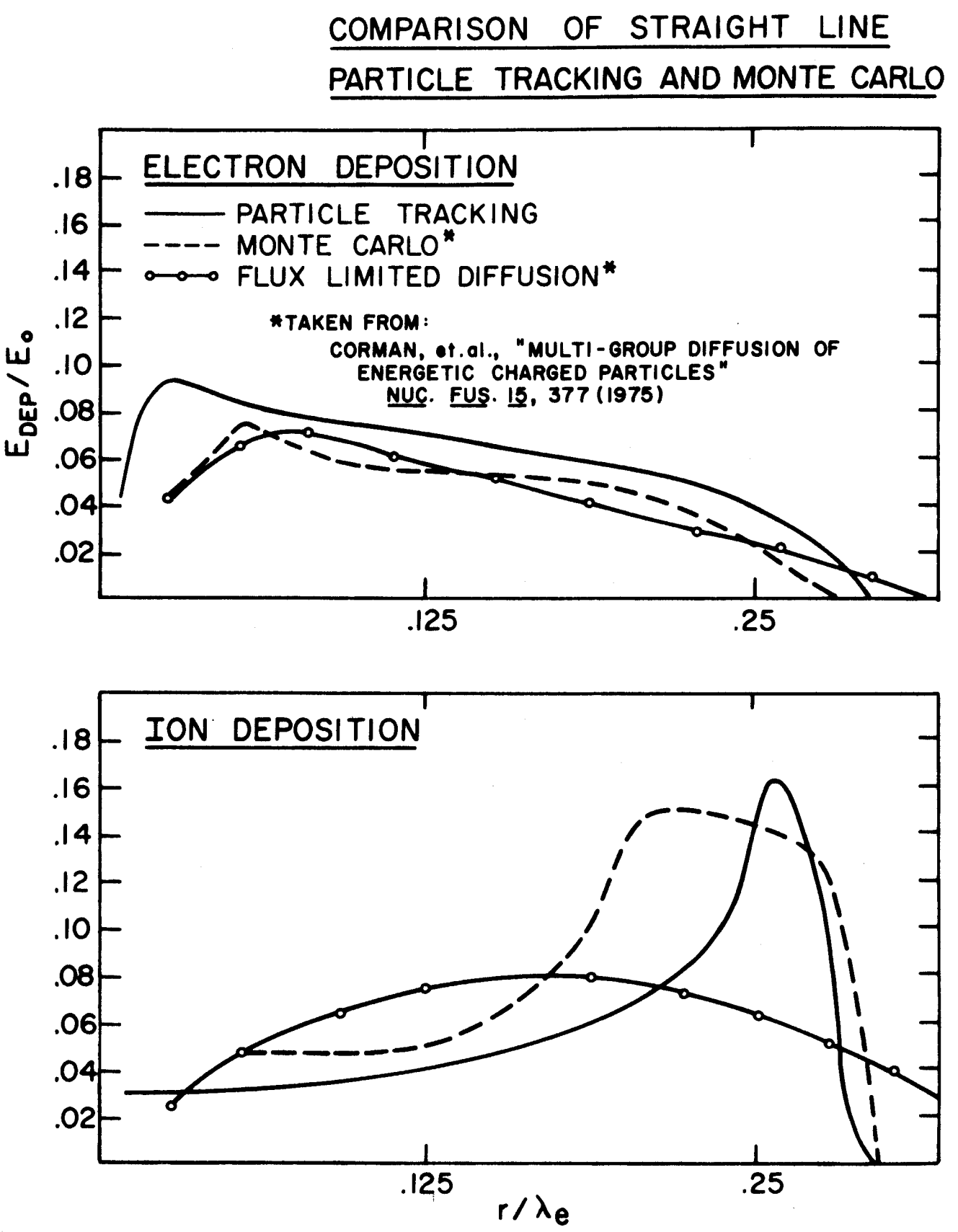
COMPARISON OF STRAIGHT LINE PARTICLE TRACKING AND MONTE CARLO
ELECTRON DEPOSITION
PARTICLE TRACKING
MONTE CARLO*
FLUX LIMITED DIFFUSION*
*TAKEN FROM:
CORMAN, et.al., "MULTI-GROUP DIFFUSION OF ENERGETIC CHARGED PARTICLES"
NUC. FUS. 15, 377 (1975)
E_{DEP}/E_o
.18
.16
.14
.12
.10
.08
.06
.04
.02
.125
.25
ION DEPOSITION
.18
.16
.14
.12
.10
.08
.06
.04
.02
.125
.25
r/λ_e

Fig. III-E-3.

source of 3.5 MeV alphas measured in units of slowing down mean free path on the electrons alone. Also plotted are the results of 100 group flux limited multigroup diffusion of the alphas. We first note that the spatial scale is considerably less than one mean free path on electrons alone so one would expect that a transport calculation is necessary. This is confirmed by the multigroup diffusion results where we see a gross error in the details of redeposition to the ions.

Fast alphas lose most of their energy to electrons along straight line trajectories until they slow down past a certain velocity, after which they lose the largest share of their energy to the ions in the larger angle collisions. This explains the broad peak in the Monte Carlo ion redeposition curve near the end of the alpha range. This peak is totally missed by the diffusion calculation although the total energy partitioning between electrons and ions is correct. The particle tracking method compares very well with both the electron and ion Monte Carlo redeposition, again, considering that no normalization is attempted. Slight adjustment of the slowing down term reproduces the Monte Carlo electron curve. The particle tracking method also predicts a peak in the ion redeposition however its peak is not as broad as the Monte Carlo peak and has its centroid farther from the origin. This discrepancy can be explained by recalling that the particle tracking method only allows straight line trajectories and this approximation will break down when scattering on the ions becomes appreciable. This method will therefore not account for back scattered alphas and will predict a peak that is narrower and further from the origin than would be expected. Techniques

for distributing the energy at the end of range to broaden the peak are being investigated. It should also be noted that this is a rather severe test of the straight line approximation because the electron temperature in this problem is 50 KeV and Fig. III-E-4 shows that at this temperature a large fraction of the alpha energy is lost to the ions (rather than to electrons along straight lines). For electron temperatures less than 50 KeV the particle tracking method should be even more valid and for temperatures greater than 50 KeV the actual mean free path of the alpha particle is long compared to typical pellet dimensions, thus little energy is deposited and the error is again small. We therefore interpret these two results as confirmation that the particle tracking model does remarkably well in predicting the coulomb collisional slowing down of the charged particle thermonuclear reaction products, and that when coupled to a Lagrangian hydrodynamics calculation it reproduces the hydrodynamic and burn results of a similar, presumably well tested, hydrodynamics code.

III-E-2. Radiation Transport - A Comparison with Published Results

Before the radiation transport code was integrated into the hydrodynamic-burn code, a comparison of our radiation treatment with the calculation of Apruzese and Davis[4] was made. Fig. III-E-5 indicates the good agreement between their calculations and ours for some simple problems. In Fig. III-E-5, J is the mean radiation intensity defined as

$$J = 1/2 \int_{-1}^{1} I(\mu)d\mu$$

where $I(\mu)$ is the specific intensity and where μ is the angle between the direction of radiation flow and the radial direction-spherical symmetry is

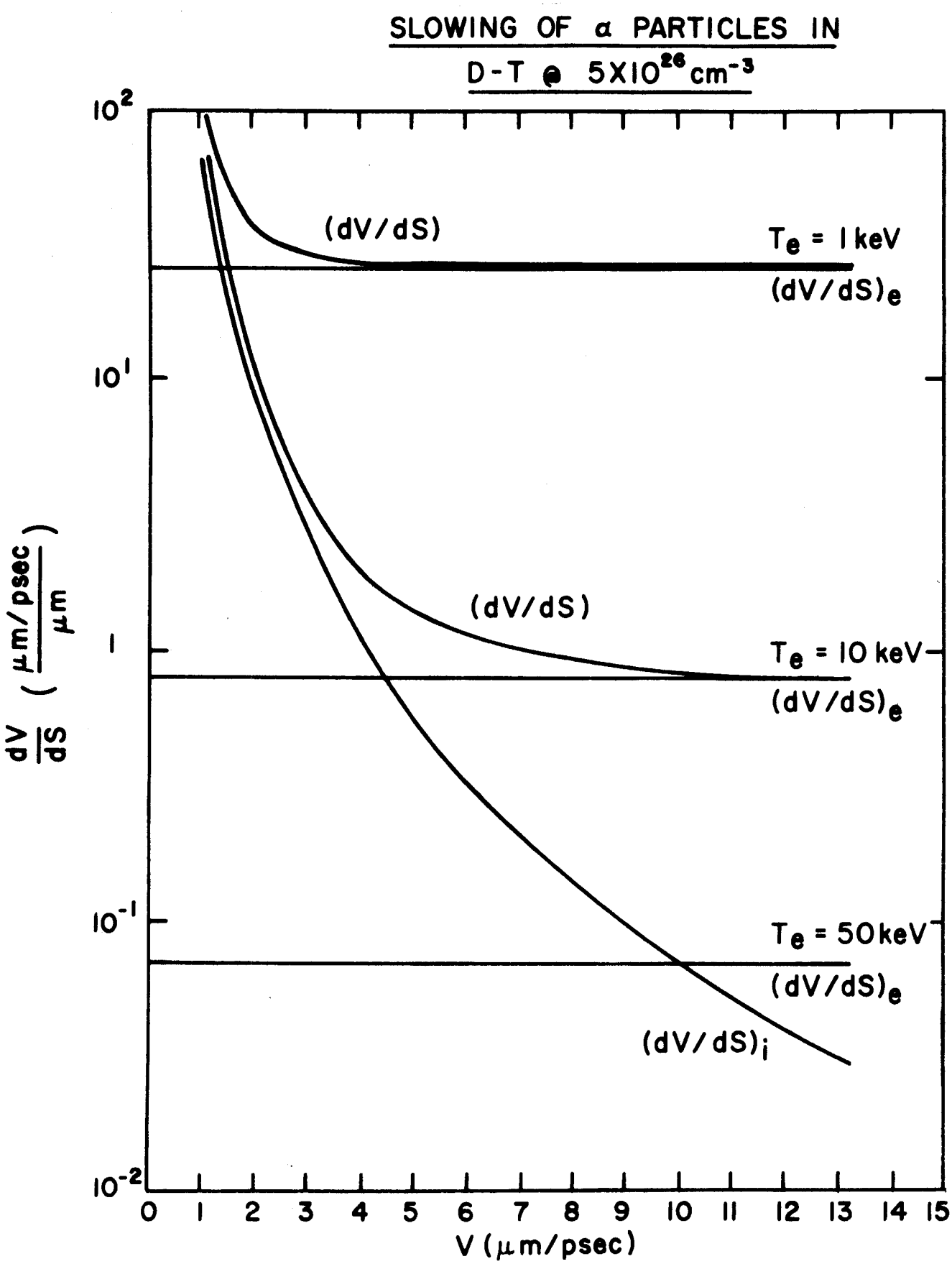
SLOWING OF α PARTICLES IN
D-T @ 5X10^26 cm^-3
10^2
10^1
1
10^-1
10^-2
dV/dS (μm/psec / μm)
(dV/dS)
Te = 1 keV
(dV/dS)e
(dV/dS)
Te = 10 keV
(dV/dS)e
Te = 50keV
(dV/dS)e
(dV/dS)i
0 1 2 3 4 5 6 7 8 9 10 11 12 13 14 15
V (μm/psec)

Fig. III-E-4.

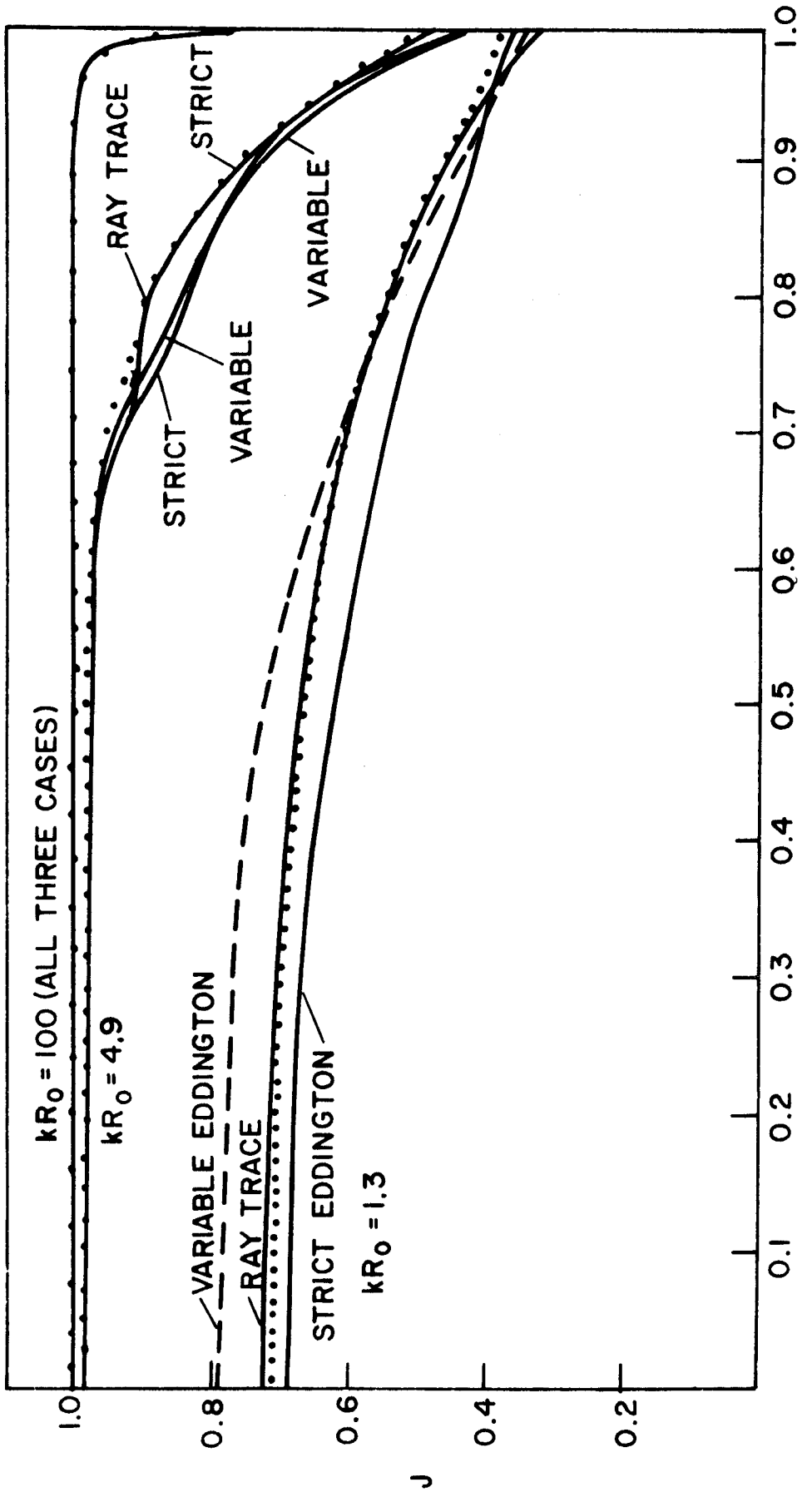

Fig. III-E-5 - Mean density J vs. radius r for optical depths of 1.3, 4.9, and 100 for ray-trace, strict Eddington, and variable Eddington transport calculations (dotted line gives our calculations).

assumed. For the three problems shown, the source function defined as the emission coefficient divided by the absorption coefficient was constant. The three cases considered were kR_o = 1.3, 4.9 and 100 where k is the absorption coefficient and where R_o is the radius of the sphere.

With the radiation included in the PHD-IV hydrodynamics-burn code, we reproduced the X-ray spectrum from a burning bare DT pellet core, computed at Lawrence Livermore Laboratory, presumably by LASNEX.[5] This comparison is shown in Fig. III-E-6 and again we are in very good agreement. Our partition of total energy between X-rays (1%) and charged particles (20%) is also in good agreement.

A far more severe test of our code is the comparison of X-ray spectra with an e-beam pellet calculation the results of which are contained in a paper by Varnado and Carlson.[6] This pellet contained approximately 200 mg of gold surrounding the DT. To make this comparison, a gold density profile was chosen to model the state of the plasma just before ignition. The gold density decreased as $1/r^3$ for the first 100 mg and was constant thereafter. The DT was assumed to be at a constant density and the DT and Au pressures were matched to be equal at their interface. Fig. III-E-7 shows the resulting X-ray spectrum at 12 nsec after ignition. The soft portion of the spectrum is in relatively good agreement with the results in Ref. 6, a 350 eV black-body. The hard portion of our spectra results from the non-LTE nature of our radiation transport calculation. However, our calculations only include bremsstrahlung emission and inverse bremsstrahlung absorption processes. If one includes photoelectric absorption and

Fig. III-E-6 - Radiation spectrum for bare DT pellet (dashed curve is Livermore spectrum scaled to a 100 MJ yield).

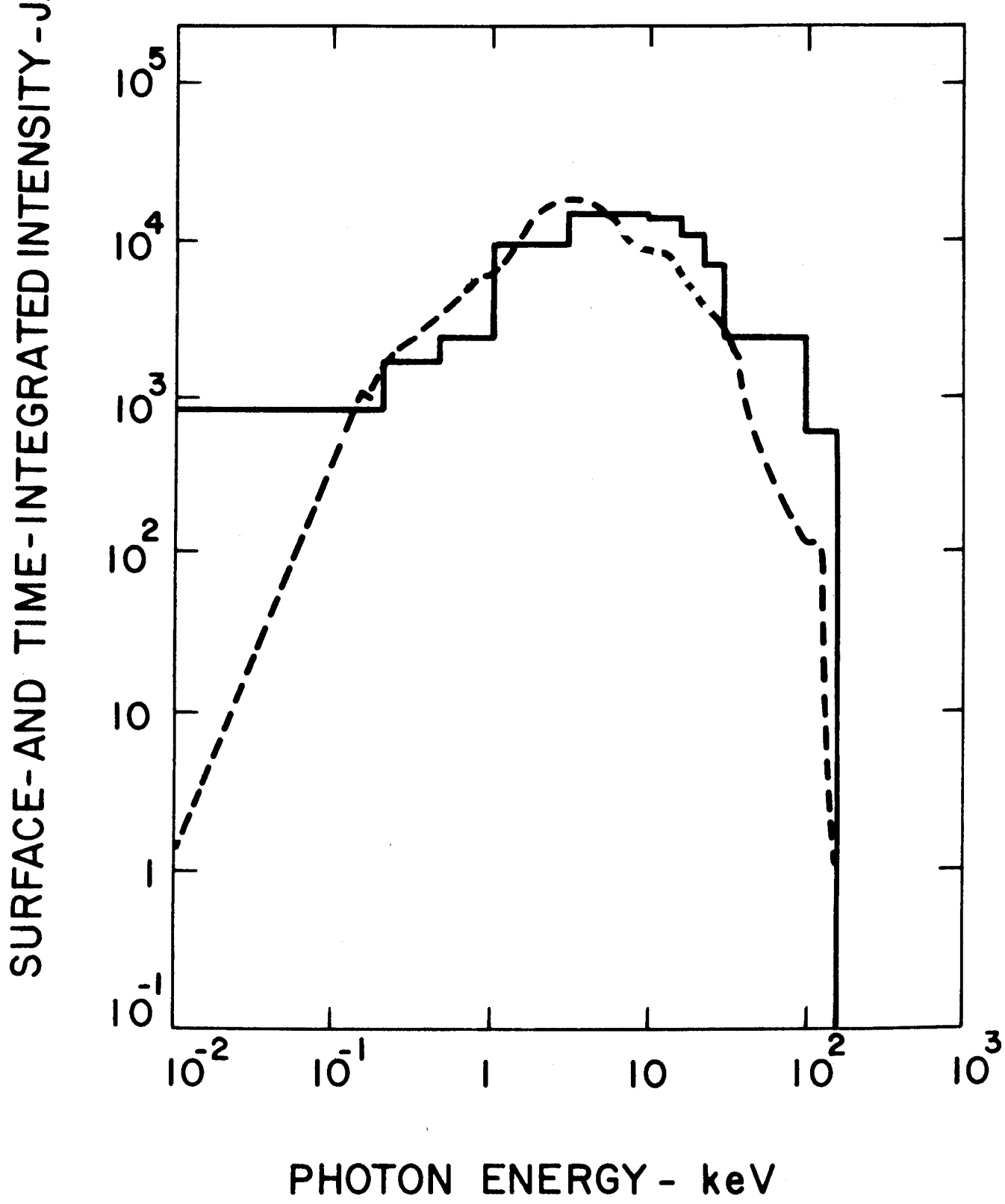

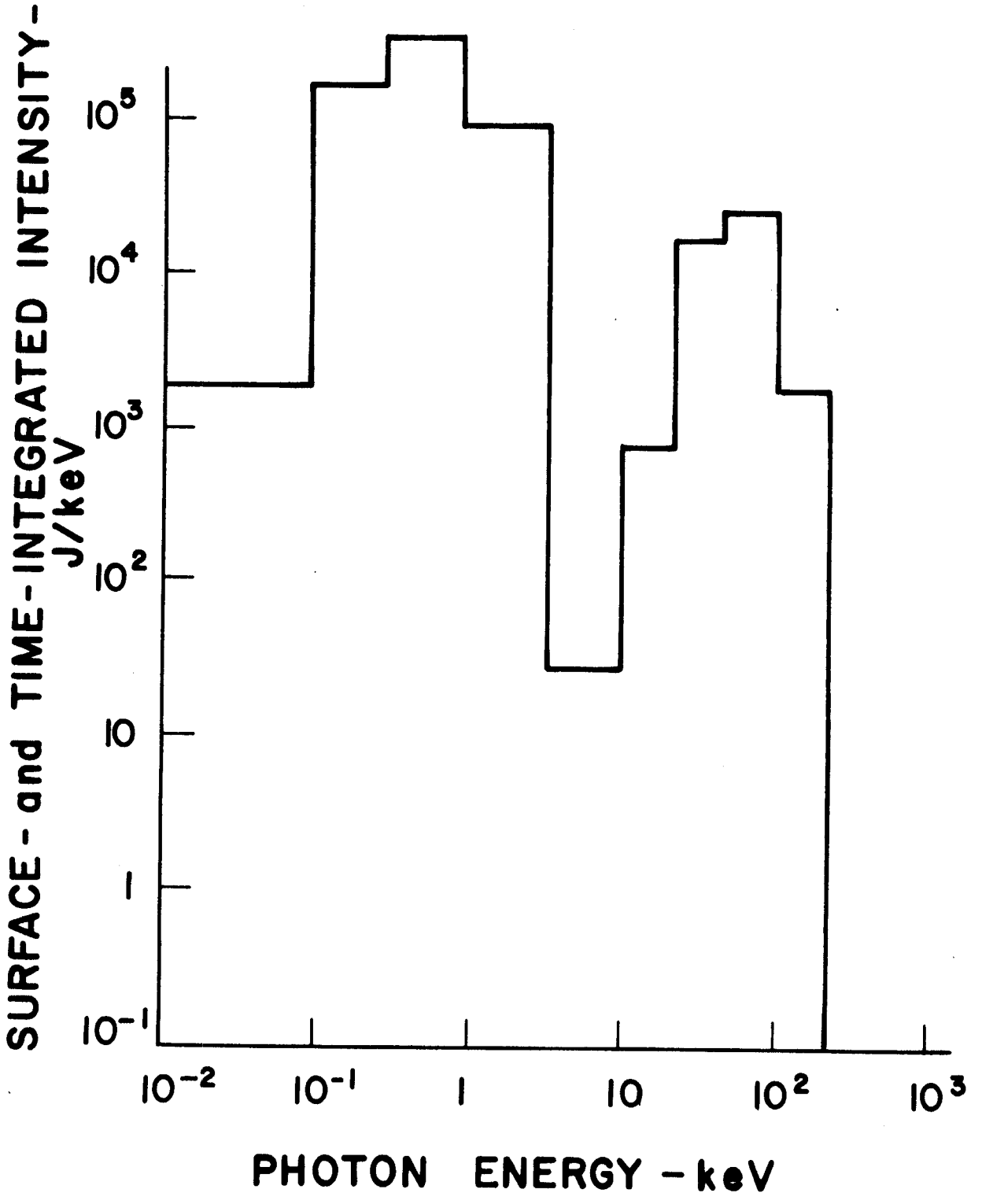

Fig. III-E-7 - RADIATION SPECTRUM FOR A DT PELLET WITH A 200 mg AU SHELL

incoherent scattering processes, this hard component of the spectrum may disappear. If we ignore the hard portion, the radiation flux peaks at about 9 nsec after ignition and decays on a time scale similar to the rise time in agreement with the results of Clauser.[7] The total photon energy emitted is approximately 4 MJ (5%), the neutron energy about 61 MJ and the charged particle energy about 11 MJ (15%).

References for Section III-E

1. G. Fraley, E. Linnebur, R. Mason and R. Morse, Phys. Fl. 17, 474 (1974).
2. Longmire, Elementary Plasma Physics, (Wiley, New York, 1967).
3. E. Corman, W. Loewe, and G. Cooper, Nuc. Fus. 15, 377 (1975).
4. Apruzese, and Davis, "Evaluation of the Radiation Field in a Spherically Symmetric Plasma", NRL Memorandum Report 3277 (1976).
5. J. Hovingh, J. Maniscalco, M. Peterson, and R. Werner, "The Preliminary Design of a Suppressed-Ablation, Laser Reduced Fusion Reactor", Lawrence Livermore Lab. Report UCRL-75368 (1973).
6. S. Varnado and G. Carlson, Nucl. Tech. 29, (1976).
7. M. Clauser, Phys. Rev. Lett. 34, 570 (1975).

III-F. Advanced Fuels

III-F-1. Introduction

The study of any type of fusion concept ultimately leads to the question of burning advanced fuels. The D-T fuel cycle produces copious quantities of 14 MeV neutrons that present difficult radiation damage problems while the tritium inventory in such D-T reactor concepts is between 10 to 100 kg representing 10^9 curies of radioactivity. To limit the tritium release to 1 curie/day requires a loss rate of 1 ppb. Advanced fuels hold the potential or reducing the radiation damage problems of 14 MeV neutrons and/or the large amounts of tritium that must be contained. The tritium breeding problem is also eliminated which leads to substantially different blanket designs. Some likely advanced fuel candidates are listed in Table III-F-1. These fuels are generally characterized by lower reaction rates than D-T, at low temperatures. Consequently, the success of burning advanced fuels will depend on increased values of ρR and/or ignition temperature. These must then be translated backward into increased laser performance in terms of energy and maximum power.

Using the PHD-IV hydrodynamic-thermonuclear burn computer code, estimates of necessary ρR and ignition temperatures were obtained for D-D and p-^{11}B fuels. These numbers are then used as "normalization points" in an analytic model of thermonuclear burn performance. Using this model, the prospect for burning advanced fuels in an inertial confinement system is analyzed.

III-F-2. Deuterium

Deuterium is an attractive advanced fuel because it has a relatively high reaction rate at low temperatures, Fig. III-C-1. The DD reaction takes two

Table III-F-1

Advanced Fuels

Fuel	Reaction Products (MeV)	Q-Value (MeV)
(D,T)	$_2He^4(3.5)$, $_0n^1(14.1)$	17.6
(D,D)	$_2He^3(.82)$, $_0n^1(2.45)$	3.65
	$_1T^3(1.01)$, $_1H^1(3.02)$	
(D,He^3)	$_2He^4(3.6)$, $_1H^1(14.7)$	18.3
(D,Li^6)	$2_2He^4(22.4)$	22.4
(P,Li^7)	$2_2He^4(22.4)$	22.4
(P,B^{11})	$3_2He^4(8.682)$	8.682

branches of about equal probability

$$ {}_1D^2 + {}_1D^2 \rightarrow {}_2He^3(.82\ MeV) + {}_0n^1(2.45\ MeV) $$
$$ \rightarrow {}_1T^3(1.01\ MeV) + {}_1p^1(3.02\ MeV). $$

It should be noted that the reaction products, ${}_2He^3$ and ${}_1T^3$, have a high probability of reacting with deuterium as they slow down

$$ {}_1T^{3*} + {}_1D^2 \rightarrow {}_2He^4(3.5\ MeV) + {}_0n^1(14.1\ MeV) $$

$$ {}_2He^{3*} + {}_1D^2 \rightarrow {}_2He^4(3.6\ MeV) + {}_1p^1(14.7\ MeV) $$

where the (*) denotes a nonthermal particle. The largest fraction of the overall Q-value is a result of the secondary reactions and the total reaction

$$ 6\ {}_1D^2 \rightarrow 2\ {}_2He^4 + 2\ {}_1p^1 + 2\ {}_0n^1 $$

has a Q-value of 43.25 MeV. This gives a specific yield of 345 MJ/mg as compared to 339 MJ/mg for DT.

A parametric study of the burn dynamics of 1 mg of deuterium configured as shown in Fig. III-F-1 was done with PHD-IV to estimate the necessary ρR and ignition temperatures. It was found that T_μ = 20 keV and ρR_μ = 10 g/cm^2 offered the best performance along with ρR values between 40 and 80 g/cm^2. These parameters gave yields of 100-200 MJ and gain on core of 200-300. However, compressing 1 mg of DD to 60 g/cm^2 requires the large compression of 177,000 times solid density. A gain on core of only 200 is also not nearly adequate. Clearly, 1 mg of DD fuel is not adequate if physically realistic compressions of 10^3-10^4 times solid density are considered. The

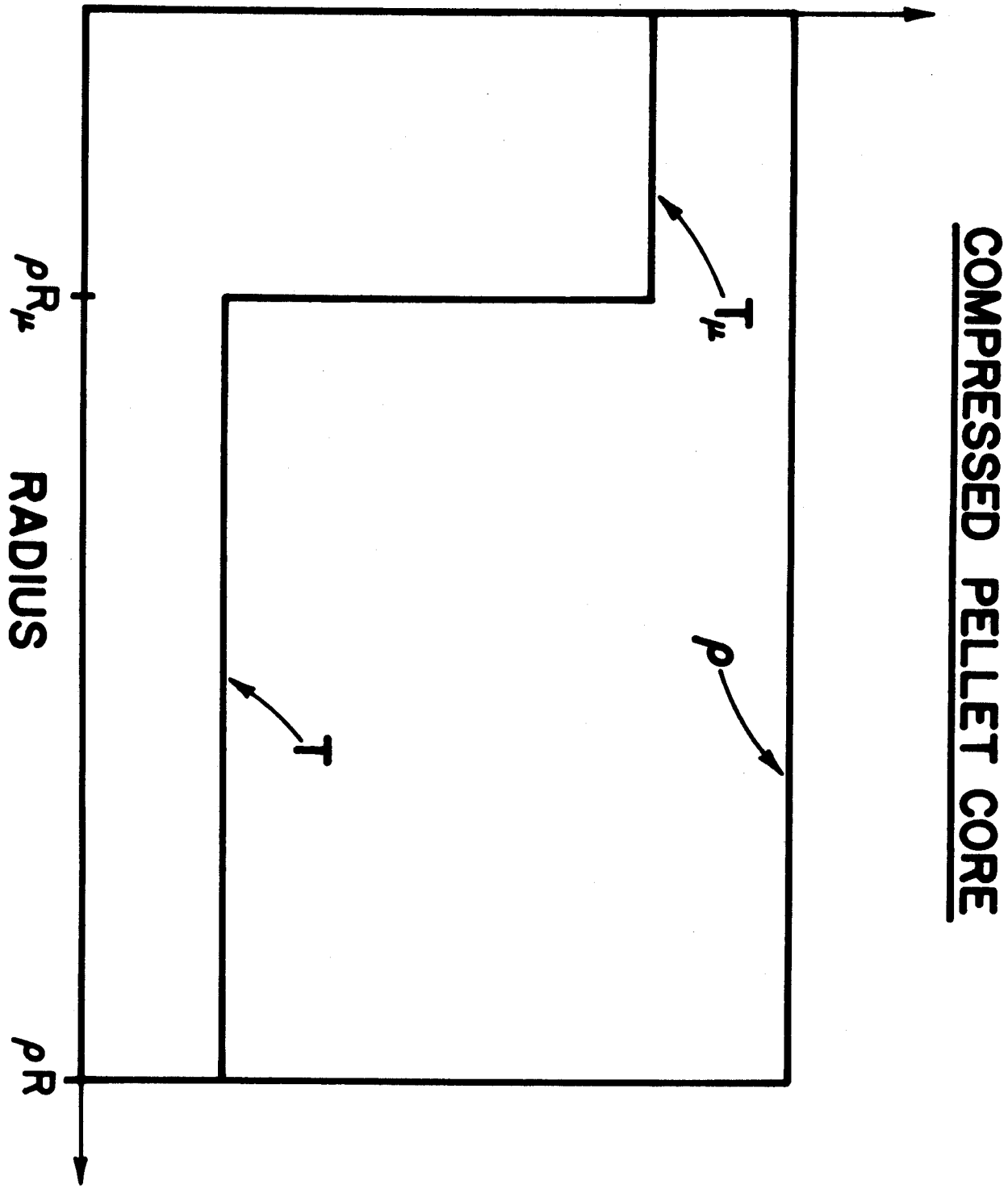

Fig. III-F-1

"free" parameter in this problem is the pellet mass which can be related to the compression by the formula

$$C = \frac{(\rho R)^{3/2}/\rho_o}{[3m/4\pi]^{1/2}} \quad .$$

Furthermore, the relation between yield and mass is given by the expression

$$Y = Y_o \; m \; f_B(\rho R)$$

where Y_o = 345 MJ/mg. PHD-IV calculations show the fractional burnup to be about 0.30.

Several conclusions can be drawn from these formulas. To avoid very high compressions, large mass pellets of large yield are necessary. Such large masses also imply large amounts of input energy, probably 100 MJ or more. The low gain on core implies a low overall pellet gain on the order of 10 rather than 100 which seems necessary for reactor applications. If total DD pellet gains of 10 are sufficient, and input energies of 100 MJ can be achieved, then DD advanced fuel fusion has merit.

Details of the DD burn propagation show that although much of the tritium reaction products are burned, there is still a substantial amount of unburned tritium remaining, typically 5×10^{-6} grams. This tritium will be recycled into later pellets thus reducing the ignition temperature and necessary ρR to support burn propagation. Careful analysis of this problem must be done to determine the extent to which it relieves the ρR requirements. In addition, this tritium must be processed, hence tritium handling problems are not totally eliminated in DD reactors. If steady state conditions are achieved at 5×10^{-6} grams of tritium per 1 mg pellet rather than the 5×10^{-4} grams necessary in a DT reactor then the tritium inventory has been reduced by two orders of magnitude to less than 1 Kg. Such a reduction in inventory greatly

relaxes the tritium containment problem. Since no tritium breeding is required, the blanket need not contain lithium or lithium bearing compounds. This could drastically alter the blanket design but has not been investigated in detail.

III-F-3. Proton-Boron-11

Another advanced fuel that has drawn a lot of attention is p-B^{11}.

$$_1p^1 + B^{11} \rightarrow 3\ _2He^4(8.682\ MeV)$$

This advanced fuel has the advantage of no neutron product at all. Only 3 alpha particles are the result of a p-B^{11} fusion (or fission if you like) with a Q-value of 8.682 MeV. The alpha particles are emitted in a continuous energy spectrum (as in β decay).

A problem with the p-B^{11} reaction is the uncertainty in the fusion cross section and hence in the reaction rate, $\langle\sigma v\rangle$. We have computed[1] our own reaction rate based on the most up-to-date data[2] and have compared our results with earlier calculations.[3-7] We find substantial differences with previous calculations.[3,4] A summary graph of very recent measurements of the p-^{11}B microscopic cross section[8,9] are shown in Fig. III-F-2.

Our code calculates the reaction rate, $\langle\sigma v\rangle$, assuming that both species have Maxwellian distributions. The integral[10] is evaluated numerically using a number of different techniques (Laguerre integration, Trapezoidal Rule, etc.) all of which give consistent results. The cross section data is in tabular form in increments of 25 keV lab. energy. Linear interpolation is also used. The value of $\langle\sigma v\rangle$ is plotted in Fig. III-F-3 and compared with the values previously reported by Fowler et. al. (FCZ).[4] Clearly, the

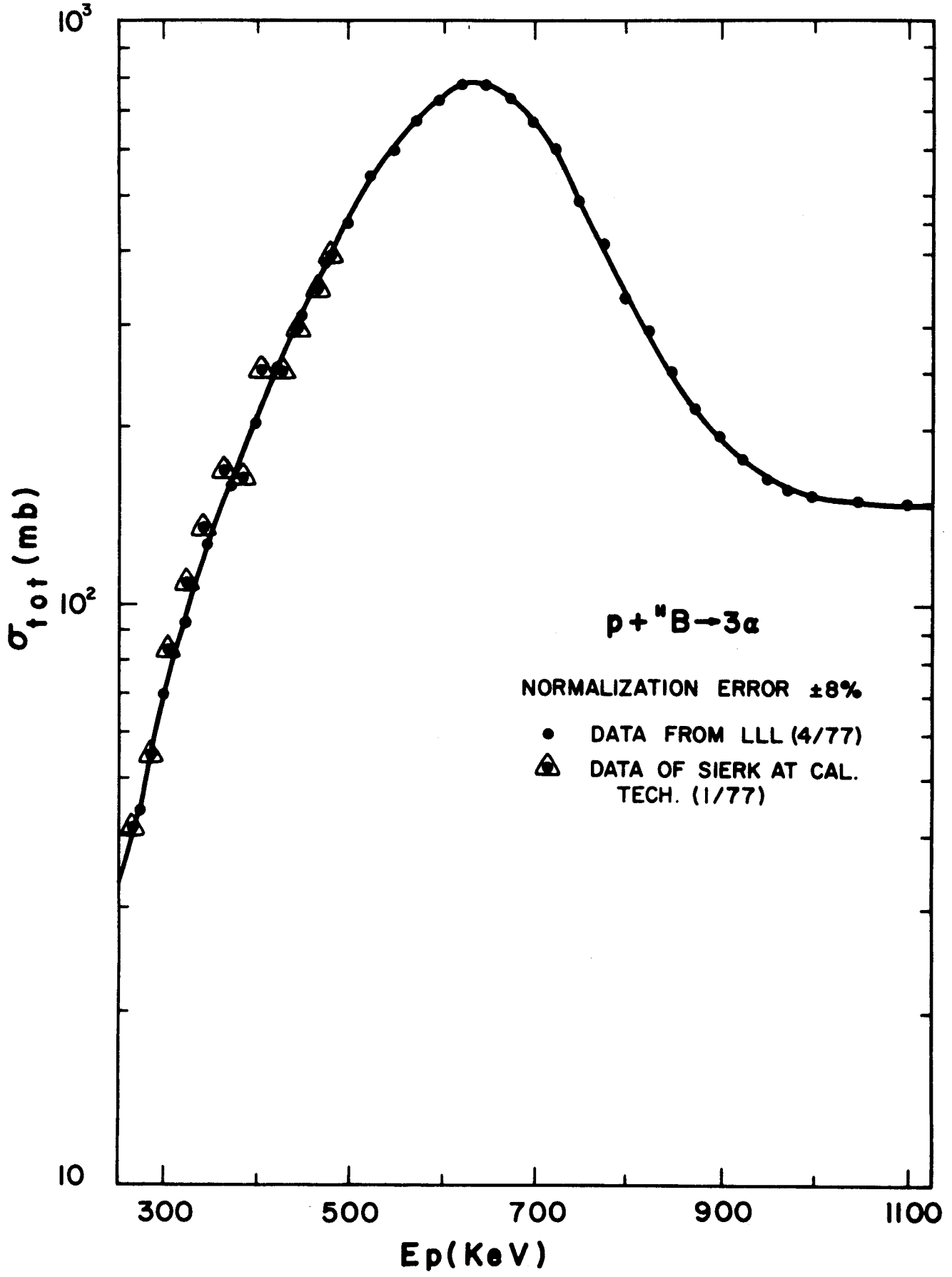
10^3
10^2
10
σ_{tot} (mb)
$p + {}^{11}B \rightarrow 3\alpha$
NORMALIZATION ERROR ±8%
DATA FROM LLL (4/77)
DATA OF SIERK AT CAL. TECH. (1/77)
300
500
700
900
1100
Ep(KeV)

Fig. III-F-2

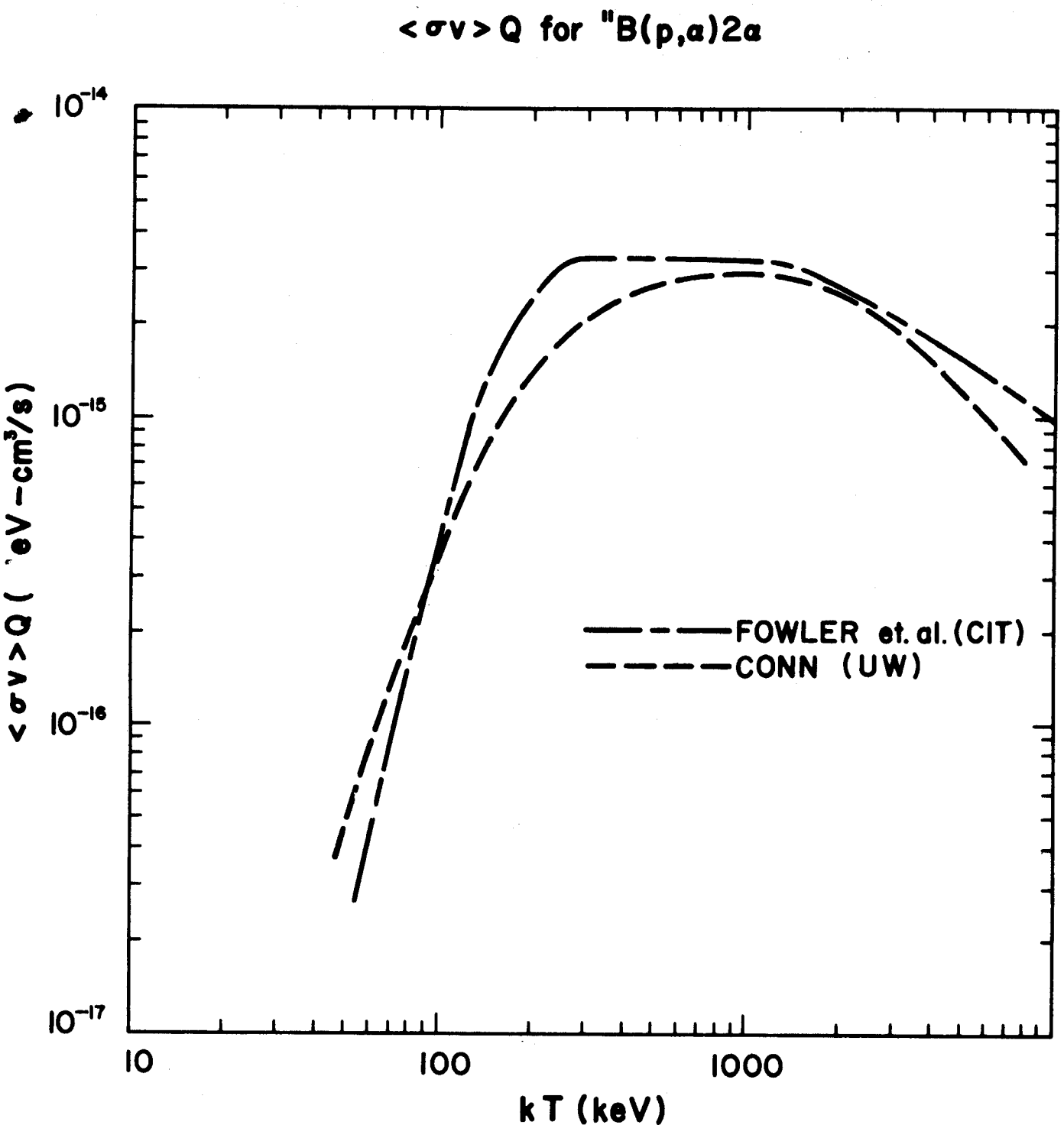
<σv>Q for ¹¹B(p,α)2α
10⁻¹⁴
10⁻¹⁵
10⁻¹⁶
10⁻¹⁷
<σv>Q (eV−cm³/s)
FOWLER et. al. (CIT)
CONN (UW)
10
100
1000
kT (keV)

Fig. III-F-3

value computed by us based on the most recent data is lower than the value of FCZ by a significant amount at temperatures below 1 MeV. At 300 keV, our value is lower by 65%. Elwyn[10] has recently used the same microscopic data to compute $\langle\sigma v\rangle$ and his results agree with those we have given.

Using the reaction rate data we have calculated, the PHD computer code was modified to calculate the burn dynamics of $p\text{-}B^{11}$. A parameter study was then done to determine the values of T_μ, ρR_μ, and ρR to burn 1 mg of $p\text{-}B^{11}$. The results are shown in Fig. III-F-4. The optimum microcore conditions are 50 g/cm^2 and 400 keV while the optimum total ρR is 500 g/cm^2. At these values, the fractional burnup is 76% and the gain on core is 170.

The high ρR and temperature necessary for burn propagation are in large part due to the excessive number of electrons present with $p\text{-}B^{11}$. The high microcore ignition temperature probably cannot be achieved by hydrodynamic processes for this implies an implosion velocity of 3×10^8 cm/sec, an order of magnitude higher than that needed for DT.

With all inertial confinement systems, advanced fuels imply greater ρR values and these can only partially be achieved through high compression. The remainder must come from large fuel masses and this implies greater yields and greater input energies. The necessary scales of yield and input energy for $p\text{-}B^{11}$ appear to rule out its use for reactor applications.

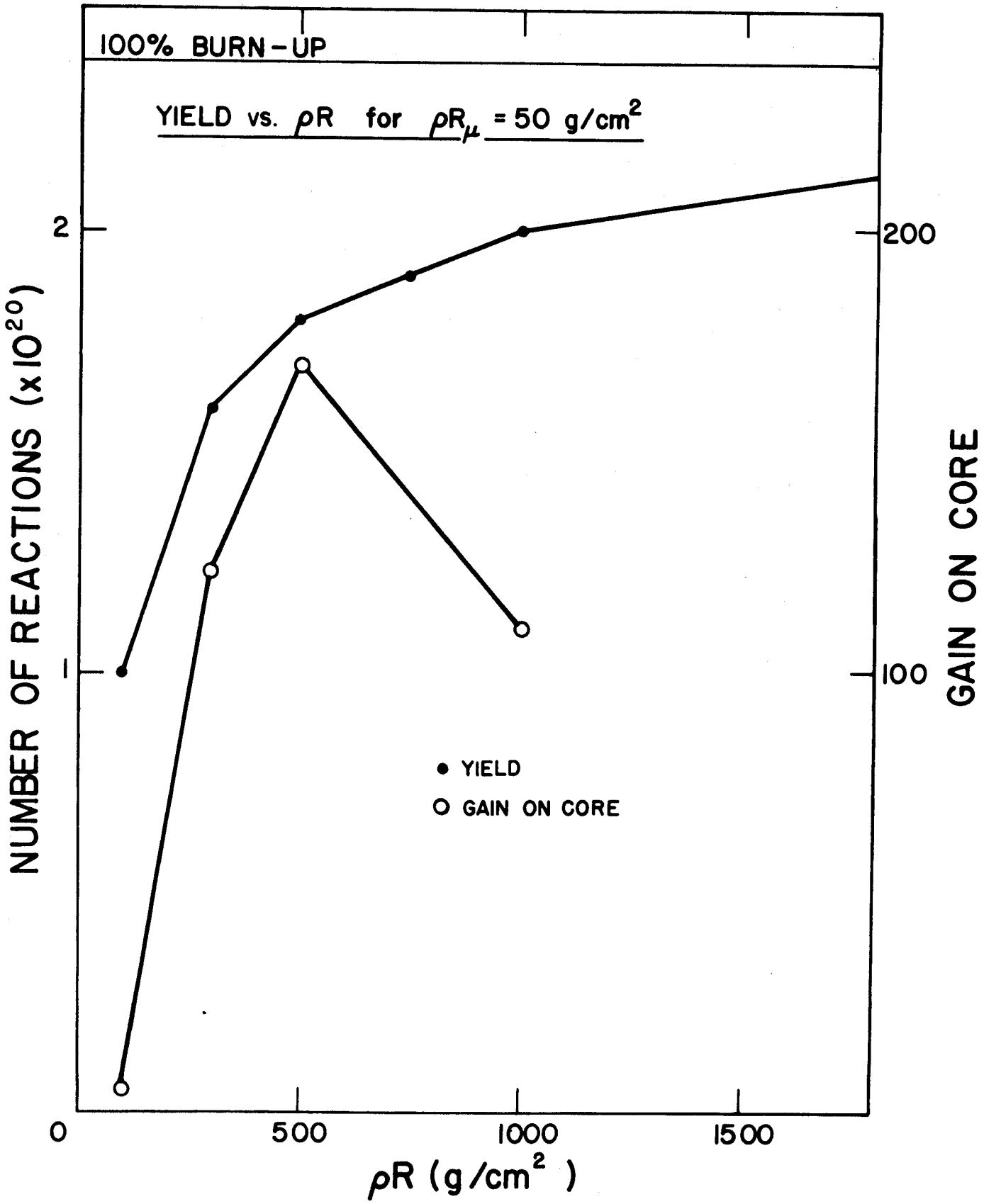
100% BURN-UP
YIELD vs. ρR for ρR_μ = 50 g/cm²
NUMBER OF REACTIONS (x10²⁰)
GAIN ON CORE
2
1
0
200
100
500
1000
1500
ρR (g/cm²)
● YIELD
○ GAIN ON CORE

Fig. III-F-4

References for Section III-F

1. M. Gordinier, R. Conn, Univ. of Wisconsin-Madison (Private Communication) (10/76).

2. T. Tombrello, Cal-Tech. (Private Communication) (10.76).

3. G. Miley, H. Towner, and N. Ivich, "Fusion Cross Sections and Reactivities", Univ. of Illinois Nuclear Engr. Program Report COO-2218-17.

4. W. A. Fowler, G. Caughlin and B. Zimmerman, "Thermonuclear Reaction Rates, II", Annual Review of Astronomy and Astrophysics, 13, 69. 1975.

5. D. C. Moreau, "Potentiality of the Proton-Boron Fuel for Controlled Thermonuclear Fusion", Princeton University Engineering Masters Thesis, May 1976.

6. T. Weaver, G. Zimmerman, L. Wood, "Prospects for Exotic Fuel Usage in CTR Systems I. $^{11}B(p,2\alpha)He^4$: A Clean High Performance CTR Fuel" Lawrence Livermore Reports UCRL-74191 and 74352.

7. J. M. Dawson, "CTF Using the p-B^{11} Reaction" (Private Communication).

8. See Ref. #3 for explicit form of the integral.

9. I. D. Proctor, H. F. Lutz, W. Bartolini (10 June 1974).

10. Segel, Hanna, Allis; Phys. Rev. 139, B818 (1965).

11. Symons, Treacy; Nuclear Physics, 46, 93 (1963).

III-G. Prospects for High Gain Pellets

Pellet gains of G = 100 are necessary for laser fusion power plant feasi assuming a laser efficiency of $\eta_L = .1$. For a laser efficiency of $\eta_L = .01$ the necessary pellet gain must be 1000. Since laser efficiencies of 10% appear to be very difficult to attain it is logical to investigate the possibility of increasing the pellet gain. Pellet gain can be expressed as the product of gain on core and hydrodynamic efficiency.

$$G = G_c \eta_H$$

$$G_c = Y/W_T$$

$$\eta_H = W/E_L$$

Y = thermonuclear yield

W_T = internal energy of the compressed core

E_L = incident laser energy

Obviously the pellet gain can be increased by increasing either G_c or η_H. Since η_H is intimately related to the very complex light absorption and implosion mechanisms we choose to analyze the simpler gain on core.

To analyze the gain on core we attempt to define the most optimum core configuration possible without treating the problem of how such a configurati might be created. The core configuration that is usually used to demonstrate the principles of ignition and thermonuclear burn is shown in Fig. III-G-1. is a uniformly compressed core of $\rho R = 3$ g/cm^2 and $\rho R_\mu = .5$ g/cm^2 with $T_\mu = 1$ In Fig. III-G-1 we also postulate a more optimum configuration. Here the core uniformly compressed but has a density variation of

$$\rho(r) = .5/r$$

This density profile has the property that if any particular radius (r^*) is chosen and the density inside this radius is held constant at $\rho = .5/r^*$ then

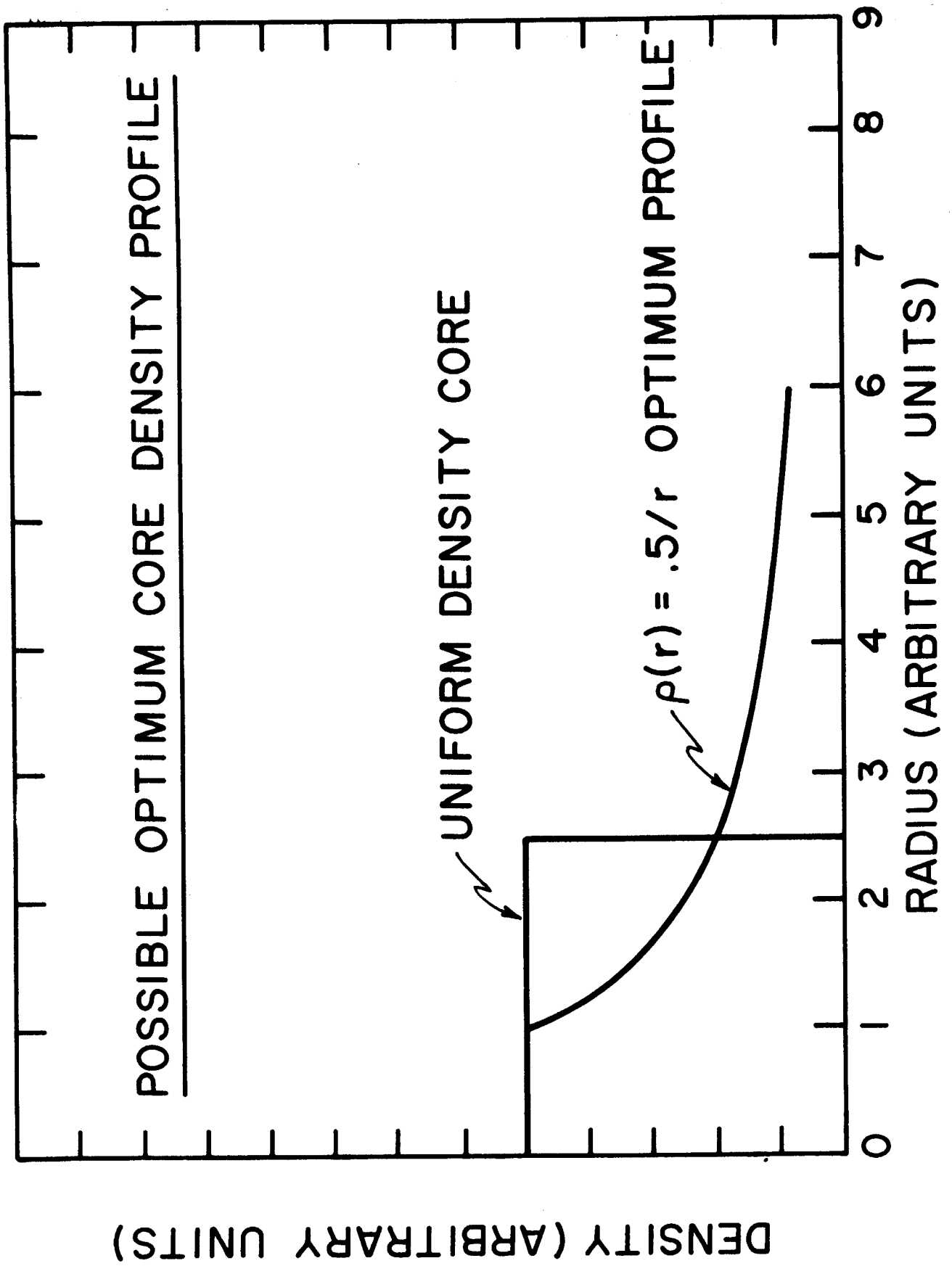
POSSIBLE OPTIMUM CORE DENSITY PROFILE
UNIFORM DENSITY CORE
ρ(r) = .5/r OPTIMUM PROFILE
DENSITY (ARBITRARY UNITS)
RADIUS (ARBITRARY UNITS)
0
1
2
3
4
5
6
7
8
9

Fig. III-G-1.

the sphere inside this radius will have $\rho r^* = .5$ g/cm^2, the necessary micro-core value. On the other hand the remainder of the core will have a density falling from this value. Therefore more mass will be necessary to achieve a given total ρR value. Assuming that fractional burn up is independent of mass, and only depends on ρR, this increased mass will provide greater yield. It remains to be determined of course whether W_T will be greater for this gre mass and thus cut down the gain on core. Another consideration in choosing the density profile is the necessity of promoting thermonuclear burn. This profile will have no trouble in this regard. Simple analysis shows

$$W_c \ (J/cm^3) = 3.225 \times 10^5 \ \rho^{5/3}$$

$$W_\mu \ (J/cm^3) = 3.83 \times 10^7 \ \rho_\mu \ T_\mu \ (Kev)$$

where W_c is the energy/cm^3 necessary to compress the core to its density ρ from solid density and W_μ is the energy/cm^3 necessary to heat the micro-core to temperature T_μ. The total energy input is then

$$W_T = 4\pi\int_o^{R_\mu} T_\mu \ 3.83 \times 10^7 [\tfrac{.5}{R_\mu}] r^2 dr + 4\pi\int_{R_\mu}^{R} 3.225 \times 10^5 [\tfrac{.5}{r}]^{5/3} \ r^2 \ dr$$

$$+ 4\pi\int_o^{R_\mu} 3.225 \times 10^5 \ [\tfrac{.5}{R_\mu}]^{5/3} \ r^2 \ dr$$

$$W_T = 8 \times 10^7 \ R_\mu^2 \ T_\mu + 1.9 \times 10^5 \ R_\mu^{4/3} + 9.6 \times 10^5 \ R^{4/3} \ (Joules)$$

The value of total ρR is

$$\rho R = \int_o^{R_\mu} \rho_\mu \ dr + \int_{R_\mu}^{R} \rho(r) \ dr$$

$$= \frac{1}{2} [1 + \ln (R/R_\mu)]$$

and the total mass is

$$M = \pi (R^2 - R_\mu^2/3)$$

Fractional burn up is estimated from computer calculations for uniformly compressed cores as (see section IV-B)

$$f_B = \begin{cases} .05\ \rho R & 0<\rho R<1 \\ .05 + .1875\ (\rho R - 1)^{.585} & 1<\rho R<3 \\ .21 + .033\ \rho R & 3<\rho R<7 \end{cases}$$

and the yield is given by

$$Y = 3.37 \times 10^{11}\ f_B\ M \quad \text{(Joules)}$$

We have now expressed ρ_μ, M, W_T, ρR, f_B, Y, and G_c as functions of R_μ and R. We investigate two different cases:

(I) $y \simeq 100$ MJ and $G_c \simeq 20000$

(II) $y \simeq 1000$ MJ and $G_c \simeq 20000$

If the hydrodynamic efficiency were $\eta_H = .05$ then these cases would imply pellet gains of 1000 with input laser energies of 100 KJ and 1 MJ. Table III-G-1 summarizes the results for case I. With a microcore radius of 10 microns, implying a compression of 2347 times solid density, the necessary conditions were met. They were also met at microcore radii of 20 μ and 30 μ but not greater than this. This implies that a compression of the micro core of at least 782 times solid density is necessary to achieve gains of 1000 <u>if the incident laser energy is 100 KJ</u>. In Table III-G-2 the results of case II are given and we see that the necessary conditions are still achievable with a compression of only 235 times solid density <u>if the incident energy is 1 MJ</u>. As the microcore radius gets larger, the total core radius must also increase to provide the same yield, thus implying that the fractional burn-up goes down, due to the increased mass. An economy of scale can be observed in Table III-G-3 where the results for different radii and a fixed microcore radius are given. As the available energy W_T goes up,

Table III-G-1

Summary of Case I - 100 KJ Yield

μ-Radius (cm)	μ-Compression	Radius (cm)	Mass (g)	ρR (g/cm^2)	Fractional Burnup	Internal Energy (J)	Yield (J)	Gain on Core
1.-3	2347	2.-2	1.3-3	2.	.24	5.3+3	1.+8	1.9+4
2.-3	1174	3.-2	2.8-3	1.85	.22	9.3+3	2.1+8	2.26+4
3.-3	782	3.-2	2.8-3	1.65	.19	9.7+3	1.9+8	1.9+4

Table III-G-2

Summary of Case II - 1 MJ Yield

μ-Radius (cm)	μ-Compression	Radius (cm)	Mass (g)	ρR (g/cm^2)	Fractional Burnup	Internal Energy (J)	Yield (J)	Gain on Core
1.-3	2347	6.-2	1.1-2	2.55	.29	2.27+4	1.1+9	4.9+4
2.-3	1174	6.-2	1.1-2	2.2	.26	2.3+4	9.9+8	4.3+4
3.-3	782	6.-2	1.1-2	2.0	.24	2.3+4	9.0+8	3.9+4
4.-3	587	7.-2	1.5-2	1.93	.23	2.9+4	1.2+9	4.1+4
5.-3	465	7.-2	1.5-2	1.82	.22	3.0+4	1.1+9	3.8+4
6.-3	391	7.-2	1.5-2	1.73	.21	3.1+4	1.1+9	3.5+4
7.-3	335	7.-2	1.5-2	1.65	.20	3.2+4	1.0+9	3.2+4
8.-3	293	7.-2	1.5-2	1.58	.19	3.3+4	9.7+8	2.9+4
9.-3	261	7.-2	1.5-2	1.53	.18	3.5+4	9.2+8	2.7+4
10.-3	235	8.-2	2.-3	1.54	.18	4.2+4	1.2+9	2.9+4

Table III-G-3

Summary of Different Core Radii at Fixed μ-Core Radius

μ-Radius = 3.-3 cm Compression = 782

Radius (cm)	Mass (g)	ρR (g/cm^2)	Fractional Burnup	Internal Energy (J)	Yield (J)	Gain on Core
1.-2	3.-4	1.1	.1	2.9+3	1.0+7	3.6+3
2.2-2	1.2-3	1.45	.17	6.0+3	7.0+7	1.2+4
3.-2	2.8-3	1.65	.20	9.8+3	1.9+8	1.9+4
4.-2	5.0-3	1.80	.21	1.4+4	3.6+8	2.6+4
6.-2	1.1-2	2.0	.24	2.3+4	9.0+8	3.9+4
8.-2	2.0-3	2.14	.25	3.4+4	1.7+9	5.0+4
10.-2	3.1-2	2.25	.26	4.5+4	2.8+9	6.2+4

the yield goes up but so does the gain on core. The yields, however, become unmanageably large as more energy is added. How this analysis translates into a laser pulse shape is impossible to predict since the implosion process is not specified. The laser energy is of course fixed once a value for the hydrodynamic efficiency is chosen and the maximum laser power might be crudely estimated because this will depend on the maximum compression of the pellet. With this in mind, the lowest microcore density which will still provide the yield and gain is desirable. For the case of 100 KJ of laser energy this will be a compression of about 782. With 1 MJ of laser energy incident the compression can be less than 235 thus the maximum laser power for the 1 MJ case will be less than for the 100 KJ case.

This analysis will be developed further in the future, but for now several conclusions can be made.

1) Density profiles can be defined that give gain on core in excess of 20000 which might imply total pellet gains of 1000 for incident laser energies of 100 KJ to 1 MJ.
2) As laser energy is reduced, the necessary compression to reach $G_c \geq$ 20000 is increased, implying greater maximum laser power.
3) Yield increases more than linearly as input laser energy increases, thus there is an economy of scale; however, the yield quickly reaches unmanageably large values for laser energies in excess of 1 MJ.
4) With 100 KJ of laser light (assuming $\eta_H = .05$) a maximum compression of only 782 times solid density is necessary to produce a yield 100 MJ.

IV. Pellet Design for SOLASE

IV-A. Basic Pellet Physics

In any controlled thermonuclear reactor concept the fundamental requirement is always to produce more energy from the fusion reactions than was required to initiate them. To produce only as much thermonuclear energy as was required to start the reaction is called breakeven. This so-called breakeven experiment is considered the next most significant milestone in fusion research, and its achievement is expected in the early 1980's. However, this milestone will come with plasma conditions that are different from those necessary to build a reactor because it is thermonuclear ignition and self-sustained burning that will provide the energy multiplication needed to produce a net power generating plant once all of the recirculated power is included. Breakeven conditions do not so strongly necessitate this thermonuclear ignition and burn. It will be the purpose of the following discussion to outline the necessary plasma performance needed for reactor applications rather than for the near term breakeven experiments. Current experimental results will be discussed only to contrast the state of the art with the necessities of eventual reactor applications.

In the context of laser driven compression of spherical pellets of DT fusion fuel[1-3] the most fundamental plasma performance characteristic is the pellet gain (G).

$$G = Y/E_L \quad . \tag{1}$$

The pellet gain is defined as the ratio of thermonuclear energy produced (Y) to the laser energy incident on the pellet (E_L). For breakeven the gain must equal unity but for power plant applications the necessary gain is determined by the laser efficiency and plant thermal efficiency. The relation between these quantities is given by the expression[4]

$$G = \left[\frac{1}{\eta_L(\eta_{th}-\eta_p)}\right] - 1 \qquad (2)$$

where η_L = laser efficiency

η_{th} = gross plant thermal efficiency

η_p = net plant thermal efficiency.

In Fig. IV-A-1 the gain is plotted as a function of the difference between η_{th} and η_p for different η_L. It is seen that if (1) the gross thermal efficiency is determined to be 40% from thermodynamic considerations, (2) the net plant efficiency must be at least 30% from economic and environmental considerations, and (3) the laser efficiency is assumed to be 10%,then the pellet gain must be 100. For a laser efficiency of 5% the pellet gain must be 200. Therefore, for realistic gross and net plant efficiencies and optimistic laser efficiency a pellet gain of 100 to 200 is necessary for reactor applications. The SOLASE design requires a pellet gain of 150 because the laser design, with multi-passed amplifiers, has an efficiency of 7%. For a 1 MJ laser this gain implies a pellet yield of 150 MJ.

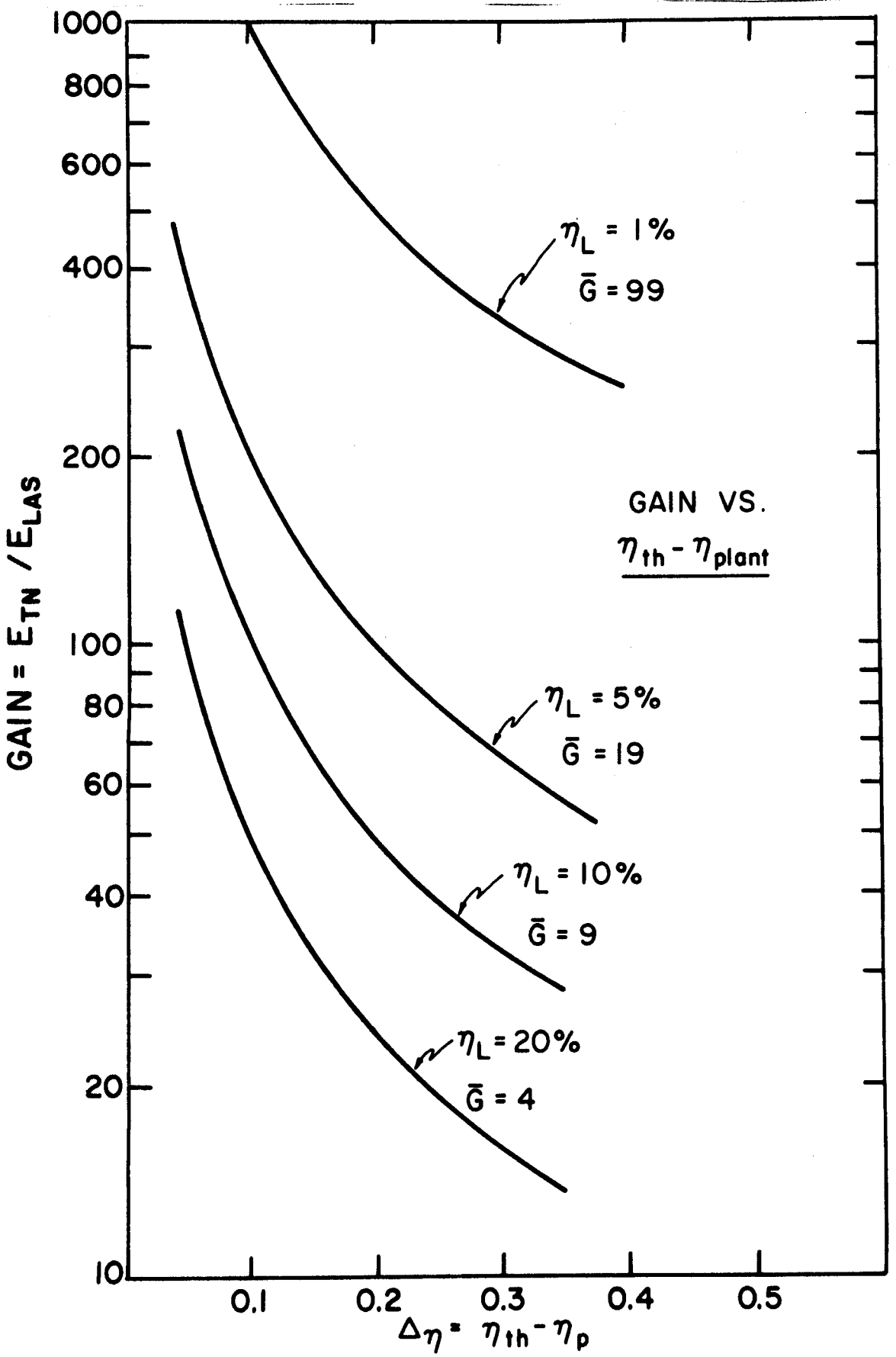
1000
800
600
400
200
100
80
60
40
20
10
GAIN = E_{TN} / E_{LAS}
0.1
0.2
0.3
0.4
0.5
$\Delta\eta = \eta_{th} - \eta_p$
η_L = 1%
$\bar{G}$ = 99
η_L = 5%
$\bar{G}$ = 19
η_L = 10%
$\bar{G}$ = 9
η_L = 20%
$\bar{G}$ = 4
GAIN VS.
$\eta_{th} - \eta_{plant}$

Fig. IV-A-1.

To determine whether such pellet performance is consistent with the physics of pellet dynamics the details of this dynamical process must be investigated. To do this the pellet behavior can be separated into two parts. The first part is the laser light absorption and implosion of the DT fuel, shown schematically in Fig. IV-A-2. This part ends at the time of ignition, when there is a hot central microcore surrounded by cool isentropically compressed DT and possibly a high Z tamper material. Once ignition occurs, the second part of the dynamics, thermonuclear burn propagation,[5-6] begins and is shown in Fig. IV-A-3 as the propagation of a temperature front out through the initially cold DT fuel. The first part of the dynamics can be simply characterized by the efficiency with which laser light energy is transferred into the DT fuel. This is called the hydrodynamic efficiency and is expressed as

$$\eta_H = E_c/E_L$$

where E_c is the internal energy of the compressed DT fuel material at the time of ignition. The second part of the dynamics is characterized by the energy gain of the DT fuel. This is given by

$$G_c = Y/E_c \ .$$

Then the total pellet gain is

$$G = \eta_H \, G_c \ .$$

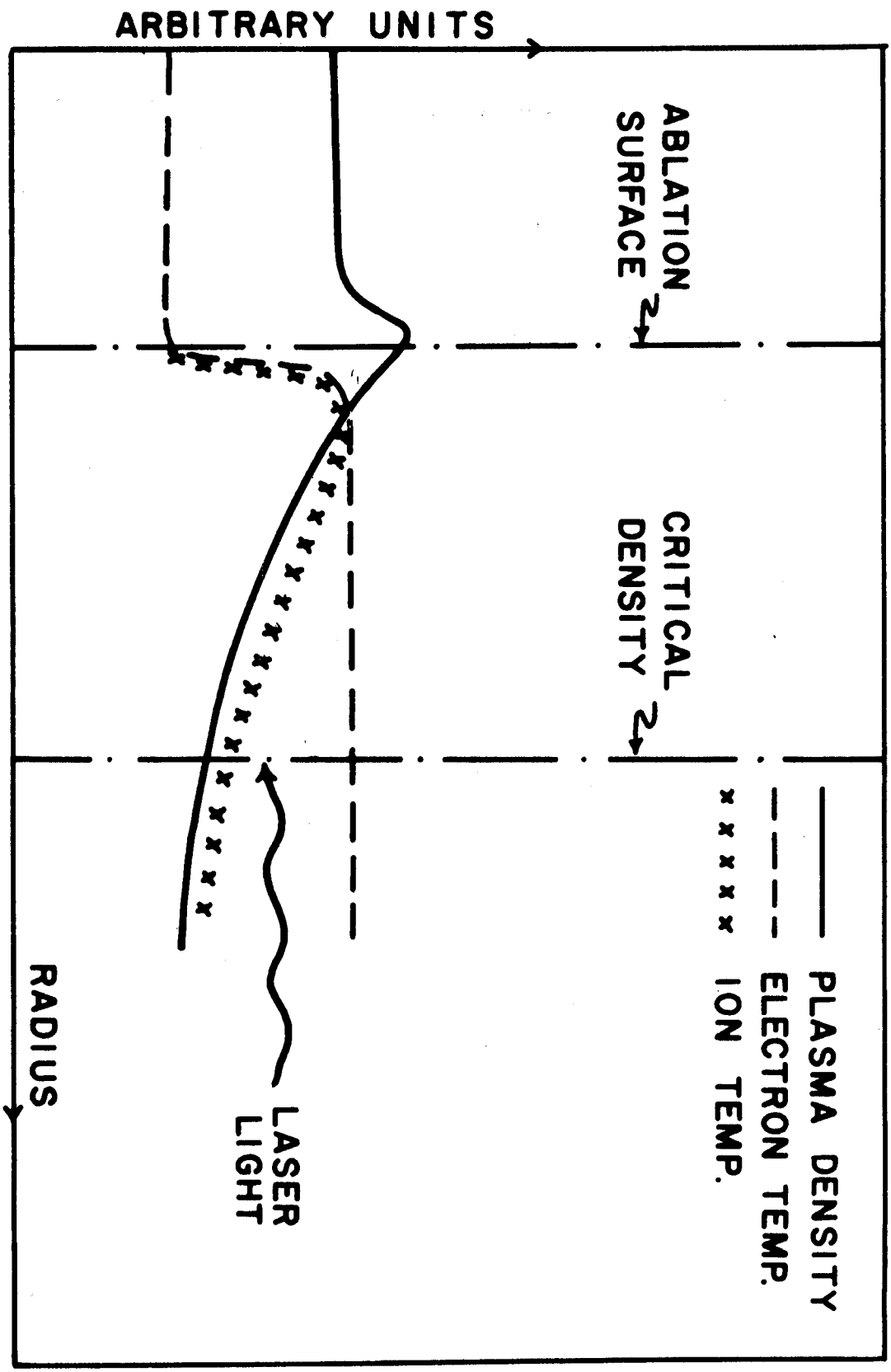

LASER-PELLET INTERACTION SCENARIO

Fig. IV-A-2.

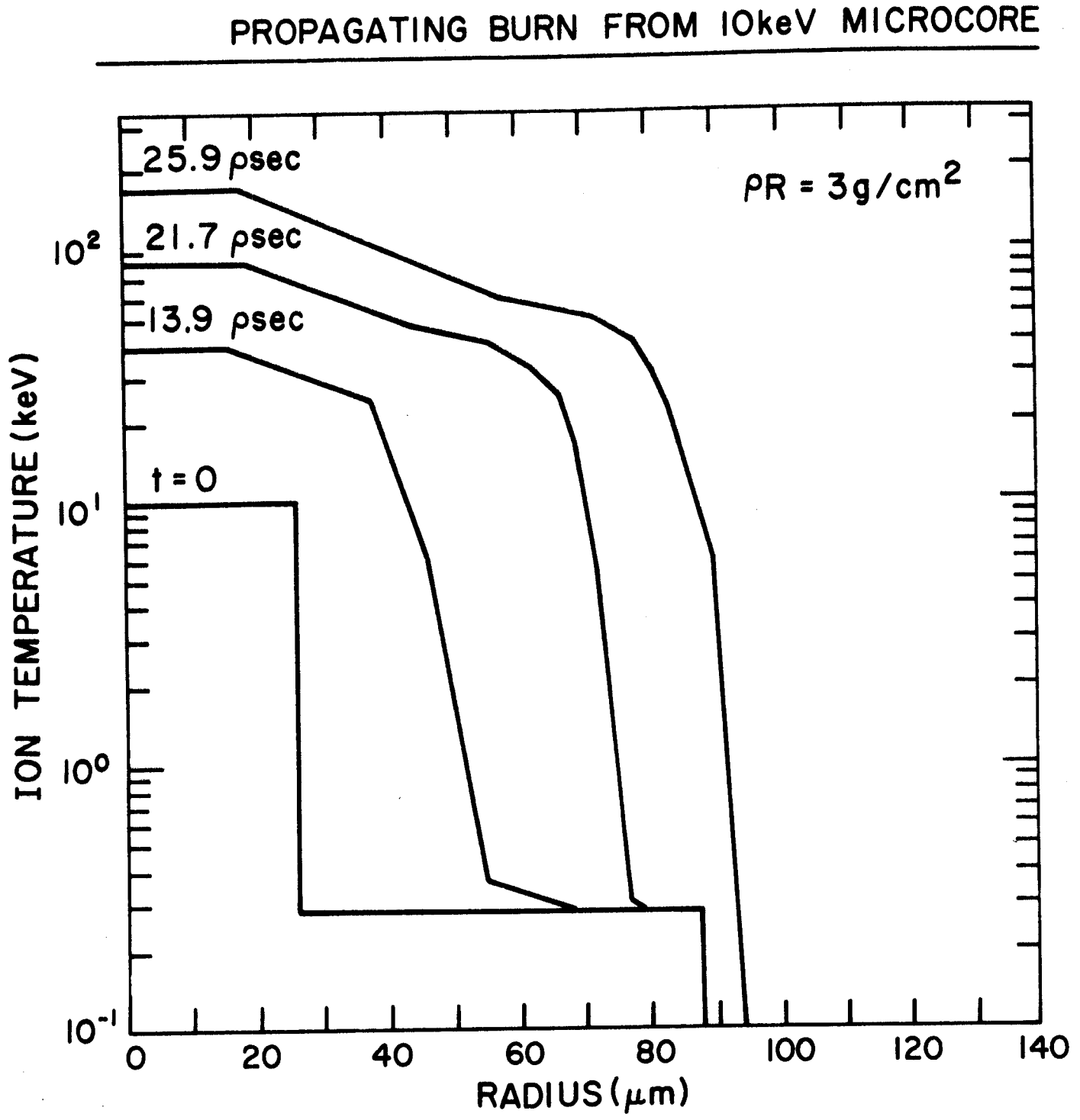
PROPAGATING BURN FROM 10keV MICROCORE
25.9 ρsec
21.7 ρsec
13.9 ρsec
t = 0
ρR = 3g/cm²
ION TEMPERATURE (keV)
10²
10¹
10⁰
10⁻¹
0
20
40
60
80
100
120
140
RADIUS (μm)

Fig. IV-A-3.

Pellet performance can now be estimated by studying the dependence of the two factors (η_H and G_c) on specific pellet designs. For SOLASE this is done in a parametric fashion using the PHD-IV computer code and simplified analytic scaling laws. A generic analysis is usually attempted because specific pellet designs are beyond the scope of this study. However, these generic analyses do indicate the necessary magnitudes of G_c and η_H for reactor pellet performance and comparison of these performance characteristics with current laser fusion experiments is a valuable measure of ultimate feasibility.

In Section IV-B the thermonuclear burn process is discussed along with the results of the PHD-IV parameter studies. In Section IV-C the implosion process is discussed and estimates of the hydrodynamic efficiency are obtained. Section IV-D discusses pellet material considerations, Section IV-E gives the details of the model pellet used for the SOLASE analysis and Section IV-F discusses the conclusions of this pellet design work.

References for Section IV-A

1. J. Nuckolls, L. Wood, A. Thiessen, and G. Zimmerman, Nature 239, 139 (1972).

2. J. Clarke, H. Fisher, and R. Mason, Phys. Rev. Lett. 30, 89 (1973).

3. K. Brueckner and S. Jorna, Rev. Mod. Phys. 46, 325 (1974).

4. R. Conn, et al., "Studies of the Technological Problems of Laser Fusion Reactors," UWFDM-190, 1976.

5. G. Fraley, E. Linnebur, R. Mason, and R. Morse, Phys. Fl. 17, 474 (1974).

6. H. Fisher, E. Linnebur, R. Mason, and R. Morse, Bull. Am. Phys. Soc. 18, 683 (1973).

IV-B. Thermonuclear Burn

The pellet yield and gain on core are dependent upon the thermonuclear burning of the DT fuel. The DT reaction is

$$ {}_1D^2 + {}_1T^3 \rightarrow {}_2He^4\ (3.5\ MeV) + {}_0n^1\ (14.1\ MeV) $$

and is greatest for temperatures between 10-100 keV, Fig. IV-B-1. Typical ignition temperatures for laser fusion pellets are about 10 keV. Using this energy of 10 keV/particle for a deuteron, triton, and their two electrons the energy gain of a single DT reaction is

$$ 17.6\ MeV/(4 \times 10\ keV) = 440\ . $$

If 100% of the DT fuel were to burn then the gain on core would only be 440 and this is not great enough to provide an overall pellet gain of 150. (Fractional burnup is typically 30-50% and implosion efficiencies are 5-10%). Other mechanisms must, therefore, be utilized to increase the gain on core. One such mechanism is self-heating and thermonuclear burn propagation.[1] Self-heating is accomplished by redeposition of the energy from the 3.5 MeV alpha particle reaction product. In inertial confinement systems this alpha particle must be slowed down by the plasma via Coulomb interaction. Test particle calculations[2] reveal that the range of a 3.5 MeV alpha in a 10 keV DT plasma is about 0.4 g/cm^2. The DT plasma pellet core must therefore have at least this much "size" in order to stop the alphas and self-heat. However, if burn

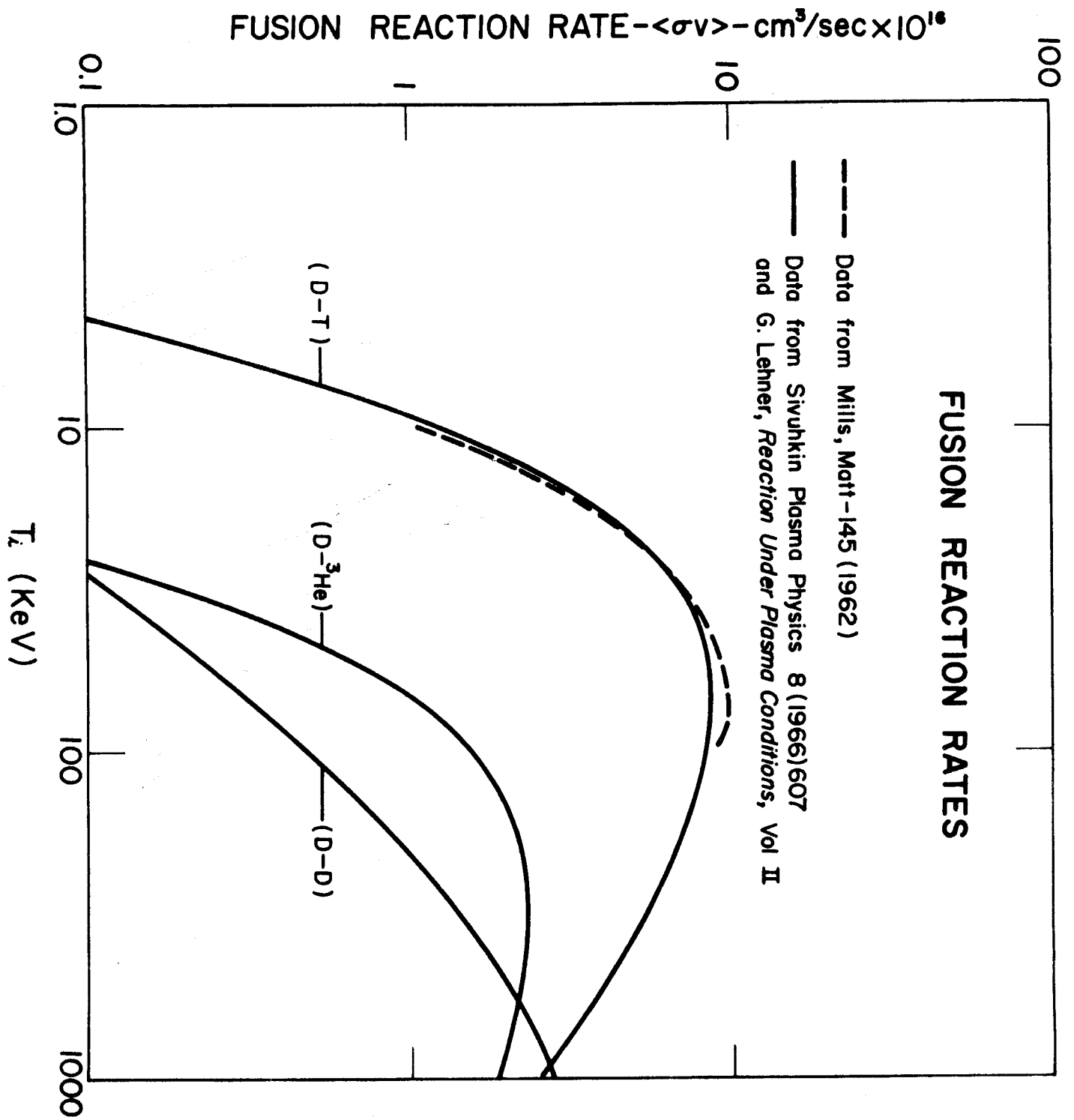
FUSION REACTION RATE-<σv>-cm³/sec×10¹⁶
0.1
1
10
100
FUSION REACTION RATES
Data from Mills, Matt-145 (1962)
Data from Sivukhin Plasma Physics 8 (1966)607
and G. Lehner, Reaction Under Plasma Conditions, Vol II
(D-T)
(D-³He)
(D-D)
Tᵢ (KeV)
1
10
100
1000

Fig. IV-B-1.

propagation is utilized then only a hot central microcore need have this size, Fig. IV-B-2. This part of the plasma will then self-heat to higher temperatures and the alpha particles escaping from it will be stopped in the surrounding plasma. This plasma will be initially cold but will heat up to burn temperatures due to the alpha particle energy redeposition. The layer of plasma next to the hot central microcore will then begin to burn and will heat the next layer of plasma. Each layer will have a thickness roughly equal to the range of the 3.5 MeV alpha particle. This process results in a temperature wave propagating out through the DT fuel as shown in Fig. IV-A-3. This process was studied extensively in Ref. (1) for pellet core masses of 0.1 μg to 10 μg. However, such small masses are not suitable for reactor applications due to the small energy yield per pellet. This analysis was therefore redone for larger pellet masses and the results are reported in Section IV-B-1.

The pellet core size, in relation to the alpha particle range, can best be expressed in terms of the spherical plasmas' density-radius product, ρR. In order for the DT fuel to self-heat its ρR value must be at least 0.4 g/cm^2. The ρR value of the total core must be greater than this if burn propagation is desired. Optimum values of ρR for the total core, and hot microcore are computed using the PHD-IV hydrodynamics code. The computer simulation results are then used to "normalize" the following simple theory of thermonuclear burn performance.

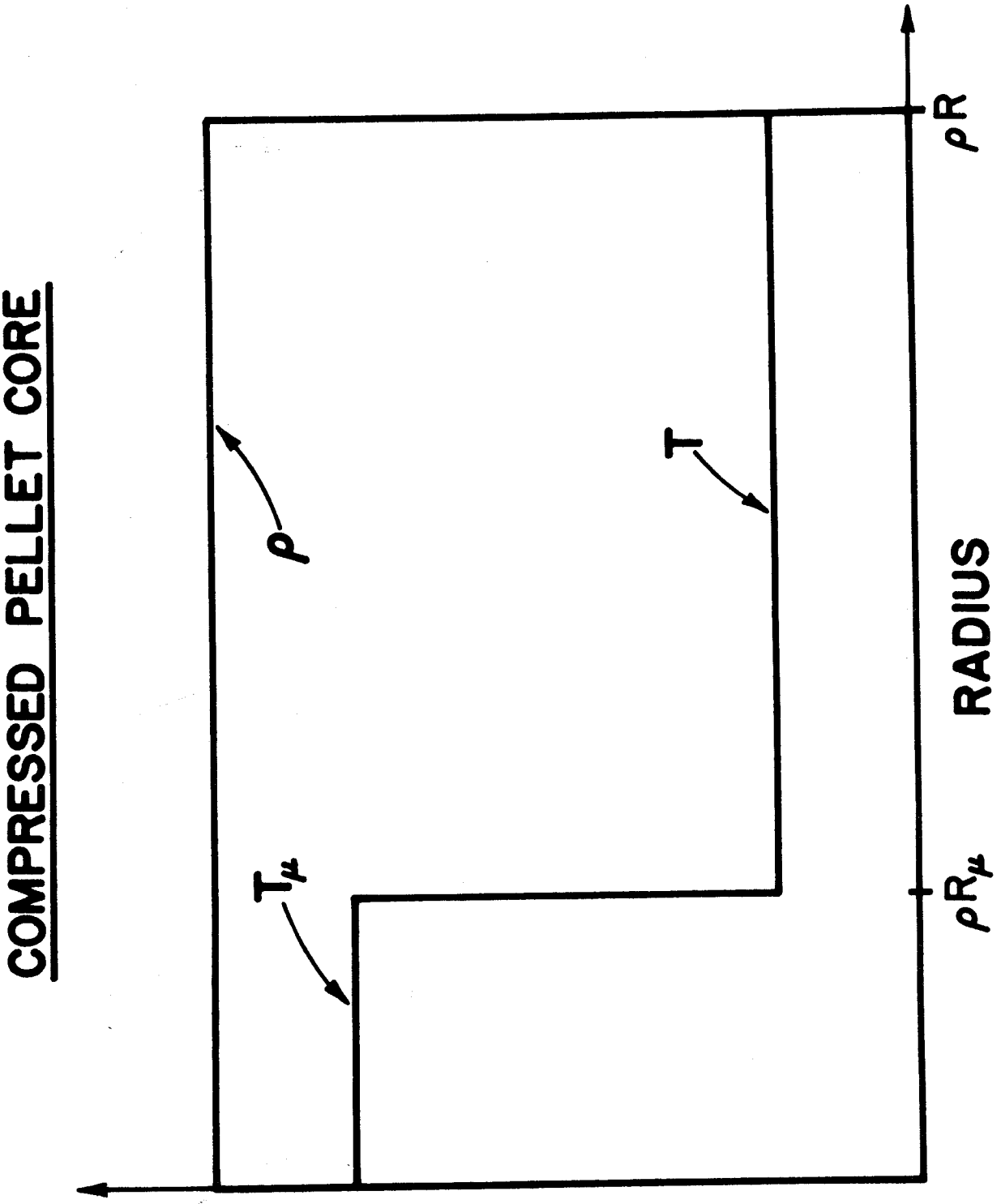

Fig. IV-B-2,

One can assume that the thermonuclear yield from the DT fuel is linearly proportional to the mass and the fractional burn up

$$Y = Y_o \, m \, f_B(\rho R) \tag{1}$$

where the fractional burn up is assumed to only be a function of ρR. The energy invested in the core of fuel is equal to the sum of energy in the microcore and the energy in the isentropically compressed surrounding fuel. The isentropically compressed fuel has an energy

$$E_{fuel} = 3\rho \, kT \, \frac{V}{m_{DT}} \quad . \tag{2}$$

If the fuel is compressed along an isentrope from an initial temperature T_o, then

$$T = T_o \, (\rho/\rho_o)^{2/3} \tag{3}$$

hence

$$E_{fuel} = 3\rho \, (kT_o) \, (\rho/\rho_o)^{2/3} \, \frac{V}{m_{DT}} \quad . \tag{4}$$

This expression can be rearranged into the more convenient form

$$E_{fuel} = 3 \, (\tfrac{4\pi}{3})^{1/3} \, \left(\frac{kT_o}{m_{DT}\rho_o^{2/3}}\right) \, m^{2/3} \, \rho R \tag{5}$$

where m is the total fuel mass. Assuming the temperature of the micro-core is much greater than the final temperature of the isentrope along which compression takes place, the additional energy invested in the microcore is

$$E_{\mu c} = 3\rho K T_{\mu} \frac{V_{\mu}}{m_{DT}} = 3\, m_{\mu}\, kT_{\mu}/m_{DT} \ . \qquad (6)$$

Therefore, an expression for the total energy invested in the core is

$$E_c = \frac{3k_B}{m_{DT}} \{(\frac{4\pi}{3})^{1/3} \frac{1}{\rho_o^{2/3}} (\rho R)\, m^{2/3}\, T_o\, [1-(\frac{\rho R_{\mu}}{\rho R})^3] + mT_{\mu} (\frac{\rho R_{\mu}}{\rho R})^3 \}$$

The gain on core can now be expressed analytically using the formulas for Y and E_c. The only unknown in these expressions is the fractional burn up as a function of ρR, $f_B(\rho R)$. This function is obtained from the computer simulation studies. If the energy invested in the hot micro-core is much less than the total energy invested in the core (which is true for reactor size pellets), then the gain on core can be expressed as

$$G_c = Y_o\, m f_B(\rho R) \left\{ 3\, (\frac{4\pi}{3})^{1/3} (\frac{kT_o}{m_{DT}\rho_o^{2/3}})\, m^{2/3}\, \rho R \right\}^{-1} \qquad (8)$$

or

$$G_c = G_o\, m^{1/3}\, g(\rho R) \qquad (9)$$

where $G_o = Y_o\left\{3\left(\frac{4\pi}{3}\right)^{1/3}\left(\frac{kT_o}{m_{DT}\rho_o^{2/3}}\right)\right\}^{-1}$ and $g(\rho R) = f_B(\rho R)/\rho R$.

From this simple expression we see that the gain on core is a function of both the fuel mass and the ρR value to which it is compressed. A similar theory has been developed by Kidder.[3]

IV-B-1. Bare Pellet Core Burn Calculations

To study the thermonuclear burn process the pellet core is modelled as shown in Fig. IV-B-2. The density is assumed to be uniform but the temperature profile consists of a hot microcore characterized by ρR_μ and T_μ and a cold surrounding plasma at temperature T. The total pellet core is characterized by its ρR value. The temperature of the cold compressed fuel is computed from the formula

$$T = T_o(\rho/\rho_o)^{2/3} \qquad (10)$$

which is the temperature along an isentrope corresponding to a fuel compression of ρ/ρ_o. The initial temperature and density (T_o and ρ_o) are taken as 1 eV and 0.213 g/cm^3. These calculations assume that the ablated part of the pellet that surrounds the core does not play any role in the burn dynamics. The PHD-IV hydrodynamics-thermonuclear burn computer code[4] is used to study the behavior of this model pellet core for the following ranges of parameters:

$$0.1\ \text{mg} \leq \text{mass} \leq 1.\ \text{mg}$$

$$1\ \text{g/cm}^2 \leq \rho R \leq 7\ \text{g/cm}^2 \qquad (11)$$

$$0.1\ \text{g/cm}^2 \leq \rho R_\mu \leq 0.7\ \text{g/cm}^2$$

$$T_\mu = 10\ \text{keV}\ .$$

The results of this study are given in Table IV-B-1 and the dependence of yield on ρR is shown in Fig. IV-B-3. It is seen that for this range of masses the separation of yield dependence on core mass and ρR is justified. The yield is a linear function of mass and a strong function of ρR for values less than 3 g/cm^2. For ρR values greater than 3 g/cm^2 the yield does not improve very much. This dependence on ρR can be explained by looking at the details of the burn and hydrodynamic disassembly process. At ρR = 3 g/cm^2 the pellet disassembly and fuel depletion due to burn have about an equal effect on quenching the burn. For ρR < 3 g/cm^2 the pellet core disassembly is the dominant mechanism affecting the fractional burn up while for ρR > 3 g/cm^2 the pellet inertial confinement time is great enough to allow fuel depletion to quench the burn. The dependence of yield on the ρR value of the 10 keV microcore is shown in Fig. IV-B-4. This dependence is of a threshold nature with almost constant yield for ρR_μ > 0.38 g/cm^2. The fractional burn up for these calculations is plotted in Fig. IV-B-5. Analytic expressions can be fit to the simulation results for use in the

Table IV-B-1

Summary of Burn Parameter Study

MASS	ρR	(ρR_{μ}) = .3	(ρR_{μ}) = .4	(ρR_{μ}) = .5	(ρR_{μ}) = .7
.1	1	3.41-2* 7.99	.32 37.4	1.54 99 0	2.8 68.8
.1	2			7.4 1804	
.1	3	2.27-3 .626	7.7 2034	10.22 2525	10.2 2048
.1	5	1.18-3 .2	12.8 2155	13 2168	13 2103
.1	7	3.55-2 4.3	14.5 1756	14.6 1764	14.6 1749
.316	1	.109 8.93	.971 38.1	5.03 106	
.316	2	.019 3.2	.763 99	23.2 2220	
.316	3	.009 1.21	27.2 3369	32.0 3602	
.316	5	.012 .278	40.55 3313	40.83 3289	
.316	7	2.5-3 .147	45.8 2702	46.4 2649	
1.	1	.344 9.5	3.3 41.3	16.5 110	30 74.8
1.	2			76.3 2649	
1.	3	2.2-2 1.3	83.6 4292	104 4786	101 3415
1.	5	8.4-3 .306	129 4641	130 4597	131 4303
1.	7	5.6-3 .147	146 3795	148 3836	148 3754

* First number is yield in mega joules
Second number is the gain on core assuming perfect adiabatic compression from 1 ev.
Micro core temperature - 10 Kev

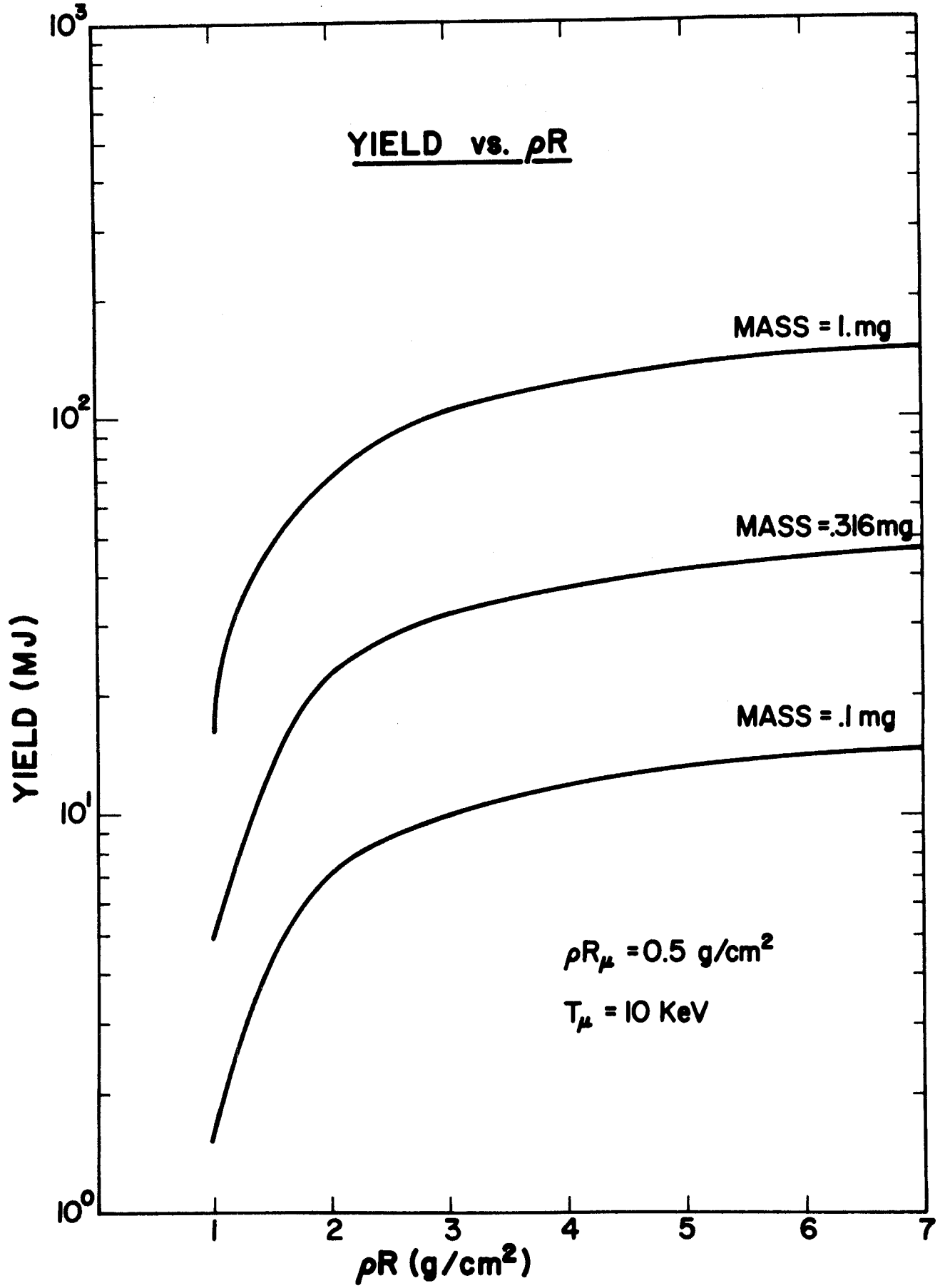
YIELD vs. ρR
MASS = 1. mg
MASS = .316mg
MASS = .1 mg
ρR$_\mu$ = 0.5 g/cm^2
T$_\mu$ = 10 KeV
YIELD (MJ)
ρR (g/cm^2)
10^3
10^2
10^1
10^0
1
2
3
4
5
6
7

Fig. IV-B-3.

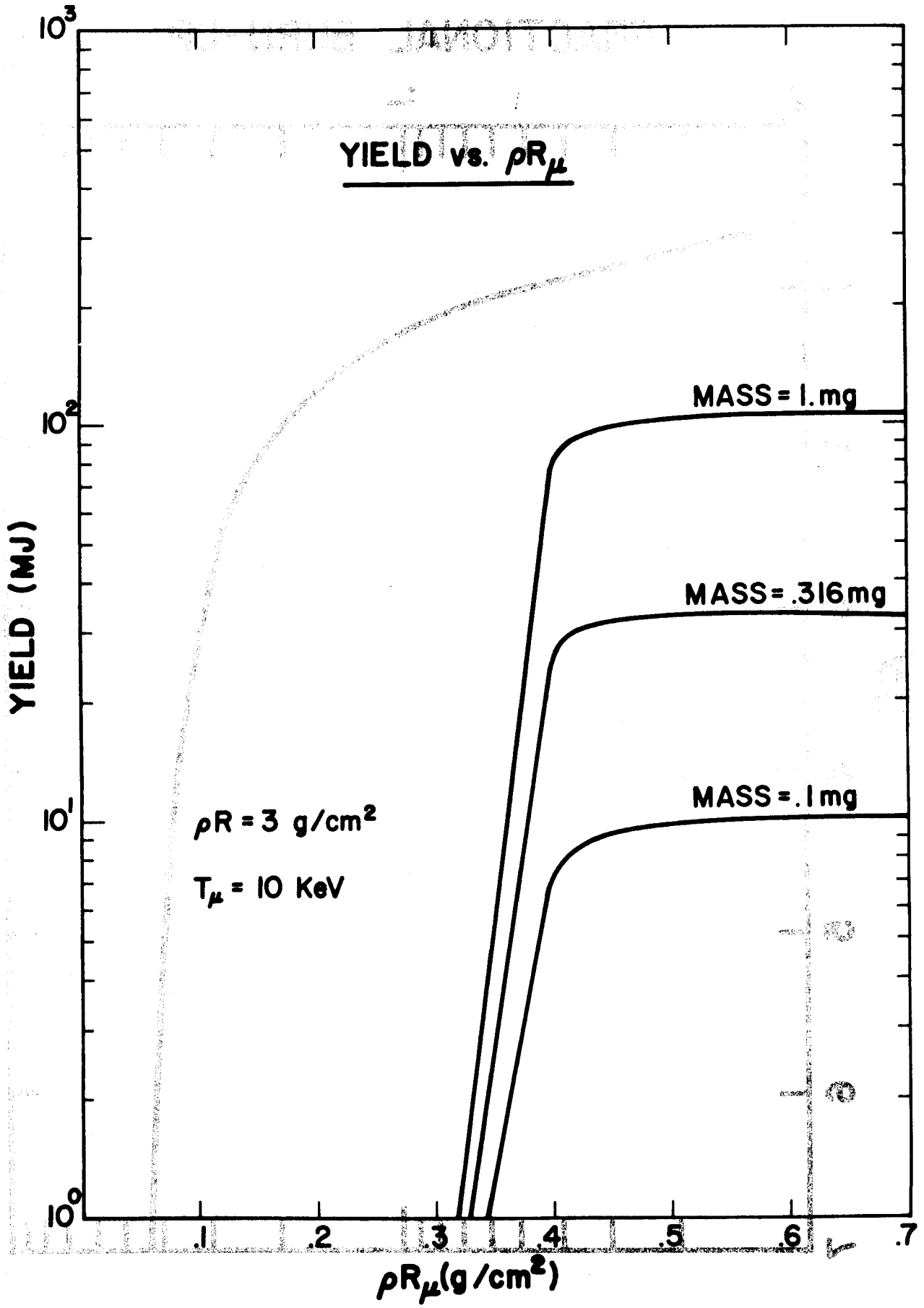
YIELD vs. ρR_μ
YIELD (MJ)
10^3
10^2
10^1
10^0
MASS = 1. mg
MASS = .316 mg
MASS = .1 mg
$\rho R = 3$ g/cm^2
$T_\mu = 10$ KeV
.1
.2
.3
.4
.5
.6
.7
ρR_μ(g/cm^2)

Fig. IV-B-4.

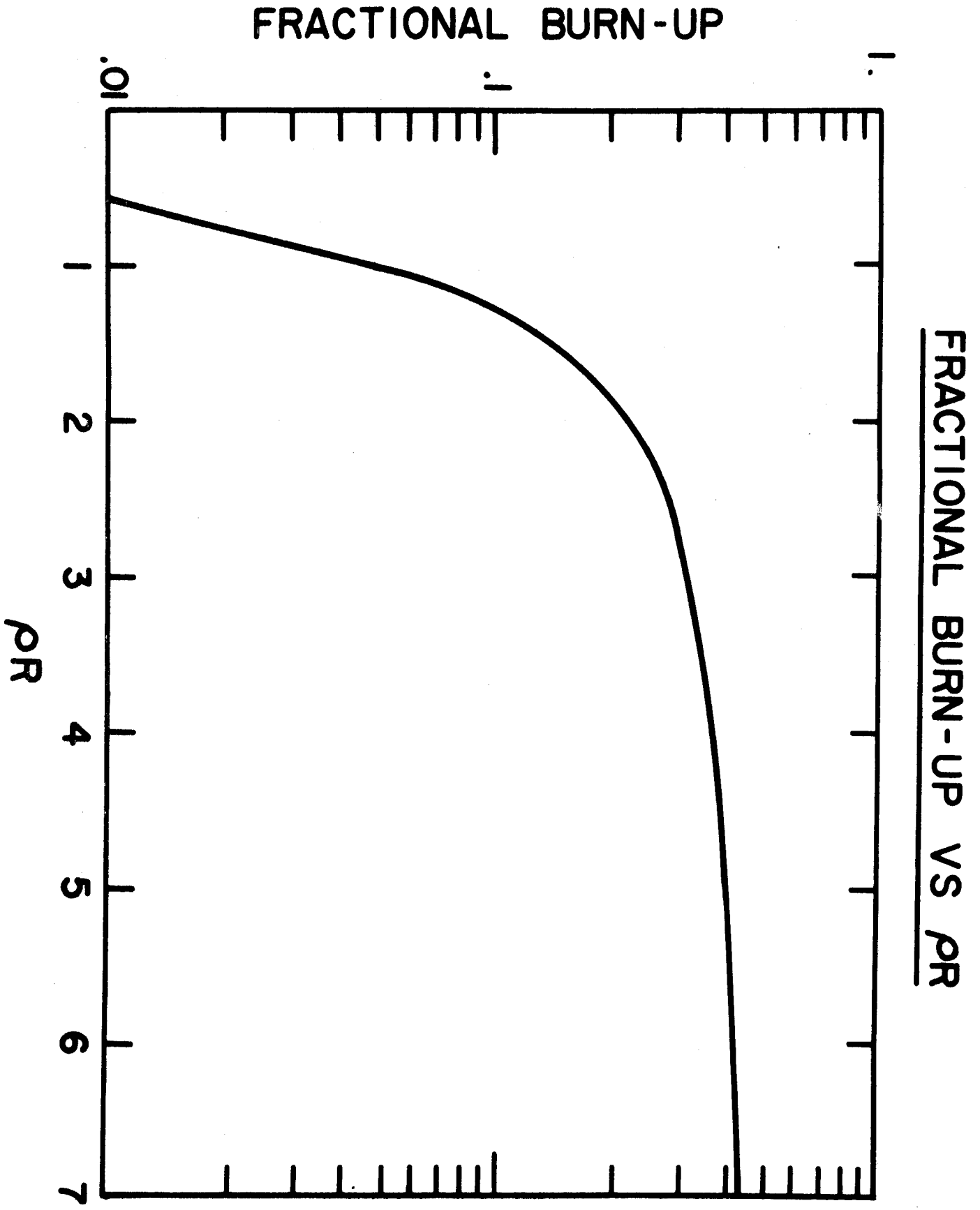

Fig. IV-B-5.

simple theory of pellet gain on core described in Section IV-B. The yield and fractional burn up are given by

$$Y = 10^3 m H\,(\rho R_\mu - 0.38) \begin{cases} [16 + 60\,(\rho R-1)^{.585}\,] & 1 < \rho R < 3 \\ [71 + 11\,\rho R\,] & 3 < \rho R < 7 \end{cases} \quad (12)$$

and

$$f_B = m H(\rho R_\mu - 0.38) \quad \begin{cases} [0.047 + 0.178\,(\rho R-1)^{.585}\,] & 1 < \rho R < 3 \\ [0.211 + 0.033\,\rho R\,] & 3 < \rho R < 7 \end{cases} \quad (13)$$

where Y is the yield in MJ, m is the core mass in grams, ρR and ρR_μ are in g/cm^2, and H is a step function. Using these analytic formulas, iso-yield contours can be plotted for mass and ρR. These contours are shown in Fig. IV-B-6 for 100, 150 and 500 MJ yields. The gain on core for each of these mass-ρR pairs is plotted in Fig. IV-B-7. The gain on core is maximized for $\rho R = 3\ g/cm^2$. For 100 MJ the optimum mass is 1 mg and for 150 MJ the optimum mass is 1.5 mg. The maximum gain on core for 150 MJ yield is 5495. This, however, assumes a perfect isentropic compression from an initial temperature of 1 eV. Such a perfect compression is quite unlikely unless the laser pulse can be very accurately shaped in time.

This large value of G_c is, of course, the result of thermonuclear burn propagation. A chronology of the burn dynamics for the $\rho R = 3\ g/cm^2$, mass = 1 mg, $(\rho R)_\mu = 0.5\ g/cm^2$, T_μ = 10 Kev pellet core is shown

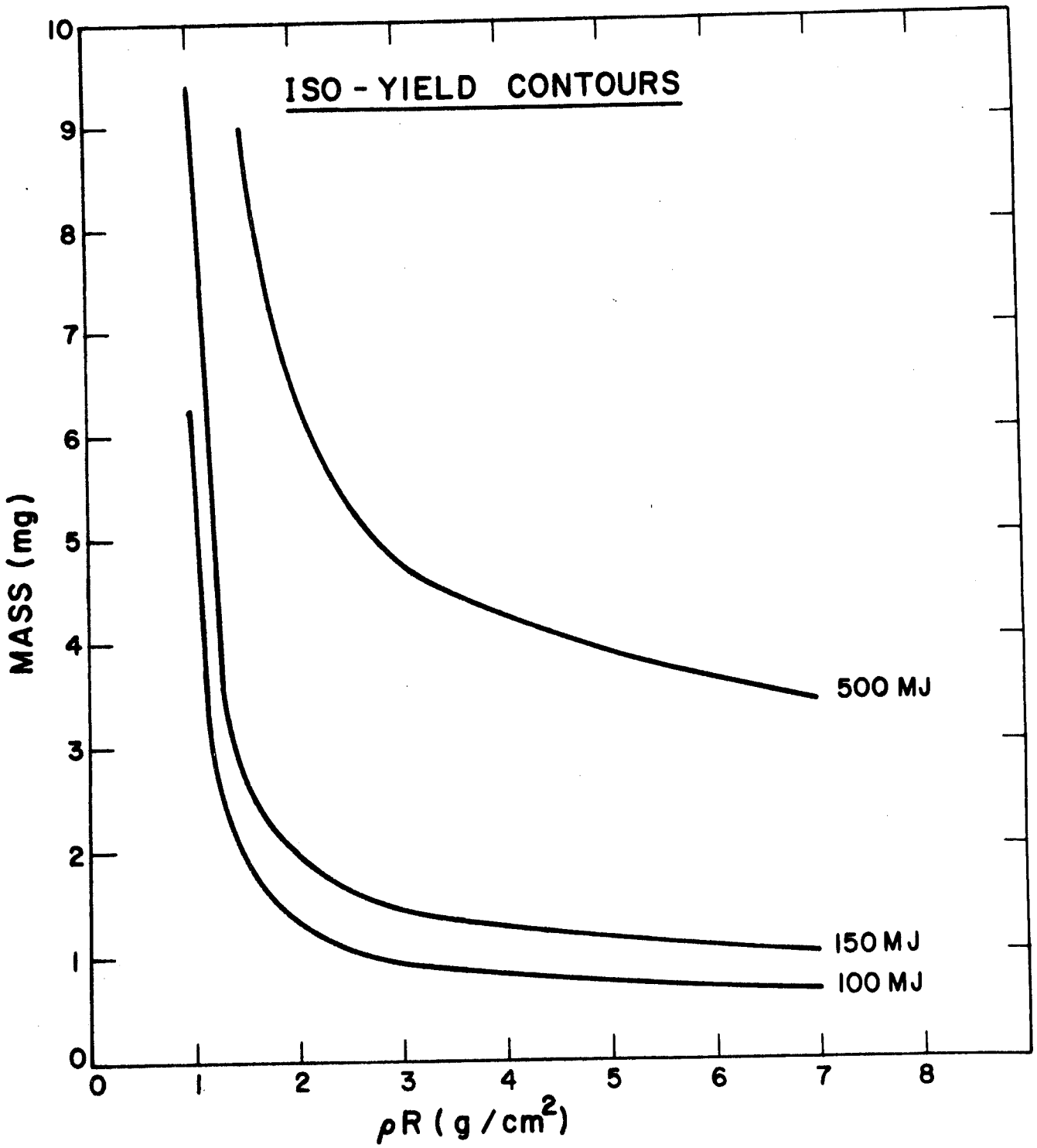
ISO - YIELD CONTOURS
MASS (mg)
ρR (g / cm²)
500 MJ
150 MJ
100 MJ
0
1
2
3
4
5
6
7
8
9
10

Fig. IV-B-6.

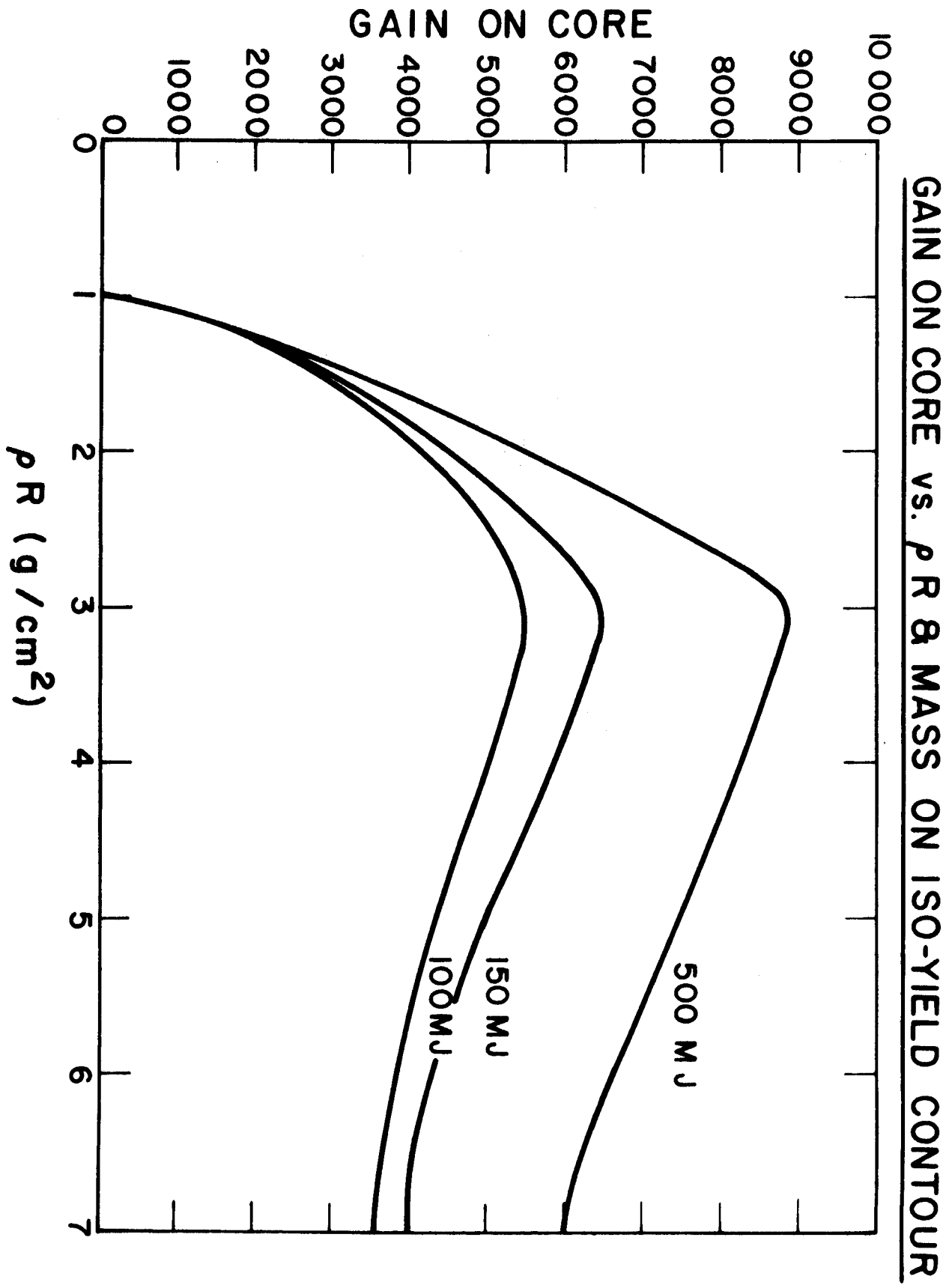
GAIN ON CORE
0
1000
2000
3000
4000
5000
6000
7000
8000
9000
10 000
ρR (g/cm²)
0
1
2
3
4
5
6
7
100 MJ
150 MJ
500 MJ
GAIN ON CORE vs. ρR & MASS ON ISO-YIELD CONTOUR

Fig. IV-B-7.

as temperature and density "snap shots" in Fig. IV-B-8 to 12. The same core uniformly heated to 10 KeV is shown in Fig. IV-B-13 to 17. The total and differential yield as a function of time for the two pellets are shown in Fig. IV-B-18 and 19. These figures show that the uniform temperature core burns to its depletion limit about 25 picoseconds sooner than the hot microcore pellet, but they both produce essentially the same total yield. The energy invested in the uniform temperature core is, however, 55 times the energy invested in the pellet with a hot microcore, hence the gain on core for the uniformly heated pellet is only 87. In the microcore case there were 3.6×10^{19} 14 Mev neutrons produced and 1.28×10^{17} 2.45 Mev neutrons. This comparison clearly demonstrates the necessity of burn propagation.

Energy from the pellet comes in three forms: neutrons, charged particles, and X-rays. For the bare DT pellet cores discussed thus far, 80% of the yield is assumed to be in the form of 14.1 MeV neutrons and 19% and 1% are computed as escaping charged particle and X-ray energy. The charged particle energy is in two forms: nonthermal DT and DD reaction products that escape the pellet core before thermalizing and the blow off plasma that results from the hydrodynamic disassembly of the pellet core. For the 3 g/cm^2, 1 mg pellet core, 33% of the reaction product charged particles escape and they carry 19% of the total charged particle energy. The time integrated spectra of the ${}_2He^4$, ${}_2He^3$, T^3, and ${}_1p^1$ reaction products are plotted in Figs. IV-B-20 and 21. The average alpha

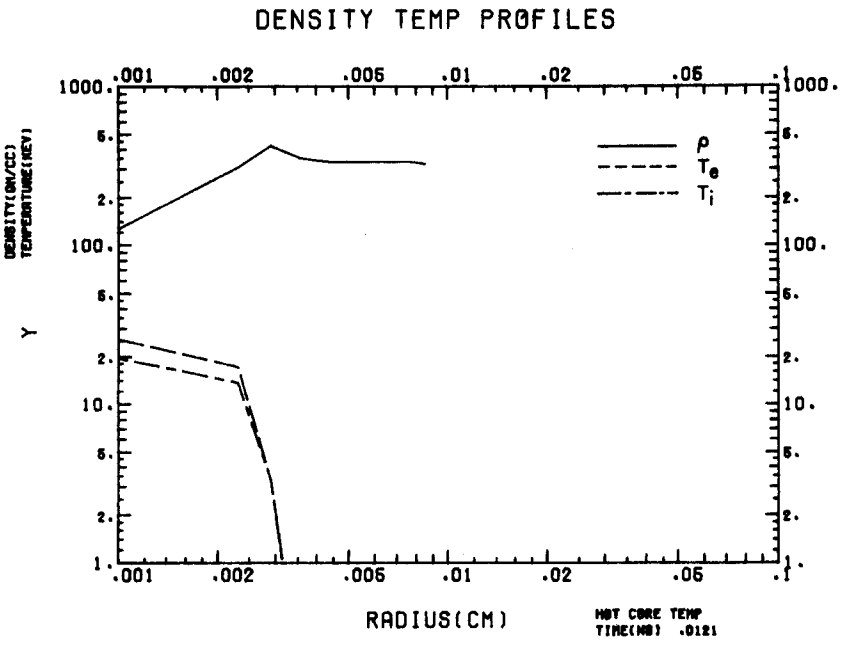

Fig. IV-B-8.

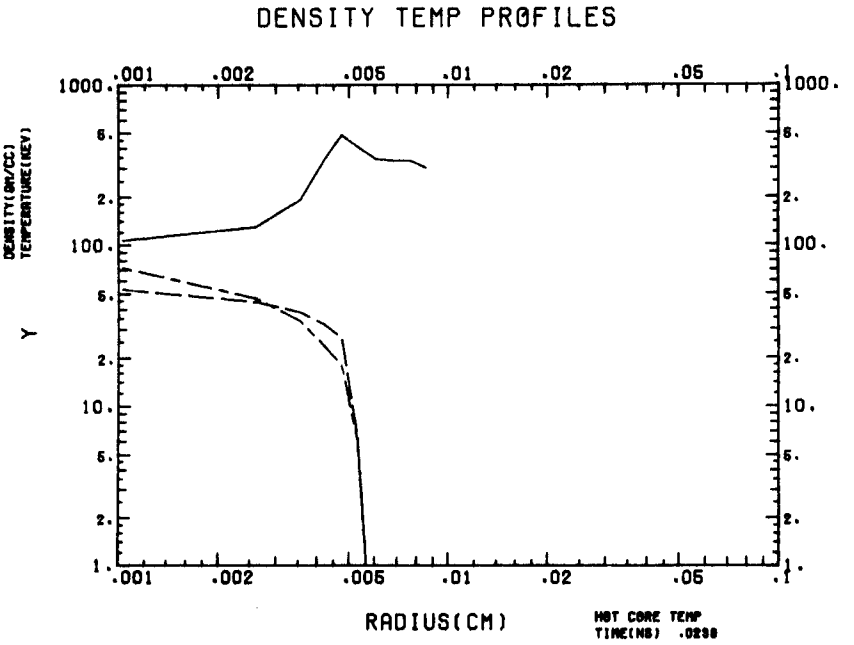

Fig. IV-B-9.

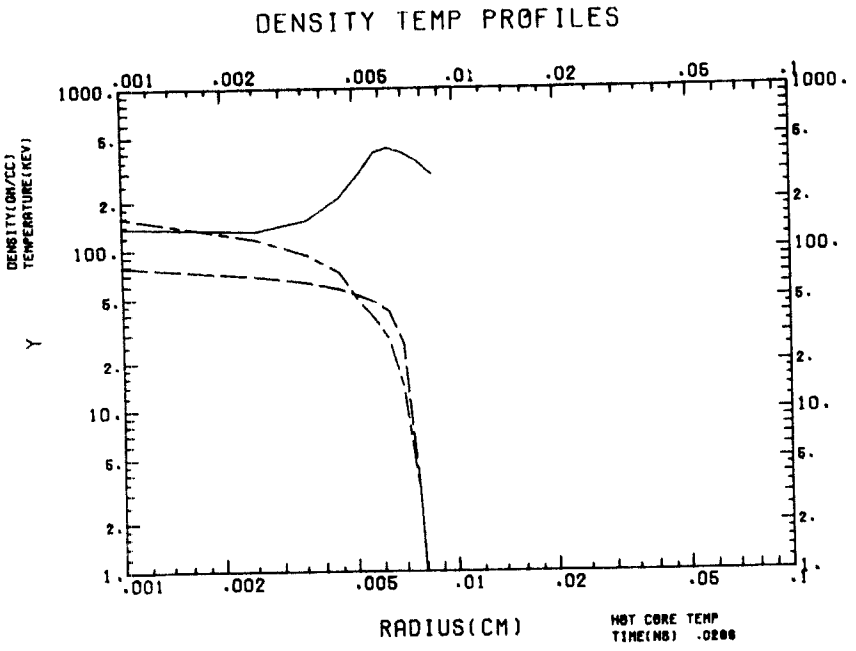

Fig. IV-B-10.

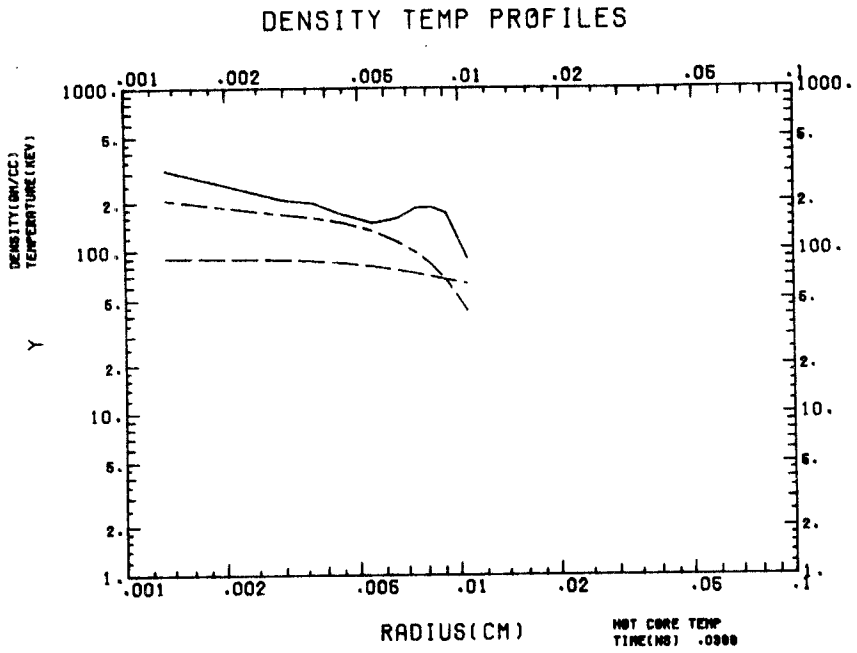

Fig. IV-B-11.

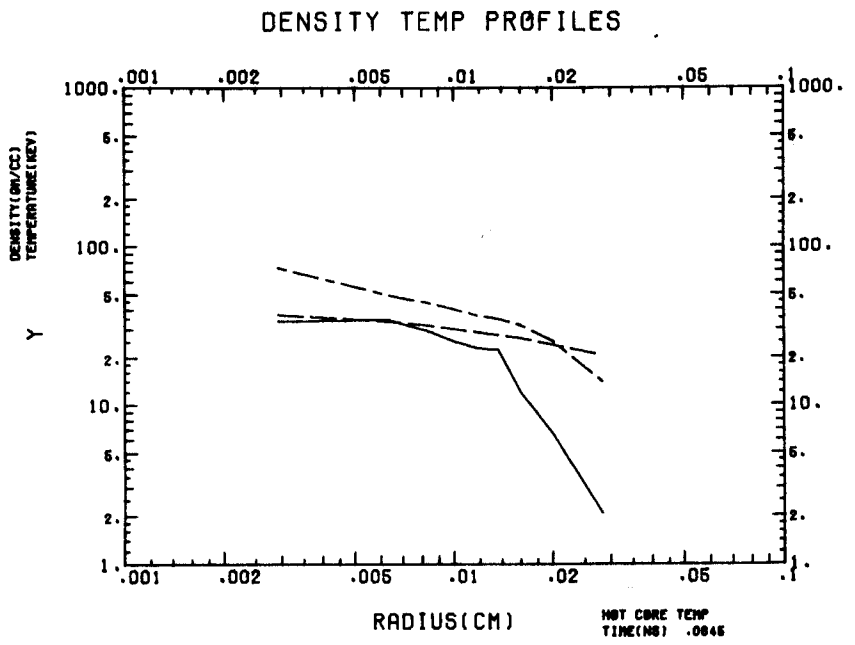

Fig. IV-B-12.

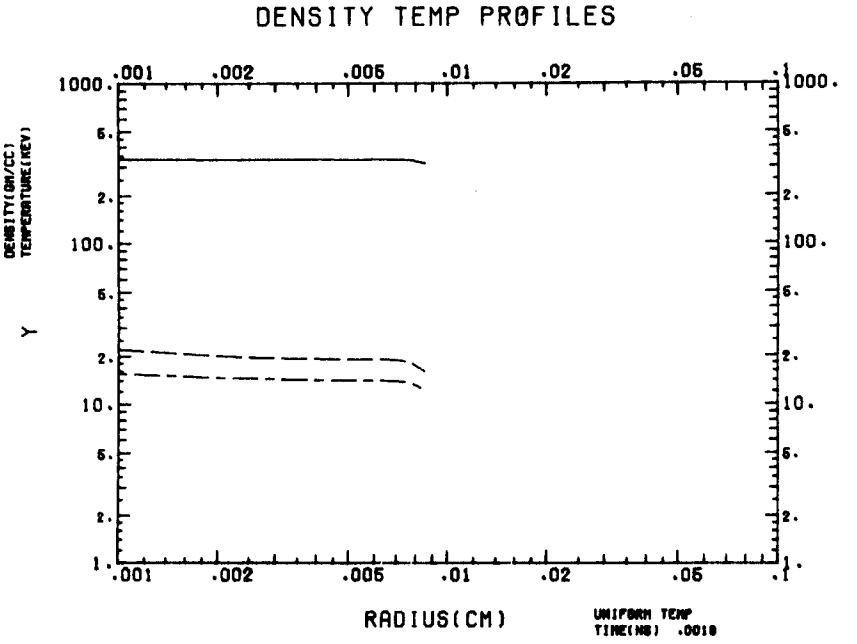

Fig. IV-B-13.

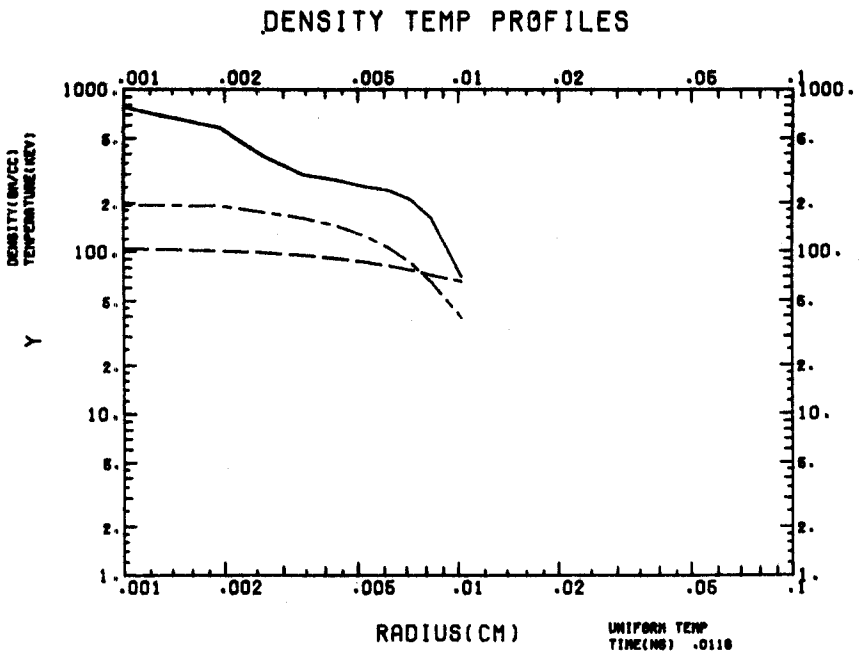

Fig. IV-B-14.

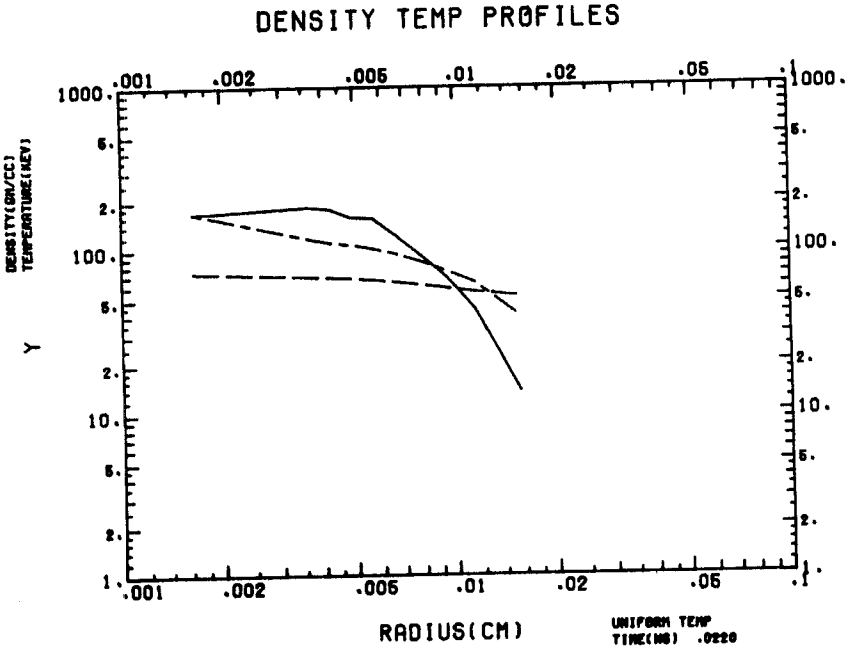

Fig. IV-B-15.

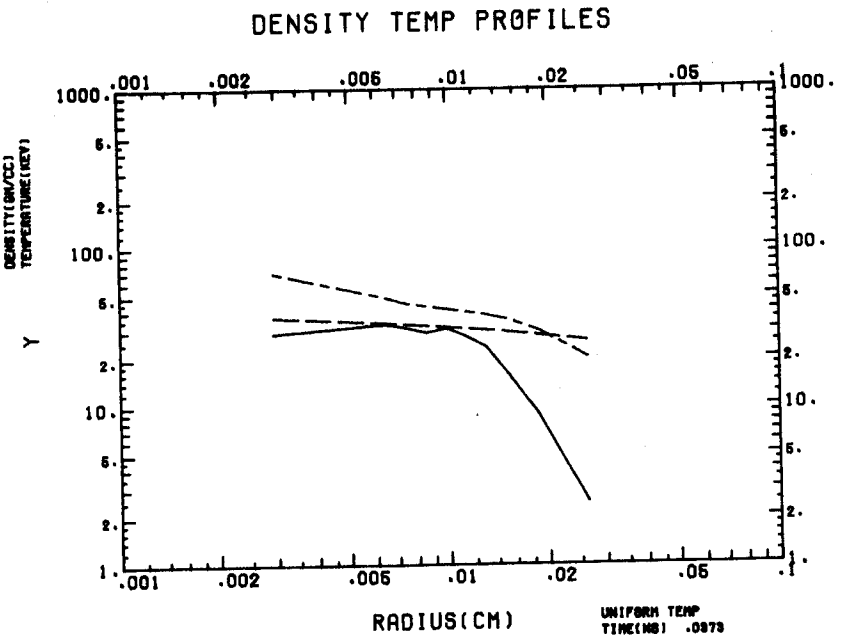

Fig. IV-B-16.

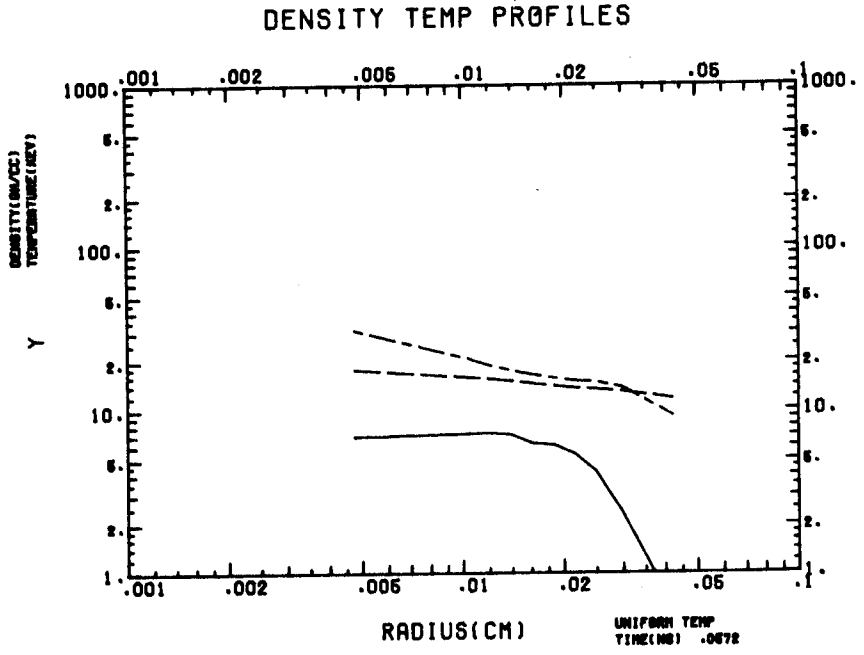

Fig. IV-B-17.

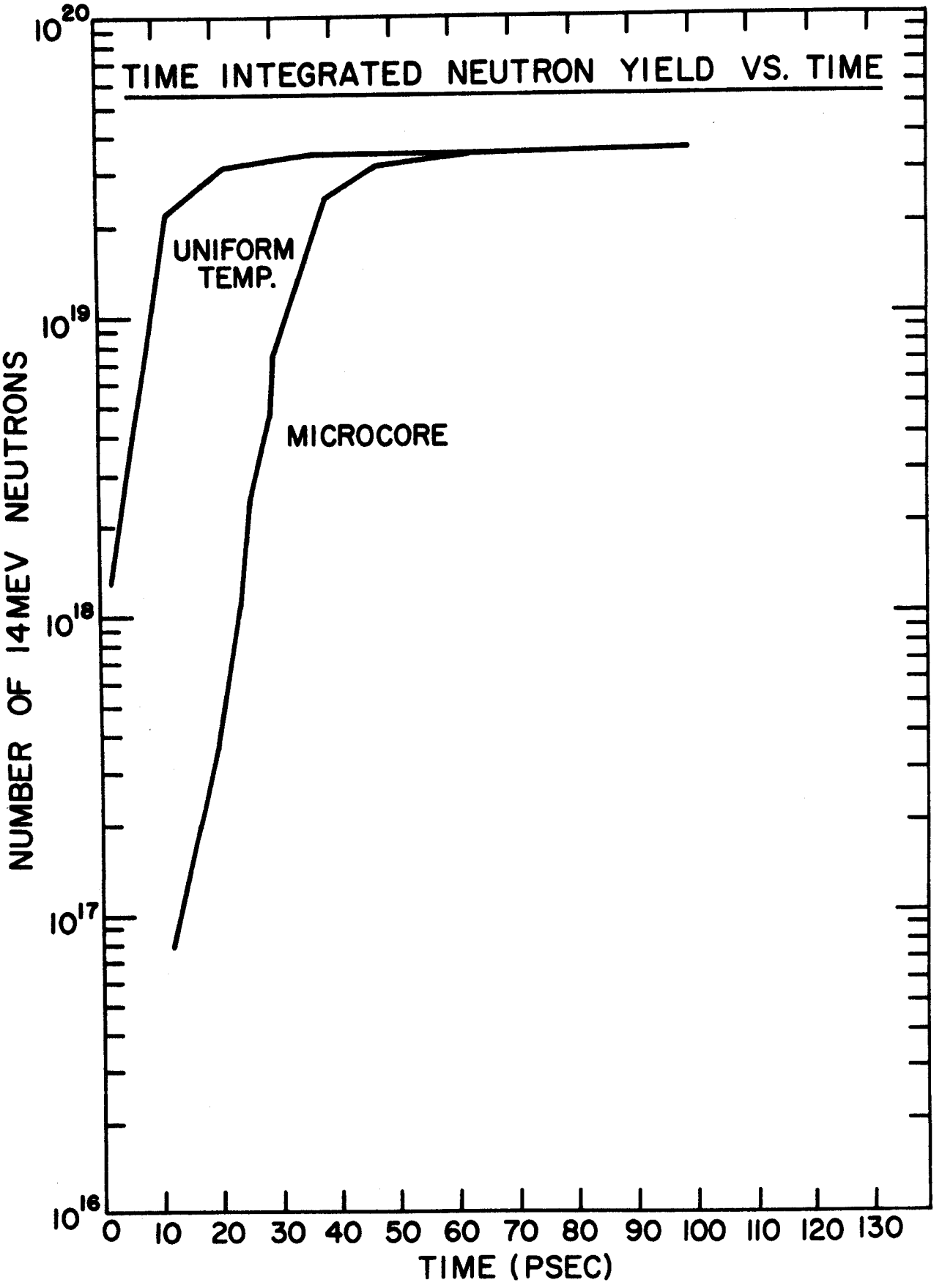
TIME INTEGRATED NEUTRON YIELD VS. TIME
UNIFORM TEMP.
MICROCORE
NUMBER OF 14MEV NEUTRONS
10^{20}
10^{19}
10^{18}
10^{17}
10^{16}
0 10 20 30 40 50 60 70 80 90 100 110 120 130
TIME (PSEC)

Fig. IV-B-18.

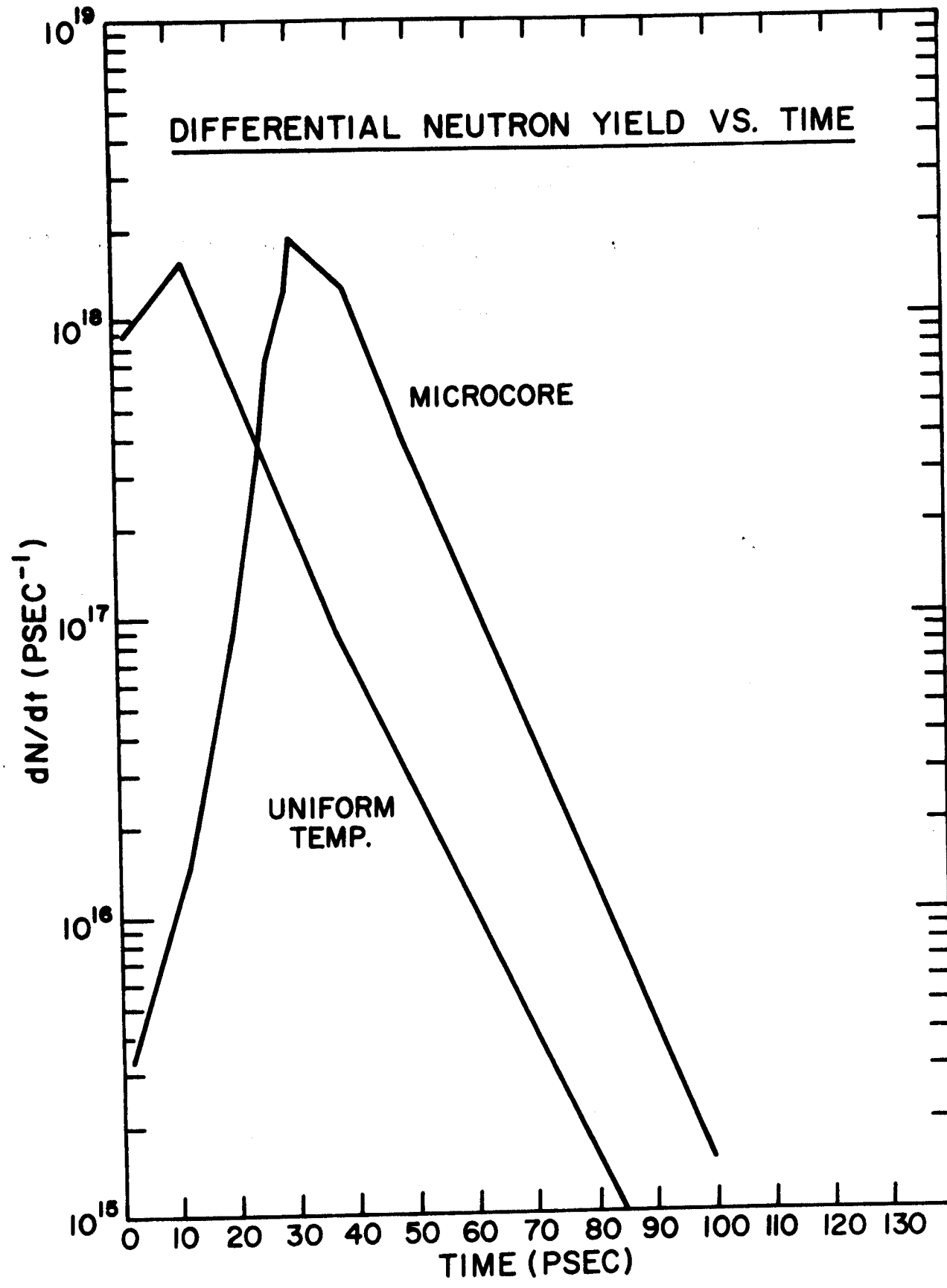
DIFFERENTIAL NEUTRON YIELD VS. TIME
MICROCORE
UNIFORM TEMP.
dN/dt (PSEC⁻¹)
10¹⁹
10¹⁸
10¹⁷
10¹⁶
10¹⁵
0 10 20 30 40 50 60 70 80 90 100 110 120 130
TIME (PSEC)

Fig. IV-B-19.

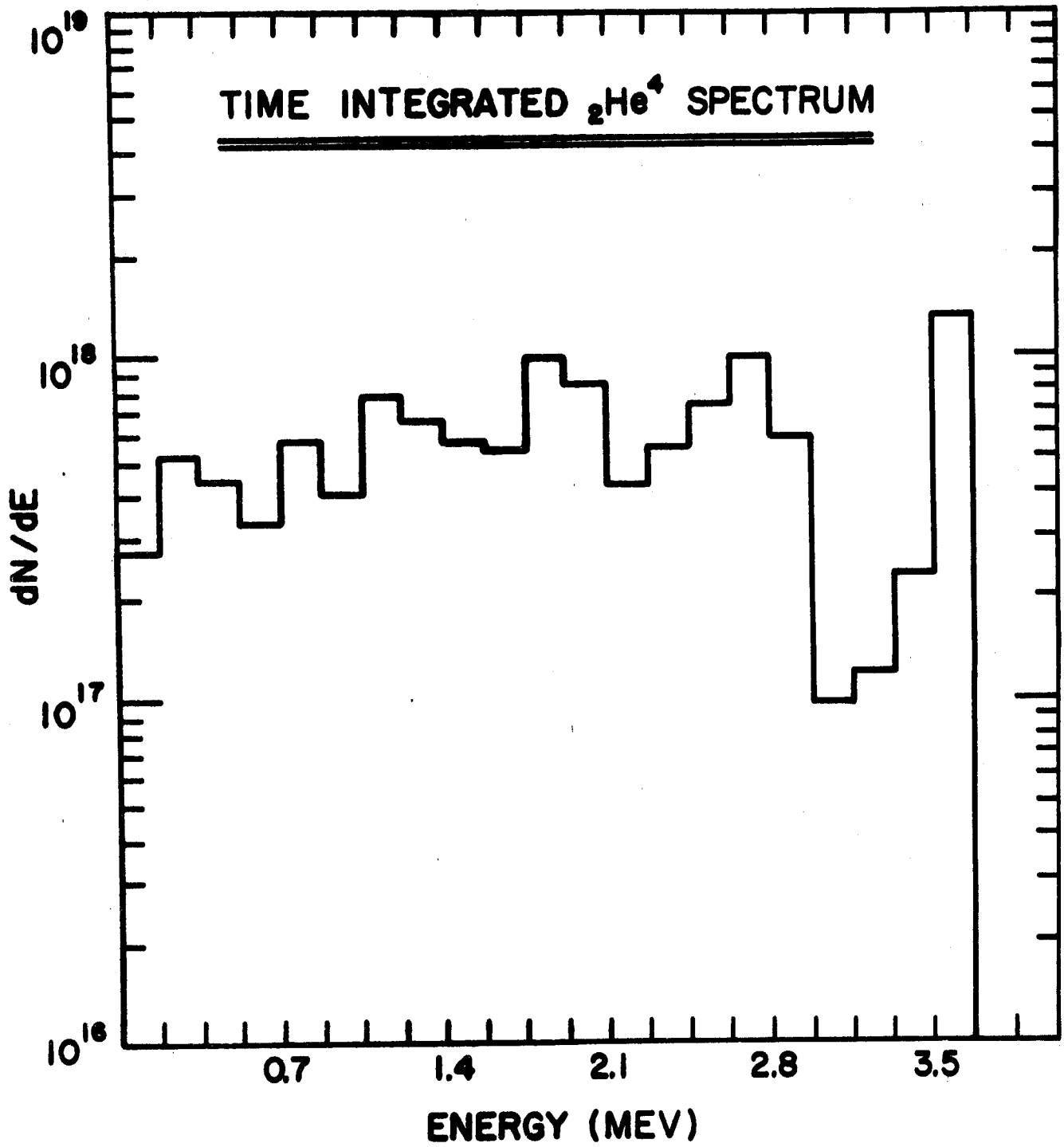
TIME INTEGRATED $_2He^4$ SPECTRUM
10^{19}
10^{18}
10^{17}
10^{16}
dN/dE
0.7
1.4
2.1
2.8
3.5
ENERGY (MEV)

Fig. IV-B-20.

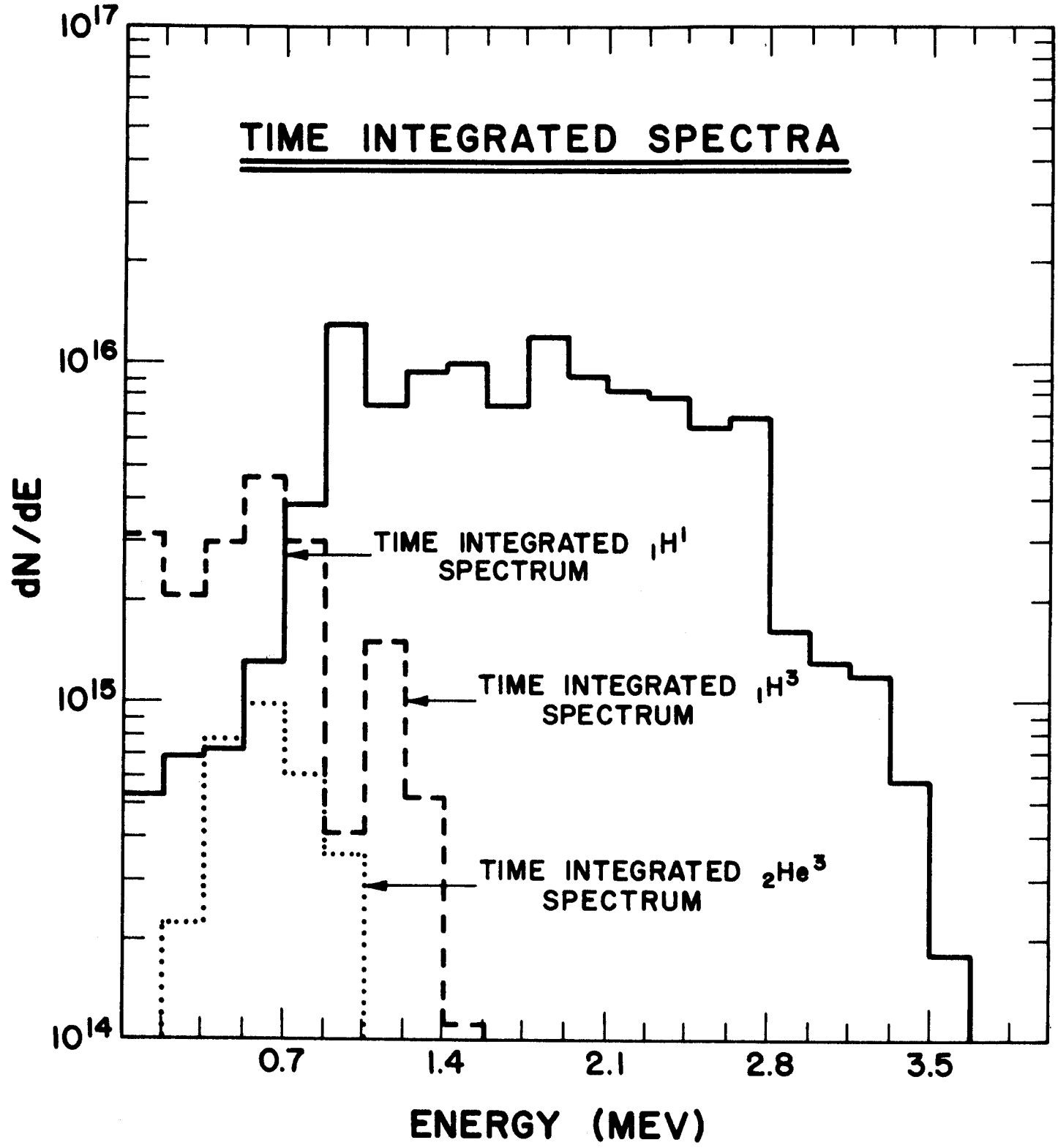
TIME INTEGRATED SPECTRA
10^{17}
10^{16}
10^{15}
10^{14}
dN/dE
TIME INTEGRATED $_1H^1$ SPECTRUM
TIME INTEGRATED $_1H^3$ SPECTRUM
TIME INTEGRATED $_2He^3$ SPECTRUM
0.7
1.4
2.1
2.8
3.5
ENERGY (MEV)

Fig. IV-B-21.

particle energy is 1.84 MeV in the laboratory frame of reference. The average energy per ion in the disassembling plasma is computed by allowing the PHD-IV simulation to run until the fluid velocity reaches a free streaming limit. This average velocity is 8×10^8 cm/sec. This corresponds to 668 keV deuterons, 1000 keV tritons, and 1330 keV alphas. The X-ray spectrum for the bare core is plotted in Fig. IV-B-22. It is quite hard and nonthermal; however, it can be approximated as an 8 keV black body.

None of these spectra account for transport through the ablated pellet surrounding the compressed core. If the remainder of the pellet is specified, these spectra can be used as source distributions for the transport of X-rays and charged particles to the first wall.

X - RAY SPECTRUM OF 100 MEGAJOULE D - T FUSION MICROEXPLOSION.

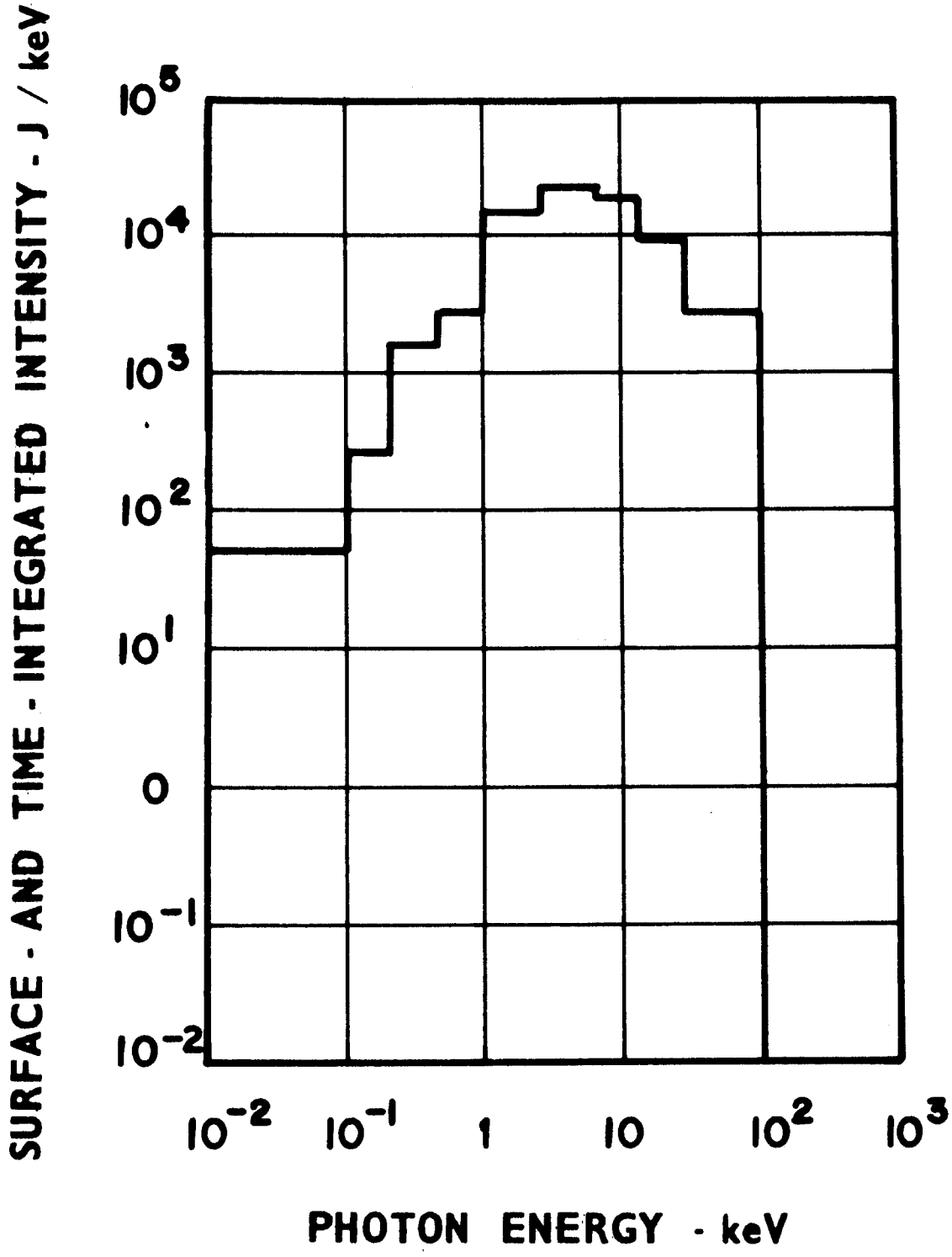

Fig. IV-B-22.

IV-B-2. Tamped Pellet Core Burn Calculations

There is good reason to believe that bare DT pellet cores are not a realistic model of reactor style laser fusion pellets. Almost every proposed pellet design for the next generation of laser systems[10-11] uses a high atomic number pusher-tamper to aid in the implosion process by increasing the ρR of the compressed core and by protecting the DT fuel from preheat caused by high energy electrons and photons generated in the pellet corona region. Preheat must be carefully controlled if isentropic compressions are to be achieved.[5] In addition to affecting the implosion dynamics, this high Z material will affect the burn dynamics and the charged particle and X-ray spectra emitted by the compressed core. Since these spectra are very important to the design of the reactor first wall it is essential to determine the effect of high Z materials in the pellet. For the pellets proposed for near breakeven experiments the ratio of high Z tamper mass to DT fuel mass is typically 10-100.[6-7] For reactor pellets with 1 mg of DT fuel this implies masses of 10-100 mg of high Z material.

With a lack of good information about reactor pellet designs, a parameter study, using PHD-IV, was done to determine the effect of high Z tampers on output spectra. In this study 1 mg of DT compressed to 3 g/cm^2 was surrounded by varying amounts of mercury. Due to a lack of opacity data for high Z materials a very simple equation of state model was employed. Ideal gas equations of state were used for the DT and high Z material. Ionization states were approximated by equilibrating ionization change with temperature change where LTE estimates of the ionization stages were used. The rate of ionization was assumed instantaneous compared to the hydrodynamic time scale. Recombination was assumed to be collisional (3 body) and electron

energy loses by ionization and gain by recombination were included in the radiation hydrodynamics. Only thermal bremsstrahlung emission and inverse bremsstrahlung absorption were considered. The bremsstrahlung emission into 4π steradians was given by:

$$J_{ff}(\nu)\, d\nu = 8.05 \cdot 10^{-46} \frac{N_e N_i}{\sqrt{kT_e}} \sum C_z Z'^2 e^{-\frac{h\nu}{kT}} g_{ff}\, d\nu$$

$$\text{ergs/cm}^3 - \text{sec}$$

where C_z is the concentration of atomic element Z, Z' is the mean ion charge of element Z, N_e and N_i are the electron and ion number densities and g_{ff} is the Gaunt factor averaged over a Maxwellian velocity distribution. The Born approximation was used and the Gaunt factor was written as:

$$g_{ff} = \frac{\sqrt{3}}{\pi} k_o(x)\, e^x$$

where $$x = h\nu/2kT_e$$

and where $k_o(x)$ is given in terms of the modified Bessel function of imaginary argument

$$k_o(x) = \pi/2\, [i\, H_o(x)]$$

Absorption coefficients corrected for induced emission were obtained from the emission functions by Kirchoff's law,

$$\sigma(\nu) = \frac{J(\nu)}{B(\nu)} = \frac{(hc)^2}{2} \frac{J_{ff}(\nu)}{(h\nu)^3} \left(e^{\frac{h\nu}{kT}} - 1\right) .$$

Thompson scattering for free electron at rest was assumed.

Recombination and line emission and their absorption counterparts are important radiation processes in high Z materials, but because of their added complexity and the crude approximations already made, these processes were neglected. This very simple model of the radiative processes is in fact substantiated by a comparison with published results of radiation hydrodynamics using the CLYDE computer code[8] which does contain sophisticated equations of state for high Z materials. This comparison is discussed in section III-E-2.

Since our goal was to gain an estimate of how fractional burnup, X-ray and charged particle spectra change with tamper mass, absorption and implosion effects were ignored. Consequently, our calculation started with a compressed core of DT surrounded by a layer of mercury. Table IV-B-1 lists three calculations of this type. For the results displayed in Table IV-B-1, the initial number density (electron and ion) was uniform (1.61×10^{26} cm^{-3}) throughout and the temperature was 10 keV at the center of the DT and .136 keV everywhere else. Table IV-B-2 displays similar calculations except that the initial mercury density was not uniform. In the latter case, pressure balance was assumed in the core contact region but the mercury density decreased as $1/r^3$ thereafter. Since these are strictly model calculations with no justification for the final density configuration it was felt that these two models would be sufficiently different to span the range of final density profiles. These qualitative results suggest that a mercury mass exists for maximizing the conversion of energy to X-rays for both of the postulated density profiles.

Fig. IV-B-23 shows time plots of the X-ray energy leaving the pellet surface for the four cases given in Table IV-B-1. The corresponding time

Table IV-B-1

DT (mg)	Hg (mg)	X-rays MJ	X-rays %	Charged Particles MJ	Charged Particles %	Neutrons MJ	Neutrons %	Total Energy MJ
1	0.0	1	1	20	19.4	82	79.6	103
1	2	14	.8	21	12	142	80	177
1	10	23	10	23	10	191	80	237
1	50	18	6	41	14	237	80	296

Table IV-B-2

DT (mg)	Hg (mg)	X-rays MJ	X-rays %	Charged Particles MJ	Charged Particles %	Neutrons MJ	Neutrons %	Total Energy MJ
1	10	23	10	22	10	187	80	232
1	50	28	11	23	9	205	80	256
1	100	25	10	25	10	203	80	253

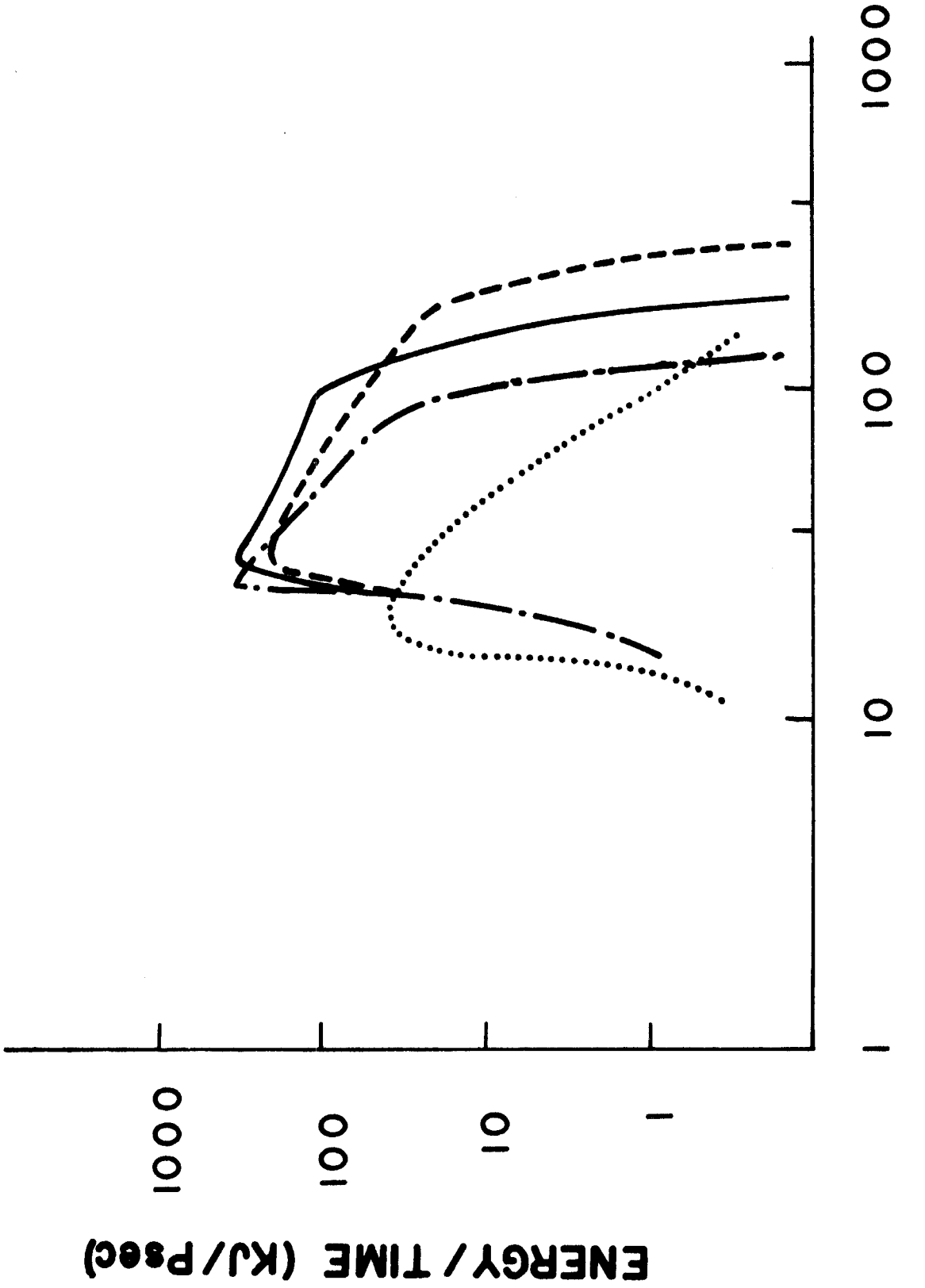

FIG. IV-B-23 **RADIATION ENERGY LEAVING THE PELLET'S SURFACE.**
THE CURVES REFER TO THE FOLLOWING CASES: BARE DT (DOTTED), 2mg OF Hg (DASH-DOT), 10 mg OF Hg (SOLID) AND 50mg OF Hg (DASH).

plots for the calculations given in Table IV-B-2 yield similar characteristics. Figures IV-B-24 to 28 display the time-integrated X-ray spectra approximately 2 nsec after burn begins. These results suggest that both the X-ray transit time and spectra are significantly altered by the amount of high Z material in the pellet. For example, the results indicate that the width of the X-ray energy pulse to the wall is greatly increased and the X-ray spectra significantly altered when the mercury mass is increased and when the density profile is altered.

Because these calculations were done for a specific high Z material and for special initial conditions, it is of interest to explore some of the more general qualitative physical processes suggested by our calculation. By focussing on the more important interconnected hydrodynamic, burn dynamic and radiation processes during and after burn, some understanding of the previous resu and some qualitative understanding of more complex pellet designs can be made.

Consider the radiation processes within a DT pellet surrounded by a high Z material. When burn starts the temperature of the DT significantly rises and with this increase comes a corresponding increase in the radiation energy density. As the burn develops, radiation penetrates the high Z layer. If the high Z shell is sufficiently thick and dense the radiation is absorbed and most reemitted back into the DT. The radiation becomes trapped.

At the same time a thermal conduction wave begins propagating through the high Z material. As the wave propagates outward the high Z layer becomes more ionized. The ionization state changes the radiation emission, absorption and scattering functions and, therefore, the radiation transport. For example, the absorption process for a highly ionized high Z layer will tend to be inverse bremsstrahlung at low frequencies and photoelectric absorption

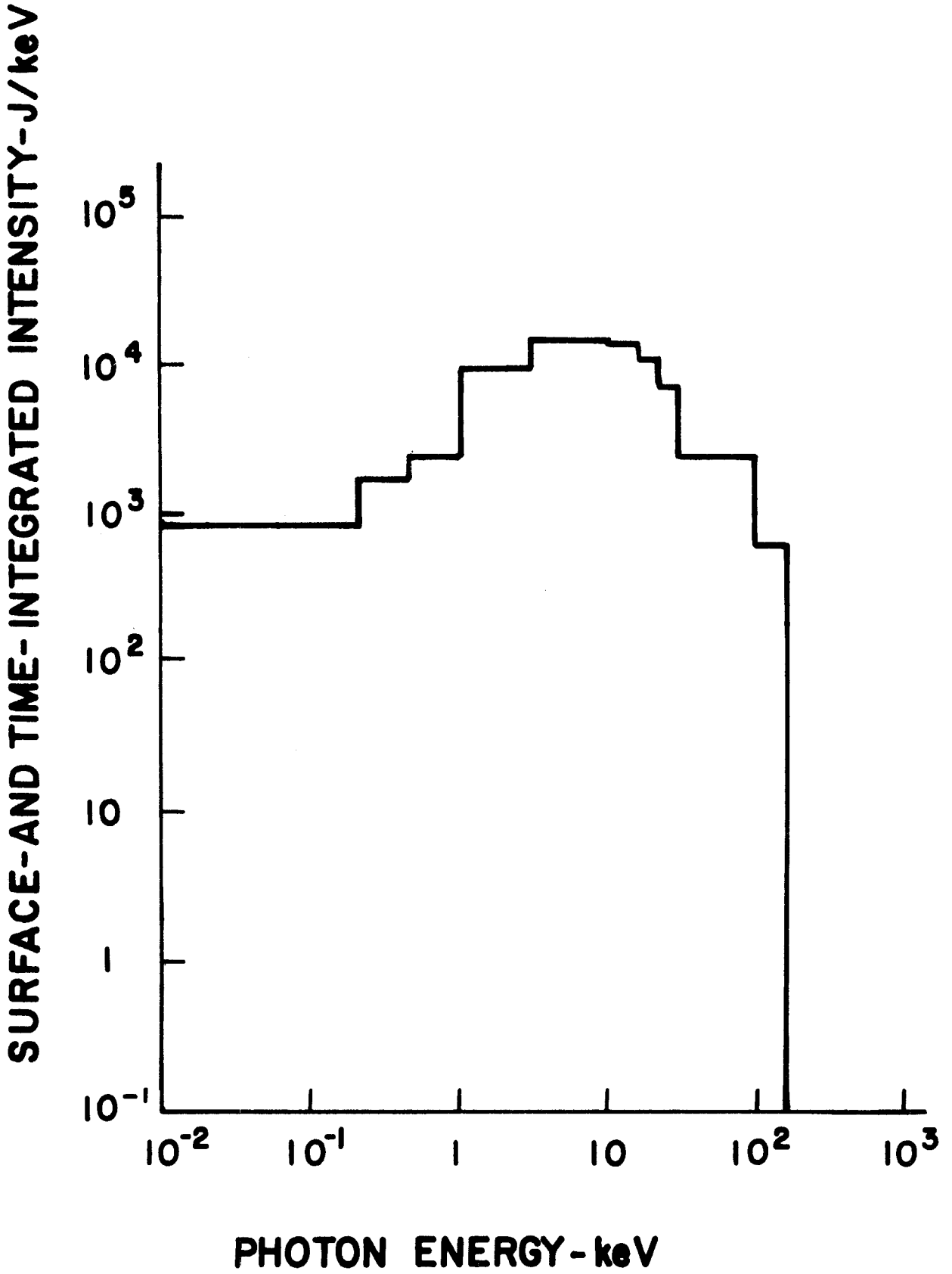

FIG. IV-B-24 **RADIATION SPECTRUM FOR BARE DT PELLET. (10 FREQUENCY GROUPS)**

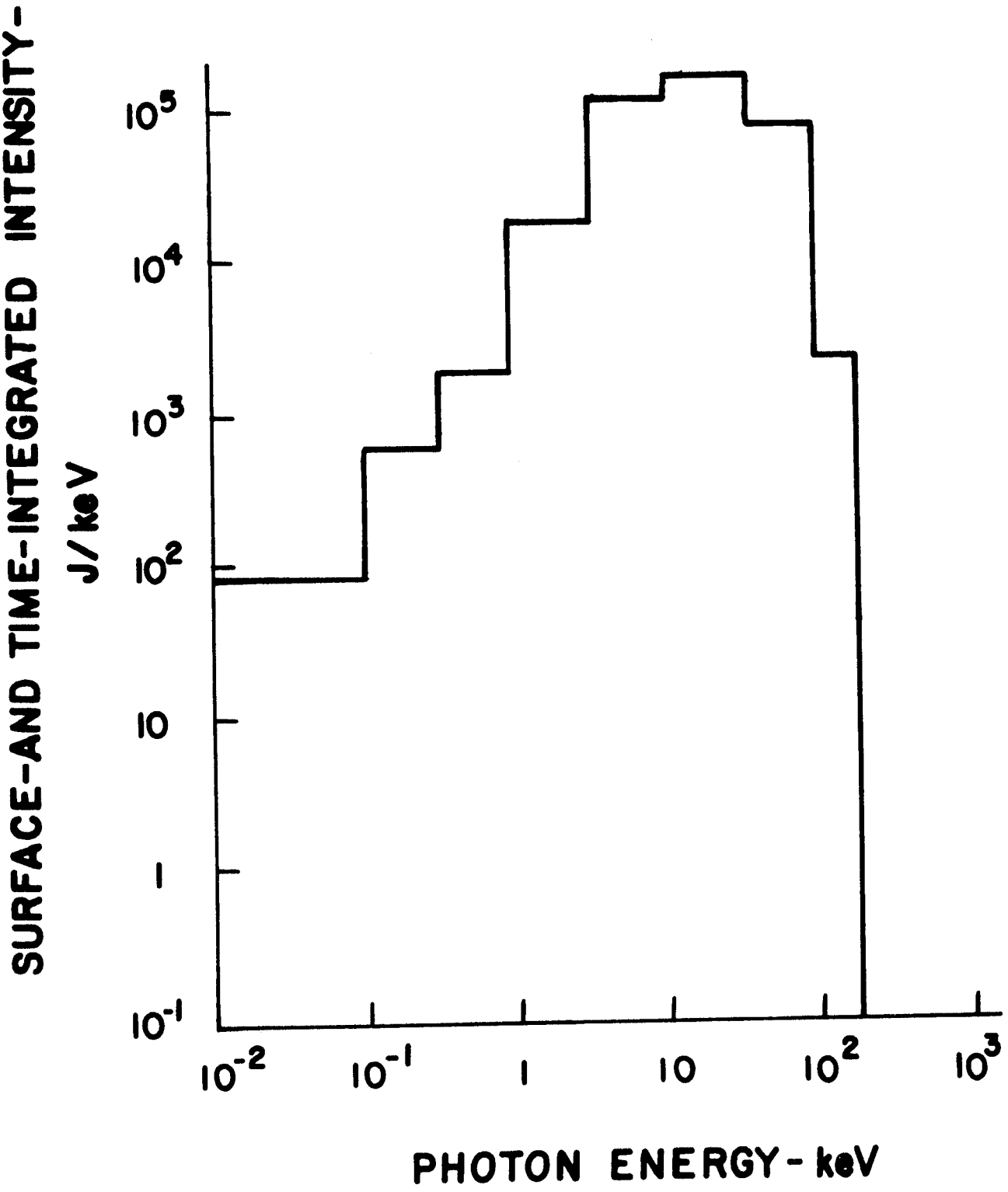

FIG. IV-B-25 **RADIATION SPECTRUM FOR A DT PELLET WITH A 2 mg Hg SHELL.**

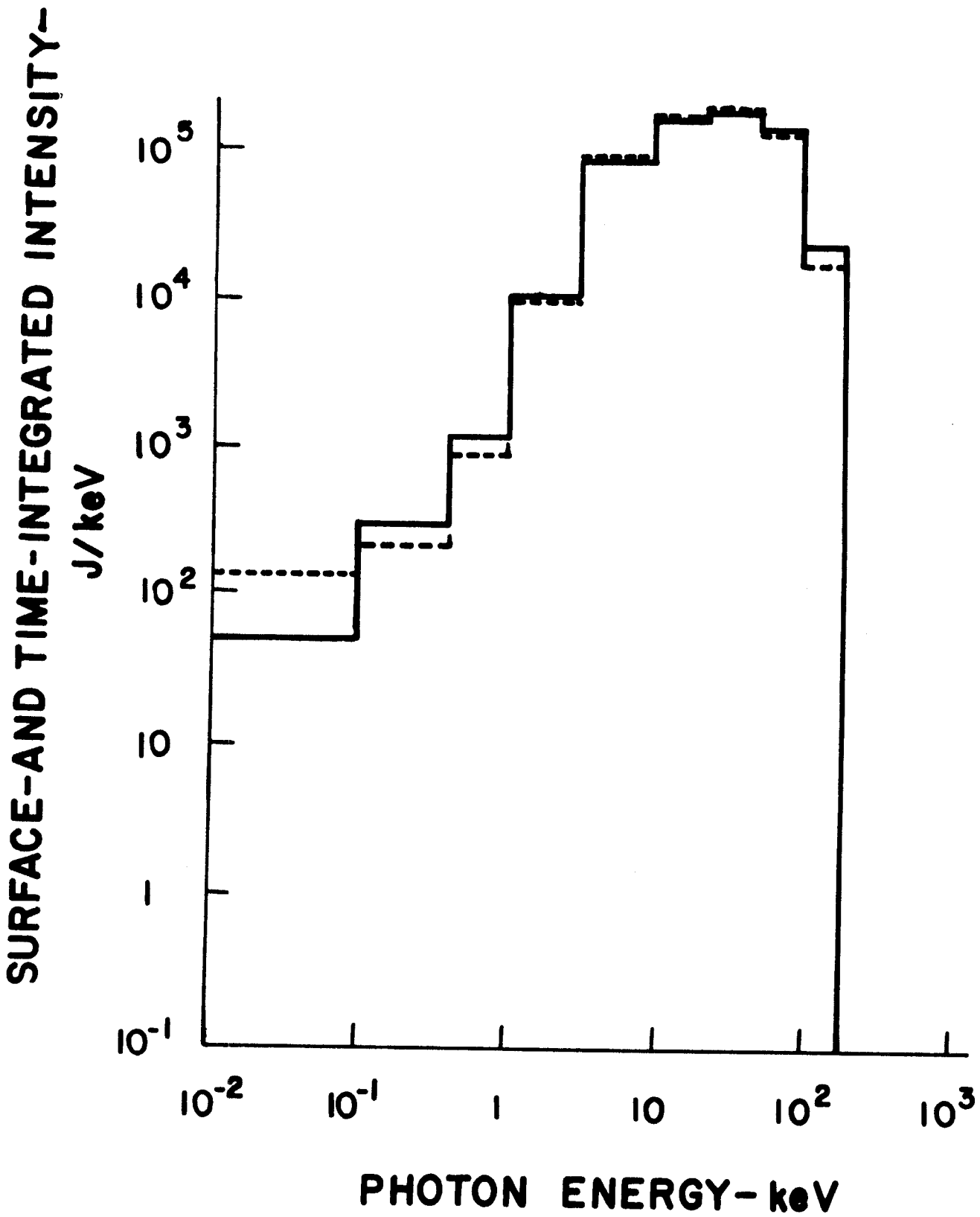

FIG. IV-B-26 RADIATION SPECTRUM FOR A DT PELLET WITH A 10 mg Hg SHELL. (SOLID CURVE ASSUMED UNIFORM Hg DENSITY)

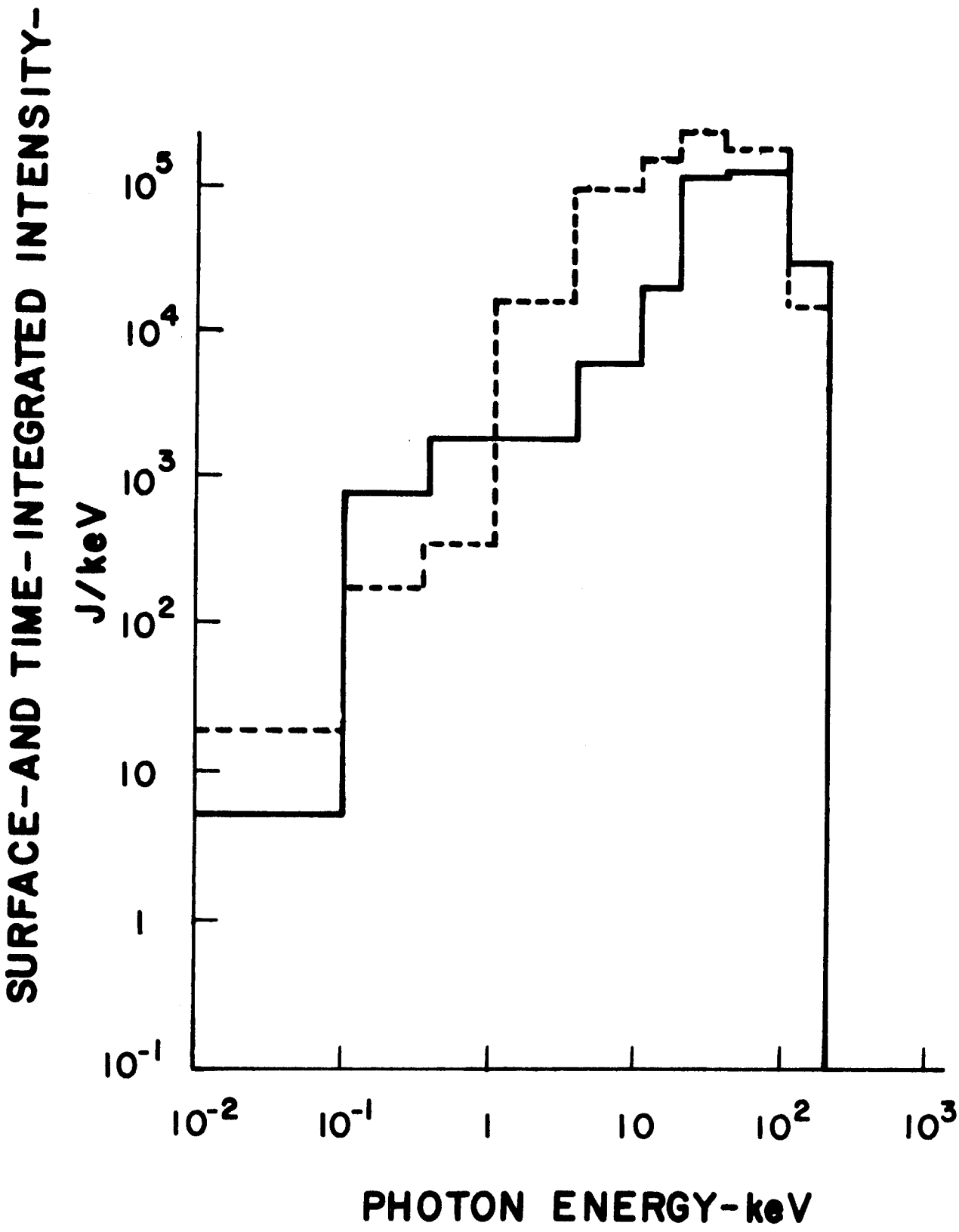

FIG. IV-B-27 RADIATION SPECTRUM FOR A DT PELLET WITH A 50 mg Hg SHELL. (SOLID CURVE ASSUMED UNIFORM Hg DENSITY)

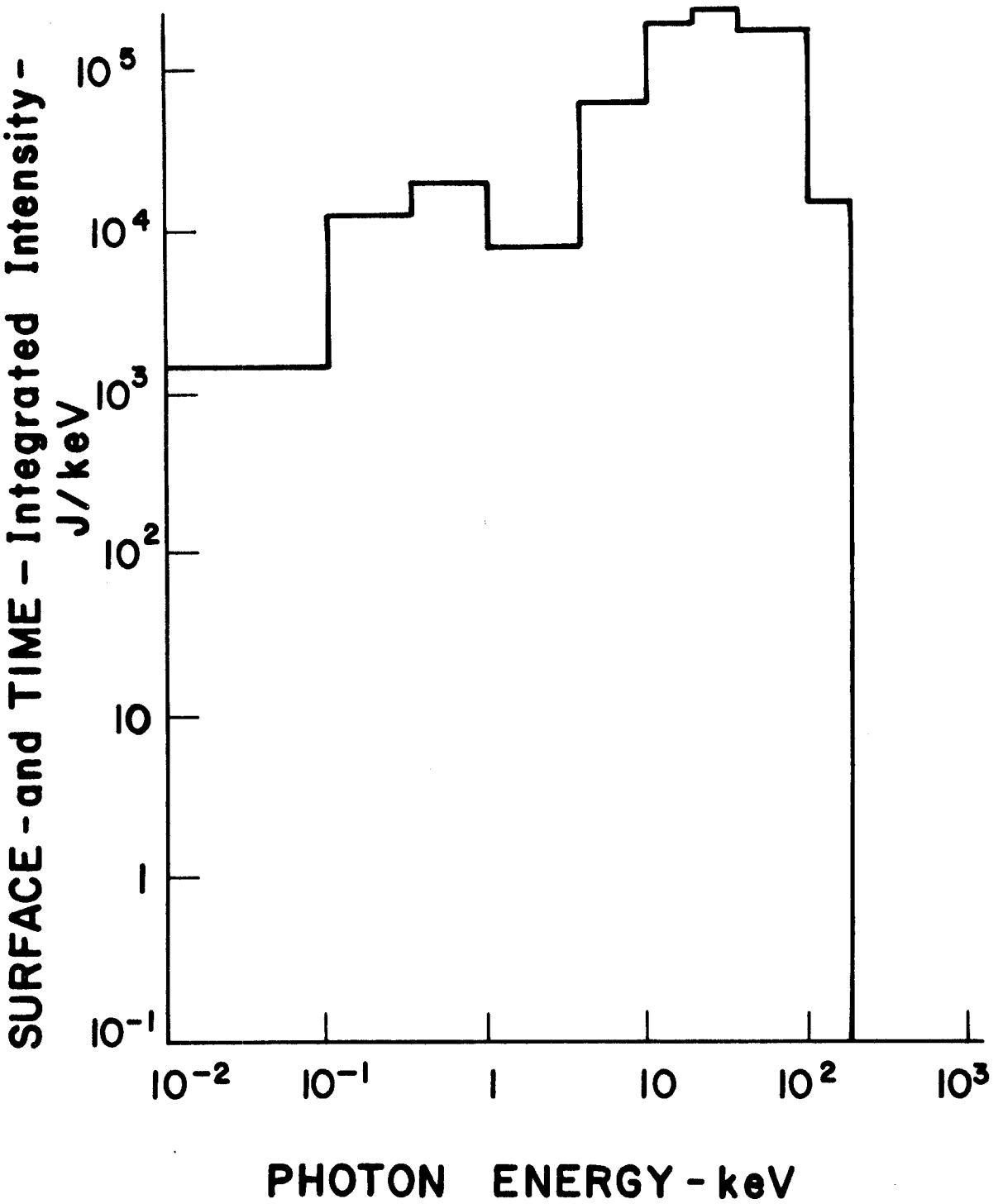

FIG. IV-B-28 RADIATION SPECTRUM FOR A DT PELLET WITH A 100 mg Hg SHELL

at high frequencies. The emission will increase as the temperature increases. Further, if the energy released during burn significantly ionizes the high Z layer, the pellet may become transparent to much of the radiation and the surface-emitted-X-rays will tend to be hard. In contrast, if the energy released is small compared to the amount needed to significantly ionize the layer, radiation mean free paths will remain small and the surface-emitted-X-rays will tend to be soft.

As the conduction wave propagates outward, the inner surface of the high Z layer ablates inward. The ablation process will impart more momentum to the shell if the penetration depth of the DT debris is small compared to the shell's thickness. For example, if the debris is stopped in the inner surface of the shell, the pressure of the inner surface rises considerably because both its temperature and ionization state are rapidly increasing. As a result, much of the debris energy is converted into momentum. On the other hand, if the DT debris penetrates deeply into the high Z layer, the shell is heated without substantial conversion of energy into momentum.

Because a conduction wave increases the plasma temperature and therefore the radiation emission, and because radiation tends to flow outward rather than inward from the pellet's surface, radiation cooling increases when the conduction wave reaches the pellet's surface. For low energy photons, radiation loss is generally a surface effect because the photon mean free path is small. On the other hand, because high energy photons tend to have much larger mean free paths, hard X-rays from the DT burning core and from the inner surface of the mercury shell may reach the pellet surface without substantial absorption.

The pellet density structure during and after burn completion will significantly affect the total radiation energy and momentum of the pellet debris and the resulting radiation spectrum. If the inner DT and high Z layer collide with a massive lower density outer layer of ablated pellet material, some kinetic energy of the inner layer is lost in the process of heating the lower density outer region. The outer layer then radiates away much of this increased thermal energy. As the pellet expands outward, more thermal energy is transferred into particle kinetic energy and low energy photons, and ionization recombination increases both the electron thermal and radiation energies.

Concluding, our results suggest the following pellet characteristics. If two pellets with equal DT but different high Z masses are brought to similar ignition condition, the pellet with the larger high Z mass will tend to produce softer X-rays, lower particle energies and longer X-ray transit times. Also, the greater the high Z compression achieved during implosion and the greater the amount of high Z mass compressed, the smaller the X-ray energy content. Again, since detailed designs of reactor pellets are not available this analysis has been an attempt to present generic results. The sensitivity of the model was tested by varying the density profile of the tamper material in a plausible fashion.

References for Section IV-B.

1. G. Fraley, E. Linnebur, R. Mason, and R. Morse, Phys. Fl. 17, 474 (1974).

2. C. Longmire, Elementary Plasma Physics, (Wiley, New York, 1967), p. 203.

3. R. Kidder, Nucl. Fus. 16, 405 (1976).

4. G. Moses and G. Magelssen, "PHD-IV, A Plasma Hydrodynamics Code", Univ. of Wisconsin Fusion Research Program Report UWFDM-194, 1977.

5. J. Lindl, Nucl. Fus. 14, 511 (1974).

6. R. Perkins, "The Laser Program at LASL", Los Alamos Scientific Laboratory Report LA-77-174 (1977).

7. Lawrence Livermore Laboratory Annual Laser Fusion Report UCRL-50021-75, p. 264 (1975).

8. S.G. Varnado, G.A. Carlson, Nucl. Tech. 29, 415 (1976).

IV-C. Pellet Implosion

The pellet implosion process must isentropically compress the DT fuel to a ρR value of about 3 g/cm^2 and it must collapse the center of the pellet at an implosion velocity of about 3×10^7 cm/sec to shock heat the microcore to 10 keV temperatures. Both of these conditions are important to high gain pellets. It has been proposed that the implosion be accomplished by uniformly irradiating spherical droplets of DT with light from a high power laser, Fig. IV-A-2. The outer surface of the droplet heats, ionizes, and ablates outward. The electrons in this cloud of plasma continue to absorb more laser radiation. The laser radiation is only able to penetrate into the plasma up to the critical density where the electron plasma frequency is equal to the incident laser frequency. The transport of energy from the critical density inward is via the mechanisms of thermal conduction and hydrodynamic motion. As the plasma surface is heated and ablates outward a shock front is formed that converges inward toward the center, pushing cold DT ahead of it to higher and higher densities along a Fermi degenerate adiabat. To maintain this isentropic compression requires a detailed understanding of the thermal conduction transport mechanism and a very precisely programmed laser pulse.

IV-C-1. An Example Pellet Implosion

To more fully understand the dynamics of the pellet implosion process a typical bare DT ball implosion is simulated using the PHD computer code. The initial pellet characteristics and the laser pulse shape are given in Fig. IV-C-1 and Table IV-C-1. We start with a rather idealized solid pellet surrounded by a lower density atmosphere (presumably prepared by a laser prepulse). The initial electron and ion temperatures are set at 1 eV and the D-T

DT PELLET INITIAL CONDITIONS

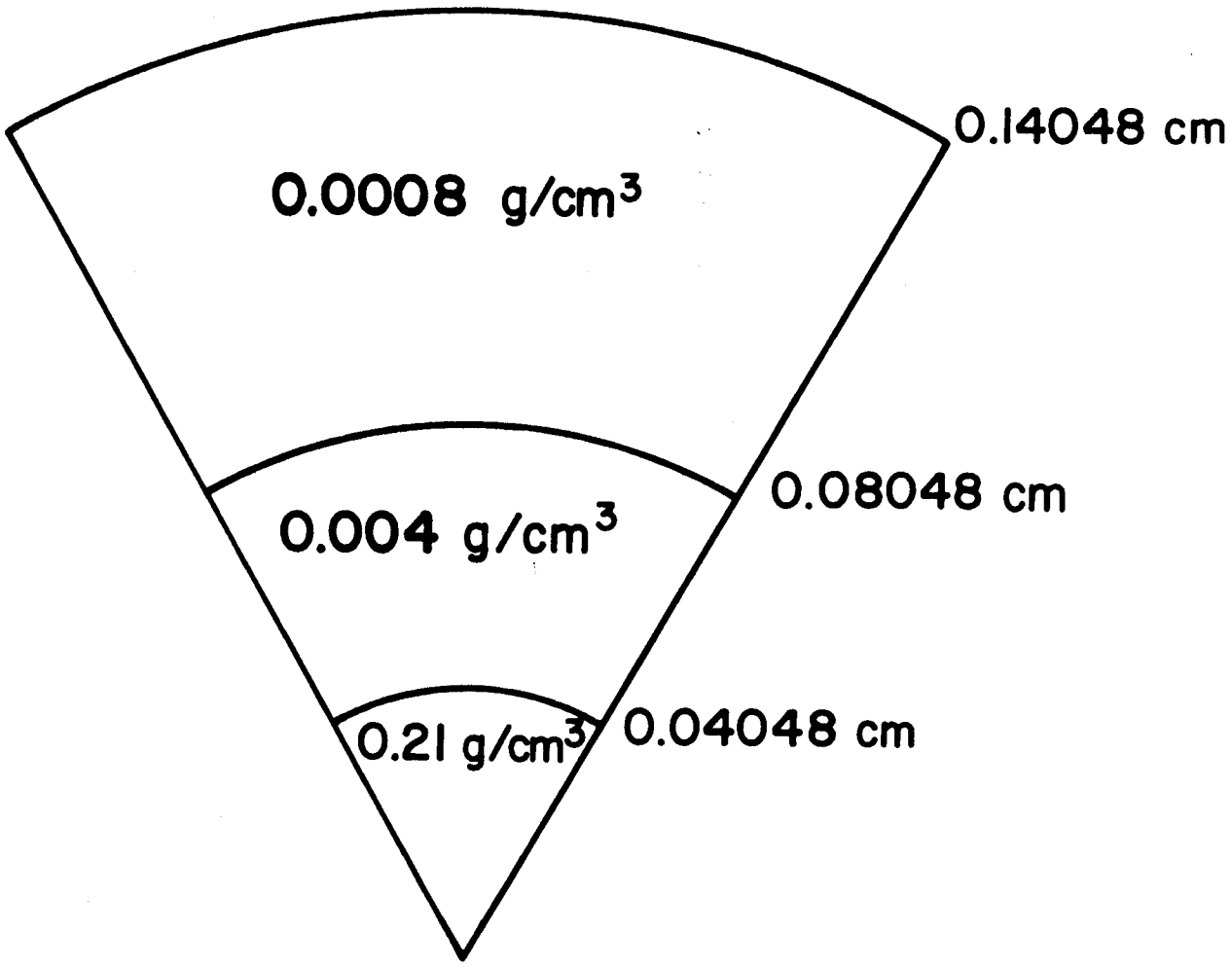

Fig. IV-C-1.

Table IV-C-1

Laser Pulse Shape

$$\dot{E}(t) = \dot{E}_1 \left\{ \frac{(t_1 - t_2)}{R(t_1 - t_2) - (t_2 - t)} \right\}^M \qquad R = \left(\frac{\dot{E}_1}{\dot{E}_2} \right)^{1/M}$$

t_1 (nsec)	t_2	$\dot{E}_1$ (watts)	$\dot{E}_2$	M
0	28	10^{10}	4×10^{12}	2
28	28.6	4×10^{12}	1.65×10^{13}	2
28.6	29	10^{13}	8×10^{14}	2

Wavelength = 2 μm

plasma is assumed to be fully ionized with Z = 1 everywhere. The charge of the plasma is specified initially and remains the same throughout the calculation. The initial pressure is determined by the temperature and density. The boundary pressure condition is specified to be very small to simulate a vacuum boundary. The temperature boundary condition is $\partial T/\partial X = 0$. This will allow no conduction of energy across the outer boundary, which is appropriate for a vacuum boundary condition. 35 spatial zones are used, with an attempt to include equal mass in each zone. Unequal zone masses foul-up the fluid motion calculation. All physical coefficients are taken at their nominal values and no radiation energy is accounted for in this calculation.

The purpose of this simulation is to examine the compression and heating of the pellet. About 41 kilojoules of energy will be absorbed by the pellet with most deposition occuring in the final one nansecond of the laser pulse. The first 28 nanoseconds are used to adiabatically compress the pellet.

Fig. IV-C-2 to 5 are "snapshots" of the relevant dynamic variables at 7.8112 nanoseconds. The time step is now 9.2464×10^{-2} nanoseconds and is being limited by the change in electron temperature at a radius of 6.99×10^{-2} cm. In Fig. IV-C-2 we see the formation of a heat front at about 7×10^{-2} cm with electron temperatures of 8×10^{-2} keV behind the front. Just at the front, a shock front has started to form, where the plasma has been locally compressed about a factor of three times its initial density. The outer edge of the pellet is blowing off (ablating) and the density gradient is very steep. The electron and ion temperature behind the heat front are starting to decouple due to the relatively long electron-ion equilibration time. Electron and

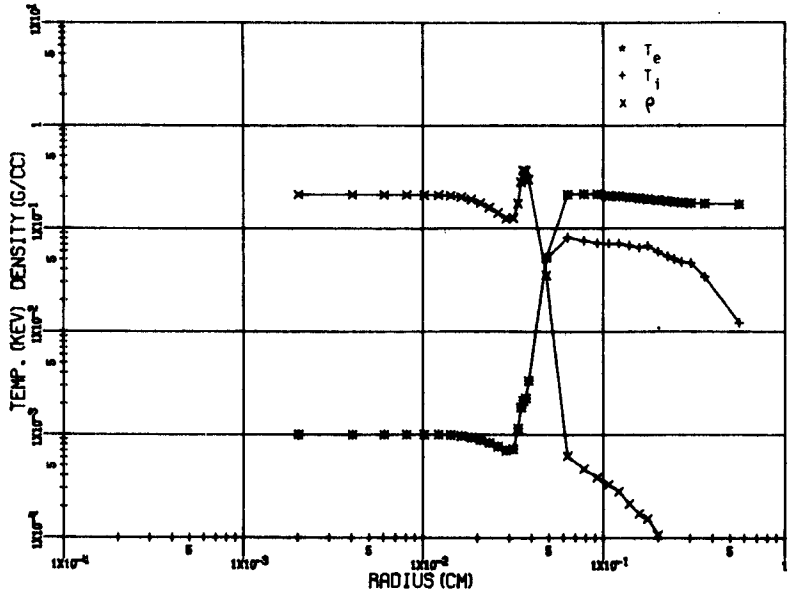

- Temperature and density @ 7.8112 nsec

Fig. IV-C-2.

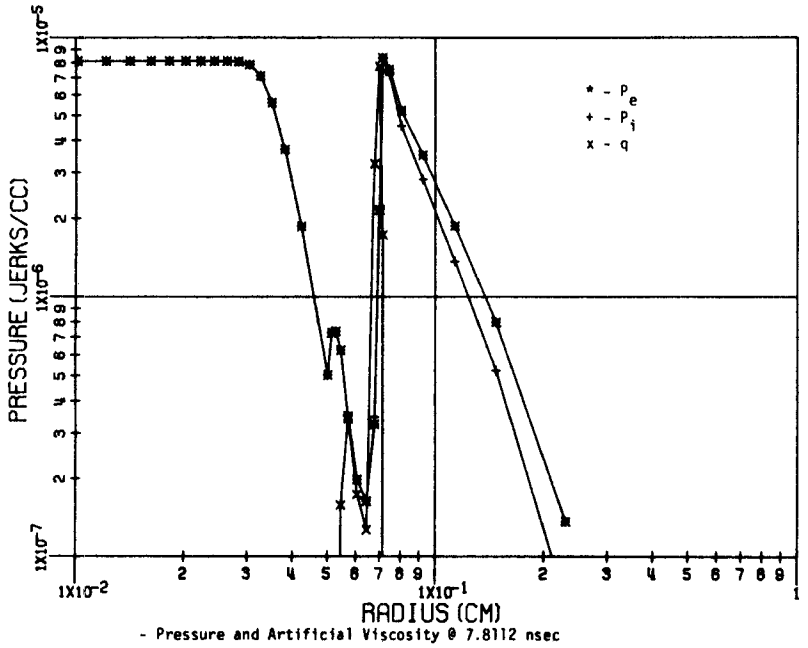

- Pressure and Artificial Viscosity @ 7.8112 nsec

Fig. IV-C-3.

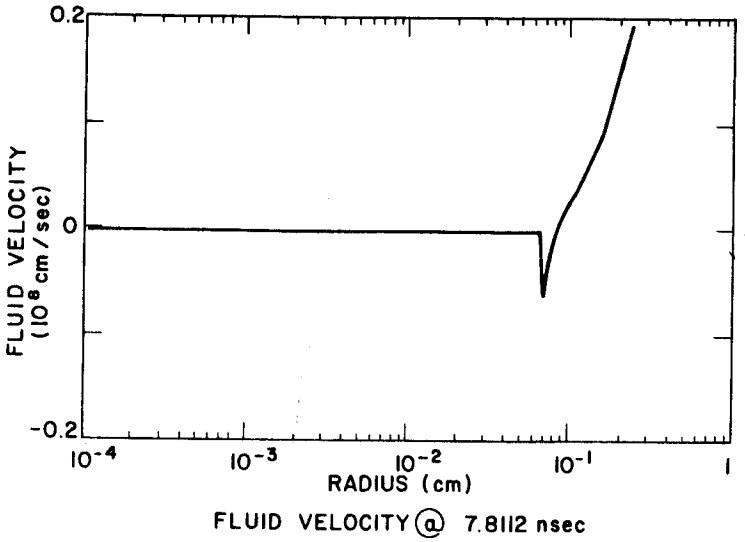

Fig. IV-C-4.

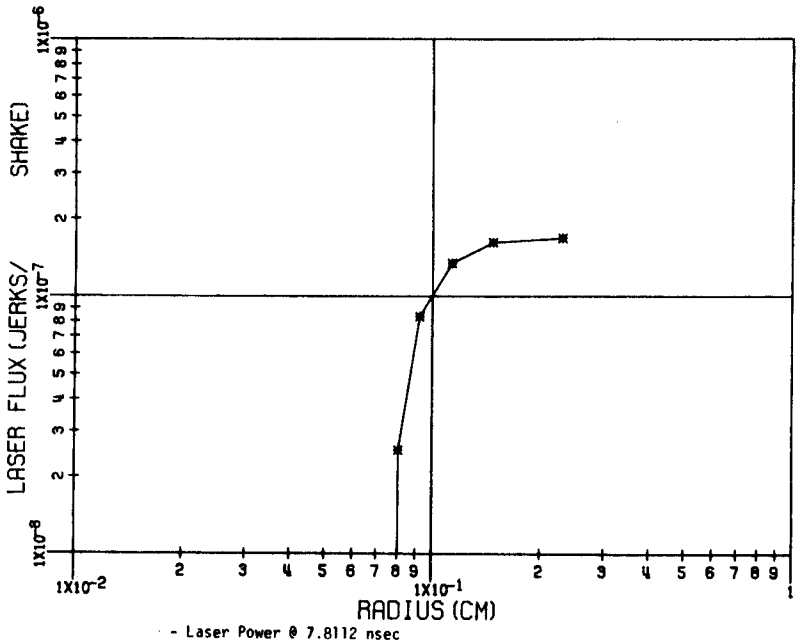

Fig. IV-C-5.

ion pressures and artificial viscosity are plotted in Fig. IV-C-3. We note that the artificial viscosity is zero everywhere except in the shock, where its value is the same order as the ion pressure. This effectively doubles the $P(\nabla \cdot \underline{u})$ term in the ion temperature equation and gives the effect of shock heating. The fluid velocity is plotted in Fig. IV-C-4. It shows that the outer edge of the pellet is expanding outward while the plasma just inside the outer surface is being driven inward due to the rocket effect. At this early stage of implosion most of the pellet remains motionless. Fig. IV-C-5 shows the laser intensity as a functional radius in the plasma. It propagates up to the critical density where the remainder of the energy is dumped. The attenuation at this time is rather constant throughout the corona. The electrons and ions actually contain less thermal energy than they did initially. This is because as the plasma expands, the ions convert thermal energy to directed or fluid motion and hence they are cooled. Thus, even though the laser has provided more than twice the initial plasma energy, most of the energy at this time has gone into fluid motion.

Our next look at the pellet is at 20.776 nanoseconds where the time step is now 1.7925×10^{-1} nanoseconds. Fig. IV-C-6 clearly shows the distinct heat front with decoupled electron and ion temperatures behind it. Just ahead of the front, a shock has formed while ahead of the shock the density and temperature are still at their initial values. Within the shock, the artificial viscosity is comparable to the ion pressure. Behind the shock the plasma is ablating outward, driving the shock inward.

At 28.684 nanoseconds the laser pulse is very rapidly rising in intensity. The time step is reduced to 1.2188×10^{-2} nanoseconds. The

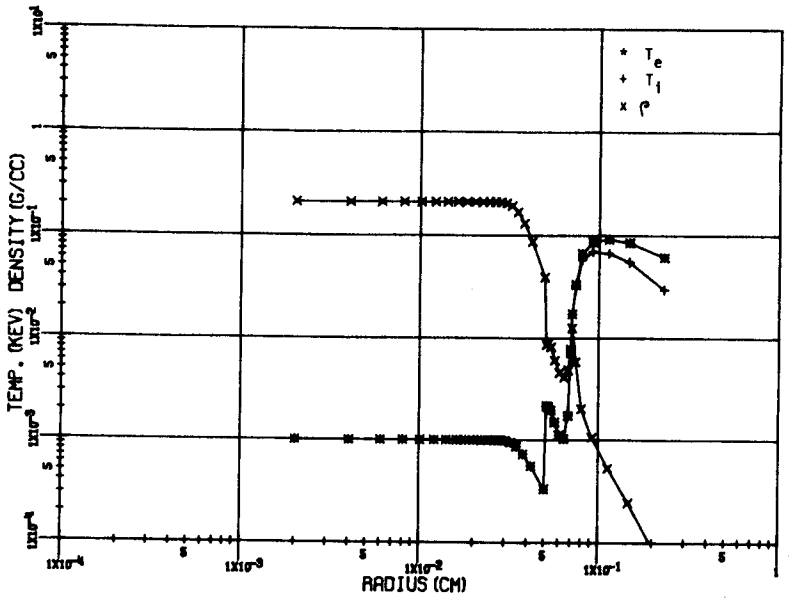

Temperature and Density @ 20.776 nsec

Fig. IV-C-6.

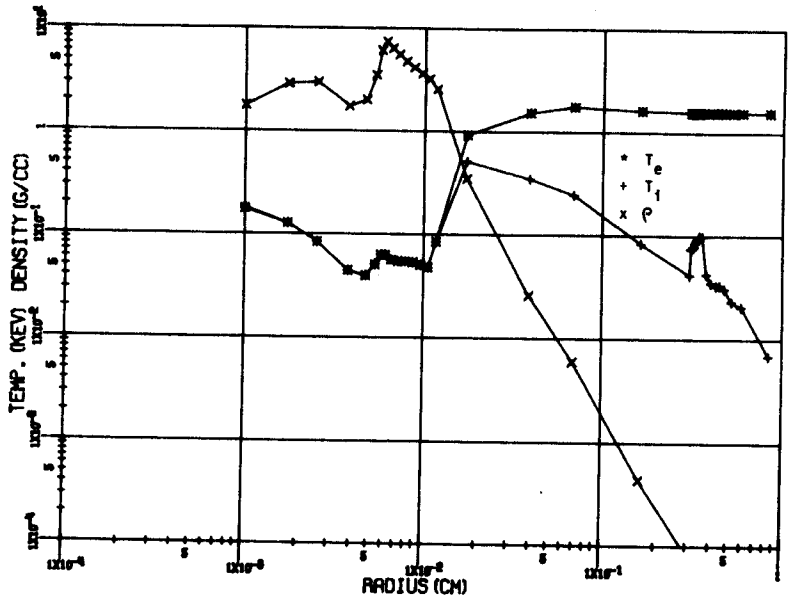

Temperature and Density @ 28.684 nsec.

Fig. IV-C-7.

density and temperature in the pellet core are beginning to rise due to compression (Fig. IV-C-7). The critical density surface is now behind the heat front and energy is carried to the front by electron thermal conduction. The ion temperature in the corona is low due to expansion cooling while the electrons remain hot due to their greater conductivity. The density falls very rapidly outside the ablation surface. Most of the plasma mass remains in the core but more and more of it will pass through the ablation surface and be lost. Maximum compression is now 35 times solid density. The heat front still remains behind the ablation surface, providing good implosion conditions. Very little energy (3.4%) is being absorbed from the laser beam until it reaches the critical density where it is all artificially absorbed (Fig. IV-C-8). This clearly indicates that the success of this numerical experiment depends on the as yet unknown absorption mechanism ("anomalous") at the critical density. A large fraction of the total system energy is still in the fluid motion. The laser has now delivered 1000 times the initial plasma energy, yet it has been deposited in such a short time that only about one half of the plasma has been heated.

At 28.918 nanoseconds the corona electron temperature is well over 1 keV and the ion temperature drops quickly with the density. The time step is down to 5.2563×10^{-3} nanoseconds and most of the core mass is moving inward. Maximum compression is 100 times solid density (Fig. IV-C-9). There is now more thermal energy in the electrons than in the fluid motion and the laser has supplied more than 5000 times the initial plasma energy.

At 28.994 nanoseconds the time step is 9.7486×10^{-4} nanoseconds. The electrons have been heated to almost 10 keV and the heat is transported from the critical density surface to the thermal front by electron thermal

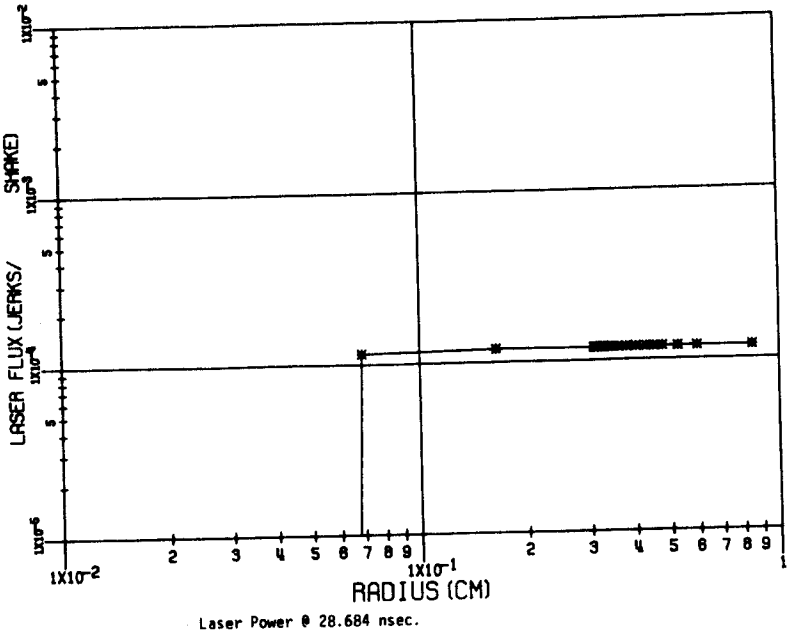

Fig. IV-C-8.

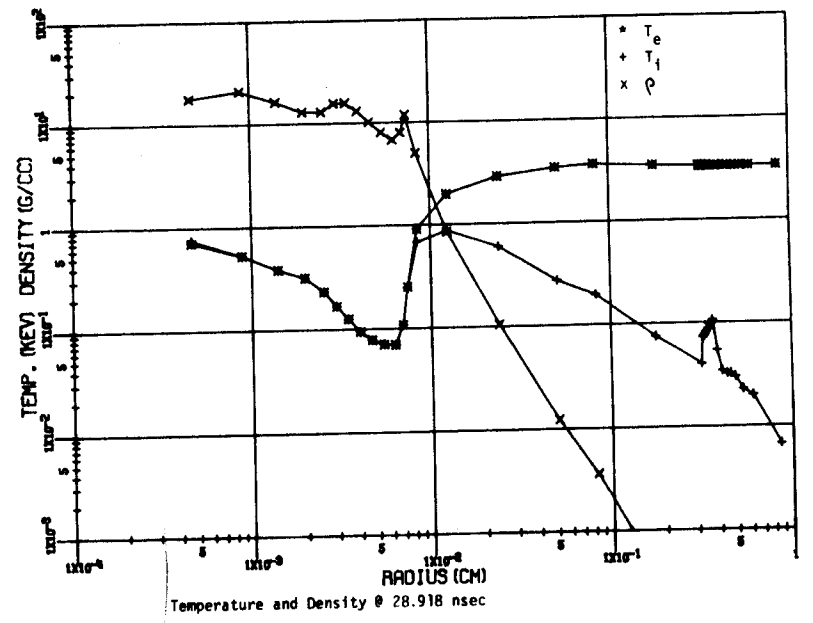

Fig. IV-C-9.

conduction. Maximum compression is in the shock and is 156 times solid density. The inner part of the pellet core has reflected at the center and is now moving outward, Fig. IV-C-10. This is a non-optimum condition caused by shock waves converging to the center too quickly. This preheats the core before the final compression takes place. Electron and ion temperatures in the core remain equal due to the very short equilibration time at these high densities. We note that almost none of the laser energy is absorbed except at the critical density, again indicating that the validity of this example rests on the anticipated absorption of the laser radiation at the critical density (Fig. IV-C-12).

At 29.008 nanoseconds the laser pulse is complete. Electron and ion temperatures and plasma density are actually lower in the core now than at 28.918 nanoseconds since the initial shock wave has reflected and passed back out of the core (Fig. IV-C-13). The strongest shock is still converging to the center with the heat front at the same position behind it.

Fig. IV-C-14 to 16 at 29.018, 29.025, and 29.036 nanoseconds show the final stages of compression. At 29.025 nanoseconds the ion temperature rises above the electron temperature due to compression. At this time the maximum compression is 333 times solid density and only 5% of the initial pellet mass is converging toward the center. The remainder of the mass has been ablated to provide the very strong compression. At 29.036 nanoseconds we observe the largest compression recorded on the graphic output. The center zone is compressed to 892 times solid density. This was not the maximum compression, however; it came at 29.033 nanoseconds and was 3080 times solid density. At this time the ion temperature was 14.1 keV and the electron temperature was 7.3 keV. No thermonuclear burn calculation

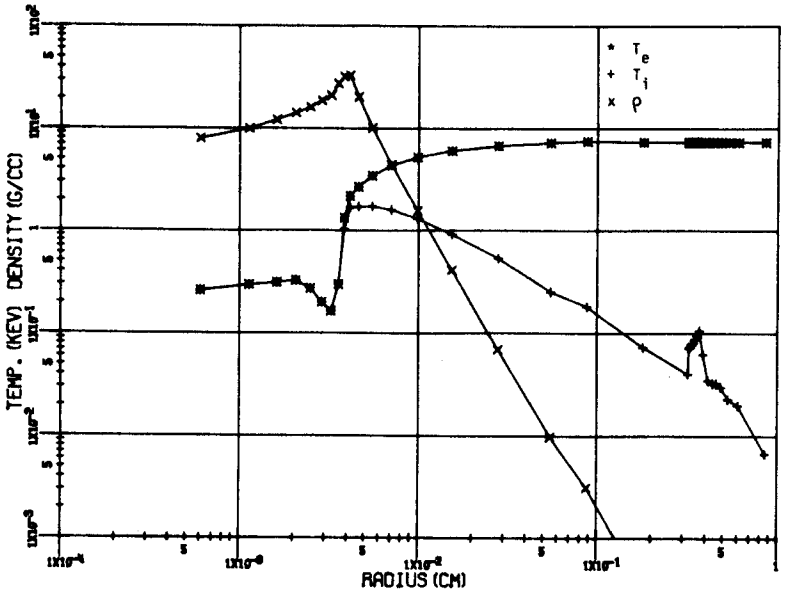

Temperature and Density @ 28.994 nsec

Fig. IV-C-10.

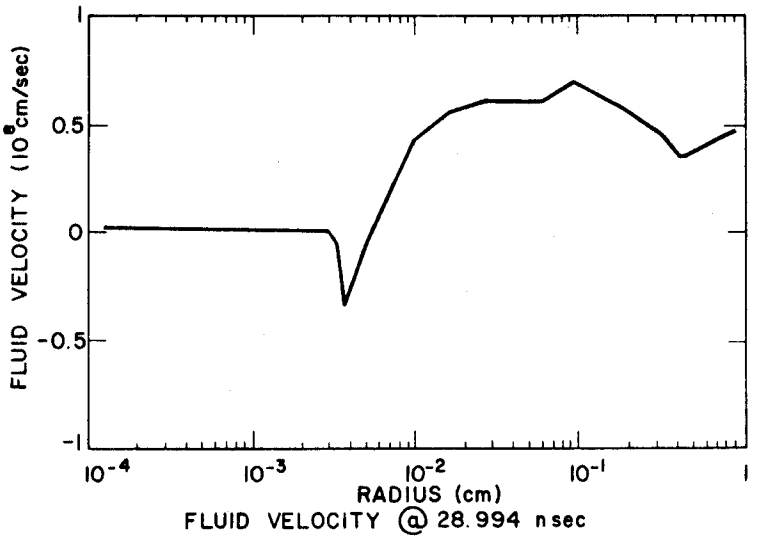

FLUID VELOCITY @ 28.994 nsec

Fig. IV-C-11.

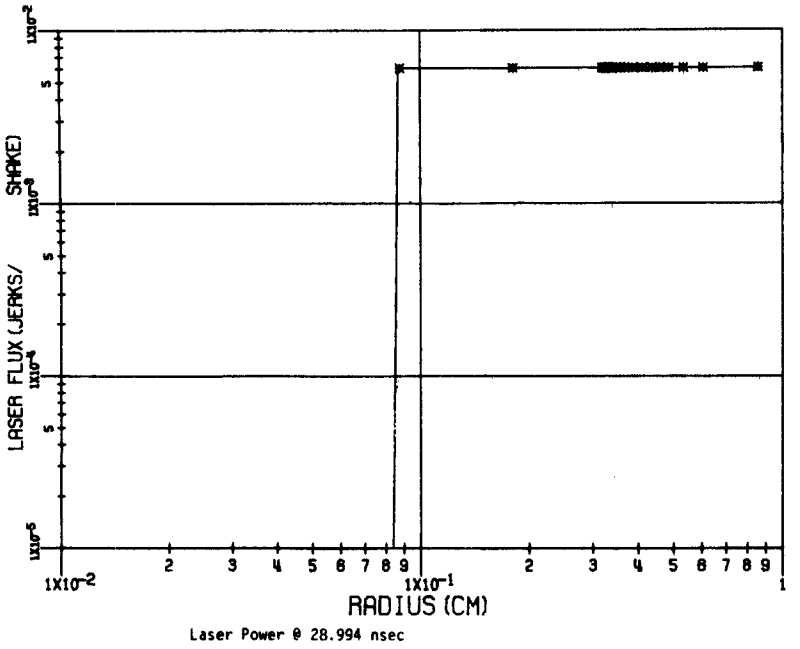

Fig. IV-C-12.

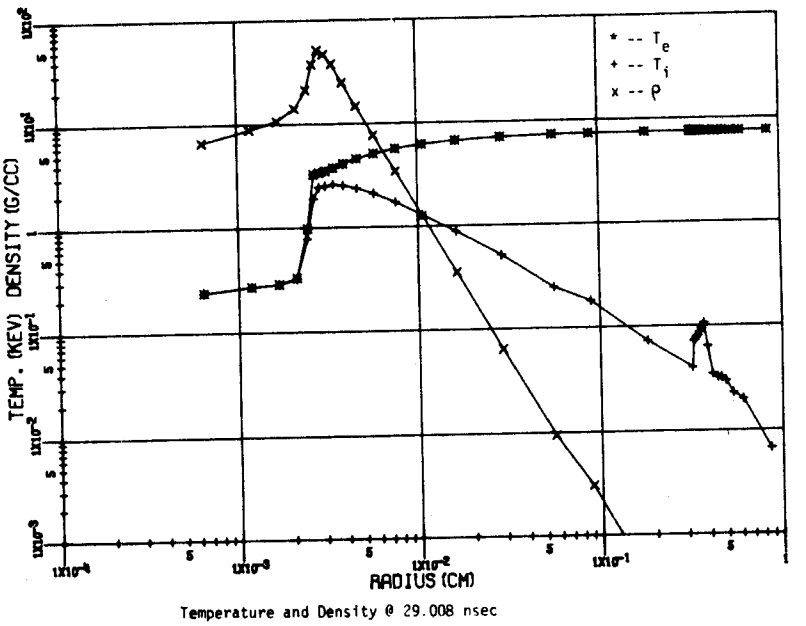

Fig. IV-C-13.

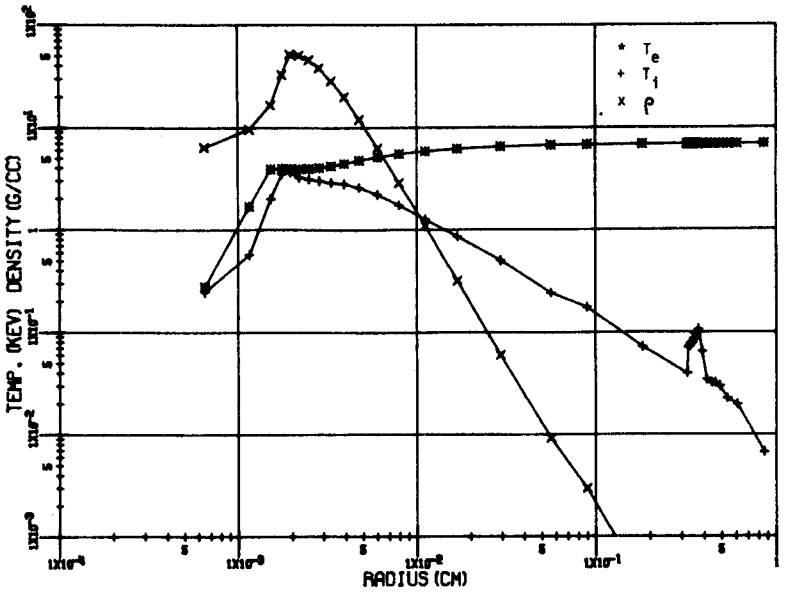

Temperature and Density @ 29.018 nsec.

Fig. IV-C-14.

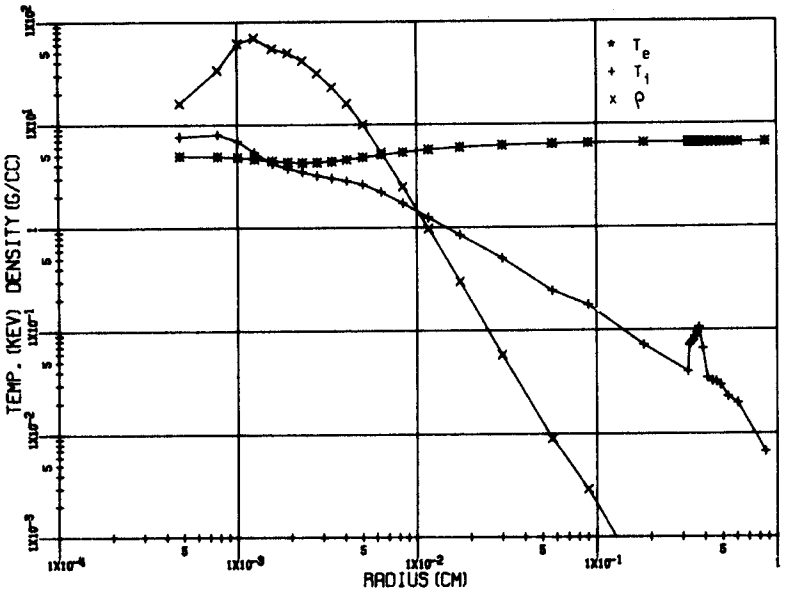

Temperature and Density @ 29.025 nsec.

Fig. IV-C-15.

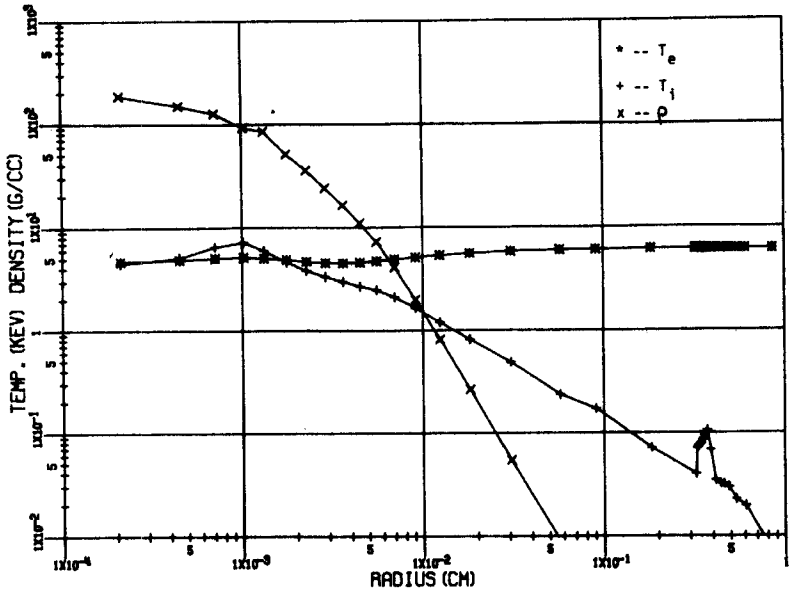

Figure 26 - Temperature and Density @ 29.036 nsec

Fig. IV-C-16.

was done in this calculation but these conditions are very favorable for bootstrap thermonuclear heating and burn propagation.

It must be emphasized that this calculation, characteristic of early laser fusion calculations,[1] is very idealized and is infact physically unrealistic. The major problem is the "dump" model for laser light absorption. At the very high intensities needed to implode a ball of DT, the electrons are heated to temperatures far in excess of those temperatures where inverse bremsstrahlung absorption is efficient. In addition anomalous absorption mechanisms generate non thermal electrons that further degrade the implosion.

In addition to laser absorption problems the energy must be transferred to the ablation surface via electron thermal conduction. This transport process must be well understood in order to maintain the relative position between the temperature front and the ablation surface. It is this positioning of the temperature front at the ablation surface that drives the implosion. In principle the laser pulse can be programmed to provide the correct behavior so long as the heat transport characteristics are well understood. This is not the case at this time because experiments indicate that the thermal conduction may be inhibited by as much as 30-100 times its anticipated theoretical value.[2-4] Such uncertainties must be resolved before the ablation driven isentropic implosion can be achieved.

IV-C-2. Sphere vs. Shell Targets

One method of reducing the sensitivity of the implosion process to the laser pulse shape is to use levitated DT shells rather than spheres. This significantly reduces the maximum laser power needed to implode the target.[5]

The PdV work necessary to implode a sphere requires a maximum P because the dV part (or volume reduction) is minimal. However for a shell there is a great deal of volume reduction and hence the maximum pressure (or equivalently, laser intensity) is much less than for a sphere. Brueckner[6] reports the implosion of a high aspect ratio ($R/\Delta R > 1$) shell using a linear laser pulse. The shell implosion will of course perform better if a shaped laser pulse is used. Typically, more energy is delivered sooner in the pulse for a shell than for a sphere. This results in a very high implosion velocity, which is of course desireable to achieve ignition temperatures.

The basic problem with shell implosions is the Rayleigh-Taylor fluid instability.[7] For very thin shells ($R/\Delta R > 8$) it is predicted[8] that the amplitude of fluid instabilities will grow in magnitude to the size of the shell thickness and break up the shell before it can be fully imploded. This is a very serious problem for laser fusion because highly levitated shell targets offered the opportunity to achieve high gain implosion and thermonuclear burn with laser energies of 1 MJ. Very high aspect ratio shells simulated in one dimensional geometry have been reported to provide gains of 1000.[9] Although much pessimism exists regarding the theoretical stability of these shell targets there is no reported experimental evidence of these fluid instabilities. With the next generation of lasers there should come isentropic implosion experiments and many of these instability questions should be answered.

IV-C-3. Exploding Pusher Targets

The target most often used for laser driven implosion experiments today is the glass microballoon filled with 10-30 atmospheres of DT gas.[10]

This glass microballoon is typically only about 50-75 μm in diameter with a wall thickness of 1 μm. Hence it is a highly levitated shell ($R/\Delta R \sim 30$) with nanogram amounts of DT and glass. These shell targets do not suffer from fluid instabilities because their implosion is not ablatively driven. They operate via the exploding pusher mechanism[11] and consequently their performance is mostly a function of the laser peak power rather than the total energy delivered onto the target. In the exploding pusher mode, the laser energy is delivered to the target in a time that is short compared to the implosion time. The glass shell absorbs the energy and a supersonic conduction wave quickly brings the shell to isothermal conditions. Then on the longer hydrodynamic time scale the shell explodes with about equal amounts of glass traveling inward and outward. The inward flowing glass compresses the DT gas inside and shock heats it (nonisentropic compression) to several kilo electron volts. This combination of moderate compression (to approximately solid density) and relatively high ion temperature provide the greatest number of neutrons for current laser systems. These targets are used because the current lasers are not capable of providing both enough energy to compress the pellet and enough power to implode it to a high velocity to cause central heating. It is suspected that longer, more energetic but lower power pulses, could be used to compress the DT fuel to higher compressions (10-100 times solid density) but the resulting temperature would not be high enough to produce significant amounts of neutrons. The central compression would need to be diagnosed in other fashions such as studying the line emission of impurity dopings in the DT.[12]

There has always been much debate regarding the acceptibility of CO_2 lasers for laser fusion because of their long wavelength, 10 μm. The efficiency of classical inverse bremsstrahlung absorption scales as $(\text{wavelength})^{-2}$. However experiments have shown that inverse bremsstrahlung is not the dominant absorption mechanism. It was also anticipated that the anomalous absorption of CO_2 lasers would generate nonthermal electrons of a higher average energy than Nd laser light and that these would seriously degrade the implosion performance. This hypothesis has not been demonstrated by the experimental evidence though. It might therefore be concluded that the apparent lag in significant CO_2 laser implosion results compared to Nd glass laser results for the current laser systems probably comes from the difficulty of producing high power, short pulses with the CO_2 laser. If this is in fact true there should be a narrowing of the gap between Nd and CO_2 laser results as these laser systems grow in size. At 100 KJ of laser energy there should be enough energy available to drive isentropic implosions and the ultra-short (10-100 psec) pulses will no longer be necessary.

The result of the glass microballoon experiments has been to demonstrate the basic principle of laser driven compression and to achieve thermonuclear reactions. As stated earlier, these target experiments have been optimized to produce the greatest number of neutrons within the constraints of the available laser systems. To do this the maximum achievable compression is sacrificed to provide temperatures high enough to produce significant numbers of neutrons. The highest neutron yields at this time are about 10^9 with the laser energy about 100 J. This is a pellet gain of 3×10^{-5} or 5.3×10^6 times less than is needed for a laser fusion reactor.

IV-C-4. Multishelled Targets

Many laser fusion target designs for near term laser systems involve multi shell construction,[13-14] Fig. IV-C-17. These concentric shells are designed to provide a multiplication of implosion velocity through conservation of momentum.[15-16] When a heavy outer shell collides with a lighter inner shell the velocity is multiplied roughly as the ratio of the shell masses. This effect can be used for longer, lower power laser pulses that would not accelerate a single shell to the necessary implosion velocity of 3×10^7 cm/sec. The low density cushion material between the shells serves to smooth out the momentum transfer as they collide. This is again an attempt to design a pellet that matches the characteristics of available lasers. The efficiency of the double shell implosion is less than a single shell provided the proper laser pulse is available to implode the single shell. This inefficiency makes their scalability to reactor grade performance uncertain.

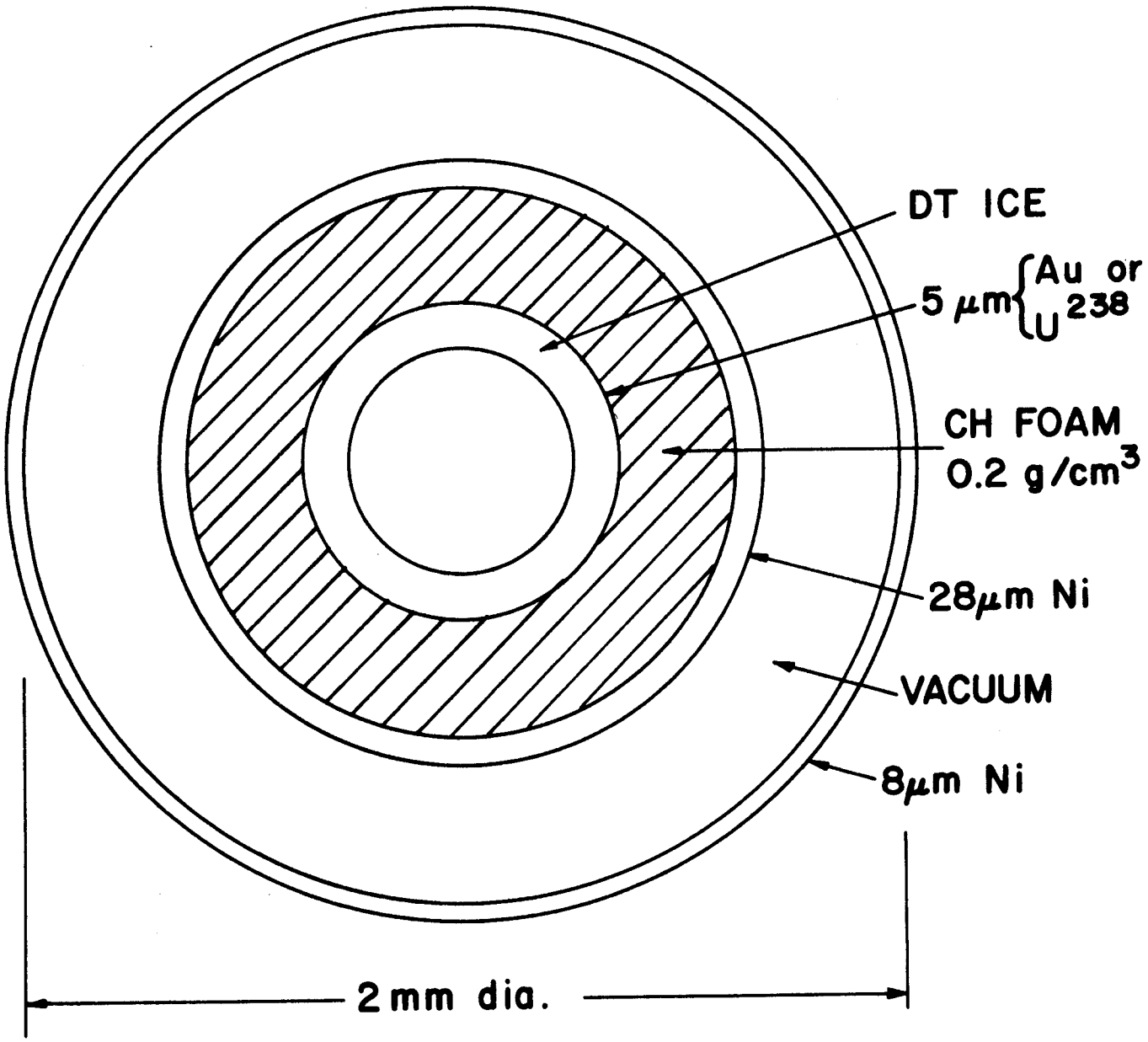

MULTI SHELL LASER TARGET

Fig. IV-C-17.

References for Section IV-C

1. "Laser Program Annual Report," Lawrence Livermore Lab. Report UCRL-50021-74, 394 (1974).

2. Conference on Transport Processes in Laser Produced Plasmas, Mt. Larsen National Park (1976), Acadia National Park (1977).

3. R. Malone, R. McCrory, and R. Morse, Phys. Rev. Lett. 34, 721 (1975).

4. F. Mayer, Proceedings of IEEE Conference on Anomalous Absorption of High Frequency Waves, Ann Arbor, Michigan, 1976.

5. Ref. 1, p. 393.

6. K. Brueckner and S. Jorna, Rev. Mod. Phys. 46, 325 (1974).

7. Lord Rayleigh, Scientific Papers, II, p. 200-207 (Cambridge, England, 1900).

8. R. Kidder, Nucl. Fus. 16, 3 (1976).

9. Y. Afanas'ev, et. al., Nucl. Fus. 15, 119 (1975).

10. G. Charatis, et al., "Experimental Study of Laser Driven Compression of Spherical Glass Shells," Fifth Conf. on Plasma Physics and Controlled Nuclear Fusion Research, 1974.

11. Ref. 1, p. 371.

12. D. Bailey, Conf. on Transport Processes in Laser Produced Plasmas, Acadia National Park, Bar Harbor, Maine, 1977.

13. R. Perkins, "The Laser Program at LASL," LA-77-174.

14. "Laser Program Annual Report," Lawrence Livermore Lab. Report UCRL-50021-75, 264 (1975).

15. R. Mason, Nucl. Fus. 15, 1031 (1975).

16. G. Fraley, et. al., "Implosion, Stability and Burn of Multi-Shell Fusion Pellets," IAEA-CN-33/F5-5, p. 543.

IV-D. Pellet Material Considerations

The compatibility of pellet materials with the first wall and last mirror is a consideration that is important to all conceptual laser fusion reactor designs. At the high operating temperatures of laser fusion reactors there are many troublesome chemical reactions. For instance, in the case of SOLASE, with a graphite first wall, the production of hydrocarbons from hydrogenic species in the pellet dictates the cavity pumping rate. The details of these considerations are discussed in Chapter XVI of this report and will not be introduced here. These problems are important to the pellet design, however, for they place limits on the types and amounts of materials that are allowed in the pellet.

To achieve a yield of 150 MJ the SOLASE pellet design uses a 45% burn-up of 1 mg of DT fuel. The remaining unburned deuterium and tritium represent hydrogen that is available to react with the first wall. Clearly, for SOLASE, it is desirable to limit the amount of hydrogen in the pellet to only the DT fuel. This poses some contradiction to current pellet designs that contain CH_2 or other plastic low Z ablators. To ease the hydrogen isotope separation problem, any hydrogen in the pellet other than the fuel should be deuterium rather than protium.

The most likely approach to reactor style pellet designs will be substitution of acceptible materials for experimentally convenient materials. For instance, a thin layer of gold is often used as a high-Z fast electron shield in current pellet designs. The mass of this gold is most often at least ten times

the mass of the DT fuel. Extrapolated to reactor size pellets, when the DT mass is 1 mg, this represents a consumption of 720 grams of gold per hour. Such quantities of gold are available and affordable; however, the efficiency of the recovery process will determine the fraction of gold that is unrecoverable. Should this fraction be too high, or should the cost of the equipment necessary to recover an acceptible fraction be too high, then the use of a substitute material such as mercury or lead must be considered. In the SOLASE design, low temperature condensates such as lead or gold should be avoided, thus mercury is an obvious choice. A more exotic material that might serve the same purpose is xenon. Xenon can be diffused into the glass or plastic shell along with the 1 mg of DT and when the pellet is cooled to cryogenic temperatures the xenon will freez onto the inside surface of the shell before the DT, thus providing a high-Z layer surrounding the solid DT. However, the Z-value of Xe is only 54 compared to 80 for Hg and 79 for Au; hence, its acceptibility as a pusher-tamper-hot electron shield must yet be verified. If Xe is acceptible then its use reduces the first wall chemical erosion due to carbide formation; however, problems still exist in separating the three noble gas constituents of the exhaust, Ne, He, and Xe. For SOLASE, such pellet materials as iron and nickel must be avoided because they will plate out on the first wall. When high-Z or intermediate-Z material must play a structural role in the pellet design, it might be replaced by a thin glass shell coated with a high-Z material like mercury. Substitutions such as these must be verified using pellet design computer codes and ultimately by experiment.

The ratio of pellet mass devoted to non-fuel materials to the DT fuel mass for several different laser fusion pellets recently reported in the literature are given in Table IV-D-1. The general trend is clearly toward more and more non-fuel pellet material, to alleviate such problems as hydrodynamic instabilities, hot electron and hard X-ray preheat, and fuel tamping. Extrapolated to reactor grade pellets with 1 mg of fuel this trend implies 10-1000 mg of non-fuel materials. Such large quantities per pellet imply that the handling and recovery equipment for non-fuel materials will be an important consideration in the overall fuel cycle. To minimize the complexity of the fuel cycle it is desirable to have as few different materials in the pellet as possible. In addition, the mass of non-fuel materials should be minimized in order to reduce the magnitude of the materials handling equipment. The interaction of non-fuel materials with the first wall and exhaust gas processing equipment is a problem unique to inertial confinement fusion and may prove to be equally as troublesome as the plasma impurity problem in magnetic confinement approaches. Greater emphasis should be given to this problem once pellet designers begin to place more confidence in specific pellet designs that can be analyzed in detail.

Table IV-D-1

Mass of DT and Other Materials in Laser Fusion Pellet

I. Ball and Shell Target*

DT - 0.0388 μg
SiO_2 - 117.3 μg
Au - 10.46 μg
CH - 5.33 μg
H_2 - 0.1 μg

$\frac{\text{OTHER mass}}{\text{DT mass}} = 3432$

II. Vacuum Insulation Target**

DT - 0.83 μg
Au - 36 μg
CH - 154 μg
Ni - 2022 μg

$\frac{\text{OTHER mass}}{\text{DT mass}} = 2659$

III. Glass Microballoon Target***

DT - 1 ng
SiO_2 - 30 mg

$\frac{\text{OTHER mass}}{\text{DT mass}} = 30$

*"Laser Program Annual Report," UCRL-50021-75, p.

**R. Perkins, "The Laser-Fusion Program at LASL," LA-UR-77-174.

***G. Choratis, et. al., Glass Microballoon Experiments, IAEA Tokyo Meeting, 1974.

IV-E. Model Pellet for SOLASE

In addition to the parametric analyses done for first wall protection and fuel cycle for SOLASE it was also desirable to analyze a specific pellet design. This of course is a difficult task if no workable pellet design can be given. However, good estimates of important characteristics for a model pellet can be made. The pellet design chosen for this analysis is shown in Fig. IV-E-1. It consists of 1 mg of DT fuel frozen on the inside of a 2.5 mg glass capsule. It is estimated that 1-2 mg of DT is necessary to produce 150 MJ depending on the fractional burnup. The thickness of the glass capsule is designed to withstand the pressures necessary to diffuse 1 mg of DT into it (see Chapter IX). The glass capsule is surrounded by a mercury layer. For the purposes of computing thermonuclear burn and the resultant X-ray and ion spectra the glass shell is ignored and the mercury mass is varied from 0-100 mg (see section IV-B). A value of 10 mg is chosen as the standard case for purposes of studying the neon filled cavity scheme for first wall protection. Since no implosion calculation is performed, this amount of mercury is simply postulated to vary in density as $1/R^3$ when the DT pellet core reaches ignition conditions at a ρR value of 3 g/cm^2. With the additional ρR added by the tamper, the yield is 232 MJ rather than 150 MJ. However, the total ρR of fuel and tamper can in principle be adjusted to reduce the yield to 150 MJ. The X-ray and ion spectra, Fig. IX-E-2 to 5, for this 10 mg case (with output energy normalized back to a total yield of 150 MJ) are used to compute the effectiveness of the gas protection scheme. Outside of the mercury layer is 2-3 mg of CD_2 to serve as an ablator material during the implosion process.

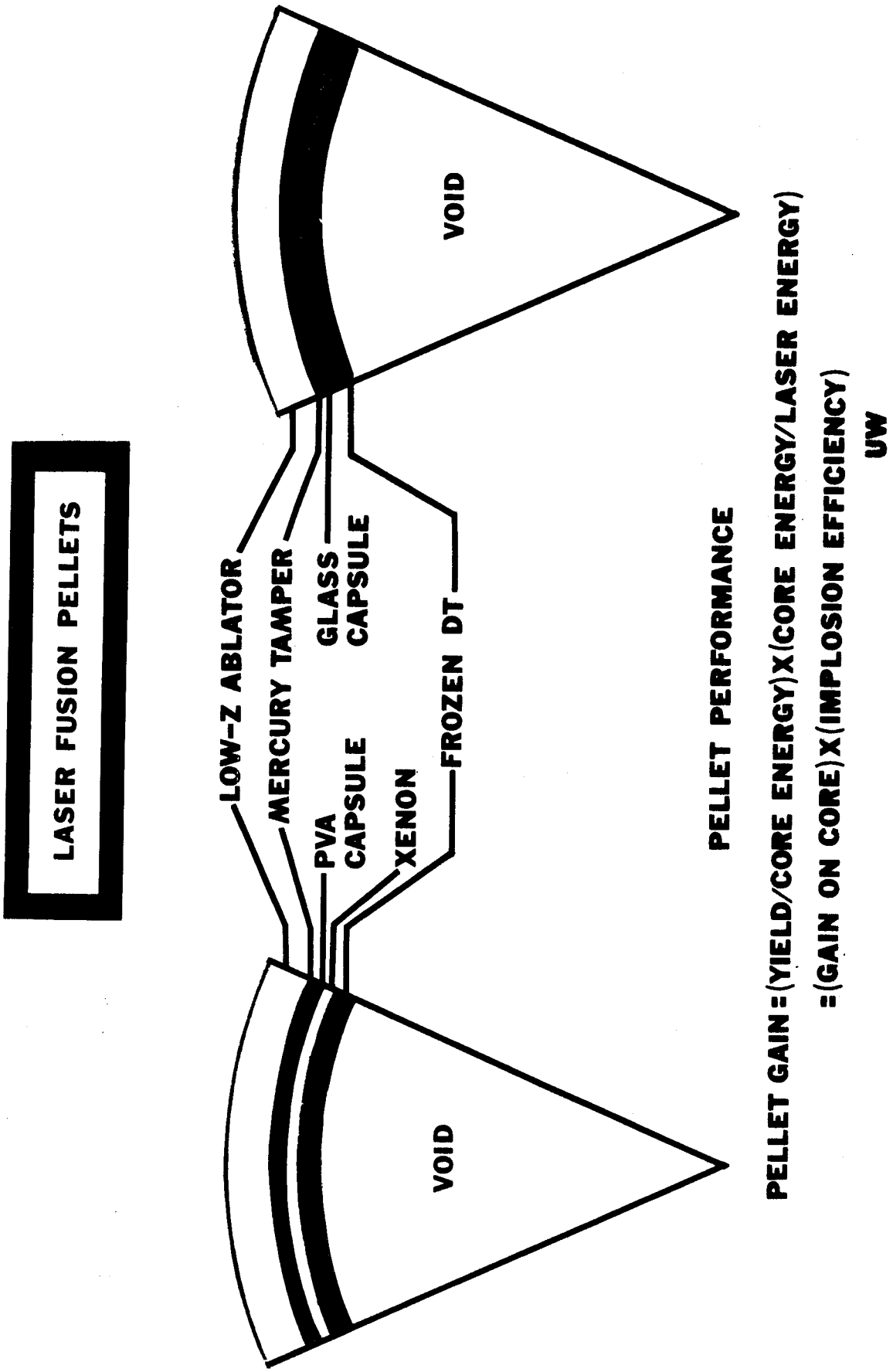
LASER FUSION PELLETS
LOW-Z ABLATOR
MERCURY TAMPER
GLASS CAPSULE
PVA CAPSULE
XENON
FROZEN DT
VOID
VOID
PELLET PERFORMANCE
PELLET GAIN = (YIELD/CORE ENERGY) X (CORE ENERGY/LASER ENERGY)
= (GAIN ON CORE) X (IMPLOSION EFFICIENCY)
UW

Fig. IV-E-1.

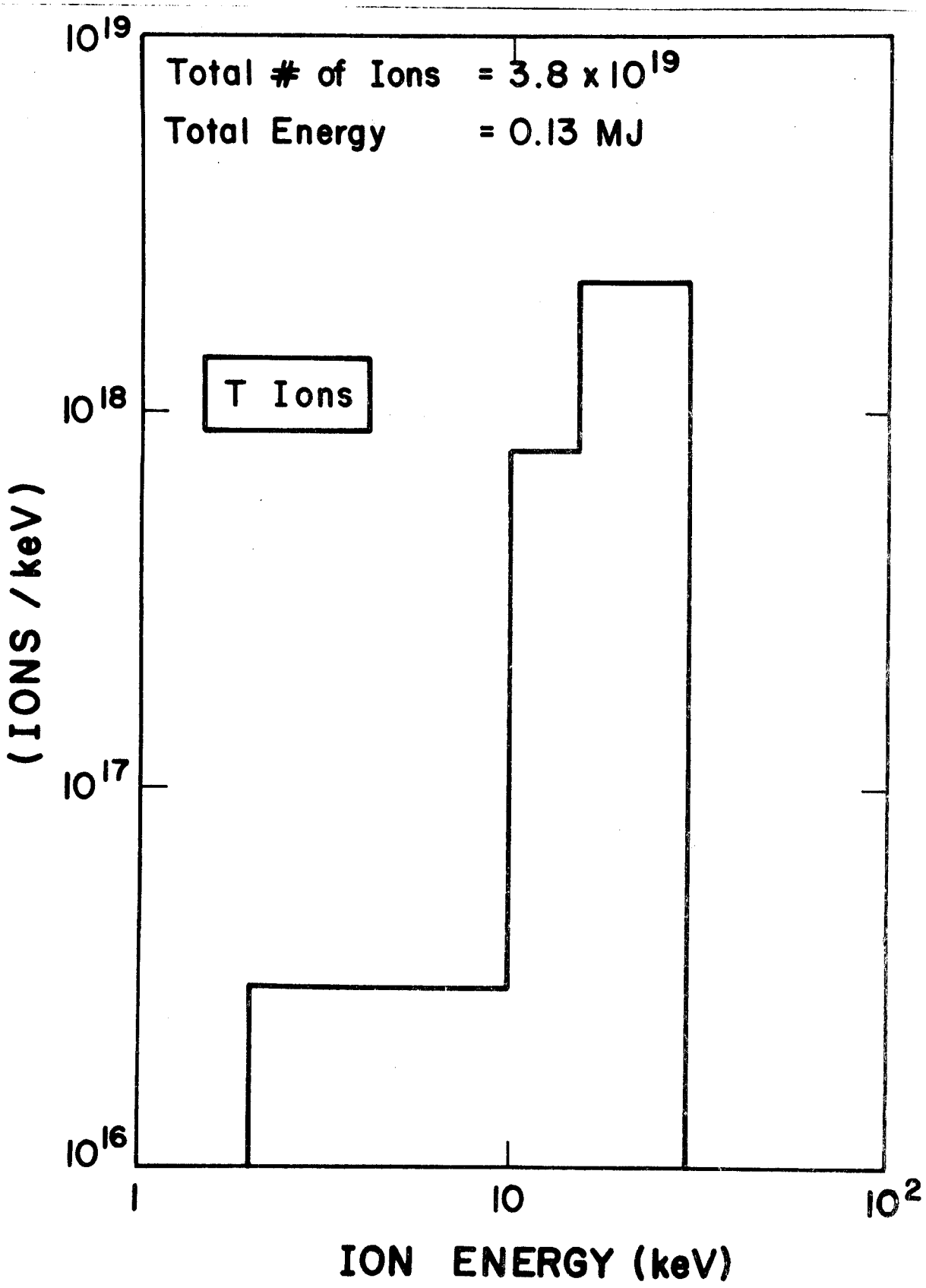
Total # of Ions = 3.8 x 10^19
Total Energy = 0.13 MJ
T Ions
10^19
10^18
10^17
10^16
(IONS / keV)
1
10
10^2
ION ENERGY (keV)

Fig. IV-E-2.

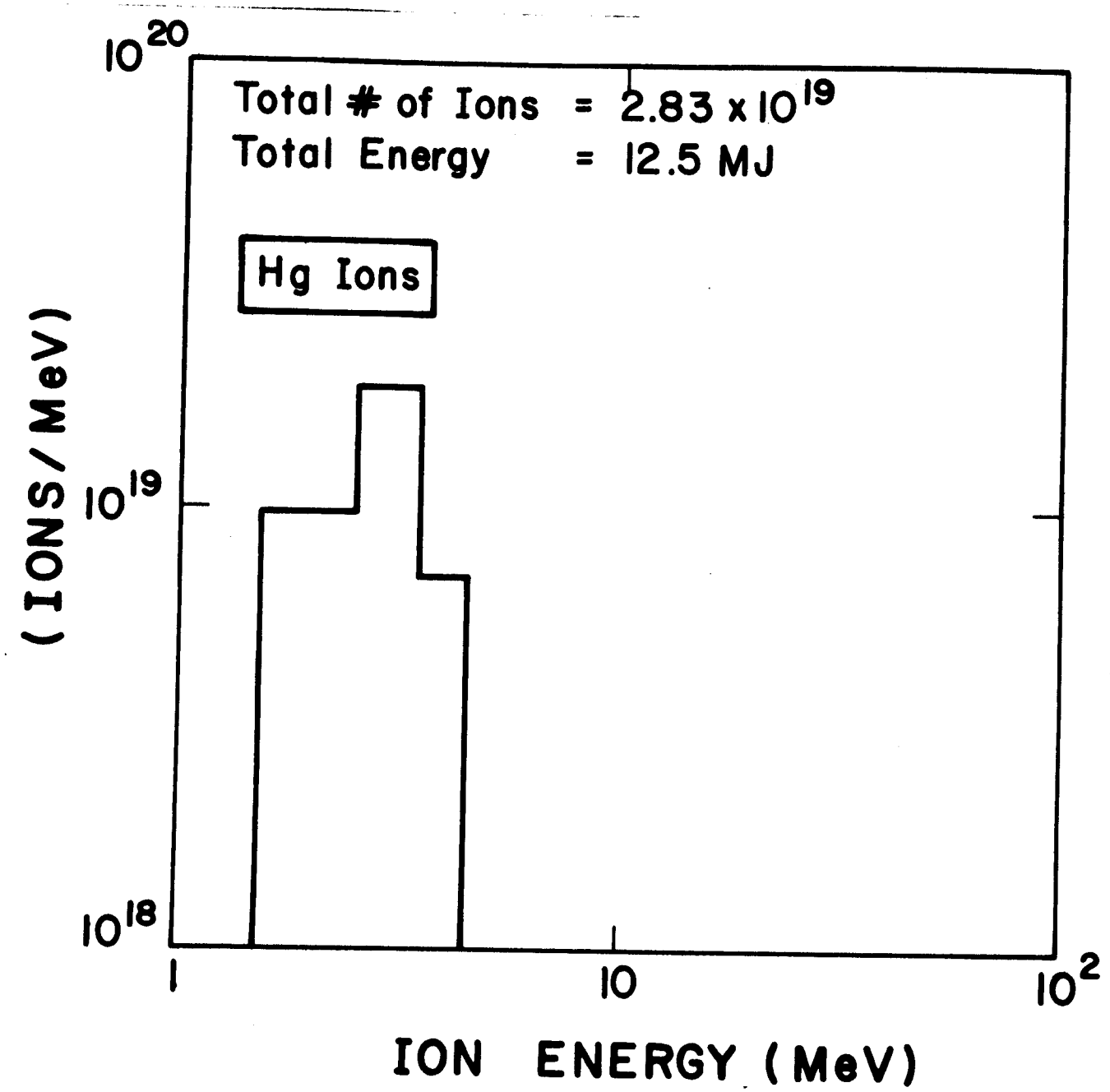
Total # of Ions = 2.83 x 10^19
Total Energy = 12.5 MJ
Hg Ions
10^20
10^19
10^18
(IONS/MeV)
1
10
10^2
ION ENERGY (MeV)

Fig. IV-E-3.

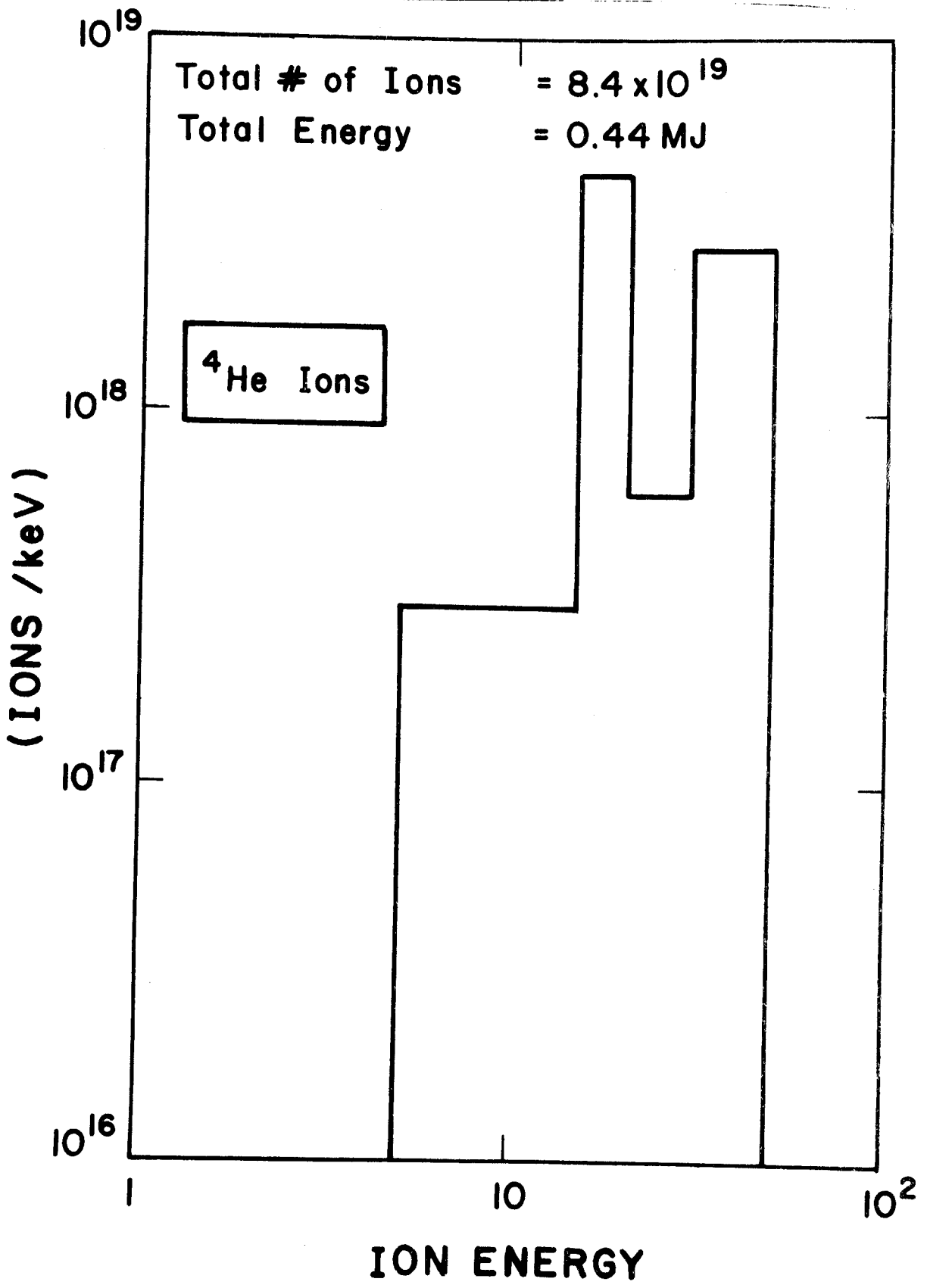
Total # of Ions = 8.4 x 10^19
Total Energy = 0.44 MJ
4He Ions
10^19
10^18
10^17
10^16
(IONS /keV)
1
10
10^2
ION ENERGY

Fig. IV-E-4.

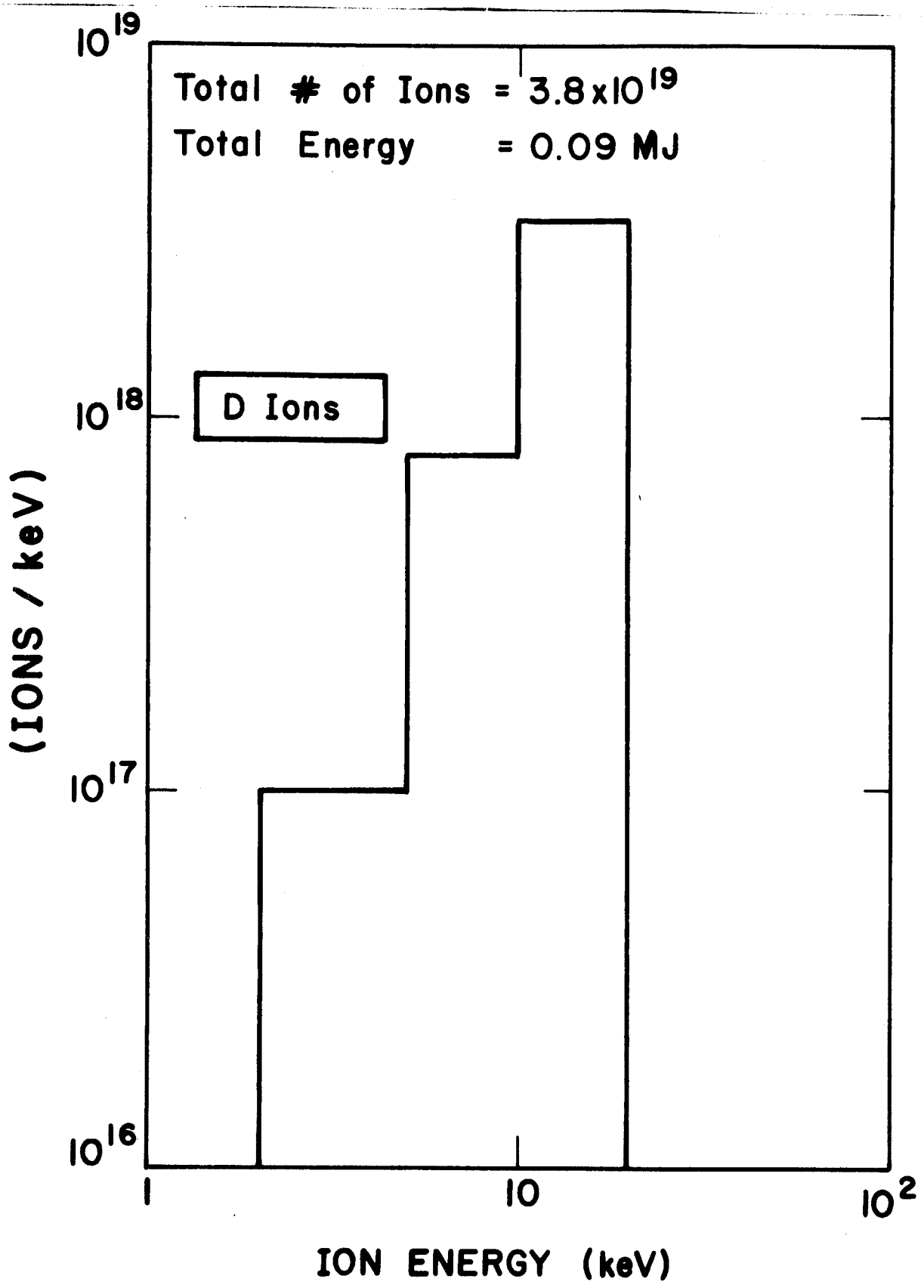
Total # of Ions = 3.8x10^19
Total Energy = 0.09 MJ
D Ions
(IONS / keV)
10^19
10^18
10^17
10^16
1
10
10^2
ION ENERGY (keV)

Fig. IV-E-5.

For the purposes of the fuel cycle analysis, only the quantity of each material in the pellet is necessary. Their exact configuration and role during implosion and burn are not important. The important materials for SOLASE are the hydrogenic species hence the fractional burnup of the DT must be specified. This is chosen to be 45% to be consistent with a 150 MJ yield and 1 mg of DT. The amount of mercury is not critical to the fuel cycle design except to determine the size of the mercury reprocessing equipment. The amount of mercury and its configuration at ignition is very important to the computation of the pellet spectra. The amount of ablator material is also very important to the fuel cycle design if it contains a large fraction of hydrogen. The best situation for the graphite first wall and blanket reactor concept would be a pellet design with no hydrogen except for the DT fuel. However, to postulate such a pellet composition for our model pellet would be totally inconsistent with published pellet designs so CD_2 was chosen as an ablator material.

In conclusion, this model pellet design and analysis is not meant to be totally consistent, but represents an attempt to specify order of magnitude estimates of pellet design characteristics that are important to the detailed design of the first wall and fuel cycle. The problem of laser-plasma interaction and the actual implosion of this pellet are not considered. Remarks concerning this part of the laser fusion problem are in the next section.

IV-F. Feasibility of Achieving Reactor Pellet Performance

Quite simply stated, there is no indication from our analysis or the published literature that single shell pellets can be designed to meet the performance levels necessary for laser fusion reactor applications if 1 MJ lasers with

a 5-10% efficiency are used. This laser efficiency implies pellet gains of 100 to 200. These gains do not seem likely with reasonable laser pulse shapes. Early statements about laser fusion feasibility assumed near isentropic compression of pellets with very carefully shaped laser pulses. It should come as no surprise that very little energy is needed to do work on a system along a reversible path and consequently the pellet gain was large. However, it is very difficult to follow so closely along an isentrope. Very small perturbations in the laser pulse shape degrade the isentropic compression considerably thus requiring more energy to implode the target to the same ρR value. This of course reduces the gain. A related matter is the hydrodynamic implosion efficiency. It is typically about 5% in most ablatively driven implosion calculations and this value is simply too small. Values of 10-20% are necessary to balance the inefficiency due to nonisentropic effects. In addition, the process of laser absorption and thermal transport are complicated by the presence of hot electrons. These electrons can preheat the core and degrade the implosion even further. Experimental evidence shows that only about 50% of the incident laser energy is absorbed hence the useful energy from a 1 MJ laser pulse is thereby reduced to 500 kJ. It is of course the energy source as a function of time that drives the isentropic implosion so the time dependence of the laser light absorption efficiency must be accurately known to predict the laser pulse shape needed to provide the necessary energy source shape. This appears to be very difficult.

In general, under the most optimistic circumstances, the performance of laser fusion pellets will only just meet the requirements for reactor applications. It is highly doubtful that all of these optimistic predictions will be true (many have already been proven false by experiment).

Many of these difficulties could be relieved if high aspect ratio shells proved to be stable when imploded. These targets are less sensitive to the laser pulse shape and require much lower peak laser powers, thus reducing the hot electron problem. The efficiency of laser light absorption remains a problem though. More than 50% of the laser light must be absorbed and this is not the case in experiments today. Recently reported complex pellet designs[1] offer the possibility of achieving gains of 150 or even much more if they prove to be successful. These pellets (Fig. IV-F-1) are really two single shell pellets, one inside the other. The DT fuel is located in two different parts of the pellet. The massive outer shell is imploded at a velocity less than that necessary for ignition and compresses the low density gas between the inner and outer pellet. This compressed gas acts as a spring and subsequently implodes the inner pellet at a higher velocity. The inner pellet implodes, ignites, and burns with a gain of about 50. The exploding inner pellet delivers 10 MJ of X-ray and ion debris onto the inner surface of the outer pellet, thus igniting it. Burn then propagates through the more massive outer shell, providing a total gain of possibly 500. Hence the inner pellet gain of 50 can be multiplied by 10 by "propagating" the burn into the outer pellet where ρR is achieved by more DT mass rather than high compression. This is in fact an implementation of the ideas for high gain pellets given in Section III-G and first reported in the preliminary SOLASE design.[2]

Should such pellet design concepts be only marginally successful they may offer the possiblity of achieving gains of at least 150, (i.e. that which is needed for the SOLASE concept). Should they be highly successful, then their high gain would reduce the laser demands considerably, both in pulse repetition frequency and efficiency.

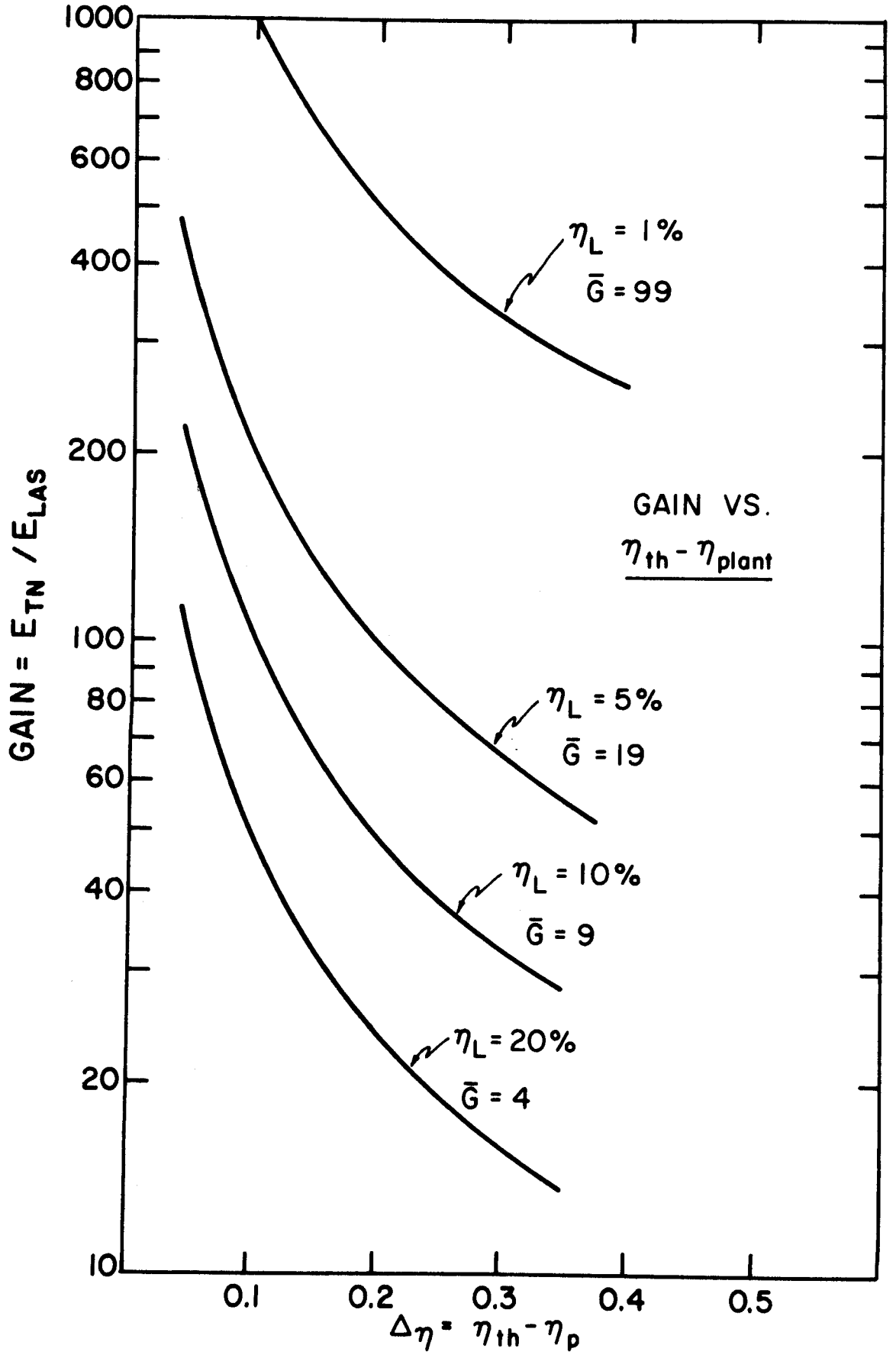
1000
800
600
400
200
100
80
60
40
20
10
GAIN = E_{TN} / E_{LAS}
η_L = 1%
$\bar{G}$ = 99
GAIN VS.
$\eta_{th} - \eta_{plant}$
η_L = 5%
$\bar{G}$ = 19
η_L = 10%
$\bar{G}$ = 9
η_L = 20%
$\bar{G}$ = 4
0.1
0.2
0.3
0.4
0.5
$\Delta\eta = \eta_{th} - \eta_p$

Fig. IV-F-1.

As with the single shell pellets, these double shells have a higher probability of success if the incident energy is large. The maximum gain achievable increases with increasing fuel mass (and hence input energy), therefore the probability of achieving a gain of 100-200 is improved. With more mass the necessary ρR value is achieved with less compression and the pellet becomes less sensitive to nonadiabatic processes. In other words, a 5 MJ laser and yields of 500 MJ are far more likely than a 1 MJ laser and yields of 100 MJ.

References for Section IV-F

1. J. Lindl, "High Gain Targets for Advanced Laser Systems", Bull. Am. Phys. Soc. 22, 1078 (1977).

2. R. Conn, et. al., "Studies of the Technological Problems of Laser Driven Fusion Reactors", University of Wisconsin Report UWFDM-190, II-F-1 (1976)

V. Optics & Illumination Studies

V-A. Laser Fusion Optics

V-A-1. Introduction

The design of a laser beam transport system entails a large number of interrelated decisions. Plasma physics studies of the laser-pellet interaction tell us that about 1 MJ of laser energy and a peak power of 100-1000 TW are needed to achieve a respectable gain.[1] Estimates of the ideal laser wavelength for efficient laser-plasma coupling vary from 2000 Å to a micron or more.[2] Some recent experiments suggest that 10.6 μm radiation may be as effective as 1 μm radiation.[3] Although these uncertainties sometimes give the impression that one is erecting glass castles on quicksand, one may nevertheless explore the advantages and disadvantages of long/short wavelengths from a practical point of view. As concrete values we have chosen 1.06 μm and 10.6 μm for our numerical examples.

Some of the questions we shall address in this section are

- Are mirrors preferrable to lenses?
- How large do the beam apertures have to be?
- How far away should we place the final optical element?
- How many beams are needed?

The principal determining factors to be weighed in answering these questions are uniformity of illumination, damage to optical components, beam quality, diffraction and positioning errors, besides the usual considerations of cost and reliability. In general, we shall find that optical components are cheaper and less susceptible to damage at longer wavelengths, but that there is some disadvantage due to diffraction.

In a conceptual design study such as SOLASE, the amount of detailed calculation is necessarily limited. Thus, many necessary but routine optical components have been noted rather schematically, or not at all. Turning mirrors are represented as 45° lines; polarizers are black boxes, etc. The error budget calculation was omitted in lieu of detailed optical figure and abberation specifications. Expensive physical optics codes have been eschewed in favor of simple geometrical optics calculations.

Instead we have elected to study in depth a few neglected areas. For example, nothing was found in the literature concerning the feasibility of uniform illumination at the large f/nos. appropriate to a reactor. A detailed study was accordingly made of symmetric illumination schemes[4] at moderately large f/nos. (Sec. V-B). The results show little advantage in using twenty rather than twelve beams, with eight beams running a poor third. We also explored the close relationship of net laser light absorption to the illumination geometry(Sec. III-C-3). While refractive energy losses were found to be small, it appears to be difficult to maintain sufficiently small average angles of incidence to assure strong resonance absorption. However, density profile steepening could well alleviate this drawback. Again, a detailed study of nonclassical absorption requiring expensive 2-D codes was deemed beyond the scope of this study.

Another key area we chose to study in depth was the last mirror design, including radiation damage and heating effects. In general we find no deterioration in optical quality at 15 m, provided that the mirror is uncoated. In Section V-C we study the imaging properties of parabolic mirrors, an area about which suprisingly little has been written.

Indeed, all laser fusion design groups seem to rely exclusively on packaged computer codes for calculating the effects of tilt errors on target irradiance. Instead we obtain simple and useful formulas for tilt error bounds and perturbed target irradiance. It should be noted that classical aberration theory does not apply to far off-axis rays. The size and shape of the final paraboloidal mirrors required for SOLASE is determined. The image shape corresponding to a circular incident beam is calculated analytically for large f/no., and is found to be nearly circular, with its centroid shifted a small amount from the optical axis. The effective f/no. is found to be nearly independent of turning angle. Analytic formulas are derived for the "natural" irradiance cast on a spherical target by an unperturbed paraboloidal mirror.

We were particularly interested in the relative merits of 45° and 90° turning angles for our final parabolic mirrors. (135° mirrors are excessively large.) The tilt error bounds turned out to be rather indecisive. On the other hand, 45° mirrors are smaller - and therefore cheaper. The most compelling advantage of smaller turning angles is the smaller caustic surface and concomitant intensity distortion. Indeed, if the caustic intersects the pellet surface, a hot spot would develop. A simple condition is derived for this to occur, based on a new expression for the caustic curve. The final choice of turning angle then depends on one's ability to control tilt errors during the operation of a large scale reactor (See Section V-A-9).

It is fairly certain that if laser fusion works at all, it will utilize some sort of gas phase laser, this being the only kind of laser expected to

achieve a high repetition rate and an efficiency of 10% or better. Limitations on the size of the electric field needed to produce a discharge seems to require annular apertures. Since annular apertures make annular beams, we are led to consider toric optics, which may be either reflective or refractive ("catoptric"). Again reflective optics is preferable, due to ease of fabrication and freedom from self-focusing. While we have not carried out a detailed analysis of the design of the toric optics required to reduce and combine the annular beams used in SOLASE, we have included a calculation of the diffraction spreading produced by a coherent annular beam.

V-A-2. Mirrors Yes, Lenses No

Several limitations dictate against the use of lenses as the final optical elements of a laser fusion reactor. The first of these is the large aperture size demanded by self-focusing and material damage thresholds. While glasses are inherently tougher than metals with respect to surface damage (low absorption), the dielectric coatings needed to reduce the natural 4% surface reflectance of glass are at least as vulnerable as metallic surfaces. Also, large aperture ($r \approx 1m$) aspheric lenses are more expensive than mirrors of comparable size. On the other hand, large aperture diamond-turned mirrors are now routinely fabricated without hand polishing, at moderate cost.[5] At present, diamond-turning looks very favorable for 10.6 μm radiation, and is well under development for 10.6 μm radiation. A more drastic drawback exists with the CO_2 laser, wherein two transitions are simultaneously pumped (to increase the efficiency), so that refractive optics is out of the question.

But by far the most serious objection to the use of lenses is self-focusing. At the anticipated peak powers, the nonlinear optical effects would result in intolerable distortions of the focal region.[6] Mirrors are entirely free of such effects.

Another basic problem with lenses is the change in material properties produced by months of neutron and X-radiation. One cannot actively cool a lens, so that its bulk temperature may be high enough to allow severe swelling as well as substantial changes in the refractive lenses. Worst of all, color center formation will soon render the lens opaque!

V-A-3. Surface Damage Thresholds and Aperture Size

Depending on the particular design parameters, the aperture area may be constrained by the need to avoid surface damage due to large energy fluxes, or by various destructive nonlinear optical effects loosely termed "self-focusing," which occur at large beam power densities.

In a typical laser fusion experiment, one finds scores of dielectric coatings, which currently constitute the weak link in transporting high laser energy fluxes.[7] The lowest damage thresholds seem to occur in polarizers, with AR coatings the next most vulnerable. Damage mechanisms in dielectric films seem to be quite complex, and are presently under intensive investigation.[
Gross failure is caused by avalanche ionization, with multiphoton processes becoming important at smaller λ. Dielectric films suffer deformation due to residual stress and thermal cycling, while the degree of damage depends on various parameters such as substrate roughness, interlayer roughness, residual stress, and standing wave intensity. Lack of quality control in the

manufacturing process often leaves impurities, particulate inclusions and defects in a highly variable degree. Although controlled experimentation is difficult, considerable progress is being made in this area.

For bare metal mirrors, the theoretical damage threshold is limited by surface melting. For a square pulse

$$\Phi = \frac{\sqrt{\pi K \rho C_p}\,(T_m - T_o)\sqrt{t}}{2(1-R)} \quad J/cm^2 \ , \tag{1}$$

where K is the thermal conductivity, ρ the mass density, C_p the specific heat, T_m the melting temperature and R is the reflectivity (wavelength dependent!). The threshold for a copper mirror subject to a 1 nsec CO_2 pulse is about 13.5 J/cm^2 at λ = 10.6 μm, but only 7.43 J/cm^2 at λ = 1.06μm, due to the decreased reflectivity at shorter wavelengths. We shall assume a working value for copper of

$$\Phi_{max} = 5 J/cm^2 \ .$$

(In current CO_2 systems a value of 2-3J/cm^2 is used because of salt window damage.) Silver and aluminum mirrors are less desirable because of their lower melting temperatures. Molybdenum, while possessing an even higher melting temperature, is suitable at λ = 10.6 μm where R = 98%, but fails at λ = 1.06 μm where its reflectivity drops to only 58%. Attempts to enhance the reflectivity by dielectric coatings have generally been frustrated at high powers by the failure of the coatings themselves.

Defining a spatial <u>fill factor</u>

$$ff = \frac{\langle \Phi \rangle}{\Phi_{max}} \ , \tag{2}$$

we can calculate the total beam area needed to handle a given total laser energy E_L:

$$A_{TOT} = \frac{E_L}{\langle\Phi\rangle} = \frac{E_L}{ff\ \Phi_{max}} \quad . \tag{3}$$

Uniform Illumination

The illumination studies described in Section V-B show that uniformity is optimal for the cubic exponential beam profile

$$\Phi_L = \Phi_o\ e^{-(r/a)^3} \quad , \tag{4}$$

with a = 0.7. Here the beam radius r is measured in units of the maximum beam radius and Φ_o is the value on axis. The resulting fill factor is ff = 0.43, which for E_L = 1 MJ yields a total aperture area $A_{TOT} = 4.66 \times 10^5$ cm^2. Setting $A_{TOT} = N\pi R_M^2$ (N beams) we obtain the following table:

	uniform	nonuniform
N	R_M(cm)	R_M(cm)
6	158	115
8	136	99.7
10	122	89.2
12	111	81.4
16	96.5	70.5
20	86.3	63.1
24	78.8	57.6

Table V-A-1

Our optimal illumination studies suggest that at least 12 and possibly 20 beams are needed to achieve 90% uniformity on target, indicating beam radii in the range 86-111 cm. (The actual beam radius can be somewhat smaller since it strikes the mirror at an angle).

Nonuniform Illumination

In this mode, precise beam tailoring is not necessary. We want instead to maximize the fill factor. Using the "top-hat" profile

$$\Phi_L = \Phi_o \, e^{-(r/a)^p} \tag{5}$$

with p = 5 and a = 1, we find ff = 0.8. An 80% fill factor seems a reasonable goal in the presence of beam loss due to Fresnel diffraction and nonlinear effects in whatever glass is present in the system. Again taking E_L = 1 MJ and Φ_{max} = 5 J/cm^2 we find $A_{TOT} = 2.5 \times 10^5$ cm^2. The resulting aperture sizes are listed in Table 1 alongside the values for uniform illumination. Here we see an immediate advantage to non-uniform illumination; fewer beams can be used (6 or 8) at the same aperture area.

V-A-4 Self-Focusing

Most amorphous materials suffer an increase in refractive index with increasing laser intensity, so that a plane wave whose intensity decreases radially will eventually collapse on itself, as shown in Fig. V-A-1. This is called whole-beam self-focusing[6], and occurs in Nd:glass at about 10^{10} W/cm^2. In general, the onset of whole beam self-focusing may be anticipated by means of the "B-integral",

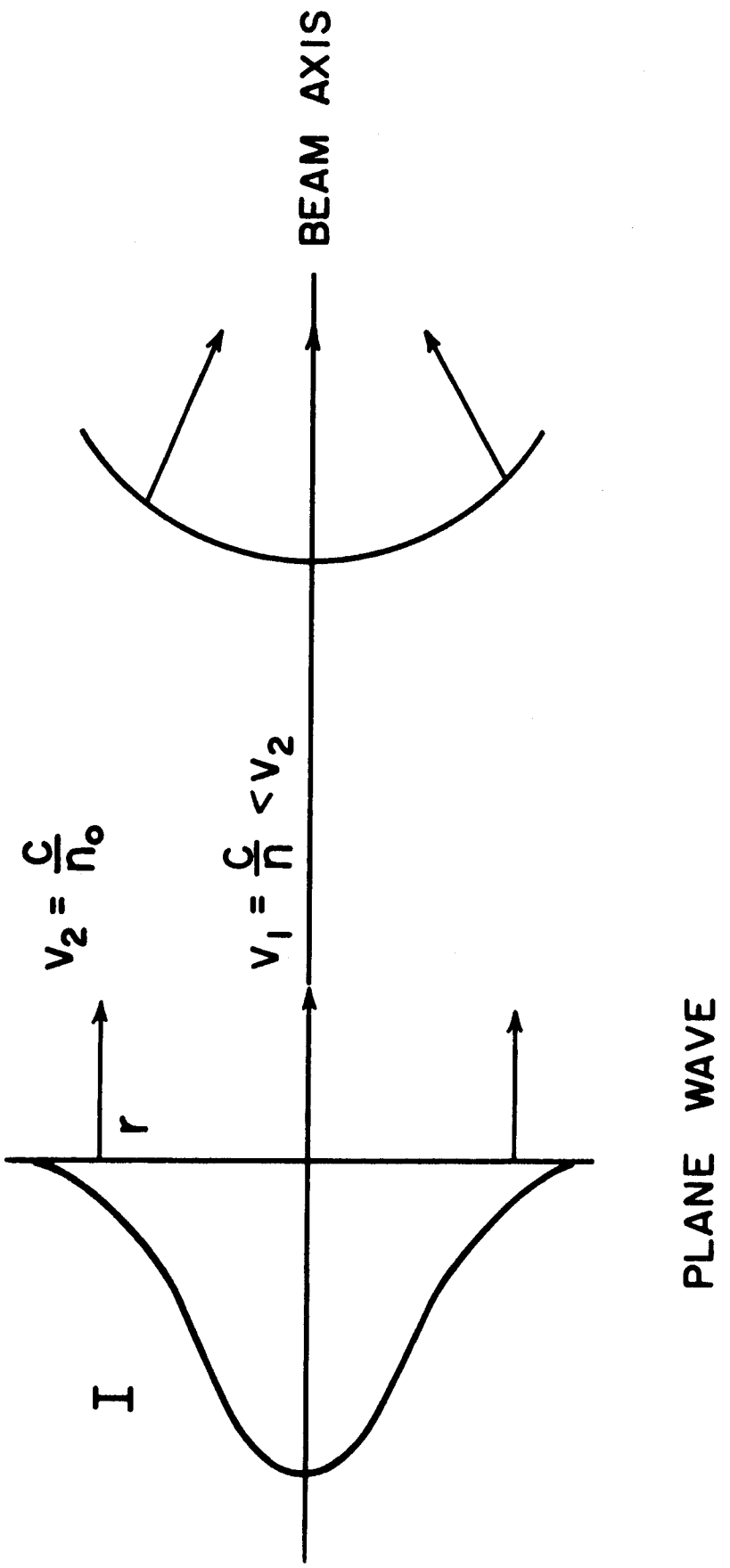

FIGURE V-A-1

$$B = \frac{2\pi}{\lambda} \int \frac{n_2}{n} \langle E^2 \rangle \, d\ell \quad , \tag{6}$$

where λ is the vacuum wavelength, and n_2 is the nonlinear part of the refractive index

$$n = n_0 + n_2 \langle E^2 \rangle \quad . \tag{7}$$

The time averaged field is related to the beam intensity via

$$\langle E^2 \rangle = \frac{4\pi}{nc} \Phi \, . \tag{8}$$

A related nasty phenomenon is small-scale self-focusing,[6] which is the exponential growth of tiny ripples into fiercely intense filaments. While the mathematical theory is more complicated in this case, it turns out that the growth rate of the most unstable (spatial) mode is given by eq. (6). In practice one finds damage due to small-scale self-focusing for beam fluctuations of 5-10 GW/cm^2. Such ripples may arise from Fresnel diffraction at any of the many apertures in a laser chain, from dust on optical surfaces, or particulate inclusions. Self-focusing can also produce serious nonlinear beam divergence, with attendant loss of beam energy. Diffraction rings may be minimized by the use of semi-opaque "soft apertures", as well as by pinhole filters, at the expense of some energy loss. Both large- and small-scale self-focusing are now well understood theoretically; such calculations form an essential part of the design of any high-power laser system. While most present-day systems are limited to about a terawatt per beam, larger peak powers can be handled by means of larger apertures.

Even in a gas laser a certain amount of refractive material is unavoidable, for example in windows, spatial filters and Faraday rotators. In this case we can use the B-integral to derive an upper bound for the maximum length of refractive material in the system.

To avoid whole-beam self-focusing it is required that

$$B < 4\pi \quad , \tag{9}$$

and to avoid small-scale self-focusing the more stringent condition

$$B < 2\pi \tag{10}$$

must be obeyed.[6] Suppose we have a peak power P_{max} and a total aperture area A_{TOT}. Then

$$\Phi = \frac{P_{max}}{A_{TOT}} = \frac{nc \langle E^2 \rangle}{4\pi} \quad . \tag{11}$$

Thus, to avoid small-scale focusing, we require as an upper bound (ignoring gain and changing beam area as we proceed down the laser chain),

$$\frac{8\pi^2 n_2 \ell P_{max}}{\lambda N c A_{TOT}} < 2\pi \quad . \tag{12}$$

Taking $n = 1.5$, $n_2 = 5 \times 10^{-14}$ esu, $\lambda = 1$ μm and $P_{max} = 10^{15}$ W $= 10^{22}$ ergs/sec gives

$$\ell / A_{TOT} < 7.2 \times 10^{-4} \text{ cm}^{-1} \tag{13}$$

Thus, if $A_{TOT} = 2.5 \times 10^5$ cm^2 (nonuniform illumination),

$$\ell_{max} = 179 \text{ cm} \quad , \tag{14}$$

and if $A_{TOT} = 4.7 \times 10^5$ cm^2 (uniform illumination),

$$\ell_{max} = 336 \text{ cm} \quad . \tag{15}$$

These are to be interpreted as absolute upper bounds on ℓ. As a check, note that Φ at the exit aperture is 4 GW/cm^2 and 2.15 GW/cm^2, for nonuniform and uniform illumination, resp., just below the "threshold" of 10 GW/cm^2. These numbers show that in this case, providing an aperture large enough to prevent surface damage automatically takes care of self-focusing problems, allowing up to a few meters of low-n_2 glass in the system.

V-A-5 The Case Against Uniform Illumination

Most pellet designs in the current literature require 90-95% illumination uniformity in order to avoid the Rayleigh-Taylor instability of the inwardly accelerating ablation surface. In section V-B we describe the beam optics requirements to achieve such high uniformity. We show here that while high uniformity is feasible in a research facility, the very different geometrical constaints inherent in a reactor design make uniform illumination unlikely. First, with 12 or 20 beam illumination, the small solid angle alloted to beams in a reactor leads to angles of incidence on the pellet in excess of 40°. At such angles, laser energy absorption drops precipitously.

Another difficulty arises in controlling the spatial beam profile. While high frequency noise may be spatially filtered, grosser structure may not. The results of section V-B show that precise beam tailoring is needed to achieve high uniformity. Further, accurate beam overlapping is limited by the pointing errors of the many optical elements. Moreover, even if the illumination were perfect, the target itself cannot be projected into the focal volume to within about 100 μm. The three-dimensional effects of targetting errors are difficult to estimate. However, a back-of-the-envelope calculation gives $\delta\Phi/\Phi \approx -2\delta r/r \approx 20\%$, unacceptably large. In conclusion, uniform illumination is impractical in a reactor situation, where many beams are required to hit a rapidly moving small target from some 15 m distance. In a research experiment stationary targets are irradiated by beams located closer to the target, with much longer times available for alignment.[9] Nevertheless, it would seem difficult to produce the carefully manicured beam profiles needed for high uniformity.

V-A-6 Thermal Distortion

In Section V-A-3 we saw that the maximum energy density on a bare metal mirror is limited by surface melting. For longer pulse widths, however, thermal distortion can play a dominant role, especially when the optical train contains many components.[10,11] As SOLASE has many more mirrors than windows, we shall give details for mirrors only. Physically, distortion of a mirror surface (and thence the wavefront) is due to two effects; bowing of the hot surface layer relative to the cool, stationary underlayer; and differential thermal expansion due to the spatial beam profile. In windows, the wavefront distortion arises from differences in optical path length through the laser heated material. Although only bulk heating occurs, the cool rim of the window constrains the hotter center, causing it to bulge.

As a consequence of wavefront distortion, the on-axis irradiance will be reduced by

$$\frac{\Delta I}{I} = \left(\frac{2\pi}{\lambda}\right)^2 \sigma^2 , \qquad (16)$$

where σ is the rms wavefront error. Following Bennett, we adopt the Maréchal criterion $\sigma \leq \lambda/14$, thus limiting the on-axis reduction to 20%. For a train of N perfectly figured mirrors receiving equal irradiance, the Maréchal criterion leads to the following limiting flux density;

$$\Phi_{TD} = \frac{\rho C_p \lambda}{2\sqrt{10}\,\pi\, N(1-R)\alpha\, (1+3\chi+3\chi^2)^{1/2}} , \qquad (17)$$

where, for copper, ρ = 8.993 g/cm^3, Cp = 0.3851 J/gm/^{o}K, α = 16.8 x 10^{-6}/^{o}K and

$$\chi = \sqrt{\pi}\left(\frac{R_M}{d}\right)^2 , \qquad (18)$$

and where R_M and d are the mirror radius and thickness. At λ = 10.6 μm, $1 - R = 8.7 \times 10^{-3}$ giving (R_M = 1.5 d, N = 5)

$$\Phi_{10.6} = 86.2 \text{ J/cm}^2 .$$

However, at λ = 1.06 μm, $1 - R = 15 \times 10^{-3}$, reducing the threshold to

$$\Phi_{1.06} = 4.73 \text{ J/cm}^2$$

Inclusion of figure errors can reduce these values to the point where the Maréchal criterion cannot be met at any energy density. Figure V-A-2 shows the Bennett limits for a train of 5 copper mirrors along with the surface melting thresholds. Thus, for CO_2 lasers, surface melting is the determining factor for pulses shorter than 40 nsec, but thermal distortion would appear to be the limiting effect down to 400 psec for Nd-glass lasers.

These thermal distortion thresholds should be taken as indicative and not accurate representations of the SOLASE design. They are meant only to emphasize the potential severity of thermal distortion vis a vis target illumination. The honeycomb structure of the SOLASE mirror should afford sufficient stiffness to raise the thresholds above the surface melting values. This point will be investigated further in the coming months. It may also be possible to coat some of the mirrors in the train sufficiently far from the chamber that the neutron fluence will not render the dielectric coatings opaque. We are also investigating the effect of non-square pulse shapes on damage thresholds.

In conclusion, we have seen that thermal distortion can be a very serious problem at shorter wavelengths and larger pulse widths.

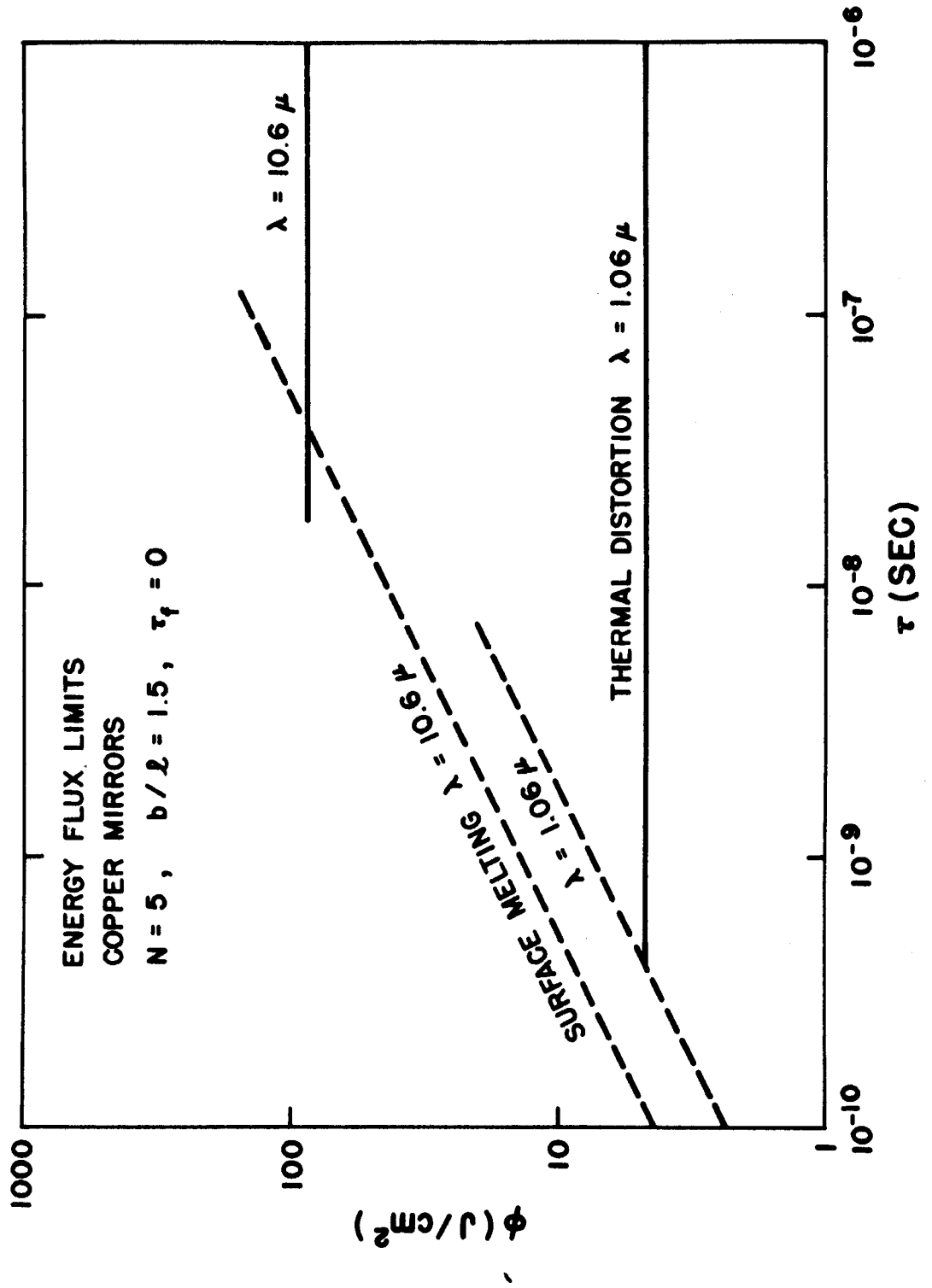
ENERGY FLUX LIMITS
COPPER MIRRORS
N = 5 , b / ℓ = 1.5 , τf = 0
λ = 10.6 μ
λ = 1.06 μ
SURFACE MELTING λ = 10.6 μ
λ = 1.06 μ
THERMAL DISTORTION λ = 1.06 μ
1000
100
10
1
φ (J/cm²)
10⁻⁶
10⁻⁷
10⁻⁸
10⁻⁹
10⁻¹⁰
τ (SEC)

Fig. V-A-2.

V-A-7. Location and Protection of Final Mirrors

High quality bare metal mirrors are so delicate that they can be rendered useless by breathing on them.[12] This statement graphically illustrates the point that protection of the final mirrors in a reactor environment is a nontrivial problem deserving considerable thought. Our first impulse is to put them as far away from the action as possible. Fig. V-A-3 depicts one possible scheme.[13] This is more readily accomplished in the case of nonuniform illumination, the distance being limited only by diffraction and pointing errors. Uniform illumination places constraints on the f/no. so that apertures must go up proportionally as distance is increased. Cost and manufacturing difficulty of large aperture mirrors then become the limiting factors.

The final mirror surfaces will be directly exposed to X-rays, neutrons and secondary gamma-rays, and possibly macroscopic debris from imperfect implosions, as well as the laser itself. Charged particles and charge-exchange neutrals will be effectively stopped by the buffer gas, as shown in Sec. XI-B-6. The hot neon or xenon buffer gas will be kept away from the mirrors by maintaining a net inward flow of fresh gas from inlets located near the mirrors, toward the suppression chamber. The buffer gas also attenuates the X-rays to the point where the mirror surface temperature rise is less than 100°C, as described in detail in Sec. XI-B-6.

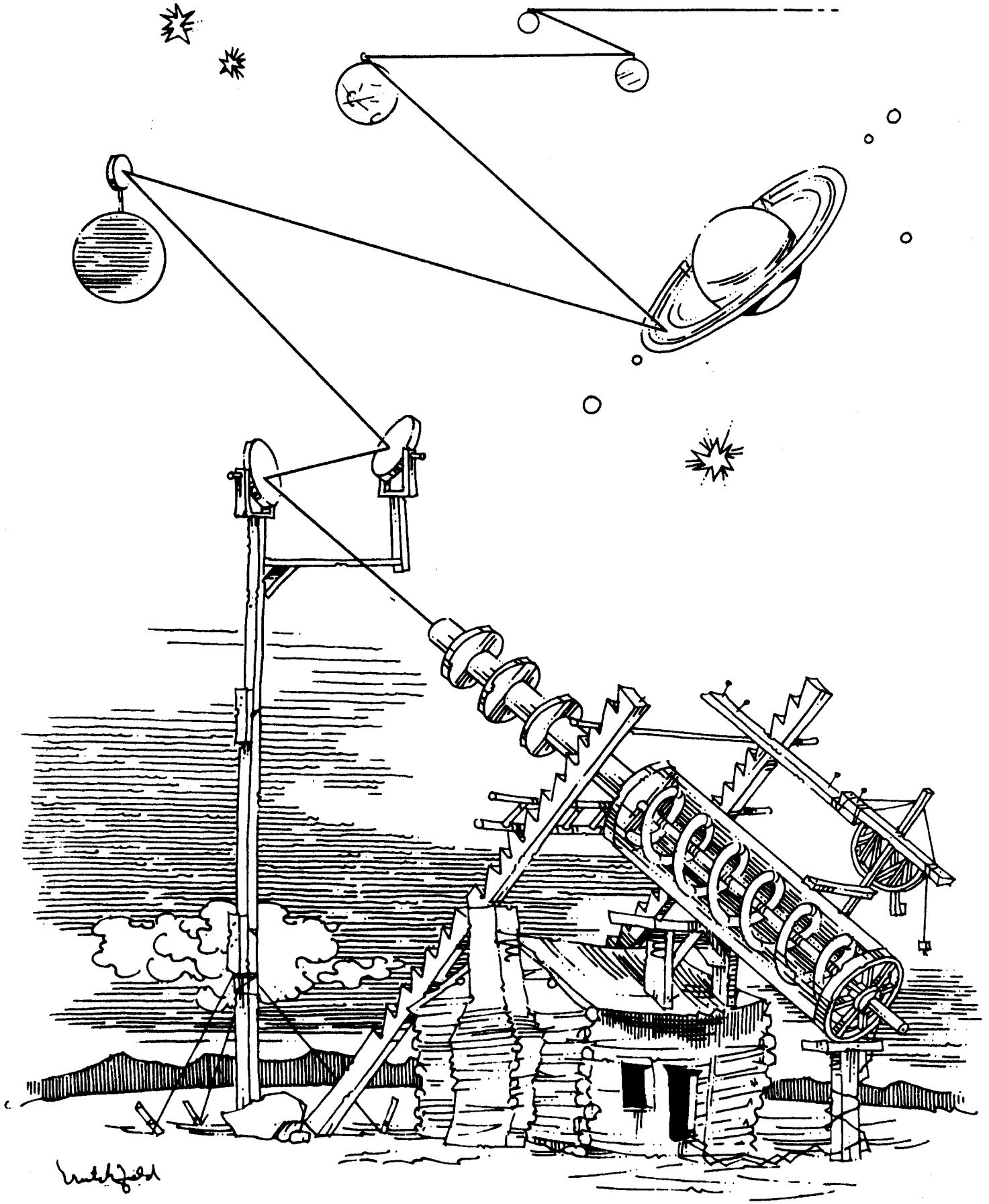

FIGURE V-A-3

V-A-8. Diffraction at an Annular Aperture

The aperture size of a gas laser amplifier is limited by the voltage required to produce the requisite electric field. A typical value for CO_2 is 40 cm, too small to produce the beam energy needed for SOLASE. This problem is customarily solved by the use of annular apertures of aspect ratio $\varepsilon \equiv r_1/r_2 \simeq 0.8$. In SOLASE these beams are reduced and combined to yield almost circular beams (actually low aspect ratio annuli). We demonstrate here the hazards of handling high aspect ratio annular beams and the folly of trying to focus them.

Figure V-A-4 depicts light focused onto a screen at distance L from an annular aperture of inner and outer radii r_1 and r_2. By Babinet's superposition principle,[14] the field due to the annular aperture is the difference between that produced by a disk of radius r_2 and one of radius r_1. The resulting irradiance in the far-field region is

$$I(y) = \frac{I_{max}}{(1-\varepsilon^2)^2}\left[\frac{2J_1(t)}{t} - \varepsilon^2\frac{2J_1(\varepsilon t)}{\varepsilon t}\right]^2 , \qquad (19)$$

where I_{max} is the on-axis irradiance and $t = 2\pi r_2 y/\lambda L$. Eq. (19) is valid in the focal region of a lens. In the absence of focusing the Airy-type pattern is obtained only if $t \ll y/r$. We shall assume the presence of a lens of f/no. $F = L/2r_2$ in what follows.

The on-axis focal irradiance is related to the (uniform) aperture irradiance I_0 by

$$I_{max} = \frac{\pi^2 r_2^2}{\lambda^2 L^2}(1 - \varepsilon^2)^2 . \qquad (20)$$

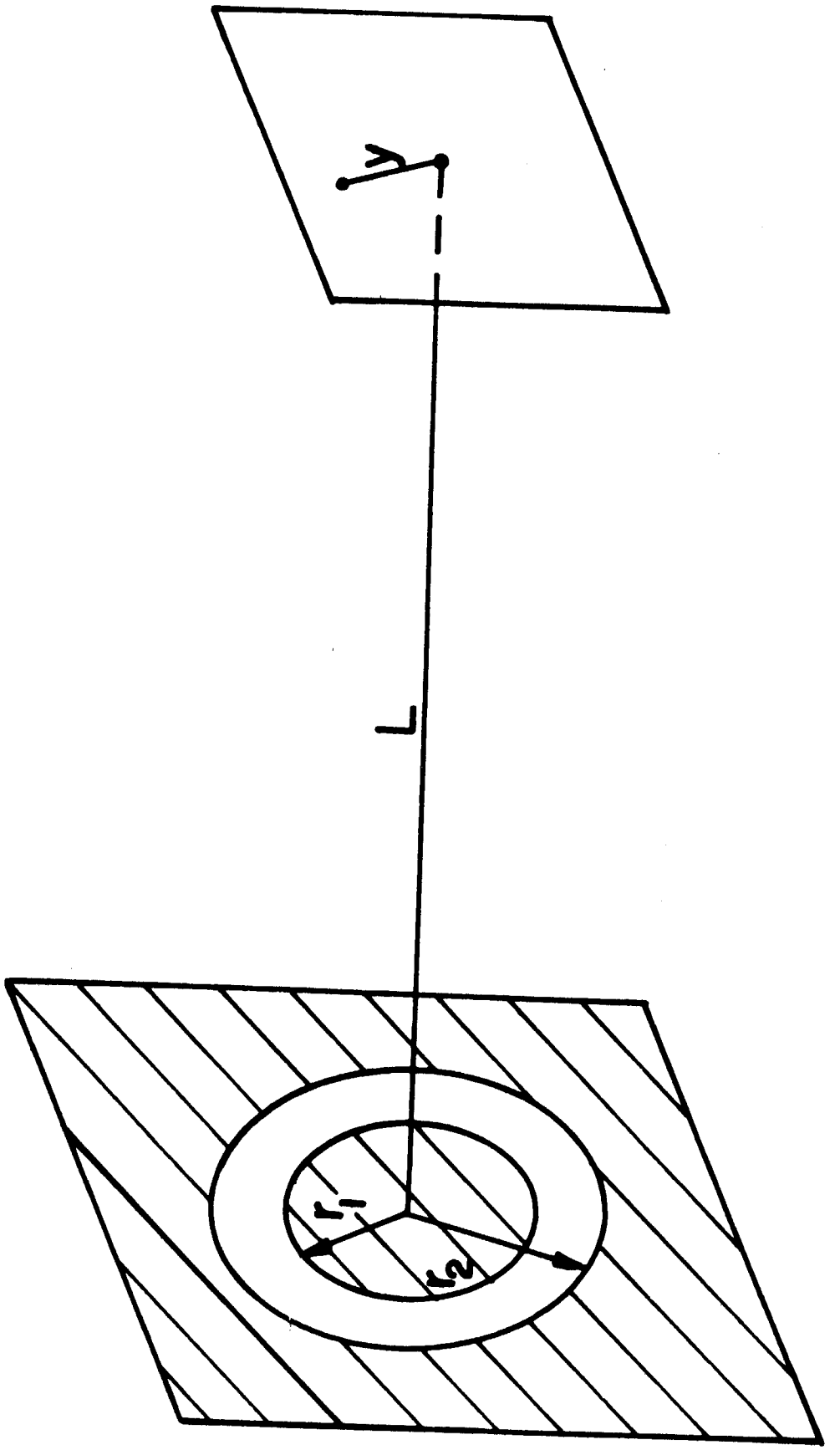

FIGURE V-A-4

When $r_1 \to 0$ the familiar Airy pattern is recovered. The "spot size" is customarily defined by the location of the first minimum,

$$y_o = 0.61 \frac{\lambda L}{r} \tag{21}$$

enclosing 83.8% of the beam power. We have chosen a reference parameter set λ = 10.6 μm, r_2 = 1 m, and L = 10 m corresponding to an f/5 lens. This gives a spot size y_o = 60 μm, which is adequate for illuminating 2 mm radius targets. Other parameters (except ε) may be represented by a simple scaling of this reference case.

Figure V-A-5 shows I(y) for ε = 0, 0.5 and 0.75. Note that the central maxima decrease and narrow with increasing ε. A more useful way of measuring the focusability of these beams is the integrated power contained within a specified radius. This quantity is plotted in Fig.V-A-6. for various ε. Clearly, in order to focus a reasonable amount of power on 2 mm radius pellets, an aspect ratio of no more than 0.75 can be used.

In practice large gas amplifiers are constructed of individual angular segments,[15] so that coherence may be lost between different portions of the annulus. In this case the ideal diffraction model presented here would not apply.

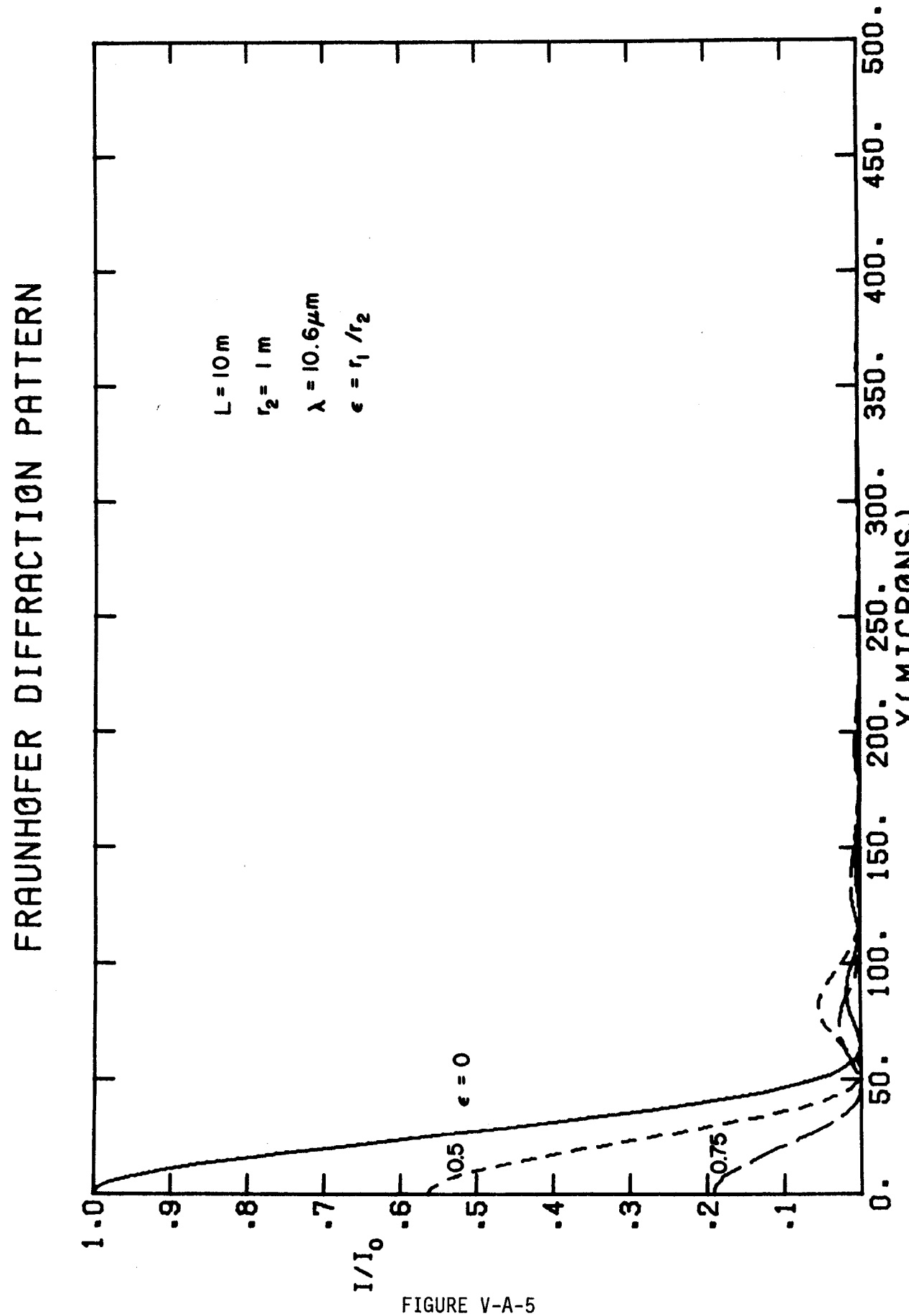
FRAUNHOFER DIFFRACTION PATTERN
L = 10 m
r_2 = 1 m
λ = 10.6μm
ε = r_1 / r_2
ε = 0
0.5
0.75
I/I_o
1.0
.9
.8
.7
.6
.5
.4
.3
.2
.1
0.
50.
100.
150.
200.
250.
300.
350.
400.
450.
500.
Y(MICRONS)

FIGURE V-A-5

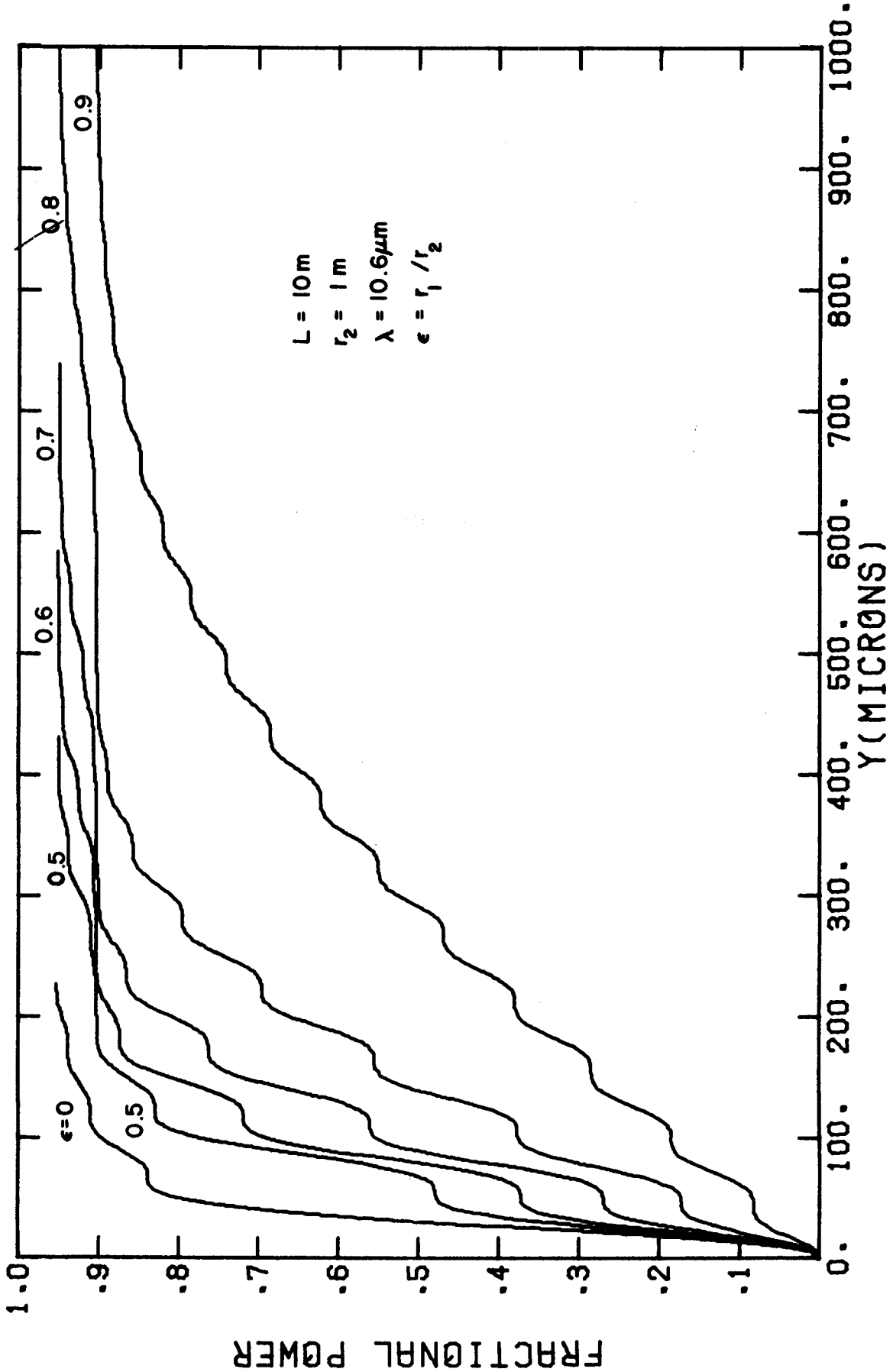
FRACTIONAL POWER
1.0
.9
.8
.7
.6
.5
.4
.3
.2
.1
0.
100.
200.
300.
400.
500.
600.
700.
800.
900.
1000.
Y(MICRONS)
L = 10m
r_2 = 1 m
λ = 10.6μm
ε = r_1 / r_2
ε=0
0.5
0.5
0.6
0.7
0.8
0.9

FIGURE V-A-6

V-A-9 Pointing Errors

Many optical surfaces have to be in near-perfect alignment in order to illuminate the very small target pellet. Further, many degrees of freedom must be actively controlled in directing 12 or more beams to the target. While we have not attempted to construct a complete error budget, we may nevertheless assess the demands on the final mirrors placed by target size and focal distance. Present day experience indicates that large-aperture mirrors may be controlled to about 1 μrad.[9]

From Section V-C-4, the mirror pitch angle must be controlled to within

$$\delta\phi < \delta\phi^* = \frac{R_T \sin\alpha}{2r_o},$$

where r_o is the focal length and α measures angular position on the pellet. Taking R_T = 2 mm, r_o = 15 m and $\alpha = 30°$, we find $\delta\phi^*$ = 33 μrad. However, it must be remembered that several surfaces, say N, are involved so that if N = 10, $\delta\phi^*$ is reduced by $\sqrt{N}$ to about 10 μrad. This is still above the "practical" value of 1 μrad quoted above. In one design,[16] a focal length of r_o = 100 m is called for. This leads to $\delta\phi^*$ = 5 μrad, now within a factor of two. Surely when a complete error budget is calculated, including targetting errors, such large focal lengths will prove to be impractical.

V-A-10 Consequences of Laser Wavelength Choice

It is useful and instructive to list all of the areas affected by the choice of laser wavelength.

V-A-10-a Laser-Plasma Coupling

Inverse bremsstrahlung absorption goes as λ^{-2}, strongly favoring shorter wavelengths. However, for fixed plasma density scale height, resonance absorption is maximized at larger angles of incidence for larger λ.

V-A-10-b Corona-Core Coupling

The critical radius is smaller for shorter λ, predicting more efficient corona-core coupling. However, the recent experiments of Giovanelli et al.,[3] cast doubt on the merits of shorter wavelengths. Theoretical estimates of the ideal wavelength range from 2000 Å to several microns.

V-A-10-c Rayleigh-Taylor Instability

Implosion symmetry seems to improve with increasing critical radius and hence with increasing λ.

V-A-10-d Self-Focusing

All other things being equal, the threshold power for self-focusing goes as λ, favoring long wavelengths. Thus, self-focusing is usually not a problem in CO_2 systems.

V-A-10-e Gas Breakdown Threshold

When a buffer gas is used in the target chamber, it is desirable to avoid breakdown if possible. From Sec. XI-B-5, the threshold intensity for breakdown goes as λ^{-2}, strongly favoring shorter wavelengths. Self-defocusing in the partially ionized beam is also more serious at longer wavelengths.

V-A-10-f Diffraction

As was shown in Sec. V-A-8, diffraction beam loss can be a problem at longer wavelengths. In general, beam spreading $\sim\lambda$.

V-A-10-g Optical Surface Requirements

In general, mirrors must be figured to $\lambda/4$, obviously easier (and cheaper!) at longer wavelengths. While inexpensive large aperture mirrors are routinely produced by diamond turning for λ = 10.6 μm, the state-of-the-art is less advanced for wavelengths below 1 μm.

V-A-10-h Mirror Surface Damage Thresholds

From Sec. V-A-3, the limiting flux density (W/cm^2) is proportional to λ^P, again favoring longer wavelengths.

V-A-11 Mirror Mechanical Design Considerations

One of the important structural characteristics for the mirrors is a high ratio of flexural stiffness to weight in order to minimize transverse deflections and slope changes. Solid mirrors with the necessary stiffness would be prohibitively massive. Rib-stiffening would lead to a more efficient overall design but local deflections (Fig. V-A-7.) could be unacceptable. The best configuration for achieving high stiffness and low weight without local effects is a sandwich construction - essentially two face plates separated by a light core such as aluminum foil honeycomb (Fig. V-A-8). Typical characteristics of such components are shown in Fig. V-A-9 for unit flexural elements. An additional advantage of the honeycomb is that it can also be designed to accommodate appropriate cooling for the unit.

Transverse deflections and slope changes of a sandwich mirror do not depend upon the thickness of the face plates since both the flexural stiffness and the gravitational loading are proportional to this parameter. Thus the faces can be kept relatively thin with the stiffness and therefore deflections governed by the core dimension.

A continuous uniform support condition is advantageous for symmetric surface deflections. Statically indeterminant supports would generally reduce deflections but lead to additional design complications of the substructure to which such members would be attached. A ring support is one possible scheme for consideration. The largest deflections and rotations are produced when the support is located at the outer edge (Fig. V-A-10). Reducing the support to a center post results in deflections and slopes approximately half of the largest values of the preceding case.

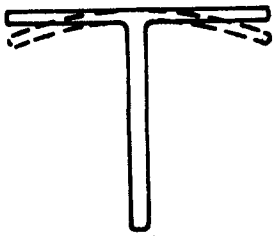

Fig. V-A-7.

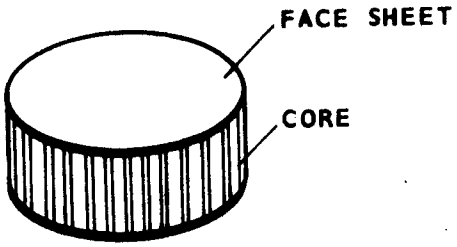

Fig. V-A-8.

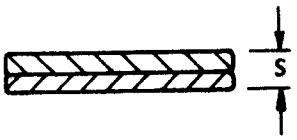

STIFFNESS = 1

RELATIVE DEFLECTION = 1

APPROXIMATE WEIGHT = 1

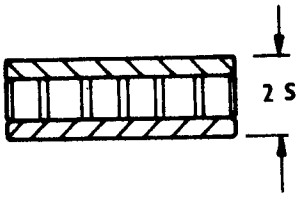

STIFFNESS = 7

R. D. = 1.4×10^{-1}

A. W. = 1

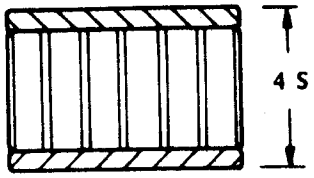

STIFFNESS = 37

R. D. = 3×10^{-2}

A. W. = 1

Fig. V-A-9.

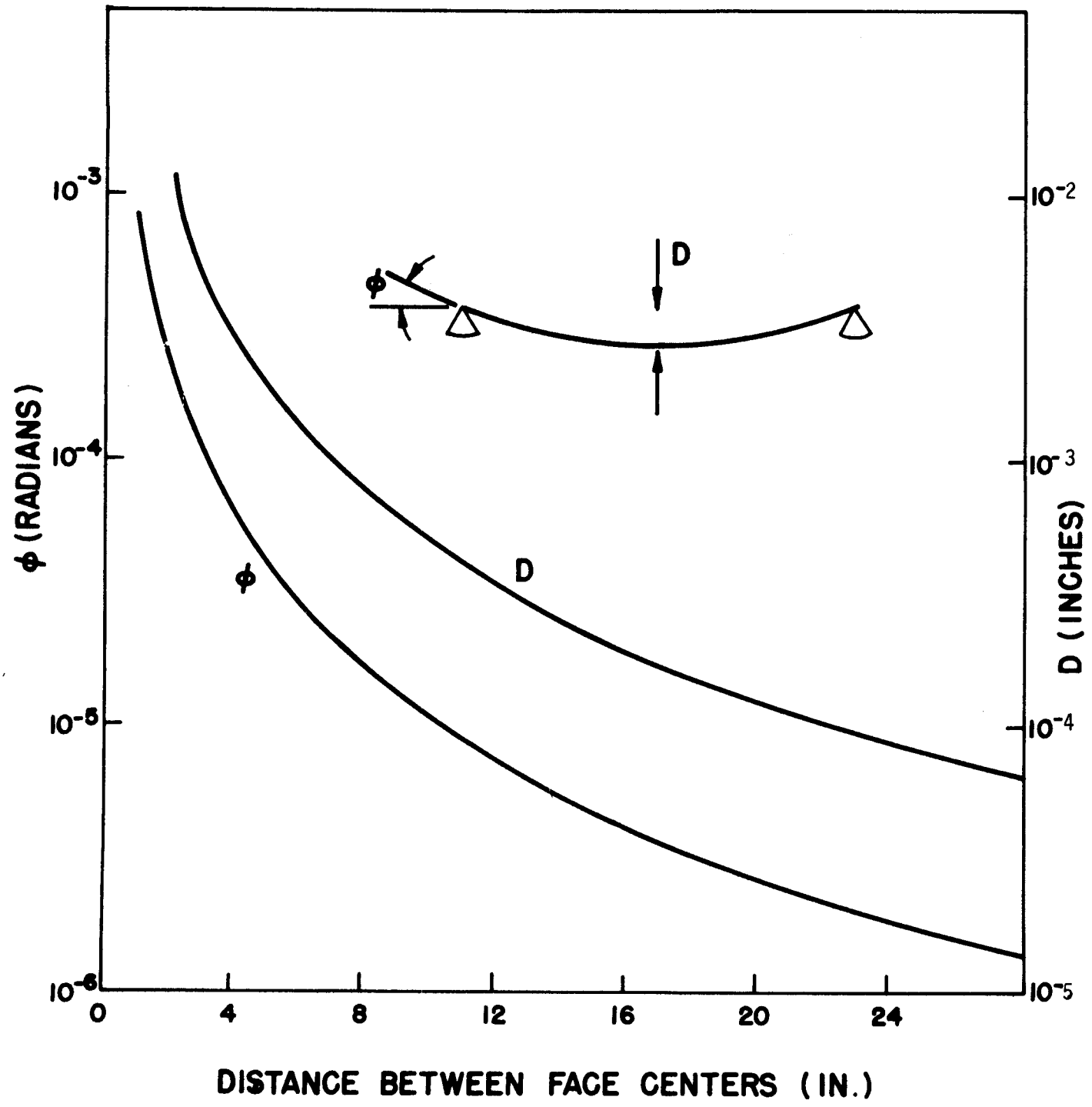
10^{-3}
10^{-4}
10^{-5}
10^{-6}
10^{-2}
10^{-3}
10^{-4}
10^{-5}
φ (RADIANS)
D (INCHES)
φ
D
D
φ
0
4
8
12
16
20
24
DISTANCE BETWEEN FACE CENTERS (IN.)

Fig. V-A-10.

Overall plate deflections can be kept to relative minima if the support is located such that deflections of the edge and center are equal. Any change in the radial position of the support from this will increase one or the other. This particular support location corresponds to approximately 67.3% of the outer radius. With this criterion, maximum deflections and rotations have been determined as shown in Fig. V-A-11. It can be seen that reasonable core thicknesses can be used to keep these deflections within design limits.

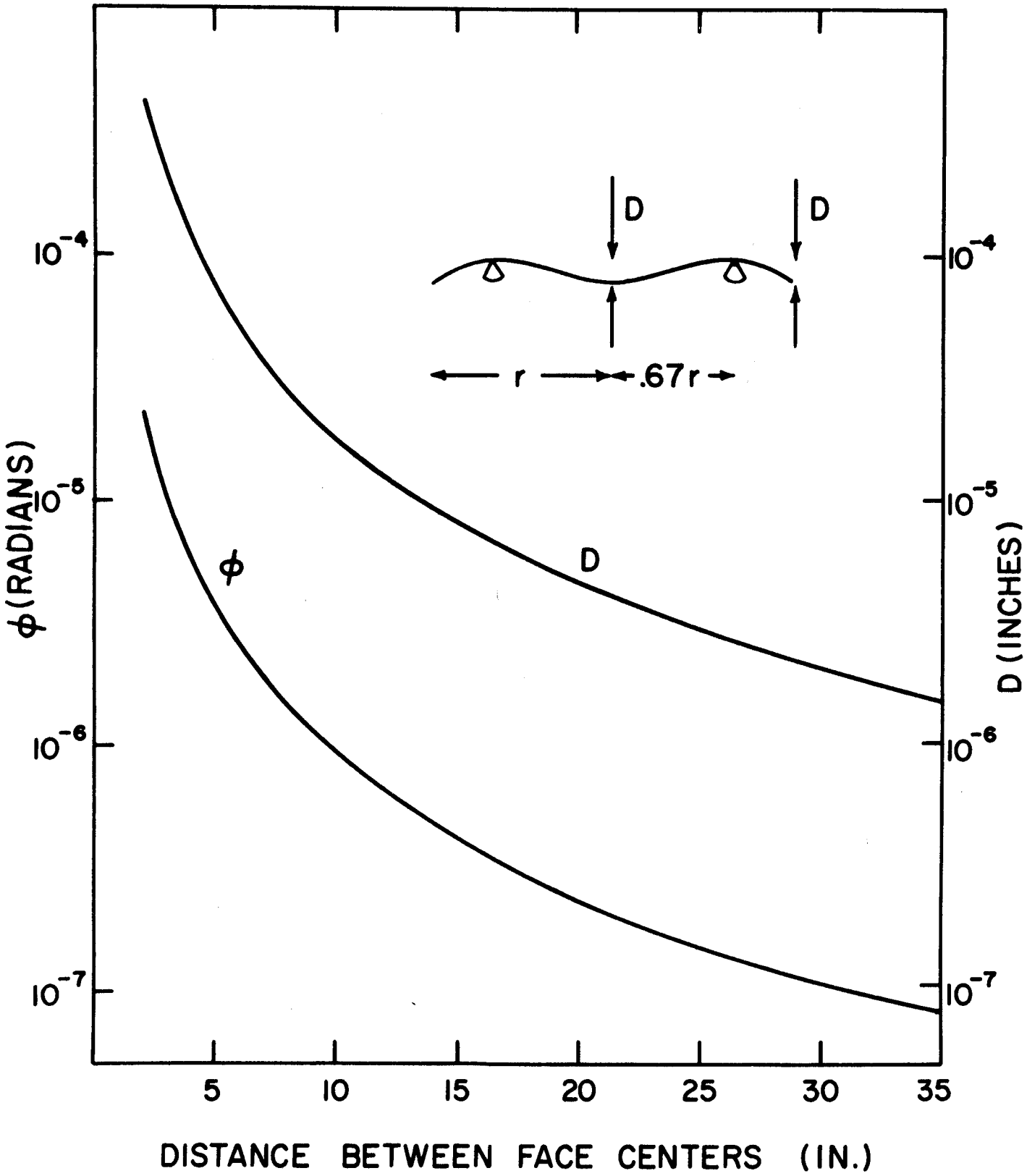
D
D
r
.67r
10^{-4}
10^{-5}
10^{-6}
10^{-7}
ϕ (RADIANS)
D (INCHES)
ϕ
D
5
10
15
20
25
30
35
DISTANCE BETWEEN FACE CENTERS (IN.)

Fig. V-A-11.

References for Section V-A

1. R. E. Kidder, Nucl. Fusion 16, 3 (1976).

2. R. L. McCrory and R. L. Morse, LA-6420-MS, July 1976.
   J. D. Lindl, UCRL-79735, Bull. Am. Phys. Soc. 22, 1078 (1977).

3. D. V. Giovanielli, Bull. Am. Phys. Soc. 21, 1047 (1976).

4. J. E. Howard, Appl. Optics 16, 2764 (1977).

5. T. T. Saito and L. B. Simmons, Appl. Optics 13, 2647 (1974).
   T. T. Saito, Appl. Optics 14, 1773 (1975).

6. L^3 1974 Annual Report, UCRL-50021-74, p. 200 et. seq.

7. A. J. Glass and A. H. Guenther, Electro-Optics System Design, June 1976, p. 28.

8. A. J. Glass and A. H. Guenther, Laser-Induced Damage in Optical Materials, 7th ASTM Symposium Proceedings, 1975 (NBS Special Pub. 435).

9. E. S. Bliss et. al., Bull. Am. Phys. Soc. 22, 1158 (1977).

10. H. E. Bennett, in Laser Induced Damage in Optical Materials: 1974, A. J. Glass and A. H. Guenther, eds. (NBS Special Publication 462, 1976), p. 11.

11. M. S. Sparks, J. Appl. Physics 42, 5029 (1971).

12. W. J. Spawr and R. L. Pierce, "Metal Mirror Selection Guide," SOR Report No. 74-004, Spawr Optical Research, Corona, CA, May 1976.

13. Drawing by William Crutchfield, from M. Tuchman, Art and Technology, Viking Press (N.Y.) 1971, p. 20, reproduced by permission of the artist.

14. M. Born and E. Wolf, Principles of Optics, 2nd Ed., Pergamon Press (Oxford), 1964.

15. W. H. Reichelt, D. J. Blevins and W. C. Turner, LA-UR 77-468.

16. M. J. Monsler and J. A. Maniscalco, private communication.

V-B. Optimal Illumination Studies

V-B-1. Introduction

In the laser fusion process, a small sphere of deuterium-tritium fuel is heated and compressed to thermonuclear burn conditions by intense laser beams.[1] The thermonuclear yield (and therefore the plant efficiency) depends sensitively on the implosion symmetry, which, at least in its early phase, demands very uniform irradiance over the pellet surface.[2] Many schemes have been proposed for illuminating fusion targets, ranging from one[3] to several hundred beams[4] in various combinations of lenses[5] and mirrors.[6] In this section we describe the calculation of irradiance on a spherical surface due to N overlapping beams, with N = 4, 6, 8, 12 or 20, corresponding to the symmetry of the five Platonic solids. Provision is currently made for the following spatial beam profiles; flat, Gaussian, and "supergaussian." Ideal lenses were employed as focusing elements, although aplanatic lenses could equally well have been used.

Basically, our task is to provide a specified uniformity of illumination over the entire pellet surface, keeping the rays as normal to the surface as possible. The required degree of uniformity is determined chiefly by its effect on growth of the Rayleigh-Taylor instability,[2] while the angles of incidence must be held down in order to maximize inverse bremsstrahlung absorption, and minimize refraction in the blowoff layer.[7]

To control pellet irradiance, we have at our disposal four independent quantities; N, the number of beams, δ, the shift of the beam focus relative to the pellet center, F, the f/no. of the focused beam, and the beam profile $I_0(r)$, where r is the beam radius on the last optical element (lens or mirror). The beam profile may depend on 2-3 parameters, so it would seem we have a formidable parameter space to deal with. In practice, however, only a few values of N are considered, F then being determined by the maximum solid angle allotted to optics. Of course, the optics must be sufficiently distant from the target so that the beam aperture is adequate to handle the energy and power per beam as well as the radiation and debris from the target. The total aperture area is determined in practice by material damage constraints on the beam energy, rather than self-focusing constraints on the beam power.[8]

A more complete treatment of the uniformity problem would entail following the energy deposition in the early phases of the corona expansion, taking into account refraction and lessened energy absorption near the beam edges where the angles of incidence are largest.

V-B-2. The Platonic Solids

A sphere may be partitioned into N equal-solid-angle wedges by means of the five Platonic solids, illustrated in Fig. V-B-1. A sphere may also be divided into two equal solid angle portions by

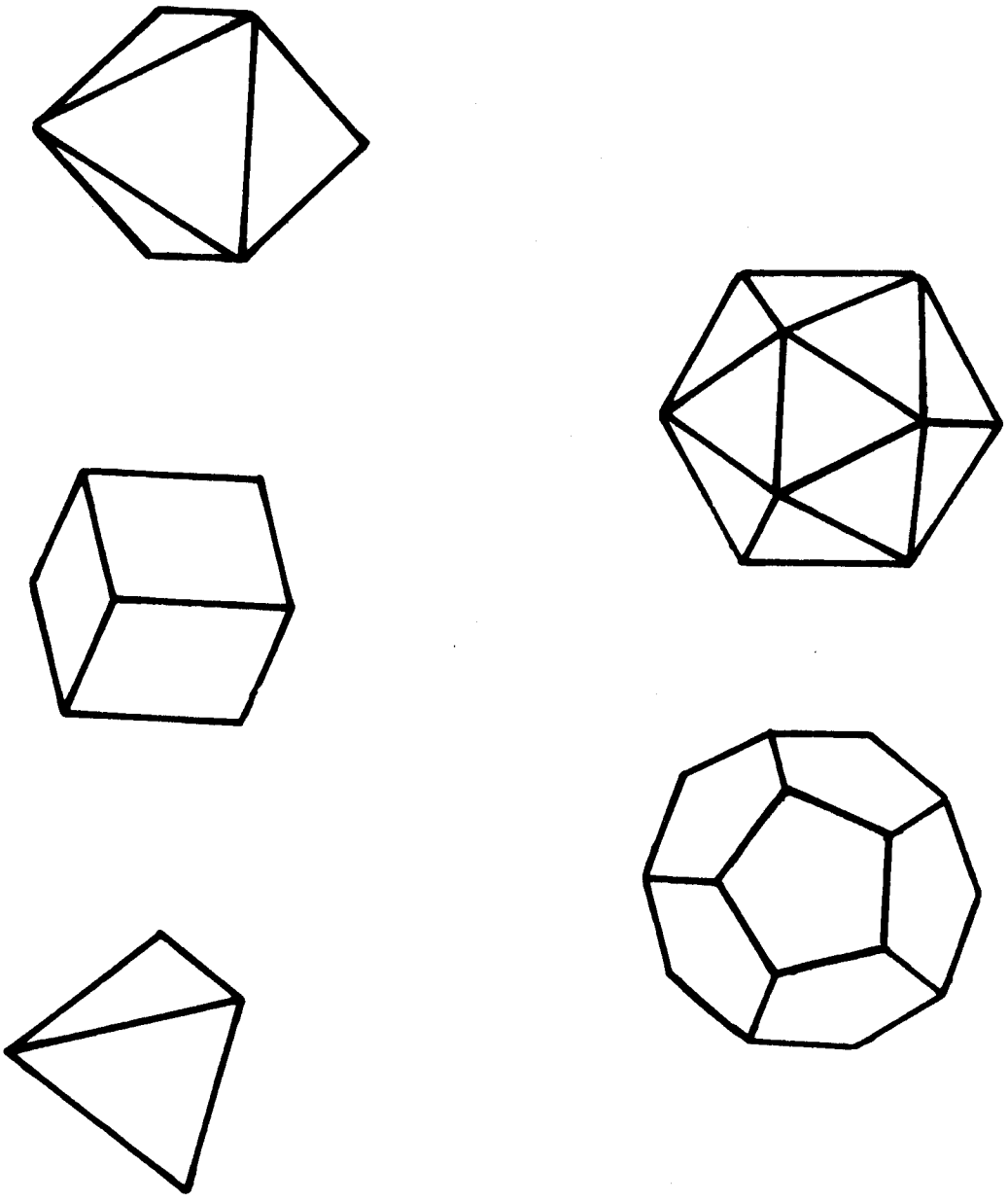

Figure V-B-1

means of a plane cut through its center.* Other partitions are possible. For example, beams placed at each of the 12 vertices of an icosahedron allows symmetric placement of 32 beams. The Ω-10 facility at the University of Rochester[9] is designed for 24 beams.

Each Platonic solid being made up of N regular polygonal faces, it is customary to classify them according to the number of sides (p) of the polygons and the number of adjacent faces (q) at a vertex. Given the number of faces N_S, it is easy to show that the number of edges and vertices are given by

$$N_E = 1/2\ p\ N_S \tag{1}$$

$$N_V = \frac{p}{q} N_S\ . \tag{2}$$

These numbers are related by Euler's formula,[10]

$$N_V + N_S - N_E = 2\ . \tag{3}$$

We shall also need the dihedral angle α and the wedge angle β, as depicted in Fig. V-B-2.

---

* I have recently learned of the existence of a sixth degenerate Platonic solid, the "dihedron," a double plane polygon enclosing no volume.[11]

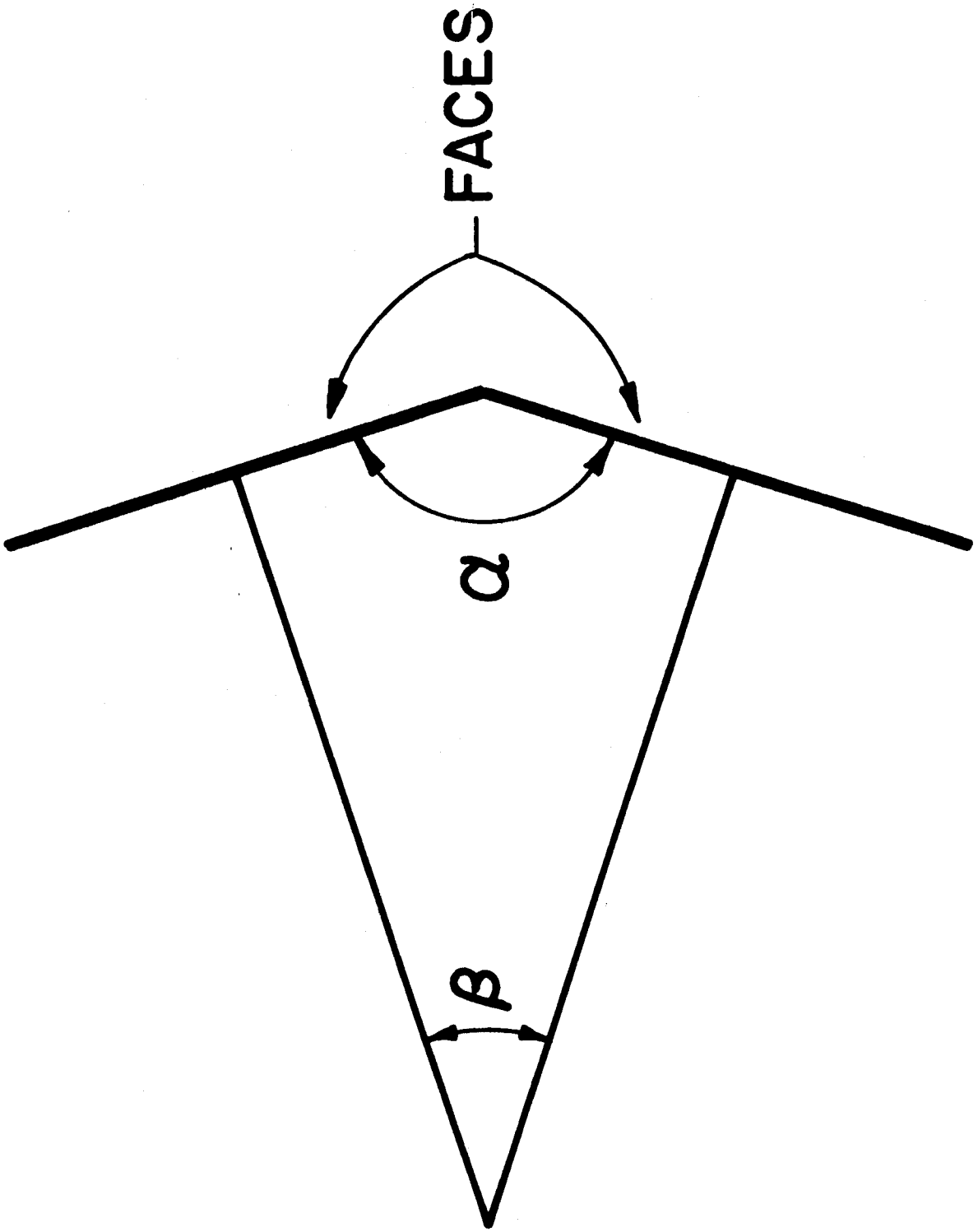

Figure V-B-2

$$\sin\frac{\alpha}{2} = \cos\frac{\beta}{2} = \frac{\cos(\pi/q)}{\sin(\pi/p)} \qquad (4)$$

$$\beta = \pi - \alpha \ .$$

Table V-B-1 lists these parameters for all of the Platonic solids. Since laser beams are circular rather than prismatic, it is necessary to overlap them in order to cover the entire pellet surface. Uniform illumination may be obtained by simultaneously varying the degree of overlap and contouring the beam profile. In Section V-B-4 we shall use Table V-B-1 to determine the coordinates of all beams relative to a common origin and combine irradiances in the overlap regions.

V-B-3. Irradiance Profiles

Assuming ideal lenses, each beam contributes an irradiance[6]

$$I(\theta) = I_o(r)\left(\frac{f}{R_T}\right)^2 \frac{1 + \delta\cos\theta}{(\cos\theta + \delta)^3} \ W/cm^2 \ , \qquad (5)$$

where $I_o(r)$ is the flux incident on the lens, r is the beam radius, R_T the target radius, f is the focal length, and

$$\delta = \Delta x/R_T \qquad (6)$$

measures the focal shift relative to the target center (Fig. V-B-3).

The angle of incidence Ψ is given in terms of the beam half-angle ξ and δ by

$$\sin\Psi = \delta\sin\xi \ . \qquad (7)$$

The beam half angle is related to the f/no. by

$$\cot\xi = 2F \ . \qquad (8)$$

	N_S	N_E	N_V	p	q	α	β
Tetrahedron	4	6	4	3	3	70.53	109.47^o
Hexahedron	6	12	8	4	3	90^o	90^o
Octahedron	8	12	6	3	4	109.47^o	70.53^o
Dodecahedron	12	30	20	5	3	116.57^o	63.43^o
Icosahedron	20	30	12	3	5	138.18^o	41.82^o

Table V-B-1. Properties of the Platonic Solids

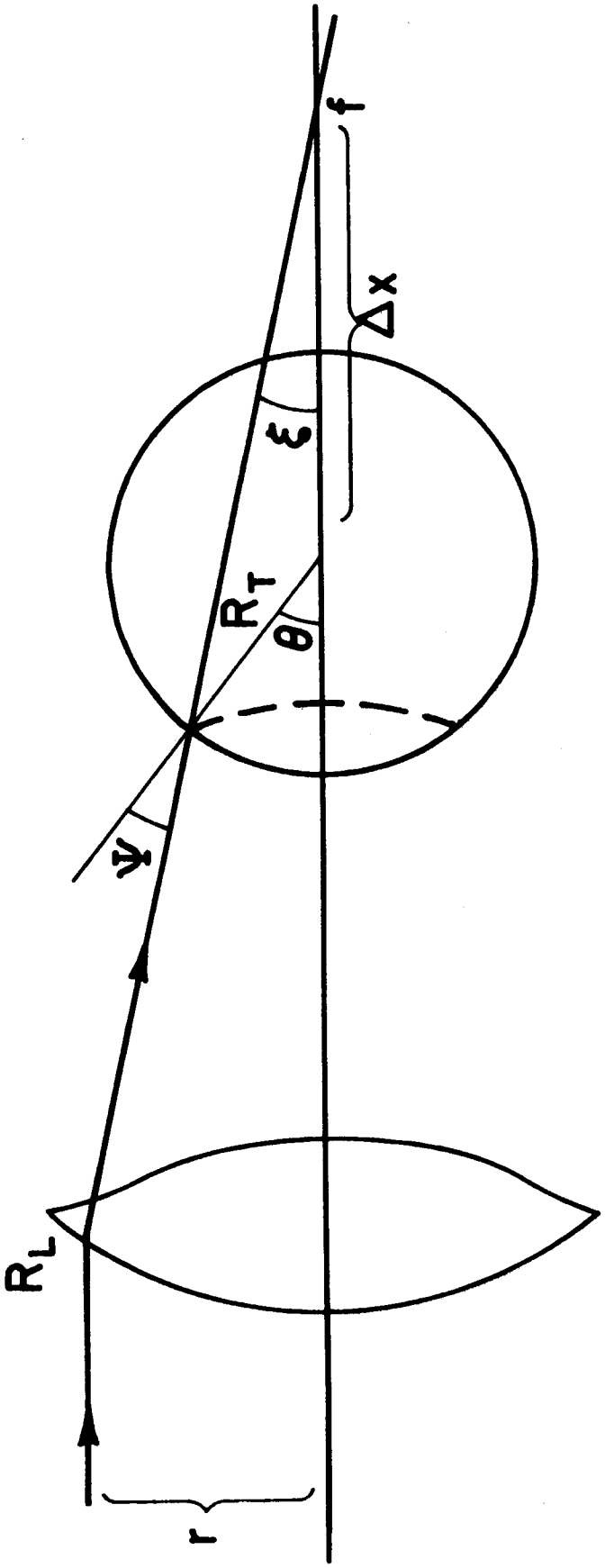

Figure V-B-3

Thus, the maximum angle of incidence is given by

$$\sin\Psi_{max} = \frac{\delta}{\sqrt{1+4F^2}} \quad . \tag{9}$$

It is essential that Ψ_{max} be made as small as possible in order to minimize laser energy lost through refraction in the pellet corona.[7]

Now when we come to optimize pellet illumination uniformity, the outcome will be a certain spot size as measured by the pellet central angle θ_{max}. From Fig. V-B-3, the corresponding focal shift is given by

$$\delta = 2F \sin\theta_{max} - \cos\theta_{max} \quad . \tag{10}$$

So the price we pay for uniformity is given by combining eqs. (9) and (10):

$$\sin\Psi_{max} = \frac{2F \sin\theta_{max} - \cos\theta_{max}}{\sqrt{1+4F^2}} \quad , \tag{11}$$

which is just another way of writing

$$\Psi_{max} = \theta_{max} - \xi \quad . \tag{12}$$

Equation (12) shows that if θ_{max} is large, then ξ must also be large in order to keep Ψ_{max} small. From eq. (8), we see that large ξ naturally translates into small f/no.

Unlike a research facility such as SHIVA,[5] the beam transport system in a laser fusion reactor (LFR) can only take up a small fraction of the

solid angle subtended to the target. Whereas SHIVA has about 50% of its solid angle devoted to beams, an LFR is limited to about 10% for economic reasons. Each beam occupies a solid angle

$$\Delta\Omega = 2\pi(1 - \cos\xi) , \tag{13}$$

so that the total fractional solid angle taken up by N beams is

$$\gamma = \frac{N\Delta\Omega}{4\pi} = \frac{N}{2}\left[1 - \frac{2F}{\sqrt{1+4F^2}}\right] . \tag{14}$$

Solving for F, we find, for $\gamma << 1$,

$$F_{min} = \frac{\frac{1}{2}\left(1 - \frac{2\gamma}{N}\right)}{\sqrt{1 - \left(1 - \frac{2\gamma}{N}\right)^2}} \simeq \frac{1}{4}\sqrt{\frac{N}{\gamma}} . \tag{15}$$

This is the minimum f/no. required to occupy less than a specified solid angle fraction. Table V-B-2 lists F_{min} for $\gamma = 0.1$ and 0.2. For $\gamma << 1$, the maximum angle of incidence is

$$\Psi_{max} \simeq \theta_{max} - 2\sqrt{\frac{\gamma}{N}} . \tag{16}$$

The small-angle results, eqs. (15) and (16) are not substantially changed by the use of aplanatic lenses, for which

$$\csc\xi = 2F \tag{17}$$

replaces eq. (8). In general, the angles of incidence decrease as more beams are added, assuming equal target coverage and fixed γ. However, it will be seen that in the important cases N = 12 and 20, the optimal values of θ_{max} are nearly equal, independent of γ, so that the angles of incidence are actually somewhat larger for 20 beams.

N	$\gamma = 0.1$	$\gamma = 0.2$
4	1.58	1.12
8	2.24	1.58
12	2.74	1.94
20	3.54	2.50

Table V-B-2. Minimum f/nos. for Specified Maximum Solid Angle Taken up by Beams

We are now in a position to design a pellet illumination scheme, proceeding as follows:

1. Choose a definite fractional solid angle γ, say 10%.
2. Choose the number of beams, say N = 12 or 20.
3. This fixes the minimum f/no. by eq. (15).
4. Next choose a beam profile, say Gaussian.
5. Vary δ until the uniformity exceeds the desired value, say 90%. This number directly affects the Rayleigh-Taylor growth rate.[2]
6. The optimum δ and F determines θ_{max} from eq. (10):

$$\sin\theta_{max} = \frac{2F\delta + \sqrt{1 + 4F^2 - \delta^2}}{1 + 4F^2} \quad . \tag{18}$$

7. Eq. (11) or (18) determines Ψ_{max}.
8. Ψ_{max} determines the amount of laser energy lost due to refraction.
9. If Ψ_{max} is too large, one has two main options:
   (a) relax the uniformity requirement (5)
   (b) relax the solid angle requirement (1).

V-B-4. Calculating Beam Overlap

Before carrying out the above optimization procedure, we have to learn how to calculate the irradiance due to a number of overlapping spots. We shall examine here only the cases N = 8, 12, and 20; octahedral, dodecahedral and icosahedral. High uniformity is not possible using 4 or 6 beams, so these configurations will not be considered further in this paper.

First of all, by symmetry we need only look at a single pie slice-shaped region, as depicted in Fig. V-B-4 for the icosahedron (only 3 nearest neighbor spots are shown). In this case, only spots O and A need be included. In general, however, several spots (located at points Q_k) may contribute to the irradiance at point P according to eq. (5) with θ_{PQ_k} given by

$$\cos\theta_{PQ_k} = \cos\theta\,\cos\theta_k + \sin\theta\,\sin\theta_k\,\cos(\phi - \phi_k) \qquad (19)$$

as shown in Fig. V-B-4.

The coordinates of the neighboring beams are conveniently found by means of the Schlegel diagram.[10] This is simply a two-dimensional projection of the polyhedron gotten by bringing one face up to the eye.

V-B-4-a. Octahedron

We wish to locate points Q_k, k = 1,6 w. r. t. point O, using the Schlegel diagram depicted in Fig. V-B-5. The 8th (opposite) point will be ignored. The fundamental pie slice has its 60° wedge at point O, with one side along the arc OQ_k. From Table V-B-1, the angular side $\beta = 70.53°$. We want to solve the spherical triangle OQ_1Q_4 for the angular side θ_4. By the cosine law, $\cos\theta_4 = -1/3$ so that $\theta_4 = \pi - \beta$. Thus,

$$\begin{array}{ll} \phi_1 = 0 & \theta_1 = \beta = 70.53^\circ \\ \phi_2 = 120^\circ & \theta_2 = \beta \\ \phi_3 = 240^\circ & \theta_3 = \beta \\ \phi_4 = 60^\circ & \theta_4 = 180^\circ - \beta = 109.47^\circ \end{array}$$

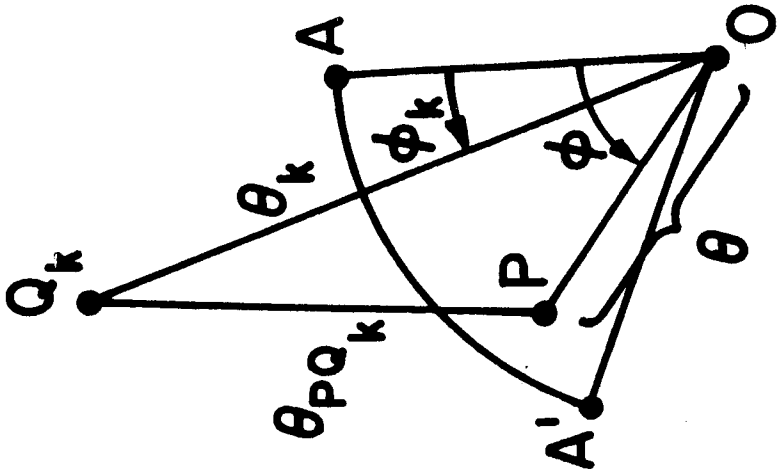

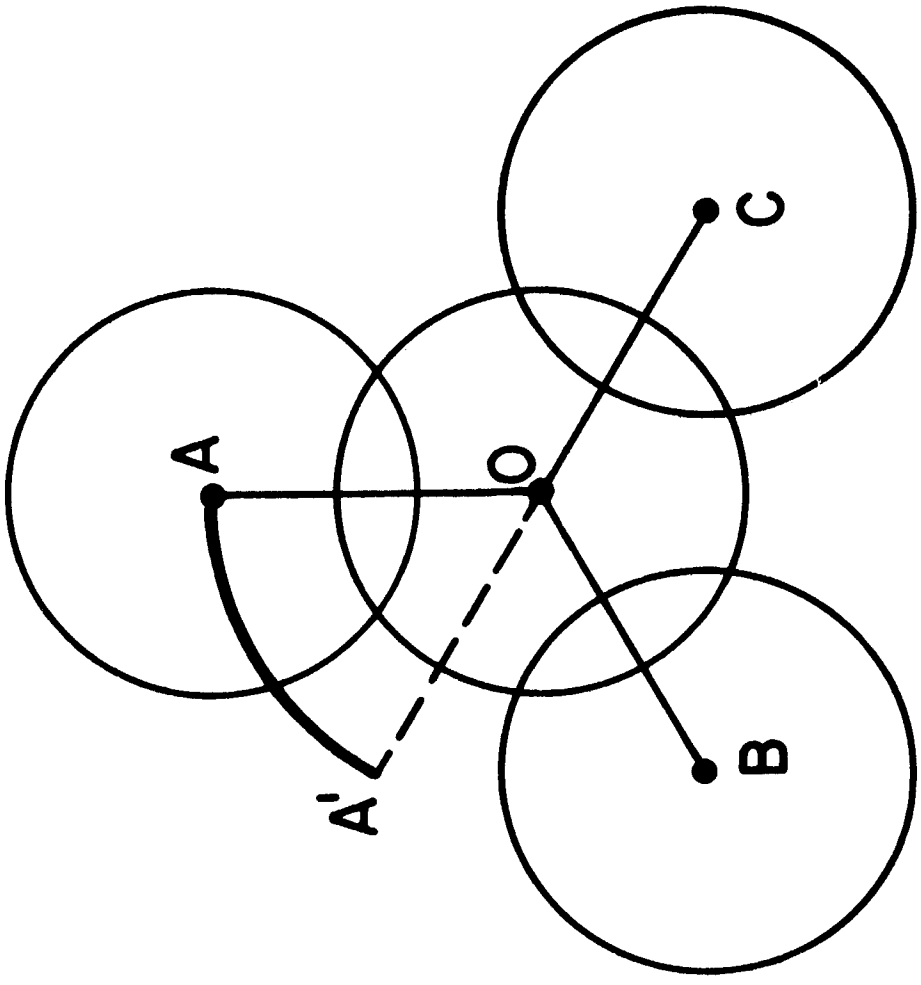

Figure V-B-4

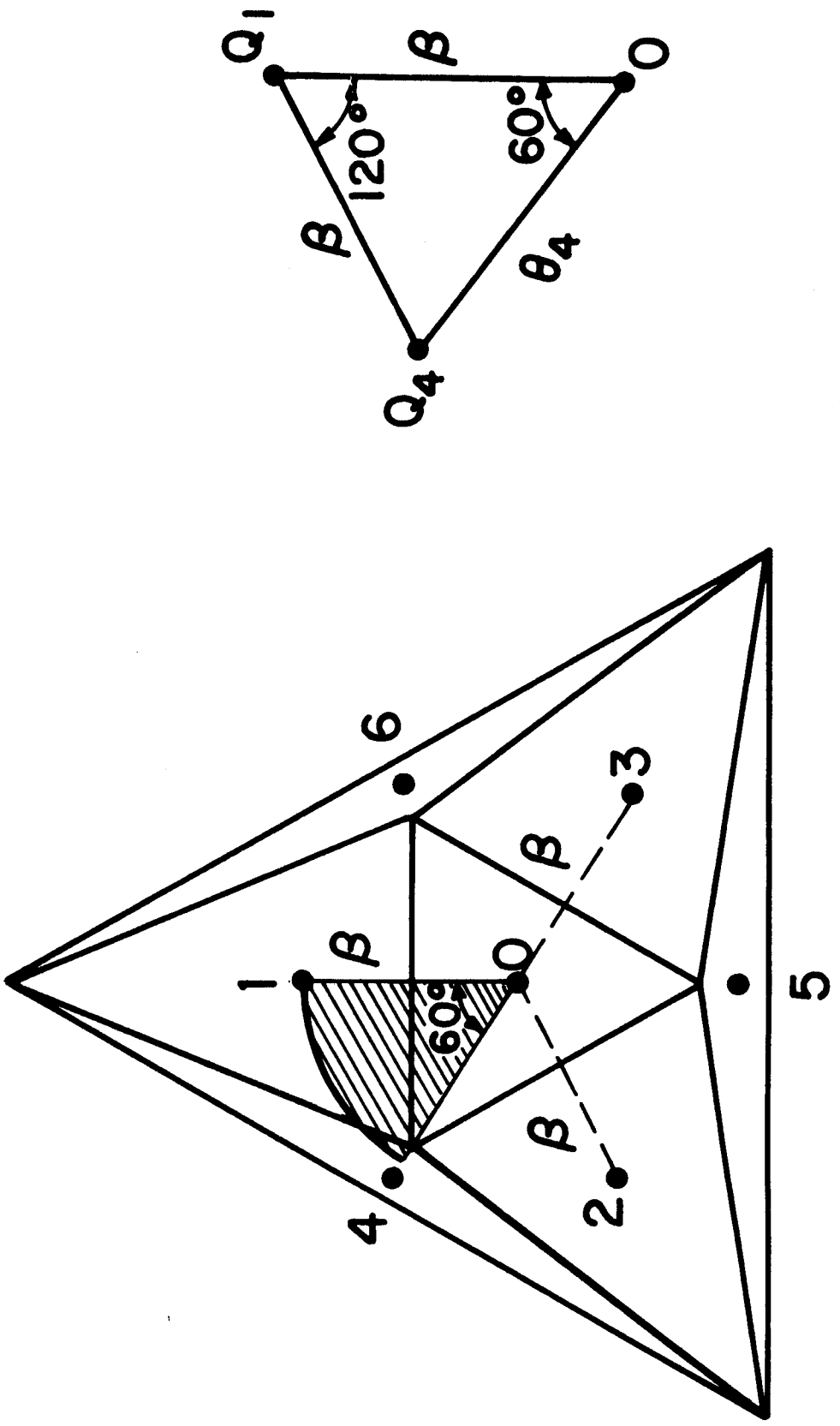

Figure V-B-5

$$\phi_5 = 180^0 \qquad \theta_5 = \theta_4$$
$$\phi_6 = 300^0 \qquad \theta_6 = \theta_4$$

V-B-4-b. Dodecahedron

Figure V-B-6 shows the Schlegel diagram; again the opposite 12th face is ignored. In this case, the fundamental pie slice subtends a 36° angle. From Table V-B-1, $\beta = 63.43°$. Solving the spherical triangle OQ_1Q_6 we find $\theta_6 = \pi - \beta$. Thus,

$$\phi_1 = 0 \qquad \theta_1 = \beta = 63.43^0$$
$$\phi_2 = 72^0 \qquad \theta_2 = \beta$$
$$\phi_3 = 144^0 \qquad \theta_3 = \beta$$
$$\phi_4 = 216^0 \qquad \theta_4 = \beta$$
$$\phi_5 = 288^0 \qquad \theta_5 = \beta$$
$$\phi_6 = 36^0 \qquad \theta_6 = \pi - \beta = 116.57^0$$
$$\phi_7 = 108^0 \qquad \theta_7 = \theta_6$$
$$\phi_8 = 180^0 \qquad \theta_8 = \theta_6$$
$$\phi_9 = 252^0 \qquad \theta_9 = \theta_6$$
$$\phi_{10} = 324^0 \qquad \theta_{10} = \theta_6$$

V-B-4-c. Icosahedron

Figure V-B-7 depicts the Schlegel diagram; only the inner hexagonal portion is needed for $\theta_{max} \leq 72°$. Solving the spherical triangle OQ_1Q_4 gives

$$\cos\theta_4 = 1 - \frac{3}{2}\sin^2\beta ,$$

where $\beta = 41.82°$. Thus, $\theta_4 = 70.53°$, which is just the octahedron wedge angle! In this case, we must also calculate the angle ϕ_4. By the sine law,

$$\sin\phi_4 = \frac{\sin\beta \sin 60°}{\sin\theta_4} = \frac{\sqrt{3}}{2\sqrt{2}} ,$$

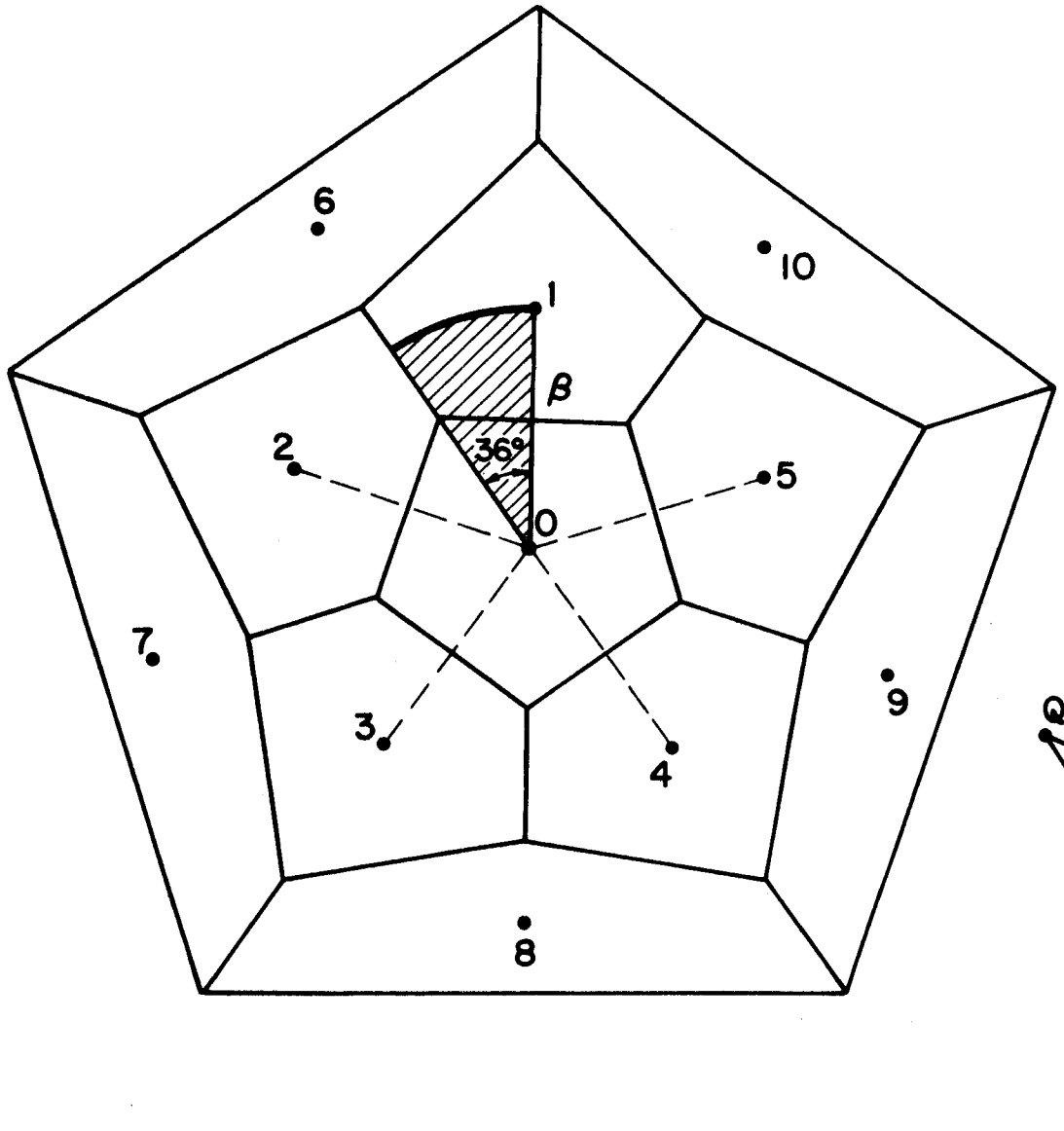

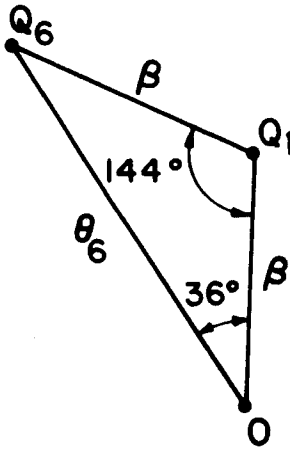

Figure V-B-6

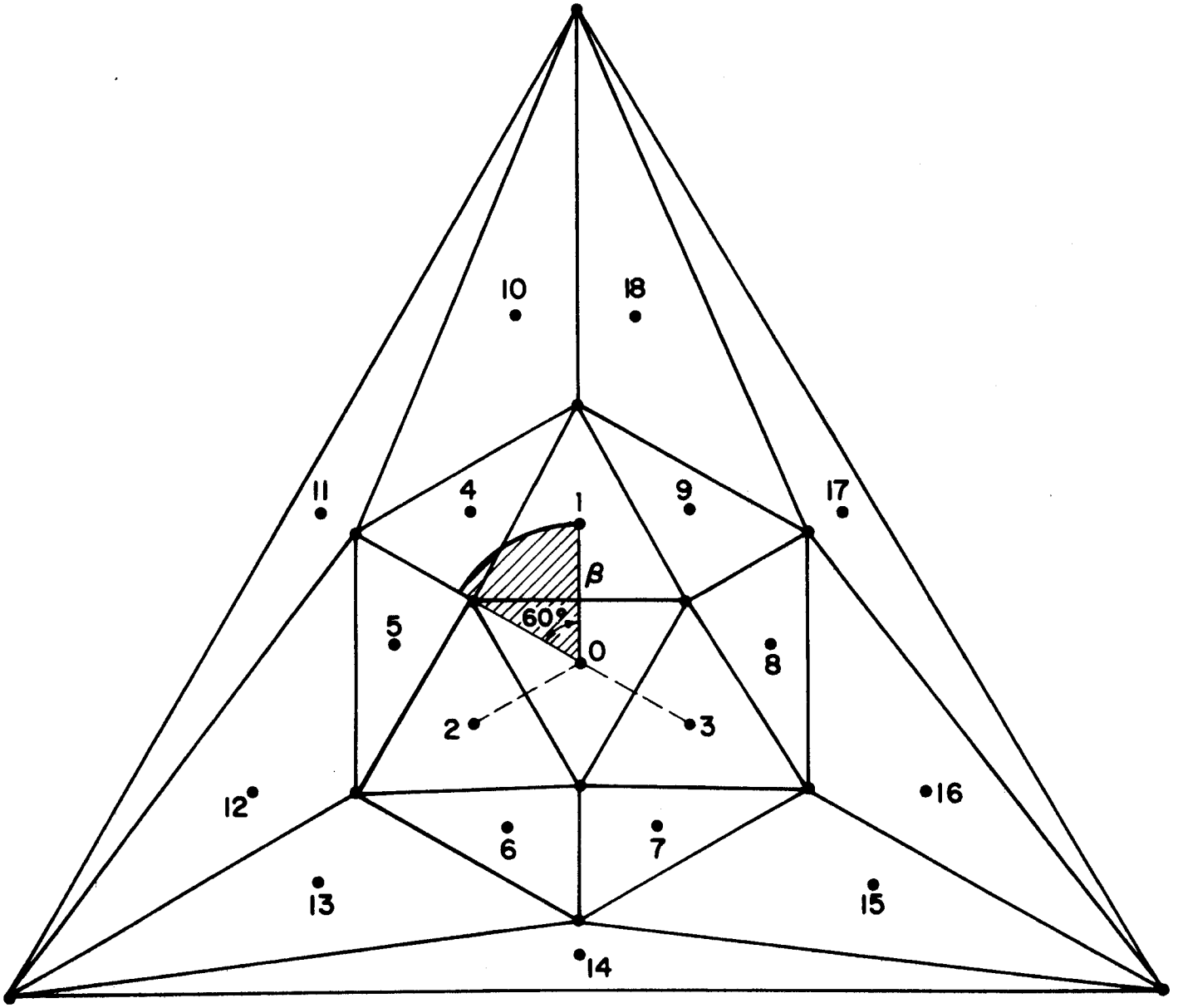

Figure V-B-7

so that $\phi_4 = 37.76°$. The coordinates of points 10-18 may be found by solving spherical triangles 0-4-11 and 0-1-18. The results are

$$\phi_1 = 0 \qquad \theta_1 = \beta = 41.82^0$$
$$\phi_2 = 120^0 \qquad \theta_2 = \beta$$
$$\phi_3 = 240^0 \qquad \theta_3 = \beta$$
$$\phi_4 = 37.76^0 \qquad \theta_4 = 70.53^0$$
$$\phi_5 = 120^0 - \phi_4 \qquad \theta_5 = \theta_4$$
$$\phi_6 = 120^0 + \phi_4 \qquad \theta_6 = \theta_4$$
$$\phi_7 = 240^0 - \phi_4 \qquad \theta_7 = \theta_4$$
$$\phi_8 = 240^0 + \phi_4 \qquad \theta_8 = \theta_4$$
$$\phi_9 = 360^0 - \phi_4 \qquad \theta_9 = \theta_4$$
$$\phi_{10} = 60^0 - \phi_4 \qquad \theta_{10} = 180^0 - \theta_4$$
$$\phi_{11} = 60^0 \qquad \theta_{11} = 180^0 - \beta$$
$$\phi_{12} = 60^0 + \phi_4 \qquad \theta_{12} = 180^0 - \theta_4$$
$$\phi_{13} = 180^0 - \phi_4 \qquad \theta_{13} = 180^0 - \theta_4$$
$$\phi_{14} = 180^0 \qquad \theta_{14} = 180^0 - \beta$$
$$\phi_{15} = 180^0 + \phi_4 \qquad \theta_{15} = 180^0 - \theta_4$$
$$\phi_{16} = 300^0 - \phi_4 \qquad \theta_{16} = 180^0 - \theta_4$$
$$\phi_{17} = 300^0 \qquad \theta_{17} = 180^0 - \beta$$
$$\phi_{18} = 300^0 + \phi_4 \qquad \theta_{18} = 180^0 - \theta_4$$

V-B-4-d. Minimum Value of θ_{max} for Total Coverage

Having located the positions of all beams, we can now calculate the irradiance on a sphere with an arbitrary amount of overlap. From Fig. V-B-4, we see that the condition for the spots to just touch is

$$\theta_{max} = \beta/2 \ . \qquad (20)$$

Thus, a focal shift of at least

$$\delta_{min} = 2F \sin\beta/2 - \cos\beta/2 \qquad (21)$$

is needed in order to achieve uniform irradiance. When the beams overlap sufficiently, there will be no unilluminated areas on the pellet. To calculate θ_{max} for 100% coverage, we must look at each case individually.

Octahedron

Figure V-B-8 depicts the four nearest neighbor beams. In order to cover the small rectangular area in the center, we solve the triangle O1P. The law of sines gives

$$\sin\theta_m^* = \sin 60^o \sin\beta = \left(\frac{1}{2}\sqrt{3}\right)\left(\frac{2}{3}\sqrt{2}\right) = \sqrt{2/3} \quad , \qquad (22)$$

or

$$\theta_m^* = \tan^{-1}\sqrt{2} = 54.74^o \ .$$

Dodecahedron

Figure V-B-9 shows the three nearest neighbor spots. To wipe out the triangular hole in the center, we solve the spherical triangle OP2 and find

$$\sin\theta_m^* = \frac{\sin 36^o}{\sin 60^o} \sin\beta = 0.607 \ , \qquad (23)$$

so that

$$\theta_m^* = 37.38^o \ .$$

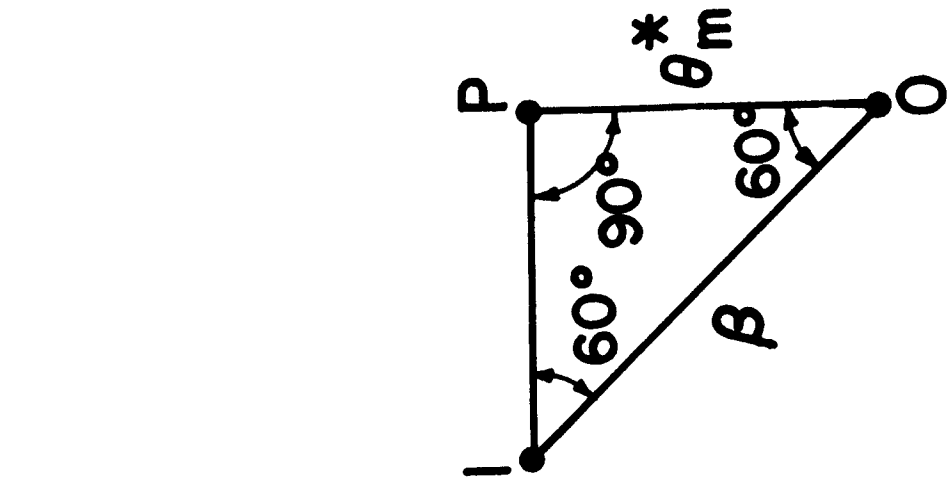

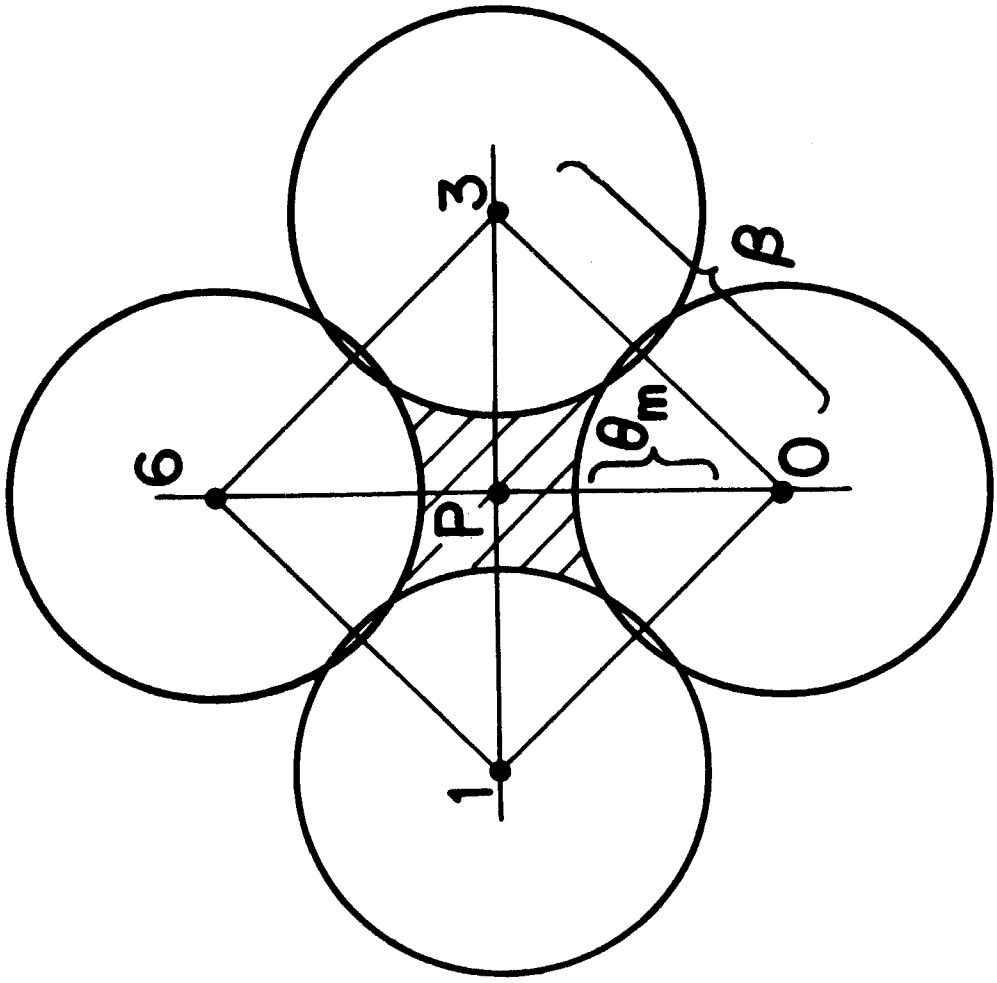

Figure V-B-8

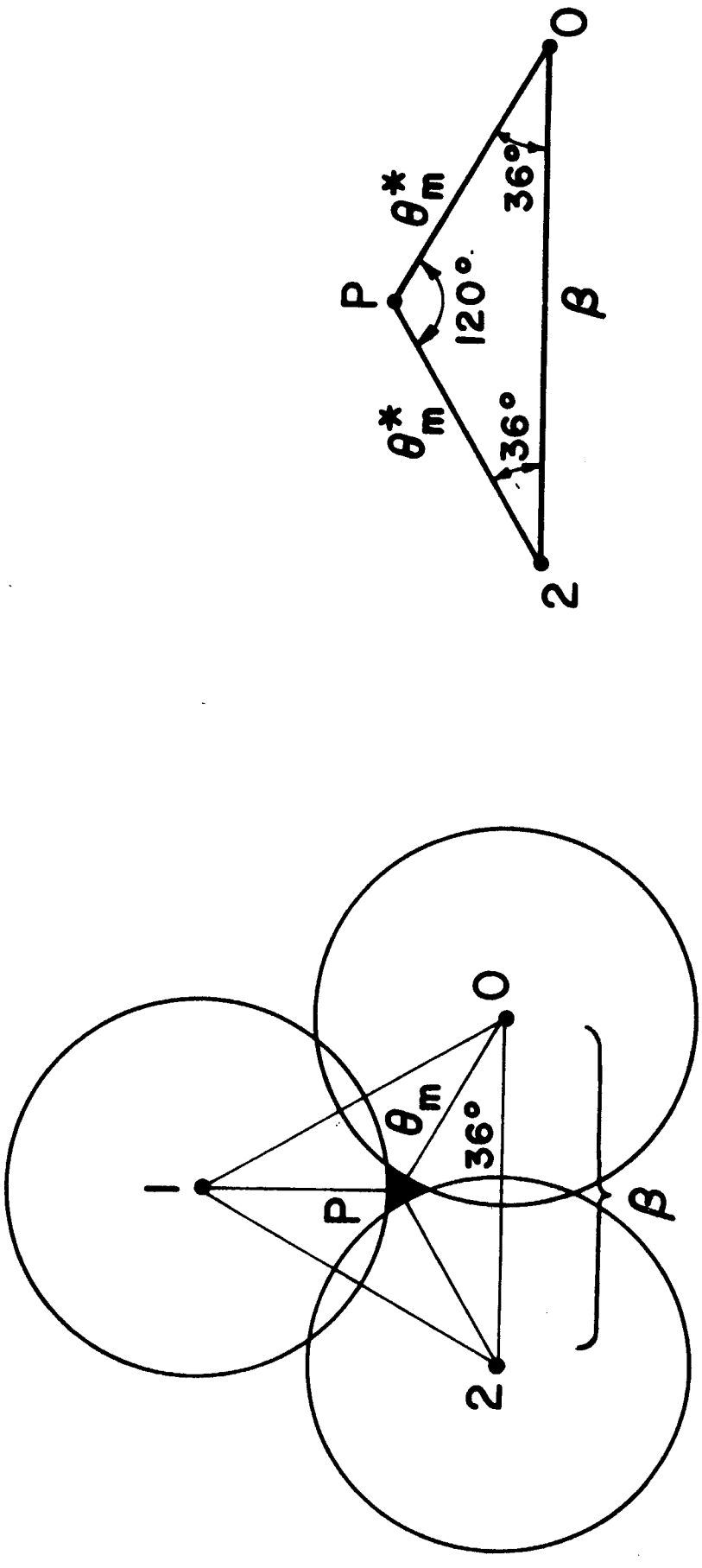

Figure V-B-9

Icosahedron

Figure V-B-10 shows the five nearest spots. Solving the spherical triangle OP2 gives

$$\sin\theta^*_m = \frac{\sin 60° \sin\beta}{\sin 72°} = 0.607 \ . \qquad (24)$$

Thus, $\theta^*_{max} = 37.38°$, the same value as for the 12 beam case!

V-B-5. Numerical Results

A computer program, PLATO, has been written to calculate irradiance profiles over the fundamental region for each of the configurations described in Section V-B-4. We first examine SHIVA-type designs,[5] using 8, 12 and 20 f/1.5 lenses. Next, reactor-type configurations are considered, with optics limited to 10 or 20% of the total solid angle seen by the target. (Of course, SHIVA was never intended to resemble a reactor; its 20 beams take up 51% of the total solid angle). In all cases, greater than 90% uniformity is realizable using 12 or 20 beams, with 8 beams running a poor third. However, good uniformity for the high f/nos. typical of reactor configurations can only be achieved at the expense of large angles of incidence and consequent loss of laser energy by refraction in the plasma corona.[7]

V-B-5-a. Optimization

In following the optimization procedure outlined in Section V-B-3, we first fix F = 1.5 and treat the cases N = 8, 12 and 20 separately. Spatial beam profiles were chosen from the two-parameter family of "supergaussian" forms,

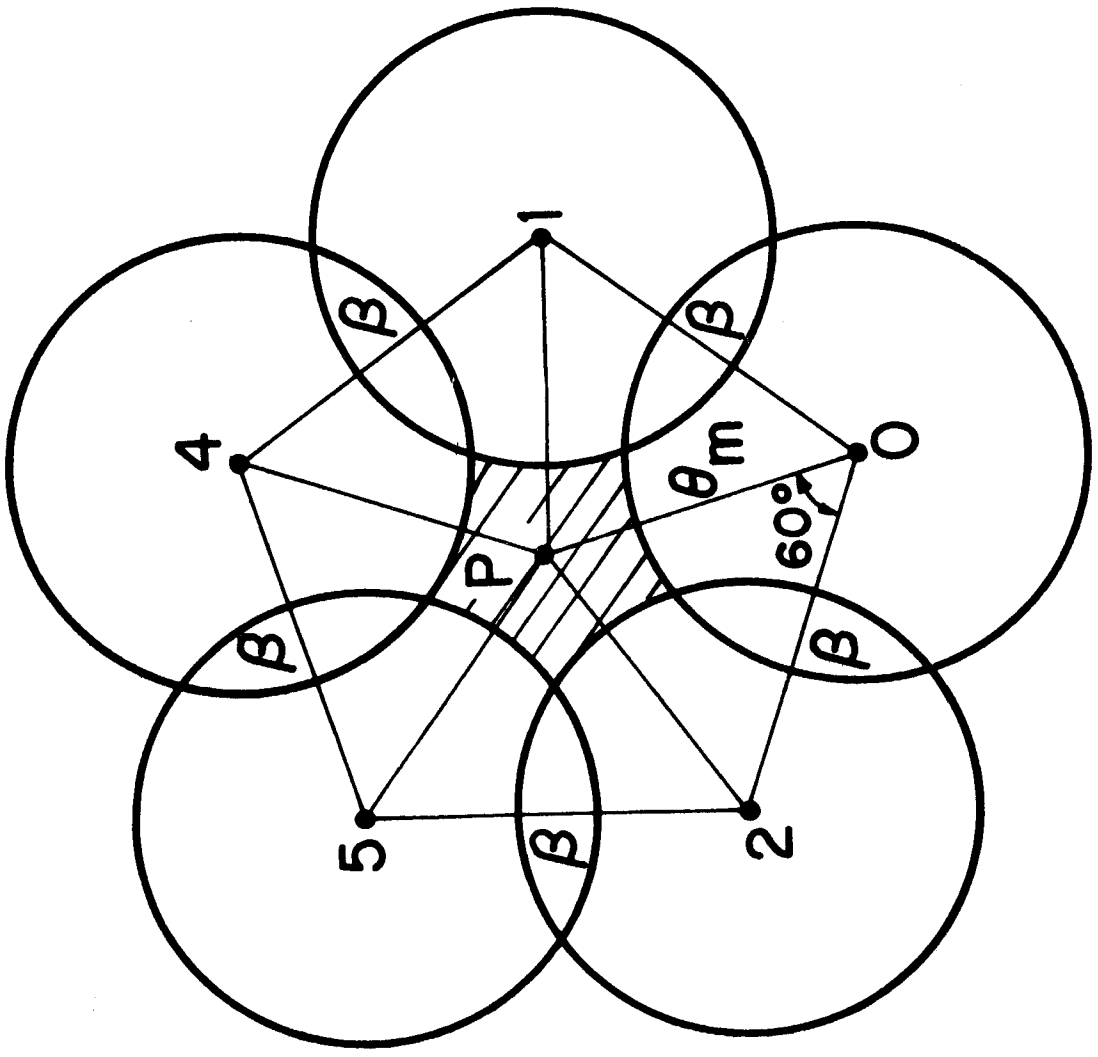

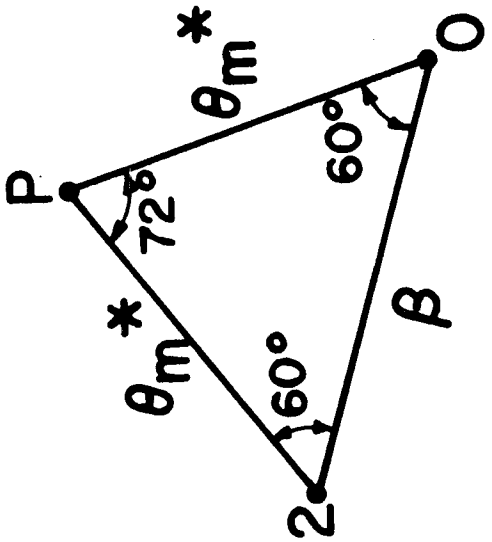

Figure V-B-10

$$I_o(r) = \bar{e}^{(r/a)^p}, \tag{25}$$

with p = 2, 3, 4 and 5. The parameter a is related to the half width at half-maximum by

$$x_{1/2} = a(\ell n 2)^{1/p} . \tag{26}$$

The irradiance, including overlap from all beams, is then computed on a mesh (θ,ϕ) over the fundamental region, for a number of values of θ_{max}. Extracting the maximum and minimum, we calculate the uniformity

$$\eta = 1 - (I_{max} - I_{min})/(I_{max} + I_{min}) . \tag{27}$$

To interpret this criterion, consider a sinusoidal ripple of amplitude A superimposed on a DC signal of magnitude B. It is natural to express the deviation from constancy or A/B and the uniformity as 1-A/B. In contrast, the Livermore studies[5] use $\eta_L = I_{min}/I_{max} \leq \eta$. Note that both η and η_L vary between 0 and 1.

Figures V-B-11 to 13 show η as a function of θ_{max} for Gaussian profiles (p = 2), having width parameters a = 0.5, 1.0 and 0.70 (Fig. V-B-14). Clearly, best uniformity is obtained for a = 0.7, the optimal value for this profile. Notice the great improvement in going from 8 to 12 beams, and the smaller but non-negligible improvement in going from 12 to 20 beams. Although the curves

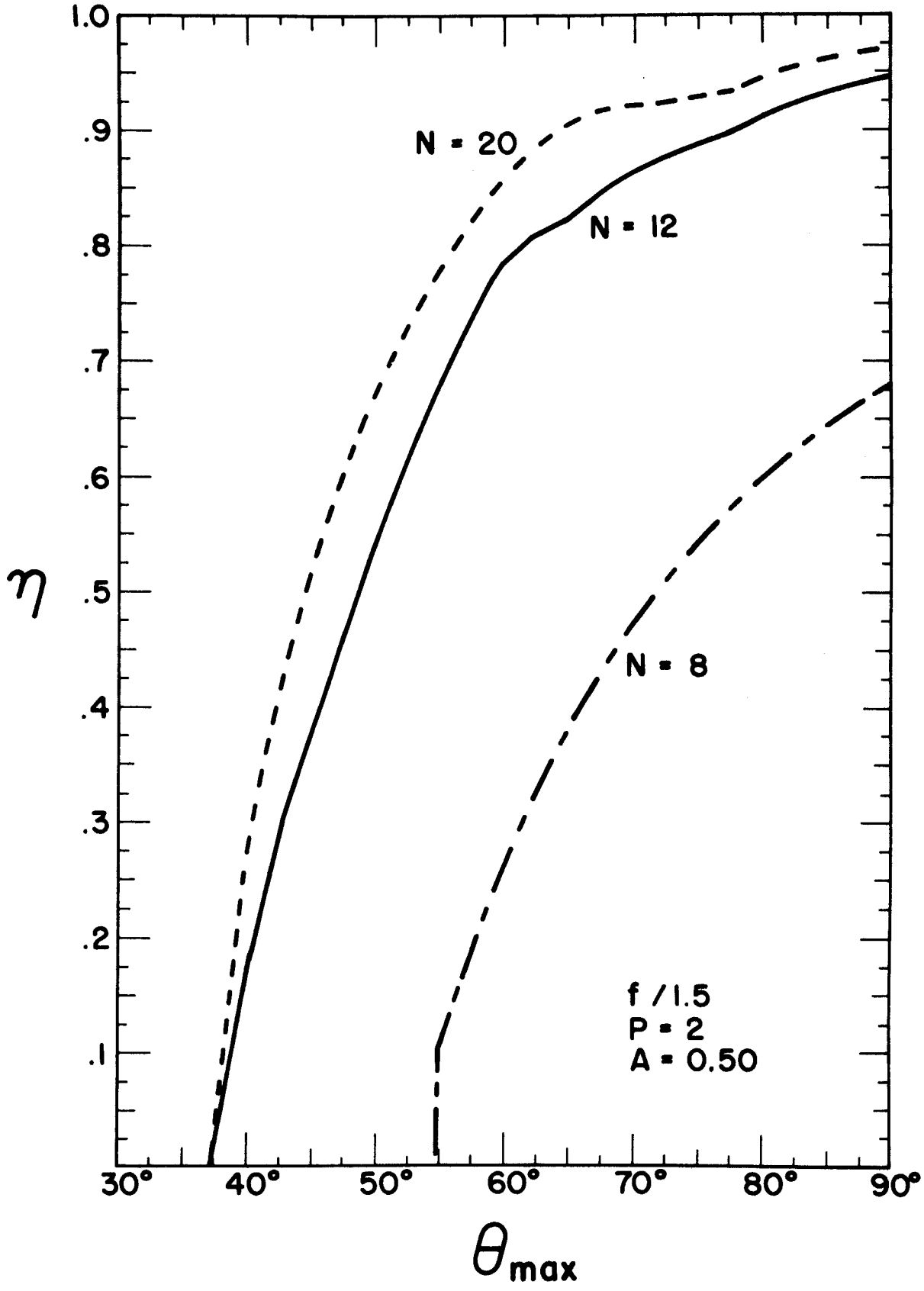

Figure V-B-11

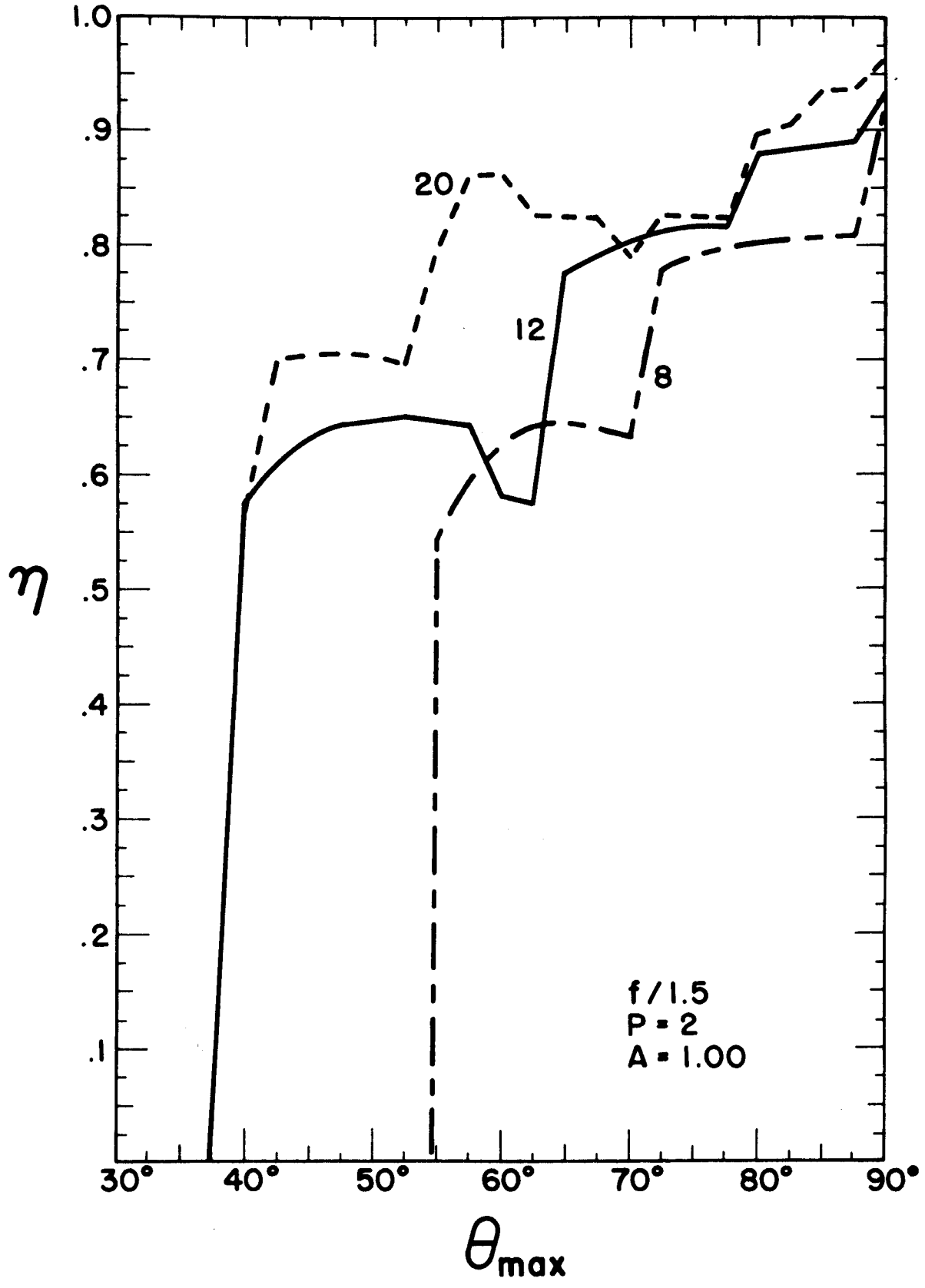

Figure V-B-12

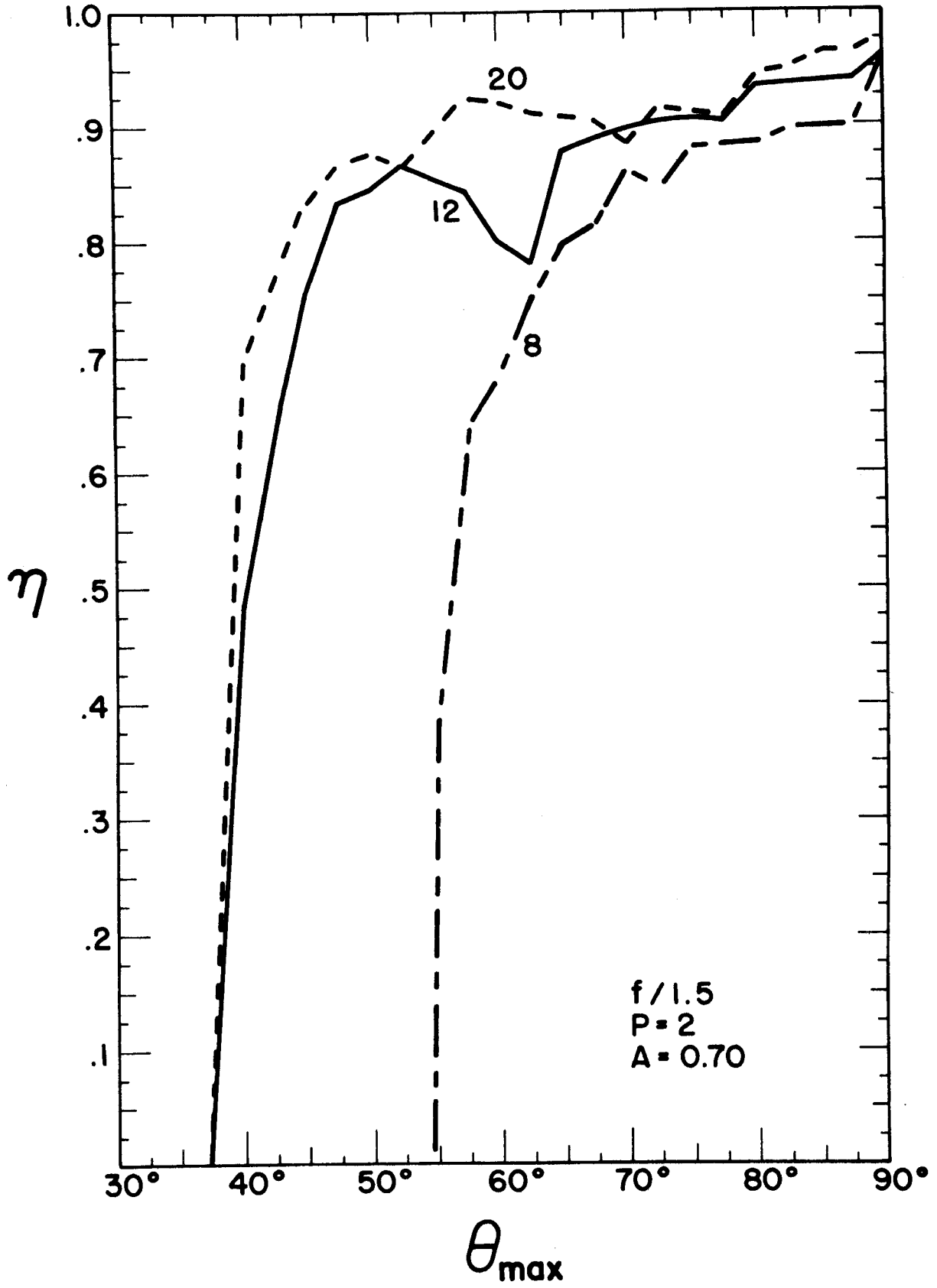

Figure V-B-13

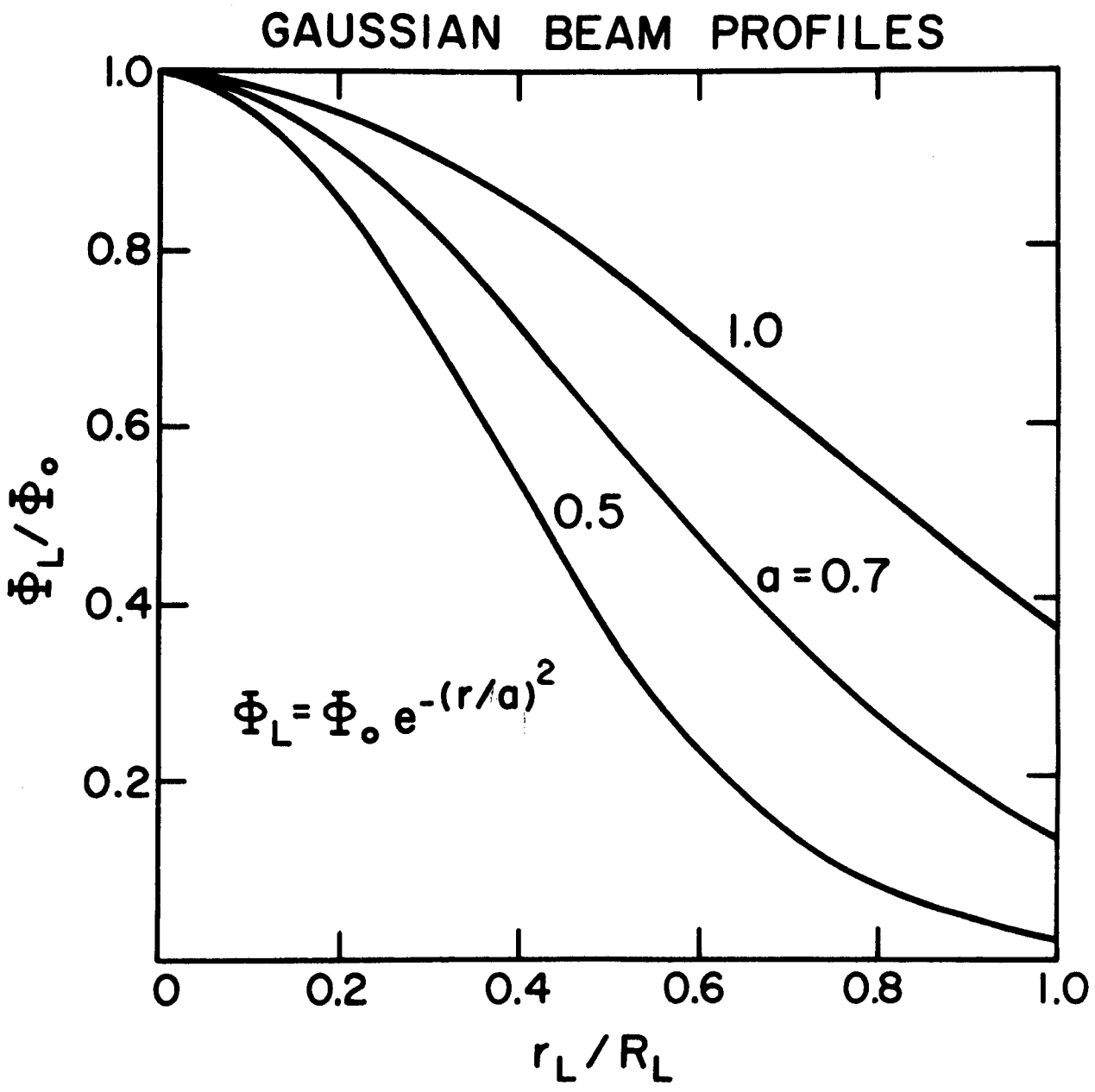
GAUSSIAN BEAM PROFILES
1.0
0.8
0.6
0.4
0.2
0
0.2
0.4
0.6
0.8
1.0
Φ_L/Φ_o
r_L/R_L
1.0
0.5
a = 0.7
$\Phi_L = \Phi_o e^{-(r/a)^2}$

Figure V-B-14

sometimes cross, the 12 and 20 beam cases always seem to improve (or worsen) together. Also note that $\eta = 0$ at $\theta_{max} = 54.7°$ for 8 beams and at $\theta_{max} = 37.4°$ for 12 or 20 beams, as predicted in section V-B-4. As we shall see, a practical illumination system requires $\theta_{max} \lesssim 50°$ in order to keep the angles of incidence reasonably small.

Figure V-B-15 shows optimum uniformity curves for the cubic exponential profile (p = 3, Fig. V-B-16). Again all three configurations are optimized together with a = 0.70. In this case better than 95% uniformity is obtained for 20 beams and over 93% using 12 beams, considerably better than that found using the Gaussian profile. Only slight improvement was realized by varying p near p = 3, while the results for p = 4 and 5 were much worse.

The remarkable closeness of the uniformity curves for 12 and 20 beams up to $\theta_{max} \simeq 50°$ suggests little advantage in choosing 20 beams rather than 12. However, the 12 beam curve is rather sharply peaked and might therefore be vulnerable to positioning errors. To investigate this question, let us calculate the change in the focal shift corresponding to a variation in θ_{max} of 2.5°, roughly the half-width of the peak in the 12 beam curve in Fig. V-B-15. From eq. (10) we have

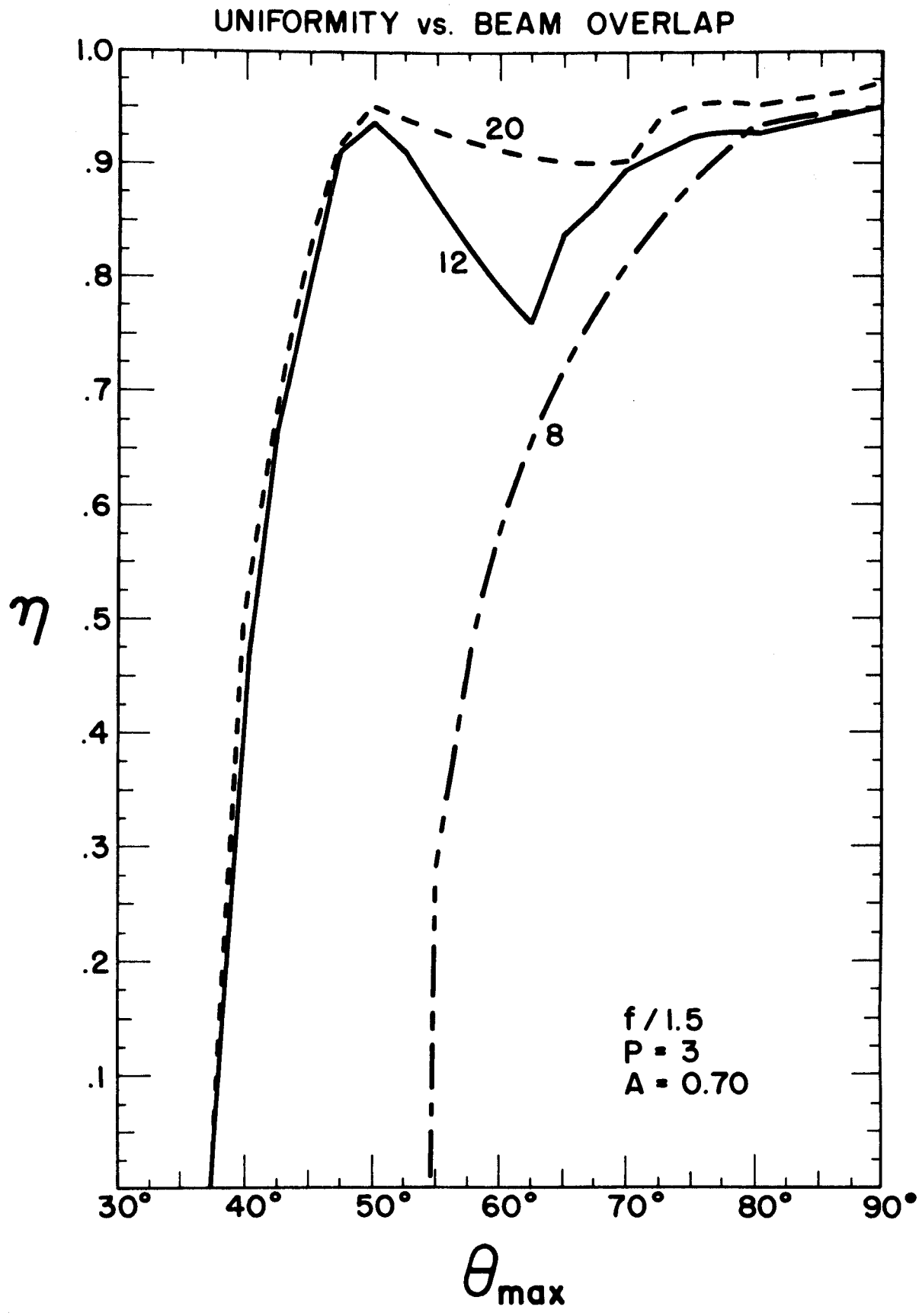
UNIFORMITY vs. BEAM OVERLAP
1.0
.9
.8
.7
.6
.5
.4
.3
.2
.1
η
20
12
8
f / 1.5
P = 3
A = 0.70
30°
40°
50°
60°
70°
80°
90°
θmax

Figure V-B-15

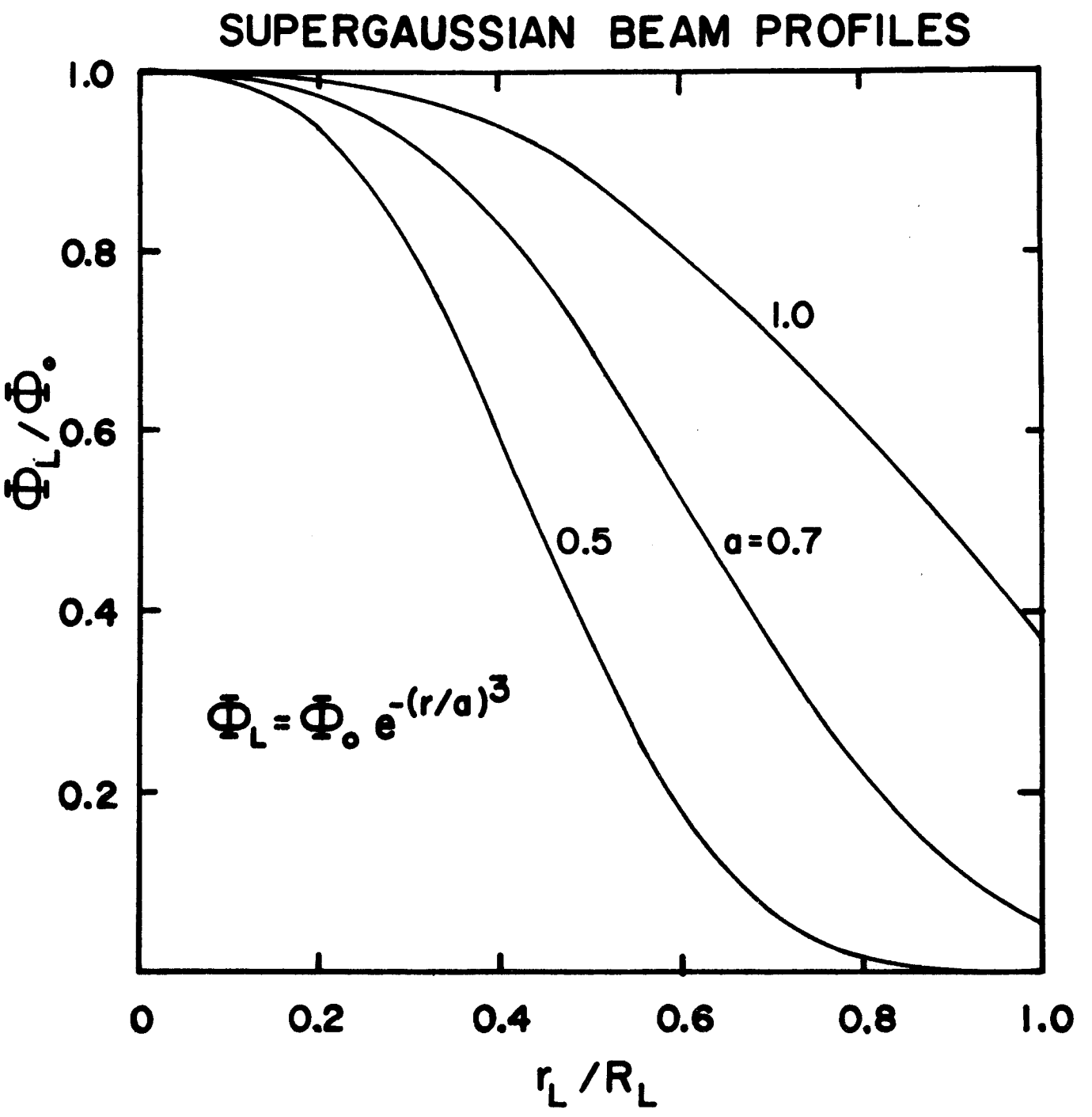
SUPERGAUSSIAN BEAM PROFILES
1.0
0.8
0.6
0.4
0.2
$\Phi_L / \Phi_\circ$
1.0
0.5
a=0.7
$\Phi_L = \Phi_\circ e^{-(r/a)^3}$
0
0.2
0.4
0.6
0.8
1.0
r_L / R_L

Figure V-B-16

$$\delta(\Delta x) = (2F\cos\theta_{max} + \sin\theta_{max})\, R_T\, \delta\theta_{max}\,, \tag{28}$$

which gives, for $F = 1.5$ and $\theta_{max} = 50^{o}$,

$$\delta(\Delta x) = 0.047\, R_T\, \delta\theta_{max}\,. \tag{29}$$

Setting $\delta\theta_{max} = 2.5^{o}$, we get $\delta(\Delta x) \simeq 12$ μm for $R_T = 100$ μm and $\delta(\Delta x) \simeq 120$ μm for $R_T = 1000$ μm.

While laser beams are routinely focused on target to within 5 μm in current laser fusion experiments,[5] maintaining optical alignment of many beams in a reactor environment at a repetition rate of 10-20 Hz is quite another matter. By the time each beam makes several reflections as it wends its way from laser to target, the accumulated jitter could be expected to exceed tens of microns. Thus, it seems reasonable to expect positioning to within 100 μm and thereby to control θ_{max} to within 2.5^{o} on reactor-size pellets. Smaller pellets can be uniformly illuminated with 12 beams only if sufficient time is available between shots to maintain alignment.

As we have seen, good uniformity also depends critically on the choice of spatial beam profile. Beam tailoring may be effected by soft apertures and Pockels cells.[13] While spatial filters[14] effectively eliminate fine structure, they are unable to remove gross beam inhomogeneities. It is therefore futile to

attempt fine beam tailoring unless the laser train produces a reasonably smooth beam to begin with. The sharp edge on the ideal optimal profile depicted in Fig. V-B-16 may also produce undesirable distortions of the focal region through self-focusing.[15] For this reason (among others) mirrors, rather than lenses, should be used as focusing elements.

A quantity relevant to system efficiency is the fill factor

$$ff = \frac{1}{\pi R_L^2} \int_0^{R_L} I_0(r)\, 2\pi r dr \ , \qquad (30)$$

which measures how well the beam fills the aperture. Table V-B-3 lists fill factors for a number of supergaussian profiles. Note that for a Gaussian,

$$ff = a^2 \left(1 - e^{-1/a^2}\right) . \qquad (31)$$

Now we see that there is something special about the optimal case a = 0.70; it is practically a stationary point for the variation of ff with index p. There is less than a 2% change in ff as p varies from 2 to 5. Table V-B-3 also illustrates the fact that considerable laser energy can be wasted in beam-tailoring. In the Appendix we derive a relationship between the fill factor and the beam overlap angle.

The 90% uniformity level required to prevent rapid growth of the Rayleigh-Taylor instability is based on analytic studies[2] and numerical simulation.[5] No direct physical measurement has yet been made of this effect. However, recent studies[7]

p \ a	.5	.70	.75	1.0
2	.2454	.4263	.4674	.6321
3	.2257	.4310	.4841	.6998
4	.2216	.4326	.4926	.7468
5	.2218	.4346	.4978	.7813

Table V-B-3. Fill Factors for Supergaussian Beam Profiles

show that the growth rate may be greatly reduced by controlling the radial density profile in the pellet. Thus, the 90% figure cited should be regarded as tentative, awaiting experimental confirmation.

All of the uniformity curves in Figs. V-B-13 and 14 exceed 95% as θ_{max} approaches 90°. The catch is that the angles of incidence increase with θ_{max} to the point where refractive loss of laser energy becomes prohibitively large. This is illustrated in Fig. V-B-17, which shows Ψ_{max} as a function of θ_{max} for various f/nos. For example, using f/1.5 lenses, the smallest possible value of Ψ_{max} is 18° for 12 or 20 beams. Based on the present studies and those at Livermore, 90% uniformity may be obtained around θ_{max} = 50° at the least, for which Fig. V-B-17 gives Ψ_{max} = 32°. The reflectivity of the pellet corona is approximately $\exp(-2p\cos^3\Psi)$, where p is the optical thickness, indicating large refractive losses as $\Psi \to 90°$. However, a detailed calculation,[7] averaging over the optimal beam profile shows only a few percent net energy loss due to oblique incidence when θ_{max} = 50°. Thus, uniform illumination of over 90% can be realized without excessive refractive energy loss.

Another reason for preferring smaller angles of incidence is to maximize resonance absorption.[16] In this process, the p-polarized component of the electric field is strongly absorbed in a range of incident angles depending on the density scale height in the

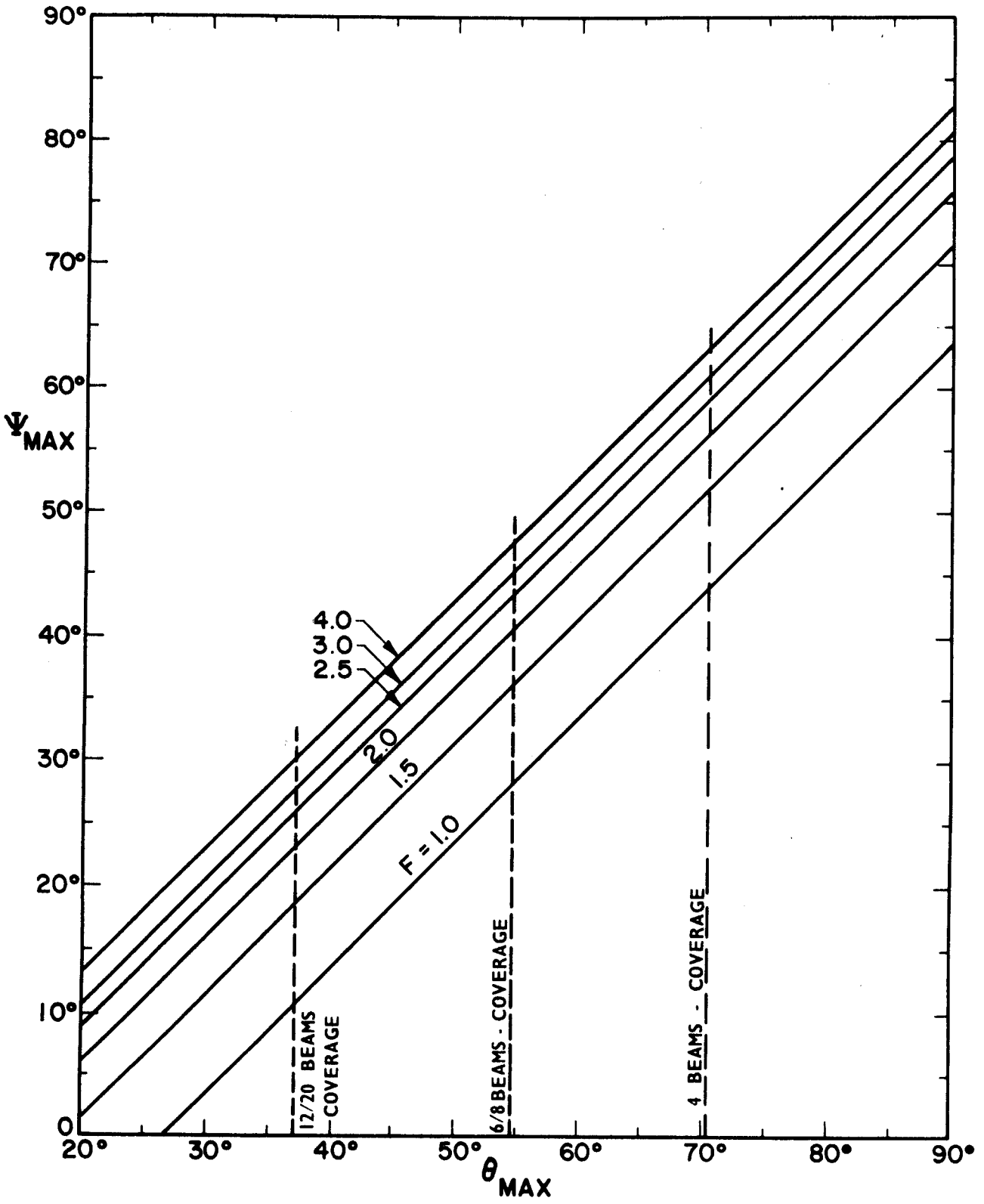
90°
80°
70°
60°
50°
40°
30°
20°
10°
0
Ψ_{MAX}
20°
30°
40°
50°
60°
70°
80°
90°
θ_{MAX}
4.0
3.0
2.5
2.0
1.5
F=1.0
12/20 BEAMS COVERAGE
6/8 BEAMS - COVERAGE
4 BEAMS - COVERAGE

Figure V-B-17

pellet corona. While the optimal angle of incidence varies from case to case, it is always less than 10°, so that the average angles of incidence ($\Psi \simeq \frac{2}{3} \Psi_{max}$) cited above are too large for effective resonance absorption. However, other effects, such as expansion of the critical surface[7] and self-steepening[17] of the plasma density profile, can improve the match of incident angle to resonance angle.

V-B-5-b. Solid Angle-Limited Designs

Next we turn to the reactor-type cases where the f/nos. are limited by the fractional solid angle allotted to optics, as listed in Table V-B-2. As before, we consider 8, 12 and 20 beams, but use only the optimal cubic exponential beam profile, with a = 0.70. Figures V-B-18 and 19 show the resulting uniformities for $\gamma = \Delta\Omega/4\pi$ = 0.1 and 0.2. Again the 8 beam configuration runs a poor third. What is perhaps surprising is that the curves are almost identical for N = 20, with only a few percent difference in the N = 12 curves. However, due to the larger f/nos., the angles of incidence are somewhat larger in the γ = 0.1 cases (Fig. V-B-17). For example, for 20 beams at θ_{max} = 50°, Ψ_{max} = 38.5° and 42°, for γ = 0.2 and 0.1, resp. For N = 12, Ψ_{max} = 36° and 39.5°. That is, decreasing γ by a factor of two only increases Ψ_{max} by 10%, a very favorable trade-off indeed!

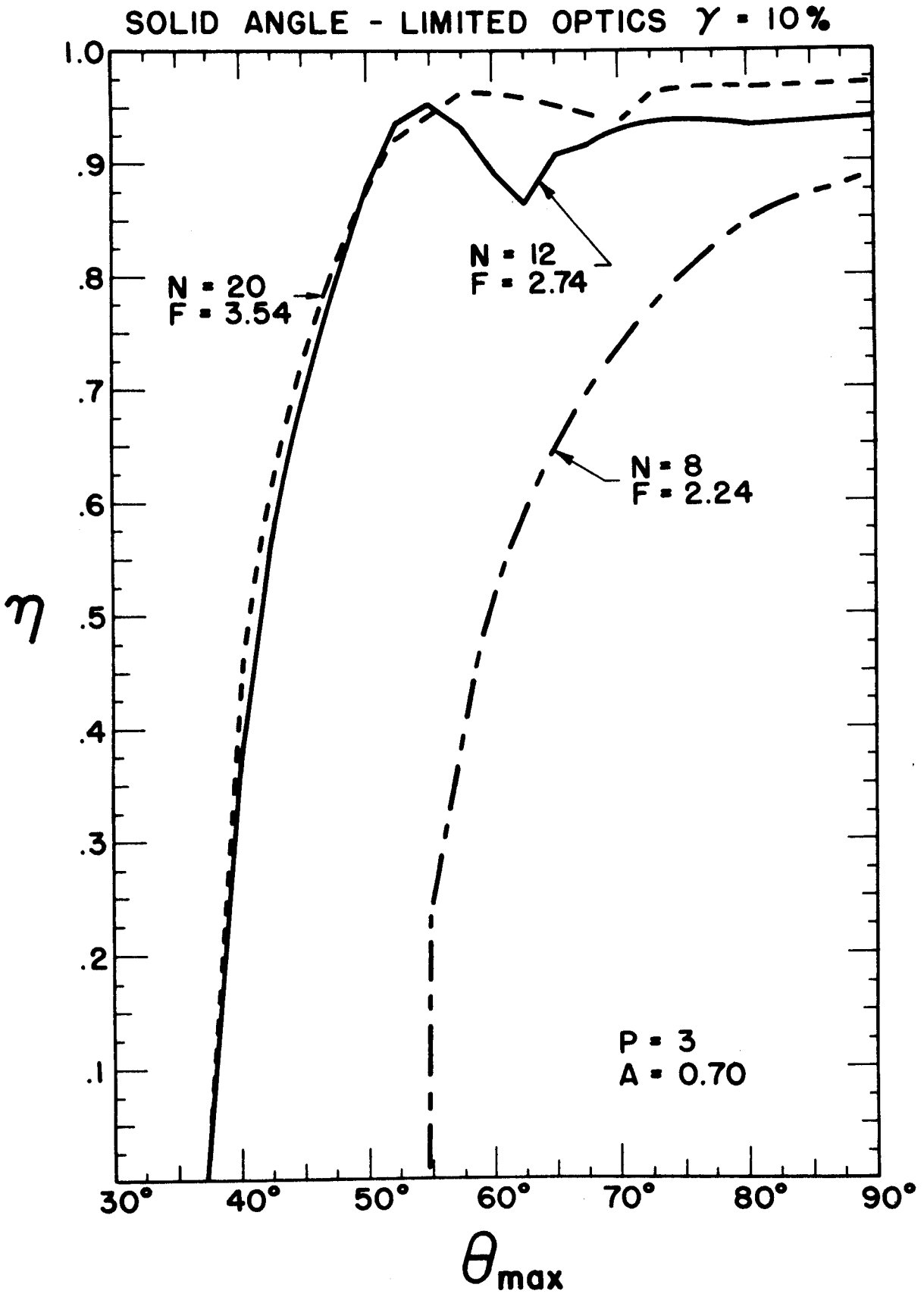
SOLID ANGLE - LIMITED OPTICS γ = 10%
1.0
.9
.8
.7
.6
.5
.4
.3
.2
.1
η
N = 20
F = 3.54
N = 12
F = 2.74
N = 8
F = 2.24
P = 3
A = 0.70
30°
40°
50°
60°
70°
80°
90°
θmax

Figure V-B-18

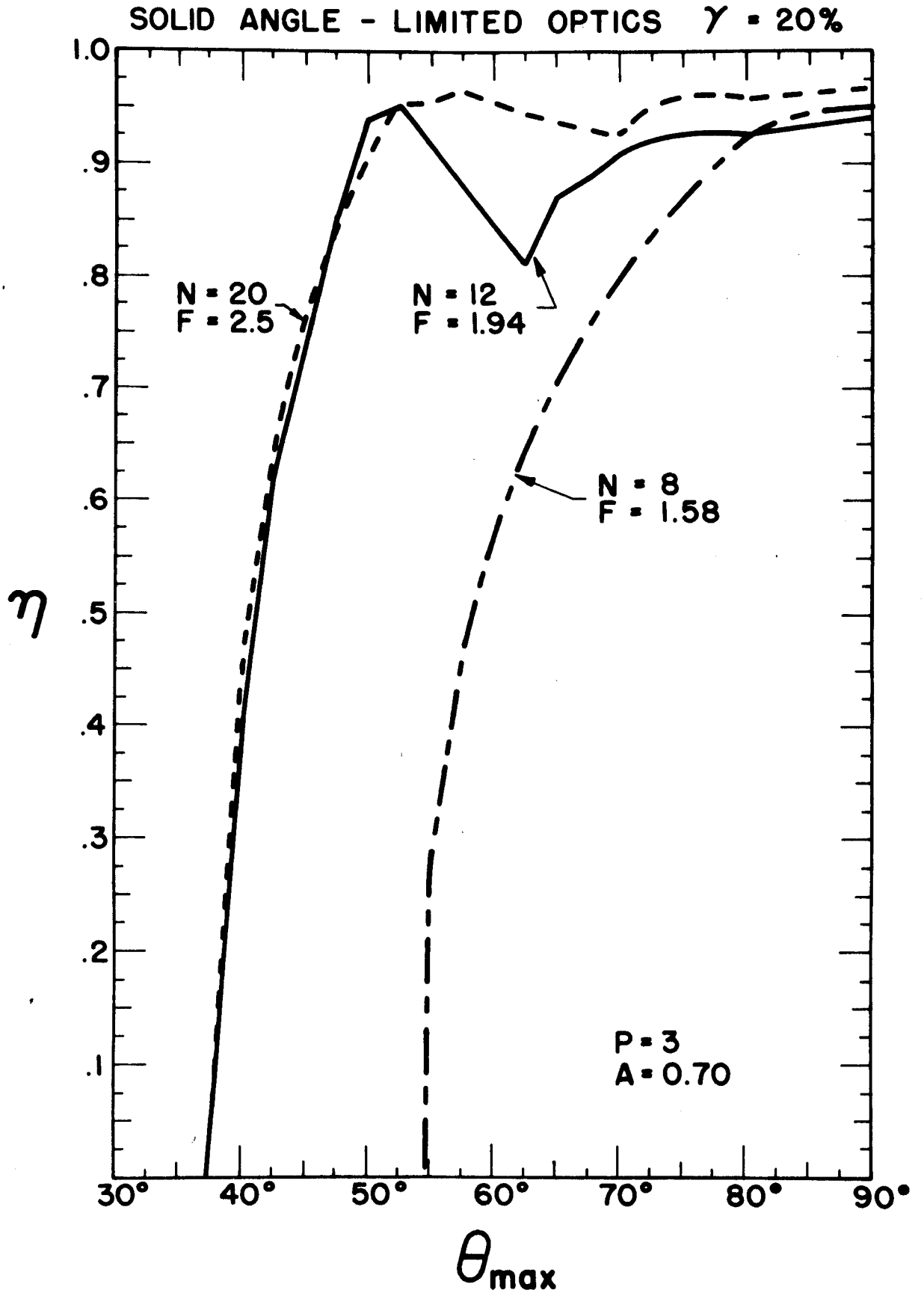
SOLID ANGLE - LIMITED OPTICS γ = 20%
1.0
.9
.8
.7
.6
.5
.4
.3
.2
.1
η
N = 20
F = 2.5
N = 12
F = 1.94
N = 8
F = 1.58
P = 3
A = 0.70
30°
40°
50°
60°
70°
80°
90°
θmax

Figure V-B-19

V-B-6. Discussion

We have described the calculation of illumination uniformity on spherical targets for 8, 12 and 20 overlapping beams arranged according to the symmetry of the Platonic solids, using ideal thin lenses as the final optical elements. Due to the extreme symmetry of these configurations, only a small triangular region had to be examined. Other, less symmetrical, illumination schemes would require looking at a larger portion of the sphere and therefore entail more programming. On the other hand, it would be easy to modify PLATO to employ aplanatic lenses, or parabolic mirrors. Further, spatial beam profiles of arbitrary complexity may be used in place of the present family of supergaussian.

Optimization studies were made using f/1.5 lenses in each of the 8, 12 and 20 beam configurations. Generally, the best uniformity was obtained for a cubic exponential having a width parameter $a \simeq 0.70$. While the maximum uniformity was found to be comparable for 12 or 20 beams, the 12 beam case seemed vulnerable to misalignment. Eight beam illumination was always found to run a poor third. Typical angles of incidence were $\Psi_{max} \simeq 32^{o}$, indicating considerable loss of energy through refraction. However, by averaging over the angles of incidence and the spatial beam profile, the net refractive loss due to oblique incidence was found to be negligible. In an attempt to reduce this loss, we have also computed 12 beam illumination with

f/1.14 lenses, which take up the same total solid angle as 20 f/1.5 lenses. The result is shown as the plotted circles in Fig. V-B-15. Best uniformity is obtained near $\theta_{max} = 50°$, where $\Psi_{max} \simeq 25^{o}$, reducing refraction losses somewhat. Optimization studies using aplanatic lenses[12] show negligible differences from the above results.

The equality of the coverage angles, θ_m^*, for the dodecahedron and icosahedron is probably due to their close geometrical relationship. (Mathematically they are reciprocals[10] and share the same group properties). Similarly, it may be shown that the coverage angle for the cube is identical to that of its reciprocal, the octahedron. The tetrahedron, on the other hand, is self-reciprocal and has a coverage angle $\theta_m^* = 70.53^{o}$. Thus, we would anticipate much better uniformity for 6 beams ($\theta_m^* = 54.7^{o}$) than for 4 beams, but only slight improvement in going from 6 to 8 beams.

Appendix: Theorem on Uniformity

After the numerical work on uniformity was completed we discovered a functional relationship between the optimal beam overlap angle and the fill factor. There are no restrictions on the beam profile except that its maximum occur on the optical axis. In addition we require $\theta_{max} < \beta$, the beam separation, so that the center of the beam is not overlapped. This is true for 12 beams, but not for 20.

If uniform irradiance is attained, its value must be close to the individual beam maxima:

$$\Phi_{max} \approx \Phi_u \approx \frac{NP_b}{4\pi R_T^2} \quad . \tag{1}$$

The power per beam is related to the fill factor by

$$P_b = \langle \Phi_L \rangle A_L = ff \; \Phi_{L_{max}} A_L \quad . \tag{2}$$

The lens flux is related to the target flux by the inverse square law:

$$(\Delta+R)^2 \; \Phi_{max} = f^2 \Phi_{L_{max}} \quad . \tag{3}$$

Combining these results and using the definition of f/no, we obtain

$$ff = \frac{16F^2}{N(1+\delta)^2} \; , \tag{4}$$

where

$$\delta \equiv \frac{\Delta}{R_T} = 2F \sin \theta_{max} - \cos \theta_{max} \quad .$$

From Fig. V-B-14, $\theta_{max} = 50^{o}$, F = 1.5, N = 12, giving ff = 0.425.

From Table V-B-3, the numerical value is ff = 0.431.

For large F, Eq. (4) reduces to

$$ff = \frac{4}{N \sin^2\theta_m} \quad .$$

It is remarkable that Eq. (4) is independent of the details of the beam profile and the beam geometry. Although we have used it here only as a check on our work, it would have proved useful in optimizing 12 beam uniformity.

References for Section V-B

1. J. Nuckolls, L. Wood, A. Thiessan and G. Zimmerman, Nature 239, 139 (1972). K. A. Brueckner and S. Jorna, Rev. Mod. Phys. 46, 325 (1974).

2. R. E. Kidder, Nucl. Fusion 16, 3 (1976). S. E. Bodner, Phys. Rev. Lett. 33, 761 (1974). J. D. Lindl and W. C. Mead, Phys. Rev. Lett. 34, 1273 (1975).

3. G. H. McCall and R. L. Morse, Laser Focus, Dec. 1974, p. 40. J. F. Holzrichter et al., Bull. Am. Phys. Soc. 20, 1266 (1975).

4. N. G. Basov et al., Lebedev Institute Preprint No. 74, Moscow (1976).

5. Lawrence Livermore Laboratory Laser Program Annual Report (1974), UCRL-50021-74.

6. C. E. Thomas, Appl. Optics 14, 1267 (1974).

7. J. E. Howard, Univ. of Wisconsin Nuclear Engineering Dept. Report UWFDM-188, 1977.

8. Univ. of Wisconsin Nuclear Engineering Dept. Report UWFDM-191, Section III-B, 1977.

9. Laser Focus, May 1976, p. 48.

10. H. S. M. Coxeter, Introduction to Geometry, 2nd ed., Wiley (New York) 1969, p. 152.

11. F. Klein, Lectures on the Icosahedron, Dover (N.Y.), 1956.

12. W. A. Kleinhaus, Appl. Optics 15, 14 (1976).

13. Lawrence Livermore Laboratory Laser Program Annual Report (1974), UCRL-50021-74, p. 135.

14. Ibid., p. 169.

15. Ibid., p. 200.

16. J. P. Freidberg, R. W. Mitchell, R. L. Morse and L. I. Rudsinski, Phys. Rev. Lett. 28, 795 (1972).

17. K. G. Estabrook, E. J. Valeo and W. L. Kruer, Phys. Fluids 18, 1151 (1975).

V-C. Imaging Properties of Off-Axis Paraboloidal Mirrors

V-C-1. Introduction

Off-axis parabolic mirrors are useful for simultaneously turning and focusing a collimated beam. Traditionally difficult to fabricate, their use has become much more practical with the advent of the diamond-turning technique.[1,2] In this section, geometric optics is employed to calculate the shape of the image and the irradiance cast on a spherical target by a circular beam. The target is assumed to be large enough that diffraction effects may be ignored. For moderately large f/no. the reflected beam is found to be nearly circular, with its geometric center shifted by a small amount from the optical axis. The target irradiance, on the other hand, can be highly asymmetric unless the beam intensity falls off rapidly at the beam edge. An expansion in powers of inverse f/no. is used to obtain closed form expressions for the image shape and target irradiance. Numerical studies are carried out for parameters relevant to the design of a laser fusion reactor.

Since laser fusion reactor targets are small ($\sim$ 1 mm) and focal lengths long[3,4] ($\gtrsim$ 10 m), pointing errors must be held to about one sec of arc. Conventional analysis of Seidel aberrations is limited to regions near the optical axis of axisymmetric systems, and does not apply to far off-axis rays.[5] Nevertheless, since spherical aberration is absent at all ray heights, one may readily calculate aberrations due to various tilt errors. This is done analytically in Sec. 4. A simple expression is also derived for the perturbed target irradiance under small tilt errors, based on a new calculation of the caustic curve. These simple formulas allow one to carry out detailed design studies without recourse to ray tracing codes.

Figure V-C-1 depicts a circular beam of radius r_B incident on a parabolic mirror, such that the optical axis is turned through an angle ϕ, and the focal distance measured along the optical axis is r_o.

A paraboloid may be described in cylindrical coordinates by

$$R^2 = 4a(a-z) \ , \tag{1}$$

and in spherical polar coordinates by

$$r = \frac{2a}{1+\cos\phi} = 2a-z \ , \tag{2}$$

where a is the latus rectum. Here z is measured to the left of O' in order that the turning angle ϕ be the spherical polar angle. The distance from ray to axis is

$$R = \frac{2a\sin\phi}{1+\cos\phi} = 2a \tan\phi/2 \tag{3}$$

which may be inverted to yield

$$\sin\phi = \frac{4aR}{4a^2+R^2} \tag{4}$$

$$\cos\phi = \frac{4a^2-R^2}{4a^2+R^2} \ . \tag{5}$$

The radius of curvature is

$$R_c = \frac{[1+(R')^2]^{3/2}}{|R''|} \ , \tag{6}$$

or

$$R_c = 2a \sec^3\phi/2 \ . \tag{7}$$

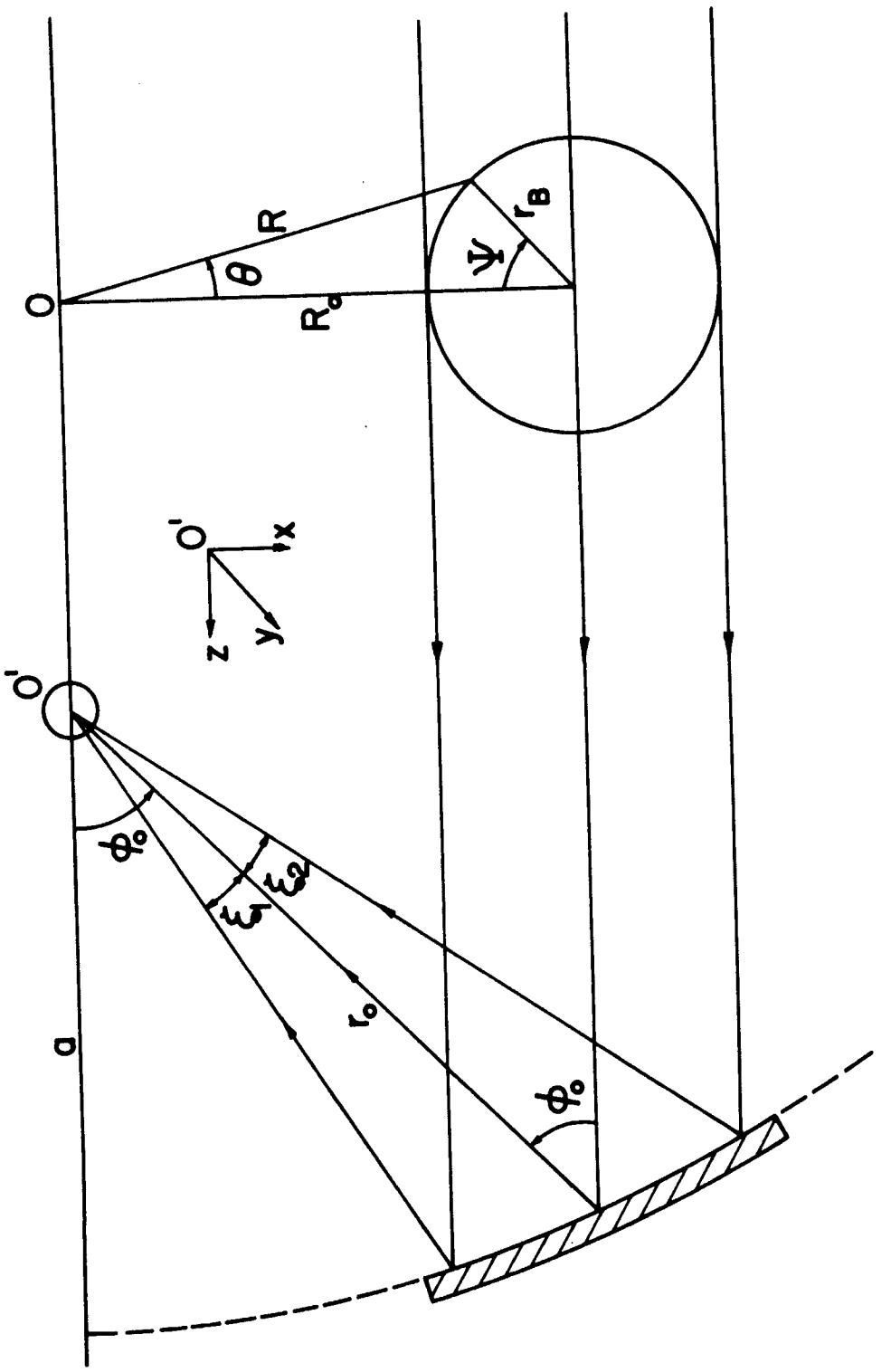

Figure V-C-1

The arc length of the mirror is given by

$$S = \int_{R_1}^{R_2} \sqrt{1+(dz/dR)^2}\, dR \ , \tag{8}$$

or

$$S = 2a \int_{u_1}^{u_2} \sqrt{1+u^2}\, du \ , \tag{9}$$

where

$$u \equiv R/2a \ . \tag{10}$$

Carrying out the integral, we obtain

$$S = au_2 \sqrt{1+u_2^2} - au_1 \sqrt{1+u_1^2} + a \ln \left[\frac{u_2+\sqrt{1+u_2^2}}{u_1+\sqrt{1+u_1^2}} \right] . \tag{11}$$

When $r_B << 2a$ this reduces to

$$S \simeq 2r_B \sec(\phi_o/2) \ , \tag{12}$$

accurate to 3 figures when $r_o = 10$ and $r_B = 1$. It should be noted that Eq. (12) gives the long dimension of the approximately elliptical spot projected on the mirror, and that S is independent of r_o when $r_B << r_o$.

A typical final mirror for a laser fusion reactor would have $\phi_o = 90°$, $r_o = R_o = 10$ m and $r_B = 1$ m, so that a = 5 m and S = 2.83 m. Such a mirror is well beyond the state-of-the-art of diamond turning ($R_o = 80$ cm), and would be prohibitively expensive to produce by conventional methods. Thus, it may be necessary to design the beam transport system for a laser fusion reactor in a way that minimizes the final turning angle.

Also note that

$$\phi_1 = 83.97°, \quad \xi_1 \equiv \phi_0 - \phi_1 = 6.03°$$

$$\phi_2 = 95.45°, \quad \xi_2 = \phi_2 - \phi_0 = 5.45° ,$$

indicating about a 10% distortion in the image contour.

Figures V-C-2 to 4 illustrate parabolic mirrors for a focal distance r_0 = 10 m and a beam radius r_B = 1 m, for turning angles ϕ_0 = 45°, 90°, and 135°. Note that the major diameter exceeds 6 m when ϕ_0 = 135°. The growth of mirror size with increasing ϕ_0 is plotted in Fig. V-C-5, which allows for the fact that only about 80% of the mirror surface is usable. We now examine the shape of the image of a circular beam in detail.

V-C-2. Image Distortion

We are interested in the shape of the image and the irradiance on a small ($R_T \simeq 1$ mm) spherical target, and the image outline at some distance from target, where the beam ports are to be placed. Figure V-C-6 depicts the image of a circular beam in a plane normal to $\vec{r}_0$, at an arbitrary distance $\tilde{r}_0$ from the focus.

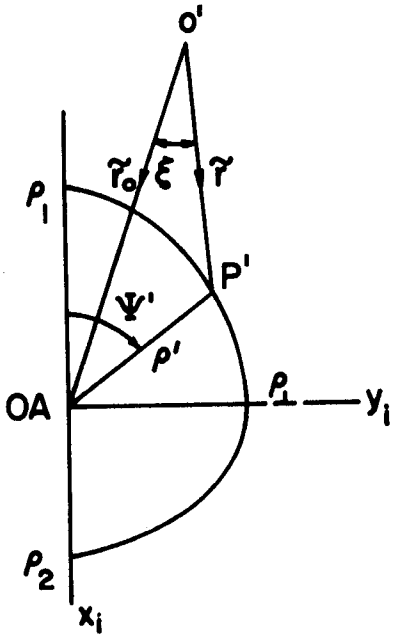

Figure V-C-6

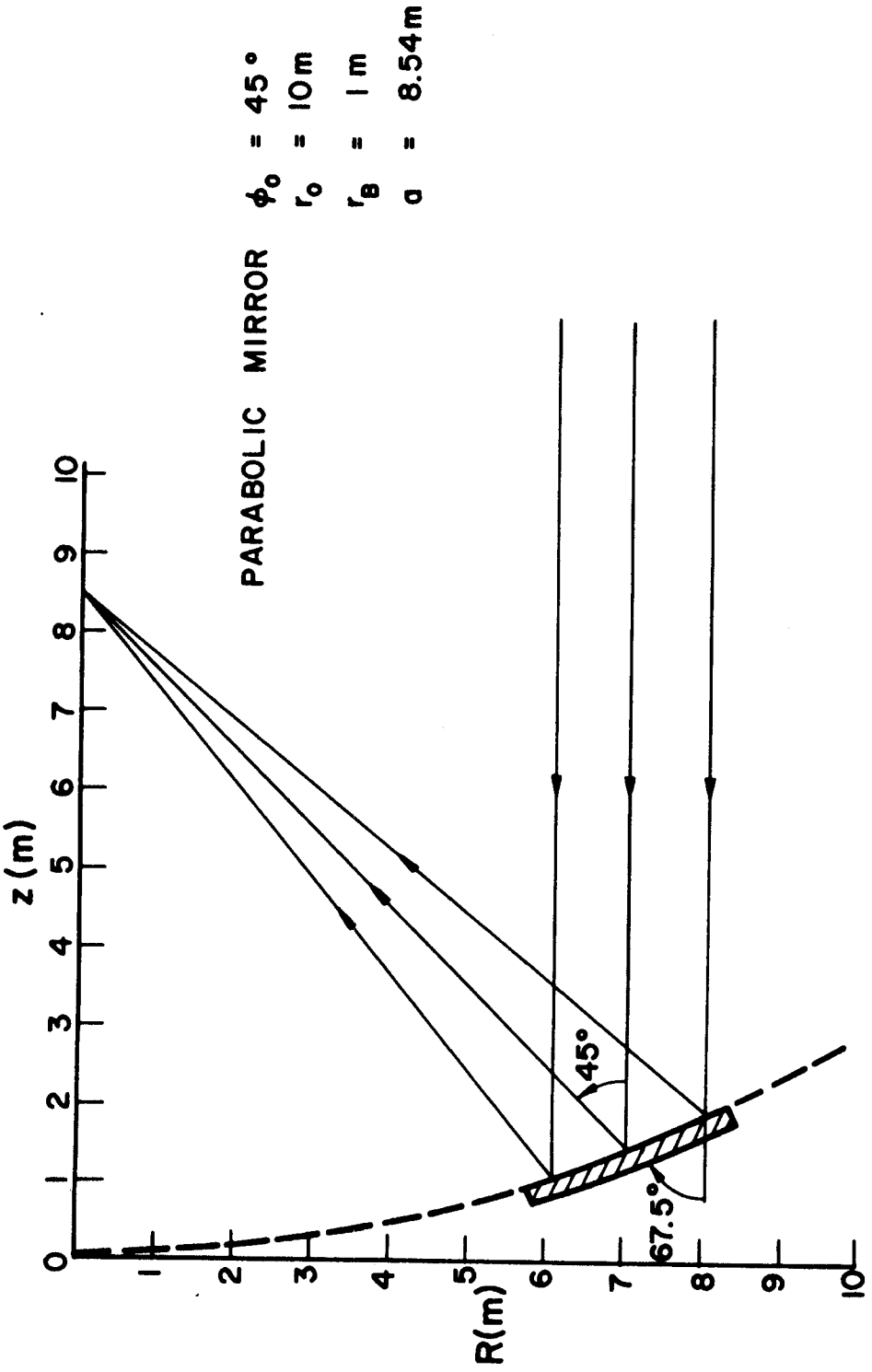
PARABOLIC MIRROR ϕ_o = 45°
r_o = 10m
r_B = 1m
a = 8.54m
z(m)
R(m)
45°
67.5°
0
1
2
3
4
5
6
7
8
9
10

Figure V-C-2

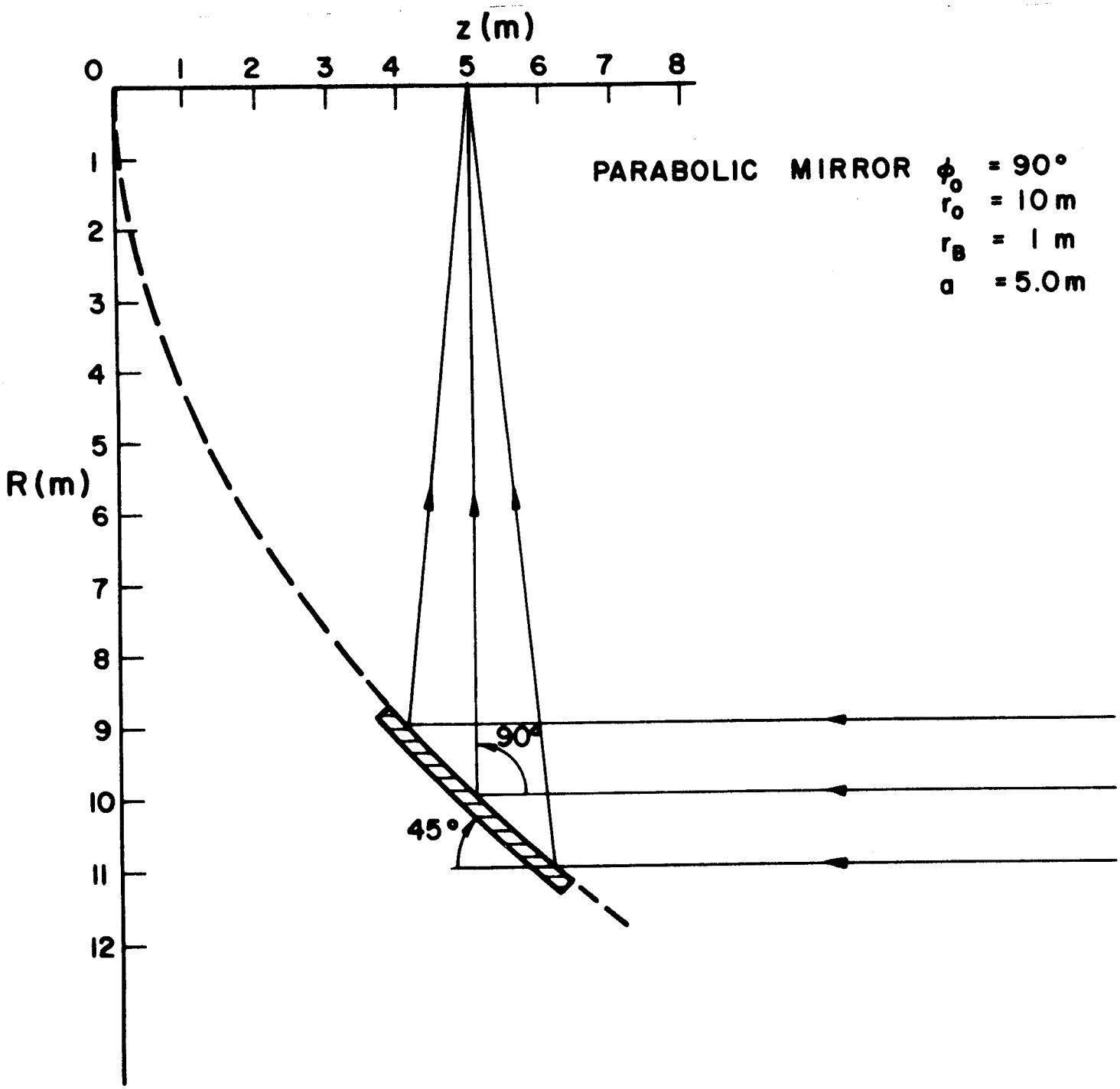
z (m)
0 1 2 3 4 5 6 7 8
R(m)
1 2 3 4 5 6 7 8 9 10 11 12
PARABOLIC MIRROR
ϕ_0 = 90°
r_0 = 10 m
r_B = 1 m
a = 5.0m
90°
45°

Fig. V-C-3.

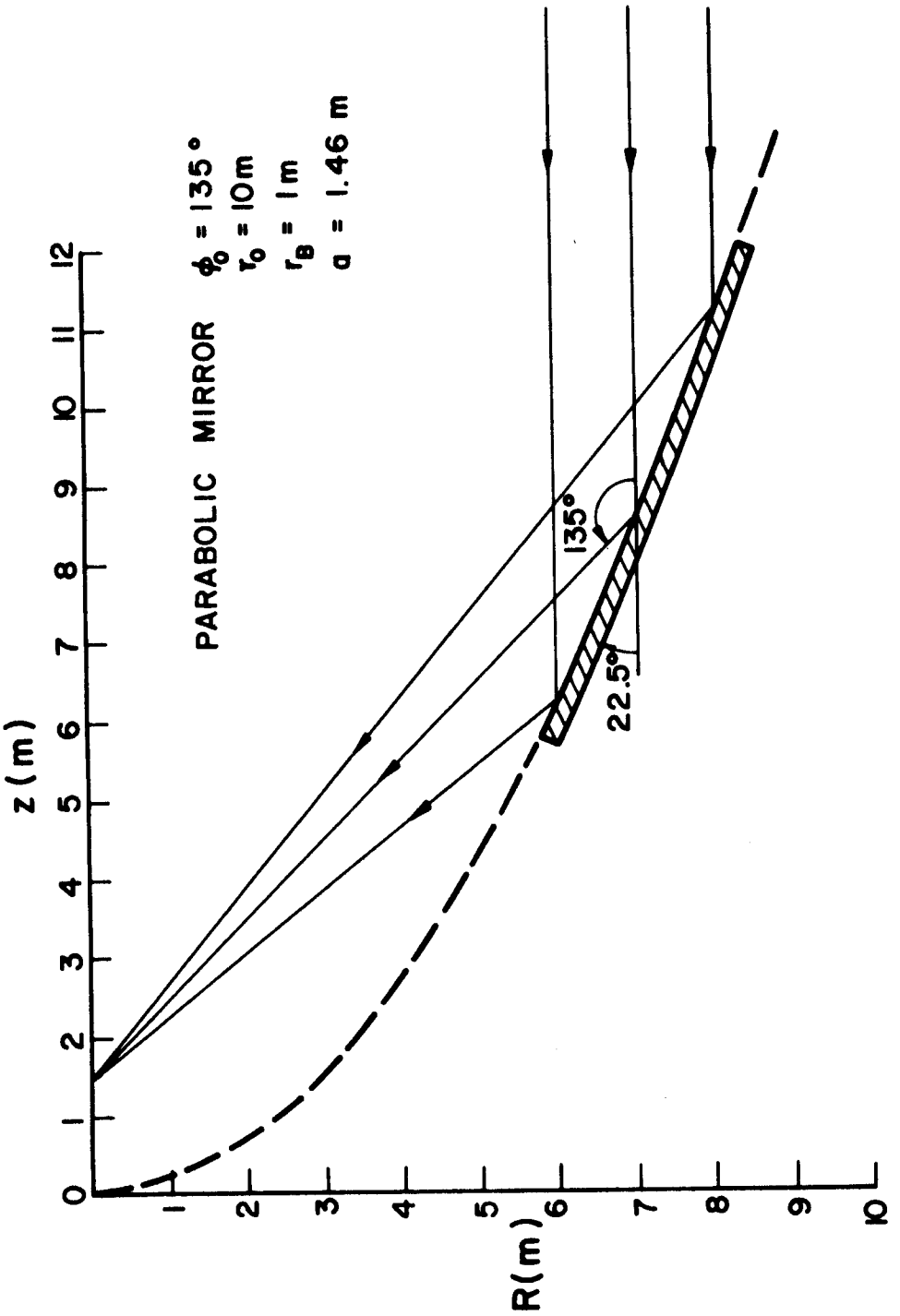
PARABOLIC MIRROR
$\phi_0 = 135°$
$r_0 = 10m$
$r_B = 1m$
$a = 1.46$ m
135°
22.5°
z(m)
R(m)
0
1
2
3
4
5
6
7
8
9
10
11
12

Figure V-C-4

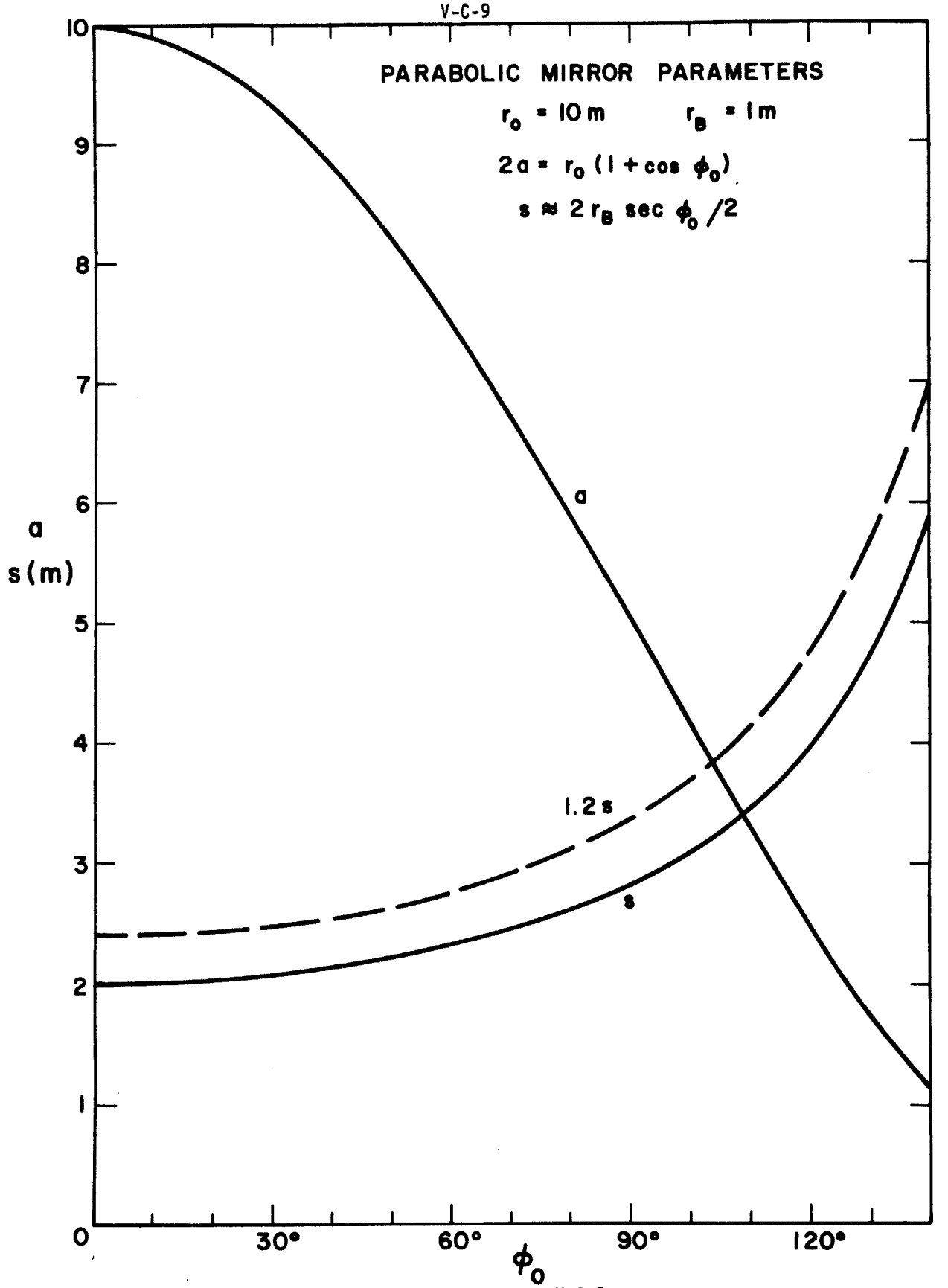
PARABOLIC MIRROR PARAMETERS
r_0 = 10 m r_B = 1 m
$2a = r_0 (1 + \cos \phi_0)$
$s \approx 2 r_B \sec \phi_0 / 2$
a
1.2 s
s
a
s(m)
ϕ_0
0
1
2
3
4
5
6
7
8
9
10
30°
60°
90°
120°

Figure V-C-5

Let us identify a point P on the edge of the object disk by polar coordinates (r_B,Ψ) and its image P' by (ρ',Ψ'). The polar coordinates of point P with respect to the origin at O are

$$R^2 = R_o^2 + r_B^2 - 2R_o r_B \cos\Psi \tag{13}$$

$$\sin\theta = \frac{r_B}{R}\sin\Psi \ . \tag{14}$$

The reflected ray $\vec{r}(r,\theta,\phi)$ is then determined by Eqs. (2), (3) and (14). In most laser fusion applications the spot size is sufficiently small that ξ may be used in place of ρ' in measuring port radii.

The angles ξ and Ψ' in Fig. V-C-6 locate the vector $\vec{r}$ with respect to a new spherical polar coordinate system having its z axis along $\vec{r}_o$, as shown in Fig. V-C-7. (We have reversed the sense of $\vec{r}$ and $\vec{r}_o$ relative to Fig. V-C-1).

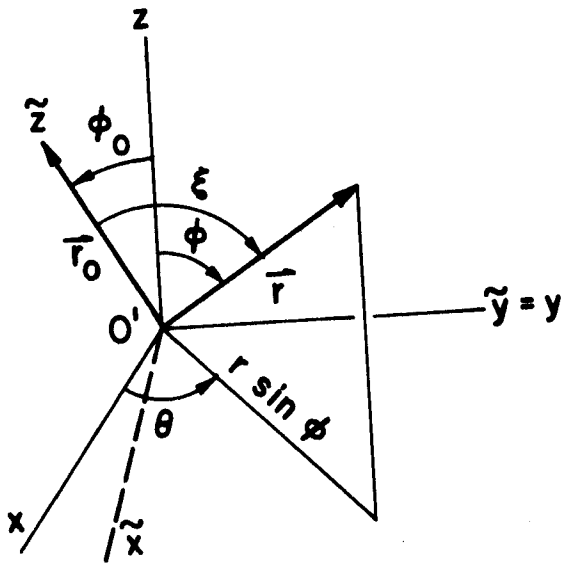

Figure V-C-7

Rotating the z axis through the angle ϕ_o in the x-z plane, we have

$$\begin{aligned} \tilde{x} &= x\cos\phi_o - z\sin\phi_o = r\sin\xi\cos(\pi-\Psi') \\ \tilde{y} &= y \qquad\qquad\qquad\quad = r\sin\xi\sin(\pi-\Psi') \\ \tilde{z} &= x\sin\phi_o + z\cos\phi_o = r\cos\xi \ , \end{aligned} \tag{15}$$

where

$$x = r \sin\phi \cos\theta$$

$$y = r \sin\phi \sin\theta$$

$$z = r \cos\phi \ . \tag{16}$$

Thus,

$$\cos\xi = \sin\phi_o \sin\phi \cos\theta + \cos\phi_o \cos\phi \tag{17}$$

$$\tan\psi' = \frac{\sin\phi \sin\theta}{\sin\phi_o \cos\phi - \cos\phi_o \sin\phi \cos\theta} \tag{18}$$

$$\sin\xi \sin\psi' = \sin\phi \sin\theta \ . \tag{19}$$

Any pair of Eqs. (17)-(19) determine the image in beam-centered coordinates. It is useful to introduce the smallness parameter

$$\varepsilon = r_B/r_o \ . \tag{20}$$

Eqs. (11)-(13) may then be expanded in powers of ε, with the result that

$$\psi' = \psi + 1/2 \ \varepsilon \sin\psi \tan\phi_o/2 + \ldots \tag{21}$$

$$\xi = \varepsilon + 1/2 \ \varepsilon^2 \cos\psi \tan\phi_o/2 + \ldots \tag{22}$$

It follows that

$$\boxed{\xi^2 \sin^2\psi' + (\xi\cos\psi' - \Delta\xi)^2 = \varepsilon^2 + \mathcal{O}(\varepsilon^4) \ ,} \tag{23}$$

where

$$\boxed{\Delta\xi \equiv \frac{1}{2}\,\varepsilon^2\,\tan\phi_0/2\ .} \tag{24}$$

That is, to lowest order the image is circular, with its center shifted a distance $\Delta\xi$ from the optical axis in the $-\phi$ direction. Higher order contributions to ξ and ψ' are very tedious to calculate.

The angles ξ_1 and ξ_2 delimiting the spot size in the median plane are then

$$\xi_{1,2} = \varepsilon(1 \pm \frac{1}{2}\,\varepsilon\,\tan\phi_0/2)\ . \tag{25}$$

The following semi-empirical formula is more accurate:

$$\xi_{1,2} = \varepsilon(1 \mp \frac{1}{2}\,\varepsilon\,\tan\phi_0/2)^{-1}\ . \tag{26}$$

Since the image is nearly circular, it makes sense to define an effective f/no.,

$$F = \frac{1}{2}\cot\bar{\xi} \simeq \frac{1}{2\varepsilon}\ , \tag{27}$$

independent of ϕ_0.

Equation (26) is accurate to 0.3% for $\varepsilon \leq 0.2$ and $\phi_0 \leq 135^0$; Eq. (27) is good to within 2% for $\varepsilon \leq 0.2$ and $\phi_0 \leq 90^0$. As an important physical consequence, note that an auxiliary beam used to align the optical axis will not pass through the center of the beam port.

When $\phi_o = 90^o$ we have the exact formulas,

$$\tan\xi_1 = \varepsilon \left(\frac{1-\varepsilon/2}{1-\varepsilon}\right) \tag{28}$$

$$\tan\xi_2 = \varepsilon \left(\frac{1+\varepsilon/2}{1+\varepsilon}\right) \tag{29}$$

in agreement with Eq. (22) to $O(\varepsilon^2)$.

For r_o = 10 m and r_B = 1 m, Eq. (30) predicts about a 10% asymmetry, in agreement with the previous estimate. Fig. V-C-9 depicts the complete images for the same parameters, with ϕ_o = 45°, 90° and 135°; Figs. V-C-10 and 11 show the same contours for r_o = 5 m and 15 m. These results indicate considerable advantage in maintaining $r_B << r_o$ and $\phi_o \leq 90°$. Since r_B is contrained by damage thresholds to at least one meter, we see that $r_o \gtrsim 10$ m is a reasonable choice of focal length. This value is also consistent with current laser fusion reactor designs.[3]

Besides distorting the shape of the beam profile, an off-axis parabolic mirror also modifies the two-dimensional irradiance profile. The next section takes up this question in detail.

V-C-3. Two-Dimensional Irradiance Profiles

The target and beam irradiances are related by conservation of energy;

$$I_T dA_T = I_B dA_B , \tag{30}$$

where

$$dA_B = R dR d\theta \tag{31}$$

$$dA_T = R_T^2 \sin\phi \, d\phi d\theta . \tag{32}$$

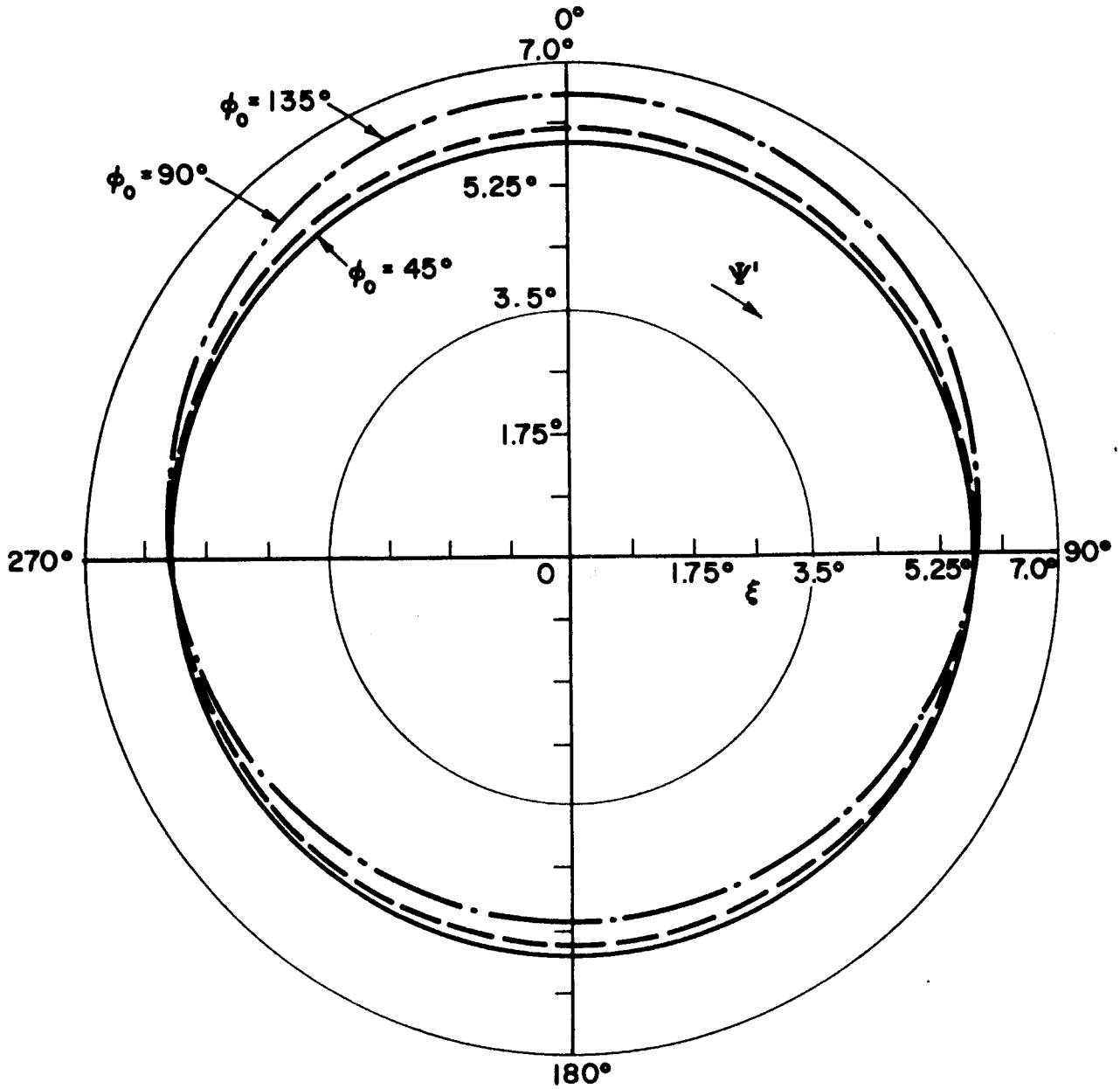
0°
7.0°
ϕ_0 = 135°
ϕ_0 = 90°
ϕ_0 = 45°
5.25°
3.5°
1.75°
Ψ'
270°
90°
0
1.75°
3.5°
5.25°
7.0°
ξ
180°

Figure V-C-9

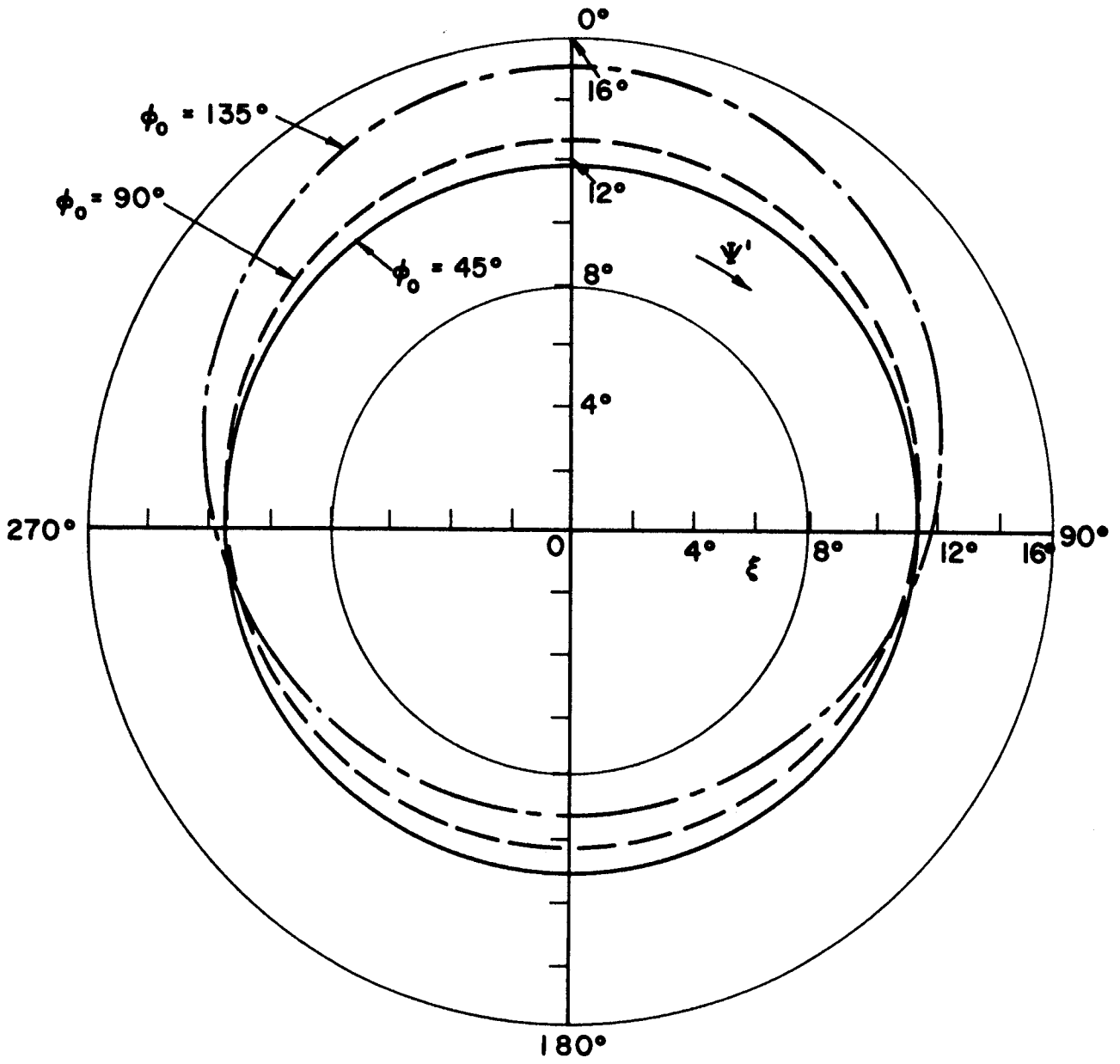

Figure V-C-10

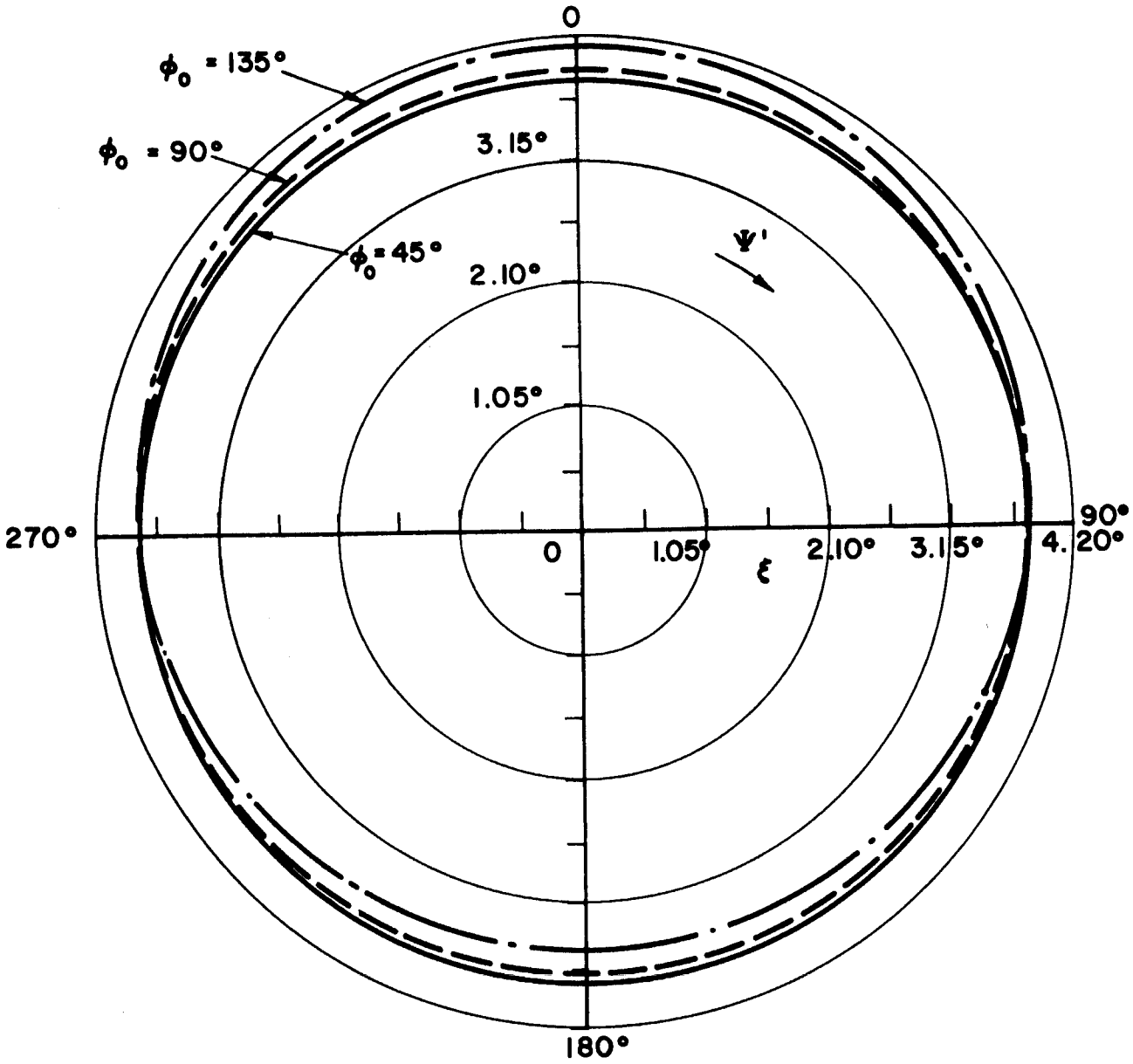
0
ϕ_0 = 135°
ϕ_0 = 90°
ϕ_0 = 45°
3.15°
2.10°
1.05°
Ψ'
270°
90°
0
1.05°
2.10°
3.15°
4.20°
ξ
180°

Figure V-C-11

Thus

$$I_T = \frac{I_B(\rho)RdR}{R_T^2 \sin\phi d\phi} , \tag{33}$$

where $0 < \rho < r_B$. Using Eq. (5) we have

$$\sin\phi \, dR = Rd\phi , \tag{34}$$

so that

$$\boxed{I_T = \left(\frac{2a}{R_T}\right)^2 \frac{I_B(\rho)}{(1+\cos\phi)^2} .} \tag{35}$$

In normalized form,

$$I_T(\theta,\phi) = \frac{I_B(\rho)}{I_o} \left(\frac{r}{r_o}\right)^2 , \tag{36}$$

where $I_o \equiv I_B(o)$.

Irradiance profiles are shown in Fig. V-C-12-18 for focal lengths of r_o = 5, 10 and 15 meters, encompassing the range of interest for most laser fusion reactor designs. $I(\xi)$ is given in the meridional plane (along the x_i axis) and in the normal direction (along the y_i axis) in each figure, for turning angles ϕ_o = 45°, 90° and 135°. Results are given for a flat beam profile and a Gaussian

$$I_B(\rho) = I_o \, e^{\alpha(\rho/r_B)^2} , \tag{37}$$

with α = 2; the case α = 1 is also depicted for r_o = 5 m. The flat profile curves are seen to be highly skewed, worsening with decreasing r_o and

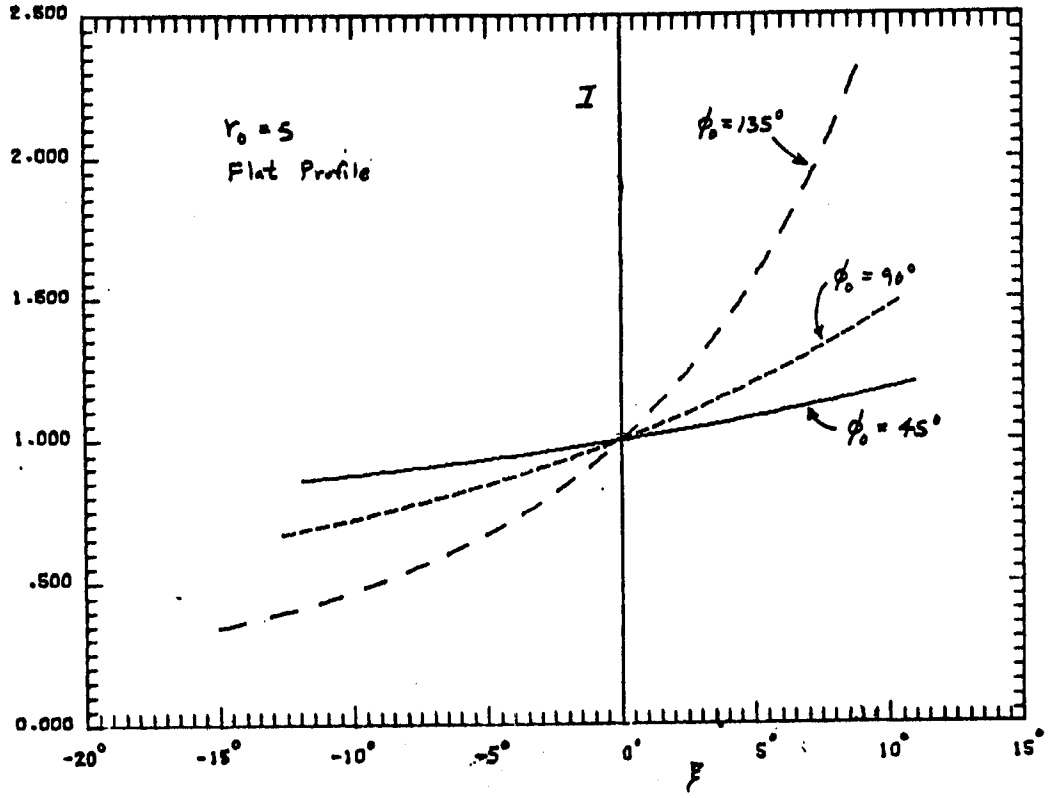
2.500
2.000
1.500
1.000
.500
0.000
I
$r_0 = 5$
Flat Profile
$\phi_0 = 135°$
$\phi_0 = 90°$
$\phi_0 = 45°$
-20°
-15°
-10°
-5°
0°
5°
10°
15°
ξ

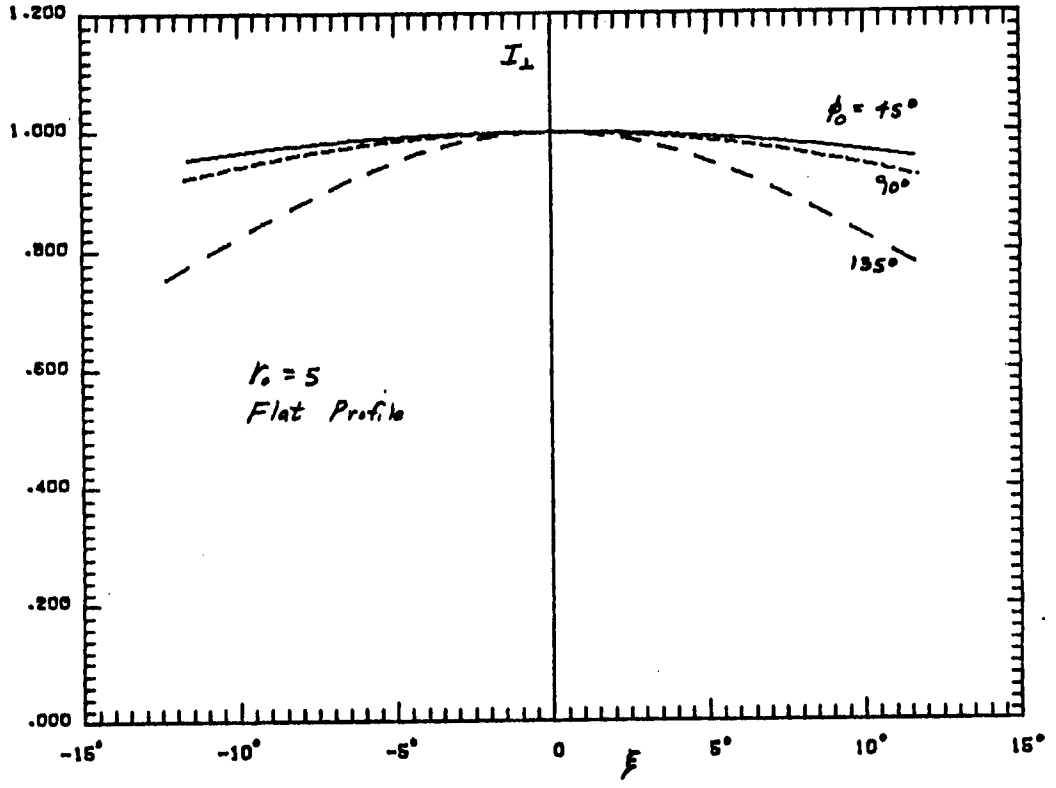
1.200
1.000
.800
.600
.400
.200
.000
$I_\perp$
$\phi_0 = 45°$
90°
135°
$r_0 = 5$
Flat Profile
-15°
-10°
-5°
0
5°
10°
15°
ξ

Figure V-C-12

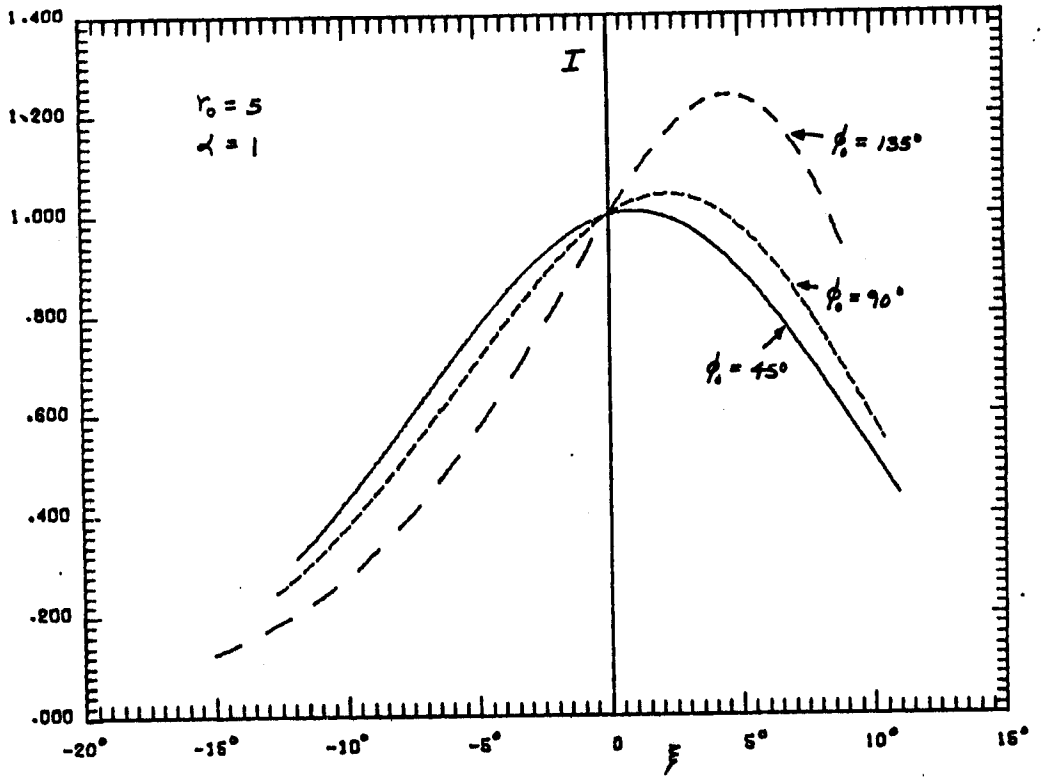
I
$r_0 = 5$
$\alpha = 1$
$\phi_0 = 135°$
$\phi_0 = 90°$
$\phi_0 = 45°$
1.400
1.200
1.000
.800
.600
.400
.200
.000
-20°
-15°
-10°
-5°
0
5°
10°
15°
ξ

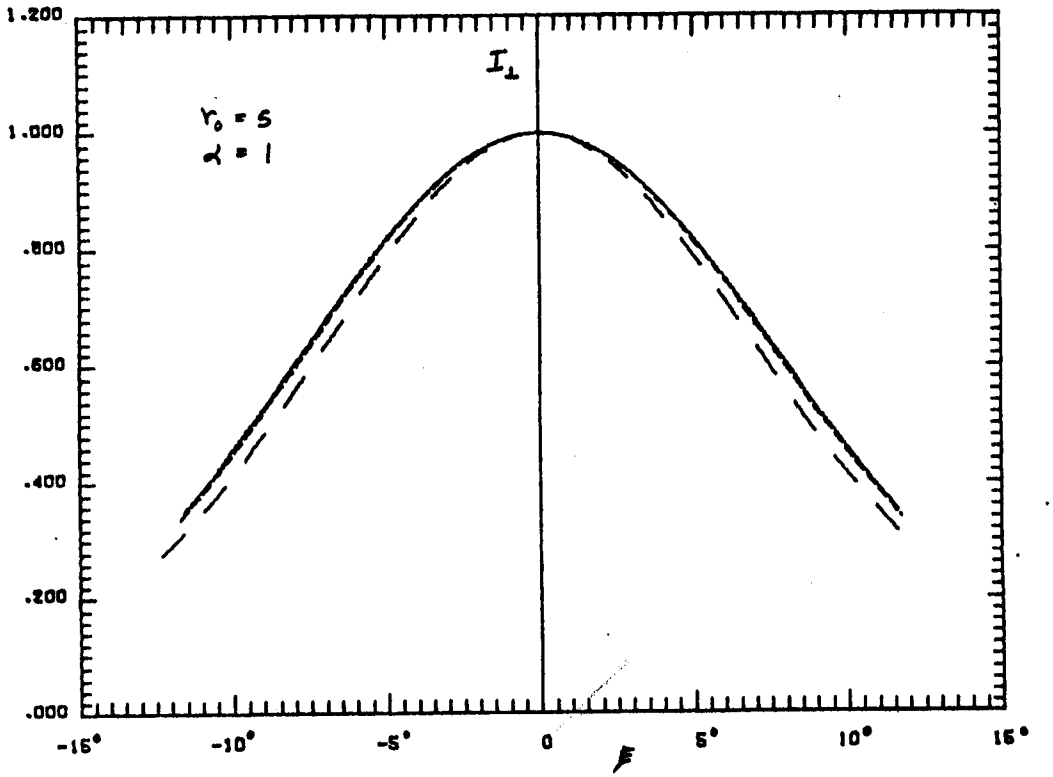
$I_\perp$
$r_0 = 5$
$\alpha = 1$
1.200
1.000
.800
.600
.400
.200
.000
-15°
-10°
-5°
0
5°
10°
15°
ξ

Figure V-C-13

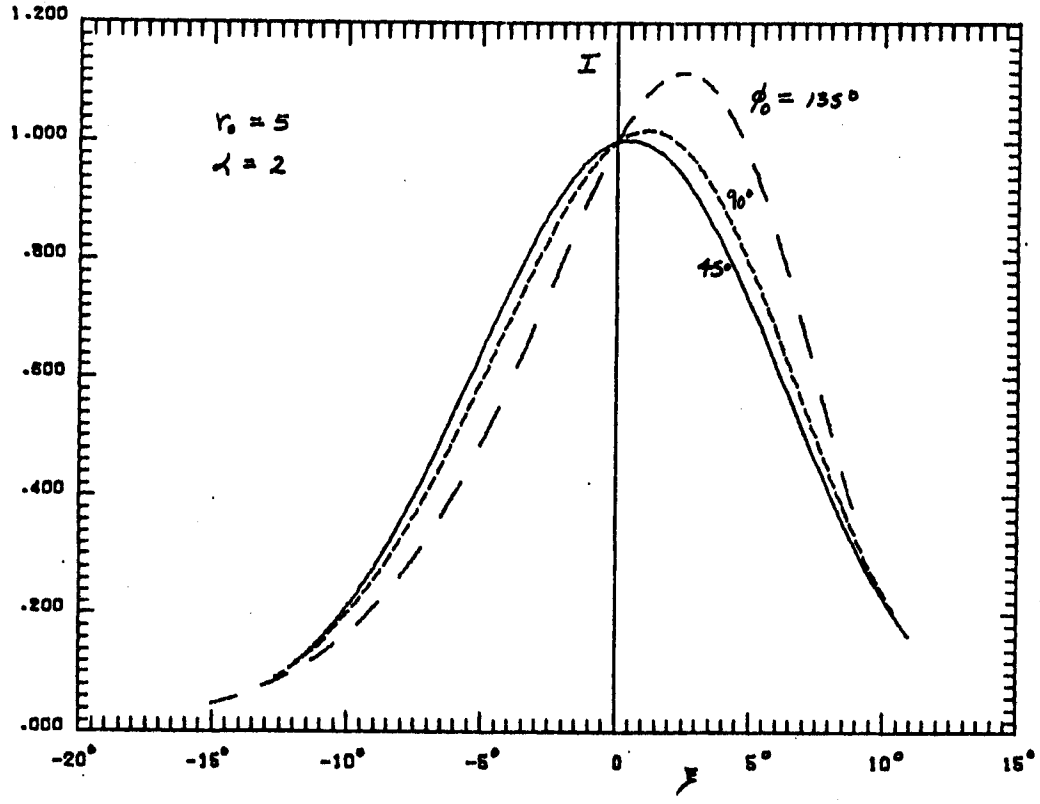
1.200
1.000
.800
.600
.400
.200
.000
I
$r_0 = 5$
$\alpha = 2$
$\phi_0 = 135°$
90°
45°
-20°
-15°
-10°
-5°
0
5°
10°
15°
ξ

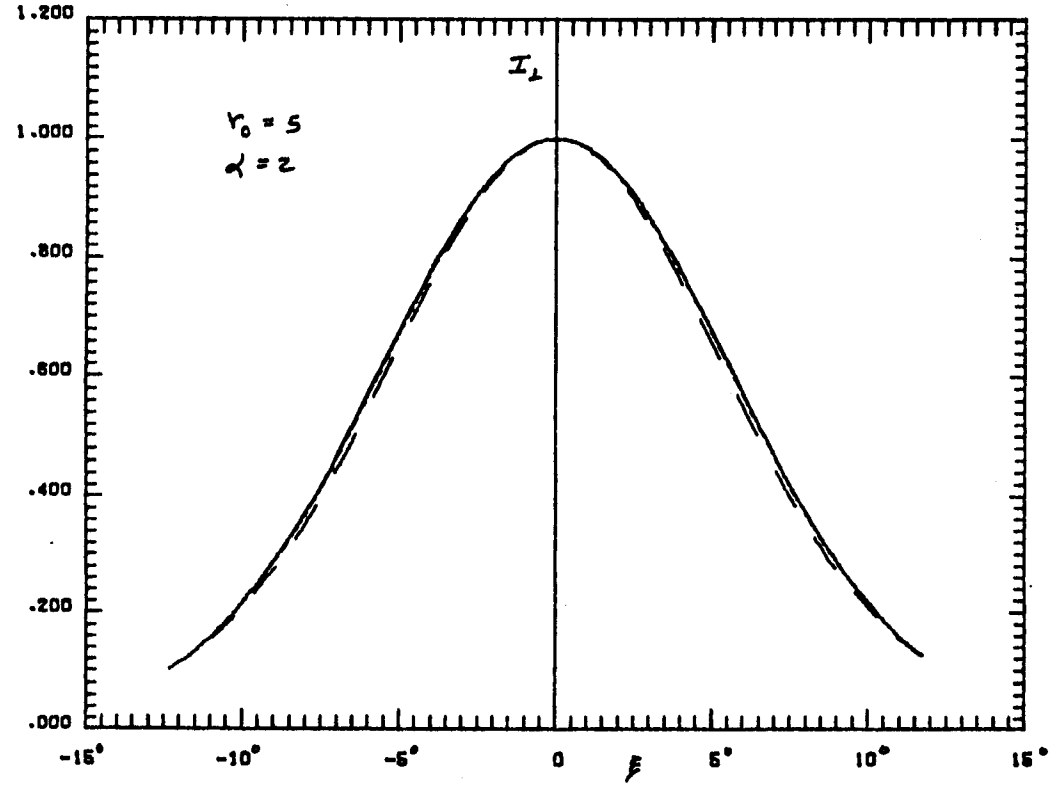
1.200
1.000
.800
.600
.400
.200
.000
$I_\perp$
$r_0 = 5$
$\alpha = 2$
-15°
-10°
-5°
0
5°
10°
15°
ξ

Figure V-C-14

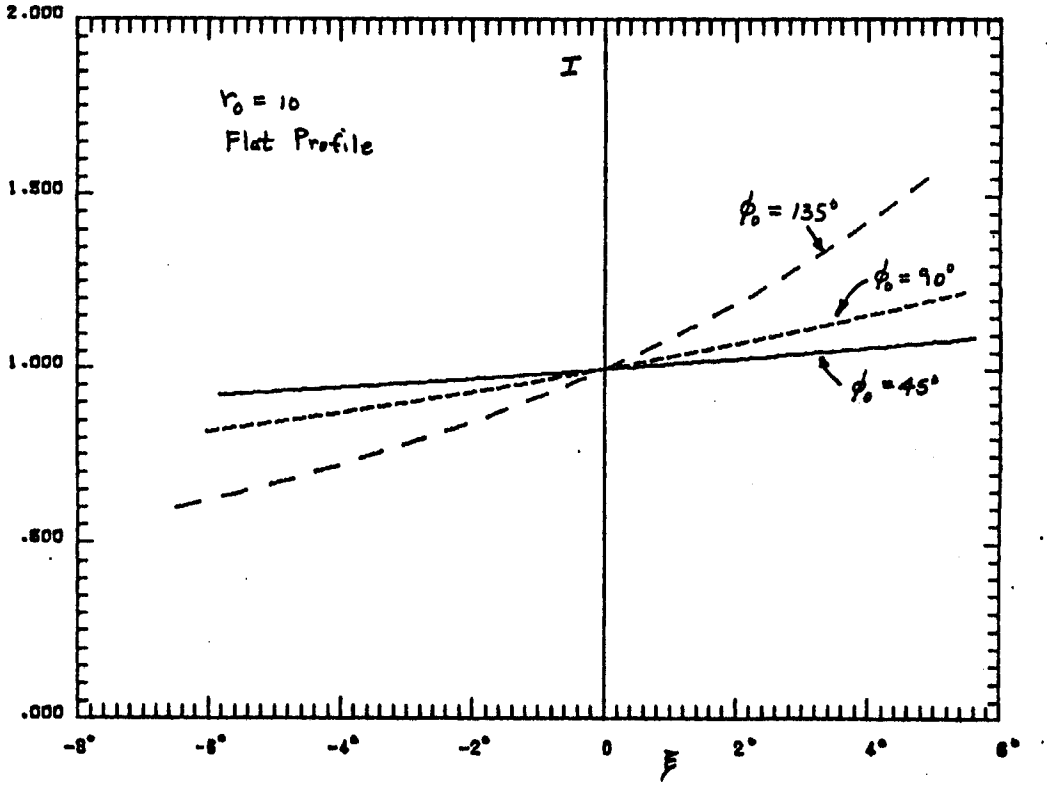
2.000
1.500
1.000
.500
.000
I
r_0 = 10
Flat Profile
ϕ_0 = 135°
ϕ_0 = 90°
ϕ_0 = 45°
-8°
-6°
-4°
-2°
0
2°
4°
6°
ξ

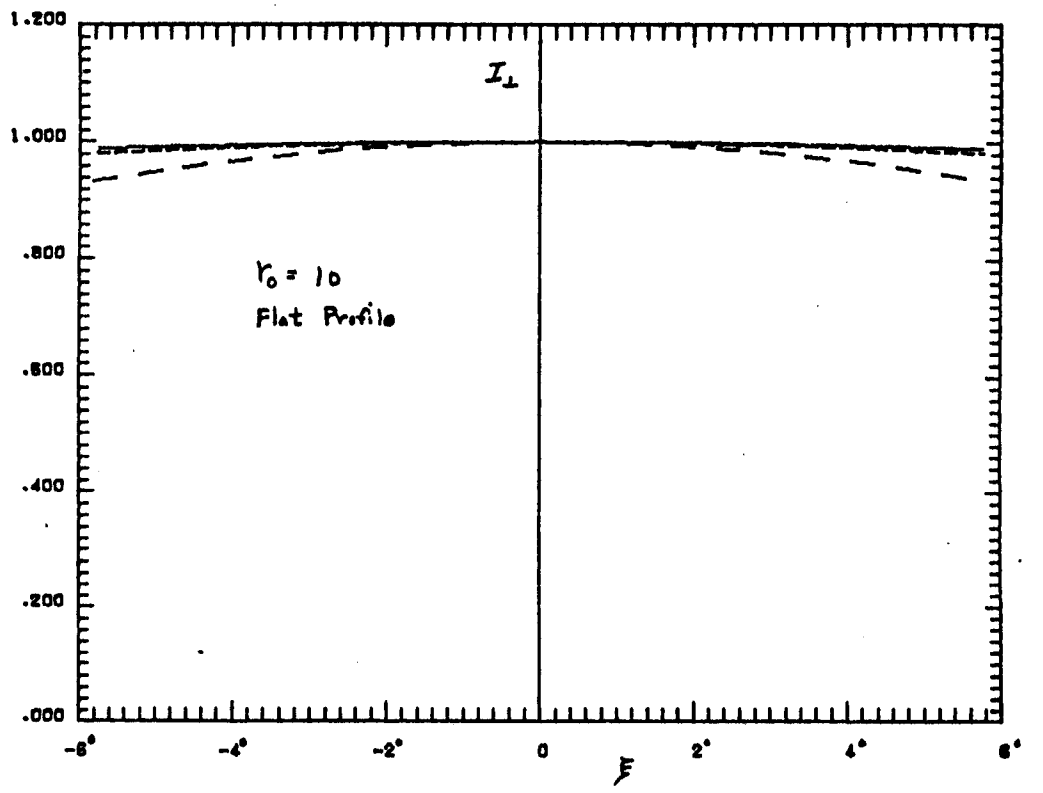
1.200
1.000
.800
.600
.400
.200
.000
$I_\perp$
r_0 = 10
Flat Profile
-6°
-4°
-2°
0
2°
4°
6°
ξ

Figure V-C-15

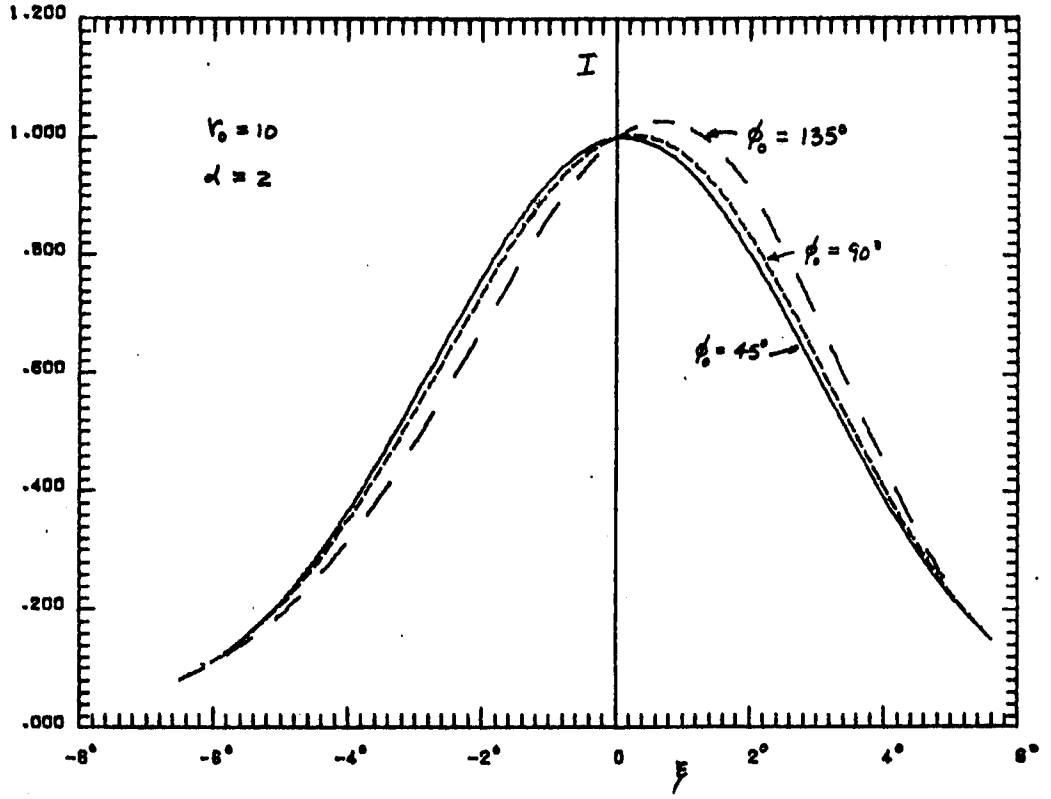
I
$r_0 = 10$
$\alpha = 2$
$\phi_0 = 135°$
$\phi_0 = 90°$
$\phi_0 = 45°$
1.200
1.000
.800
.600
.400
.200
.000
-8°
-6°
-4°
-2°
0
2°
4°
6°
ξ

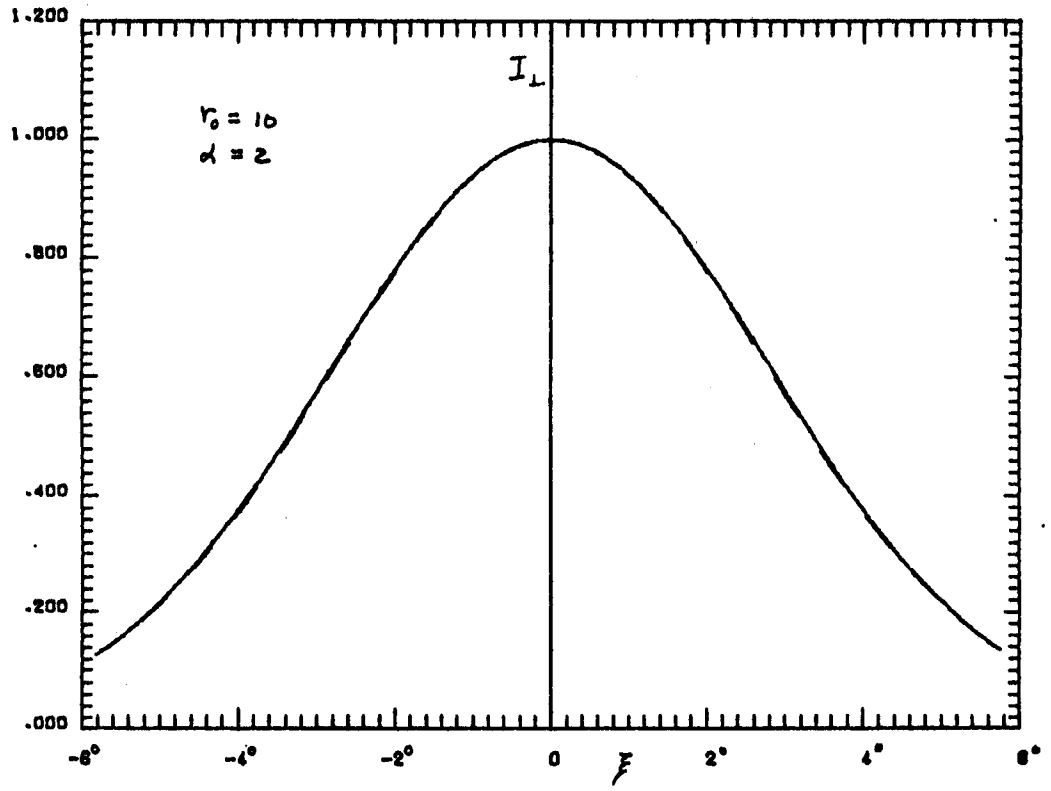
$I_\perp$
$r_0 = 10$
$\alpha = 2$
1.200
1.000
.800
.600
.400
.200
.000
-8°
-4°
-2°
0
2°
4°
6°
ξ

Figure V-C-16

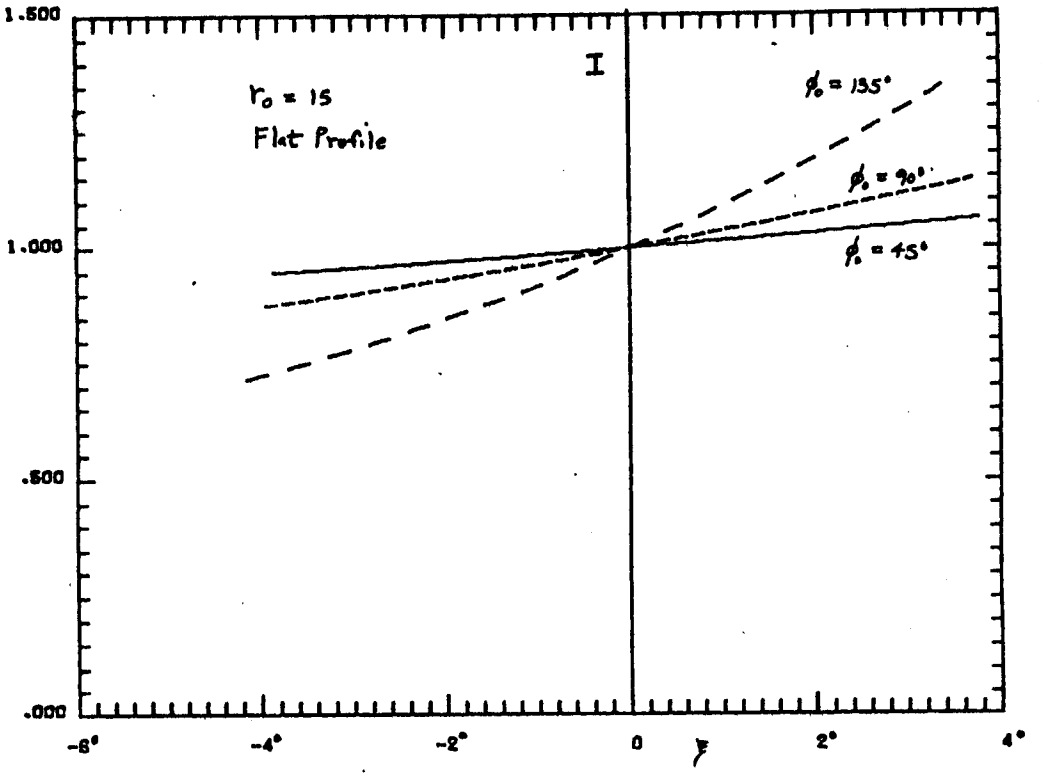
1.500
1.000
.500
.000
I
r_o = 15
Flat Profile
ϕ_o = 135°
ϕ_o = 90°
ϕ_o = 45°
-6°
-4°
-2°
0
2°
4°
Y

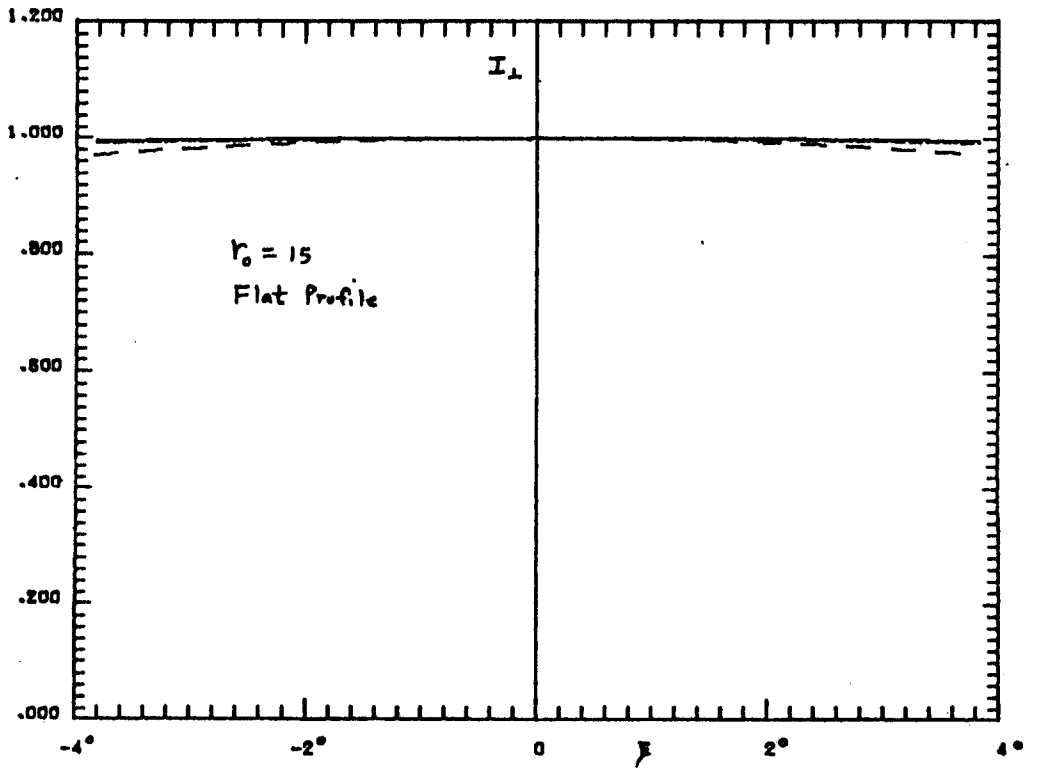
1.200
1.000
.800
.600
.400
.200
.000
$I_\perp$
r_o = 15
Flat Profile
-4°
-2°
0
2°
4°
Y

Figure V-C-17

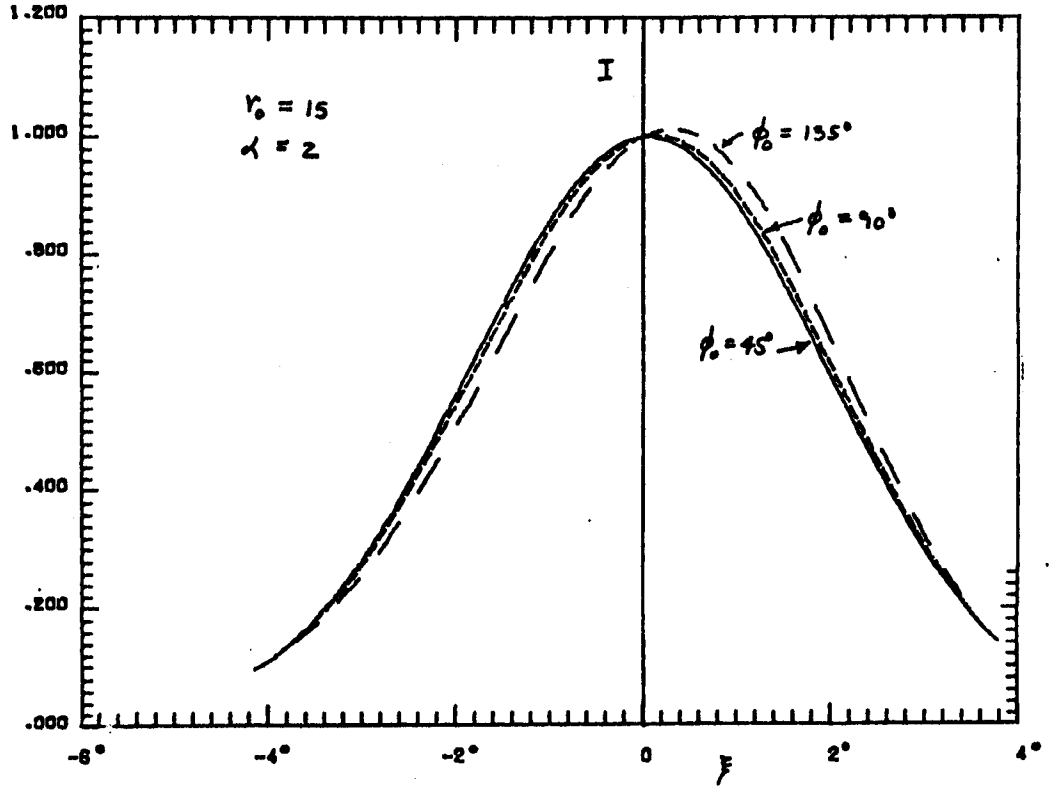
1.200
1.000
.800
.600
.400
.200
.000
I
$r_0 = 15$
$\alpha = 2$
$\phi_0 = 135°$
$\phi_0 = 90°$
$\phi_0 = 45°$
-6°
-4°
-2°
0
2°
4°
ξ

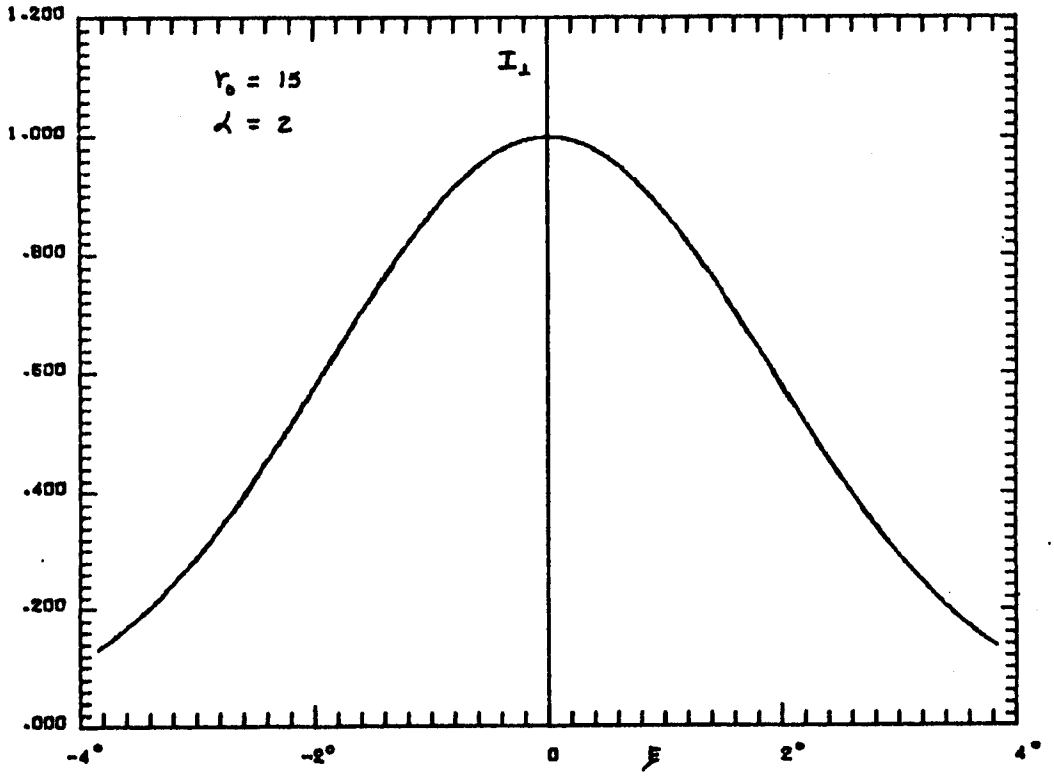
1.200
1.000
.800
.600
.400
.200
.000
$I_\perp$
$r_0 = 15$
$\alpha = 2$
-4°
-2°
0
ξ
2°
4°

Figure V-C-18

increasing ϕ_o. The asymmetry is much less severe, however, for the Gaussian profiles, especially for the case $\alpha = 2$. The reason for this improvement is that the largest distortion, occurring at the beam edge, is scaled down by the rapidly decreasing Gaussian. The required symmetry depends on the details of the target design. These results show that quite symmetric irradiances obtain for $r_o \geq 10\ r_B$ and $\phi_o \leq 90^o$, using paraboloidal mirrors alone as final focusing elements.

Again taking advantage of the smallness of ξ, we may readily obtain an explicit formula for $I(\xi)$ along the x_i axis. The result is, in normalized form,

$$I_T(\xi) \simeq [1 + 2t\xi + \frac{1}{2}(1 + 5t^2\ \xi^2)]\ \exp\ [-\alpha(\xi/\epsilon)^2\ (1 + t\xi)]\ , \qquad (38)$$

where

$$t \equiv \tan\phi_o/2$$

and

$$-\xi_1 < \xi < \xi_2\ .$$

V-C-4. Mirror Positioning and Pointing Errors

Illuminating a 1 mm radius target from a distance of 10 m or more with a large off-axis paraboloid and keeping it on target is a formidable technical task. Six degrees of freedom must be controlled in an explosive environment. Further, it is not clear how positive feedback control can be accomplished or how often corrections would have to be made. Current large scale laser fusion experiments allow hours between shots for alignment, as compared to perhaps 50 msec between pulses in a reactor.[3]

In this section analytic ray tracing is employed to calculate tolerances on each of the six positioning coordinates for arbitrary values of ϕ_o, r_o, r_B, and R_T. In each case we assume a stationary target and collimated beam, allowing only motions of the mirror.

V-C-4-a. Translational Positioning Errors

Any purely translational error δx, δy or δz preserves the parallel relation between the incident ray and the axis of the paraboloid. Consequently, the focal point simply follows the displacement without magnification or confusion of the focal region. Since stepping motors capable of 0.5 μm motions are in existence today,[6] translational errors should not be problematical.

V-C-4-b. Rotational Positioning Errors

Consider rotations about the x, y and z axes with origin at the intersection of the optical axis with the mirror. As the ray displacements on target are proportional to the focal distance r_o, such errors can be quite serious.

V-C-4-b-i. Rotation About the y-axis ($\delta\phi$)

Figure V-C-19 shows the deflection of the principal ray (or any ray in the median plane $\theta = 0$). Simple triangulation gives the axial aberration,

$$\delta z = r \frac{\sin(2\delta\phi)}{\sin\phi'} \simeq \frac{2r\delta\phi}{\sin\phi} . \qquad (39)$$

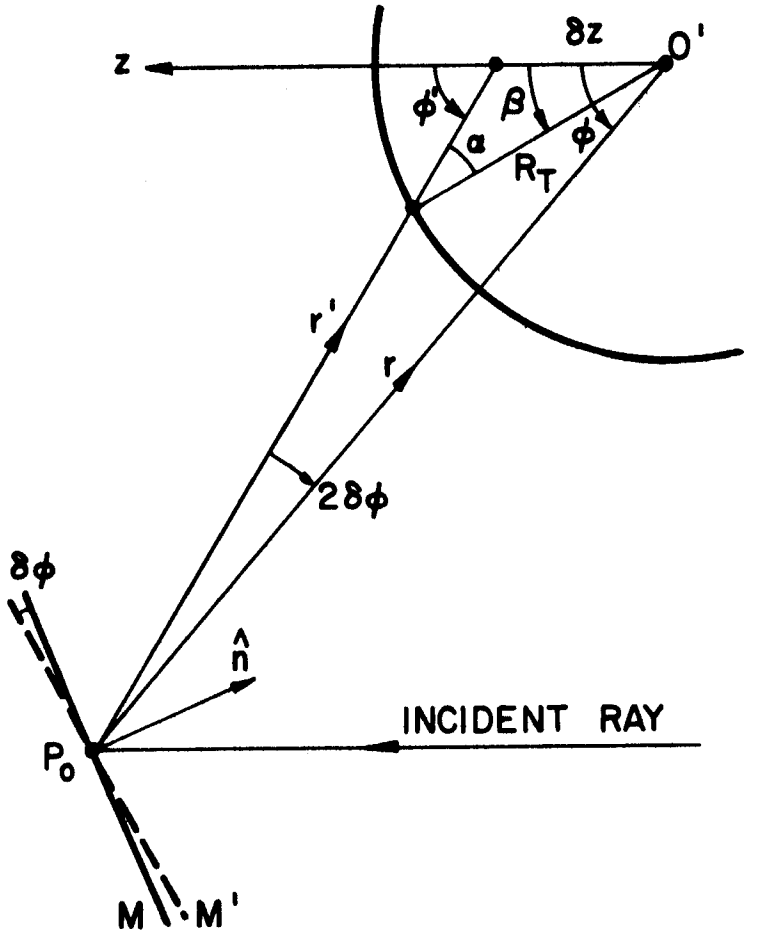

Figure V-C-19

The angle of incidence α and target central angle β are given by

$$\sin\alpha = \frac{\delta z}{R_T} \sin\phi' \simeq \frac{2r\delta\phi}{R_T} \tag{40}$$

$$\beta = \phi'-\alpha \simeq \phi-\alpha \ . \tag{41}$$

Using the general method outlined in Appendix A, it can be shown that the deflection of meridional rays out of the median plane differ by terms proportional to θ, which we have assumed to be small. Similarly, when $\Delta\phi = \phi - \phi_0 << \phi_0$ it follows from Eq. (39) that a general ray lying in the median plane is deflected by

$$\delta z = \delta z_0 \left[1 + \left(\frac{1-2\cos\phi_0}{\sin\phi_0}\right) \Delta\phi\right] \ , \tag{42}$$

where δz_0 is the deflection of the principal ray. Since $\Delta\phi \leq \xi \simeq \varepsilon$, the fanning of the rays (corresponding to classical coma and astigmatism) is seen to be negligible. Eq. (42) points out the curious fact that ray fanning is a second order effect when $\phi_0 = 60^0$. While ray fanning is unimportant for tilt error control, it does markedly affect the irradiance distribution on the pellet surface, as we shall see in the next section.

Rather than impose a limit on the axial aberration δz, we choose to require that the arc length displacement δs be less than a specified fraction of the pellet circumference. Since $\delta s \simeq \alpha R_T$, this is equivalent to limiting the angle $\phi - \beta \simeq \alpha$.

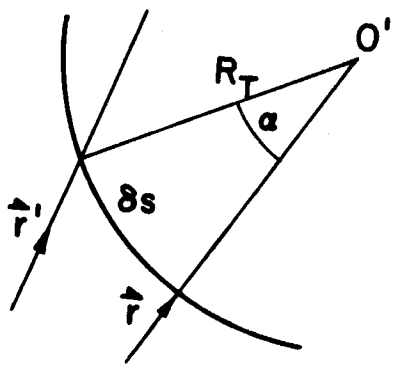

Figure V-C-20

From Eq. (40) we then have

$$\delta\phi \leq \frac{R_T \sin\alpha}{2r_o} . \tag{43}$$

The precise value of α will depend on the particular pellet design. As an upper bound on α we have the condition to just miss the pellet, $\alpha = 90^o$,

$$\delta\phi_{max} = R_T/2r_o . \tag{44}$$

The deflection of a general ray, for which $\theta \neq 0$, is complicated by the fact that the axis of rotation is no longer normal to the local meridional plane, with the result that the reflected ray does not lie in the unperturbed meridional plane. That is, $\theta \neq$ constant for the perturbed ray. This calculation has been carried out using the general method described in Appendix A, with negligible difference from Eq. (44), due to the smallness of θ.

V-C-4-b-ii. Rotation About the z-axis ($\delta\theta$)

In this case the incident rays remain parallel to the axis of the paraboloid. The result is a simple lateral motion of the focus, as depicted in Fig. V-C-21. The lever arm is now R_o and the deflection simply

$$\delta y \simeq R_o \delta\theta = r_o \sin\phi_o \, \delta\theta . \tag{45}$$

Introducing the angle of incidence α, we obtain a criterion analogous to Eq. (43),

$$\delta\theta \leq \frac{R_T \sin\alpha}{r_o \sin\phi_o} \quad . \tag{46}$$

In this case there is some advantage in going to smaller ϕ_o.

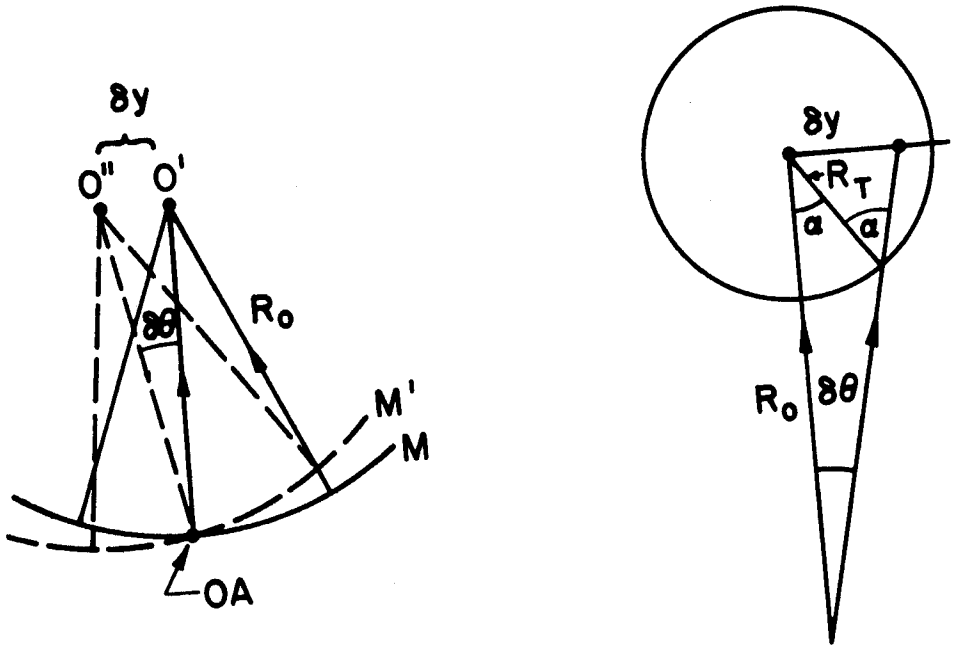

Figure V-C-21

V-C-4-b-iii. Rotation About the x-axis ($\delta\eta$)

As before, due to the smallness of θ, we need only consider an unperturbed ray lying in the median plane. Fig. V-C-22 is a top view of the mirror, showing how the axis of the paraboloid is rotated through the angle $\delta\eta$. Since the perturbed ray does not lie in a meridional plane, we must use the general vectorial method described in Appendix A.

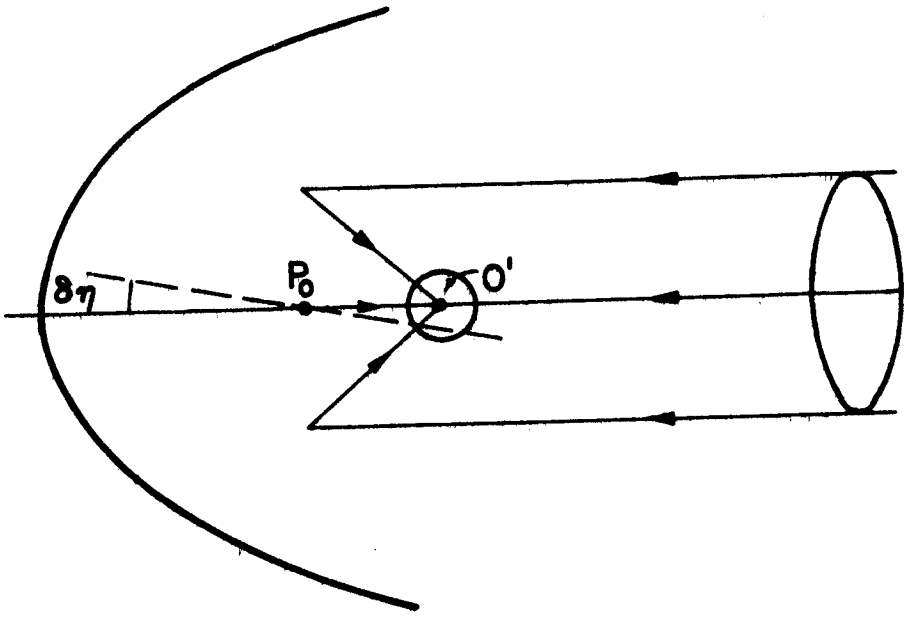

Figure V-C-22

The perturbed unit ray is

$$\hat{r}' = \hat{r} + 2\cos(\phi'/2)\hat{n}'. \tag{47}$$

In order to calculate the perturbed normal $\hat{n}'$, we introduce (yet another!) coordinate system (x,y,z) centered at the point P_0 where the optical axis strikes the mirror, as sketched in Fig. V-C-23.

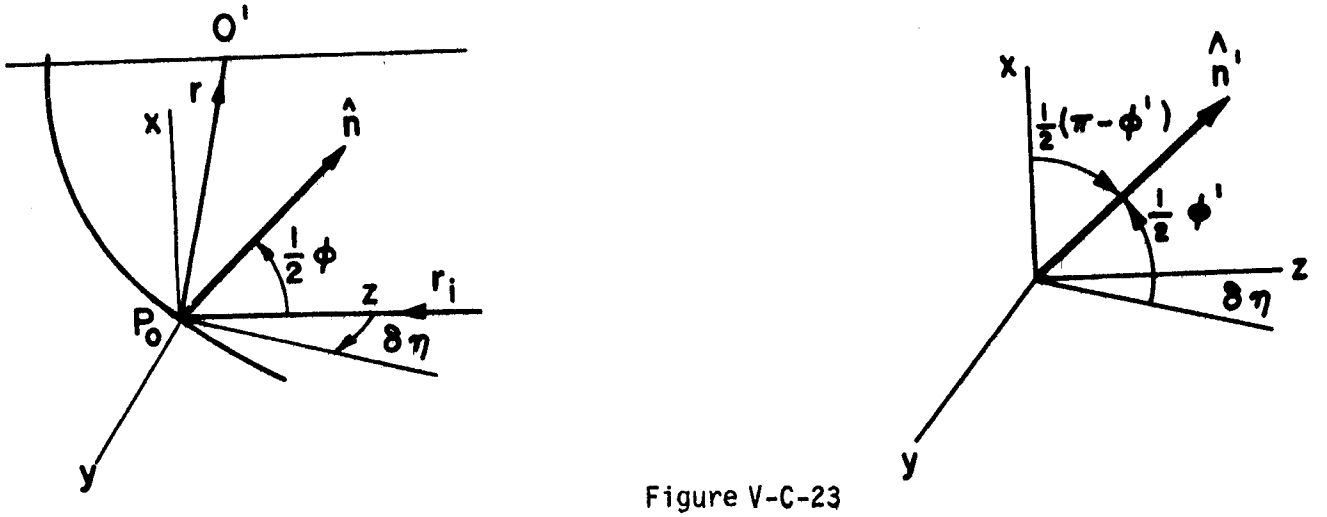

Figure V-C-23

The unperturbed normal is

$$\hat{n} = (\sin\phi/2,\ 0,\ \cos\phi/2) \ . \tag{48}$$

From Fig. V-C-23, the perturbed normal is then approximately

$$\hat{n}' = (\sin\phi/2,\ \delta\eta\ \cos\phi/2,\ \cos\phi/2) \ . \tag{49}$$

Thus,

$$\hat{r}' = (\sin\phi,\ 2\delta\eta\ \cos^2\phi/2,\ \cos\phi) \ . \tag{50}$$

The ray displacement at the focus is

$$\delta\vec{r} = r_o(\hat{r}' - \hat{r}) \ , \tag{51}$$

or

$$\delta x = \delta z = 0$$

$$\delta y = r_o\ \delta\eta\ (1 + \cos\phi_o) = 2a\ \delta\eta \ . \tag{52}$$

To impose a meaningful limit on $\delta\eta$, we again introduce the angle α:

$$\delta y = R_T \sin\alpha \ , \tag{53}$$

which gives

$$\delta\eta \leq \frac{R_T \sin\alpha}{r_o(1+\cos\phi_o)} \ , \tag{54}$$

with a rather weak dependence on ϕ_o.

In summary, we have derived the three angular constraints (roll, pitch and yaw!)

$$\delta\phi \leq \frac{R_T \sin\alpha}{2r_o} \tag{55}$$

$$\delta\theta = \frac{2\delta\phi}{\sin\phi_o} \tag{56}$$

$$\delta\eta = \frac{2\delta\phi}{1+\cos\phi_o} . \tag{57}$$

Fig. V-C-24 plots these tolerances as functions of turning angle, with $\delta\phi$ normalized to unity. The tightest tolerance is on $\delta\phi$, due to the fact that the reflected ray is perturbed by twice the tilt angle. The minimum in $\delta\theta$ is easily understood geometrically. The behavior of $\delta\eta$ is less well understood at present and should be viewed with some skepticism until numerical verification has been obtained. To get an idea of the order of magnitude of these tolerances, let R_T = 1 mm, r_o = 15 m and $\alpha = 30^o$. Then $\delta\phi$ = 16.5 rad, or about 3 sec of arc.

V-C-5. Perturbed Irradiances

Using the simple ray deflection formulas derived in Sec. V-C-4 we may calculate pellet irradiance under the three small tilt perturbations $\delta\phi$, $\delta\theta$ and $\delta\eta$. We have seen that the fanning of rays is an $O(\varepsilon)$ effect, so that to lowest order the focal spot is simply translated. While it is sufficient to look at the deflection of the principal ray in estimating allowable tilt errors, more precision is called for in calculating irradiance variations over the translated spot, being themselves of $O(\varepsilon)$.

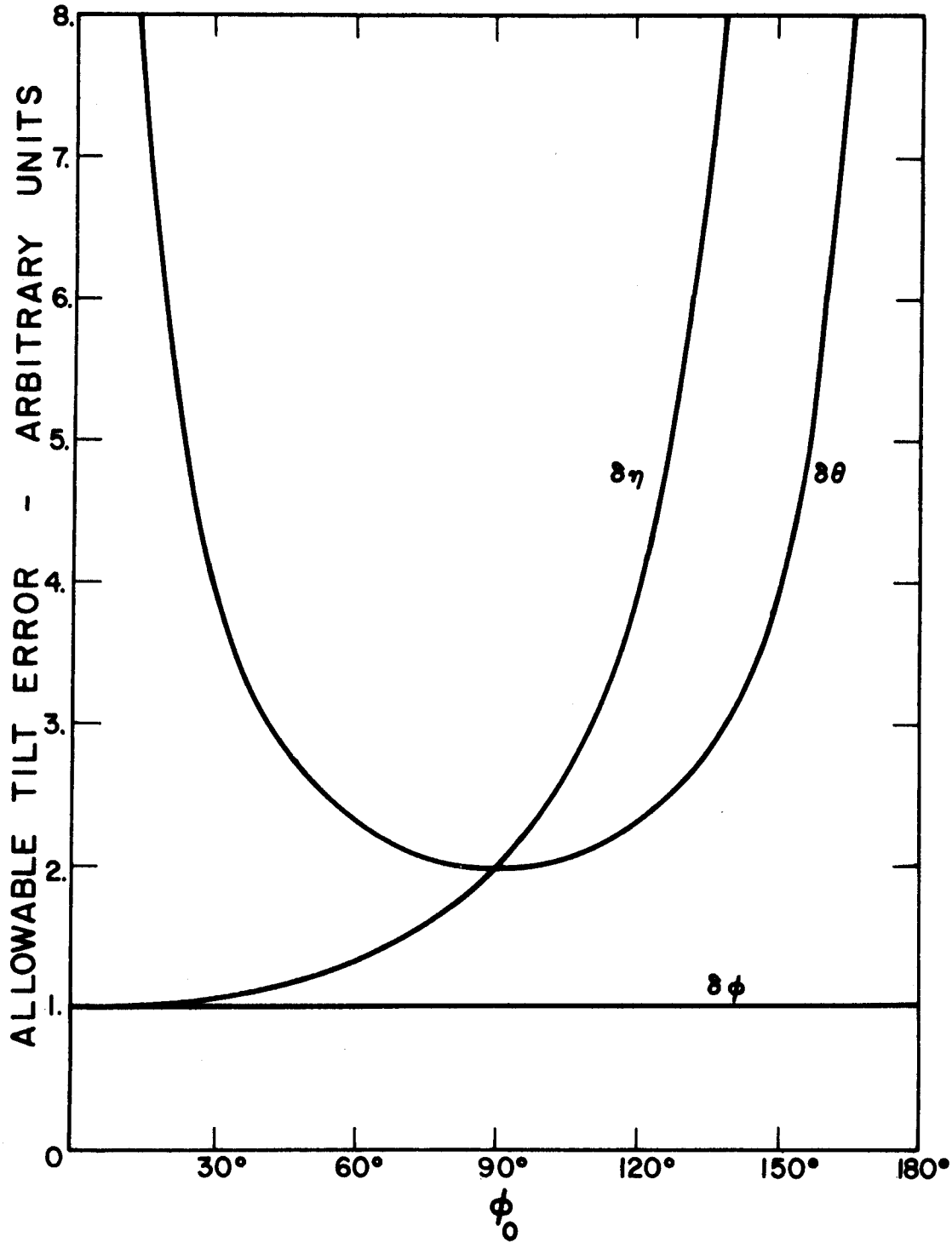
ALLOWABLE TILT ERROR - ARBITRARY UNITS
8.
7.
6.
5.
4.
3.
2.
1.
0
δη
δθ
δφ
30°
60°
90°
120°
150°
180°
φ0

Figure V-C-24

V-C-5-a. Translation of the Target in the z-direction

A simpler related problem is the calculation of irradiance under translations of the pellet itself, in which case ray fanning may be completely ignored. We first consider an axial translation δz, as illustrated in Fig. V-C-25.

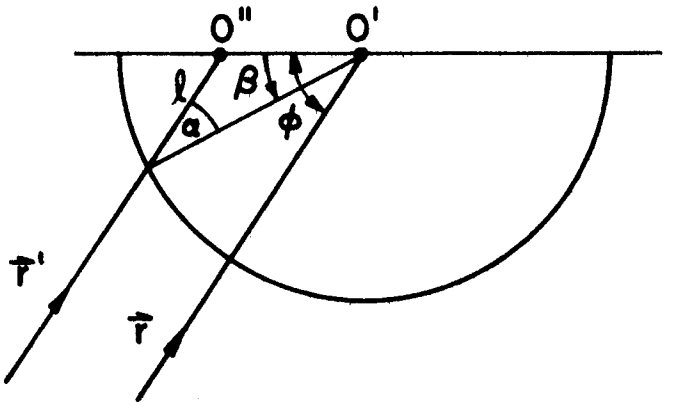

Figure V-C-25

Note that δz is positive when the pellet is moved away from the (virtual) vertex of the paraboloid. Denoting perturbed quantities by primes, energy conservation gives

$$I_T' \, dA_T' = I_B \, dA_B \, , \tag{58}$$

where

$$dA_B = R \, dR \, d\theta \tag{59}$$

and

$$dA_T' = R_T^2 \sin\beta \, d\beta \, d\theta \ . \tag{60}$$

As before,

$$\sin\Phi \, dR = R \, d\Phi \ , \tag{61}$$

so that

$$I_T' = I_B \left(\frac{R}{R_T}\right)^2 \frac{d\Phi/d\beta}{\sin\Phi \sin\beta} \ . \tag{62}$$

To simplify this result, we have from Fig. V-C-25

$$\ell d\phi = R_T \cos\alpha \, d\beta \tag{63}$$

$$\ell \sin\phi = R_T \sin\beta \ . \tag{64}$$

Thus,

$$I_T' = I_B \left(\frac{R}{R_T}\right)^2 \frac{\cos\alpha}{\sin^2\beta} \ . \tag{65}$$

Using the relations

$$\alpha + \beta = \phi \tag{66}$$

$$\sin\alpha = \Delta \sin\phi \ , \tag{67}$$

where $\Delta \equiv \delta z/R_T$, we may manipulate Eq. (65) into the form

$$\boxed{I_T' (\phi,\delta z) = \frac{I_T(\phi)\cos\alpha}{(\cos\alpha - \Delta\cos\phi)^2} \ ,} \tag{68}$$

where the unperturbed irradiance is given by Eq. (35).

As Fig. V-C-26 shows, the projected spot is now elongated rather than circular. Restricting our attention to the irradiance along the arc δs lying in the median plane, we can express I_T' as a function of the angle $\Delta\beta$, just as we wrote $I_T(\xi)$ in the unperturbed case. To do this, we have from Fig. V-C-25,

$$\cot\phi = \frac{\cos\beta - \Delta}{\sin\beta} , \tag{69}$$

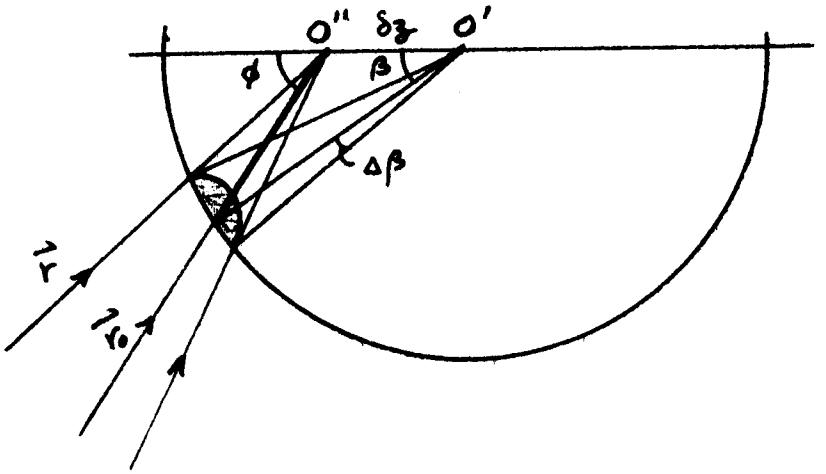

Figure V-C-26

V-C-5-b. Target Irradiance Under the Rotation $\delta\phi$

The perturbed rays no longer come to a sharp focus and one must determine the intersection of two contiguous rays for each turning angle ϕ. This point (corresponding to O" in Fig. V-C-25) may lie above or below the z axis. The locus of such points forms the caustic surface, as discussed in Appendix B. Figure V-C-27 illustrates the geometry required to solve this problem.

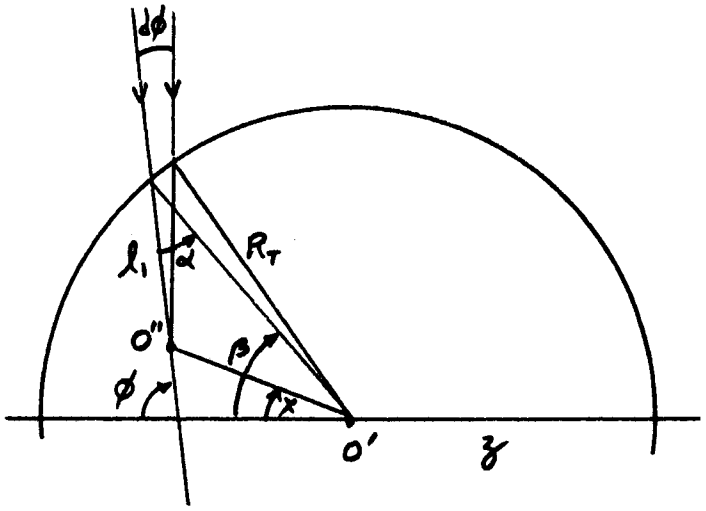

Figure V-C-27

As before, we exploit energy conservation

$$I_T' \, dA_T' = I_B \, dA_B$$

with $dA_B = RdRd\theta$. Examination of Fig. V-C-27 shows that the target area element is

$$dA_T' = (R_T \, d\beta) \, (\ell_i \sin\phi) \, d\theta \, , \qquad (70)$$

so that

$$I_T' = \frac{I_B \, R^2 \, d\phi/d\beta}{R_T \, \ell_i \sin^2\phi} \, , \qquad (71)$$

where Eq. (59) has been used to eliminate dR. Simple triangulation yields

$$\ell_1 \sec\alpha \, d\phi = R_T \, d\beta \tag{72}$$

$$\ell_1 \sin(\phi-\chi) = R_T \sin(\beta-\chi) \, . \tag{73}$$

From Appendix B

$$\boxed{\chi = \frac{3}{2}\phi - \frac{\pi}{2} \, ,}$$

which transforms Eq. (73) to

$$\ell_1 \cos\phi/2 = R_T \cos(\tfrac{3}{2}\phi - \beta) = R_T \cos(\alpha + \phi/2) \, . \tag{74}$$

Combining, we have

$$I_T' = I_B \left(\frac{R}{R_T}\right)^2 \frac{\cos\alpha \cos^2\phi/2}{\cos^2(\phi/2+\alpha) \sin^2\phi} \tag{75}$$

or

$$\boxed{I_T' = I_T \frac{\cos\alpha \cos^2\phi/2}{\cos^2(\phi/2+\alpha)} \, ,} \tag{76}$$

where I_T is the unperturbed irradiance. The irradiance (76) may be evaluated for given ϕ and $r\delta\phi$ by substituting

$$\sin\alpha = \frac{2r\delta\phi}{R_T} = \frac{2a\delta\phi}{R_T} \sec^2\phi/2 \, . \tag{77}$$

The irradiance is infinite when the caustic intersects the pellet surface; that is, when $\chi = \beta \Rightarrow \alpha + \phi/2 = \pi/2$. From Eq. (77) we conclude that a hot spot occurs when

$$\boxed{\delta\phi \geq \frac{R_T}{2a} \cos^3\phi/2 \ .} \tag{78}$$

This result may be derived directly from the caustic equation (B13), by setting $\ell = R_T$ and replacing $\delta\phi$ by $2\delta\phi$. The latter step takes into account the fact that here we are tilting the mirror rather than the beam.

Figures V-C-28 and 29 depict I_T'/I_T versus ϕ for various tilt errors with r_o = 10 m, $\phi_o = 45^o$ and R_T = 1 mm. The location of the singularity ϕ^* in each case is found by solving Eq. (78) for ϕ. In both cases the effect on I_T' in the operating range near ϕ_o is minimized by keeping $\delta\phi$ below 10 μrad. However, the resonance between ϕ_o and ϕ^* is easier to avoid at smaller ϕ_o. This resonance may be quantified by eliminating a between Eq. (78) and

$$a = r_o \cos^2\phi_o/2 \ , \tag{79}$$

so that

$$\cos^3\phi^*/2 = \frac{2r_o\delta\phi}{R_T} \cos^2\phi_o/2 \ . \tag{80}$$

Overlap occurs when $\phi^* \simeq \phi_o$, or when

$$\delta\phi^* \simeq \frac{R_T}{2r_o} \cos\phi_o/2 \ . \tag{81}$$

The tilt error must be kept below this value to avoid hot spots. For example, if r_o = 10 m, $\phi_o = 90^o$, and R_T = 1 mm, $\delta\phi^*$ = 35.4 μrad, but if r_o = 100 m, $\delta\phi^*$ = 3.54 μrad, which might be hard to attain. Of course, smaller pellets would add to the difficulty.

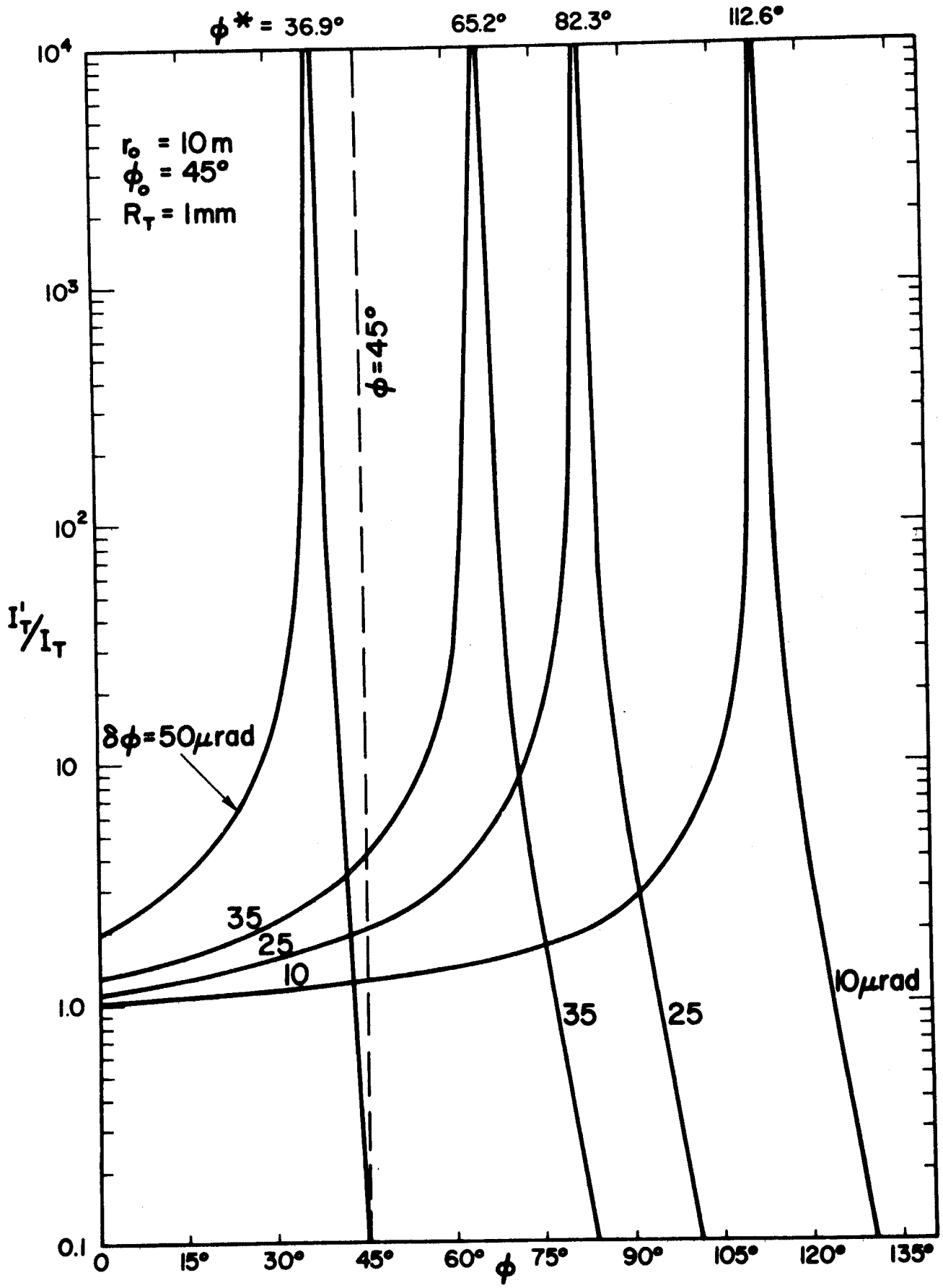
φ* = 36.9°
65.2°
82.3°
112.6°
10^4
10^3
10^2
10
1.0
0.1
r_o = 10 m
ϕ_o = 45°
R_T = 1mm
φ=45°
I'_T/I_T
δφ=50μrad
35
25
10
10μrad
35
25
0
15°
30°
45°
60°
φ
75°
90°
105°
120°
135°

Fig. V-C-28.

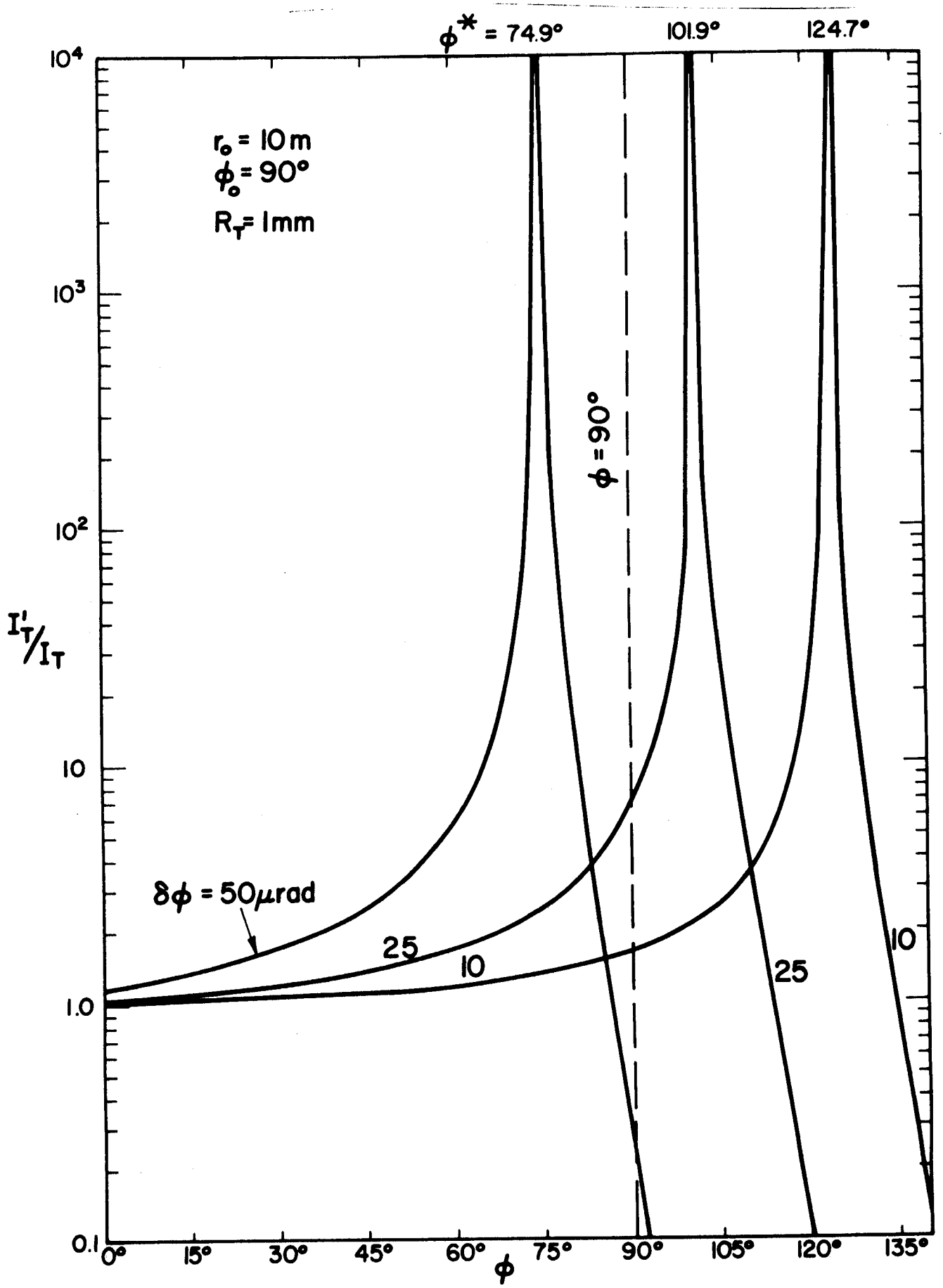
ϕ^* = 74.9°
101.9°
124.7°
r_o = 10 m
ϕ_o = 90°
R_T = 1mm
10^4
10^3
10^2
10
1.0
0.1
I'_T/I_T
ϕ = 90°
$\delta\phi$ = 50μrad
25
10
10
25
0°
15°
30°
45°
60°
75°
90°
105°
120°
135°
ϕ

Fig. V-C-29.

V-C-6. Discussion

We have studied the imaging properties of far off-axis paraboloidal reflectors in the parameter range encountered in laser fusion applications. The shape of the image disk was calculated analytically by means of an expansion in small inverse f/no. and was found to be a shifted circle in lowest order. The f/no. itself was shown to be nearly independent of turning angle for large f/no. Closed form expressions were derived for the irradiance cast on a spherical target centered at the mirror focus. Excellent agreement was found between numerical calculations and the analytic formulas. The asymmetry of the target irradiance was found to increase with decreasing f/no. and increasing turning angle (large turning angles necessitate excessively large mirrors).

The effect of various tilt errors on the focus was also exhibited, first by calculating ray deflections and then by a detailed examination of the perturbed target irradiance. Maximum allowable roll, pitch and yaw tilts were shown to depend differently on turning angle, with pitch being the most restrictive motion. Since the pitch angle error limit is independent of ϕ_o, there is no obvious advantage to using a 45^o rather than a 90^o turning mirror.

An analytic expression was derived for the perturbed target irradiance under a small pitch angle tilt, based on a new expression for the caustic curve. This calculation also yields a simple criterion for the caustic to intersect the target surface. In practice the tilt angles will vary in some limit cycle, say $\phi \pm 25$ μrad. If $\phi_o = 90^o$, Fig. V-C-29 predicts occasional large irradiances and possible breakup of the pellet. These modulations can easily be 10-100 times the natural pattern produced by a perfectly aligned mirror. Smaller turning angles are, therefore, strongly favored for reducing these hot spots.

Appendix A: General Method for Calculating Perturbed Rays

Consider incident and reflected rays $\hat{r}_i$ and $\hat{r}$, each making an angle $\phi/2$ with the normal $\hat{n}$, all being coplanar. The origin is taken at the point P_o where $\hat{r}_i$ intersects the mirror.

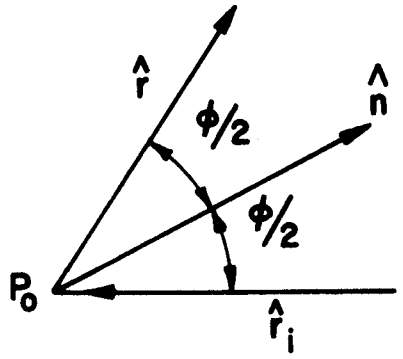

Since they are coplanar, there exists a number α such that

$$\hat{r} = \hat{r}_i + \alpha\hat{n} \ . \tag{A1}$$

Then

$$\alpha = \hat{n} \cdot \hat{r} - \hat{n} \cdot \hat{r}_i = 2 \cos\phi/2 \ , \tag{A2}$$

so that

$$\hat{r} = \hat{r}_i + 2 \cos\phi/2 \ \hat{n} \ . \tag{A3}$$

This result is entirely general and applies to any reflecting surface. Given a small tilt angle it is straightforward to calculate the perturbed normal $\hat{n}'$. The ray displacement at the target is then

$$\delta\vec{r} = r(\hat{r}' - \hat{r}) \ , \tag{A4}$$

where r is the focal distance and

$$\hat{r} = (\sin\phi, \cos\phi, 0) \tag{A5}$$

$$\hat{r}' = \hat{r}_i + 2 \cos(\phi'/2) \ \hat{n}' \ . \tag{A6}$$

Appendix B: Caustics for Tilted Paraboloid

Consider the paraboloid

$$R^2 = 4\,az \tag{B1}$$

with rays incident at angle $\delta\phi$ with axis of symmetry, as depicted in Fig. V-C-30.

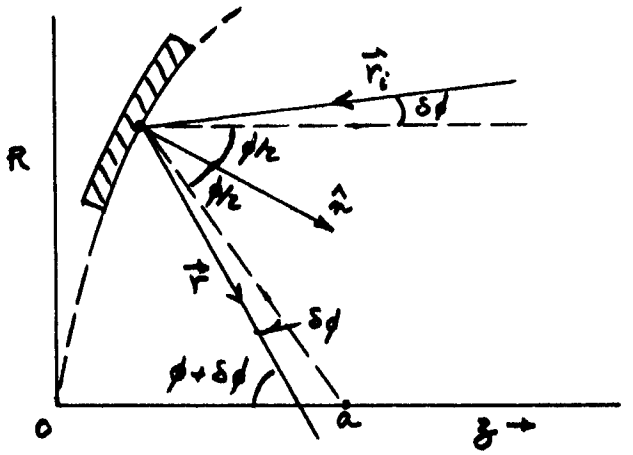

Figure V-C-30

This is just one of the three possible tilt errors.

The caustic is formed by the intersections of the reflected rays $\vec{r}$, with either ϕ or R taken as variable parameter and $\delta\phi$ fixed. The reflected ray is

$$R - R_0 = -(z - z_0)\tan(\phi + \delta\phi)\,, \tag{B2}$$

where R_0 and z_0 are the coordinates of the ray-mirror intersection point. Using

$$R_0 = 2a\tan\phi/2 \tag{B3}$$

we find

$$R = 2a\ \tan\phi/2 - (z - a\ \tan^2\phi/2)\ \tan(\phi + \delta\phi)\ , \qquad \text{(B4)}$$

or

$$F(R,z,\phi,\delta\phi) = R - 2a\ \tan\phi/2 + (z - \tan^2\phi/2)\ \tan\ (\phi + \delta\phi)\ , \qquad \text{(B5)}$$

where a has been scaled out. The envelope equation is[7]

$$\frac{\partial F}{\partial \phi} = 0\ , \qquad \text{(B6)}$$

which yields

$$\cos^2\phi/2\ (z - \tan^2\phi/2) = \cos^2(\phi + \delta\phi)\ [1 + \tan\phi/2\ \tan(\phi + \delta\phi)] \qquad \text{(B7)}$$

$$R = 2\ \tan\phi/2 - (z - \tan^2\phi/2)\ \tan\ (\phi + \delta\phi)\ . \qquad \text{(B8)}$$

The caustic may be obtained by eliminating ϕ between Eqs. (B7) and (B8). As a check note that the trivial solution $R = 0$, $z = 1$ results for $\delta\phi = 0$. The general solution has been obtained by Stalzer.[8] The result may be written

$$27t(\Delta z - Rt)^2 = (R + zt)(R - 8t + t\Delta z)^2, \qquad \text{(B9)}$$

where $\Delta z \equiv z - 1$ and $t \equiv \tan(\delta\phi)$. However, since $\delta\phi << \delta$ is always well satisfied in laser fusion applications, we may Taylor expand (B8) and (B9) to obtain

$$R \cong \frac{2(1 - 2\cos\phi)}{1 + \cos\phi}\ \delta\phi \qquad \text{(B10)}$$

$$\Delta z \cong -\frac{2\sin\phi(1 + 2\cos\phi)}{(1+ \cos\phi)^2}\ \delta\phi\ . \qquad \text{(B11)}$$

Eliminating ϕ between (20) and (21), we find

$$\boxed{\Delta z \cong -\frac{\sqrt{3}}{9}(8-R)(1+R)^{1/2},} \qquad \text{(B12)}$$

where $\delta\phi$ has been scaled out. This expression agrees with Stalzer's result (B9) in the limit $\delta\phi \to 0$. Eq. (B12) is plotted in dimensionless form in Fig. V-C-31. The left hand portion is due to rays reflected from the upper portion of the mirror depicted in Fig. V-C-30 and the right hand portion is produced by the lower half (if a complete mirror is present.)

In applying these results to the design of a laser fusion illumination system, one would seek to keep $a\delta\phi$ sufficiently small that the caustic would fall entirely inside the (spherical) target. Figure V-C-32 shows the caustics produced by tilt errors of ± 25 μrad for a paraboloid with latus rectum $a = 5$m, superimposed on a target 1 mm in radius (with $\delta\phi$ doubled because we are tilting the mirror rather than the beam). While the caustic is entirely interior to this pellet for all turning angles of interest ($\phi \leq 90°$), a hot spot would be produced on a smaller target wherever the caustic intersects the surface.

One may go further and use Eqs. (B10) and (B11) to calculate the perturbed target irradiance. This work is in progress. It is useful for this calculation to express the caustic in polar coordinates (ℓ,χ) as shown in Fig. V-C-31. The rather suprising result is

$$\ell = a\delta\phi \sec^3\phi/2 \qquad \text{(B13)}$$

$$\chi = \frac{3}{2}\phi - \frac{\pi}{2}, \qquad \text{(B14)}$$

so that

$$\boxed{\ell = a\delta\phi \sec^3\left(\frac{\chi}{3} + \frac{\pi}{6}\right).} \qquad \text{(B15)}$$

If the mirror is tilted instead of the beam, $\delta\phi$ must be replaced by $2\,\delta\phi$ in Eqs. (B13) and (B15).

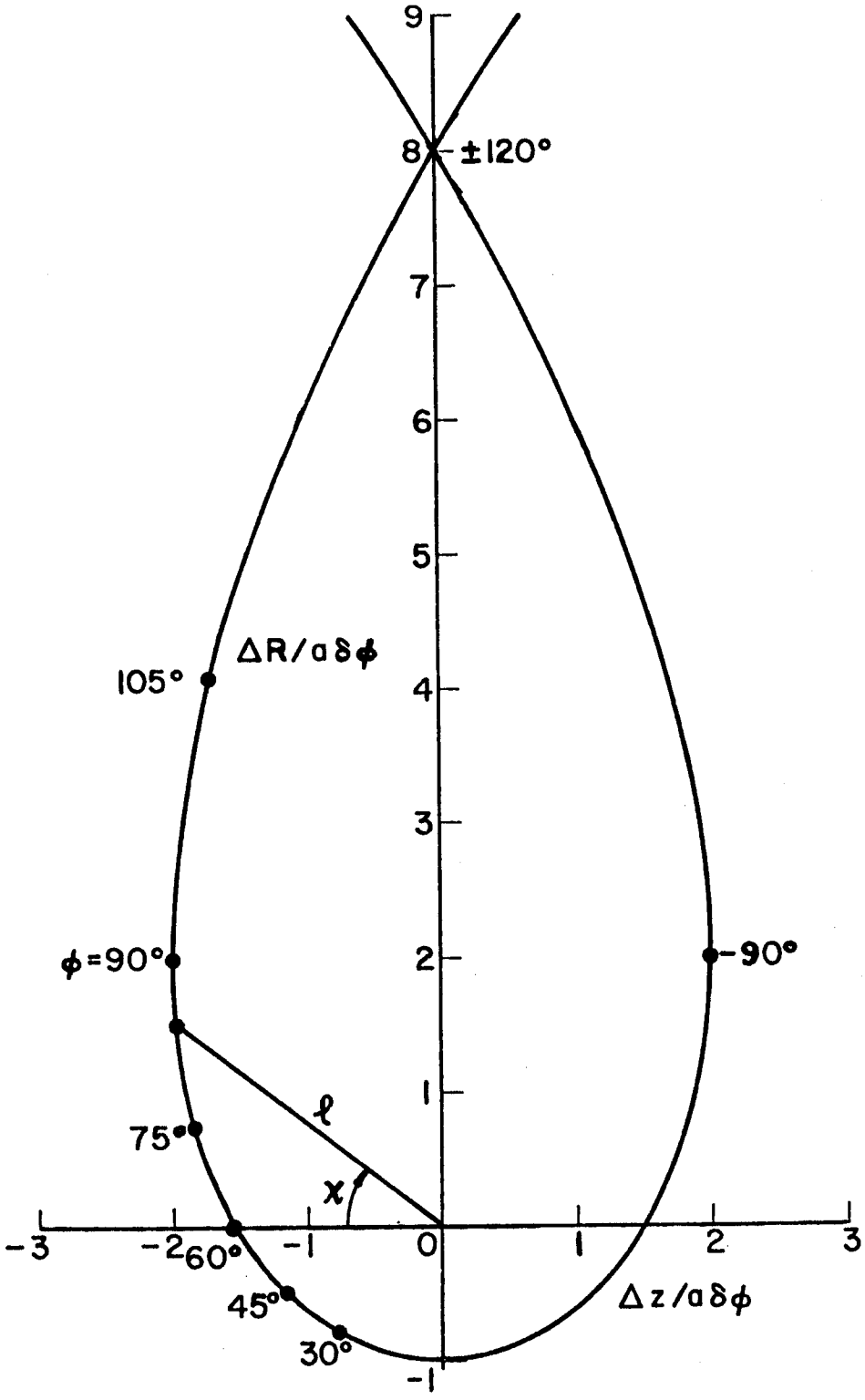

Fig. V-C-31.

CAUSTICS FOR PARABOLIC MIRROR

$a = 5m \quad R_T = 1mm \quad \delta\phi = 25\mu rad$

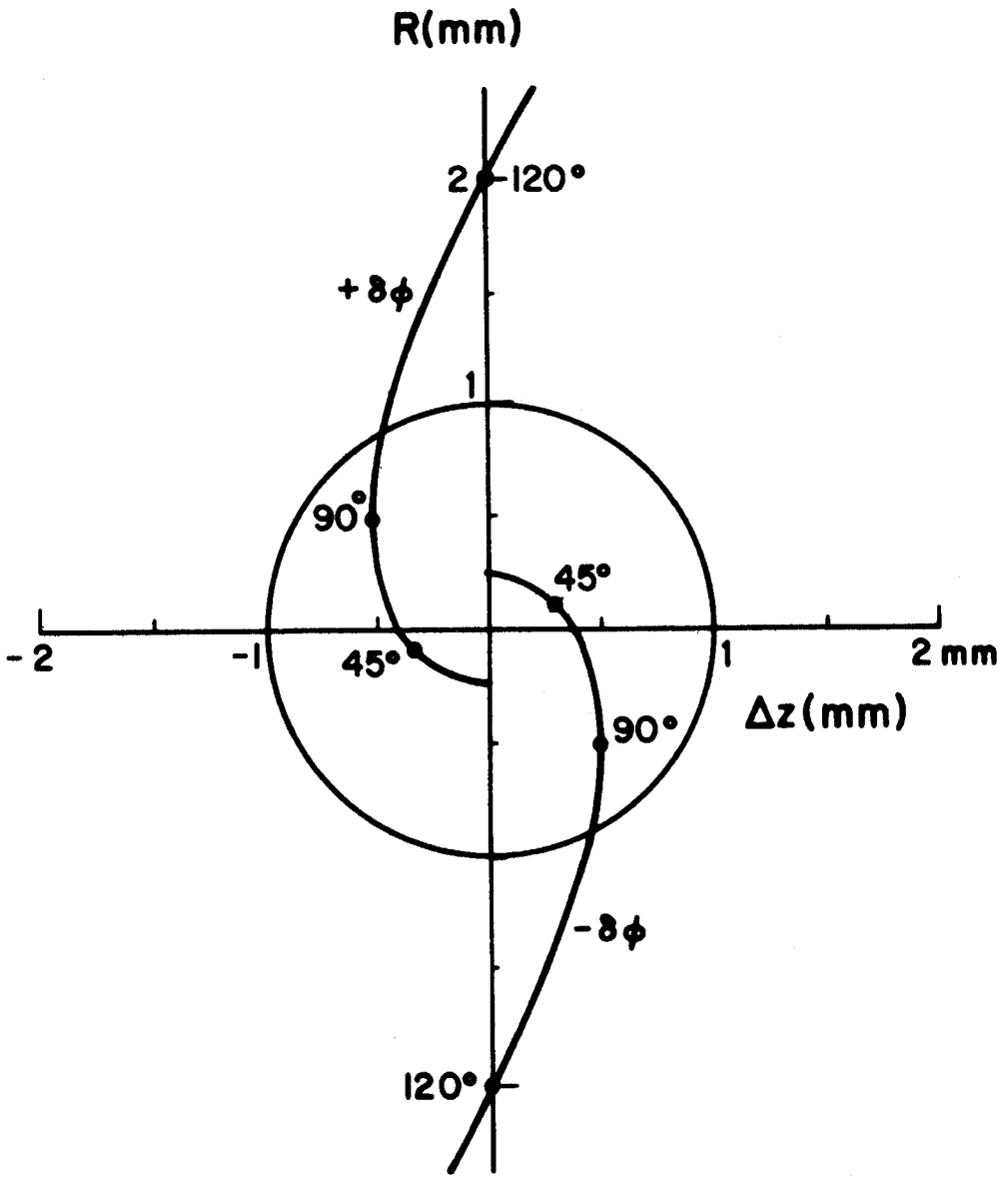

Figure V-C-32

Acknowledgement

It is a pleasure to thank Prof. A. D. Code for helpful discussions.

References for Section V-C

1. W. H. Reichelt, D. J. Blevins and W. C. Turner, LA-UR 77-468.

2. T. T. Saito, Applied Optics 14, 1773 (1975).

3. U. of Wis. Nuclear Engineering Report UWFDM-190, 1977.

4. J. A. Maniscalco, UCRL-78682, September 1976.

5. H. P. Brueggemann, Conic Mirrors, Focal Press Limited (London), 1968.

6. S. S. Glaros and A. J. Glass, Sixth Symposium on Engineering Problems of Fusion Research, San Diego, November 1976, p.

7. J. Morgan, Introduction to Geometrical and Physical Optics, McGraw-Hill (New York, 1953), p. 420.

8. H. J. Stalzer, Jr., Applied Optics 4, 1205 (1965).

VI-A. The Beam Transport System

VI-A-1. Introduction

The beam transport system is a critical element of any laser fusion reactor. Regardless of the laser's performance, if the energy cannot be satisfactorily delivered to the pellet the reactor will not be a viable system. The beam transport system must repetitively deliver the laser's output, with minimal distortion or energy loss, to an extremely precise location. These specifications would be difficult to meet under ideal circumstances but the problems are compounded by the reactor environment in which the optics will be subjected to vibrations, shock waves, nuclear radiation, and pellet debris. These problems are particularly severe for the last mirror and are discussed separately in section VI-B. This section discusses the layout of the SOLASE beam transport system and problem areas not specifically related to the last mirror.

The SOLASE beam transport system will have the following general characteristics. There will be six final amplifiers. From each of these, four separate beams will be extracted giving a total of 24 beams. These will then be combined in pairs resulting in 12 beams that will be focused on the pellet. The beams will be annular as a result of the amplifiers being annular. There will be optical delay lines as a result of extracting multiple beams from each amplifier.

VI-A-2. Multipassing Considerations

In order to increase the efficiency of the SOLASE laser the technique of multipassing is used as discussed in section VIII-B-4. This method requires that the beams pass through the amplifiers at different angles so that the beams can be separated by merely allowing them to travel a

sufficient distance. In the SOLASE design, each beam will make an angle of 60 mrad with the axis of the final amplifier, forming two X's that are perpendicular to each other. The distance between the input and output mirrors is 100 m.

Since the next-to-last-amplifying stage generates 10% of the total laser energy, it is desirable to multipass this stage as well. Because of the large dimensions required (~ 100 m) it is desirable to minimize the additional building space that will be required. This is accomplished in SOLASE by placing the two stages side-by-side and utilizing the same length of building to separate the beams from each amplifier as shown schematically in Fig. VI-A-1. Thus, at one end of the building, the beam is input to the first stage and extracted from the final stage and at the other end the output of the first will be expanded and then reflected into the final stage.

VI-A-3. Beam Combining

The laser pulses as they are extracted from the SOLASE laser will be large, thin annuli with inner and outer diameters of 313 and 357 cm respectively and have an energy density of 3 J/cm^2. Such beams would not only be difficult and awkward to handle but would also require unnecessarily large mirrors and beam transport tubes. Thus, to facilitate the handling of the beams, they will be both reduced in size and combined in pairs. The beams will be reduced in size by both "filling in" the annulus (see Fig. VI-A-2) and increasing the energy density to 5 J/cm^2.

The fact that the beams are annular provides an interesting method of combining beams as shown schematically in Fig. VI-A-2. To combine beams in pairs, one beam is reduced to as small an annulus as possible

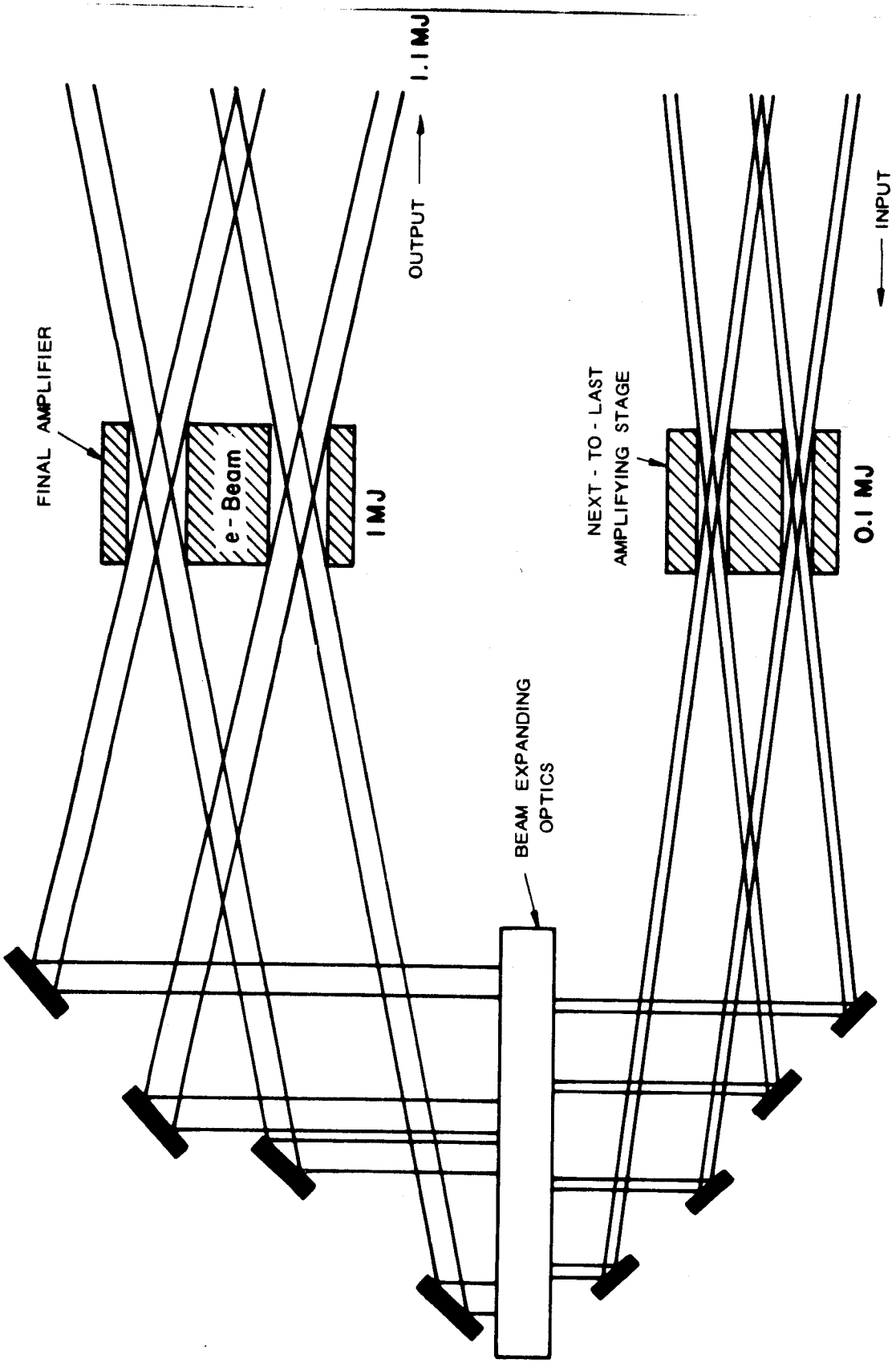

MULTIPASSING FINAL TWO AMPLIFYING STAGES IN SOLASE

Figure VI-A-1

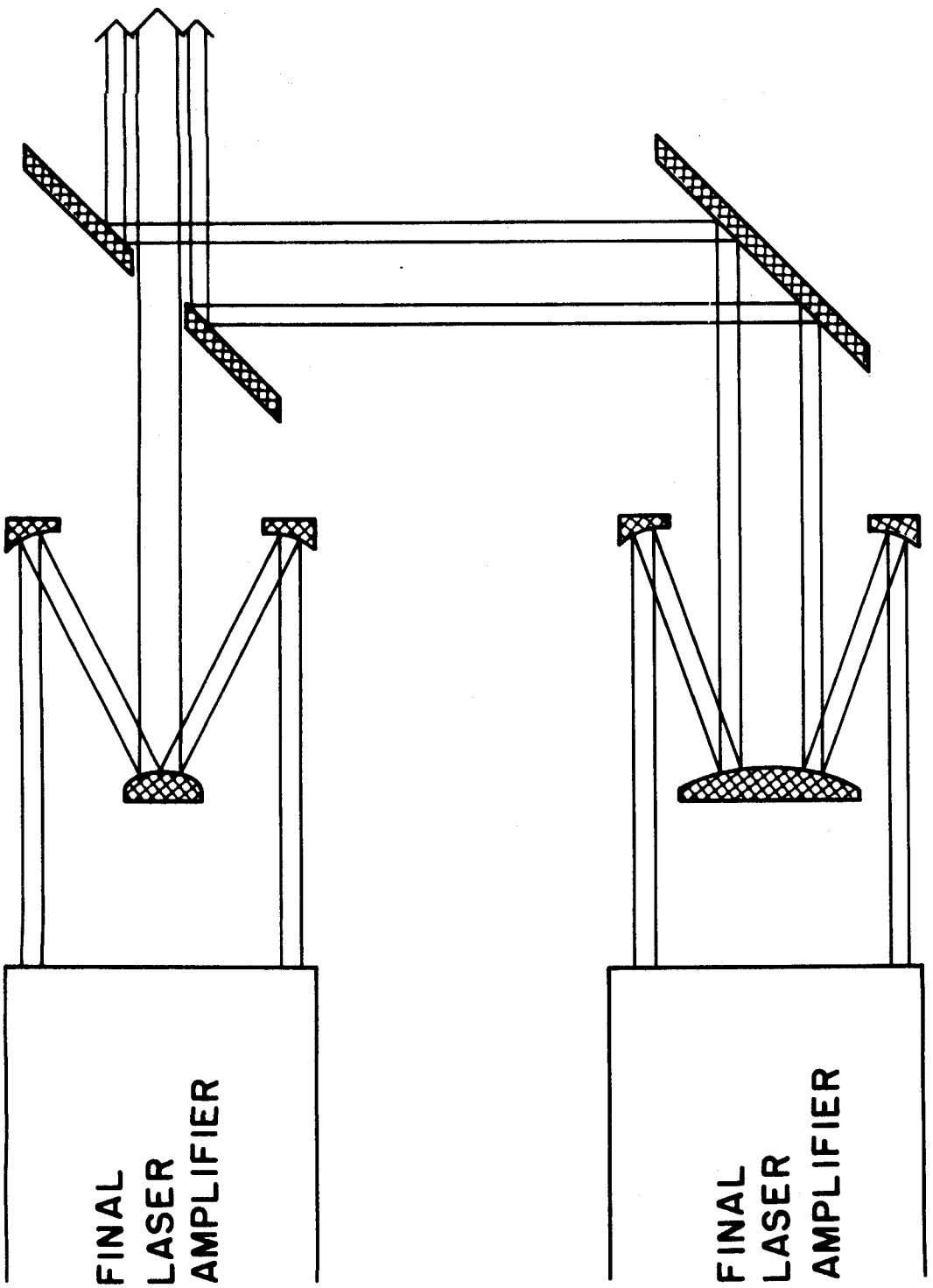

COMBINING TWO ANNULAR LASER BEAMS

Figure VI-A-2

and the other is reduced to a size that just encircles the first. These beams can now be combined by using the series of mirrors as shown in the figure. A detailed design of the optics has not been attempted. It should also be noted that more than two beams could be combined by this method if desired.

The ease with which annular beams can be combined allows not only easier handling of the beams but also allows a more optimum and realistic integration of two aspects of the laser system: the size of the final amplifiers and the number of beams desired on target. The number of beams desired is a compromise between providing a sufficient number of beams so that relatively uniform illimination could be obtained if necessary and minimizing the number of beams to both reduce the complexity of the system and maximize the accessibility to the reactor. Twelve beams were chosen as a reasonable compromise. With respect to the size of the final amplifiers it was desired to limit the energy extracted by a single amplifier chain to a value that would be representative of a typical laser. The limit will probably range from about 10 to 100 kJ depending on the laser so an average value of about 50 kJ was chosen. This requires 22 to 24 beams for a 1.1 MJ system. Thus, to make these two requirements compatible, the twenty-four beams from the final amplifiers are combined in pairs to yield the twelve beams that will be focused onto the pellet.

VI-A-4. The Optical Delay Lines

A consequence of multipassing is the need for optical delay lines. In the SOLASE design four successive beams will be extracted from each amplifier during each pumping cycle. There will be a delay of about

0.1 μs between passes to allow for the collisional repopulation of the upper laser level. Thus, in order to have all beams reach the target simultaneously, the first three beams extracted must each be delayed the appropriate amount. This will require delay lines of approximately 100, 66.7, and 33.3 m for the first, second, and third beams extracted. A schematic of the delay lines and beam transport system is shown in Fig. VI-A-3. In this figure, which is to scale, the solid beam lines represent the beams passing through the amplifiers at the various angles while the dashed lines represent the delay lines and the remainder of the beam transport system. Note that differences in height of the various lines have not been indicated in the figure but were accounted for in the laying out of the system. It should also be noted that this layout requires an equivalent number of mirrors as would a system without delay lines. The actual number of mirrors required depends on the particular beam line and varies from 4 to 6. In addition the beams must be reduced and combined which will require 2 reflections for one of each pair combined and 4 for the other. Thus, the beams must undergo 6 to 10 reflections after the final amplifier.

VI-A-5. The Last Mirror Placement

The placement of the last mirrors involves two basic considerations: one is consideration of parameters such as the distance the mirrors are to be placed from the pellet and the turning angle. These questions have been addressed in section VI-B-1. It was decided to place the mirrors 15 m from the center and have the final turning angle be 90°. The other consideration is the overall mirror configuration which will be discussed here.

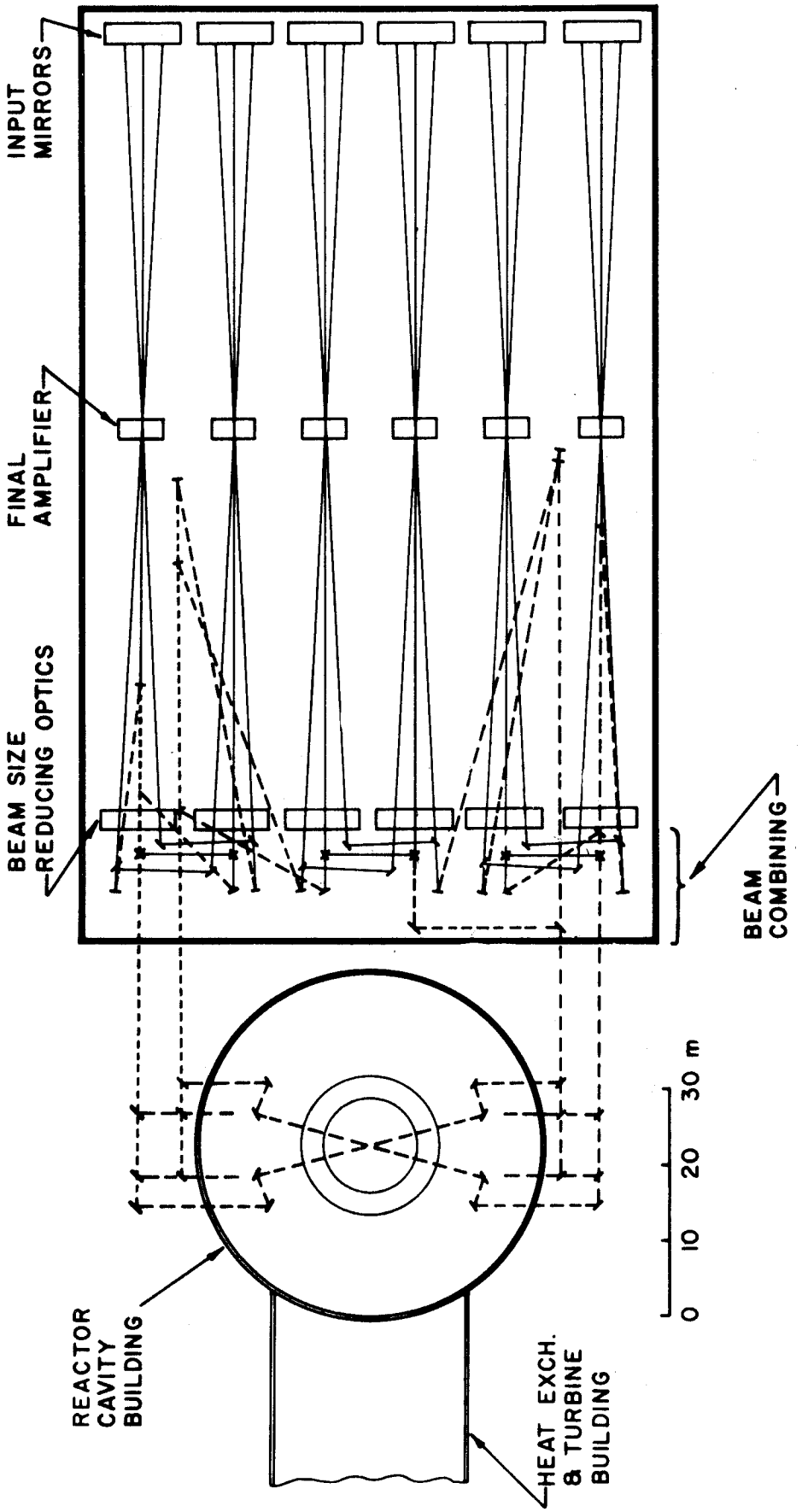
INPUT MIRRORS
FINAL AMPLIFIER
BEAM SIZE REDUCING OPTICS
BEAM COMBINING
REACTOR CAVITY BUILDING
HEAT EXCH. & TURBINE BUILDING
0
10
20
30 m

Figure VI-A-3

The placement of the last mirrors will depend primarily on the illumination requirements of the laser-pellet interaction. Of the many possible illumination patterns the two most likely to be employed will probably be "uniform" and two-sided illumination. For SOLASE we have chosen a mirror configuration that can be "inverted" to provide either two-sided illumination as shown in Fig. VI-A-4 or reasonably uniform illumination as shown in Fig. VI-A-5. (Note for several reasons as discussed in section V-A-5 it is virtually impossible to obtain truly uniform illumination in practice). Since it is not known at this time which illumination scheme may ultimately be required, we have chosen the two-sided configuration because it results in a more compact system, allowing greater accessibility to the reactor cavity. However, inverting the design to obtain uniform illumination requires no fundamental change in design.

In this design, the last mirrors will be placed six each on opposite sides of the reactor in the smallest hexagonal array allowable (see Fig. VI-A-6). Opposite mirrors will "see" each other so that a laser pulse that misses a pellet will pass through a port on the opposite side and travel back through the beam transport system. This design depends critically on the ability to both prevent parasitic oscillations that could be established in the cavity formed by each pair of amplifier chains that are connected through the center of the reactor chamber, and prevent damage to the optical elements in the event of a miss and the full beam energy is propagated back through the amplifier chain. The parasitic problem is greatly reduced by the combination of the large distance the light must

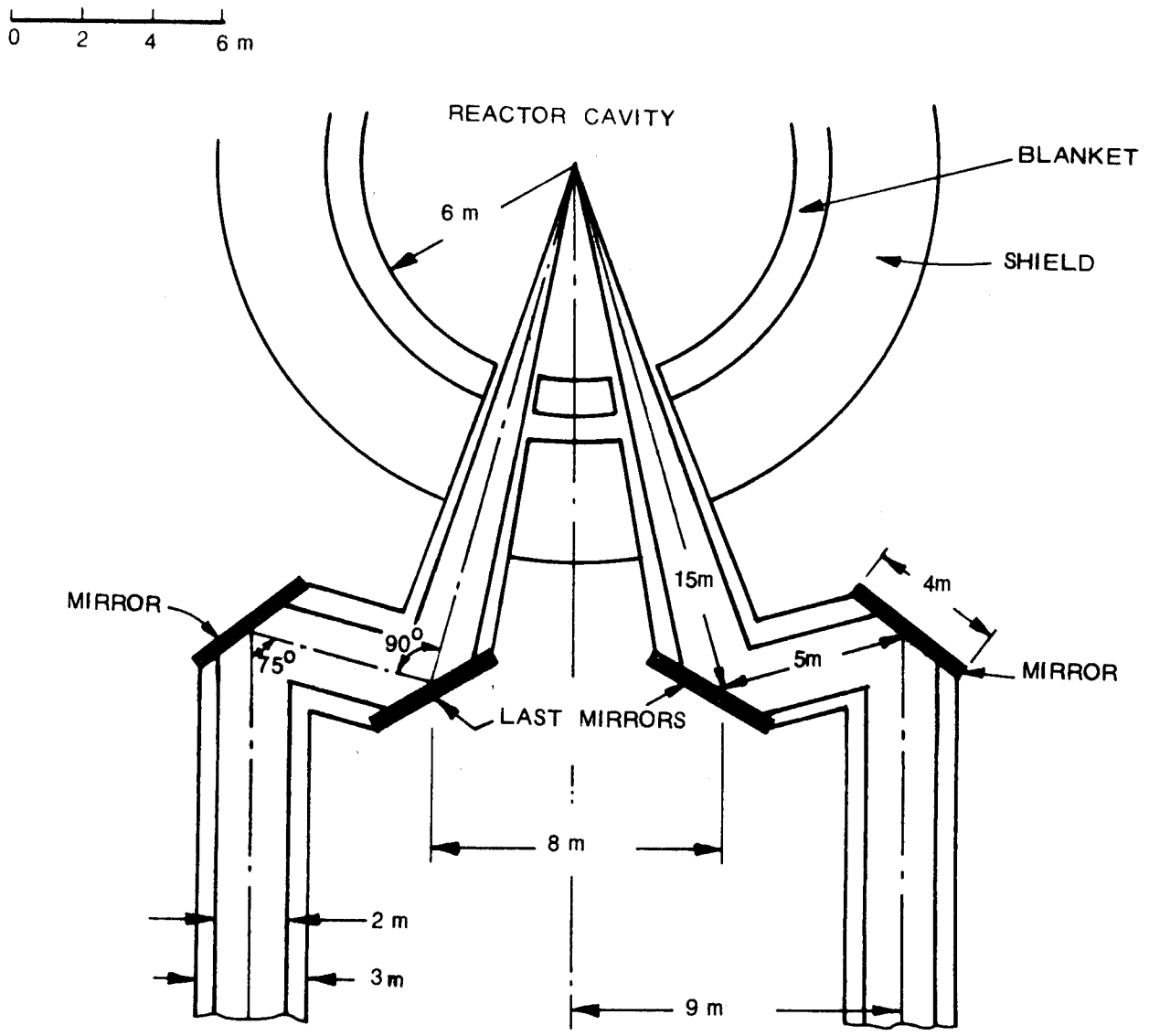

TOP VIEW
LAST MIRROR PLACEMENT
FOR SOLASE

Figure VI-A-4

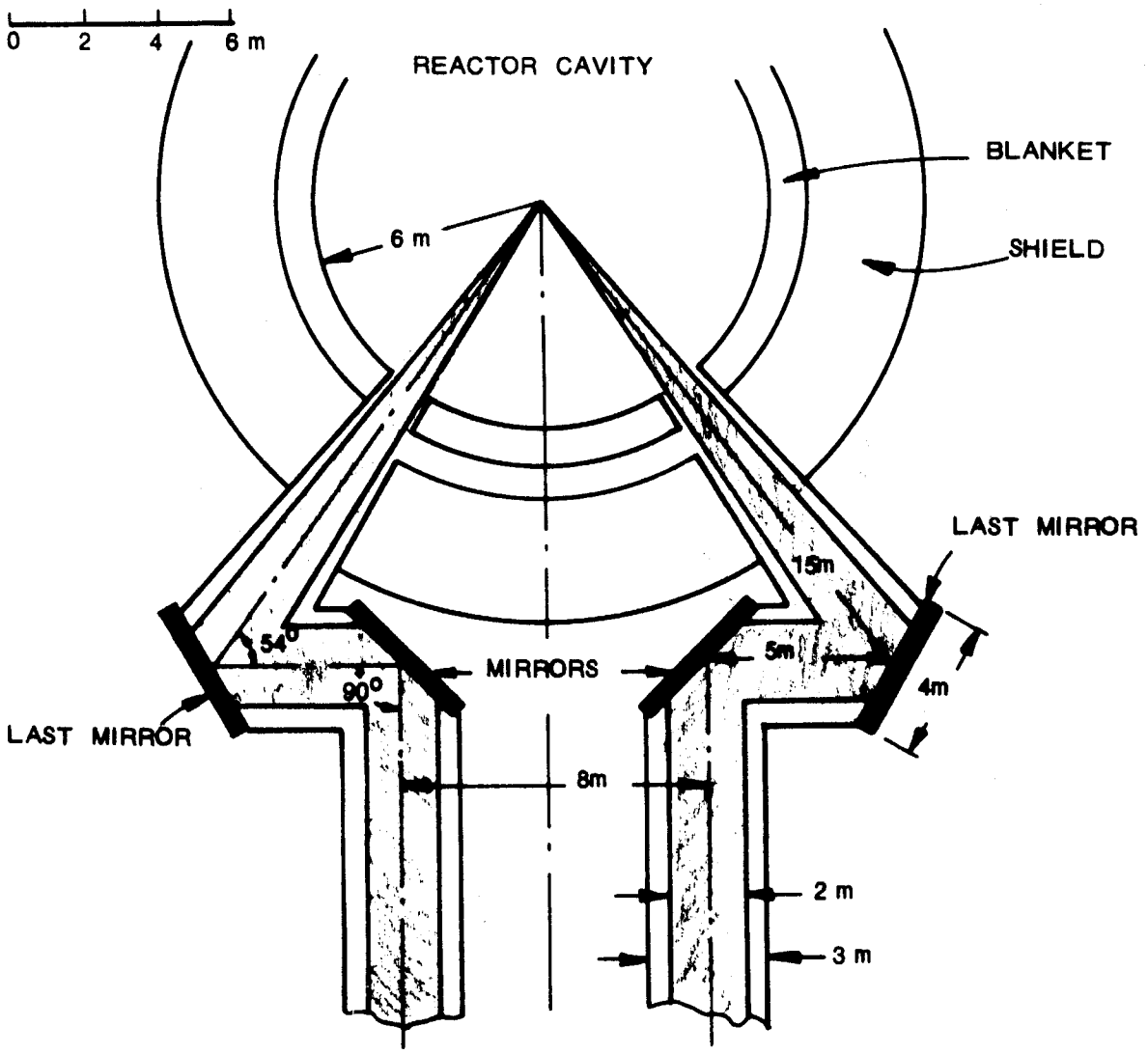

TOP VIEW
LAST MIRROR PLACEMENT
ALTERNATE CONFIGURATION

Figure VI-A-5

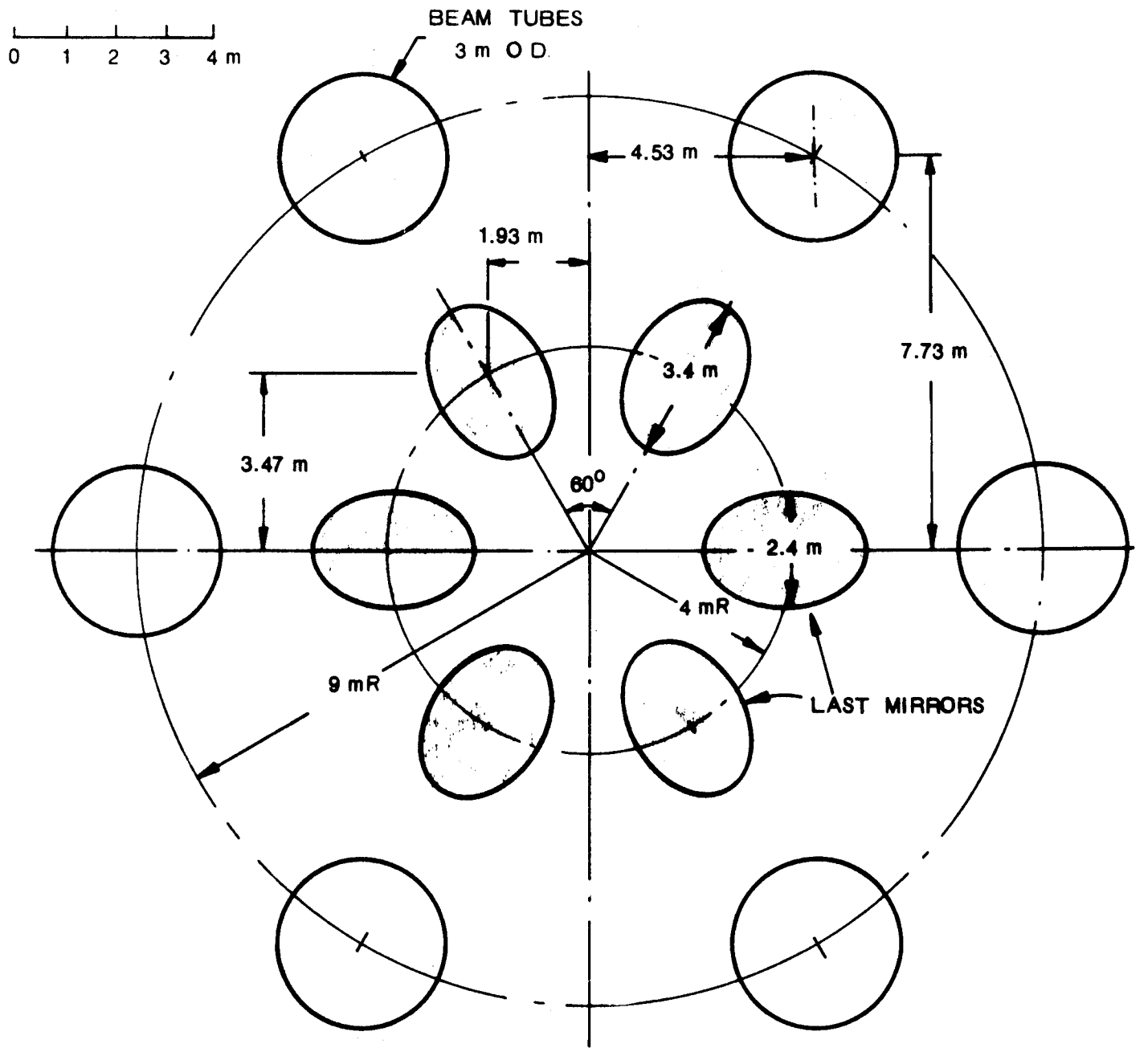

END VIEW
LAST MIRROR PLACEMENT
FOR SOLASE

Figure VI-A-6

travel and the short pumping time and can be further reduced by the use of faraday rotators and saturable absorbers. The protection problem might be solved by either faraday rotators or a gas breakdown scheme (see section VIII-B-8). These methods should work adequately for light reflected from the target but it is not clear that either could stop a sufficient fraction of the full beam energy to prevent damage.[1] This issue must be examined closely. Should no method prove adequate (it only takes one failure of the protection system to damage a large portion of the optics train) the beam ports will have to be skewed so that they no longer see each other and the affected sections of the reactor wall must be designed to tolerate a full laser pulse.

The final turning angle for all mirrors will be 90° as shown in Fig. VI-A-4. The bend in the beam line is necessary to reduce neutron streaming along the beam lines. Shielding considerations may further require that these beam lines not all lie in the same plane as depicted in the figure or alternatively that the beam line after the bend be parallel to the beam line between the last mirror and pellet (see chapter III). However, neither of these modifications necessitate any fundamental changes in the beam transport design.

VI-A-6. Additional Considerations

There are several areas of import to the beam transport system which have not been thoroughly evaluated. These include the alignment of the system; the effects of the medium in the beam lines on the laser pulse; the placement of a window in the beam line to isolate the reactor and laser buildings; and the optical differences between a multipassed and a single passed system. Each of these are discussed below.

The alignment of the optical system will be extremely difficult due to the large number of components and the small tolerances to which they must be aligned. In addition to initially aligning the system, it must be maintained in this precise alignment during operation. This will undoubtedly require continuous monitoring and adjusting of the various components.

Unfortunately there is little experience in aligning such large arrays of optics. In this regard Livermore's Shiva and Los Alamos' Antares lasers should provide valuable experience. However, these lasers will not require "on-line" alignment nor will their problems be complicated by the need to inject targets. To include this ability in an automatic, high-repetition rate system will require a very sophisticated diagnostic, feedback, and correction system.

Since the ultimate goal is to have the laser beams hit a very small target that has been injected toward the center of the reactor chamber, the alignment problem involves the coupling of two systems: the optics and the pellet injector. The pellet injector must be capable of repetitively delivering the pellet to a precise location with a given velocity. (The injector is discussed in greater detail in Chap. IX.) To determine if an injected pellet will arrive at both the proper time and place, it must be accurately tracked for both position and velocity. The time of injection and the pellet's velocity must be measured to provide an accurate trigger signal to fire the lasers. The position must be monitored

to provide diagnostics in order to make the proper adjustments should the injector drift out of alignment and to stop the firing of the laser if it is determined that the laser beams would miss the pellet. This tracking might be accomplished by a system of low power lasers, but any scheme will be complicated by the reactor's harsh environment.

The optics must be aligned such that each beam is focused to a precise location with respect to both the pellet and the other beams. As with the pellet injector, diagnostics must be provided to detect misalignments and provide the information to make the necessary corrections. This system would probably also consist of a series of low power monitoring lasers. It should be strongly emphasized that the diagnostics for both the pellet injector and optics must not only detect whether the system is misaligned but how it is misaligned in order that proper corrections can be made.

Another aspect of the alignment question to consider is whether either mid-course corrections can be made in the pellet's trajectory or whether the optical alignment can be adjusted during a pellet's flight to correct for variations in its trajectory. Neither task appears trivial.

One method considered for correcting the pellet's trajectory was the placing of a charge on the pellet and electrostaticly changing the trajectory. However, from our initial considerations this method did not appear promising. Clearly this and other potential methods should be examined more thoroughly.

With regard to the optics, the actual moving of the large mirrors would be very difficult on the time scales required. An alternative is to utilize

adaptive optics in which a "rubber mirror" can be adjusted to give the change in wavefront necessary to slightly shift the focal region to the desired location. The time response of state-of-the-art adaptive optics is quite adequate for laser fusion applications. However, it is not clear at this time whether the adaptive optic would be effective if placed early in the amplifier chain (at which point it would small in size) nor whether it is credible to consider large (2-3 m) adaptive optics that would be necessary if placed at the end of the chain. However, the advantages of adaptive optics certainly warrant further consideration.

Another problem to consider is the effect of the medium in the beam lines on the laser pulse. There are several processes that could have adverse effects on the beam. These processes include catastrophic self-focusing, thermal blooming, turbulence, and laser-induced gas breakdown.

Self-focusing is a non-linear effect in which the effective index of refraction of a material increases with increasing beam intensity. Because the intensity is not uniform across the pulse, self-focusing will eventually cause the beam to collapse upon itself.

When the media through which the laser beam is passing absorbs a fraction of the beam's energy the effect known as thermal blooming can occur. In this process the energy is absorbed non-uniformly which in turn heats the gas non-uniformly. This creates a density gradient in the medium and this a gradient in the index of refraction which distorts the beam. Other sources of thermal gradients and turbulence also result in density gradients and thus index of refraction gradients that can distort

the beam. Turbulence can arise from many sources such as equipment vibrations and shocks generated by the discharging amplifiers and pellet explosions.

Laser-induced gas breakdown of the medium is the final process to consider. This process occurs when the laser beam is intense enough to ionize a significant fraction of the medium through which it is propagating (see Sec. XI-B-5). The plasma that forms will be opaque to the laser beam,preventing further propagation of the light. The threshold for breakdown depends upon several parameters including the intensity and wavelength of the light and the pressure and composition of the gas.

A preliminary examination of these processes indicates that a laser beam could propagate through a medium at atmospheric pressure provided that the medium is properly controlled and conditioned. Specifically all turbulence must be suppressed and all temperature gradients minimized to eliminate all density gradients. All absorbing gases must be removed (such as CO_2 and H_2O for a CO_2 laser) to prevent thermal blooming and residual temperature gradients. A one nanosecond, 10.6 μm laser pulse with an energy density of 5 J/cm^2 is sufficiently below the breakdown threshold of atmospheric air that it should propagate without breaking down the gas. However, the air must be maintained free of dust particles since their presence will greatly reduce the breakdown threshold. Also since the threshold varies approximately as the inverse of the wavelength squared, breakdown will be less critical for shorter wavelength lasers. Self-focusing does not appear to be a problem.[2] Thus, it appears that

the beam could propagate in an atmospheric medium prior to focusing. However, the cost of conditioning the gas will probably be excessive. Alternatively, the lines could be evacuated to a pressure of about 0.1-1 torr. This should minimize all these problems and be both simplier and cheaper than conditioning the gas. Also if a high pressure medium is utilized, a window will be required to separate the beam lines into two regions since the reactor cavity region must be maintained at a low pressure. (There are other advantages to having such a window and the problems associated with one are discussed next.) Finally, all these problems should be examined in greater detail because even if the individual effects are small, their cumulative effect along the entire length of beam line could become significant.

It is desirable to consider placing a window in each beam line in order to isolate the reactor and laser buildings from each other. There are two advantages of having such a window: to contain tritium in the reactor building under normal operating conditions and to allow different ambient conditions in the two sections of beam line. The desirability of containing tritium should be obvious. This will minimize the area in which tritium is present, reducing both the working hazards in the laser building and the cost of the tritium recovery system. This window could be used in conjunction with a valve that would seal the beam line in the event of the window's breaking. It may also prove desirable to have a window in order to maintain different ambient conditions in the two sections of beam lines. The reactor cavity and adjacent beam lines in

SOLASE will be filled with a low pressure (<1 torr) gas such as Ne or Xe. It would probably be desirable to use a cheaper gas such as N_2 in the laser building beam lines instead of the expensive Ne or Xe. This would require an isolating window. A window would also be required, if it were decided to operate the laser building beam lines at atmospheric pressure.

There will be difficulties encountered in designing such a window, however. This window must span the entire beam line (2 to 2-1/2 meters in diameter), possibly withstand a large pressure differential, and simultaneously remain a high quality optical component that will pass the laser pulse with minimal distortion. It will be difficult to meet these requirements. A solution may be to build the window, not of a single optical component, but of several smaller ones. This could be advantageous for several reasons. The smaller components could be produced with higher optical quality than a single large component. In addition some materials such as NaCl may prove very difficult to manufacture in such large sizes. Also windows composed of smaller components might be made structurally stronger so that they would be less susceptible to deformation. Of course the effects of a segmented window on the beam quality must be closely examined. If no pressure differential exists, it may be possible to use a very thin sheet of plastic or other transparent material which would serve to isolate the two regions of beam lines but would have minimal optical effect on the laser pulse.

An alternative to a solid window is the aerodynamic window in which rapidly flowing gas forms a shock wave that acts as a window in that it can effectively isolate two media and withstand pressure differentials. Such a window also has the advantage in that it will not suffer any permanent optical damage being a gas. Thus, aerodynamic windows appear attractive.

Initial considerations, however, indicate that if the aerodynamic window directly replaces the solid window discussed above the pumping power requirements would be excessive because the apertures are so large. (Extrapolating data from Ref. 3, it is estimated that the mass flow rate in these windows would be about 4 times that in the lasers which will require up to 27 MW in pumping power.) Since the mass flow requirements are proportional to the aperture's size, reducing the aperture would reduce flow requirements. This might be accomplished by greatly increasing the distance of the last mirror from the chamber and placing the aerodynamic window near the edge of the reactor cavity, at which point the beam will have been significantly reduced in size by the focusing process. This configuration would have the additional advantage of preventing shock waves and most pellet debris from hitting the last mirror. However, a major problem to now consider is the possibility of gas breakdown in the window since the beam will be substantially more intense. Also with this particular configuration, energetic tritium atoms could possibly penetrate the window reducing its effectiveness for tritium containment. In general tritium entrapment and removal from the window gas could present additional costs and complications. Pumping power requirements could also be reduced if the window did not have to with-

stand a pressure differential, which will likely be the case. This type of gas window would still allow different gases to be utilized in the two regions of the beam lines, but the consequences of tritium entrapment in the window gas must be more thoroughly evaluated.

Thus, aerodynamic windows appear to suffer from several serious drawbacks. However, their potential advantages are such that they warrant further investigation. It is possible that improved designs or novel methods of incorporating these into the beam transport system can overcome the disadvantages.

A final area that should be analyzed is the optical differences between multipassed and single passed systems. As mentioned in section VI-A-4, the optical delay lines will constitute one major difference between the two systems. The increased distance a beam must travel in the delay lines will increase the diffraction losses. However, the maximum increase in path length relative to the overall path length is small (about a factor of 4) so that increased losses should be relatively small.

In some cases, delay lines may require an increase in the number of reflections. This will increase losses due to both partial absorption of the light by the mirror and greater alignment errors. However, the additional reflections required should usually be small and in the SOLASE design no additional reflections are required.

Another difference to be examined is that the beams must pass through the amplifiers at different angles in a multipassed system. This will

result in different reflection losses than in a single pass system, but since the angles of incidence are small the differences between the two systems should be small. Another difference could arise if the reflections are not suppressed and unwanted parasitic oscillation modes develop.

Each of the differences although expected to be small should be examined more thoroughly.

VI-A-7. Summary of the Beam Transport System

The basic layout of the beam transport system has been presented. Except for the last mirror this area has not been examined in great detail. However, several problem areas have been identified. These include the protection of the optics in the event that a laser pulse misses a target; maintaining the alignment of the optics and pellet injector; the effects of the medium in the beam lines on the laser pulse; and the development of a window to isolate the reactor building from the laser building. It would also be informative to analyze the optical differences between a single pass and multiple pass system.

References for Section VI-A

1. Walter Reichelt, private communication.

2. L.A. Booth, D.A. Freiwald, T.G. Frank, and F.T. Finch, "Prospects of Generating Power with Laser-Driven Fusion," Proc. of the IEEE, 64, 1460-1482 (1976).

3. E.M. Parmetier and R. A. Greenberg, "Supersonic Flow Aerodynamic Windows for High Power Lasers," AIAA Journal, II, 943-949 (1973).

VI-B. Final Mirror Design for SOLASE

VI-B-1. Fabrication

We have elected to use diamond-turned bare metal mirrors because of their durability, resistance to surface damage and simplicity of fabrication.[1] The optimal reflective surface for wavelengths greater than 7000 Å is copper, having both high reflectivity and a high melting point. As Fig. VI-B-1 shows,[2] silver and aluminum remain reflective at shorter wavelengths, but are more susceptible to melting. Moreover, silver tarnishes rapidly. While dielectric coatings greatly enhance reflectivity, they are difficult to apply over large areas and are vulnerable to damage from neutrons, X-rays, as well as the laser itself. As will be seen below, the average absorbed laser power in copper at $\lambda = 1$ μm is quite modest and may easily be removed by actively cooling the mirror substrate.

In order to keep the weight down, the large final mirrors are constructed of 2.5 cm thick aluminum alloy plated with 1 mm of copper. This thickness is sufficient to allow several retoolings when damage occurs, and also serves as a thermal buffer zone to prevent the transient surface temperature from reaching the aluminum. The thermal response of the surface layer to X-rays and laser light is treated in Sec. VI-B-2. While BeCu offers a somewhat greater stiffness/weight ratio, the Al alloy is much cheaper and has proven to be quite satisfactory in present day experiments.[3] The technology required to plate Cu on large areas of Al is also well developed. As discussed in Sec. V-A-11, a honeycombed sandwich

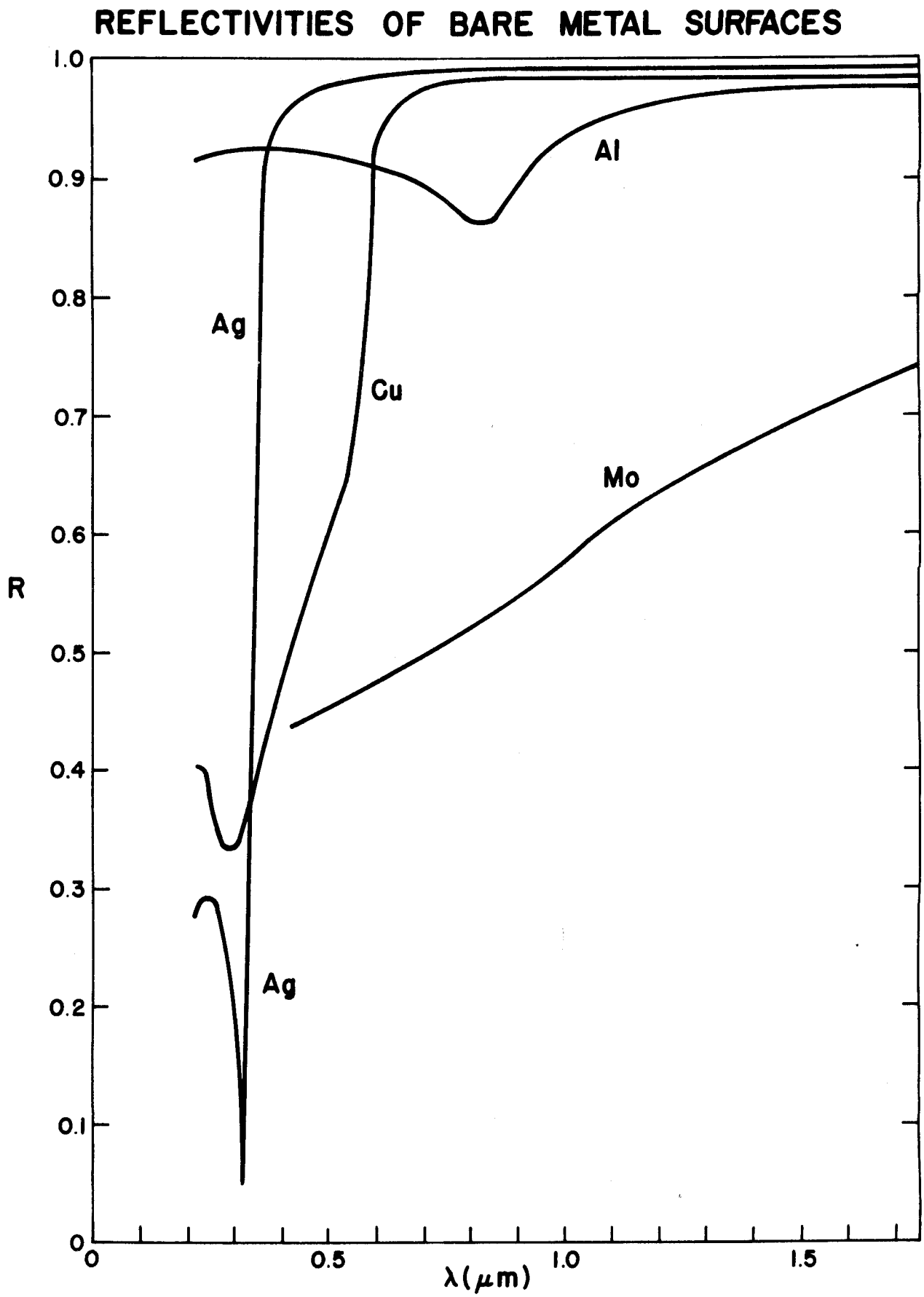
REFLECTIVITIES OF BARE METAL SURFACES
1.0
0.9
0.8
0.7
0.6
0.5
0.4
0.3
0.2
0.1
0
R
Al
Ag
Cu
Mo
Ag
0
0.5
1.0
1.5
λ(μm)

Figure VI-B-1

of two face plates offers the greatest stiffness/weight ratio.

The physical dimensions of the final mirror are determined by the incident beam radius, the turning angle and the damage threshold for surface melting under the intense laser radiation. Since the beam radius does not change between the beam combining optics and the last mirror, this beam radius is determined by the mirror in this line having the smallest turning angle. It may be seen from Fig. VI-A-6 that this angle is about 30°. From Sec. V-A-3 it follows that if a mirror suffers a maximum energy flux Φ (J/cm^2) at normal incidence, the oblique flux is reduced to $\Phi \cos(\phi_o/2)$ where ϕ_o is the turning angle. Assuming a fill factor of 0.8, a beam radius of 86 cm was calculated for nonuniform illumination. Allowing for some difficulty in producing a large fill factor in combining annular beams (which may themselves have to be segmented) we choose a beam radius r_B = 1m.

Having determined the beam radius, we may now calculate the size of the last two mirrors, both of which will certainly have to be cooled. It may also be necessary to cool the many mirrors involved in the delay lines and beam combining systems. From Fig. VI-A-4 we see that the penultimate (flat) mirror turns the beam through 75° and the final parabolic mirror turns the beam thorough 90°. (It may prove necessary to reduce these angles somewhat to reduce their physical size and to reduce pointing errors. It should be pointed out however, that the final beams' cone angle - and f/no. - are independent of the turning angle. That is, the solid angle taken up by beams depends only on r_B and the

focal length.) From Sec. V-C-1, the mirror major diameter is

$$S \approx 2\, r_B \sec \phi_o/2, \qquad (1)$$

exact for flats and approximate for paraboloids. The average lengths and customary 20% oversize values are plotted in Fig. V-C-5. The values for the 75° and 90° mirrors are, in meters,

ϕ_o	S	1.2S
75°	2.52	3.03
90°	2.82	3.38

Table VI-B-1

The final mirrors for SOLASE will be elliptical, 3.4 m x 2.4 m, as depicted in Fig. VI-A-6.

It would be very desirable to reduce the size of these huge mirrors, as they would be costly and difficult to fabricate. Indeed, the dimension $R_o = r_o \sin\phi_o = 15$m determines the size of the diamond turning facility needed so that segmenting would not help. It may be possible to diamond turn the mirrors by fly-cutting in which the tool is rotated, rather than by the piece. We are currently considering alternate designs with drastically smaller turning angles in order to reduce R_o to a meter or two. These design changes would require somewhat longer focal lengths, which would have the additional benefit of reducing the neutron leakage, a serious problem with the present design.

VI-B-2 Thermal Response to Radiation

The last mirror is directly exposed to fast neutrons, X-rays, secondary γ-rays, and of course the laser light. Charged particles are virtually 100% absorbed by the buffer gas, as discussed in Section XI-B-6. The laser and X-radiation produce surface heating which is eventually conducted into the mirror substrate. The laser radiation is potentially most damaging, as surface melting can take place if insufficient area is provided. Section V-A-3 explains how to avoid this catastrophe. It may be shown that negligible energy is radiated away from the mirror surface for the temperatures encountered in SOLASE. The neutrons and secondary gammas of course contribute only bulk heating; void growth may be suppressed by cooling the mirrors. Assuming 15 MJ of X-radiation it is straightforward to show that this source potentially dominates the bulk heating. The actual delivery of X-ray energy depends strongly on its black body temperature because of the buffer gas attenuation. An uncertain amount of this absorbed energy is subsequently reradiated to the mirrors, as explained in Section XI-B-4. The results of this section show that the maximum possible power delivered to the last mirrors is well within the state of the art of active cooling.

VI-B-2-a Laser Light

The maximum energy density per pulse is $ff\Phi^*$ J/cm^2, where ff is the fill factor and Φ^* is the working flux, about half the damage threshold of 10 J/cm^2. For non-uniform illumination, ff $\approx$ 0.8. This energy is absorbed in a very thin surface layer and is rapidly conducted into the body of the mirror. The resulting absorbed power per unit volume is

$$\left\langle \frac{dP}{dV} \right\rangle_L \simeq \frac{(1-R)\ ff\Phi^*\ \nu_r}{d}\ W/cm^3\ , \qquad (2)$$

where ν_r is the laser rep rate, R is the reflectivity and d is the mirror thickness. Taking ν_r = 20 Hz, R = 0.98 and d = 2.54 cm gives

$$\left\langle \frac{dP}{dV} \right\rangle_L = 0.63\ W/cm^3\ , \qquad (3)$$

a very small amount of power.

VI-B-2-b X-Rays

The X-ray energy flux for 15 MJ delivered over 15 m is

$$\Phi_x = \frac{E_x}{4\pi R^2} = 0.531\ J/cm^2\ . \qquad (4)$$

The corresponding volumetric power absorption, assuming zero reflectivity, is

$$\left\langle \frac{dP}{dV} \right\rangle_x = \frac{\Phi_x\ \nu_r}{d} = 4.17\ W/cm^3\ . \qquad (5)$$

This is much greater than the absorbed laser power, mainly due to our assumption of zero reflectivity.

Because of absorption in the buffer gas, not all of the X-ray energy reaches the mirrors and cavity wall immediately. Some of the absorbed energy is reradiated, but an uncertain fraction is carried off as internal heat in the circulating gas. As discussed in Section XI-B-4, a quantitative estimate of this fraction is enormously complex to carry out. The volumetric heating rate, taking into account absorption in the buffer gas, is plotted vs. black body temperature in Fig. VI-B-2. Data is shown for the present SOLASE design using 0.5 torr of neon, and the improved design using 0.25 torr of xenon.

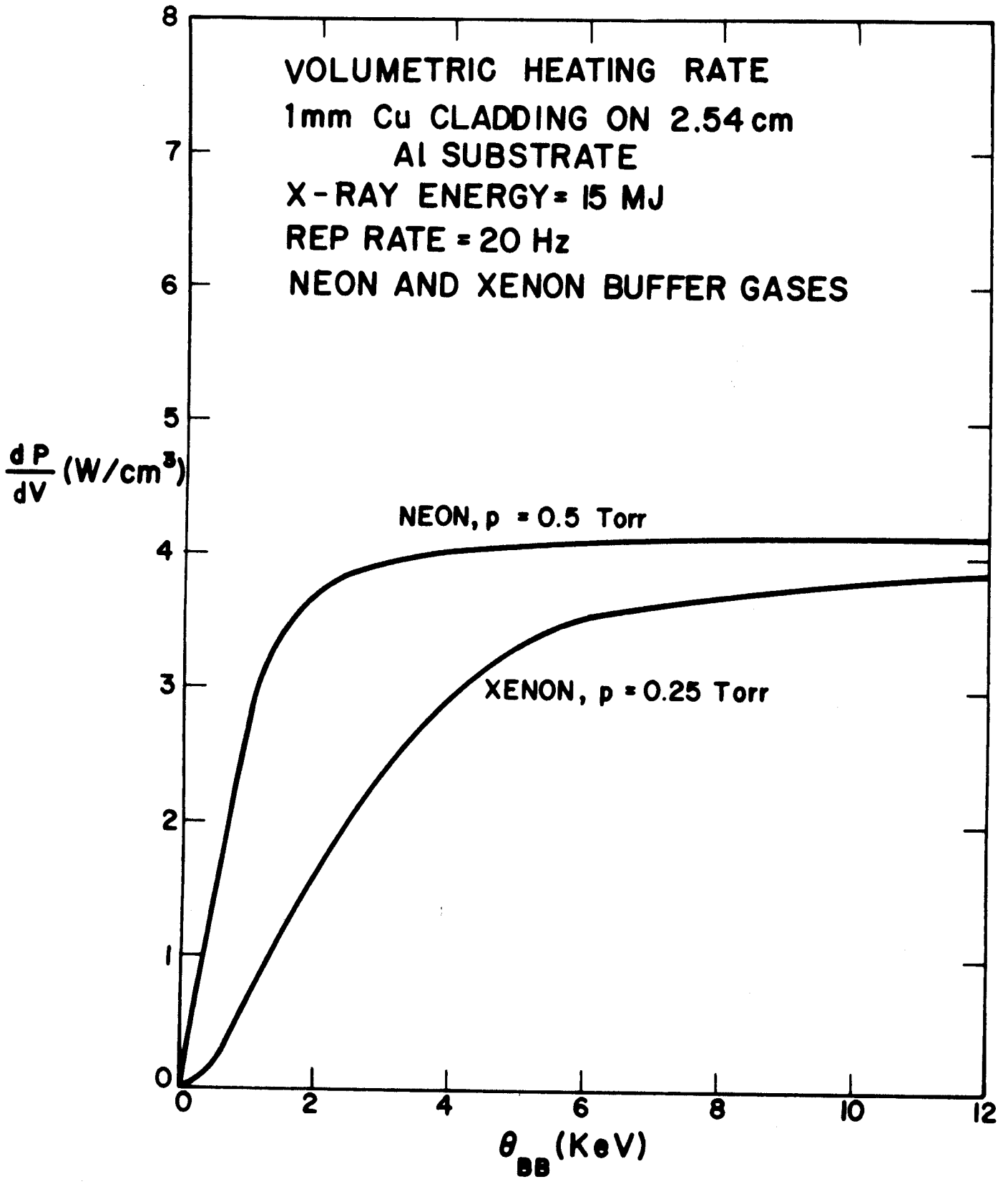
VOLUMETRIC HEATING RATE
1mm Cu CLADDING ON 2.54 cm
Al SUBSTRATE
X-RAY ENERGY = 15 MJ
REP RATE = 20 Hz
NEON AND XENON BUFFER GASES
NEON, p = 0.5 Torr
XENON, p = 0.25 Torr
dP/dV (W/cm³)
θBB (KeV)
0
1
2
3
4
5
6
7
8
0
2
4
6
8
10
12

Fig. VI-B-2.

The X-rays also produce a significant surface temperature rise for $\theta_{BB} \tilde{<} 5$ Kev, as Figs. VI-B-3 and VI-B-4 show for neon and xenon, respectively. Here the use of xenon has a dramatic effect, keeping the temperature rise below 100°C for all black body temperatures. The reradiated energy is released over a time greater than 1 ms, producing negligible surface effects.

Since the X-rays are penetrating, one might be concerned that thermal cycling could weaken the Cu-Al interface. As a worse case, let us consider a 10 kev black body spectrum passing through 0.5 torr of neon, and look at the temperature fall-off through the 1 mm Cu cladding. As Fig. VI-B-5 shows, the temperature rise at the interface is very small. Even if the cladding were reduced to 100 μm, the temperature excursion would only be a few degrees. Softer spectra give higher temperature rises confined to thinner layers.

VI-B-2-c Neutrons and Secondary Gamma Rays

The bulk heating rate due to direct (14 Mev) and thermal neutrons and their secondary gammas has been computed for a number of substrate materials by a Monte Carlo method.[4] The volumetric heating rates for an aluminum substrate are, neglecting the thin copper cladding,

$$\left(\frac{dP}{dV}\right)_n = 1.80 \text{ W/cm}^3 \qquad (6)$$

$$\left(\frac{dP}{dV}\right)_\gamma = 1.65 \text{ W/cm}^3 \ . \qquad (7)$$

The total heating rate is therefore less than

$$\left(\frac{dP}{dV}\right)_{Tot} = 8.25 \text{ W/cm}^3 \ . \qquad (8)$$

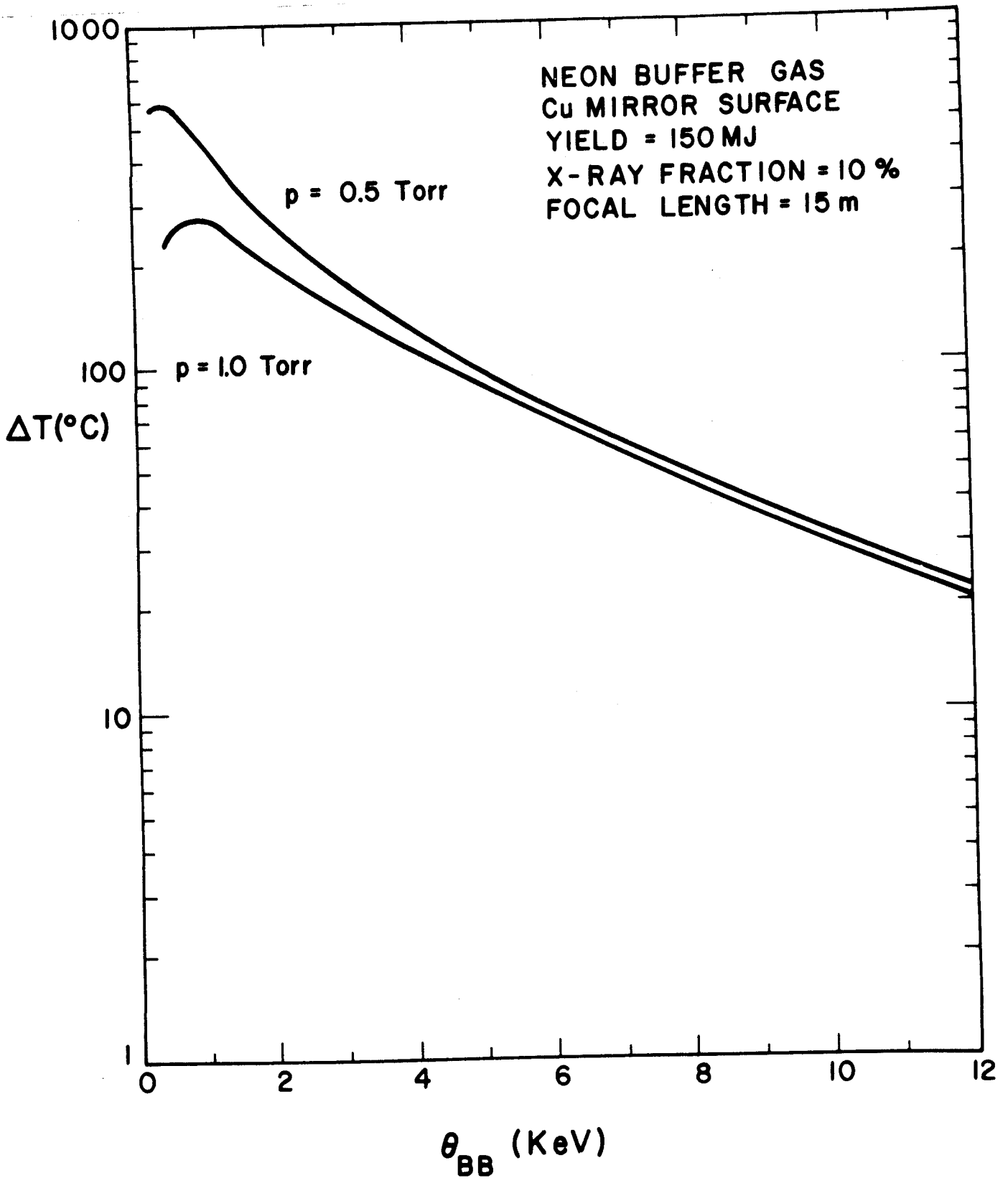
NEON BUFFER GAS
Cu MIRROR SURFACE
YIELD = 150 MJ
X-RAY FRACTION = 10 %
FOCAL LENGTH = 15 m
p = 0.5 Torr
p = 1.0 Torr
ΔT(°C)
1000
100
10
1
0
2
4
6
8
10
12
θBB (KeV)

Fig. VI-B-3.

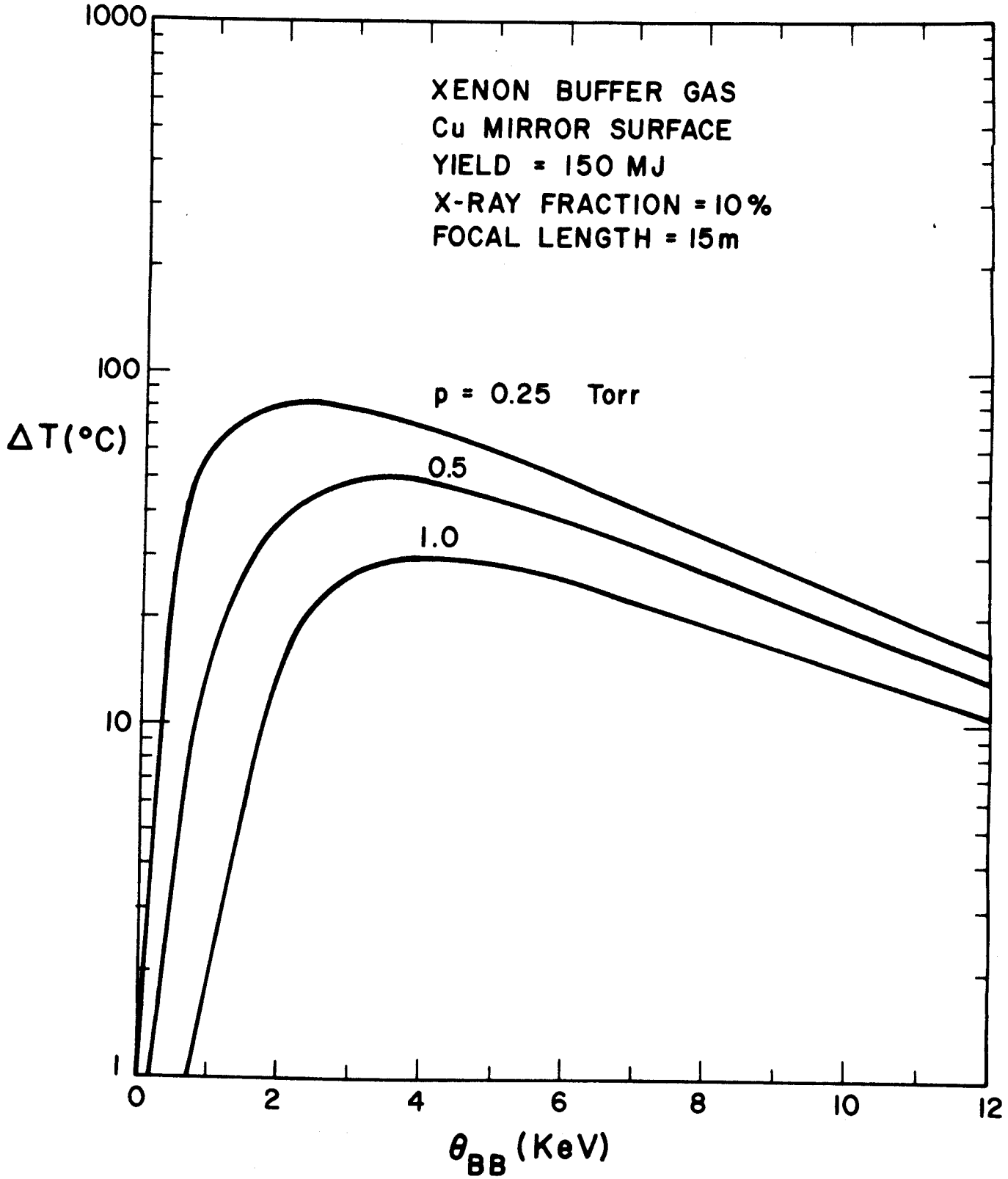
XENON BUFFER GAS
Cu MIRROR SURFACE
YIELD = 150 MJ
X-RAY FRACTION = 10%
FOCAL LENGTH = 15m
p = 0.25 Torr
0.5
1.0
ΔT(°C)
1000
100
10
1
0
2
4
6
8
10
12
θBB (KeV)

Fig. V-B-4.

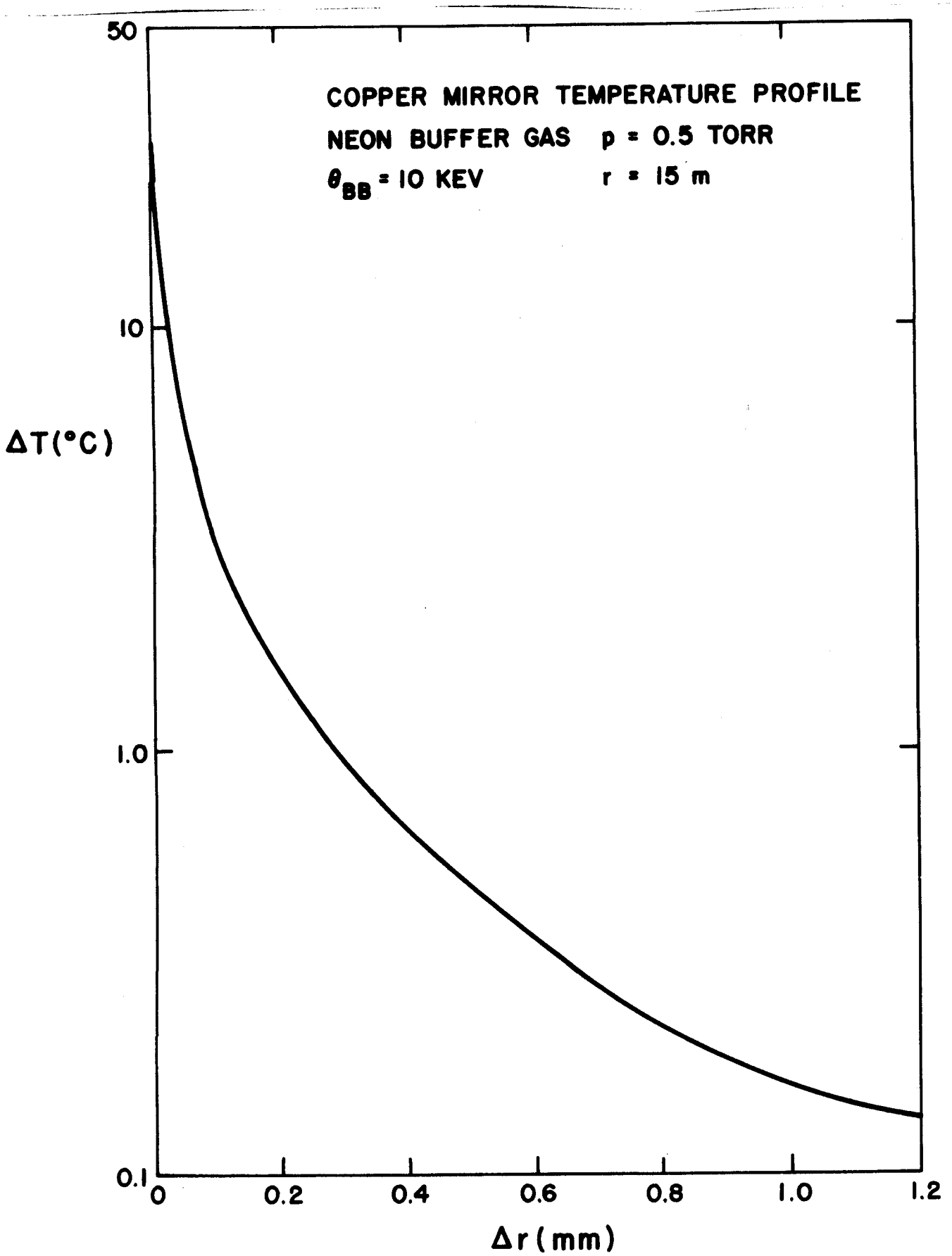
COPPER MIRROR TEMPERATURE PROFILE
NEON BUFFER GAS p = 0.5 TORR
θ_{BB} = 10 KEV r = 15 m
50
10
1.0
0.1
ΔT(°C)
0
0.2
0.4
0.6
0.8
1.0
1.2
Δr (mm)

Fig. VI-B-5.

Unfortunately, much of the literature on mirror cooling technology is classified, and for this reason we have not attempted a detailed analysis of this problem. The point is that although the instantaneous heating rates are high in a laser fusion reactor, the average rates are low, compared to steady state devices, where incident laser fluxes in excess of 150 KW/cm^2 are encountered.[5]

References for Section VI-B

1. T. T. Saito, Appl. Opt. 14, 1773 (1975).
2. G. Hass, M. R. Kingslake, ed., Applied Optics and Optical Engineering, Vol. III, Academic Press (New York, 1965), pp. 309-330.
3. W. H. Reichelt, D. J. Bleums and W. C. Turner, LA-UR 77-468.
4. C. W. Maynard and M. Ragheb, private communication.
5. W. J. Spawr and R. L. Pierce, "Metal Mirror Selection Guide", SOR Report No. 74-004, Spawr Optical Research, Corona, Ca., May 1976.

VII. Lasers for Laser Fusion

VII-A. Introduction

In any laser fusion scheme, the laser is, of course, of primary importance. Its performance (or lack thereof) could be the difference between the success or failure of a reactor system. Due to an incomplete physical understanding of the laser-pellet interaction, the exact requirements needed for the ideal laser are still in question. However, for simple shell targets the necessary characteristics have been divided into two classes: those that are necessary to implode and burn a pellet and those necessary to make a practical and economic reactor system.

From the requirements listed in Table VII-A-1, one can infer a number of properties that would be exhibited by the ideal laser. First, the wavelength range of 3000-6000 Å implies an electronic transition. This wavelength range is desirable to efficiently couple laser energy into the pellet. The lower cutoff at 3000 Å is dictated by two-photon absorption damage suffered by optical components and the lack of efficient reflectors at shorter wavelengths. Recent experiments indicate less wavelength dependence than originally thought and may allow wavelengths of at least 2-3 μm and possibly even 10 μm.

The short pulse widths of 0.1-1 nsec are necessary to obtain a satisfactory implosion and imply two things of the laser. The first is that the energy must be stored directly in the upper laser level as collisional processes are too slow to repopulate the level during the pulse. This again suggests an electronic transition. The second is that the upper laser level should have

and decide on the one which optimizes the system. The next section evaluates both "proven" laser systems and potential systems in light of these requirements.

VII-B. Survey of Lasers for Laser Fusion

VII-B-1. The Iodine Laser

The iodine laser is based on the photodissociation of any of many different perfluoroalkyl iodides[3,4] which yield excited atomic iodine upon dissociation. The two compounds giving the best results to date[4] are i-C_3F_7I and n-C_3F_7I with C_2F_5I, CF_3I and CD_3I also giving reasonable results. A typical reaction would then be

$$i\text{-}C_3F_7I + h\nu \rightarrow C_3F_7 + I^*$$

which results in lasing on the $^2P_{1/2} \rightarrow {}^2P_{3/2}$ transition (1.315 μm) of iodine. The absorption band for the photodissociation process in C_3F_7I peaks at 270 nm, has a band width of ~ 36 nm, and has an average absorption coefficient of 1.14×10^{-2} $(Torr/cm)^{-1}$.[5]

The lasing levels actually have a hyperfine structure[4] as shown in Fig. VII-B-1. In addition, these levels can be further split by the magnetic fields generated by the flashlamps. This leads to complications in energy extraction. It has been determined that the lower levels mix rapidly enough on subnanosecond time scales that they may be considered as one state but that the upper levels do not.[6] Thus, in order to extract the maximum energy, both transitions must be amplified which gives a maximum extraction efficiency of 66%.[6] If only the transition with the higher gain ($F = 3 \rightarrow F = 4$) were to be amplified, the efficiency would drop to 46%.[6]

A list of the important parameters of the iodine laser is given in Table VII-B-1. To date, the laser has been pulsed to 500J with a pulse width of 500 psec.[7]

THE IODINE LASER

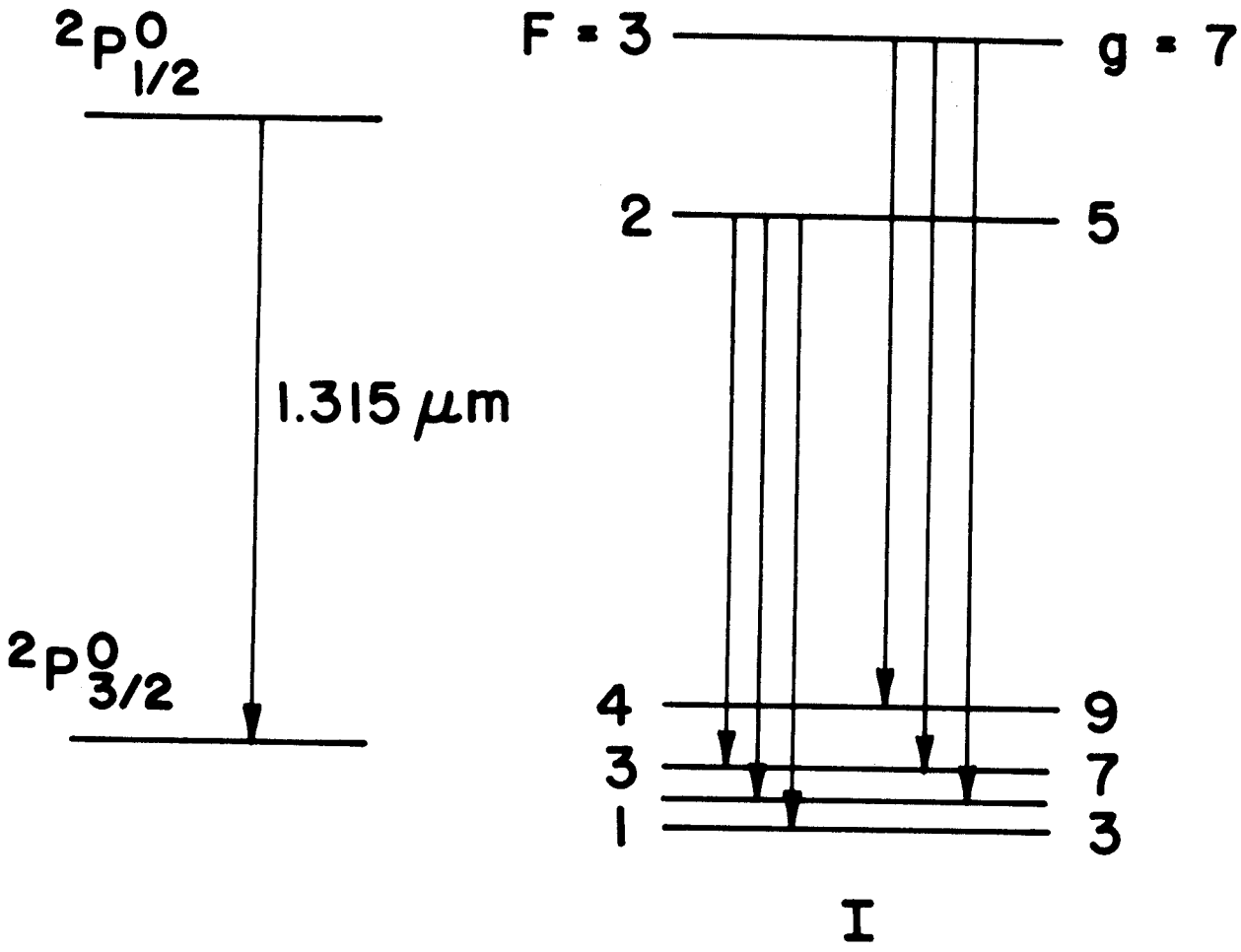

$$C_3F_7I + h\nu \longrightarrow C_3F_7 + I^*$$

I^* LASES AT 1.315 μm

Fig. VII-B-1

VII-B-2. Advantages of Iodine Lasers

The primary advantage of the iodine laser is that its wavelength is the shortest of the "proven" high-power gas lasers, although at 1.315 μm it still may be longer than desirable.

Table VII-B-1

Properties of the Iodine Laser

Wavelength	1.315 μm
Small Signal Gain	~0.1 cm^{-1}
Stimulated Emission Cross Section	$1.37 \times 10^{-16}/P_{tot}$ ~1.37×10^{-19} at 1000 torr
Pulse Width	0.1 - 1 nsec
Extractable Energy	0.72 J/l-Torr(C_3F_7I)
Efficiency	~0.5%

A second great advantage is that pulse lengths as short as 0.1 nsec can be effectively extracted. An additional advantage is that iodine is flash pumped. This allows one to go to very large apertures in order to increase the total energy out without increasing the energy density. This is an advantage over discharge-pumped lasers whose apertures are limited by the electric field that can be applied. Finally, the iodine laser has shown that it is capable of producing high energy pulses.

VII-B-3. Disadvantages of the Iodine Laser

Although an attractive system, the iodine laser suffers from a serious drawback: its efficiency. If standard flashlamps are used to pump the laser, this efficiency will be limited to about 1/2 to 1%, which is probably low for a pure laser fusion reactor. Another problem is that of regeneration of the

laser medium since not all the gas recombines to form the original molecule after having been dissociated. Thus, some chemical reprocessing must be done which will reduce the net efficiency even further. A potential problem could result from the use of flashlamps. State-of-the-art flashlamps are simply not adequate. There appears to be no insurmountable problem in designing lamps which can be pulsed at the necessary repetition rates but a serious question to consider is the failure rate. If this rate is too high, it could lead to excessive maintenance requirements.

VII-B-4. Possible Improvements

The question to be asked now is whether these disadvantages can be alleviated. The poor efficiency observed is not something inherent to the system (~20% quantum efficiency) but is the result of using flashlamps, since only a small fraction of their output lies in the proper absorption band. Thus a method of improving the efficiency is to utilize non-equilibrium flash sources such as electron-beam generated fluorescence of molecules such as XeBr* that exhibit strong spontaneous emission in the absorption band of C_3F_7I. It is thought that use of such a source would increase the efficiency, but only to ~1 or 2%.[8] This might also help to eliminate the possible drawbacks of flashlamps. The flashlamps themselves can probably be improved by such methods as doping to yield net efficiencies of 1 - 1.5%. There appears to be little one can do to improve the regeneration problem. Fortunately, the molecule which gives the best laser response (i-C_3F_7I) also seems to have the best regeneration properties. It is thought that shortening the pump time would improve the regeneration. Recently, a method for the regeneration of CF_3I has been proposed[9] that would utilize either a laser or low power RF field

to selectively break the C-C bond of C_2F_6, a principal reaction product, and would allow the spontaneous reaction,

$$CF_3 + I_2 \rightarrow CF_3I + I$$

to proceed. Calculations indicate that this process should not significantly reduce the net efficiency of the iodine laser system. Experiments are currently being conducted to test the validity of this proposal.

An alternative approach which should probably be more thoroughly explored than it has been to date is the dissociation of the iodine by direct electron impact. Pumping by this method has been demonstrated[10] but it has not been demonstrated whether a significant increase in the efficiency could be realized with electron pumping. Nor has it been demonstrated that an electron pumped laser can be effectively scaled to the required size. Because the iodine laser is basically attractive, it would seem worthwhile to pursue electron pumping to determine if the efficiency could be improved by this method. The use of electron pumping would result in a tradeoff of advantages with a flash pumped system. One would lose the advantage of being able to go to large apertures of the flash system but would gain a more compact system which would possibly be more reliable.

VII-B-5. Summary of Iodine Lasers

To summarize, the iodine laser is a very attractive system except for the fundamental problem of efficiency. This drawback would appear to eliminate this laser from any practical, pure-laser-fusion reactor scheme. However, when considering some form of hybrid system in which the efficiency requirement could be greatly relaxed, the iodine laser becomes quite promising. Also if

shorter wavelengths should prove to be essential, this would work greatly to the advantage of the iodine laser as opposed to a CO_2 laser, for example.

VII-B-6. The HF Chemical Laser

The hydrogen fluoride chemical laser, as the name implies, is based on any of a large number of chemical reactions which yield HF in an excited state. Thus, it is actually the chemical reaction that pumps the laser, creating a population inversion on many vibrational-rotational transitions of HF. A simplified potential energy diagram is shown in Fig. VII-B-2. Lasing occurs on transitions with wavelengths varying from approximately 2.7-3.2 μm.

Although a number of reactants yield a laser, the ones which promise the greatest electrical efficiency are F_2 and H_2 because they can undergo the following chain reaction:

$$F + H_2 \rightarrow (HF)^* + H \qquad (1)$$

$$H + F_2 \rightarrow (HF)^* + F \qquad (2)$$

in which the products of each reaction feed the other. Reaction (2) has the most energy available and populates higher vibrational levels ($v \leq 6$) of HF than does reaction (1) ($v \leq 3$) but unfortunately distributes the energy relatively uniformly[11] which minimizes the inversion. Reaction (1) on the other hand, preferentially populates the upper levels ($v = 3,2$) and contributes most to the inversion.[11] Generally, the proposed high power HF lasers would utilize an electron beam initiated chain reaction between H_2 and F_2. In addition to H_2 and F_2, these gas mixtures will usually contain a small percent of oxygen to stabilize the mixture,[12] some SF_6 to both increase the electron beam's energy deposition in the gas and increase the initial

The Hydrogen-Fluoride Chemical Laser

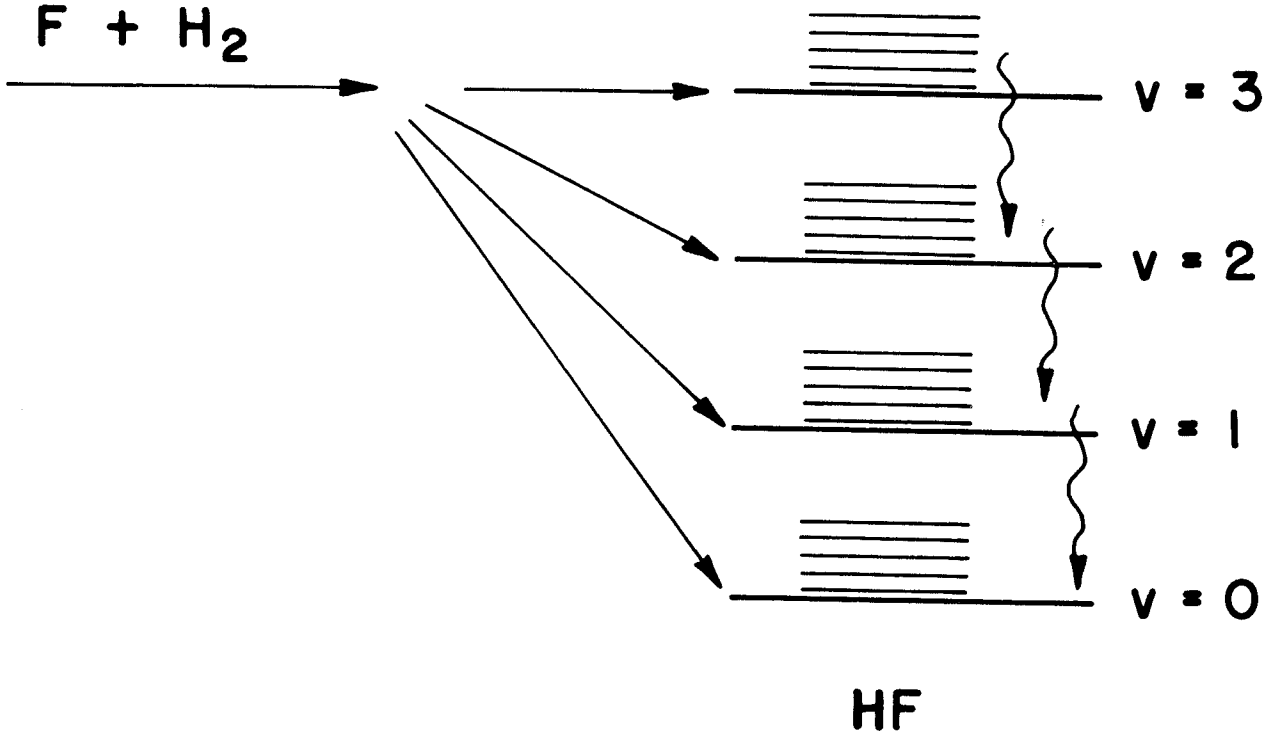

$$H + F_2 \longrightarrow (HF)^* + F$$

$$F + H_2 \longrightarrow (HF)^* + H$$

LASES AT ~2.7-3.0 μm

Fig. VII-B-2

atomic flourine concentration,[13] and sometimes a diluent such as He, Ar, or N_2. Other systems using SF_6 instead of F_2 may also be used. This would have the disadvantages of lower electrical efficiency and probably higher costs, but a higher chemical efficiency would make the net efficiency about the same and the difficulties of gas handling would be greatly reduced.

The general characteristics of the HF laser are shown in Table VII-B-2. The performance to date has been most impressive as far as total energy out at 4 kJ but the pulse width was rather long, being 26 nsec.[14]

VII-B-7. Advantages of the HF Laser

The primary advantage of the HF laser is the very large energies that can be extracted. The second primary advantage is the relatively high efficiency of the system. The electrical efficiency should be at least 10%[15] for SF_6 and C_2H_6 mixtures, and probably about 100% for H_2 and F_2 mixtures,[16,17] while the chemical efficiency should be about 35% and 10% for the SF_6 and F_2 mixtures respectively. Thus, the total efficiency is quite reasonable. However, the cost of regeneration of the gases will reduce the net efficiency to about 3-5%. The high electrical efficiency is also advantageous from the standpoint of relaxing the requirements on the power supplies.

VII-B-8. Disadvantages of the HF Laser

The wavelength of HF at 2.7-3.0 μm is not ideal but it is still in the range of iodine and because of the high efficiency there is the possibility of up conversion. The major difficulties with HF are its high gain and the fast relaxation of the lasing levels. The high gain means that there will be problems with prepulsing which can destroy the pellet before the main pulse arrives, and parasitic oscillations which reduce the energy available to the

Table VII-B-2

Properties of the HF Laser

Wavelength	~2.7 - 3.0 μm
Small Signal Gain	0.1 - 1.0 cm^{-1}
Stimulated Emission Cross Section	$4.4 \times 10^{-7}/\Delta\nu$ cm^2
	~2.5×10^{-17} at 1 atm HF
Pulse Width	26 nsec (~1 nsec)
Extractable Energy	150 - 185 J/l
Efficiency (Electrical)	~100%
Efficiency (Chemical)	10-15%

main pulse. The fast relaxation means that HF is not a storage medium - one must extract the energy as it is generated. Thus, one loses a primary advantage of lasers, their pulse compressing ability. Because of this, the pulse lengths of HF tend to be of the order of the pumping rate which is coupled to both the pressure and electron-beam pulse lengths. With state-of-the-art systems this results in unacceptably long pulses.

A final problem is the need for safe and controlled handling of multi-atmospheres of H_2 and F_2. Of particular difficulty will be the rapid mixing and burning that will be required for the high repetition rates necessary.

VII-B-9. Possible Improvements

The problem of HF not being a storage medium can be effectively eliminated if the rate of reaction can be increased enough that the instantaneous energy available is sufficient to meet fusion requirements. There are two ways of increasing the reaction rate. The first is to increase the pressure which increases both the rate of reaction and the total energy available. Calculations by Jensen[17] indicate that by increasing the pressure to 13 atm. of F_2 and 3 atm. of H_2 that a power level of 1 TW/liter can be achieved with state-of-the-art electron beams. Of course, handling such high-pressure mixtures would be extremely difficult. The second approach is to increase the rate of production of atomic fluorine. This could be done by decreasing the time interval over which the electron beam energy is dumped into the gas and by using additives such as SF_6 which improve fluorine production. However, at best the burn time will still be a few nanoseconds long.

Since such high powers can apparently be extracted without energy storage, it has been suggested that prepulsing can be eliminated by running an off

target beam through the amplifier until the primary beam arrives.[18] Since no energy is stored, no energy is lost to the amplified beams. Such a scheme has been demonstrated at low energies.[18] It was found that problems of parasitics can be eliminated if a beam is extracted during the entire pumping time and if this beam fills the entire amplifier volume. A 4 nsec beam has been successfully switched from a 30 nsec pulse by changing the plane of polarization of the incoming beam by 90° for 4 nsec and passing the outgoing, amplified beam through a dielectric set at the Brewster angle so that the original beam was passed but the 4 nsec pulse was reflected. It has yet to be demonstrated that this method will work effectively at the much higher energies required. Even if successful, this method will decrease the net efficiency as much of the energy is wasted. An alternative is to successively pass several short, smaller beams in varying directions through different regions of the amplifier (see Fig. VII-B-3). It is thought that a sufficient amount of the amplifier volume will be filled with each beam to suppress parasitics. In such a manner, much more usuable energy could be extracted in several short pulses.

Recent experiments at Sandia Laboratories have shown that energy can be effectively extracted from a high energy HF amplifier.[19] In these experiments 200J were extracted from a one stage amplifier in a 20 nsec pulse. Thus, the problems associated with a high gain system do not appear insurmountable. Currently, experiments are being conducted to determine the beam quality that can be obtained from the HF amplifier.

It should be pointed out that since the pulse width of HF is related to the reaction rate,[14] increasing the pressure not only increases the total power but also decreases the pulse width. However, to efficiently take advantage of this the electron beam pulse widths must be reduced to the

same time scale which implies 1 to 5 nsec electron beam pulses, which may not be practical. This, coupled with the development of short pulse, multiline oscillators, could yield pulses at least as short as 5 nsec.

Two other suggestions have been made which should be mentioned.[20] The first is to utilize a traveling wave excitation scheme in which instead of exciting the entire volume of the amplifier simultaneously, one excites only a small portion of the volume, sweeping this excitation pulse along in front of the beam to be amplified. In this manner, one does not allow time for the parasitics to build up or relaxation to occur. The second idea is to suppress oscillation on $\Delta v = 1$ transitions and force oscillations on the $\Delta v = 2$ transitions, as has been observed in DF.[21] This would accomplish two things. First, it would effectively double the frequency and secondly, it would reduce the gain since $\Delta v = 2$ transitions have smaller stimulated emission coefficients. Thus, it would help to alleviate a couple of the problems associated with HF.

Finally, to help minimize the effects of the regeneration of HF into H_2 and F_2, it has been suggested that the heat generated by the chemical reaction be used to generate electricity.[17] This could substantially reduce the net energy cost of the electrolysis of the HF. Utilizing such a scheme, Jensen[17] has claimed a net efficiency of approximately 8% could be obtained for a large optimized system.

VII-B-10. Summary of the HF Laser

To summarize, the HF chemical laser has several serious problems in view of the requirements of laser fusion. How successful any of the proposed

MULTIBEAM EXTRACTION FOR HF AMPLIFIER

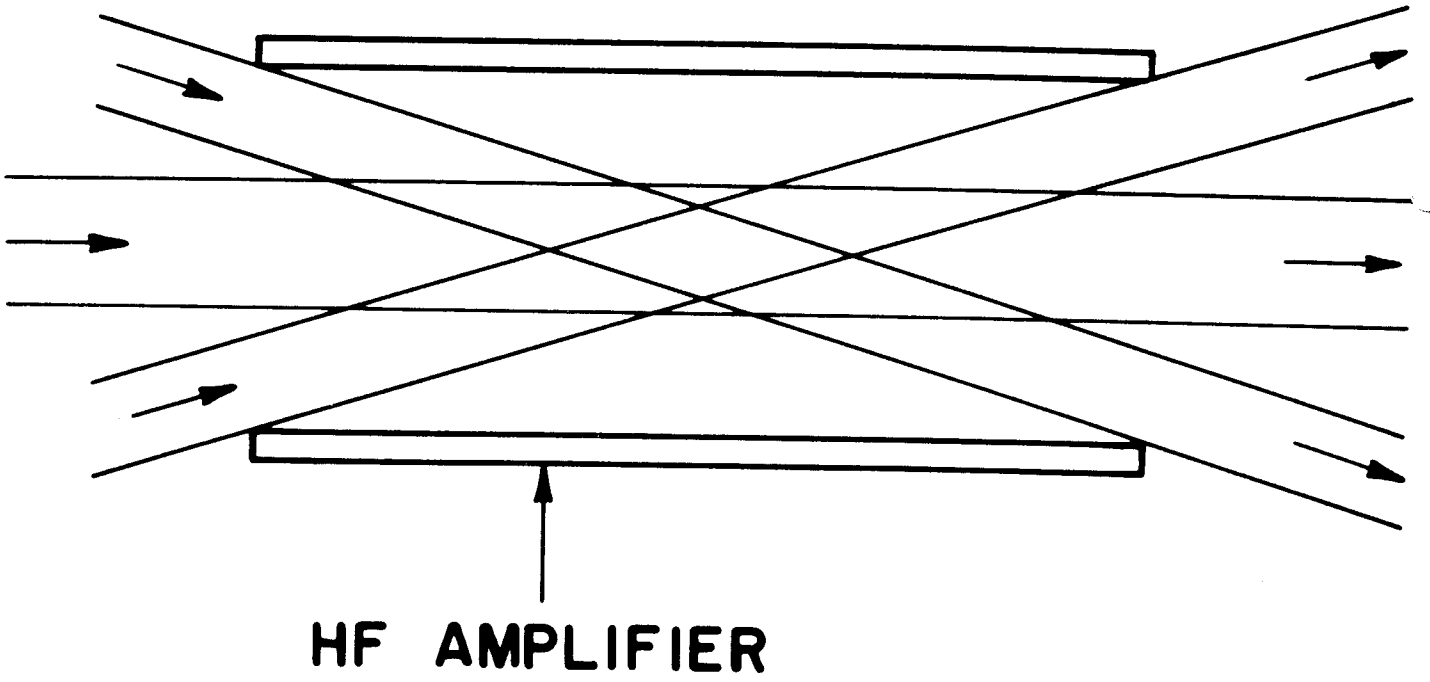

Fig. VII-B-3

solutions will be remains to be seen. However, given that it has a high potential efficiency and a wavelength that is not too unreasonable, it would seem that a search for solutions would certainly be worthwhile. The possible 100% electrical efficiency would also greatly relax the requirements on the power supplies as compared to a 10% efficient system. Thus, even in light of its difficulties, the HF laser is an attractive system to consider for laser fusion applications.

VII-B-11. The CO_2 Laser

Unlike either the iodine or HF lasers, the CO_2 laser is not a chemical laser but is pumped directly by electron impact or by vibrational excitation transfer from excited nitrogen molecules. A simplified potential energy diagram of the CO_2 system is shown in Fig. VII-B-4. Lasing generally occurs on the vibrational-rotational transitions between the (001) and (100) levels of CO_2 ($\sim$ 10.6 μm) but can also occur between the (001) and (020) levels ($\sim$ 9.6 μm) which becomes quite important for short pulse extraction.[22] The three numbers identifying the levels refer to the various vibrational modes of the CO_2 molecule. The upper laser level (001) is the first asymmetric stretch mode, while the lower (100) level is the first symmetric stretch mode and the (020) level is the second bending mode.

The CO_2 laser is potentially very efficient having a quantum efficiency of over 40%. Also a substantial percentage of the direct electron impact energy into the CO_2 molecule is eventually channeled into the upper laser level.

The CO_2 Laser

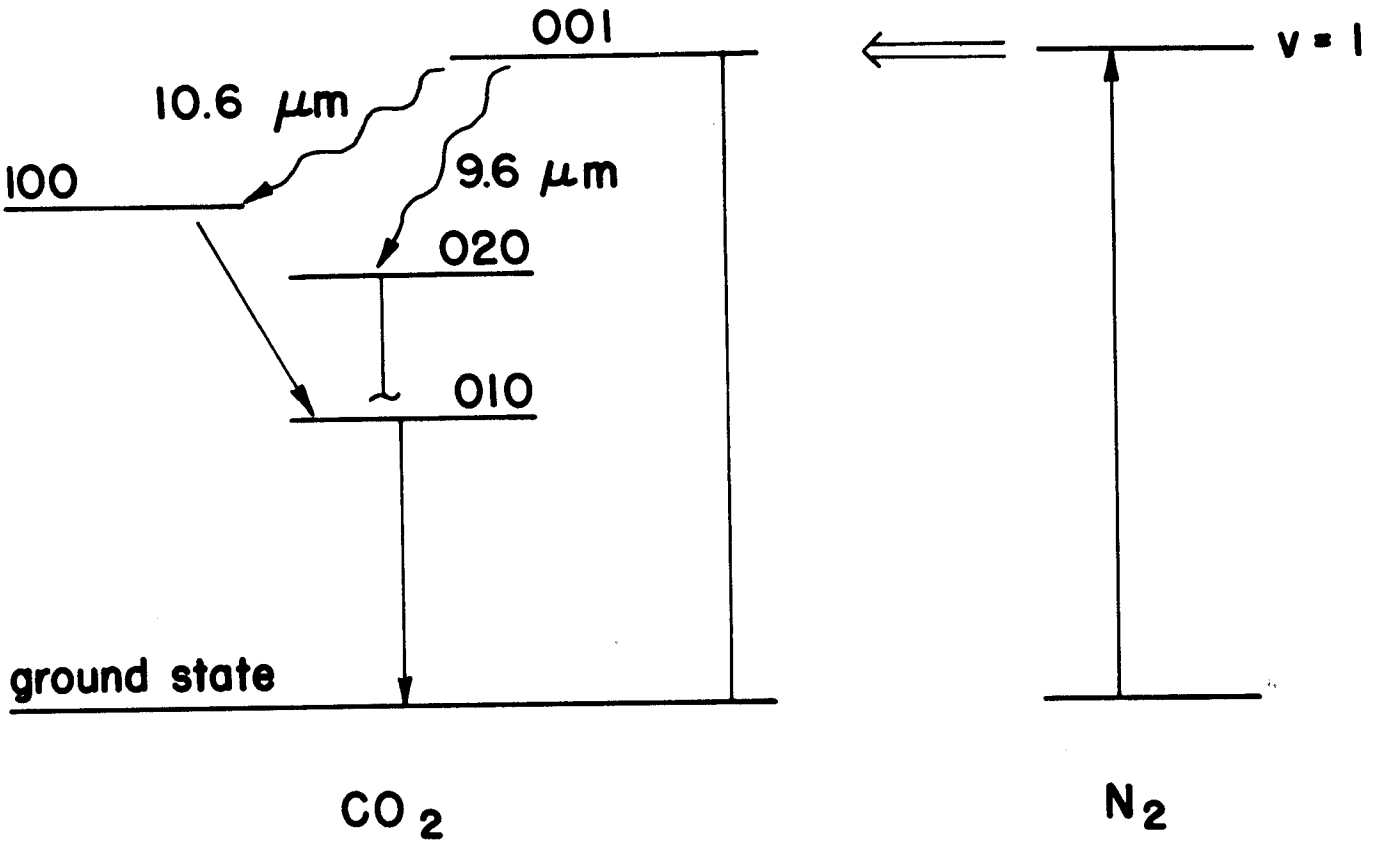

$$CO_2 + e \longrightarrow CO_2^{*} + e$$

$$CO_2 + N_2^{*} \longrightarrow CO_2^{*} + N_2$$

$$\downarrow$$

LASES AT 10.6, 9.6 μm

Fig. VII-B-4

In addition, much of the energy going into the N_2 is channeled into its first vibrational state which is rapidly transferred directly to the CO_2's upper laser level. As a result, overall efficiencies of about 30% can be obtained. Unfortunately, in the nanosecond time scales required, all the advantageous collisional processes become insignificant - the short pulse will interact only with those rotational levels which are directly connected to transitions in the incoming pulse. This greatly reduces the efficiency of the CO_2 laser. In order to obtain the maximum energy available, one must amplify as many rotational transitions as possible on both the 10.4 and 9.4 μm bands. Even this will limit the efficiency to about 2-5% unless one can successfully develop multipass amplifiers.

The general characteristics of the CO_2 laser are given in Table VII-B-3. The performance to date for CO_2 is ~600 J in 1.4 nsec.[23]

VII-B-12. Advantages of the CO_2 Laser

The most fundamental advantage of CO_2 is that it is capable of high energy output in relatively short pulses (.25-1 nsec). Also, the efficiency at 2-5% is not too unreasonable. Finally, it is a very well characterized system and relatively simple in design (as compared to handling high-pressure HF for example).

VII-B-13. Disadvantages of the CO_2 Laser

The principal disadvantage of the CO_2 laser appears to be its wavelength. Just how serious this is has not been fully determined. Another problem is a gain which is higher than desirable which leads to problems of parasitic oscillations, prepulsing, and isolation of the amplifiers.

TABLE VII-B-3

PROPERTIES OF THE CO_2 LASER

Wavelength	10.6 μm, 9.6 μm
Small Signal Gain	0.05 cm^{-1}
Stimulated Emission cross section (single line)	$\frac{1.5 \times 10^{-18}}{P(atm)}$ cm^2
Pulse Width	0.25 - 1 nsec
Extractable Energy	5 J/l
Efficiency	~ 2 - 5%

VII-B-14. Possible Improvements

If shorter wavelengths prove to be essential, the CO_2 laser's potential will be greatly reduced since up conversion to even 2.5 μm would be very costly in terms of the net efficiency of the system.

The pulsed CO_2 laser efficiency is low because energy is stored in collisionally-coupled levels and not available during a nanosecond pulse. This suggests that if one makes not just one but several successive passes through the amplifier that the efficiency could be significantly increased provided that there is sufficient time between passes to collisionally repopulate the upper laser level.[24] In such a scheme one would take advantage of the favorable collisional processes in CO_2 to increase the efficiency while still extracting the energy in nanosecond pulses.

The problem of high gain can be solved in part by developing better isolating components. Also calculations indicate that there is an inherent buildup time for parasitic oscillations of about 1/2 μsec.[25] Therefore, if pumping can be accomplished in less than this time, the effects of parasitics can be minimized. Calculations also indicate that 95% of maximum gain can be reached by discharge pumping[25] in the 1/2 μsec allowed.

A second approach to alleviating the gain problem is to eliminate He from the laser mix. It has been found that more energy can be extracted for a given gain and energy input in a heliumless mixture

than with the usual laser mix.[23] By doing this one not only reduces the gain problem but increases the efficiency. Unfortunately, much higher voltages are required for a heliumless mixture putting an added burden on the power supplies although for a given energy input the current requirements would be greatly reduced.

VII-B-15. Summary of the CO_2 Laser

The CO_2 laser appears to be an attractive system with apparently no insurmountable problems in scaling to the required power levels. Also the efficiency, while not ideal, is not too unreasonable. The main question is whether 10.6 μm will prove too long to effectively couple energy into the targets.

VII-B-16. Brand X Lasers

As can be easily concluded from the above, no known laser is ideal for laser fusion, particularly if wavelengths in the range of 3000-6000 Å prove to be essential. Therefore, a major search continues for the brand X laser.

Much effort has concentrated on atomic oxygen and the other group VI elements, sulfur, selenium and tellurium and elements with similar properties to these, nitrogen, carbon, lead and tin. These elements are characterized by having low lying electronic transitions which have small stimulated emission cross sections and relatively long lifetimes.[26] The fact that these states lie close to the ground state means that the quantum efficiencies are quite reasonable. Also since all the energy is stored in a single state, this energy can be readily extracted in short pulses. As an example, a

potential energy diagram of oxygen is shown in Fig. VII-B-5 and its characteristics are listed in Table VII-B-4. Such characteristics make these systems near ideal candidates for laser fusion lasers.

To date, atomic oxygen itself has not been observed to lase. However, the rare-gas oxides ArO, KrO and XeO have lased.[27,28] The oxides have the disadvantages of greatly reduced lifetimes ($\sim 10^{-6}$ sec) as compared to atomic oxygen itself ($\sim$ 1 sec) and reduced beam quality due to the high pressures required. Electron beams were used to excite mixtures of either O_2 or N_2O and the rare gas. The exact pumping mechanism is still in question. It has also been proposed that the atomic oxygen be pumped by the photodissociation of N_2O by Kr_2^* or Ar_2^* superfluorescence.[29] This is advantageous since there is near unity probability of dissociating $O(^1S_o)$ state atoms from N_2O for wavelengths of approximately 1250-1400 $\mathring{A}$. Gain has been observed using this method[30] with Ar fluorescence.

The main problem with oxygen appears to be the difficulty in developing an efficiently pumped system. The lack of a detailed understanding of the system makes it difficult to predict whether an efficient pumping scheme can be found. However, it is thought that efficiencies of 1 or 2% may be realistically obtainable.

Another group of lasers that have received great attention are the various excimer systems. Such systems have great potential and are extremely attractive for several reasons. First, the efficiencies by which the upper states are formed can be very high (as much as 30-50% of the energy

The Oxygen System

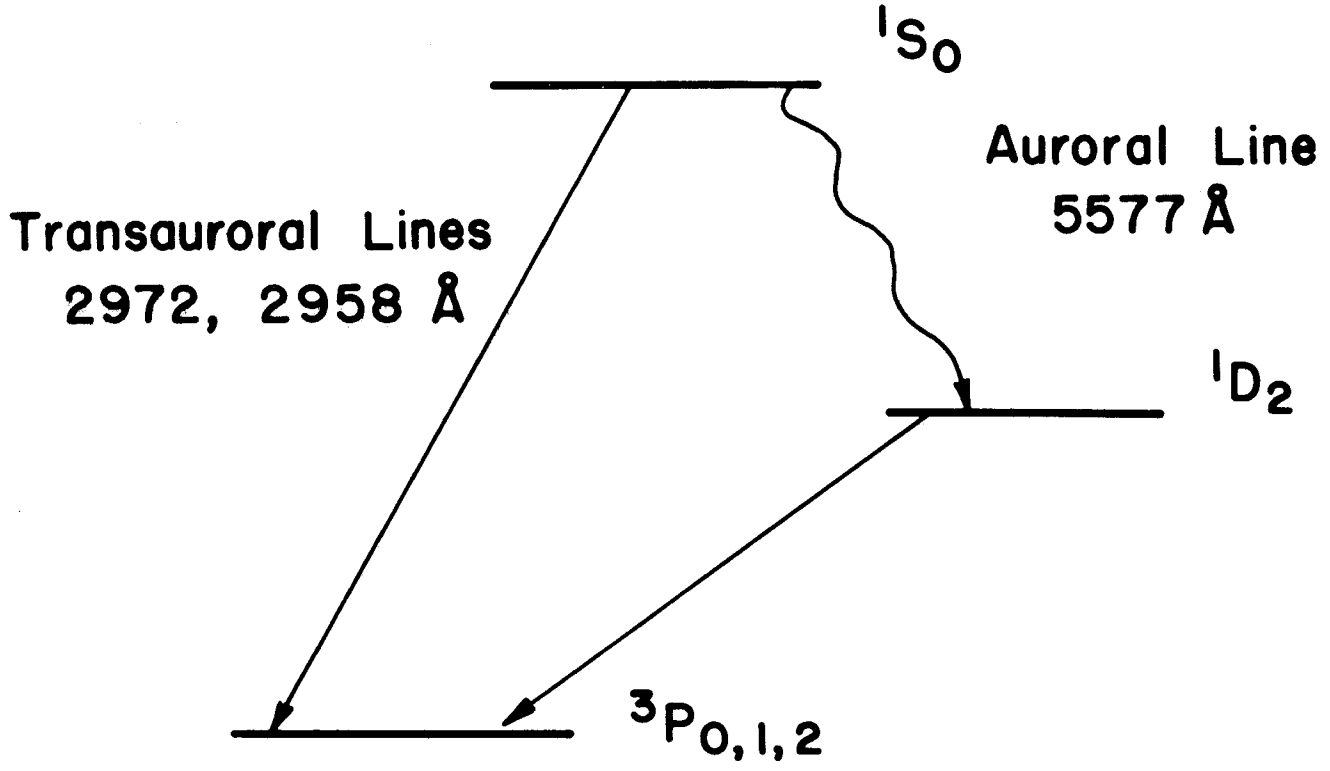

$$XO + \Delta E \longrightarrow X + O^*$$

$$O^* \downarrow$$

LASES AT 5577 Å

Fig. VII-B-5

TABLE VII-B-4

PROPERTIES OF ATOMIC OXYGEN

Wavelength	5577 Å
Small Signal Gain	0.005 cm^{-1}
Stimulated Emission cross section	8.7×10^{-20} cm^2
Extractable Energy	5 J/l

PROPERTIES OF THE RARE-GAS OXIDES

	ArO	KrO	XeO
Wavelength (Å)	5576	5578	5300-5500
Stimulated Emission cross section (cm^2)	$\frac{3 \times 10^{-21}}{P(atm)}$	$\frac{1 \times 10^{-20}}{P(atm)}$	$\frac{2.9 \times 10^{-19}}{P(atm)}$

Schematic of a Typical Excimer System

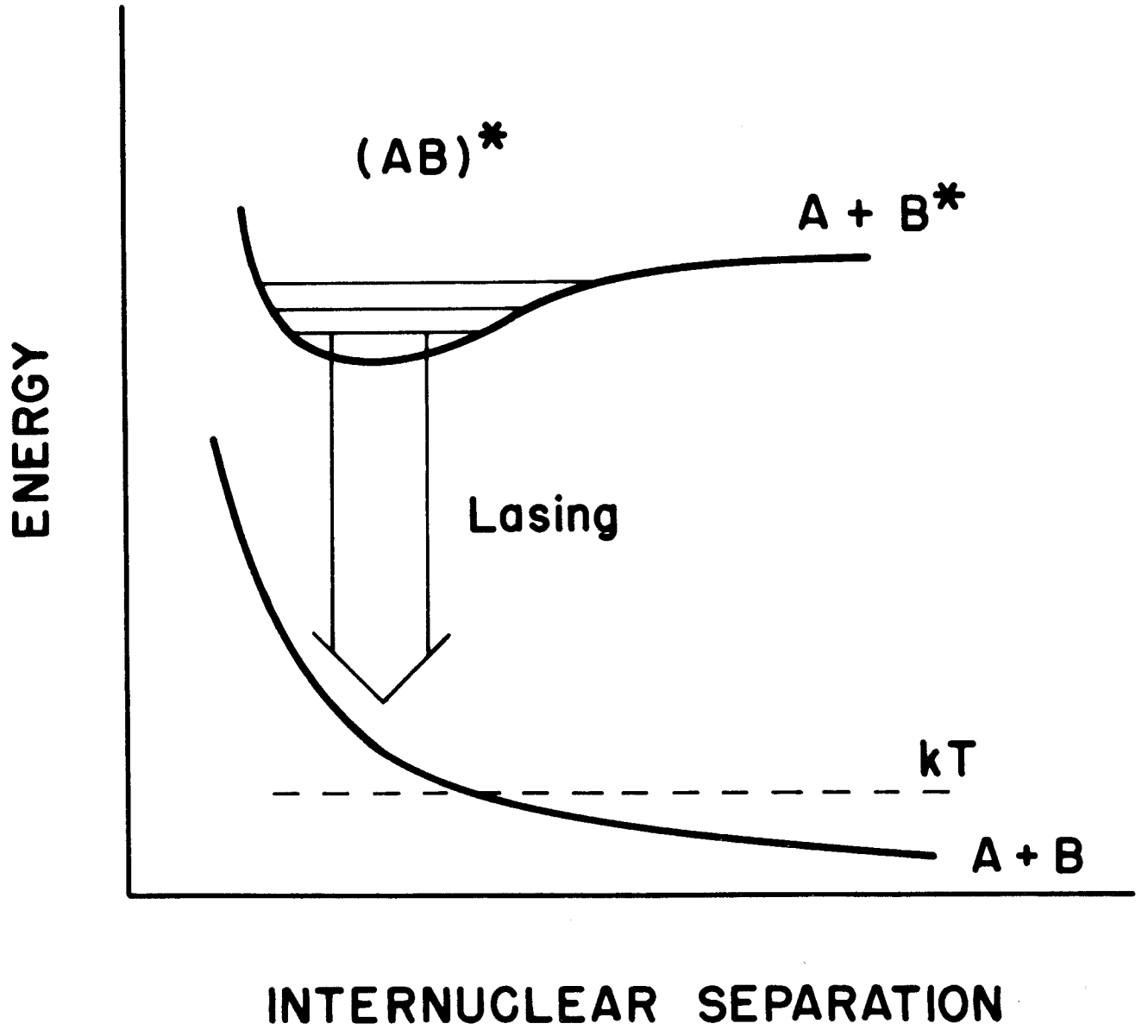

Fig. VII-B-6

deposited in the gas is transferred to the excited state). Secondly, excimers of interest exist only in the excited states, having dissociative ground states. Thus, essentially all the energy in the upper states can be extracted. Thirdly, due to the dissociative ground states (see Fig. VII-B-6) the excimers lase over a continium, resulting in broad bandwidths which allows very short pulse extraction.

Several excimer lasers have been developed. The Kr_2*, Xe_2*, KrF*, and ArF* lasers are all potentially efficient, high-power systems. However, their wavelengths are much too short and would cause severe two-photon damage to optical components and in addition there is a lack of efficient reflectors at these wavelengths. The XeF* laser's wavelength at 3540 Å is more reasonable but this laser suffers from a bound ground state. A number of metal vapor-rare gas excimers have been proposed but none have been proven and many suffer from strong self absorption. The search continues, however, with work being done on systems such as Hg_2* and HgCd*.

As an alternative to finding new, more suitable excimer lasers, there is the possibility of converting the rare gas-halide laser's near uv wavelengths to the more usable optical wavelengths. This has been demonstrated for the XeF laser.[31] In this experiment the lasers 351 nm radiation was converted by Raman scattering from a Ba vapor to 585 nm. The efficiency was quite high as nearly unit-photon conversion from 351 to

585 nm was found. Similar schemes for other uv lasers should be readily found. If such a method proves scalable, these excimer lasers would become very attractive candidates for laser fusion.

Another system that has been proposed is a gaseous phase neodymium or other rare earth laser. If successful, this would eliminate the problems associated with the glass such as heat removal, but if the laser were still flash pumped, the efficiency would probably not be greatly improved.

A laser candidate that has recently been reported is the S_2 laser.[32] It is attractive because it lases on several vibrational-rotational transitions with wavelengths ranging from 365 to 570 nm and is also thought to be scalable. However, it has at least two disadvantages. One is that the upper laser lifetimes are very short (~ 20 nsec) which will require very short pumping times. The other disadvantage is that it must be operated at elevated temperatures (~ 500°C) which increases the complication and operating costs of the laser.

Another interesting class of lasers, the mercury-mono-halides, has also been recently discovered.[33,34] Two have been reported to date: HgCl and HgBr. (It is possible that HgI may also lase). These are of particular interest because HgCl lases at 5576 Å and HgBr at 5018 Å; and they appear scalable. Lasing was obtained by electron-beam excitation of high-pressure mixtures of Ar and Xe containing low partial pressures of Hg and either CCl_4 or HBr. The detailed kinetics of the formation of excited HgCl and HgBr are not fully understood. The measured efficiency

of converting the electron-beam's energy that is deposited in the gas to optical energy was about 0.5% for HgCl and 0.25% for HgBr. Neither system was optimized so that higher efficiencies would be expected in the future. It may also be possible to discharge pump these lasers which could substantially improve their efficiencies.[33,34] The disadvantages of these systems are that the upper state lifetimes (~ 20 nsec) are much shorter and the stimulated emission cross sections (~ 10^{-16} cm^2) much larger than desirable for laser fusion applications. Also, analogous to the S_2 laser, the cavity must be heated to increase the mercury's vapor pressure to useful levels.

VII-C. A Summary of the Laser Survey

To summarize, there is no laser candidate that obviously will meet the ideal requirements for laser fusion. The group VI lasers appear to have great potential but it has not been demonstrated that they can be pumped efficiently. Although no ideal laser candidate exists, there are lasers such as CO_2 and iodine that appear to be scalable to minimum energy (~ 1 MJ), power (~ 1000 TW), and pulse width (~ 1 nsec) requirements. It should be clear, however, that the development of all potential systems that have been discussed as well as the search for new lasers must continue if a suitable laser is to be found.

Another conclusion that can be drawn from this survey is that there are more laser candidates with potential efficiencies of 1 or 2% than with potential efficiencies greater than 2%. Thus, if a plant can be designed that can operate economically with a 1 or 2% efficient laser, the number of potential laser candidates greatly increases so that the probability of finding a suitable laser should also increase.

A similar situation exists with respect to the required wavelength: the broader the range of allowable wavelengths, the greater the probability of finding a suitable laser. However, unlike efficiency, the wavelength of a given laser can in general be converted to a more suitable wavelength but this process will usually decrease the net efficiency significantly. Thus, it is preferable to have as broad of a range of allowable wavelengths as possible as opposed to relying on frequency conversion to maximize the probability of finding a suitable laser for laser fusion.

VII-D. Design Study System

As stated above, there is no known or proposed system which obviously will meet the requirements for laser fusion. Which laser will prove

optimum will depend much upon the ultimate wavelength, efficiency, and power requirements imposed by the physics of the laser pellet interaction as well as developments in the lasers themselves. Thus, choosing the "right" specific laser for our design at this time is virtually impossible, the choice thus becoming somewhat arbitrary. In light of this, we have chosen the CO_2 laser for our design. This is not to be construed as an endorsement for CO_2, but rather as a way to give a concrete basis to a generic design. It was felt that in order to meet the basic requirements for a laser fusion laser (a flowing gas system, 1 MJ total energy out, and energy densities dictated by the optics and not the laser medium) that the ultimate laser's electrical, mechanical and optical parameters will not be dramatically different from those of the CO_2 design. Of course, each laser will have its own particular requirements for such things as optical components, possible chemical reprocessing and flash as opposed to discharge pumping which will not be specifically considered in our design. However, the total design should be quite similar and specific modifications readily made. (For example, flash pumped systems such as I*, O*, or Nd^{+3} will likely use electron-beam generated fluorescence to improve efficiencies and, thus, utilize the electron beam technology developed for CO_2). Thus, the CO_2 laser, which is relatively simple in operation, well characterized and apparently scalable, should provide a good basic design for the laser system of our laser fusion reactor.

References for Section VII

1. W. Krupke and C. Rhodes, "Ideal Laser Characteristics for Fusion," LLL Laser Program Annual Report (1974), 446-447 (UCRL-50021-74).

2. J. Wilson and D. O. Ham, "Specifications for a Fusion Laser," Laser Focus, 12, no. 11, 38-41 (1976).

3. J. V. V. Kasper and G. C. Pimentel, "Atomic Iodine Photodissociation Laser," Appl. Phy. Lett. 5, 231-233 (1964).

4. C. C. Davis, R. J. Pirkle, R. A. McFarlane, and G. J. Wolga, "Output Mode Spectra, Comparative Parametric Operation, Quenching, Photolytic Reversibility, and Short Pulse Generation in Atomic Iodine Photodissociation Lasers," IEEE J. Quantum Electron, QE-12, 334-352 (1976).

5. R. W. F. Gross, "High Power Iodine Lasers for Laser Fusion," in Laser Induced Fusion and X-ray Laser Studies, ed. S. F. Jacobs, M. O. Scully, M. Sargent III and C. D. Caatrell III (Addison-Wesley Pub. Co., Pon Mills, Ontario, 1976), Chap. 7, 311-368.

6. G. Brederlow, K. J. Witte, E. Fill, K. Hohla and R. Volk, "The Astrix III Pulsed High-Power Iodine Laser," IEEE J. Quantum Electron, QE-12, 152-155 (1976).

7. Laser Focus, 12, no. 12, 4 (1976).

8. J. C. Swingle, C. E. Turner, Jr., J. R. Murray, E. V. George and W. F. Krupke, "Photolytic Pumping of the Iodine Laser by XeBr*," Appl. Phys. Lett. 28, 387-388 (1976).

9. George A. Fisk, "The Effects of Chemical Kinetics and Starting Material Regeneration on the Efficiency of an Iodine Laser Amplifier," SAND 77-0880, Sandia Laboratories (1977).

10. L. D. Pleasance and L. A. Weaver, "Laser Emission at 1.32 μm From Atomic Iodine Produced by Electrical Dissociation of CF331," Appl. Phys. Lett. 27, 407-409 (1975).

11. G. Emanuel, N. Cohen and T. A. Jacobs, "Theoretical Performance of an HF Chemical CW Laser," J. Quant. Spectrose Radiation Transfer, 13, 1365-1393 (1973).

12. F. K. Truby, "Stability of Multi-atmosphere H_2-F_2-O_2 Mixtures for HF Laser Studies," Appl. Phys. Lett. 29, 247-249 (1976).

13. R. A. Gerber, E. L. Patterson, L. S. Blari and N. R. Greiner, "Multi-kilojoule HF Laser Using Intense-Electron-Beam Initiation of H_2-F_2 Mixtures," Appl. Phys. Lett. 25, 281-283 (1974).

14. Laser Focus, 12, no. 6, 24-28 (1975).

15. E. L. Patterson and R. A. Gerber, "Characteristics of a High-Energy Hydrogen Fluoride (HF) Laser Initiated by an Intense Electron Beam," IEEE J. Quantum Electron, QE-11, 642-647 (1975).

16. J. A. Mangano, R. L. Limpaecher, J. D. Dougherty and F. Russell, "Efficient Electrical Initiation of an HF Chemical Laser," Appl. Phys. Lett. 27, 293-295 (1975).

17. R. J. Jensen, "HF Chemical Lasers," in Progress in Lasers and Laser Fusion, ed. A. Perlmutter and S. M. Wildmayer (Plenum Press, New York, 1975), p. 53-70.

18. R. W. Getzinger, N. R. Greiner, K. D. Ware, J. P. Carpenter, and R. G. Wenzel, "Controlled Energy Extraction and Sharp Nanosecond Pulses From an HF Amplifier," IEEE J. Quantum Electron, QE-12, 556-558 (1976).

19. J. B. Gerardo, private communcation.

20. K. L. Kompa, "High Power Chemical Lasers: Problems and Perspectives," in Laser Interaction and Related Phenomena, ed. H. J. Schwarz and H. Hora (Plenum Press, New York, 1974), p. 115-132.

21. S. N. Sucherd and G. C. Pimentel, "Deuterium Fluoride Vibrational Overtone Chemical Laser," Appl. Phys. Lett. 18, 530-531 (1971).

22. B. J. Feldman, "Short-Pulse Multi-line and Multi-band Energy Extraction in High-Pressure CO_2-Laser Amplifiers," IEEE J. Quantum Electron, QE-9, 1070-1078 (1973).

23. F. Skoberne, Laser Fusion Program Progress Report (LA-6245-PR), July 1976, p. 11.

24. W. T. Leland and Mary Kircher, "The Relation of CO_2 Discharge Kinetics to the Efficiency of Short Pulse Amplifiers," LA-UR 74-637, Los Alamos Scientific Laboratory (1973).

25. L. J. Denes, L. H. Taylor, L. E. Kline, R. J. Spreadburg and R. V. Babcock, "Pumping Characteristics of Multi-atmosphere CO_2 Amplifiers," 29th Annual Gaseous Electronics Conference, Cleveland, Ohio, 1976.

26. J. E. Murray, "Group VI Elements as Potential High-Energy Visible-Laser Sources," LLL, Laser Program Annual Report (1974), 448-450 (UCRL-50021-74).

27. H. T. Powell, J. R. Murray and C. K. Rhodes, "Laser Oscillation on the Green Bands of XeO and KrO," Appl. Phys. Lett. 12, 730-732 (1974).

28. H. T. Powell, "Rare Gas-Oxygen Excimer Lasers," LLL, Laser Program Annual Report (1974), 451-456 (UCRL-50021-74).

29. J. R. Murray and C. K. Rhodes, "The Possibility of a High-Energy-Storage Visible Laser on the Anroral Line of Oxygen," LLL Report UCRL-51455 (1973).

30. W. M. Hughes, N. T. Olson and R. Hunter, "Experiments on 558 nm Argon Oxide Laser System," Appl. Phys. Lett. 28, 81-83 (1976).

31. N. Djeu and R. Burnham, "Efficient Raman Conversion of XeF Laser Output in Ba Vapor," Appl. Phys. Lett. 30, 473-475 (1977).

32. Stephen R. Leone and Kenneth G. Kosnik, "A Tunable Visible and Ultraviolet Laser on $S_2(B^3\Sigma_u^- - X^3\Sigma_g^-)$", 30, 346-348 (1977).

33. J. H. Parks, "Laser Action on the $B^2\Sigma_{1/2}^+ \rightarrow X^2\Sigma_{1/2}^+$ Band of the HgCl at 5576 Å," Appl. Phys. Lett. 31, 192-194 (1977).

34. J. H. Parks, "Laser Action on the $B^2\Sigma_{1/2}^+ \rightarrow X^2\Sigma_{1/2}^+$ Band of HgBr at 5018 Å," Appl. Phys. Lett. 31, 297-300 (1977).

SOLASE

A CONCEPTUAL LASER FUSION REACTOR DESIGN

R.W. Conn
S.I. Abdel-Khalik
G.A. Moses
F. Beranek
E.T. Cheng
G.W. Cooper
R.B. Droll
T. Henderson*
J. Howard
T.O. Hunter
E.M. Larsen
G.L. Kulcinski
E.G. Lovell
G.R. Magelssen
C.W. Maynard
K.R. Okula
M. Ortman
M.M.H. Ragheb
W.B. Rensel*
D. Solomon*
R.L. Spencer
I.N. Sviatoslavsky
W.F. Vogelsang
R.D. Watson
W.G. Wolfer

UWFDM-220

VOLUME II

Fusion Research Program
Nuclear Engineering Department
The University of Wisconsin
Madison, Wisconsin 53706

December 1977

*KMS Fusion Inc., Ann Arbor, Michigan

"LEGAL NOTICE"

"This work was prepared by the University of Wisconsin as an account of work sponsored by the Electric Power Research Institute, Inc. ("EPRI"). Neither EPRI, members of EPRI, the University of Wisconsin, nor any person acting on behalf of either:

"a. Makes any warranty or representation, express or implied, with respect to the accuracy, completeness, or usefulness of the information contained in this report, or that the use of any information, apparatus, method, or process disclosed in this report may not infringe privately owned rights; or

"b. Assumes any liabilities with respect to the use of, or for damages resulting from the use of, any information, apparatus, method or process disclosed in this report."

Acknowledgment

Any effort as substantial as a conceptual fusion reactor design inevitably involves more people than those who appear on the title page. It is a pleasure to acknowledge the Electric Power Research Institute for its financial support of this research under contract RF-237-3. Dr. Noel Amherd of EPRI monitored this work and his efforts in organizing review meetings so that we could receive early feedback from others in the field is greatly appreciated. We also appreciate the encouragement of our University which contributed to this work both financially and by providing an environment supportive of research. This is of course a long standing tradition at Madison but it is important to note that this tradition remains in a healthy state.

Finally, we gratefully acknowledge the help of our secretarial staff -- Mrs. Connie Linehan, Ms. Gail Herrington, Mrs. Bonnie Smart, and Mrs. Linda Kraft -- and our support staff, particularly Mr. Dennis Bruggink -- who together were responsible for the typing, reproduction, and distribution of this report.

Preface

Inertial confinement fusion is a rapidly growing part of the search to achieve commercial power applications from the fusion process. Experiments are planned over the next five years with enough energy and power on target to determine if the targets designed can produce the gains required for reactor applications. With this perspective, it is auspicious to consider the technological aspects of ICF reactors. We have found that a conceptual reactor study is an ideal way of exploring such a problem and the SOLASE system is the product of such an effort. We hope that the results, analysis, and analytical methods described here will be helpful to others in the field and to those who must make policy regarding a broadly based program aimed at ICF reactor development.

Abstract

The SOLASE conceptual laser fusion reactor has been designed to elucidate the technological problems posed by inertial confinement fusion reactors. This report contains a detailed description of all aspects of the study including the physics of pellet implosion and burn, optics and target illumination, last mirror design, laser system analysis, cavity design, pellet fabrication and delivery, vacuum system requirements, blanket design, thermal hydraulics, tritium analysis, neutronics calculations, radiation effects, stress analysis, shield design, reactor and plant building layout, maintenance procedures, and power cycle design. The reactor is designed as a 1000 MW_e unit for central station electric power generation. This should be typical of central station power plants produced by a mature (rather than a developing) technology. The net plant efficiency is 30% and the recirculating power fraction is 25%. The laser energy on target is 1 MJ and 20 targets are exploded per second, each with a gain of 150. The gas phase laser relies on multipassing to achieve an efficiency of 6.7%. No particular laser wavelength is specified. A buffer gas of neon or xenon is used to prevent particle debris and X-rays from directly impacting the cavity first wall. The reactor cavity is spherical with a radius of 6 m and is constructed of graphite designed to guide the flow of lithium oxide (Li_2O) which serves as both the tritium breeding and heat transport medium. The neutron wall loading is 5 MW/m^2 and the tritium breeding ratio is 1.33. The overall radioactivity levels of the blanket are very low and the activity at 50 years after shutdown is just 3 Ci. The target is illuminated from two sides by 12 beams, 6 on each side, and the last mirrors are copper diamond turned on an aluminum backstructure. The mirrors are cooled to 50°C to minimize neutron radiation effects. The reactor system itself is highly accessible and a detailed but relatively simple procedure is outlined for blanket replacement. The 16 blanket segments making up the sphere are so inexpensive that replacement rather than maintenance of the blanket modules has been the design philosophy.

The major technological conclusions developed from this study include the following: 1. An energy gain on target of 100-200 or higher is difficult to achieve with a 1 MJ laser. High gain targets have been reported and their performance must be verified by experiment. 2. A laser driver with an efficiency of about 5% and matching all other requirements including those of the pellet must be developed. The requirement is that the product of laser efficiency and pellet gain, $\eta_L G$, exceed about 10. However values of η_L less than 1-2% will imply high laser costs because of power supplies regardless of target gain. 3. Power supplies and switches with lifetimes of 10^8-10^9 shots are needed. 4. A basic manufacturing procedure is needed for the mass production of targets. 5. Target delivery can be by pneumatic guns but accuracy, trajectory determination, and coordination with the laser firing is required. 6. Automatic methods for maintaining alignment in the entire optical train will be necessary. 7. The gas protection method is an attractive approach to cavity design that can be verified in principle on current and near term experiments. 8. Permeation filling of targets will imply that the tritium inventory will be dominated by the time to fill targets. In SOLASE, the inventory can vary from 10 kg to 25 kg of tritium depending on the encapsulating material. 9. The performance of the graphite blanket design requires verification and data is needed on radiation effects at temperatures above 1400°C. 10. The design and protection of the last mirror poses no insuperable problems unless dielectric coatings (required if

$\lambda_L \lesssim 8000$ Å) are used. Color center formation at low neutron fluences can so increase light absorption that visible lasers may not be usable. Much more work is required here. 11. Vacuum requirements are modest if set by wall erosion. 12. An unprotected dry wall cavity designed with conventional structural metals will not survive a microexplosion at economically reasonable wall loadings (neutron wall loading greater than 1 MW/m^2). 13. The blanket tritium inventory using Li_2O can be low ($\sim$ 1 kg) and tritium release rates through the steam generators and reheaters is low enough that no intermediate loop in the power cycle appears necessary. 14. Accessibility of the reactor cavity is very good simplifying blanket maintenance or replacement methods.

The issues outlined here and others discussed in the report are those one would have to pursue vigorously to allow the employment of laser fusion reactors beginning in the early part of the next century. Results from experiments carried out over the next five to seven years with ever increasing energy and power on target, taken together with results from reactor studies such as SOLASE, should provide the basis to determine if an ambitious engineering-oriented program aimed at reactor development is justified.

TABLE OF CONTENTS

	Page
I. Overview of SOLASE	
I-A. Introduction	I-A-1
I-B. Initial Questions	I-B-1
I-C. Description of SOLASE	I-C-1
I-C-1. Pellet performance in SOLASE	I-C-8
I-C-2. Targets for laser fusion	I-C-27
I-C-3. Injection of targets	I-C-33
I-C-4. Optics, target illumination, and mirror mechanical design	I-C-37
I-C-5. The laser system	I-C-43
I-C-6. Laser gas handling,power supplies,beam layout	I-C-51
I-C-7. Reactor cavity & blanket design	I-C-56
I-C-8. Radiation damage	I-C-67
I-C-8-a. Radiation effects to graphite	I-C-67
I-C-8-b. Stress & failure analysis for the blanket-determination of blanket lifetime	I-C-71
I-C-8-c. Radiation effects to dielectric coatings on mirrors	I-C-83
I-C-9. Vacuum system & mechanical design	I-C-94
I-C-10. The fuel cycle & tritium processing	I-C-98
I-C-11. Power flows in SOLASE	I-C-108
References for Chapter I	I-C-115
II. Summary & Conclusions	
II-A. Brief Summary of SOLASE & General Conclusions	II-A-1
II-B. Summaries of Specific Topics & Conclusions by Subject Area	
II-B-1. Laser pellet physics & pellet design	II-B-1
II-B-2. Lasers for laser fusion & for SOLASE	II-B-6
II-B-3. Illumination & optics design	II-B-9
II-B-4. Pellets for laser fusion reactor applications	II-B-11
II-B-5. Cavity design & first wall protection	II-B-13
II-B-6. Blanket design	II-B-16
II-B-7. Radiation effects to materials	II-B-17
II-B-7-a. The blanket	II-B-17
II-B-7-b. The lithium oxide	II-B-19
II-B-7-c. Radiation effects to dielectric coatings on mirrors	II-B-19
II-B-8. Tritium	II-B-20
II-B-9. Mechanical design & blanket replacement	II-B-21
II-B-10. Neutronics	II-B-21
II-B-11. The power cycle	II-B-22
II-B-12. General	II-B-23
References for Chapter II	II-B-27
III. Laser Fusion Physics	
III-A. Introduction to General Ideas of Inertial Confinement	III-A-1
III-A-1. Laser requirements for laser fusion	III-A-3
III-A-2. Implosion scenario	III-A-5
References for Section III-A	III-A-8
III-B. Efficiencies & Pellet Gain Requirements for Laser Fusion Reactors	III-B-1
III-C. Laser Plasma Modelling	III-C-1
III-C-1. Hydrodynamics	III-C-1
III-C-1-a. Introduction	III-C-1

TABLE OF CONTENTS (contd)

	Page
III-C-1-b. One fluid - 2 temperature model	III-C-2
III-C-1-c. Equation of state	III-C-5
III-C-1-d. Transport coefficients	III-C-6
References for Section III-C-1	III-C-9
III-C-2. Burn dynamics	III-C-10
III-C-2-a. Reaction rates	III-C-10
III-C-2-b. Charged particle transport	III-C-12
References for Section III-C-2	III-C-16
III-C-3. Laser light absorbtion	III-C-17
III-C-3-a. Introduction	III-C-17
III-C-3-b. Classical absorption	III-C-20
III-C-3-c. Absorption at oblique incidence	III-C-27
III-C-3-c-i Slab geometry	III-C-27
III-C-3-d. Total power absorbed at oblique incidence	III-C-37
III-C-3-e. Effect of expanding critical radius	III-C-44
III-C-3-f. Resonance absorption & density profile steepening	III-C-54
References for Section III-C-3	III-C-56
III-C-4. Radiation	III-C-57
III-C-4-a. Introduction	III-C-57
III-C-4-b. The radiation transport equation	III-C-57
III-C-4-c. Radiation processes in a laser fusion plasma	III-C-59
III-C-4-c-i Introduction	III-C-59
III-C-4-c-ii Description of atomic states of a plasma	III-C-61
III-C-4-c-iii The distribution of ion states	III-C-62
III-C-4-c-iv A mean ion representation for computing radiative properties	III-C-66
III-C-4-c-v Emission processes	III-C-67
References for Section III-C-4	III-C-74
III-C-5. Hydrodynamic stability	III-C-76
References for Section III-C-5	III-C-78
III-C-6. Hot Electrons	III-C-79
III-C-6-a. Introduction	III-C-79
III-C-6-b. Creation	III-C-79
III-C-6-c. Propagation	III-C-80
References for Section III-C-6	III-C-83
III-D. Numerical Modelling	III-D-1
References for Section III-D	III-D-3
III-E. Comparison of PHD-IV Results With Other Published Results	III-E-1
III-E-1. Thermonuclear burn - A comparision with other published results	III-E-1
III-E-2. Radiation transport	III-E-9
References for Section III-E	III-E-14
III-F. Advanced Fuels	III-F-1
III-F-1. Introduction	III-F-1
III-F-2. Deuterium	III-F-1
III-F-3. Proton-Boron-11	III-F-10
References for Section III-F	III-F-15
III-G. Prospects for High Gain Pellets	III-G-1

TABLE OF CONTENTS (contd)

	Page
IV. Pellet Design for SOLASE	
IV-A. Basic Pellet Physics	IV-A-1
References for Section IV-A	IV-A-8
IV-B. Thermonuclear burn	IV-B-1
IV-B-1. Bare core pellet burn calculations	IV-B-7
IV-B-2. Tamped pellet core burn calculations	IV-B-28
References for Section IV-B	IV-B-41
IV-C. Pellet Implosion	IV-C-1
IV-C-1. An example pellet implosion	IV-C-1
IV-C-2. Sphere vs. shell targets	IV-C-16
IV-C-3. Exploding pusher targets	IV-C-17
IV-C-4. Multishelled targets	IV-C-20
References for Section IV-C	IV-C-22
IV-D. Pellet Material Considerations	IV-D-1
IV-E. Model Pellet for SOLASE	IV-E-1
IV-F. Feasibility of Achieving Reactor Pellet Performance	IV-F-1
References for Section IV-F	IV-F-4
V. Optics and Illumination Studies	
V-A. Laser Fusion Optics	V-A-1
V-A-1. Introduction	V-A-1
V-A-2. Mirrors Yes, Lenses No	V-A-4
V-A-3. Surface Damage Thresholds and Aperture Size	V-A-5
V-A-4. Self-Focusing	V-A-8
V-A-5. The Case Against Uniform Illumination	V-A-13
V-A-6. Thermal Distortion	V-A-14
V-A-7. Location and Protection of Final Mirrors	V-A-17
V-A-8. Diffraction at an Annular Aperture	V-A-19
V-A-9. Pointing Errors	V-A-24
V-A-10. Consequences of Laser Wavelength Choice	V-A-25
V-A-10-a. Laser-Plasma Coupling	V-A-25
V-A-10-b. Corona-Core Coupling	V-A-25
V-A-10-c. Rayleigh-Taylor Instability	V-A-25
V-A-10-d. Self-Focusing	V-A-26
V-A-10-e. Gas Breakdown Threshold	V-A-26
V-A-10-f. Diffraction	V-A-26
V-A-10-g. Optical Surface Requirements	V-A-26
V-A-10-h. Mirror Surface Damage Thresholds	V-A-26
V-A-11. Mirror Mechanical Design Considerations	V-A-27
References for Section V-A	V-A-32

TABLE OF CONTENTS (contd)

		Page
V-B.	Optimal Illumination Studies	V-B-1
	V-B-1. Introduction	V-B-1
	V-B-2. The platonic solids	V-B-2
	V-B-3. Irradiance profiles	V-B-6
	V-B-4. Calculating beam overlap	V-B-12
	V-B-4-a. Octahedron	V-B-13
	V-B-4-b. Dodecahedron	V-B-16
	V-B-4-c. Icosahedron	V-B-16
	V-B-4-d. Minimum value of θ_{max} for total coverage	V-B-18
	V-B-5. Numerical results	V-B-23
	V-B-5-a. Optimization	V-B-23
	V-B-5-b. Solid angle-limited designs	V-B-38
	V-B-6. Discussion	V-B-41
	Appendix: Theorem on Uniformity	V-B-43
	References for Section V-B	V-B-45
V-C.	Imaging Properties of Off Axis Paraboloidal Mirrors	V-C-1
	V-C-1. Introduction	V-C-1
	V-C-2. Image distortion	V-C-5
	V-C-3. Two-dimensional irradiance profiles	V-C-13
	V-C-4. Mirror positioning & pointing errors	V-C-26
	V-C-4-a. Translational positioning errors	V-C-26
	V-C-4-b. Rotational positioning errors	V-C-26
	V-C-4-a-i. Rotation about the y-axis ($\delta\phi$)	V-C-27
	V-C-4-a-ii. Rotation about the z-axis ($\delta\theta$)	V-C-29
	V-C-4-a-iii. Rotation about the x-axis ($\delta\eta$)	V-C-30
	V-C-5. Perturbed Irradiances	V-C-33
	V-C-5-a. Translation of the target in the z-direction	V-C-35
	V-C-5-b. Target irradiance under the rotation $\delta\phi$	V-C-38
	V-C-6. Discussion	V-C-43
	Appendix A: General Method for Calculating Perturbed Rays	V-C-44
	Appendix B: Caustics for Tilted Paraboloid	V-C-45
	References for Section V-C	V-C-50
VI.	Optics and Beam Transport for SOLASE	
VI-A.	The Beam Transport System	VI-A-1
	VI-A-1. Introduction	VI-A-1
	VI-A-2. Multipassing considerations	VI-A-1
	VI-A-3. Beam combining	VI-A-2
	VI-A-4. The optical delay lines	VI-A-5
	VI-A-5. The last mirror placement	VI-A-6
	VI-A-6. Additional considerations	VI-A-12
	VI-A-7. Summary of the beam transport system	VI-A-21
	References for Section VI-A	VI-A-21

TABLE OF CONTENTS (contd)

	Page
VI-B. Final Mirror Design for SOLASE	VI-B-1
VI-B-1. Fabrication	VI-B-1
VI-B-2. Thermal response to radiation	VI-B-5
VI-B-2-a. Laser light	VI-B-5
VI-B-2-b. X-rays	VI-B-6
VI-B-2-c. Neutrons and secondary γ-rays	VI-B-8
References for Section VI-B	VI-B-12
VII. Lasers for Laser Fusion	
VII-A. Introduction	VII-A-1
VII-B. Survey of Lasers for Laser Fusion	VII-B-1
VII-B-1. The iodine laser	VII-B-1
VII-B-2. Advantages of iodine lasers	VII-B-3
VII-B-3. Disadvantages of the iodine laser	VII-B-3
VII-B-4. Possible improvements	VII-B-4
VII-B-5. Summary of iodine lasers	VII-B-5
VII-B-6. The HF chemical laser	VII-B-6
VII-B-7. Advantages of the HF laser	VII-B-8
VII-B-8. Disadvantages of the HF laser	VII-B-8
VII-B-9. Possible improvements	VII-B-10
VII-B-10. Summary of the HF laser	VII-B-12
VII-B-11. The CO_2 laser	VII-B-14
VII-B-12. Advantages of the CO_2 laser	VII-B-16
VII-B-13. Disadvantages of the CO_2 laser	VII-B-16
VII-B-14. Possible improvements	VII-B-18
VII-B-15. Summary of the CO_2 laser	VII-B-19
VII-B-16. Brand X lasers	VII-B-19
VII-C. A Summary of the Laser Survey	VII-C-1
VII-D. Design Study System	VII-D-1
References for Chapter VII	VII-D-3
VIII. Laser & Power Supplies for SOLASE	
VIII-A. Introduction	VIII-A-1
VIII-B. The Laser Design	VIII-B-1
VIII-B-1. General description of CO_2 laser	VIII-B-1
VIII-B-2. Laser mixture & discharge parameters	VIII-B-4
VIII-B-3. Engineering extraction from an amplifier	VIII-B-8
VIII-B-4. Multipass extraction	VIII-B-12
VIII-B-5. Laser master oscillator and preamplifiers	VIII-B-19

TABLE OF CONTENTS (contd)

	Page
VIII-B-6. Efficiency of the SOLASE laser	VIII-B-27
VIII-B-7. The gas handling system	VIII-B-30
VIII-B-8. Additional problem areas	VIII-B-32
VIII-B-9. The SOLASE laser as a generic laser	VIII-B-43
VIII-B-10. Conclusions of laser design	VIII-B-48
References for Section VIII-B	VIII-B-51
VIII-C. Power Supplies for Laser Fusion Reactors	VIII-C-1
VIII-C-1. Introduction	VIII-C-1
VIII-C-2. General supply design considerations	VIII-C-3
VIII-C-3. The capacitor bank	VIII-C-4
VIII-C-4. Switching	VIII-C-12
VIII-C-4-a. Spark gaps	VIII-C-13
VIII-C-4-b. Semiconductor switches	VIII-C-18
VIII-C-5. General design of the laser power supplies	VIII-C-22
VIII-C-6. Final amplifiers design	VIII-C-24
VIII-C-7. Power supply conclusions	VIII-C-29
References for Section VIII-C	VIII-C-31
Appendix - Beam Extraction from a Multipassed Annular Amplifier	VIII-1
IX. Target Fabrication & Delivery Considerations	
IX-A. Present Inertial Confinement Target Requirements	IX-A-1
IX-A-1. Glass Microshell$_{TM}$ Pellets	IX-A-4
IX-A-1-a. Fabrication procedures	IX-A-4
IX-A-1-b. Shell quantities & sizes	IX-A-8
IX-A-1-c. DT permeation & storage	IX-A-9
IX-A-2. Polymeric Microshell$_{TM}$ Pellets	IX-A-13
IX-A-2-a. Fabrication procedures	IX-A-13
IX-A-2-b. Permeation fueling, storage & shelf life	IX-A-15
IX-A-3. Cryogenic Targets	IX-A-16
IX-A-3-a. Present status	IX-A-17
IX-A-3-b. Cryogenic reactor pellet considerations	IX-A-19
IX-B. Reactor Pellet Requirements	IX-B-1
IX-B-1. Representative reactor pellets	IX-B-2
IX-B-2. Fabrication & processing of reactor pellets	IX-B-4
IX-B-2-a. Fabrication techniques	IX-B-4
IX-B-2-b. Storage requirements	IX-B-6
IX-B-2-c. Pellet cost estimates	IX-B-9
IX-C. Pellet Injection	IX-C-1
IX-C-1. Electrostatic injection & deflection	IX-C-1
IX-C-2. Pneumatic Injection	IX-C-2
References for Chapter IX	IX-C-6

TABLE OF CONTENTS (contd)

	Page
X. Cavity Design Concepts	
X-A. Pedagogy	X-A-1
X-A-1. Wall protection -- problem definition	X-A-2
References for Section X-A	X-A-15
X-B. Wall Protection Concepts	X-B-1
X-B-1. The wetted wall concept	X-B-2
X-B-2. The liquid Li "waterfall" concept	X-B-4
X-B-3. Magnetic protection	X-B-7
X-B-3-a. Diffusion of the magnetic field into the conducting wall	X-B-9
X-B-3-b. Diffusion of the magnetic field in the plasma	X-B-10
X-B-3-c. Time of flight spreading of the particles	X-B-11
References for Section X-B	X-B-18
X-C. Thermal & Mechanical Response of ICTR First Walls	X-C-1
X-C-1. Thermal response to photon irradiation without buffer gas	X-C-1
X-C-1-a. Temperature rise produced by the reflected laser light	X-C-6
X-C-1-b. Temperature rise produced by the X-rays	X-C-10
X-C-2. Thermal response to pulsed ion sources with no buffer gas	X-C-15
X-C-3. Effect of residual chamber gas on wall thermal response	X-C-24
X-C-4. Surface evaporation rate	X-C-36
X-C-5. Stress analysis for ICTR walls	X-C-42
X-C-5-a. Impulsive heat deposition in a semi-infinite medium	X-C-42
X-C-5-b. Energy deposition in a finite elastic layer	X-C-43
X-C-5-b-i. Series solutions	X-C-43
X-C-5-b-ii. Wave solutions	X-C-47
X-C-5-b-iii. Stress wave results	X-C-49
X-C-6. Structural design considerations for the first wall	X-C-52
References for Section X-C	X-C-60
XI. Cavity Design for SOLASE	
XI-A. General Description of the SOLASE Cavity	XI-A-1
XI-B. Analyses of the Gas Protection Concept	XI-B-1
XI-B-1. Charged particle attenuation	XI-B-2
XI-B-2. X-ray attenuation	XI-B-7
XI-B-3. Pressure impulse at the first wall	XI-B-12
XI-B-4. Gas cooling -- energy transfer to the wall	XI-B-19

TABLE OF CONTENTS (contd)

	Page
XI-B-5. Laser induced gas breakdown	XI-B-32
XI-B-5-a. Introduction	XI-B-35
XI-B-5-b. Theory of Hacker, Cohn & Lax	XI-B-37
XI-B-5-c. Classical microwave breakdown theory	XI-B-39
XI-B-5-c-i. Breakdown threshold for He	XI-B-42
XI-B-5-c-ii. Breakdown threshold for Ne	XI-B-44
XI-B-5-c-iii. Low collision frequency limit	XI-B-46
XI-B-5-c-iv. The diffusion limit	XI-B-47
XI-B-5-d. Multiphoton absorption	XI-B-47
XI-B-5-e. Target intensity for SOLASE	XI-B-49
XI-B-5-f. Breakdown thresholds for SOLASE	XI-B-52
XI-B-5-g. Consequences of breakdown	XI-B-54
XI-B-5-h. Conclusions	XI-B-55
XI-B-6. Postscript: Xe as a buffer gas	XI-B-56
XI-B-6-a. Ion stopping power	XI-B-56
XI-B-6-b. X-ray attenuation	XI-B-59
XI-B-6-c. Pressure Impulse to the First Wall	XI-B-61
XI-B-6-d. Gas Cooling & Reradiation to First Wall	XI-B-61
XI-B-6-e. Disadvantages of Using Xenon	XI-B-62
References for Section XI-B	XI-B-63
XI-C. Summary: First Wall Protection in SOLASE	XI-C-1
XII. Blanket Design and Analysis	
XII-A. Introduction	XII-A-1
References for Section XII-A	XII-A-2
XII-B. Blanket Design for SOLASE	XII-B-1
XII-B-1. The Li_2O/Graphite Blanket Concept	XII-B-1
References for Section XII-B-1	XII-B-10
XII-B-2. Thermal-Hydraulic Design of the SOLASE Blanket	XII-B-11
References for Section XII-B-2	XII-B-20
XII-B-3. Closure	XII-B-26
XIII. Blanket Neutronics Analyses and Shield Design for SOLASE	
XIII-A. Introduction	XIII-A-1
XIII-B. Time-Integrated (Steady State) Neutronics Studies	XIII-B-1
XIII-B-1. Calculational Method	XIII-B-1
XIII-B-2. Blanket Model and Survey Calculations	XIII-B-2
XIII-B-3. Final Blanket Model and Nuclear Analysis	XIII-B-9
XIII-B-3-a. Tritium Breeding	XIII-B-11
XIII-B-3-b. Nuclear Heating	XIII-B-11
XIII-B-3-c. Gas Production and DPA	XIII-B-11
XIII-B-3-d. Neutron Scalar Fluxes & Leakages	XIII-B-16
References for Section XIII-B	XIII-B-21
XIII-C. Time Dependent Neutronics	XIII-C-1
XIII-C-1. Neutron Source	XIII-C-2
XIII-C-2. Computational Techniques	XIII-C-7
XIII-C-2-a. Energy Dependent Quadrature	XIII-C-7
XIII-C-2-b. Discrete Cross Section Expansion	XIII-C-8
XIII-C-3. SOLASE Calculation	XIII-C-15
References for Section XIII-C	XIII-C-25

TABLE OF CONTENTS (contd)

		Page
XIII-D.	Shield Design	XIII-D-1
	XIII-D-1. Concrete Shield Design	XIII-D-1
	XIII-D-2. Lead Acetate Shield	XIII-D-3
XIII-E.	Radioactivity	XIII-E-1
	XIII-E-1. Calculational Methods	XIII-E-1
	XIII-E-2. System Geometry and Material Composition	XIII-E-5
	XIII-E-3. Induced Activity in Blanket and Shield	XIII-E-10
	XIII-E-4. After Shutdown Gamma Dose Rates	XIII-E-25
	XIII-E-5. Conclusions Concerning Radioactivity in the Laser Fusion System	XIII-E-34
	References for Section XIII-E	XIII-E-36
XIII-F.	Calculated Neutron and γ Irradiation Response of Candidate Laser Mirror Materials	XIII-F-1
	XIII-F-1. Introduction	XIII-F-1
	XIII-F-2. Calculational Model	XIII-F-3
	XIII-F-3. Results of Calculations and Discussion	XIII-F-5
	XIII-F-4. Summary	XIII-F-12
	References for Section XIII-F	XIII-F-14
XIV.	Mechanical Design, Assembly and Disassembly of SOLASE	
XIV-A.	General Description	XIV-A-1
XIV-B.	Graphite Blanket and Back Structure	XIV-B-1
XIV-C.	Shield	XIV-C-1
XIV-D.	Assembly and Disassembly	XIV-D-1
XV.	Radiation Damage and Materials Considerations	
XV-A.	Radiation Effects in Graphite	XV-A-1
	XV-A-1. Behavior of Point Defects in Graphite	XV-A-1
	XV-A-2. Dimensional Changes of Polycrystalline Graphites	XV-A-3
	XV-A-3. Irradiation Creep of Graphite	XV-A-15
	XV-A-4. Changes of Elastic Properties and Strength	XV-A-21
	XV-A-5. Fatigue Strength of Graphite	XV-A-25
XV-B.	Stress and Failure Analysis of the Blanket	XV-B-1
	XV-B-1. Procedure for Lifetime Analysis	XV-B-1
	XV-B-2. Inelastic Stress Analysis	XV-B-4
	XV-B-3. Results of the Stress Analysis	XV-B-11
	XV-B-4. Discussion of the Results	XV-B-30
XV-C.	Effects of Radiation on Lithium Oxide	XV-C-1
	XV-C-1. An Assessment of Radiation-Enhanced Densification	XV-C-1
	XV-C-2. The Densification Model	XV-C-1
	References for Chapter XV	XV-C-5

TABLE OF CONTENTS (contd)

		Page
XVI.	The Fuel Cycle and Tritium Processing	
	XVI-A. Introduction	XVI-A-1
	XVI-B. Reactor Fueling Cycle	XVI-B-1
	XVI-B-1. Compatibility of Wall and Pellet	XVI-B-1
	XVI-B-1-a. General Description and Pellet Composition	XVI-B-1
	XVI-B-1-b. Exhaust Gas Compositions	XVI-B-1
	XVI-B-2. Vacuum System Design and Requirement	XVI-B-11
	XVI-B-2-a. General Description	XVI-B-11
	XVI-B-2-b. Pump Selection	XVI-B-14
	XVI-B-2-c. System Conductance and Pump Capacity	XVI-B-17
	XVI-C. Reactor Exhaust and Fuel Logistics	XVI-C-1
	XVI-C-1. Separation and Recycling of Reactor Exhaust	XVI-C-1
	XVI-C-1-a. Neon Cleanup Scheme	XVI-C-3
	XVI-C-1-b. Hydrogen Isotope Recovery	XVI-C-7
	XVI-C-2. Fuel Supply Logistics	XVI-C-8
	XVI-D. Tritium Breeding and Extraction	XVI-D-1
	XVI-D-1. The Lithium Oxide Blanket	XVI-D-1
	XVI-D-2. Extraction of Bred Tritium	XVI-D-1
	XVI-D-3. Lithium Oxide - Wall Interactions	XVI-D-7
	XVI-E. Tritium Control System	XVI-E-1
	XVI-E-1. Primary and Secondary Containments	XVI-E-1
	XVI-E-1-a. Fueling, Exhaust and Extraction Systems	XVI-E-1
	XVI-E-1-b. Steam Generators and Steam Reheaters	XVI-E-5
	XVI-E-2. Tertiary Containment	XVI-E-9
	XVI-F. Conclusions	XVI-F-1
	References for Chapter XVI	XVI-F-2
XVII.	Power Conversion System for SOLASE	
	XVII-A. Steam Generator and Reheater Design	XVII-A-2
	XVII-B. Particle Transport System	XVII-B-1
	References for Chapter XVII	XVII-B-5

VIII. Laser and Power Supplies for SOLASE

VIII-A. Introduction

The estimated performance characteristics currently thought necessary of a laser fusion laser are discussed in Chapter VII and are listed here in Table VIII-A-1. The SOLASE laser design will be based on the more conservative of these estimates. For example, the laser system must deliver 1 MJ of energy to the pellet. This requires that the laser energy output be greater than 1 MJ since some energy will be lost in the beam transport system. Until a better estimate can be made, it is assumed that approximately 10% of the energy is lost in transport, requiring a total laser output of about 1.1 MJ (this may be optimistic). In addition, the SOLASE la must have a peak power of ~ 1000 TW and a pulse shape that closely approximates th ideal shape. The wavelengths thought necessary are still subject to considerable debate and so no choice of wavelength has been made for SOLASE.

For the particular operating parameters chosen for the SOLASE reactor, the laser must have an efficiency of at least 7% in order for SOLASE to be an economical reactor. This efficiency includes all plant recirculating power costs and so the laser itself must have a higher operating efficiency than 7%. Another parameter that has been chosen is a laser pulse repetition rate of 20 per second.

Prevention of damage to the various optical components in the system will also place a requirement on the laser: the energy density of the laser

Table VIII-A-1

Requirements of the Laser for Laser Fusion

Performance Requirements

Energy	$\sim 10^5 - 10^6$ J
Peak Power	~100 - 1000 TW
Pulse Width	0.1 - 1 nsec
Wavelength	3000 - 6000 Å (0.3 - 10 μm)
Pulse Shape	$P(t) \sim \frac{P_o}{(1 - t/t_o)^2}$

Practical Considerations

Efficiency	$\geq$ 2-10%
Pulse Repetition Rate	10 - 100 sec^{-1}
Small Signal Gain	0.001 - .01 cm^{-1}
Stored Energy Density	$10^2 - 10^3$ J/liter
Stimulated Emission Cross Section	$10^{-19} - 10^{-20}$ cm^2
Low Capital Costs and Low Maintenance	

pulse cannot exceed the optical damage threshold of any component in the optical chain. These damage thresholds for nanosecond pulses range from about 1 to 10 J/cm^2. For purposes of our generic design a value of 5 J/cm^2 has been chosen to represent the damage threshold of the average optical element. An important consequence of this is that the damage threshold combined with the total energy requirement determines the minimum total aperture of the laser. Thus, upon choosing the number of final amplifiers, the aperture size of each will be essentially fixed.

The number of final amplifiers chosen will depend on two principal criteria: namely, how large a single amplifier can be made and still operate successfully, and how many beams are required to illuminate the target satisfactorily. Determining the optimum number of beams required to illuminate the target is a complicated problem for which there is insufficient knowledge at this time. For SOLASE we have chosen to use 12 beams as a compromise between the ability to illuminate the target uniformly if required (see Chapter V) and the desire to minimize the complexity of the beam transport system and to maximize the accessibility of the reactor. To minimize the size of each amplifier, 24 beams will be extracted from the final amplifier and then combined in pairs to form the 12 beams that will illuminate the target. In SOLASE the technique of multipassing (see Section VIII-B-4) will be employed in which four separate beams will be extracted in successive passes from each amplifier during each pumping cycle. Thus, to generate the desired 24 beams only 6 final amplifiers will be required.

As discussed in Chapter VII, the SOLASE laser is intended to be generic in design. Such a laser could be designed by assuming a brand X laser that has all the ideal characteristics required for laser fusion. However, since it is extremely unlikely that such a laser will be discovered, the design would be rather fanciful and by definition would avoid many difficulties that will undoubtedly have to be surmounted. Therefore, in order to give our generic design a strong basis in reality we have chosen to utilize the parameters of the CO_2 laser in designing the SOLASE laser. The CO_2 laser was chosen, not because we feel that it will meet all the requirements for laser fusion, but because it does exhibit many of the features that will be desirable in a laser fusion laser. For example, it is a flowing-gas laser as will probably be essential. It also has a reasonable gain and operating efficiency. Thus, its electrical and mechanical properties should not be dramatically different from any laser that is ultimately utilized. Only optically might the CO_2 laser be substantially different, but we have chosen not to specify a particular wavelength in our design. Thus, the SOLASE design should be generic but still represent a realistic system in which typical problems have been encountered and solutions suggested. Section VIII-B-10 will discuss the generic aspects of the SOLASE design and those aspects

more specific to CO_2 and how these latter might change for alternative laser systems.

The following section, VIII-B, will discuss the details of the SOLASE laser design. Specific mixture, pressure and discharge parameters will be chosen. Using these parameters, calculations of the energy that can be extracted are performed. Next the technique of multi-passing is discussed and this finalizes the final amplifier design. The master oscillator, net laser efficiency, and problems that will be encountered but are not fully resolved will also be discussed.

Section VIII-C discusses the power supplies and switching for the SOLASE laser. First the general requirements of the supply system are presented. This is followed by discussions of the capacitors, switches, and the possible improvements in their lifetimes. Finally a general design of the power supply system for SOLASE is presented.

VIII-B. The Laser Design

VIII-B-1. General Description of the CO_2 Laser

As discussed in the previous section, CO_2 laser parameters will be used as a design basis for a generic laser fusion laser. Thus, it is beneficial to review briefly the CO_2 laser system.

The CO_2 laser is a gas phase, molecular laser. A simplified energy level diagram is shown in Fig. VIII-B-1. Lasing can occur on a variety of vibrational-rotational transitions on either the 10 μm

The CO_2 Laser

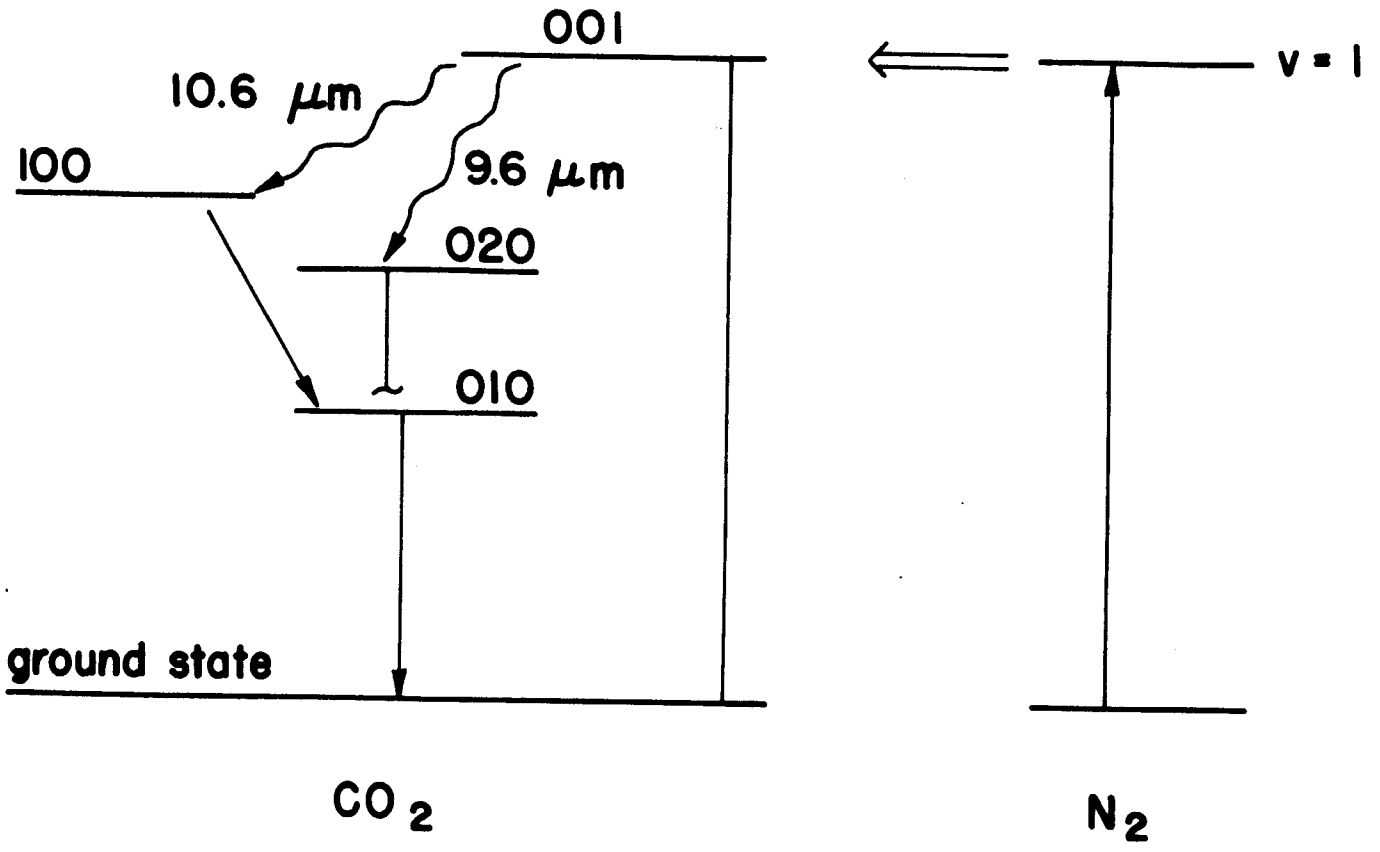

$$CO_2 + e \longrightarrow CO_2^* + e$$

$$CO_2 + N_2^* \longrightarrow CO_2^* + N_2$$

$$CO_2^* \longrightarrow \text{LASES AT } 10.6,\ 9.6\ \mu m$$

Fig. VIII-B-1.

band or the 9 μm band. This laser is generally pumped by an electric discharge. Energy is channeled into the upper laser level by several pathways. One is by direct electron impact which either excites the CO_2 molecule directly into the upper laser level or into a higher lying state that eventually relaxes into the upper laser level. The discharge can also excite the vibrational levels of N_2, a gas generally present in the laser mixture. The first vibrational level of N_2 is resonant with the CO_2 upper laser level which results in rapid collisional transfer of energy to the upper laser level of CO_2. Since the N_2 levels are optically metastable and because there is a strong mixing among N_2 levels, the majority of energy deposited in the N_2 is selectively transferred to CO_2. These highly favorable pumping pathways coupled with a high quantum efficiency results in a very efficient ($\gtrsim$ 30%) laser under optimum operating conditions.

Since the electron cross sections for exciting CO_2 have a peak value for certain electron energies, there will be an optimum E/N value (electric field/gas number density) for efficient pumping.[1] (The E/N value is a measure of the electron's average energy). This optimum value is generally lower than the E/N value that is fixed by the discharge physics but can be obtained by adding a source of ionization external to the discharge. This can be accomplished by use of an electron-beam to provide additional ionization. Thus, an electron-beam-sustained discharge can be the most efficient method of pumping of CO_2.

Although CO_2 has the potential of being extremely efficient, on nanosecond time scales the advantageous collisional processes have insufficient time to contribute to the pumping process. Thus, only energy stored directly in the upper laser level contributes to the energy output for a nanosecond pulse.[2] Consequently, for short pulse extraction one should lase on as many transitions as possible to obtain maximum efficiency. However, even with multi-line and multi-band extraction the efficiency will be limited to a few percent. This efficiency could be improved by utilizing a multi-passing technique which allows time for the collisional repopulation of the upper laser level.[3] That is, instead of making a single pass through an amplifier to extract energy, one makes several passes through each amplifier allowing time for the repopulation of the upper state between passes. This could be accomplished by either a single beam making multiple passes or multiple beams making single passes through an amplifier. In this manor energy can be extracted which has been stored in the laser system but is otherwise unavailable for short laser pulses. Thus, the efficiency can be substantially improved. Multi-passing is discussed in greater detail in Section VIII-B-4 and Appendix VIII-A.

VIII-B-2. Laser Mixture and Discharge Parameters

A CO_2 laser medium consists of a mixture of gases, primarily He, N_2 and CO_2. The N_2 is beneficial in selectively exciting the upper laser level in CO_2 while the He helps to depopulate the lower level and cool the gas in general. A number of mixtures have been investigated. Until

recently, a 3/0.25/1:$He/N_2/CO_2$ mixture was thought to have among the best performance characteristics. However, Los Alamos has been investigating heliumless mixtures and found that a 0/1/4:$He/N_2/CO_2$ mixture has a number of advantages over more conventional helium-rich mixtures. These advantages include: a larger bandwidth which is desirable for short pulse extraction; shorter rotational relaxation times, which increases the energy available; larger saturation energy, which increases the extractable energy; larger heat capacity, which results in lower temperature rises; better efficiency - particularly at higher gains; lower currents for a given energy input; and finally lower costs due to the elimination of He. The disadvantages are that much higher voltages are required, uv photo-ionization techniques cannot be used because photo absorption cross sections are too large, and the lack of He could reduce the rate of depopulation of the lower state which could adversely affect multi-pass extraction. The advantages of the heliumless mixture dominate, however, and our design will be based on a 0/1/4:$He/N_2/CO_2$ mixture.

Having chosen a mixture, one must now choose the operating discharge parameters. In determining the optimum discharge parameters several factors must be considered. One is that pumping to provide lower small signal gains is generally more efficient than pumping for maximum gain. A lower gain, however, requires a larger system in order to extract comparable energy. Another factor is that pumping faster is generally more efficient

but places more stringent requirements on the power supplies. Thus, choosing the optimum parameters will involve compromises.

The optimum E/N value for a 0/1/4 mixture at 600 torr is about 6 kV/cm. Figure VIII-B-2 shows a plot of the small signal gain versus the pumping time for various current densities at the optimum E/N value.[4] To pump to a moderate gain of 0.04/cm in 2 μs will require a current density of 5 A/cm^2 and a total energy input of 60 J/ℓ. However, these values are only valid for an operating pressure of 600 torr which is not an optimum pressure.

Ideally, the pressure should be as high as possible because the extractable energy density increases with pressure. However, there are several factors that limit the maximum pressure allowable, one is laser-induced, gas breakdown in which the electric field of the laser pulse causes the formation of a plasma through which the laser beam can no longer propagate. For a given laser intensity, there will be a pressure above which breakdown will always occur. Another, more ill-defined limit results from the fact that increasing the pressure requires a proportional increase in the applied electric field. Thus, there will be an effective limit to the pressure for a fixed electrode gap beyond which either the voltage cannot be raised or uniform pumping is no longer obtainable. A final limitation is due to the adverse affect high pressure has on beam quality which determines the focusability of the laser beam. Thus, there is a limit to the operating pressure of the laser. Taking these factors

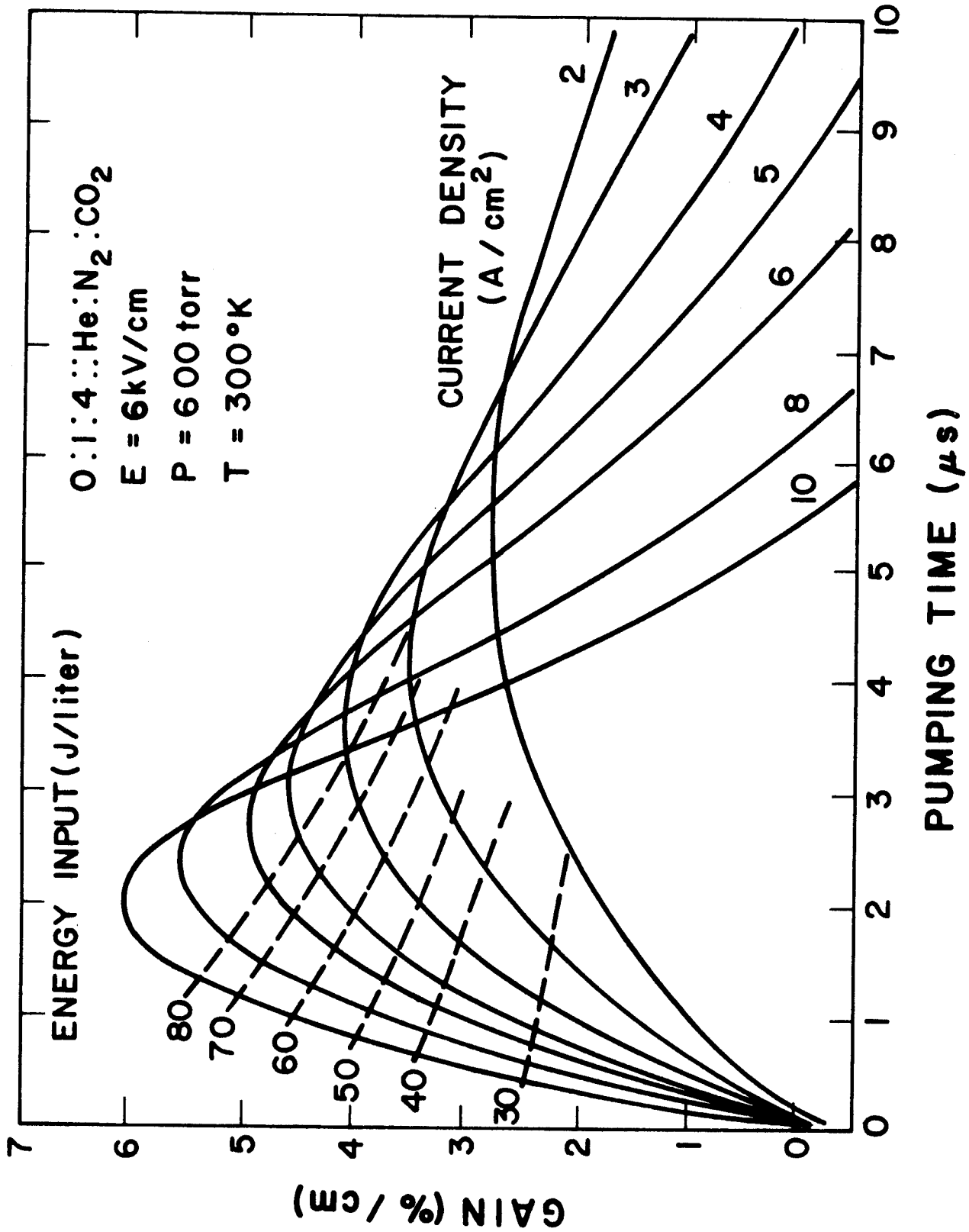

Fig. VIII-B-2. (after ref. 4)

into consideration, the operating pressure was chosen to be 1800 torr. The discharge parameters at this pressure can be calculated from those measured at 600 torr by using the scaling laws

$$F = F_0(P/P_0) \quad (1)$$

$$J = J_0(P/P_0) \quad (2)$$

$$E = E_0(P/P_0) \quad (3)$$

and

$$T = T_0(P_0/P) \quad (4)$$

where F is the electric field, J is the current density, E is the energy density, T is the pumping time and P is the pressure. F_0, J_0, E_0, T_0, and P_0 are these parameters at 600 torr. In using these scaling laws the small signal gain remains constant. Thus, for a small signal gain of 0.04/cm, the discharge parameters at 1800 torr are F = 18 kV/cm, J = 15A/cm^2, E = 180 J/ℓ and T = 2/3 μs.

A final important parameter is the saturation energy. This parameter is fixed by the mixture, the pressure, and the number of lines that are lasing. Figure VIII-B-3 shows the saturation energy for a 0/1/4 mixture as a function of pressure for multi-line (4) and single line extraction.[5] Choosing multi-line extraction, the saturation energy at 1800 torr is 0.28 J/cm^2.

VIII-B-3. Energy Extraction From an Amplifier

Having determined the basic parameters of the laser an estimate can be made of the energy that can be extracted from an amplifier. To calculate the energy extraction, the theory of pulse propagation in laser

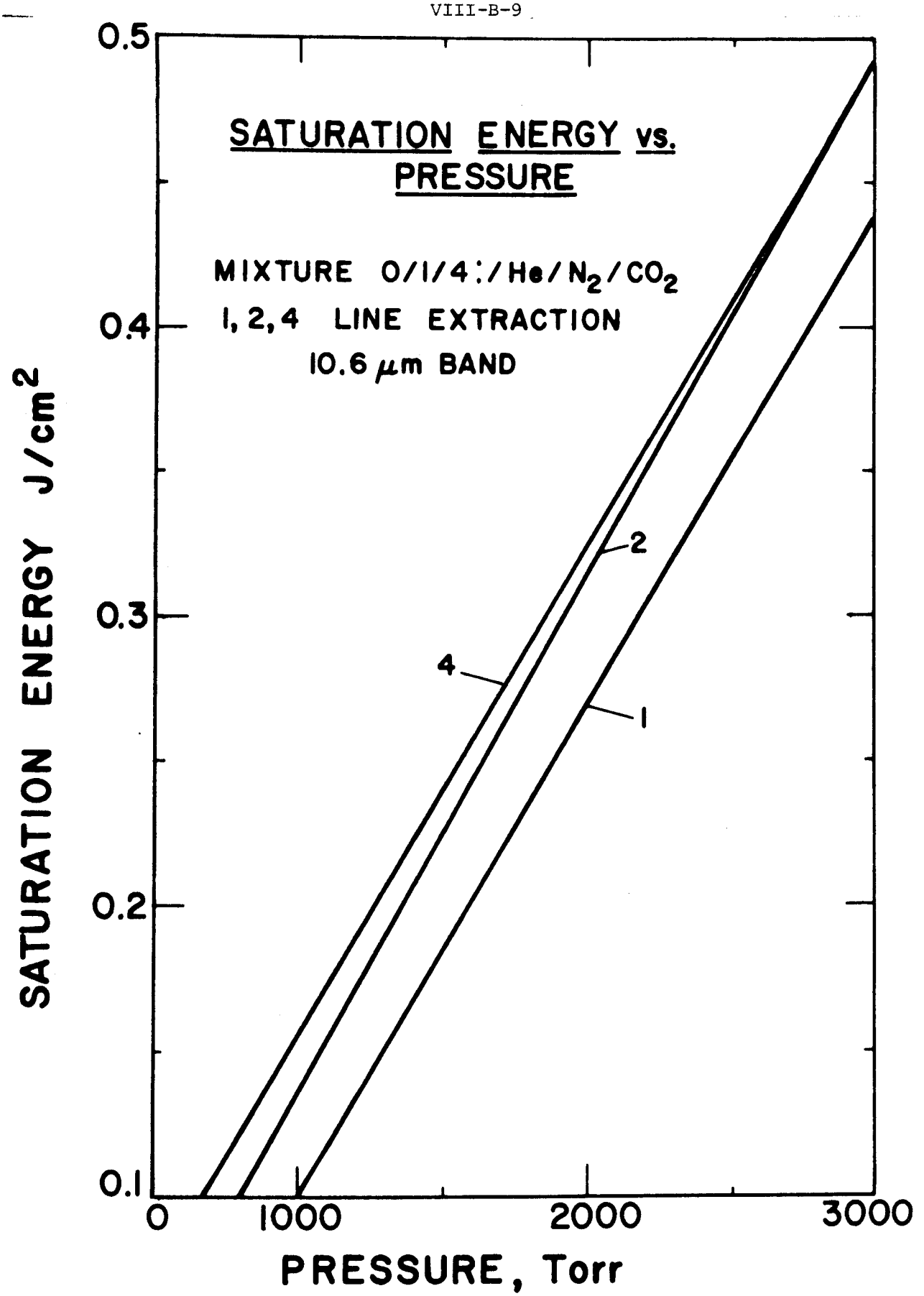
SATURATION ENERGY vs. PRESSURE
MIXTURE 0/1/4 : / He / N_2 / CO_2
1, 2, 4 LINE EXTRACTION
10.6 μm BAND
SATURATION ENERGY J/cm²
0.5
0.4
0.3
0.2
0.1
0
1000
2000
3000
PRESSURE, Torr
1
2
4

Fig. VIII-B-3.

amplifiers developed by Frantz and Nodvik will be used.[6] Assuming a uniform plane wave, the energy density out of an amplifier is given by

$$e^{E_o/E_s} - 1 = e^{g_o L} \left(e^{E_i/E_s} - 1\right) \qquad (5)$$

where E_o, E_i, and E_s are the output, input and saturation energy densities respectively; g_o is the small signal gain; and L is the length of the amplifier. For most efficient extraction the input flux must saturate the amplifier. In this case Eq. 5 reduces to

$$E_o = E_i + E_s\, g_o L \ . \qquad (6)$$

It is obvious from this relation that it is desirable for E_s to be as large as possible. Since E_s is proportional to the pressure (see Figure VIII-B-3), the desirability of increasing the pressure as discussed in the previous section becomes clear. The saturation energy and the small signal gain have previously been fixed at 0.28 J/cm^2 and 0.04/cm respectively; only the length of the amplifier, L, is left to be determined. To maximize the output the length should be as long as possible. Practical experience has indicated that parasitics become a major problem for $g_o L$ products greater than about 10. Thus,

the length must be limited to about 2.5 m for a gain of 0.04/cm. Substituting these values into Eq. 6 indicates that the maximum increase in energy density out is about 3 J/cm^2. This fortunately is of the same order as the optical damage threshold limit. Assuming 3 J/cm^2 to be the final output density and substituting the values of the parameters into Eq. 5 yields a value of 0.309 J/cm^2 for the input energy density.

From the total energy output and the output energy density, the aperture size can be calculated. For a 1.1 MJ output and 3 J/cm^2 the total aperture required is $\sim 3.67 \times 10^7$ cm^2. In the SOLASE design there will be six final amplifiers from each of which four successive beams will be extracted for a total of 24 beams. Thus, the aperture per beam is $\sim 15{,}270$ cm^2.

Assuming the usual circular geometry for this final amplifier, the diameter of this aperture will be 140 cm. This would require an applied voltage of $\sim$ 2.5 MV. It would be extremely difficult to pump this amplifier uniformly and the handling of such large voltages would present increased design complications. As an alternative, Los Alamos has proposed an annular amplifier. With this configuration the aperture could theoretically be made as large as desirable while maintaining a reasonable spacing between the discharge electrodes by increasing the size of the annulus but keeping the annular thickness constant. (However, diffraction losses may limit the actual size obtainable as discussed in Chap. V). Even with this configuration, the annulus must be composed of individual segments in order to keep currents below the level that results in magnetic pinching of the E-beam and non-uniform energy deposition. Because of the

practicality of annular amplifiers, they will be incorporated into the SOLASE design.

Knowing the aperture size, the total input energy required to drive an amplifier can be calculated and is found to be 4720 J per amplifier per pass. Since the total energy out per amplifier per pass is 45.8 kJ, the input energy comprises over 10% of the total output energy. It would, therefore, seem desirable to multi-pass the next to last stage of the amplifier chain as well as that of the last stage to improve the overall efficiency (see Section VIII-B-4). Finally assuming the same basic parameters as for the final amplifier, the next to last amplifier will require an aperture of 1573 cm^2 and an input driving energy of 486 J.

VIII-B-4 Multi-Pass Extraction

Continuous wave or long pulsed CO_2 lasers can be highly efficient due to favorable collisional processes which selectively excite the upper laser level. Unfortunately, on the nanosecond time scales required for laser fusion only the energy stored directly in the upper laser levels can be extracted since the collisional processes are too slow to significantly repopulate the upper laser levels during the pulse.[2] This results in relatively-low, short-pulse extraction efficiency even with multi-line and multi-band extraction. However, the fact that energy is stored in these collisionally-coupled states suggests that this energy could be extracted by making multiple passes through the amplifier and allowing sufficient time between passes for collisions to repopulate the upper laser levels.[3]

There are two basic approaches that could be used in multi-pass extraction: passing a single beam several times through an amplifier or passing several different beams through a single amplifier. In either case a method of switching or otherwise separating the beams is necessary. If a single beam is used, the beam must be switched out after the final pass. If multiple beams are used each must be switched to a path of appropriate length such that all beams arrive at the target simultaneously. At present there are no methods of electrically or mechanically switching beams of such high energy in the time scales required. The alternative is to make each pass through the amplifier at a slightly different angle and allow the beams to travel far enough that they physically separate. This eliminates the need to actively switch beams since each beam can be controlled independently. Figure VIII-B-4 schematically illustrates this technique for single beam, double pass extraction and two beam extraction.

The disadvantage of this technique is that because the beams pass through the amplifier at an angle, the fraction of the pumping volume that can be extracted is reduced. This tends to offset the gain in efficiency. For typical SOLASE parameters the volume extracted could range from about 50 to 70%. Thus, the gain in efficiency could be reduced by as much as a factor of two. Details of the volume extraction are given in Appendix VIII-A.

Even with the reduced volumetric extraction, multi-passing can result in a significant increase in the CO_2 laser's efficiency and will be incorporated into the SOLASE design. In particular, four separate

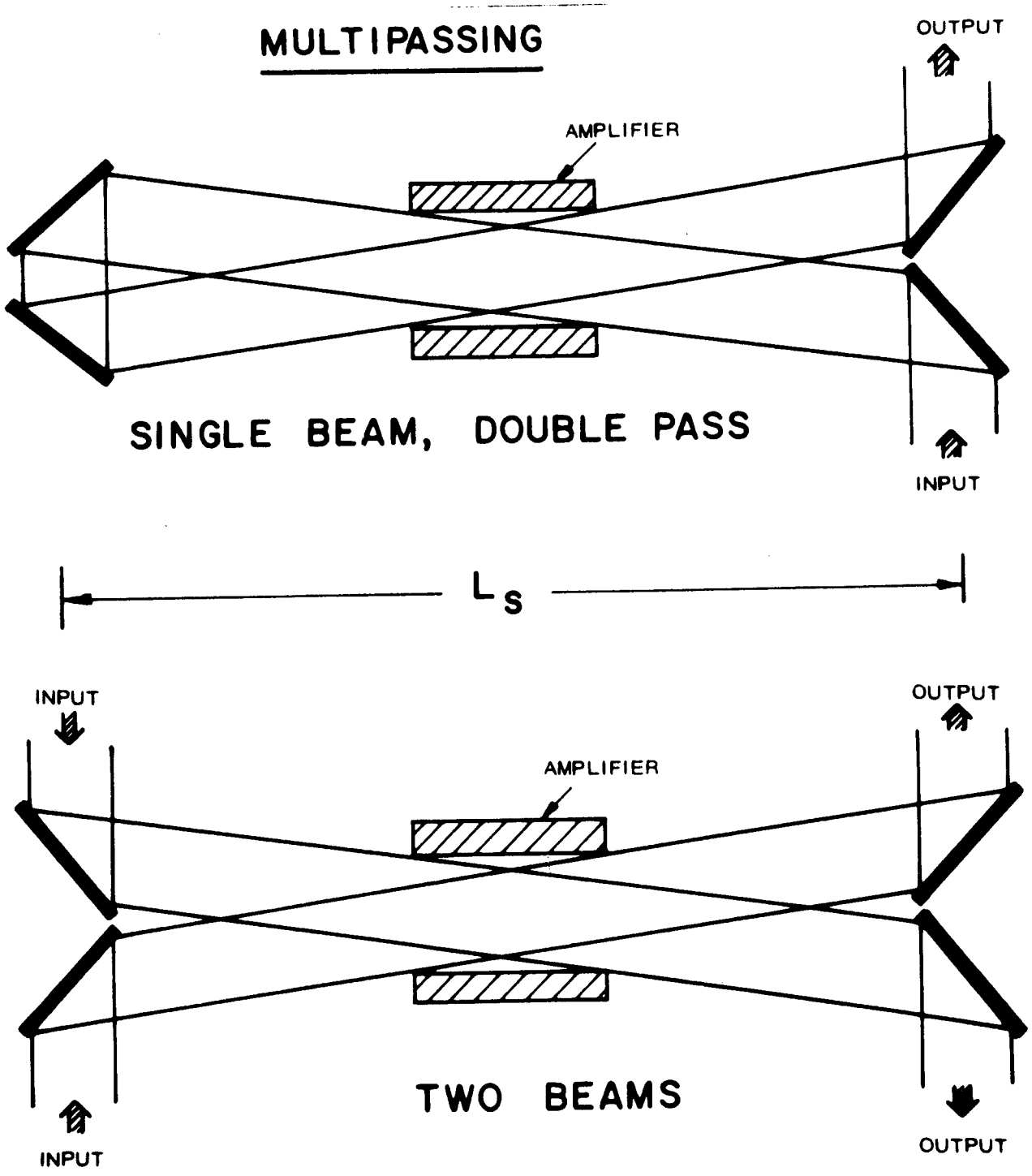
MULTIPASSING
OUTPUT
AMPLIFIER
SINGLE BEAM, DOUBLE PASS
INPUT
L_s
INPUT
OUTPUT
AMPLIFIER
TWO BEAMS
INPUT
OUTPUT

Fig. VIII-B-4.

beams will be extracted from each amplifier. Four beams were chosen as the minimum number necessary to increase the efficiency to meet SOLASE design requirements. (As many as 8 or 9 beams could be advantageously extracted at a cost of ever increasing complexity of the system). Four separate beams will be extracted from each amplifier as opposed to four passes of a single beam in order to minimize capital costs and to help maintain the highest beam quality allowable. In each case the building must be equally long not because of comparable volumetric extraction, but because of energy density limitations, the single beam system would require four times as many amplifiers as the four beam system and the corresponding building costs would be that much greater. (Note, an alternative is to make the area of the apertures of the single beam amplifiers four times larger, but this would result in a very large and probably impractical amplifier).

For successful operation of a four beam, multi-pass amplifier, the passage of each beam through the amplifier must be separated by sufficient time to allow the upper laser level to repopulate. At 1800 torr, this time[3] is approximately 0.12 μs. After passing through the amplifiers each beam must be delayed the appropriate amount in order that all beams reach the target simultaneously.

In designing a multiple pass system there are many parameters that can affect the final efficiency. For example, increasing the distance between input and output (L_s in Fig. VIII-B-4) allows the angle at which the beams pass through the amplifier to be decreased - increasing the

volume extracted and thus increasing the efficiency. This can be seen in Fig. VIII-B-5 where the efficiency of the final amplifier versus the distance between input and output mirrors is plotted. Clearly, a study optimizing the trade-offs between increasing the operating efficiency of the laser and minimizing capital costs should be done. For SOLASE, parameters were chosen that provide the minimum operating efficiency of the laser necessary for a viable reactor while minimizing the capital costs. However, this may not be the optimum configuration.

The SOLASE multi-pass laser has the following design parameters (detailed calculations are given in Appendix VIII-A). The amplifier, as discussed in the previous section, will have a length of 2.5 m and a small signal gain of 0.04/cm. As shown in Fig. VIII-B-6, the amplifier will be a segmented annulus with inner and outer diameters of the pumping volume being 298 and 372 cm respectively. There will be twenty-four, 34 x 37 cm segments spaced 5 cm apart at the inner radius. The laser beam itself will also be annular with inner and outer diameters of 313 and 357 cm respectively. The distance between input and output mirrors is 100 m. The angle the beams make with respect to the center axis of the amplifier is 60 mrad. With these values of the parameters, 59% of the volume can be extracted per pass. This corresponds to an aperture area of $\sim$ 17,750 cm^2. Since only 15,270 cm^2 is required for a uniform plane wave of 3J/cm^2 to yield the required output, this design allows for an 86% geometric utilization factor (a quantity that accounts for the fact that the entire aperture does not contribute equally to the energy extracted).

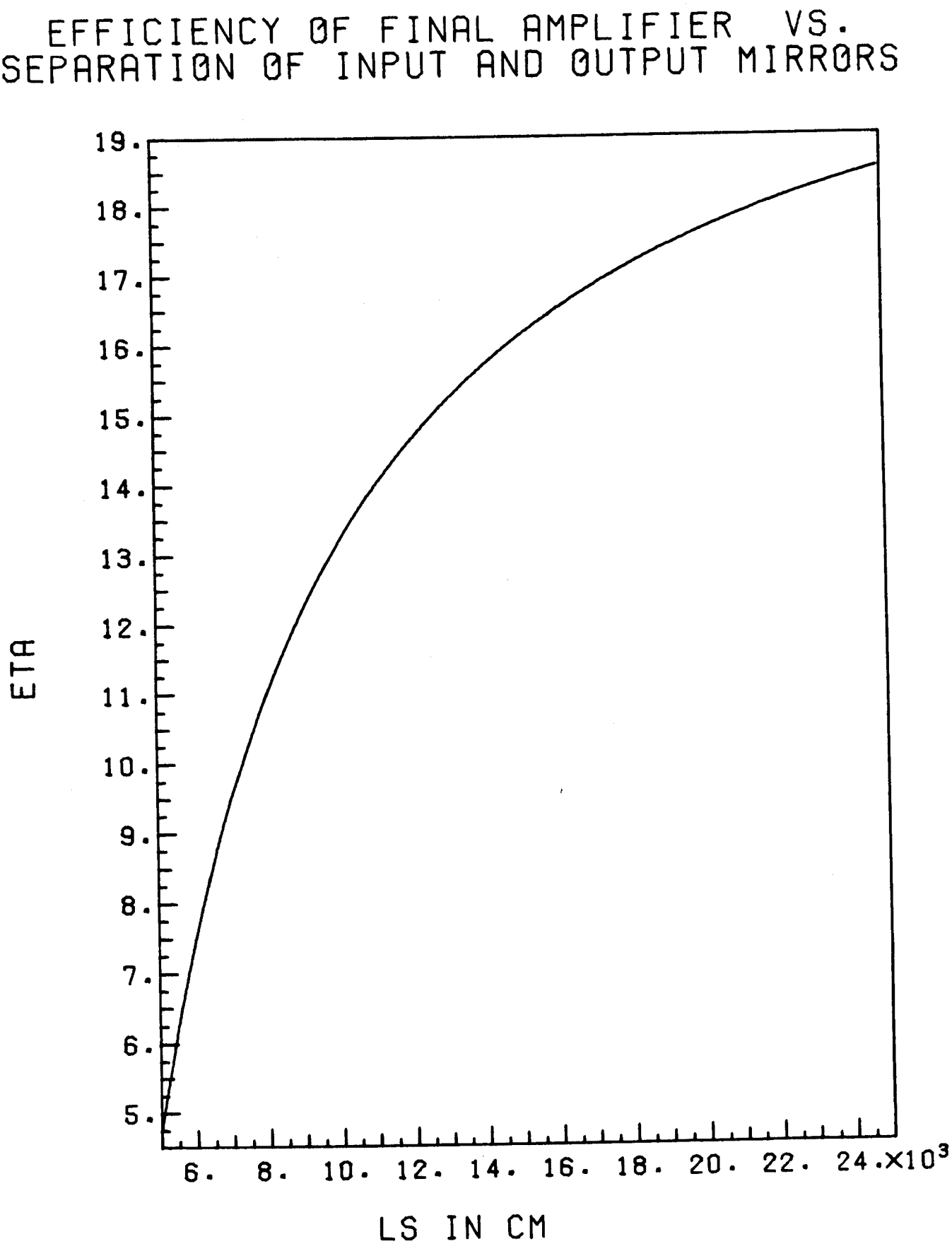
EFFICIENCY 0F FINAL AMPLIFIER VS.
SEPARATI0N 0F INPUT AND 0UTPUT MIRR0RS
ETA
19.
18.
17.
16.
15.
14.
13.
12.
11.
10.
9.
8.
7.
6.
5.
6. 8. 10. 12. 14. 16. 18. 20. 22. 24.X10³
LS IN CM

Fig. VIII-B-5.

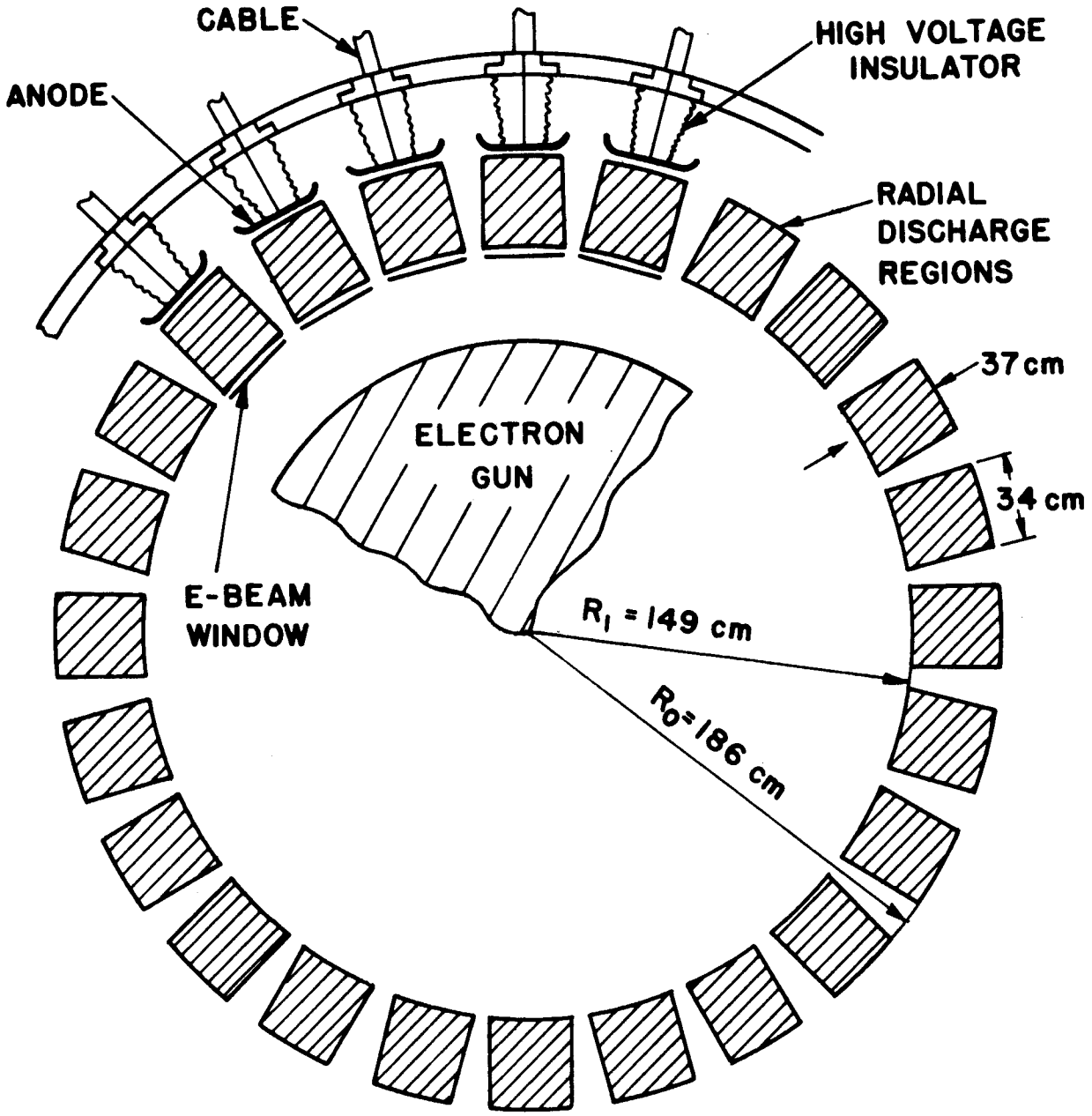

END VIEW OF ANNULAR AMPLIFIER FOR SOLASE

Fig. VIII-B-6.

From energy extraction calculations the next to last stage amplifiers will be generating 10% of the total output energy of the laser. Thus, it is desirable to multi-pass these stages as well to obtain maximum efficiency. Similar to the final amplifiers, these will be annular amplifiers comprised of 24 segments. Their pumping volumes will have inner and outer diameters of 130 and 156 cm respectively and a length of 2.5 m. The individual segments will be 12 by 13 cm each. The laser beam at this stage will be annular with an inner and outer diameter of 136.5 and 149.5 cm respectively. Again the distance between input and output mirrors is 100 m. With these parameters 50.5% of the volume can be extracted and the geometric utilization factor is 83.5%.

Further details of the layout of the multi-passing system with associated delay lines are given in Chapter VI.

VIII-B-5. Laser Master Oscillator and Preamplifiers

The master oscillator and the associated components of the front end of the laser chain form a critical element of the laser system. If the front end does not produce a pulse of exacting characteristics, the resulting pulse will not have the proper characteristics to satisfactorily implode and burn a pellet, regardless of the final amplifier performance.
This section presents some general characteristics desirable of the front end system; some problems that will be encountered and some possible solutions to these; and a general front end design for SOLASE.

The master oscillator generates the initial laser pulse that is subsequently amplified into the high energy pulse required for laser fusion.

This oscillator must meet several requirements. It must produce a pulse that is of proper shape in both space and time, that is of sufficient beam quality, and that is composed of the desired transitions if lasing on multiple lines is possible. The master oscillator must also be capable of switching out this pulse on command with very low jitter. Finally the oscillator (as well as the remaining amplifiers) must be optically isolated to prevent prepulses that can destroy the pellet prior to the arrival of the main pulse.

The initial characteristics of the pulse are important because they largely determine the final pulse characteristics and the detailed characteristics of the final pulse can be crucial in obtaining a satisfactory implosion of the pellet (see Chapter IV). The initial beam profile is important because the beam flux will saturate the large amplifiers and, as a result, minute variations in the initial profile can become large distortions by the completion of the amplification process[7] (see Sec. VIII-B-8). High beam quality is essential in the initial pulse because this determines, in part, the ultimate focusability of the beam; that is, how much of the beam's energy can actually be focused onto the target. If multiple lasing transitions are possible (as with CO_2) the oscillator must be forced to lase on all lines desired because only these transitions will be extracted from an amplifier. Conversely those transitions that are not desired must be suppressed.

The capability of command triggering of the oscillator is essential in synchronizing the laser with the pellet. Because the pellet is

injected into cavity at a comparatively slow velocity, the laser pulse must be triggered relative to the pellet injection. However, the pellet is traveling with a sufficient velocity that a jitter in the triggering of the laser of more than about $\pm$ 100 nsec would result in an effective miss of the target; that is, while the beams might still hit the target, they would hit sufficiently off center to result in an unsatisfactory burn. The actual triggering of the laser pulse should not be a major problem as the expected jitter will only be ~ 1-10 nsec. The more difficult problem will probably be the monitoring of the pellet injection to determine when to trigger the laser (see Chapter IX).

The need to optically isolate the amplifiers may prove in general to be one of the most difficult problems to solve. The total gain of the laser system will be of the order of 10^9. Thus, even very small signals resulting from self-lasing can be amplified to high energy if allowed to pass unchecked through the amplifier chain. This can "rob" the main pulse of available energy, but more importantly a prepulse arriving at the target prior to the main pulse can melt a pellet preventing the implosion and burn of the pellet. For state-of-the-art experimental targets as little as 50 μJ of prepulse energy can melt a target.(8)

The design of a master oscillator that gives the desired pulse will be specific to each variety of laser but each will incorporate many of the same basic features and techniques. Thus, only CO_2 designs will be described upon which the SOLASE design will be based.

The master oscillator for a CO_2 laser could assume several forms. One would be a TEA (transverse, electric, atmospheric) laser oscillator that generates a relatively long pulse, ~ 50-100 nsec. From this long pulse a short pulse of appropriate length will be electro-optically switched out. These long pulses frequently have a random structure due to a self-mode-locking phenomena. To obtain reproducable outputs these pulses must be "smoothed." This can be accomplished by introducing a low pressure, CO_2 discharge into the laser cavity[9] as shown in Fig. VIII-B-7. This results in a gain profile curve for each transition of a wide pressure-broadened base with a narrow peak. This extra peak will force the laser to oscillate in a single longitudinal mode, smoothing the pulse. A state-of-the-art Pockel's cell combined with a series of polarizers can be used to switch out pulses as short as a nanosecond. For much shorter pulses (~ 0.25 nsec) two Pockel's cells in series can be used. In this case, the plane of polarization is rotated past the usual 90^o to 180^o in the first cell. Thus, the cell is only transparent as the polarization sweeps past 90^o during the rise and fall of the voltage pulse. The second Pockel's cell is used to block transmission of the second pulse.

An alternative to electro-optically switching-out a short pulse from a longer pulse is to generate the short pulse by mode-locking the laser. In this system, the parameters would be adjusted to produce a mode-locked pulse of the appropriate length. In actuality a train of pulses is produced of which one must be switched-out electro-optically. CO_2 oscillators have been both passively and actively mode-locked at both high and low pressures.

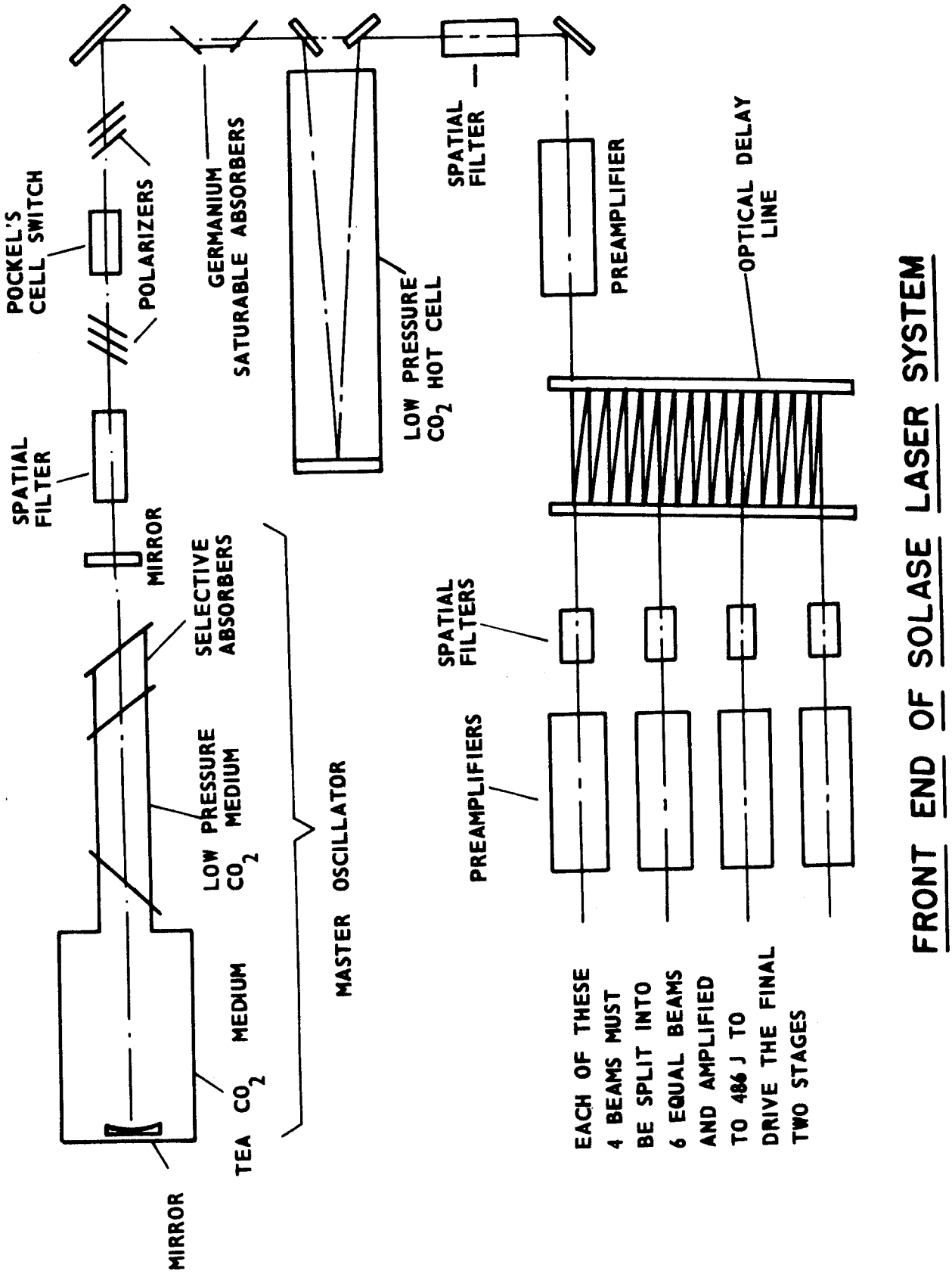
FRONT END OF SOLASE LASER SYSTEM
POCKEL'S CELL SWITCH
POLARIZERS
GERMANIUM SATURABLE ABSORBERS
SPATIAL FILTER
LOW PRESSURE CO_2 HOT CELL
SPATIAL FILTER
PREAMPLIFIER
OPTICAL DELAY LINE
SPATIAL FILTER
MIRROR
SELECTIVE ABSORBERS
LOW PRESSURE CO_2 MEDIUM
MASTER OSCILLATOR
SPATIAL FILTERS
PREAMPLIFIERS
TEA CO_2 MEDIUM
MIRROR
EACH OF THESE 4 BEAMS MUST BE SPLIT INTO 6 EQUAL BEAMS AND AMPLIFIED TO 486 J TO DRIVE THE FINAL TWO STAGES

Fig. VIII-B-7.

A variation of this mode-locking technique is the injection mode-locking of a high-pressure, relatively-high-energy TEA CO_2 laser. In this technique a low-energy, short pulse generated by either of the above methods is injected into a high-pressure laser, forcing it into mode-locked oscillations. This has been successfully used to generate a near diffraction limited, 1 J pulse from an unstable resonator, TEA CO_2 oscillator.[10] Thus, this method could be utilized to generate relatively high energy pulses if desired.

There are several methods of isolating the oscillator in the case of CO_2. The electro-optic switches that will probably be used in most master oscillators will provide some isolation, but it will not be sufficient for laser fusion applications. Additional isolation can be provided by saturable absorbers - a saturable absorber being an absorber whose absorption coefficient decreases as the intensity of light increases. Thus, with an ideal saturable absorber all low intensity self-lasing pulses will be absorbed while the high intensity primary pulse is transmitted with minimal attenuation.

Several different materials have been found for CO_2 that approximate saturable absorbers to various degrees of success. Many gases have been tried - most notably SF_6 but also NH_2O and C_2H_4. These have the disadvantage that they do not completely saturate, primarily as a result of secondary absorptions from excited states.[11] As an alternative, various triatomic molecules are being investigated which should be less likely

to absorb from excited states. A second disadvantage of the gaseous absorbers are that they are wavelength dependent and must, therefore, be used in combinations if a single gas does not serve as a saturable absorber for all transitions.

A second type of saturable absorber is p-type germanium.[12] This has an advantage over the gases in that it is a broad-band absorber over the range of 9 to 11 μm. The primary disadvantage is that being a solid, germanium can suffer permanent optical damage. Recently, the damage threshold has been improved such that it is now comparable to that of NaCℓ windows. Thus, optical damage should not limit its use.

Another interesting approach to isolating CO_2 oscillators is to utilize a hot, low pressure CO_2 gas cell. This does not act as a saturable absorber but as a selective absorber, absorbing only narrow-band CO_2 radiation.[13] Thus, it will absorb the narrow-band prepulses but will pass with little attenuation the broad-band primary pulse. This has an additional advantage of being a linear process, independent of intensity, and thus does not create spatial distortions in the beam. Isolation of the amplifiers will be further discussed in Section VIII-B-8.

To obtain the maximum short pulse extraction efficiency in CO_2, multi-line extraction must be used. In order to extract on multiple lines from an amplifier, the initial laser pulse must be composed of these transitions. The transitions that oscillate can be controlled by

introducing selective absorbers into the cavity (see Figure VIII-B-7). Some absorbers are needed to decrease the gain of strong transitions to allow weaker lines to oscillate. Other absorbers are needed to completely suppress certain lines that one does not wish to oscillate.

The general SOLASE front end laser design will consist of the following and is shown schematically in Fig. VIII-B-7. The master oscillator will be a TEA CO_2 laser which produces a long pulse that is smoothed by a low pressure CO_2 discharge. Selective absorbers will be used to force oscillations on four lines of the 10 μm band. A pulse of desired length will be switched out electro-optically by use of Pockel's cells and polarizers. Further isolation will be provided by p-type germanium saturable absorbers and a hot, low pressure CO_2 cell of sufficient length to provide necessary isolation. The beam will then pass through spatial filters to improve beam profile and quality. After passing through a preamplifier, the beam will be put into an optical delay line. At appropriate time intervals (~ 0.12 μs) the beam in the delay line will be split with one beam continuing in the delay line and the other being directed on to an amplifier chain. In this manner the four beams that make the four successive passes through each amplifier are generated. Each of these four beams must be further split into six beams and amplified to ~ 486 J to drive the next-to-last amplifier. During the preamplifying stages, isolators, beam expanders, and spatial filters will be provided as necessary. Also at a point

in the amplification process in which the beam is still relatively low in energy, the center portion of the beams will be discarded, leaving only an annular beam. Finally diagnostics must be provided to monitor the pellet injection and provide the trigger pulse for the master oscillator. Diagnostics must also be provided to detect failures of laser components and maintain alignment of the amplifier chain and beam transport system.

VIII-B-6. The Efficiency of the SOLASE Laser

The power costs of the laser will be the principal recirculating power cost of the reactor. The laser's efficiency will, therefore, be one of the primary factors in determining the economic viability of the reactor and should be examined closely.

For SOLASE to be an economical reactor, the net efficiency of the laser including all recirculating power costs must be at least 7%. To increase the CO_2 laser efficiency to this level, the technique of multi-passing was employed. The basic electrical to optical efficiency can be readily estimated.

The first step in calculating the efficiency is to determine the efficiency of converting the energy deposited in the gas to optical energy out. For each amplifier chain the total energy out is ~ 183 kJ (45.8 kJ per pass). The energy deposited in the gas by the discharge in the final two stages is 180 J/ℓ. The electron beam energy deposited is approximately 5 J/ℓ. The total energy deposited in the last two stages is then ~ 1.57 MJ. The front end of the laser must generate ~ 2000 J to

drive the final two amplifiers. Assuming the front end of the laser is ~ 3% efficient, the front end requires an input of 0.067 MJ which gives a total of ~ 1.64 MJ of energy for the entire amplifier chain. Thus, the efficiency of converting the energy deposited in the gas to optical energy is ~ 11.2%. Next the electrical to load efficiency must be included. This depends on the detailed design of the power supply system and can only be estimated here. In a well designed system this should be between 80 and 90%. (Such high efficiencies have not as yet been demonstrated). Assuming an average value of 85%, the net electrical to optical efficiency is ~ 9.5%.

To obtain a final overall efficiency all recirculating power costs must be included. Those costs directly associated with the laser include: the pumping, cooling, and reprocessing of the laser medium; the heating of the electron-beam's cathode if necessary; the flowing and cooling of oil in the capicitor banks; the laser triggering of switches; the flowing, cooling, pressurizing, and reprocessing of the switch's dielectrical material if spark gaps are used; the cooling of windows and mirrors; and the replacement and/or reprocessing of spent components such as mirrors, capacitors, switches and electron-beam foils. Additional plant recirculating power costs would include such items as the tritium cycle, pellet manufacture, and pumping on the reactor chamber. The power requirements of all of these depend significantly on the details of the individual systems and thus all power costs have not been estimated.

An estimate has been made of the cost of pumping the laser medium in order to remove heat by replacing the gas in the amplifiers after each shot. The flow rate necessary to replace the gas in the final two chambers is 1.7×10^5 ℓ/sec. Assuming a pressure drop of 2 atm. the pumping power required is 4.5 MW/amp or a total of 27 MW for the laser system. This will reduce the net laser efficiency from 9.5% to 8.4%. If the system can be designed with a substantially lower pressure drop the power requirement can be reduced accordingly.

If hot cathode electron guns are used, as much as 3-7 MW will be required to heat the filaments. While this power represents a relatively small fraction of the total laser's recirculating power requirement, it is a significant fraction of the "excess" power available for miscellaneous recirculating power costs. (Note, for the 9.5% efficient laser described, approximately 82 MW can be consumed and still maintain the minimum 7% overall efficiency). Thus, the desirability of the much less power intensive grid-controlled, cold cathodes becomes clear.

The efficiency of the SOLASE laser was fixed somewhat arbitrarily by the choice of the particular multi-passing parameters which are chosen to give approximately the minimum laser efficiency necessary to yield the required efficiency and to minimize capital costs. However, the efficiency can be increased by increasing the distance between the input and output mirrors of the final amplifier. This allows the angle

between the beams and the amplifiers center axis to be decreased, increasing the fraction of volume extracted and therefore increasing the efficiency. This is shown in Figure VIII-B-5 in which the final amplifier efficiency is plotted as a function of distance between input and output mirrors. In this plot neither the cost of generating the input beam nor the electrical to load efficiency has been included, but still it indicates the increases that could be expected. Ultimately a study should be done that optimizes the trade-offs between recirculating power costs and capital costs. It should also be mentioned that the efficiency can also be increased by increasing the number of passes through the amplifier up to a maximum of 8 or 9 but this is at the cost of greatly increasing the complexity of the system.

VIII-B-7. The Gas Handling System

For any gas laser a gas handling system will be essential. In all gas lasers the gas must be flowed in order to remove heat since the heating of a lasing gas generally results in greatly reduced operating efficiencies. Thus, a laser system must have pumps to flow the gas and heat exchangers to remove the heat. In the SOLASE design this system must handle $\sim 10^6$ ℓ/sec and other systems would require pumping capacities of the same order.

In addition, a great many laser systems undergo a chemical change in the pumping process. In these cases the gas must also be flowed to remove the spent gas and replenish with a fresh lasing mixture. Upon

removal, the spent gas must be chemically reprocessed before being reused in the laser. In the case of CO_2, approximately 10^5 metric tons/day flows through the lasers. Thus, even systems in which the mass flow rate is about two orders of magnitude lower - roughly a minimum flow rate that might be expected - the chemical reprocessing plant could be a major system depending on the extent of reprocessing necessary. For CO_2 lasers the need for reprocessing is greatly reduced. Mixtures can be pulsed many times with little degradation of the output. The principal limiting factor in the life of a mixture is the dissociation of CO_2 into CO and O. Some dissociation, however, can actually be beneficial since CO, like N_2, can selectively excite CO_2 by collisional-excitation-transfer. Thus, for SOLASE bleeding off a small fraction of the gas and reprocessing only this portion will probably be sufficient.

Since CO_2 and N_2 are relatively cheap, one might consider discarding the wastes rather than reprocessing. However, with a mass flow rate of about 4×10^5 metric tons/day the cost of replacing even a fraction of a percent of this could be prohibitive. In addition a primary constituent of the waste would be CO which would probably be regarded as a pollutant and one might be required to convert it to CO_2 before releasing it to the environment. This would greatly diminish the advantage to be gained by discardir

Finally it should be noted that even systems that ideally require no reprocessing will require some in practice. This is because some gas will leak from the system requiring make-up and impurities will build-up in the system requiring their removal.

VIII-B-8. Additional Problem Areas

There are a number of problems that will be encountered but have not been fully addressed as yet. These include the propagation of shock waves, the uniformity of excitation, the isolation and protection of laser components from light that is reflected from the target, and pulse shaping.

Shock waves if present in the laser medium can completely destroy the optical quality of the laser beam. The shock waves will be formed by the rapid deposition of energy into the medium and the stresses present in the system. The formation and propagation of shocks is relatively slow compared to the pumping and extraction processes. Thus, for single pulse operation, shocks have little effect on the operation of the laser. However, in repetitively pulsed systems the shock from one pulse continues to form and will adversely affect later laser pulses. Thus, an essential criteria for an amplifier is that it be designed to dampen out all shocks prior to the extraction of the next pulse.

Another problem is obtaining uniform excitation - particularly in large systems. A result of non-uniform excitation is that the gain profiles are no longer uniform. This can result in poor beam quality. In addition, local "hot spots" can occur in which the energy density can exceed optical damage thresholds, damaging the optical components.

In CO_2 lasers the uniformity of excitation is largely determined by the uniformity of the energy deposition of the electron beam. Difficulties can arise in large systems because of the current-induced, magnetic pinching of the electron-beam. For a given propagation distance

of the electron beam the total current must be below a certain limit or the induced magnetic field will pinch the beam beyond tolerable limits.[14]

One solution to this problem is to divide the amplifier into a number of smaller independent sections such that each carries a current less than that required to pinch the electron beam. Another approach that has been suggested is to apply a counter-acting magnetic field to eliminate the pinching.

Another problem will be the optical isolation of the amplifiers. This problem has already been addressed with regard to isolating the master oscillator to eliminate prepulsing. However, as indicated in Section VIII-B-5 self-oscillations can occur throughout the system and careful attention must be made to eliminate all possible feedback loops that could start unwanted oscillations. This will probably require additional saturable absorbers in the amplifier chain. It may also prove desirable to introduce a saturating gas absorber directly into the laser medium to help prevent both axial and cross oscillations. Of course, adding such a gas is contingent upon the gas not affecting the laser performance in any adverse way.

The other isolating problem results from reflections from the target. There are two aspects to this problem. One is the formation of a feedback loop by reflections off of the target. This can lead to self-lasing that can melt the target. This can be minimized by introducing saturable absorbers into the beam transport system. However, it can also be solved by placing the target a sufficient distance away. If the time-of-flight

of the light to the target is comparable to the pumping time of the laser, there will be insufficient time for the oscillations to build up. This will generally be the case in a reactor scale system. This problem is also aided by the motion of the target since it will only be "seen" by the lasers for a few microseconds, the exact time depending on its velocity and size.

The second aspect is that fraction of light from the main pulse that is reflected back from the pellet. In this case the light propagating back toward the oscillator can be sufficiently amplified by the residual gain in the system to damage optical components in the system. Thus, it is essential that sufficient isolation be provided to protect the laser system.

One method is to use Faraday rotators. These will allow the transmission of the outgoing pulse but will stop the reflected light. A general problem of Faraday rotators is making them large enough for this application. Another is that they can suffer permanent optical damage. In the particular case of CO_2 no satisfactory Faraday rotator materials have been found.

Another possible isolating technique is to utilize an ionization switch. In this case a plasma is formed in the path of the reflected beam which will stop the transmission of the beam by both absorption and scattering of the reflected light. The plasma could be self-induced by focusing the beam to a point to increase the intensity to a level that will breakdown the gas. The location of this focal region is quite critical. Since the main pulse must be transmitted through this focal region, the focal region must be placed at a point in the amplifier chain

at which the focused main pulse intensity remains below breakdown threshold. However, it also must be located at a point that will stop the reflected pulse before it can be amplified to an intensity that will damage the optical components. It may prove necessary to aid the breakdown of the returning pulse by externally supplying ionization by a discharge or electron beam. This would relax the restrictions on placement of the focal region. This ionization switch has proved very successful in stopping reflected pulses. If the above criteria can be met, this technique will probably provide the best and least expensive protection for the optics from reflected pulses.

A somewhat more exotic protection would be provided automatically if frequency conversion were utilized in the system. That is, for reasons other than protection it may be desirable to convert either long wavelengths to shorter wavelengths or very short wavelengths to longer wavelengths. This would provide protection from reflected light because the reflected light would no longer be of the oscillating frequency; therefore, it could not be amplified to high intensities. However, unless an extremely efficient method of frequency conversion can be found, it is very doubtful that it will be used for isolation alone, but its use will have the additional advantage of providing optical isolation if the use of frequency conversion is essential for other reasons.

A final problem results from the need to pulse shape. In order for most computer simulations of the imploding and burning of a pellet to give a satisfactory yield, the laser pulse must assume a very specific

temporal shape (see Chapter IV). A representative "ideal" pulse shape is shown in Fig. VIII-B-8. Physically, however, it will be very difficult to generate a pulse of this shape. This is a result of requiring that the beam flux saturate the amplifier for efficient energy extraction. The difficulty arises because the portions of the beam with different intensities see different gains - the low intensity components see higher gains and are amplified more strongly than the high intensity components. For example, Figure VIII-B-9 shows the distortion in the spatial profile that could occur.[7] Such distortions due to intensity can also occur temporally because the leading edge can deplete the population inversion so that the trailing edge sees a substantially reduced gain.[7] These temporal effects can be seen in Figure VIII-B-10. Comparing the final pulse in Figure VIII-B-10 with the ideal in Figure VIII-B-8, one notes that nature tends to give the opposite shape from that desired. Still it may be possible to tailor an incoming pulse that would yield the desired output pulse shape, but the input pulse must be controlled very exactly since even minute variations would result in intolerably shaped output pulses. It would seem desirable, if not essential, to find an alternative method of pulse shaping.

One method that has been proposed is to use a pulse stacker.[15] In this technique a beam is split into a number of individual beams and then recombined to form a pulse approximating the desired shape (see Figure VIII-B-11). The difficulty with this technique is that it must

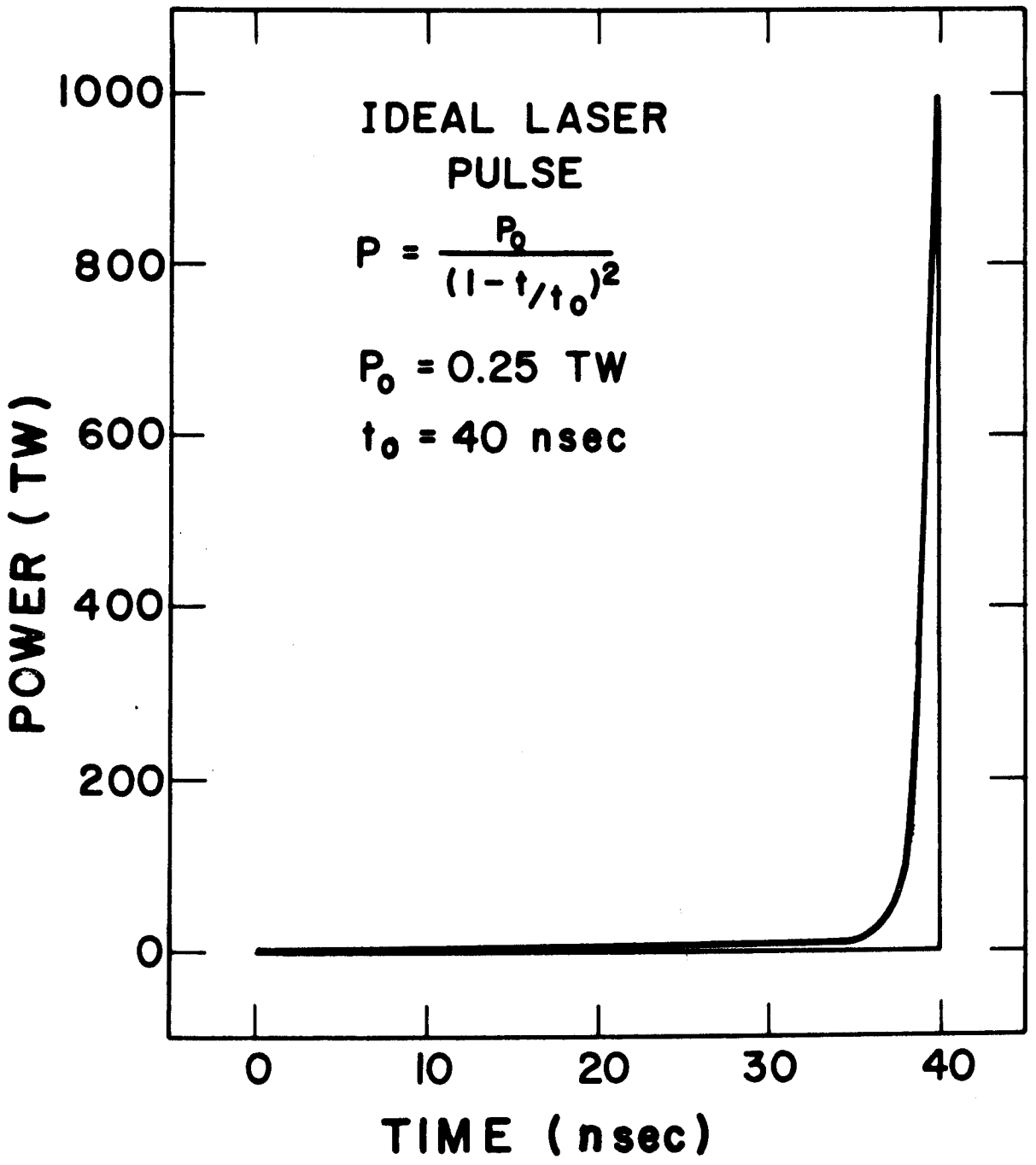
IDEAL LASER
PULSE
$P = \frac{P_0}{(1 - t/t_0)^2}$
$P_0 = 0.25$ TW
$t_0 = 40$ nsec
POWER (TW)
1000
800
600
400
200
0
0
10
20
30
40
TIME (nsec)

Fig. VIII-B-8.

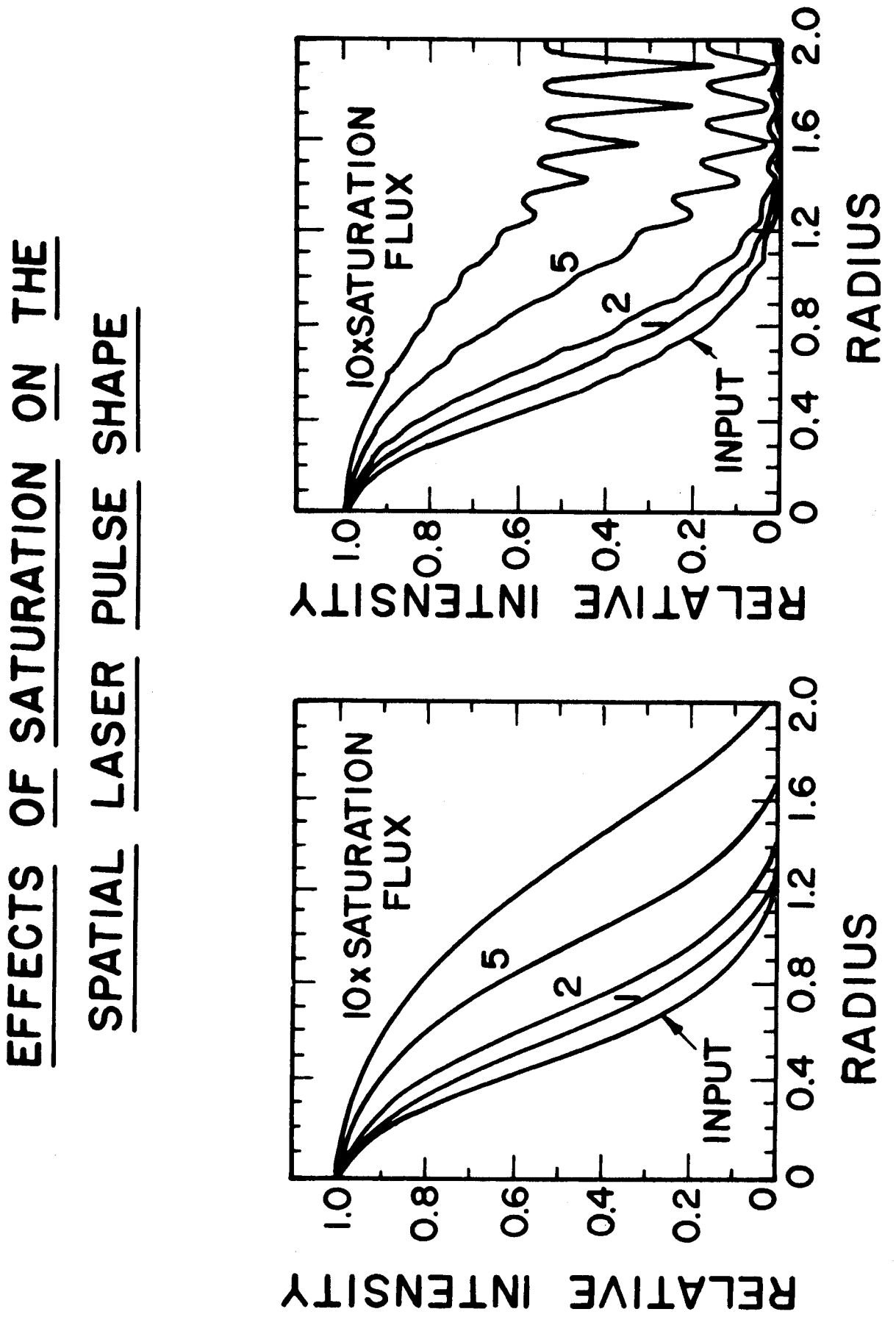

Fig. VIII-B-9. (after ref. 7)

EFFECTS OF SATURATION ON THE TEMPORAL LASER PULSE SHAPE

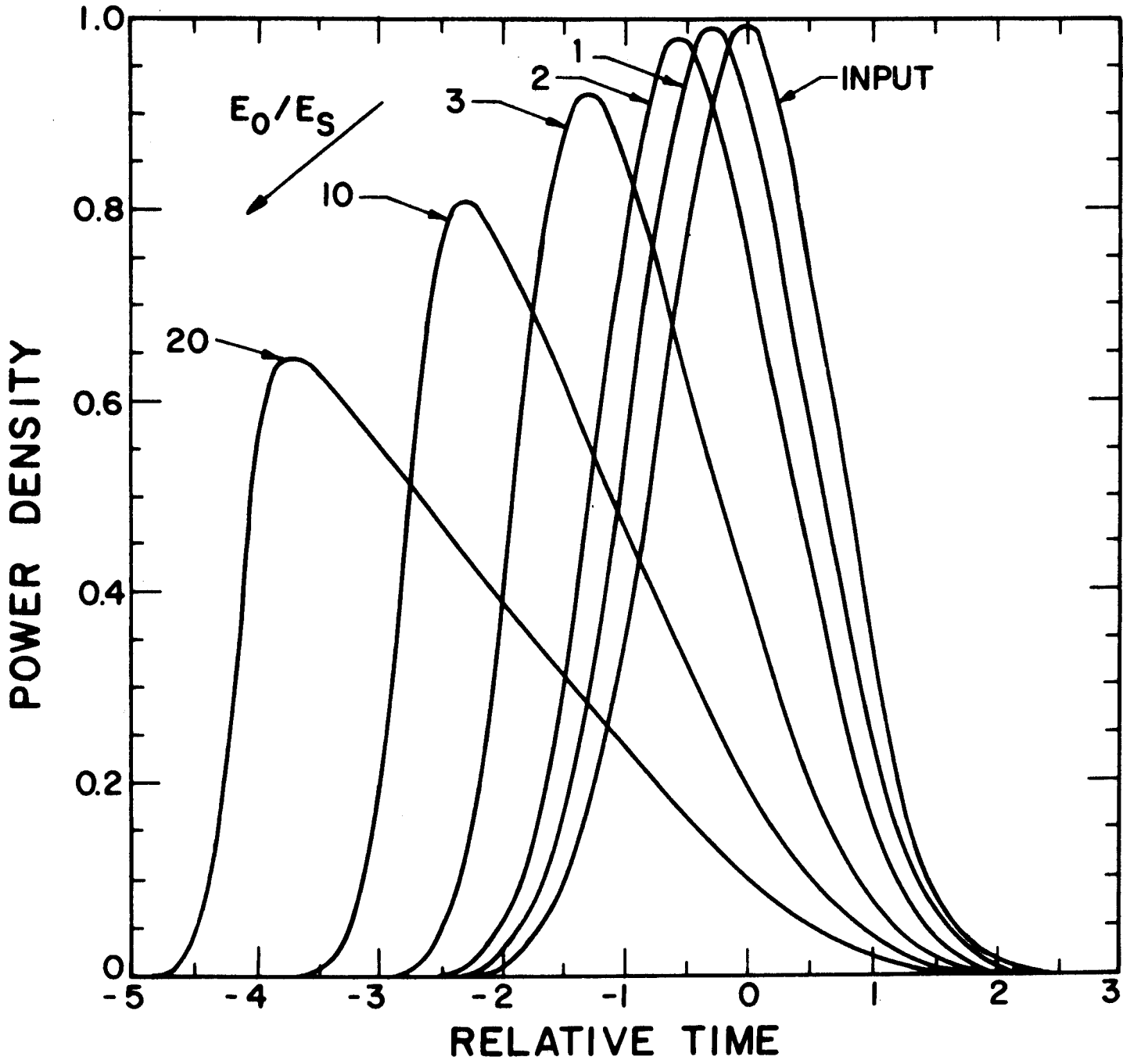

Fig. VIII-B-10. (after ref. 7)

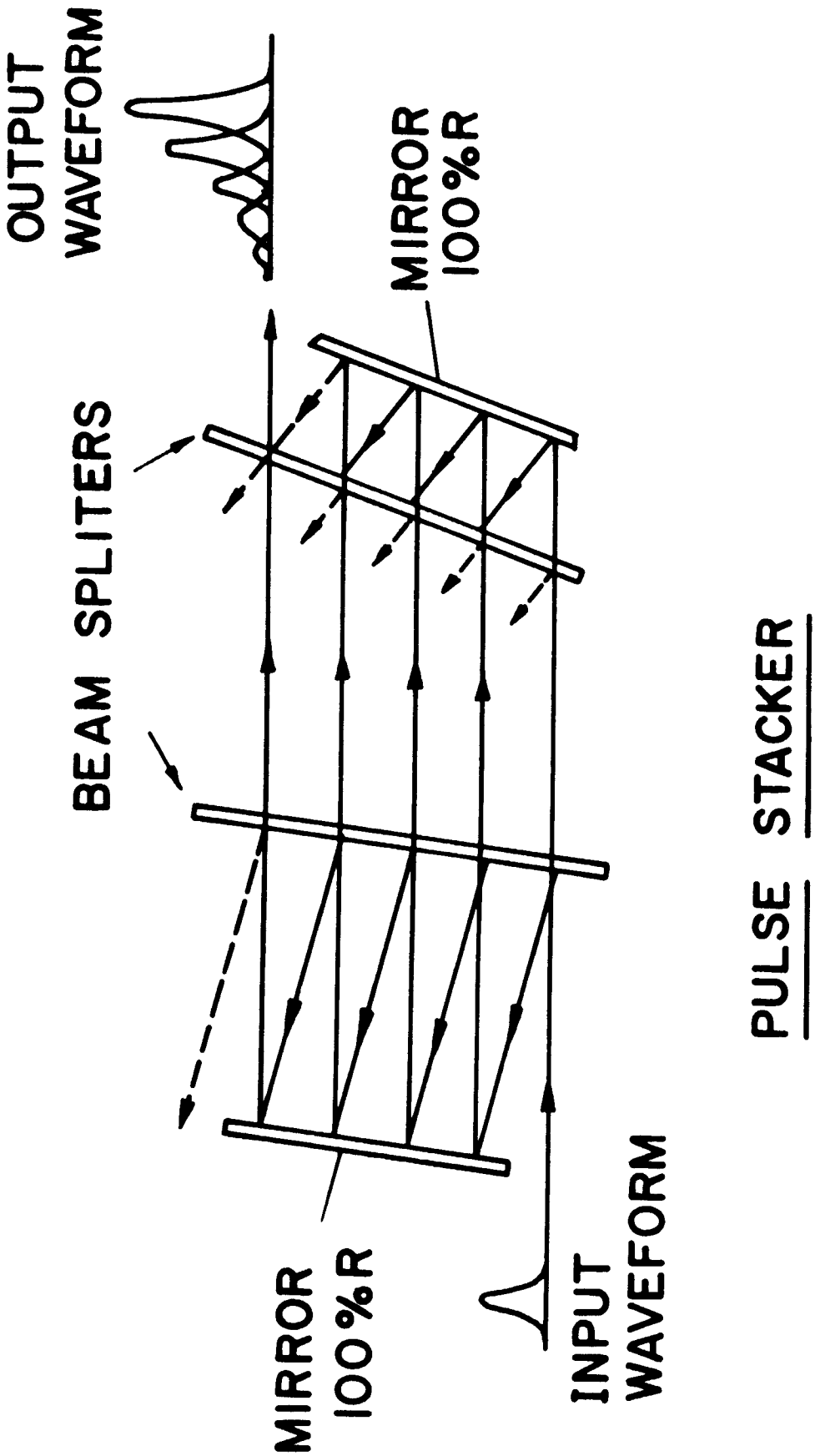
PULSE STACKER
OUTPUT WAVEFORM
MIRROR 100%R
BEAM SPLITERS
MIRROR 100%R
INPUT WAVEFORM

Fig. VIII-B-11.

be accomplished after the final amplifier to avoid saturation effects and this may prove impractical at such high energies.

Another possible method that is specific to CO_2 (although it may be applicable to certain other lasers as well) is to take advantage of the multi-line output. By selecting the proper transitions and carefully controlling the discharge parameters, the time behavior of the gains for the various transitions would be adjusted such that they oscillate at different times, the sum of the outputs of the individual transitions giving a pulse of the desired shape.[2] Saturation effects would still be important, but the method would provide better control over the final output pulse shape.

A final method is to use the fact that there are a number of essentially independent amplifier chains in the laser system. Thus, one could "turn on" the amplifiers at different times - beginning with just a few, then gradually adding more amplifiers until all were on for the final peak. This would approximate the ideal pulse as shown in Figure VIII-B-12. However, another aspect to consider is the uniformity of illumination required which is most stringent in the early stages of illumination. Unfortunately, it is early in the pulse that this method would provide the poorest uniformity as only light from a few amplifiers would be illuminating the pellet. Thus, even if the temporal shape of one of these pulses were satisfactory, the uniformity requirements could eliminate this as a viable pulse shaping technique.

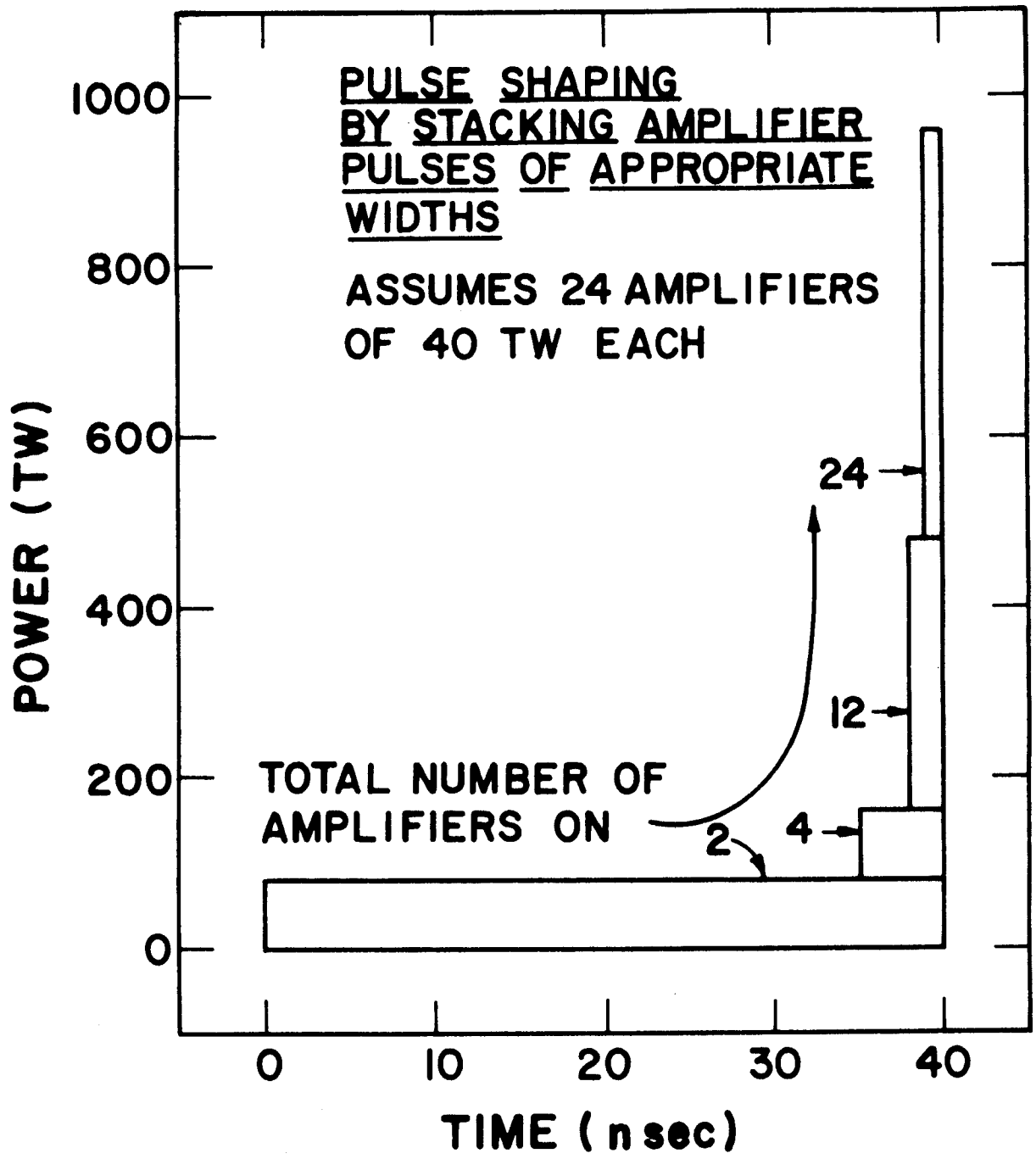
PULSE SHAPING
BY STACKING AMPLIFIER
PULSES OF APPROPRIATE
WIDTHS
ASSUMES 24 AMPLIFIERS
OF 40 TW EACH
TOTAL NUMBER OF
AMPLIFIERS ON
2
4
12
24
POWER (TW)
1000
800
600
400
200
0
0
10
20
30
40
TIME (n sec)

Fig. VIII-B-12.

An analogous approach might be applied for a laser with a SOLASE design in which each final amplifier is composed of a number of individual segments. In this case, instead of turning entire amplifiers on in sequence, one turns segments within each amplifier on in sequence. In this manner greater uniformity of illumination would be maintained throughout the pulse as equal amounts of light from each amplifier would be striking the pellet at all times during the pulse. These segments would be turned on by controlling the input pulse to each. Since the input is initially one beam, the beam must be chopped appropriately so that each segment's energy is extracted with a pulse of proper length and at the proper time. Also each segment must be sufficiently isolated such that light diffracted from one beam does not enter and extract energy from an adjacent segment. Although this may be difficult to accomplish it is probably feasible.

Thus, it appears possible to shape a pulse to approximate the ideal shape but it will be extremely difficult to reproduce it exactly. The more closely the required pulse shapes approach the "natural" pulse shapes that result from saturated amplification, the more realistically one could expect the pulses to be trailored to the desired shape.

VIII-B-9. The SOLASE Laser as a Generic Laser

This section discusses those aspects of the SOLASE laser system which tend to be generic to a laser fusion laser; those that tend to be more specific to a CO_2 laser; and how these latter might vary for alternative systems. For a laser design to be considered generic, its principal

design parameters should be representative of those parameters thought desirable of a laser fusion laser. They should also be indicative of the parameter ranges exhibited by the various potential laser candidates. On this basis, the SOLASE laser, although based on CO_2, can be considered a generic laser design.

One simple but important aspect in which the SOLASE laser is representative is that it is a flowing, gas laser which will be essential for heat removal. The principal operating parameters of the SOLASE laser such as the electrical efficiency (9.5%), the applied voltage (666 kV), the current density (15 A/cm^2), the pumping time (0.67 μs), the gain (0.04/cm), and the pressure (1800 torr) all tend to be in the parameter range that one would expect of a fusion laser. These operating parameters are also generally within the range of parameters assumed by the various potential laser systems. In addition, the final energy density of the SOLASE laser is limited by optical damage thresholds as will be the case for other laser systems. Thus, the final electrical and mechanical parameters of the SOLASE laser should not be dramatically different from those indicative of a laser fusion laser.

Unlike the electrical and mechanical aspects, an optical system designed specifically for a CO_2 laser could be quite different from a design for lasers with shorter wavelengths. For this reason (among others) the wavelength was not specified in the SOLASE design and the optics were analyzed parametrically where possible. The front end of the laser

design, however, was discussed specifically with respect to a CO_2 laser, but because a given component in general will function correctly only for a specific wavelength and all systems will require analogous components, the front end design can also be considered generic. In addition the triggering and timing requirements will be similar for all systems.

The optimum pumping processes will vary for the different lasers. The SOLASE laser is pumped by an electron-beam-sustained discharge with the primary alternatives being electron-beam pumping, flash pumping, and simple or uv-preionized discharge pumping (lasers can also be pumped chemically but the reaction is generally initiated by one of the above methods). The principal differences between these include the method by which the energy is delivered to the load, the characteristics of the load, and the time interval over which the energy must be delivered. Thus, detailed designs depend on the specific laser chosen but the general power supply characteristics should be roughly equivalent in all cases. However, the fact that the SOLASE laser is discharge pumped virtually dictates that the amplifier aperture be annular while electron-beam or flash pumping could conceivably retain the more conventional circular apertures.

One major aspect of the SOLASE laser that tends to be specific to CO_2 lasers is the multi-passing technique used to increase the efficiency of the laser. This technique will be limited, in part, to laser systems in which the upper laser level is selectively pumped by collisional-excitation-transfer. In such systems the collisional pumping will be too slow to contribute to the lasing during the nanosecond time scales required for laser fusion. Thus, multi-passing could be beneficial in such systems. However, multi-passing can also be beneficial in a quite different laser system: the HF chemical laser, which is another principal candidate for a fusion laser. In this case, multi-passing is useful not because of collisional pumping but because of the relatively slow rate of the chemical reaction that pumps this laser. Because of the finite reaction rate, the HF pulses are usually at least 20 nsec in length. With some difficulty the pulse widths could be reduced to a limiting value of about 5 nsec, which is currently thought to be too long for laser fusion applications. Thus, in order to obtain maximum efficiency from the HF laser, one must extract, not a single nanosecond pulse, but a series of successive nanosecond pulses for the duration of the natural pulse width of the laser. This would best be accomplished by the multi-passing technique[16] as discussed for CO_2 but, unlike CO_2, there would be no delay between successive pulses - each would immediately follow the previous one. It should be pointed out that HF being a high gain laser is more suited to multi-passing than CO_2 because a larger fraction

of the pumping volume could be extracted for equal sized systems.

Since multi-passing is applicable to two of the possible laser candidates for laser fusion and since it could find application in various brand X lasers, we feel that multi-passing techniques were definitely worth our consideration for the SOLASE design. However, since multi-passing will not be applicable to all laser systems, the difference between multi-passed and single-passed systems should be discussed. One major difference will be the size and/or number of final amplifiers required. If the output per beam is the same in the two systems, the single pass system will require four times as many amplifiers (a total of 24). This number could be reduced to 12 amplifiers (the minimum number required for 12 beams on target) by increasing the size of the amplifiers but this is still twice as many as in the multipass design. Thus, there will be a trade-off in capital costs because the single pass system will require additional space to house a larger number of amplifiers but will not require the long distances necessary to separate beams in a multipassed system. Another difference is that the optical layout of the multipassed system should be relatively more complex, but this should not be a limiting factor.

A final point should be made concerning multipassing. For CO_2, multi-passing offers a simple method of increasing the laser's short pulse extraction efficiency from only 2-5% to 10% or greater. In other systems for which multipassing is inapplicable there will be no general way of

significantly increasing a laser's efficiency. Thus, a reactor may have to be designed for a 1 or 2% efficient laser if the laser-pellet interaction physics requires a specific laser to be used. Because of the vast differences in economic and pellet design criteria implied in raising the laser efficiency from 2 to 10%, this is probably the most critical area in which the SOLASE laser design cannot be considered generic.

Thus, in general the SOLASE laser design characteristics are representative of most lasers that might ultimately be utilized for laser fusion. In this sense the SOLASE laser can be considered a generic design.

VIII-B-10. Conclusions of Laser Design

In this section we presented a "generic" design of a laser fusion laser - specifically a design that meets the parameters dictated by the SOLASE reactor design. The laser design was based on the parameters of a CO_2 laser. The laser is a flowing-gas laser that is pumped by an electron-beam-controlled discharge. The final amplifiers have an annular configuration and are multipassed to improve efficiency.

It was not the purpose of this study to give complete and detailed design of the laser system but only to design a laser in sufficient detail to help identify problem areas requiring further research and to help assess the likelihood of developing such lasers. As a result of this approach, the actual SOLASE laser design tends to be optimistic in that in many respects it represents the best achievable performance that one could

expect from a CO_2 laser. While such a performance is possible, in practice the performance would probably be degraded somewhat by the failure to completely eliminate such problems as parasetics, non-uniform excitations, and density gradients (shock waves) in the amplifiers. However, in order to have a practical and economic laser one would desire that the laser operate as close to optimum as feasible and in addition if many problems are not largely eliminated the system will fail to function as a laser fusion laser. (For example, failure to eliminate prepulses could result in the destruction of the target prior to the arrival of the main pulse). Thus, it can almost be considered essential that a laser operate near its optimum potential.

Our studies indicate that there are lasers that could be scaled to meet basic laser fusion requirements of energy on target (1 MJ), peak power (1000 TW), and pulse width (1 nsec FWHM). In general, problems although difficult, do not appear insurmountable but because solutions are usually specific to a given laser system, no absolute statements can be made. The laser, however, may be required to meet other criteria which are dictated by pellet physics and reactor design: namely, the pulse shape, the wavelength, and the efficiency. The pulse shape can be tailored to some degree but only with difficulty and usually the tailored pulse will only approximate the designed shape. The wavelength, in general, can be varied but only at the cost of significantly reducing the net laser efficiency. There is essentially nothing that can be done to significantly improve a laser's efficiency except in special

cases where multipassing techniques might be effective. Thus, any innovations in pellet design and/or reactor design (such as hybrid reactors) that relax these three requirements will greatly improve the probability of developing a suitable laser.

The principal problem areas appear to be optical isolation; non-uniform excitation; pulse shaping; and shock and turbulence suppression. These problems will be encountered to some degree in scaling all laser systems. Thus, research should continue in these areas, although it should be emphasized that solutions will in general be specific to a given laser system. It would also be desirable to experimentally investigate the concept of multipassing both CO_2 and HF laser systems. Of course, improvements in both optics and power supplies are also essential to the development of a successful laser system and are discussed elsewhere in this report.

To conclude, it appears in general that the problems to be encountered in scaling a laser are difficult but not insurmountable. The probability of developing a suitable laser will depend critically on the efficiency, wavelength, and pulse shape requirements imposed on the laser.

References for Section VIII-B

1. W. L. Nighan, "Electron Energy Distributions and Collision Rates in Electrically Excited N_2, CO, and CO_2," Phys. Rev. A, 2, 1989-2000 (1970).

2. B. J. Feldman, "Short-Pulse Multiline and Multiband Energy Extraction in High-Pressure CO_2-Laser Amplifiers," IEEE J. Quantum Electron, QE-9, 1070-1078 (1973).

3. W. T. Leland and M. Kircher, "The Relation of CO_2 Discharge Kinetics to the Efficiency of Short Pulse Amplifiers," LA-UR 74-637, Los Alamos Scientific Laboratory (1973).

4. "Laser Fusion Program at LASL," LA-6510-PR, p. 24 (1976).

5. T. Ganley, private communication.

6. L. M. Frantz and J. S. Nodvik, "Theory of Pulse Propagation in a Laser Amplifier," J. Appl. Phys., 34, 2346-2349 (1963).

7. J. B. Trenholme and K. R. Manes, "A Simple Approach to Laser Amplifiers," UCRL-51413, Lawrence Livermore Laboratory (1972).

8. "Laser Fusion Program at LASL," LA-6510-PR, p. 15 (1976).

9. "Laser Fusion Program at LASL," LA-6510-PR, p. 35-36 (1976).

10. A. J. Alcock, P. B. Corkum and D. J. James, "A Simple Mode-Locking Technique for Large Aperture TEA CO_2 Lasers," Appl. Phys. Lett., 30, 148-150 (1977). A. J. Alcock, P. B. Corkum, D. J. James, and K. E. Leopold, "Injection Mode-Locking of a Multi-Atmosphere TEA CO_2 Laser," IEEE J. Quantum Electron, QE-13, 89-91 (1977).

11. "Laser Fusion Program at LASL," LA-6510-PR, p. 48 (1976).

12. "Laser Fusion Program at LASL," LA-6510-PR, p. 44-47 (1976).

13. "Laser Fusion Program at LASL," LA-6510-PR, p. 49 (1976).

14. K. Boyer, D. B. Henderson, and R. L. Morse, "Spatial Distribution of Ionization in Electron-Beam-Controlled Discharge Lasers," J. Appl. Phys., 44, 5511-5512 (1973). D. B. Henderson, "Electron Transport in Gas Discharge Lasers," J. Appl. Phys., 44, 5513-5516 (1973).

15. C. E. Thomas and L. D. Siebert, "Pulse Shape Generation for Laser Fusion," Appl. Optics, 15, 462-465 (1976).

16. "Feasibility Study Relating to the Use of High Gain Lasers, Particularly HF, in Controlled Fusion Applications," SAND 76-0094, Sandia Laboratories, p. 103-107 (1976).

VIII-C. Power Supplies for Laser Fusion Lasers

VIII-C-1. Introduction

The laser power supply system represents one of the most critical components of the entire laser fusion reactor system. State-of-the-art power supply systems cannot meet the requirements that will be imposed by a laser fusion reactor. Major advances must be made in several areas before a practical, economic system can be developed.

Generally, the power supply system will consist of three primary components - a D.C. power supply, an energy storage unit, and switches to transfer the energy from the store to the load. The D.C. power supply's function is to charge the main energy storage unit. The energy storage unit will generally be a large capacitor bank for laser applications. Its purpose is to store a large amount of energy that can be rapidly transferred to the load - in this case the laser medium. The switches, of course, serve to prevent transfer of energy from the capacitor bank to the load until desired and then pass this energy as efficiently as possible.

The type of system that will be utilized will depend on the type of laser chosen. Some lasers, such as HF would probably best be pumped by electron beams. Others would use more conventional supplies for simple discharge pumping or the operation of flashlamps. The CO_2 laser operates best with a combination of the two: an electron-beam-sustained discharge.

The performance requirements for the power supplies are quite severe. The power supplies will have to deliver, depending on the particular laser, about 10-100 MJ per pulse with an output voltage of ~ 0.1-2 MV

in ~ 0.01-10 μs and at repetition rates of 1-30 times per second. They must also be reliable and have lifetimes equivalent to about a years operation: that is, 10^8 to 10^9 shots.[1-3] To date, large energy, short pulse supplies have been designed for single shot experimental applications. In these systems, state-of-the-art components, such as capacitors and switches, have lifetimes of 10^4 to 10^6 shots[2-6] which are completely adequate for experimental work but would last only on the order of hours at repetition rates required for laser fusion. Use of these components would certainly result in excessive maintenance costs and probably excessive reactor down time unless very redundant systems were utilized. In addition to having a long lifetime, the system must also be reliable: that is, it must have a high probability of functioning as designed on every shot. For example, in order to be reliable, the switches must have a very low prefire probability ($<10^{-6}$) to prevent an excessive number of prefires. As with lifetime, improvements in reliability will be required, particularly with regard to the reliability of large arrays of components.

One reason that components fail to meet laser fusion requirements is that there has been no previous application having such performance requirements and therefore the problems encountered have not been thoroughly addressed. For this reason, one could expect significant improvements in the future, but the problems are difficult enough that the solutions will not come easily. Possible improvements that can be made in capacitors and switches will be discussed in sections VIII-C-3 and VIII-C-4. General design considerations are discussed next in section VIII-C-2.

VIII-C-2. General Supply Design Considerations

In order to meet laser fusion design requirements, the lifetimes of the components must be improved. To obtain reasonable performance will require increases in lifetimes of 2 to 4 orders-of-magnitude[1-6] in many cases. The problem is actually greater than just developing individual components with lifetimes of 10^8 or 10^9 shots because the entire system, consisting of many thousands of components, must exhibit an overall lifetime and reliability of this order which will be much more difficult to obtain. It is probable that the system may suffer from relatively frequent failures. Thus, the power supply system should be designed to minimize the consequences of a failure.

One unfortunate characteristic of low-inductance, repetitively-pulsed supplies is that a failure of one component can be rapidly propagated to other components.[7,8] Thus, a small repair job rapidly becomes a large repair job. By modularizing the system (that is, each power amplifier is supplied not by one large capacitor bank, but by several smaller, isolated ones) a failure will remain relatively localized. Also fuses should be incorporated where possible to protect remaining circuitry.

Modularization should also allow repairs to be "hotworked" on a given module while the rest remain on-line. This is particularly advantageous if the plant can operate at reduced capacity while repairs are being made. To be successful, this would require that the pellet give a satisfactory, although reduced yield when the laser's energy has been decreased due to the loss of a module. If, on the other hand, there is a threshold effect that decreases the pellet yield to essentially zero with a reduction in

laser energy, then economics may dictate that the laser system be shutdown during repairs. In either case, it is desirable to have designed a system that maximizes the ease of repair.

Unless extremely reliable and long-lived systems are developed, the ability to rapidly detect faults will also be essential. The more rapidly a fault can be detected, the sooner a module can be shutdown to prevent fault propagation and to make repairs. The on-line detection of weak or faulty components will be difficult and will require the development of sophisticated monitoring systems.

Redundancy must also be considered in designing a system. The extent to which the system is made redundant can vary widely. At one extreme, the entire laser-power supply system could be duplicated; at the other, for example, packages of switch arrays could be developed that could properly function even with the failure of one or two switches within the package.[9] The reliability and repairability of a given power supply system must be carefully evaluated and weighed against the increased capital costs and complexity of adding redundancy to the system.

VIII-C-3. The Capacitor Bank

The capacitor bank represents an area in which major improvements must be made in order to have a practical, repetitively pulsed system. Most high energy, high power capacitors have been designed for single shot, experimental applications for which lifetime ratings of 10^3 to 10^5 shots are generally more than adequate. Indeed, much effort has been made to develop cheaper capacitors at the expense of derating their life-

times when available capacitors are overrated for a given application.[4,5] However, such capacitors would last only on the order of an hour when pulsed at 20 times per second. Even if these capacitors could be rapidly exchanged and the materials readily recycled - as would probably be desirable in any case - doing so on an hourly basis is clearly unreasonable: the lifetimes of the capacitors must be extended considerably.

Conventional capacitors generally consist of a series of aluminum foils, which are separated by a dielectric material.[10] One of the most successful dielectrics to date has been kraft paper which has been impregnated with castor oil.[11] A cut away drawing of a typical high energy, high power capacitor is shown in figure VIII-C-1. Failure of the capacitor occurs when the dielectric breaks down, no longer standing off the voltage between the plates. Aside from manufacturing defects, failures are a result of electrical and thermal stresses which cause deterioration of the dielectric. As one reduces these stresses the lifetime of the capacitor should increase accordingly. Thus, it is worthwhile to examine the sources of the various stresses.

The electrical stresses are a result of the large voltage differentials that exist between foils. A schematic of the foil construction for the capacitor is shown in figure VIII-C-2a. A deficiency of this design[3] is that the voltage difference between foils (a,b) along the dielectric surface (the margin) is twice that between foils separated by the dielectric (a,a'). This creates a corona along the surface which can carbonize the surface until breakdown occurs. Significant electrical stresses also result from voltage reversals or ringing of the capacitors. The greater

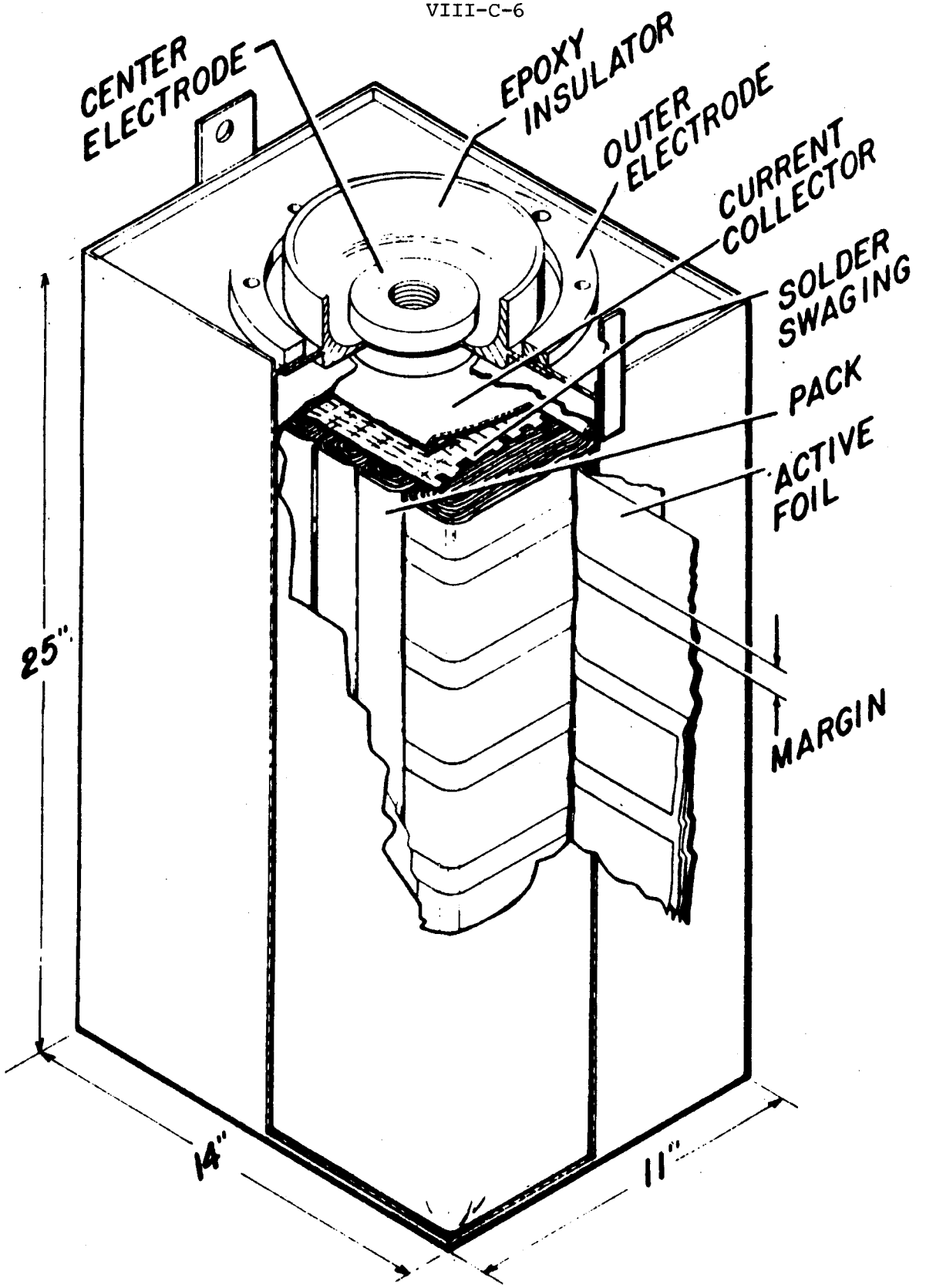

Fig. VIII-C-1.

Schematic of a typical high voltage capacitor (After Ref. 10).

FOIL PLACEMENT IN CAPACITORS

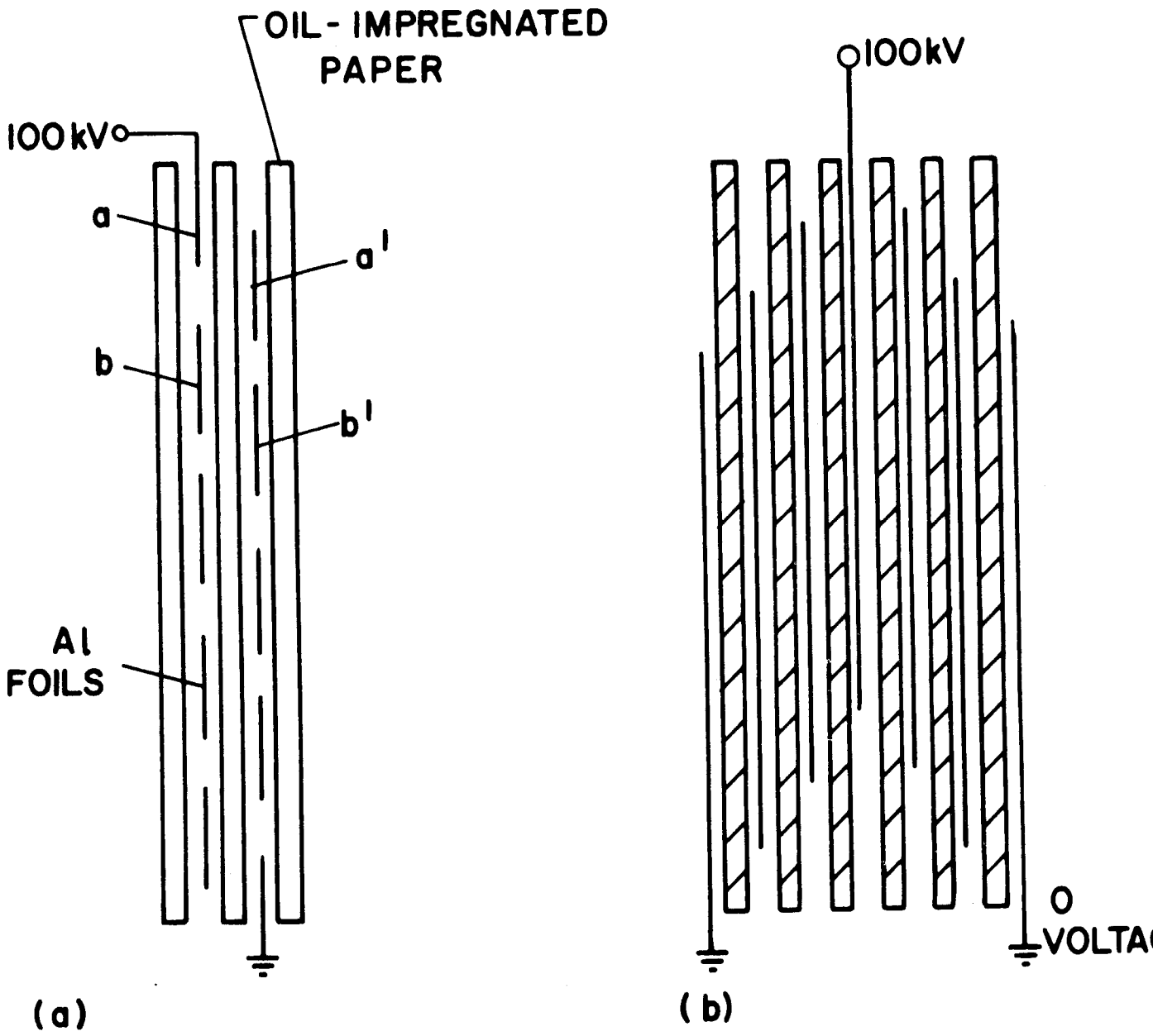

Fig. VIII-C-2.

(a) Schematic of typical capacitor foil placement.
(b)Schematic of proposed foil placement for improved capacitor performance. (After Ref. 3)

the voltage reversal a capacitor routinely experiences, the shorter will be its life.[7] Another source of stress is the phenomenon of "current crowding".[3] This results when a number of foils are connected in parallel to a single busbar as depicted in figure VIII-C-3a. Since the current is always conducted on the external surface of a conductor, the current from each foil must find its way to the external surface of the busbar. This results in "tortuous" current paths and high, localized currents, a combination which produces large magnetic stresses in the capacitor. These large currents also cause increased thermal stresses in the capacitor. In addition to these thermal stresses, the normal heating of the capacitor during operation reduces the life of the capacitor. Obviously to improve the life of a capacitor one must reduce the stresses, improve the resistance of the materials to stress, or perferably do both.

It is possible that improved dielectrics will be found that will allow greater operating stresses and temperatures, but it seems unlikely that improved materials alone could result in a 3 or 4 order of magnitude increase in the lifetime that is desirable. Thus, a major effort must be made to reduce the stresses in the capacitors in order to significantly prolong their life.

The electric stresses in a capacitor increase as the operating voltage approaches the rated voltage of the capacitor. Thus, reducing the operating electric field relative to the maximum allowable field will increase the lifetime of a capacitor. However, since the energy storage density is proportional to the square of the electric field, reducing the electric field will require increasing the volume of the capacitor for a

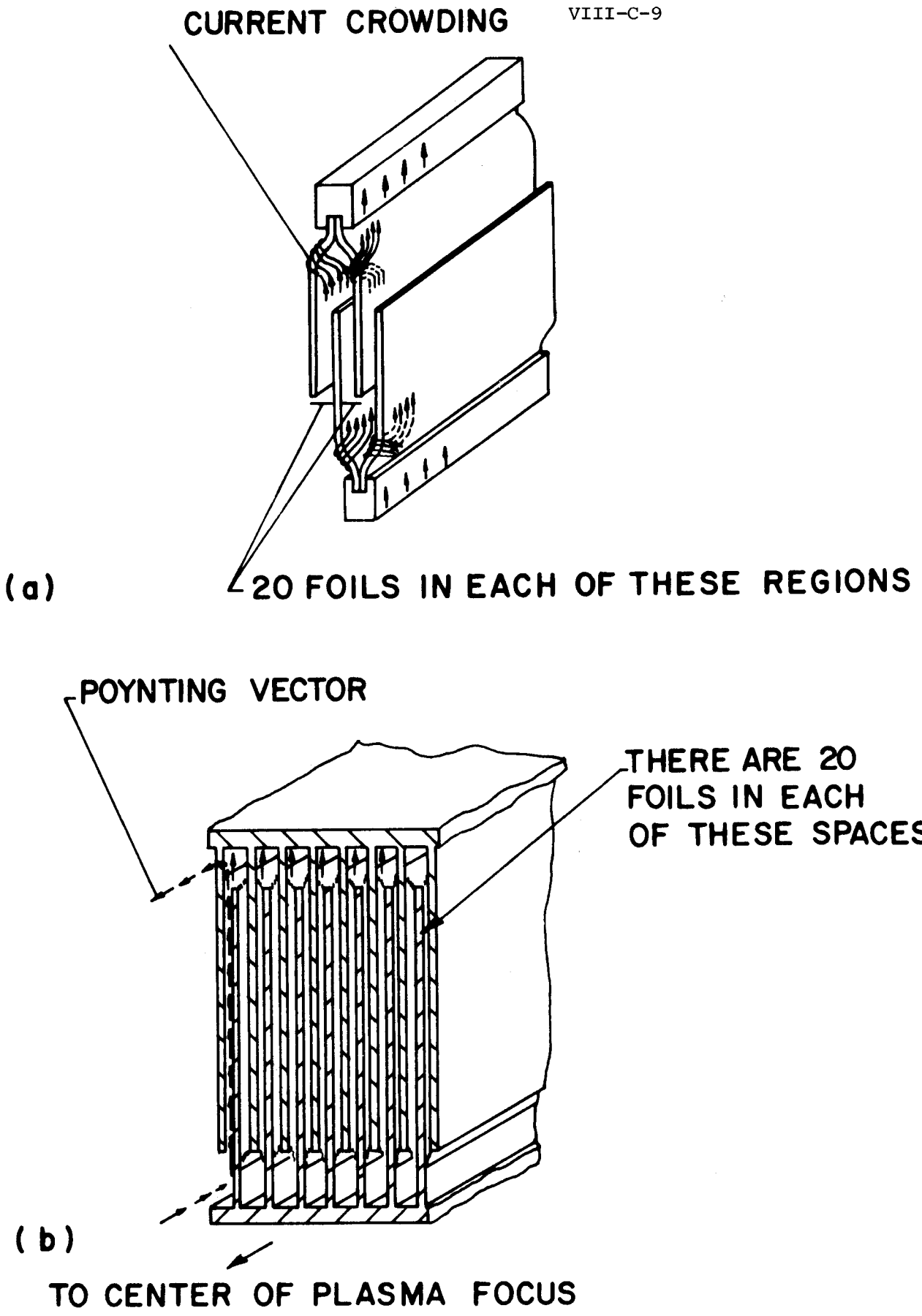

Fig. VIII-C-3.
(a) Schematic of Current Crowding in a Typical Capacitor.
(b) Schematic of improved Foil-busbar Connections
to Eliminate Current Crowding. (After Ref. 3)

constant total stored energy. This has two disadvantages, it increases capital costs and increases the difficulty of designing a low inductance system, but this increase in volume will probably be essential for a sufficiently long lived system. The maximum allowable field[3] between foils is about 4 kV/mil. At this value the surface stress corona will carbonize paths across the margins eventually shorting out the capacitor. Reducing the field to 1 kV/mil eliminates the corona but requires a 16 fold increase in volume for constant total energy.[3]

The stresses can also be reduced by redesigning the foil placement as suggested by O. Zucker et al.[3] Their design, shown in Fig. VIII-C-2b, is a variation of the previous staggered foil design (Fig. VIII-C-2a) in which all foils are separated by a dielectric sheet. This design not only will reduce stresses and edge effects but also should have greater volume efficiency.

O. Zucker et al.[3] have also addressed the current crowding problem discussed above and have offered an improved design as shown in Fig. VIII-C-3b. In this design the electromagnetic energy must exit through the dielectric material. Since there are no multifoil connections there can be no current crowding. They have also suggested that the foils that are connected to either the upper or lower plate be thicker than the remaining foils to allow stronger connections.

A final method of reducing electrical stresses is to minimize ringing in the capacitors. If ringing can be minimized or entirely eliminated for normal operation, the lifetime will be greatly increased.

The remaining consideration is the reduction of thermal stresses in the capacitors. The elimination of current crowding as discussed above helps to prevent localized hot spots but does not reduce normal resistive heating of the capacitors. It has been determined for some capacitors that for every 10°C temperature rise above the rated temperature the lifetime is cut in half.[5] This strongly suggests that active cooling of the capacitors will be necessary. To facilitate cooling, the capacitor should be designed with a large surface area to volume ratio and probably not be "canned". Instead the capacitors will be suspended in an oil bath. This oil can then be flow around and through the capacitors to remove the heat. Such a design should also facilitate the recovery of spent capacitor materials. (Recycling the capacitor materials where possible will probably be desirable as the materials comprise about 50% of the capacitor's costs.[5])

A final item should be emphasized with respect to capacitor failures. There are two periods in the life of a capacitor during which the probability of failure is high: at the very beginning of their life and toward the end.[7] The initial failures are due primarily to material and manufacturing defects and the latter to the wearing out of the materials. The early failures can be largely avoided by maintaining a strong quality assurance program in the manufacture of the capacitor and by conducting power "burn-in" tests on the capacitor. This test consists of subjecting the capacitor to conditions similar to or exceeding the normal operating conditions in the reactor for a specific length of time. If a capacitor has a manufacturing defect the capacitor will generally fail during such a test. Of course, testing every capacitor would prove very costly and probably impractical as well. However, if a satisfactory quality assurance

program exists, the testing of selected capacitors should be sufficient to determine whether to accept or reject a "batch" of capacitors. In this manner the unnecessary failures due to manufacturing defects should be avoided and the capacitors actually utilized in the reactor can be expected to have normal lifetimes.

A number of suggestions have been made which should improve the life of a capacitor. Until such capacitors are built and tested, no estimate can be made of the increase in the lifetimes that could be expected. Clearly the lifetime versus replacement costs must be looked at carefully in determining the economic viability of the plant.

VIII-C-4. Switching

The performance requirements for the switches are very severe. Depending on the laser system, they must be capable of standing off hundreds of kilovolts to several megavolts, and then on command conduct currents upwards of mega-amperes with essentially no resistance. All this must be done at repetition rates of 1-30 pps. Another requirement is that it must have low inductance to allow fast risetimes (1-10 nsec). Often in large systems, switches must be combined in parallel and/or series to meet these requirements. This adds another requirement - that a system of switches can be triggered synchronously. A final requirement is that they have sufficiently long lifetime and reliability to make an economical, practical system.

Conventional switches such as thyratrons which have found application in pulse systems such as radar power supplies can handle neither the voltages nor the power that will be necessary.[3] Instead spark gap switches have generally been employed in high voltage, high power applications and until recently, spark gaps were the only switch that could operate at such levels

with sufficiently short risetimes. However, there are now semiconductor switches that have overcome previous deficiencies and have become more suitable for such applications.

VIII-C-4-a. Spark Gaps

A spark gap switch consists simply of two electrodes that are separated by a dielectric medium. It is closed by formation of arc between the electrodes. Thus, the dielectric must be able to stand off the required voltage and then, on command, be capable of conducting the current with little impedance. Solid, liquid, gaseous, and vacuum dielectric mediums have all been successfully utilized. Also there are a number of successful methods for initiating conduction: over-volting, field distortion, and laser triggering. The difficulty has not been the initiating conduction in the spark gap but doing so with as little as 1 nanosecond of jitter which will be required. Success has been found for both the field distortion and laser triggering methods. In field distortion triggering, a large voltage pulse is applied between one of the two main electrodes and a third trigger electrode. The resulting change in the electric field patterns causes the gap to break down.[12] In laser triggering, a high energy laser pulse is focused in the gap creating an ionization path leading to break down.[13] There may also be a surface electrode effect as the laser vaporizes and ionizes a portion of the electrode at which it is aimed. Both field distortion and laser triggered spark gaps have been operated with nanosecond jitter times.[12,13]

It is generally felt that lifetimes of at least 10^8 and probably 10^9 shots will be required of the switches for laser fusion applications.[1,2] This greatly exceeds the lifetimes of state-of-the-art spark gaps. Spark gaps that carry currents of about 100 kA (a level desirable for laser

fusion[1,2,14]) currently require maintenance every 10^4 shots.[2,3] Spark gaps that switch at an average power level comparable to the levels expected for laser fusion applications but having much lower peak currents (~20kA) have exhibited lifetimes in excess of 10^6 shots.[6] Prefire probabilities must also be reduced. Spark gaps typically used in state-of-the-art electron beams have prefire probabilities[15] of about 10^{-4}. This probability should be lowered to about 10^{-6} for a reliable system. Thus, substantial improvements must be made if spark gaps are to perform satisfactorily.

One of the most serious problems appears to be the erosion of the electrode material due to the high currents being switched. Some erosion can be tolerated but eventually the gap will no longer function as designed. Another problem occurring in spark gaps is that of prefires in which the gap breaks down prior to the desired time. Prefires can result from two causes: flashovers in which arcing occurs along the housing of the gap and "whiskers". Whiskers are small needle like formations on the electrodes created by the intense fields and at whose end points even more intense fields exist leading to premature breakdown. Flashovers are a problem not only because the switch closes at the wrong time and thus wastes energy but because it will generally leave a carbonized path. This increases the probability of future flashovers and eventually results in a sufficiently conducting path that the gap no longer stands off the voltage. In addition flashovers can cause the housing to crack, necessitating its replacement. Maintaining the integrity of the housing in general, will be a problem due to the mechanical and electrical stresses imposed.

There are many possible improvements that could be made to extend the life of a spark gap. It is possible that a better electrode material will be found that would greatly reduce the erosion rate. However, as with the capacitor it is doubtful that a material improvement alone can be expected to extend the life sufficiently - other improvements must be found. For example, it may be possible to automatically replenish electrode material as it is consumed. This could be simply a large rotating electrode[3] of which only a small area is conducting in any given pulse or some more exotic method of continually or periodically rebuilding the electrode. An example of the latter might be to make the electrode porous and force a liquid such as water through the electrode to form a thin film.[16,17] It is this renewable film that will primarily be vaporized, preserving the actual electrode material. This will also tend to cool the electrode, further reducing the erosion rate. It should be pointed out that some form of active cooling will be essential in repetively pulsed systems.

Reducing the prefire probability may be accomplished in many ways. One is to simply reduce the operating voltage with respect to the self breakdown voltage, but this may increase the jitter. Flashovers can also be reduced by keeping the insulting housing walls clean. Debris from the electrodes frequently deposits on the housing walls, resulting in a conducting path being formed and increasing the probability of a flash-over. Thus, decreasing the erosion rate will help to reduce flashovers. Also the addition of spatter shields that protect the housing walls from direct deposition of erosion products have proven beneficial.[6] If

gaseous or liquid dielectrics are used, they can be rapidly flowed. This will help to remove debris and cool the electrodes. This will also keep the dielectric free of impurities so that it maintains its dielectric strength. It is probable that a method of actively cleaning the gap must also be found.

A different approach to reducing flashovers has proven successful.[12] Instead of having a continuous insulator for a housing, the wall is composed of sections separated by metal rings. With this design currents cannot "track" along the entire length of the housing. Thus, some tracking can be tolerated without resulting in flashovers. Prefires due to whiskers may possibly be minimized by frequently removing them with a chemically active gas or liquid. If a large rotating electrode is used the whiskers could probably be removed mechanically.

It is likely, however, that the most effective way to increase the life of the spark gaps is to increase the number of gaps carrying the load. Since most problems such as electrode erosion will be proportional to the current carried, distributing the load over a larger number of gaps will increase their lifetime. This is indicated by the difference in the lifetimes of the 20 and 100 kA peak current spark gaps discussed above. Of course, increasing the number of gaps increases the complexity of the circuit, the problem of synchronously triggering the gaps, and the cost of the system. However, an increased number of parallel switches would decrease the total inductance of the switches which is advantageous.

Of the various types of dielectric media (solid, liquid, gaseous and vacuum) none are ideal, each having advantages and disadvantages. The

solids have high dielectric constants which allows narrow gap spacings. This is desirable as narrowing the gap decreases the inductance of the switch. However, a solid can be used only once since a hole is punched through it during the pulse. Thus, the solid must be replaced after each pulse. The problem of automatically replacing the spent dielectric should not be insurmountable, but the cost of replacing the solid dielectric 10^9 times a year in each of the 10^3 to 10^4 switches should be carefully examined.

Liquids also have high dielectric constants which also allows for small gap spacings (i.e. low inductance). This is particularly true if the gap is pulse charged. Because of their high dielectric strength, liquid spark gaps can be more compact which would more readily allow incorporation of a large rotating electrode structure than would the larger gaseous spark gaps. A liquid can also be readily flowed, removing impurities and cooling the gap. Liquids have the disadvantage that strong shocks are propagated by the medium which strongly stress the housing. If laser triggering is used these shock waves can crack the focusing lens. In certain cases these shocks can cause intolerable vibrations in the optics of the laser being pumped.

Gases have lower dielectric constants than either liquids or solids and therefore have wider gaps and higher inductances. However, like liquids they can be readily flowed but unlike liquids the shock problems are relatively minor although still present. Expansion volumes can be incorporated into the design to further reduce shocks. To increase the dielectric constant the gas can be pressurized, but this is at the cost of both

pressurizing the gas and designing gap housings to withstand the increased pressures.

Compared to other types, there is little experience with vacuum spark gaps. The inductance will be higher than in other gaps. The recovery time (the time required after a pulse before it can be recharged) should be very short[18] allowing rapid pulsing (~ 1 KHz) but this is not a particular advantage in laser fusion applications where only 1-30 pps will be required. Also erosion rates tend to be higher, since vaporized electrode material must conduct the current.

To conclude, spark gaps have a number of problems that seriously reduce their lifetime. Several improvements have been suggested but the extent to which these will increase the life of the gap is difficult to estimate, but 10^8 shot lifetimes are thought to be reasonably obtainable.[1] It should be emphasized, however, that developing a single switch with a lifetime of 10^8 shots is quite different from developing a reliable system of several thousand switches with a system lifetime of 10^8 shots. Of the several varieties of spark gaps, field distortion and laser triggered gaps with a liquid or gaseous dielectric media appear the most suitable for a laser fusion system.

VIII-C-4-b. Semiconductor Switches

A second class of switches of promising potential are the semiconductor switches. There are a variety of such switches, transistors, thyristors, and silicon controlled retifiers among others. The operation of each of these is similar. In the open circuit state, a p-n junction

is maintained depleted of mobile charge and acts as an insulator. To close the switch, charge is injected into this region in sufficient quantity that the impedance is significantly reduced and large currents can flow. In the past these switches have been able to stand off sufficient voltage and carry sufficient current for our application when used in proper parallel and series combinations, but they have suffered from too slow a risetime. Slow risetimes result in inefficient energy use at best and essentially unusable output at worst. For example, thyristors would take upwards of 100 μsec to turn-on, while we wish to pump the CO_2 laser in only 2/3 μsec.

The slow risetimes are a result of the physics of the turn-on process. Charge must be injected into the depleted region to initiate this process. At first only a small fraction of the area of the switch is conducting (see Fig. VIII-C-4). Only by the relatively slow process of diffusion do the conductors gradually spread over the entire area. Thus, in the initial stages of turn-on, the switch will burn up if one attempts to force the maximum current for which the switch is rated through the small conducting area. There are a number of "tricks" one can employ to increase the initial conducting area and thereby reduce the turn-on time, but all of these ultimately rely on inherently slow diffusion processes. Recently, however, a technique of using a laser to trigger the switch has been developed.[19] In this method, photons from a laser are focused into the switch to generate electron-hole pairs. This, unlike the former methods is a volumetric source producing ionization throughout the switch. Thus, the entire area can be initially conducting resulting in very fast risetimes.

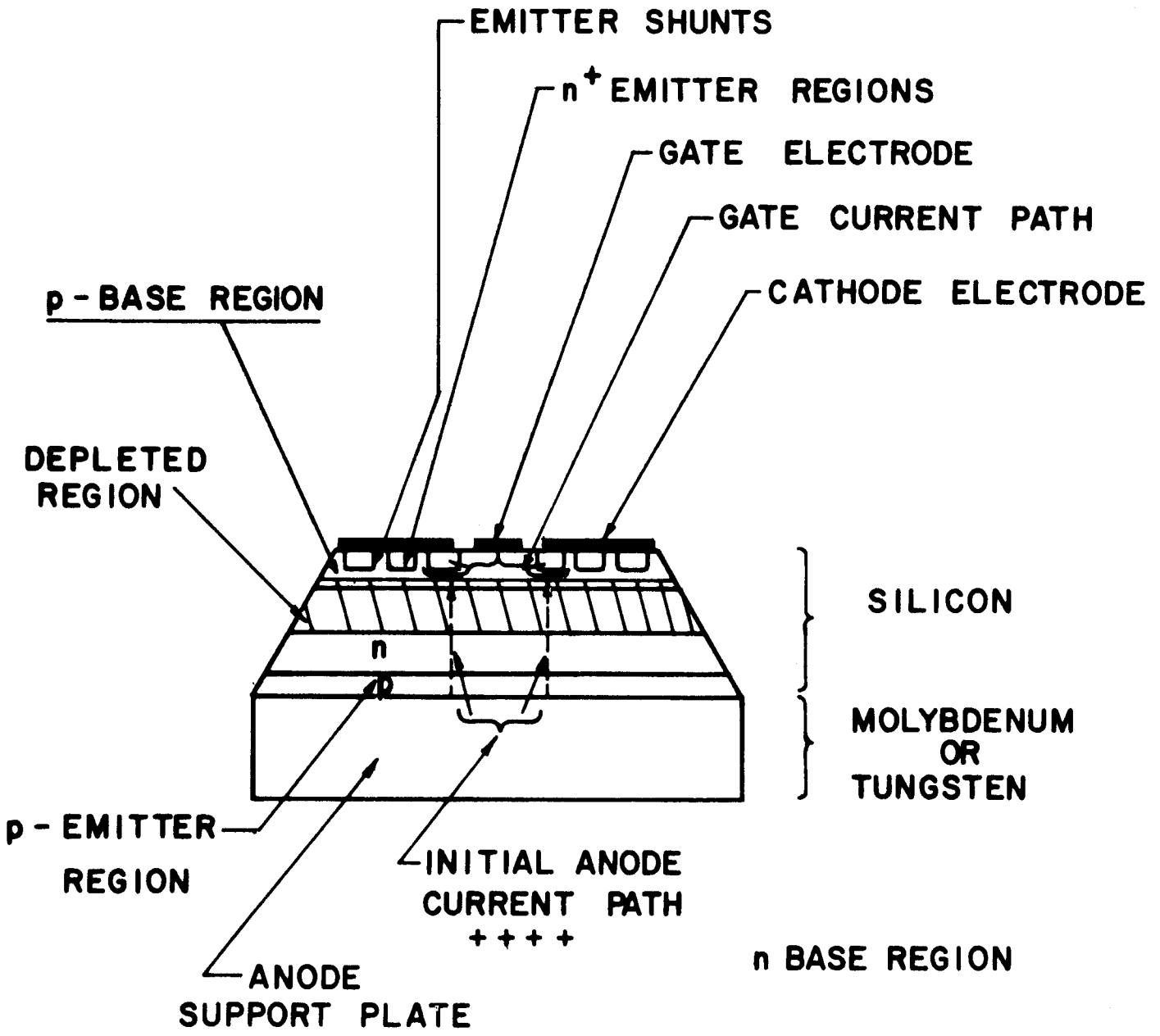

SCHEMATIC OF A SEMICONDUCTOR SWITCH

Fig. VIII-C-4.
(After Ref. 19)

State-of-the-art switches[19,20] can carry currents of about 5 kA and can stand off 1-5 kV. Thus, the switches must be operated in both large series and parallel arrays. In this regard it is desirable to improve the voltage stand-off and current carrying parameters of individual switches in order to reduce the number of components required. Arrays of up to 10 switches in series have been successfully triggered by a laser,[9] but it has yet to be determined if the much larger arrays that will be necessary can be successfully triggered synchronously. It appears that laser triggering will serve both as an isolator separating the trigger from the switch and as an excellent method to synchronously trigger all switches by properly adjusting the path length of the light to each particular switch.

The major advantage of semiconductor switches is their lifetime which should exceed 10^7 shots.[3] This has been verified for slow risetime switches in high power, industrial applications, but not for fast risetime switches. This lifetime is substantially greater than state-of-the-art spark gaps and is approaching a year's operating life at 20 pps. It is thought that semiconductor switch packages can be designed that can both be hotworked and incorporate redundancy so that if one or two individual switches fail the package as a whole will continue to function properly[9] (at least for a certain period of time). A disadvantage of semiconductor switches is that they tend to be expensive. However, overall, this class of switches appears to have great potential in laser fusion applications.

VIII-C-5. General Design of the Laser Power Supplies

In this section we describe the power supply system for the laser of the SOLASE reactor. Detailed electrical circuits will not be presented, but a more general description will be given. However, the specific output parameters that the supplies must deliver will be given.

The most efficient method of pumping a CO_2 laser is by an electron-beam-sustained discharge because the electronic cross sections for the pumping of CO_2 peak at values of E/N (electric field/gas number density) that can only be obtained by providing a source of ionization external to the discharge.[21] The electron beam provides this source. By carefully controlling the e-beam current, the E/N can be adjusted to maximize the pumping efficiency. Another consequence of having this optimum range of E/N values is that only when the applied voltage level is in this range does one get efficient pumping. Thus, energy deposited during the rise-and falltimes of the pulse does not contribute significantly to the pumping of the laser but instead is deposited as heat. This is detrimental in two ways: the energy deposited as heat is not available to excite the laser and the heating of the laser medium reduces the efficiency of the lasing process. Clearly then, the rise-and falltimes of the discharge pulse should be as short as possible to obtain maximum pumping efficiency.

The main energy store for the primary discharge supply could be either a capacitive run down circuit or a pulse-forming network[22] (PFN).

A PFN is generally more efficient, requiring much less energy storage capacity. Also the shape of the discharge pulse can be controlled but generally the greater control required the greater will be the circuit complexity.[22] Los Alamos has had initial success with a Type C Guillemin/Marx network.[23]

In using a PFN, it is important that the PFN be carefully matched to the load. Mismatching can result in decreased energy deposition and degraded rise-and falltimes. A critical element in determining the characteristics of the load is the e-beam. If the e-beam output can be closely controlled, the load can be well characterized and a PFN designed to match it. This criteria tends to eliminate state-of-the-art cold cathode e-beams[22] since they have poor shot-to-shot repeatability. In addition the current pulse is not flat and there is a minimum operating current density which is frequently higher than desirable. However, cold cathode devices are simpler than other types of e-beams, do not require filament currents, require only "soft" vacuums and have been successfully utilized in CO_2 laser systems. Because of these advantages, attempts are being made to minimize the deficiencies by using such techniques as a resistively self-biased grid that would both provide blade ignition voltage and allow low current densities.[23] If this is successful, cold cathodes would become quite attractive.

The principal alternative to the cold cathode e-beam is the grid-controlled, hot-cathode e-beam.[22] This has the advantage of better controlled currents and more desirable current density ranges. Some

disadvantages are that power must be supplied to heat the cathode (although this should be small, relative to the total laser power requirements) and that they require hard vacuums.

Another variety of e-beams are the plasma cathode guns.[22] These utilize a discharge between a hollow cathode and a grid to generate electrons. These devices are in the early stages of development and may or may not prove applicable to large systems. However, state-of-the-art devices require substantially more operating power per unit area than do hot cathodes which makes them less attractive for continuous power applications. Thus, until significant advances in cold cathode systems are made, hot-cathode electron guns appear most suitable for our laser system.

VIII-C-6. Final Amplifier Design

Each of the six final amplifiers will be a segmented annulus, 37 cm thick. The pumping volume will consist of twenty-four 34 x 37 cm sections evenly spaced around an annulus of inner and outer radii of 149 and 186 cm respectively (see Fig. VIII-C-5). The e-beams will be either radial, hot cathode or grid-controlled, cold cathode devices located in the center of the amplifier. Pulse forming networks will provide the primary energy source for the pumping of the laser. Each segment could be operated independently or in small groups of about 2 to 4 segments. The maximum number of segments that could be grouped will be determined by circuit inductance. However, arguments of reliability would

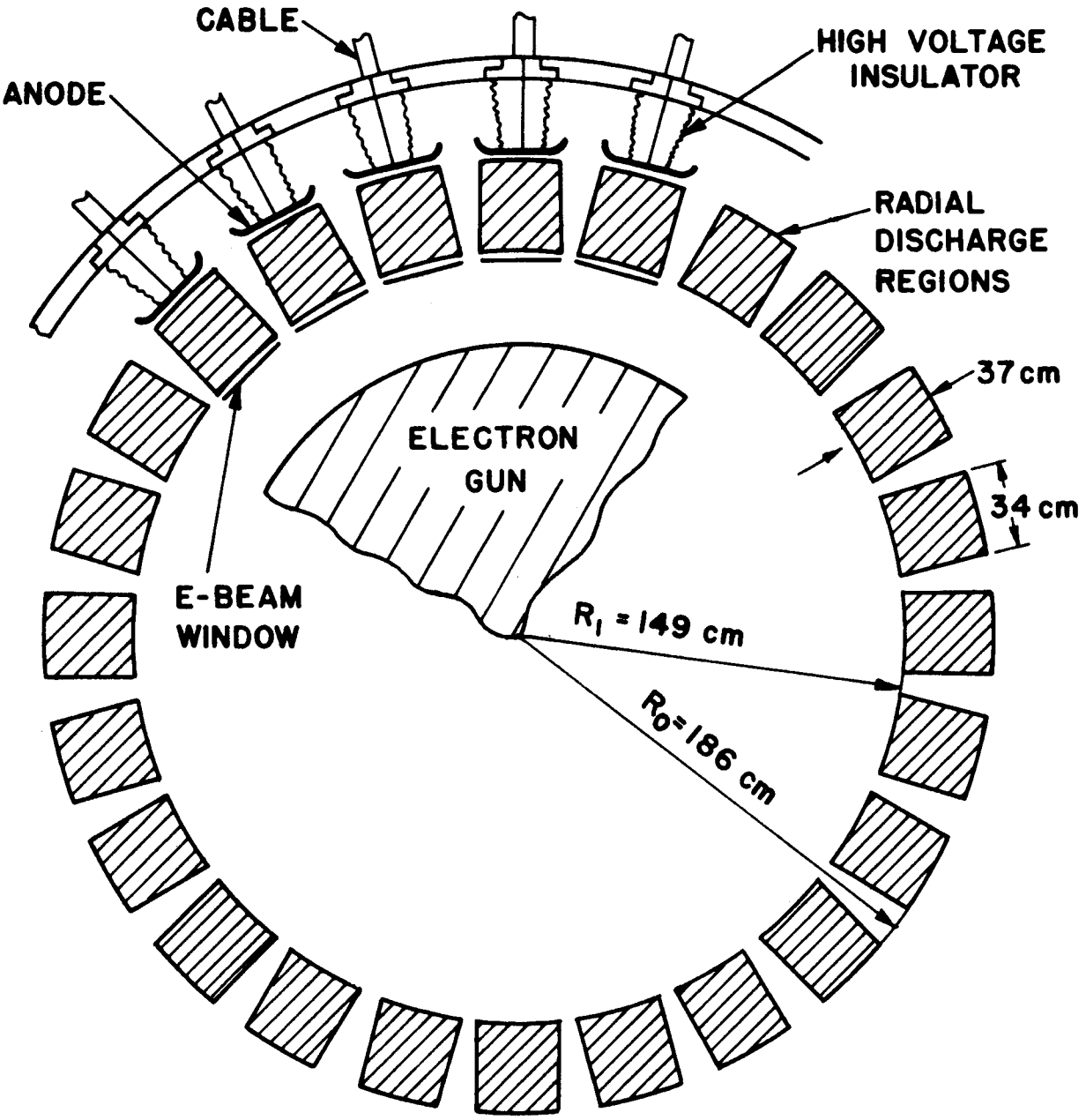

END VIEW OF ANNULAR AMPLIFIER FOR SOLASE

Fig. VIII-C-5.

favor independent operation of the segments so that if a supply fails only 1 segment in 24 would be lost as opposed to say 4 in 24 - the former loss possibly having a less detrimental effect on the pellet yield. It may prove necessary to segment the amplifier along its length as well.

Similar reliability arguments can be made for the e-beams. However, one of the advantages of annular amplifiers is that one e-beam could serve all 24 segments which greatly reduces the number of components and the complexity of the system. Thus, with both the PFN's and e-beams, a careful evaluation of the system's reliability versus the number of individual units must be made in determining the final design.

The power supplies will be designed so that either on-line repairs can be made or so that the entire faulty unit can be replaced by a new unit without shutting down the reactor. The desirability of such a design depends on the ability and practicality of operating the reactor at reduced capacity until the fault is repaired. If feasible, this appears clearly superior to shutting down the reactor. In either case, however, it is desirable to repair a fault as rapidly as possible and the systems should be designed to facilitate repairs as much as possible.

The design of the capacitor bank will incorporate the stress reducing features discussed in Section VIII-C-3 and the capacitors for each PFN will be placed in a bath of oil which will be flowed for cooling. Providing arrays of semiconductor switches with satisfactory risetimes are developed, laser triggered semiconductor switches will be used because of their long lifetimes.

Table VIII-C-1 Power Supply Parameters for the Final Amplifier

Discharge Supply Parameters	Per Segment	Total Amplifier
Electric Field	18 kV/cm	18 kV/cm
Total Applied Voltage	666 kV	666 kV
Current Density	15 A/cm^2	15 A/cm^2
Total Current	0.128 MA	3.06 MA
Pumping Time	2/3 μs	2/3 μs
Total Energy Deposited	56.6 kJ	1.36 MJ
Electron Beam Parameters		
Beam Energy	~ 700 keV	~ 700 keV
Current Density	~ 0.144 A/cm^2	~ 0.144 A/cm^2
Total Current	~ 1.22 kA	~ 19.38 kA
Pulse Width	3 μs	3 μs
Total Energy Deposited	~ 2.52 kJ	~ 60.38 kJ

Table VIII-C-2 Power Supply Parameters for the Next-to-Last Amplifying Stage

Discharge Supply Parameters	Per Segment	Total Per Amplifier
Electric Field	18 kV/cm	18 kV/cm
Total Applied Voltage	234 kV	234 kV
Current Density	15 A/cm^2	15 A/cm^2
Total Current	45 kA	1.08 MA
Pumping Time	2/3 μs	2/3 μs
Total Energy Deposited	7.02 kJ	168 kJ
Electron Beam Parameters	**Per Segment**	**Total Per Amplifier**
Beam Energy	~ 250 keV	~ 250 keV
Current Density	~ 0.144 A/cm^2	~ 0.144 A/cm^2
Total Current	~ 0.43 kA	~ 10.6 kA
Pulse Width	3 μs	3 μs
Total Energy Deposited	~ 0.34 kJ	~ 8.1 kJ

The electrical output requirements for both the PFN's and the e-beams of the SOLASE final amplifiers are given in Table VIII-C-1. The requirements are given on both a per amplifier and per segment basis. Similarly, Table VIII-C-2 gives the power supply requirements for the next-to-last stage of the amplifier chain.

VIII-C-7. Power Supply Conclusions

The power supply system is an area in which major technical advances are essential if there are to be practical and economical laser fusion reactors. Difficulties arise primarily from inadequate lifetimes and reliability of state-of-the-art components. Although capacitors and switches have been emphasized in this report other components such as high voltage cables and electron-beam foils will suffer similar lifetime problems. Since state-of-the-art components are primarily designed for single-shot experimental work, substantial improvements should be possible when lifetime questions are addressed.

The lifetime that will be required depends on several factors including: the repairability of the system, the overall consequences of a failure, and the costs of the components. The exact lifetime required, therefore, will depend on the specific details of a given design, but it will probably be desirable to be able to operate at least a year before major maintenance is required (although the system should be designed to tolerate a few, isolated failures). Thus, the power supply lifetime should be at least 10^8 to 10^9 shots.

The power supplies must also be designed to have high reliability. That is, they must have a high probability of performing as designed on every shot. In particular, the reliability of large arrays of components must be thoroughly investigated.

Another problem that must be overcome is the need to remove the residual heat from the supplies, which will generally require active cooling of the various components. This may or may not prove difficult depending on the component but because state-of-the-art components in general cannot be cooled, designs incorporating active cooling should be developed.

Another area that needs development is that of fault detection. Unless extremely reliable, long-lived supplies are developed, the rapid detection and identification of faults will be essential. This will require the development of rather sophisticated diagnostic tools in order to have an adequate detecting capability.

The power supply system should be designed to maximize the ease of repair and allow hotworking where possible. If the supplies can be modularized, the overall reliability should be improved and any fault propagation should be confined to a relatively small portion of the supply. Of course, designing all components to be as inexpensive, as simple, and as rugged as possible is always desirable.

To conclude it is absolutely essential to develop power supplies that are sufficiently reliable and long-lived but still have a reasonable cost. Without major advances to meet these requirements, it is doubtful that economically viable laser fusion reactors can be built.

References for Section VIII-C

1. "Summary of Workshop Discussions," in Proc. of the Workshop on Switching Requirements and R & D for Fusion Reactors, EPRI ER-376-SR, 1977.

2. K. B. Riepe, "Switching Requirements for Laser Fusion," in Proc. of the Workshop on Switching Requirements and R & D for Fusion Reactors, EPRI ER-376-SR, 1977.

3. O. Zucker, W. Bostik, R. Gullickson, J. Long, J. Luce, and H. Sahlin, "The Design of a Repetitively Pulsed Megajoule Dense-Plasma Focus," Lawrence Livermore Lab., UCRL-51872 (1975).

4. E. L. Kemp, "The Study of Capacitive Energy Storage for a Theta-Pinch PTR Compression Coil," in the Proc. of the Fifth Symposium on Engineering Problems of Fusion Research (IEEE Pub. No. 73CH0843-3-NPS, 1973), p. 303-307.

5. J. R. Hutzler and W. L. Gagnon, "Development of a Reliable, Low-Cost, Energy-Storage Capacitor for Laser Pumping," in Energy Storage, Compression and Switching, ed. W. H. Bostik, V. Nardi, and O. Zucker (Plenum Press, N.Y., 1976), p. 343-348.

6. H. Milde, C. Schubert, and R. Harrison, "Repetitive High Power Switching Technology," in Proc. of the Workshop on Switching Requirements and R & D for Fusion Reactors, EPRI ER-376-SR, 1977.

7. J. Hutzler, G. Dabrowski, M. Young, and W. Lupton, "Reliable Capacitors for Large Energy Storage Facilities," in the Proc. of the Fifth Symposium on Engineering Problems of Fusion Research (IEEE Pub. No. 73CH0843-3-NPS, 1973), p. 466-470.

8. K. Prestwich, "Proposal for Repetitive Rate Technology," prepared for ERDA, Division of Laser Fusion by Sandia Laboratories, May 1976.

9. A. Greenwood, "Technical Approaches to Switching Problems Associated With Fusion Research," Proc. of the Workshop on Switching Requirements and R & D for Fusion Reactors, EPRI ER-376-SR, 1977.

10. G. P. Boicourt, "The Diagnosis of Underdrying in Paper Castor Oil Capacitors," in the Proc. of the Sixth Symposium on Engineering Problems of Fusion Research (IEEE Pub. No. 75CHI097-5-NPS, 1975), p. 336-342.

11. G. P. Boicourt, "Some Properties of Castor Oil Affecting its Performance as a Capacitor Impregnant and Their Significance to Future Impregnant Research," in Proc. of the Sixth Symposium on Engineering Problems of Fusion Research (IEEE Pub. No. 75CHI097-5-NPS, 1975), p. 343-348.

12. S. Mercer, I. Smith, and T. Martin, "A Compact, Multiple Channel 3 MV Gas Switch," in Energy Storage, Compression, and Switching, ed. W. Bostik, V. Nardi, and O. Zucker (Plenum Press, N.Y., 1976), p. 459-462.

13. A. Guenther, G. Zigler, J. Bettis, and R. Copeland, "Laser Triggered Switching of a Pulsed Charged Oil Filled Spark Gap," in Energy Storage, Compression and Switching, ed. W. Bostik, V. Nardi, and O. Zucker (Plenum Press, N.Y., 1976), p. 441-450.

14. I. Smith, "Fast Pulse Switching for Electron Beam and Laser Reactor Concepts," in Proc. of the Workshop on Switching Requirements and R & D for Fusion Reactors, EPRI ER-376-SR, 1977.

15. T. H. Martin, private communication.

16. J. C. Martin, "Million Volt Repetitive Spark Gaps," in Proc. of the Workshop on Switching Requirements and R & D for Fusion Reactors, EPRI ER-376-SR, 1977.

17. O. Zucker, "R & D Recommendations for Future ERDA Switch Requirements," in Proc. of the Workshop on Switching Requirements and R & D Fusion Reactors, EPRI ER-376-SR, 1977.

18. A. Guenther and J. Bettis, "Laser Triggered Switching," in Laser Interaction and Related Plasma Phenomena (Plenum Press, 1971), p. 131-171.

19. D. Page, "Some Advances in High Power, High dI/dt, Semiconductor Switches," in Energy Storage, Compression and Switching, ed. W. Bostik, V. Nardi, and O. Zucker (Plenum Press, N.Y., 1976), p. 415-421.

20. W. L. Nighan, "Electron Energy Distributions and Collision Rates in Electrically Excited N_2, CO, and CO_2," Phys. Rev. A, 2, 1989-2000 (1970).

21. K. Riepe and R. Stapleton, "Electron-Beam-Controlled Gas Lasers: Discussion from the Engineering Viewpoint Part II. Problems in the Electrical Design of Very High Energy Systems," in Proc. of the Fifth Symposium on Engineering Problems of Fusion Research (IEEE Pub. No. 73CH0843-3-NPS, 1973), p. 626-632.

22. K. Riepe and H. Jansen, "Pulsed Power System for the LASL High Energy Gas Laser Facility," Los Alamos Scientific Lab., LA-UR-76-2299 (1976).

Chapter VIII, Appendix -- Beam Extraction From a Multipassed Annular Amplifier

In order to effectively use the technique of multipassing each beam must pass through the amplifier at a slightly different angles (see section VIII-B-4). An inherent result of this is that a single beam will not extract the entire pumping volume. The fraction that will be extracted depends on parameters such as the angle the beam makes with respect to the amplifier, the length of the amplifier, and the relative diameters of the beam and amplifier. This fraction can be estimated using rather simple geometry.

A schematic of the geometry for SOLASE is shown in Fig. VIII-1 of Appendix A. The laser beam and amplifier are annular with inner and outer diameters denoted by w_{bi}, w_{bo} and w_{ai}, w_{ao} respectively. The length of the amplifier is L_a. The angle that the laser beam makes with respect to the central axis of the amplifier is ϕ. Four beams will be passed through each amplifier. At both the input and output these beams must be physically separated so that they can be handled independently. For practicality it is assumed that the beams must separate sufficiently that there is space for optical mountings that are 20% larger in diameter than the beams themselves. The distance between these input/output mirrors is denoted by L_S.

With these definitions the volume fraction can now be calculated. From the figure it can be seen that

$$\tan\phi = \frac{x}{L_a} \quad , \tag{1}$$

$$\cos\phi = \frac{w_{bi}}{w_{ai}+x} \quad , \tag{2}$$

and

$$\cos\phi = \frac{w_{bo}}{w_{ao}-x} \tag{3}$$

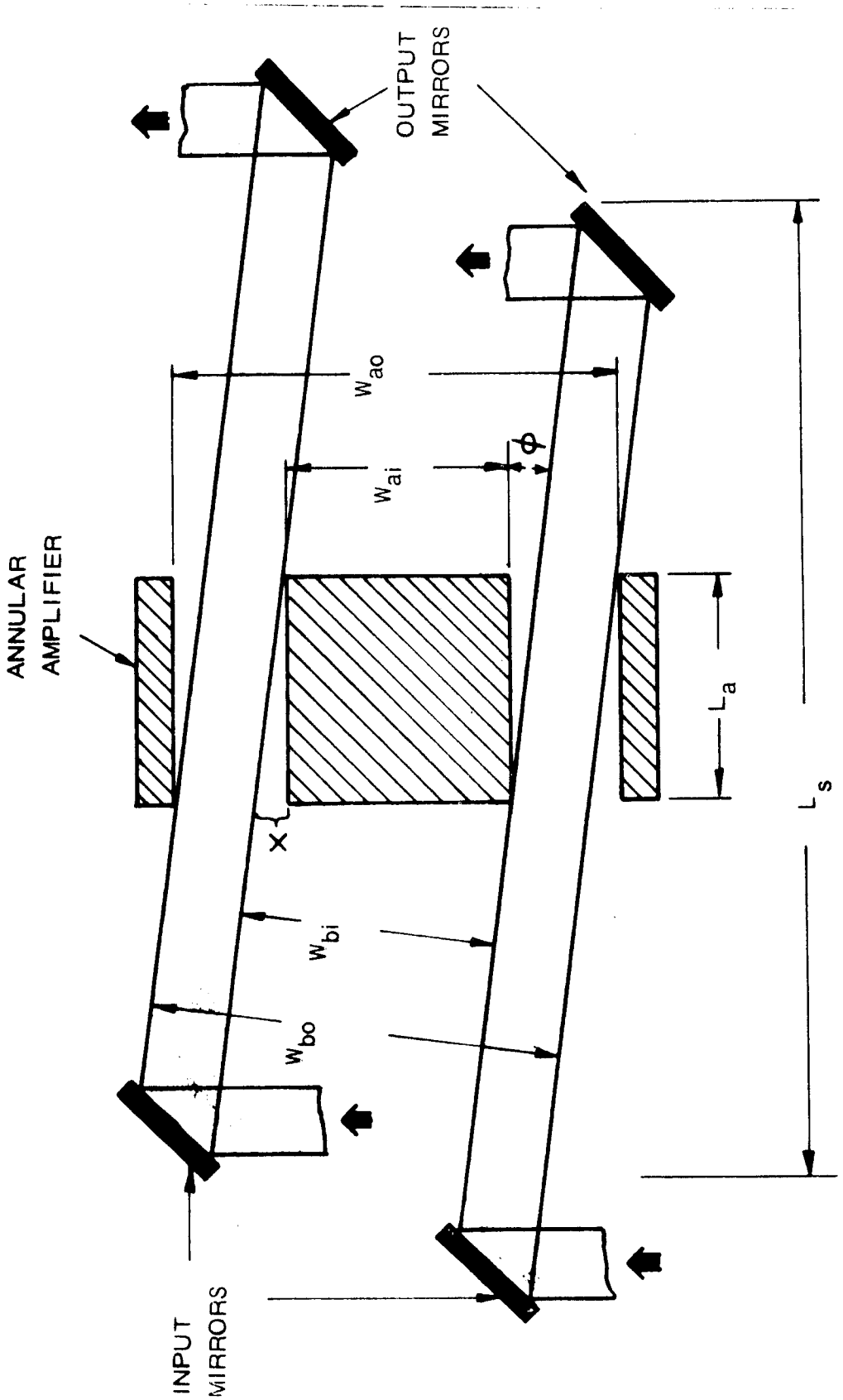
OUTPUT MIRRORS
ANNULAR AMPLIFIER
INPUT MIRRORS
W_{ao}
W_{ai}
ϕ
W_{bi}
W_{bo}
X
L_a
L_s

Fig. VIII-1.

Eliminating the variable x between Eq. 1 and 2 and between Eq. 1 and 3 yields

$$\cos\phi = \frac{w_{bi}}{w_{ai} + L_a \tan\phi} \tag{4}$$

and

$$\cos\phi = \frac{w_{bo}}{w_{ao} - L_a \tan\phi} \tag{5}$$

For small angles, Eq. 4 and 5 reduce to

$$\frac{w_{bi} - w_{ai}}{L_a} \cong \phi \tag{6}$$

and

$$\frac{w_{ao} - w_{bo}}{L_a} \cong \phi \tag{7}$$

From the figure it can also be determined that

$$\tan\phi = \frac{1.7\, w_{bo}}{L_S} \tag{8}$$

where 1.7 is a geometric factor that accounts for separation of the four beams including the optical mountings. For small angles Eq. 8 reduces to

$$\phi \cong \frac{1.7\, w_{bo}}{L_S} \tag{9}$$

Eliminating the angle ϕ between Eq. 7 and 9 yields

$$w_{bo} = \frac{w_{ao}}{L_a} \left(\frac{1}{\frac{1.7}{L_S} + \frac{1}{L_a}} \right) . \tag{10}$$

The beams inner diameter can now be calculated by using

$$w_{bi} = w_{ao} + w_{ai} - w_{bo} \tag{11}$$

Assuming that the size of the amplifier (w_{ao}, w_{ai}, L_a) and L_S are given then the size of the laser beam that can be extracted is readily calculated from Eq. 10 and 11. From these values the volume fraction that can be extracted can be found. Since the volume is proportional to the diameter squared, the fraction extracted is given by

$$\frac{w_{bo}^2 - w_{bi}^2}{w_{ao}^2 - w_{ai}^2} = f_1 \qquad (12)$$

For example, SOLASE has the following parameters: w_{ao} = 372 cm, w_{ai} = 298 cm, and L_S = 100 m. Substituting into the above formulas yields: w_{bo} = 357 cm, w_{bi} = 313 cm, and ϕ = 60 mrad. The fractional volume extracting is then 0.595. This fraction is important in determining the efficiency of the laser.

For SOLASE the annulus of the amplifier is not continuous but is composed of twenty-four 34 x 37 cm segments. Thus, the actual volume extracted will be reduced by an additional factor

$$\frac{24x37x34}{\frac{\pi}{4}\left(w_{ao}^2 - w_{ai}^2\right)} = f_2 = 0.775$$

The total beam area extracted is then

$$\frac{\pi}{4}\left(w_{bo}^2 - w_{bi}^2\right) \cdot f_2 = 17{,}750 \text{ cm}^2.$$

Since only 15,270 cm^2 are necessary for a uniform beam of 3 J/cm^2 to give a total output of 45.8 kJ, the allowable geometric utilization factor is

$$\frac{15{,}270}{17{,}750} = 0.86 .$$

IX. Target Fabrication and Delivery Considerations

IX-A. Present Inertial Confinement Target Requirements

Present inertial confinement experiments are limited to laser and e-beam systems. It is useful to classify the pellets used in these experiments by the type of material used to retain the high pressure D-T fuel mixture. In the majority[1] of neutron-producing laser-induced implosions, including the first,[2] the fuel container material has been glass. In recent experiments polymeric materials,[3] e.g., poly (vinyl alcohol), have been used either as the primary container or as a low-Z coating on the exterior of glass-shell or metal-shell containers.

Shell diameters, shell wall thicknesses, fill pressures, etc., are dictated by the characteristics of available lasers and in particular by available laser power. Primarily because of the latter consideration, total target mass is still < 3 μg. With this limitation the glass targets of interest, i.e., those suitable for producing thermonuclear neutrons, have diameters in the range of 50 μm to 300 μm with walls ranging from 0.5 μm to ~ 5 μm.

The glasses from which these targets are fabricated have in general been either sodium-borosilicates or calcium-sodium-borosilicates. These are chosen because of their high intrinsic tensile strength and high fabricability. In addition, deuterium and tritium will controllably permeate shells of these materials at moderately high temperatures and will be retained by the shells at room temperature for several months with no measurable losses.[4] Because of the laser energy expended in compressing the fuel gases in shells filled to high pressures, the internal fill pressures of target pellets have

not exceeded 130 atm*, although the high tensile strength of the silica glasses presently available will allow fill pressures up to ~ 10^3 atm. Polymer shells, because they are weaker than glass and more permeable at room temperature, are much more difficult to fill with deuterium and tritium at elevated pressures and store than glass shells. These problems have been circumvented to some extent by processing and storing the pellets cryogenically.(5)

Although only small quantities of microshells are needed for present experiments (a typical laser-fusion laboratory can irradiate no more than ten targets per day), considerable effort is required for target fabrication because the microshells selected for targets must be of extremely high quality and extensively and accurately characterized. As a result, from the large numbers of microshells normally produced (10^7 to 10^9 per batch), fewer than ten out of every 10^5 shells have the required dimensions and quality. The yields from commercially available shells are factors of ten smaller than this. Automatic search and segregation procedures have been developed to minimize the labor content and are briefly discussed below.

Shells which are acceptable for laser-fusion experiments are required to be spherical to better than 0.1% (i.e., $\frac{\Delta r}{r} \leq 10^{-3}$) with wall nonuniformities less than 10% (i.e., $\frac{\Delta w}{w} < 10^{-1}$). Although these high quality shells are obtained by relatively low-labor-content procedures, the search for the optimum match of laser and target parameters requires that each target selected for irradiation be accurately characterized geometrically.

---

*Fill pressures are defined as the total pressure of the fuel gases within the shell at room temperature.

Interferometric[6] and radiographic[7] inspection techniques have been developed which allow nondestructive characterization. The radiographic procedure is particularly amenable to computerization and automatic sampling and is now being extended for use as a sampling technique for multilayered reactor pellets.

The current characterized target, when finally presented to the laser, is mounted on a glass or polymeric fiber, 1 μm to 10 μm in diameter, which is in turn attached to a tapered rod. The target is stationed at the focus of the laser beams with a positioning accuracy of better than 10 μm relative to the center of the focal volume. This procedure is obviously unusable in a working reactor but in the current experiments it serves to minimize uncertainties in the uniformity and orthogonality of the pellet illumination. Techniques such as electromagnetic and inertial suspension which will allow levitated pellets to be illuminated are currently being investigated as a preliminary step in developing the rapid pellet injection that will be required in a power reactor.

In addition to these targets, cryogenic pellets (i.e., fueled shells maintained at temperatures at or below 20 K) are of great interest at this stage in the laser-fusion program. Interest stems not only from the expected enhancement of neutron yields from such targets,[8,9] but also from the awareness that since reactor-type pellets may well be cryogenic, the development of the technology should begin as early as possible. Within the last year, cryogenic targets in which the fuel is condensed as a liquid film on the interior surface of glass microshells have been irradiation, and a significant enhancement in neutron yield has been observed.[9,10]

It appears that present technology can be readily extended or modified to solve the problems of fabricating and processing reactor-type pellets. This can best be appreciated by considering the state of the art and its natural extensions as described in the following sections.

IX-A-1. Glass Microshell™* Pellets

Technology capable of producing hollow glass microspheres already existed prior to the earliest laser-fusion experiments. Unfortunately, commercial microspheres, although in a useful size range (20 to 170 μm in diameter and walls 0.4 to 2 μm thick), were mostly too small and too thin and required extensive processing to cull the very few suitable for laser targets. Work on glass-shell fabrication was therefore initiated early in the KMS program with the primary objective of developing techniques to produce an abundance of shells having the utmost uniformity and sphericity and with diameters as large as 500 μm and wall thicknesses up to 10 μm. Since then, in order to meet the requirements of e-beam experiments, these limits have been raised to 5000 μm diameter and 300 μm wall thickness.

A second objective was to develop techniques amenable to large-volume production of uniform shells of very nearly identical size and aspect ratio. (Aspect ratio = diameter of shell/shell wall thickness.)

IX-A-1-a. Fabrication Procedures

Hollow glass spheres have been made by two principal techniques. One technique uses the re-boil phenomenon which occurs in oxide glasses when a previously melted and homogenized glass is remelted and internally generated gases expand, causing small melted glass particulates to form small

---

*Trademark of KMS Fusion, Inc.

glass shells. This technique is likely the basic technique for a large variety of commercial microspheres.

The second technique makes use of the gases produced during reaction and fusion within the particulate material in a mixture of finely divided, previously unreacted glass-forming constituents.[11] As in the first technique, the gases cause rapid expansion of the molten glass globules into glass microshells. To date, all the large, thick-walled shells employed in inertial confinement experiments have been fabricated with variations of this basic technique. A major effort in this area has been undertaken to investigate this reactive expansion process using a variety of sythesis methods for the glass percursor particulate and a variety of glass-melting and expansion arrangements.

The usual procedure after blending and pulverizing the constituents is to introduce the powder into the top of the vertical tubular furnace where it forms a glass and expands into a shell as it traverses a heated zone. An alternative, but much more limited method, is the use of a gas-flame powder-spray torch for melting and blowing the powder into glass shells. The various steps involved in the manufacturing of glass microshell pellets are outlined in the process flow chart shown in Figure IX-A-1.

Although the particular glass composition chosen dictates the details of each process, the main features of these procedures are: (1) formation of a homogeneous solution of all metal oxide convertible components (essention if glass homogeneity on a microscopic scale is to be assured); (2) conversion of the gel formed from this solution into a dry solid while

TYPICAL GLASS MICROSHELL™ PELLET MANUFACTURING PROCESS

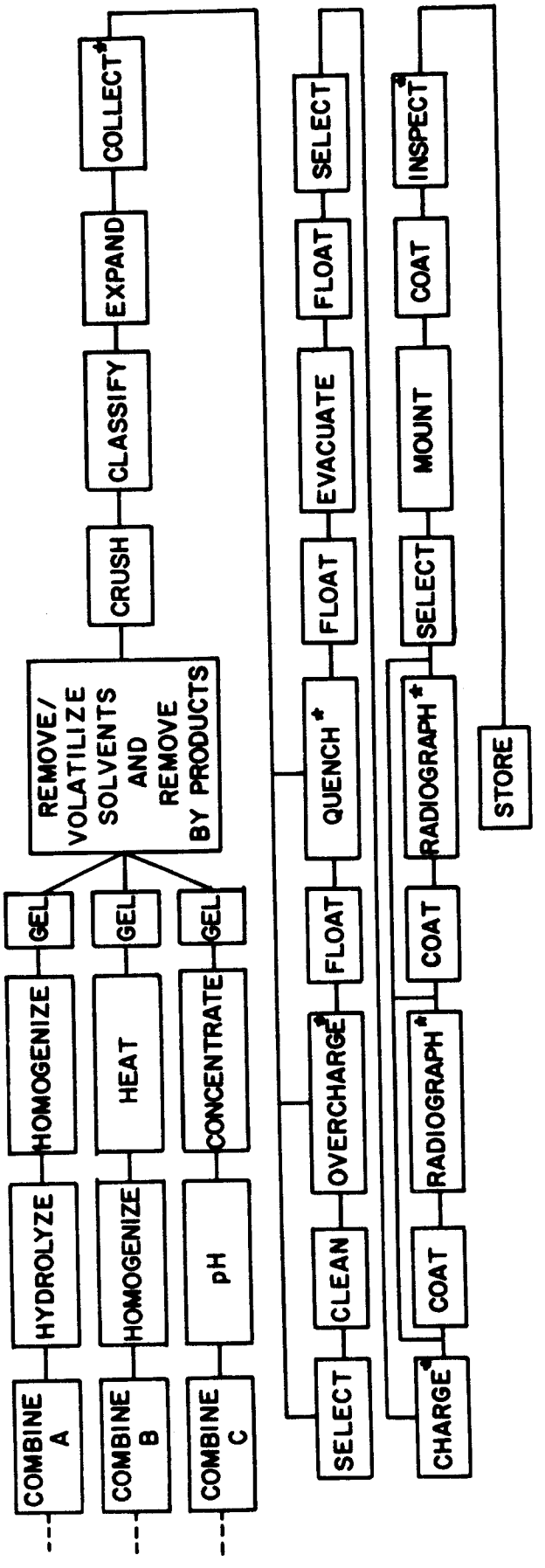

Fig. IX-A-1.

maintaining compositional homogeneity; (3) crushing and classification of the solid into a desired size range; (4) conversion of the glass precursor components from solid particulate state into molten metal oxide glass droplets and expanding the droplets into tiny spherical shells.

The glasses in commercial microshells are not formulated with any regard for possible use in laser fusion targets; shells from these glasses find their principal application as low-density and/or heat-resistant fillers. It is thus fortuitous that the compositions in some commercial shells impart a reasonable permeability (to the hydrogen isotopes) and the high tensile strength required for laser fusion targets.

All data collected to date indicate that the composition of the glass in a shell determines its gas-holding ability. Permeation properties, i.e., transport of the gas through the shell wall, appear to follow the same relationships as those observed on a macroscopic scale. Other properties such as strength and resistance to static fatigue are also related to composition, as experimentally established with bulk glass samples, but these properties have not been studied in sufficient detail in glass shells to be able to quantify any relationship between properties and composition.

One objective of the KMS development program has been to maintain the excellent fuel-gas retention exhibited by sodium borosilicate glass microspheres while extending the range of size and aspect ratio well beyond what is commercially available. This objective has been partially achieved. Improvements in sphericity, uniformity and surface topography of the larger shells are presently the main areas of investigation.

Experiments have also been started in which the solid glass particles or precursors are heated while levitated on gas jets or while being acoustically positioned in a zero-g environment. The main thrust of these experiments is to examine alternative means of high volume low-cost production of large shells to obtain in-depth knowledge of the phenomena involved in shell blowing. It may also be possible that for the very large shells, i.e., those with diameters greater than 5000 μm, well established molding and casting techniques can be applied to the fabrication of hemispheres. These hemispheres can subsequently be joined by techniques or combinations of techniques such as electron beam welding and heating during fall through a vertical furnace. At this juncture it appears that the proposed reactor pellet specifications and the associated problems, i.e., size, quality, large-volume production, etc., can be met by building on the basic technology already established.

IX-A-1-b. Shell Quantities and Sizes

Glass shells can be produced in large quanitites as evidenced by the availability of truckloads of Microballoons$_{TM}$[8] and Microspheres$_{TM}$[9]. The limitation on the number of shells fabricated per unit time is primarily a function of furnace size and temperature.

In order to form a glass shell from a particle it is necessary to raise the temperature of the particle to a point where the viscosity of the molten glass will permit expansion and coalescense of bubbles of the entrapped or chemically generated gas to form a shell. During free fall through the vertical tubular furnace, large particles of precursor powder will usually traverse the heated zone in a time too short to raise the

temperature of the particle to the point where adequate flow can occur. For these, increasing the furnace length and temperature can result in improved shell quality. Such improvement with increased temperature has been observed experimentally for several glass compositions and is being explored further with new and longer furnace systems which permit the particles to dwell in the hot zone for longer periods and so attain higher temperatures. The maximum shell size with acceptable uniformity is now about 500 μm, although occasionally shells with fair to good quality as large as 800 μm have been observed. Fabrication of shells approaching 1000 μm may be possible by a reasonable extrapolation of existing techniques, but still larger sizes may require one of the approaches discussed above.

IX-C-1-c. DT Permeation and Storage

The rate at which the isotopes permeate glass depends on the driving pressure, the composition of the glass, the temperature of the glass and its thickness. Since the filling and the emptying of glass are both permeation processes, the gas-fill time and storage life of glass shells likewise depend on the above parameters. In addition, the useful life of a pellet is further dependent on factors such as resistance to weathering, abrasion, mechanical fatigue, and radiation damage, all of which can cause early failure of the stressed glass.

The maximum allowable fill temperature is just below the point at which the shells begin to fuse together. This point occurs between 300°C and 500°C for the majority of the glasses of interest. At 300°C, 400-μm-diameter shells with 3-to-4-μm-thick walls will be filled to pressures equal to the driving pressure in approximately 120 hours.

Here it is worth noting that by changing the glass composition we can change the fill time by factors of ten. In addition, when the shells are filled at a constant external pressure the majority of the gas permeates the shells in the first few hours. After that, however, the driving pressure, i.e., the pressure difference across the shell wall, is sufficiently low that it may take several days to reach the final fill pressure.

Specifically, the fill pressure, $P(t)$, at time t varies exponentially with time as $P(t)=P_0\ [1-\exp\ (t/\tau)]$, where P_0 is the external pressure. It also follows that by increasing the external pressure during filling so that the driving pressure remains large, fill times can be greatly decreased. Note: the driving pressure, or the pressure difference across the shell wall, is limited to the pressure which will cause the shells to buckle. Larger and thicker shells, such as may be required for reactor pellets, would, under the same conditions, take longer - perhaps as long as a week or ten days. However, for higher strength shells, e.g., shells fabricated from high-silica glasses, which could be filled by maintaining high driving pressures and high filling temperatures, it is quite likely that fill times (for well-classified batches) would be no more than a few hours.

An in-depth study of the extended shelf life of DT-filled glass shells is yet to be undertaken. As a consequence, the data generated in the routine use of DT-filled shells give an insight into shelf life only in terms of out-permeation, but not in terms of fatigue and permature failure. Moreover, since the bulk of the DT-filled shells comes from glasses of similar composition, data on gas retention as a function of composition are also sparse. However, the available data are encouraging. For example, a batch of specially processed commercial borosilicate glass shells stored at 25°C did not show a measurable gas loss in two years. Although not quantitative, data are available which indicate that the rate at which shells fail by rupturing or breaking is very high during the first few hours after filling. The rate of failure then decreases very rapidly, with the majority of the weaker shells failing within the first few weeks. Afterwards, the failure rate is quite slow but it does continue throughout the entire storage period.

Studies with D_2-filled glass microshells, though also limited, substantiated the observed correlation of composition with permeation. Silica shells at 25°C emptied in a few weeks; low-sodium glasses maintained a 70-atm gas fill for several months before gas losses became noticeable. The newest soda lime glasses showed the lowest permeability; in accelerated shelf life tests at elevated temperatures, shells from this glass lost their fill at half the rate of the batch which had hitherto (at room temperature) retained its fill for two years.

Radiation damage to glass from tritium has thus far been notable only in that the glass slowly turns yellow. However, during long-term storage the damage from the β-decay of tritium does not appear to be significant;

90% of the filled shells survive in storage for one year, and the losses suffered are most likely due to fatigue since similar losses are observed with D_2-filled shells.

Glass has a theoretical tensile strength of ~ 10^6 psi. It is well known, however, that the actual strength of glass is highly dependent on surface condition. For this reason, while the maximum observed tensile strength for pristine glass is ~ 5 x 10^5 psi, the average strength of the usual aged glass in bulk is considerably lower, viz. in the range of 5000 to 20000 psi. It is readily apparent that the processing history of glass will have an effect on its strength.

The tensile load that DT-filled shells have survived is 15000 to 50000 psi, as calculated from data using the hoop-stress relationship. Compared with pristine glass, this is a rather low value (though better than for bulk glass), indicating considerable surface damage imparted by normal handling and processing. The damage is probably caused by abrasion during shell-shell or shell-container contact, with resultant stress sites and microcracks, and by solvent corrosion during cleaning. Such stress sites and microcracks can cause eventual failure under load through stress corrosion and fatigue. The cleaning, sorting, and gas-fill processes to which glass shells are subjected are severe, embodying methods and agents sure to cause abrasion and solvent corrosion. If high-pressure fills are required by reactor pellets, then present processing techniques will have to be improved.

IX-A-2. Polymeric Microshell$_{TM}$ Pellets

As discussed above, glass is attractive as a fuel container material because of its high mechanical strength and low permeability. However, it has been suggested that fuel containers fabricated from materials having lower average atomic number ($\bar{Z}$) may prove to be advantageous in that they should incur less radiative loss and produce less radiative preheating.[12]

Interest in polymers as candidate low-$\bar{Z}$ materials stems primarily from the ease of fabrication into spherical shells. Unfortunately, not all polymers are capable of containing the fuel gases for the intervals usually required for presentation to the laser. Research is therefore being directed at determining the most suitable polymers, their characteristics and ways of enhancing these characteristics, e.g., by cryogenic processing.

IX-A-2-a. Fabrication Procedures

Polymer shells of high quality have been fabricated by two basic techniques: spray drying and microencapsulation. A number of these shells filled with fuel have been irradiated, and the results have been encouraging.

The technique of spray drying to produce hollow particles was developed as early as 1957 for use as a fill-type insulation material and as a cellular filler in the manufacture of molded articles. These applications, however, do not require high quality nor spherical uniformity. To obtain a polymer shell by spray drying, the polymer must be soluble in a volatile solvent and form a solution with a viscosity low enough to be atomized into droplets of a controlled size distribution, which, when introduced into a zone of heated gas, will form uniform, hollow shells. The shell forms as the rapid evaporation of the solvent produces a liquid film of concentrated polymer

solution strong enough to trap solvent vapor, which then inflates the film to form a bubble. As the film solidifies, a permanent bubble or microshell results.

Parameters such as nozzle velocity, solution composition and concentration, and temperature profile of the heated zone must be controlled to obtain polymer shells of laser-target quality. Techniques for precise control of the majority of these parameters have been established. Emphasis is now on quality control during large-volume production.

Microencapsulation, which had its first development in the pharmaceutical industry to impart time-release properties to drugs, has been successfully adapted to the production of laser fusion targets. Two methods have been tried, each involving the formation of a polymer coating around a droplet of volatile liquid, which, when vaporized by heat, inflates the polymer.

In the first method, termed in-situ polymerization microencapsulation, a water-immiscible solution consisting of a polymerizable monomer, a volatile solvent and a polymerization initiator is dispersed as uniform droplets in an aqueous medium which contains surface-active agents to stabilize the droplets and prevent agglomeration. As polymerization of the monomer occurs the polymer is deposited at the interface of the droplet and the aqueous suspending medium. Polymer capsules containing a volatile liquid result. When heated above the softening point of the polymer, the pressure developed by the volatile solvent expands the capsules into polymeric bubbles.

The second microencapsulation method is coacervation. The primary difference between the two methods is that in coacervation, an already

polymerized compound is employed as the wall material instead of using monomer. The polymer is put into solution and within this solution a volatile liquid, immiscible in the solvent, is dispersed in droplets. The polymer is slowly forced out of solution and deposits on the droplets as a gel which then chemically hardens to form polymer capsules enclosing the volatile liquid. As before, the capsules are inflated by heating to produce the desired microspheres.

The advantages of the microencapsulation method are that the size distribution and wall thickness of the product can be controlled more precisely than in spray drying and much larger shells can be achieved. The encapsulation of fusionable fuel is also practicable. However, not all polymers are conducive to microencapsulation and expansion by heating.

Thus far, most of the microencapsulation work has been done with poly (methyl methacrylate). Shells made of poly (methyl methacrylate) range in size from a few micrometers to several millimeters, with wall thicknesses up to six micrometers.

IX-A-2-b. Permeation Fueling, Storage and Shelf Life

Using the two techniques described above, a large number of different types of polymer shells have been fabricated and tested. Fuel-fill tests have been done on poly (methyl methacrylate), poly (vinyl alcohol-co-vinyl butyral), poly (styrene-carboxymethyl cellulose) and poly (2-hydroxypropyl methacrylate). Poly (vinyl alcohol), PVA, had the lowest hydrogen permeation constant of all the materials investigated, but it must be kept dry to retain tensile strength and minimize elongation. Coatings of PVA have

been applied to other polymers and have significantly reduced out-permeation. Sodium carboxymethyl cellulose has permeation characteristics similar to those of PVA but the quality of the cellulose shells is thus far inferior.

It has been observed that exposure to DT for ~ 100 hours causes significant deterioration of the polymer due to radiation damage. For exposures of 5 hours or less, no appreciable damage is observable. Damage is caused by β-decay of tritium. For exposures up to 5 hours, the major effect appears to be some embrittlement of the polymer and a decrease in elongation. If the fusion reactor pellet were to include a polymer shell without a permeation barrier, and without structural support from another layer of material, maximum shell storage time would probably be of the order of five or six hours.

IX-A-3. Cryogenic Targets

It has been proposed that the yields from spherical shell targets can be increased by condensing the fuel gases uniformly on the inner surfaces of the shells. In recent experiments with cryogenic targets, enhanced neutron yields have indeed been observed.[13] The suitability of cryogenic targets as reactor pellets is still to be demonstrated in light of the severe thermal environment of the reactor cavity. The principal problem, of course, is whether the cryogenic field layer will remain in the condensed phase until the pellet is irradiated.

Two basic techniques for producing cryogenic targets are under investigation at many laboratories. The first of these is based on transfer by conducting heat through a metal fiber in direct thermal contact with the pellet and the second is based on heat transfer by cold helium gas (T ~ 5K).

The gaseous-helium cooling technique has as its goal the processing of large quantities of shells in a manner suitable for power-plant operations. The contact-cooling technique is not amenable to reactor pellet delivery requirements. It is very useful, however, in conducting laser-target-interaction experiments and in furnishing essential data on the condensation of the fuel gases.

IX-A-3-a. Present Status

Contact conduction cooling is based on removing heat from the spherical shell through a small conductive fiber which is attached to a liquid-helium cryostat. The fiber (usually Cu) serves both as a support for the pellet and as a thermal conductor. This technique was designed to allow laser-target interaction experiments to be performed on a well-positioned target in a manner which produced minimum obstruction to plasma-diagnostic instruments and particle-detectors. The fuel is condensed as a continuous liquid film on the inner surface of the shell while the outer surface is exposed to the room-temperature environment. The fuel is held in this configuration by carefully controlling the temperature at the contact point so as to maintain the proper balance between evaporation from the warmer regions of the shell and condensation at the colder regions.

The results of some of the initial experiments with these liquid-film targets are shown in Table IX-A-1.[5] The important conclusion is that these cryogenic shells exhibit greater yields than the yields from equivalent noncryogenic shells exhibit greater yields than the yields from equivalent noncryogenic targets. In addition, the diagnostic data[14] contribute to the fundamental understanding of the hydrodynamics of the implosion process; which is, of course, critical to target design.

TABLE IX-A-1

FIRST EXPERIMENTAL RESULTS FROM LASER IRRADIATION OF CRYOGENIC TARGETS*

DIA (WALL) μm	ENERGY ON TARGET J	TEMP K	PRESSURE atm**	NEUTRON YIELD
		CRYOGENIC TARGETS		
63 (1.3)	40.7	20	123	9.4×10^6
58 (1.3)	72.8	20	123	8.3×10^6
66 (1.3)	71.8	20	123	4.6×10^6
67 (1.3)	46.4	20	123	3.7×10^6
62 (1.3)	44.3	20	123	3.3×10^6
57 (1.3)	54.5	15	123	2.7×10^6
57 (1.3)	59.0	20	123	0.3×10^6
		NONCRYOGENIC TARGETS		
57 (1.2)	106.3	40	123	2.8×10^6
51 (1.3)	56.0	300	98	0.3×10^6
53 (1.3)	50.5	300	98	0.2×10^6
52 (1.4)	57.0	300	98	0.2×10^6
66 (1.3)	95.0	300	31	0.2×10^6
53 (1.3)	66.0	300	31	0.1×10^6

*The DT fuel was condensed as a continuous liquid film on the inner surfaces of glass shells

**Fill pressures are defined as the total pressure of the fuel gases within the shell at room temperature

IX-A-3-b. Cryogenic Reactor Pellet Considerations

With the fill densities of interest ($\gtrsim$ 30 mg/cc), the fuel, as it cools, will liquefy before solidifying. The gaseous-helium cooling technique relies upon the random tumbling of the filled shell in a 5 K helium-gas environment. This tumbling will result in a sufficiently uniform solid layer if the shell tumbles many times during solidification. This procedure is extremely simple and is applicable to batch processing of large quantities of shells. Experiments are presently underway to determine the uniformity of the cryogenic layers produced in this way.

An inherent difficulty with cryogenic pellets is maintenance of the solid condensate during pellet injection. If, for example, one assumes a nominal 4-mm-diameter reactor pellet exposed to ~ 2000°C throughout delivery, the radiant energy impinging on the pellet, initially at 5 K, is sufficient to completely vaporize the fuel in 5 ms. For an injection rate of 20 sec^{-1} a reasonable delivery time is 25 msec, which means that if all the energy is absorbed by the pellet it will become noncryogenic long before arrival at the center of the reactor cavity.

The above estimates assume that the pellet has an absorptivity (α) equal to unity, i.e., the pellet is black to radiation at 2000°C. It is possible, however, to add a reflective coating which can reduce the absorbed energy to a few percent. It may be possible, for example, to coat the pellet with a thin layer of gold (for which the reflectivity is ~ 98%) which can extend the lifetime so that the pellet would still be cryogenic upon laser irradiation. This assumes the heat load on the pellet is that due only to radiation from the walls, as would be the case in a complete vacuum. If the heat transfer

by the cavity gas is also considered, the picture changes. Table IX-A-2 shows the times that the pellet will remain in a given phase at gas pressures of 0.1, 1 and 10 Torr for 3 possible chamber gases.[15] It is evident from this table that even at the lowest cavity pressure now being considered (0.1 Torr) the fuel will not be solid when it arrives at the target position. At 0.1 Torr the major portion of the fuel is in the liquid phase. In this case, it is possible that the wetting action of the fluid and its surface-tension forces may be sufficient to maintain complete coverage over the inner surface, although uniform coverage is highly unlikely. Lowering the chamber pressure to 0.01 Torr, however, reduces the heating rate to the point that approximately a quarter of the fuel is still solid.

An alternative, which appears feasible, is to coat the pellet with an ablative layer, which while ablating will maintain the pellet at cryogenic temperatures. Solid and liquid hydrogen have been used in this mode and have maintained solid DT fuel mixtures exposed to room temperature for ~ 20 seconds.[16] The pellet lifetime will of course depend on the temperature of the environment and the amount of hydrogen surrounding the pellet. In the experiments just cited, the mass of the hydrogen ablator was approximately 0.6 mg. For the reactor environment, the hydrogen mass must be at least 11 mg which would correspond to a protective layer ~ 1.2 mm thick. Instead of hydrogen this ablative layer may be 30 mg of neon, which is in fact more compatible with the SOLASE design. The ablator masses required are shown in Table IX-A-3.

In any event, the lifetime of cryogenic pellets in the environment of the reactor cavity is a problem generic to all conceptual reactor designs.

TABLE IA-A-2

CRYOGENIC PELLET LIFETIME

EXCHANGE GAS	P (Torr)	Q TOTAL (W)	ELAPSED TIME, msec			FUEL CONDITION AT 25 ms	
			5 → 18.7 K	All Melt	All Vapor	Solid/Liq Fraction	Liq/Vapor Fraction
NEON	10.0	12.50	1.5	4.6	25.2		0.01
	1.0	6.621	2.8	8.8	47.5		0.58
	0.1	2.513	7.5	23.1	125.0		0.98
	0.01	1.914	9.8	30.3	164.0	0.26	
AIR	10.0	13.84	1.4	4.2	22.7		
	1.0	6.593	2.9	8.8	37.7		0.58
	0.1	2.656	7.1	21.8	119.0		0.97
	0.01	1.932	9.7	30.0	163.0	0.25	
HELIUM	10.0	44.89	0.4	1.3	7.0		
	1.0	13.50	1.4	4.3	23.3		
	0.1	3.371	5.6	17.2	93.4		0.90
	0.01	2.0	9.4	29.0	157.0	0.20	

Calculations based upon mol equivalent D_2 fuel

TABLE IX-A-3

ABLATOR MASS AND THICKNESS REQUIRED TO SURVIVE 25 msec

EXCHANGE GAS	P (Torr)	Q_{in}, J		ABLATOR MASS, mg		ABLATOR THICKNESS, mm		ABLATOR O.D., mm	
		H_2	Neon	H_2	Neon	H_2	Neon	H_2	Neon
NEON	10.0	6.9	3.4	13.5	32.7	1.43	0.32	7.25	5.05
	1.0	6.2	3.1	12.2	20.4	1.33	0.30	7.07	5.01
	0.1	5.8	3.0	11.3	28.9	1.27	0.29	6.94	4.98
	0.01	5.7	2.9	11.2	28.6	1.26	0.29	6.92	4.98
AIR	10.0	7.0	3.4	13.8	33.2	1.45	0.33	7.29	5.06
	1.0	6.2	3.1	12.1	20.4	1.33	0.30	7.06	5.01
	0.1	5.8	3.0	11.3	28.9	1.27	0.29	6.94	4.98
	0.01	5.7	2.9	11.2	28.6	1.26	0.29	6.92	4.98
HELIUM	10.0	10.3	4.7	20.2	45.5	1.85	0.43	8.09	5.26
	1.0	7.0	3.4	13.8	33.1	1.45	0.33	7.30	5.05
	0.1	5.9	3.0	11.5	29.2	1.29	0.29	6.97	4.99
	0.01	5.7	2.9	11.2	28.7	1.26	0.29	6.92	4.98

Calculations based upon maximum ablator thickness

Its solution will depend on the temperature of the cavity, the background pressure in the cavity, the velocity of the injected pellet, the distance over which the pellet must travel and the heat capacity of the pellet. In the case of SOLASE, with such high temperature and background pressure the pellet heat capacity must be enhanced by the addition of an ablator material. For lower temperature and pressure this may not be necessary if the pellet is massive enough. It should be noted that it is still necessary to address the means by which the hydrogen or neon layer is applied so as to assure adherence during injection.

IX-B. Reactor Pellet Requirements

As previously defined, the reactor pellet is a spherical shell that contains a 50:50 deuterium-tritium fuel mixture and is coated with layers of various materials. The fuel gases are condensed uniformly on the inner surface of the shell. The primary functions of the coatings or layers are to increase laser coupling and/or decrease fuel preheating.

Reactor-pellet requirements can be stated only in general terms, since presently available data are insufficient to define the optimum pellet design. However, the basic specifications assume a spherical structure consisting of 4 layers. The first, or innermost layer, is the condensed fuel mixture, which has a total mass of 1 mg. The second layer is usually the structural shell which serves to contain the fuel during processing. The dimensions of this layer are determined primarily by its materials and mechanical properties rather than the physics of laser-pellet interactions. The third is a high-Z layer with a mass of 1 mg or more, needed only when the Z of the structural shell is not sufficiently high. The outermost layer is chosen to be a low-Z, low-density ablator.

In choosing the reactor-pellet materials, consideration must also be given to their compatibility with the cavity materials. The principal problems appear to be condensation, carbide and alloy formation, and the resulting degradation or erosion of the first wall and liner. This is discussed in detail in Chapter XVI.

IX-B-1. Representative Reactor Pellets

The reactor pellets can be conveniently classified according to the material out of which the container or structural shell is composed. For the reason discussed in sections on shell fabrication, the two most probable classes of container materials are glasses and polymers. Of these, based on present technology, the silicate glasses and poly (vinyl alcohol) are the most promising candidates. Possible alternatives to glass and polymeric containers are iron and beryllium. Iron has an intermediate atomic number, putting it in a class with glass, while beryllium has a low atomic number, comparable to that of most of the polymers of interest.

Numbering the shells or layers from inside out and starting with the material in contact with the fuel layer, Table IX-B-1 lists the materials which satisfy the pellet requirements and have the highest probability of being fabricable into small uniform shells. It is worth noting that another particularly interesting class of reactor pellets is that in which the container is fabricated from a high-Z material. The significant factor is only one coating material is required, which reduces the fabrication steps.

A preferred high-Z material is xenon. The basis for this preference is the expectation that xenon will not react with the cavity materials and will remain as a gas which can be easily pumped from the chamber. The other high-Z materials thus far considered are expected to react with and rapidly

TABLE IX-B-1

REACTOR PELLET MATERIALS

CONTAINER MATERIAL (pertinent properties)	SHELL (LAYER) MATERIAL LAYER NUMBER* 1	2	3
GLASS (strength, H_2-permeability)	High Z[1] Materials	Glass	Low ρ, low Z[2] Materials
POLYMER (heavy atom-permeability)	Xe and High Z[1] Materials	PVA	Low ρ, low Z[2] Materials
HIGH Z CONTAINER	---	W-25 Re[3] 50 Mo-50 Re	Low ρ, low Z[2] Materials

(1) High Z coating materials - Ta, W, Pb, Hg, Pt, Au, Pd

(2) Low density, low Z layers - CH_2, $LiBH_4$ (foams); Be, B, B_4C, LiH or LiD (open structures)
H_2, D_2 (low density frost)

(3) Candidate high Z materials - tensile strengths > 2×10^5 psi
shell fabricability - unknown

*The layers are numbered in sequence starting with the innermost layer, which is next to the DT fuel layer

degrade the first wall and liner. An additional benefit will accrue from freezing the xenon on the inner surface of the polymer, since in doing this the xenon can act as a radiation shield, preventing the tritium β-particles from depositing their energy in the polymer container and thereby degrading it. Storing the pellets at a temperature below 164 K, the triple point temperature of xenon, and continually removing the energy due to β-heating (1.8×10^{-4}W per pellet) should significantly increase the shelf life of the polymer shells (shelf life and cryogenic storage are discussed in greater detail below).

From the reactor point of view, the ideal pellet materials would contain no oxygen and would produce only volatile nonreactive agents. The configuration which comes closest to this is a DT-filled, deuterated polymeric shell (e.g., polystyrene, polyethylene, or parylene) with xenon deposited on the inner and perhaps on the outer surface of the shell. The outermost layer would be a low density foam, again of a polymer containing no oxygen.

IX-B-2. Fabrication and Processing of Reactor Pellets

Detailed descriptions of reactor-pellet fabrication procedures are not yet possible since the pellet's design is incomplete. However, addressing the classes of pellets discussed in the previous section, it is possible to describe representative procedures which can be useful in defining problem areas, or areas which are important because of their commonality with all schemes.

IX-B-2-a. Fabrication Techniques

Three steps appear in all candidate pellet-processing schemes:

a. permeation (fuel) filling

b. final cryogenic processing (immediately prior to injection)

c. deposition technology (for low-Z ablators, high-Z layers)

The present processes leading to selection of glass and polymer shells of suitable quality are shown in some detail in Figure IX-A-1. These processes will of course require modifications, but the basic techniques, e.g., radiographic inspection, cleaning, and floatation, which are well established procedures will probably remain part of the selection process.

If the high-Z layer is sufficiently permeable to hydrogen and is not degraded by the hydrogen during the filling operation, it will be deposited prior to filling in order to avoid coating tritium-filled shells. This layer will probably be deposited on the inner shell by electroless or electrolytic deposition and/or chemical vapor deposition. Physical vapor deposition (e.g., electron beam evaporation) is also possible, but for high-volume processing, the deposition rates may be too slow or the energy consumption too high to be practical. Again from Table IX-B-1, examples of possible materials are tantalum, lead, tungsten and gold, with the specific selection being based on the compatibility of pellet and cavity materials and on the material requirements for high-gain pellets. It may also be possible to eliminate this layer by increasing the Z of the polymer shells by incorporating a heavy halogen (bromine, iodine).

The optimum pellet design may require that the high-Z or the ablator layer have a density less than their normal bulk density. Obtaining these low densities can be accomplished by mixing or interspersing the materials with a foaming agent during deposition. Subsequently, the density can be reduced by <u>in situ</u> foaming. Similar techniques have been used commercially to fabricate lower-density glass bricks and aluminum blocks.

The technology to perform all the fabrication operations for any of the representative pellets is already in existence. High-volume processing for power-plant reactors will require only limited extensions and modifications of well-established techniques.

IX-B-2-b. Storage Requirements

Storage requirements for reactor fuel pellets are derived primarily from considerations of: (1) safety, (2) shelf life and material properties of fabricated pellets, and (3) energy costs for pellet fabrication and storage.

The main safety concern is with the large tritium inventory resulting from storing large quantities of pellets. The principal hazard with tritium is its easily ingested oxide species, HTO, DTO and T_2O and to a much lesser extent the diatomic species HT, DT and T_2. Permissible occupational-exposure concentrations of T_2 and T_2O in air are 2×10^{-3} $\mu Ci/cm^3$ and 5×10^{-6} $\mu Ci/cm^3$ respectively. The levels established for the general public are 10% of these.

At a pellet usage rate of 20 sec^{-1}, 1.728×10^6 pellets will be consumed per day. At 1 mg of fuel per pellet, this corresponds to a tritium consumption of 9.95 MCi per day. To avoid interruptions in power plant operation caused by lack of reactor pellets requires a stockpile of fueled pellets. The number of pellets stockpiled is determined by the number of days required to bring the tritium fueling operations back on line. The estimate of the number of required days is, of course, dependent on the complexity of the operations. The permeation filling operations and equipment (e.g. high pressure autoclaves, heaters, controllers) are inherently simple so that down

time should be minimal. In addition, by virtue of their simplicity, the filling stations should be sufficiently inexpensive to warrant redundant systems. It would appear then that the inventory would be dictated by the time required to fill a batch of shells. This time is dependent on the permeability of the shell materials, but times in excess of one week are highly improbable. The tritium inventory in pellets for one week is 69.7 MCi. This extensive inventory combined with the low permissible tritium concentrations implies strict control and prevention of any tritium release to the environment.

Several storage techniques are feasible. Of these, cryogenic storage appears the most attractive. As previously discussed, the outpermeation of the fuel through any of the shell materials may be reduced to a negligible level by storing the DT-charged pellets at low temperatures. Cryogenic temperatures can also reduce the pressure-induced stresses and radiation damage. As described above, condensed high-Z deposits such as xenon can also effectively shield the container material.

The largest power investment during storage is that required to remove the heat continually produced by the β-decay of tritium. The β-decay power generated by a week's inventory of pellets is 2.27 kW. Essentially all of this will be deposited in the shells' walls. The simplest conceivable cooling system consists of flowing cooling gases over the pellets. The power consumption for such a procedure can be bounded by considering the inventory of pellets to be loosely packed in an enclosure through which gaseous helium flows. The flow required to maintain the pellets at room temperature is about 90 g/sec, assuming an inlet temperature 6K° below and an outlet temperature 1 K° below

room temperature. The pellets can be enclosed in a volume of 0.8 m^3. The flowing helium will experience a negligible pressure drop in transit (e.g., across a cube of volume 0.8 m^3 the pressure drop will be < .02 psi with a flow velocity < 10 ft/sec). The heat transfer coefficients are sufficiently high that the pellets will be only ~ 0.07 K° warmer than the local temperature of the gaseous helium. The compressor power, assuming a driving fan which is only 5% efficient, is about 1.5 kW.

The total power consumed is therefore approximately 3.8 kW which is negligibly small for the proposed circulating power of 335 MW. However, as previously discussed, storage at cryogenic temperatures is desirable since it can reduce pressure-induced stresses and radiation damage. For storing polymer shells cryogenic temperatures may be unavoidable, particularly if they must be stored for a week or more. Using cooling techniques like those just described for room-temperature storage would require about 60 kW to maintain a week's supply of DT-filled polymer shells at liquid-nitrogen temperature (80 K) and about 1.7 MW to maintain them at liquid-helium temperatures (5 K). Neither of these power requirements is too large to preclude storage at either temperature; however, the large difference between them makes it worthwhile to investigate storage at 80 K with a final refrigeration to 4 K just prior to injection.

Suitable cryogenic storage vessels and refrigeration systems can readily be developed from existing commercial products. As an additional safety factor, metal hydride absorber systems for adsorption of leakage T_2 and its oxides can be incorporated within the pellet-storage vessels and secondary-containment vessels.

An alternative to cryogenic storage is high-pressure-gas storage. But storage under gas significantly increases the danger of gas release and puts more severe requirements on equipment performance - on valves, fittings, materials, etc. Moreover, some refrigeration will still be required to remove the heat generated by the β-activity.

IX-B-2-c. Pellet Cost Estimate

Direct material costs are shown in Table IX-B-2 and preliminary estimates of pellet manufacturing costs for a pellet consisting of a layered sphere are shown in Table IX-B-3[17]. This table assumes an investment in plant of $100,000,000 which is a reasonable goal. To attain this investment level requires a substantial expenditure for manufacturing development between now and the time that a prototype reactor begins operation. If one is forced to assume today's technology and the present state of pellet development an investment in plant would reach as high as $500,000,000 which is presently unacceptable. It is apparent from Table IX-B-3 that materials are a small fraction of the total pellet cost. Labor is taken as being proportional to capital charges, which include amortization, taxes, interest on debt and return on equity.

Although 4.67¢ per pellet is the cost shown in Table IX-B-3, no specific estimates have been made on the developmental costs. Past projects of similar scale have shown that the commitment of the appropriate level of effort has to have extremely difficult objectives.

It is therefore both timely and appropriate to begin the large and critical task of defining the lower limit of pellet manufacturing costs.

TABLE IX-B-2

Direct Materials Costs[a]

Material	Total Weight (kg/yr)	Material Unit Cost ($/kg)	Total Material Cost/Year ($/year)	Cost per Net Pellet ($/pellet)	Weight per Pellet (mg)[d]
Deuterium[c]	1.11×10^2	1000.0	1.11×10^5	0.00022	0.40
Glass[b]	9.7×10^4	7.63	7.39×10^5	0.00146	2.52
Mercury[b]	1.54×10^4	66.0	1.016×10^6	0.00201	10.0
Plastic[b]	1.05×10^4	1.10	1.155×10^4	0.00002	10.65
TOTAL			1.877×10^6	0.00371	23.57

(a) 20 pellets/sec, 80% plant factor $\Rightarrow 5.046 \times 10^8$ pellets/year

(b) No recovery in manufacturing

(c) Assumes 45% fractional burnup of deuterium in the pellet and 100% recovery of unburned deuterium

(d) The total weight per year is not equal to the total weight of one years' worth of pellets because of manufacturing inefficiency.

TABLE IX-B-3

ESTIMATED PELLET COST

	EFFECT OF INCREASING DEVELOPMENTAL COSTS		
MATERIALS (a)	$ 4,480,000	$ 4,480,000	$ 4,480,000
LABOR	7,000,000	3,500,000	1,750,000
CAPITAL CHARGES (b)	18,000,000	9,000,000(d)	4,500,000(e)
TOTAL	$29,480,000	$16,980,000	$10,730,000
COST PER PELLET (c)	4.67¢	2.69¢	1.70¢

(a) All materials, supplies and utilities

(b) @ 18% of investment in plant

(c) Plant factor 0.9 assumed

(d) Assumes a $50,000,000 investment in plant

(e) Assumes a $25,000,000 investment in plant

IX-C. Pellet Injection

Experiments on inertial confinement fusion targets to date have employed mechanical supports to hold and position the target in the focal volume. Typical support mechanisms are the so-called ball and disc and the stalk or post mount. Typically, a spherical target in the range of 30 to 500 μm OD is placed on a thin film or fiber and positioned in the focal volume by means of an x, y, z micrometer stage. The mechanical connection typically extends through the target-chamber wall to allow for external alignment control. Inside the target chamber a thin rod or tube extends from the x, y, z positioner and terminates in a target holder. These mechanical supports may perturb the plasma dynamics.

Development of noncontact pellet-suspension systems is in process. This kind of suspension has been accomplished with varying degrees of success by levitating the pellet with lasers, gas jets, acoustically, electrostatically, electromagnetically and by inertial processes. For the requirements of present laser fusion experiments it appears that pellet noncontact suspension can be best attained utilizing inertial or ballistic noncontact techniques. Emphasis should be placed on the development of these two techniques since they both involve technology applicable to the power-plant reactor.

IX-C-1. Electrostatic Injection and Deflection

Electrostatic and pneumatic injection are the two injection modes which have been given the most attention. The state-of-the-art for both techniques is highly advanced and their application to the reactor might appear straightforward but such is not the case. Electrostatic injection appears desirable because of the possibility of correcting the trajectory of pellets while in flight. The method consists of depositing an electrical charge on the pellet

and accelerating the pellet in an electric field to the desired velocity. While the pellet is in flight, one can in principle make position and velocity measurements electronically, evaluate these data and use them for in-flight trajectory correction by fields between sets of deflector plates.

An analysis of this scheme in the framework of the reactor radiation and temperature environment reveals some severe shortcomings.[16] During both acceleration and deflection, the resultant velocity and trajectory correction depend on the charge-to-mass ratio of each individual pellet. Control of this charge-to-mass ratio is not possible in the reactor environment. Trajectory corrector plates would have to establish the electrical deflection fields inside the high temperature region of the reactor. There is no known reliable way to accomplish this. In addition, the system requires velocity and position measuring schemes that would function reliably in an environment of at least 2000°C. To our knowledge, no such system is available.

It is, however, possible that electrostatic injection schemes may prove to be a useful approach for single-shot experiments with contactless pellets in a test-chamber environment at approximately room temperature. In this case, the absence of high temperatures as well as the freedom of choice for the velocity at the focal volume makes the electrostatic acceleration method appear feasible and even desirable.

IX-C-2. Pneumatic Injection

The scheme of pellet injection which appears the most feasible employs a pneumatically operated launching device which injects the pellet along a vertical trajectory. In this configuration, the pellet will

traverse a distance of about 12 m to the cavity center at a speed which is compatible with the timing requirements inherent in the laser injector synchronization and the maximum lifetime of a pellet in the 2000°C environment of the reactor chamber.

The proposed pneumatic injection system which is now being studied at KMS Fusion is based on the principles of air guns which have been in existence for nearly 250 years. The extensive technical experience in this field has led to the development of small-bore (4.5 mm and less) guns of extreme accuracy and reliability. With presently available high-precision air guns, projectiles can be delivered into an area of radius less than ~0.7 mm at a distance of 12 m with a generally horizontal trajectory. This is still a slightly greater circle of uncertainty than that required for the delivery of fuel pellets into the laser focal volume of future laser fusion reactors. For a vertical trajectory, inprovement in this accuracy or a decrease in the spread of projectile impact points can be expected. Further increases in accuracy may require delivery from shorter distances, e.g., insertion of the barrel into the cavity.

A repetition rate of 20 pellets per second or greater is also feasible with pneumatic devices. This has recently been demonstrated with a gas operated "BB-machine gun".

A major advantage of a pneumatic injection system is its relative ruggedness and insensitivity to ionizing radiation. It is also worth noting that the accelerating gas can be the same as that in the cavity. During operation approximately 100 torr-ltr/sec of gas is introduced into the cavity. This additional gas load can be easily handled with the proposed chamber pumping speed of 5×10^5 torr-ltr/sec.

The system is, however, sensitive to high temperatures and to temperature changes. The pneumatic injection system must be kept at a constant temperature both to maintain mechanical dimensions and to protect the fuel pellets from heating during loading and acceleration. A combination of cooling the injector, synchronized rotating shutter and a gently curved barrel can meet these requirements.

If trajectory correction is needed, this can only be done by correcting the gun's aim. This can be accomplished in a straight forward manner by feeding back a sequence of trajectory measurements and correcting until the desired trajectory is obtained. However, predicting or obtaining coincidence of laser firing and the pellet's arrival in the focal volume is much more difficult. The measurements required to do this, i.e., measurements of pellet position as a function of time, cannot be accomplished with either optical or electrical methods because of the high temperature of the cavity (which results in an unacceptably high radiation background) and the requirement that the pellet be located within 100 μm of the target position. For a delivery rate of 20 sec^{-1} and a flight time of 1/40 sec the pellet's velocity will be approximately 480 m/sec, which means it will remain within the target volume (as defined by the requirement for 100-μm positioning accuracy) for 0.42 μsec. Since laser jitter is expected to be less than 0.1 μsec, it appears feasible, once the trajectory is established, to trigger the laser to fire at the instant the pellet arrives at the focal volume.

Ultimately, the determination of proper pellet positioning in the target volume and the laser timing must be based on variation in yield as a function of laser power on a shot-to-shot basis. The yield can be monitored

by measuring the neutron flux or any of the other emitted radiations. It is conceivable that when the yield decreases the pellet trajectory could be checked by firing surrogate pellets, i.e., pellets which do not contain DT. Position measurements could be made external to the severe reactor environment and the gun re-aimed until the surrogate pellets pass through the desired positions. Once the trajectory is established, then the fueled pellets can be fired and illuminated to establish proper timing.

It should be noted that this procedure entails the loss or inefficient use of pellets. It also means that the average reactor power level will be lowered. To compensate for this, the firing rate would have to be increased. If we assume 10% down-time for trajectory and timing adjustments (any number appreciably greater than this is unacceptable for power plant operations), then the firing rate becomes 22 sec^{-1}, which is easily handled. However, the effective pellet costs must also be increased by as much as 10% since the test-fired pellets may produce little or no energy. The fuel cycle materials capacity has been computed using this rate of 22 sec^{-1}.

The fusion reactor chamber and its structure will probably vibrate due to the 20-Hz injection cycle. A likely remedy is to isolate the pellet-injection system and the optics from the vibrating structure, while rigidly maintaining their positions with respect to each other.

With the exception of improvements in aiming accuracy by a factor of about 7, the technology to meet the requirements of pellet injection is fairly well established. The questions of reliability under long periods of thermal cycling and nuclear irradiation still remain to be answered. The problems of delivery of cryogenic pellets will require extensive investigation.

References for Chapter IX

1. J. Holtzrichter, H. Ahlstrom, E. Store, J. Swain, IEEE Second International Conference on Plasma Science, Ann Arbor, Michigan (1975), 85. Similar experiments are being conducted at the University of Rochester and Los Alamos Scientific Laboratory. Also, recently, laser-driven shell target implosions have been reported by BASOV, et al., Proceedings of Nobel Symposium on Non-Linear Effects in Plasmas, Plenum Press (1976).

2. G. Charatis, J. Downward, R. Goforth, B. Guscott, T. Henderson, S. Hildum, R. Johnson, K. Moncur, T. Leonard, F. Mayer, S. Segall, L. Siebert, D. Solomon, C. Thomas, Plasma Physics and Controlled Nuclear Fusion Research (Proc. Int. Conf. Tokyo, 1974), IAEA, Vienna (1975), Vol. II, 317.

3. R.R. Johnson, Plasma Physics 28, 28-46, Plenum Publishing Co. (1977).

4. D.E. Solomon and T.M. Henderson, J. Phys. D: Appl. Phys. 8 (1975).

5. T.M. Henderson, D.E. Solomon, R.B. Jacobs, G.H. Wuttke, D.L. Musinski and R.J. Simms, "Laser Interactions and Related Plasma Phenomena," 4A, 305, edited by H.J. Schwarz and H. Hora, Plenum Press, New York, 1977.

6. R.R. Stone, D.W. Gregg and D.C. Souers, J. Appl. Phys. 46, 2693 (1975).

7. T.M. Henderson, D.E. Cielaszyk, R.J. Simms, Rev. Sci, Instrum. 48 (1976).

8. R.J. Mason, Los Alamos Report UC-20, 1975 (unpublished).

9. J. Nuckolls, L. Wood, A. Thiessen and G. Zimmerman, Nature 239, 139 (1972).

10. T.M. Henderson, R.R. Johnson, Appl. Phys. Lett., 31, 18 (1977).

11. U.S. Patent 4,021,253, May 3, 1977.

12. Trademark of Emerson and Cuming, Inc.

13. P.M. Campbell, P. Hammerling, R.R. Johnson, J.J. Jubis, F.J. Mayer, D.C. Slater, Plasma Physics and Controlled Nuclear Fusion Research, Vol. I, 227 (1976).

14. T.M. Henderson, D.L. Musinski, R.B. Jacobs, G.H. Wuttke, and R.J. Simms, "Cryogenic Laser Fusion Targets by Point Contact Conduction Cooling," (to be published), J. Appl. Phys.

15. T.M. Henderson, R.B. Jacobs, D.E. Solomon, G.H. Wuttke, Advances in Cryogenic Engineering 21, 455 (1975).

16. R.J. Simms and T.M. Henderson, KMSF Report KMSF-U754.

17. W.B. Rensel and D.E. Solomon, KMSF Report KMSF-U752.

18. D.A. Burgeson, KMSF Report KMSF-U753.

19. Ibid.

X. Cavity Design Concepts

X-A. Pedagogy

The energy release from the exploding pellets of inertially-confined fusion systems consists of energetic neutrons, photons, and charged particles which eventually dissipate their kinetic energies in the walls surrounding the reactor cavity. The X-rays and charged particles emanating from the microexplosion and the reflected laser light from the pellet deposit their energy in an extremely thin surface layer causing rapid surface heating of the first wall. The energy from the 14 MeV neutrons and high energy gammas is deposited in relatively large volumes and does not pose significant heat transfer problems.

The photon and ion irradiations may cause excessive wall erosion by evaporation, spallation and sputtering. In addition, the wall may experience significant cyclic stresses leading to fatigue failure. Protection of the first wall from damage due to these irradiations is the main objective of the designer. Neutron-induced damage must, of course, be assessed in conjunction with the above described problems. In this and the following sections, the main problems associated with cavity and chamber design for laser fusion reactors are discussed. Different wall protection schemes, viz gas stopping, magnetic protection, wet walls, and free falling lithium are described and critically compared. Our aim is to identify the limitations imposed by these concepts as well as

areas of uncertainty which require further attention. The design philosophy adopted in SOLASE and the models developed to support such a design are presented in Section XI.

X-A-1. Wall Protection -- Problem Definition

Calculations of the implosion of bare D-T pellets indicate that approximately 1% of the energy yield is in the form of X-rays.[1-5] In addition to the D-T fuel, reactor-type pellets will contain other materials for fuel containment purposes as well as implosion and burn dynamics requirements. The X-ray energies and spectra produced by these pellets may be considerably different than those for bare D-T pellets. Typical X-ray spectra for three different pellets are shown in Figs. X-A-1 through X-A-3. Structured pellets with large amounts of high-Z materials may produce high X-ray energy fractions with soft spectra (Fig. X-A-3). This tends to exacerbate the surface heating problem since soft X-rays have a very short range. The majority of the X-rays are produced during the thermonuclear burn which lasts about 10 ps; however, for structured pellets, the X and gamma radiation occurs over a longer time interval (Section IV). A long pulse duration is desirable since it allows the energy deposited in the surface layer to be removed by heat conduction (Section X-C).

Approximately 75% of the thermonuclear energy yield is carried away by the neutrons. The neutron energy spectrum closely resembles a 14 MeV monoenergetic source (Fig. X-A-4). These neutrons are released during the

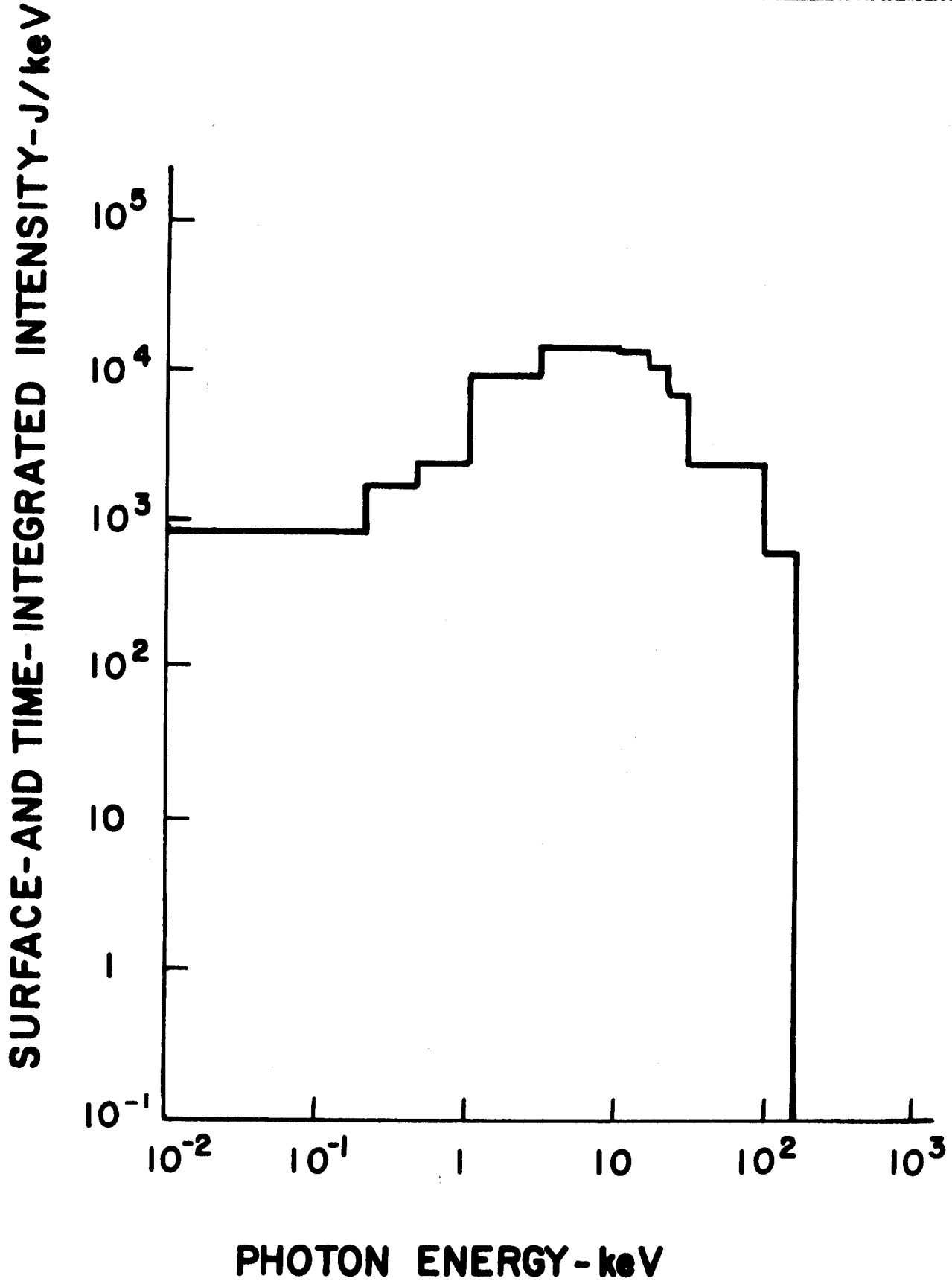

RADIATION SPECTRUM FOR BARE DT PELLET. (10 FREQUENCY GROUPS)

Fig. X-A-1.

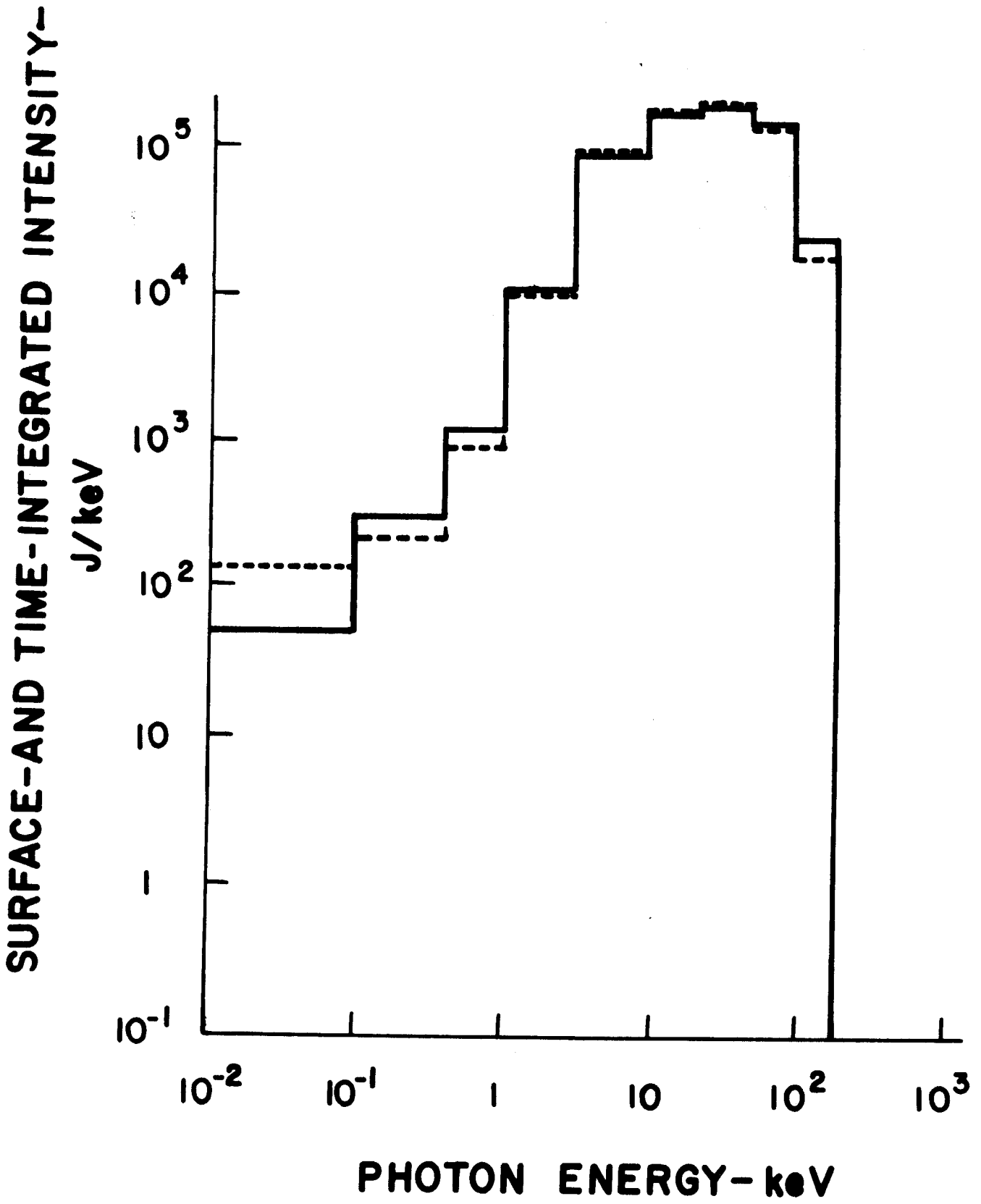

RADIATION SPECTRUM FOR A DT PELLET WITH A 10 mg Hg SHELL. (SOLID CURVE ASSUMED UNIFORM Hg DENSITY)

Fig. X-A-2.

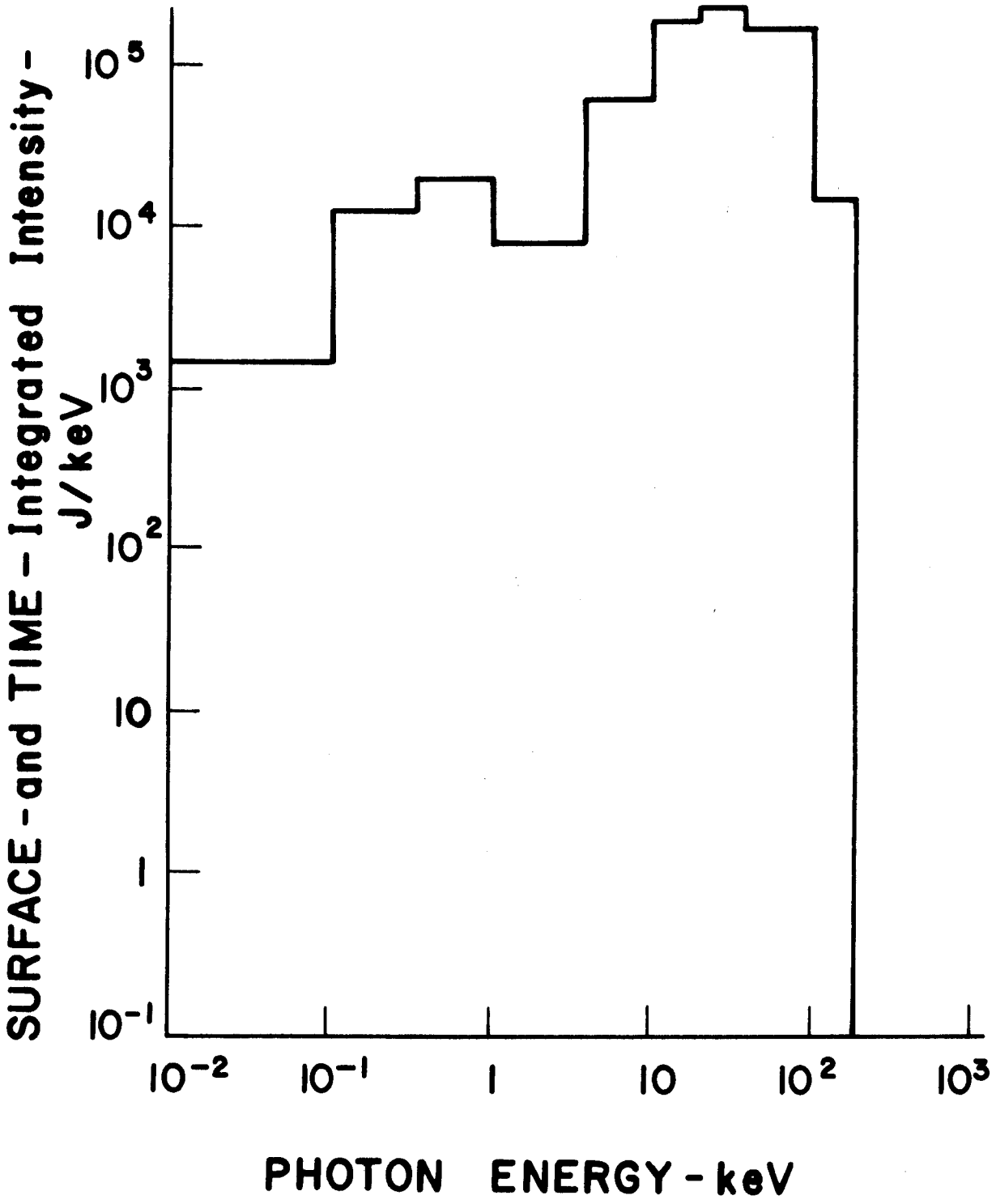

RADIATION SPECTRUM FOR A DT PELLET WITH A 100 mg Hg SHELL

Fig. X-A-3.

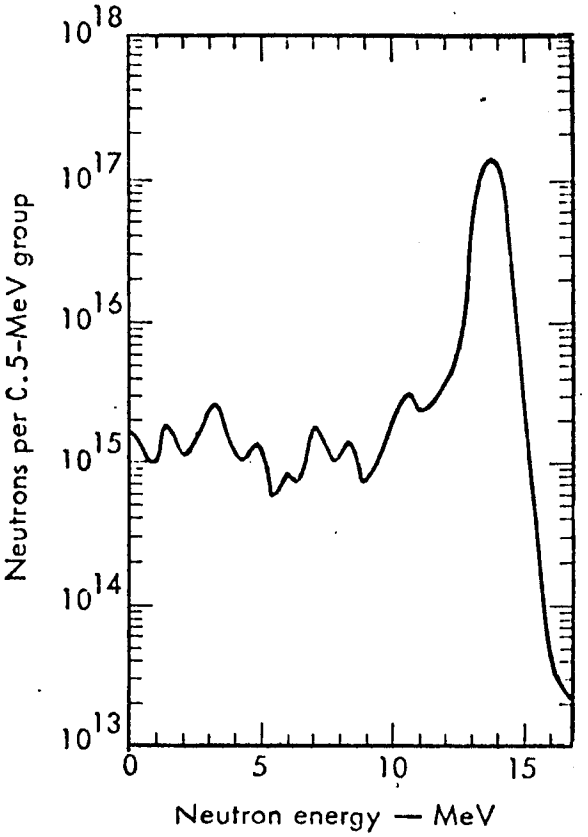

Neutron Pulse Spectrum of a Megajoule DT Fusion Micro-explosion [from (1)]

Fig. X-A-4.

burn time of 10 ps. Depending on the cavity diameter (a few meters), they arrive at the first wall approximately 10 ns after the X-rays. The energy deposition by the neutrons occurs primarily in the blanket regions in neutron-slowing-down times, a few microseconds for 14 MeV neutrons in lithium.

A significant portion (20-25%) of the energy yield from the micro-explosion is released in the form of energetic charged particles. For some pellet designs, the alpha particles escaping from the pellet may carry as much as one-third of that energy; the remainder is associated with the pellet debris (Section IV). These include the unburned deuterons, tritons and trapped alphas, as well as any non-hydrogenic pellet constituents. The arrival times at the first wall of free-streaming charged particles and of the debris plasma depend on chamber geometry and dimensions, and on the kinetic energy and spectra of the particles. These times are also affected by the presence of a magnetic field or significant amounts of residual gas in the chamber. Typical charged particles spectra for a structured pellet with a 10 mg Hg shell are shown in Figs. X-A-5 through X-A-8. The energy spectrum of the debris is nearly Maxwellian with the average energy equal to the energy deposited in the pellet from the laser and burn divided by the number of particles. The time interval for deposition of the charged particles energy in the front wall is of the order of a few microseconds (Section X-C). Much shorter times are associated with the 2 MeV alphas.[6] Knowledge of

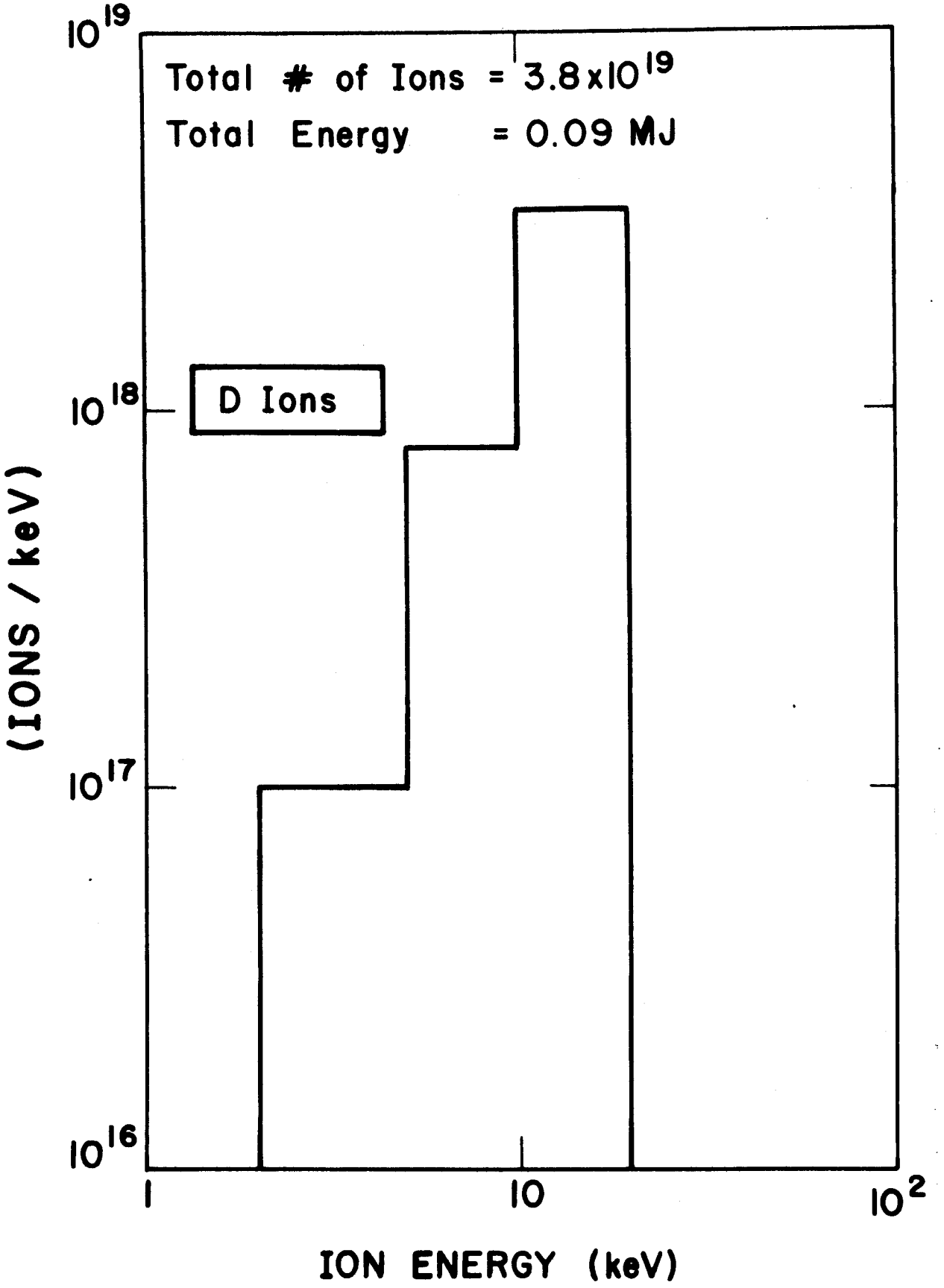
Total # of Ions = 3.8x10^19
Total Energy = 0.09 MJ
D Ions
10^19
10^18
10^17
10^16
(IONS / keV)
1
10
10^2
ION ENERGY (keV)

Fig. X-A-5.

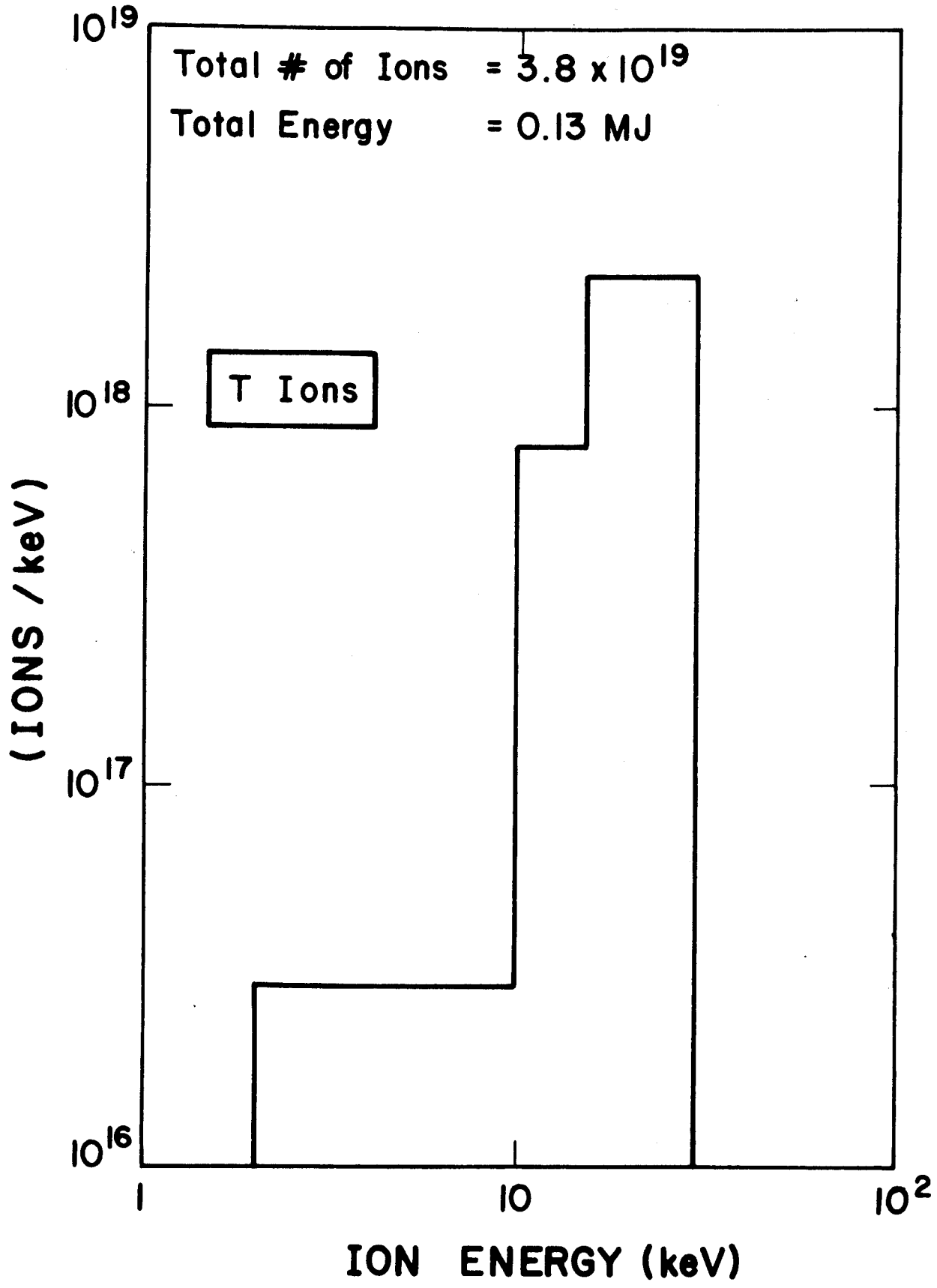
Total # of Ions = 3.8 x 10^19
Total Energy = 0.13 MJ
T Ions
10^19
10^18
10^17
10^16
(IONS / keV)
1
10
10^2
ION ENERGY (keV)

Fig. X-A-6.

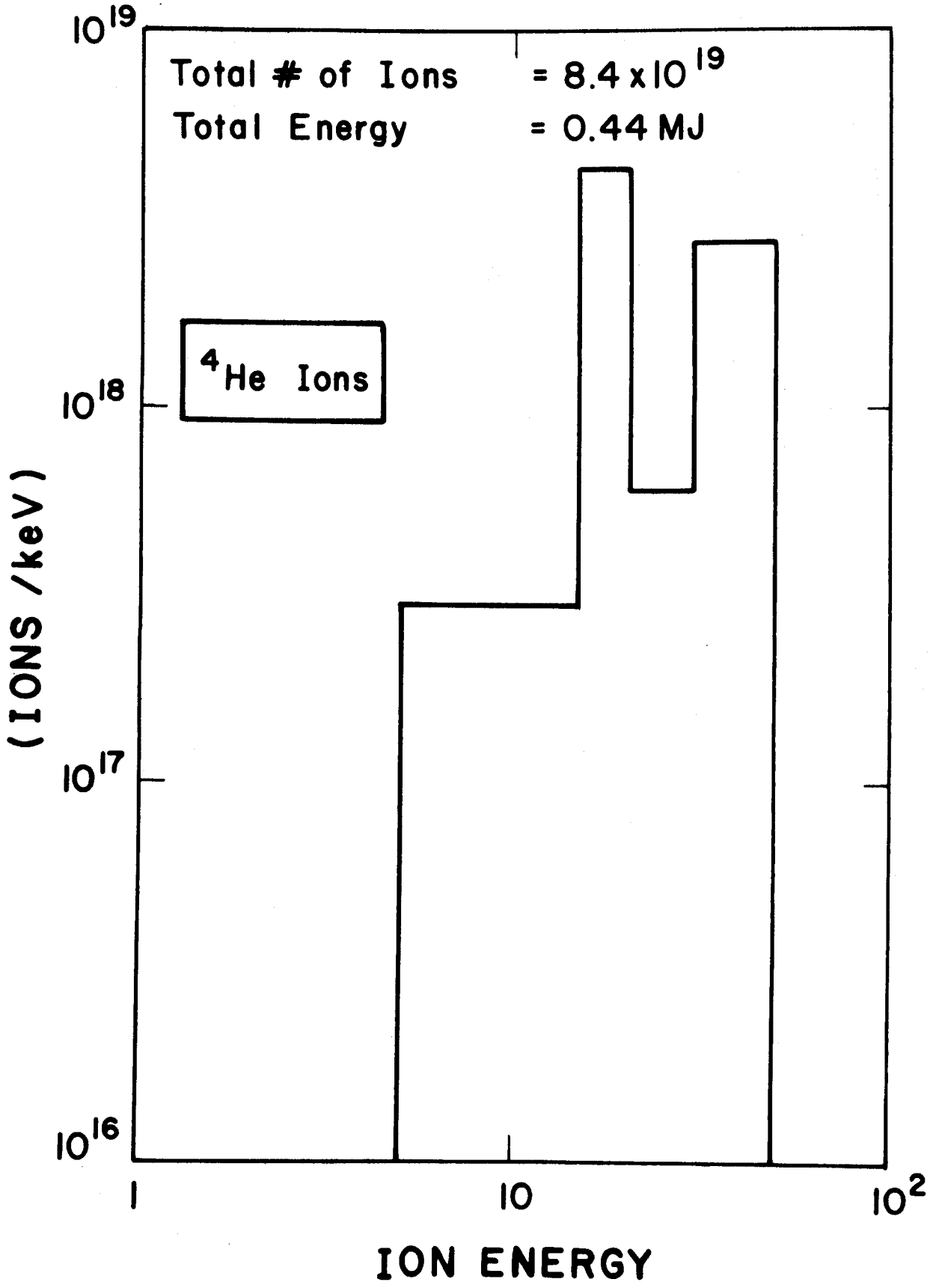
Total # of Ions = 8.4 x 10^19
Total Energy = 0.44 MJ
4He Ions
10^19
10^18
10^17
10^16
(IONS /keV)
1
10
10^2
ION ENERGY

Fig. X-A-7.

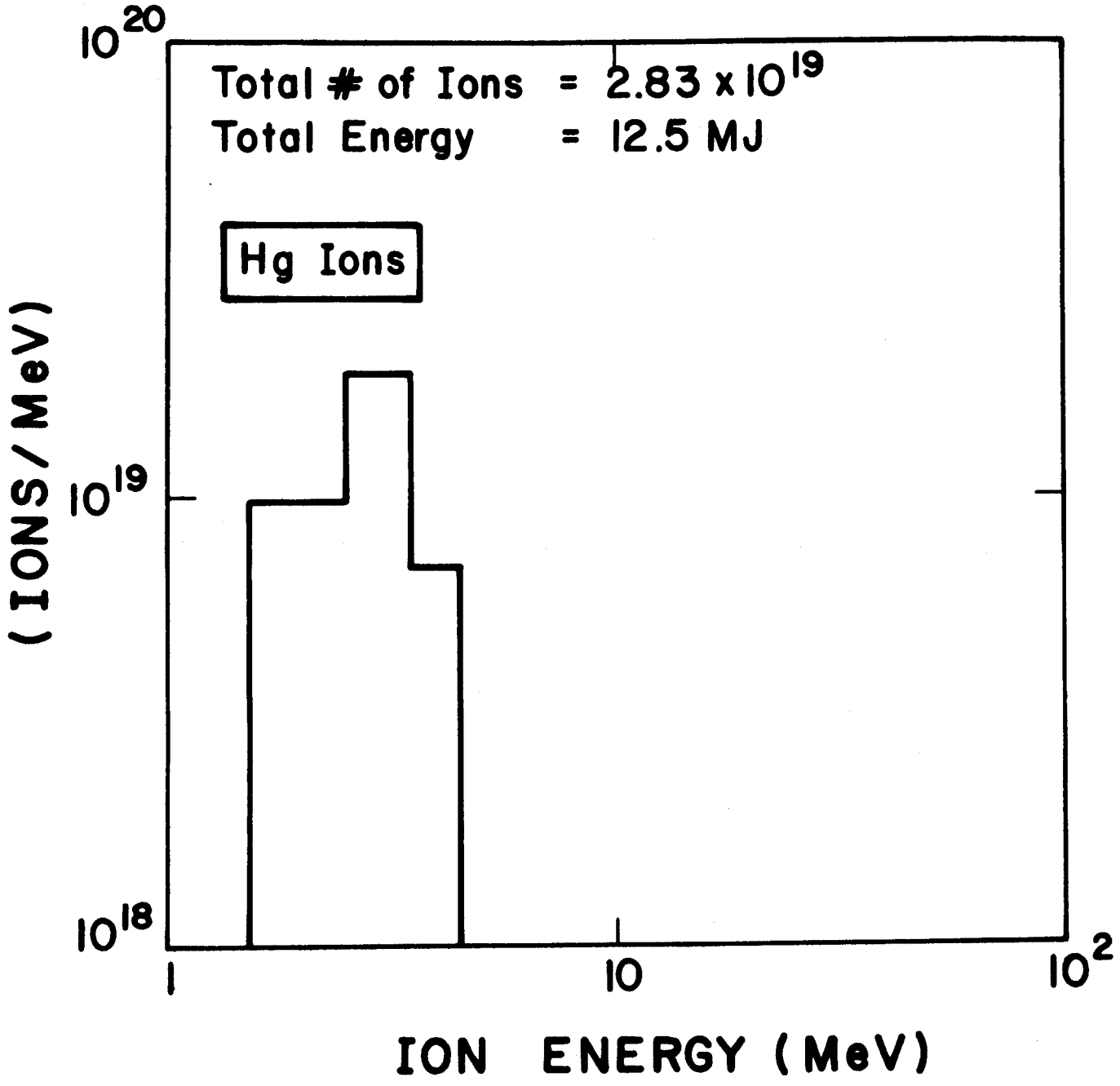
Total # of Ions = 2.83 x 10^19
Total Energy = 12.5 MJ
Hg Ions
10^20
10^19
10^18
(IONS/MeV)
1
10
10^2
ION ENERGY (MeV)

Fig. X-A-8.

the spatial energy deposition as a function of particle energy, and the arrival time of each particle is necessary for evaluating the thermal response of the wall.

A significant fraction of the incident laser light can be reflected from the DT plasma surrounding the pellet by such processes as Brillouin and Raman instabilities before it reaches the critical plasma density.[1] This reflection may persist for time periods of the order of 100 ps. The reflectivity increases for plasmas with longer density gradients. The reflected photon energy will be deposited in the first wall in a series of pulses with diminishing amplitudes which depend on the wall surface absorptivity. Like the X-rays and charged particles, the reflected laser light will result in rapid surface heating in the first wall because of its short range.

The rapid surface heating of the first wall results in high stress levels due to the thermal gradients in the material. The coupling between the energy equation and the equation of motion makes the problem difficult to solve. However, for X-rays, the characteristic thermal time for energy deposition, $\tau_T \equiv 1/\mu^2\alpha$, is considerably larger than the characteristic mechanical time, $\tau_m \equiv 1/\mu c$, which, in turn, is larger than the energy deposition period τ (see Table X-A-1). Here μ is the energy attenuation coefficient, α is the thermal diffusivity, and c is the wave velocity in the first wall material. This means that for X-rays the time variation

Table X-A-1

Energy Attenuation Factors and the Pulse Time, and Mechanical and Thermal Characteristic Times for Laser Fusion Reaction Products in Typical First Wall Materials (from Ref. [1])

Parameter	Photons	Soft X-rays	Charged Particles	Neutrons
μ, m^{-1}	10^{8}	10^{5}-10^{6}	10^{5}-10^{6}	1-10
τ, s	10^{-10}	10^{-11}	10^{-6}	10^{-11}
τ_m, s	10^{-11}	10^{-9}-10^{-8}	10^{-9}-10^{-8}	10^{-4}-10^{-3}
τ_T, s	10^{-11}	10^{-7}-10^{-5}	10^{-7}-10^{-5}	10^{3}-10^{5}

effects produced by heat conduction are small compared with the time variation effects in the pressure wave. Hence, a simple instantaneous heat deposition model can be used to determine the temperature rise. For structured pellets the X-rays are produced over a longer time interval than that given in Table X-A-1.Under these conditions, the instantaneous heat deposition model may yield highly conservative estimates of surface temperature. The approximate theory of uncoupled dynamic thermoelasticity and viscoelasticity can be used to determine the moving stress pulse produced by the X-rays.[1] Similar conclusions can be made for neutron energy deposition.

For the reflected laser light, the three time constants, s, τ, τ_T, and τ_m are of the same order and the simple uncoupled models will yield conservative estimates of both temperature and stress. For the ion loading, τ_m is considerably smaller than both τ_T and τ. Therefore, the stress due to the charged particle energy deposition can be determined by quasi-static thermoelastic or viscoelastic theory while the temperature history can be determined using classical diffusion theory.

Analytical models for assessing the surface-heating and stress problems have been developed. Details of these models are given in Section X-C. Application of these models to the SOLASE cavity design is given in Section XI. In the following section (X-B), we shall describe and compare different wall protection concepts proposed to date.

References for Section X-A

1. A. J. Glass and K. L. Cummings (Eds.), "Laser Program Annual Report," Lawrence Livermore Laboratory (1975).

2. L. A. Booth (Compiler), "Central Station Power Generation by Laser-Driven Fusion," Los Alamos Scientific Laboratory Report LA-4858-MS, Vol. I (1972).

3. J. M. Williams, et al., "Engineering Design for Laser Controlled Thermonuclear Reactors," Proc. 5th Symposium on Engineering Problems of Fusion Research, Princeton, NJ (1973).

4. T. G. Frank, et al., "Heat Transfer Problems Associated With Laser Fusion," Proc. 6th National Heat Transfer Conference, St. Louis (1976).

5. J. Hovingh, et al., "The Preliminary Design of a Suppressed Ablation Laser-Induced Fusion Reactor," Proc. 1st Topical Meeting on the Technology of Controlled Nuclear Fusion, CONF-740402-P1, San Diego (1974).

6. J. Hovingh, "First Wall Studies of a Laser-Fusion Hybrid Reactor Design," Proc. 2nd Topical Meeting on the Technology of Controlled Nuclear Fusion, Richland, Washington.

X-B. Wall Protection Concepts

Several conceptual laser fusion reactor designs have been developed during the past few years primarily by LASL and LLL. Compared to SOLASE, these studies have been limited in scope dealing primarily with the problems of cavity design and wall protection. This, one may argue, is the main problem facing the designer. However, one must realize that the reactor cavity represents a small subsystem of the entire reactor design. It is extremely important to investigate how a given wall protection scheme will affect the overall system design. It is our experience that as analysis of a promising concept grows in detail, including synergistic effects, more and more difficult problems, not previously identified, have arisen rendering the concept unattractive. With this caveat in mind, we compare the different wall protection schemes proposed so far, including that for SOLASE.

One obvious solution to the wall protection problem is to make the cavity sufficiently large to reduce the wall loading, and hence, the surface temperatures and stress levels. The economic penalties involved in the increased cavity and blanket cost ($\alpha\ d^2$), and containment building cost ($\alpha\ d^3$) may be significant, especially for large-yield, low-repetition-rate type systems. Hence, there is a need for developing viable protection schemes which do not depend on size alone. The first wall and blanket are designed for optimum neutron wall loading as dictated by radiation damage considerations while a scheme is provided to protect the wall from the pellet debris and X-rays. Four different schemes have been proposed,

viz a wet wall, a liquid wall ("waterfall"), a magnetically-protected dry wall, and a gas-protected dry wall. The merits and demerits of these different design concepts are discussed below. Our aim is to identify the limitations imposed by these concepts as well as areas of uncertainty which require further attention.

X-B-1. The Wetted-Wall Concept

In the wetted-wall concept developed by LASL,[1,2] a thin film of liquid lithium is allowed to flow over a porous niobium first wall in a spherical cavity. The ions and photons produced by the microexplosion deposit their energy in the film which prevents surface heating of the metallic wall. However, the energy deposited in the film causes a significant amount of lithium to evaporate resulting in a periodic impulse load on the metallic wall and blanket structure. After each microexplosion, the ablated lithium is pumped out of the cavity through a supersonic spray condenser; this limits the repetition rate to $\sim 1\ sec^{-1}$. The liquid lithium film is replenished by radial outflow from the blanket through the porous first wall.

While the wetted-wall concept appears to be a clever way of protecting the first wall, numerous questions remain to be answered before its feasibility can be established. First, it is critical to prove that a stable liquid film can be reestablished over the entire wall surface after each microexplosion. Experimental and analytical studies have shown that falling liquid films can experience Marangoni-type instabilities

as a result of local temperature gradients.[3,4] This may lead to growing rivulets or drops of liquid running down the wall causing dry hot regions in the first wall. When a hot spot is formed, the local surface tension falls below that of the adjacent film surface. A force is thereby created which tends to pull the liquid away from the hot spot and thus perpetuate or enlarge the depression. Additional details on falling film stability may be found in Ref. 3,4.

The vapor pressure of lithium at the film surface temperature ($400^{o}C$) is $\sim 2 \times 10^{-4}$ torr. Laser-induced-gas breakdown experiments[5-7] in the alkali-metals strongly suggest that lithium vapor at $\sim 10^{-4}$ torr will breakdown at laser intensities of $\sim 10^{12}$ W/cm^2 (λ = 6940 $\overset{o}{A}$). The breakdown problem is exacerbated at longer wavelengths. These intensities are substantially lower than the on-target intensities thought necessary for laser fusion ($\sim 10^{16}$ W/cm^2). Although the resulting plasma frequency would be much lower than the cut-off frequency for propagation of the laser light, serious questions arise as to whether the energy can be effectively delivered to the target. This is due to the phenomena of self-defocusing of the laser beam[8] and inverse bremsstrahlung absorption which will limit the laser energy reaching the target.

The problem of lithium purification needs special attention since structured pellets may contain significant amounts of non-hydrogenic species. It is also important to show that the pressure pulses produced by the

ablated lithium will result in acceptable stress levels in the wall and blanket structure. The problems of fatigue and stress corrosion should be examined.

The suppressed ablation system developed by LLL is a modification of the wet wall design.[9] Lithium ablation is suppressed by using a niobium liner consisting of pyramidal elements to effectively increase the surface area of the cavity. This liner will presumably lower the energy fluxes to a level where excessive lithium ablation does not occur. In addition to wall design complexity, this concept involves similar uncertainties to those of the wet-wall design.

X-B-2. The Liquid Lithium "Waterfall" Concept

This concept has recently been proposed by LLL for large-yield ($\sim 10^3$-10^4 MJ/pellet), low-rep-rate inertial confinement systems.[10] A similar concept has been investigated by BNL[11] for ion beam systems. Here, a thick fall of liquid lithium ($\sim$ 40 cm thick) with an annular cross section is used to protect the metallic first wall from the microexplosion. The fall impacts onto a lithium pool at the bottom of the cavity and is continuously recirculated to the top of the cylindrical vacuum chamber. The X-rays and pellet debris deposit their energy in the lithium. Also, most of the neutrons' energy is deposited directly in the lithium fall which serves as the primary heat transport and tritium breeding medium.

This concept appears to offer several advantages over the wetted-wall design; however, it is still in a preliminary stage of development and many questions remain to be answered before its feasibility can be established. The main advantages of this concept are: the lithium fall protects the first wall from the photon and ion irradiations and attenuates the neutron flux so that wall damage by the high energy neutrons is considerably reduced. This allows higher wall loadings. High breeding ratio and energy multiplication can be obtained. Due to the time necessary to reestablish the waterfall and pump the cavity, this concept appears suitable for ion-beam systems where large yields and low repetition rates are expected and where the lithium vapor in the chamber will not adversely affect beam focusing onto the pellet.

The uncertainties involved in this concept deal mainly with the dynamics of the lithium fall. It must be shown that, at the required velocity and thickness, the fall will not disassemble prior to reaching the bottom of the cavity. The radial momentum imparted on the lithium fall by the vapor produced during the microexplosion and its possible impact onto the surrounding structure should be examined. It is also important to determine the magnitude of the pressure pulse produced by the evaporated lithium from the pool at the bottom of the chamber. This impulse load will be transmitted directly to the wall and support structure.

It remains to be shown how the areas which are not shielded by the lithium fall (~ 20% of the 4π steradians[10]), including the beam ports' ends, will be protected. Also, the flow characteristics in the wake of the beam ports protruding through the free falling lithium need to be examined. In addition, similar to the wetted-wall design, the problem of lithium purification from the pellet debris needs special attention.

X-B-3. Magnetic Protection

Magnetic protection has been proposed by LASL as a means of limiting the temperature rise produced in the first wall by the charged particles.[12,13] A pre-SOLASE conceptual laser fusion reactor based on the magnetic protection concept has also been developed by the University of Wisconsin.[14] A cylindrical cavity with hemispherical end caps is used (Fig. X-B-1). A solenoid surrounding the cylindrical portion of the cavity is used to divert the charged particles away from the first wall. The magnetic field acts to hinder expansion perpendicular to the axis of the cylinder while allowing the expansion along this axis to proceed unimpeded. The explosion debris is thus channeled to the ends of the cylinder where it is absorbed on the hemispherical end caps. The energy sinks need not be spherical; they can be designed to equalize the incident energy flux at their surface. Compared to the cavity wall, the sinks are relatively far away from the explosion center. Since the particles must travel farther, there can be more time-of-flight spreading of their spatial distribution, allowing the rate of thermal conduction from the surface layer to compete with the energy deposition rate. This can lead to a lower surface

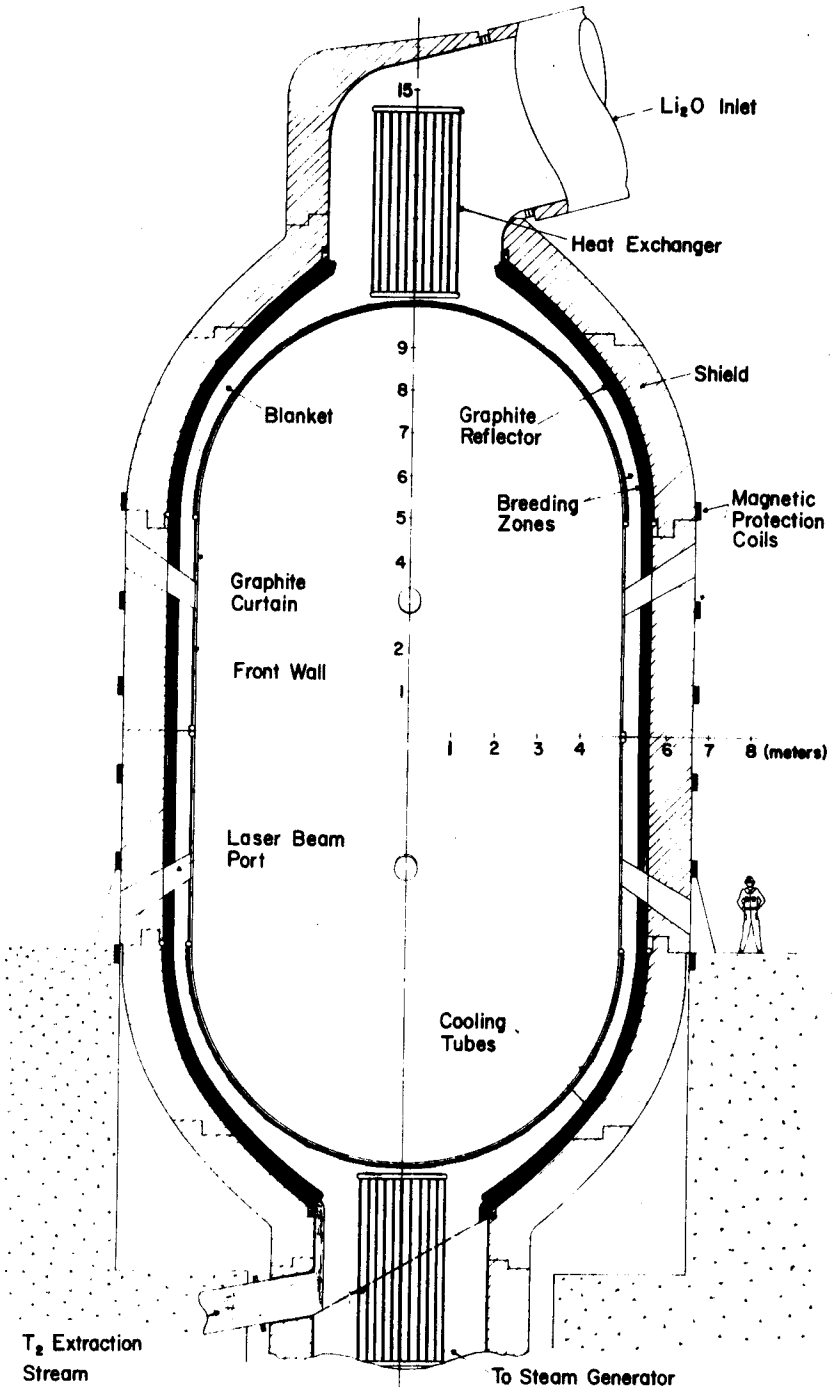

Fig. X-B-1.
Schematic Diagram of the pre-SOLASE Reactor Cavity
Based on the Magnetic Protection Scheme.

temperature. Other means for protecting the wall from the reflected laser light and soft X-rays such as a carbon liner should be provided.[14] An impulse load produced by the expanding plasma against the magnetic field will be imparted onto the first wall; however, the stress levels can be held to acceptable levels.

In the pre-SOLASE design, the photon and ion energy deposited in the carbon liner is radiated to a boiling-water cooled stainless steel wall. In such designs, the neutron wall loading is limited to ~ 4 MW/m^2 since the back temperature of the liner should be kept below ~ 2000^oC in order to prevent excessive evaporation from its front surface.

The principal drawback to magnetic protection is that the exploding plasma is unstable to flute modes, which give rise to transport across the restraining magnetic field. However, for this application confinement is not required. The relevant concern is that the growth rate for the flute modes be small enough to allow time for the debris to stream out the cylindrical chamber. (Note that this requirement makes it desirable for the energy sinks to be close to the explosion center, in opposition to the time-of-flight spreading condition mentioned above. Thus, some optimum distance must be determined). Previous studies indicate that flute growth times may be roughly 5 times longer than transit times out the chamber.[15] However, these results are based on rough estimates and in view of the critical nature of this problem, further study is required.

In the following we present some of the results obtained for our pre-SOLASE design.[14] These results pertain to a 0.4 mg DT pellet with a fractional burn-up of 30% and a yield of 150 MJ. There are approximately 2×10^{18} fast alphas with an average energy of 2 MeV. The debris forms initially a D-T plasma with 260 keV of radial kinetic energy and 26 keV of thermal energy (values at a radius of 2 cm).

If we assume that both groups expand as hot plasmas, then the helium plasma expands first, compressing the field until the radial motion is stopped. This helium plasma continues its expansion along the axis, relieving the pressure, as the field begins to push the plasma back toward the axis. The D-T plasma then streams through the helium plasma and recompresses the field; it too then streams out the ends.[15] If we assume that a particle's velocity component along the axis, v_z, is unchanged by the magnetic field (only approximately true) and that the explosion is isotropic, then the particles are uniformly distributed in v_z. An estimate of the time for an element of D-T plasma on the cylinder axis to reach the energy sink is 3×10^{-6} s, so in 3×10^{-5} s roughly 90% of the plasma has left the chamber. We will now take this characteristic time and investigate some of the relevant processes which occur.

X-B-3-a. Diffusion of the Magnetic Field into the Conducting Wall

If we assume that the field is suddenly compressed against the conducting wall with the helium plasma expansion time, $\tau = 5 \times 10^{-7}$ s,

then the diffusion problem can be approximated by a one-dimensional problem in which there is a jump in the magnetic diffusion coefficient at a point, and B is held constant to the left of the jump point. Solving this problem by matching classical solutions in the two regions gives for the current distribution in the wall (as a function of depth x and time t),

$$j(x,t) \propto \frac{e^{-x^2/4kt}}{N4\pi kt} \text{ , where } k = \frac{c^2}{4\pi\sigma}$$

and σ is the electrical conductivity of the wall material. The half width of this profile is

$$\Delta x = \left(\frac{c^2 \ell n 2}{\pi\sigma}\right) t \ .$$

Setting $t = 3 \times 10^{-5}$ s, we find that a copper shell ($\sigma \simeq 5 \times 10^{17}$ s) would give $\Delta x \simeq .01$ cm, and a stainless steel shell ($\sigma \simeq 10^{16}$ s) would give 0.6 cm. Hence, several millimeters of conducting metal shell should allow the field to be compressed and protect the copper coils from large voltage pulses caused by the expanding plasma.

X-B-3-b. Diffusion of the Magnetic Field into the Plasma

Since hot plasmas have high conductivities and correspondingly small skin depths, we expect the above analysis also to apply here. Indeed, a 200 eV D-T plasma has a conductivity like that of stainless

steel. Since the electrons start out at 20 KeV (thermal) at a radius of 2 cm, for at least radii not too much larger than 2 cm, the field will be excluded because of the high conductivity. At larger radii, we might expect some field penetration due to lower electron temperatures. In addition, if any high Z materials get swept up in the plasma, the conductivity would be further decreased. As the skin depths begin to be of the same size of the radius, the 1-dimensional analysis is no longer applicable. The details of the time evolution of the electron temperature must also be known more exactly to predict the amount of field penetration into the plasma.

X-B-3-c. Time-of-Flight Spreading of the Particles

If we assume that the 26 KeV temperature given by the hydrodynamics has meaning in the terms of a local Maxwellian in a frame moving with the plasma, we may estimate how much the particles are spread in time when they reach the energy sinks. As an illustration we consider 260 KeV deuterons with a 26 KeV thermal spread, interpreted to mean that their distribution function is proportional to Exp $[-\frac{1}{2} m \frac{(v-v_o)^2}{kT}]$. The particles then arrive at a distance z from the source spread in time according to the factor: Exp $[-\frac{1}{2}\frac{mv_o^2}{kT}(1 - \frac{z}{v_o t})^2]$. In the present case, we find a spread of about 0.3×10^{-6} s. This spread will reduce the maximum surface temperature of the sinks.

We now turn to a preliminary analysis of the problem of designing the shape of the energy collecting surfaces at the cylinder ends. This surface can be described by a function z(r) with z = 0 and r = 0. The conditions that determine the shapes are:

(1) The surface is to be as far from the explosion center as possible (i.e., the surface is to be convex, as viewed from the source).

(2) The energy absorbed per unit area is to be constant over the surface. We derive the desired shape in terms of the radial distribution of the particles projected on a plane perpendicular to the cylinder axis. For purposes of illustration we make the simplifying assumption that this distribution is constant in time which is approximately true if the conducting walls which compress the field are at a constant radius over the entire chamber, including the energy sinks. The radial distribution $f(r)$ is normalized by $2\pi \int_0^{R_{max}} f(r)rdr = 1$. An element of surface area at $z(r)$ is given by $dA = 2\pi r\sqrt{1+(\frac{dz}{dr})^2}\, dr$, while the number of particles incident on this strip is $dN = \frac{N}{2}(2\pi r f(r)dr)$. If we require the energy per unit area to be some constant C we find

$$\frac{dz}{dr} = -\sqrt{\frac{N^2}{4C^2} r^2(r) - 1} \ .$$

We pick the negative sign for the square root to make the surface convex.

It is interesting to consider some special cases.

(a) Let $f(r)$ be determined by a thin spherical shell of radius R projected on a plane perpendicular to the axis,

$$f(r) = \frac{1}{2\pi R^2\sqrt{1-(r/R)^2}} \ ;$$

then the collector shapes are as illustrated in Figure (X-B-2).

(b) Let f(r) be determined by the projection of a solid sphere on a plane,

$$f(r) = \frac{3\sqrt{1-(r/R)^2}}{2\pi} ;$$

then the collector shapes are as illustrated in Figure (X-B-3). Note that solutions do not exist for this last case all the way to R. This occurs because at some $r < R$, $\frac{dN}{dA}$ tends to 0 independent of the collector shape, making it impossible to maintain constant energy deposition per unit area. We see that the problem of finding the right collector shape may not have a solution, and it may be necessary to settle for some non-uniformity in the energy per unit area on the collector.

There is another variable in the problem, however, which we ignored in making these simplifying assumptions. The radius of the conducting wall against which the field is compressed may be varied. In particular, it may be held constant along the cylinder, and then be allowed to increase in the energy sink region. As the plasma enters this region, the restraining magnetic pressure will drop, allowing the plasma to expand radially as it traverses the sink region. By varying both the collector shape and the conducting wall radius, it may be possible to achieve uniform wall loading for a wider variety of radial distributions, f(r). A good example of the effect mentioned above is contained in reference 16.

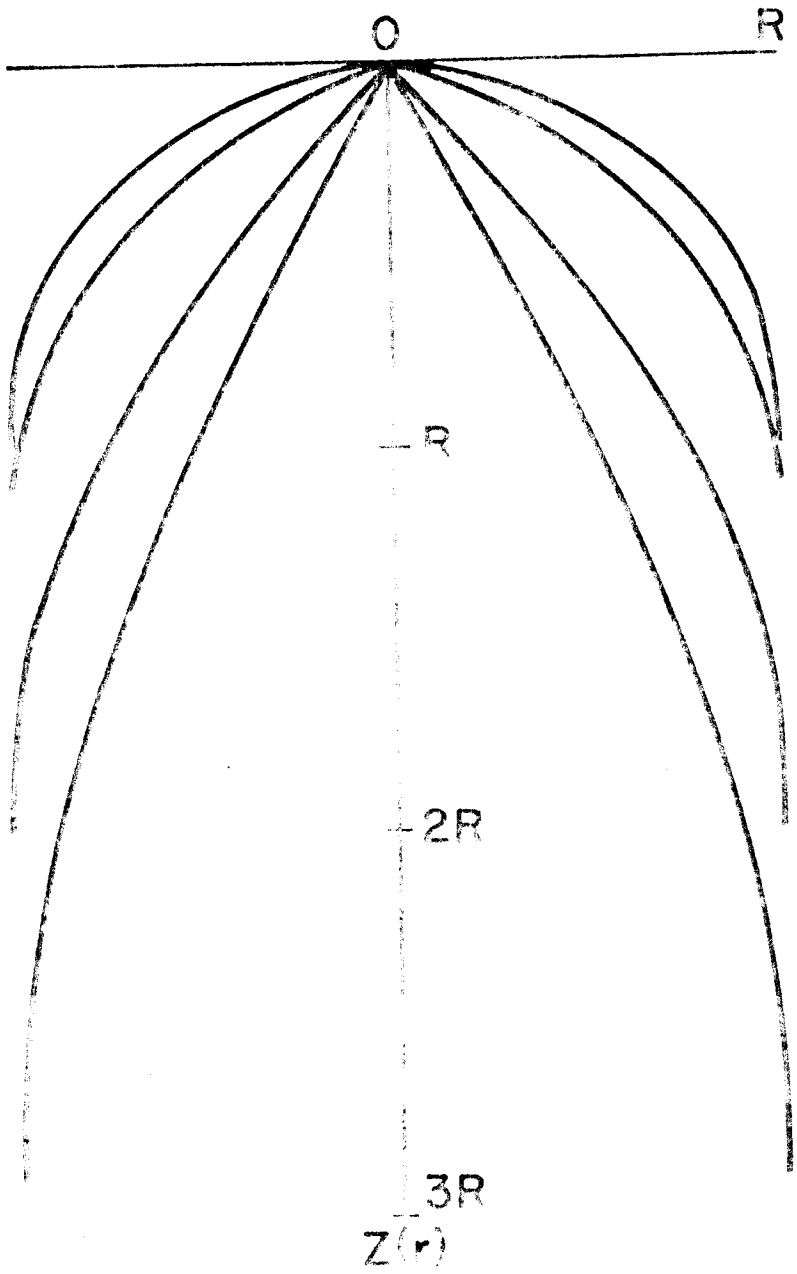

ENERGY SINK SHAPE FOR A SHELL LIKE EXPLOSION.
R = PLASMA RADIUS

Fig. X-B-2.

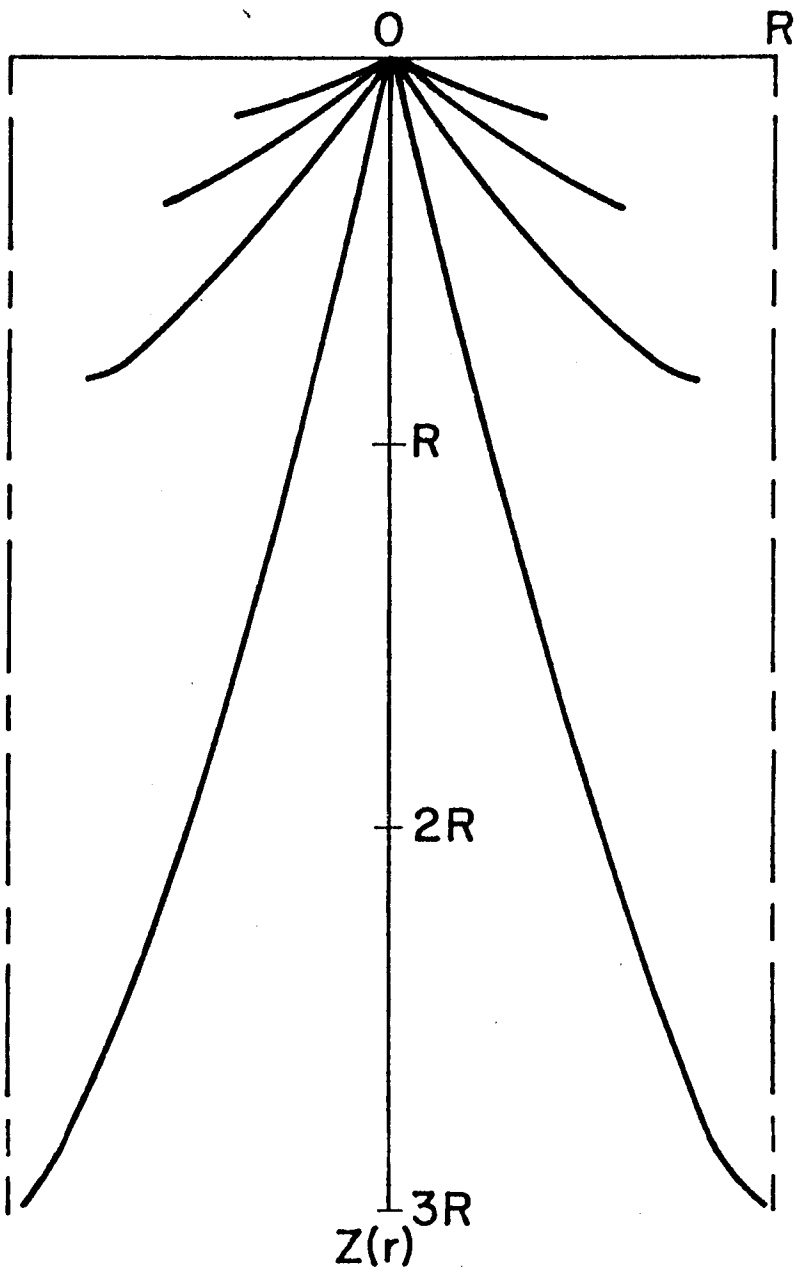

ENERGY SINK SHAPE FOR A SOLID SPHERE EXPLOSION.
R = PLASMA RADIUS

Fig. X-B-3.

In conclusion, magnetic protection appears attractive; however, it is important to establish that the growth rate for the flute instability is sufficiently small. A detailed analysis of the exploding plasma as it is decelerated by the magnetic field in cylindrical geometry is needed.

X-B-4. Gas Protection

The SOLASE reactor design is based on the gas protection concept. The reactor cavity is filled with a buffer gas (neon) which attenuates the charged particles and soft X-rays before reaching the first wall. The energy deposited in the gas is removed by radiation to the chamber walls and external cooling of the hot gas removed by the vacuum system. (A steady stream of cold gas is allowed into the cavity). The energy is radiated from the gas to the front wall over a relatively long time period ($> \sim 1$ ms) so that surface heating and thermal ablation of the wall become insignificant. The shock wave generated in the gas after each micro-explosion is weak and imparts a relatively small periodic impulse loading on the front wall.

Neon is selected as the fill gas because it has the highest laser-induced gas breakdown threshold among all gases, followed closely by helium.[16] In addition, neon has a relatively high stopping power for ions and X-rays and is inert so there is no worry of chemical reactions with the first wall. A disadvantage of neon is its high ionization potential (21 eV) that leads to an inefficient reradiation of the absorbed energy (Section XI). This implies that much of the absorbed

energy must be pumped out of the cavity in the form of hot gas. However, it is the high ionization potential that leads to the high gas breakdown threshold so it is best that it remains as high as possible.

In order to ascertain the viability of this wall protection concept, numerous questions have been addressed. These include:

(1) How does the gas attenuate the charged particles as a function of Z, energy per ion, and gas density?

(2) How does the gas attenuate the X-rays as a function of the spectrum and gas density?

(3) How much energy is reradiated from the gas to the front wall and on what time scale? How does the wall respond thermally to the modified photon spectra and to the pulsating heat flux loads?

(4) Does a shock wave develop in the gas as a result of the energy deposition and how much momentum does this shock transfer to the first wall?

(5) Can the laser beams be propagated through the gas without experiencing gas breakdown? How does this depend on gas density, laser wavelength, and pulse shape?

These questions have been analyzed in detail; the analyses are presented in Section XI.

References for Section X-B

1. L. A. Booth (compiler), "Central Station Power Generation by Laser-Driven Fusion," Los Alamos Scientific Laboratory, LA-4858-MS (1972).

2. J. M. Williams, et al., "A Conceptual Laser Controlled Thermonuclear Reactor Power Plant," Proc. 1st Topical Meeting on the Technology of Controlled Nuclear Fusion, San Diego (1974).

3. V. Ludviksson and E. N. Lightfoot, "Hydrodynamic Stability of Marangoni Films," AIChE Journal, 14, 620 (1968); V. Ludviksson, "Dynamics of Thin Liquid Films," Ph.D. Thesis, Chemical Engineering Department, University of Wisconsin (1968).

4. R. B. Bird, et al., Lectures in Transport Phenomena, AIChE Continuing Education Series, 4, p. 66, et seq. (1969).

5. E. Panarella, "Theory of Laser Induced Gas Ionization," Foundations of Physics, 4, 227 (1974).

6. J. Rizzo and R. C. Klewe, "Optical Breakdown in Metal Vapors," Brit. J. Appl. Phys., 17, 1137 (1966).

7. K. Kishi, et al., "Two-Photon Ionization of Cesium and Sodium Vapors," J. Phys. Soc., Japan, 29, 1053 (1970).

8. D. Henderson, "Laser Pulse Propagation Through Ionizable Media," Los Alamos Scientific Laboratory, LA-5086-MS (1972).

9. J. Hovingh, et al., "The Preliminary Design of a Suppressed Laser Induced Fusion Reactor," Proc. 1st Topical Meeting on the Technology of Controlled Nuclear Fusion, San Diego (1974).

10. J. A. Maniscalco and W. R. Meier, "Liquid-Lithium 'Waterfall' Inertial Confinement Fusion Reactor Concept," Trans. ANS, 26, 62 (1977).

11. J. Powell, et al., "A Liquid-Wall Boiler and Moderator (BAM) for Heavy Ion-Pellet Fusion Reactors," Trans. ANS, 26, 64 (1977).

12. L. A. Booth and T. G. Frank, "A Technology Assessment of Laser-Fusion Power Development," Los Alamos Scientific Laboratory Report LA-UR-76-2060, presented at the Second ANS Topical Meeting on the Technology of Controlled Nuclear Fusion, Richland (Sept. 1976).

13. D. A. Freiwald, T. G. Frank, E. A. Kern, and L. A. Booth, "Laser Fusion Generating Stations Based on the Magnetically Protected Reactor Cavity," Los Alamos Scientific Laboratory Report LA-UR-75-2035, presented at the ANS 1975 Meeting, San Francisco (Nov. 1975).

14. R. W. Conn, et al., "Studies of the Technological Problems of Laser Fusion Reactors," UWFDM-190, University of Wisconsin (Dec. 1976).

15. T. Frank, D. Freiwald, T. Merson, J. Devaney, "A Laser Fusion Reactor Concept Utilizing Magnetic Fields for Cavity Wall Protection, Los Alamos Scientific Laboratory Report LA-UR-74-495, presented at the First ANS Topical Meeting on the Technology of Controlled Nuclear Fusion, San Diego (April 1974).

16. R. G. Tomlinson, et al., "The Breakdown of Noble and Atmospheric Gases by Ruby and Neodymium Laser Pulses," Physics of Quantum Electronics, Kelly, Lax, and Tannenwald (Eds.), p. 520, et seq., McGraw Hill, New York (1966).

X-C. Thermal and Mechanical Response of ICTR First Walls

In this section, the surface-heating problems associated with the pulsed photon and ion irradiations of the first walls and liners of inertially-confined fusion reactor cavities are investigated. Analytical models for predicting the thermal response of these surfaces as a function of the different design and operational parameters of the system and the nature of the incident irradiations are developed. The effectiveness of residual gas as a means for protecting the wall from the ions and soft X-rays is assessed. The models presented here are quite general; application of these models to the SOLASE design is given in Section XI. The analyses presented here have been carried out parametrically. This approach is necessary since pellet design is in its infancy and a wide range of pellet materials, and output characteristics is possible. Careful analysis of the effects of these parameters on the different reactor subsystems, including synergistic effects, should guide pellet designers in their research for suitable pellet(s) for reactor applications.

X-C-1. Thermal Response to Photon Irradiation Without Buffer Gas

Reactor cavities are either spherical or cylindrical with diameters considerably larger than the first wall or liner thickness. Hence, the wall (or liner) can be represented by a slab as shown in Fig. X-C-1. If the pressure inside the cavity is sufficiently low, the photons will not be attenuated and will deposit their energies directly in the wall. Under these conditions, radiative and convective heat flux at the wall's inner surface can be ignored. The outside surface can be assumed to remain at a

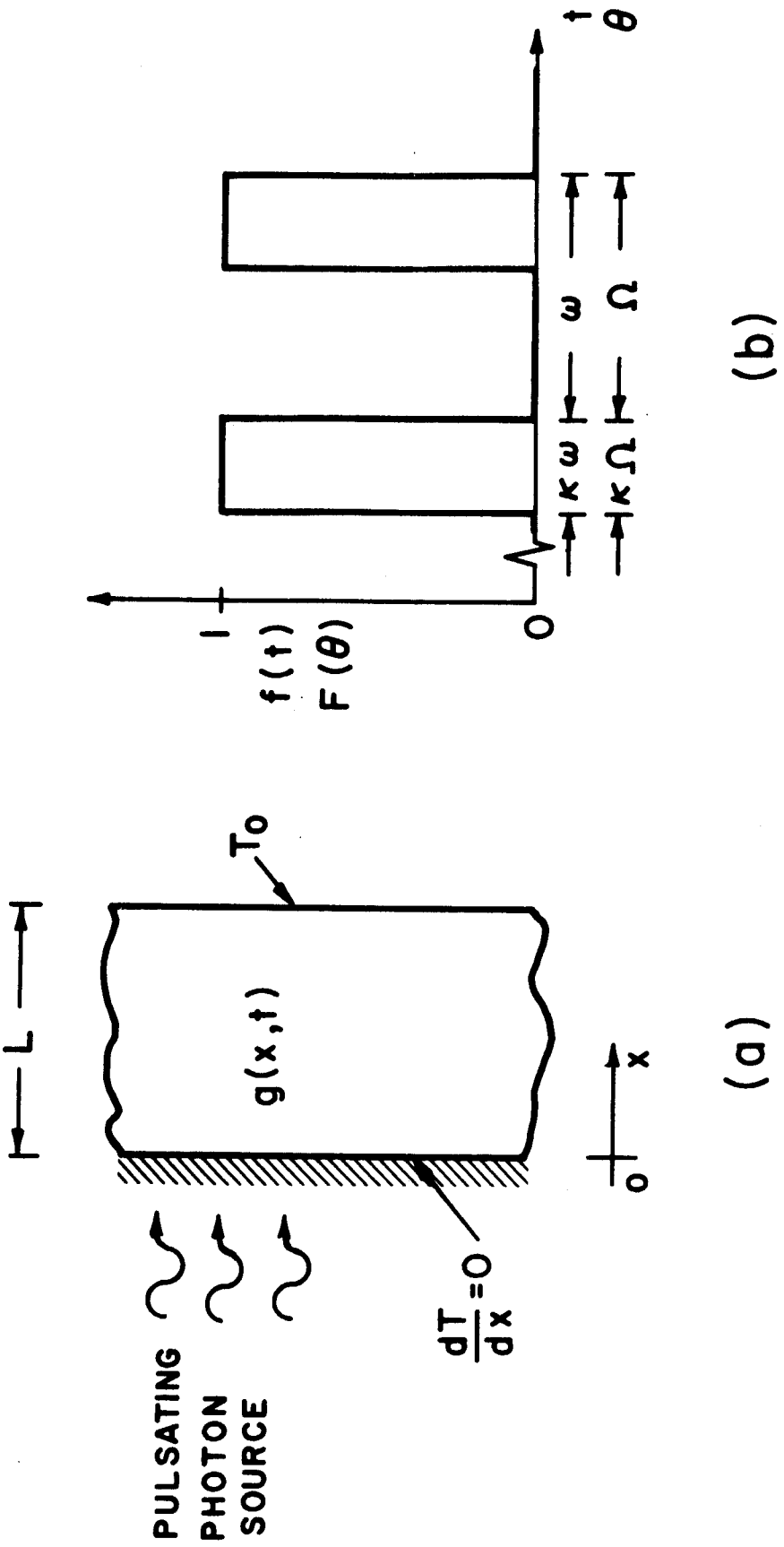
t
θ
ω
Ω
κω
κΩ
1
0
f(t)
F(θ)
(b)
T₀
L
g(x,t)
x
0
(a)
PULSATING
PHOTON
SOURCE
dT/dx=0

Fig. X-C-1.

constant temperature T_o. This condition can be physically realized if the thermal time constant of the wall (or liner) is considerably larger than the time between pulses. Under these conditions, the pulsating volumetric heating loads are rectified and a constant heat flux is radiated or convected from the back surface. The initial temperature distribution in the wall is assumed to be uniform and equal to T_o. This assumption should not affect the sustained transient solution in which we are interested.

For a pulsating flux of monoenergetic photons, the volumetric heat generation rate, g, can be represented by:

$$g(x,t) = (g_o \, \bar{e}^{\mu x}) \, f(t) \tag{1}$$

where g_o is the volumetric heat generation rate at the surface, μ is the absorption coefficient, and f(t) is the on/off control function shown in Fig. X-C-1. The time between pulses and the pulse width are assumed to be constant and equal to ω and $\kappa\omega$ respectively. The surface heat generation rate g_o is related to the incident flux ϕ_o, absorption coefficient μ, and photon energy ε_p by the relation: $g_o = \phi_o \mu \, \varepsilon_p$. The incident flux ϕ_o is assumed to remain constant during the "on" period so that g_o is not a function of time. It is a straightforward matter, however, to extend the analysis to include any temporal flux variations.

We introduce the nondimensional variables:

$$\left.\begin{aligned} u &\equiv (T - T_o) \,/\, [(g_o/\mu) \, \kappa\omega/\rho cL] \\ \xi &\equiv x/L \\ \theta &\equiv \alpha t/L^2 \end{aligned}\right\} . \tag{2}$$

In Eq. (2), the nondimensional temperature $u(\xi,\theta)$ is the ratio between the actual temperature rise and that obtained if the incident photons' energy were to be deposited uniformly and adiabatically. In terms of these nondimensional variables, the heat conduction equation, boundary conditions, and initial condition for the above stated problem are:

$$\frac{\partial^2 u}{\partial \xi^2} + Q(\xi)\, F(\theta) = \frac{\partial u}{\partial \theta} \tag{3a}$$

$$\left.\begin{aligned} \frac{\partial u}{\partial \xi}(o,\theta) &= o \\ u(1,\theta) &= o \end{aligned}\right\} \tag{3b}$$

$$u(\xi,o) = o\ . \tag{3c}$$

The nondimensional heat generation function $Q(\xi)$ is given by: $Q(\xi) = A\, \bar{e}^{b\xi}$; $o \leq \xi \leq 1$, where $A \equiv b/\kappa\Omega$, $b \equiv \mu L$, and $\Omega \equiv \alpha\omega/L^2$. The on/off function $F(\theta)$ is shown in Fig. X-C-1.

The sustained transient solution, $\tilde{u}(\xi,\theta)$, for the above stated problem is given by:

$$\tilde{u}(\xi,\theta) = 2 \sum_{n=1}^{\infty} \cos\left[\left(\frac{2n-1}{2}\right)\pi\xi\right] \left\{\frac{b^2}{b^2+\left(\frac{2n-1}{2}\pi\right)^2}\right\}$$

$$\left\{1 + \bar{e}^{b}\left(\frac{2n-1}{2b}\pi\right)\sin\left(\frac{2n-1}{2}\pi\right)\right\} \left\{\frac{\exp\left[-\left(\frac{2n-1}{2}\pi\right)^2 \delta\Omega\right]}{\left(\frac{2n-1}{2}\pi\right)^2 \kappa\Omega}\right\}$$

$$\left\{\left[\exp\left[\left(\frac{2n-1}{2}\pi\right)^2 \delta\Omega\right]-1\right] + \frac{\exp\left[\left(\frac{2n-1}{2}\pi\right)^2 \kappa\Omega\right]-1}{\exp\left[\left(\frac{2n-1}{2}\pi\right)^2 \Omega\right]-1}\right\}$$

$$(o \leq \delta \leq \kappa) \tag{4}$$

and,

$$\tilde{u}(\xi,\theta) = 2\sum_{n=1}^{\infty} \cos\left[\left(\frac{2n-1}{2}\right)\pi\xi\right] \left\{\frac{b^2}{b^2+\left(\frac{2n-1}{2}\pi\right)^2}\right\} \left\{1 + \bar{e}^{b}\left(\frac{2n-1}{2b}\pi\right)\sin\left(\frac{2n-1}{2}\pi\right)\right\} \left\{\frac{\exp\left[-\left(\frac{2n-1}{2}\pi\right)^2 \delta\Omega\right]}{\left(\frac{2n-1}{2}\pi\right)^2 \kappa\Omega}\right\} \left\{\frac{\exp\left[\left(\frac{2n-1}{2}\pi\right)^2 \kappa\Omega\right]-1}{1-\exp-\left[\left(\frac{2n-1}{2}\pi\right)^2 \Omega\right]}\right\}$$

$$(\kappa \leq \delta \leq 1) \ . \qquad (5)$$

In Eqs. (4) and (5), the fraction δ is defined by: $\theta = (N + \delta)\Omega$, where N is an integer much larger than unity.

Equations (4) and (5) can be used to determine the nondimensional transient temperature distribution in the liner resulting from the pulsating exponential heat deposition given by Eq. (1). After a large number of pulses, the surface temperature will vary in a cyclic manner between a maximum value, u_{max}, at $\delta=\kappa$ and a minimum value, u_{min}, at $\delta=1$. These temperature extremes are of particular significance when estimating the stress levels produced in the liner. These are necessary for determining whether spallation will take place.

For smaller values of Ω, i.e. when the time constant of the liner is considerably larger than the time between pulses, u_{min} will depend only on

the nondimensional absorption coefficient b, while u_{max} will depend on both b and the nondimensional pulse width κ. Plots of u_{min} and u_{max} as functions of b and κ for $\Omega = 0.01$ are shown in Fig. X-C-2. These results are quite general inasmuch as they can be used for arbitrary geometry, material absorption coefficient (i.e. photon energy), repetition rate, wall loading, and pulse width. In the following, we show how these results can be directly used to determine surface temperature rise produced by the reflected laser light for different lasers and pellet "reflectivities". These results shown in Fig. X-C-3 are also used, along with superposition techniques, to determine the surface temperature rise produced by the X-rays emanating from the microexplosion.

X-C-1-a. Temperature Rise Produced by the Reflected Laser Light

For low-energy photons, the attenuation coefficient μ in the exponential heat deposition curve of Eq. (1) may be estimated by considering the attenuation of electromagnetic radiation in a homogeneous, isotropic, conducting medium with zero surface reflectivity. The result is $\mu = 8\pi/\lambda$ where λ is the wavelength.[1] Therefore, the results shown in Fig. X-C-2 can be readily used to determine the surface temperature rise produced by the reflected laser light for a given geometry and operating conditions.

A 6.5 mm thick graphite wall in a 12 m diameter cavity is considered. For a 1 MJ laser with a repetition rate of 20 sec^{-1} and a pellet" reflectivity" of 15%, the surface temperature rise is plotted in Figs. X-C-3, 4 for different laser wavelengths and pulse widths. These results can be easily used for other conditions since $\Delta T_{surface}$ is linearly proportional to the

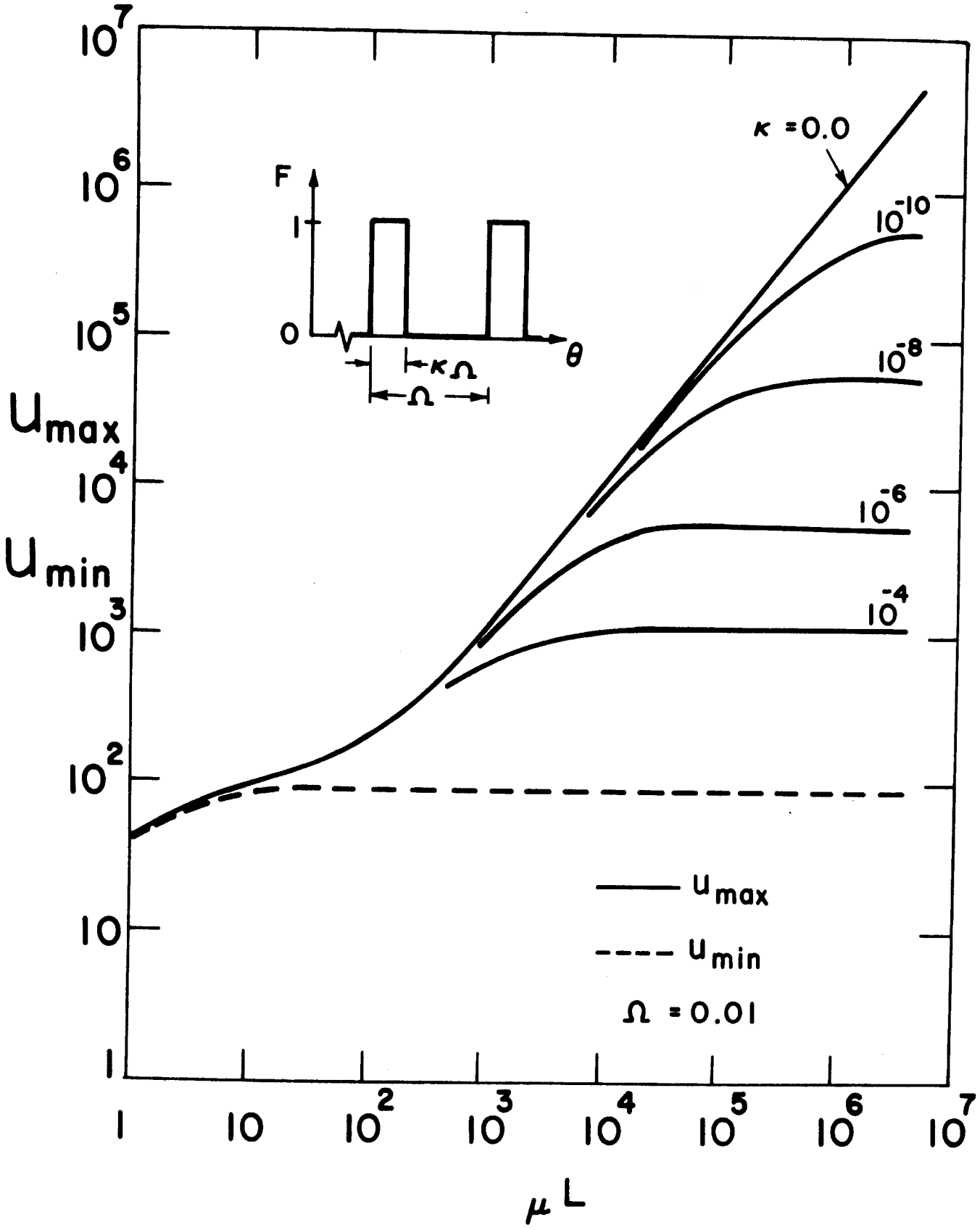
10^7
10^6
10^5
10^4
10^3
10^2
10
1
U_{max}
U_{min}
F
1
0
θ
κΩ
Ω
κ = 0.0
10^{-10}
10^{-8}
10^{-6}
10^{-4}
u_{max}
u_{min}
Ω = 0.01
1
10
10^2
10^3
10^4
10^5
10^6
10^7
μL

Fig. X-C-2.

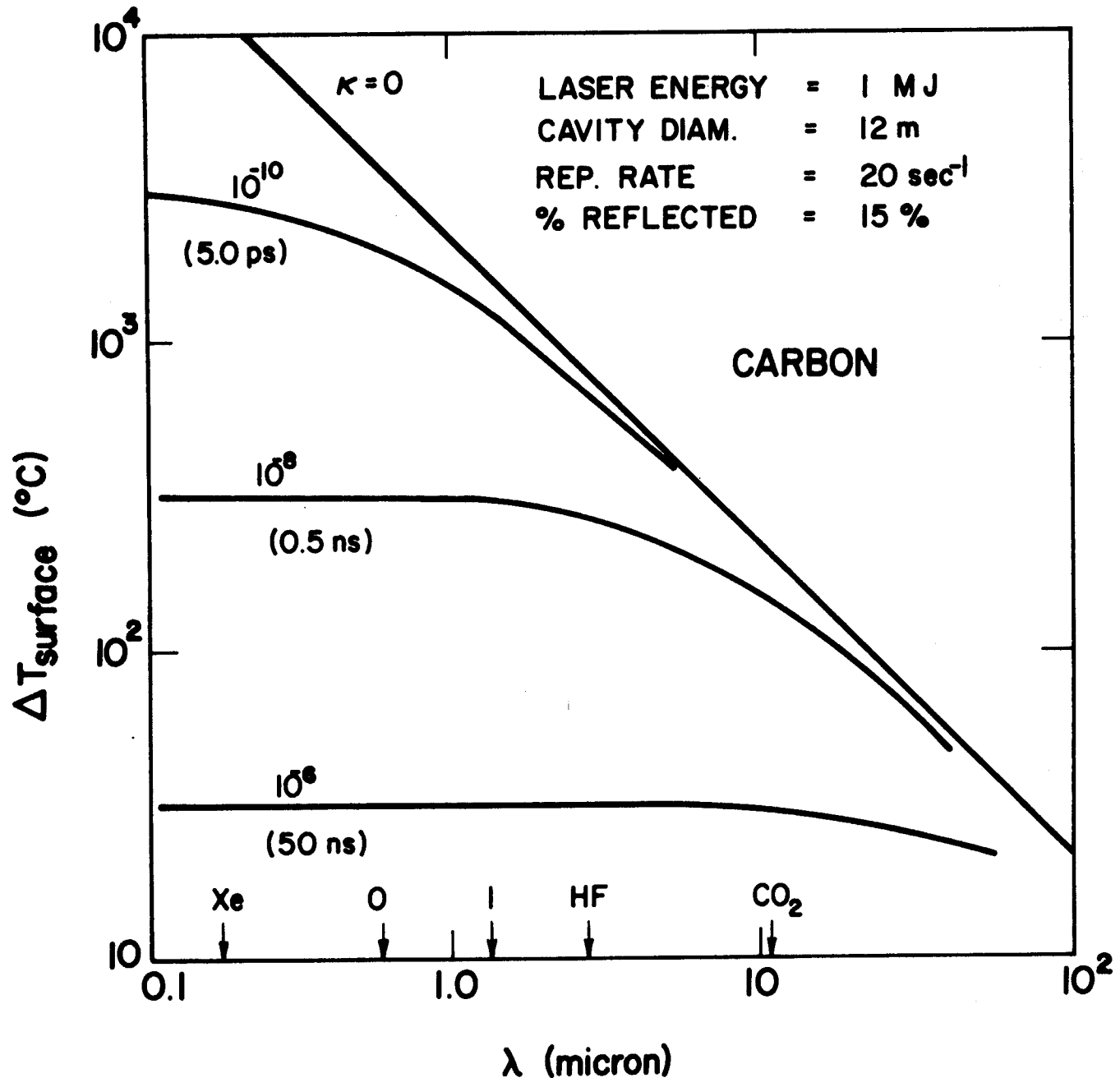
10^4
10^3
10^2
10
$\Delta T_{surface}$ (°C)
κ = 0
LASER ENERGY = 1 MJ
CAVITY DIAM. = 12 m
REP. RATE = 20 sec^{-1}
% REFLECTED = 15 %
10^{-10}
(5.0 ps)
CARBON
10^{-8}
(0.5 ns)
10^{-6}
(50 ns)
Xe
O
I
HF
CO_2
0.1
1.0
10
10^2
λ (micron)

. Fig. X-C-3.

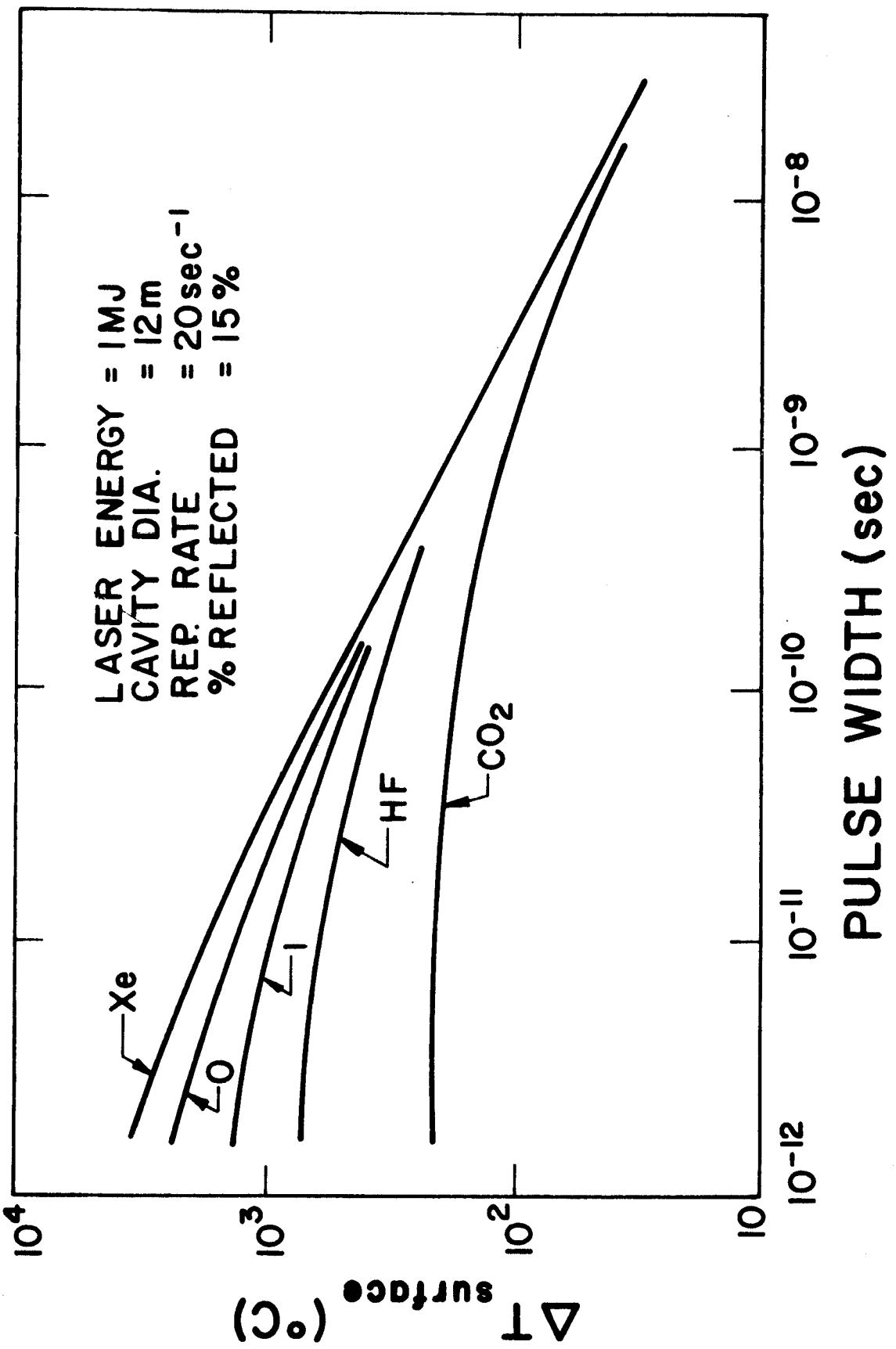
LASER ENERGY = 1MJ
CAVITY DIA. = 12m
REP. RATE = 20sec⁻¹
% REFLECTED = 15%
Xe
I
O
HF
CO2
ΔT surface (°C)
10⁴
10³
10²
10
10⁻¹²
10⁻¹¹
10⁻¹⁰
10⁻⁹
10⁻⁸
PULSE WIDTH (sec)

Fig. X-C-4.

incident flux. It should be emphasized that the results shown in Figs. X-C-3, 4 do not account for any evaporation which may take place at the liner surface. Figure X-C-3 is quite valuable inasmuch as it allows us to estimate the maximum tolerable pellet reflectivity corresponding to the onset of liner sublimation or spallation.

X-C-1-b. Temperature Rise Produced by the X-rays

It is important to be able to determine the thermal response of the liner when subjected to a pulsating photon source with an arbitrary spectrum. This task can be readily accomplished by extending the solution for mono-energetic photons by means of superposition techniques. The X-ray spectra produced by the microexplosions are approximated by black-body radiations in the range of 0.1-2.0 keV. This range is sufficiently wide to cover pellet designs of interest.

The spectrum is divided into M bands with average photon energies ϵ_i, i = 1,2, . . ., M. Let ζ_i be the fraction of the incident energy within band i so that:

$$\sum_{i=1}^{M} \zeta_i = 1. \tag{6}$$

The surface flux from the pulsating black-body source is given the symbol S so that the incident energy within a single pulse per unit surface area is equal to $S\kappa\omega$. We assume that the incident photons within the different bands will result in exponential heat deposition curves with absorption coefficients μ_i, i = 1, 2, . . ., M, so that the corresponding net heat generation rate g(x,t) can be represented by:

$$g(x,t) = f(t)\, S \sum_{i=1}^{M} \zeta_i\, \mu_i\, \bar{e}^{\mu_i x} . \tag{7}$$

The linearity of Eqs. (3a, b) allows the superposition of monoenergetic results so that:

$$u(\xi,\theta) = \sum_{i=1}^{M} \zeta_i \, u_i(\xi,\theta) \tag{8}$$

where $u_i(\xi,\theta)$ is the solution to Eqs. (3a-c) given by Eqs. (4) and (5) with b equal to b_i.

For graphite, the absorption coefficients are curve fitted for five ranges of photon energies: (0.01-0.284 kev), (0.284-0.80 kev), (0.80-4.00 kev), (4.0-20.0 kev), and (20.0-100.0 kev) using the relations of the form:[2]

$$(\mu/\rho) \ (cm^2/g) = \sum_{j=1}^{4} a_j/\varepsilon_p^j \ , \tag{8a}$$

where ε_p is the photon energy in kev. The constants a_j, j = 1 - 4 for the five ranges of photon energies are given in Table X-C-1.

A 6.5 mm thick graphite liner in a 12 m diameter cavity is considered. For a pellet yield of 150 MJ, a repetition rate of 20 sec^{-1}, and an X-ray fraction of 1%, the periodic surface temperature rise is shown in Fig. X-C-5 for different black-body temperatures and pulse durations. Obviously, softer spectra produce higher surface temperature jumps because of their shorter range. The case $\kappa = 0$ corresponds to instantaneous deposition of the X-ray energy into the wall. Similar results for niobium are shown in Fig. X-C-6.

Again, it should be emphasized that the results shown in Figs. X-C-5, 6 do not account for any evaporation which may take place at the liner surface. However, these results should help in determining the conditions corresponding to the onset of liner sublimation or spallation.

Table X-C-1

Parameters a_j for the Absorption Coefficients of Graphite Given by Eq. (8a)[2]

Photon Energy (kev)	a_1	a_2	a_3	a_4
0.01-0.284	-6.531×10^{2}	3.748×10^{2}	-5.790	2.678×10^{-2}
0.284-0.80	-9.022×10^{2}	1.760×10^{3}	1.549×10^{3}	-2.280×10^{2}
0.80-4.0	-7.363	-1.537×10^{1}	2.672×10^{3}	-4.482×10^{2}
4.0-20.0	1.640	-9.428×10^{1}	2.872×10^{3}	-5.583×10^{2}
20.0-100.0	5.621×10^{-4}	-2.533	1.169×10^{3}	9.909×10^{3}

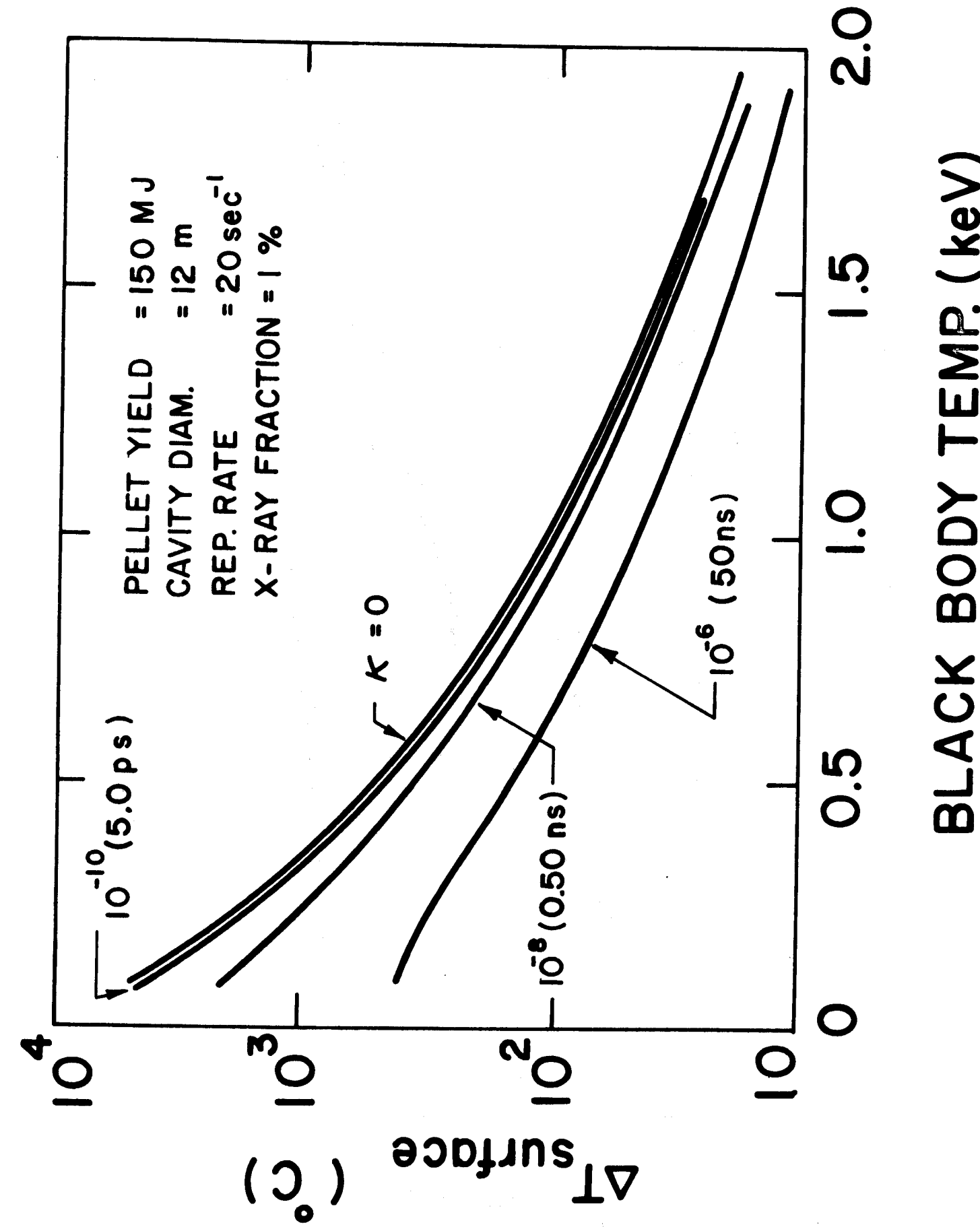
PELLET YIELD = 150 MJ
CAVITY DIAM. = 12 m
REP. RATE = 20 sec⁻¹
X-RAY FRACTION = 1 %
K = 0
10⁻¹⁰ (5.0 ps)
10⁻⁸ (0.50 ns)
10⁻⁶ (50ns)
ΔT surface (°C)
10⁴
10³
10²
10
0
0.5
1.0
1.5
2.0
BLACK BODY TEMP. (keV)

Fig. X-C-5

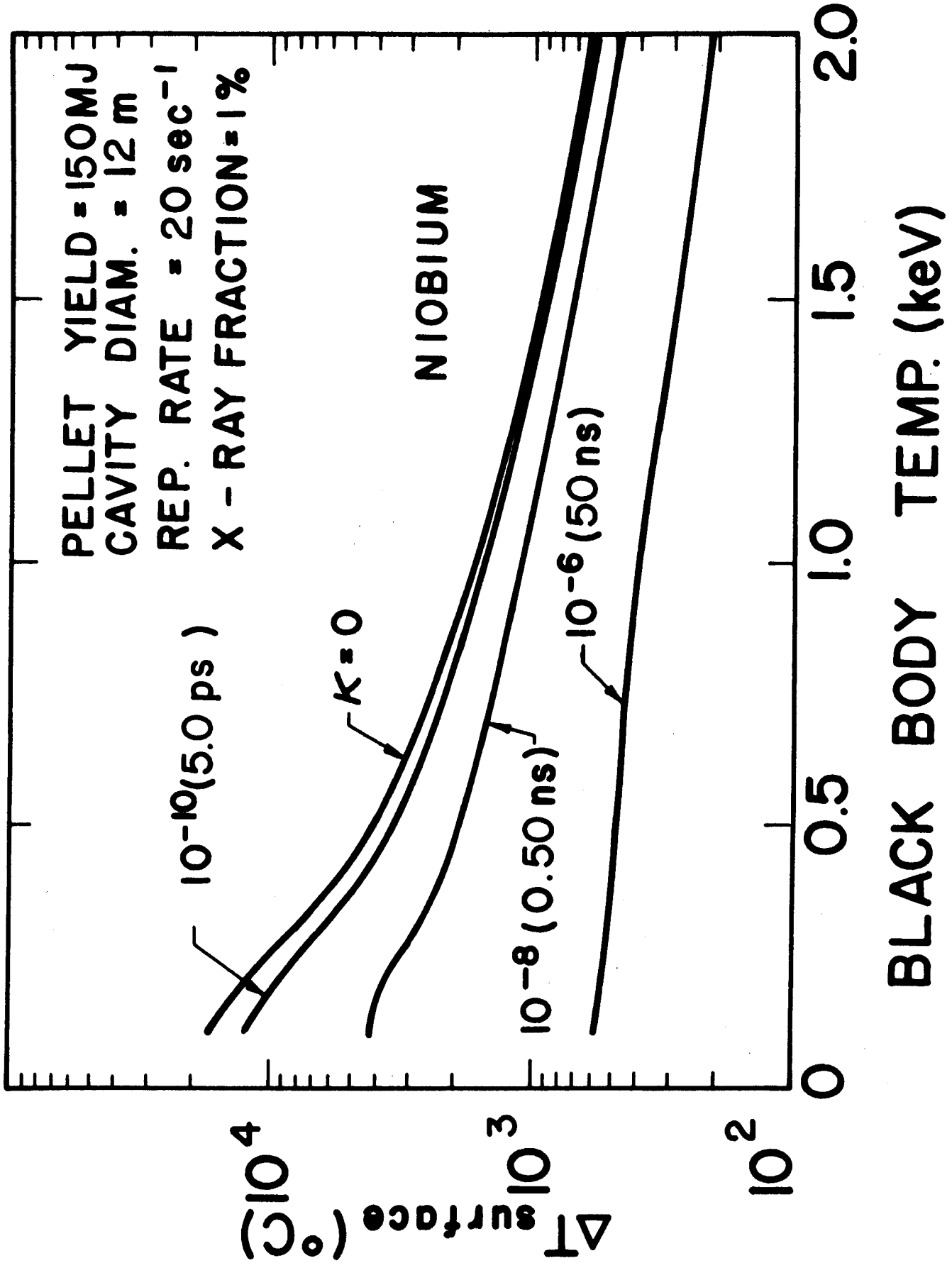
PELLET YIELD = 150MJ
CAVITY DIAM. = 12 m
REP. RATE = 20 sec⁻¹
X - RAY FRACTION = 1%
NIOBIUM
10⁻¹⁰(5.0 ps)
K = 0
10⁻⁶ (50 ns)
10⁻⁸ (0.50 ns)
ΔT surface (°C)
10⁴
10³
10²
0
0.5
1.0
1.5
2.0
BLACK BODY TEMP. (keV)

Fig. X-C-6.

X-C-2. Thermal Response to Pulsed Ion Sources with No Buffer Gas

The thermal response of the wall (or liner) to ion pulses can be determined upon knowledge of the spatial energy deposition as a function of particle energy and arrival time of each particle. A model has been developed whereby a given spectrum of particles is initiated at the cavity center and each particle is allowed to propogate uncollided to the point of impact. The resulting particle arrival density is combined with their slowing-down characteristics to yield the spatial and temporal distribution of energy deposition. This, in turn, is used to determine the thermal response of the wall.

The particle energy loss is usually calculated as a function of its local kinetic energy. For electronic losses described by modified Linhard slowing down model,[3] the rate of energy loss is given by

$$\frac{dE}{dx} = - C \left(\frac{E}{E_o}\right)^{1/2} . \tag{9}$$

For a particle with incident energy E_1, Eq. (9) can be transformed from spectral to spatial dependence as:

$$\frac{dE}{dx}(x) = \frac{xC^2}{2E_o} - C\left(\frac{E_1}{E_o}\right)^{1/2} . \tag{10}$$

The particle range, $x_m(E_1)$, is given by:

$$x_m(E_1) = \frac{2(E_o E_1)^{1/2}}{C} . \tag{11}$$

The particles from a pulsed source will arrive at a given location with an arrival density function f(t) given by:

$$\int_t f(t)dt = -\int_E S(E)dE \ . \qquad (12)$$

Here, the integral is equal to the total number of incident particles per unit surface area, and S(E) is the particle energy spectrum at x = 0. If the kinetic energy of the particles is primarily directed along the propagation axis (i.e. small thermal component), the arrival density would be given by:

$$f(t) = 2S(E)\ E^{3/2}/B \qquad (13)$$

where, $B = 2.284 \times 10^{-6}\ RA^{1/2}$. Here, R is the distance travelled by the particles (i.e. cavity radius) in meters and A is the particle mass in amu.

The volumetric heating rate is related to the arrival density function by : $g(x,t) = f(t)\ \frac{dE}{dx}\ (x)$. Therefore,

$$\left.\begin{aligned} g(x,t) &= f(t)\ [\frac{A_1}{t} - A_2\ x]; \quad x < \frac{2BE^{1/2}}{Ct} \\ &= 0 \qquad\qquad\qquad\quad ; \quad x > \frac{2BE_o^{1/2}}{Ct} \end{aligned}\right\} \qquad (14)$$

where $A_1 \equiv (CB/E_o^{1/2})$, $A_2 \equiv C^2/2E_o$, and $(B/\sqrt{E}_{max} < t < B/\sqrt{E}_{min})$. Here, E_{min} and E_{max} are the limits of the spectrum.

For a semi-infinite solid with an insulated boundary at x = 0, and volumetric heat source g(x,t), the transient temperature distribution is given by:(4)

$$T(x,t) = \iint_{tx} \frac{g(x',t')}{\rho c} G(x,t,x',t')\, dx'\, dt'$$

where G is Green's function given by:

$$G(x,t,x',t') = \frac{1}{2\sqrt{\pi\alpha(t-t')}} \left\{ \exp\left[-(x - x')^2/4\alpha\,(t - t')\right] + \exp\left[-(x + x')^2/4\alpha\,(t - t')\right] \right\} .$$

For the volumetric heat source given by Eq. (14), the above equation yields:

$$T(x,t) = \frac{1}{\rho c} \int_{t_{min}}^{t_{max}} f(t') \left\{ Q_1(t',t,x) + Q_2(t',t,x) + Q_3\,(t',t,x) \right\} dt' \qquad (15)$$

where

$$\left.\begin{aligned} Q_1(t',t,x) &= \frac{A_1}{2t'} \left[\operatorname{erf}(F_1) + \operatorname{erf}(F_2)\right] , \\ Q_2(t',t,x) &= \frac{A_2 x}{2} \left[\operatorname{erf}(F_2) - \operatorname{erf}(F_1) - 2\operatorname{erf}(F_o)\right] , \\ Q_3(t',t,x) &= A_2 \sqrt{\frac{\alpha(t-t')}{\pi}} \left[\bar{e}^{F_2^2} + \bar{e}^{F_1^2} - 2\bar{e}^{F_o^2}\right] , \\ F_o &\equiv x/2\sqrt{\alpha(t-t')} , \\ F_1 &= (x_m - x)/2\sqrt{2\alpha(t-t')} , \\ F_2 &= (x_m + x)/2\sqrt{2\alpha(t-t')} , \end{aligned}\right\}$$

and

$$\left.\begin{aligned} x_m &= 2BE_o^{1/2}/Ct' . \end{aligned}\right\} \qquad (16)$$

The above analysis has been carried out for intermediate energy ions characteristic of pellet debris which can be described by the modified Linhard slowing down model[3] (Eq. 9). For heavier ions, the inclusion of nuclear stopping will alter the deposition profiles to be more spatially uniform. Incorporation of this effect yields a result similar to Eq. (15). In all cases, the time integral is performed numerically so that arbitrary spectra can be accommodated. The use of the semi-infinite solid model to predict the temperature response of the liner to ion irradiation should be quite accurate since the ion's range is extremely short compared to practical wall thicknesses.

Results are shown for 200 kev Maxwellian spectra in a 12 m diameter cavity. Figure X-C-7 shows the arrival flux density of He and Si particles as a function of time. Figure X-C-8 shows the time-dependent energy deposition rate at various distances from the front surface for helium in carbon. The corresponding temperature response is shown in Fig. X-C-9. Similar results for silicon ions in carbon and helium ions in tantalum are shown in Figs. X-C-10 and 11 respectively.

The results shown in Figs. X-C-9 through X-C-11 have been normalized to an ion wall loading of 1 J/cm^2 per pulse. Ion fluxes for conceptual laser fusion reactors can be much higher than 1 J/cm^2 per pulse; assuming 23% of the energy yield to be carried by the charged particles, the ion flux for SOLASE is $\sim$7.6 J/cm^2 per pulse. The resulting temperatures would be too high for wall survival and protective measures must be employed. In the following, we shall investigate the effectiveness of buffer gas as a means

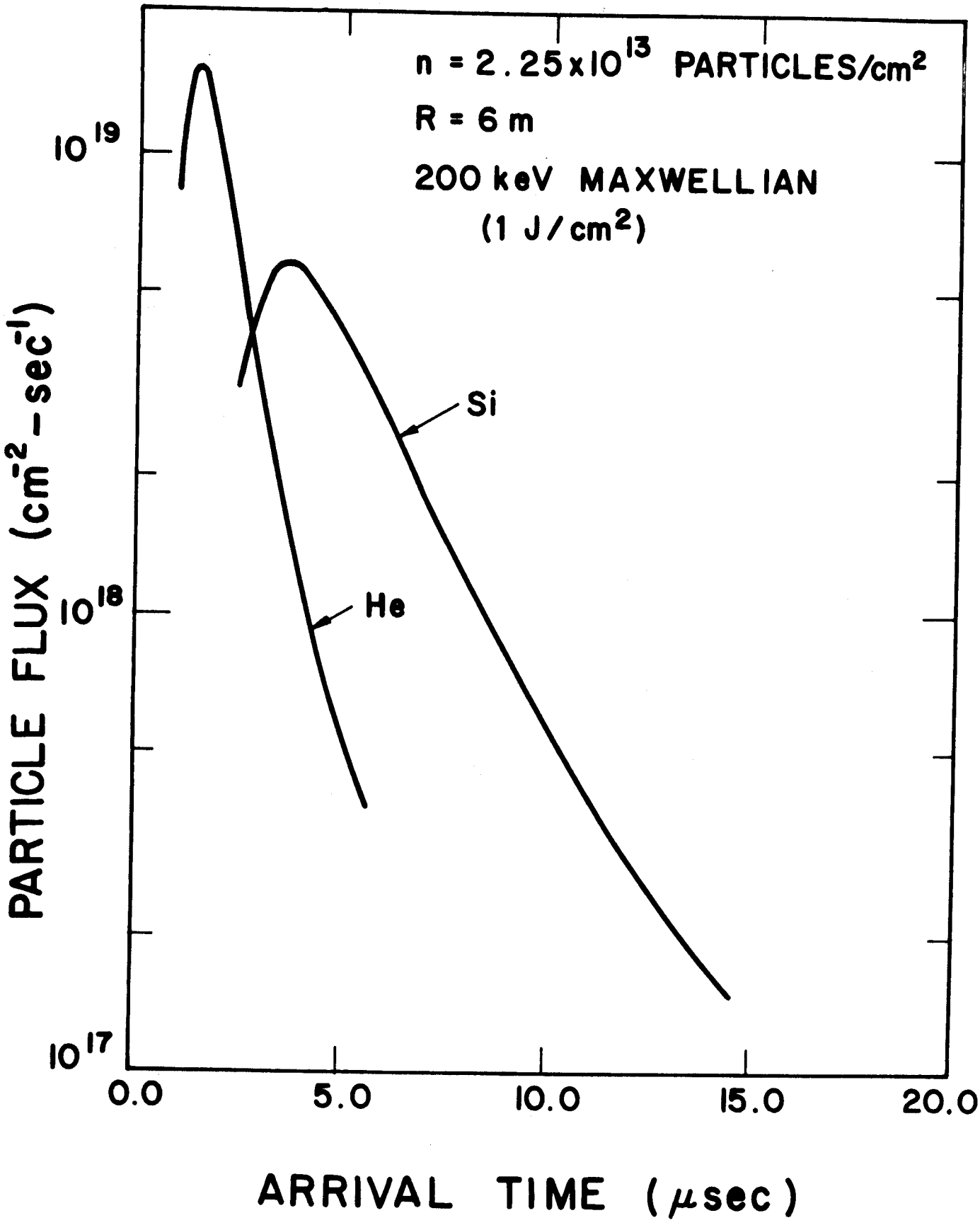
n = 2.25x10^13 PARTICLES/cm^2
R = 6 m
200 keV MAXWELLIAN
(1 J/cm^2)
Si
He
PARTICLE FLUX (cm^-2-sec^-1)
10^19
10^18
10^17
0.0
5.0
10.0
15.0
20.0
ARRIVAL TIME (μsec)

Fig. X-C-7.

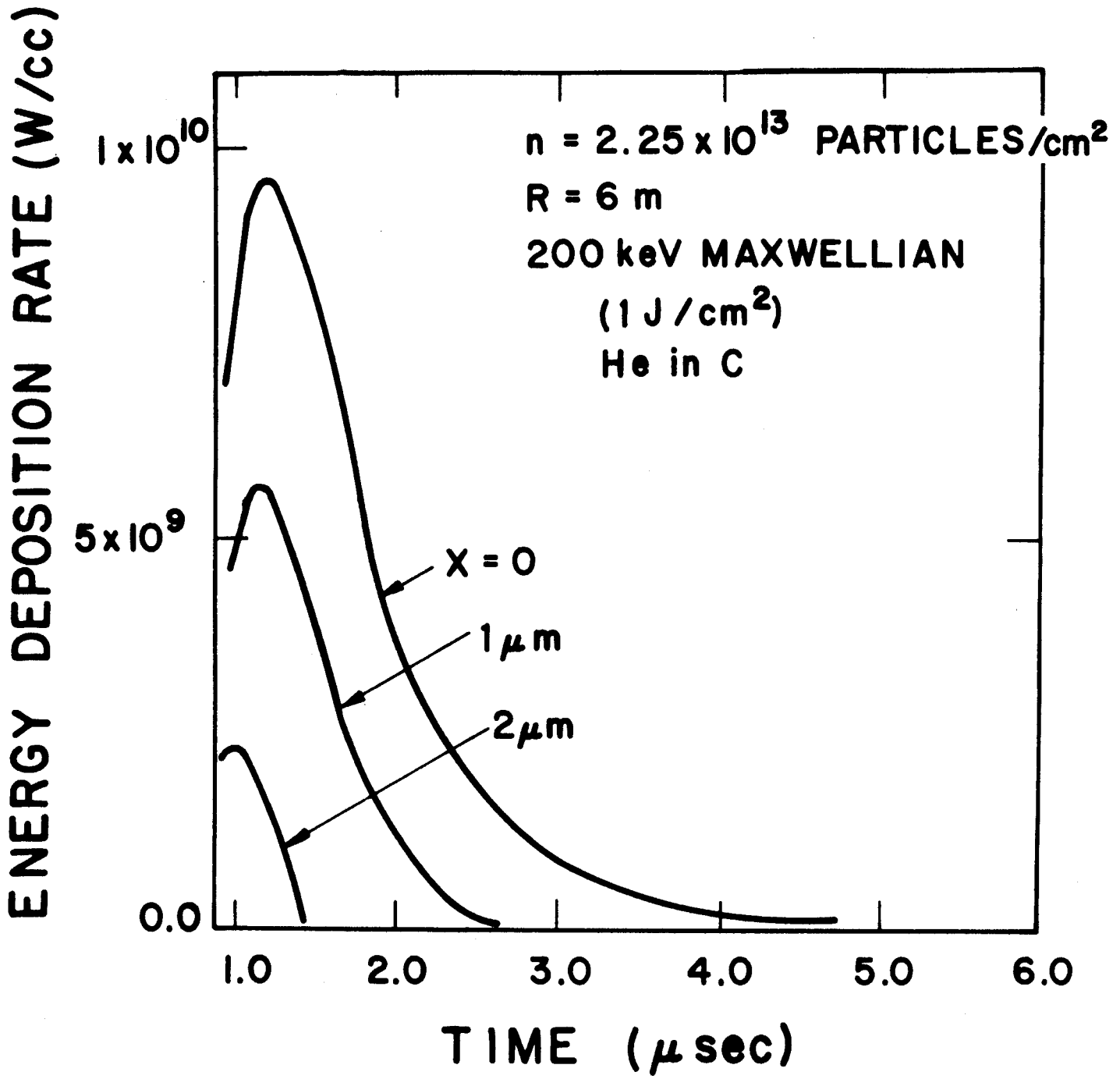
ENERGY DEPOSITION RATE (W/cc)
1 x 10^10
5 x 10^9
0.0
n = 2.25 x 10^13 PARTICLES/cm^2
R = 6 m
200 keV MAXWELLIAN
(1 J/cm^2)
He in C
X = 0
1 μm
2 μm
1.0
2.0
3.0
4.0
5.0
6.0
TIME (μsec)

Fig. X-C-8.

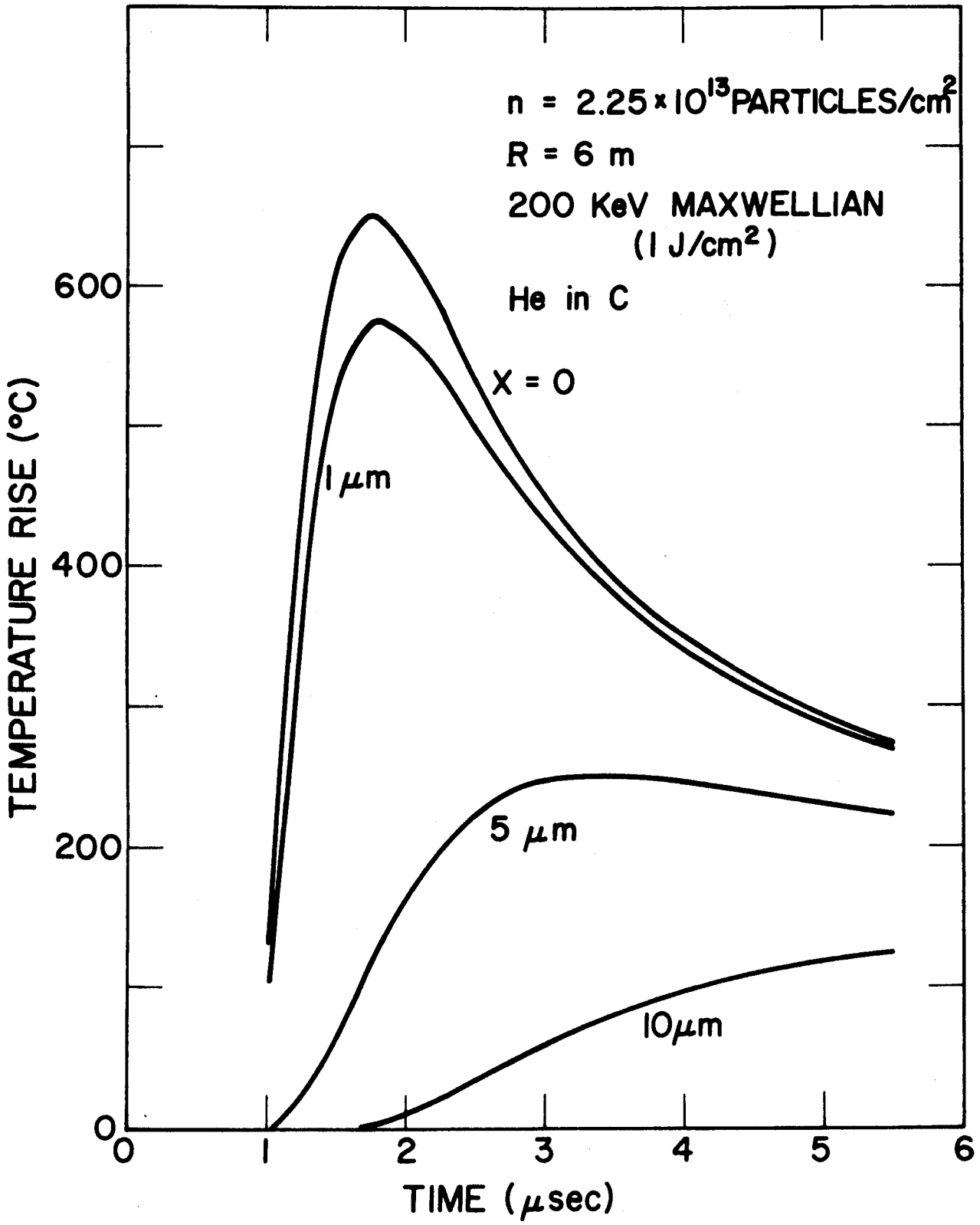
n = 2.25 × 10^13 PARTICLES/cm^2
R = 6 m
200 KeV MAXWELLIAN
(1 J/cm^2)
He in C
X = 0
1 μm
5 μm
10μm
TEMPERATURE RISE (°C)
0
200
400
600
0
1
2
3
4
5
6
TIME (μsec)

Fig. X-C-9.

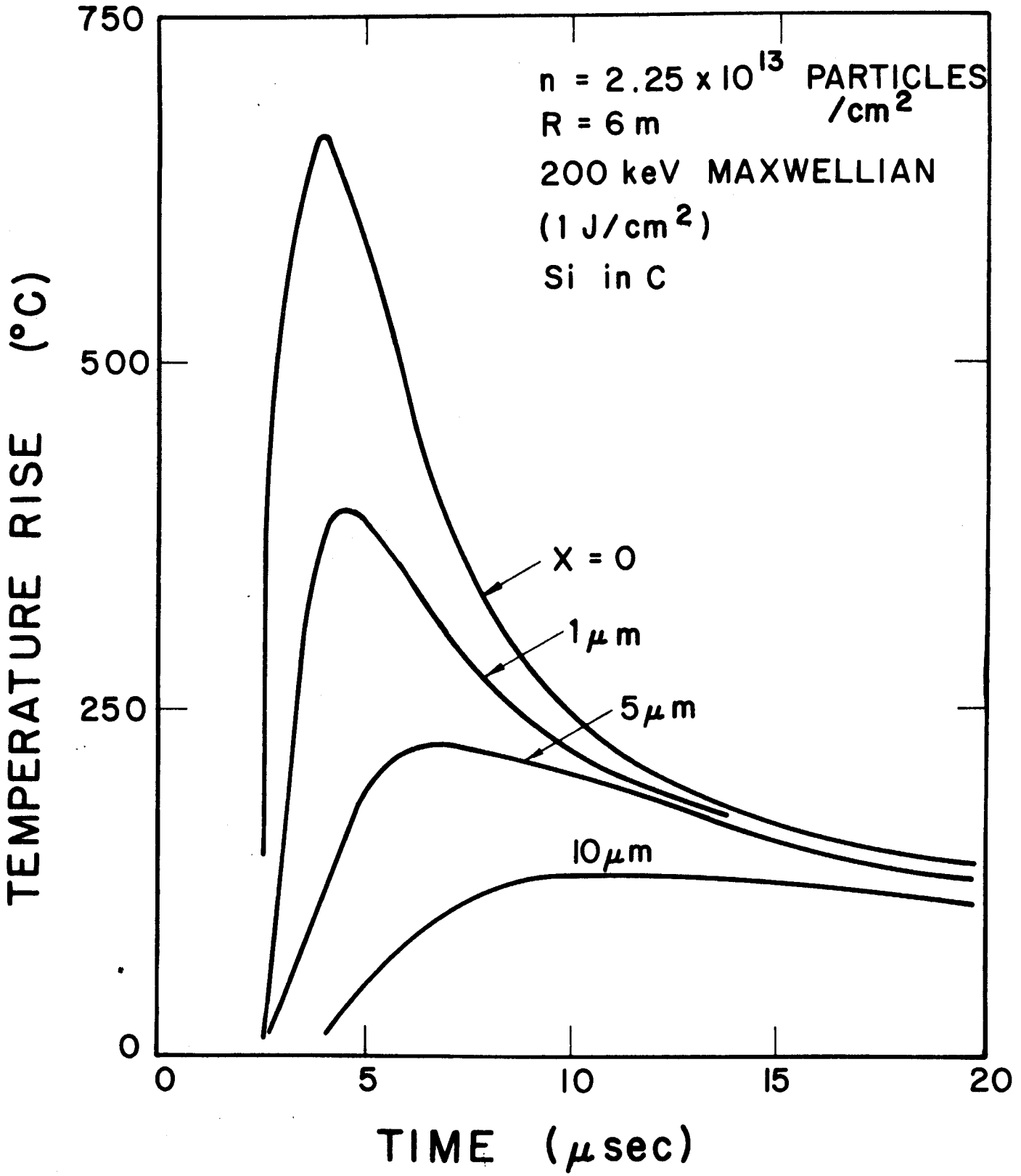
750
500
250
0
0
5
10
15
20
TEMPERATURE RISE (°C)
TIME (μsec)
n = 2.25 x 10^13 PARTICLES /cm^2
R = 6 m
200 keV MAXWELLIAN
(1 J/cm^2)
Si in C
X = 0
1μm
5μm
10μm

Fig. X-C-10.

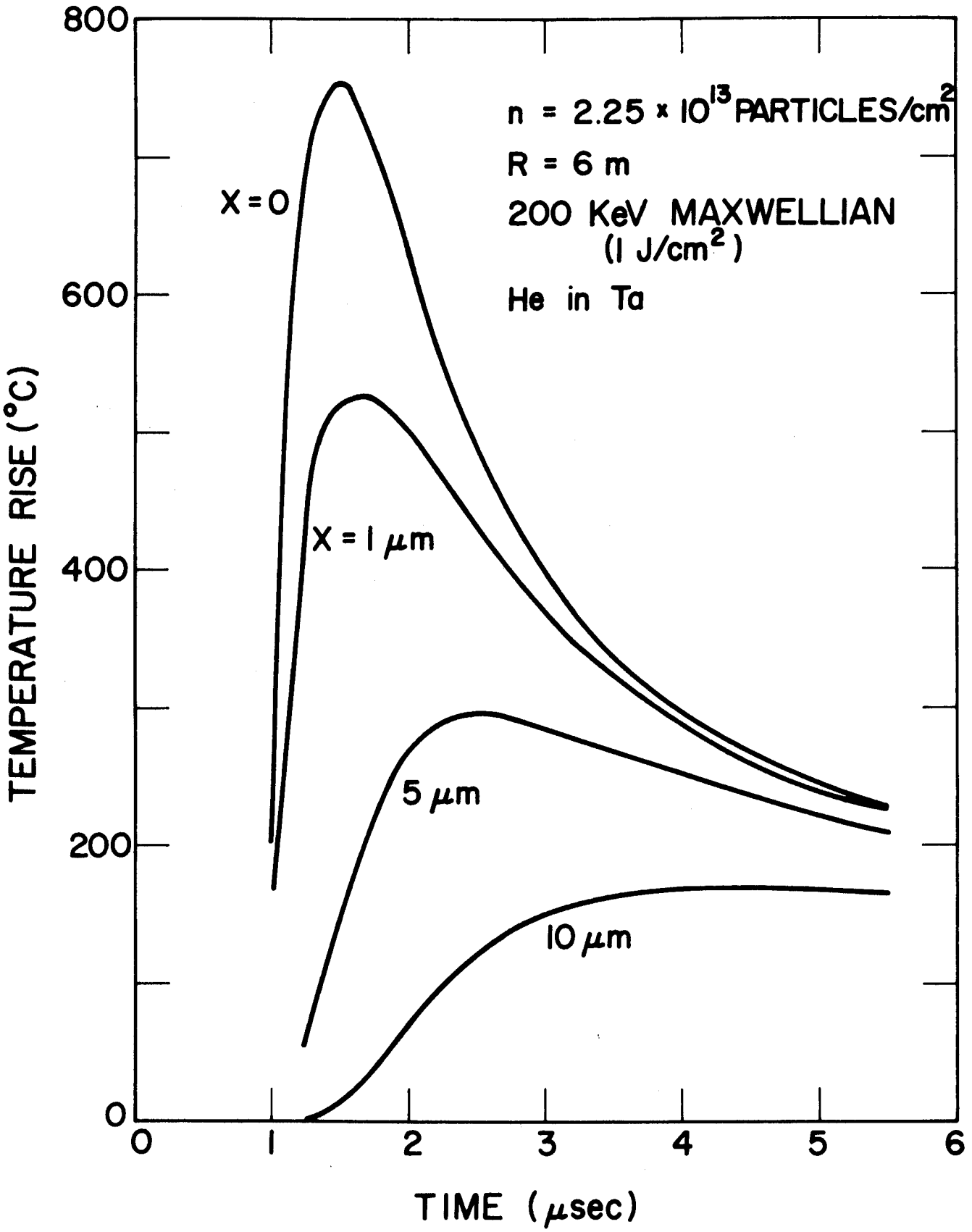
800
600
400
200
0
0
1
2
3
4
5
6
TEMPERATURE RISE (°C)
TIME (μsec)
n = 2.25 × 10^13 PARTICLES/cm^2
R = 6 m
200 KeV MAXWELLIAN
(1 J/cm^2)
He in Ta
X = 0
X = 1 μm
5 μm
10 μm

Fig. X-C-11.

for protecting the wall from the ions and soft X-rays emanating from the microexplosion.

X-C-3. Effect of Residual Chamber Gas on Wall Thermal Response

The gas pressure inside the reactor cavity has to be sufficiently low to allow laser propagation and focusing onto the pellet. Neon has the highest laser-induced gas breakdown threshold followed closely by helium.[5] Thus, for a given laser intensity, neon can be maintained at the highest pressure and still transmit the laser beams. For example, for 1 μm light with an on-target intensity of 10^{16} W/cm^2, the reactor cavity can be filled with neon at a pressure of about 1 torr. (See Section VI and XI for details) At such pressures, the gas can significantly modify the X-ray spectra incident on the wall by absorbing the low-energy photons (Fig. X-C-12). These photons would have produced high surface temperature excursions because of their short range. Figure X-C-13 shows how a black body spectrum initiated at the center of a neon-filled, 12 m diameter cavity is modified. The wall will, therefore, be subjected to harder X-ray spectra than those produced by the microexplosion. Hard X-rays are benign and produce small surface temperature jumps. (Fig. X-C-5).

Typical results showing the surface temperature rise produced by the modified X-ray spectra are shown in Figs. X-C-14, 15. These results pertain to a 6.5 mm thick graphite liner in a neon-filled, 12 m diameter cavity. The results are plotted against the black body temperature characterizing the original spectrum produced by the microexplosion. Figure X-C-15 shows the surface temperature rise for different gas pressures and black body

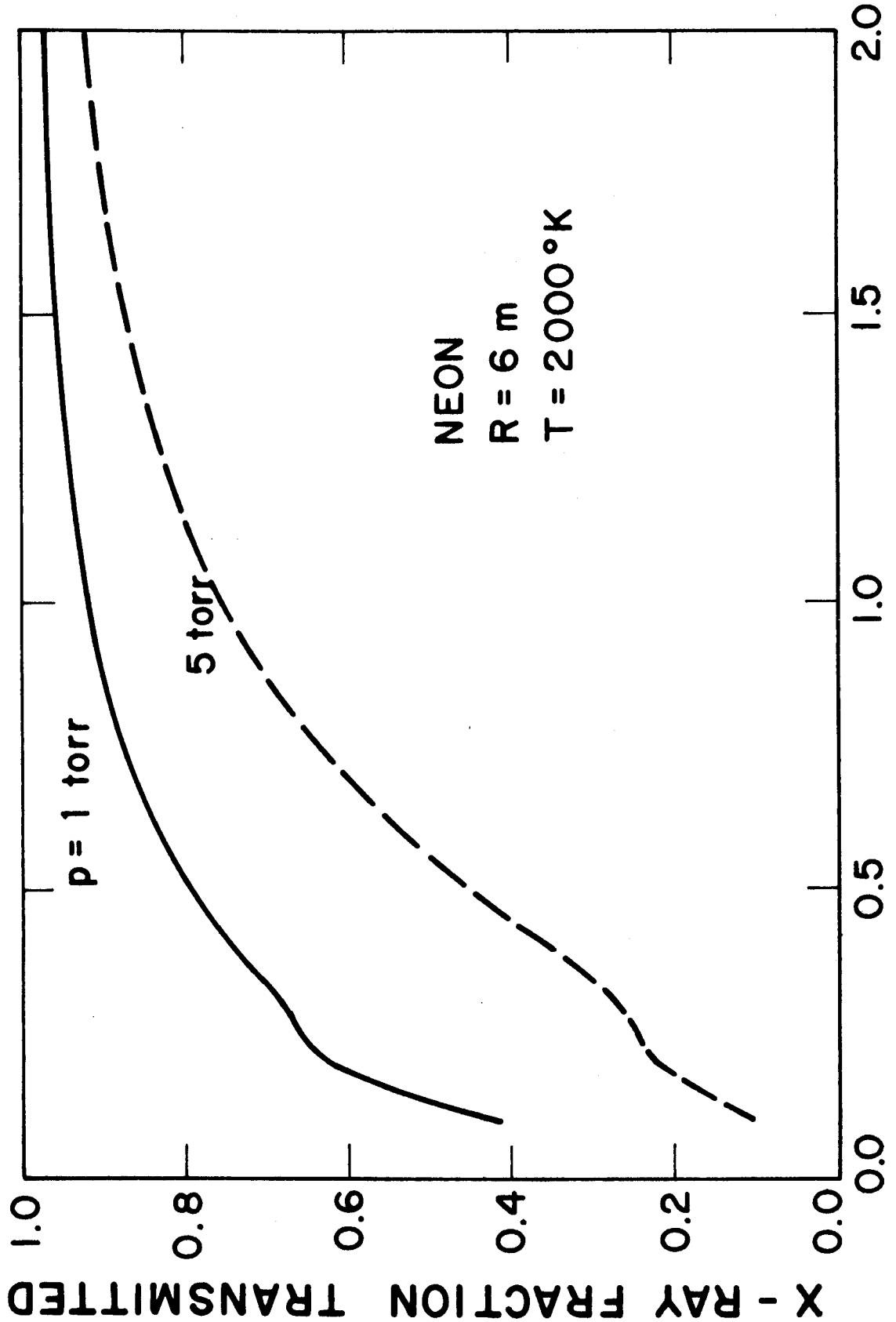
X - RAY FRACTION TRANSMITTED
1.0
0.8
0.6
0.4
0.2
0.0
0.0
0.5
1.0
1.5
2.0
BLACKBODY TEMPERATURE (keV)
NEON
R = 6 m
T = 2000°K
p = 1 torr
5 torr

Fig. X-C-12.

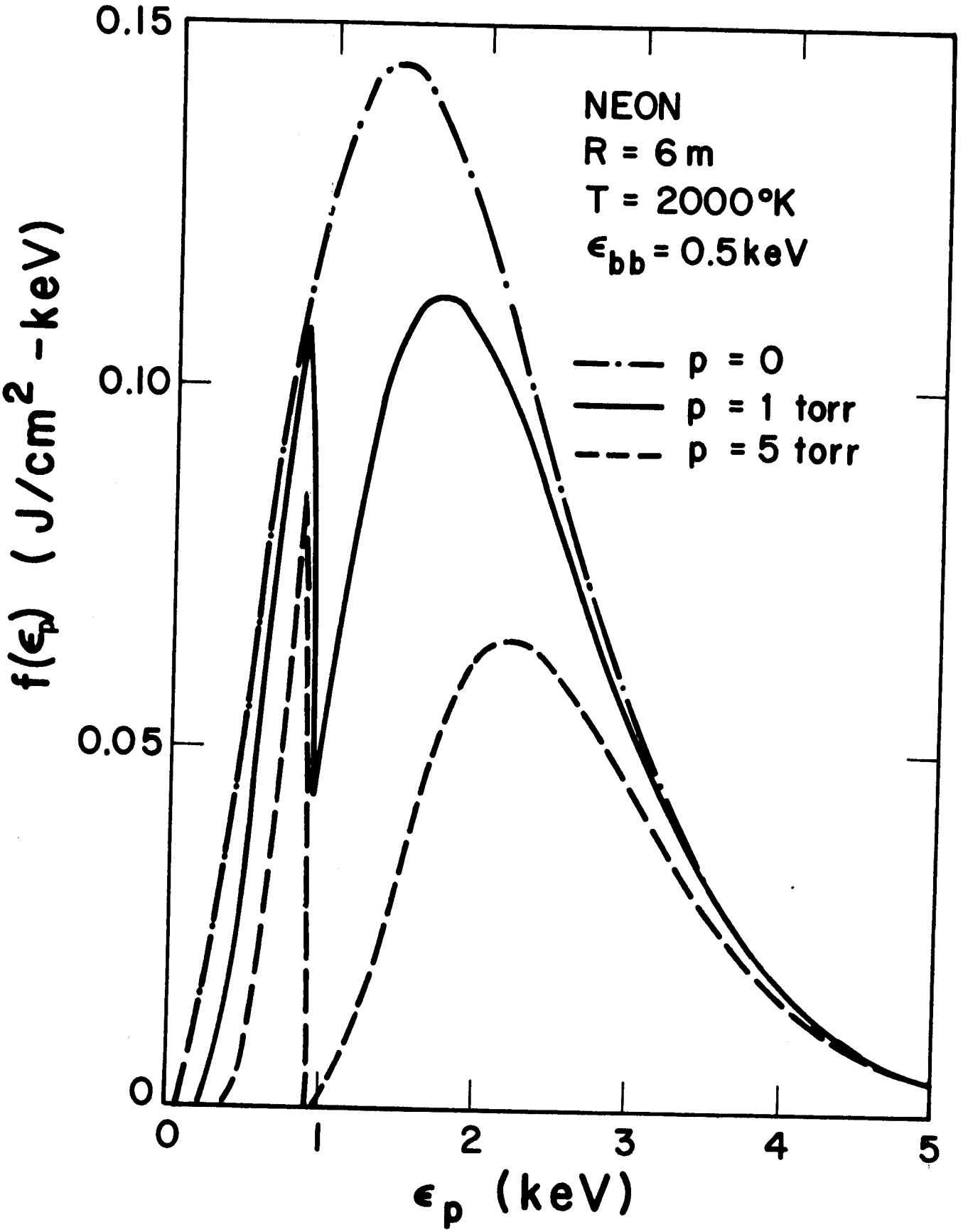
NEON
R = 6 m
T = 2000°K
ϵ_{bb} = 0.5 keV
p = 0
p = 1 torr
p = 5 torr
$f(\epsilon_p)$ (J/cm^2-keV)
ϵ_p (keV)
0.15
0.10
0.05
0
0
1
2
3
4
5

Fig. X-C-13.

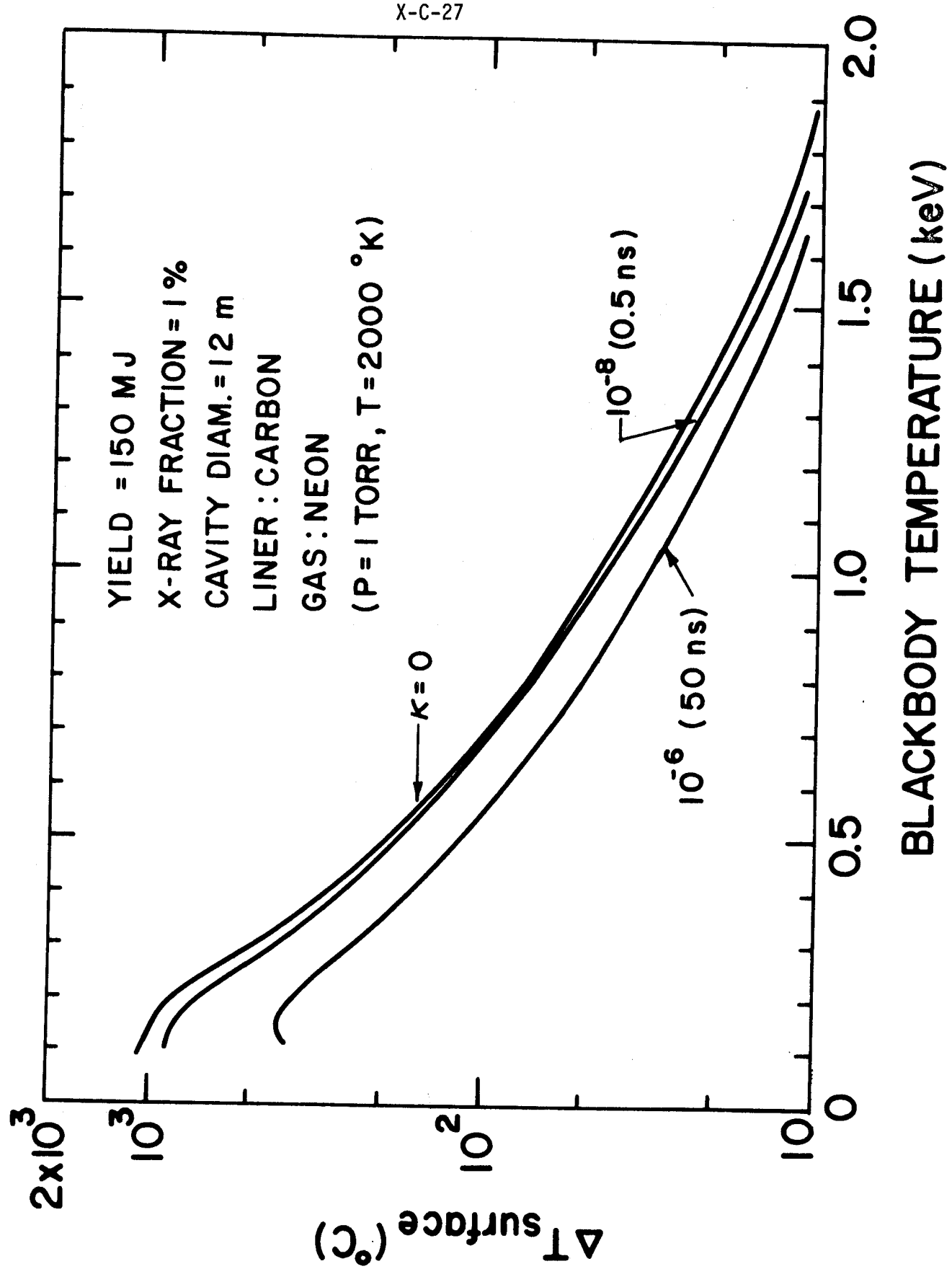
YIELD = 150 MJ
X-RAY FRACTION = 1 %
CAVITY DIAM. = 12 m
LINER : CARBON
GAS : NEON
(P = 1 TORR, T = 2000 °K)
κ = 0
10^-8 (0.5 ns)
10^-6 (50 ns)
ΔT surface (°C)
2x10^3
10^3
10^2
10
0
0.5
1.0
1.5
2.0
BLACKBODY TEMPERATURE (keV)

Fig. X-C-14.

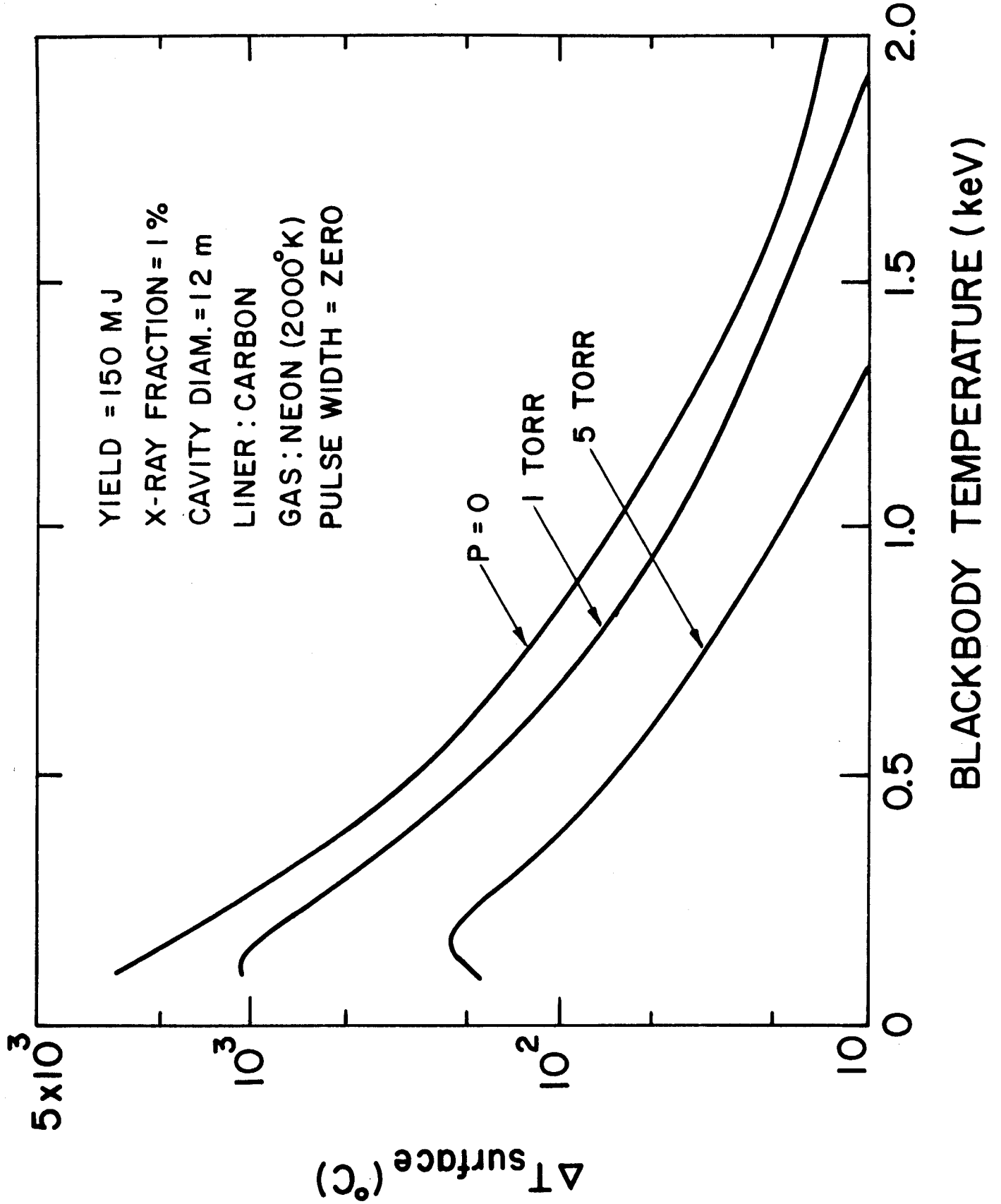
YIELD = 150 MJ
X-RAY FRACTION = 1 %
CAVITY DIAM. = 12 m
LINER : CARBON
GAS : NEON (2000°K)
PULSE WIDTH = ZERO
P = 0
1 TORR
5 TORR
ΔT surface (°C)
5x10^3
10^3
10^2
10
0
0.5
1.0
1.5
2.0
BLACKBODY TEMPERATURE (keV)

Fig. X-C-15.

temperatures with zero pulse width. These results show that gas protection can be quite effective especially if the X-rays produced by the microexplosion are soft as may be the case with structured pellets. (Section IV)

In addition to absorbing the soft X-rays, the gas can stop the ions produced by the microexplosion. If the wall radius exceeds the mean ion range by approximately a factor of 2, all the ions' kinetic energy will be deposited in the chamber gas. The neon pressure corresponding to a mean range of 6 m is shown in Fig. X-C-16 for a variety of ions. These data are based on ion range calculations using Lindhard theory in the EDEPI code.[6] These results indicate that most of the non-hydrogenic pellet constituents can be stopped in the gas at sufficiently low pressures. Calculations pertaining to specific pellet designs for the SOLASE reactor are presented in Section XI.

The energy deposited in the gas by the X-rays and ions will be removed by radiation to the chamber walls and external cooling of the hot gas removed through the vacuum system. (A steady stream of cold gas is allowed into the system). Unless the energy is radiated to the wall over a sufficiently long period, excessive surface heating and ablation would result. The temporal distribution of the radiant heat flux depends on the radiation transport through the gas, as well as system characteristics (Section XI). Here we consider the two limiting cases shown in Fig. X-C-17. For case a, the radiant heat flux during each pulse is assumed to remain constant and equal to q_o over a period $\kappa\omega$, where ω is the time between pulses. For case b, the surface heat flux during each pulse is assumed to decay exponentially so that for the (N+1) pulse: $q = q_o \exp[-(t-N\omega)/\tau]$; $N\omega \leq t \leq (N+1)\omega$, where

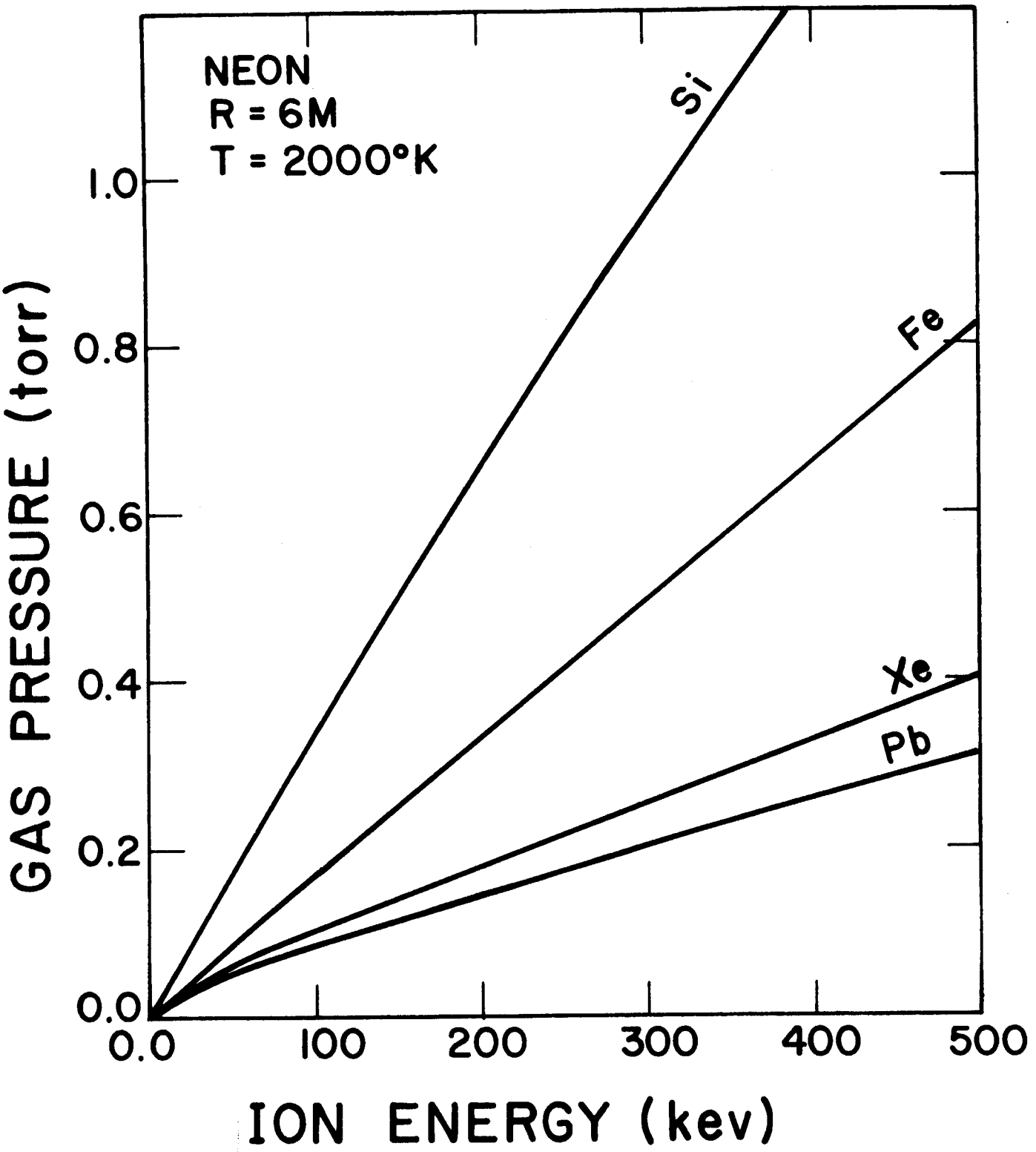
NEON
R = 6M
T = 2000°K
Si
Fe
Xe
Pb
GAS PRESSURE (torr)
0.0
0.2
0.4
0.6
0.8
1.0
0.0
100
200
300
400
500
ION ENERGY (kev)

Fig. X-C-16.

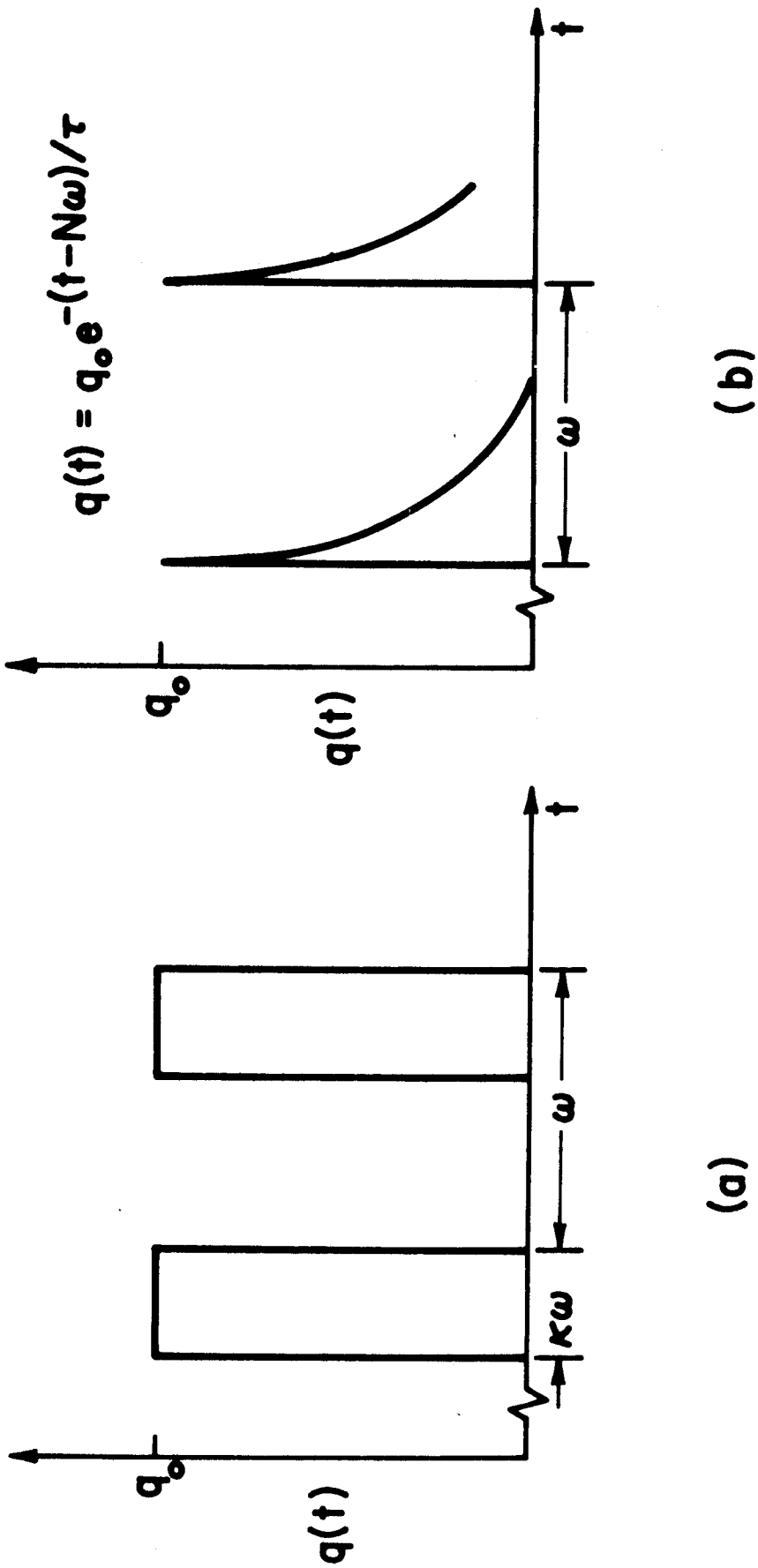

Fig. X-C-17.

τ is a reference time.

The thermal response of a finite slab of thickness L subjected to a sequence of these heat flux pulses can be readily obtained by either superposition or variation of parameters techniques.[4] The back surface of the slab (x=L) is assumed to remain at a constant temperature T_o. For case a, the sustained transient solution $\tilde{u}_a(\xi,\theta)$ is given by:

$$\tilde{u}_a(\xi,\theta) = 2 \sum_{m=0}^{\infty} \frac{\cos(\frac{2m+1}{2}\pi\,\xi)}{(\frac{2m+1}{2}\pi)^2}$$

$$\left\{ \frac{\left\{\exp - [(\frac{2m+1}{2}\pi)^2\,\delta\,\Omega]\right\}\left\{\exp\,[(\frac{2m+1}{2}\pi)^2\,\kappa\,\Omega] - 1\right\}}{\left\{\exp\,[(\frac{2m+1}{2}\pi)^2\,\Omega] - 1\right\}} \right.$$

$$\left. + \left\{ 1 - \exp - [(\frac{2m+1}{2}\pi)^2\,\delta\,\Omega]\right\} \right\} \quad (0 \le \delta \le \kappa) \qquad (17)$$

and,

$$\tilde{u}_a(\xi,\theta) = 2 \sum_{m=0}^{\infty} \frac{\cos(\frac{2m+1}{2}\pi\,\xi)}{(\frac{2m+1}{2}\pi)^2}$$

$$\left\{ \frac{\left\{\exp\,[(\frac{2m+1}{2}\pi)^2\,\kappa\,\Omega] - 1\right\}\left\{\exp\,[\frac{2m+1}{2}\pi)^2\,(1-\delta)\,\Omega]\right\}}{\left\{\exp\,[(\frac{2m+1}{2}\pi)^2\,\Omega - 1\right\}} \right\}$$

$$(\kappa \le \delta \le 1) \qquad (18)$$

Here, the non-dimensional temperature $u_a(\xi,\theta)$ is defined by: $u_a \equiv (T-To)/q_oL/k$. The variables ξ, θ, Ω, δ, and κ have been defined before.

For case b, the sustained transient solution $\tilde{u}_b(\xi,\theta)$ is given by:

$$\tilde{u}_b(\xi,\theta) = 2 \sum_{m=0}^{\infty} \frac{\cos(\frac{2m+1}{2}\pi\,\xi)}{[(\frac{2m+1}{2}\pi)^2 - \tau^*]} \left\{ \frac{\{\exp[\frac{2m+1}{2}\pi)^2 (1-\delta)\Omega]\}\ \{\exp -[\Omega\,\tau^*] - 1\}}{\{\exp[(\frac{2m+1}{2}\pi)^2\,\Omega - 1]\}} + \exp -[\delta\,\Omega\,\tau^*] \right\} \quad (19)$$

where $\tau^* \equiv L^2/\alpha\tau$, and $u_b \equiv (T-T_o)/(q_oL/k)$.

Typical results showing the surface temperature rise in a graphite wall subjected to a train of heat flux pulses of types a and b are shown in Figs. X-C-18 and 19 respectively. These results do not account for any evaporation which may take place at the surface. It is obvious that the surface temperature rise, and hence the maximum surface temperature will decrease as the pulse width is increased. For the case shown, in order to prevent excessive evaporation and spallation of the wall, the energy deposited in the gas has to be radiated over a period $\geq \sim 1$ ms. This, in turn, can be used to determine the necessary amount of gas in the chamber to provide such a long cool-down period. Specific calculations pertaining to the SOLASE cavity design are given in Section XI.

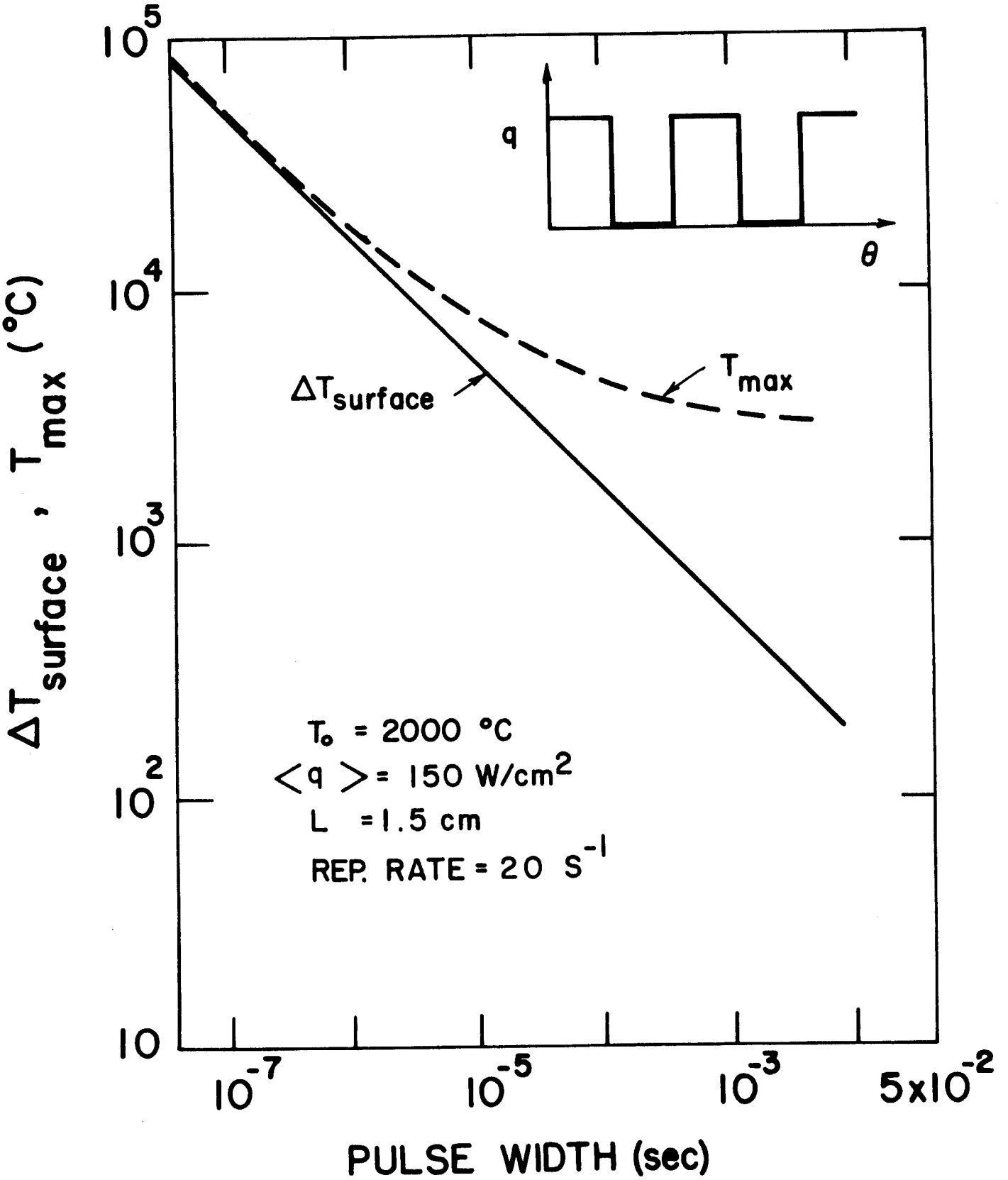
10^5
10^4
10^3
10^2
10
$\Delta T_{surface}$, T_{max} (°C)
q
θ
$\Delta T_{surface}$
T_{max}
T_o = 2000 °C
$\langle q \rangle$ = 150 W/cm^2
L = 1.5 cm
REP. RATE = 20 S^{-1}
10^{-7}
10^{-5}
10^{-3}
5×10^{-2}
PULSE WIDTH (sec)

Fig. X-C-18.

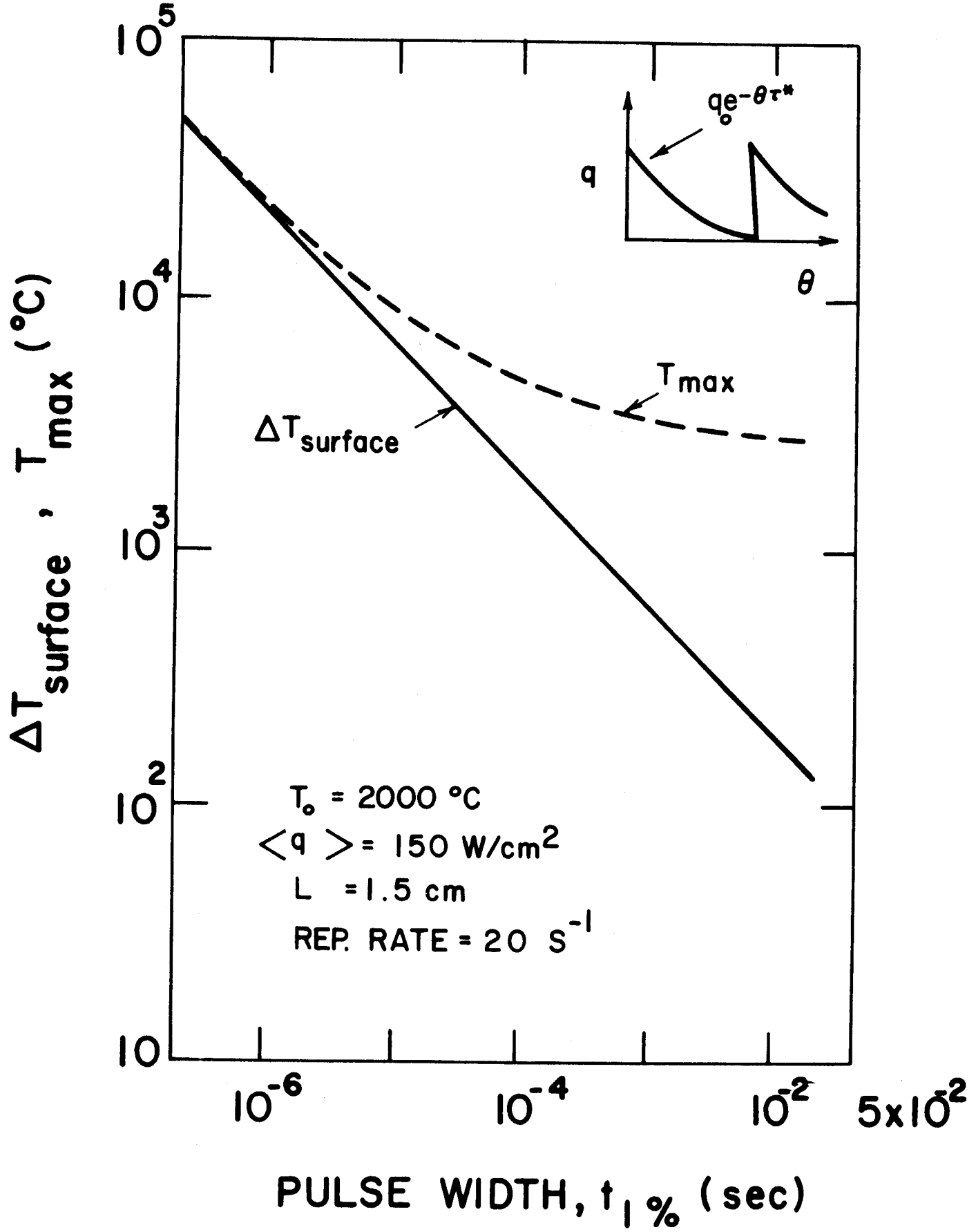
10^5
10^4
10^3
10^2
10
$\Delta T_{surface}$, T_{max} (°C)
$qe^{-\theta\tau^*}$
q
θ
T_{max}
$\Delta T_{surface}$
T_o = 2000 °C
$\langle q \rangle$ = 150 W/cm^2
L = 1.5 cm
REP. RATE = 20 s^{-1}
10^{-6}
10^{-4}
10^{-2}
5×10^{-2}
PULSE WIDTH, $t_{1\%}$ (sec)

Fig. X-C-19.

X-C-4. Surface Evaporation Rate

The evaporation rate from a surface at temperature T can be estimated from the equilibrium vapor pressure p of the solid material above the surface. The evaporation rate $\dot{n}(T)$ is given by:[7]

$$\dot{n}(T) = \frac{3.5 \times 10^{22}}{\sqrt{M}} \frac{p}{\sqrt{T}} \left(\frac{\text{atoms}}{\text{cm}^2 \text{ sec}}\right) \tag{20}$$

where M is the molecular weight, p is in torr, and T is in °K. Vapor pressure data for several first wall materials are given in reference (7). For graphite, the vapor pressure can be estimated using the relation:

$$p = 4 \times 10^{13} \exp\left[\frac{-9.7 \times 10^4}{T}\right] \text{ torr.} \tag{21}$$

Upon knowledge of the surface temperature history and the corresponding vapor pressure, one can determine the evaporation rate as a function of time. Typical results showing the surface temperature history for a graphite wall subjected to black body radiation with no gas protection are shown in Fig. X-C-20; the corresponding evaporation rates for back surface temperatures of 1500°C and 2000°C are shown in Fig. X-C-21 and 22 respectively. These can be integrated to determine the amount of material ablated per pulse (Figs. X-C-23, 24). These results indicate that for a back surface temperature of 2000°C, the evaporation rates are significantly higher than those for T_{back} = 1500°C. This, of course, is a result of the sharp increase in the vapor pressure for carbon as the temperature is increased beyond ~2000°C. This means that cavity designs with metallic first walls and protective graphite liners will have an

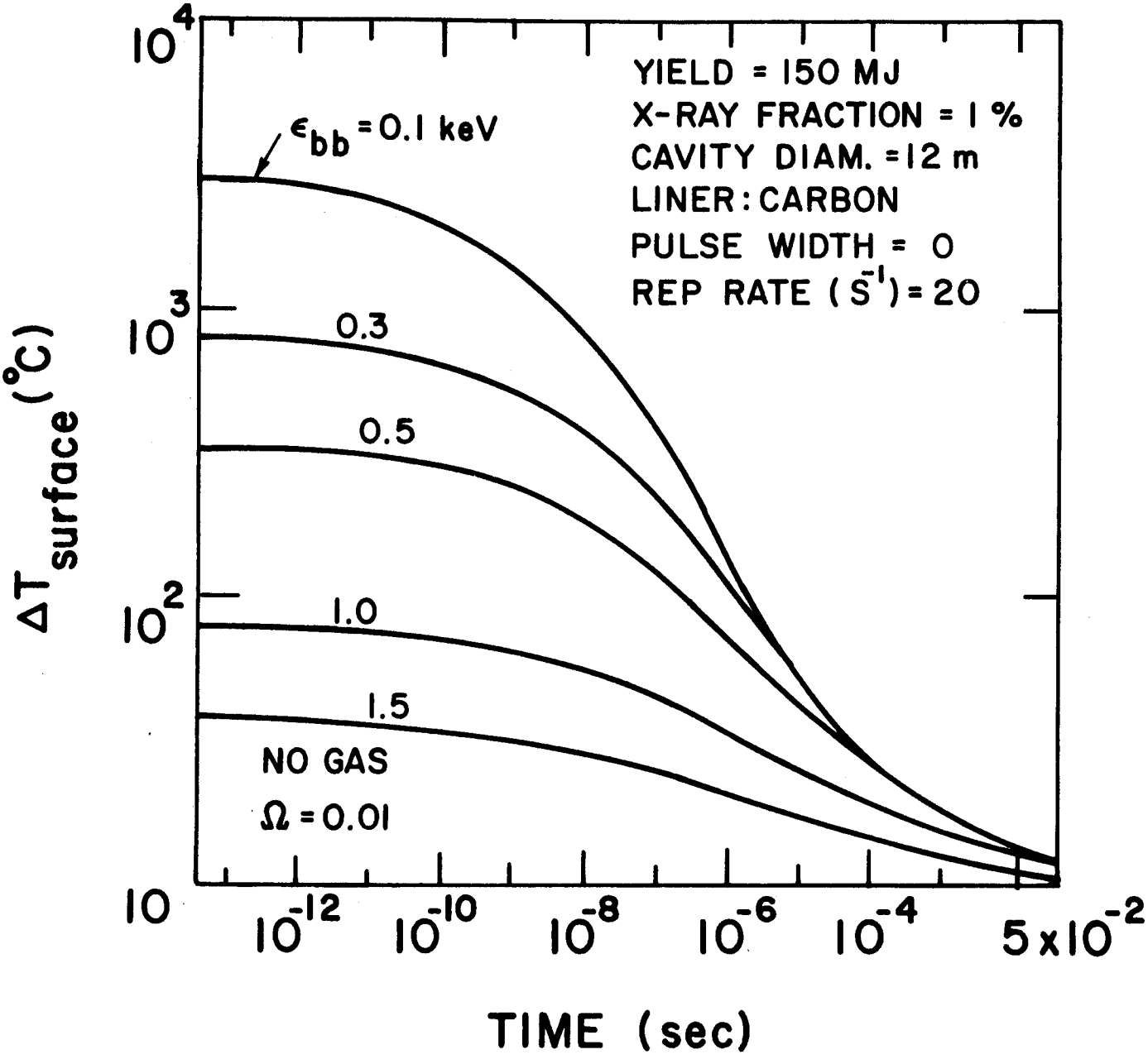
YIELD = 150 MJ
X-RAY FRACTION = 1 %
CAVITY DIAM. = 12 m
LINER: CARBON
PULSE WIDTH = 0
REP RATE (S^{-1}) = 20
ϵ_{bb} = 0.1 keV
0.3
0.5
1.0
1.5
NO GAS
Ω = 0.01
$\Delta T_{surface}$ (°C)
10^4
10^3
10^2
10
10^{-12}
10^{-10}
10^{-8}
10^{-6}
10^{-4}
5×10^{-2}
TIME (sec)

Fig. X-C-20.

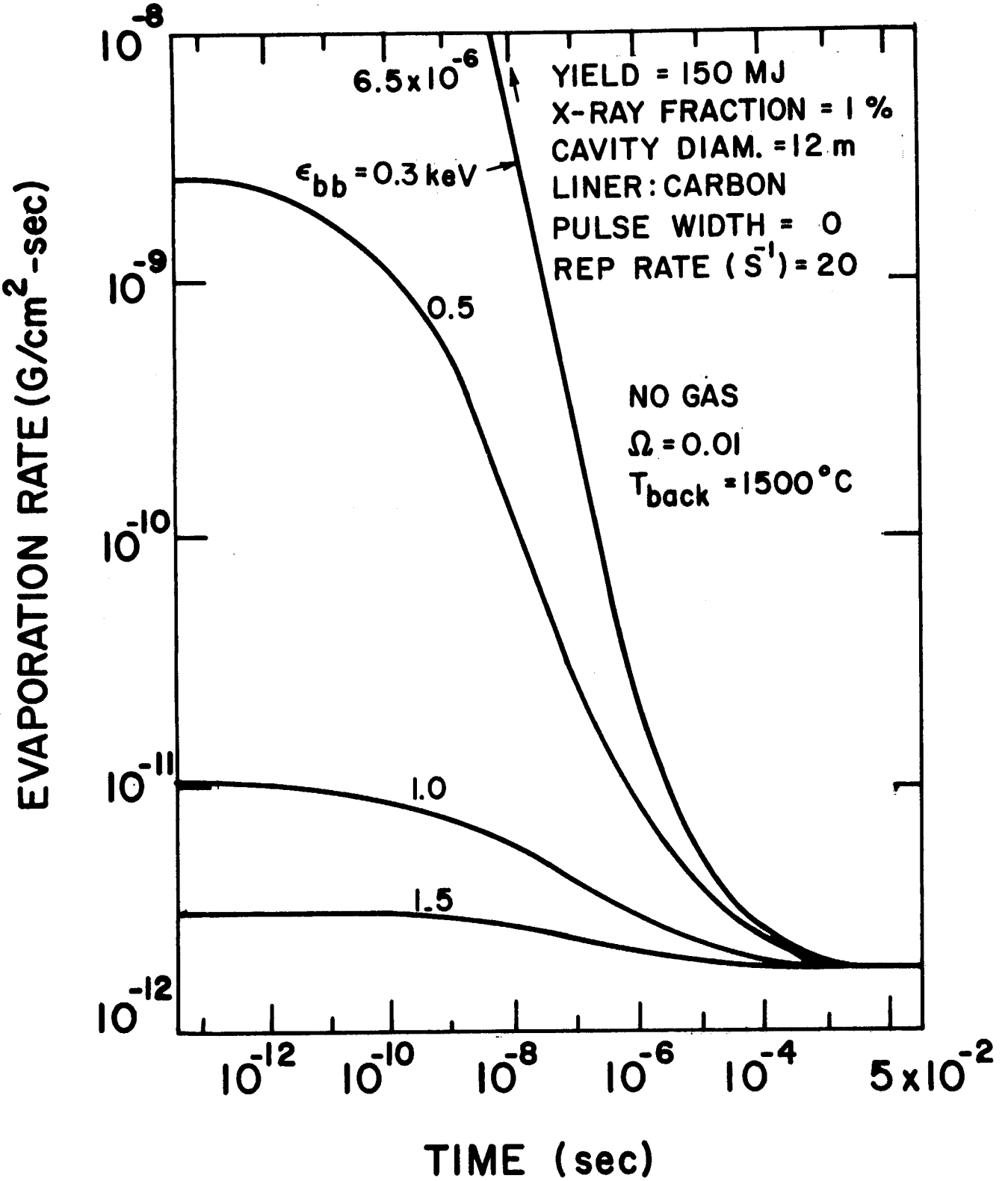
EVAPORATION RATE (G/cm²-sec)
TIME (sec)
YIELD = 150 MJ
X-RAY FRACTION = 1 %
CAVITY DIAM. = 12 m
LINER: CARBON
PULSE WIDTH = 0
REP RATE (S⁻¹) = 20
NO GAS
Ω = 0.01
T_back = 1500°C
ε_bb = 0.3 keV
6.5x10⁻⁶
0.5
1.0
1.5
10⁻⁸
10⁻⁹
10⁻¹⁰
10⁻¹¹
10⁻¹²
10⁻¹²
10⁻¹⁰
10⁻⁸
10⁻⁶
10⁻⁴
5x10⁻²

Fig. X-C-21.

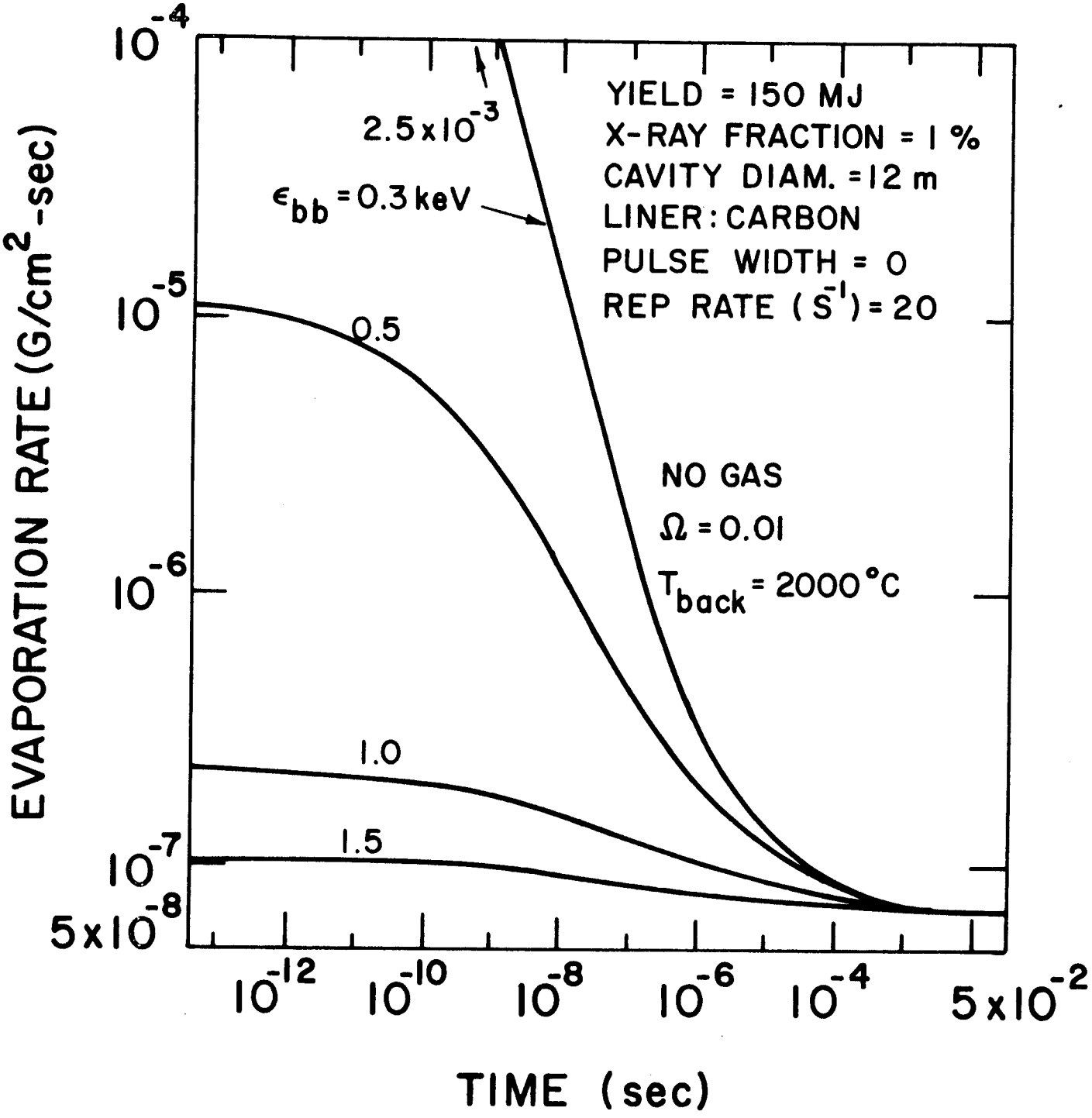
EVAPORATION RATE (G/cm²-sec)
TIME (sec)
YIELD = 150 MJ
X-RAY FRACTION = 1 %
CAVITY DIAM. = 12 m
LINER: CARBON
PULSE WIDTH = 0
REP RATE (S⁻¹) = 20
NO GAS
Ω = 0.01
T_back = 2000°C
2.5x10⁻³
ε_bb = 0.3 keV
0.5
1.0
1.5
10⁻⁴
10⁻⁵
10⁻⁶
10⁻⁷
5x10⁻⁸
10⁻¹²
10⁻¹⁰
10⁻⁸
10⁻⁶
10⁻⁴
5x10⁻²

Fig. X-C-22.

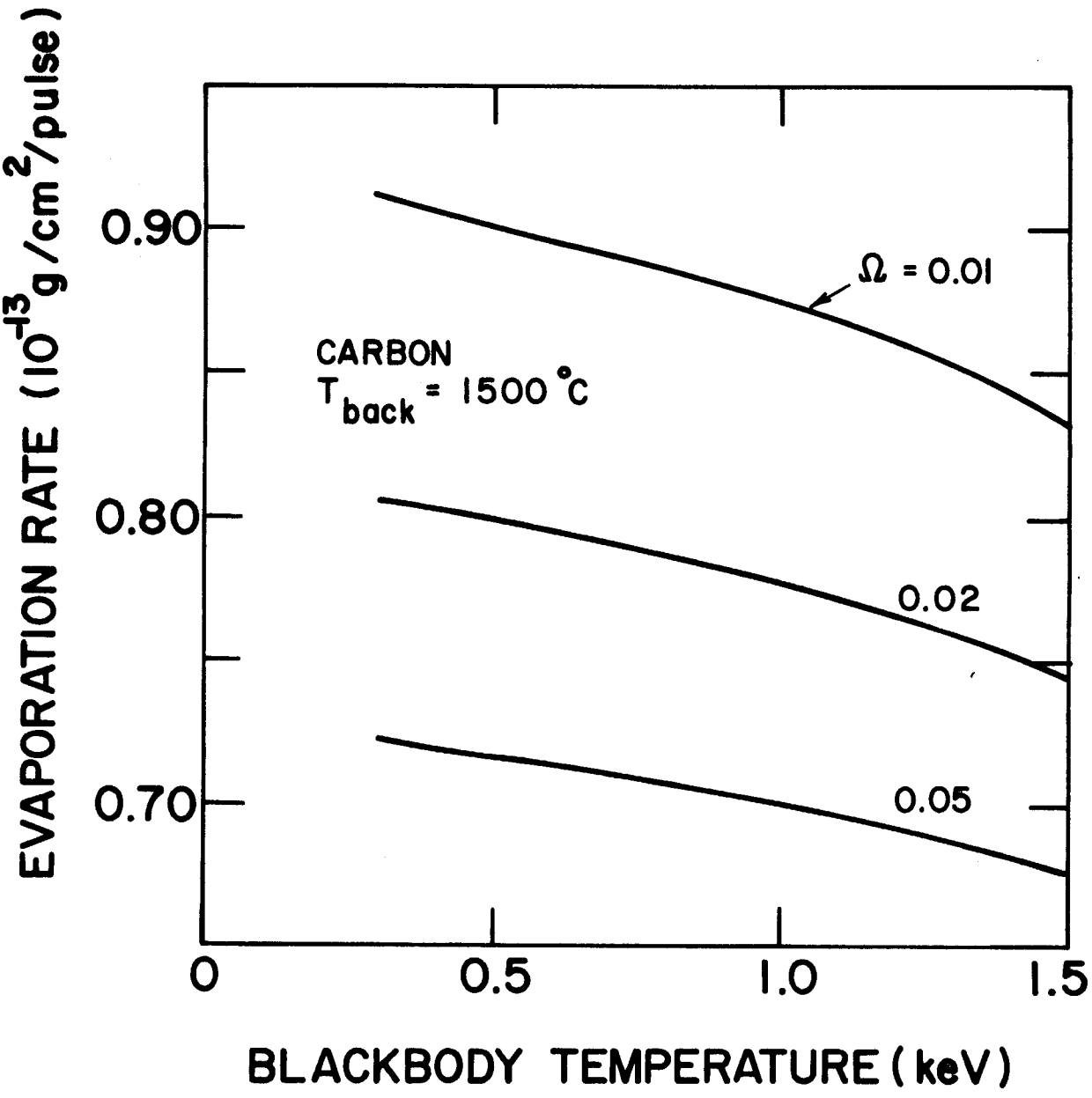
EVAPORATION RATE (10^{-13} g/cm^2/pulse)
0.90
0.80
0.70
CARBON
T_{back} = 1500 °C
Ω = 0.01
0.02
0.05
0
0.5
1.0
1.5
BLACKBODY TEMPERATURE (keV)

Fig. X-C-23.

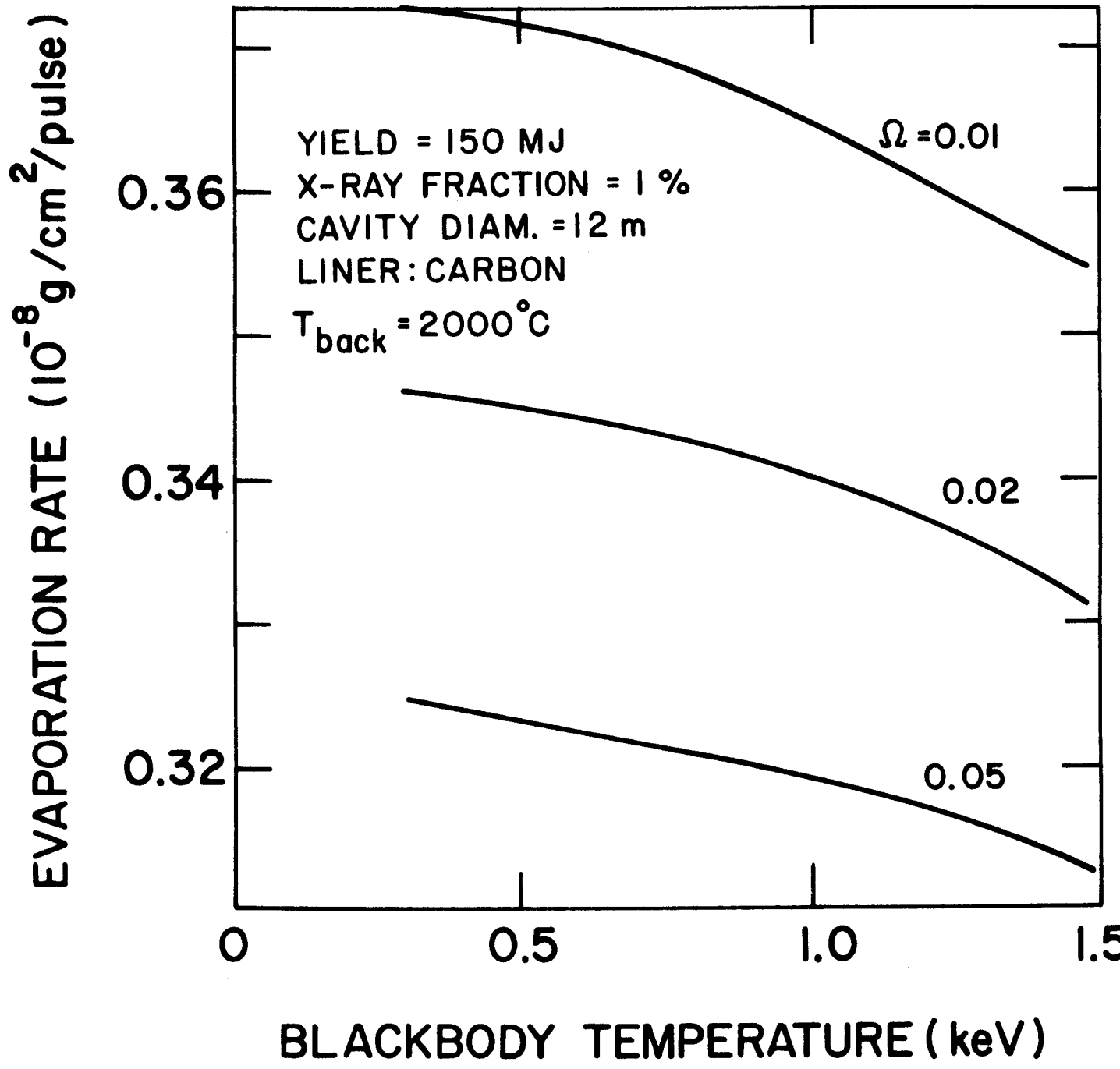
EVAPORATION RATE (10^{-8} g/cm^2/pulse)
0.36
0.34
0.32
YIELD = 150 MJ
X-RAY FRACTION = 1 %
CAVITY DIAM. = 12 m
LINER: CARBON
T_{back} = 2000°C
Ω = 0.01
0.02
0.05
0
0.5
1.0
1.5
BLACKBODY TEMPERATURE (keV)

Fig. X-C-24.

upper bound on the wall loading dictated by the ability to radiate the ion and photon energy deposited in the liner to the cold first wall since the liner's back surface has to be kept below ~1800°C to avoid excessive evaporation at the front surface.

X-C-5. Stress Analysis for ICTR Walls

X-C-5-a. Impulsive Heat Deposition in a Semi-Infinite Medium

Estimates of the stress levels produced in the front wall (or liner) can be made from solutions for impulsive energy deposition in an elastic half-space.[8] The volumetric heat generation rate is given by:

$$g(x,t) = g_0 e^{-x/\ell}[H(t) - H(t - t_0)] \tag{22}$$

where ℓ is the deposition length ($\ell \equiv 1/\mu$), t_0 is the deposition time, and H is the Heavyside step function. The heat conduction equation, boundary conditions, and initial condition are similar to those described in the previous section with T_0 = zero. When the deposition time approaches zero, the resulting temperature response becomes:

$$T(x,t) = T_s \exp(-x/\ell)\, H(t) \tag{23}$$

where $T_s = Q/\rho c_p \ell$ is the surface temperature rise and Q is the deposited energy.

For uniaxial motion, the equilibrium equation in terms of stress and temperature is

$$\frac{\partial^2 \sigma}{\partial x^2} - \frac{1}{c^2}\frac{\partial^2 \sigma}{\partial t^2} = \frac{3\alpha K}{c^2}\frac{\partial^2 T}{\partial t^2} \quad . \tag{24}$$

Here σ is the normal stress in the x direction, K is the bulk modulus, c is the dilational wave speed ($c = K + \frac{4}{3} G)/\rho$), α is the thermal expansion coefficient, G is the shear modulus, and ρ is the material density. In terms of the nondimensional variables: $\bar{x} \equiv x/\ell$, $\bar{t} \equiv tc/\ell$, and $\bar{\sigma} = \sigma/3\alpha T_s K$, the solution to Eq. (24) is:

$$\bar{\sigma} = -\frac{1}{2} \{\exp [-(\bar{x} - \bar{t})] + \exp [-(\bar{x} + \bar{t})]\} H(t)$$

$$+ \cosh (\bar{t} - \bar{x}) H(\bar{t} - \bar{x}). \qquad (25)$$

Initially, the wave is entirely compressive; however, the tensile component grows until in the limit for arbitrarily large values of time, the peak tensile and compressive stresses, $\bar{\sigma}_{max}$, are $\pm$ 0.50. The growth of the tensile component is very rapid, e.g. for $\bar{t} = 2$ when the front is at $\bar{x} = 2$, the maximum tensile stress $\bar{\sigma}$ is equal to 0.49. Therefore, the limiting fully-developed values can be used for estimates involving deposition in layers of finite thickness. With a reflection of the compressive stress from the outer free surface, the instantaneous maximum tensile stress is:

$$\sigma = 3\alpha T_s K = \alpha T_s E/(1 - 2\nu) \qquad (26)$$

where E and ν are the elastic modulus and Poisson's ratio respectively. This result agrees with the quasi-static magnitude of $\alpha TE(1 - k\nu)$ in which k = 0, 1, and 2 for uniaxial, biaxial, and triaxial states respectively.

Results are shown in Fig. X-C-25 for stainless steel and nearly-isotropic graphite. The fatigue limit for the graphite does not include temperature compensation and is based on a fraction of the instantaneous fracture strength.

X-C-5-b. Energy Deposition in a Finite Elastic Layer

X-C-5-b-i. Series Solutions

The wall model considered is a layer with finite thickness L. The governing differential equation in terms of the x displacement component u(x,t) is:

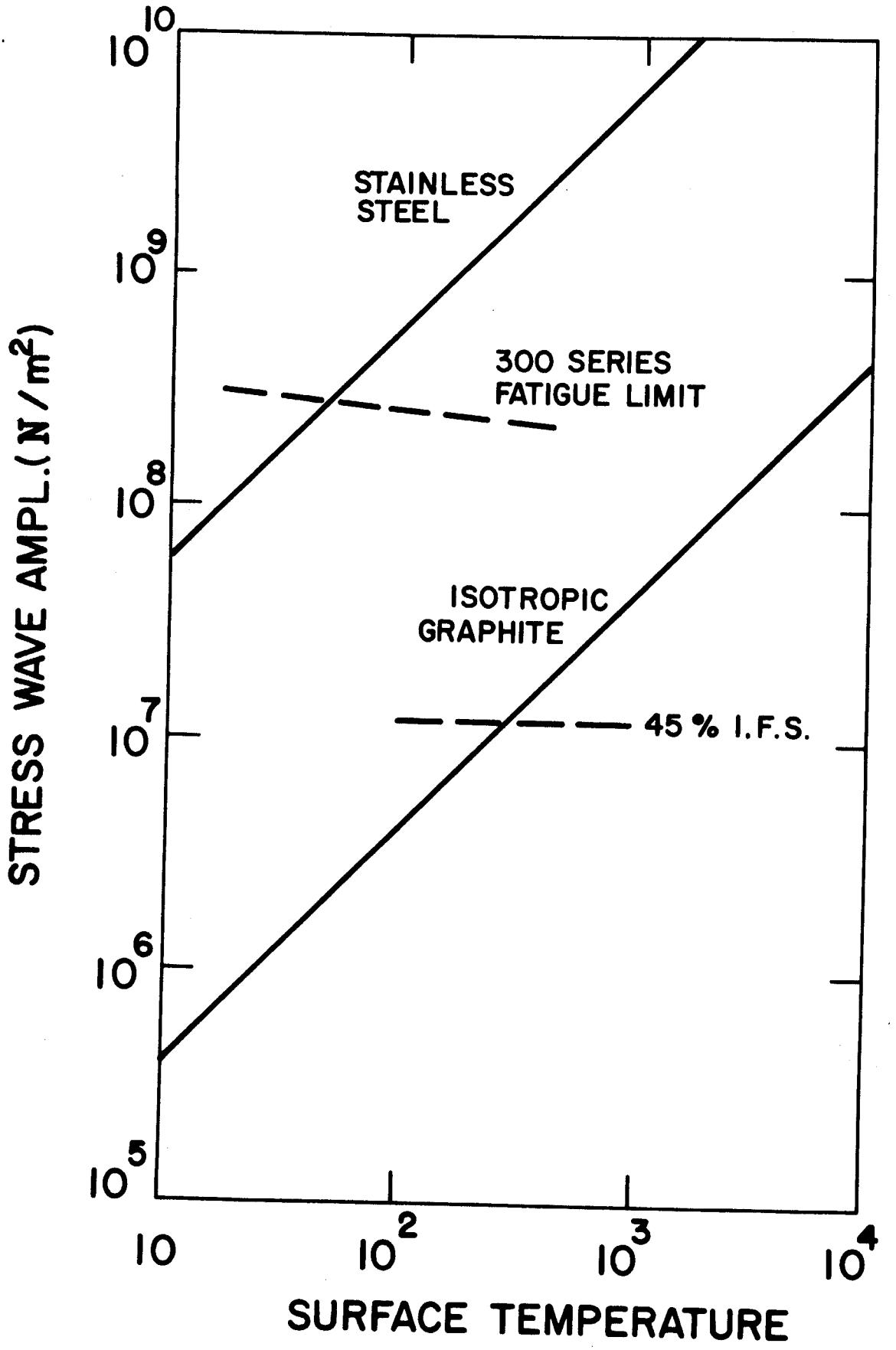
STAINLESS STEEL
300 SERIES FATIGUE LIMIT
ISOTROPIC GRAPHITE
45 % I.F.S.
STRESS WAVE AMPL. (N/m²)
SURFACE TEMPERATURE
10¹⁰
10⁹
10⁸
10⁷
10⁶
10⁵
10
10²
10³
10⁴

Fig. X-C-25.

$$c^2 \frac{\partial^2 u(x,t)}{\partial x^2} - \frac{\partial^2 u(x,t)}{\partial t^2} = a \frac{\partial T}{\partial x}(x,t) \tag{27}$$

where $a \equiv (1 + \nu)\, \alpha c^2/(1 - \nu)$. The boundary and initial conditions are:

$$\left.\begin{aligned} \sigma(o,t) &= \sigma(L,t) = o \\ u(x,o) &= \frac{\partial u}{\partial t}(x,o) = o \end{aligned}\right\} . \tag{28}$$

Define:

$$\left.\begin{aligned} \bar{T}(x,t) &= T(x,t) \quad ; \quad o \leq x \leq L \\ &= -T(x,t) \quad ; \quad -L \leq x \leq o \end{aligned}\right\} . \tag{29}$$

Thus $\bar{T}(x;t)$ is an odd function of x which can be expressed as:

$$\bar{T}(x,t) = \sum_{n=o}^{\infty} T_n(t) \sin (n\pi x/L) \; ; \tag{30}$$

$$(-L \leq x \leq L)$$

and

$$T_n(t) = \frac{2}{L} \int_o^L T(x,t) \sin (n\pi x/L)\, dx \; .$$

The solution to Eq. (27) can be expressed as an infinite series:

$$u(x,t) = \sum_{n=o}^{\infty} u_n(t) \cos (n\pi x/L) \; . \tag{31}$$

Therefore,

$$u_n'' + \omega_n^2 u_n = - \omega_n s T_n \tag{32}$$

where, $\omega_n = n\pi c/L$ and $s = a/c$. The solution to Eq. (32) is:

$$u_n(t) = A \sin \omega_n t + B \cos \omega_n t - s \int_0^t T_n(\xi) \sin \omega_n (t-\xi) d\xi. \tag{33}$$

The initial conditions on displacement and velocity yield:

$A = B = 0$. The resulting stress is given by:

$$\sigma(x,t) = -\sum_{n=0}^{\infty} [\rho c \omega_n u_n(t) + \rho a T_n(t)] \quad \sin \frac{n\pi x}{L} . \tag{34}$$

Evaluation of $\sigma(x,t)$ from Eq. (34) is straightforward. For example, consider the case:

$$T(x,t) = T^* e^{ax} \quad (a < 0, \; T^* > 0)$$

$$T_n(t) = 2\omega_n T^* (1 - e^{aL} \cos n\pi)/cL \, [a^2 + (\omega n/c)^2],$$

and

$$u_n(t) = - (sT_n/\omega_n)(1 - \cos \omega_n t).$$

Hence,

$$\sigma(x,t) = - \sum_{n=0}^{\infty} T_n \rho a \cos (\omega_n t) \sin (\omega_n x/c) . \tag{35}$$

This solution offers a relatively convenient means of determining the stress solution provided that the temperature gradient is not severe so that the summation can be truncated after a reasonable number of terms. Under these conditions, the results given by Eq. (35) are in close agreement with those given by the half-space solution. However, if a severe temperature gradient exists, considerable error may result in the

magnitude of the maximum stress and the shape of the wave profile unless an extremely large number of terms are taken in the summation.

X-C-5-b-ii. Wave Solution

In the following, an alternative solution to Eq. (27) subject to the boundary and initial conditions (28) is developed. The boundary conditions can be written as:

$$c^2 u_x(o,t) = a\, T(o,t) \tag{36}$$

and

$$c^2 u_x (L,t) = a\, T(L,t). \tag{37}$$

If the temperature distribution does not change appreciably during wave generation, one can assume that $T_t = 0$ and $T = T(x)$. Define:

$$\phi_x(x) = \frac{a}{c^2} T(x), \tag{38}$$

and

$$V(x,t) = u(x,t) - \phi(x). \tag{39}$$

Therefore,

$$u_{xx} = V_{xx} + \phi_{xx} = V_{xx} + \frac{a}{c^2} T_x. \tag{40}$$

Equation (27) can be written as

$$c^2 \left(V_{xx} + \frac{aT_x}{c^2}\right) - V_{tt} = a\, T_x \tag{41}$$

or,

$$c^2 V_{xx} - V_{tt} = 0. \tag{42}$$

The initial conditions become:

$$V(x,o) = - \phi(x) , \tag{43}$$

and $$V_t(x,0) = 0 \ . \tag{44}$$

The solution to Eq. (42) subject to (43) and (44) is:

$$v(x,t) = F(x + ct) + G(x - ct) \tag{45}$$

where,

$$V(x,o) = F(x) + G(x) = - \phi(x) \tag{43à}$$

and

$$V_t(x,o) = cF(x) - cG(x) = 0. \tag{44à}$$

Thus,

$$F(x) = G(x) = - \frac{1}{2}\phi(x) \tag{46}$$

$$v(x,t) = \frac{-1}{2}[\phi(x + ct) + \phi(x - ct)] \tag{47}$$

$$u(x,t) = \phi(x) - \frac{1}{2}[\phi(x + ct) + \phi(x - ct)] \tag{48}$$

and the stress becomes:

$$\sigma(x,t) = - \frac{\alpha\rho c^2(1+\nu)}{2(1-\nu)} \ [T(x + ct) + T(x - ct)]. \tag{49}$$

The stress boundary conditions require that: $T(ct) = - T(-ct)$ and $T(L + ct) = - T(L - ct)$. If $T = f(x)$, $(0 \leq x \leq L)$, then the preceding conditions require that $T = - f(x)$, $- L \leq x \leq 0$, and $T(x) = T(x + 2L)$.

The preceding wave solution can be extended to obtain a closed form solution for general temperature distribution of the form:

$$T(x,t) = (pt + q)\ f(x) + (mx + n)\ g(t) \tag{50}$$

where p, q, m, and n are constants. The corresponding stress is given by:

$$\sigma(x,t) = \frac{\rho a}{2} \{q\ [f(x + ct) + f(x - ct)] + \frac{p}{c}\ [f(x + ct) - f(x - ct)] - (mx + n)\ g(t)\}. \tag{51}$$

For m = n = 0:

$$T(x,t) = (Pt + q)\, f(x)$$

$$\sigma(x,t) = -\rho \frac{a}{2}[(q + P/c)f(c + ct) + (q - p/c)f(x - ct)$$

The actual temperature distribution can be represented by the piece-wise linear functions for which this solution can be used.

X-C-5-b-iii. Stress Wave Results

Typical results showing the generation of stress waves as a result of the reflected laser light are given in Figs. X-C-26 and X-C-27 for a 1.5 cm thick graphite wall. These figures correspond to a laser wavelength of 1.3 μm and 10.6 μm respectively. Initially the stress is entirely compressive with the peak value at the inner surface of the wall (Fig. X-C-26a). As the wave travels into the material, tensile and compressive peaks develop and stabilize at equal numerical values. Figure X-C-26b shows the wave passing through the mid-surface (x = 0.75 cm) of the wall. When it reaches the wall's outer boundary (x = 1.5 cm) the stress wave is reflected from this free surface. It can be seen in Fig. X-C-26c that the amplitude at this time is twice the value of the developed wave and is also tensile. Materials with relatively low tensile strengths could be susceptible to spallation under such conditions. In the absence of dissipation or spallation, the wave history will now be the same as the initial passage except for the sign reversal.

Figure X-C-27 shows comparable results for a 10.6 μm laser. The increase in wavelength from 1.3 to 10.6 μm reduces the peak stress by approximately a factor of ten.

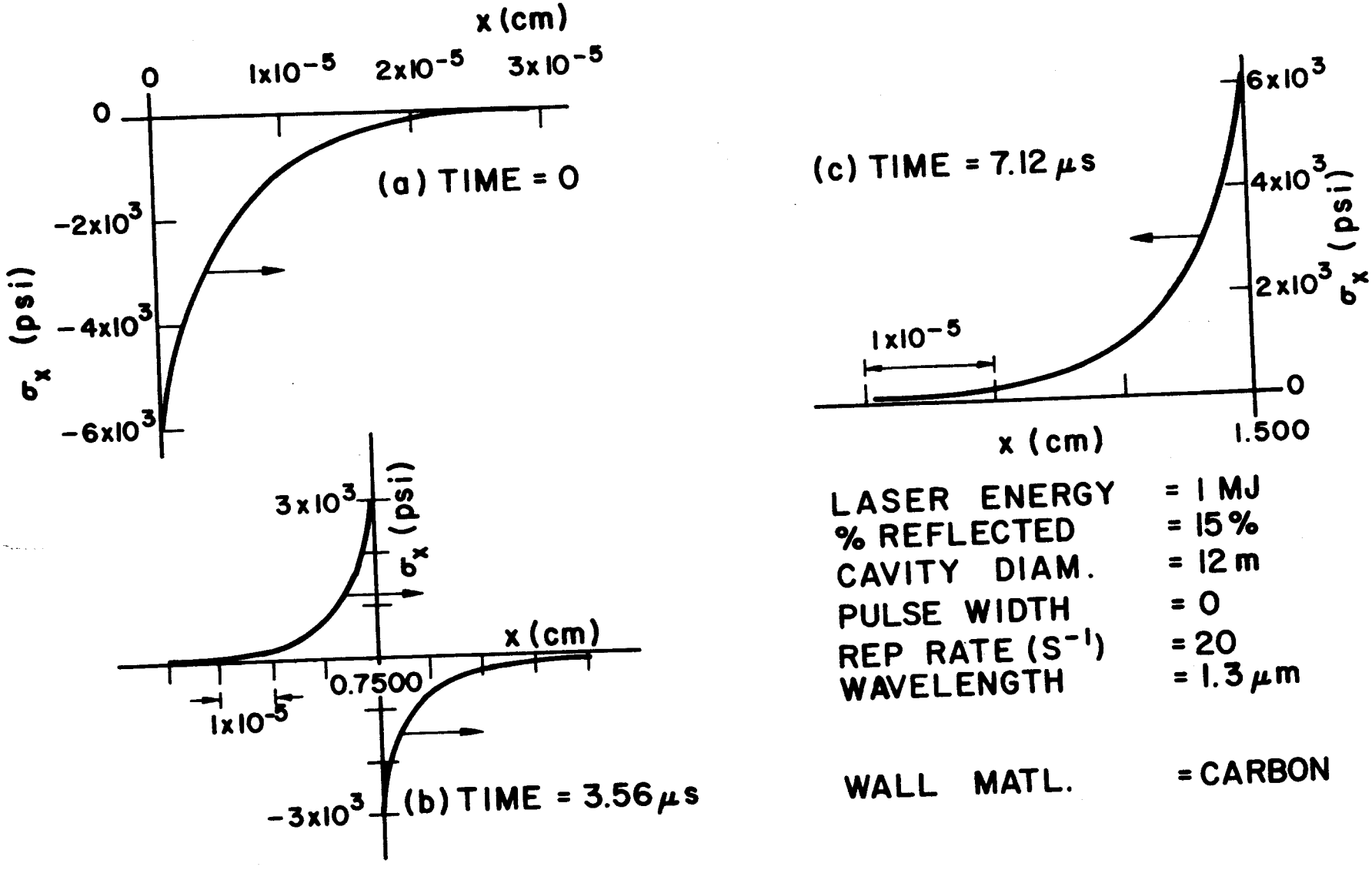
x (cm)
0
1x10-5
2x10-5
3x10-5
0
-2x10^3
-4x10^3
-6x10^3
σx (psi)
(a) TIME = 0
3x10^3
σx (psi)
x (cm)
0.7500
1x10-5
-3x10^3
(b) TIME = 3.56 μs
(c) TIME = 7.12 μs
6x10^3
4x10^3
2x10^3
σx (psi)
1x10-5
0
x (cm)
1.500
LASER ENERGY = 1 MJ
% REFLECTED = 15%
CAVITY DIAM. = 12 m
PULSE WIDTH = 0
REP RATE (S-1) = 20
WAVELENGTH = 1.3 μm
WALL MATL. = CARBON

Fig. X-C-26.

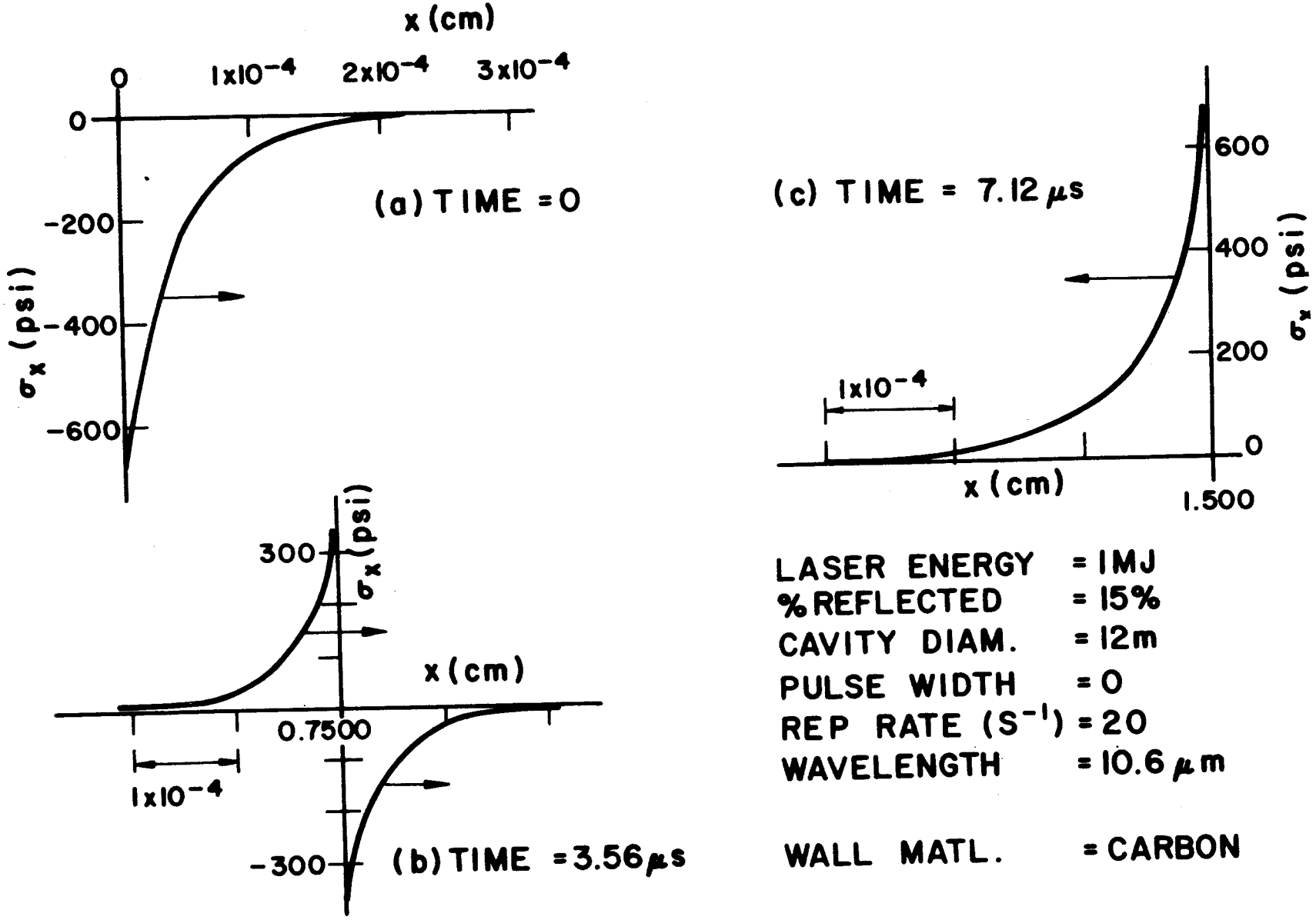
x (cm)
0
1x10⁻⁴
2x10⁻⁴
3x10⁻⁴
0
-200
-400
-600
σx (psi)
(a) TIME = 0
300
σx (psi)
x (cm)
0.7500
1x10⁻⁴
-300
(b) TIME = 3.56 μs
(c) TIME = 7.12 μs
600
400
200
0
σx (psi)
1x10⁻⁴
x (cm)
1.500
LASER ENERGY = 1MJ
% REFLECTED = 15%
CAVITY DIAM. = 12m
PULSE WIDTH = 0
REP RATE (S⁻¹) = 20
WAVELENGTH = 10.6 μm
WALL MATL. = CARBON

Fig. X-C-27.

Stress waves produced from X-ray energy are qualitatively similar to those resulting from reflected laser light. Parameters considered were a pellet yield of 150 MJ, an X-ray fraction of 1% and a repetition rate of 20 Hz. Highest stresses are produced by the largest surface temperature increases, i.e., instantaneous deposition. This case is shown in Figure X-C-28 for a black body temperature of 1 keV.

From these results it can be seen that such stress waves are generally characterized by an extremely small pulse width and high gradients. Amplitudes are not prohibitively high compared with static fracture strengths. However with wave speeds of 2×10^5 cm/sec and thus excursion frequencies of 7×10^4 Hz for a 1.5 cm wall, the question of fatigue degradation from stress waves merit further consideration. At this point insufficient data on fatigue and stress dissipation are available for the proposed carbon wall material.

X-C-6. Structural Design Considerations for the First Wall

In addition to the transient thermal stress, the first wall will be mechanically loaded by the surface shock pressure produced by the energy deposition in the buffer gas. (For magnetically protected cavities, the wall will experience a similar dynamic load produced by the expanding plasma against the magnetic field). A complete spherical shell would be the optimal design in this case sustaining the pressure by uniform membrane stress. However, with segmentation, each shell sector will now respond independently and carry the load through flexural action. For a simple wall, stress design limits could be met by increasing the wall

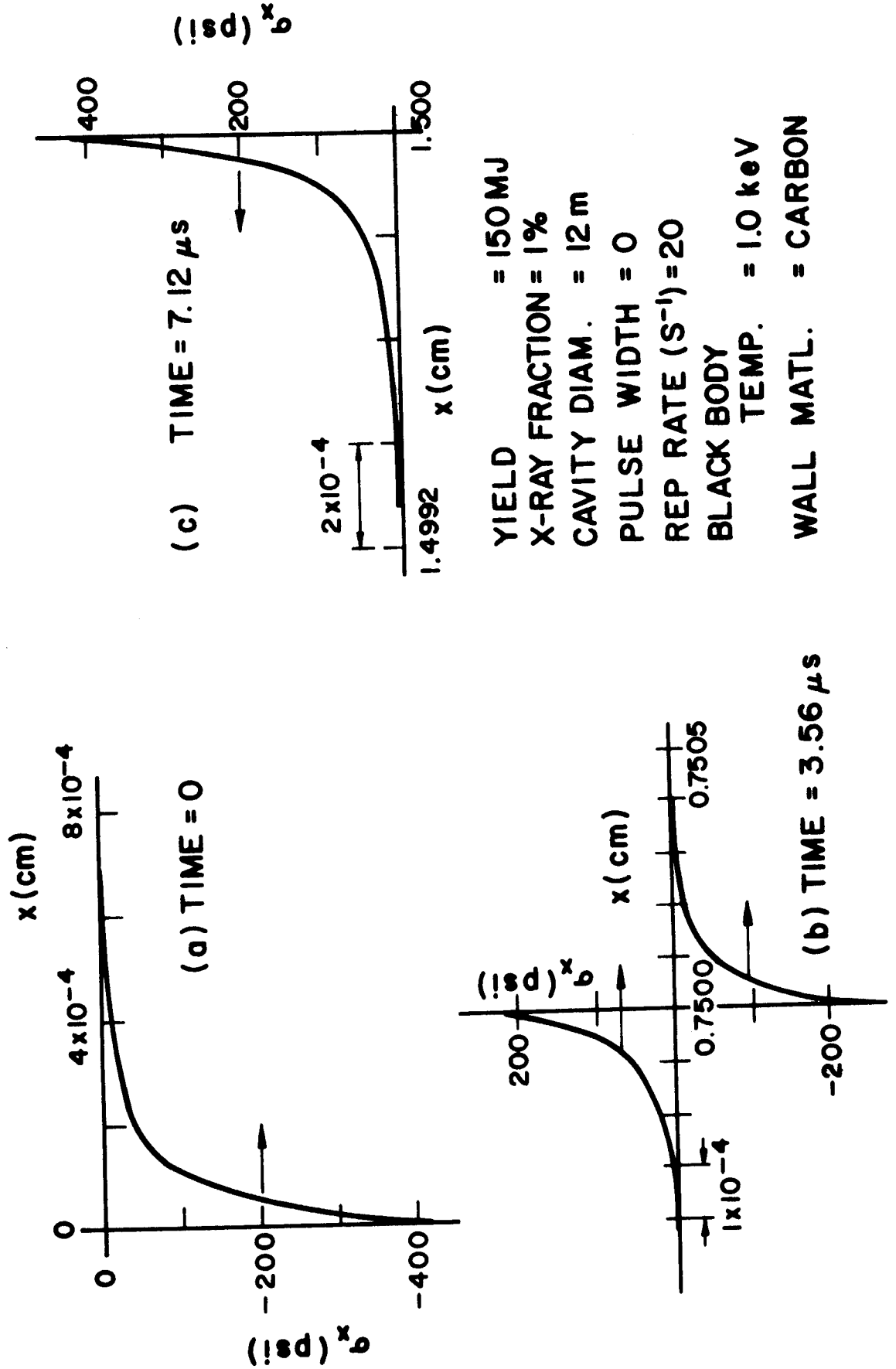
(a) TIME = 0
x (cm)
8x10⁻⁴
4x10⁻⁴
0
0
-200
-400
q_b^x (psi)
(b) TIME = 3.56 μs
x (cm)
0.7505
0.7500
1x10⁻⁴
200
-200
q_b^x (psi)
(c) TIME = 7.12 μs
400
200
1.500
2x10⁻⁴
1.4992
x (cm)
q_b^x (psi)
YIELD = 150 MJ
X-RAY FRACTION = 1%
CAVITY DIAM. = 12 m
PULSE WIDTH = 0
REP RATE (S^{-1}) = 20
BLACK BODY TEMP. = 1.0 keV
WALL MATL. = CARBON

Fig. X-C-28.

thickness (Fig. X-C-29a). The inefficiency of this approach suggests alternate methods of increasing the flexural stiffness. A double-walled plate (analogous to an I-beam in two dimensions) is considerably stiffer and thus stressed at a much lower intensity (Fig. X-C-29b). Diagonal lace elements (curved plates) serve to separate faces, transmit shear and stiffen against tangential loads (a minor consideration in this application). The natural extension of this design is a complete cellular unit (Fig. X-C-29a) This design has been used in SOLASE (Sections XI, XII). In addition to being structurally sound, this configuration allows for partitioning of the LiO_2 flow and is neither a difficult nor expensive configuration to fabricate.

The radial dividers effectively separate the first wall into smaller plates, each of which will have zero slope change and maximum flexural stress at the divider support. Circumferential stiffeners, such as ribs on the wall surface, are not possible since they would interfere with the LiO_2 through the blanket. Each plate will be conservatively considered flat; its curvature will enhance its structural integrity. In addition, if the aspect ratio of the plate (i.e., in this case the meridonial length to circumferential span) is greater than 2, the stresses are for all practical purposes no different than a plate with infinite aspect ratio. With these considerations the maximum stress is determined as a function of thickness and span between radial dividers.

The response of the plate can be obtained by multiplying static stresses and deflections by a dynamic load function. The maximum value of the function depends upon the ratio of the pressure pulse duration (τ) to the

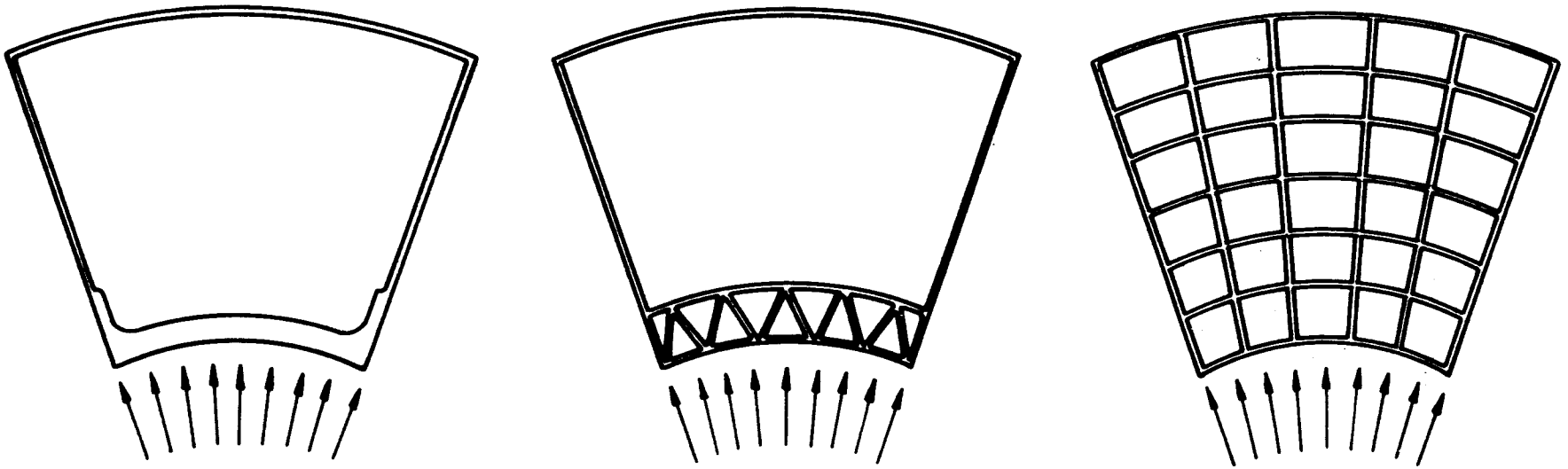
(a) SIMPLE FIRST WALL
(b) COMPOUND WALL
(c) COMPLETE CELL CONFIGURATION

Fig. X-C-29.

natural period of the structural component (T). Considering that the effect of the pressure can be adequately represented by a rectangular pulse, it can be seen from Fig X-C-30 that the maximum dynamic load factor is two. Using this as an extreme value, design curves are now established for maximum stress as a function of wall thickness and partition spacing as shown in Figs. X-C-31 and 32.

Detailed calculations pertaining to the SOLASE cavity are given in Section XI.

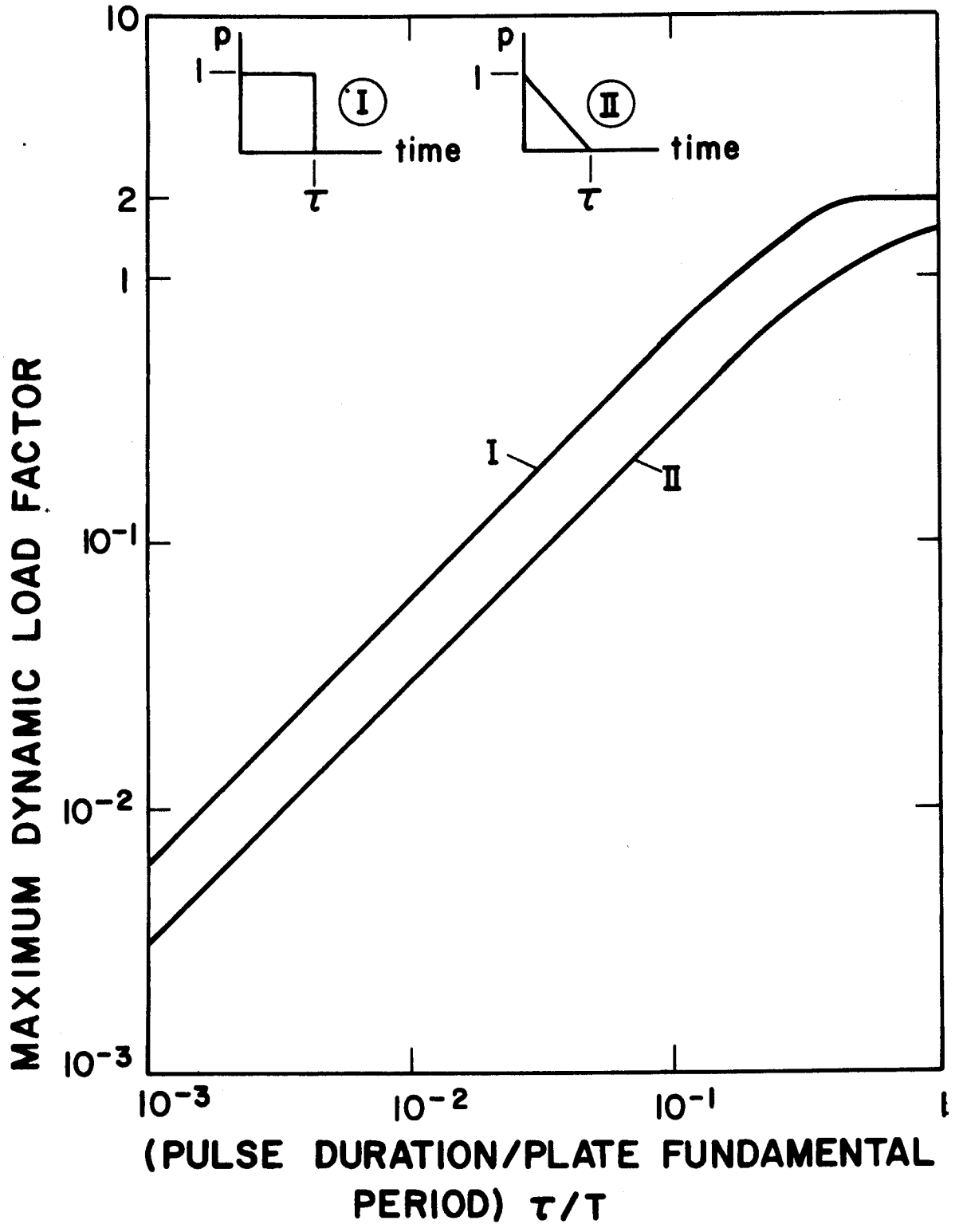
10
2
1
10^{-1}
10^{-2}
10^{-3}
p
1
I
time
τ
p
1
II
time
τ
I
II
MAXIMUM DYNAMIC LOAD FACTOR
10^{-3}
10^{-2}
10^{-1}
(PULSE DURATION/PLATE FUNDAMENTAL PERIOD) τ/T

Fig. X-C-30.

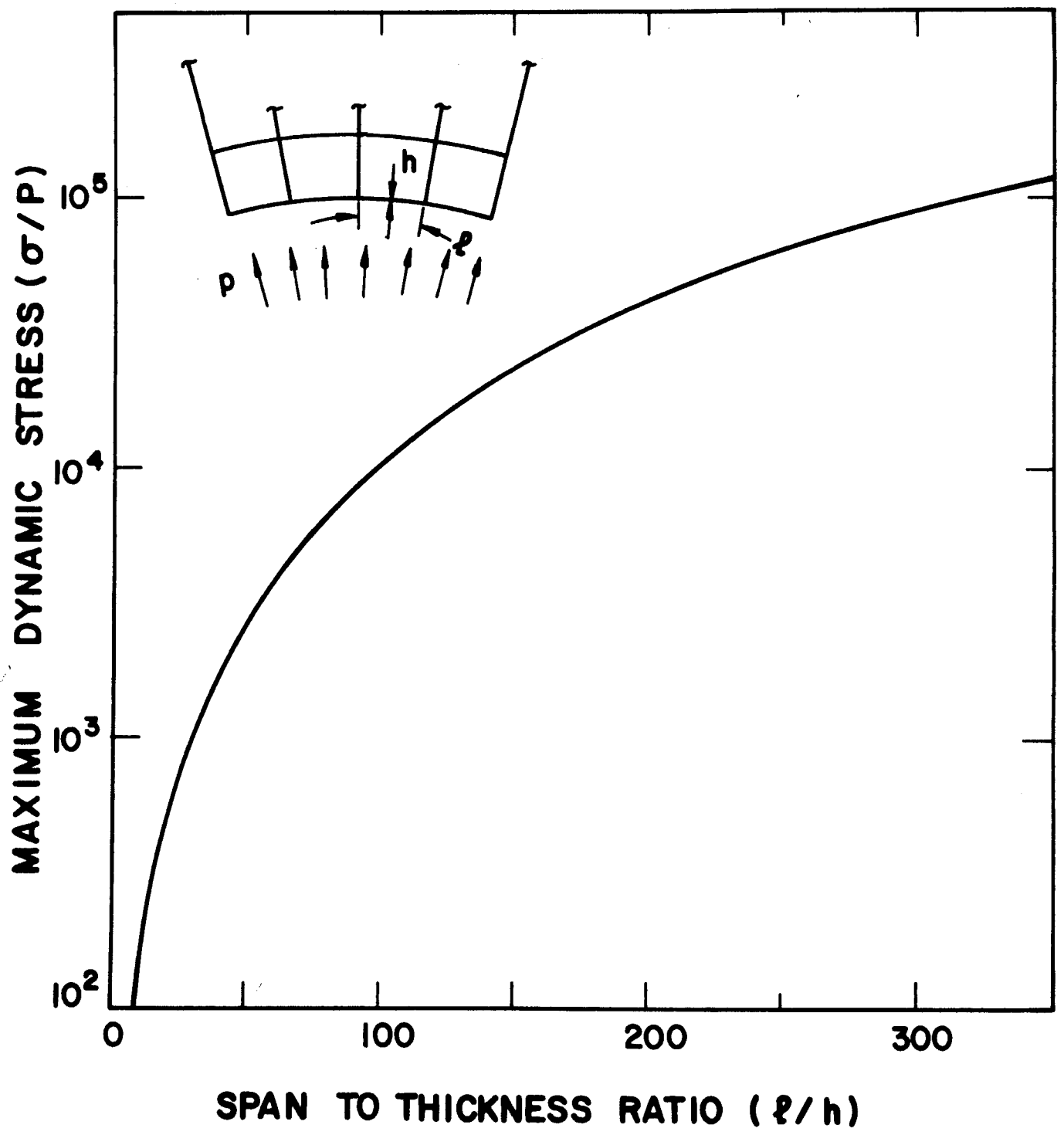
MAXIMUM DYNAMIC STRESS (σ/P)
10^5
10^4
10^3
10^2
h
ℓ
p
0
100
200
300
SPAN TO THICKNESS RATIO (ℓ/h)

Fig. X-C-31.

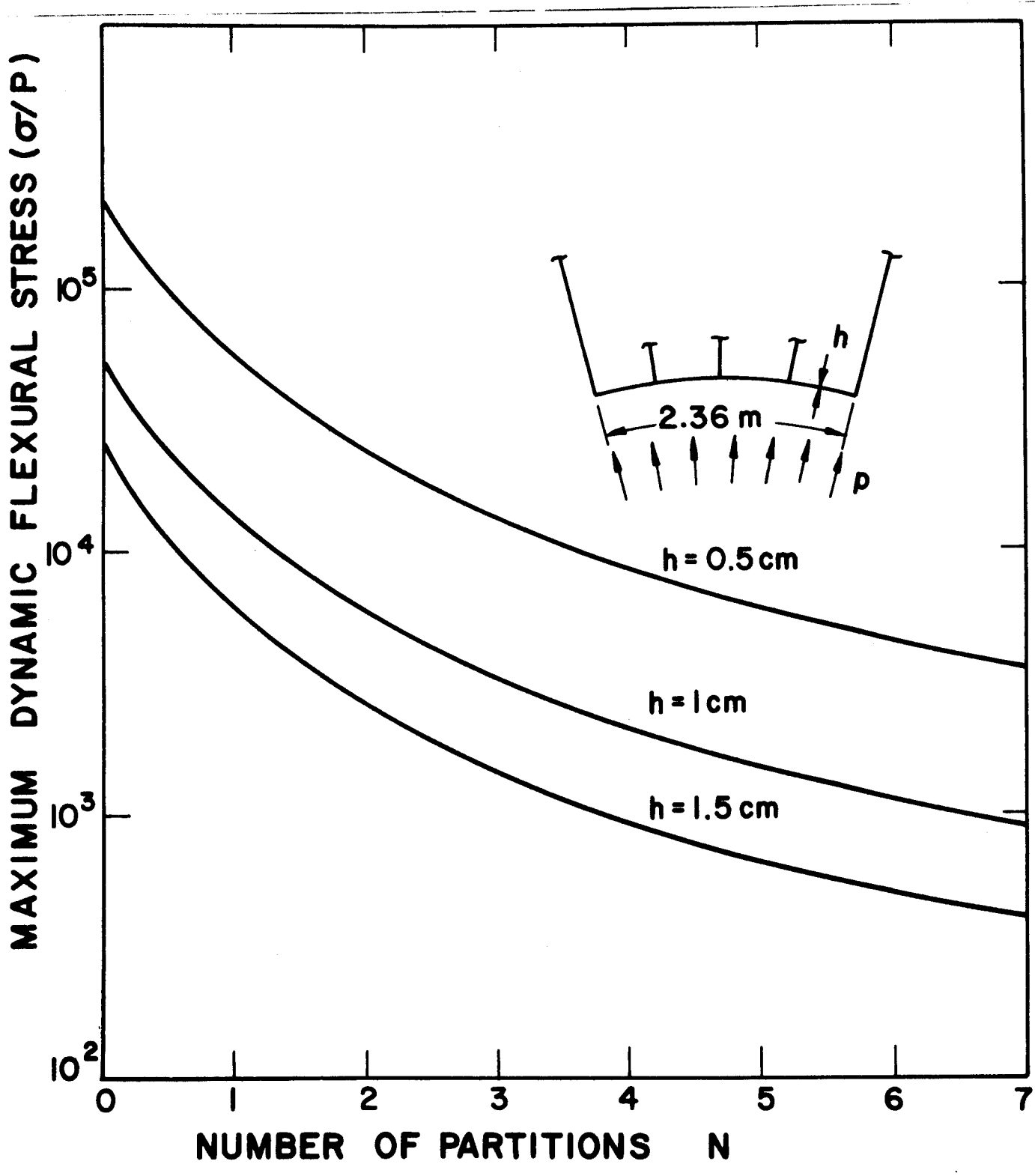
MAXIMUM DYNAMIC FLEXURAL STRESS (σ/P)
10^5
10^4
10^3
10^2
0
1
2
3
4
5
6
7
NUMBER OF PARTITIONS N
h = 0.5 cm
h = 1 cm
h = 1.5 cm
h
2.36 m
p

Fig. X-C-32.

References for Section X-C

1. J. Hovingh, "First Wall Studies of a Laser-Fusion Hybrid Reactor Design", Proc. 2nd Topical Meeting on the Technology of Controlled Nuclear Fusion, Richland, Washington (1976).

2. F. Biggs and R. Lighthill, "Analytical Approximations for X-ray Cross Sections II", SC-RR-71-0507, Sandia Laboratories (1971).

3. J. Lindhard, M. Scharff and H. E. Schiott, Mat. Fys. Medd. Dan. Vid. Selsk., 33, 14 (1963).

4. H. S. Carslaw and J. C. Jaeger, Conduction of Heat in Solids, Second Edition, Oxford University Press (1959).

5. R. G. Tomlinson, E. K. Damon, and H. T. Buscher, "The Breakdown of Noble and Atmospheric Gases by Ruby and Neodymium Laser Pulses", Physics of Quantum Electronics, Kelley, Lax and Tannenwald (Eds.), p. 520, McGraw Hill, New York (1966).

6. I. Manning and G. P. Meuller, "Depth Distribution of Energy Deposition by Ion Bombardment", Computer Physics Communication, 6 (1973).

7. R. Behrish, "First Wall Erosion in Fusion Reactors", Nuclear Fusion, 12, 695 (1972).

8. L. W. Morland, "Generation of Thermoelastic Stress Waves by Impulsive Electromagnetic Radiation," AIAA Journal, 6, 1063-1066 (1968).

XI. Cavity Design for SOLASE

In this section, the cavity design for SOLASE and the models developed to support such a design are presented. Section XI-A deals with the overall description of the cavity and blanket. The buffer gas protection concept is analyzed in Section XI-B; the analyses include: charged particles and X-ray attenuation, shock strength and magnitude of the pressure pulse experienced by the first wall, gas cooling and energy transfer to the front wall, and laser-induced gas breakdown. The thermal and mechanical responses of the first wall are analyzed in Section XI-C. The analyses have for the most part been carried out parametrically. This approach is necessary since pellet design is in its infancy and a wide range of pellet materials, and output characteristics is possible. Careful analysis of the effects of these parameters on the different reactor subsystems, including synergistic effects, should guide pellet designers in their search for suitable pellet(s) for reactor applications.

XI-A. General Description of the SOLASE Cavity

A general view of the SOLASE cavity and blanket is shown in Fig. XI-A-1. The cavity is spherical with a 6 m radius. It is filled with neon gas at less than 1 torr pressure, sufficient to protect the first wall from the ions and soft X-rays produced by the microexplosion. Hard X-rays deposit their energy directly in the front wall of the blanket but produce a relatively small surface temperature rise because of their long range. The energy deposited in the gas is radiated to the front wall over a relatively long time period (> 1 ms) so that surface heating and thermal ablation of the wall become insignificant. A shock wave is generated in the gas after each microexplosion. The propagating shock imparts an impulse load on the front wall. These

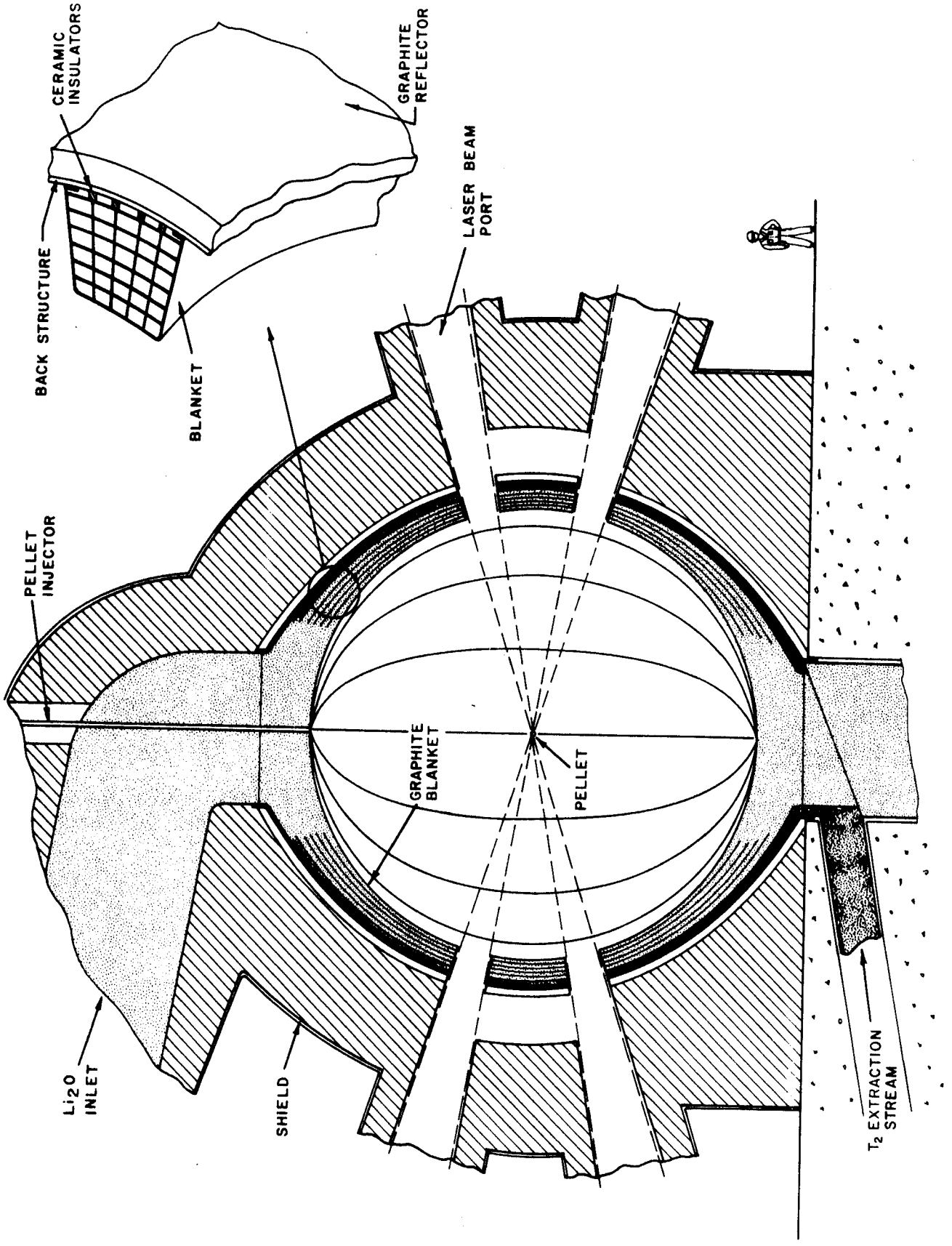

Fig. XI-A-1. Schematic Diagram of the SOLASE Cavity.

periodic loads, however, are quite small and can easily be accommodated (Section XI-B). This protection scheme is generic inasmuch as it can accomodate a wide range of spectra and ion-and-X-ray energy fractions for the 150 MJ pellet yields considerd. Maps showing the ranges of pellet output parameters over which this protection scheme will operate successfully are given in Section XI-C.

Neon is selected as the fill gas because it has the highest laser-induced gas breakdown threshold among all gases, followed closely by helium (Section XI-B). In addition, neon has a relatively high stopping power for ions and X-rays and is inert so there is no worry of chemical reaction with the first wall.

The spherical cavity is divided along longitudes into sixteen blanket segments each with a honeycomb type construction (Fig. XI-A-1). The entire blanket is constructed from graphite. Either nuclear grade graphite or chopped-fiber type graphite composite can be used. Lithium oxide particles, 100-200 μm in diameter, flow under gravity through the blanket and serve the dual purpose of tritium breeding and heat transport. The tangential spacers parallel to the front wall allow the velocity distribution of the Li_2O particles to be tailored to match the radial heat deposition curve (Chapter XII). The radial supports provide structural rigidity and allow impulse loadings on the front wall to be transmitted to the support structure behind the blanket. This design eliminates the need for metallic first walls and liners since the front wall of the blanket can readily accomodate the microexplosion both thermally and mechanically.

The pulsed surface heat flux radiated by the gas is rectified in the blanket's front wall and directly convected and radiated to the flowing

lithium oxide. The lithium oxide particles enter the blanket at 400°C and leave at 600°C except for the outermost zone where the exit temperature is 850°C. (The hot stream contains ~2% of the total flow rate and is used for tritium extraction (Chapter XVI)). The back surface of the front wall will operate at ~1400°C with the front surface temperature reaching ~1800°C after each microexplosion. These temperatures are sufficiently high that excessive swelling of the graphite should not be a problem. Also, at these temperatures the vapor pressure of carbon remains low so that thermal ablation of the graphite is insignificant. Detailed thermal hydraulic and neutronic analyses for the blanket are given in Chapters XII and XIII respectively. Radiation damage considerations are discussed in Chapter XV.

Possible chemical reactions between the first wall and pellet materials have been investigated. At the first wall temperatures of interest (~1800°C), the unburned hydrogen isotopes will react with graphite to form acetylene. The reaction rates have been used to determine the vacuum system throughput required to limit the wall erosion rate to ~1 mm/yr. For pellet designs of interest, the necessary vacuum system throughputs and the corresponding pumping powers are reasonably low (~3×10^4 torr-l/sec, 10 MW). Details of these analyses are given in Chapter XVI. Special attention has also been given to possible non-hydrogenic pellet constituents and their compatibility with the first wall. The use of lead or mercury in the pellet does not pose significant problems since they do not form stable carbides (Chapter XVI).

The remainder of this section is devoted to analyses of the gas protection concept and determination of the thermal and mechanical response of the first wall.

XI-B. Analyses of the Gas Protection Concept

In this section, the gas protection concept utilized in SOLASE to attenuate the charged particles and soft X-rays before reaching the first wall is analyzed. Our aim is to answer the questions posed in Section X-B-4, namely:

(1) How does the gas attenuate the charged particles as a function of Z, energy per ion, and gas density?

(2) How does the gas attenuate the X-rays as a function of the spectrum and gas density?

(3) How much energy is re-radiated from the gas to the front wall and on what time scale? How does the wall respond thermally to the modified photon spectra and to the pulsating heat flux loads?

(4) Does a shock wave develop in the gas as a result of the energy deposition and how much momentum does this shock transfer to the first wall?

(5) Can the laser beams be propagated through the gas without experiencing gas breakdown? How does this depend on gas density, laser wavelength, and pulse shape?

The amount of buffer gas necessary to adequately attenuate the charged particle debris and X-rays depends on the ion and X-ray spectra produced by the microexplosion. These spectra depend on the amount of DT fuel and other non-fuel materials in the pellet (Chapter IV). Since a complete pellet design is unavailable, parametric studies of the ion and X-ray spectra as a function of pellet materials have been conducted

for a wide range of masses using the PHD-IV plasma hydrodynamics code (chapter IV). For the purpose of the following analysis, a pellet consisting of 1 mg DT and 10 mg Hg is used. This pellet has been selected in order to illustrate the phenomena involved in this protection concept, and to produce a consistent set of results to be used in our design calculations.

XI-B-1. Charged Particle Attenuation

As the compressed pellet burns and explodes, the hot DT and alpha particle mixture accelerates the surrounding mercury to a high velocity (2×10^8 cm/sec). This acceleration ceases when all of the particle species in the pellet are moving radially outward at the same velocity. The velocity spectra of the different species (deuterium, tritium, helium and mercury) can then be constructed from the hydrodynamics code output and these are shown in Figs. XI-B-1 through XI-B-4. The mercury ions with their large mass carry almost all of the charged particle energy. In addition, the 10 mg of mercury does not allow any non-thermal alpha particles to escape from the thermally expanding plasma. Ion attenuation calculations based on the Lindhard stopping theory[1,2] indicate that the mercury ions are the

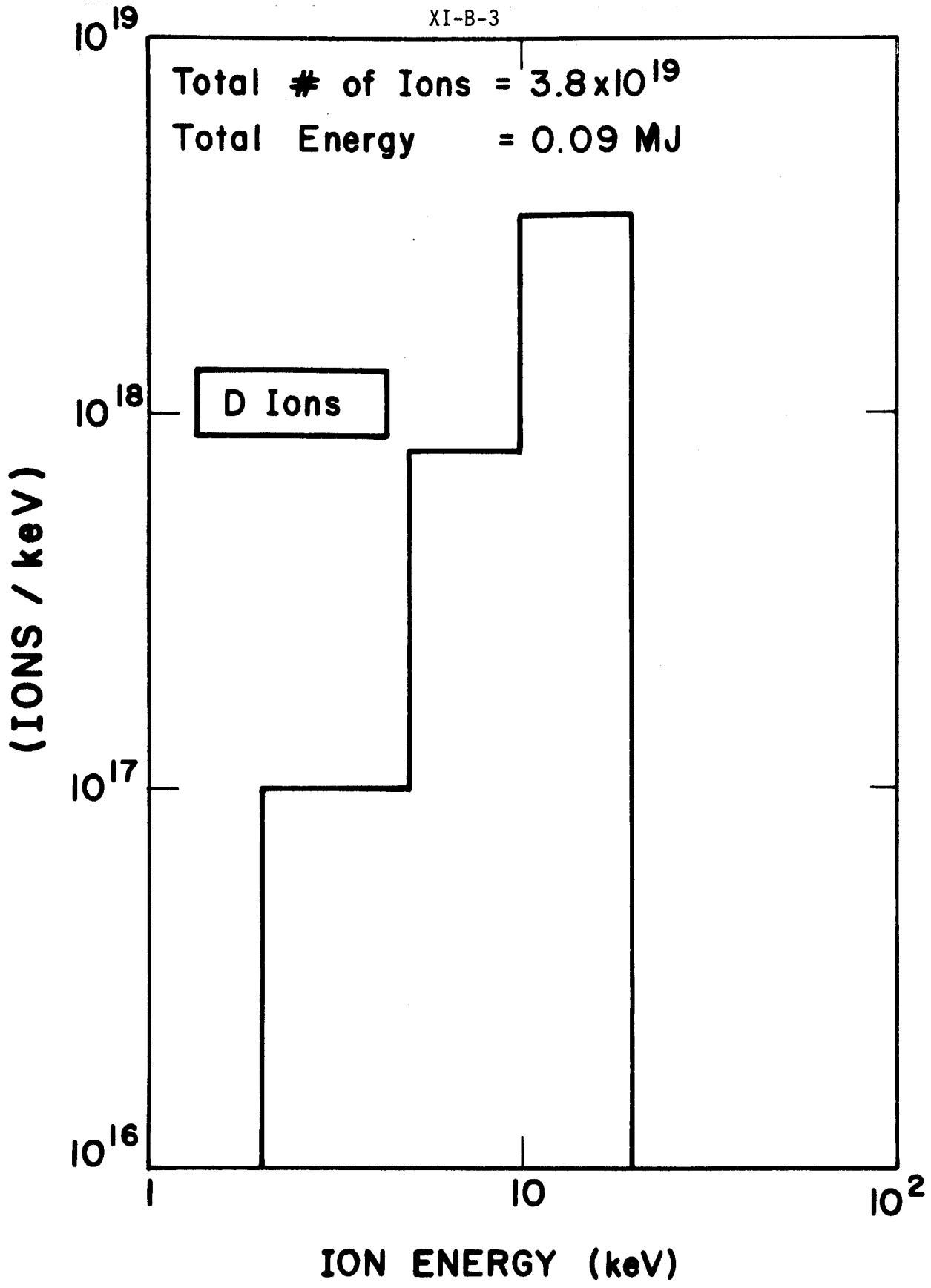

Fig. XI-B-1.

Deuterium particle spectrum from a 150 MJ pellet with 10 mg of mercury surrounding the DT fuel.

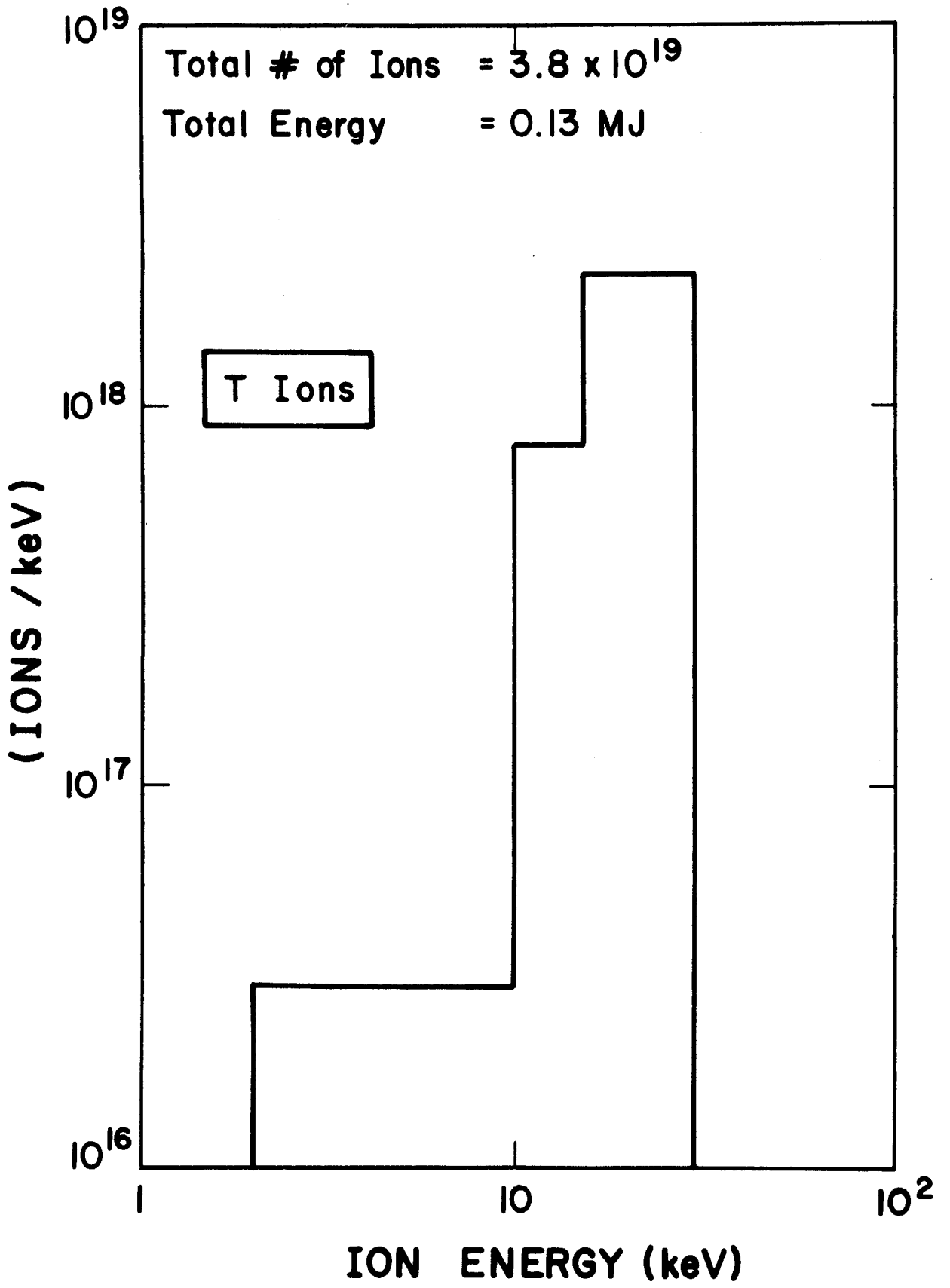

Fig. XI-B-2.

Tritium spectrum from a 150 MJ pellet
with 10 mg of mercury surrounding the DT fuel.

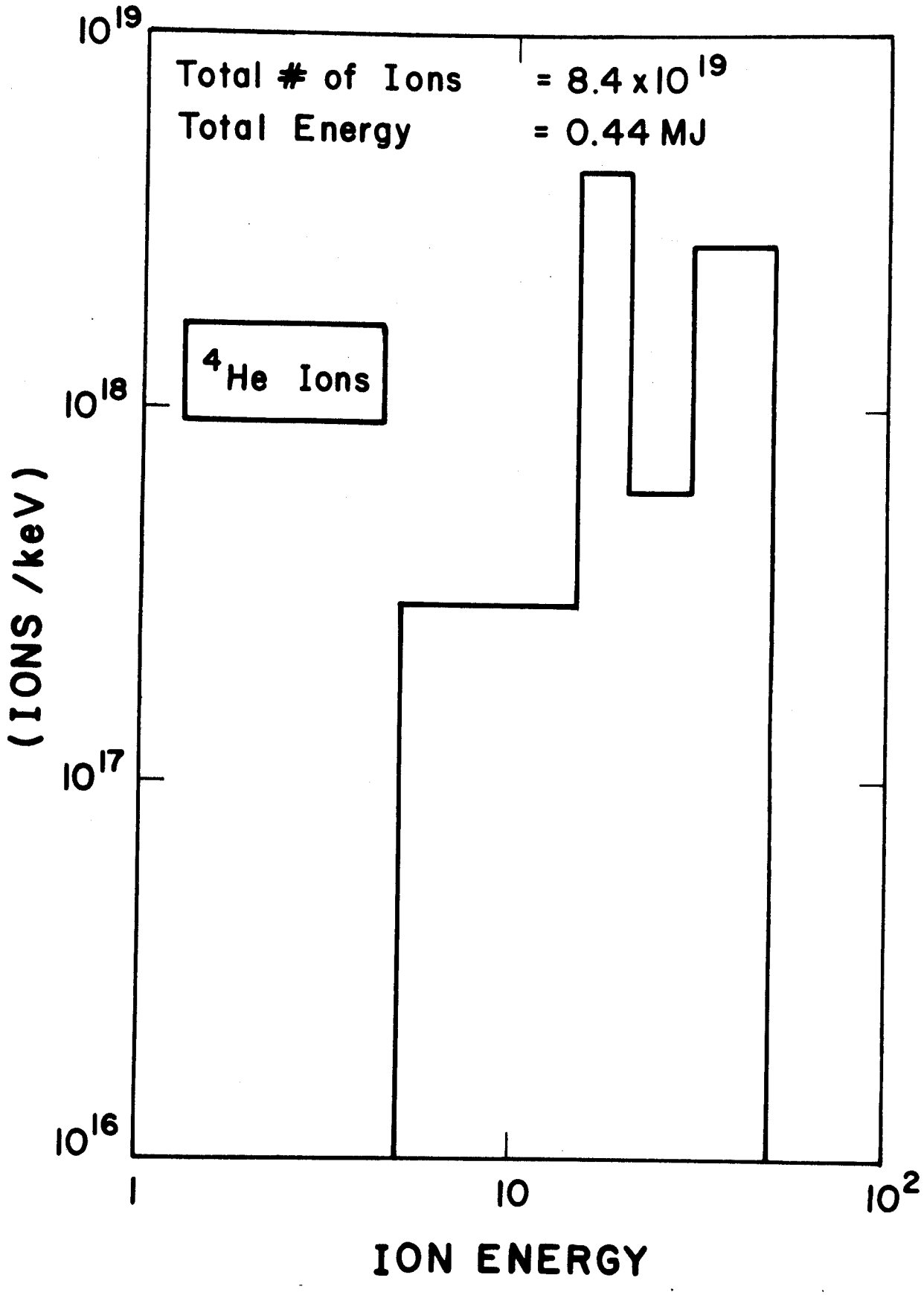

Fig. XI-B-3.

Alpha particle spectrum from a 150 MJ pellet with 10 mg of mercury surrounding the DT fuel.

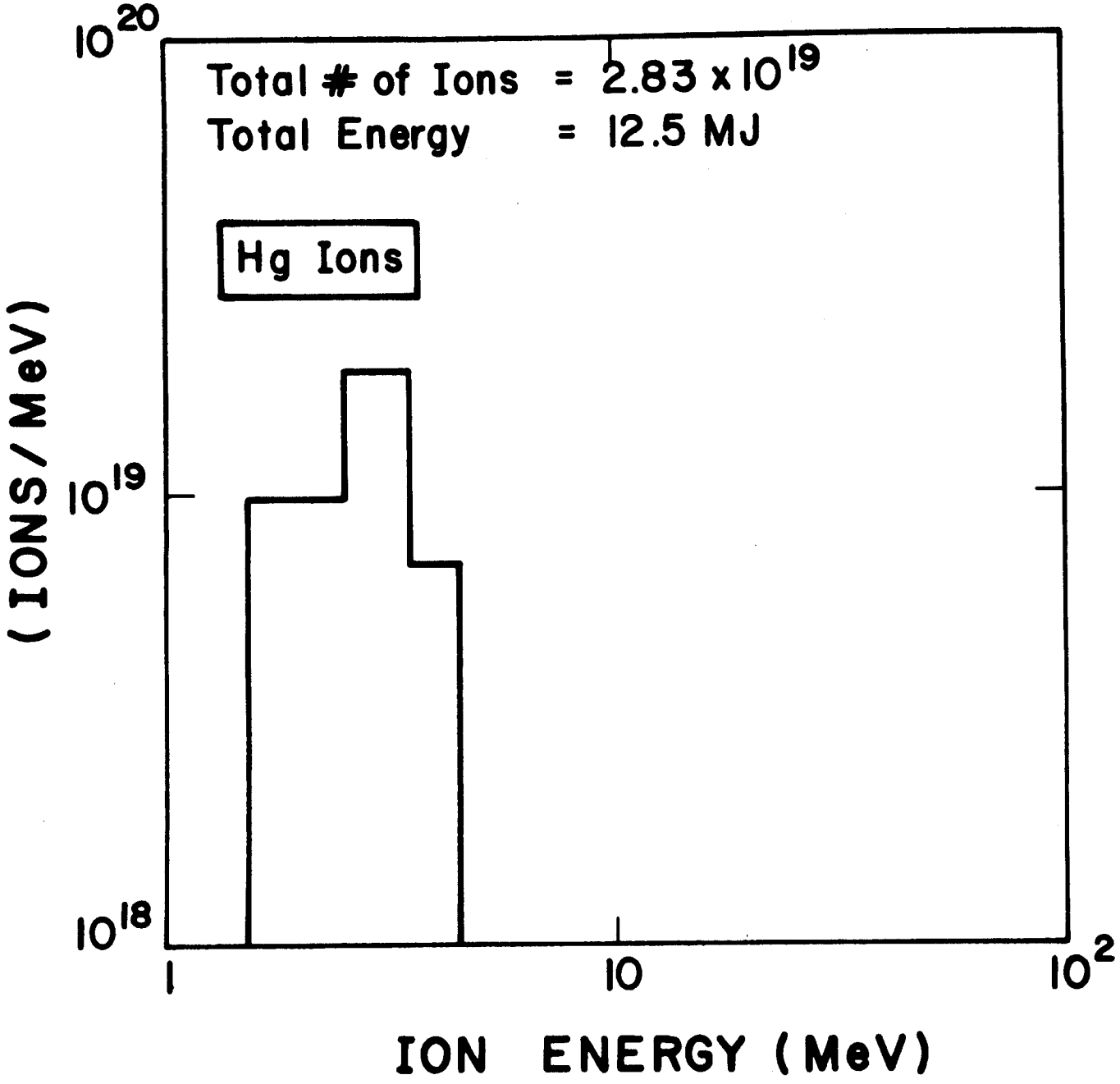

Fig. XI-B-4.

Mercury ion spectrum from a 150 MJ
pellet with 10 mg of mercury surrounding the DT fuel.

most penetrating of the particle species from this pellet and that they are nearly completely stopped by 6 meters of neon at a density of $1.5 \times 10^{16} cm^{-3}$. Mean ranges and rms deviations for the ions in this pellet are given in Table XI-B-1. The ion energy deposition as a function of radius is given in Fig. XI-B-5 for mercury in neon. This energy deposition profile is important for the computation of the dynamics of the shock wave resulting from this energy source (Section XI-B-3).

Table XI-B-1

Ranges In Neon ($1.5 \times 10^{16} cm^{-3}$) For Different Particles Found In The Pellet. (The Energies Given Are The Maximum Values For Each Particle.)

Particle	Energy	Mean Range (m)	RMS Deviation
D	20 keV	2.3	0.1
T	30 keV	3.4	0.2
^4He	90 keV	3.6	0.2
Hg	4.2 MeV	4.9	0.8

XI-B-2. X-Ray Attenuation

The mercury surrounding the DT fuel absorbs much of the fusion reaction product energy, heats up, and radiates. The detailed dynamics of this process are discussed in Chapter IV. For the particular pellet used in this analysis, the X-ray spectrum predicted by the PHD-IV code is quite hard. The frequency-dependent code results along with a 20 keV black body spectrum are plotted in Fig. XI-B-6. This spectrum is harder than the spectrum from

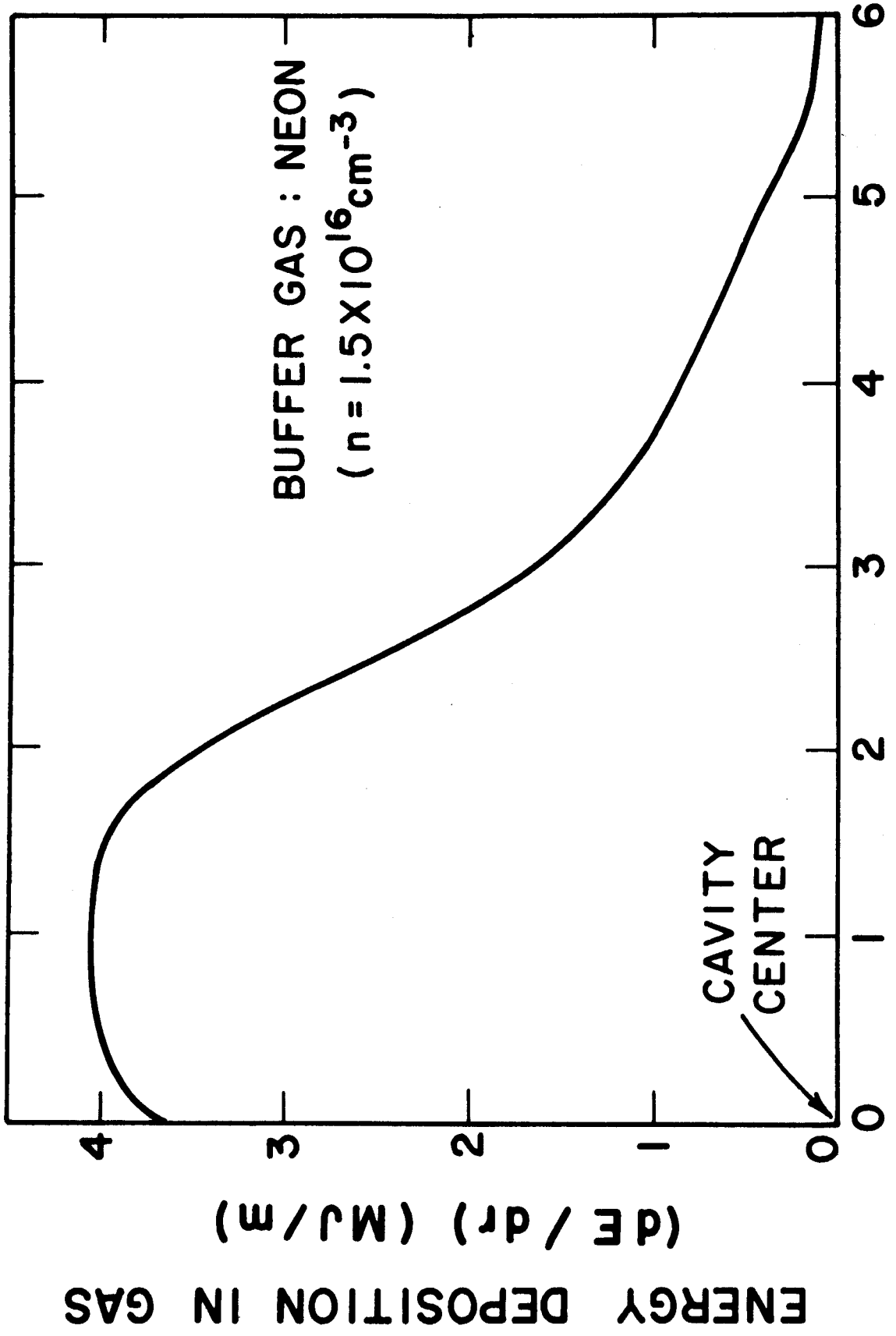

Fig. XI-B-5.
Energy deposition due to mercury ions in neon as a function of radius.

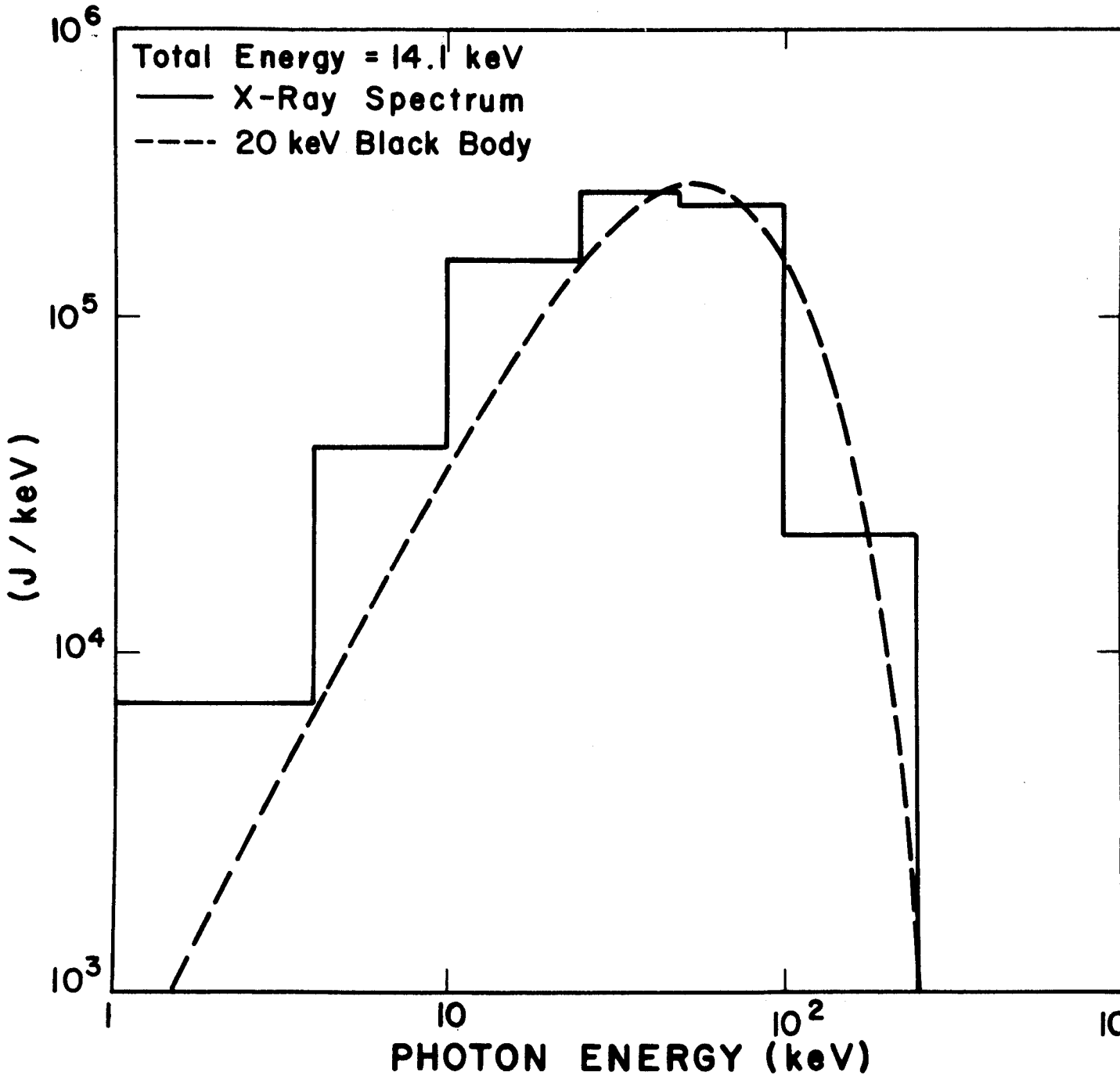

Fig. XI-B-6.

Time integrated x-ray spectrum from a 150 MJ pellet with 10 mg of mercury around it. The dashed curve is a 20 KeV blackbody spectrum.

bare DT pellets and about 10% of the thermonuclear energy is carried away by X-rays which is nearly equal to the energy carried away by charged particles. Because this spectrum is so hard, the neon is ineffective at attenuating it. For instance, even a 2 keV photon has a mean free path of 15 meters in the gas. The photo-electric cross section for neon is plotted in Fig. XI-B-7. It is seen that this cross section is highest at low energies (<100 ev) so that most of the attenuation of any spectrum will be for soft photons. The mean free paths of photons with energies less than 100 ev will be on the order of centimeters. This is, of course, the desired effect since these low energy photons are also the most damaging to the first wall because of their short range in carbon (Section X-C). The PHD-IV code predicts that the X-rays are emitted from this reference pellet in a 2 nsec pulse. This finite pulse length significantly relaxes the attenuation requirements of the neon gas. Besides, the hard X-rays produced by this pellet result in negligible wall surface temperature rise. Plots showing the maximum allowable fraction of energy in X-rays as a function of the spectrum and pulse duration are given in Section XI-C.

Due to uncertainties in the exact pellet spectra it is important that the graphite first wall-neon fill gas combination used in SOLASE will perform adequately over a range of pellet debris and X-ray spectra. This is indeed the case as discussed in Section XI-C. The neon gas will protect the first wall from X-rays with energies less than 100 ev and the first wall needs no protection from X-rays with energies greater than ~1 keV. Between

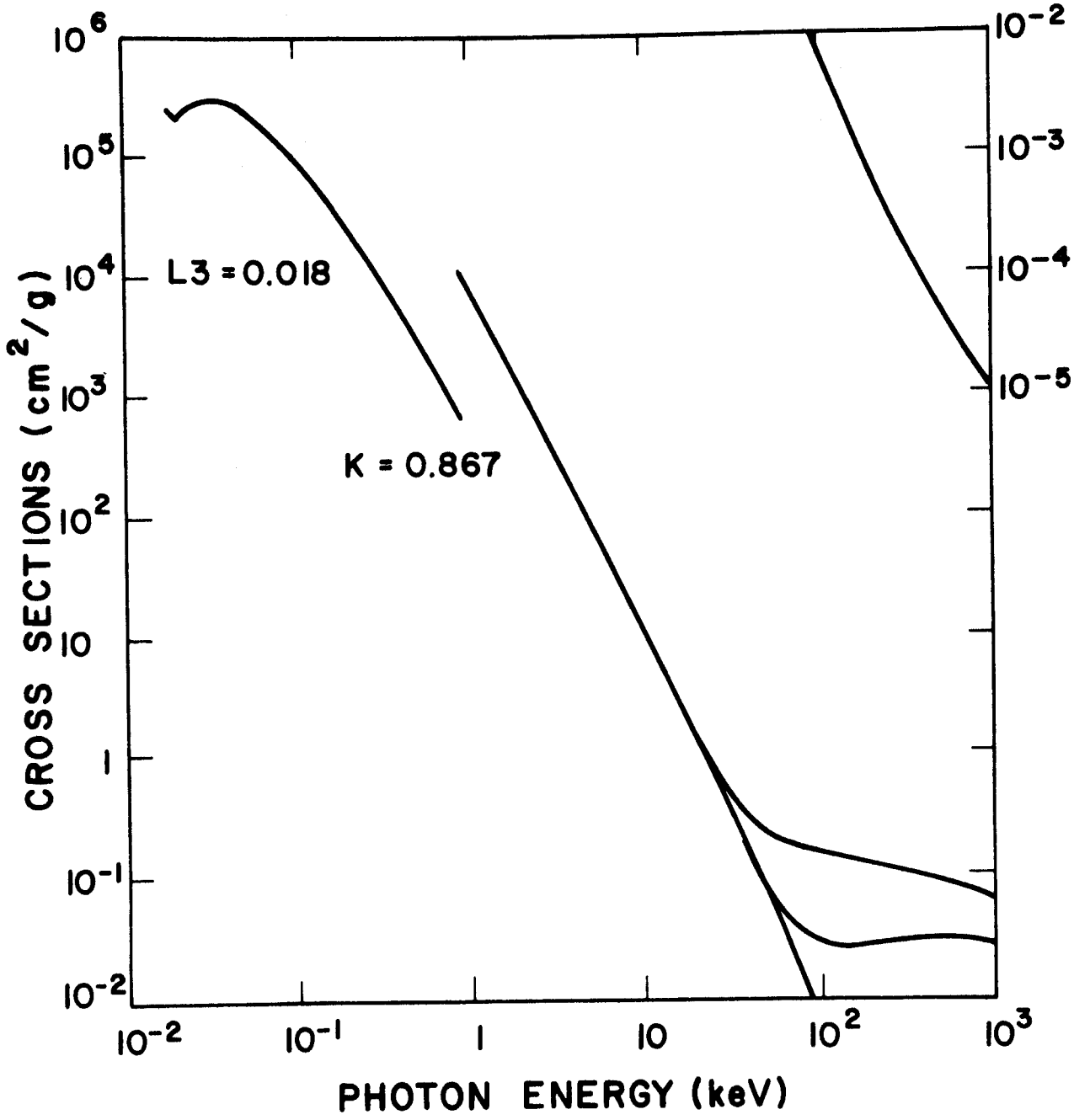

Fig. XI-B-7.

The absorption coefficient of neon. The mass density of the neon in the chamber is 5×10^{-7} g/cm^3.

these two energies there can be problems if the X-ray fraction is too large. However, the laser fusion pellet explosions investigated in this study indicate that with as much as 10 mg of nonfuel material in the pellet, the X-ray spectrum is still very hard. In fact, an order of magnitude "over-estimate" of the black body temperature of this spectrum could still be tolerated. The SOLASE concept is not limited to these hard spectra though, and could prove to be applicable to e-beam or ion-beam fusion pellets if the X-ray spectrum is softer than 100 ev.

XI-B-3, Pressure Impulse at the First Wall

When the background neon gas in the chamber absorbs the pellet X-ray and ion energy, it not only heats up but also experiences hydrodynamic motion. This motion may be in the form of an outward directed shock front and the subsequent momentum transfer at the first wall must be computed to insure that the wall can withstand such an overpressure. Several limiting cases are studied to observe the effects of differing assumptions regarding the energy absorption. If there were no gas in the cavity then the momentum transfer would be due to the outward expanding mercury shell and the reaction of the wall to the ablated carbon (if any). A rough estimate of the pulse width and momentum of the mercury arriving at the first wall is given by:

$$\left.\begin{aligned} \Delta t &\simeq R\left(\frac{1}{V_{min}} - \frac{1}{V_{max}}\right) \simeq 10^{-6} \text{ seconds,} \\ \text{and} \quad M &= 2 \times 10^{6} \text{ g cm/sec} \end{aligned}\right\} \qquad (1)$$

The magnitude of the pressure pulse corresponding to these values is

$$P = \frac{1}{4\pi R^2} \frac{M}{\Delta t} = 300 \text{ torr.} \qquad (2)$$

When a background gas is introduced into the chamber, the energy of the explosion is distributed over a much larger gas mass (500 g of neon), causing the impulse to be greater. If all the energy is absorbed in a small volume near the center of the cavity, then the self-similar strong shock theory of Sedov[3] may be applied. Since only an estimate of the impulse produced is needed, the approximate method of Chernyi[4] is sufficient. In this approximation, the entire mass of gas swept by the shock is assumed to be in a thin shell at the shock radius. The pressure, density and fluid velocity in the shell are assumed to be constant and equal to their values at the shock front. The volume inside the shell is assumed to have negligible mass but a high temperature and uniform pressure equal to one half that of the shell. Under these assumptions, the fluid variables in the shell are given by:

$$\left.\begin{array}{ll} \text{density:} & \rho_1 = \frac{\gamma+1}{\gamma-1}\rho_o \\ \text{pressure:} & P_1 = \frac{2}{\gamma+1}\rho_o D^2 \\ \text{fluid velocity:} & U_1 = \frac{2}{\gamma+1} D \end{array}\right\} \qquad (3)$$

where ρ_o is the initial gas density and D is the shock speed. The shock speed is given by:

$$D = \left[\frac{3}{4\pi} \frac{(\gamma-1)(\gamma+1)^2}{3\gamma-1} \frac{E}{\rho_o R^3}\right]^{1/2} \qquad (4)$$

where E is the explosion energy, R is the radius of the shock front and γ is an effective adiabatic exponent for the hot neon gas. Two quantities of interest are the fraction of the total energy that is in kinetic energy and the magnitude of the total gas momentum. These are given by:

$$\frac{T}{E} = \frac{2(\gamma-1)}{3\gamma-1} \tag{5}$$

and

$$M = \left[\frac{16\pi}{3}\frac{\gamma-1}{3\gamma-1}\rho_o R^3 E\right]^{1/2} \tag{6}$$

The maximum pressure at the wall may be computed by assuming that the shock reflects there and re-shocks the gas. The pressure is then given by[5]:

$$P_2 = \frac{3\gamma-1}{\gamma-1} P_1 \tag{7}$$

These results can be applied to the SOLASE cavity where E = 13 MJ, $\rho_o = 5 \times 10^{-7}$ g/cm^3 and R = 600 cm. Since the neon is heated sufficiently to cause partial ionization, an effective γ of about 1 must be used. A value of $\gamma = 1.2$ has been used successfully for high temperature air[6] and is also used in this case. With these values the kinetic energy fraction becomes

$$T/E = 0.15,$$

the total momentum becomes

$$M = 1.3 \times 10^8 \text{ g cm/sec},$$

and the peak pressure after reflection becomes

$$P_2 = 470 \text{ torr}.$$

Because of the steep pressure gradients and high pressures the results of this strong shock theory should give an upper bound on all of the above quantities.

These results indicate that if the explosion energy is stopped in a volume that is small compared to the cavity volume then the overpressure at the first wall is not significantly different from that experienced when there is no gas in the cavity. The first wall response would be considerably different however because in the case of no gas the high energy mercury ions would act as a surface heating source and would ablate a layer of carbon. This problem has not been treated in this analysis.

For the purposes of the SOLASE cavity design, neither of these two extremes is strictly appropriate. If it is assumed that the X-ray spectrum is sufficiently hard that the gas need not attenuate it then the gas pressure should be only great enough to attenuate the ions over a distance slightly less than the cavity radius. In this case, the neon gas will be more uniformly heated and the subsequent hydrodynamic response cannot be approximated by a simple analytical theory. For this reason a Lax-Wendroff fluid dynamics code similar to that developed by Goldberg and Abarbanel[7] was written and applied to this problem. For initial conditions, the fluid density was assumed uniform. The initial temperature distribution (Fig. XI-B-8) was constructed to be consistent with the energy deposition profile in Fig. XI-B-5. The fluid motion was followed until the pressure peaked. Shocks were observed to develop, but they were

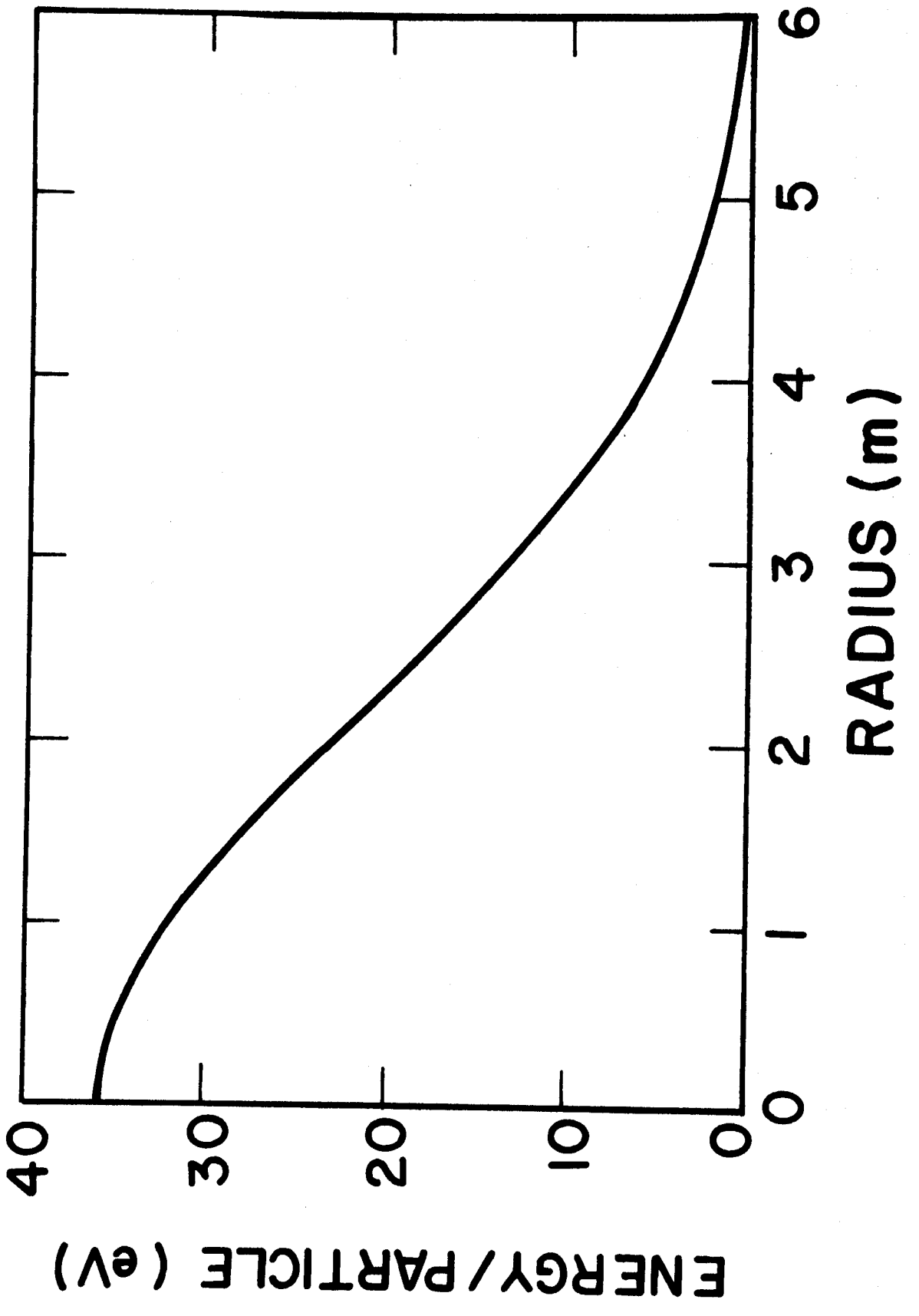

Fig. XI-B-8.

Initial energy per particle distribution used in the fluid calculation; the total energy is 13 MJ (γ = 1.2)

weak due to the rather gentle initial conditions. In spite of this, the peak values of the kinetic energy fraction and the total momentum were about half the values predicted by the strong shock theory. The peak pressure at the wall was about 90 torr and was spread over about 5×10^{-4} seconds as shown in Fig. XI-B-9. The momentum transferred to the wall, obtained by integrating the pressure profile over time, was about 2×10^{8} g cm/sec, a hundred times larger than that estimated for the mercury alone. The mechanical response of the wall to these pulsating loads is discussed in Section XI-C.

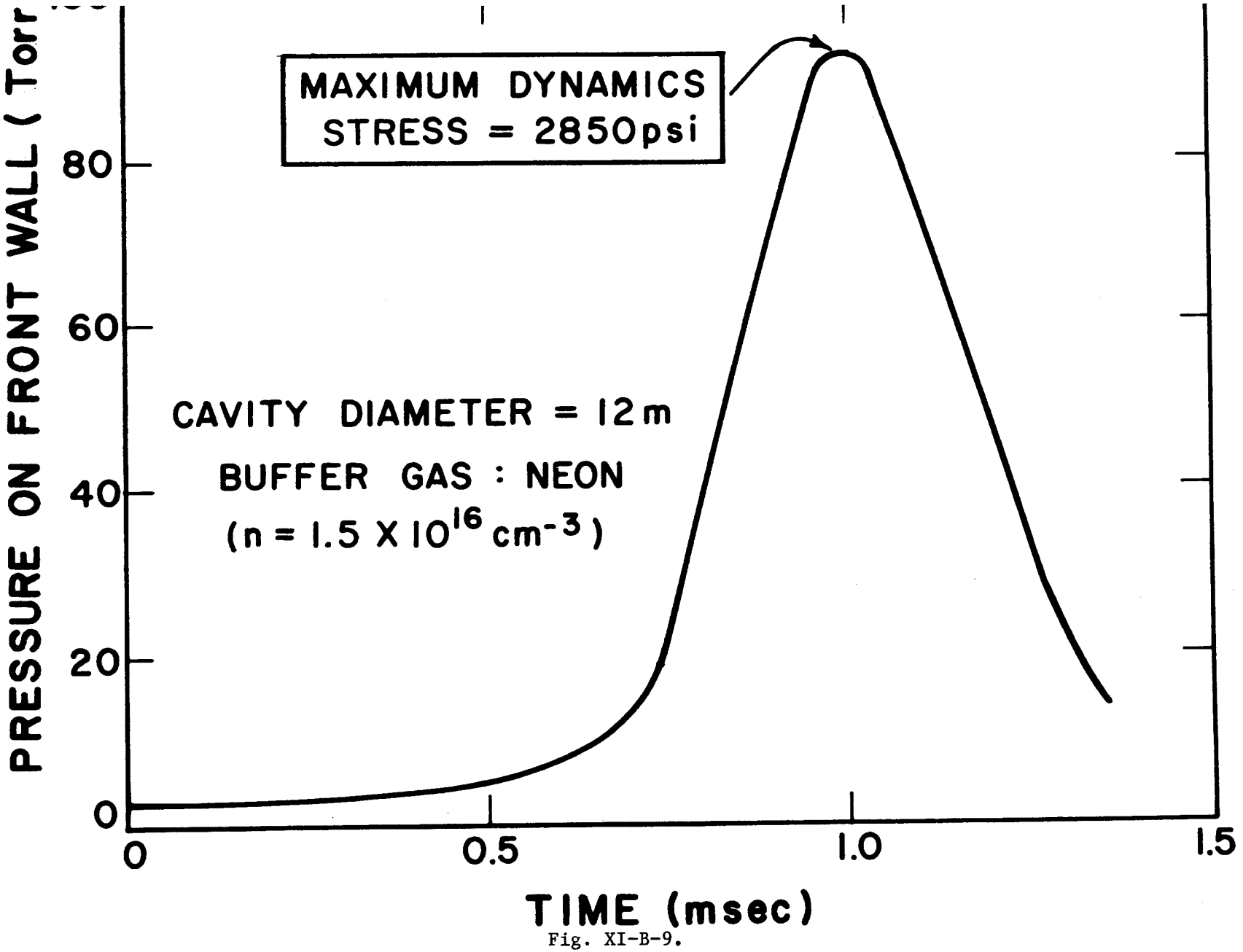

Fig. XI-B-9.

Pressure as a function of time at the liner for the initial conditions shown in Fig. XI-B-8.

XI-B-4. Gas Cooling -- Energy Transfer to the Wall

Once the ion energy is absorbed by the neon gas, this energy must be extracted. The neon will of course radiate the energy to the first wall over some time interval. The exact length of this time interval is crucial to the performance of the gas protection scheme. Should the energy be re-radiated in less than $\sim 10^{-3}$ second, the first wall surface temperature would rise significantly. However, if the radiation time is about 0.05 second then the hot gas would be removed through the pumping system before it could radiate an appreciable fraction of its energy. In this second case, the energy must be extracted in heat exchangers outside the reactor cavity. To estimate this radiation time we must study three radiative processes: bremsstrahlung, line radiation, and recombination. This problem is simplified by noting that bremsstrahlung is too weak at the anticipated temperature and density of the neon gas and line radiation does not carry much energy. Radiative recombination will be responsible for transporting most of the charged particle energy since most of this energy goes into ionizing the gas. Radiative recombination is not the only recombination process. The process of 3-body recombination also participates, but below $n = 10^{17}$ cm^{-3} the radiative process dominates.[8] Hence, to estimate the rate at which energy goes to the wall, we first calculate the recombination rate in the gas.

The simplest way to calculate the recombination rate is to assume thermodynamic equilibrium in translation, excitation and ionization. The translational degrees of freedom will quickly come to equilibrium compared to the millisecond times of interest here, but for the ionization to be in equilibrium, recombination must occur at a faster rate than energy is

lost. This may be the case. Figures XI-B-7 and 10-14 show the photo-electric cross-sections for the first six states of neon. At equilibrium, kT is less than the ionization potential I of the main ion species in the gas, so there are many recombination photons of energy near I. Such photons have mean free paths less than a meter, and their transfer of energy between the different ionization states of the gas will drive the ionization toward equilibrium. There is justification, then, for calculating the energy emission rates due to recombination by assuming local thermodynamic equilibrium.

The mean ionization state and total energy per neon atom as functions of temperature must be known before the energy release times can be calculated. These quantities can be satisfactorily calculated using the approximate method of Raizer.[9] In this method, the Saha equations, which determine the fraction of each ionized species present, are transformed into a single differential equation by replacing the discrete ionization potentials of the different neon ions by a piece-wise linear function I(m) such that $I(0) = 0$, $I(1) = I_1$, etc., where I_i is the ionization potential of the neon ion with $Z = (i-1)$. The result of the analysis is that the mean ionization state, or mean number of free electrons per atom, m, is given as a function of temperature by the solution of the equation

$$I(m + 1/2) = kT \ln \left(\frac{AT^{3/2}}{m\, n}\right) \tag{8}$$

where n is the atom density and $A = 2\left(\frac{2\pi mek}{h^2}\right)^{3/2} = 6.04 \times 10^{21}/cm^3/eV^{3/2}$.

This method is only useful for $m > 1$, but below $m = 1$ the first Saha equation alone gives m(T) fairly accurately except very near m=1:

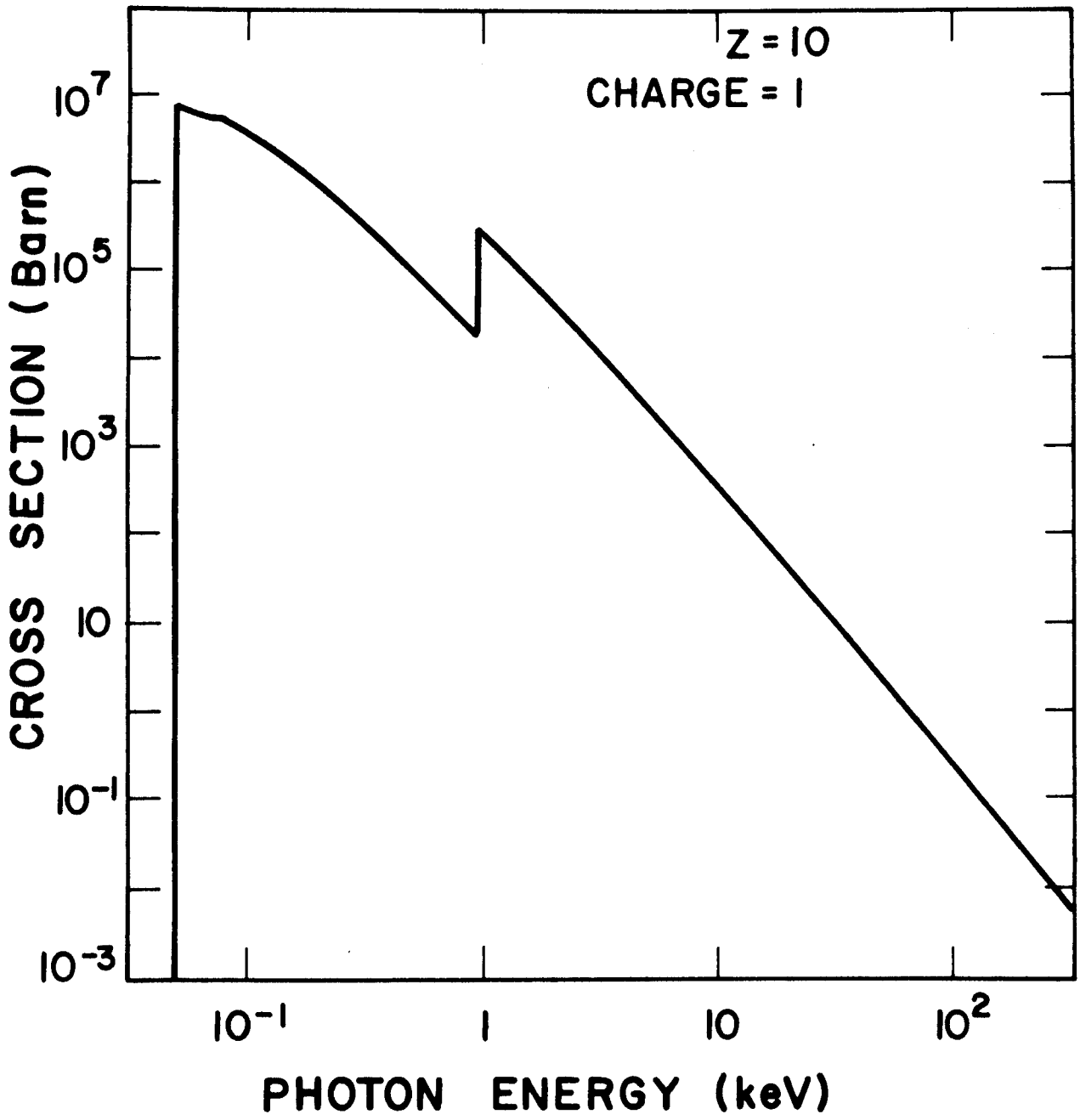

Fig. XI-B-10.

Photoelectric cross section for singly ionized neon. (From Ref. 10)

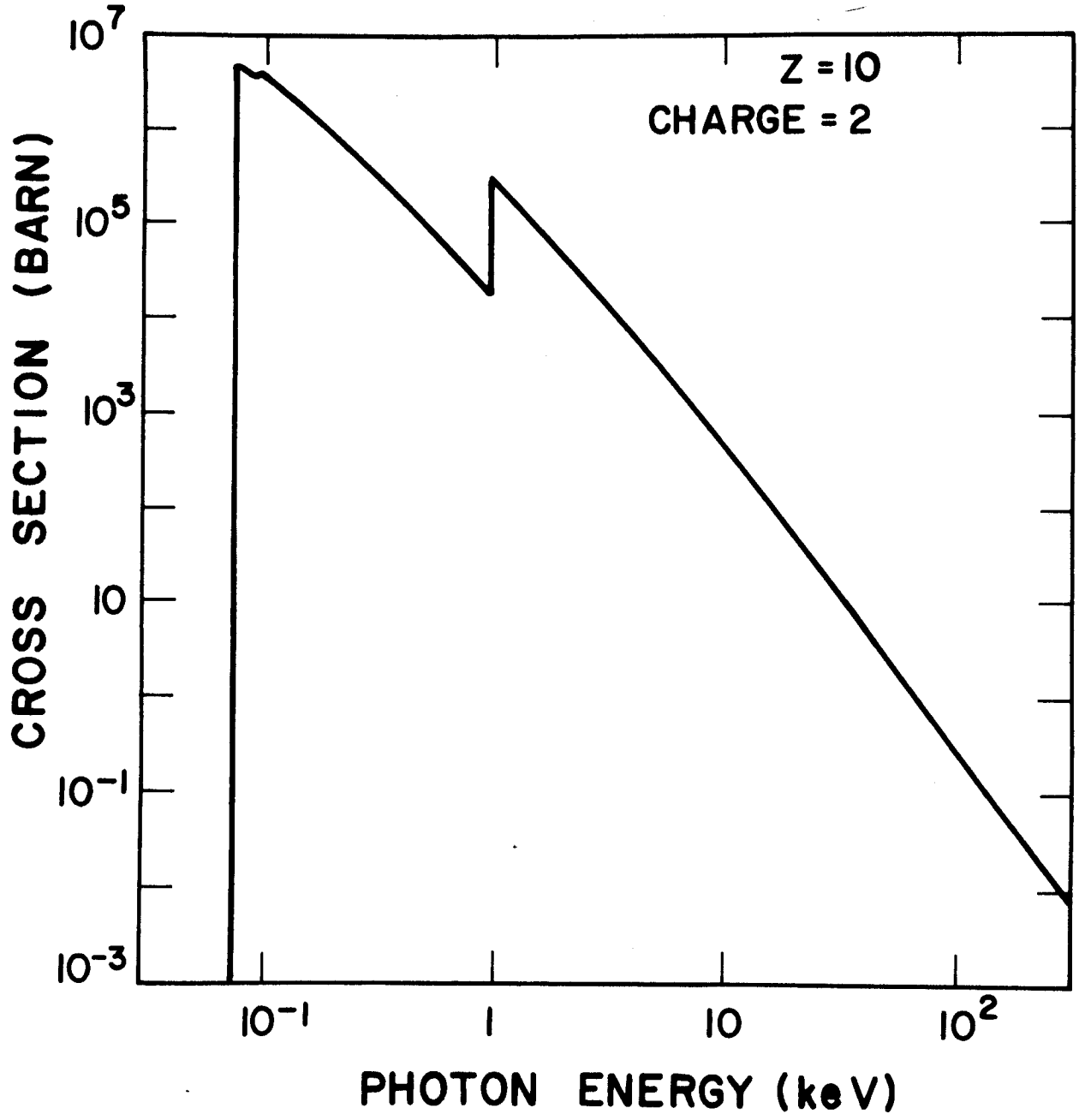

Fig. XI-B-11.

Photoelectric cross section for doubly ionized neon (from Ref. 10).

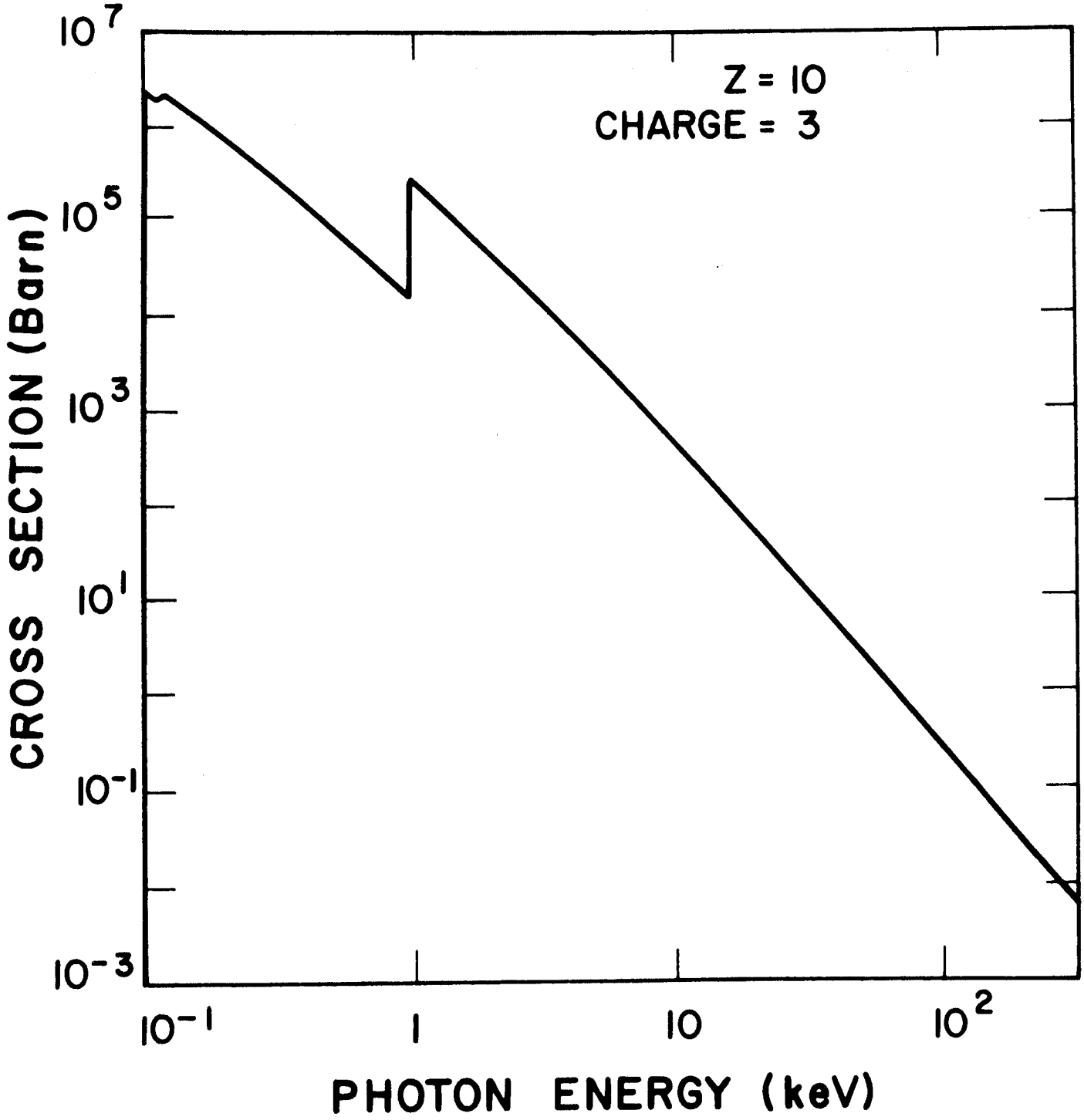

Fig. XI-B-12.
Photoelectric cross section for triply ionized neon. (from Ref. 10)

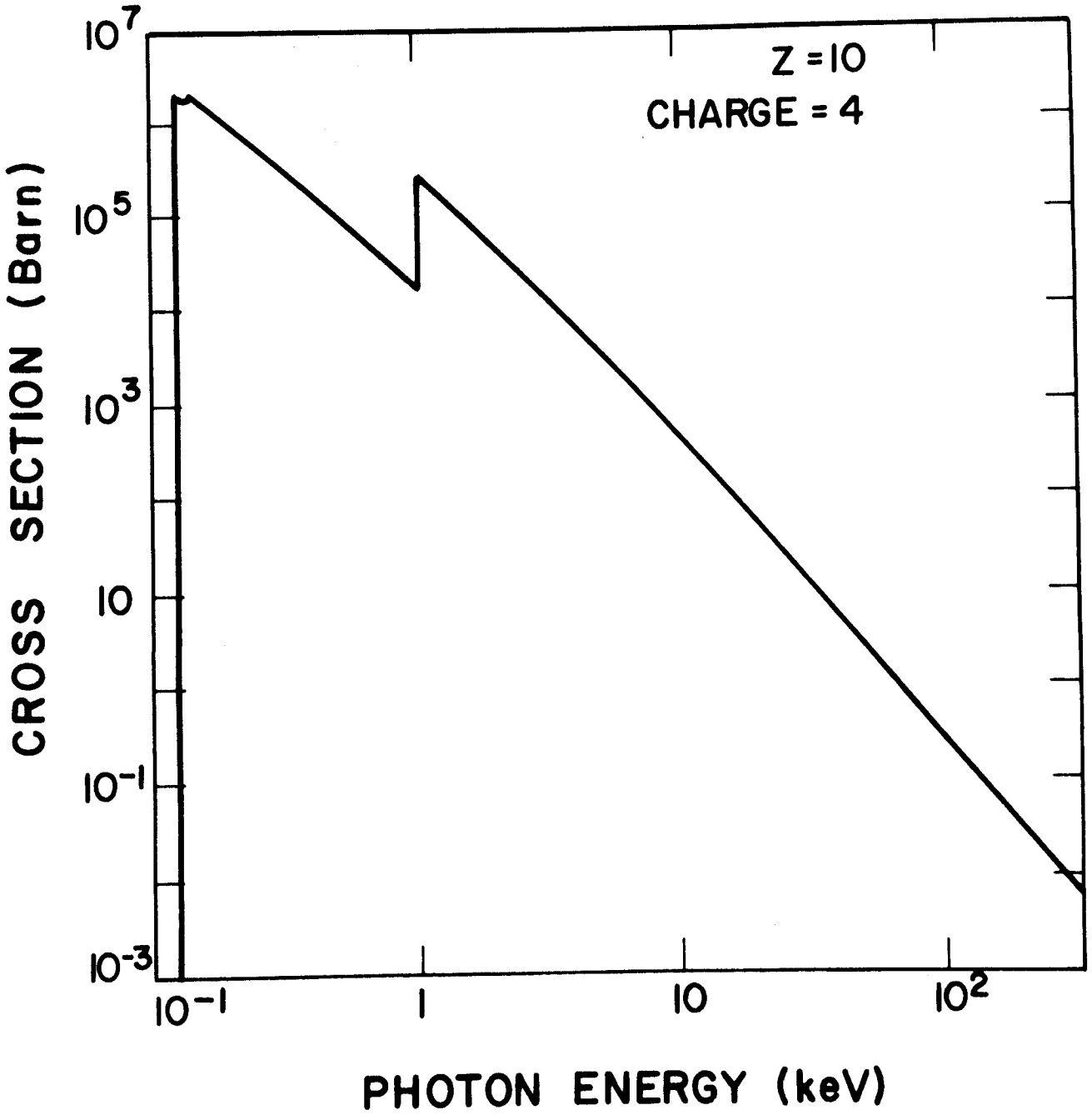

Fig. XI-B-13.

Photoelectric cross section for quadruply ionized neon (from Ref. 10).

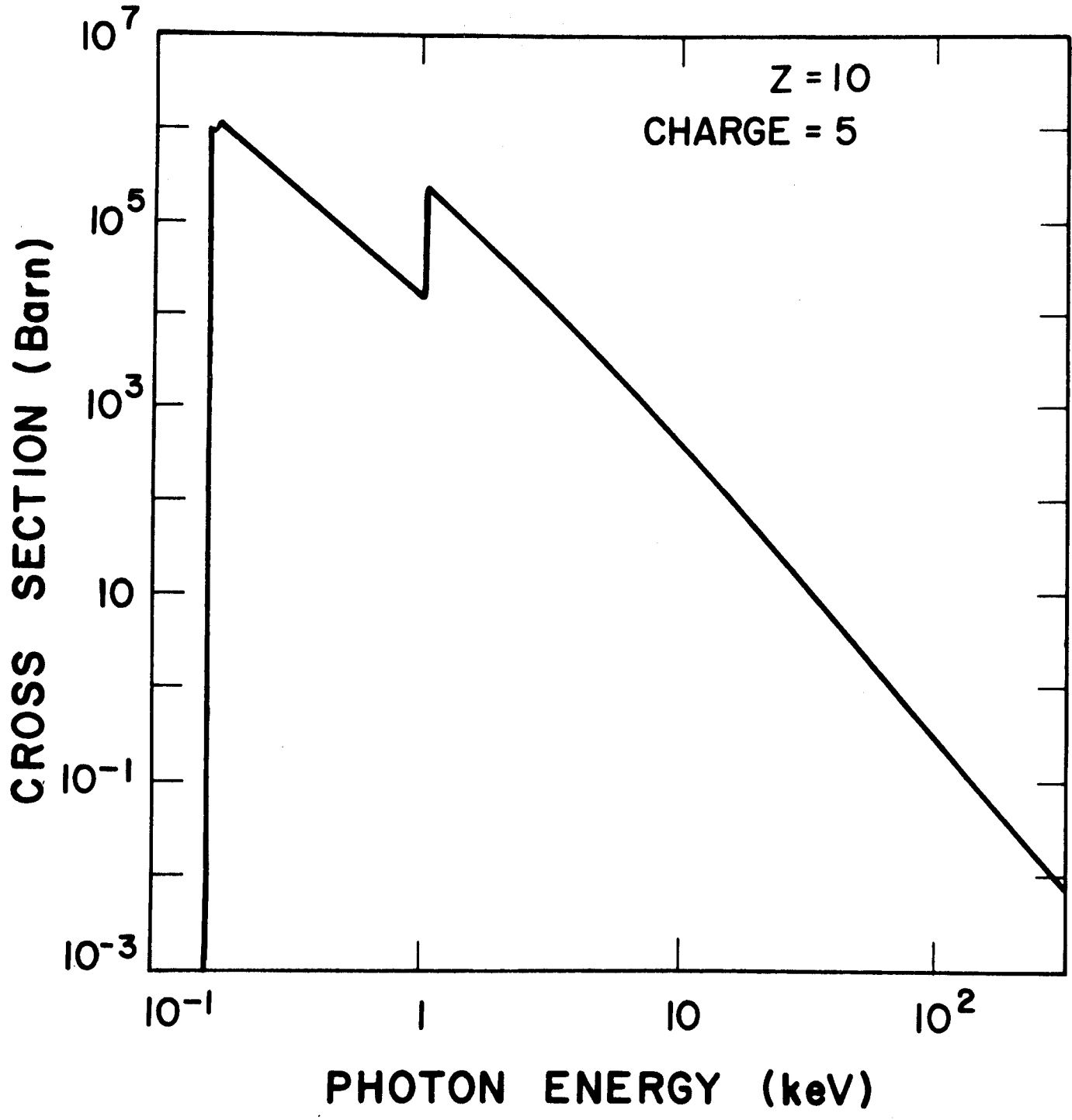

Fig. XI-B-14.
Photoelectric cross section for quintuply ionized neon (from Ref. 10).

$$\frac{m^2}{1-m} = 2\,\frac{g_+}{g_o}\,\frac{1}{n}\,\left(\frac{2\pi m_e\, kT}{h^2}\right)^{3/2} e^{-I_1/kT} \qquad (9)$$

$$= K(n,T)$$

where g_+ is the weight of the ionized atom and g_o is the weight of the ground state. The solution is

$$m(T) = \sqrt{K^2/4 + K} - K/2 \,. \qquad (10)$$

In the region near m=1 the two solutions merge in some way unknown from either one. Fortunately, exact calculations exist which give some guidance on how to match the solutions. Figure XI-B-15 shows a comparison between a careful calculation[10] and the approximate calculation.

Once the mean ionization state is known (Fig. XI-B-16), the total energy per atom may be approximately determined by assuming that only the ionization potentials and kinetic energies of the ions and electrons contribute. Good agreement with careful calculations[11] is obtained by assuming that electrons 1 through $[m]^*$ are removed from all atoms and that the $[m]+1$ electron is removed from the fraction $m-[m]$ of the atoms, i.e. if $K=[m]$

$$E(T) = \frac{3}{2}\,(1+m)\,kT + \sum_{j=1}^{K} I_j + (m-K)\,I_{K+1} \qquad (11)$$

Figure XI-B-17 shows E(T) for neon at the density $n=1.5\times10^{16}\,cm^{-3}$.

With this information, the recombination rate as a function of temperature may be calculated, as well as the energy emission rate. The number of recombination events per unit volume per unit time into the ground state is given by[12]:

$$Z_{rec} = n_+\; n_e \int_o^\infty f_e(v)\; v\sigma_c(v)\; \left(1 + \frac{1}{e^{h\nu/kT} - 1}\right) \qquad (12)$$

where n_+ is the ion density, n_e is the electron density,

---

* $[x] \equiv$ the greatest integer less than x.

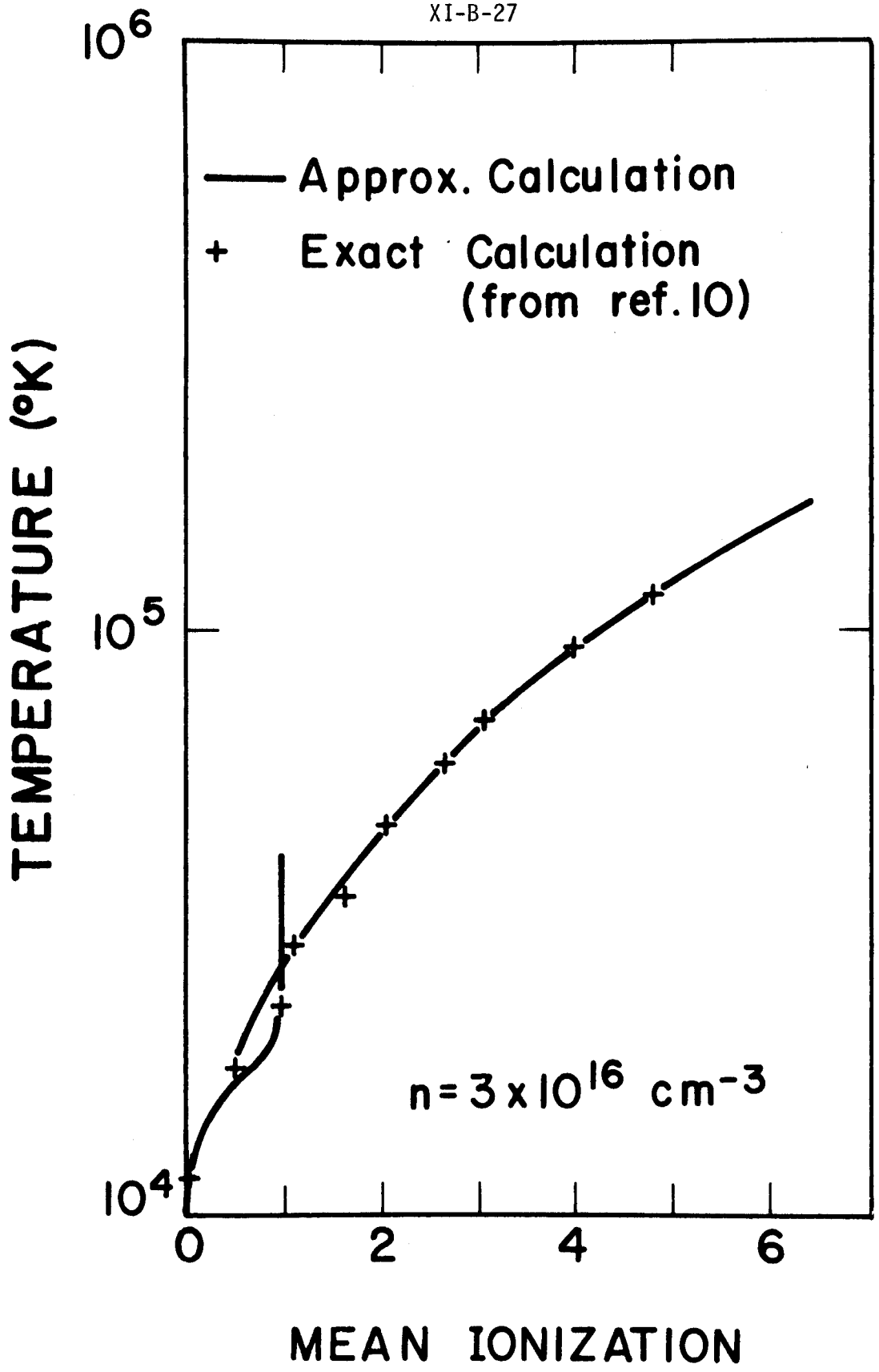

Fig. XI-B-15.

The solid lines are the results of the approximate method of Raizer for calculating the mean ionization. The crosses are from ref. 10.

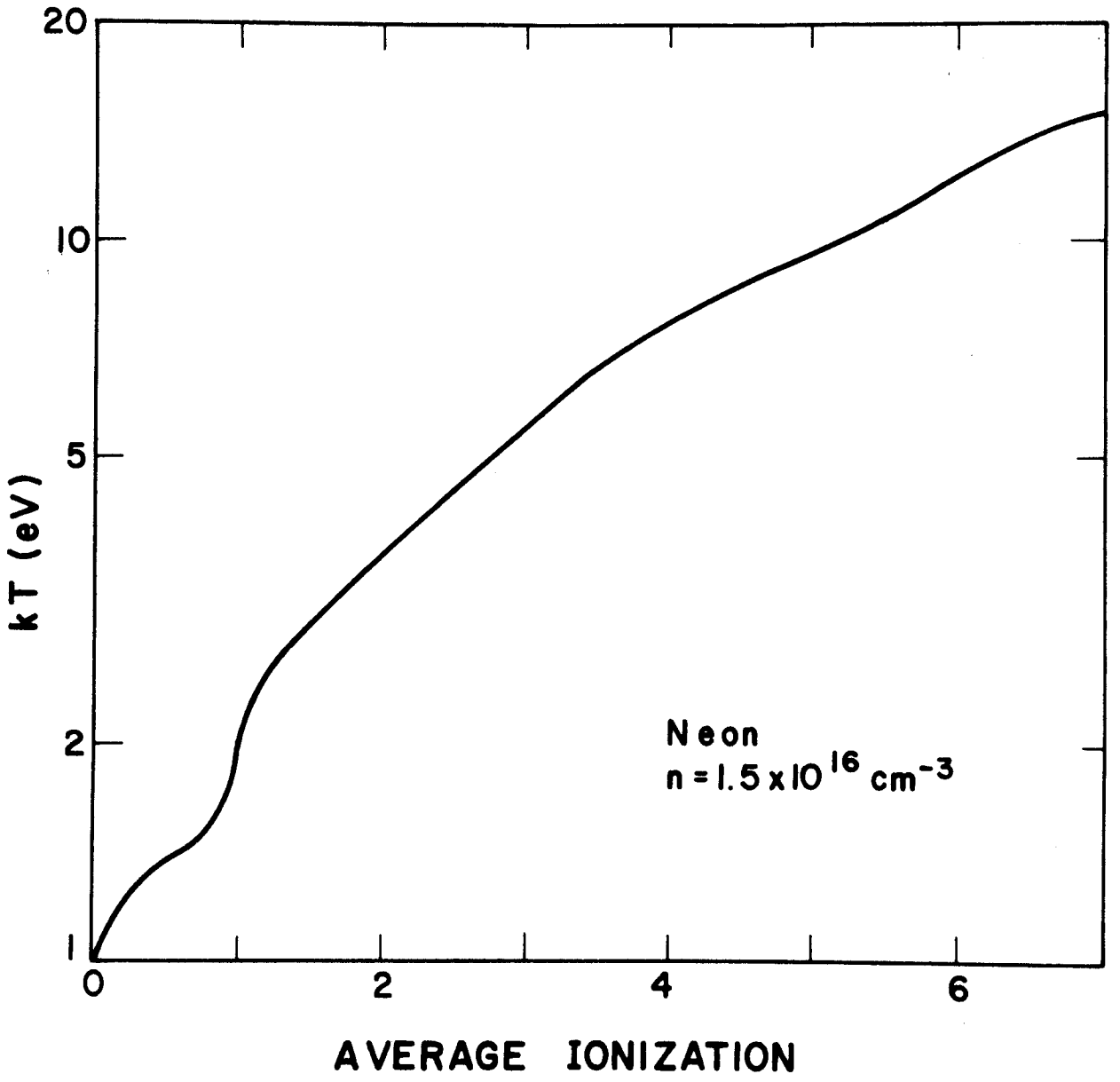

Fig. XI-B-16.
Mean ionization as a function of temperature for neon at a density of 1.5×10^{16} cm^{-3}.

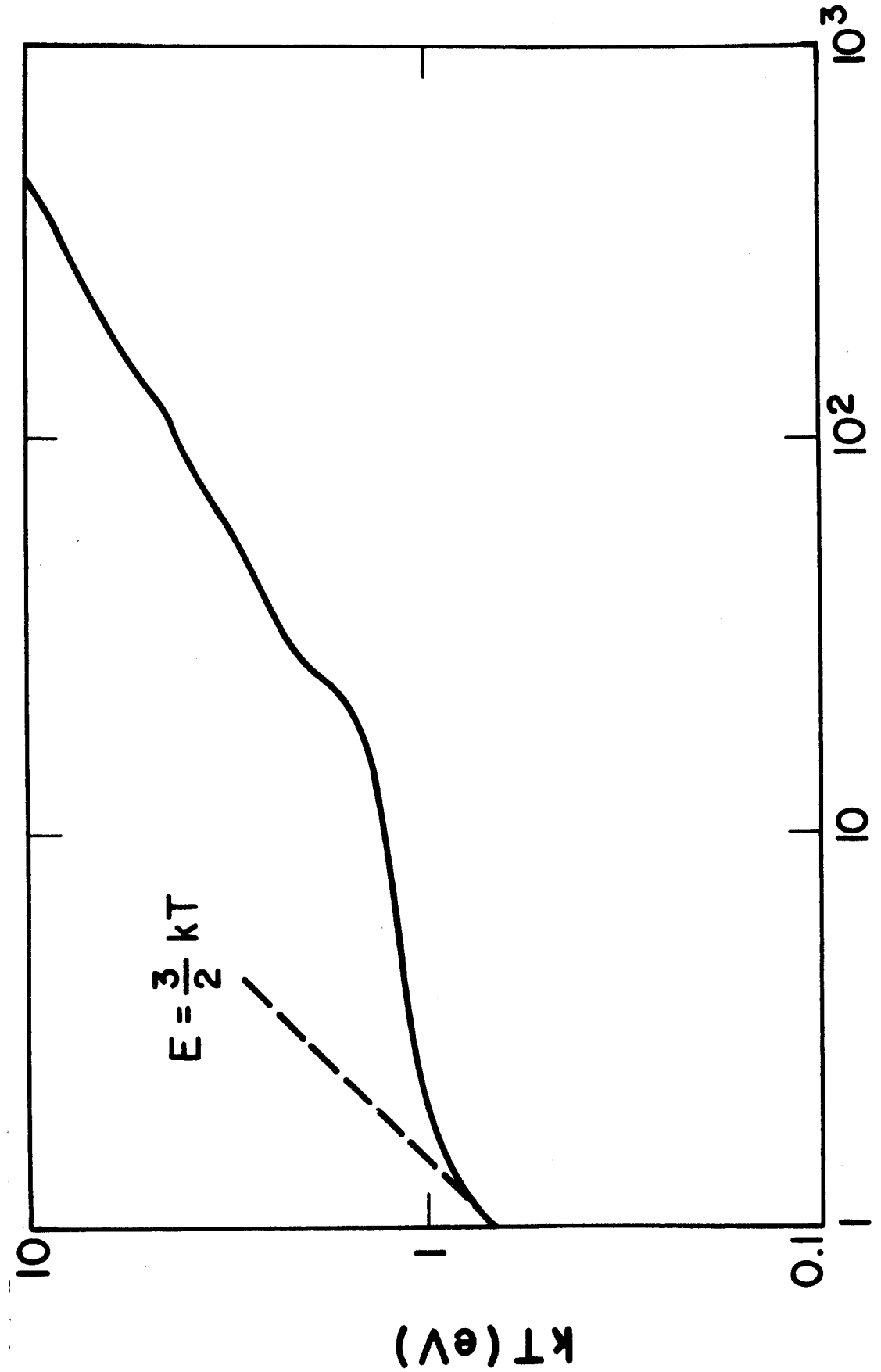

Fig. XI-B-17.
Energy per neon atom as a function of temperature at a density of 1.5×10^{16} cm^{-3}.

$$f_e(v) = 4\pi \left(\frac{m}{2\pi kT}\right)^{3/2} v^2 e^{-\frac{mv^2}{2kT}} , \tag{13}$$

$\sigma_c(v)$ is the recombination cross section into the ground state and

$\frac{1}{e^{h\nu/kT}-1}$ is the induced recombination term, which we neglect.

The photon energy and electron energy are connected by the photoelectric equation,

$$h\nu = \frac{1}{2} mv^2 + I . \tag{14}$$

The recombination cross section is related to the corresponding photo-ionization cross section through the principle of detailed balancing:

$$\sigma_c(v) = \frac{g_o}{g_+} \frac{h^2\nu^2}{me^2v^2c^2} \sigma_\nu(h\nu) . \tag{15}$$

Because $f_e(v)$ is only significant for $v^2 \leq \frac{2kT}{m}$, $\sigma_\nu(h\nu) = \sigma_\nu(\frac{mv^2}{2} + I)$ only contributes to the integral from $h\nu = I$ to $h\nu = I + kT$. Since $kT \approx \frac{I}{10}$, no great error is committed by replacing $\sigma_\nu(h\nu)$ by $\sigma_\nu(I)$ and removing it from the integral. The integral is then easily performed to give:

$$Z_{rec} = \frac{2g_o}{g_+} \frac{n_+ n_e}{m_e^2 c^2} \left(\frac{me}{2\pi kT}\right)^{1/2} (2(kT)^2 + 2kTI + I^2) \sigma_\nu(I) \tag{16}$$

This only accounts for recombination into the ground state. We may approximately account for recombination into the excited states by assuming that the excited states are hydrogen-like and using hydrogen cross sections. This calculation[13] yields the following approximate formula for the additional recombination rate:

$$Z_{rec}^{exc} = 2.7 \times 10^{-13} n_+ n_e Z^2 \, Tev^{-3/4}/cm^2/s . \tag{17}$$

To estimate the emission coefficient, we multiply the recombination rates by an average photon energy for that event. For recombination into the ground state this energy is approximately I. For recombination into the excited states we used

$$h_\nu \approx \frac{1}{2}(I - \varepsilon_1) + kT \tag{18}$$

where ε_1 is the energy of the first excited state. The resulting emission coefficient for various ionization states is shown in Table XI-B-2. Note that the subsequent line emission from the recombinations into excited states have been ignored.

These emission rates would give the total power radiated by the gas if it were optically thin. The optically thin emission can give a lower bound on the time for the energy to come out and is worth calculating. If we assume that 13 MJ is distributed evenly in the gas, the energy per unit volume is 1.4×10^4 J/m^3. This corresponds roughly to T = 1.2 eV, m = 0.2 and an emission coefficient J = 2.7×10^6 J/m^3/s.
The power emitted from the gas in the chamber would be

$$P = 2.4 \times 10^3 \text{ MW}$$

and the energy relaxation time would be

$$\tau = \frac{E}{P} = 5 \times 10^{-3} \text{ s.}$$

This energy radiation time is in the appropriate range for good performance of the gas filled cavity first wall protection scheme. However, several of the assumptions made are not strictly correct and therefore the conclusions cannot be so strongly stated. The gas is not optically thin. The photons are successively absorbed and re-emitted and consequently take longer to

Table XI-B-2

Neon at $n = 1.5 \times 10^{16}$ cm^{-3}

Ionization State m	T (eV)	Energy per unit volume (J/m^3)	Ground State Emission ($J/m^3/s$)	Total Emission ($J/m^3/s$)
.009	0.9	3.7×10^3	3×10^3	6×10^3
.2	1.2	1.5×10^4	1.5×10^6	2.7×10^6
.57	1.4	3.8×10^4	1.2×10^7	2.2×10^7
1	2.22	6.8×10^4	3.3×10^7	5.7×10^7
1.5	2.9	1.3×10^5	3×10^8	4.4×10^8
2	3.7	1.9×10^5	6.7×10^8	9.8×10^8
2.5	4.5	2.8×10^5	1.9×10^9	3×10^9
3	5.6	3.8×10^5	3.4×10^9	5.2×10^9
3.5	6.7	5.3×10^5	7.3×10^9	1.1×10^{10}
4	7.7	6.8×10^5	1.2×10^{10}	1.8×10^{10}
4.5	8.6	8.6×10^5	2.8×10^{10}	3.8×10^{10}
5	9.7	10^6	4.7×10^{10}	6×10^{10}

reach the wall. A detailed radiation transport calculation coupled to the fluid motion is necessary before such quantities as the power incident on the first wall as a function of time and the fraction of energy that must be removed from the gas in the vacuum system can be accurately known. In regard to the second problem it should be noted that the gas ceases to effectively radiate at a temperature of about 1 ev so at least this much energy (about 3 MJ for SOLASE) must be removed prior to reaching the vacuum system. To minimize the energy content of the gas at 1 ev, the gas pressure should be kept at the minimum value consistent with ion attenuation in 6 meters. This will of course depend on the ion spectra of the exploding pellet. Should the ion spectra be harder than those used for the SOLASE calculations then a greater gas pressure would be necessary and more energy would be extracted through the vacuum system. In addition, the problem of laser gas breakdown would become more severe. However, if the ion spectra were less energetic than those used for the SOLASE design, the gas pressure could be less than 0.5 torr and both the vacuum system and breakdown problems would be relieved.

In any of these situations it is clear that the energy is not radiated to the first wall too fast, (i.e., in less than 10^{-3} seconds) hence the gas filled cavity would appear to perform adequately for pellets with a reasonable amount of high Z material. This amount of high Z material should be enough to stop the alpha particle reaction products and DT debris and 10 mg of mercury is adequate to meet this need. This amount is also very consistent with the proposed pellet designs for the next generation of laser systems. Since detailed reactor type pellet designs are not available we simply scale these breakeven pellets up to the size needed for reactor yields. When more

detailed reactor pellet designs become available, this analysis can be redone in a more exact fashion.

XI-B-5. Laser-Induced Gas Breakdown

XI-B-5-a. Introduction

In the SOLASE design, low pressure neon gas is used to protect the cavity walls from soft X-rays and charged particles. As the converging laser beams traverse the gas filled region from mirror to target, the intensity may grow to the point where a spark occurs. Even if the electron density is sub-critical, breakdown may interfere with target illumination due to:

(a) The momentum of the resulting shock wave

(b) Defocusing associated with ∇n

(c) Formation of localized density peaks where $n > n_{crit}$.

(d) Stimulated Raman scattering off plasmons in the ionized gas.

Gas breakdown is reviewed by DeMichelis,[14] Morgan,[15] and Ready.[16] The operating gas density (usually expressed as pressure at $0^{o}C$) depends on the chamber size and the X-ray and charged particle spectra from a given pellet. The breakdown threshold Φ^* (in W/cm^2) depends on pressure, focal volume (diffusion length), laser pulse width, and the ionization potential of the gas. Elastic losses are usually negligible at low pressures. Inelastic losses are important only for non-noble gases, not under consideration in these studies, except perhaps as impurities. Our first choice for a buffer gas is neon having the highest breakdown threshold, with helium running a close second.

The theoretical portion of this section is based mainly upon the work of Hacker, Cohn and Lax,[17] incorporating ionization rate, diffusion length and pulse width. For the low pressures ($\lesssim$ 0.5 Torr) and moderately long ($\sim$1 nsec) pulse width envisioned for SOLASE, the threshold is nearly independent of pulse width, and classical microwave breakdown theory applies.[18,19] The SOLASE pulse is nevertheless short enough that hydrodynamic effects[20] may be ignored. The theoretical expressions are then evaluated for helium and neon using published cross section data.

Close to the pellet, the focal cone has narrowed to the point where the electron-atom collision mean free path greatly exceeds the radius of the focal volume, so that neither diffusion nor a cascade can take place. Nevertheless, breakdown can still occur via multiphoton absorption.[16] The corresponding threshold is about two orders of magnitude smaller than the cascade threshold at 0.5 Torr; both theory and experiment predicting breakdown at about 2×10^{13} W/cm^2. While helium does as well as neon in this respect, neon has the superior stopping power for soft X-rays and charged particles.

For SOLASE, the average power on target is about 2×10^{14} W/cm^2, so that breakdown should occur within 5 cm from the (2 mm radius) target. The most serious consequence of breakdown for target illumination is light scattering due to stimulated Raman scattering off plasmons in the ionized neon.[21] Preliminary calculations show the magnitude of this forward scattering to be tolerable for SOLASE-size pellets. In fact, due to the very weak pressure dependence of the multiphoton threshold, it may be possible to raise the pressure to perhaps 1 Torr without loss of beam quality.

XI-B-5-b. Theory of Hacker, Cohn and Lax

Perhaps the most believable model in the recent literature is that of Hacker, Cohn and Lax[17] (HCL), in which breakdown in the focal region of a lens (sans target) is treated. Approximating the focal volume as a long cylinder, they find

$$\Phi^* = \frac{\pi m c^3 U_i}{e^2 \lambda^2} \left(\frac{D}{\nu_c \Lambda^2} + \frac{\ell n (n_b/n_o)}{\nu_c \tau} + \frac{m}{2M} \right) \text{ W/cm}^2 \qquad (19)$$

where

U_i = ionization potential

λ = laser wavelength

D = diffusion coefficient

ν_c = collision frequency

Λ = diffusion length

n_b = breakdown electron density $\approx 10^{18} \text{cm}^{-3}$

n_o = initial electron density $\approx 10^{4} \text{cm}^{-3}$

τ = laser pulse width

m = electron mass

M = mass of neutral atom

The first term arises from diffusion losses, the second from the finite pulse width and the last from elastic losses.

For helium, eq. (19) becomes

$$\Phi^* \sim \frac{U_i}{\lambda^2} \left(\frac{1.22 \times 10^{-3}}{\Lambda^2 p^2} + \frac{13.4}{p\tau} + 6.6 \times 10^{-5} \right), \qquad (20)$$

with Λ in cm, p in Torr and τ in nsec. Making plausible estimates for Λ and the size of the focal volume, HCL fit their experimental data quite well. A similar result holds for neon, except that an average collision frequency must be estimated (see following section).

The following sketch illustrates a typical SOLASE laser-target goemetry using f/7.5 optics (not to scale).

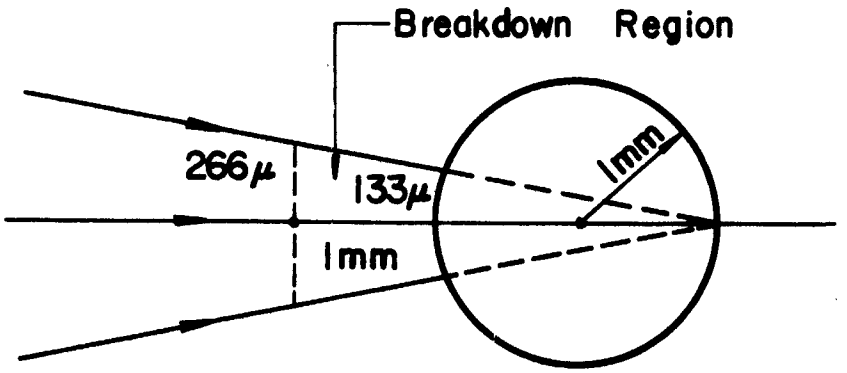

Figure XI-B-18

Let us suppose breakdown to be likely only in the region very near the target, say in the last millimeter. Ignoring axial diffusion, we assume an average diffusion length of

$$\Lambda = \frac{r}{2.4} \approx 100 \ \mu m \ .$$

Eq. (20) then becomes

$$\Phi^* \sim \frac{U_i}{p\lambda^2}\left(\frac{1}{p} + \frac{1}{\tau}\right) . \tag{21}$$

If $\tau \geq 1$ nsec and $p \lesssim 0.1$ Torr, diffusion clearly dominates and the breakdown intensity is simply

$$\Phi^* \sim \frac{U_i}{\lambda^2 p^2 \Lambda^2} . \tag{22}$$

Even if the $1/\tau$ term is appreciable, as it is at 0.5 Torr, eq. (22) still gives a useful lower bound on Φ^*. Things can only be better at shorter pulses.

XI-B-5-c. Classical Microwave Breakdown Theory

A great deal of theoretical and experimental work has been done at microwave frequencies.[18-19] Since these sources are continuous and the gas volumes well-defined cylinders or rectangular boxes, the pulse width is effectively infinite and the diffusion length unambiguous, with some implicit assumptions concerning the initial conditions.

Theoretical treatments of this problem may be divided into two general classes; those which employ kinetic theory and those which do not. Both approaches are based on the Townsend criterion, which is simply the threshold for the ionization rate to exceed diffusion losses:

$$\nu_i = D/\Lambda^2 , \tag{23}$$

where ν_i is the ionization rate and the diffusion coefficient is

$$D \equiv \frac{1}{3n}\int \frac{v^2}{\nu_c} f(v)\, d^3v . \tag{24}$$

Strictly speaking, the momentum transfer collision frequency ν_m should be used in place of ν_c.

As an individual electron accelerates in the oscillating electric field of the laser or microwave beam it gains energy (on the average) between collisions with neutral gas atoms, until it has sufficient energy to ionize an atom. When this happens the electron loses most of its energy, but produces a new electron. When the Townsend criterion is met, the electrons rapidly cascade to breakdown. Elastic collisional losses are negligible at low pressures; inelastic losses are not present in noble gases. Attachment and recombination are usually negligible under these conditions and are therefore excluded from eq. (23). The finite laser pulse width affects the electron multiplication rate and in general must be included in eq. (23), as in the previous section.

In the kinetic theory description, a complicated differential equation must be solved for the distribution function, to be inserted into eq. (24) for the diffusion coefficient. The second class of simplified theories use an unperturbed Maxwellian distribution function in eq. (24), with Λ chosen to fit the particular experiment. While the more complex theory describes the microwave experiments to within the experimental error, the lower level description is adequate for our purposes, where Λ is only approximately known and the mean free paths are rather long.

The electron continuity equation is

$$\frac{\partial n}{\partial t} = \nu_i n + \nabla^2(Dn) \ , \qquad (25)$$

with appropriate initial values and boundary conditions. In general both ν_i and D may depend on position while ν_i may depend on time via the laser pulse shape. It is expedient and not altogether inaccurate to take ν_i and D

as constants, in which case eq. (25) is separable. Taking

$$n(\vec{r},t) = X(\vec{r})T(t) \quad , \tag{26}$$

we obtain a result of the form

$$n = n_o \sum^{\infty} A_n X_n e^{(\nu_i - k_n^2 D)t} \quad , \tag{27}$$

where $-k_n^2$ is an eigenvalue of the Laplacian operator, i.e.

$$\nabla^2 X_n + k_n^2 X_n = 0 \quad . \tag{28}$$

Unless excluded by peculiar initial conditions, the Townsend criterion is to be evaluated for the most rapidly growing mode of eq. (27) corresponding to the smallest eigenvalue of eq. (28). The coefficients A_n, of order unity, are of little consequence here.

In cylindrical geometry the solutions of eq. (28) are Bessel functions, with $k_n = X_n R$, R being the cavity radius and $J_o(X_n) = 0$. Since min $\{X_n\}$=2.405 we have

$$\Lambda_1 = R/2.405 \quad . \tag{29}$$

Ignoring the small elastic losses and assuming $\omega_L >> \nu_c$, the absorbed power is $P = U_i \nu_i$, giving

$$\nu_i = \frac{e^2 E^2}{m \nu_c U_i} \left(\frac{\nu_c}{\omega}\right)^2 \quad , \tag{30}$$

where the inverse Bremsstrahlung expression has been used. The laser intensity and field strength are related by

$$\Phi = \frac{cE^2}{4\pi} \quad , \tag{31}$$

so that

$$\nu_i = \frac{e^2}{\pi mc^3} \frac{\lambda^2 \nu_c \Phi}{U_i} \quad .$$

The Townsend criterion (23) then yields the breakdown threshold,

$$\Phi^* = \frac{\pi mc^3}{e^2 \lambda^2} \frac{U_i D}{\nu_c \Lambda^2} \quad , \tag{32}$$

precisely the first term of the HCL equation (19).

XI-B-5-c-i. Breakdown Threshold for Helium

Helium has been thoroughly studied both experimentally and theoretically, having a high ionization potential and a nearly energy-independent collision frequency. The diffusion coefficient is

$$D = \frac{1}{3} \left\langle \frac{v^2}{\nu_c} \right\rangle \quad . \tag{33}$$

As Fig. XI-B-19 shows, ν_c is very nearly energy-independent for $\varepsilon > 5$ eV. Thus

$$D \approx \frac{\theta_e}{m\nu_c} \quad , \tag{34}$$

where we have used

$$\bar{\varepsilon} = \frac{1}{2} m\langle v^2 \rangle = \frac{3}{2} \theta_e \quad . \tag{35}$$

HCL take $\bar{\varepsilon} = \frac{1}{4} U_i \simeq 6$ eV $\Rightarrow$ $\theta_e \simeq 4$ eV. Then

$$D = \frac{7.04 \times 10^{15}}{\nu_c} \quad . \tag{36}$$

Using

$$\nu_c \approx 2.37 \times 10^9 \, p(\text{Torr}) \tag{37}$$

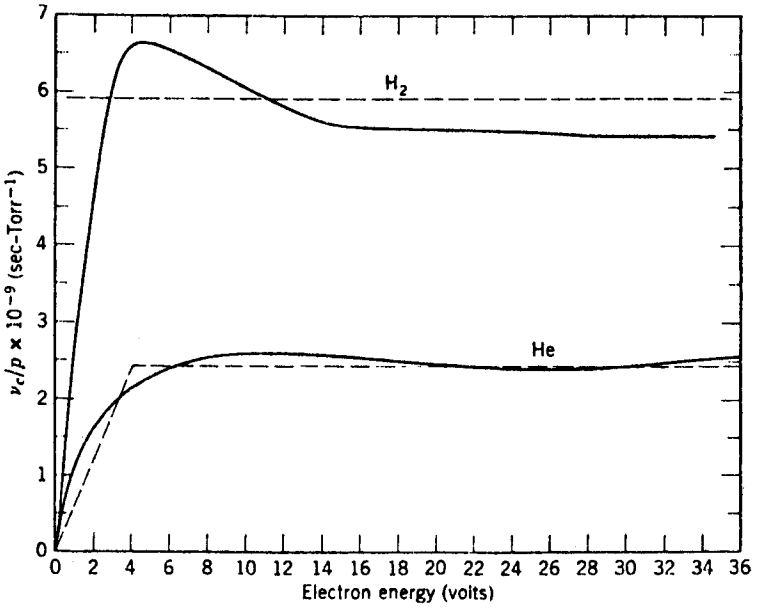

Fig. XI-B-19, from Ref. 19, P. 23.

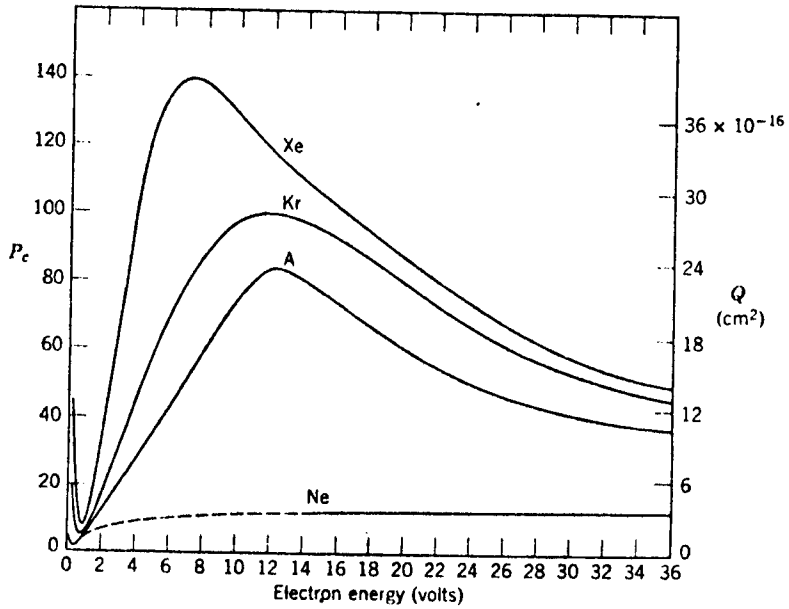

Fig. XI-B-20, from Ref. 19, P. 20.

we find

$$\boxed{\Phi^* = \frac{1600}{\lambda^2 \Lambda^2 p^2} \ W/cm^2} \qquad (38)$$

with λ and Λ in cm and p in Torr.

Evaluating the second term in the HCL expression (20) yields

$$\Phi^* = \frac{1600}{\lambda^2 \Lambda^2 p^2} (1 + 1.10 \times 10^4 \ \Lambda^2 \ p) \ . \qquad (38a)$$

The second term will be needed when we consider diffusion lengths greater than 100 μm.

XI-B-5-c-ii. Breakdown Threshold for Neon

In the case of neon, the "collision probability" P_c is reasonably constant, as attested to by Fig. XI-B-20. From the definition of P_c,

$$P_c \ p\ell = 1 \ , \qquad (39)$$

where the free path is given by

$$\ell = v/\nu_c \ , \qquad (40)$$

we find

$$D = \frac{1}{3}\langle v\ell \rangle = \frac{\langle v \rangle}{3P_c p} \qquad (41)$$

$$\bar{\nu}_c = \langle v/\ell \rangle = P_c p \langle v \rangle \ . \qquad (42)$$

Thus

$$D/\nu_c = \frac{1}{3P_c^2 p^2} \qquad (43)$$

and

$$\Phi^* = \frac{\pi m c^3}{e^2} \ \frac{U_i}{3P_c^2} \ \frac{1}{\lambda^2 \Lambda^2 p^2} \qquad (44)$$

From Fig. XI-B-20, $P_c \approx 10\ cm^{-1}\ Torr^{-1}$, and with $U_i = 21.6$ eV we find

$$\boxed{\Phi^* = \frac{3860}{\lambda^2 \Lambda^2 p^2}\ W/cm^2\ ,} \qquad (45)$$

a little more than twice the threshold for helium.

Working out the second term in the HCL expression (19) leads to <v>. Rather than guess at this average, which depends on the details of a complicated distribution function, we simply approximate $\nu_c \approx 2 \times 10^9\ p$ (Fig. XI-B-21) with the result

$$\Phi^* = \frac{3860}{\lambda^2 \Lambda^2 p^2}\ (1 + 0.483 \times 10^4\ \Lambda^2\ p)\ . \qquad (45a)$$

XI-B-5-c-iii. Low Collision Frequency Limit

When the collision time greatly exceeds the laser pulse width, neither diffusion nor cascading can take place. For helium,

$$\nu_c = 2.4 \times 10^9 \, p \ ,$$

so that

$$\tau_c \cong \frac{4 \times 10^{-10}}{p} \text{ sec} \ll \tau_L = 10^{-9} \text{ sec}$$

when $p \geq 1$ Torr; when $p = 0.5$ Torr we are on the borderline, and when $p = 0.1$ Torr, $\tau_c = 4$ nsec $> \tau_L$, in which case the electrons are collisionless. As Fig. X-B-21 shows, the collision frequency for neon is strongly energy dependent. Taking $\nu_c \approx 2 \times 10^9 \, p$ gives about the same results as for helium.

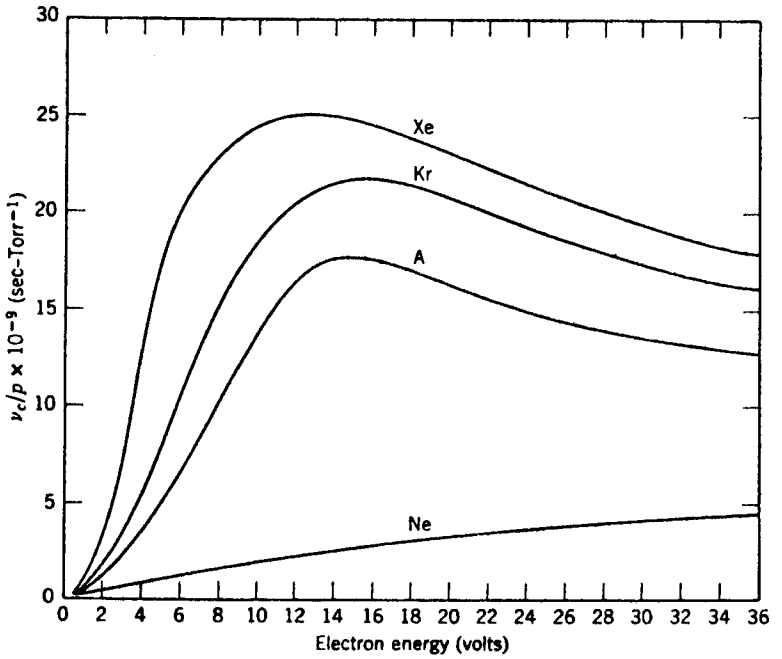

Fig. XI-B-21 from Ref. 19, P. 24.

XI-B-5-c-iv. The Diffusion Limit

From Fig. X-B-20, we have, for neon,

$$\ell = \frac{1}{p_c p} \cong \frac{1}{10p} . \tag{46}$$

Thus, at p = 0.5 Torr, ℓ = 2 mm, much longer than the diffusion length near the pellet. In fact, when $\Lambda \simeq 100$ μm, anything below p = 10 Torr cannot be correctly described as diffusion nor is a cascade possible. The electrons are now free-streaming, with a characteristic length $R \simeq 2\Lambda$, which might be expected to lower the threshold somewhat. Similar results hold for helium, where P_c = 10-20 cm^{-1} $Torr^{-1}$. Thus, the cascade-diffusion picture is valid only further upstream toward the laser, where the focal volume exceeds the mean free path. Since the diffusion lengths are proportionally larger, the second term would have to be retained in the HCL formula (20).

XI-B-5-d. Multiphoton Absorption

When the conditions for cascade ionization are not met, breakdown can still take place through multiphoton absorption. In this process a number of photons are simultaneously absorbed in a time consistent with the uncertainty principle. The ionization rate for absorbing k photons is, following Morgan[15]

$$\nu_{mp} = AF^k , \tag{47}$$

where

$$A = \frac{\sigma^k}{\nu^{k-1}(k-1)!} \quad , \tag{48}$$

F is the photon flux, and σ is the photon absorption cross section for exciting an atom from the k^{th} to the $(k+1)^{th}$ state.

The number of electrons/unit volume liberated in a time τ is then

$$n_e = n\nu_{mp}\tau \quad , \tag{49}$$

where n is the neutral gas density and the laser pulse is assumed to be square. Defining breakdown as the liberation of n_e^* electrons/cm^3, Morgan finds

$$F^* = \frac{\nu}{\sigma}\left[\frac{n_e^*(k-1)!}{n\nu\tau}\right]^{1/k} \quad , \tag{50}$$

so that

$$\Phi^* = h\nu F^* \quad . \tag{51}$$

Since $n = 3.56 \times 10^{16}$ p, we see that the threshold depends very weakly on pressure (k = 19 for Nd-glass radiation in helium). Taking $n_e^* = 10^{13}$ cm^{-3} as the electron density at breakdown at p = 1 Torr and taking $\sigma = 10^{-16}$ cm^2, we find $\Phi^* = 1.2 \times 10^{12}$ W/cm^2, a rather low estimate.

More refined treatments of multiphoton absorption have been carried out semi-classically by Keldysh[22] and by Bebb and Gold[23-25] using time-dependent perturbation theory. In these theories resonances between energy levels of the gas and harmonics of the laser frequency play a major role. In Bebb and Gold's most elaborate calculation,[25] for ruby light,

Coulomb wave functions are used as final state wave functions. The result is $\Phi^* = 3.7 \times 10^{13}$ W/cm^2. Naively scaling this value to $\lambda = 1.06$ μ, we find

$$\Phi^* = \left(\frac{1.17}{1.78}\right)^2 3.7 \times 10^{13} = 1.6 \times 10^{13} \text{ W/cm}^2 , \qquad (52)$$

close to the experimental value $\Phi^* = 2.2 \times 10^{13}$ W/cm^2 reported by Agostini, et al.[26] Ireland[27] finds $\Phi^* = 4 \times 10^{13}$ W/cm^2 for Nd glass radiation in argon. Kraysuk's[28] result for ruby light in neon scales to 2.6×10^{13} W/cm^2 for $\lambda = 1.06$ μm. We therefore take $\Phi^* = 2 \times 10^{13}$ W/cm^2 as a working value near p = 0.5 to 1 Torr.

It should be noted that serious discrepancies persist in a number of experiments using Nd and ruby radiation in the noble gases. The new generation of high power lasers at Livermore and Los Alamos could be profitably employed in resolving these very puzzling inconsistencies.

XI-B-5-e. Target Intensity for SOLASE

The SOLASE design calls for 100-1000 TW (temporally) maximum power P incident on 2 mm radius pellets. Under uniform illumination the (spatial) average power density Φ_u (with beam overlap) will be equal to the spatial maximum. Thus, for 100 TW peak power,

$$\Phi_{max} = \Phi_u = \frac{P}{4\pi R_T^2} = 2 \times 10^{14} \text{ W/cm}^2 . \qquad (53)$$

This is the minimum possible Φ_{max}. More or less beam overlap can only increase Φ_{max} and thereby increase the likelihood of breakdown near the pellet surface.

The SOLASE irradiance (53) exceeds the estimated breakdown threshold (52) by an order of magnitude. To find the distance z from the target where breakdown will occur, recall from Section V-B that the optimal beam overlap angle is about 50^{o}, corresponding to a focal shift Δ of about eleven pellet radii. From Fig. XI-B-22,

$$\Phi^{*} = \Phi_{max} \left(\frac{R_T + \Delta}{R_T + \Delta + z} \right)^2 , \tag{54}$$

so that

$$z = (R_T + \Delta) \left(\sqrt{\Phi_{max}/\Phi^{*}} - 1 \right) = 5.2 \text{ cm} . \tag{55}$$

If P_{max} = 1000 TW, we find z = 21.6 cm, less desirable if Raman scattering is present.

Under non-uniform illumination, the power per beam is again fixed, but now a fill factor near unity may be assumed. Following the reasoning of the appendix to Section V-B, it can be shown that

$$\Phi_{max} = \frac{16F^2}{Nff} \left(\frac{R_T}{R_T + \Delta} \right)^2 \Phi_u , \tag{56}$$

where $\Phi_u = 2 \times 10^{14}$ W/cm^2. Let us assume that breakdown <u>will</u> occur and not be alarmed at the high target irradiance produced by overlapping square beams (ff=1). Our motive is now to arrange for breakdown to take place as close to the pellet as possible. With F = 7.5 and ff=1, Eq. (56) becomes

$$\Phi_{max} = \frac{75\Phi_u}{(1+\delta)^2} , \tag{57}$$

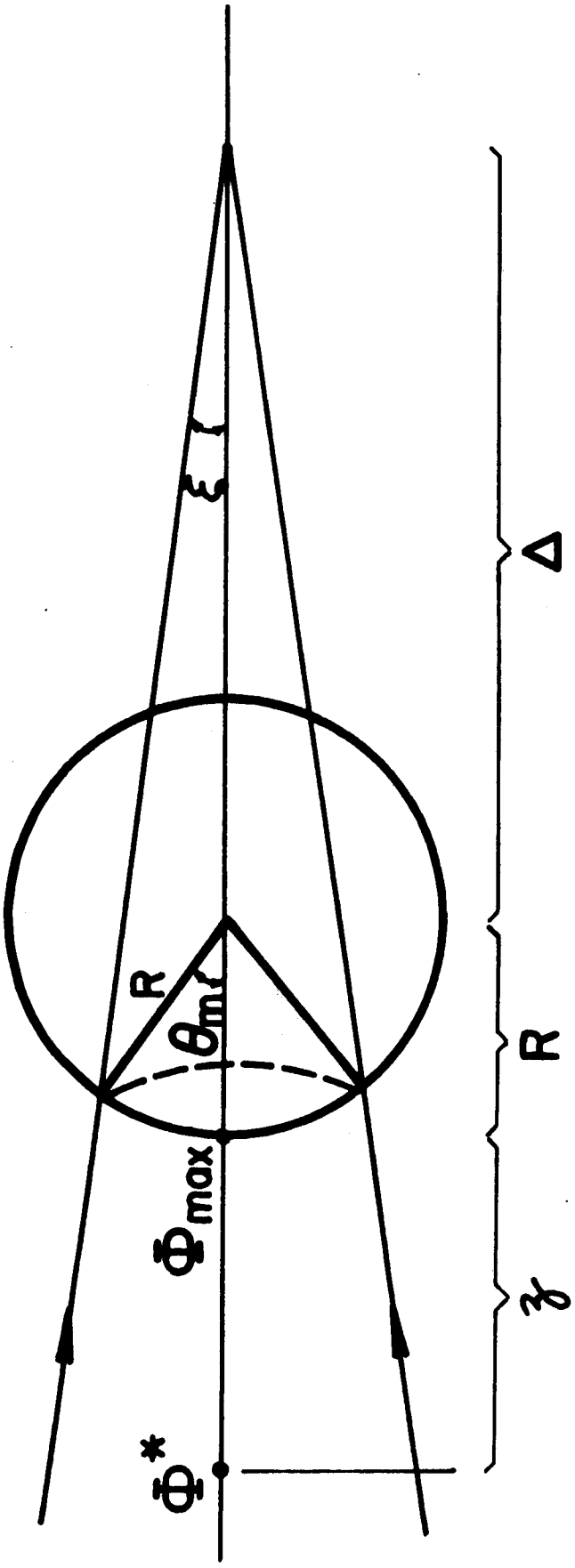

Fig. XI-B-22.

where $\delta = \Delta/R_T$. As a worst case, take $\delta = 0$; then $\Phi_{max} = 1.5 \times 10^{16}$ W/cm^2 and z = 5.28 cm. The maximum possible shift is $\delta = \csc\xi = 15.03$, at which point the marginal rays just skim the surface of the pellet. In this case, $\Phi_{max} = 0.3\ \Phi_u = 6 \times 10^{13}$ W/cm^2. Of course, we have to back off somewhat because of extreme refractive losses. A reasonable value is $\theta_{max} = 30°$ ($\delta = 6.63$) which gives $\Phi_{max} = 2.57 \times 10^{14}$ W/cm^2 and z = 3.95 cm, somewhat closer than the uniform illumination case. In the next sections we examine the consequences of breakdown.

A preliminary calculation[30] indicates that under SOLASE conditions, we are dealing with tunneling rather than multiphoton absorption. (Keldysh's theory encompasses both effects.) The transition between them is given by

$$\Phi < \Phi_x \Rightarrow \text{multiphoton absorption}$$

$$\Phi > \Phi_x \Rightarrow \text{tunneling} ,$$

where

$$\Phi_x = \frac{9\Phi_T}{16k^2}$$

$$k = U_i/h\nu = 19$$

$$\Phi_T = 6.23 \times 10^{12}\ \theta_e^3\ (\text{ev}) .$$

The electron temperature for $\Phi = 2.6 \times 10^{14}$, p = 0.5 torr is less than 22eV. Thus, $\Phi_T = 6.35 \times 10^{16}$ and $\Phi_x = 9.9 \times 10^{12}$, so that tunneling is implicated.

XI-B-5-f. Breakdown Thresholds for SOLASE

Figure XI-B-23 displays Φ^* as a function of pressure for λ=1.06 μm radiation in neon. The slanted lines represent the cascade breakdown

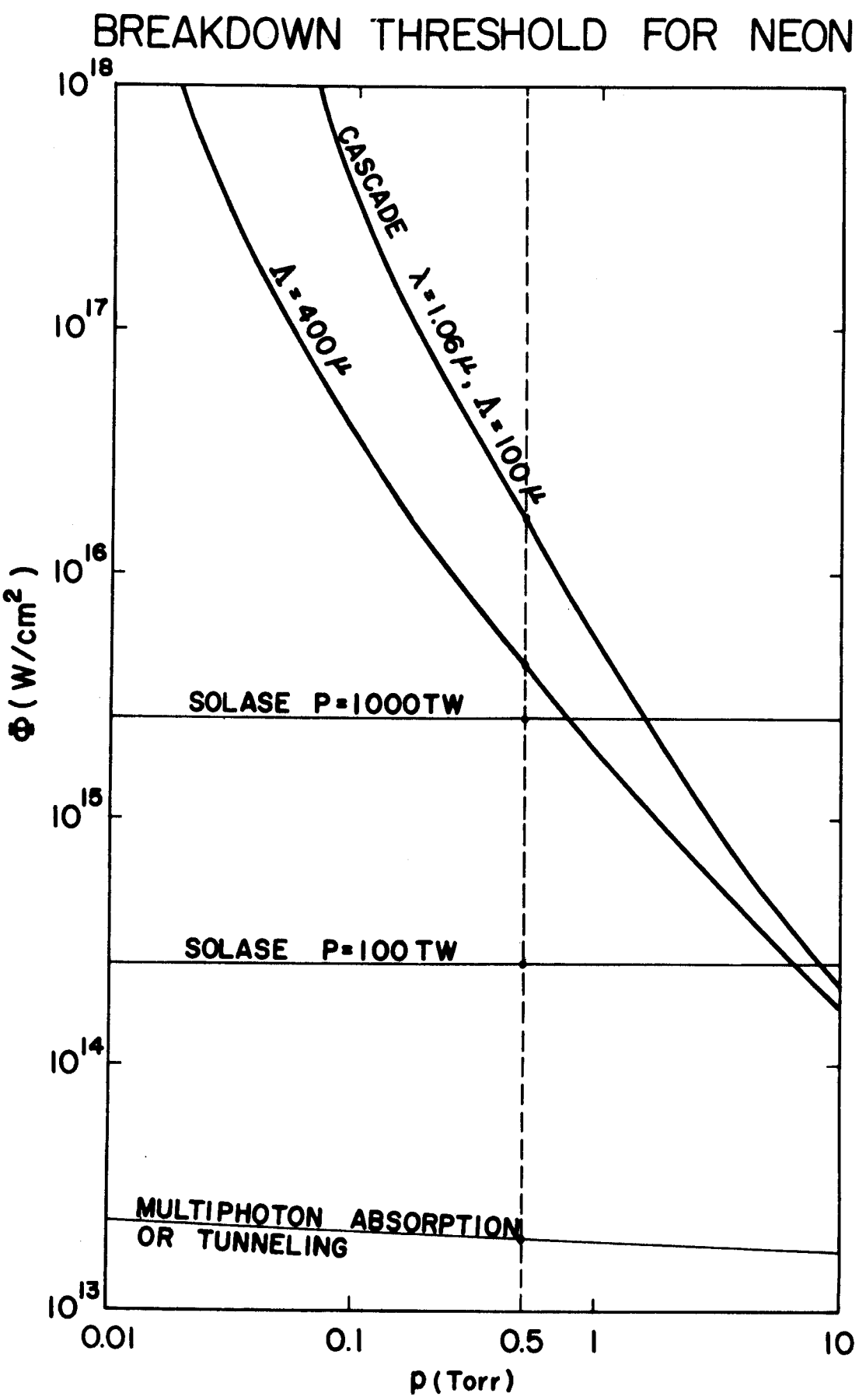
BREAKDOWN THRESHOLD FOR NEON
10^{18}
10^{17}
10^{16}
10^{15}
10^{14}
10^{13}
Φ (W/cm^2)
CASCADE λ=1.06μ, Δ=100μ
Δ=400μ
SOLASE P=1000TW
SOLASE P=100 TW
MULTIPHOTON ABSORPTION OR TUNNELING
0.01
0.1
0.5
1
10
p (Torr)

Fig. XI-B-23

threshold, assuming a diffusion length of Λ = 400 μm, corresponding to the last (non-uniform) case discussed in the previous section. The multiphoton absorption threshold is shown as the lower horizontal line at 2×10^{13} W/cm^2, while the SOLASE working irradiances are shown as the horizontal lines at 2.6×10^{14} and 2.6×10^{15} W/cm^2, corresponding to 100 and 1000 TW, resp. The corresponding thresholds for λ = 10.6 μm would be two orders of magnitude smaller.

According to the figure, an operating peak power of 100 TW is easier to handle than 1000 TW, because at the higher level both cascade and multiphoton breakdown are predicted (if $\Lambda > 400$ μm), whereas only multiphoton breakdown occurs at the lower level.

XI-B-5-g. Consequences of Breakdown

We have seen that breakdown may be expected to occur via multiphoton absorption at about 4 cm from SOLASE pellets. At the low electron number densities envisioned ($n \lesssim 10^{16}$ cm^{-3}) attenuation by inverse Bremsstrahlung is certainly negligible. The laser pulse width (1 nsec) is too short for hydrodynamic effects[20] to develop. If it turns out that larger (~ 50 nsec) pulses are required, then hydrodynamic effects would have to be considered. Although shocks may form, the mean free paths (~ 2 mm) are rather long and shock speed too slow to reach the pellet from 4 cm away within 1 nsec. That is, the light outruns the shock. Refractive losses due to partial ionization[31] are small at λ = 1.06 μm and could be countered by shaping the beam profile at λ = 10.6 μm.

Very recently Sparks and Sen[21] have suggested that considerable beam loss could occur by enhanced stimulated Raman plasmon scattering.

In this process laser photons are scattered in the forward direction in a cone of angle

$$\theta_e = \lambda_L / 5\lambda_D \ , \tag{58}$$

where λ_D is the Debye length. The electron temperature in our case at $z = 4$ cm is less than 22 eV for the 100 TW case,[30] which would predict a rather large scattering angle. The ramifications of this controversial effect are presently under active investigation.

XI-B-5-h. Conclusions

The rather benign consequences of breakdown at $\lambda = 1.06$ μm suggest that it may be possible to raise the neon pressure somewhat. By operating at 1 Torr, for example, the heavy ions could be much more effectively stopped, reducing wall sputtering to completely negligible levels. (It should be remembered that $p = 0.5$ Torr is quite marginal in this respect, as Fig. XI-B-5 shows). An additional advantage is that the reradiation time would be increased somewhat, although we have not yet obtained a useful estimate for this increase. The shock pressure, although doubled, would still only be a modest 180 Torr. Since multi-photon absorption/tunnelling is nearly independent of pressure, the breakdown intensity and its location would be virtually unchanged. The major objection to raising the pressure is the possible burden on the pumping system to remove heat from the gas, if the reradiation time is too long for this energy to be given up to the walls.

XI-B-6. Postscript: Xenon as Buffer Gas

Originally neon was chosen for the buffer gas because of its resistance to breakdown. Now that we know that breakdown is inevitable and apparently harmless, we are free to consider the other inert gases; He, Ar, Kr, and Xe. Of these, xenon has the greatest stopping power ($Z = 54$) and the lowest breakdown threshold ($U_i = 12.1$ eV). The observed breakdown threshold for xenon is about an order of magnitude less than neon's at $\lambda = 1.06$ μm. It follows from Eq. (55) that breakdown will occur about three times farther from the pellet, or at about $Z = 16$ cm. There are apparently no pernicious consequences using xenon rather than neon. The advantages are considerable. The much higher atomic number means greater stopping power for the ions and soft X-rays, ensuring longer wall lifetime. The lower ionization potential means the gas will continue radiating somewhat below 1 eV, with the result that less energy remains in the gas, raising the plant efficiency.

The purpose of this section is to elucidate the advantages and disadvantages of xenon, in comparison to simply using neon at a higher pressure. All calculations are carried out for the reference target containing 1 mg of DT and 10 mg of Hg.

XI-B-6-a. Ion Stopping Power

As Table XI-B-1 shows, the energetic mercury ions have the greatest range in neon. Figure XI-B-24 shows the mean range of Hg ions for neon pressures of 0.5 and 1.0 Torr.[32] When straggling is considered, the range of 4 MeV ions approaches the wall at 0.5 Torr but is less than half the chamber size at 1.0 Torr. Figure XI-B-25 shows the mean range

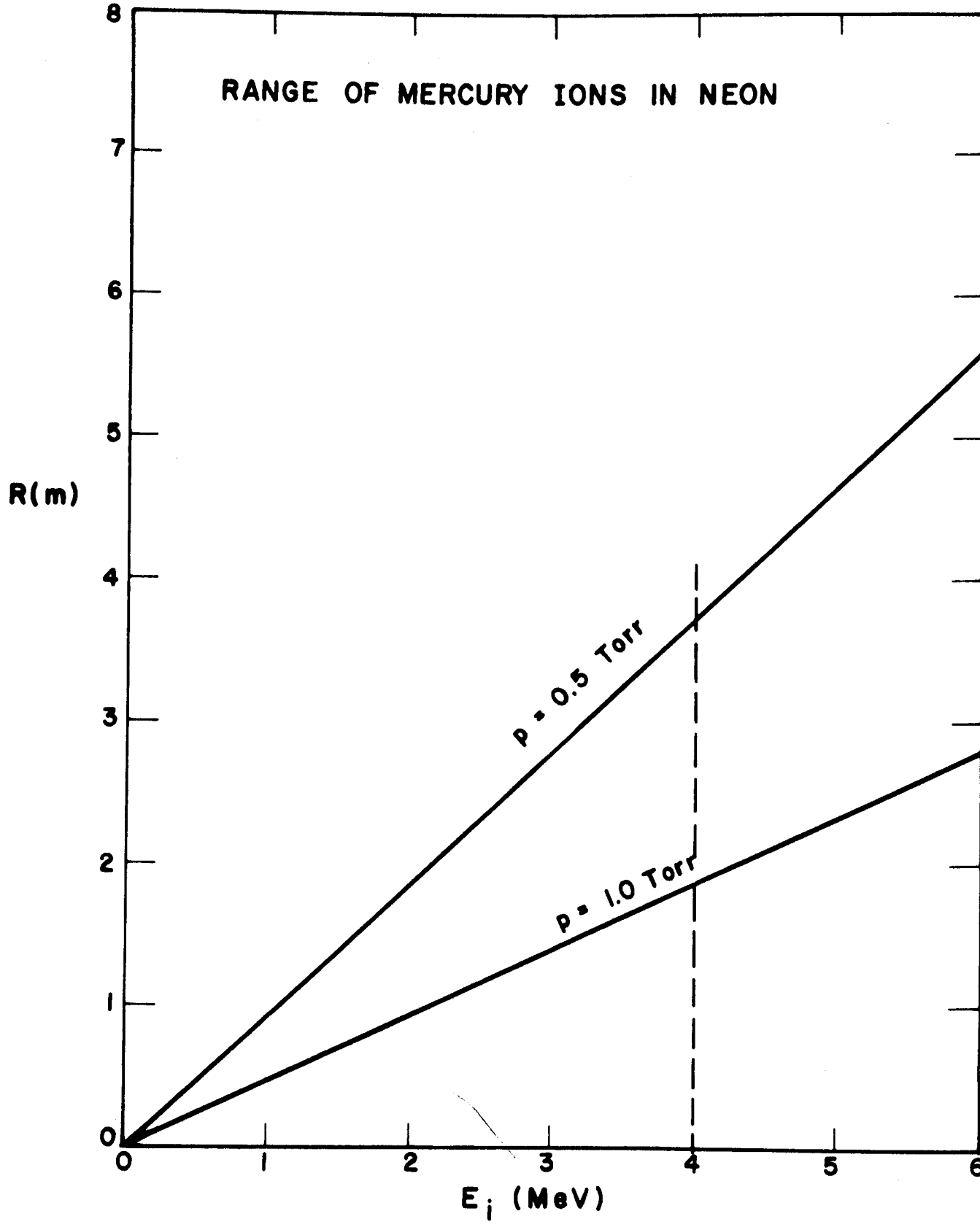
RANGE OF MERCURY IONS IN NEON
R(m)
E_i (MeV)
p = 0.5 Torr
p = 1.0 Torr
0
1
2
3
4
5
6
7
8

Fig. XI-B-24

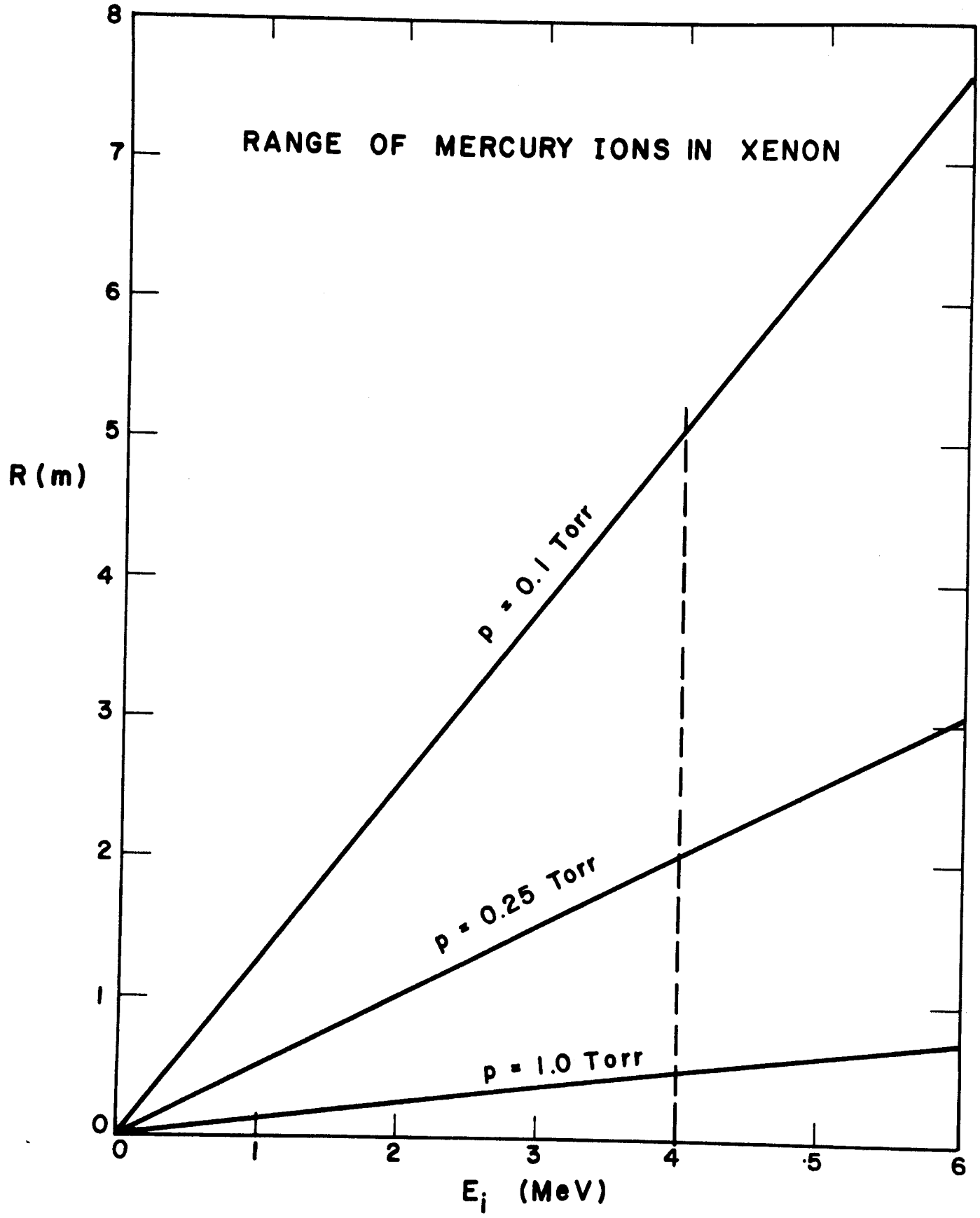
RANGE OF MERCURY IONS IN XENON
R (m)
E_i (MeV)
p = 0.1 Torr
p = 0.25 Torr
p = 1.0 Torr
0
1
2
3
4
5
6
7
8
.5

Fig. XI-B-25

of the Hg ions in xenon at pressures of 0.1, 0.25 and 1.0 Torr. In this case, 0.25 Torr seems a reasonable choice and is quite similar to using 1.0 Torr of neon. Thus, xenon offers no clear advantages over neon insofar as charged particle attenuation is concerned.

XI-B-6-b. X-Ray Attenuation

A full recalculation of the absorption and irradiation process is not possible at this point because of the difficulty in obtaining xenon equation of state data.[33] However, we can readily calculate the wall heating due to the direct unabsorbed flux. Figure X-B-26 displays the graphite wall temperature rise as a function of black body temperature, using neon and xenon as buffer gases. Here we see a definite disadvantage in using xenon. Even with 1.0 Torr of neon, the wall temperature rise exceeds 1000°C at θ_{BB} = 0.2 KeV, whereas only 150°C is reached at the same black-body temperature using 0.25 torr of xenon. We are unable to follow the rise in wall temperature below θ_{BB} = 0.1 Torr; the 0.25 Torr curve must turn over somewhat below this value. The case of 0.5 Torr of xenon is included to illustrate the expected behavior of the previous case, but shows an unexpected rise after first falling off below 1 KeV. On the basis of these results and the charged particle attenuation, we are led to choose a working pressure of 0.25 Torr of xenon. A larger pressure would be less desirable because it would tend to concentrate the ion energy near the center of the cavity. The pressure dependence of the gas breakdown threshold is very weak for mulitphoton ionization.

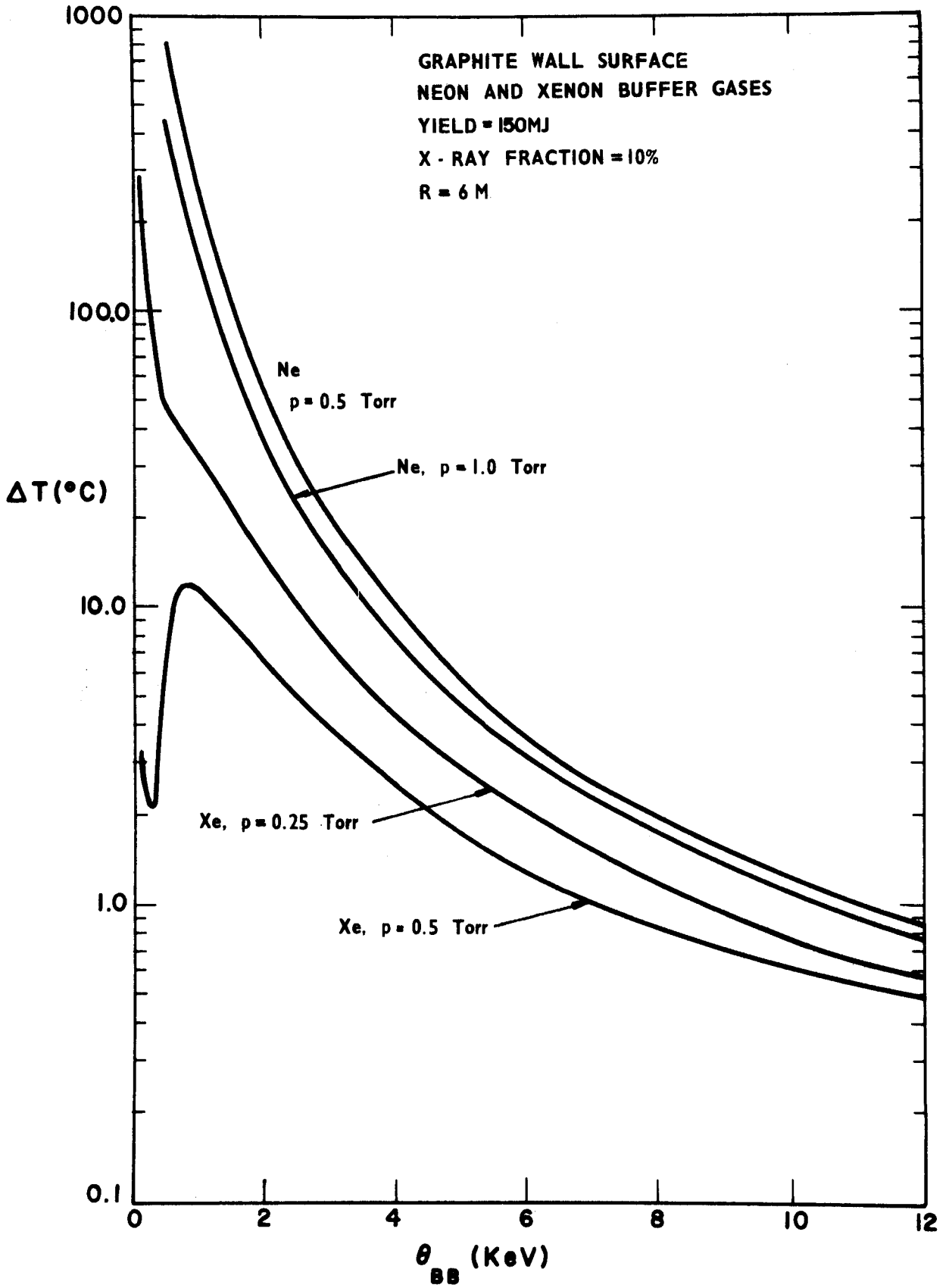
GRAPHITE WALL SURFACE
NEON AND XENON BUFFER GASES
YIELD = 150MJ
X - RAY FRACTION = 10%
R = 6 M
Ne
p = 0.5 Torr
Ne, p = 1.0 Torr
Xe, p = 0.25 Torr
Xe, p = 0.5 Torr
ΔT(°C)
1000
100.0
10.0
1.0
0.1
0
2
4
6
8
10
12
θBB (KeV)

Fig. XI-B-26.

XI-B-6-c. Pressure Impulse to the First Wall

Assuming the same absorbed charged particle energy per unit volume in both cases, the shock overpressure is independent of the buffer gas density or species. The impulse to the first wall then simply scales as time, or (see Sec. XI-B-3).

$$M_{Xe} = \sqrt{\frac{m_{Xe}\, n_{Xe}}{m_{Ne}\, n_{Ne}}}\; M_{Ne} \,. \qquad (59)$$

Comparing 0.25 torr of Xe with 1.0 torr of Ne, we then have

$$M_{Xe} = 1.28\, M_{Ne} \,.$$

This comparison is only meaningful insofar as the charged particle deposition profiles are comparable. Thus, based on Figs. XI-B-24 and 25 we chose the above Xe and Ne pressures. We do not believe that momentum transfer to the first wall presents serious problems in either case.

XI-B-6-d. Gas Cooling and Reradiation to the First Wall

It is of interest to compare the radiation rate of the xenon buffer gas with that of neon under similar conditions except for density. We assume that 13 MJ of changed particle energy are distributed evenly in the xeno gas at a density of $.75 \times 10^{16}$ cm^{-3}. Under such conditions the energy per particle, average ionization and temperature as calculated from the approximate method of Zeldovich and Raizer are:

ε = 12 eV/particle

α = .9/free electrons/atom

T = .9 eV .

This information may be used to calculate the radiation rate once the photo ionization cross-sections are known. The cross-sections are not known very exactly but are somewhere between 2 - 5 times that of neon at ionization threshold. On this assumption the energy release time assuming no absorption and re-emission is between 0.3 and 2 milliseconds. Here again this is a lower bound due to the role of photon transport. Photon mean-free-paths are less than a meter and considerable absorption and re-emission can take place, increasing the energy release time considerably. The transparency temperature for xenon is near 0.6 eV which means that at least 2 MJ will be left in the gas when radiation ceases. If transport dominates, the amount of energy remaining will be larger. These questions merit further study.

XI-B-6-e. Disadvantages of Using Xenon

An mentioned in Section XI-B-5- g, the consequences of gas breakdown do not appear to be severe in SOLASE. Collisional absorption and self-defocusing are probably still negligible in xenon due to the low number density and short laser wavelength and pulse width. The magnitude (and existence!) of stimulated Raman scattering is an area under active investigation, both theoretically[34] and experimentally[35] and remains an open question at this time.

References for Section XI-B

1. J. Lindhard, M. Scharff and H. E. Schiott, "Range Concepts and Heavy Ion Ranges, (Notes on Atomic Collisions, II)", Mat. Fys. Medd. Dan. Vid. Selsk., 33, 14 (1963).

2. I. Manning and G. P. Mueller, "Depth Distribution of Energy Deposition by Ion Bombardment", Computer Physics Communication, 6, (1973).

3. L. I. Sedov, Similarity and Dimensional Methods in Methods in Mechanics. Gostekhizdat, Moscow, 4th edition, 1957. English transl. (M. Holt, ed.), Academic Press, New York, 1966.

4. Y. B. Zel'dovich and Y. P. Raizer, Physics of Shock Waves and High Temperature Hydrodynamic Phenomena, pp. 93-99. English transl. (W. D. Hayes and R. F. Probstein, ed.), Academic Press, New York (1966).

5. Ibid, pp. 236-239.

6. Ibid, pp. 207-209.

7. S. Abarbanel and M. Goldberg, Journal of Computational Physics 10, 1-21 (1972).

8. Y. B. Zeldovich and Y. P. Raizer, op cit., pp. 405-406.

9. Ibid, pp. 201-207.

10. W. Huebner, "Equation of State and Opacity Data for Neon", private communication.

11. Ibid

12. Y. B. Zeldovich and Y. P. Raizer, op cit., p. 402.

13. Ibid, p. 405.

14. C. DeMichelis, IEEE J. Quant. Electron. QE5, 118 (1969).

15. C. Grey Morgan, Rep. Prog. Phys. 38, 621 (1975).

16. J. F. Ready, Effects of High-Power Laser Radiation, Academic Press, New York (1971).

17. M. P. Hacker, D. R. Cohn, and B. Lax, Appl. Phys. Lett. 23, 392 (1973).

18. S. C. Brown, Introduction to Electrical Discharges in Gases, John Wiley & Sons, New York (1966).

19. A. D. MacDonald, Microwave Breakdown in Gases, John Wiley & Sons, New York (1966).

20. L. C. Steinhauer and H. G. Ahlstrom, Phys, Fluids, 14, 1109 (1971).

21. M. Sparks and P. N. Sen, Phys. Rev. Lett. 39, 751 (1977).

22. L. V. Keldysh, Sov. Phys.-JETP 20, 1307 (1965).

23. A. Gold and H. B. Bebb, Phys. Rev. Lett. 14, 60 (1965).

24. H. B. Bebb and A. Gold, Phys. Rev. 143, 1 (1966).

25. H. B. Bebb and A. Gold, in Physics of Quantum Electronics, ed. P. L. Kelley, B. Lax and P.E. Tannenwald, McGraw-Hill, New York (1966), pp. 489-498.

26. P. Agostini, G. Barjot, G. Mainfray, C. Manus, and J. Thebault, IEEE J. Quantum Electron. QE-6, 782 (1970).

27. C.L.M. Ireland, J. Phys. D. Appl. Phys. 7, L87 (1974).

28. P. N. Kraysuk, P. P. Pashinin, and A. M. Prokhorov, Sov. Phys. - JETP 31, 860 (1970).

29. T. K. Chu and L. C. Johnson, Phys. Fluids, 18, 1460 (1975).

30. M. Sparks, private communication.

31. D. Henderson, unpublished.

32. T. O. Hunter and G. L. Kulcinski, Univ. of Wisconsin, Nuclear Engr. Dept. Report, UWFDM-196 (March 1977).

33. Ross Spencer, private communication.

34. J. J. Thomson, Bull. Am. Phys. Soc. 22, 1138 (1977).

35. M. Sparks, private communication.

XI-C. Summary: First Wall Protection in SOLASE

In the previous sections, we have described and analyzed the gas protection scheme utilized in SOLASE. The cavity is filled with neon (or xenon) at less than 1 torr pressure, sufficient to protect the first wall from the ions and soft X-rays produced by the microexplosion. There are four different factors which affect the gas type and pressure to be used, namely: (1) laser-induced gas breakdown, (2) pellet output spectra, (3) reradiation time for the energy deposited in the gas, and (4) strength of the shock produced by the energy deposition. We have shown that breakdown is inevitable and, for gas pressures of 0.01 - 1.0 torr and average power on target of 2×10^{14} - 2×10^{15} W/cm^2, it will occur sufficiently close to the target to be harmless. The gas pressure should be selected so that the ions are stopped before reaching the first wall. By judiciously selecting the gas pressure to match the pellet output spectra, the ion and soft X-ray energies will be deposited along most of the cavity radius in order to minimize the strength of the concomitant shock. This means that mechanical design of the first wall and blanket will place an upper bound on the gas pressure. The energy deposited in the gas must be reradiated to the first wall over a long period of time to prevent excessive surface heating of the wall. This requirement will place a lower bound on the gas pressure.

For the structured pellet examined here, we have shown that a neon pressure of about 0.5 torr is sufficient to stop all the ions before

reaching the walls of the 12 m diameter SOLASE cavity. The pressure impulse on the first wall will have a peak value of only 90 torr. The corresponding maximum dynamic stress in the first wall is less than 3000 psi (Section XII-B-2) which is tolerable. We have also shown that the energy deposited in the gas will be radiated to the first wall over a period longer than 1 ms. Our analysis assumes the gas to be optically thin; hence, the reradiation time obtained represents a lower bound. This is extremely important for wall survival. As can be seen from Fig. XI-C-1 , if the energy is rapidly reradiated from the gas, the first wall surface temperature will sharply rise after each microexplosion. For reradiation times greater than 1 ms, the surface temperature jump will be less than 200°C. This corresponds to a maximum tensile stress at the surface of less than 340 bars which is considerably lower than the maximum allowable stress. For longer reradiation times, smaller surface temperature jumps and lower stresses result. Under these conditions, evaporation of the carbon first wall will be insignificant.

One should keep in mind that while it is necessary that the reradiation time be longer than 1 ms, it is desirable that it be much less than the time between pulses (50 ms). This latter requirement means that the ion and X-ray energy deposited in the gas will be radiated to the first wall rather than being convected out along with the chamber exhaust and removed in the suppression chamber. This is desirable from an overall thermal efficiency standpoint since the lithium oxide coolant of the first wall leaves at 600°C while the water-cooled suppression chamber walls operate at only 200°C (Chapter XVII).

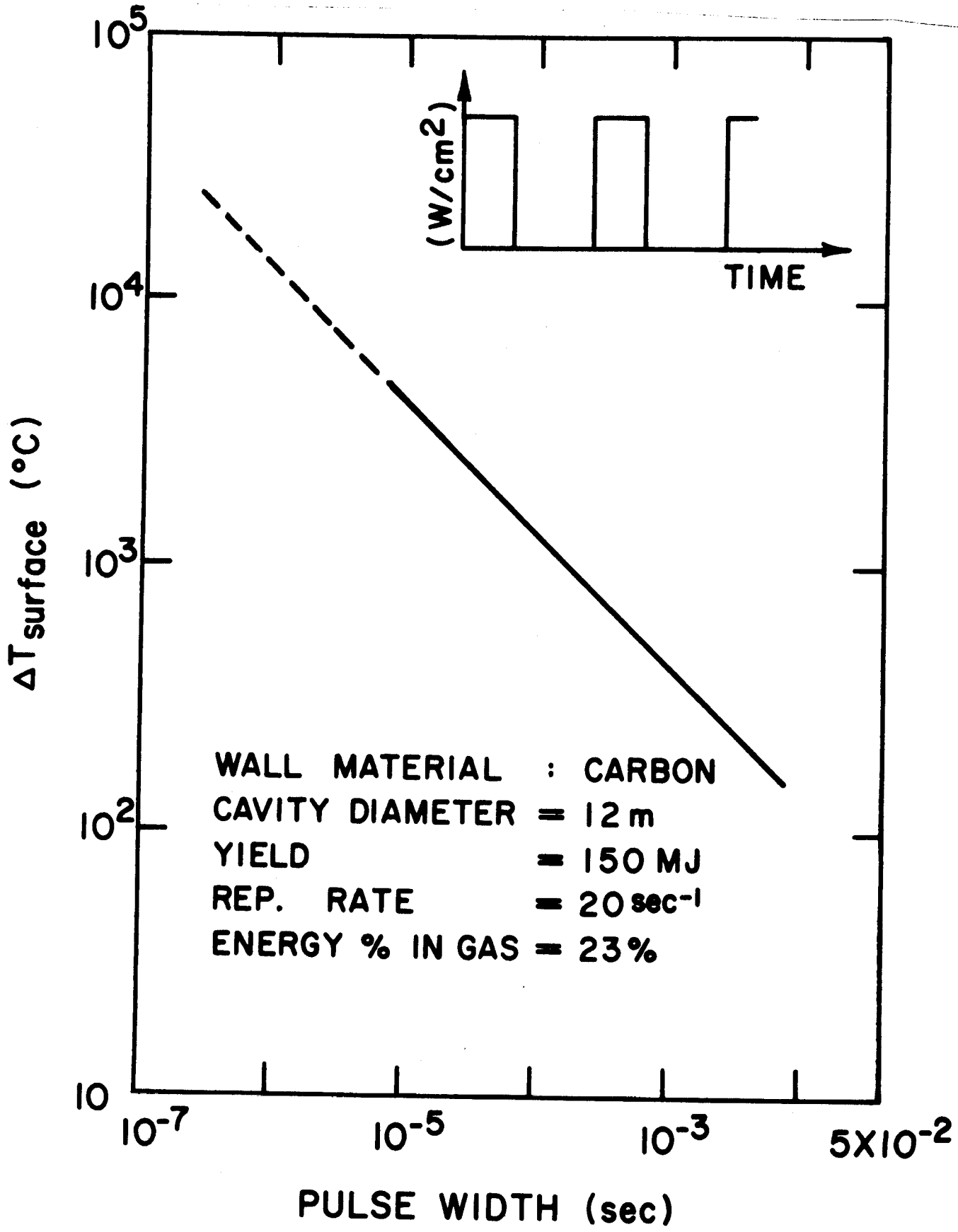
10^5
10^4
10^3
10^2
10
$\Delta T_{surface}$ (°C)
(W/cm²)
TIME
WALL MATERIAL : CARBON
CAVITY DIAMETER = 12 m
YIELD = 150 MJ
REP. RATE = 20 sec⁻¹
ENERGY % IN GAS = 23%
10^{-7}
10^{-5}
10^{-3}
$5X10^{-2}$
PULSE WIDTH (sec)

Fig. XI-C-1.

In addition to the energy radiated by the gas, the first wall will be subjected to the unabsorbed X-ray flux. Hard X-rays will not be stopped in the gas; these, however, are benign since they have a long range in carbon (Figure XI-C-2). One can set an upper bound on the allowable temperature rise in the first wall by the unattenuated X-rays so that the resultant thermal stresses are tolerable and the surface temperature remains below the point where evaporation becomes significant. For SOLASE an upper limit on $\Delta T_{surface}$ of 235°C has been set which corresponds to a maximum stress at the wall surface of 400 bars and a maximum temperature of 1800°C. One can cross-plot Figure XI-C-2 and obtain the X-ray fraction in the pellet yield which would result in $\Delta T_{surface}$ = 235°C. There results are shown in Figure XI-C-3. As can be seen if the X-ray spectrum is harder than 1 keV, the wall can withstand more than 10% of the pellet yield in X-rays. If the X-rays are extremely soft ($< \sim$ 50 eV), most of the X-rays will be absorbed in the gas so that a high X-ray fraction is allowed without $\Delta T_{surface}$ exceeding the 235°C limit. Figure XI-C-3 shows that for neon there is a window between $\sim$ 50 eV and $\sim$ 500 eV where the unabsorbed X-rays are "soft-enough" to cause significant temperature rise in the wall and "hard-enough" not to be stopped in the gas. It is for this reason that the use of xenon as a buffer gas appears more attractive, provided, of course, that the laser-induced gas breakdown will be tolerable. The analyses presented in the previous section indicate that this is indeed the case. This means that gas protection is a generic approach which can be made to operate successfully for a wide range of pellet output characteristics.

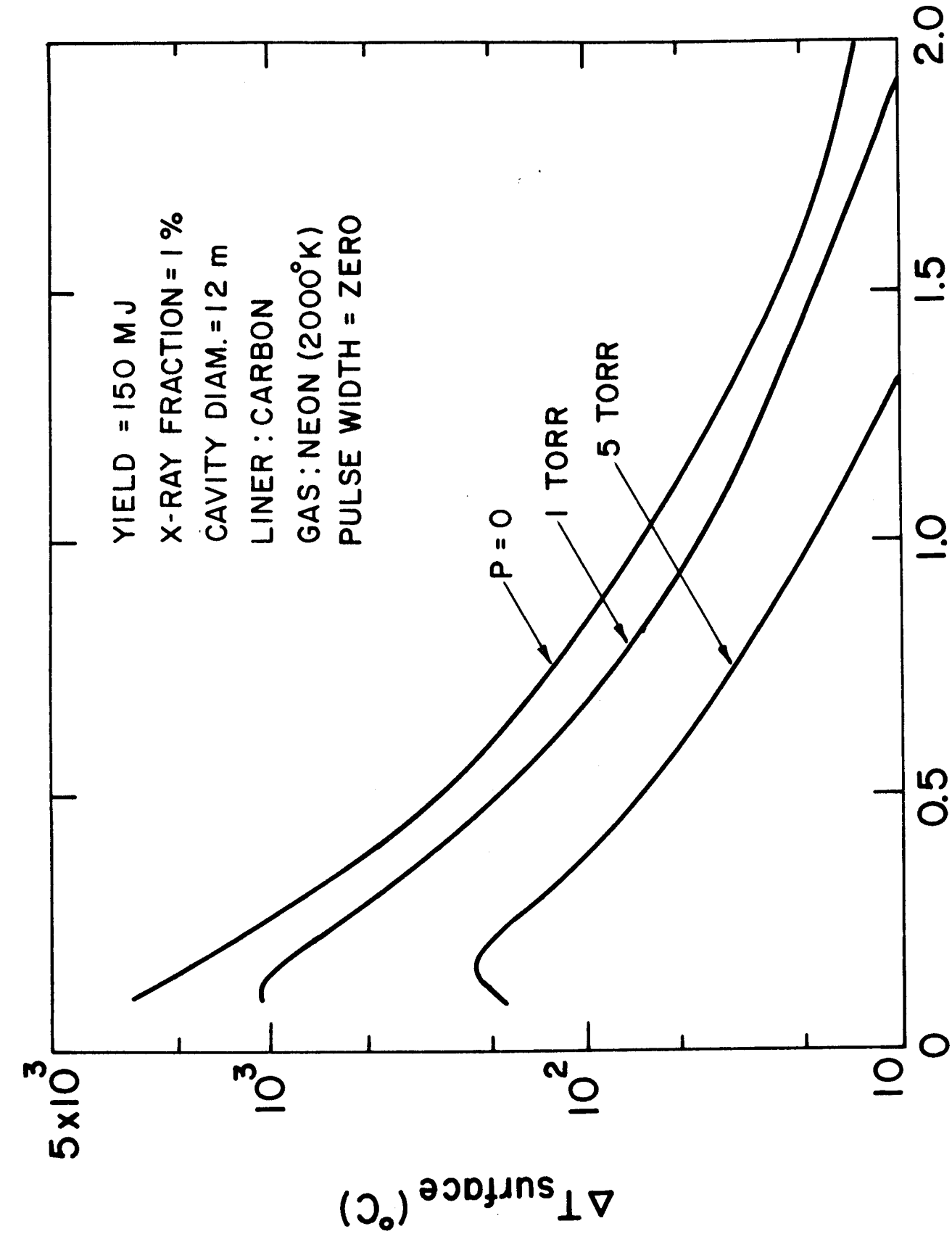
YIELD = 150 MJ
X-RAY FRACTION = 1 %
CAVITY DIAM. = 12 m
LINER : CARBON
GAS : NEON (2000°K)
PULSE WIDTH = ZERO
P = 0
1 TORR
5 TORR
$\Delta T_{surface}$ (°C)
5×10^3
10^3
10^2
10
0
0.5
1.0
1.5
2.0

Fig. XI-C-2.

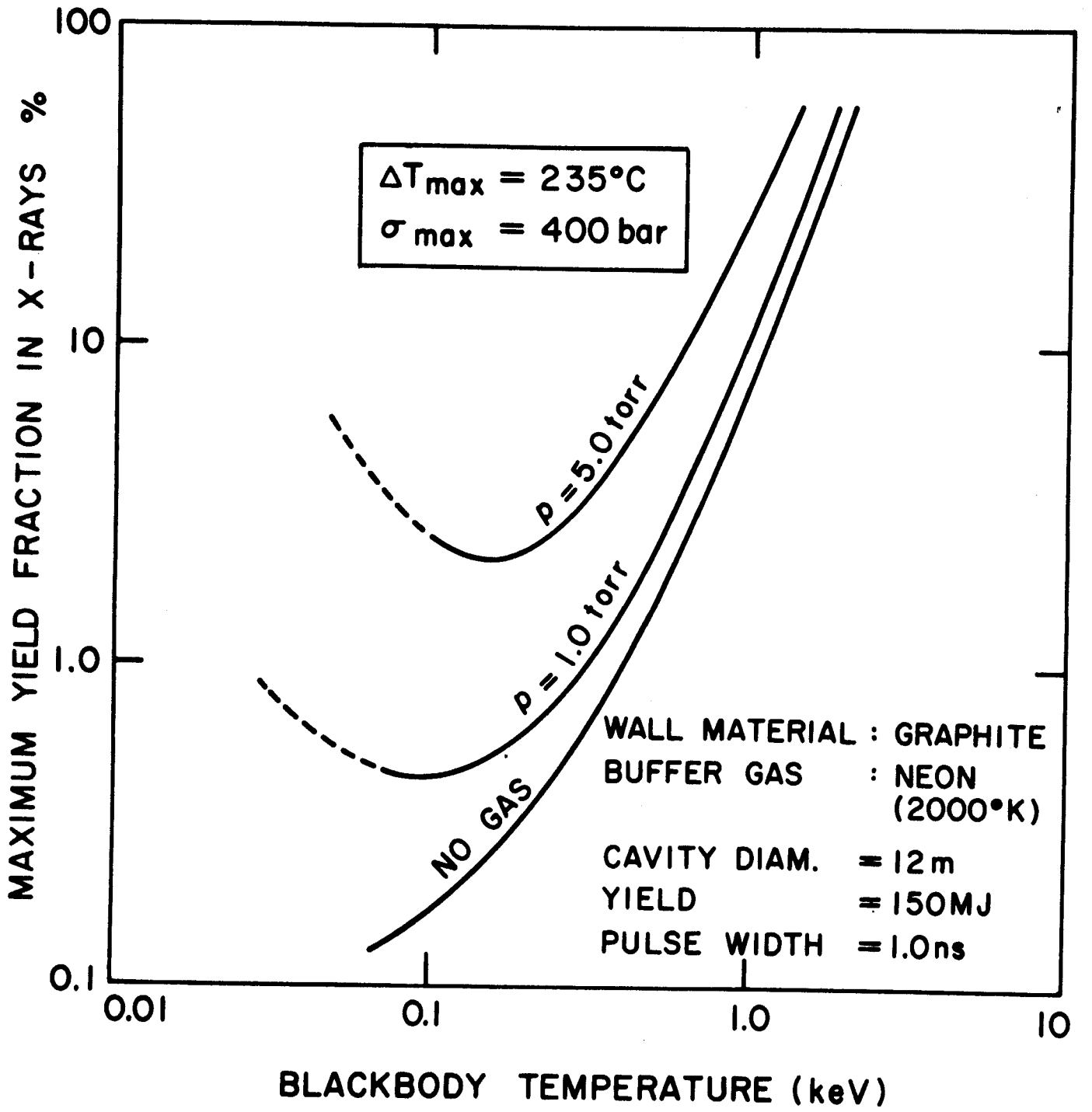
100
10
1.0
0.1
MAXIMUM YIELD FRACTION IN X-RAYS %
ΔTmax = 235°C
σ max = 400 bar
p=5.0 torr
p=1.0 torr
NO GAS
WALL MATERIAL : GRAPHITE
BUFFER GAS : NEON (2000°K)
CAVITY DIAM. = 12 m
YIELD = 150MJ
PULSE WIDTH = 1.0ns
0.01
0.1
1.0
10
BLACKBODY TEMPERATURE (keV)

Fig. XI-C-3.

In summary, the gas protection scheme utilized in SOLASE is extremely attractive. The uncertainties involved in this concept can, and should, be easily examined experimentally. Notable among these are the gas re-radiation problem and the effect of gas breakdown on pellet performance. Also, the effect of impurities on gas breakdown should be examined since that will have a direct effect on the required pumping speed. It should be noted that gas protection appears most suitable for near-term reactor applications as well. With proper X-ray spectra, it can work successfully for "standard" chamber designs with water-cooled stainless steel walls.

XII. Blanket Design and Analysis

XII-A. Introduction

The blanket of a D-T fusion reactor is the zone where tritium is bred and where most of the nuclear reaction energy (~80%) is deposited. This energy must be removed and delivered to a power conversion unit. An efficient blanket cooling scheme at a relatively high temperature is therefore required in order to attain a reasonably high overall thermal efficiency for the plant. The blanket cooling scheme should be compatible with the tritium breeding and recovery processes. It would also be desirable to operate the blanket at relatively low pressures in order to reduce the structural materials requirements and simplify the overall design of the primary loop.[1-3] In addition, the blanket design should be compatible with the first wall protection scheme.

Various cooling-breeding schemes have been suggested for fusion reactor blankets. In all these schemes, the breeding material is either pure lithium or a lithium compound. The coolants most frequently used are lithium and helium. When a lithium compound is used, it usually serves the dual purpose of breeding and cooling, and thus the tritium recovery and heat removal loops are combined. Such a scheme greatly simplifies the blanket design since only one set of feed/discharge pipes and headers is required, which in turn reduces the effort needed to repair or replace part of the blanket.[4] On the other hand, when a lithium compound is used for cooling, the heat transfer problems encountered in the design process are less conventional and thus require additional effort during the design stage.

When a lithium compound is used as a coolant and breeding medium, it has to occupy a large fraction of the blanket volume (~95%) in order to maximize the breeding ratio. In such a design around 80% of the heat is deposited in the coolant while the remaining 20% are deposited in structural materials. Thus, if the first wall is separately cooled, the blanket cooling process becomes a heat transport problem. Most of the efforts ordinarily devoted to obtaining high heat transfer coefficients and large cooling-surface areas are not needed in this case. The problem here is to select a good heat transport medium, namely, one which would have a high value of (ρc_p/pumping power).

A gravitational flow Li_2O blanket design has been suggested by Sze, et al.[4] for tokamak-type reactors. Such a design appears well suited for the geometrically-simple laser fusion reactors. It satisfies the different requirements for cooling/breeding materials and is expected to provide sufficiently high breeding ratios. The Li_2O blanket concept has been adapted for use in SOLASE. Detailed description of the SOLASE blanket and a general discussion of the merits of the Li_2O blanket concept are given below.

References for Section XII-A

1. B. Badger, et al., "UWMAK-I, A Toroidal Tokamak Power Reactor Design," UWFDM-68, Nuclear Eng. Dept., Univ. of Wisconsin (1974).

2. B. Badger, et al., "UWMAK-II, A Conceptual D-T Fueled, Helium Cooled, Tokamak Fusion Power Reactor Design, UWFDM-112, Nuclear Eng. Dept., Univ. of Wisconsin (1975).

3. B. Badger, et al., "UWMAK-III, An Advanced Noncircular Tokamak Power Reactor Design, UWFDM-150, Nuclear Eng. Dept., Univ. of Wisconsin (1976).

4. D. K. Sze, et al., "Gravity Circulated Solid Blanket Design For A Tokamak Fusion Reactor," Proc. 2nd Topical Meeting on the Technology of Controlled Nuclear Fusion, Richland (1976).

XII-B. Blanket Design for SOLASE

XII-B-1. The Li_2O/Graphite Blanket Concept

A schematic diagram of the SOLASE cavity and blanket is shown in Fig. XII-B-1. The cavity is spherical with a 6 m radius surrounded by a 60 cm thick blanket. The entire blanket is constructed from graphite. Either nuclear grade graphite or chopped-fiber type graphite composite can be used; the latter is superior because of its high strength and reduced swelling under irradiation. Lithium oxide particles, 100-200 μm in diameter, flow under gravity through the blanket and serve the dual purpose of tritium breeding

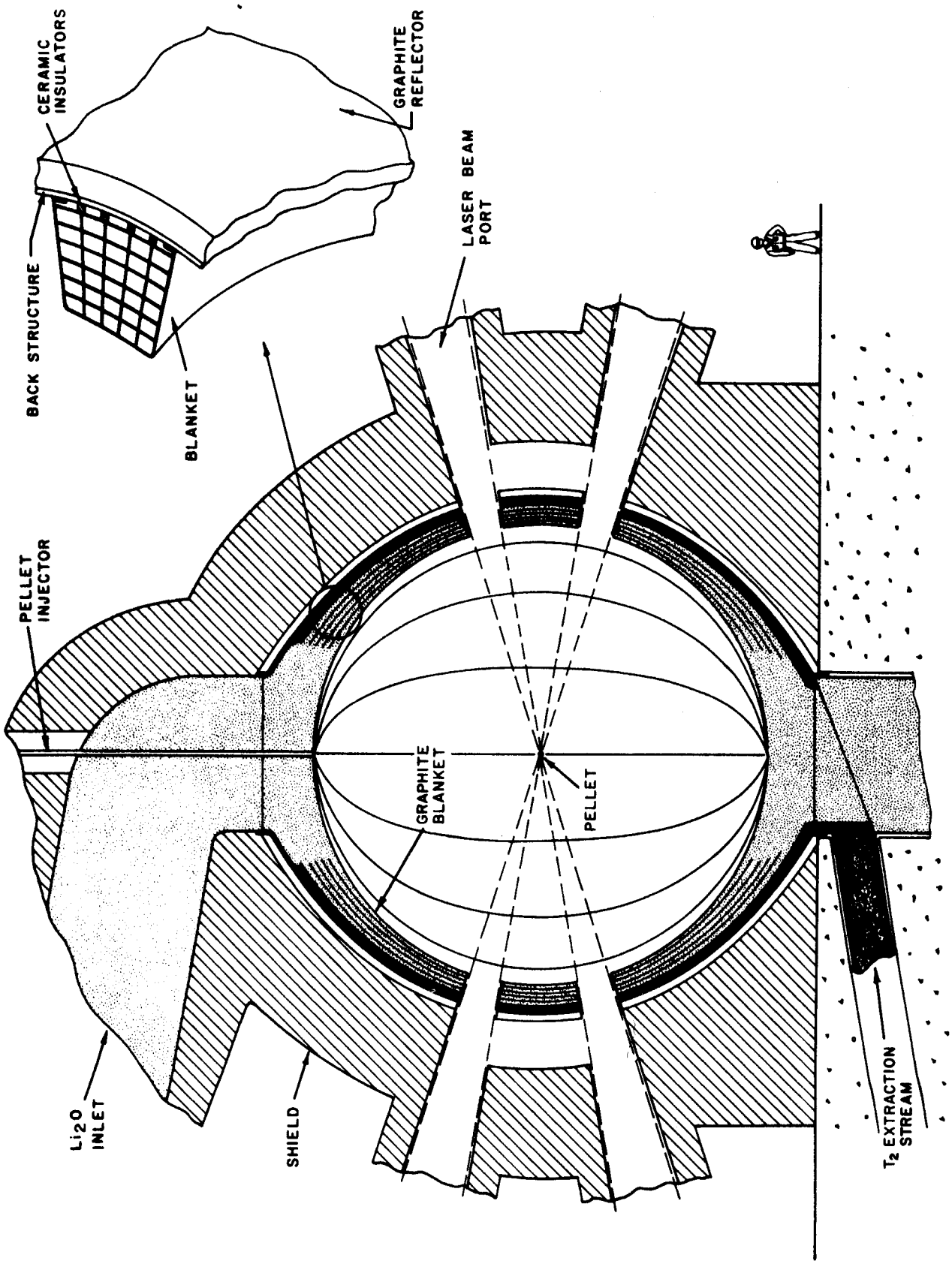

Fig. XII-B-1.
Schematic Diagram of the SOLASE Cavity

and heat transport. The spherical cavity is divided along longitudes into sixteen blanket segments each with a honeycomb type construction (Fig. XII-B-2).

Five tangential spacers, 6.5 mm thick, are used to divide each blanket segment into six breeding zones of equal thickness (10 cm). The average velocity of the Li_2O particles within each zone is controlled to match the radial heat deposition curve (Section XII-B-2). Graphite radial supports, 6.5 mm thick, are provided to maintain structural rigidity and allow impulse loadings on the blanket's front wall to be transmitted to the support structure behind the blanket. This design eliminates the need for metallic first walls and liners since the blanket's front wall can readily accommodate the microexplosion both thermally and mechanically.

The reactor cavity is filled with neon gas at less than 1 torr pressure, sufficient to protect the front wall from the ions and soft X-rays produced by the microexplosion (Chapter XI). The energy deposited in the gas is radiated to the front wall over a relatively long time period (>1 ms) so that surface heating and thermal ablation of the wall become insignificant. Hard X-rays deposit their energy directly in the front wall of the blanket but produce a relatively small surface temperature rise because they have a sufficiently long range in carbon (Section X-C). A shock wave is generated in the gas after each microexplosion. The propagating shock imparts an impulse load on the front wall. These periodic loads, however, are quite small and can easily be accommodated as will be shown later.

The pulsed surface heat flux radiated by the gas is rectified in the blanket's front wall and directly convected and radiated to the flowing

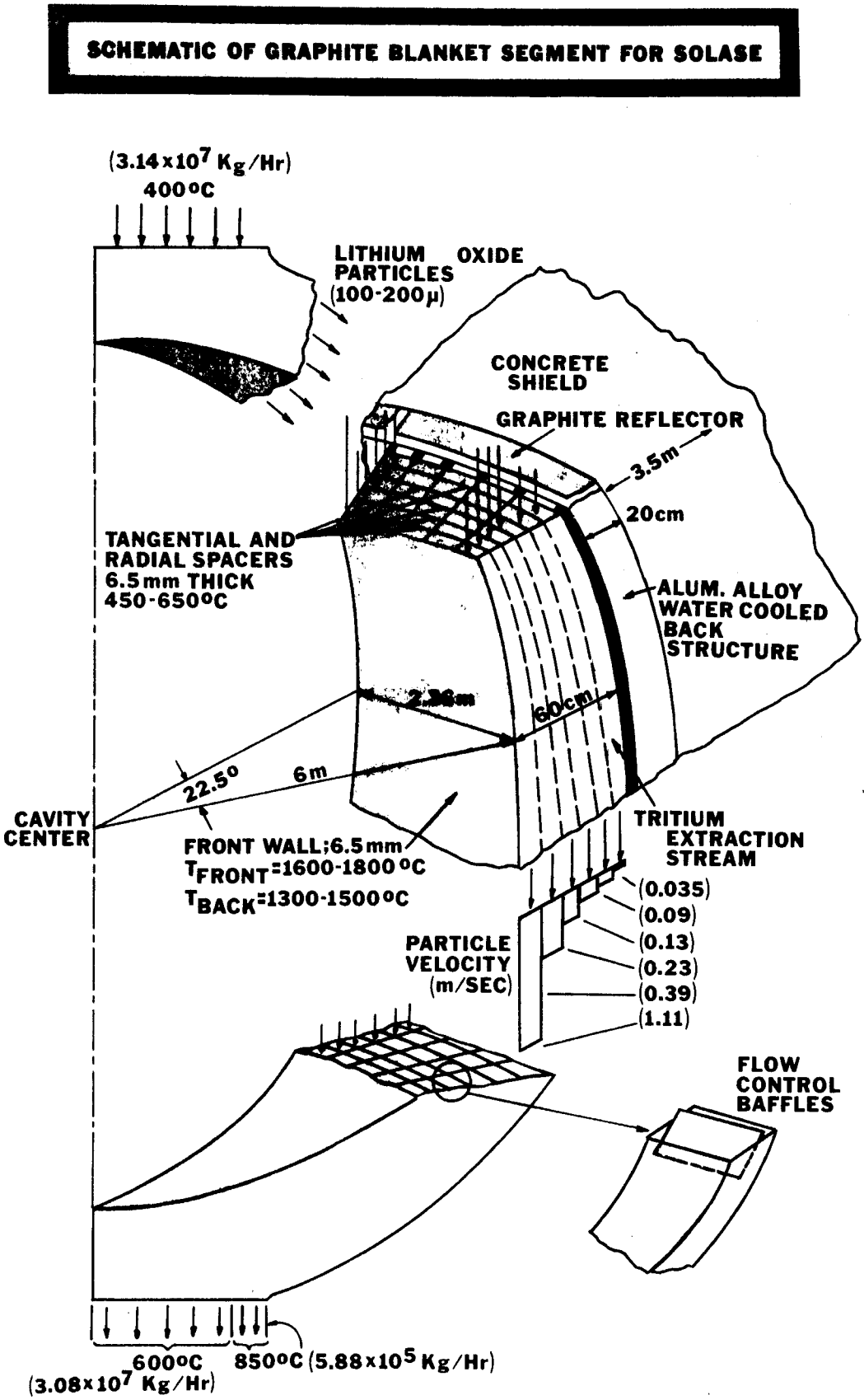

Fig. XII-B-2.

Schematic Diagram of a SOLASE Blanket Segment

lithium oxide. The combined heat transfer coefficient is low (~0.2 W/cm^2-°C) so that the front wall temperature is significantly higher than that for the Li_2O stream. The ability to "decouple" the first wall and blanket coolant temperatures is one of the main advantages of the flowing lithium oxide blanket concept. The latter temperatures are dictated by power cycle efficiency requirements while the former can be selected on the basis of radiation damage considerations. For our graphite construction, the front wall must be operated at sufficiently high temperature (>~1300°C) to avoid "run-away" swelling. This is, indeed, the case. The lithium oxide particles enter the blanket at 400°C and leave at 600°C except for the outermost zone where the exit temperature is 850°C. The hot stream contains ~2% of the total flow rate and is used for tritium extraction prior to joining the other stream on its way to the steam generators. The back surface of the front wall will operate at 1300-1500°C with the front surface temperature reaching a maximum of 1800°C after each microexplosion (Chapter XI).

The idea of temperature-decoupling works equally well for blankets with metallic first walls and protective liners. In such systems, the first wall can be maintained at temperatures well below those of the Li_2O stream without significant adverse effect on the overall thermal efficiency of the plant since a small fraction of the thermal power deposited in the blanket is transferred to the relatively cold first wall. For example, in the pre-SOLASE design,[1] the stainless steel first wall was separately cooled and maintained at ~300°C resulting in reduced swelling and significant increase in wall life. Hence, the use of lithium oxide as a coolant and breeder in fusion systems (both inertial and magnetic confinement) allows greater flexibility in system

design. The graphite blanket construction is more suitable for inertial confinement systems because of the relaxed chamber vacuum requirements.

The Li_2O stream in the outer breeding zone can be heated within the blanket to a sufficiently high temperature (850°C) compatible with tritium extraction. This allows a high degree of flexibility in designing the tritium extraction cycle since one can adjust the temperature and flow rate of the extraction stream. One controls the exit temperatures by merely adjusting the particles' flow rate, i.e., residence time within the blanket. The fact that the heat deposition rate within the blanket drops as we move away from the first wall (Chapter XIII) should not cause any difficulty. One can maintain relatively uniform exit temperatures by simply dividing the blanket into several subzones and adjusting the particles' flow rates within the different zones independently to match the local heat generation rates (Section XII-B-2). Flow channel orificing at the exit can be used to get the proper flow rates. Other, equally simple, schemes for obtaining a uniform exit temperature distribution can be surmised.

The selected Li_2O particle size (100-200 μ) is a compromise between tritium diffusion, structural erosion, particle attrition, particle fabrication and material handling problems. Structural erosion does not appear to be a serious problem for particles of this size moving at ~1 m/sec.[2] Tritium recovery is possible if the solid particles are porous (Chapter XVI).

Neon gas fills the gaps between the particles in the blanket. The void fraction in the blanket is only 40% which means that the required blanket thickness will not be large and that sufficiently high breeding ratios can be

obtained. With a blanket thickness of 60 cm, the breeding ratio for SOLASE is 1.33 (Chapter XIII).

The pressure within the blanket is only 10 torr which makes it attractive from a safety standpoint. The low pressure is selected to minimize gas leakage into the cavity. Operation of the entire Li_2O loop at such loop pressure should not cause significant problems with regard to steam generator and reheater design as well as particle transport system (Chapter XVII). It is necessary to maintain a reasonable fill gas pressure (~ 10 torr) in the primary loop so that adequate heat transfer coefficients can be obtained in the steam generators.

In this design, no intermediate heat exchanger is needed since the tritium diffusion through the primary system is sufficiently low (Chapter XVI). A Li_2O/w reaction caused by a leak in the steam generator or reheater tubes is not hazardous. The elimination of the intermediate loop should have a significant impact on system economics. It will also allow for better steam conditions and hence a higher overall thermal efficiency.

Gravitational flow of the Li_2O particles through the blanket and steam generator will, of course, require corresponding material lifts to complete the flow path. Several particle transport schemes have been used in the chemical industry;[3] among these are mechanical transport, penumatic mass lift, and penumatic-disperse phase flow. Multi-stage Archimedes lift pumps are most suitable for the low-pressure loop used in SOLASE. They offer many advantages including low particle attrition, circulation power, and equipment maintenance requirements (Chapter XVII).

Typical results showing the SOLASE blanket radioactivity as a function of time after shutdown are given in Fig. XII-B-3. These results show that the activity level of such a blanket is very low. The graphite shells are supported

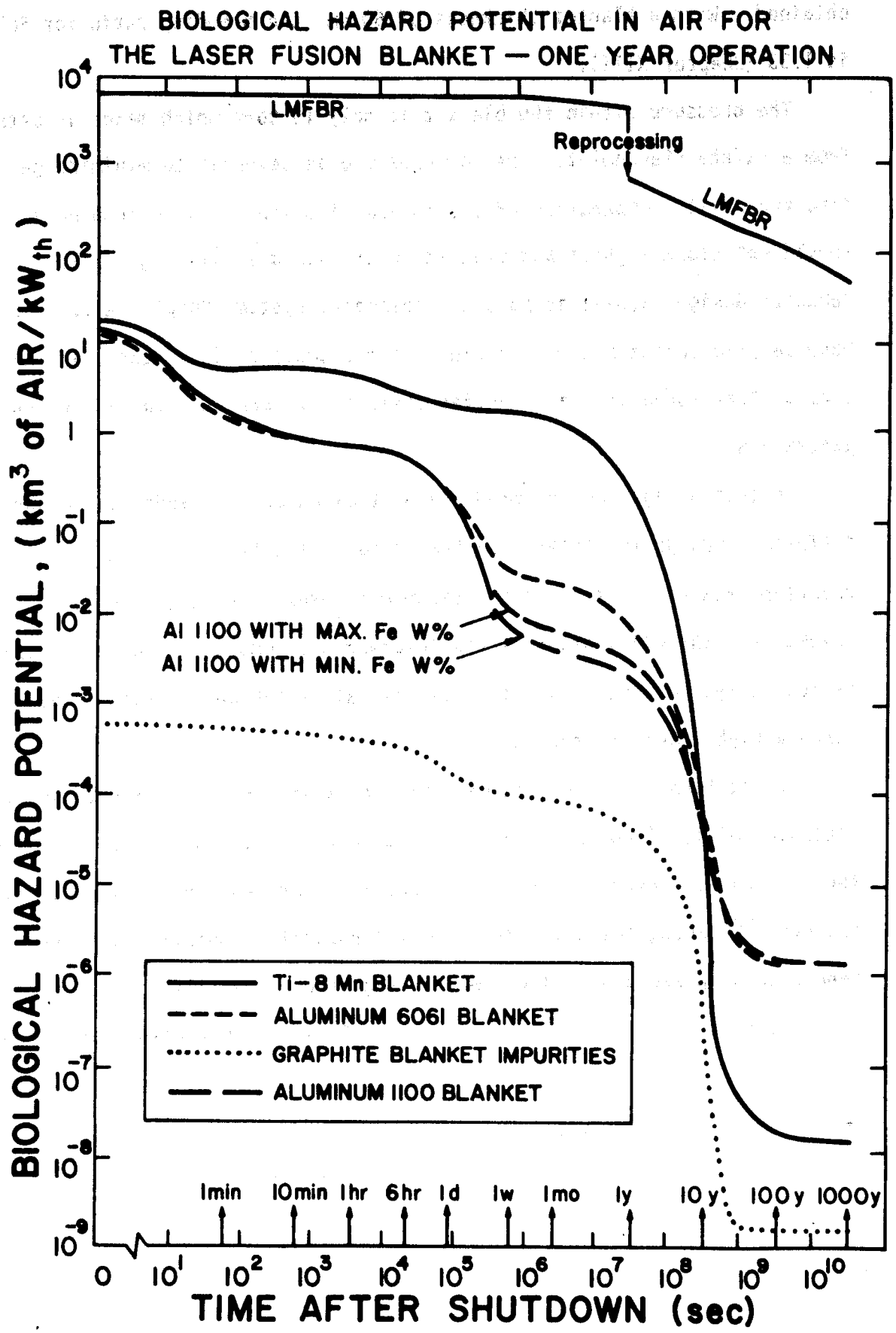

Fig. XII-B-3.

Variation of SOLASE Blanket Radioactivity After Shutdown

by an aluminum alloy structure so that the entire blanket's radioactivity drops substantially after a short period. Hence, limited hands-on maintenance appears feasible which should greatly simplify blanket replacement. Additional details regarding blanket radioactivity are given in Chapter XIII. Assembly and disassembly procedures for this modular blanket design have been developed. The blanket segments can be readily removed by opening the sphere in quadrants after halting the Li_2O flow. The estimated annual downtime for blanket segment replacement is nearly 2 weeks (Chapter XIV).

As mentioned earlier, the graphite front wall temperatures are sufficiently high that excessive swelling should not be a problem (Chapter XV). Also, at these temperatures the vapor pressure of carbon remains low so that thermal ablation of the graphite is insignificant. The tangential spacers parallel to the front wall will operate at nearly 650° since the amount of heat generated within them is low. At 650°C, volume changes in the graphite upon irradiation are also low. This means that the graphite temperature in the blanket are either above or below the temperature region (~850-1150°C) where excessive swelling limits graphite performance. The estimated lifetime of the blanket structure at 5 MW/m^2 wall loading is approximately 1 year.

Possible chemical reactions between the blanket's front wall and pellet materials have been investigated. At the front wall temperatures of interest (~1800°C), acetylene will be formed. The reaction rate depends on the concentrat of the unburned hydrogen isotopes in the chamber gas. For pellet desings of interest, the erosion rate can be limited to ~2 mm/yr with vacuum pumping power of less than 10 MW. Detailed analyses of the chemical compatibility between graphite and possible pellet materials are

discussed in Chapter XVI.

In summary, the blanket design used in SOLASE offers many advantages, including low cost, low weight, low induced radioactivity levels, the potential for hands-on maintenance, modular construction, low pressure, ability to decouple first wall and blanket coolant temperatures, adequate breeding, low tritium inventory and leakage, and sufficiently long life. It is particularly suitable for ICTRs since the vacuum requirements are not stringent and it is superior to blankets with metallic first walls and protective liners inasmuch as the neutron wall loading in such designs is limited by the ability to radiate the ion and photon energy deposited in the liner to the cold first wall. These designs, however, may be more suitable for magnetic confinement systems. Details of the thermal hydraulic design for the SOLASE blanket are given in the following section.

References for Section XII-B-1

1. R.W. Conn, et. al., "Studies of the Technological Problems of Laser Driven Fusion Reactors", UWFDM-190, Nuclear Eng. Dept., Univ. of Wisconsin (1976)

2. I. Finnie, "Erosion of Surfaces by Solid Particles," Wear, 3, 87-103 (1960)

3. F. A. Zenz and D. F. Othmer, Fluidization and Fluid Particle Systems, Reinhold (1960)

XII-B-2. Thermal-Hydraulic Design of the SOLASE Blanket

As indicated earlier, the SOLASE blanket is divided into sixteen segments each with a honeycomb construction (Fig. XII-B-2). Five tangential spacers are used to divide each blanket segment into six breeding zones of equal thickness. Lithium oxide particles enter the blanket at 400°C and leave at 600°C except for the outermost zone where the exit temperature is 850°C. The 850°C stream is used for tritium extraction prior to joining the main stream (600°C) on its way to the steam generators. The flow rates within the six breeding zones are adjusted independently to match the local heat generation rates.

Figure XII-B-4 shows the volumetric heat generation profile in the Li_2O blanket. The heat generation rate in the front zone is significantly higher than those in the outer zones. In addition, the lithium oxide flowing in the front zone will remove the heat convected and radiated from the back surface of the first wall. This is the heat radiated by the chamber fill gas (neon) to the first wall after the ions and soft X-rays have been stopped. This means that the power removed by the lithium oxide in the front zone will be much larger than those in the outer zones. Hence, the flow rates should be adjusted to match the power profile so that a uniform exit temperature distribution can be obtained.

Table XII-B-1 summarizes the flow rates and corresponding average velocities in the different blanket zones. These velocities are based on an average void fraction of 40% and an equivalent density of 1.20 g/cc. The particle velocity distribution within the blanket is shown in Fig. XII-B-5.

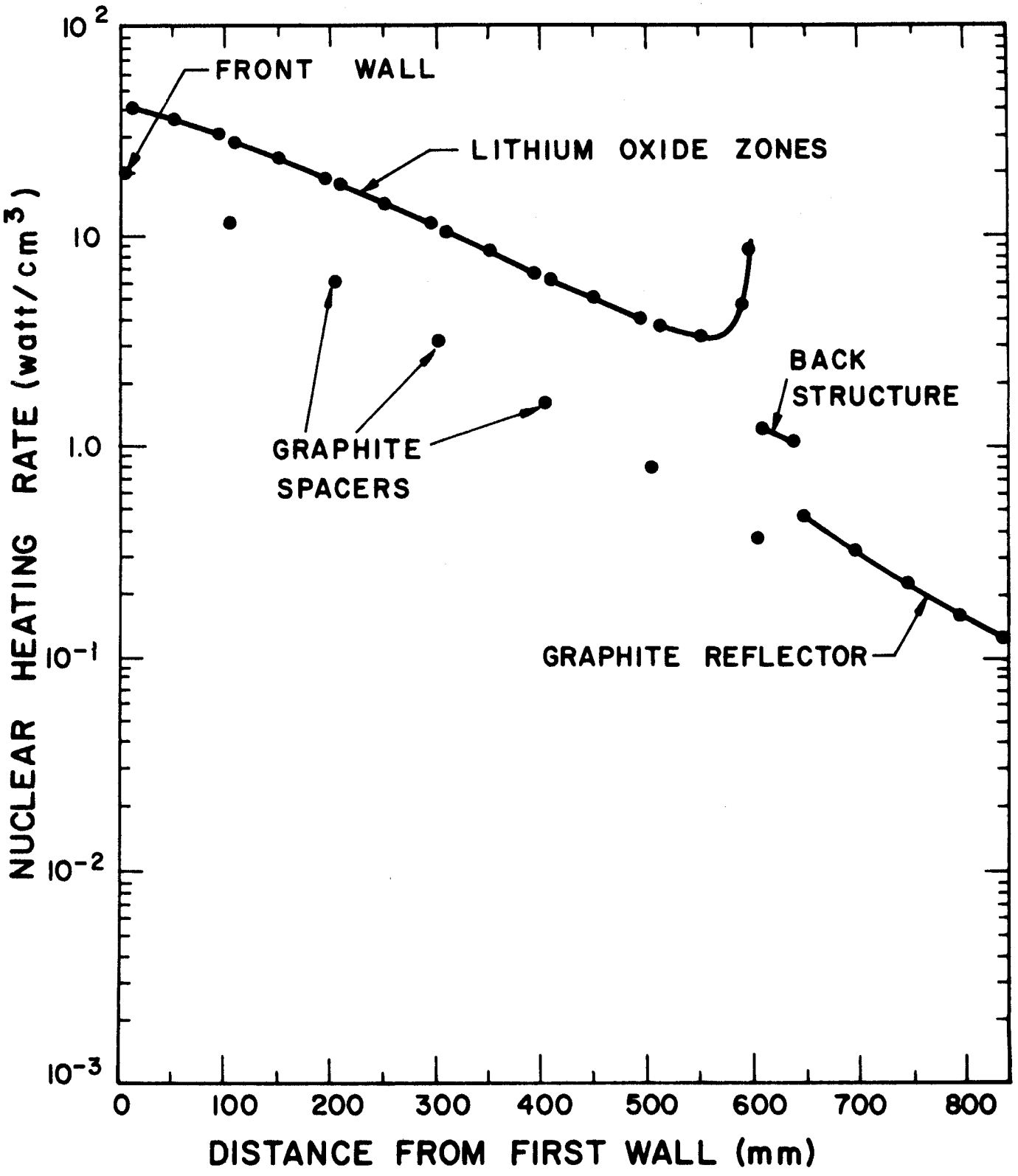

Fig. XII-B-4.

Distribution of Nuclear Heating in the SOLASE Blanket

Table XII-B-1

Blanket Thermal Hydraulic Parameters

Parameter	Blanket Zone #					
	1	2	3	4	5	6
Li_2O Inlet Temperature (^oC)	←		400			→
Li_2O Exit Temperature (^oC)	←	600			→	850
Power Removed by Li_2O (MWt)	1720	614	365	218	141	147
Li_2O Flow Rate (kg/hr)	1.72×10^7	6.13×10^6	3.65×10^6	2.18×10^6	1.41×10^6	5.88×10^5
Flow Area (m^2)	3.44	3.50	3.56	3.62	3.68	3.73
Flow Velocity (m/sec)	1.11	0.39	0.23	0.13	0.09	0.035
Particle Residence Time (sec)	17.1	49.8	86.3	149.2	236.7	588
Void Fraction	←		0.40			→
Specific Heat (cal/g^oC)			0.431			
Equivalent Density (g/cc)			1.20			
Equivalent Prandtl Number			6.03			

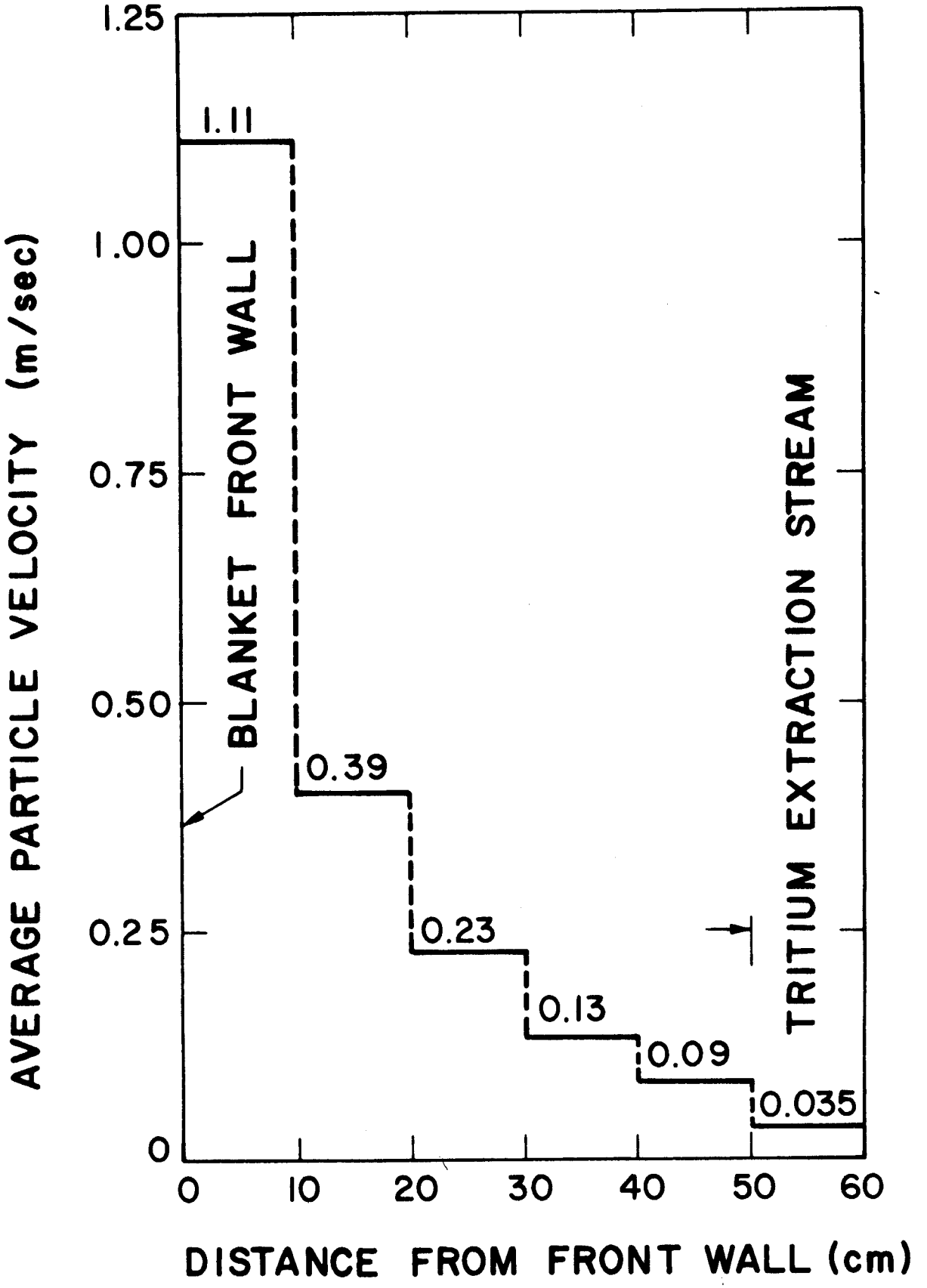

Fig. XII-B-5.

Particle Velocity Distribution Within the SOLASE Blanket

The maximum velocity is only 1.1 m/sec so that structural erosion should be insignificant for the particle sizes selected (100-200 μ in diameter).

In order to determine the inside surface temperature of the front wall, the Li_2O stream is treated as a continuum with an effective viscosity of 1.5 cp.[1] The method of Deissler and Beogli[2] is used to determine the effective thermal conductivity of the particle stream as a function of the conductivity of the solid and that of the interconnecting gas (neon at 10 torr). The conductivity of the gas is estimated using the method described in reference 3. Upon knowledge of the conductivity and viscosity of the equivalent continuum, the Reynolds and Prandtl numbers can be readily obtained. The Dittus-Boelter correlation (Eq. XII-B-1) is then used to determine the effective Nusselt number, and hence the heat transfer coefficient, for the Li_2O stream. Values of the convective heat transfer coefficients in the different blanket zones are given in Table XII-B-2.

$$Nu = 0.023\ Re^{0.8}\ Pr^{0.4} \qquad \text{(XII-B-1)}$$

The temperature distribution in the different tangential spacers has been calculated. Heat conduction along the flow direction and curvature effects have been ignored so that the temperature distributions in these spacers with uniform volumetric heating are parabolic. Values of the surface temperatures of the different tangential spacers based on the heat transfer coefficients in Table XII-B-2 are given in Table XII-B-3. The front

Table XII-B-2

Blanket Heat Transfer Parameters

Parameter	Blanket Zone Number					
	1	2	3	4	5	6
Reynolds Number	1.13×10^5	3.95×10^4	2.31×10^4	1.36×10^4	8.67×10^3	3.55×10^3
Nusselt Number	458	198	129	84.2	58.8	28.8
Convective Heat Transfer Coefficient ($W/cm^2\ ^oK$)	0.163	0.070	0.046	0.030	0.021	0.011

wall temperatures account for radiative heat transfer between the wall and the particle stream; an emissivity of 0.90 is used for the back surface of the graphite wall. The effect of the uncertainty in the value of the convective heat transfer coefficient on the front wall back surface temperature is shown in Fig. XII-B-6. The corresponding maximum front surface temperature is less than 2000°C so that surface evaporation is insignificant.

The radial supports of the blanket will act as cooling fins. For the first zone, the temperature in the radial support will drop from a maximum of 1429°C at the back surface of the front wall to a minimum of 640°C at the surface of the first tangential spacer (Table XII-B-3). The radial support can be treated as a simple rectangular fin with uniform volumetric heating so that the radial temperature distribution is given by:(4)

$$\frac{T-T_\infty}{T_0-T_\infty} = R + (1 - R) \left\{\frac{\cosh m_0 (L-x)}{\cosh m_0 L}\right\} \qquad \text{(XII-B-2)}$$

where,

$$R \equiv \text{generation ratio} = q''' / m^2 k (T_0-T_\infty)$$

$$m^2 = 2h/k\delta \ .$$

Here, q''' is the average volumetric heat generation rate, h is the heat transfer coefficient, k is the thermal conductivity of the graphite spacer, δ is the thickness of the radial support, T_0 is the base temperature and T_∞ is the temperature at x = L. Values of the radial support temperatures

Table XII-B-3

Surface Temperatures of Tangential Spacers in the SOLASE Blanket*

Temperature (^{o}C)	Front Wall	Spacer Number 1	2	3	4	5	Back Wall
$T^{(-)}$	1800	644 (659)	658 (672)	656 (669)	655 (663)	739 (753)	630
$T^{(+)}$	1429 (1521)/	640 (653)	654 (668)	654 (667)	653 (661)	745 (755)	626
T_{max}	1800	653 (670)	662 (677)	659 (672)	656 (665)	745 (755)	630

* These temperatures are calculated at the exit temperature where the lithium oxide temperature is maximum (either 600 or 850^{o}C). T^{-} is the temperature at surface closer to cavity center; T^{+} is temperature at other surface, and T_{max} is maximum temperature within the 6.5 mm thick spacers.

/ Values in parenthesis correspond to a 25% uncertainty in the heat transfer coefficients given in Table XII-B-2.

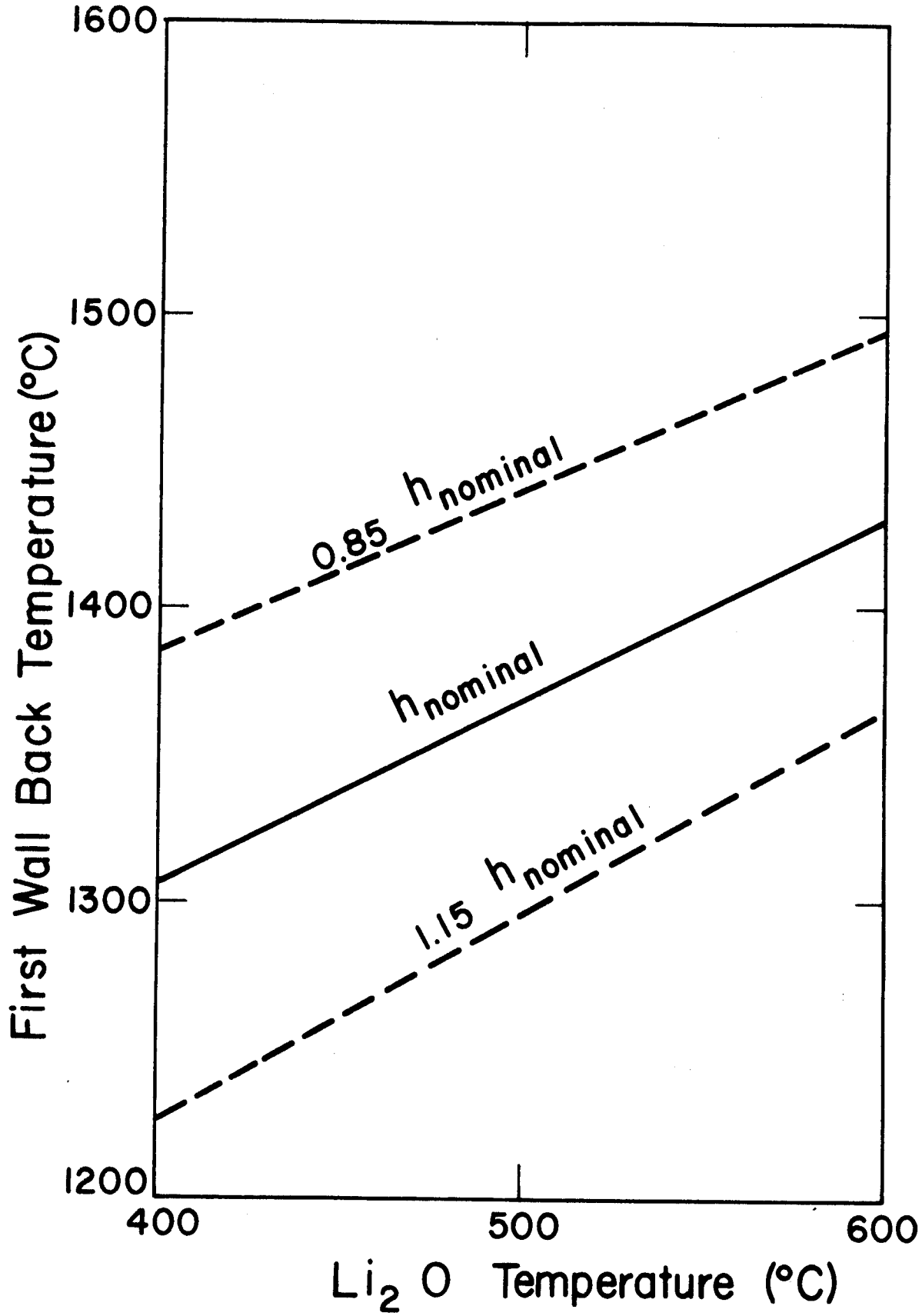

Fig. XII-B-6.
Temperature Distribution of Back Surface

at different locations are given in Table XII-B-4. These temperatures are important in calculating the stresses produced by differential swelling in the blanket (Chapter XV).

The number of radial supports in each of the sixteen blanket segments is determined so that the maximum stress produced by the impulse loading on the blanket front wall is limited to less than 3000 psi. Figure XII-B-7 shows the variation of pressure at the front wall of the blanket. This periodic impulse is produced by the shock wave generated in the cavity fill gas (neon) after the X-ray and ion energy is deposited. The dynamic load factor for different pulse shapes and durations can be obtained from Fig. XII-B-8. We have set the dynamic load factor equal to its maximum value of 2.0 and determined the maximum dynamic flexural stress (Fig. XII-B-9). Setting the maximum allowable stress to $\leq$ 3000 psi we determined the required number of radial supports to be $\geq$ 5. A schematic showing the evolution of blanket segment design in SOLASE is shown in Fig. XII-B-10.

References for Section XII-B-2

1. D. K. Sze, et al., "Gravity Circulated Blanket Design for a Tokamak Fusion Reaction", Proc. 2nd Topical Meeting on the Technology of Controlled Nuclear Fusion, Richland (1976).

2. R. G. Deissler and J. S. Boegli, "An Investigation of Effective Thermal Conductivities of Powders in Various Gases", ASME Trans. (October 1958).

3. R. B. Bird, W. E. Stewart, and E. N. Lightfoot, Transport Phenomena, Wiley (1960).

4. M. M. El-Wakil, Nuclear Heat Transport, Intext (1971).

Table XII-B-4

Temperature Distribution in Blanket Radial Support*

Location (cm)	Temperature (^{o}C)
0.0	1429
1.0	919
2.0	754
3.0	702
4.0	687
5.0	665
10.0	640

*Values correspond to nominal convective heat transfer coefficient in Table XII-B-2. These temperatures are evaluated at the lithium oxide exit where T_{Li_2O} = 600^{o}C.

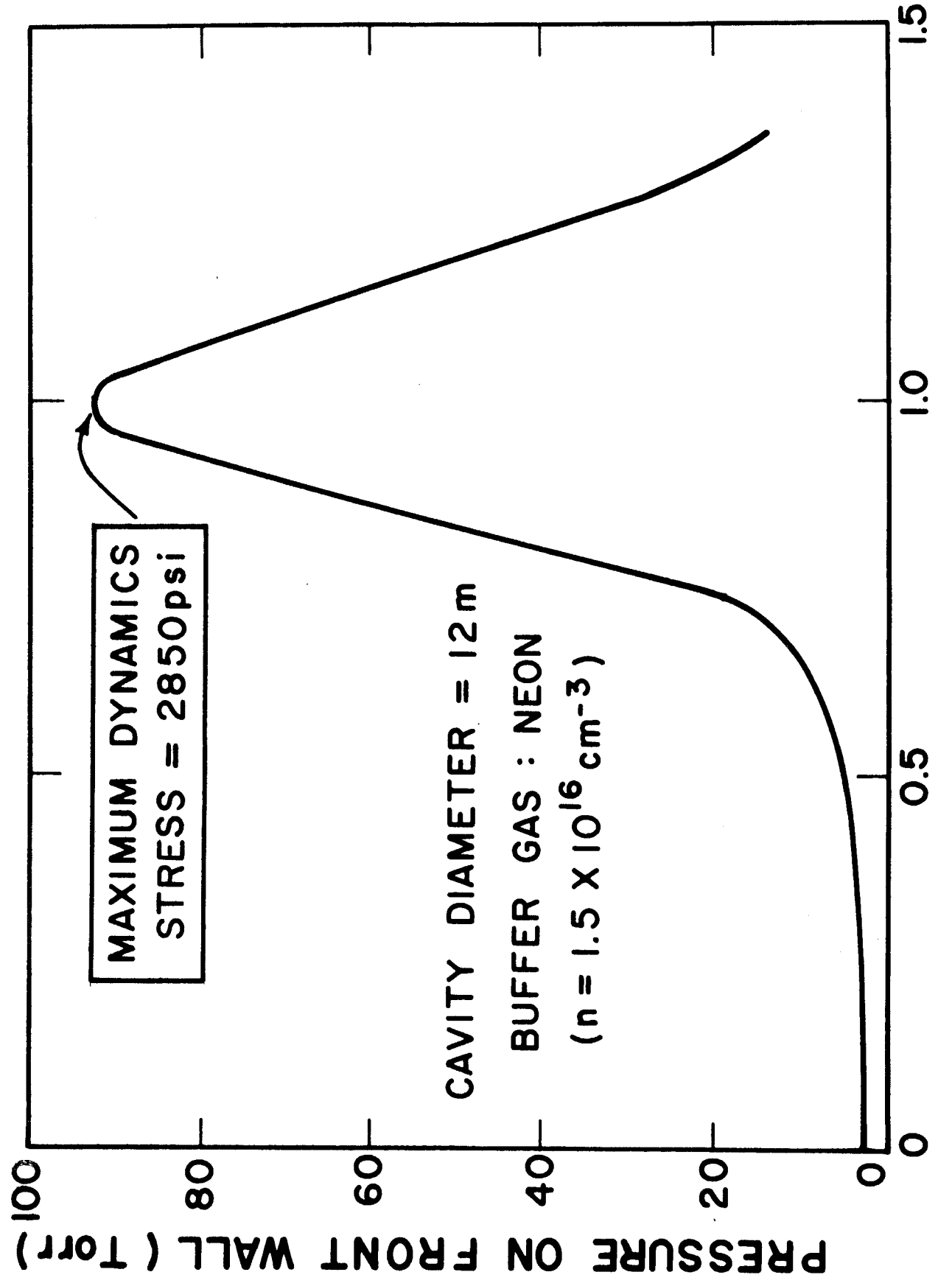

Fig. XII-B-7. Pressure as a Function of Time at the Blanket Front Wall

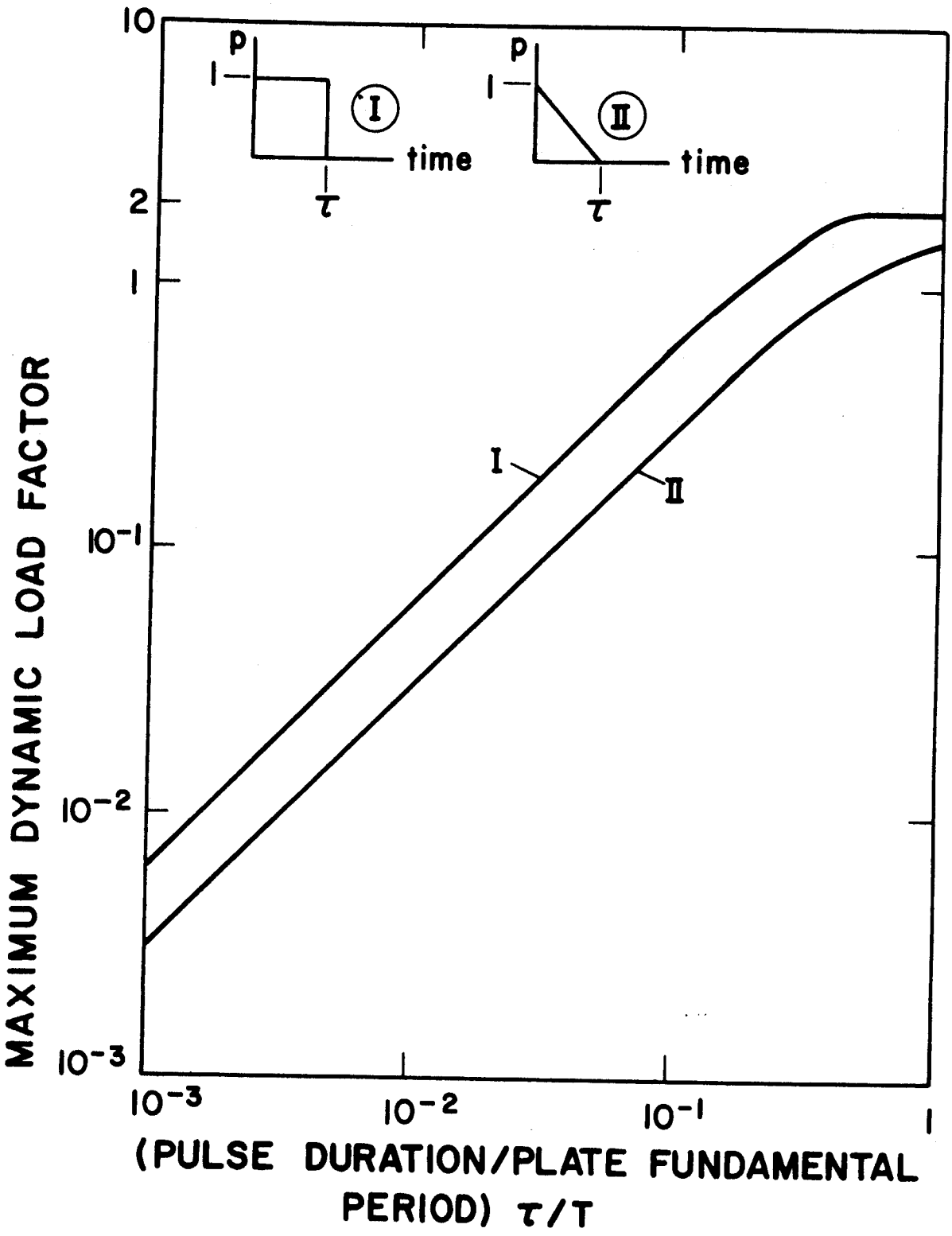
10
2
1
10^{-1}
10^{-2}
10^{-3}
p
1
I
time
τ
p
1
II
time
τ
I
II
MAXIMUM DYNAMIC LOAD FACTOR
10^{-3}
10^{-2}
10^{-1}
1
(PULSE DURATION/PLATE FUNDAMENTAL PERIOD) τ/T

Fig. XII-B-8.

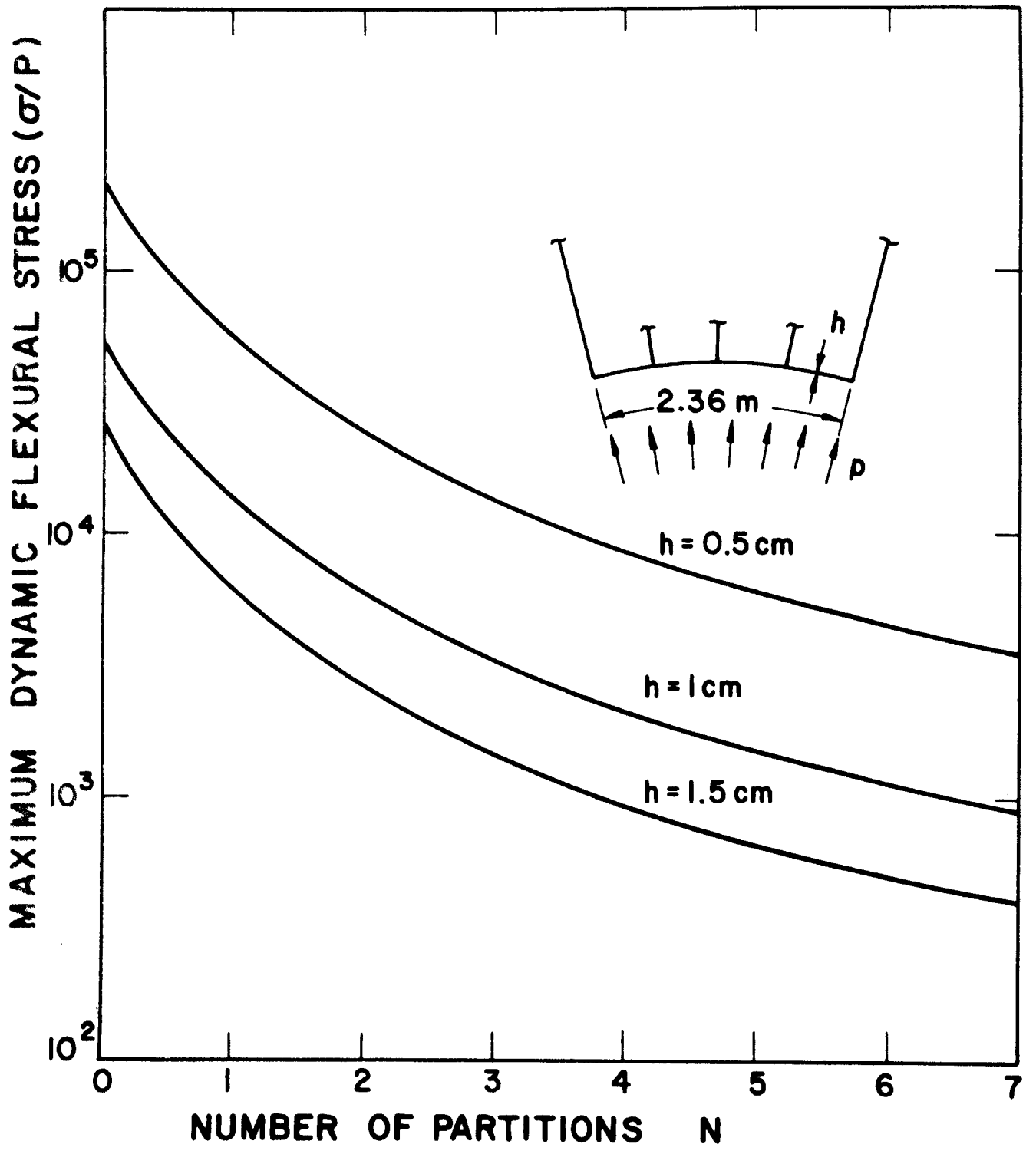

Fig. XII-B-9. Span to Thickness Ratio (1/

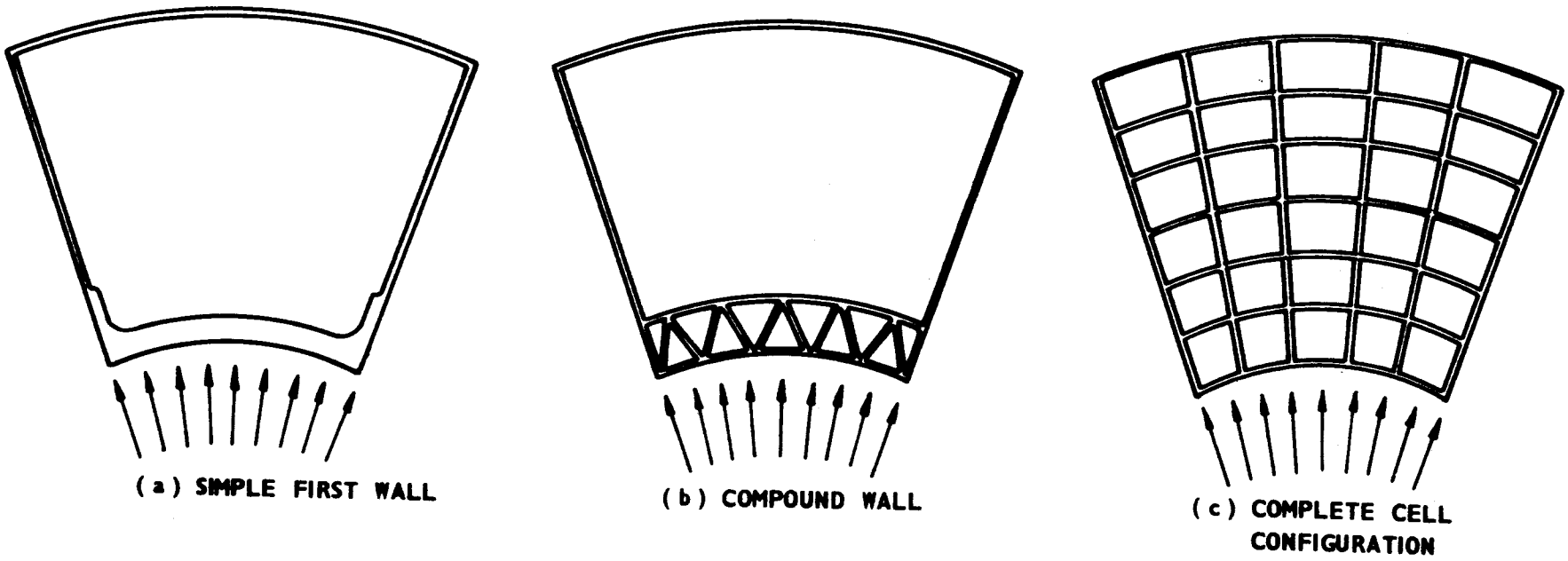

Fig. XII-B-10.
Evolution of First Wall/Blanket Structure Design for Radial Pressure.
Horizontal Section/Meridional View

XII-B-3. Closure

The unique blanket design used in SOLASE offers many advantages, including low cost, low weight, low induced radioactivity levels, the potential for hands-on maintenance, modular construction, low pressure, ability to decouple first wall and blanket coolant temperatures, adequate breeding, low tritium inventory and leakage, and sufficiently long life. The blanket's front wall can readily accommodate the microexplosion both thermally and mechanically. This blanket design is particularly suitable for ICTRs since the vacuum requirements are not stringent and it is superior to blankets with metallic first walls and protective liners inasmuch as the neutron wall loading in such designs is limited by the ability to radiate the ion and photon energy deposited in the liner to the cold first wall. These designs, however, may be more suitable for magnetic confinement systems.

XIII. Blanket Neutronics Analyses and Shield Design for SOLASE

XIII-A. Introduction

Neutronics and shielding studies are important aspects of any conceptual reactor design. Unique, however, to laser fusion is the possible importance of time dependent neutronics and associated rate effects in materials. In this chapter, we present the results of the steady state neutronics analysis of the blanket, time dependent neutronics theory and analysis of the first wall and blanket response, blanket shielding studies, calculations of blanket and shield radioactivity, afterheat, and biological hazard indicators.

The calculated neutron and gamma irradiation response of candidate laser mirror materials is exposed. A three-dimensional Monte Carlo analysis of the laser beam penetration, mirrors and shield system is under way, and reveals the existence of a serious radiation leakage problem. The findings of the latter will be reported at a future date.

XIII-B. Time Integrated (Steady State) Neutronics Studies

XIII-B-1. Calculational Method

If the time-dependent flux $\phi(\underline{r},\Omega,E,t)$ is available, the (time) overall spatial nuclear response, R(r), can be estimated as

$$R(r) = \int d\underline{\Omega} \int\int \Sigma_R(\underline{r},E)\phi(\underline{\gamma},\underline{\Omega},E,t)dtdE \ .$$

However, the time-dependent transport equation can be transformed into a time-independent form by integrating over a certain (time) period to the equation itself. Let us define

$$\Phi(\underline{r},\underline{\Omega},E) = \int \phi(\underline{r},\underline{\Omega},E,t)dt$$

and

$$S(\underline{r},\underline{\Omega},E) = \int s(\underline{r},\underline{\Omega},E,t)dt \ ,$$

the time-dependent (time integrated) form becomes

$$L(\underline{r},\underline{\Omega},E)\Phi(\underline{r},\underline{\Omega},E) = S(\underline{r},\underline{\Omega},E) \ ,$$

which is equivalent to a steady-state transport form, and the (time) overall nuclear response can be evaluated from the simple relation

$$R(\underline{r}) = \int \Sigma_R(\underline{r},E) \int \Phi(\underline{r},\underline{\Omega},E)d\underline{\Omega}dE \ .$$

In the following, the time-integrated angular flux $\Phi(\underline{r},\underline{\Omega},E)$ has been obtained numerically using the steady-state transport code, ANISN[1]. The neutron source introduced here corresponds to the neutron

density produced in the single laser induced pellet fusion event. The neutronics calculations have been performed using the P_3-S_8 approximation in spherical geometry.

The total number of neutrons produced in laser fusion explosions in a time period of one second is ~ 1.002×10^{21} assuming an equivalent time-averaged neutron wall loading of 5 MW/m^2. The radius of the cavity chamber is 6 meters. The total energy which will be recovered in this system is ~ 3000 MW. The nuclear data used is given elsewhere[2] and has been collapsed into coupled neutron-gamma cross section sets with 25 neutron and 21 gamma energy groups. The new neutron and gamma energy group structures are given in Tables XIII-B-1 and XIII-B-2, respectively.

XIII-B-2. Blanket Model and Survey Calculations

The schematic of the blanket is shown in Fig. XIII-B-1. It is structurely made of three-dimensional (woven) graphite. The cooling and breeding medium is the gravitational flowing lithium-oxide particles. Both the packing fraction of the 3-D graphite weave and the lithium oxide particles are 6
An albedo of 0.3 is used in all the calculations to simulate the effect of the shield. In the following, several survey calculations will be performed in order to meet the essential blanket design criterions. Two of the most important design criteria are as follows: the tritium breeding ratio must exceed ~ 1.10 in a one-dimensional calculation; and the energy deposition in the blanket region should be as

Table XIII-B-1

Neutron 25 Energy Group Structure in eV

Group Limits

Group	E(Top)	E(Low)	E(Mid Point)
1	1.4918 (+7)	1.3499 (+7)	1.4208 (+7)
2	1.3499 (+7)	1.2214 (+7)	1.2856 (+7)
3	1.2214 (+7)	1.1052 (+7)	1.1633 (+7)
4	1.1052 (+7)	1.0000 (+7)	1.0526 (+7)
5	1.0000 (+7)	9.0484 (+6)	9.5242 (+6)
6	9.0484 (+6)	8.1873 (+6)	8.6178 (+6)
7	8.1873 (+6)	7.4082 (+6)	7.7979 (+6)
8	7.4082 (+6)	6.7032 (+6)	7.0557 (+6)
9	6.7032 (+6)	6.0653 (+6)	6.3843 (+6)
10	6.0653 (+6)	5.4881 (+6)	5.7787 (+6)
11	5.4881 (+6)	4.4933 (+6)	4.9907 (+6)
12	4.4933 (+6)	3.6788 (+6)	4.0860 (+6)
13	3.6788 (+6)	3.0119 (+6)	3.3453 (+6)
14	3.0119 (+6)	2.4660 (+6)	2.7390 (+6)
15	2.4660 (+6)	1.3534 (+6)	1.9097 (+6)
16	1.3534 (+6)	7.4274 (+5)	1.0481 (+6)
17	7.4274 (+5)	4.0762 (+5)	5.7518 (+5)
18	4.0762 (+5)	1.6573 (+5)	2.8667 (+5)
19	1.6573 (+5)	3.1828 (+4)	9.8779 (+4)
20	3.1828 (+4)	3.3546 (+3)	1.7591 (+4)
21	3.3546 (+3)	3.5358 (+2)	1.8541 (+3)
22	3.5358 (+2)	3.7267 (+1)	1.9542 (+2)
23	3.7267 (+1)	3.9279 (+0)	2.0597 (+1)
24	3.9279 (+0)	4.1399 (-1)	2.1718 (+0)
25	4.1399 (-1)	2.200 (-2)	2.1800 (-1)

Table XIII-B-2

Gamma-Ray Energy Group Structure in MeV

Group Limits

Group	E(Top)	E(Low)	E(Mid Point)
1	14.00	12.00	13.00
2	12.00	10.00	11.00
3	10.00	8.00	9.00
4	8.00	7.50	7.75
5	7.50	7.00	7.25
6	7.00	6.50	6.75
7	6.50	6.00	6.25
8	6.00	5.50	5.75
9	5.50	5.00	5.25
10	5.00	4.50	4.75
11	4.50	4.00	4.25
12	4.00	3.50	3.75
13	3.50	3.00	3.25
14	3.00	2.50	2.75
15	2.50	2.00	2.25
16	2.00	1.50	1.75
17	1.50	1.00	1.25
18	1.00	0.40	0.70
19	0.40	0.20	0.30
20	0.20	0.10	0.15
21	0.10	0.01	0.055

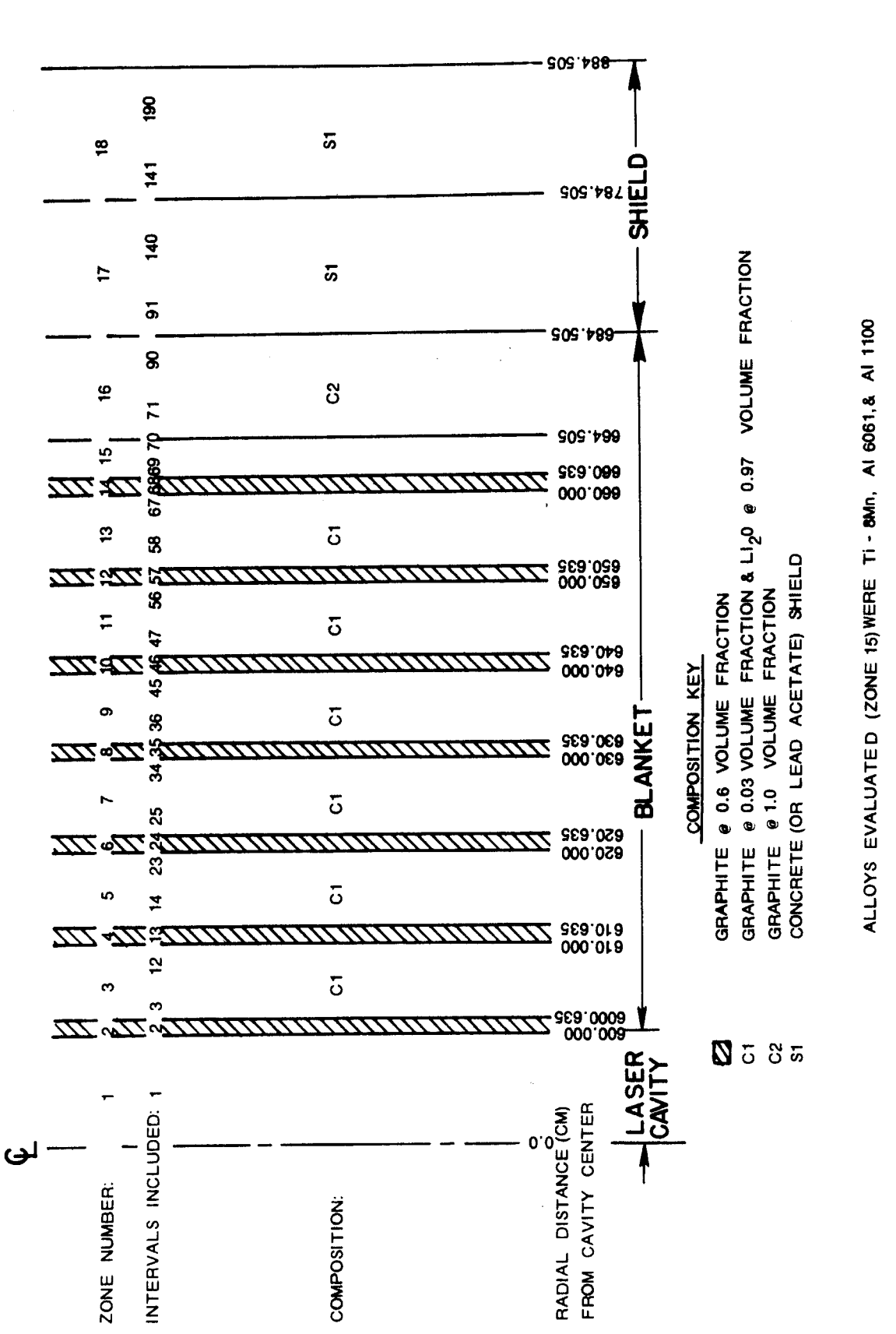
ONE-DIMENSIONAL SCHEMATIC OF LASER FUSION BLANKET & SHIELD
ZONE NUMBER:
INTERVALS INCLUDED:
COMPOSITION:
RADIAL DISTANCE (CM) FROM CAVITY CENTER
0.0
600.000
600.635
610.000
610.635
620.000
620.635
630.000
630.635
640.000
640.635
650.000
650.635
660.000
660.635
664.505
684.505
784.505
884.505
LASER CAVITY
BLANKET
SHIELD
C1
C2
S1
COMPOSITION KEY
GRAPHITE @ 0.6 VOLUME FRACTION
GRAPHITE @ 0.03 VOLUME FRACTION & Li2O @ 0.97 VOLUME FRACTION
GRAPHITE @ 1.0 VOLUME FRACTION
CONCRETE (OR LEAD ACETATE) SHIELD
ALLOYS EVALUATED (ZONE 15) WERE Ti - 8Mn, Al 6061, & Al 1100
ALL GRAPHITE WITH 5PPM OF (Si,Fe,Al, & Mg) EACH

Fig. XIII-B-1.

high as possible. The varying parameters in these survey calculations are the cooling/breeding medium and graphite reflector thicknesses. In order to perform the one-dimensional calculations, we have homogenized the structural material and the cooling/breeding material in the blanket breeding zone and the calculational model is shown in Table XIII-B-3. Here the breeding zone is a homogenized region of 9.6% graphite and 90.4% Li_2O with a density factor of 60%. The as yet to be determined thicknesses of the breeding and graphite reflector zones are "x" and "y" meters, respectively. The survey calculations are performed for two sets of graphite reflector thickness, 0.2 and 0.4 m. In turn, two calculations were done with the 0.4 m graphite reflector using a breeding zone thickness of 0.3 and 0.6 m. Also, three calculations were done for the 0.2 m reflector case with breeding zone thickness at 0.3, 0.5 and 0.6 m. The results are tabulated in Table XIII-B-4. One notes that as the graphite reflector becomes thicker (from 0.2 to 0.4 m), the tritium breeding ratio increases from 1.039 to 1.070 for a 0.3 m breeding zone thickness, and from 1.298 to 1.304 for a breeding zone thickness of 0.6 m. Thus, the maximum increment in the tritium breeding ratio is only ~3% in the range of breeding zone thickness surveyed here. The total energy increment is at most ~1%, from 14.14 to 14.27 MeV per D-T neutron for a breeding zone thickness of 0.3 m. Hence we conclude that the tritium breeding ratio and total nuclear heating in the system will not be affected significantly by the graphite reflector thickness as discussed in Ref. 3. A graphite reflector thickness of 0.2 m will be chosen for the final design.

Table XIII-B-3

Neutronic Calculational Model Zone Thickness and Material Composition

Zone No.	Thickness (m)	Material Composition
1	6	Vacuum
2	x	9.6% Graphite + 90.4% Li_2O (D.F. = 0.6)
3	y	Graphite

Table XIII-B-4

Nucleonic Characteristics for the Graphite-Structured Blanket With Varying Breeding Zone and Reflector Thicknesses

Case No.	Breeding Zone Thickness, m	Graphite Reflector Thickness, m	Tritium Breeding Ratio (T/D-T Neutron)	Total Nuclear Heating[a] (MeV/D-T Neutron)	Fraction of Total Energy[b] Deposited in the Breeding Zone, %
1	0.3	0.4	1.070	14.27	76.7
2	0.6	0.4	1.304	15.11	96.0
3	0.3	0.2	1.039	14.14	79.0
4	0.5	0.2	1.249	14.91	93.7
5	0.6	0.2	1.298	15.08	96.5

a. Nuclear energy leakage to the shield is included.

b. The blanket defined here consists of the breeding and reflector zones.

Also from Table XIII-B-4, we see that for a graphite reflector thickness of 0.2 m, the increment of the tritium breeding ratio is ~20% and as the breeding zones thickness increases from 0.3 to 0.5 m but only 5% as it is increased from 0.5 to 0.6 m. We have also found that a tritium breeding ratio of more than 1.10 cannot be obtained unless the breeding zone thickness exceeds about 0.35 m (the values mentioned here which are not listed in Table 4 are approximate estimates using the variational interpolation technique[4]). Now that the fraction of total energy deposited in the breeding zone should be as high as possible. A breeding zone thickness of ~0.35 m giving a breeding ratio of about 1.1 is not truly a good design from this standpoint since the fraction of energy deposition will only be ~83%. Hence, we will need ~0.6 m of the breeding zone thickness in order to obtain the highest value of energy deposition in the breeding zone and in the blanket overall.

XIII-B-3. Final Blanket Model and Nuclear Analysis

The final optimized blanket design is as illustrated in Table XIII-B-5. This blanket consists of a graphite first wall of 6.35 mm (zone 2), six regions of the breeding medium, each 93.65 mm with homogenized material of 3% graphite and 97% Li_2O, six additional graphite grid regions of 6.35 mm between and after breeding regions (zone 3 through 14), a 12.70 mm Al-6061 wall, a 25.0 mm H_2O zone, a 1.0 mm Al-6061 wall, and a graphite reflector of 200 mm. The density factor in the graphite wall/grid and breeding regions are 60% which represent the packing fractions. The aluminum walls and water

Table XIII-B-5

Final Blanket Model for the Neutronics Analysis

Zone No.	Thickness (mm)	Material Composition	Density Fac
1	6000	Vacuum	0.0
2	6.35	Graphite	0.6
3	93.65	3% Graphite + 97% Li_2O	0.6
4	6.35	Graphite	0.6
5	93.65	3% Graphite + 97% Li_2O	0.6
6	6.35	Graphite	0.6
7	93.65	3% Graphite + 97% Li_2O	0.6
8	6.35	Graphite	0.6
9	93.65	3% Graphite + 97% Li_2O	0.6
10	6.35	3% Graphite + 97% Li_2O	0.6
11	93.65	3% Graphite + 97% Li_2O	0.6
12	6.35	3% Graphite + 97% Li_2O	0.6
13	93.65	3% Graphite + 97% Li_2O	0.6
14	6.35	3% Graphite + 97% Li_2O	0.6
15	12.70	Al-6061	1.0
	25.0	H_2O (400°C)	0.5
	1.0	Al-6061	1.0
16	200	Graphite	1.0

region (zone 15) are the back cooling tubes where the density factor in the water region is 50% to account for boiling. The density factor in the (bulk) graphite reflector is unaffected and is taken at 100%.

The neutronics calculation has been performed for the above blanket model and the results are summarized and discussed as follows.

XIII-B-3-a. Tritium Breeding

The tritium production rates are 0.8233 and 0.5068 from $^{6}Li(n,\alpha)$ and $^{7}Li(n,n'\alpha)$ reactions per D-T neutron, respectively. The total tritium breeding ratio is therefore 1.3301 which is more than adequate. The tritium production rates by zone are tabulated in Table XIII-B-6. The spatial distribution of the $^{6}Li(n,\alpha)$ and $^{7}Li(n,n'\alpha)$ reactions per D-T neutron are given in Fig. XIII-B-2.

XIII-B-3-b. Nuclear Heating

The total nuclear heating in this blanket is 15.31 MeV per D-T neutron of which ~ 8% comes from gamma-ray heating. The nuclear energy deposition rates by zone are tabulated in Table XIII-B-7. Note the fraction of energy deposited in the blanket other than the graphite reflector zone, i.e., zone 2 through zone 15 is ~ 96.5%. The spatial nuclear heating rate is depicted in Fig. XIII-B-3. Adding the 3.52 MeV per event from alphas gives a total fusion energy of 18.83 MeV per D-T fusion event.

XIII-B-3-c. Gas Production and Displacement per Atom

Nuclear transmutation, gas production and displacement per atom rates are important measures for the radiation damage to materials. The spatial distribution of nuclear transmutations as well as gas production reactions

Table XIII-B-6

Tritium Production Rates by Zone
(T/D-T Neutron)

Zone	$^{6}Li(n,\alpha)T$ (T_6)	$^{7}Li(n,n'\alpha)T$ (T_7)	T_6+T_7
3	0.2029	0.2196	0.4225
5	0.1810	0.1359	0.3169
7	0.1476	0.0763	0.2239
9	0.1118	0.0414	0.1532
11	0.0806	0.0221	0.1027
13	0.0994	0.0115	0.1109
Total	0.8233	0.5068	1.3301

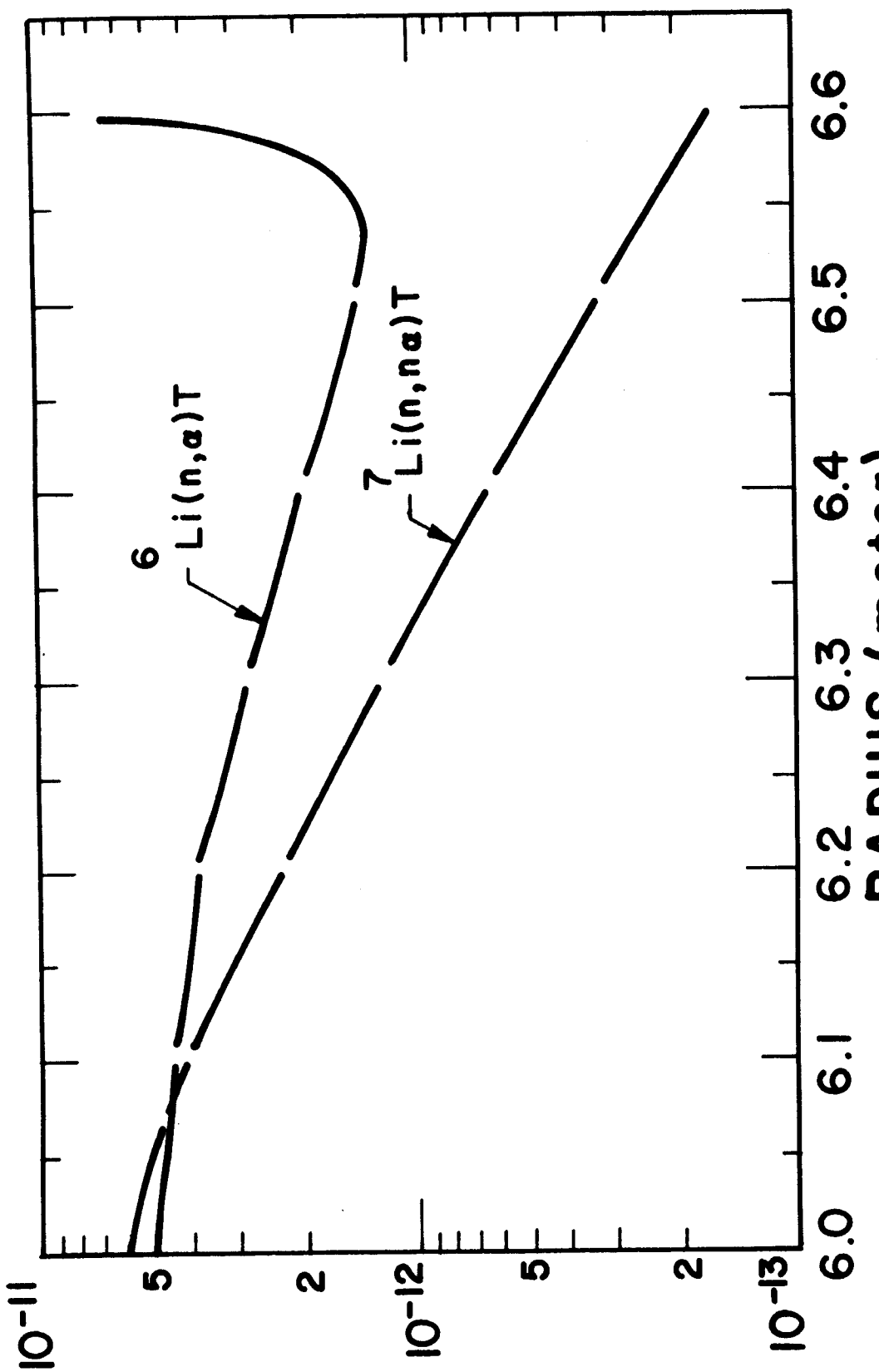

Fig. XIII-B-2.
Spatial Distribution of Tritium Production $^{6}Li(n,\alpha)$ and $^{7}Li(n,n'\alpha)$ Rates in the Blanket Breeding Region

Table XIII-B-7

Nuclear Energy Deposition Rates by Zone
(MeV/D-T Neutron)

Zone	Neutron Heating	Gamma Heating	Total Heating
2	0.1669	0.0221	0.1890
3	4.8258	0.1824	5.0082
4	0.1063	0.0278	0.1341
5	3.3440	0.1701	3.5141
6	0.0640	0.0152	0.0792
7	2.1776	0.1715	2.3491
8	0.0356	0.0153	0.0509
9	1.3876	0.1033	1.4904
10	0.0194	0.0115	0.0309
11	0.8787	0.0789	0.9576
12	0.0104	0.0090	0.0194
13	0.7662	0.0657	0.8319
14	0.0051	0.0082	0.0133
15	0.0802	0.0523	0.1325
16	0.1184	0.2427	0.3611
Subtotal	13.9862	1.1760	15.1622
Leakage to the Shield	0.0583	0.0928	0.1511
Total	14.0445	1.2688	15.3133

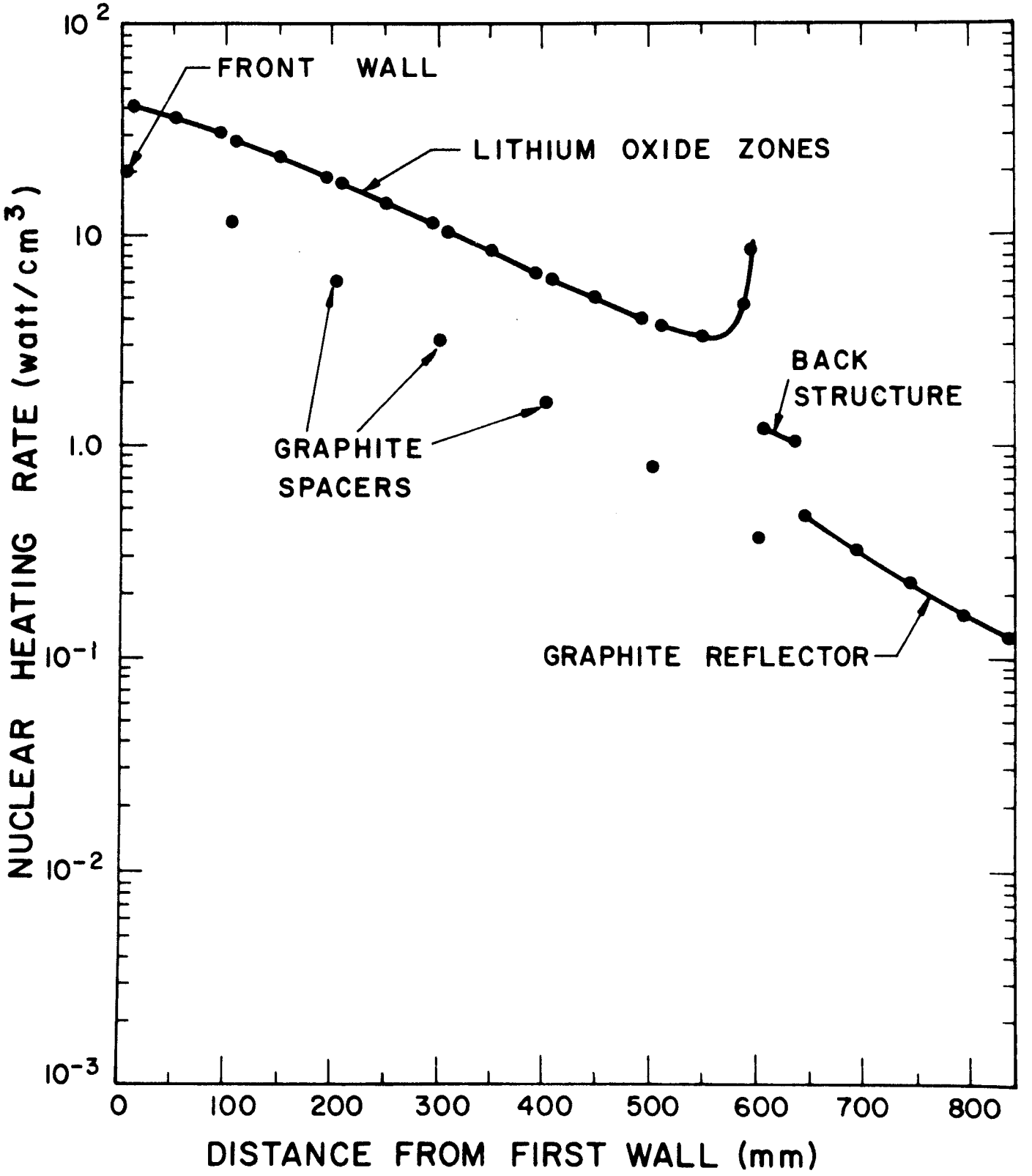

Fig. XIII-B-3.
Spatial Variation of Volumetric Heating Rate in the Blanket

such as C(n,n')3α, C(n,α), O(n,α), O(n,p) and O(n,d) reactions are given in Fig. XIII-B-4. The helium production and atom displacement rates in the graphite structure are particularly important and are depicted in Fig. XIII-B-5. Note the helium production and displacement per atom rates in the first wall are ~ 1500 appm and ~ 6.5 dpa per year per MW/m^2 wall loading, respectively.

XIII-B-3-d. Neutron Scalar Fluxes and Leakages

The neutron scalar flux at the first wall, the first breeding region, the fourth graphite grid region (zone 8), the subsequent breeding region (zone 9), the last breeding region (zone 13) and the last graphite grid region (zone 14) are sketched in Fig. XIII-B-6. Note the shape of the high energy neutron flux (> 20 KeV) is roughly preserved (albeit attenuated overall) as the breeding medium becomes thicker. The integrated neutron scalar fluxes are given in Fig. XIII-B-7. Also given in this figure are the total (neutron and gamma ray) particle and energy leakage. At the first wall, the leakage is due to neutrons only. However, at the back of the graphite reflector, the particle leakage is 0.08 with ~ 45% contributed by neutrons. The energy leakage there is about 1% of the incoming D-T neutron energy and approximately 33% is contributed by leaking neutrons.

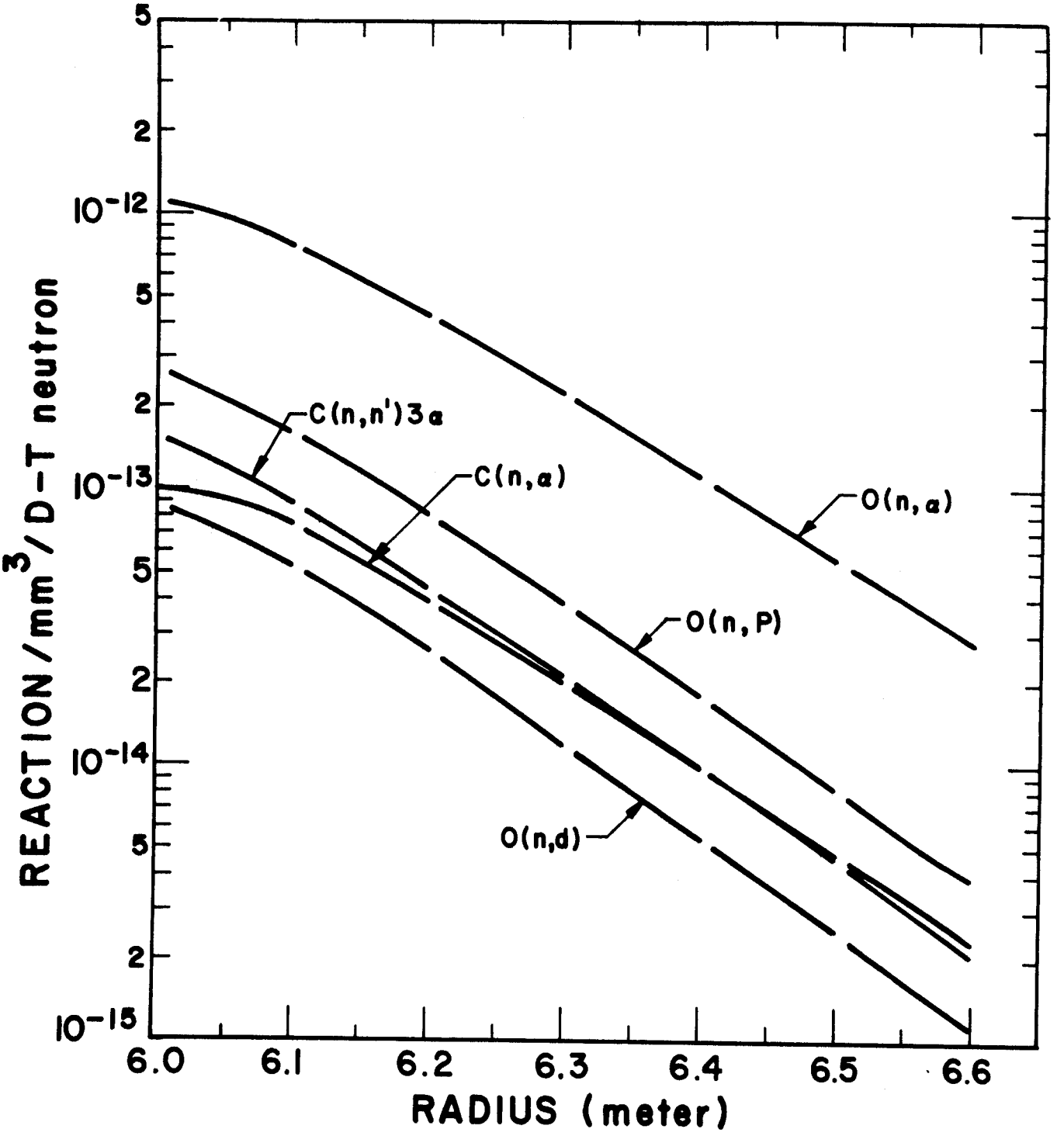

Fig. XIII-B-4.
Spatial Distribution of Gas Production Rates in the Blanket Breeding Region.

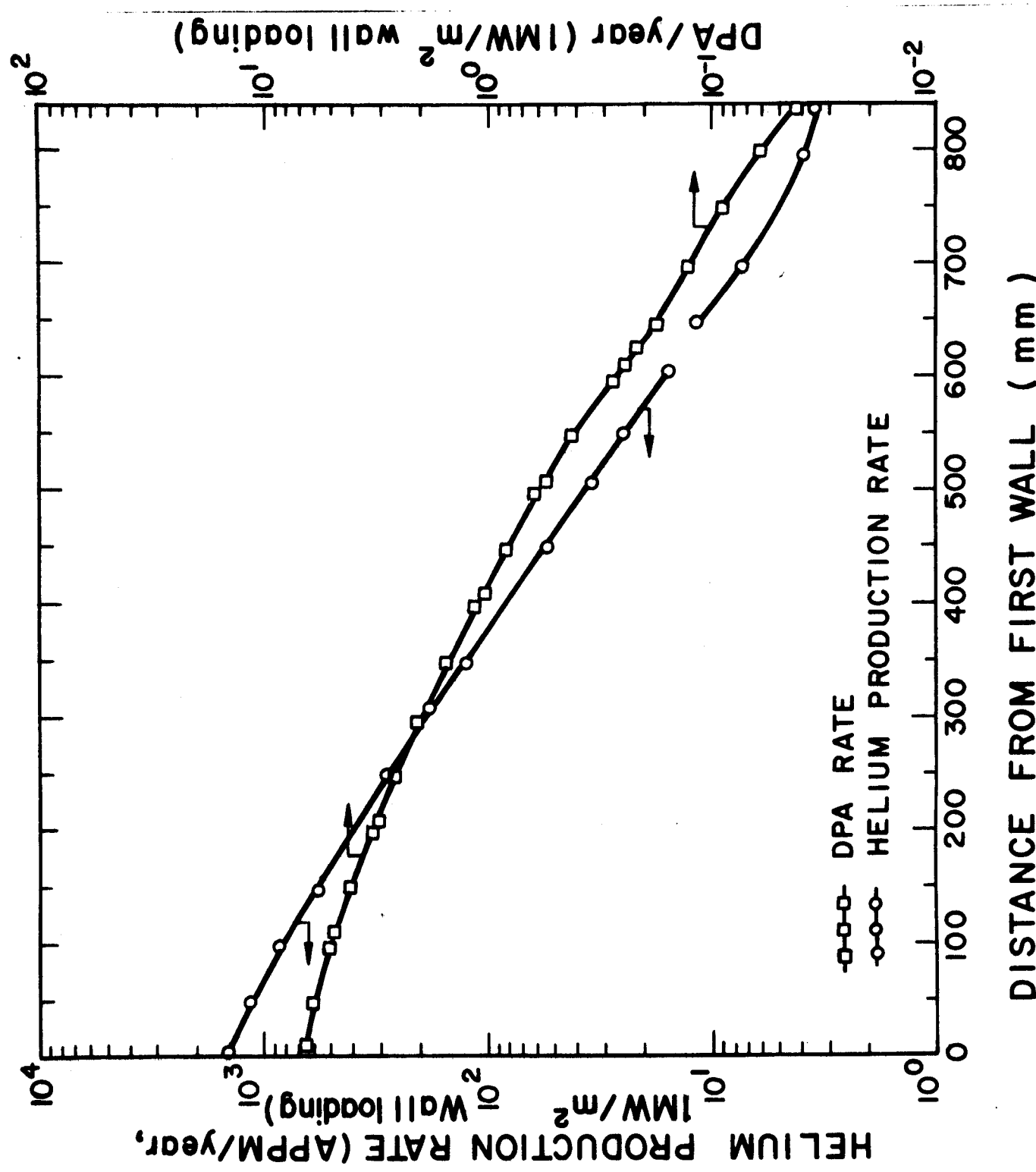

Fig. XIII-B-5.

Spatial Distribution of Helium Production and DPA Rates in the Graphite Structure in the Blanket Normalized to a Wall Loading of 1 MW/m^2.

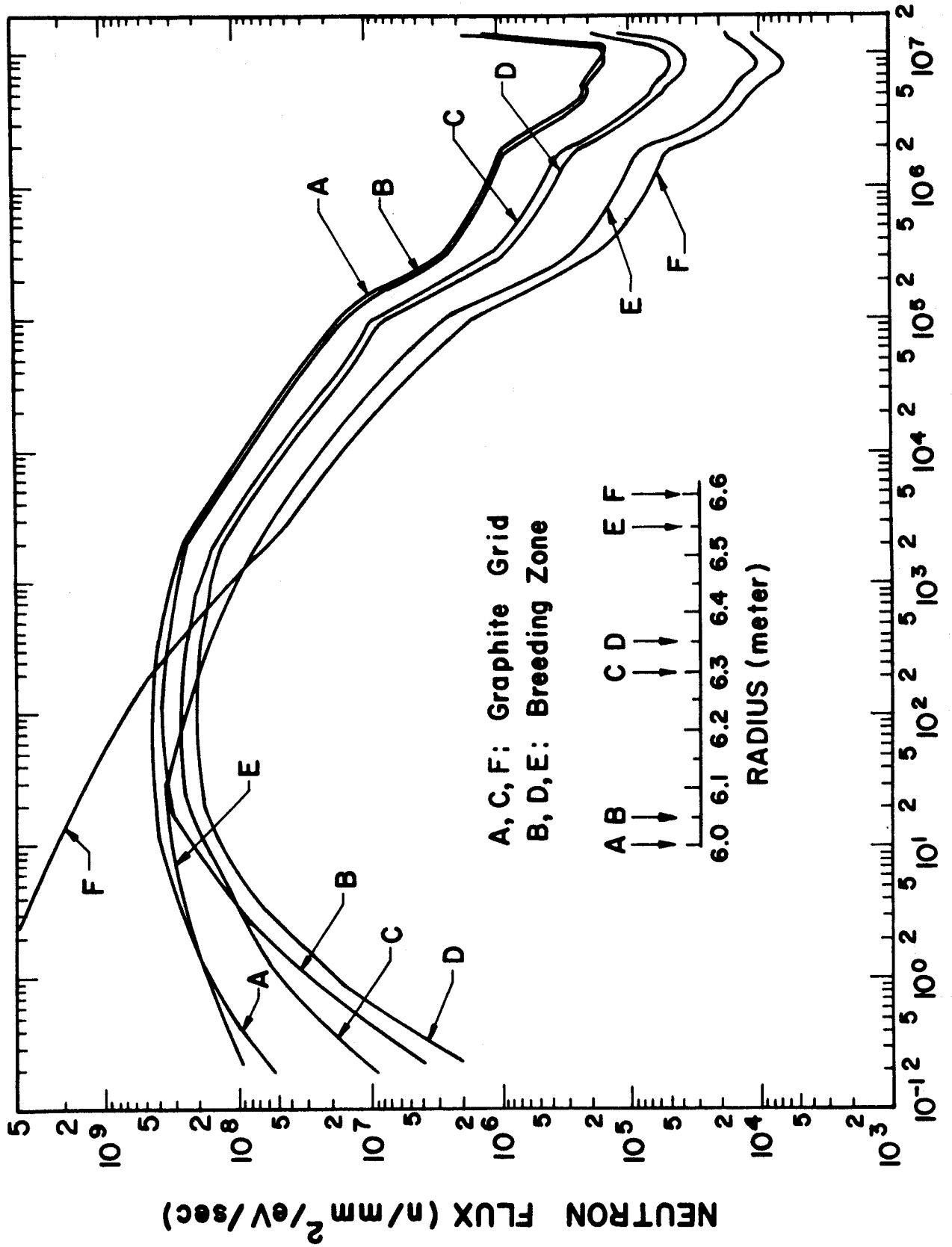

Fig. XIII-B-6

Comparison of Neutron Scalar Fluxes at Different Locations in the Blanket Breeding Region

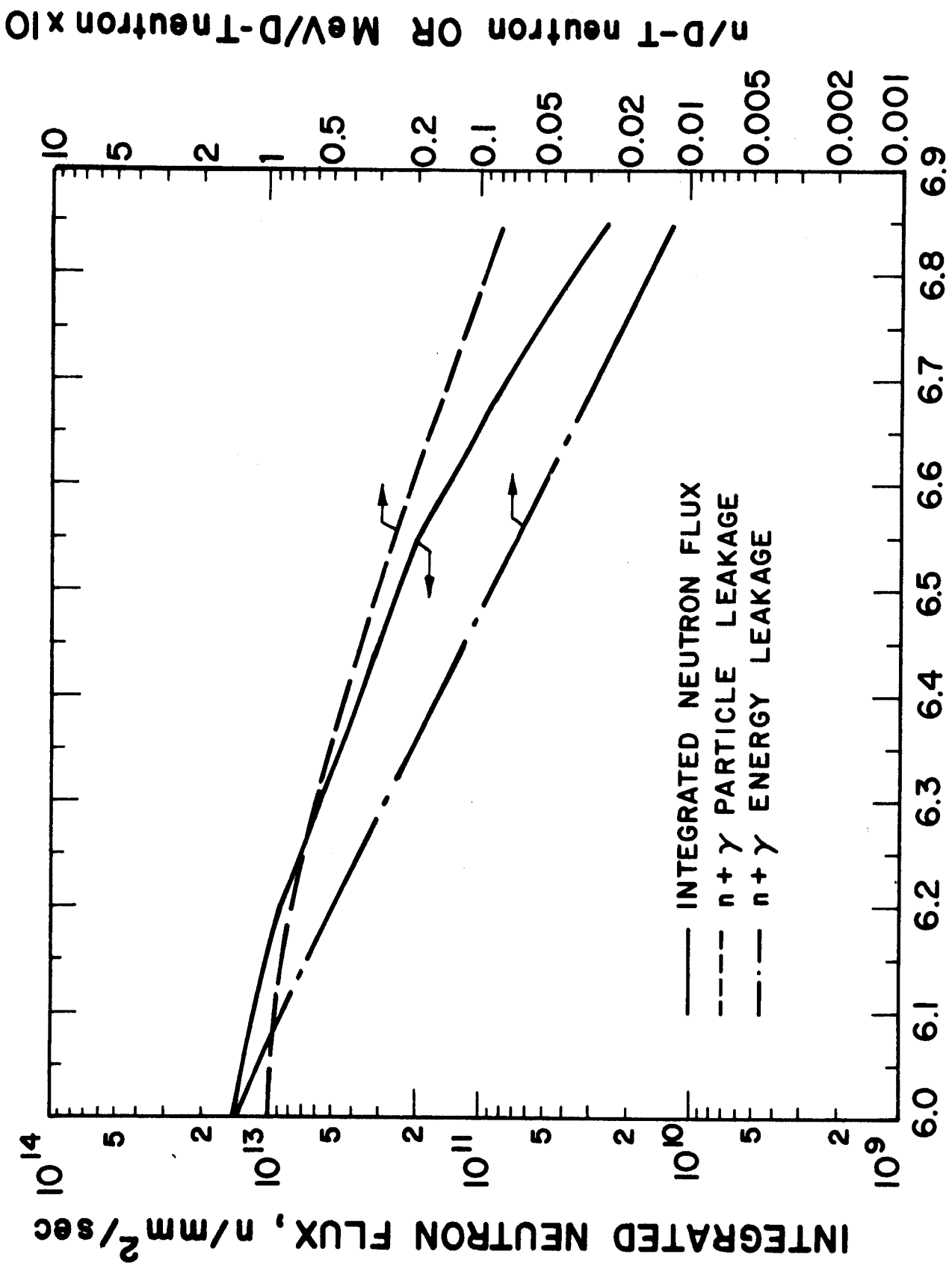

Fig. XIII-B-7
Spatial Variation of Integrated Neutron Scalar Flux, Neutron and Gamma-Ray Particle

References for Section XIII-B

1. W. W. Engle, Jr., "A User's Manual for ANISN," K-1693, Oak Ridge Gaseous Diffusion Plant (1967).

2. B. Badger, et al., "UWMAK-III," UWFDM-150, University of Wisconsin, Nuclear Engineering Department (1976), Chapter V.

3. E. T. Cheng, T. Y. Sung and D. K. Sze, Nuclear Technology 34, 362 (1977).

4. E. T. Cheng and R. W. Conn, Nucl. Sci. Eng. 62, 601 (1977).

XIII-C. Time Dependent Neutronics

Time dependent neutronics is a relatively new area of investigation in the field of fusion reactor design. Magnetic confinement reactors (MCTR) do not have to deal with transient effects due to the time width of the neutron source. However, the inertially confined fusion devices (ICTR) have such short pulse lengths that the temporal distribution of the neutrons is important. It has been reported that some radiation induced damage to metals is affected by the rate at which the damage occurs.[1] If the dpa rate (displacement per atom) is very high (1-10 dpa/sec), swelling in the metal is less than if the damage rate is lower (10^{-4}-10^{-6}dpa/sec) for the same total number of displacements. This is because a high displacement rate leads to a high recombination rate between vacancies and interstitials. If the recombination rate is high enough, the number of vacancies migrating to voids is less than if the vacancies were produced over a longer time period. Thus the swelling is less in metals undergoing high dpa rates. A more detailed explanation of this phenomenon can be found in Chapter XV of this report.

An accurate determination of the time and energy distribution of the neutron source is very important to the quality of the final damage rate results. The ICTR source spectrum will be softer and much narrower in time than an MCTR source distribution. The calculation of the neutron spectrum incident on the first wall is discussed in the first part of this section.

Computational techniques used for the neutron transport calculation are explained in the second part. The time dependent discrete ordinate particle transport code, TDA, is used for this study.[2] Several modifications have

been made on TDA reducing the necessary CPU time of a calculation. One added option discussed in this section is that of energy dependent quadrature order. An S_8 calculation can be performed for high energy neutrons while an S_2 model can be used for low energy particles.

The appearance of negative scalar fluxes raises serious doubts about the applicability of the traditional Legendre polynomial cross section expansion for discrete ordinates transport codes. A method to solve this problem which still maintains the Legendre polynomial formalism by recalculating the expansion coefficients is discussed. This technique has been tested on an artificial cross section but has yet to be implemented on a large scale.

The last part of this section deals with the SOLASE blanket calculation. The details of the calculation and the final results are given.

XIII-C-1. Neutron Source

The calculation of the energy spectrum of neutrons escaping from the pellet is an essential part of the overall time dependent neutronics study. An exact solution, however, is very difficult to obtain since it would involve a time dependent neutron transport problem in a moving medium with time dependent densities and temperatures. The calculation performed for this study includes the three major factors which influence the energy spectrum: (1) the random velocity distribution of the deuterium and tritium as characterized by their temperature; (2) the directed motion of the fuel due to the explosion; and (3) the neutron-fuel collisions within the pellet.

The study of an MCTR blanket includes the first factor in its source calculations. The fuel velocity is not of a magnitude that would affect

the energy of an emitted neutron nor is the density of the DT high enough to cause an appreciable number of n-D or n-T collisions. Also, the arrival time distribution of the neutrons at the wall is so wide (thousands of seconds) compared to the moderation times (microseconds) and thermal diffusion times (milliseconds) that the neutronics problem can be characterized as steady state.

Conversely, the pulsed nature of the ICTR study is evidenced by the fact that the pellet microexplosion (hence the neutron source) lasts 10-100 ps and the highest energy neutrons do not even reach the wall until 100 ns after the burn. Thus, the neutrons are travelling through the gaseous atmosphere in a fixed energy spectrum but a spreading time packet (at different spatial points). The width of the time distribution at the first wall is a most important parameter and is determined by the energy spectrum. All the neutrons which normally arrive at the first wall over a one second period in an MCTR are incident on the chamber over a span of tens of nanoseconds in an ICTR with the same average wall loading. Extremely high instantaneous damage rates are the result.

The source spectrum for the ICTR is calculated in conjunction with the PHD-IV hydrodynamic code developed at the University of Wisconsin.[3] This code simulates the burn of a pellet in time steps ranging in size from .01-2 ps. At each time step, an energy distribution (in the absence of neutron-fuel collisions) is calculated for the neutrons born in each spatial interval given the fuel temperature and particle velocities in that interval. Since the distance to the first wall is several meters and the arrival time of

the pulse will spread over ten or more nanoseconds, the assumption is made that all neutrons were born instantaneously at t = 0. Thus, at the end of the simulated pellet explosion, all the distributions are added resulting in the final energy spectrum. This spectrum is then transported to the walls to obtain the arrival time spectrum. An implosion of a pellet to $\rho R = 3$ g/cm^2 resulted in a Gaussian distribution with a full width half maximum (fwhm) of 1.9 MeV about a peak at 14 MeV. This results in a fwhm of 12 ns in the arrival time spectrum.

The addition of neutron-fuel collisions is accomplished every twentieth time step. The energy spectrum produced over the previous twenty time steps is folded into the differential scattering cross sections for D and T using a fuel density obtained by averaging over the previous twenty time steps. The Doppler effect caused by the directed motion of the fuel is ignored. The result in the pellet with $\rho R = 3$ g/cm^2 is that 31% of the neutrons have at least one collision with the fuel. The average energy loss is 4 MeV/collision.

Fig. XIII-C-1 illustrates the spectra with and without neutron-fuel collisions. The peak at 14 MeV is reduced by 26% because of the collisions. The small peak at ~2.8 MeV is due to the backscatter peak in the differential scattering cross section and not to DD reactions. Fig. XIII-C-2 described the arrival time spectrum at a wall located 600 cm from the neutron source. This illustrates what is meant by time of flight spreading. The numbers at the bottom of the graph indicate the energy group associated with the various times.

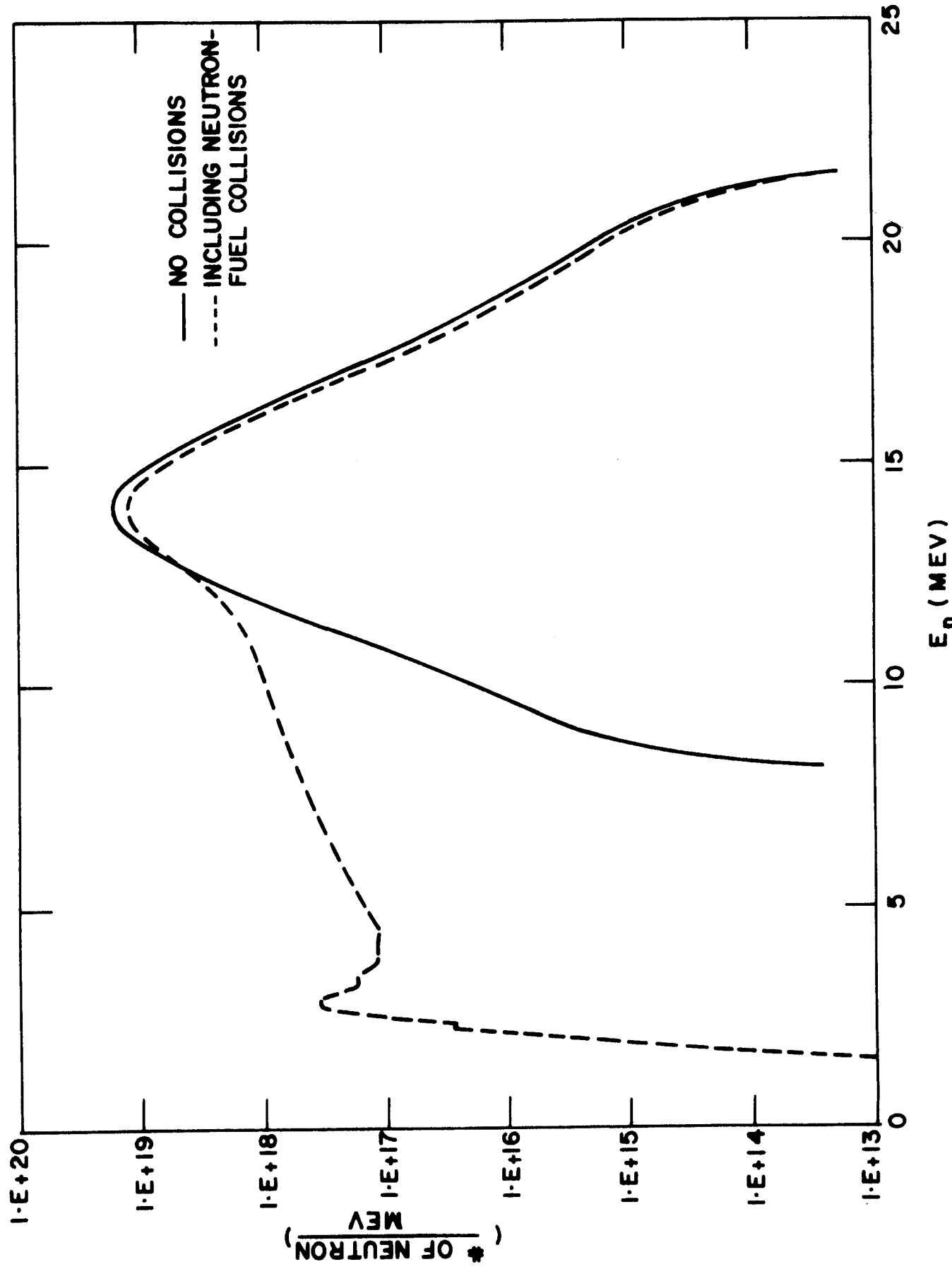
NO COLLISIONS
INCLUDING NEUTRON-FUEL COLLISIONS
1·E+20
1·E+19
1·E+18
1·E+17
1·E+16
1·E+15
1·E+14
1·E+13
0
5
10
15
20
25
E_n (MEV)
(# OF NEUTRON / MEV)

Fig. XIII-C-1

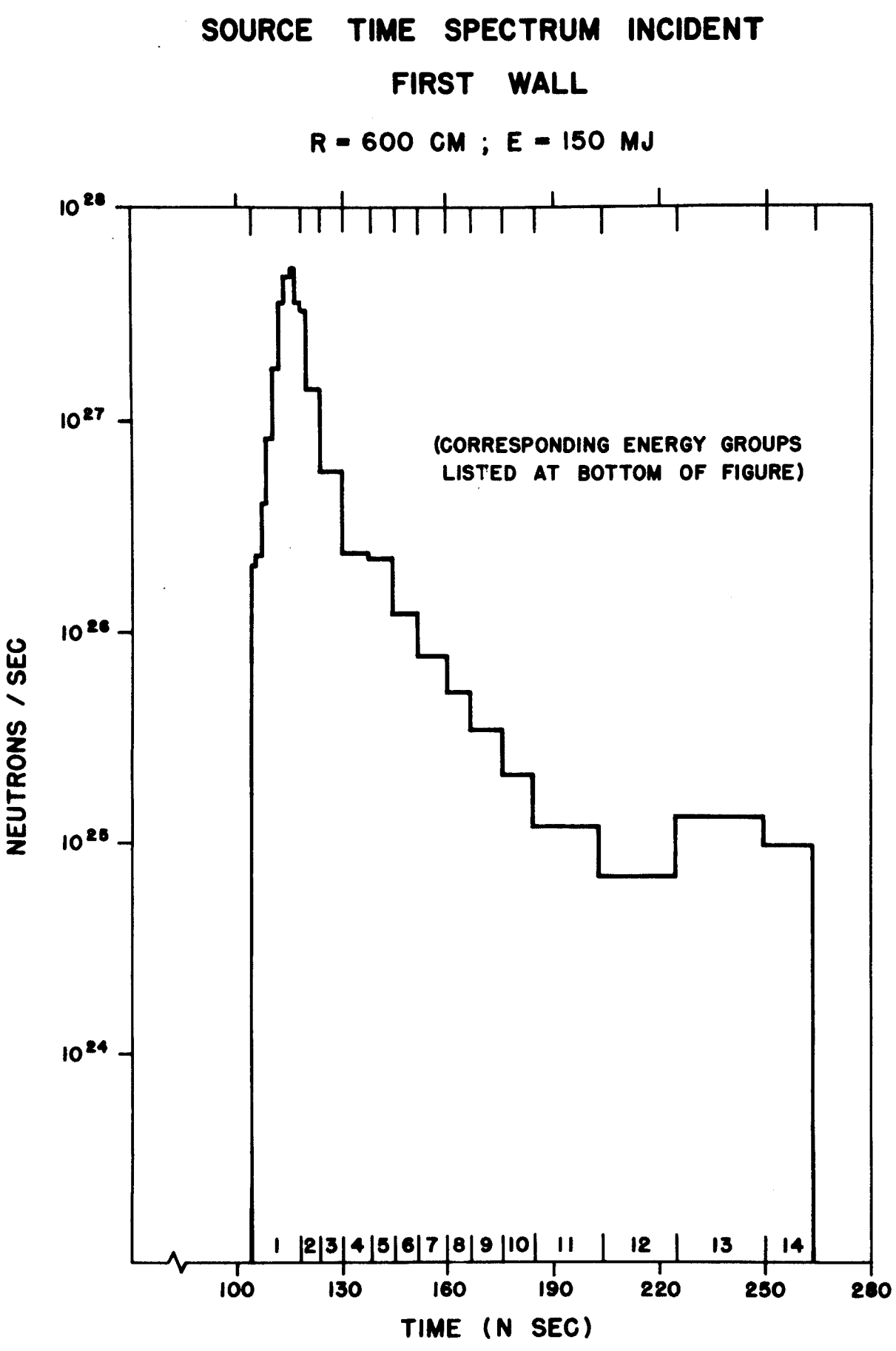
SOURCE TIME SPECTRUM INCIDENT
FIRST WALL
R = 600 CM ; E = 150 MJ
(CORRESPONDING ENERGY GROUPS
LISTED AT BOTTOM OF FIGURE)
NEUTRONS / SEC
TIME (N SEC)
10^28
10^27
10^26
10^25
10^24
100
130
160
190
220
250
280
1
2
3
4
5
6
7
8
9
10
11
12
13
14

Fig. XIII-C-2

XIII-C-2. Computational Techniques

XIII-C-2-a. Energy Dependent Quadrature

A time dependent neutronics calculation is a relatively expensive and time consuming operation. A typical calculation which followed neutrons for 10 μsec using an S_4-P_3 model required 150 minutes of CPU time on a UNIVAC 1110. An S_4 calculation is a very poor representaion to use due to the high energy of the neutrons and the anisotropy of their incidence. However, for economic reasons, it is necessary. The problem with calculations of this nature is that the same model is used to treat particles with dissimilar characteristics: the high energy source neutrons which are incident normal to the surface and have highly anisotropic differential transfer cross sections (especially for light materials) and the low energy scattered neutrons whose angular distribution is nearly isotropic with very flat differential transfer cross sections. If the high energy neutrons are treated accurately, large amounts of time are wasted dealing with slower neutrons over an unnecessarily small angular mesh. Conversely, efficient treatments of low energy particles force a poor simulation of the fast particles. The result is the use of an intermediate quadrature order with reasonable accuracy for fast neutron results yet economically practical.

The TDA code is now capable of preforming calculations with user specified energy group dependent quadrature order. The user inputs integers A,B,C,D and EP and the code runs groups 1→A with S_8, A+1→B with S_6, B+1→C with S_4, and C+1→D with S_2. When using coupled neutronics-photonics problems, the code will then use an S_{EP-1} model for the photonics. Since the running time

of the code is roughly proportional to the total number of directions (the product of the number of energy groups and the number of discrete angles per group), a suitable choice of quadrature orders allows the high and low energy particles to be treated correctly in the same computer time associated with an intermediate quadrature order for all groups.

XIII-C-2-b. Discrete Cross Section Expansion

It has been noticed in working with TDA that under certain source conditions (high energy, monodirectional neutron pulses of short time width) negative scalar fluxes occur in intervals through which the pulse had recently passed. Negative angular fluxes are noted in other published reports but are usually dismissed as a relatively minor but unavoidable inconvenience. In time dependent calculations, however, these negative angular fluxes often combine to produce negative scalar fluxes which is an intolerable problem. Not only is the flux incorrect in this time interval, but the error will propagate to later time steps and spatial intervals casting doubt on all results. Concern about the accuracy of steady state results is also raised because even though scalar fluxes in those calculations are positive, they may be inaccurate. This has yet to be studied.

The problem arises due to the combination of the discrete ordinates method to model the angular variable in the particle transport equation and the Legendre polynomial expansion used to simulate the transfer cross sections. The energy dependent steady state transport equation in plane geometry is used to briefly explain the theory involved (for explanation of symbols see Table XIII-C-1:

$$\mu \frac{\partial \Phi(x,\mu,E)}{\partial x} + \sigma(x,E)\Phi(x,\mu,E) = \int\int \sigma f(x;\ E' \rightarrow E,\ \mu_0)\Phi(x,\mu',E')d\vec{\Omega}'dE' + Q(x,\mu,E). \quad (1)$$

Table XIII-C-1

Symbol	Definition
μ	Cosine of the angle θ of neutron travel where θ is taken with respect to the axis of symmetry.
x	Spatial variable
E	Particle energy
$\Phi(x,\mu,E)$	Angular flux: the product of the neutron velocity and the probably number of neutrons at x travelling in direction μ with energy E.
$\sigma(x,E)$	Total macroscopic cross section at positio x for neutrons with energy E.
μ_o	Cosine of the angle through which a neutron is scattered $\mu_o = \Omega \cdot \Omega'$
$\sigma f(x;E' \rightarrow E,\mu_o)$	Total probability of neutron transfer from E' to E through an angle whose cosine is μ_o.
$Q(x,\mu,E)$	External source

The scattering function under the integral is expanded in an infinite set of Legendre polynomials as

$$\sigma f \equiv \sum_{\ell=0}^{\infty} \frac{2\ell+1}{4\pi} \sigma_\ell(x;E'\to E)P_\ell(\mu_o) \qquad (2)$$

with the expansion coefficients calculated by

$$\sigma_\ell(x,E'\to E) = 2\pi \int_{-1}^{1} \sigma f(x;E'\to E, \mu_o)P_\ell(\mu_o)d\mu_o. \qquad (3)$$

The Addition Theorem for Legendre polynomials is used to expand $P_\ell(\mu_o)$. The expression is then integrated over the azimuthal angle ϕ' resulting in the equation

$$\mu \frac{\partial\Phi(x,\mu,E)}{\partial x} + \sigma(x,E)\Phi(x,\mu,E) = \int_{-1}^{1} \sum_{\ell=0}^{\infty}(2\ell+1) \sigma_\ell(x,E'\to E)P_\ell(\mu)P_\ell(\mu')\Phi(x,\mu',E') d\mu' dE' + Q(x,\mu,E) \qquad (4)$$

The multigroup approximation is made by integrating the equation over several small energy groups. For a system containing G energy groups, there are G coupled integro-differential equations of the form

$$\mu \frac{\partial\Phi^g(x,\mu)}{\partial x} + \sigma^g(x)\Phi^g(x,\mu) = \sum_{g'=1}^{G} \int_{-1}^{1} \sum_{\ell=0}^{\infty} (2\ell+1) \sigma_\ell^{g'\to g}(x)P_\ell(\mu)P_\ell(\mu')\Phi^{g'}(x,u')d\mu' + Q^g(x,\mu) \qquad (5)$$

The definitions of the above terms can be found in Table XIII-C-2:

The discrete ordinates method is now used to remove the only remaining integral. The angular variable is discretized to include only N values changing the integration over to a weighted summation:

Table XIII-C-2.

Symbol	Definition
$\Phi^g(x,\mu)$	$\int_{E_g}^{E_{g-1}} \Phi(x,\mu,E)dE$
$\sigma^g(x)$	$\dfrac{\int_{E_g}^{E_{g-1}} \sigma(x,E)\omega(E)dE}{\int_{E_g}^{E_{g-1}} \omega(E)dE}$ ($\omega(E)$ describes the energy dependence of the flux).
$\sigma_\ell^{g'\to g}(x)$	$\dfrac{\int_{E_{g'}}^{E_{g'-1}} \omega(E') \int_{E_g}^{E_{g-1}} \sigma_\ell(x,E'\to E)dEdE'}{\int_{E_{g'}}^{E_{g'-1}} \omega(E')dE'}$
$Q^g(x,\mu)$	$\int_{E_g}^{E_{g-1}} Q(x,\mu,E)dE$

$$\mu_j \frac{\partial \Phi^g(x,\mu_j)}{\partial x} + \sigma^g(x)\Phi^g(x,\mu_j) = \sum_{g'=1}^{G} \sum_{\ell=1}^{\infty} (2\ell+1)\, \sigma_\ell^{g'\to g}(x) P_\ell(\mu_j) \sum_{i=1}^{N} w_i P_\ell(\mu_i)\Phi^{g'}(x,\mu_i) + Q^g(x,\mu_j). \quad (6)$$

The final approximation made is the reduction of the summation over the Legendre polynomials to a somewhat arbitrary finite order L. The final equation is now

$$\mu_j \frac{\partial \Phi^g(x,\mu_j)}{\partial x} + \sigma^g(x)\Phi^g(x,\mu_j) = \sum_{g'=1}^{G} \sum_{\ell=0}^{L} (2\ell+1)\sigma_\ell^{g'\to g}(x) P_\ell(\mu_j) \sum_{i=1}^{N} w_i P_\ell(\mu_i)\Phi^{g'}(x,\mu_i) + Q^g(x,\mu_j). \quad (7)$$

The limit, L, determines the number of integral moments of the differential transfer cross sections that are preserved by the Legendre polynomial expansion. For calculations involving low energy neutrons, an L=0 approximation can be used since these neutrons are characterized by isotopic scattering. Linearly anisotropic scattering can be modelled by setting L=1. The most common limit in published computations is L=3. As neutron energies get higher, materials become lighter or energy groups become narrower; a third order polynomial fit does a very poor job of approximating transfer cross sections. Even high order expansions (L=9) do not adequately represent these cross sections for discrete ordinates calculations.

A poor fit results because for many materials and group transfers there may be only a small angular range through which a neutron can scatter and arrive in a given group. By kinematics arguments, the transfer cross

section for scattering into that particular group through any other angle is identically zero. However, in an attempt to fit this isolated peak, the polymonial will pass through the zero cross section value at some point and become negative in a range (range A) where the true cross section is zero. The polynomial will also be positive over another range (range B) when the exact value is zero which will lead to an equally serious but less noticeable error. If the scattering term in equation 7 includes an angular transfer combination lying in a range through which there should be a zero transfer cross section, the scattering term will give either a negative or positive contribution. If the scattering angle lies in range A, a negative angular flux will appear which, in time dependent problems, may dominate the positive fluxes in other angles at later times producing a negative scalar flux. An angle lying in range B results in a positive flux but is incorrect since there should be a zero contribution. The second error is very difficult to notice but has been found in TDA results.

Other investigators have reported on the problem of negative angular fluxes and have developed methods to eliminate or reduce the severity of the problem.[4,5] However, the techniques discussed involve modification of the transport code and the data files. The method proposed in this section changes only the data files and could be used with any code which presently accepts Legendre expansion coefficients as data.

The new expansion method reduces the number of approximations made in obtaining equation 7. Presently equation 6 is more exact than 7 but cannot be solved numerically. An improvement in accuracy can obviously be made if

equation 7 can be written in a form identical to 6 but still use a finite limit on the summation over the Legendre polynomials. The two equations will be identical if the scattering terms in each are the same:

$$\sum_{\ell=0}^{\infty} (2\ell+1)\, \sigma_\ell^{g'\to g}\, P_\ell(\mu_j) \sum_{i=1}^{N} \omega_i\, P_\ell(\mu_i)\, \Phi(x,\mu_i) \equiv \sum_{\ell=0}^{L} (2\ell+1)$$

$$f_\ell^{g'\to g}\, P_\ell(\mu_j) \sum_{i=1}^{N} \omega_i\, P_\ell(\mu_i)\, \Phi(x,\mu_i)\ . \qquad (8)$$

Note that the expansion coefficients for the RHS of Equation 8 have been changed to f_ℓ to indicate that they may not be the same as the σ_ℓ of the LHS. Equation 8 can be rewritten as:

$$\sum_{i=1}^{N} \omega_i\, \Phi(x,\mu_i) \sum_{\ell=0}^{\infty} (2\ell+1)\, \sigma_\ell^{g'\to g}\, P_\ell(\mu_j)\, P_\ell(\mu_i) \equiv \sum_{i=1}^{N} \omega_i\, \Phi(x,\mu_i) \sum_{\ell=0}^{L}$$

$$(2\ell+1)\, f_\ell^{g'\to g}\, P_\ell(\mu_j)\, P_\ell(\mu_i)\ . \qquad (9)$$

This identity will hold only if

$$\sum_{\ell=0}^{\infty} (2\ell+1)\, \sigma_\ell^{g'\to g}\, P_\ell(\mu_j)\, P_\ell(\mu_i) \equiv \sum_{\ell=0}^{L} (2\ell+1)\, f_\ell^{g'\to g}\, P_\ell(\mu_j)\, P_\ell(\mu_i)\ . \qquad (10)$$

The LHS of Equation 10 is the exact value of the group transfer cross section from ordinate $\mu_{j,i}$ to $\mu_{i,j}$ integrated over the azimuthal angle. These are known and can be obtained for all unique products of $\mu_i\ \mu_j$. The result is an algebraic set of L + 1 equations with L + 1 unknowns from which the f_ℓ terms can be computed. The upper limit, L, is determined by the number of unique angular combinations which is $\frac{N(N+6)+4}{4}$ for an S_N calculation. This total number assumes that $\mu_{N+1} = -1$ and preserves the correct cross section for

scattering from a normal direction ($\mu = 1$) to all other discrete angles which is necessary for the first collided source option in TDA. The traditional Legendre expansion coefficients preserve the first L + 1 integral moments of the true cross section. Thus, the first expansion coefficient, σ_0, is the total transfer cross section. There is no reason to assume that f_0 will equal σ_0 but since discrete ordinates codes such as ANISN[6] and TDA use σ_0 as the total transfer cross section, f_0 must be set equal to σ_0:

$$\sum_{\ell=0}^{\infty} (2\ell+1)\, \sigma_\ell P_\ell(\mu_i)\, P_\ell(\mu_j) = f_0 + \sum_{\ell=1}^{L+1} (2\ell+1)\, f_\ell\, P_\ell(\mu_i)\, P_\ell(\mu_j)$$

$$f_0 = \sigma_0 .$$

There now exists a numerically solvable equation which has undergone only two approximations (multi-group and discrete ordinate) on the exact equation instead of the usual three. The form, however, is the same as is presently solved in existing neutron transport codes so the only change required is a new data set.

XIII-C-3. SOLASE Calculation

The primary purpose for the time dependent neutronics calculation is to compute the damage rate in the first wall. The neutron behavior in the back portion of the blanket is thus of little significance. Since the calculation is expensive, the number of spatial intervals required is reduced by modelling only the first 30 cm of the blanket. Reflection at the right boundary due to backscattering is represented by appropriate albedos

obtained from the steady state calculation. The sensitivity of the results in the first wall due to errors in the albedo has not been studied, but is presumed to be small.

The energy dependent quadrature order option is used in this calculation. The following table illustrates which orders are associated with which energy groups:

Energy Groups	Quadrature
1→3	S_8
4→10	S_6
11→17	S_4
18→25	S_2
26→46 (Photonics)	S_4

Within the first three energy groups are 83% of the source neutrons. These are treated with the highest quadrature. The next seven energy groups contain 15.5% of the source and are handled somewhat less exactly, but still better than the S_4 model which would have been required if all groups were to be treated with the same order. The S_4 model is used for the intermediate groups while S_2 is used for the last eight neutron groups. Preliminary testing showed that S_2 calculations in these groups results in scalar fluxes within .1% of S_8 models.

The description of the neutron source that is used as input to the code is very important. Note in Fig. XIII-C-1 that a large fraction of the

neutrons have energies greater than 13.5 MeV and are thus in the first energy group. If all these neutrons are described in the code as being born at the same time, they will all arrive at the first wall simultaneously resulting in an average over the first group which will be lower than the peak indicated in Fig. XIII-C-2. This is because the fastest neutrons (15-17 MeV) are forced to travel at the group 1 velocity of 5.245×10^9 cm/sec instead of streaming ahead causing a slowly rising pulse. In order to remedy this problem, artificial birth times are calculated for all the neutrons such that physical reality is preserved at the first wall. This is necessary to allow the peak of the pulse to appear in the calculation (rather than an average over the group) since this will cause the highest damage rates.

The results of the SOLASE time dependent neutronics calculations are summarized in Fig. XIII-C-3 to 9. The values correspond to a 150 MJ micro-explosion resulting in an average neutron wall loading of .2655 MJ/m^2/pulse (assuming an average neutron energy of 14 MeV). The dpa rate in the graphite first wall reaches a peak of 1.71 dpa/sec 12.4 ns after the leading edge of the pulse strikes the wall Fig. XIII-C-3. The maximum rate is lower in the other graphite zones due to the slowing down of the neutrons out of the energies of high dpa cross sections (Fig. XIII-C-5 to 7). Fig. XIII-C-8 displays the helium production rate and its well defined cut off point. This is because the (n,α) reaction is a threshold reaction with zero cross section below 6 MeV in graphite.

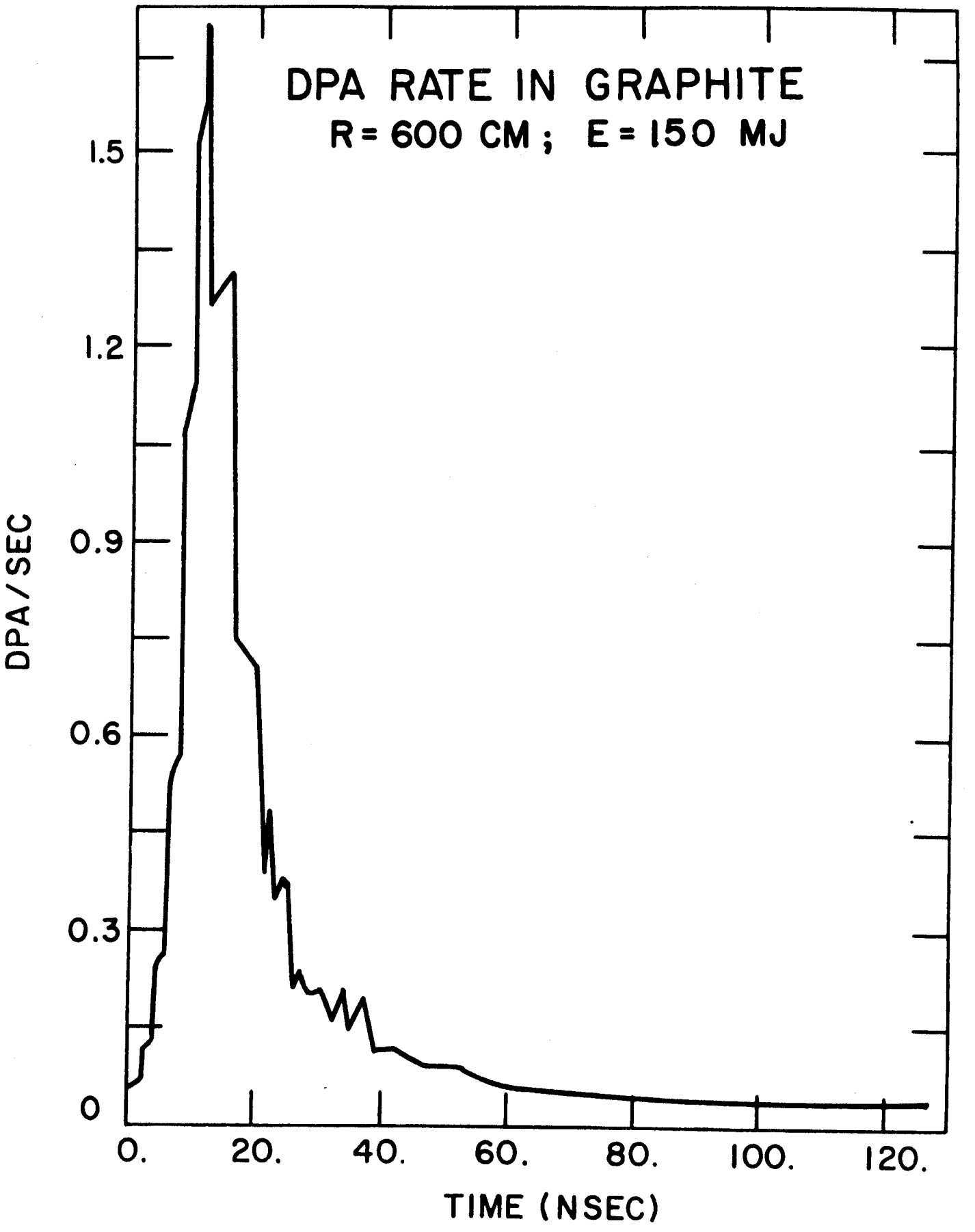
DPA RATE IN GRAPHITE
R = 600 CM ; E = 150 MJ
DPA/SEC
1.5
1.2
0.9
0.6
0.3
0
0.
20.
40.
60.
80.
100.
120.
TIME (NSEC)

Fig. XIII-C-3

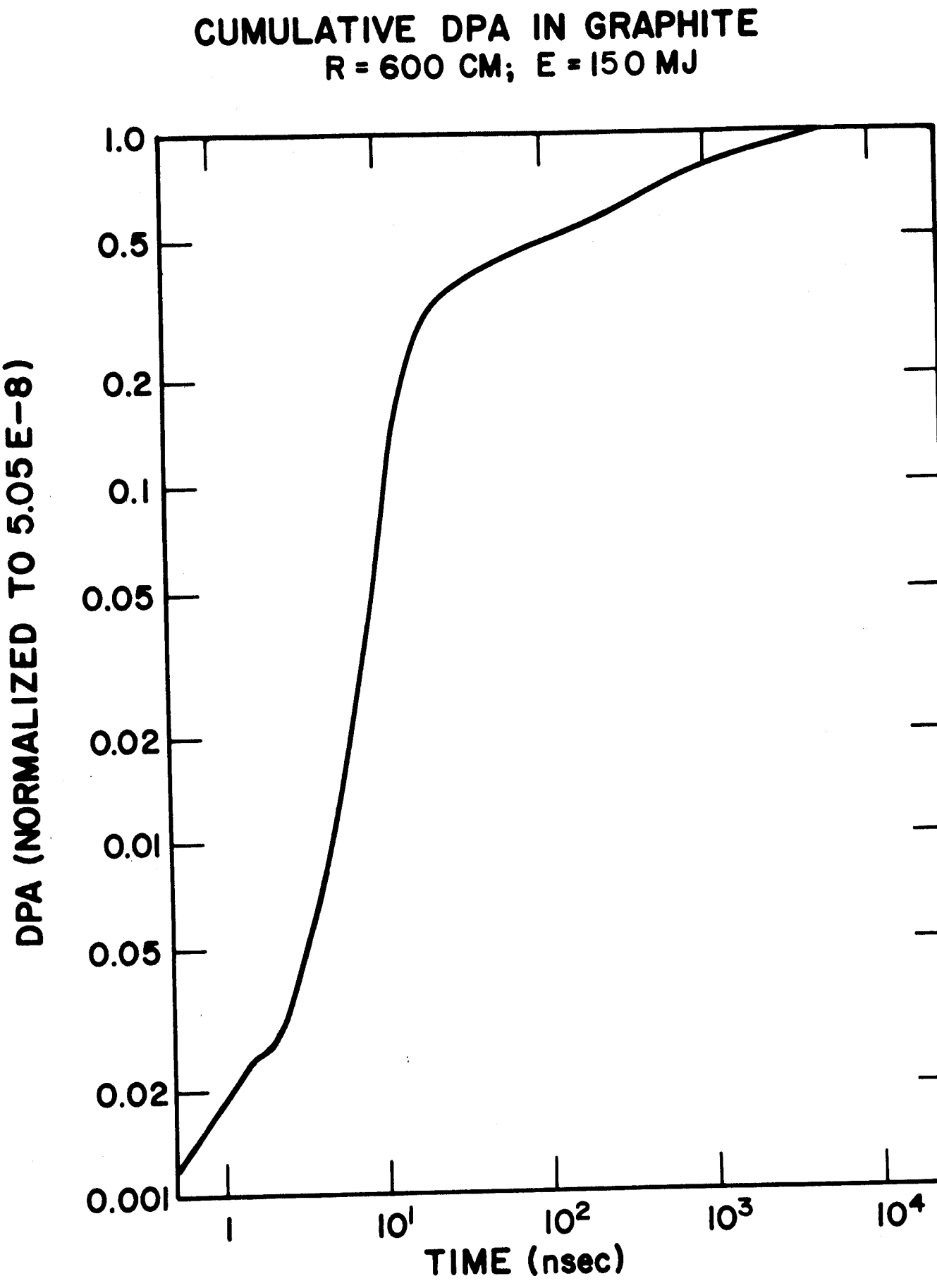
CUMULATIVE DPA IN GRAPHITE
R = 600 CM; E = 150 MJ
DPA (NORMALIZED TO 5.05E-8)
1.0
0.5
0.2
0.1
0.05
0.02
0.01
0.05
0.02
0.001
1
10¹
10²
10³
10⁴
TIME (nsec)

Fig. XIII-C-4

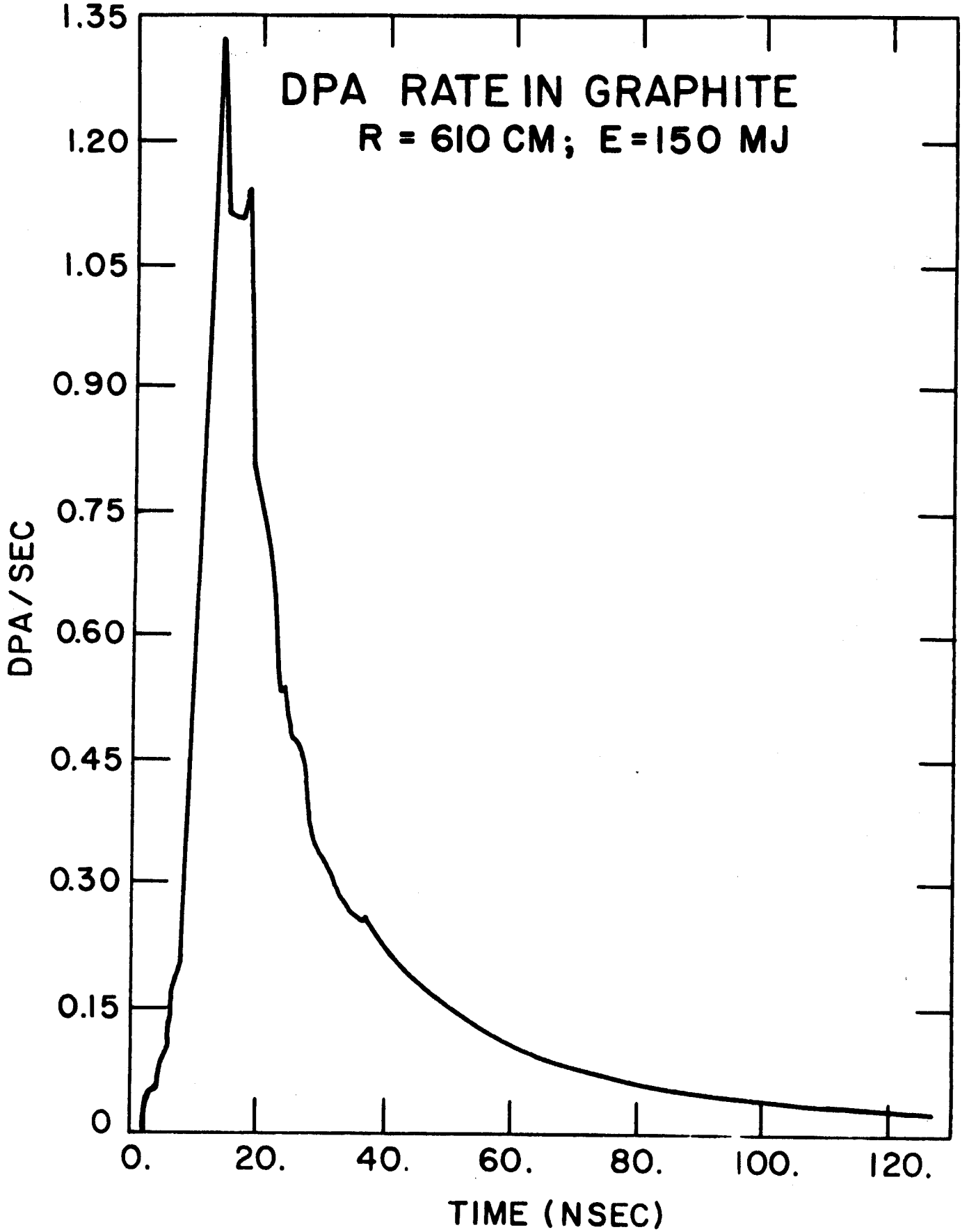
DPA RATE IN GRAPHITE
R = 610 CM; E = 150 MJ
DPA/SEC
1.35
1.20
1.05
0.90
0.75
0.60
0.45
0.30
0.15
0
0.
20.
40.
60.
80.
100.
120.
TIME (NSEC)

Fig. XIII-C-5

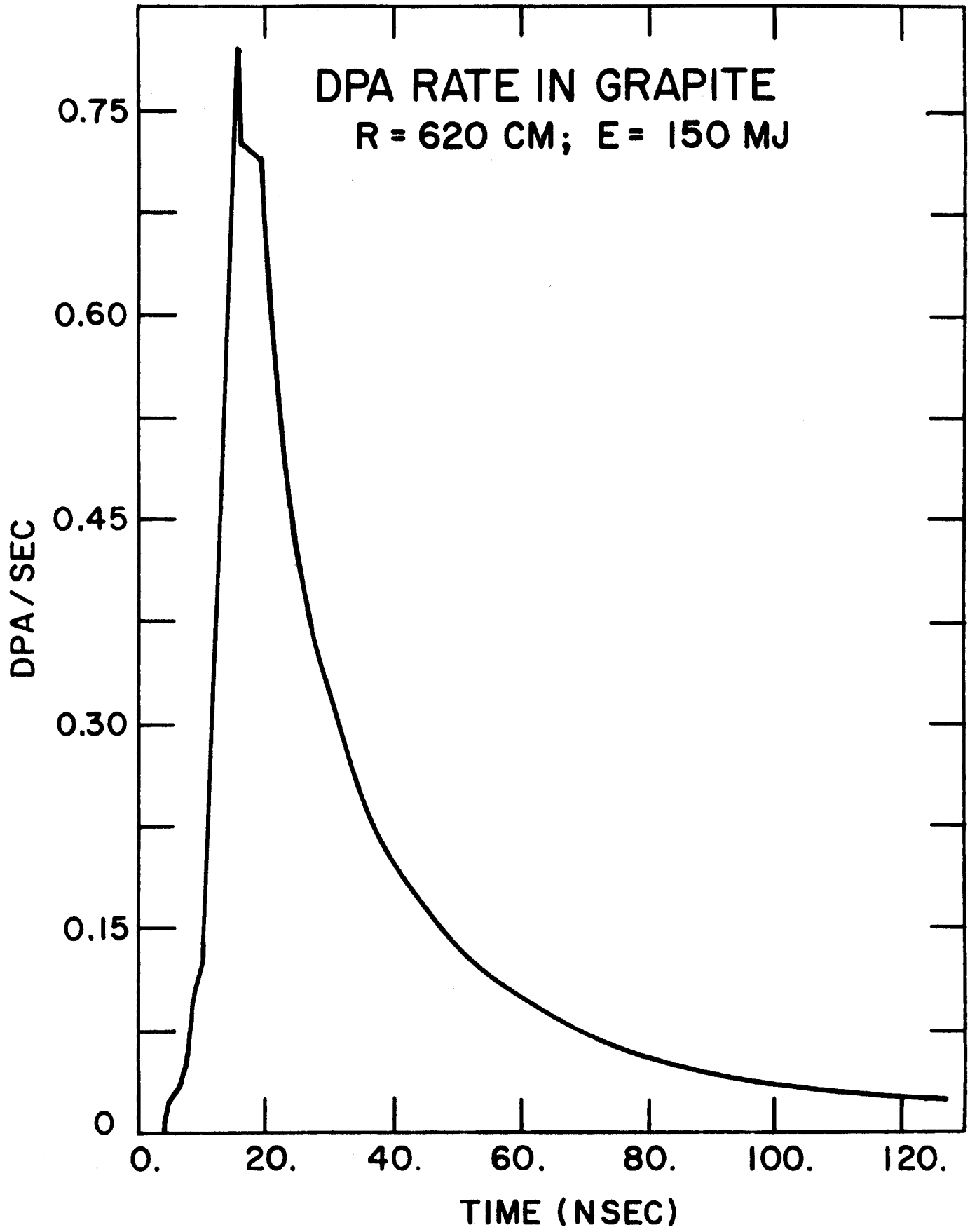
DPA RATE IN GRAPITE
R = 620 CM; E = 150 MJ
DPA/SEC
0.75
0.60
0.45
0.30
0.15
0
0.
20.
40.
60.
80.
100.
120.
TIME (NSEC)

Fig. XIII-C-6

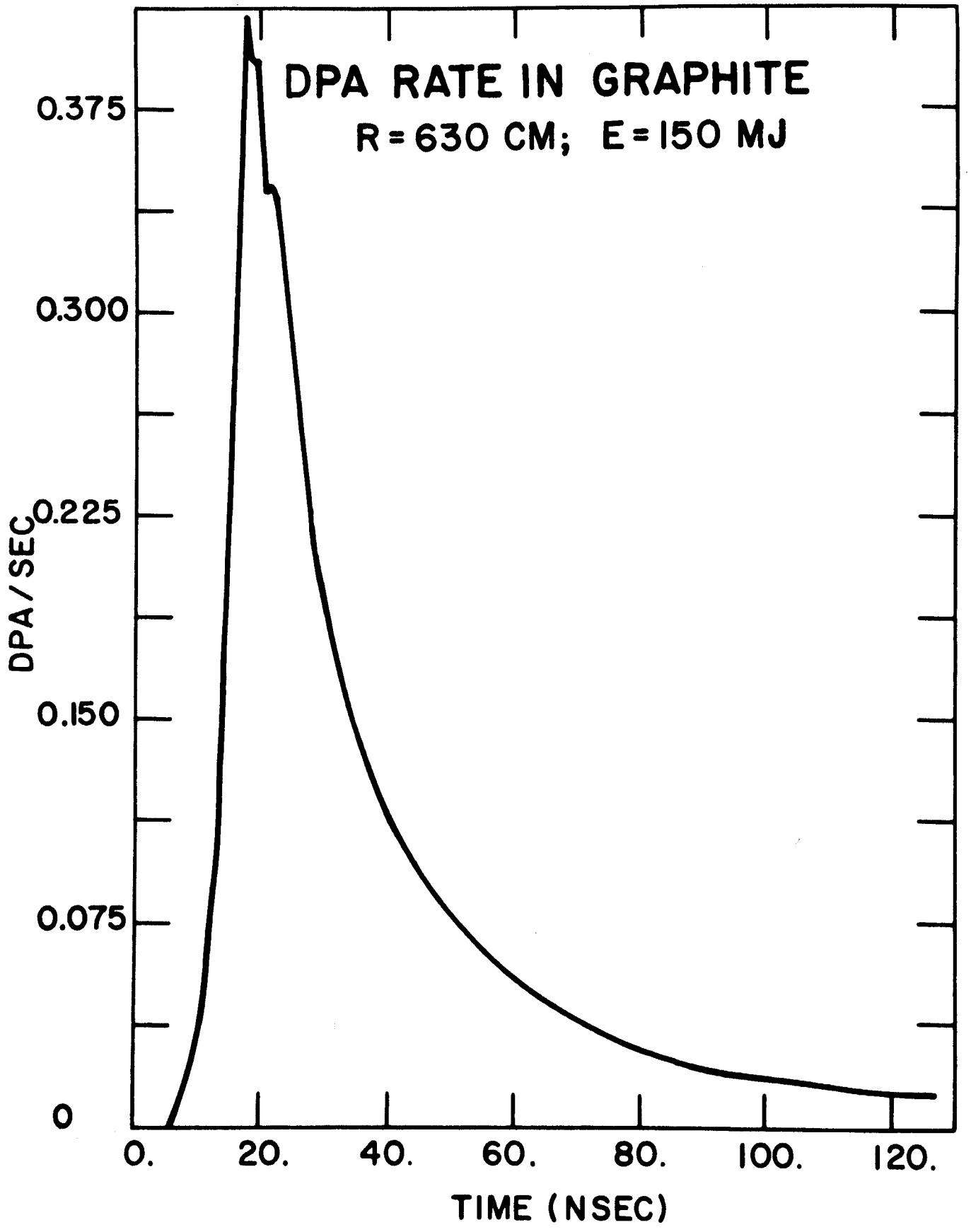
DPA RATE IN GRAPHITE
R = 630 CM; E = 150 MJ
0.375
0.300
0.225
0.150
0.075
0
DPA / SEC
0.
20.
40.
60.
80.
100.
120.
TIME (NSEC)

Fig. XIII-C-7

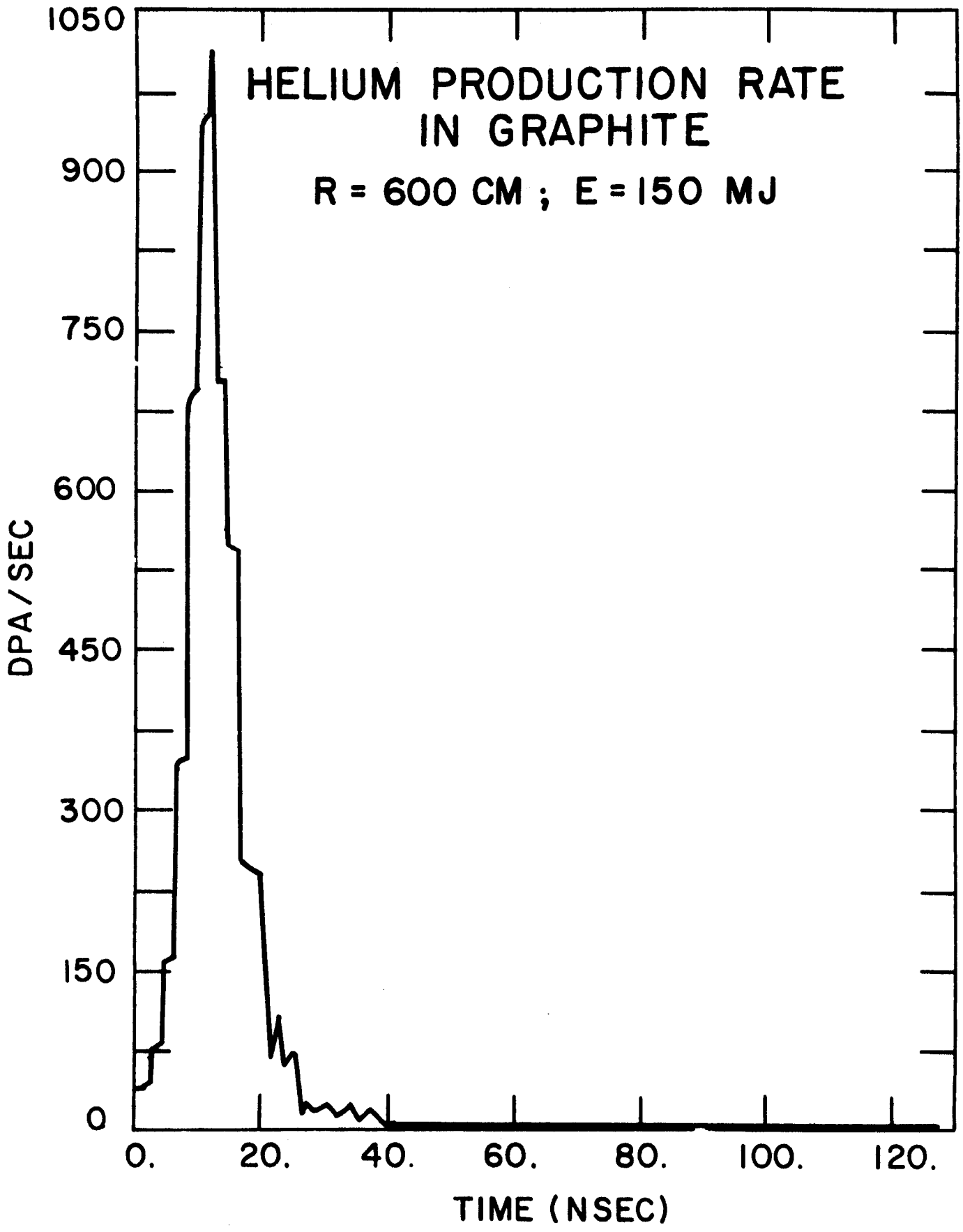
HELIUM PRODUCTION RATE
IN GRAPHITE
R = 600 CM ; E = 150 MJ
DPA/SEC
1050
900
750
600
450
300
150
0
0.
20.
40.
60.
80.
100.
120.
TIME (NSEC)

Fig. XIII-C-8

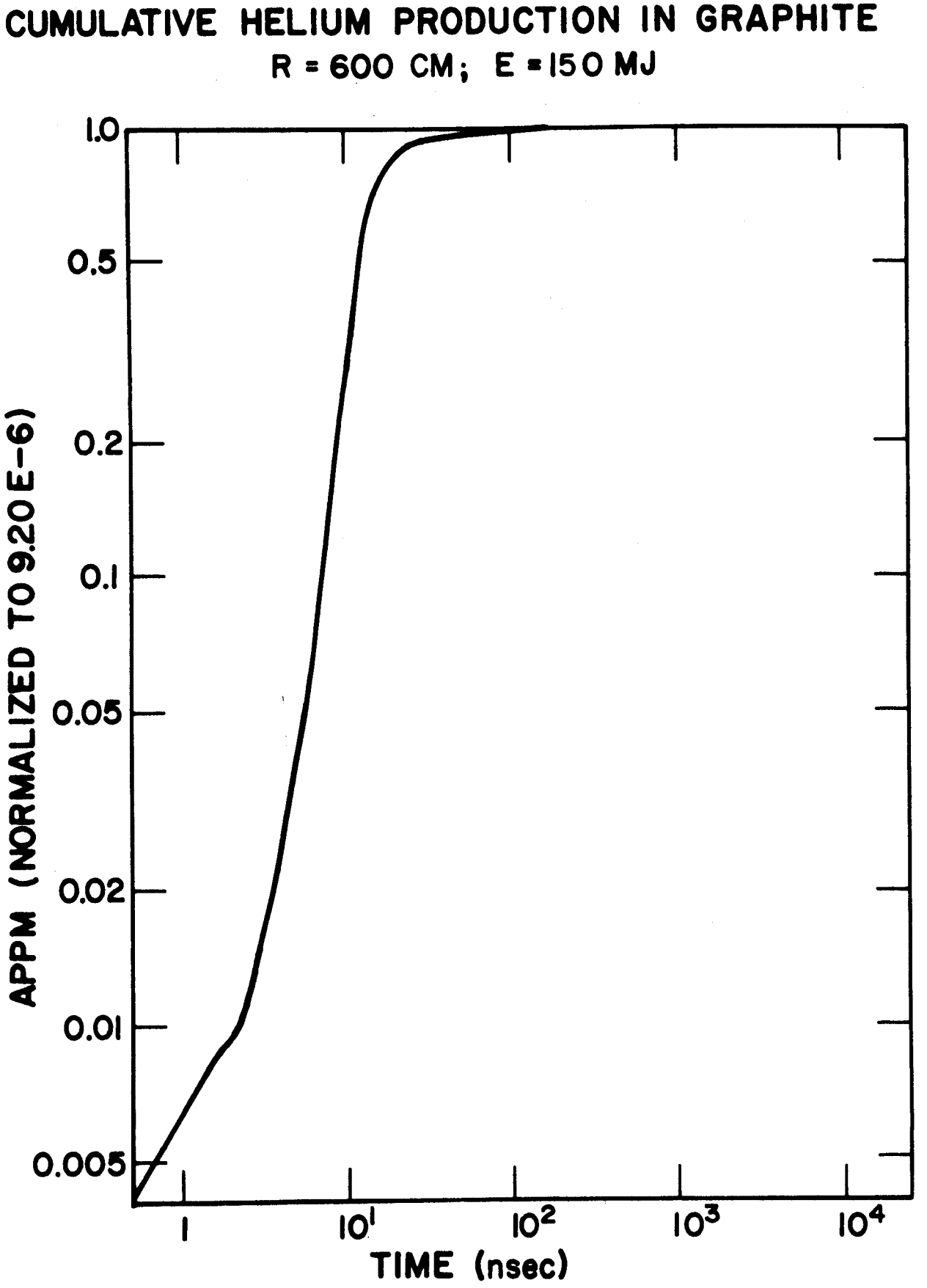
CUMULATIVE HELIUM PRODUCTION IN GRAPHITE
R = 600 CM; E = 150 MJ
APPM (NORMALIZED TO 9.20E-6)
1.0
0.5
0.2
0.1
0.05
0.02
0.01
0.005
1
10¹
10²
10³
10⁴
TIME (nsec)

Fig. XIII-C-9

References for Section XIII-C.

1. N. Ghoniem and G. L. Kulcinski, "Void Growth Kinetics Under an Irradiation Pulse," Nuclear Engineering Department Report UWFDM-138, University of Wisconsin (Oct. 1975).

2. S. A. Dupree, et al., "Time Dependent Neutron and Photon Transport Calculations Using the Method of Discrete Ordinates," Joint Los Alamos Scientific Laboratory-Oak Ridge National Laboratory Report LA-4557 (ORNL-4662) (1971).

3. G. A. Moses, "PHD (Version I) Computer Code Documentation," Nuclear Engineering Department Report UWFDM-160, University of Wisconsin (June 28, 1976).

4. J. P. Odom and J. K. Shultis, Nuclear Science and Engineering 59 (1976), 278.

5. E. A. Attia and A. A. Harms, Nuclear Science and Engineering 59 (1976), 319.

6. W. W. Engle, Jr., "A User's Manual for ANISN," Computing Technology Center, Union Carbide Corporation (March 1967).

XIII-D. Shield Design

Shielding of the reactor cavity does not pose special problems because of the simple geometries involved. Two different types of shields have been considered for the SOLASE reactor: (1) a free-standing concrete shield with an outside layer of lead (to stop the gammas) and aluminum alloy reinforcement (to minimize long term radioactivity), and (2) an aqueous solution of lead acetate enclosed in aluminum alloy containers. For either of these shield designs, the anticipated dose rates outside the shield during reactor operation are extremely low (~ 1 mrem/hr). This design criterion has been set in order to allow hands-on maintenance of auxiliary components outside the reactor during operation. In addition, these shields have been designed to have low residual radioactivity levels in accordance with the design philosophy adopted for the blanket. Radioactivity calculations for both types of shield are presented in Section XIII-E. The lead acetate shielding concept offers the advantage of fast disassembly during scheduled blanket replacement; drainage of the solution into shielded (underground) containers allows easy access to the blanket (Chapter XIV). Details of the neutronic calculations for both types of shield are described below; the mechanical design aspects are discussed in Chapter XIV.

XIII-D-1. Concrete Shield Design

A free-standing concrete shield with an outside layer of lead (to stop the gammas) and aluminum alloy reinforcement (to minimize long term radioactivity) has been designed. The concrete used has a density of 2.3 g/cm^3 with the composition shown in Table XIII-D-1. Ten percent of aluminum alloy reinforcement is allowed. The one-dimensional code ANISN has been used to

Table XIII-D-1

Concrete Composition

Element	Weight %
Calcium	24.33
Silicon	20.24
Oxygen	46.70
Carbon	4.92
Hydrogen	3.81

determine the flux attenuation as a function of shield thickness. These fluxes are then used to determine the corresponding dose values behind the shield. The tissue composition used in these calculations is given in Table XIII-D-2; it has a density of 1 g/cm^3.

Variation of the anticipated dose rate with shield thickness is shown in Figure XIII-D-1. For a 3.5 m thick shield, a dose rate of 100 mrem/hr is obtained. Addition of a 10 cm thick layer of lead outside the shield would reduce the dose rate to ~ 1 mrem/hr. This estimate is based on the fact that the average energy of the gammas escaping from the 3.5 m concrete shield is 4.4 MeV; the corresponding absorption coefficient for lead is 0.48 cm^{-1}. The most important consideration regarding the shield thickness is interference with the next-to-last turning mirror. However, for the 90° turning angle used in the SOLASE optics design this presents no problem. Mechanical design, and assembly and disassembly procedures, along with weight estimates for the shield are given in Chapter XIV.

XIII-D-2. Lead Acetate Shield

A second shield design using an aqueous solution of lead acetate enclosed in aluminum alloy canisters has also been analyzed. During scheduled blanket replacement periods, the lead acetate solution can be drained from the canisters into a shielded (underground) retention tank allowing easy removal of the canisters and access to the blanket. The blanket can then be disassembled using hands-on or semi-hands-on maintenance. The lead acetate solution consists of 221 gm of lead acetate per 100 cm^3 of water. This is the solubility limit of lead acetate at 50°C. The corresponding solution volume is 158 cm^3. These values are used to compute the number densities necessary for the neutronics calculations. Ten percent aluminum structure

Table XIII-D-2

Tissue Composition

Component	Weight %
Oxygen	76.2
Carbon	11.1
Hydrogen	10.1
Nitrogen	2.6

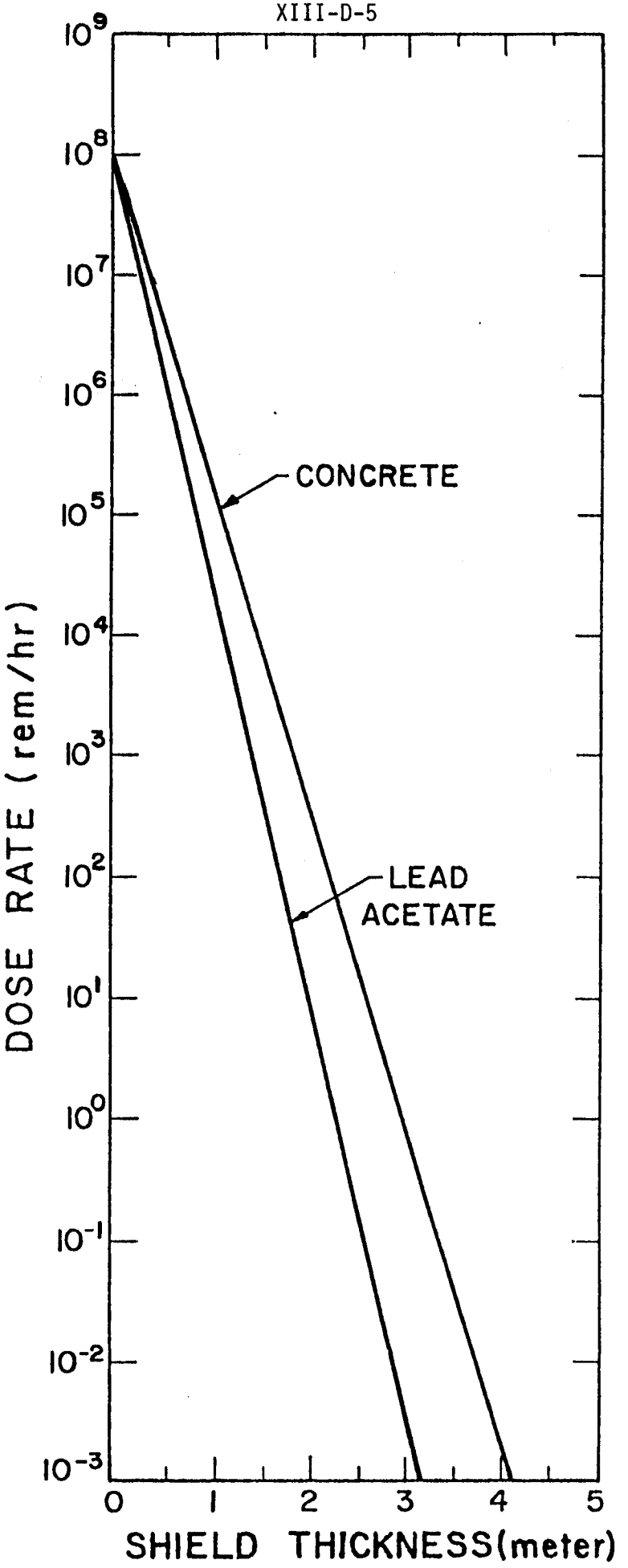
DOSE RATE (rem/hr)
10^{9}
10^{8}
10^{7}
10^{6}
10^{5}
10^{4}
10^{3}
10^{2}
10^{1}
10^{0}
10^{-1}
10^{-2}
10^{-3}
CONCRETE
LEAD
ACETATE
0
1
2
3
4
5
SHIELD THICKNESS(meter)

Fig. XIII-D-1.

is also included giving the overall composition shown in Table XIII-D-3. Demanding that the dose rate be 1 mrem/hr behind the shield, a shield thickness of 3.2 meters has been obtained.

This shield design looks very attractive when coupled with the low radioactivity blanket. It offers the potential for very easy disassembly after shutdown which is a very positive feature of the SOLASE design. The cost of the lead acetate shield is several times greater ($6 million) than the cost of the concrete shield ($1 million). However neither of these costs is great enough to warrant concern.

Table XIII-D-3

Lead Acetate Shield Composition

Component	Number Density (cm^{-3})
Lead	2.385×10^{21}
Carbon	9.540×10^{21}
Oxygen	2.902×10^{22}
Hydrogen	6.576×10^{22}
Aluminum	6.00×10^{21}

XIII-E. Radioactivity

XIII-E-1. Calculational Methods

The chronological order of calculations and procedures performed leading to radioactivity parameters and dose rates for the blanket and shield follows that employed in the recent TETR design study.[1] This includes utilization of the DKR[2] fusion reactor radioactivity code and its decay chain data library, DCDLIB,[3] for the brunt of the work.

Initially, after system geometry and composition are established, neutron multi-group fluxes are coupled with the cross-section sets contained in DCDLIB by DKR to generate automatically those linear decay chains pertinent to the laser fusion system. The chains set up for the three blankets evaluated in this section are given in Tables XIII-E-1 and XIII-E-2. Additional information can be found in the next subsection (XIII-E-2) on these particular alloys and their constituents.

With the chosen system operating time and specified after-shutdown times, DKR then solves the set-up chains for the resultant radionuclide number densities on an intervalwise basis, as well as the related activity, afterheat, and biological hazard potential (BHP). A file containing decay gamma sources also is generated for all blanket and shield intervals for use in the associated dose calculation.

Table XIII-E-1. Linear Decay Chains Constructed to Evaluate Radioactivity of the Ti-8Mn Blanket (not including those considered for impurities in the graphite)

1. $^{6}Li\ (n,p)^{6}He \longrightarrow {}^{6}Li$
   $^{7}Li\ (n,n'p)\ ^{6}He \longrightarrow {}^{6}Li$
   $(n,\gamma)\ ^{8}Li \longrightarrow {}^{8}Be$
2. $^{13}C\ (n,\gamma)\ ^{14}C \longrightarrow {}^{14}N$
3. $^{16}O\ (n,p)\ ^{16}N \longrightarrow {}^{16}O$
4. $^{46}Ti\ (n,p)\ ^{56}Sc \longrightarrow {}^{46}Ti$
   $(n,2n)\ ^{45}Ti \xrightarrow{\beta^{t},EC} {}^{45}Sc$
   $^{47}Ti\ (n,d)\ ^{46}Sc \longrightarrow {}^{46}Ti$
   $(n,p)\ ^{47}Sc \longrightarrow {}^{47}Ti$
   $(n,2n)\ ^{46}Ti\ (n,p)\ ^{46}Sc \longrightarrow {}^{46}Ti$
   $(n,2n)\ ^{46}Ti\ (n,2n)\ ^{45}Ti \xrightarrow{\beta^{t},EC} {}^{45}Sc$
   $^{48}Ti\ (n,\alpha)\ ^{45}Ca \longrightarrow {}^{45}Sc$
   $(n,d)\ ^{47}Sc \longrightarrow {}^{47}Ti$
   $(n,p)\ ^{48}Sc \longrightarrow {}^{48}Ti$
   $^{49}Ti\ (n,n)\alpha\ ^{45}Ca \longrightarrow {}^{45}Sc$
   $(n,t)\ ^{47}Sc \longrightarrow {}^{47}Ti$
   $(n,d)\ ^{48}Sc \longrightarrow {}^{48}Ti$
   $(n,p)\ ^{49}Sc \longrightarrow {}^{49}Ti$
   $(n,2n)\ ^{48}Ti\ (n,\alpha)\ ^{45}Ca \longrightarrow {}^{45}Sc$
   $(n,2n)\ ^{48}Ti\ (n,d)\ ^{47}Sc \longrightarrow {}^{47}Ti$
   $(n,2n)\ ^{48}Ti\ (n,p)\ ^{48}Sc \longrightarrow {}^{48}Ti$
4. $^{50}Ti\ (n,d)\ ^{49}Sc \longrightarrow {}^{49}Ti$
   $(n,p)\ ^{50}Sc \longrightarrow {}^{50}Ti$
   $(n,\alpha)\ ^{47}Ca \longrightarrow {}^{47}Sc \longrightarrow {}^{47}Ti$
   $(n,2n)\ ^{49}Ti\ (n,n)\alpha\ ^{45}Ca \longrightarrow {}^{45}Sc$
   $(n,2n)\ ^{49}Ti\ (n,t)\ ^{47}Sc \longrightarrow {}^{47}Ti$
   $(n,2n)\ ^{49}Ti\ (n,d)\ ^{48}Sc \longrightarrow {}^{48}Ti$
   $(n,2n)\ ^{49}Ti\ (n,p)\ ^{49}Sc \longrightarrow {}^{49}Ti$
5. $^{55}Mn\ (n,\alpha)\ ^{52}V \longrightarrow {}^{52}Cr$
   $(n,p)\ ^{55}Cr \longrightarrow {}^{55}Mn$
   $(n,2n)\ ^{54}Mn \xrightarrow{EC^{*}} {}^{54}Cr$
   $(n,\gamma)\ ^{56}Mn \longrightarrow {}^{56}Fe$

Note: Decay arrows with no specification of decay type, i.e., ($\longrightarrow$), signify beta-minus decay.

Table XIII-E-2. Linear Decay Chains Constructed to Evaluate Radioactivity of Either the Al 6061 or the Al 1100 Blankets

(not including chains constructed for the graphite impurities)

1. $^{6}Li(n,p)\ ^{6}He \longrightarrow\ ^{6}Li$
   $^{7}Li(n,n')p\ ^{6}He \longrightarrow\ ^{6}Li$
   $(n,\gamma)\ ^{8}Li \longrightarrow\ ^{8}Be$
2. $^{13}C(n,\gamma)\ ^{14}C \longrightarrow\ ^{14}N$
3. $^{16}O(n,p)\ ^{16}N \longrightarrow\ ^{16}O$
4. $^{24}Mg(n,p)\ ^{24}Na \longrightarrow\ ^{24}Mg$
   $^{25}Mg(n,p)\ ^{25}Na \longrightarrow\ ^{25}Mg$
   $^{26}Mg(n,\alpha)\ ^{23}Ne \longrightarrow\ ^{23}Na$
   $(n,p)\ ^{26}Na \longrightarrow\ ^{26}Mg$
   $(n,\alpha)\ ^{27}Mg \longrightarrow\ ^{27}Al$
5. $^{27}Al(n,\alpha)\ ^{24}Na \longrightarrow\ ^{24}Mg$
   $(n,p)\ ^{27}Mg \longrightarrow\ ^{27}Al$
   $(n,2n)\ ^{26}Al \xrightarrow{\beta^+,EC}\ ^{26}Mg$
   $(n,\gamma)\ ^{28}Al \longrightarrow\ ^{28}Si$
6. $^{28}Si(n,p)\ ^{28}Al \longrightarrow\ ^{28}Si$
   $^{29}Si(n,p)\ ^{29}Al \longrightarrow\ ^{29}Si$
   $^{30}Si(n,\alpha)\ ^{27}Mg \longrightarrow\ ^{27}Al$
   $(n,p)\ ^{30}Al \longrightarrow\ ^{30}Si$
   $(n,\gamma)\ ^{31}Si \longrightarrow\ ^{31}P$
7. $^{46}Ti(n,p)\ ^{46}Sc \longrightarrow\ ^{46}Ti$
   $(n,2n)\ ^{45}Sc \longrightarrow\ ^{45}Ti$
   $^{47}Ti(n,d)\ ^{46}Sc \longrightarrow\ ^{46}Ti$
   $(n,p)\ ^{47}Sc \longrightarrow\ ^{47}Ti$
   $^{48}Ti(n,\alpha)\ ^{45}Ca \longrightarrow\ ^{45}Sc$
   $(n,d)\ ^{47}Sc \longrightarrow\ ^{47}Ti$
   $(n,p)\ ^{48}Sc \longrightarrow\ ^{48}Ti$
   $^{49}Ti(n,n)\alpha\ ^{45}Ca \longrightarrow\ ^{45}Sc$
   $(n,t)\ ^{47}Sc \longrightarrow\ ^{47}Ti$
   $(n,d)\ ^{48}Sc \longrightarrow\ ^{48}Ti$
   $(n,p)\ ^{49}Sc \longrightarrow\ ^{49}Ti$
   $^{50}Ti(n,d)\ ^{49}Sc \longrightarrow\ ^{49}Ti$
   $(n,p)\ ^{50}Sc \longrightarrow\ ^{50}Ti$
   $(n,\alpha)\ ^{47}Ca \longrightarrow\ ^{47}Sc \longrightarrow\ ^{47}T$
8. $^{50}Cr(n,d)\ ^{49}V \xrightarrow{EC}\ ^{49}Ti$
   $(n,\gamma)\ ^{51}Cr \xrightarrow{EC}\ ^{51}V$
   $(n,2n)\ ^{49}Cr \xrightarrow{\beta^+,EC}\ ^{49}V$
   $^{52}Cr(n,p)\ ^{52}V \longrightarrow\ ^{52}Cr$
   $(n,2n)\ ^{51}Cr \xrightarrow{EC}\ ^{51}V$
   $^{53}Cr(n,d)\ ^{52}V \longrightarrow\ ^{52}Cr$
   $^{54}Cr(n,\alpha)\ ^{51}Ti \longrightarrow\ ^{51}V$
   $(n,\gamma)\ ^{55}Cr \longrightarrow\ ^{55}Mn$

Note: Decay arrows with no specification of decay type, i.e., ($\longrightarrow$), signify beta-minus decay.

Al 6061/Al 1100 Chains (continued)

9. $^{55}Mn(n,\alpha)\ ^{52}V \longrightarrow\ ^{52}Cr$

$(n,p)\ ^{55}Cr \longrightarrow\ ^{55}Mn$

$(n,2n)\ ^{54}Mn \xrightarrow{EC}\ ^{54}Cr$

$(n,\gamma)\ ^{56}Mn \longrightarrow\ ^{56}Fe$

10. $^{54}(n,\alpha)\ ^{51}Cr \xrightarrow{EC}\ ^{51}V$

$(n,d)\ ^{53}Mn \xrightarrow{EC}\ ^{53}Cr$

$(n,p)\ ^{54}Mn \xrightarrow{EC}\ ^{54}Cr$

$(n,\gamma)\ ^{55}Fe \xrightarrow{EC}\ ^{55}Mn$

$(n,2n)\ ^{53}Fe \xrightarrow{\beta^+,EC}\ ^{53}Mn \xrightarrow{EC}\ ^{53}Cr$

$^{56}Fe(n,t)\ ^{54}Mn \xrightarrow{EC}\ ^{54}Cr$

$(n,p)\ ^{56}Mn \longrightarrow\ ^{56}Fe$

$(n,2n)\ ^{55}Fe \xrightarrow{EC}\ ^{55}Mn$

$^{57}Fe(n,d)\ ^{56}Mn \longrightarrow\ ^{56}Fe$

$(n,p)\ ^{57}Mn \longrightarrow\ ^{57}Fe$

$^{58}Fe(n,\alpha)\ ^{55}Cr \longrightarrow\ ^{55}Mn$

$(n,t)\ ^{56}Mn \longrightarrow\ ^{56}Fe$

$(n,d)\ ^{57}Mn \longrightarrow\ ^{57}Fe$

$(n,\gamma)\ ^{59}Fe \longrightarrow\ ^{59}Co$

11. $^{63}Cu(n,\alpha)\ ^{60}Co \xrightarrow{\beta^{-*}}\ ^{60}Ni$

$(n,\gamma)\ ^{64}Cu \xrightarrow{EC,\beta^+,\beta^-}$ t

$^{65}Cu(n,2n)\ ^{64}Cu \xrightarrow{EC,\beta^+,\beta^-}$ t

$(n,\gamma)\ ^{66}Cu \longrightarrow\ ^{66}Zr$

12. $^{64}Zn(n,p)\ ^{64}Cu \longrightarrow\ ^{64}Zn$

$(n,2n)\ ^{63}Zn \xrightarrow{\beta^+,EC}\ ^{64}Cu$

$(n,\gamma)\ ^{65}Zn \xrightarrow{\beta^+,EC}\ ^{65}Cu$

$^{66}Zn(n,2n)\ ^{65}Zn \xrightarrow{\beta^+,EC}\ ^{65}Cu$

$^{67}Zn(n,p)\ ^{67}Cu \longrightarrow\ ^{67}Zn$

$^{68}Zn(n,\alpha)\ ^{65}Ni \longrightarrow\ ^{65}Cu$

$(n,p)\ ^{68}Cu \longrightarrow\ ^{68}Zn$

$(n,\gamma)\ ^{69}Zn \longrightarrow\ ^{69}Ga$

$(n,\gamma)^*\ ^{69m}Zn \xrightarrow{IT}\ ^{69}Zn \longrightarrow\ ^{69}Ga$

$^{70}Zn(n,\gamma)\ ^{71}Zn \longrightarrow\ ^{71}Ga$

$(n,\gamma)^*\ ^{71m}Zn \longrightarrow\ ^{71}Ga$

$(n,\alpha)\ ^{67}Ni \longrightarrow\ ^{67}Cu \longrightarrow\ ^{67}Zn$

$+ \begin{cases} 19\%\ (\beta^+) + 43\%\ (EC) \longrightarrow\ ^{64}Ni \\ 38\%\ (\beta^-) \longrightarrow\ ^{64}Zn \end{cases}$

The dose rate at a particular position is found with an auxiliary program to DKR, DOSE, which accepts an adjoint gamma flux set and the gamma decay source as input. The above adjoint flux is generated from an ANISN[4] run that uses a human tissue kerma factor set as a "source" in the proper spatial interval.

The bulk of radioactivity considerations is based on a one-year operating time for the system although in several cases activation and subsequent decay were also found for a 2-year continuous flux condition. All DKR code implementations for the laser fusion blanket and shield radioactivity study are done with a 5 MW/m^2 wall loading.

XIII-E-2. System Geometry and Material Composition

For the most part, appraisals made of the induced activity in the blanket and shield surrounding the laser fusion cavity are confined to one-dimensional analyses based on the model represented in Figure XIII-E-1. The webbed graphite blanket structure with Li_2O cooling channels is seen to be dealt with,as far as the activity calculation is concerned,by establishing zones of homogenized material, e.g., zones 3, 5, 7, 9, 11, and 13 consist of 3 volume % graphite and 97 volume % Li_2O (at 60% theoretical density). Those regions of the web that run parallel to the first wall are designated as zones 3, 4, 6, 8, 10, 12, and have a 60 vol. percent graphite makeup. Also common to all blankets considered is the water-cooled structural support plate, given

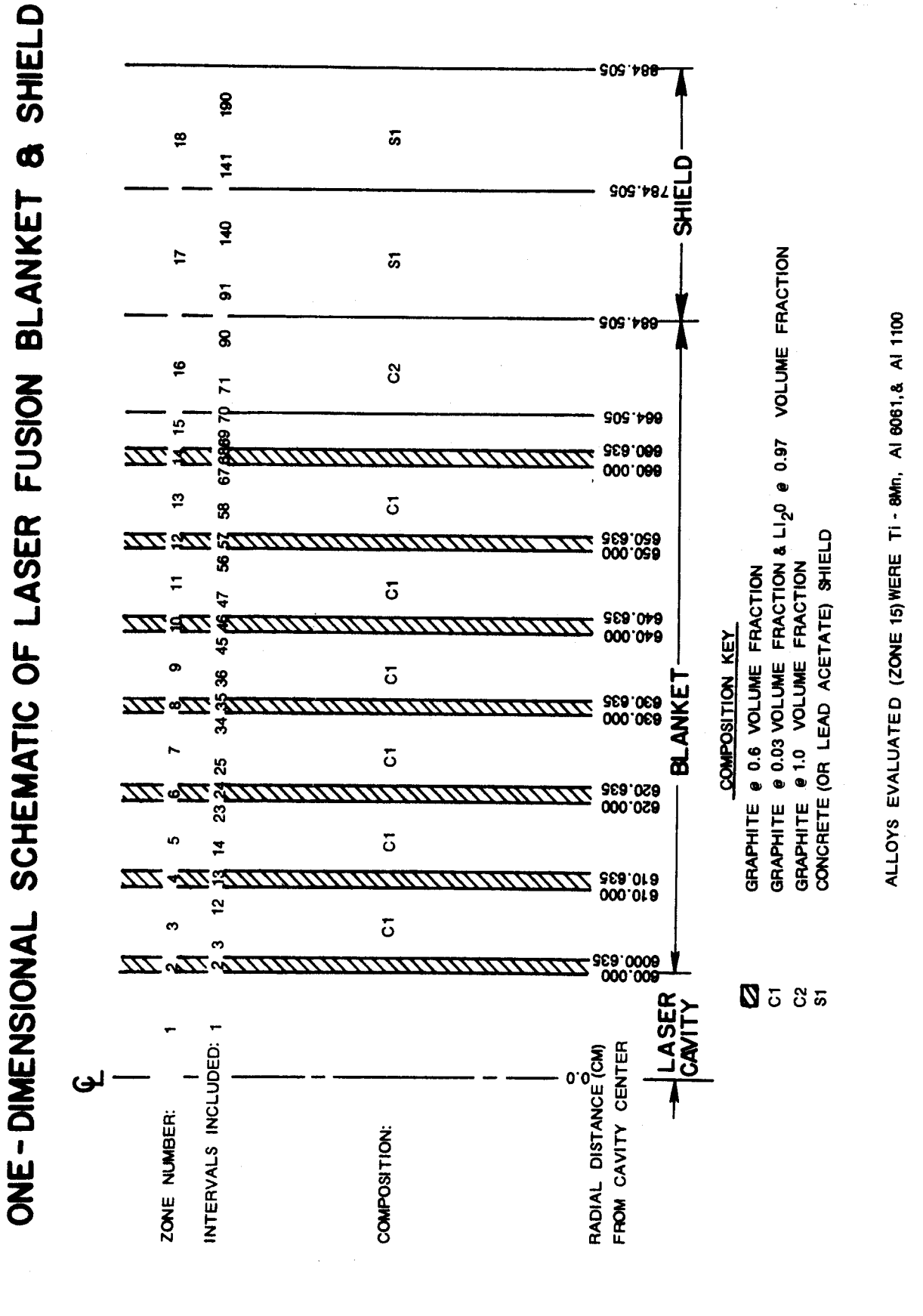
ONE-DIMENSIONAL SCHEMATIC OF LASER FUSION BLANKET & SHIELD
ZONE NUMBER:
INTERVALS INCLUDED:
COMPOSITION:
RADIAL DISTANCE (CM) FROM CAVITY CENTER
LASER CAVITY
BLANKET
SHIELD
600.000
600.635
610.000
610.635
620.000
620.635
630.000
630.635
640.000
640.635
650.000
650.635
660.000
660.635
664.505
684.505
784.505
884.505
COMPOSITION KEY
C1 GRAPHITE @ 0.6 VOLUME FRACTION
GRAPHITE @ 0.03 VOLUME FRACTION & Li_2O @ 0.97 VOLUME FRACTION
C2 GRAPHITE @ 1.0 VOLUME FRACTION
S1 CONCRETE (OR LEAD ACETATE) SHIELD
ALLOYS EVALUATED (ZONE 15) WERE Ti - 8Mn, Al 8061, & Al 1100
ALL GRAPHITE WITH 5PPM OF (Si, Fe, Al, & Mg) EACH

Fig. XIII-E-1.

as 35% alloy and 65% water (at 0.5 density factor to account for high temperature conditions) in zone 15. Completing the outer regions of the structure are a 20 cm.-graphite reflector (zone 16) and a two meter-thick shield (zones 17 and 18).

Three blanket alloys are considered in this treatment: Ti-8 Mn, Al 6061, and Al 1100.[5] Their respective elemental compositions are listed in Table XIII-E-3. The titanium alloy is one of several studied recently that looks particularly attractive from a low residual radioactivity point of view.[6] The Al 6061 contains magnesium and silicon as major alloying elements, both of which are not noted for particularly bothersome activation products. Al 1100 is a high aluminum content alloy ($\geq$ 99%) that contains no Cr, Ti, and Mg and even lower percentages of those trace elements shared in common with Al 6061. While there is substantial difference among the three, the blanket schematic indicates that the alloy chosen is present in only one 3.8 cm thick zone of the lightweight structure. Thus when a blanket is denoted as a Ti-8 Mn, Al 6061, or Al 1100 blanket, the variation referred to will be only in the alloy present in zone 15; all other nonshield regions are identical from one design to the next. For comparison purposes, a 316 SS blanket is also analyzed for activity BHP and afterheat, but it is not pursued further as a chief blanket alloy.

Two very different shields are analyzed along with the blanket possibilities, one of reinforced concrete and the other, lead acetate contained in aluminum structure. The latter especially offers

Table XIII-E-3. Blanket Materials Evaluated for the Laser Fusion Study

Alloy	Mass Density (gm/cc)	Elemental Composition	
		Element	Weight %
1. Ti-8Mn	4.71	Ti	92.
		Mn	8.
2. Al 6061	2.707	Si	0.60
		Fe	0.70
		Cu	0.275
		Mn	0.15
		Mg	1.00
		Cr	0.25
		Zn	0.25
		Ti	0.15
		Al	96.625
3. Al 1100	2.713	Si, Fe	0.741
		Cu	0.148
		Mn	0.037
		Zn	0.074
		Al	99.000

persuasive arguments for implementation; one not only has a shield that can be drained and then easily moved, but also one of low activation and excellent gamma attenuation.

Throughout all analyses, any graphite contained in either the web or the reflector of the blanket is assumed to have a 20 ppm total impurity level, or 5 ppm each of iron, silicon, aluminum, and magnesium. This is somewhat above the purity level found in present day nuclear grade graphite.[7] Standard grades could be expected to show total ash content somewhere in the 300-600 ppm range, or a factor of 200 greater than the nuclear type.

Dose rate calculations add a one-centimeter-thick tissue zone at some point of interest near or in the blanket or shield. The three positions reported on later in this section include the laser cavity center, outside the metal back structure, and outside the shield. Also, while zones 2, 4, 6, 8, 10 and 12 contain 97% Li_2O (at a density factor of 0.6) for the radioactivity analysis, the important activated products resulting from this coolant are of very short half-lives (the longest being ^{16}N with $t_{1/2}$ = 7.2 sec). Hence, the coolant contribution to the total activity or afterheat is appreciable only within the first 60 seconds after shutdown. It is chosen to report dose rates based on Figure XIII-E-1 geometry and composition but without Li_2O in the webbed blanket structure.

XIII-E-3. Induced Activity in Blanket and Shield

The radioactivity given in total curies per thermal watt of operating power following shutdown is shown in Figure XIII-E-2 for the four evaluated blankets and a separate graphite blanket impurities calculation following one year of operation. The activity at shutdown of the Al 6061 and 1100 and Ti-8 Mn blankets is seen to be in the $(3 \rightarrow 4) \times 10^{-1}$ Ci/W(th) range, about one-half that reported for the outer blankets of UWMAK-I[8] and UWMAK-III[9] and approximately a factor of 10 less than TETR. Moreover, it is immediately apparent that the three design alloys offer at least an order of magnitude activity reduction for all times greater than one minute after shutdown over that of the 316 SS blanket. It is also notable that impurities in the nuclear grade graphite throughout the blanket lead to activity levels that are only remotely comparable to the rest of the system during the interval, 3 to 18 years post-shutdown.

All three blankets (Ti-8 Mn, Al 6061, and Al 1100) indicate virtually the same very short-term (< 1 minute) and long-term (> 50 years) levels. The Li_2O zones, common to all designs, give rise to the products ^{6}He, ^{8}Li, and ^{16}N ($t_{1/2}$ = 0.8, 0.842, and 7.2 seconds, respectively), which dominate the systems' total activities, but only during the first few tens of seconds. Similarly, graphite contained in the Li_2O zones and in the reflector (zone 16) controls the activity at long times because

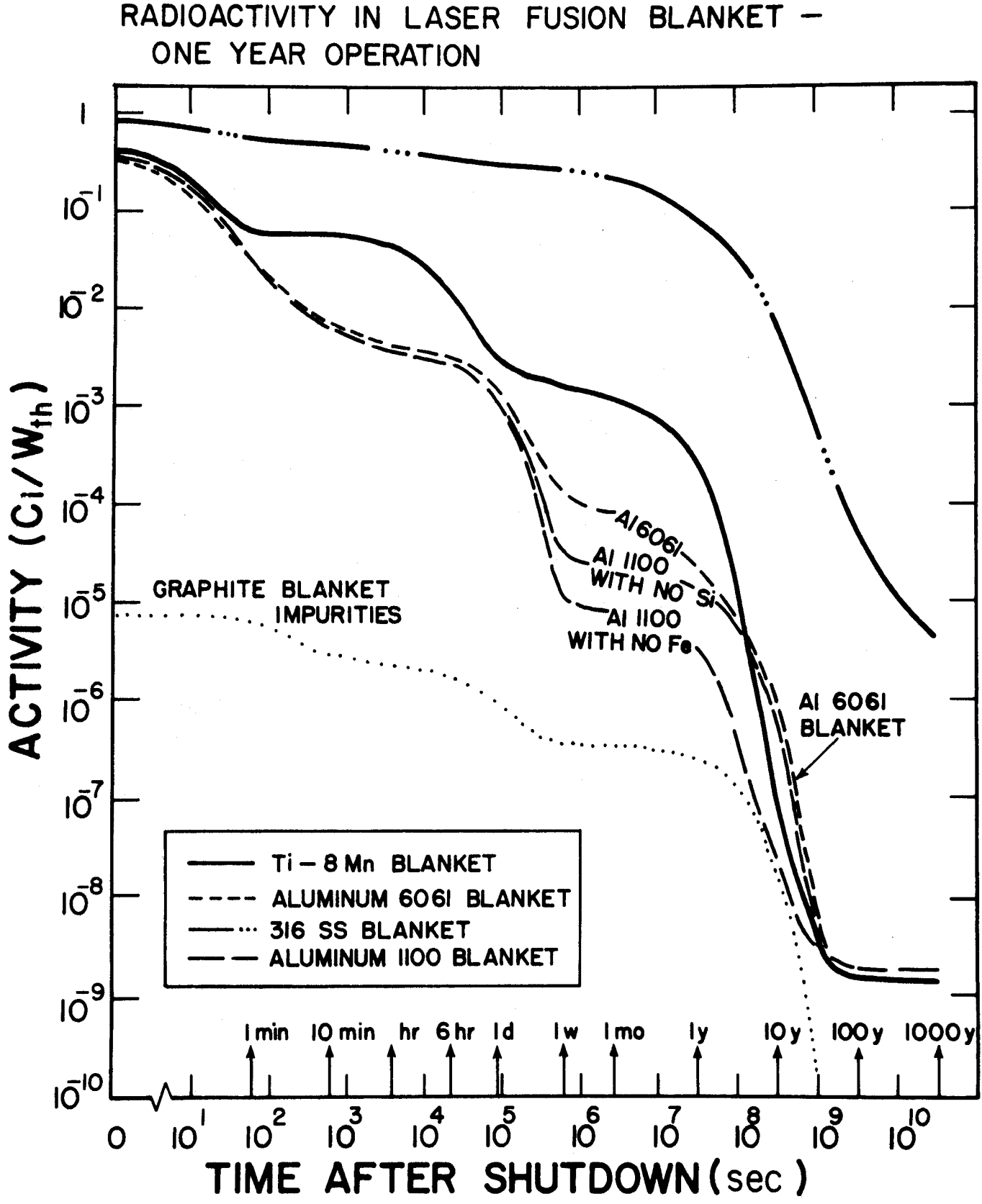

Figure XIII-E-2

of $^{14}C(t_{1/2}$ = 5730 years). It is then seen that the alloy chosen for the back structure (zone 15 of Figure XIII-E-1) influences the overall system chiefly in the one minute to 50 year time span. These characteristics of the laser fusion blanket are illustrated with a Ti-8 Mn blanket in Figure XIII-E-3; the trend is repeated in the aluminum structures as well.

A better understanding of the differences among the decay curves of Figure XIII-E-2 can perhaps be found by recognizing the chief contributors to the overall activity of each blanket type. The next set of these figures attempts to perform this function by presenting the activities of the major nuclides found in Ti-8 Mn, Al 6061, and Al 1100 blanket designs, respectively.

The set of such curves obtained for the Ti-8 Mn blanket, Figure XIII-E-4 indicates the dominance of ^{16}N (from (n,p) reactions with ^{16}O present in Li_2O) at short times and ^{14}C (from (n,γ) reactions in the graphite) after tens of years as discussed previously. However, after ^{16}N dies off, two products of manganese activation, Mn 56 ($t_{1/2}$ = 2.57 hours) and Mn 54 ($t_{1/2}$ = 297 days), govern all but approximately two decades of after shutdown time. It is only during the period of 20 hours to a few months that ^{46}Sc, 96% produced from the $^{46}Ti(n,p)$ reaction, is a sizeable part of the overall blanket curve. Another Sc isotope, ^{47}Sc ($t_{1/2}$ = 3.4 days), is roughly comparable to the ^{46}Sc activity level for nearly the first 7 hours, but its larger decay constant precludes it from ever being greater than about 20% of the total.

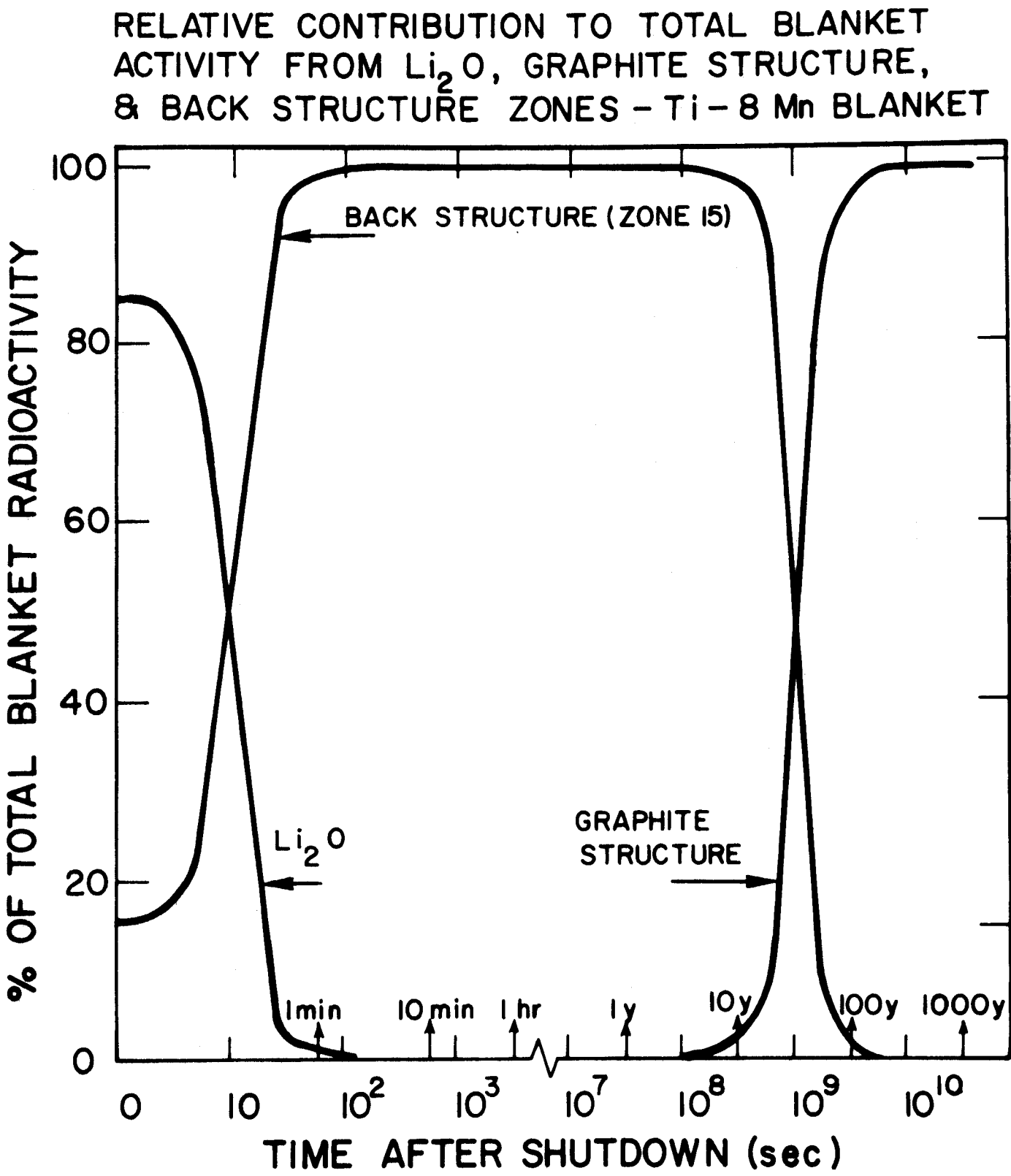
RELATIVE CONTRIBUTION TO TOTAL BLANKET ACTIVITY FROM Li_2O, GRAPHITE STRUCTURE, & BACK STRUCTURE ZONES - Ti - 8 Mn BLANKET
% OF TOTAL BLANKET RADIOACTIVITY
100
80
60
40
20
0
BACK STRUCTURE (ZONE 15)
Li_2O
GRAPHITE STRUCTURE
1min
10min
1 hr
1y
10y
100y
1000y
0
10
10^2
10^3
10^7
10^8
10^9
10^{10}
TIME AFTER SHUTDOWN (sec)

Fig. XIII-E-3

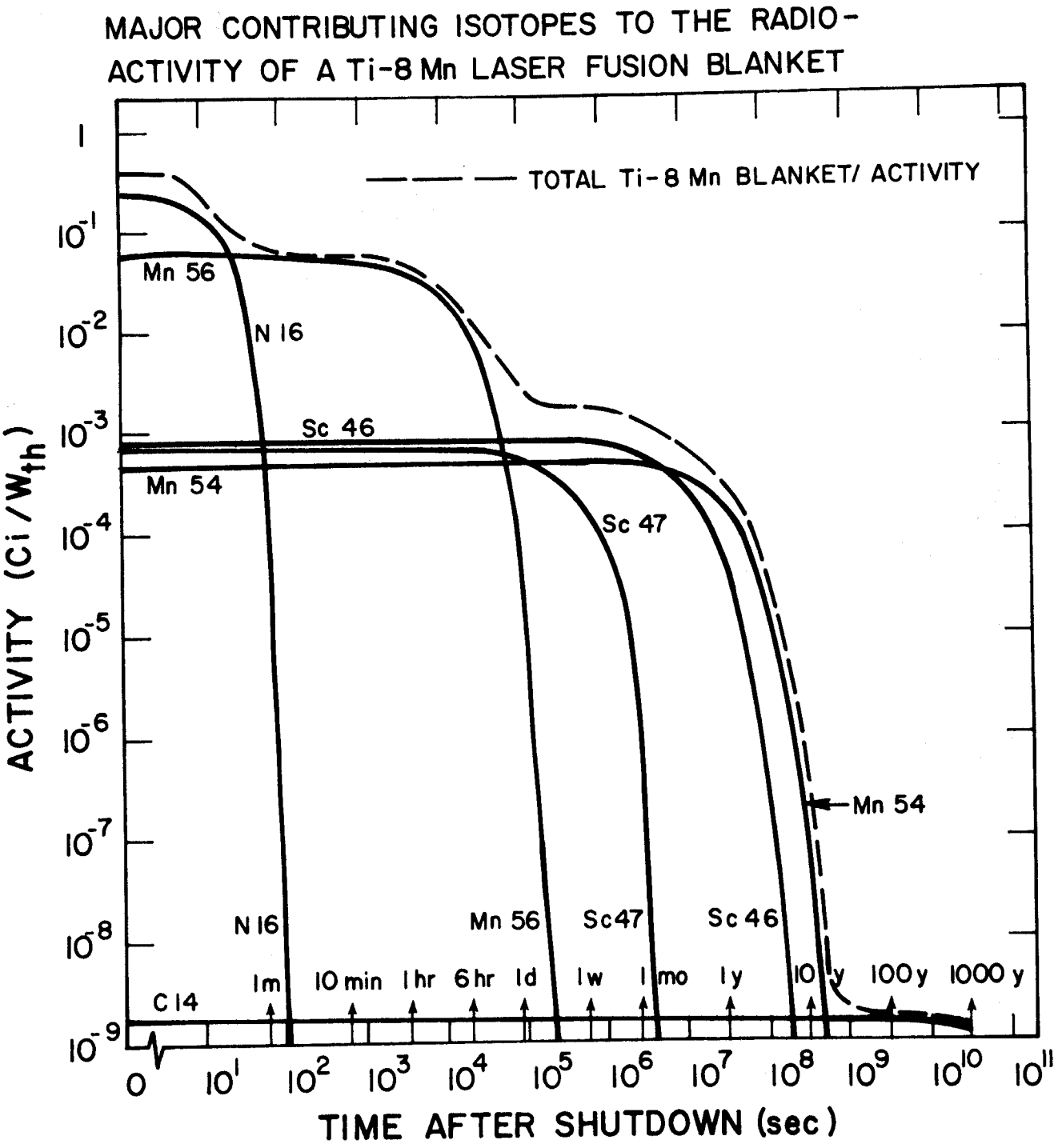
MAJOR CONTRIBUTING ISOTOPES TO THE RADIO-
ACTIVITY OF A Ti-8 Mn LASER FUSION BLANKET
TOTAL Ti-8 Mn BLANKET/ ACTIVITY
Mn 56
N 16
Sc 46
Mn 54
Sc 47
Mn 54
N16
Mn 56
Sc47
Sc 46
C 14
1m
10 min
1hr
6hr
1d
1w
1mo
1y
10 y
100y
1000 y
ACTIVITY (Ci / Wth)
TIME AFTER SHUTDOWN (sec)

Fig. XIII-E-4

Again referring to Figure XIII-E-2, the first aluminum alloy considered, Al 6061, appears to be a marked improvement over a Ti-8 Mn blanket for the initial five years. The aluminum constituent of Al 6061 experiences (n,γ) and (n,α) reactions leading to products that control nearly the first three and one-half days of decay (Figure XIII-E-5). These products, ^{28}Al ($t_{1/2}$ = 2.3 minutes) and ^{24}Na ($t_{1/2}$ = 15 hours), however, are of a short half-life nature compared to three transmutated products formed from the trace elements found in Al 6061. Half-lives of 27.8 days, 245 days, and 2.6 years characterize ^{51}Cr, ^{65}Zn, and ^{55}Fe as they dominate blanket activity in succession from 3.5 days to roughly 30 years after shutdown. Indeed, it is the ^{55}Fe which hangs up the curve for an Al 6061 blanket over that of a Ti-8 Mn design from 5 to 30 years. Again, ^{16}N and ^{14}C "frame" the short and long-term portions.

There is some gain with the Al 1100 blanket in the 3 day to 3 year time span over both Ti-8 Mn and Al 6061 systems, a noteworthy point when maintenance considerations arise. Figure XIII-E-6 shows the activity decay on a total and a per isotope basis for this particular blanket with the Fe content at its upper limit.* It is not the iron constituent, but the reduced zinc (~ a factor of 2) fraction and the zero chromium content of Al 1100 compared to Al 6061 that reduces activity in the above-mentioned period. The shaded area indicates the one week to seventy year portion of the curve where the Fe fraction is influential.

---

*The Fe constituent in Al 1100 considered could vary from 0→0.74 w%.

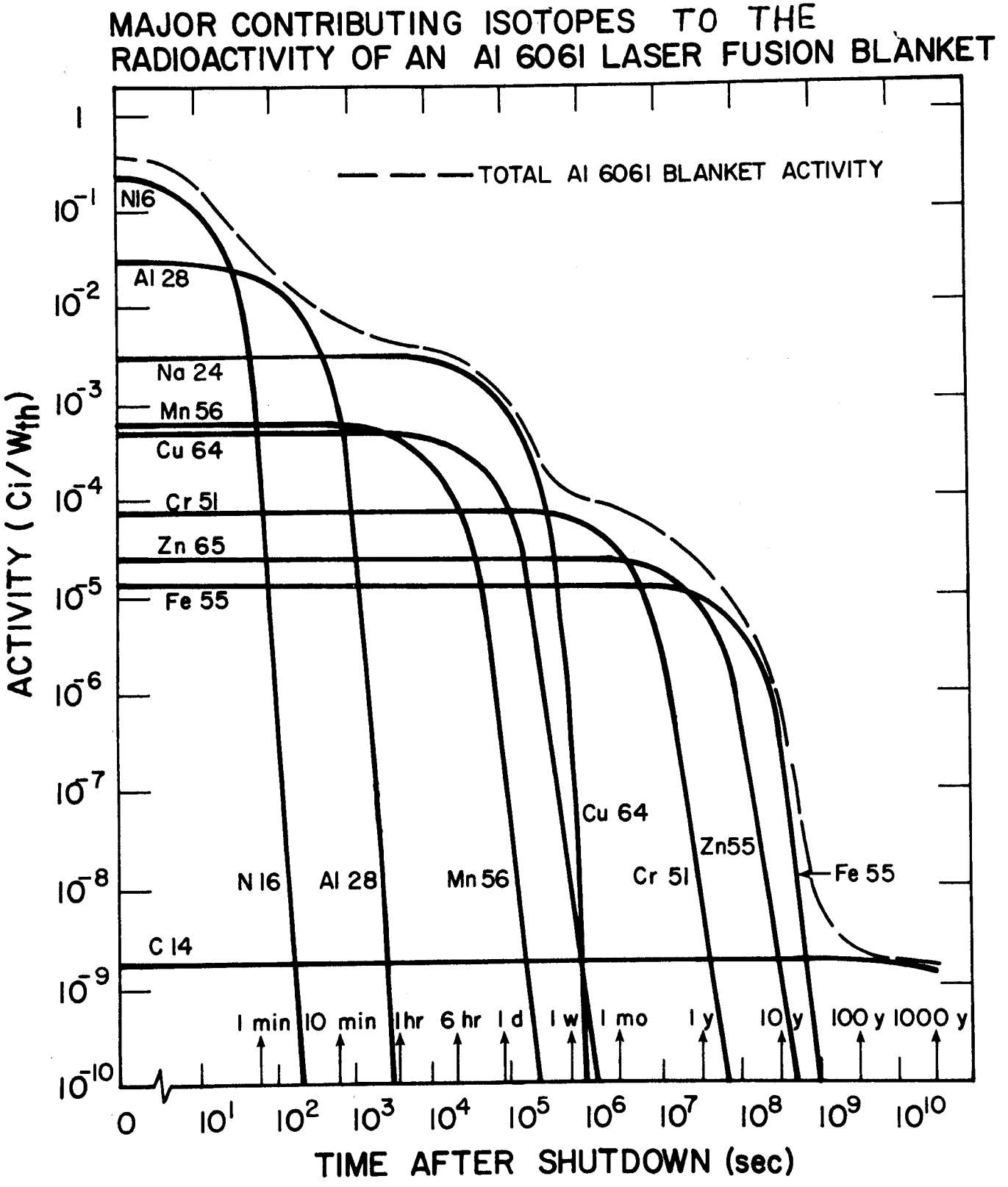
MAJOR CONTRIBUTING ISOTOPES TO THE
RADIOACTIVITY OF AN Al 6061 LASER FUSION BLANKET
TOTAL Al 6061 BLANKET ACTIVITY
N16
Al 28
Na 24
Mn 56
Cu 64
Cr 51
Zn 65
Fe 55
C 14
ACTIVITY (Ci/Wth)
TIME AFTER SHUTDOWN (sec)
1 min
10 min
1hr
6 hr
1 d
1 w
1 mo
1 y
10 y
100 y
1000 y

Fig. XIII-E-5.

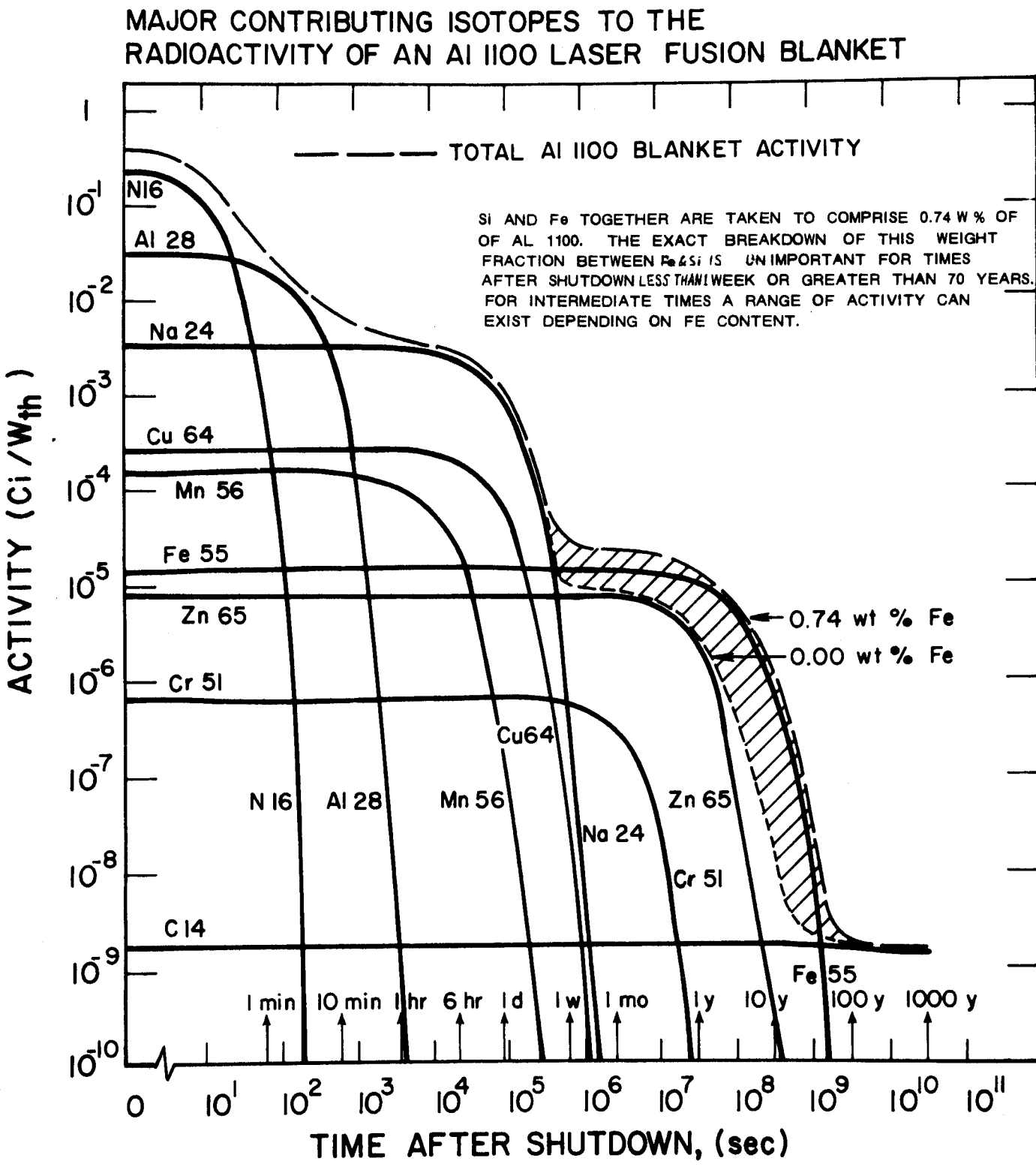
MAJOR CONTRIBUTING ISOTOPES TO THE
RADIOACTIVITY OF AN Al 1100 LASER FUSION BLANKET
TOTAL Al 1100 BLANKET ACTIVITY
Si AND Fe TOGETHER ARE TAKEN TO COMPRISE 0.74 W % OF OF AL 1100. THE EXACT BREAKDOWN OF THIS WEIGHT FRACTION BETWEEN Fe & Si IS UN IMPORTANT FOR TIMES AFTER SHUTDOWN LESS THAN 1 WEEK OR GREATER THAN 70 YEARS. FOR INTERMEDIATE TIMES A RANGE OF ACTIVITY CAN EXIST DEPENDING ON FE CONTENT.
ACTIVITY (Ci / Wth)
TIME AFTER SHUTDOWN, (sec)
N16
Al 28
Na 24
Cu 64
Mn 56
Fe 55
Zn 65
Cr 51
C 14
0.74 wt % Fe
0.00 wt % Fe
1 min
10 min
1 hr
6 hr
1 d
1 w
1 mo
1 y
10 y
100 y
1000 y

Fig. XIII-E-6

The short skewed line (---) representing the best that could be done with the alloy (no Fe) follows the activity given by ^{60}Co for the one to twenty year range. Chief isotopes other than ^{55}Fe, ^{65}Zn, and ^{51}Cr are nearly at the same levels as found in Al 6061, hence the decay curves are not significantly different when those isotopes (^{16}N, ^{28}Al, ^{24}Na, ^{14}C) are important.

While not graphically presented, the three "plateau" portions of the graphite impurity curve of Figure XIII-E-2 are produced by decay of ^{28}Al, ^{24}Na and ^{55}Fe in their respective time frames. Unless the specification for nuclear grade graphite is relaxed, these decays are seen to be not particularly crucial to the overall blanket activity.

Figure XIII-E-7 presents a set of afterheat decay curves obtained for the blankets considered that are not unlike those of the activity in shape and relative positioning. While chief contributors to the afterheat of Ti-8 Mn are the same as the activity, some differences exist with the aluminum blanket. It is found that ^{28}Al and ^{24}Na dominate over the first several weeks in Al 6061 and Al 1100 as is true for the activity, but that ^{65}Zn (0.7 Mev/^{65}Zn-decay) and ^{26}Al(3.3 Mev/^{26}Al decay and $t_{1/2} = 7.4 \times 10^5$ years) control intermediate (a few weeks to a few years) and long-term (times greater than several years) results.

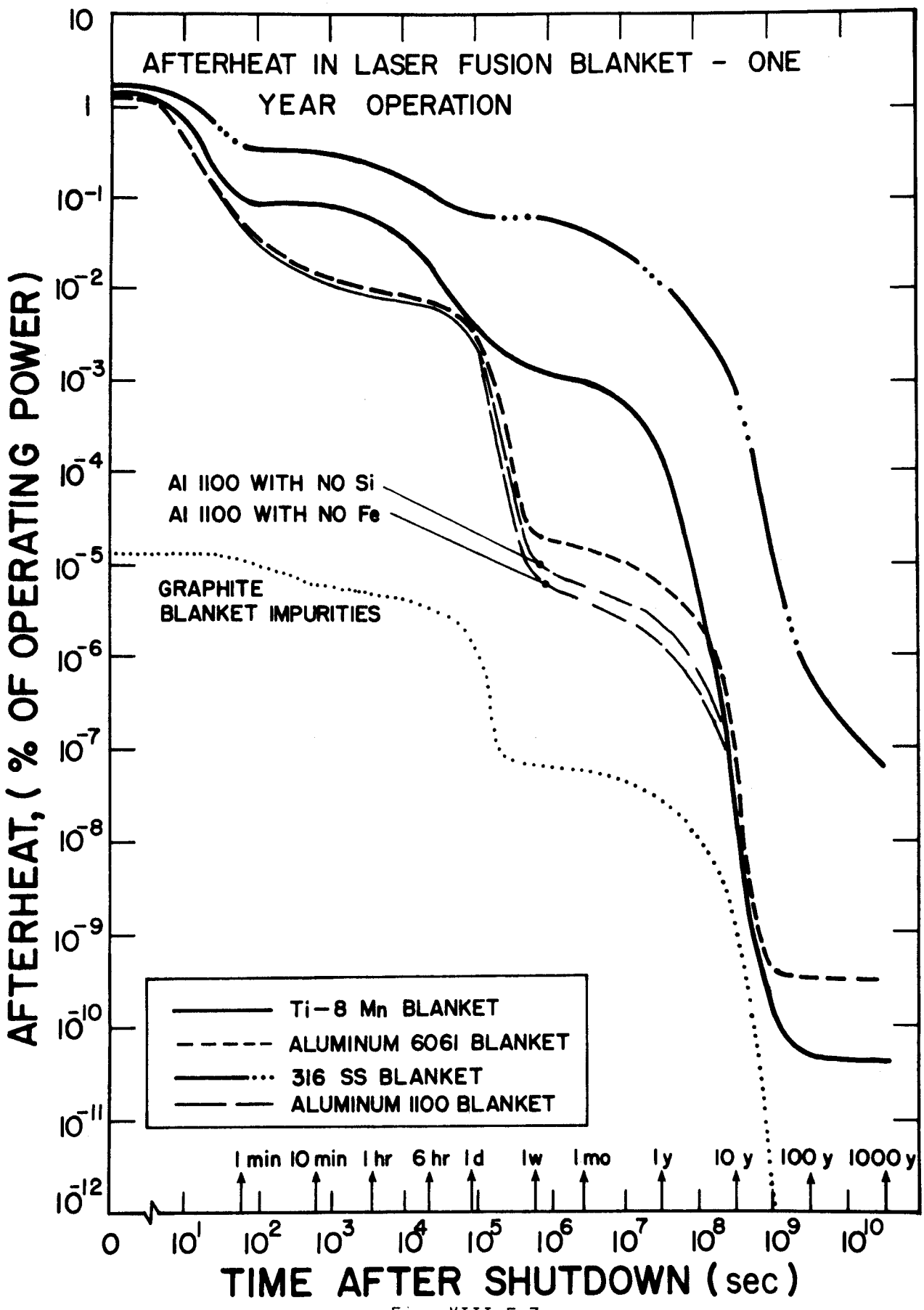
AFTERHEAT IN LASER FUSION BLANKET - ONE YEAR OPERATION
AFTERHEAT, (% OF OPERATING POWER)
TIME AFTER SHUTDOWN (sec)
Al 1100 WITH NO Si
Al 1100 WITH NO Fe
GRAPHITE
BLANKET IMPURITIES
Ti-8 Mn BLANKET
ALUMINUM 6061 BLANKET
316 SS BLANKET
ALUMINUM 1100 BLANKET
1 min
10 min
1 hr
6 hr
1 d
1 w
1 mo
1 y
10 y
100 y
1000 y

Fig. XIII-E-7

The various nuclides contained in a system can be indexed in a different fashion by noting the volume of air required to reduce each one to maximum permissible concentration on a per unit power basis. The biological hazard potential (BHP) thus attained for a particular isotope can be added to that obtained for others of a design resulting in the curves found in Figure XIII-E-8. The BHP levels illustrated here for the titanium or aluminum laser fusion blanket are markedly less than that recently obtained for a plutonium-fueled LMFBR's fuel, coolant, and cladding wastes.[10] Those nuclides which contribute the most toward the overall activity or afterheat for Ti-8 Mn are found to do the same for the BHP curve. The aluminum alloys are a bit different in that while ^{16}N, ^{28}Al, and ^{24}Na are important for times earlier than 10^5 seconds, about 28 hours, ^{55}Fe is never influential. The MPC's for nuclides important for intermediate and long times ($> 10^5$ sec) are from one order to greater than two orders of magnitude less than that of ^{55}Fe (MPC_{AIR} = 30 Ci/km^3). Hence, while this isotope of iron is dominating from about one week to 30 years in the activity curves (Figures XIII-E-5 and 6), the BHP during this time span is controlled largely by ^{65}Zn (MPC_{AIR} = 2 Ci/km^3) and ^{54}Mn (MPC_{AIR} = 1 Ci/km^3). It is the ^{26}Al (MPC_{AIR} = 0.1 Ci/km^3) which causes the BHP curves to hang above that corresponding for the Ti-8 Mn blanket. A short table (Table XIII-E-4) lists the nuclides of greatest interest for each alloy considered.

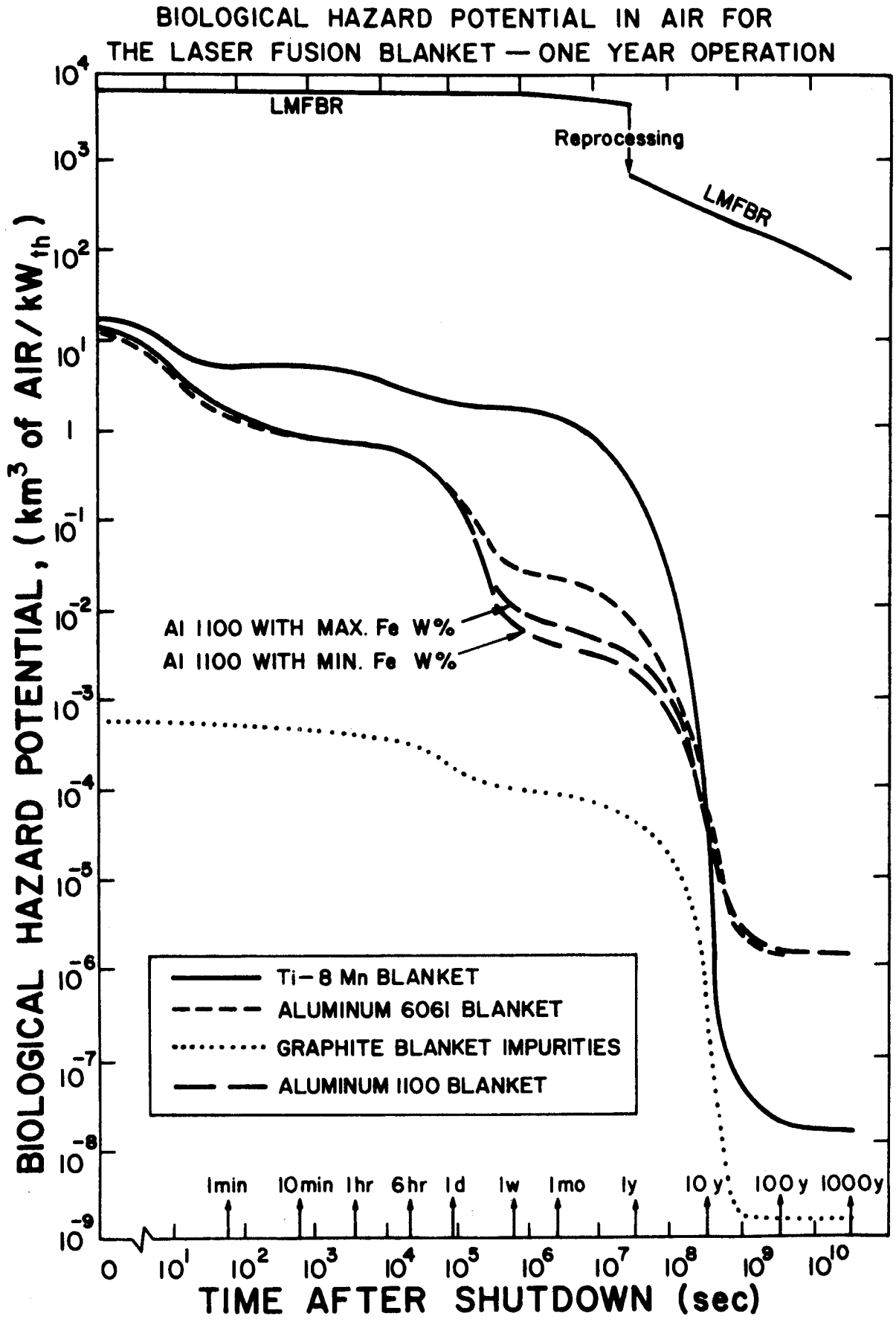
BIOLOGICAL HAZARD POTENTIAL IN AIR FOR
THE LASER FUSION BLANKET — ONE YEAR OPERATION
LMFBR
Reprocessing
LMFBR
Al 1100 WITH MAX. Fe W%
Al 1100 WITH MIN. Fe W%
Ti-8 Mn BLANKET
ALUMINUM 6061 BLANKET
GRAPHITE BLANKET IMPURITIES
ALUMINUM 1100 BLANKET
BIOLOGICAL HAZARD POTENTIAL, (km3 of AIR/kWth)
1min
10min
1hr
6hr
1d
1w
1mo
1y
10 y
100 y
1000y
TIME AFTER SHUTDOWN (sec)

Fig. XIII-E-8

Table XIII-E-4

Major Contributing Nuclides to Total Blanket Biological Hazard Potential, BHP_{AIR}

	Blanket	A $(0 \rightarrow 10^2)$ sec	B $(10^2 \rightarrow 10^5)$ sec	C $(10^5 \rightarrow 10^7)$ sec	D $>10^9$ sec
1.	Ti-8 Mn	^{16}N	^{56}Mn, ^{46}Sc, ^{54}Mn	^{46}Sc, ^{54}Mn	^{14}C
2.	Al 6061 & Al 1100	^{16}N, ^{28}Al, ^{24}Na	^{24}Na	^{65}Zn, ^{54}Mn	^{28}Al, ^{14}C

A set of activity calculations was also performed for two shields, one employing lead-acetate in an aluminum structure and the other using concrete. While the design analyzed used a 2-meter thick shield, changes late in the design extended this dimension to 3.5 meters. It is felt that though more material can now be activated, the drop-off of the neutron flux through this increased thickness will limit the increase in the shield activity parameters to perhaps 75%. Even under assumption of such an increase, corresponding parameters for the blanket will far outweigh contributions from the shield.

Figure XIII-E-9 compares the radioactivity of the two shields, showing Curie/Watt levels that are for the most part at least a factor of 10 smaller than the blanket. The notable exception occurs from approximately one minute to 3 hours when the concrete shield actually is higher ($\sim$ 7 mCi/W compared to $\sim$ 5 mCi/W). The silicon isotope, ^{31}S (via $^{30}S(n,\gamma)$ reactions), dominates concrete shield activity for the first day after shutdown while ^{14}C holds up the decay for times after a few days. The first few days activity of the lead-acetate shield is mainly due to structural activation. ^{28}Al ($\sim$ 0 $\rightarrow$ 10 minutes) and ^{24}Na ($\sim$ 10 min. $\rightarrow$ 3 days) are the two largest contributors. In the succeeding period, one week to 30 years, activation of the lead content gives ^{203}Pb, ^{203}Hg and ^{204}Tl as the controlling nuclides. Long-term results are due to ^{14}C.

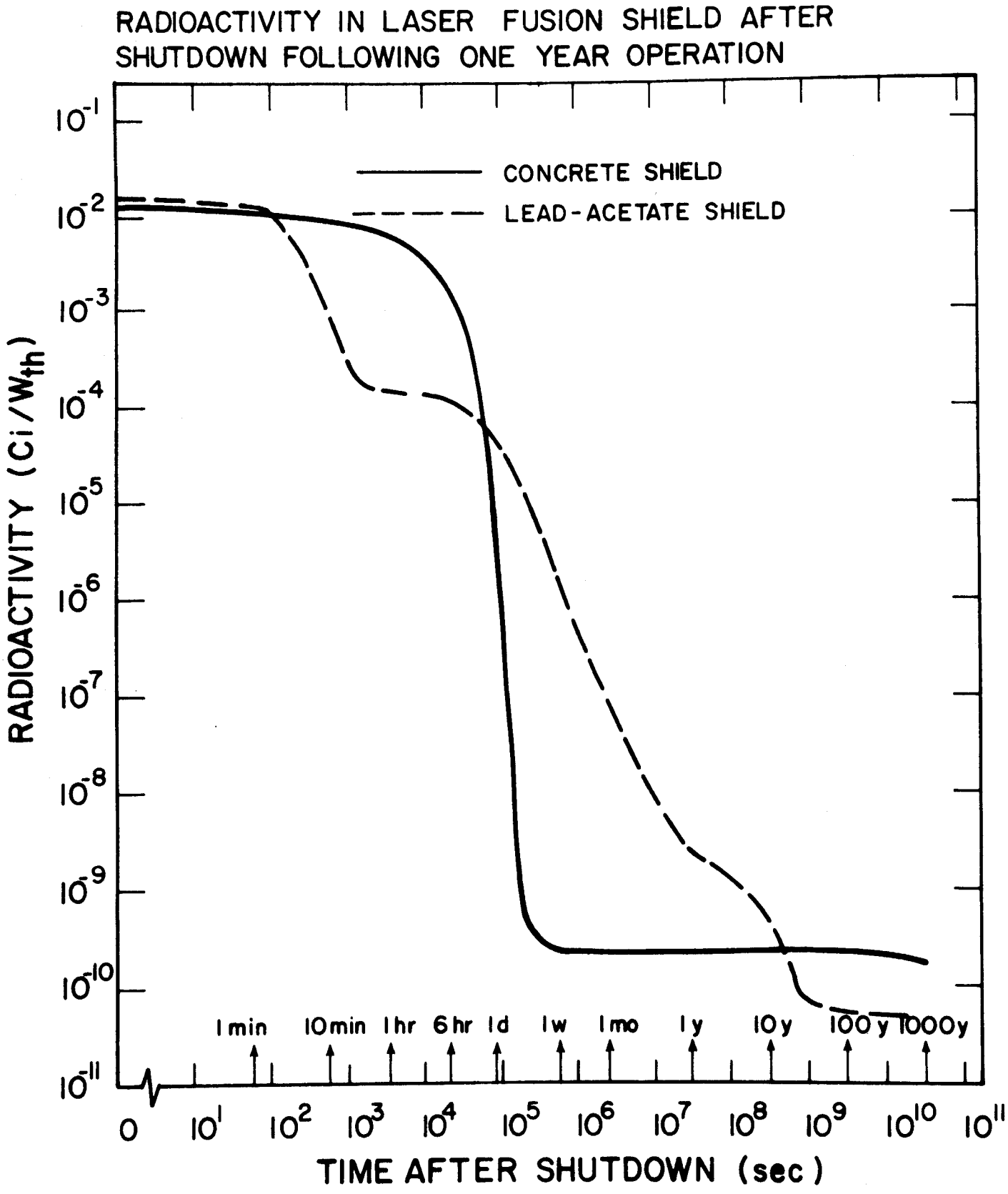
RADIOACTIVITY IN LASER FUSION SHIELD AFTER SHUTDOWN FOLLOWING ONE YEAR OPERATION
CONCRETE SHIELD
LEAD-ACETATE SHIELD
RADIOACTIVITY (Ci/Wth)
10-1
10-2
10-3
10-4
10-5
10-6
10-7
10-8
10-9
10-10
10-11
1 min
10 min
1 hr
6 hr
1 d
1 w
1 mo
1 y
10 y
100 y
1000 y
0
10¹
10²
10³
10⁴
10⁵
10⁶
10⁷
10⁸
10⁹
10¹⁰
10¹¹
TIME AFTER SHUTDOWN (sec)

Fig. XIII-E-9.

The afterheat of the shields (Figure XIII-E-10) is never any problem relative to the blankets. It is found that ^{28}Al and ^{16}N are larger factors in determining early-term concrete afterheat, but otherwise no change occurs from the activity case. The lead-acetate shield afterheat is limited after 50 years by the long-lived ^{26}Al.

Finally, Figure XIII-E-11 indicates the BHP in air for the two shields with the lead acetate curve again remaining above the concrete shield level for any time after one day. The nuclides ^{26}Al and ^{205}Pb, each with MPC_{AIR} = 0.1 Ci/km^3, hang the lead-acetate level for times longer than 60 years at a level greater than that for a Ti-8 Mn blanket or 1.1 x 10^{-7} km^3/kW(th) compared to 1.5 x 10^{-8} km^3/kW(th).

Calculations done assuming a 2-year system operation time instead of one year show no significant change to blanket activity, afterheat, or BHP except to levels resulting from ^{14}C. The long half-life of this nuclide (5730 years) relative to its formation rate during system operation allows essentially twice as much an amount to exist after 2-year operation. This change is noticeable only at 80 years or greater since other earlier dominating nuclides are insensitive to the change of a 2-year from a 1-year operation.

XIII-E-4. After Shutdown Gamma Dose Rates

For emergency and routine maintenance purposes, the laser fusion system can be characterized for various times after shutdown by a set of dose rates due to decay gammas from the activated blanket and shield

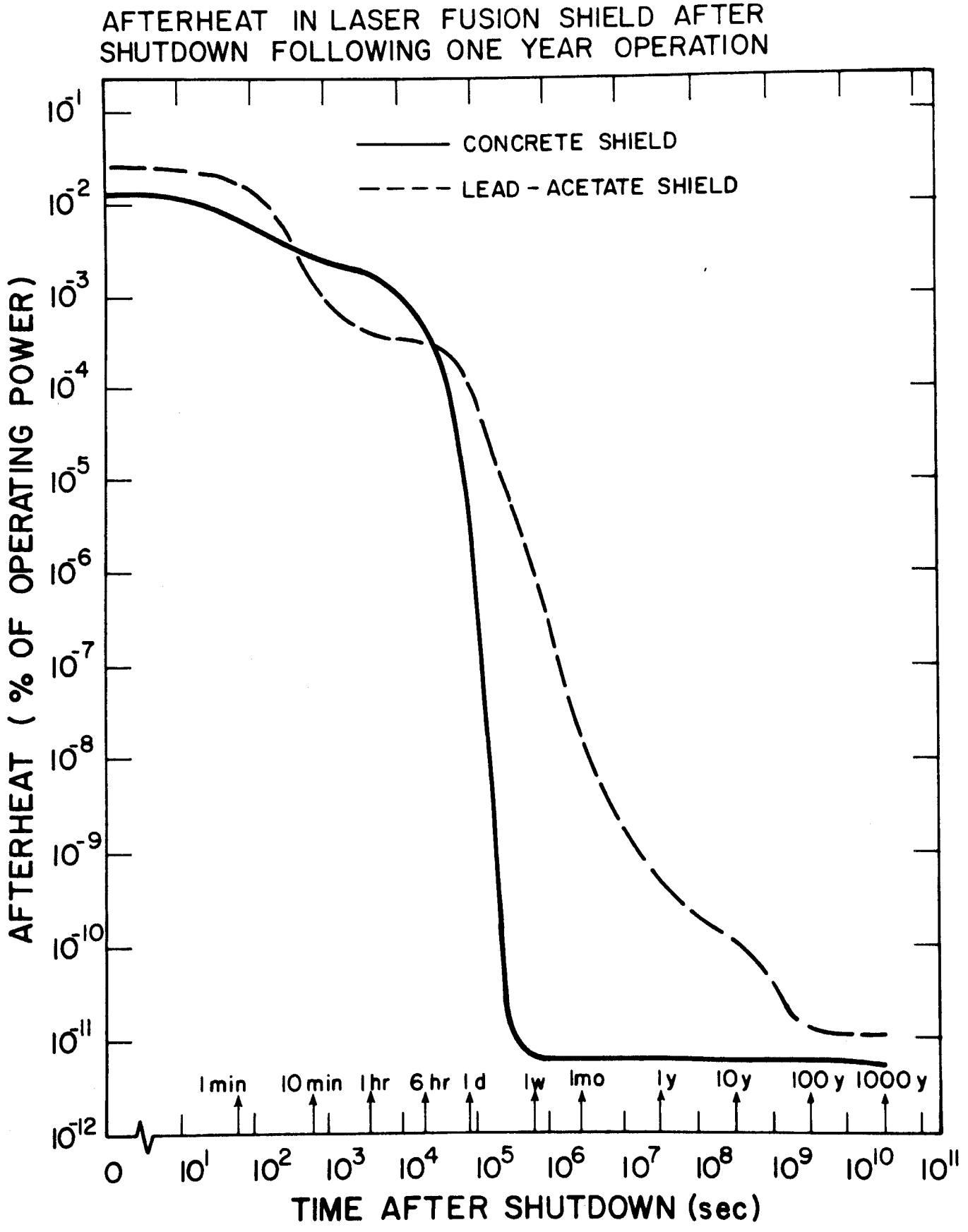
AFTERHEAT IN LASER FUSION SHIELD AFTER SHUTDOWN FOLLOWING ONE YEAR OPERATION
CONCRETE SHIELD
LEAD - ACETATE SHIELD
AFTERHEAT (% OF OPERATING POWER)
TIME AFTER SHUTDOWN (sec)
1 min
10 min
1 hr
6 hr
1 d
1 w
1 mo
1 y
10 y
100 y
1000 y

Fig. XIII-E-10

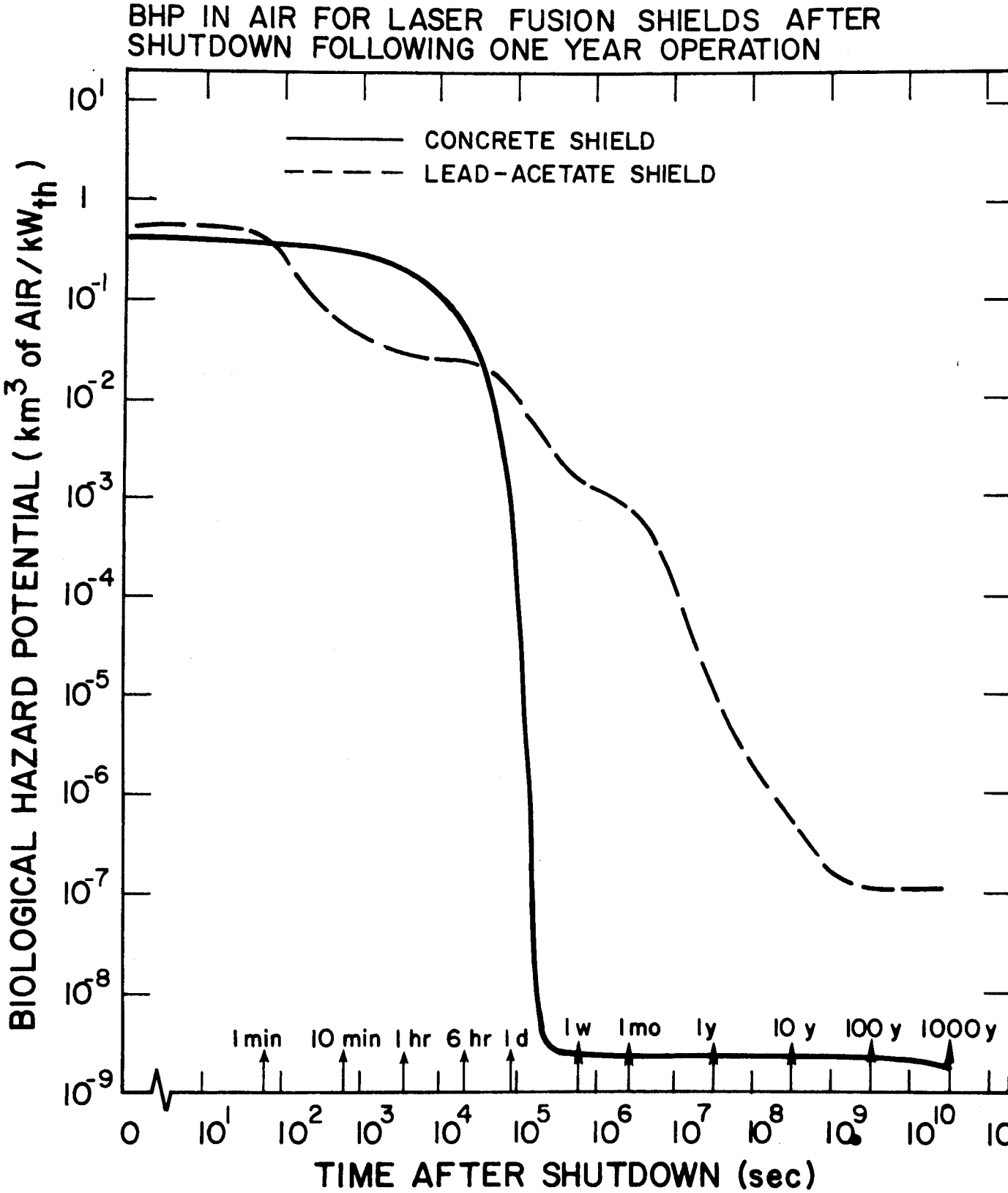
BHP IN AIR FOR LASER FUSION SHIELDS AFTER SHUTDOWN FOLLOWING ONE YEAR OPERATION
CONCRETE SHIELD
LEAD-ACETATE SHIELD
BIOLOGICAL HAZARD POTENTIAL (km3 of AIR / kWth)
10^1
1
10^-1
10^-2
10^-3
10^-4
10^-5
10^-6
10^-7
10^-8
10^-9
1 min
10 min
1 hr
6 hr
1 d
1 w
1 mo
1 y
10 y
100 y
1000 y
0
10^1
10^2
10^3
10^4
10^5
10^6
10^7
10^8
10^9
10^10
TIME AFTER SHUTDOWN (sec)

Fig. XIII-E-11

structures. Such information is given in Table XIII-E-5 for Ti-8 Mn, Al 6061 and Al 1100 blankets (sub-tables a, b and c, respectively). Three spatial locations are of particular interest in such a calculation: cavity center, outside the lead acetate or concrete shield, and outside the metallic back structure. The last position is 664.505 cm from the cavity center and assumes that shield and graphite reflector sections have been pulled out from the operating configuration.

Dose rates from the table (columns c and d) indicate that both the lead acetate and concrete shields will allow personnel outside of these structures without any waiting period after shutdown. Whereas TETR gave 0.7 to 1.9 rem/hour at shutdown and as large as 60 mrem/hour at one week for outside shield dose rates, the laser fusion system is down to virtually negligible levels, less than 5×10^{-3} mrem/hour for all shields, immediately at shutdown. Though the lead-acetate shield was shown to generate higher activity levels for times after about one day, intense gamma radiation from the 3.8 cm back support zone is better shielded by this blanket than a comparable concrete type as expected. This is reflected in Table XIII-E-5, in that for a given blanket, the lead-acetate shield (column c) is roughly twice as effective as the concrete (column d) at early times and is at least that good during the interval of one week to one year.

Dose rates received at the chamber center are in the tens of krem/hour range and differ by less than a factor of two for all three blankets

Table XIII-E-5.a. Ti-8Mn Blanket Gamma Dose Rates for Times After Shutdown

Time After Shutdown	Dose Rate (mrem/hr)			
	A. Cavity Center* (r=0.0 cm)	B. Outside Support** Plate (r=664.505 cm)	C. Outside Pb-Acetate Shield (r=884.505 cm)	D. Outside Concrete Shield (r=884.505 cm)
0	4.67+7	4.07+7	2.38-3	4.78-3
1 min.	4.62+7	4.05+7	2.21-3	4.34-3
10 min.	4.39+7	3.90+7	1.73-3	3.13-3
1 hr.	3.57+7	3.77+7	1.35-3	2.43-3
6 hr.	1.18+7	1.03+7	3.52-4	6.34-4
1 day	2.98+6	2.42+6	3.11-6	6.01-6
1 week	1.13+6	9.02+5	8.04-8	3.69-7
1 month	7.85+5	6.21+5	5.15-8	2.38-7
1 year	1.00+5	7.47+4	3.35-9	1.63-8
10 years	2.55+1	2.18+1	2.21-13	7.01-13
100 years	3.98-2	7.24-3	2.21-13	2.31-13
1000 years	3.57-2	6.51-3	2.21-13	2.08-13

*Results at cavity center are virtually the same (within 1-2%) regardless of shield (Pb-Ace or Concrete). Doses here are computed with a Pb-Acetate Shield.

**Dose rates here are computed for a system in which the shield and graphite reflector are removed and the tissue position is outside Zone 15. See Fig. XIII-E-1.

Table XIII-E-5.b. Al 6061 Blanket Gamma Dose Rates for Times After Shutdown

Time After Shutdown	Dose Rate (mrem/hr)			
	A. Cavity Center* (r=0.0 cm)	B. Outside Support** Plate (r=664.50 cm)	C. Outside Pb-Acetate Shield (r=884.505 cm)	D. Outside Concrete Shield (r=884.505 cm)
0	2.70+7	1.82+7	7.56-4	1.88-3
1 min.	2.11+7	1.41+7	5.65-4	1.39-3
10 min.	4.81+6	3.06+6	5.31-5	1.22-4
1 hr.	2.88+6	1.81+6	1.33-5	2.51-5
6 hr.	2.09+6	1.30+6	3.77-6	7.03-6
1 day	8.64+5	5.36+5	2.28-7	3.81-7
1 week	1.06+4	5.19+3	5.80-10	1.39-9
1 month	8.30+3	3.92+3	2.79-10	7.86-10
1 year	3.64+3	1.68+3	1.12-10	2.68-10
10 years	1.82+2	8.94+1	5.65-12	2.20-11
100 years	2.62-1	1.55-1	1.23-12	2.12-12
1000 years	2.58-1	1.54-1	1.23-12	2.09-12

*Results of cavity center are virtually the same (within 1-2%) regardless of shield (Pb-Ace or Concrete). Doses here are computed with a Pb-Acetate Shield.

**Dose rates here are computed for a system in which the shield and graphite reflector are removed and the tissue position is outside Zone 15. See Fig. XIII-E-1.

Table XIII-E-5.c. Al 1100 Blanket Gamma Dose Rates for Times After Shutdown

Time After Shutdown	Dose Rate (mrem/hr)		
	A. Cavity Center* (r=0.0 cm)	B. Outside Support** Plate (r=664.505 cm)	C. Outside Pb-Acetate Shield (r=884.505 cm)
0	2.73+7	1.84+7	7.47-4
1 min.	2.12+7	1.42+7	5.55-4
10 min.	4.50+6	2.88+6	4.15-5
1 hr.	2.60+6	1.64+6	3.96-6
6 hr.	2.00+6	1.26+6	1.36-6
1 day	8.60+5	5.40+5	2.10-7
1 week	(2.49→5.53)+3	(1.38→2.84)+3	(2.65→3.16)-10
1 month	(1.33→4.15)+3	(0.67→1.99)+3	(9.89→44.1)-12
1 year	(0.59→2.34)+3	(0.32→1.08)+3	(8.88→9.08)-12
10 years	(2.75→16.7)+1	(1.97→7.88)+1	3.58-12
100 years	2.67-1	1.60-1	1.26-12
1000 years	2.63-1	1.59-1	1.25-12

*Results at cavity center are virtually the same (within 1-2%) regardless of shield (Pb-Ace or Concrete). Doses here are computed with a Pb-Acetate Shield. Also, dose rates quoted in parentheses reflect (lower→upper) limits depending on Fe content in the Al 1100.

**Dose rates here are computed for a system in which the shield and graphite reflector are assumed to be removed and the tissue position is outside Zone 15. See Fig. XIII-E-1.

(27., 27.3, and 46.7 krem/hr for Al 6061, Al 1100, and Ti-8 Mn, respectively). The Al 1100 blanket clearly offers the lowest dose at intermediate times, about 4 rem/hr., at the one week point, nearly 3 orders of magnitude less than Ti-8 Mn and one-half as much as Al 6061. Though the rates are high at this position, plasma center calculations for TETR indicated ~ 84. krem/hr at shutdown, 4.8 krem/hr at one week, and 137 rem/hr at 10 years.

Although one can work at outside shield positions at shutdown, the dose rates of 2→900 rem/hr after one week outside the highly-activated back structure would suggest the need for remote maintenance operations if reflector and shield components are absent. The aluminum alloys are again superior to the Ti-8 Mn blanket, especially in the week to one year category after ^{28}Al and ^{24}Na have decayed away. However, the dose at long-term times after shutdown is lowest for a Ti-8 Mn blanket, since essentially only ^{14}C from graphite activation persists.

Some measure of shield effectiveness can be found if dose rates are computed at the same position for shield and no shield-present conditions. Figure XIII-E-12 shows the results of such a comparison for a Ti-8 Mn blanket and one of the aluminum alloy designs, Al 6061, at the outside shield radius of 884.5 cm. Without a shield gamma-rays emitted from the back structure have only 20 cm of graphite to penetrate before reaching air; doses for both blankets are of cavity-center magnitude. Addition of either a lead-acetate or concrete shield is responsible

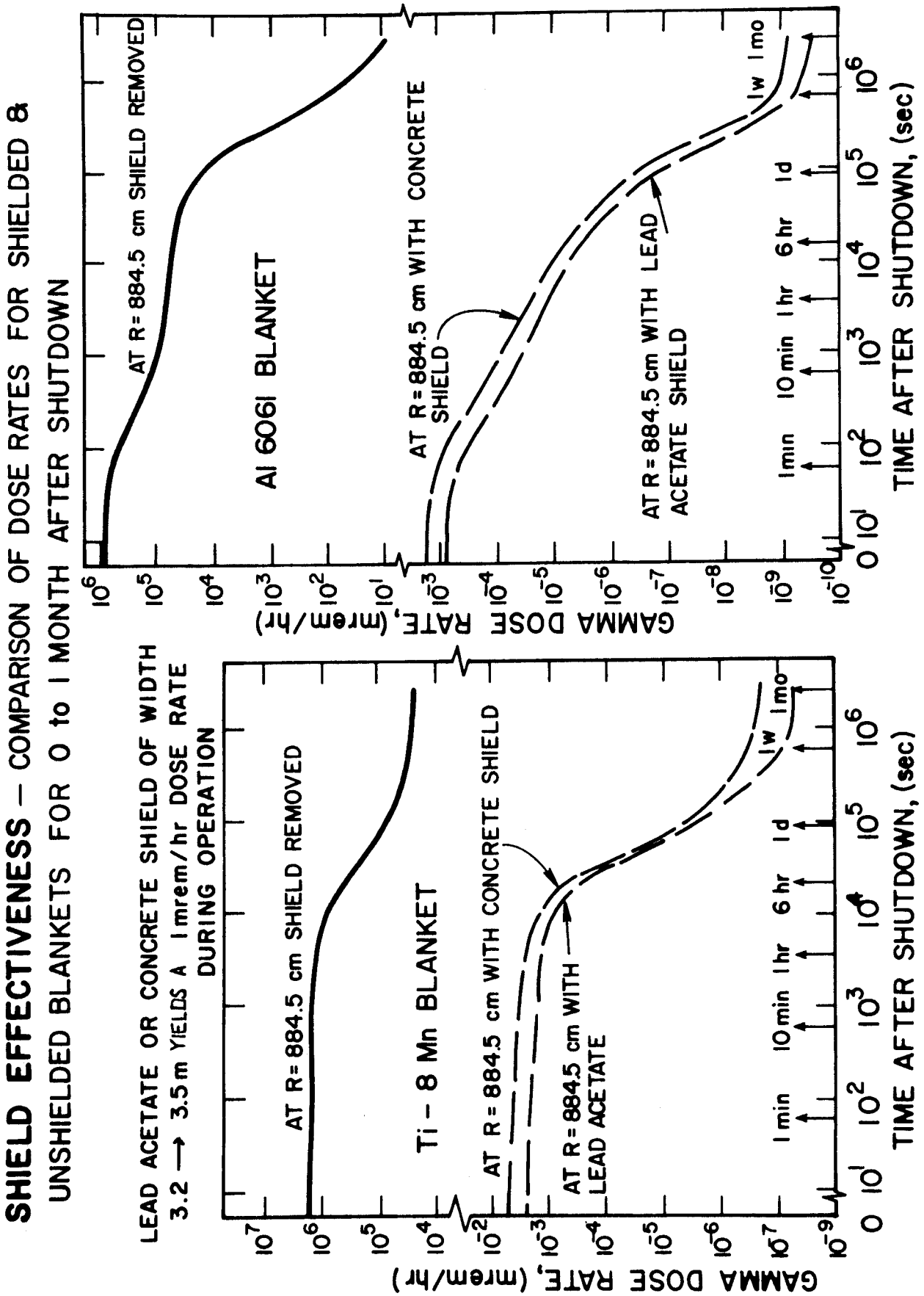
SHIELD EFFECTIVENESS — COMPARISON OF DOSE RATES FOR SHIELDED & UNSHIELDED BLANKETS FOR 0 to 1 MONTH AFTER SHUTDOWN
LEAD ACETATE OR CONCRETE SHIELD OF WIDTH 3.2 → 3.5 m YIELDS A 1 mrem/hr DOSE RATE DURING OPERATION
Ti - 8 Mn BLANKET
AT R = 884.5 cm SHIELD REMOVED
AT R = 884.5 cm WITH CONCRETE SHIELD
AT R = 884.5 cm WITH LEAD ACETATE
Al 6061 BLANKET
AT R = 884.5 cm SHIELD REMOVED
AT R = 884.5 cm WITH CONCRETE SHIELD
AT R = 884.5 cm WITH LEAD ACETATE SHIELD
GAMMA DOSE RATE, (mrem/hr)
TIME AFTER SHUTDOWN, (sec)
1 min
10 min
1 hr
6 hr
1 d
1 w
1 mo

Fig. XIII-E-12

for nearly a nine orders of magnitude reduction to the dose rates obtained at this point. Both Ti-8 Mn and Al 6061 blankets are shielded roughly twice as well with a lead-acetate shield than concrete over the first month of shutdown; however, both shielded dose rate curves lie in extremely low regimes such as to suggest that some other shield characteristic may be of more important a consideration.

XIII-E-5. Conclusions Concerning Radioactivity in the Laser Fusion System

Aside from the 3.8 cm thick back structure, there is little in the largely non-metallic laser fusion blanket and shield to activate to the levels found in earlier fusion system designs. Indeed, if near nuclear-grade graphite can be used in the blanket web and in the reflector, the most widespread isotope found in the system is ^{14}C, formed at levels that are quite acceptable with regard to the overall activity and dose.

While the graphite web and reflector as well as the Li_2O coolant remained the same for each design considered, three metallic alloys were considered for the back structure: Ti-8 Mn, Al 6061, and Al 1100. Transmutation products from the coolant (^{16}N, ^{8}He) dominate over the first several minutes after shutdown, regardless of which of the specific blankets studied. Similarly, after 30 years all blankets indicate ^{14}C, arising from graphite activation, will control long-term levels. It is in the intermediate period that the two aluminum alloy blankets offer as much as two orders of magnitude less activity (several days to one year)

than the corresponding Ti-8 Mn blanket. In no instance was it found that a comparable 316 SS design would present less of a radioactivity problem relative to any of those blankets seriously considered.

Analysis of two possible shields, one of reinforced concrete and the other of lead acetate, indicate that activity, BHP, or afterheat of this part of the structure will reach only 10 to 20% of the corresponding blanket quantity for all but two isolated cases after shutdown.

The one-dimensional dose rate results indicate that one may select any of the three blankets, and, coupled to one of the three shields, still have the ability to perform hands-on maintenance at outside shield positions at any time after shutdown. However, this possibility seems to be precluded at more interior points, i.e., the laser cavity center or near the back support, due to the higher decay gamma fluxes found at these locations. The best case alloy, Al 1100, has rem/hr magnitudes at one week after shutdown for these positions, or about 100 times less than Ti-8 Mn rates.

The calculations regarding radioactivity reviewed in this section would offer an Al 1100 blanket/lead-acetate shield as the most attractive system, although use of Al 6061 as an alternative blanket material would still yield excellent performance.

References for Section XIII-E

1. B. Badger, et al., "Tokamak Engineering Test Reactor", University of Wisconsin Report UWFDM-191, 1977.

2. T. Y. Sung and W. F. Vogelsang, "DKR: A Radioactivity Calculation Code for Fusion Reactors", University of Wisconsin Report, UWFDM-170, 1976.

3. T. Y. Sung and W. F. Vogelsang, "Decay Chain Data Library for Radioactivity Calculations", University of Wisconsin Report, UWFDM-171, 1976.

4. W. W. Engle, Jr., "A User's Manual for ANISN", K-1693 (March, 1967).

5. The Aluminum Data Book, The Reynolds Metals Company.

6. G. L. Kulcinski, T. Y. Sung and J. Davis, "Residual Radioactivity in Potential Titanium Alloys for Fusion Reactors", to be published.

7. Private communication between I. Sviatoslavsky, Nuclear Engineering Department, University of Wisconsin, and Poco Graphite, Inc., Decatur, Texas.

8. B. Badger, et al., "UWMAK-I, A Wisconsin Toroidal Fusion Reactor Design", University of Wisconsin Report, UWFDM-68, 1974.

9. B. Badger, et al., "A Non-Circular Tokamak Power Reactor Design, UWMAK-III", University of Wisconsin Report, UWFDM-150, 1976.

10. W. Häfele, J. P. Holdren, G. Kessler, G. L. Kulcinski, "Fusion and Fast Breeder Reactors", Institute for Applied Systems Analysis Report RR-77-8, (November 1976).

XIII-F. Calculated Neutron and Gamma Irradiation Response of Candidate Laser Mirror Materials

XIII-F-1. Introduction

This work presents a comparison of the calculated neutron and gamma irradiation response of candidate materials for water cooled mirrors for Laser Fusion Power Reactors. Active cooling of the last optical element is a necessity in a reactor environment even though not considered in current experiments, to avoid the excessive heating and the distortion which may be caused by the thermal gradients generated by neutron and gamma heating, laser light, and pellet alpha and X-ray radiation. Whereas pellet X-rays and debris will affect just the first few microns at the mirror surface, neutron and secondary gammas will affect the bulk of the mirror structure.

Mirror blanks can be fabricated from brazed or welded box structures. Mirror faces can be clad with copper either by electroplating or by brazing a thin copper sheet to the substrate [1]. Reichelt et al. [15] discussed mirror materials' constraints and choices, as well as fabrication techniques. For the structural materials, cost eliminates materials such as beryllium that are desirable as to their thermal distortion, rigidity, and stiffness-to-weight ratio. Beryllium is also undesirable as a mirror material, because of its (n,2n) reaction with the 14-Mev neutrons. Molybdenum has an acceptable thermal distortion because of its low coefficient of expansion even though difficult to fabricate. Titanium has good fatigue

resistance, and, like aluminum does not activate much. Copper base alloys and stainless steels, and low-expansion alloys such as Invar, are reported by Stark [1] as low-cost candidate structural materials for laser reactor mirrors.

Except for a calculation of the expected activation of candidate materials (304 stainless steel, 6061 aluminum, and pure copper) for the HEGLF [1] by pulses of 4.5×10^{17} neutrons, with the sample located at 0.305 m from a source of 14-Mev neutrons, no neutronics and photonics studies of the expected behavior of materials for laser mirrors has been reported in the literature. The best available basis for comparing candidate materials for laser mirrors under neutron irradiation effects is in terms of the neutron and gamma heating, displacements per atom (dpa), helium from α-producing transmutations, and hydrogen from (n,p) and other hydrogen isotope production reactions. Kulcinski, Doran, and Abdou [3] presented a set of calculations comparing the response of several alloys of potential interest in a single conceptual fusion reactor spectrum. Gabriel, Bishop and Wiffen [2] also presented a set of calculations of the neutronic response of a number of elements and alloys to a particular projected fusion reactor first wall neutron spectrum, where they used more recent neutron cross-section data. Since the neutron spectrum seen by the mirror will be much different from that seen by the first wall (because of the different compositions and configurations), and since heating estimates as well as the gas production rates for some elements were not reported, the present study was undertaken.

XIII-F-2. Calculational Model

The materials chosen for analysis include elements that are of potential use as structural materials for laser power reactor mirrors, namely, Al, Fe, Cu, Mo and Ti. For a conceptual laser power reactor design, a typical off-axis parabolic mirror emplaced at 15 m from the center of the reactor cavity was considered [6]. Its thickness was taken as 35 cm. The first 2.5 cm are a solid plate of the considered structure, and the rest of the structure was considered as a honeycomb structure of the same material, cooled with water. A 5 v/o metal and 95 v/o H_2O ratio was considered there. Such a mixture will act as a shielding element to the 14-Mev neutrons hitting the mirror and the inelastic scattering gammas generated by them. If a lesser amount of water is used, it must be substituted by adequate shielding at the back of the mirror, say concrete. That shielding will act in a manner similar to the water-metal mixture in slowing down neutrons and backscattering them to the mirror face; so that the present results still apply. Coating materials,being of the order of a millimeter thickness [15] and consequently almost transparent to the 14-Mev neutrons, were not included in the calculations.

All calculations have been performed for an impinging 14-Mev neutron source. A two-dimensional Monte Carlo calculation considering a conical section of a one steradian solid angle (cone half angle θ_c = 32.7705°) surrounded by a black absorber with spherical shells representing the mirror regions was considered. The 14-Mev neutron source was sampled isotropically at the head of the cone. A one-dimensional spherical

geometry calculation would not have adequately modelled the system since it would have generated a significant backscattered radiation component. The mirror will mostly see a line-of-sight 14-Mev neutron flux, with the backscattered component mostly absorbed by the lining of the laser beam ports. Spherical or cylindrical one-dimensional calculations using conceptual design first wall and blanket spectra [2,3] would then not have modelled the system adequately. The neutron source in this work is the average number of neutrons released in the fusion microexplosion per second. The total energy released per second is assumed to be 3000 MJ for a laser energy of 150 MJ at a repetition rate of 20 Hz. This corresponds to a source term of:

$$S = 1.062737 \times 10^{21} \left(\frac{\text{source neutrons}}{\text{sec}}\right)$$

for a 4π solid angle.

Since the mirror sees a 14-Mev impinging flux, quantities of interest at the face of the mirror will scale as $1/R^2$ for mirrors emplaced at other distances R from the center of the cavity.

The combinatorial geometry capability of the MORSE Monte Carlo code [10,11] was used in modelling the problem geometry. The face plate of the mirror was divided into two regions of 0.5 and 2 cm thickness respectively, while the honeycomb water-metal mixture was divided into three regions of 7.5, 10, and 10 cm thickness respectively. Volume detectors were used to estimate the integrated quantities of interest [8, 9, 10].

A coupled 25-21 multigroup neutron-gamma cross-section set was used in the calculations. The group structure has been reported in reference [8].

This is a collapsed set from the EPR 100-group neutron and 21-group gamma-ray cross section library [12, 14], in turn considering data from the ENDF/B-IV file. The methods used to calculate the irradiation response of elements of interest have been described in detail in Reference 4. Reaction cross sections of interest were adopted from References 5 and 13.

Coupled neutron-gamma multigroup Monte Carlo calculations were carried out using for each considered material 10 experiments of 50 particles each, totalling 500 histories. For the type of survey studies we are carrying out, this was found to be adequate. A typical CPU running time was 25 min on the University of Wisconsin UNIVAC-1110, for the titanium case. Much of the time expenditure was in tracking the gamma photons and the thermalized neutrons, particularly in the metal-water mixture.

XIII-F-3. Results of Calculations and Discussion

The total volumetric heating rates are necessary for the heat transfer cooling calculations. They are compared for the various mirror structural materials in Figure XIII-F-1. The neutron heating is larger than the gamma heatin in the cooling structure. But the reverse occurs in the mirror face all-metal part, where the gamma heating largely exceeds the neutron heating, except for Al where they are almost of equal magnitude.

The total heating rate in the mirror face is largest in Cu followed by Mo, Fe, Ti, then Al, whereas it is almost of the same magnitude in the honeycomb water-cooled structure. This means that the temperature gradient will be lower in the case of Al and Ti than in the cases of Cu, Fe, or Mo. The thermal gradient will lead to dimensional distortion of the mirror if not corrected by appropriate orificing and controlled cooling of the mirror. Added to the neutron and gamma heating, provision must be

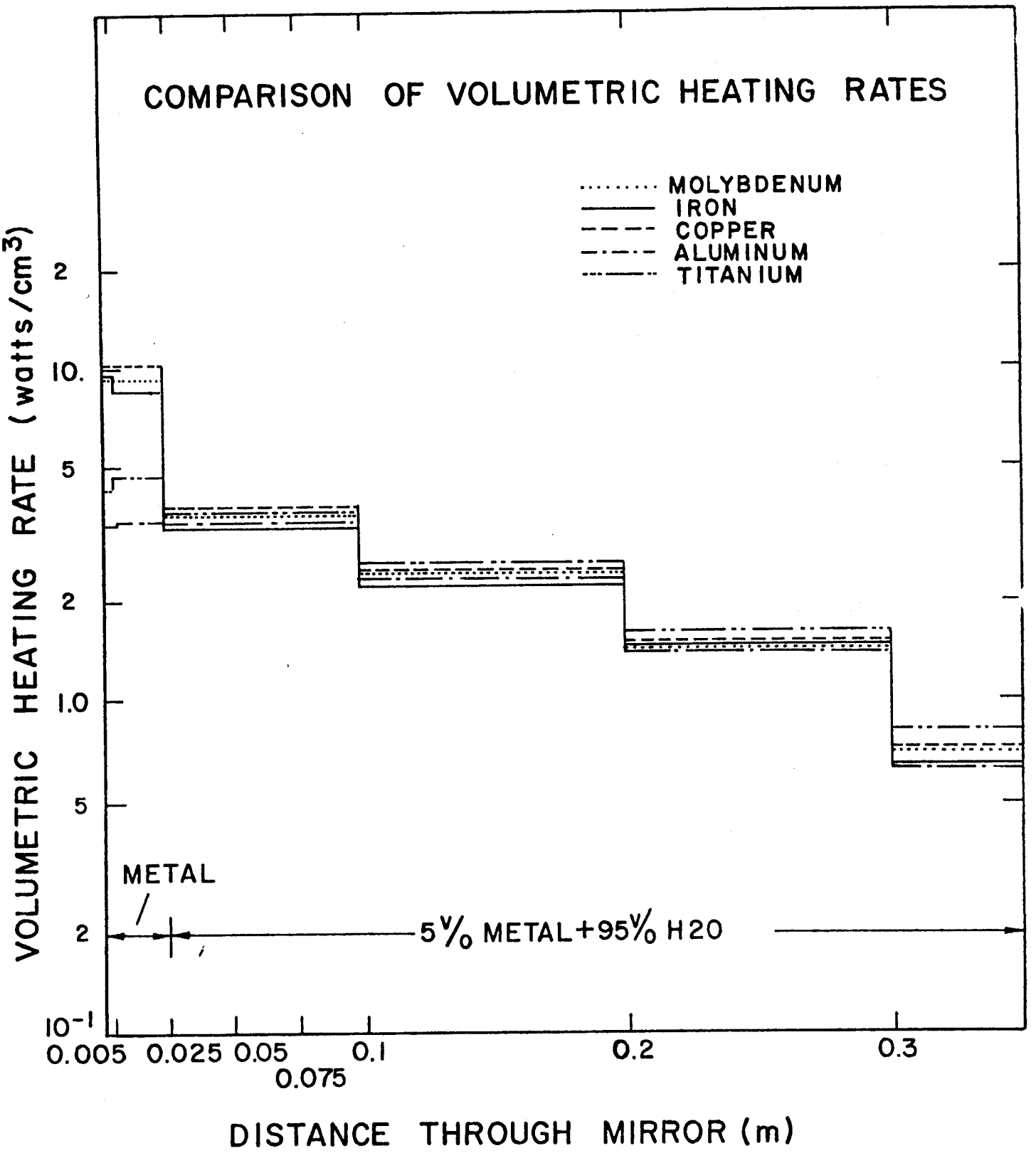

Figure XIII-F-1

made for the absorbed laser light, and further heating by the pellet X-rays and debris. Whereas neutrons and gammas affect the bulk structure, the others affect only the first few microns at the mirror face. For the laser pulse, Saito et al., [16] calculate the thickness Δx of the region of temperature region of temperature rise as: $\Delta x = \sqrt{\frac{\pi}{4} \frac{Kt}{\rho c}}$; K is the thermal conductivity, ρ the density, c the specific heat, and t the width of the incident laser pulse. For a copper surface and a one-nanosecond pulse, $\Delta x = 0.35$ μm.

Figures XIII-F-2 and XIII-F-3 compare the estimated helium gas production rat from all helium producing reactions, and hydrogen isotope production rates, respectively. Table XIII-F-1 displays these values for the two regions of the mirror face: Region 1 comprising the first 0.5 cm of the mirror, while Region II comprising the next 2 cm. One estimated standard deviation of the mean is shown for these results.

The He gas production rates vary from Al to Fe, Ti, Cu, then Mo over an order of magnitude. The hydrogen isotope gas production is of the same order of magnitude as the helium gas production, but follows in magnitude a different order from highest to lowest (at the mirror face): Fe, Al, Cu, Ti, Mo.

Figure XIII-F-4 compares the atomic displacements in (dpa/sec). Table XIII-F shows them with their associated standard deviations in Regions I and II of the mirror face. Cu will suffer the most (dpa/sec) at the mirror's face together with Ti, followed by Fe, then by Al and Mo.

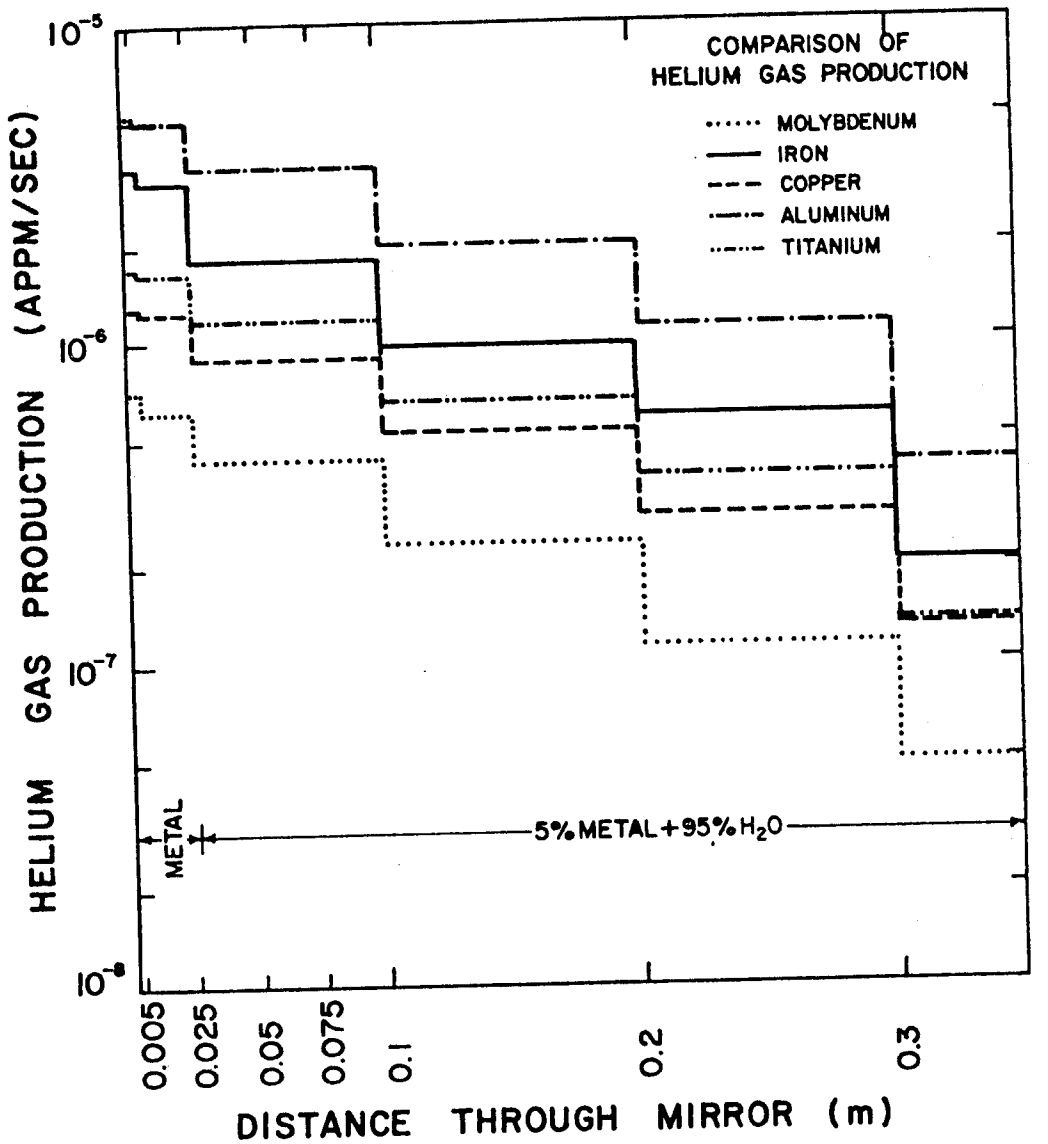

Figure XIII-F-2

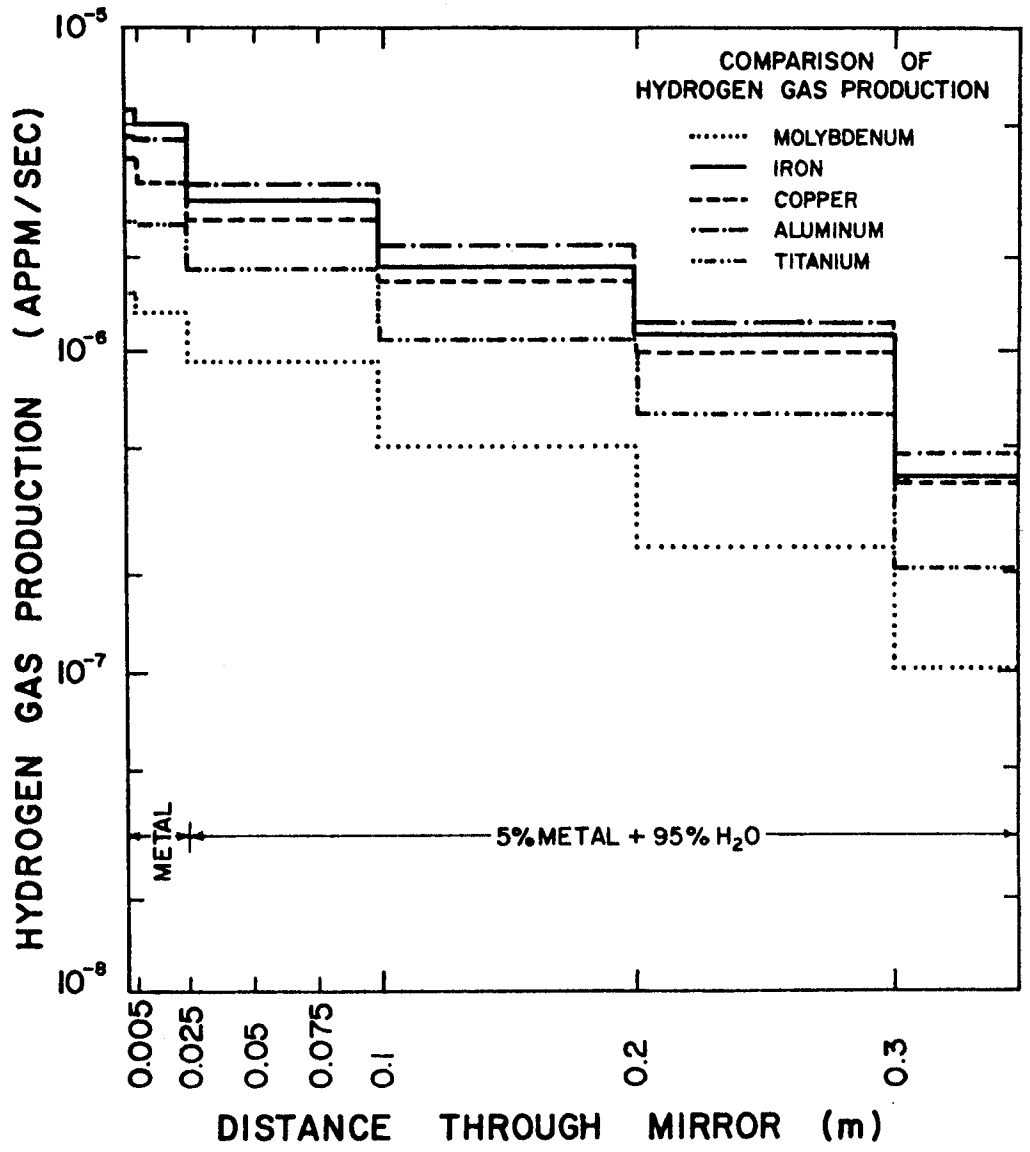

Figure XIII-F-3

Table XIII-F-1

Helium Gas Production Rates (appm/sec) in Mirror Face

Structure	Region I	Region II
Al	(5.351396 ± 1.074025)-06	(5.016463 ± 0.435780)-06
Cu	(1.291910 ± 0.154655)-06	(1.241676 ± 0.082696)-06
Fe	(3.620044 ± 0.606357)-06	(3.239260 ± 0.205823)-06
Mo	(7.108789 ± 0.900257)-07	(6.158574 ± 0.430915)-07
Ti	(1.670791 ± 0.367273)-06	(1.576560 ± 0.122499)-06

Hydrogen Gas Production Rates (appm/sec) in Mirror Face

Structure	Region I	Region II
Al	(4.719977 ± 0.909904)-06	(4.572613 ± 0.393839)-06
Cu	(3.897110 ± 0.444972)-06	(3.341781 ± 0.207926)-06
Fe	(5.561190 ± 0.898132)-06	(5.060721 ± 0.376568)-06
Mo	(1.494898 ± 0.189344)-06	(1.293884 ± 0.090507)-06
Ti	(2.604744 ± 0.568824)-06	(2.469678 ± 0.192363)-06

Atomic Displacements Rates (dpa/sec) in Mirror Face

Structure	Region I	Region II
Al	(1.171044 ± 0.167459)-07	(1.135044 ± 0.090804)-07
Cu	(2.112372 ± 0.316856)-07	(1.819247 ± 0.127347)-07
Fe	(1.530206 ± 0.247893)-07	(1.347009 ± 0.109108)-07
Mo	(9.529783 ± 1.520078)-08	(8.323508 ± 0.634543)-08
Ti	(1.987894 ± 0.296634)-07	(1.981773 ± 0.134404)-07

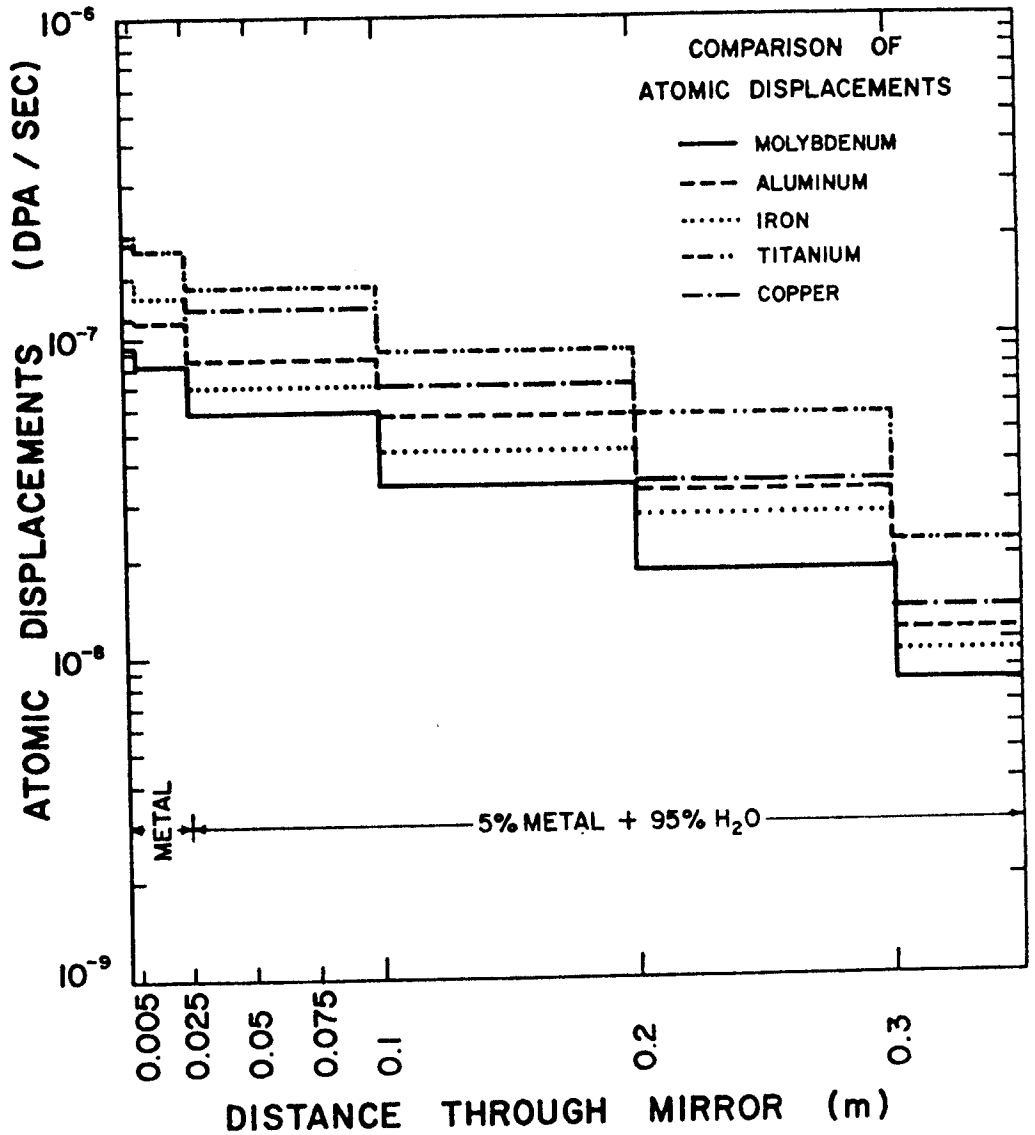

Figure XIII-F-4

Future investigations should consider specific mirror designs and take into account factors such as its alloy composition, spatial orientation, and the penetration shielding environment including the beam lining, and the shielding at the mirror back. The penetration design must be chosen to minimize the scattered components from the cavity and blanket reaching the mirror position.

XIII-F-4. Summary

This work compares estimates of the neutron and gamma irradiation response of water cooled mirrors for contemplated Laser Fusion Power Reactors for some candidate structural materials. The neutron and gamma response will affect the bulk of the structure, whereas the pellet X-rays and debris response will mostly affect the first 10 microns of the mirror face. Mo appears to suffer the fewest atomic displacements and gas production rates, but results in a high volumetric neutron and gamma heating. If easy to fabricate, it may be a good choice as a structural material due to its low coefficient of expansion. Al and Ti offer the smallest heating rates, but Al suffers the highest He gas production. Al and Ti offer the advantage of low activation, with some Ti alloys having good fatigue strength (e.g., Ti 6% Al, 6% V, 2% Sn). Ti, however, has a high atomic displacement rate. The highest hydrogen gas production will occur in Fe, and this effect may be amplified by the presence of Ni in any stainless steel alloy. Fe may also activate, substantially limiting access to the mirror. Cu, even though of high reflectivity to the laser light and of good thermal conductivity, will have the highest atomic displacement rate and volumetric heating at the mirror face, added to its

activation potential. Variations of the obtained estimates are within an order of magnitude for the quantities of interest.

Based on cost, weight, and low activation considerations, aluminum coated with copper was chosen as the structural material for the SOLASE design.

References for Section XIII-F

1. E. Stark, "Laser Fusion Program", LA-6510-PR, Los Alamos Scientific Laboratory (1976).

2. T.A. Gabriel, B.L. Bishop, and F.W. Wiffen, "Calculated Irradiation Response of Materials Using A Fusion-Reactor First-Wall Neutron Spectrum", ORNL-TM-5956, Oak Ridge National Laboratory (1977).

3. G.L. Kulcinski, D.G. Doran, and M.A. Abdou, "Comparison of Displacement and Gas Production Rates in Current Fission and Future Fusion Reactors", p. 239 in "Properties of Reactor Structural Alloys After Neutron or Particle Irradiation", ASTM STP 570, ASTM (1975).

4. T.A. Gabriel, J.D. Auburgey, and N.M. Greene, "Radiation Damage Calculations: Primary Recoil Spectra, Displacement Rates, and Gas Production Rates", ORNL/TM-5160, Oak Ridge National Laboratory (1976).

5. H. Avci, G.L. Kulcinski, "The Response of ISSEC Protected First Walls to DT and DD Plasma Neutrons", UWFDM-135, October (1975).

6. G. Cooper, J. Howard, Personal communications, Fusion Research Program, The University of Wisconsin.

7. M.H. Ragheb, E.T. Cheng, and R.W. Conn, "Monte Carlo Study of Asymmetry Effects in a Lithium Oxide Blanket for a Laser Driven Reactor", UWFDM-207, University of Wisconsin (1977).

8. M. M.H. Ragheb, E.T. Cheng, and R.W. Conn, "Comparative One-Dimensional Monte Carlo and Discrete Ordinates Neutronics and Photonics Analysis for a Laser Fusion Reactor Blanket with Li_2O Particles as Coolant and Breeder", UWFDM-193, University of Wisconsin (1977).

9. E.T. Cheng, M.M.H. Ragheb, and R.W. Conn, "Neutronics and Photonics Studies for the University of Wisconsin Laser Fusion Reactor Blanket", Trans. Am. Nucl. Soc., 26, 504 (1977).

10. MM.H. Ragheb, and C.W. Maynard, "A Version of the MORSE Multigroup Transport Code for Fusion Reactors Blankets and Shield Studies", BNL-20376, Brookhaven National Laboratory (1975).

11. RSIC Code Package CCC-203, "MORSE-CG", Radiation Shielding Information Center, ORNL (1976).

12. W.E. Ford III, R.T. Santoro, R.W. Roussin, and D.M. Plaster, "Modification Number One to the Coupled 100n-21 Gamma Cross Section Library for EPR Calculations", ORNL/TM-5249 (1976).

13. M.A. Abdou, and R.W. Roussin, "MACKLIB, 100 Group Neutron Fluence-to-Kerma Factors and Reactions Cross Sections Generated by the MACK Computer rogram From Data in ENDF Format", ORNL-TM-3995 (1974).

14. D.M. Plaster, R.T. Santoro, and W.E. Ford III, "Coupled 100-Group Gamma-Ray Cross Sections for EPR Calculations", ORNL-TM-4872 (1975).

15. W.H. Reichelt, D.J. Blevins, and W.C. Turner, "Metal Optics In CO_2 Laser Fusion Systems", LA-UR-77-468 (1977).

16. T. Saito, D. Milam, P. Baker, G. Murphy, NBS Special Publication #435, 29 (1975).

ACKNOWLEDGEMENT

Thanks are due to Mr. H. Avci, Dr. E. Cheng, and Mr. T. Wu for making some cross-section data available for the calculations, and to Professor W. Wolfer and to Mr. T. Hunter for some helpful discussions.

XIV. Mechanical Design, Assembly and Disassembly of SOLASE

XIV-A. General Description

The reactor cavity for SOLASE is spherical with an inside diameter of 12 m. It is surrounded by a 60 cm thick graphite blanket as shown in Fig. XIV-A-1. The cavity has 12 beam ports, six on each side for two-sided pellet illumination. The breeding material consisting of Li_2O microspheres enters the blanket at the top and flows by gravity to a return duct at the bottom. It is then mechanically lifted to the steam generator where it again flows by gravity. The "cold" lithium oxide leaving the steam generator is returned to the cavity using a screw lift (Fig. XIV-A-2). A small fraction of the breeding material (~2%) is made to flow at a lower velocity through the blanket. This stream leaves the blanket at a higher temperature (850°C) than the main stream and is diverted to the tritium extraction facility.

The graphite blanket consists of 16 segments attached to a back structure made of 1100-H14 aluminum alloy. The spherical back structure is divided into four quadrants with four blanket segments attached to each of them. The back structure quadrants are attached to the shield which is also divided into four segments. The shield is a free standing thick walled hollow sphere which can be opened up by moving quadrants radially away from the cavity. It is made of aluminum-alloy-reinforced concrete with an overall thickness of 3.75 m. Suppression chambers are built into the shields at the beam port locations as a protection scheme for the last mirrors.

XIV-B. Graphite Blanket and Back Structure

The blanket is divided into 16 equal segments by vertical planes going through the center of the reactor cavity. A top view of the assembled blanket segments at the point of Li_2O inlet resembles a wagon wheel with

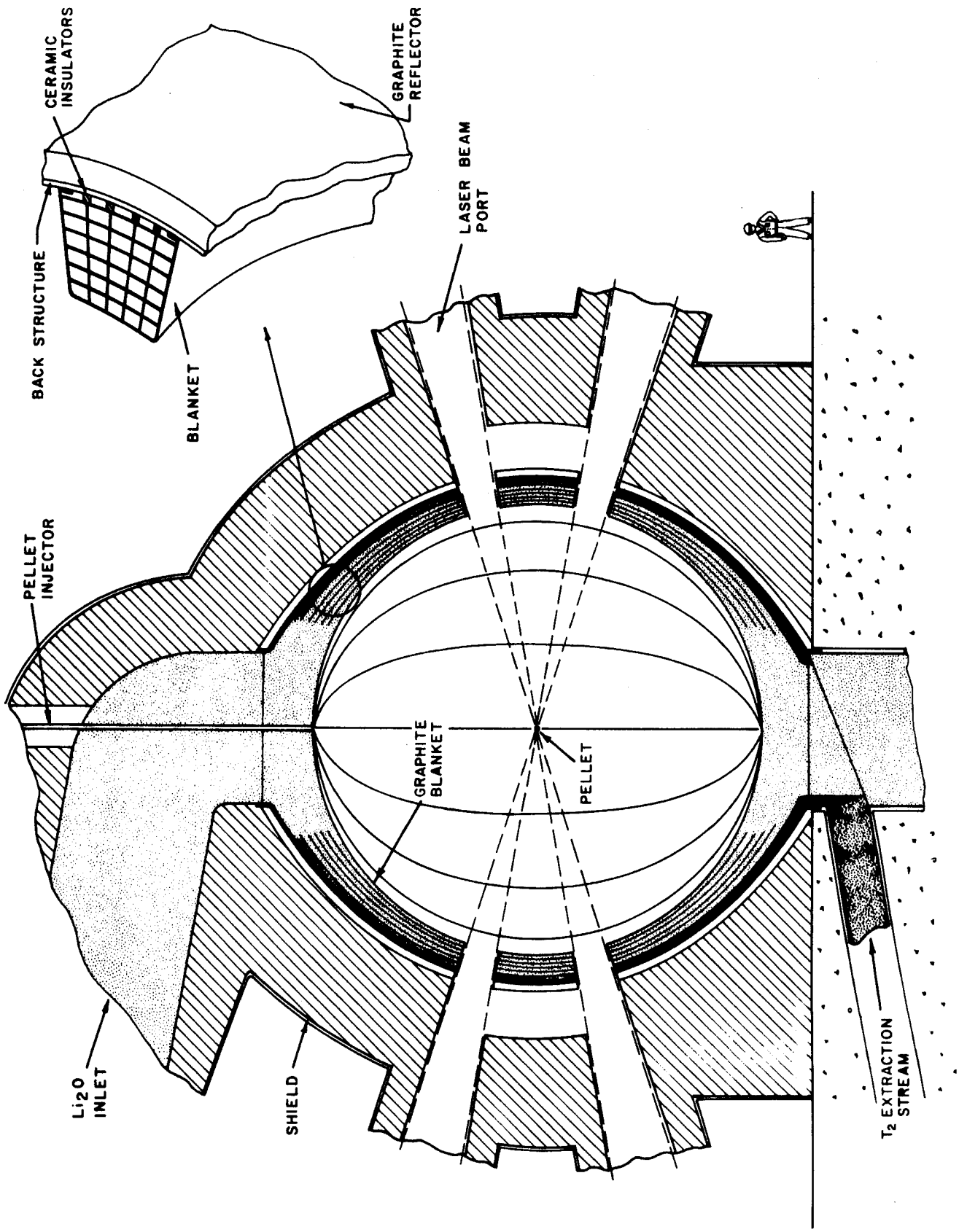

Fig. XIV-A-1. Overall Cross-Sectional View of Reactor Cavity.

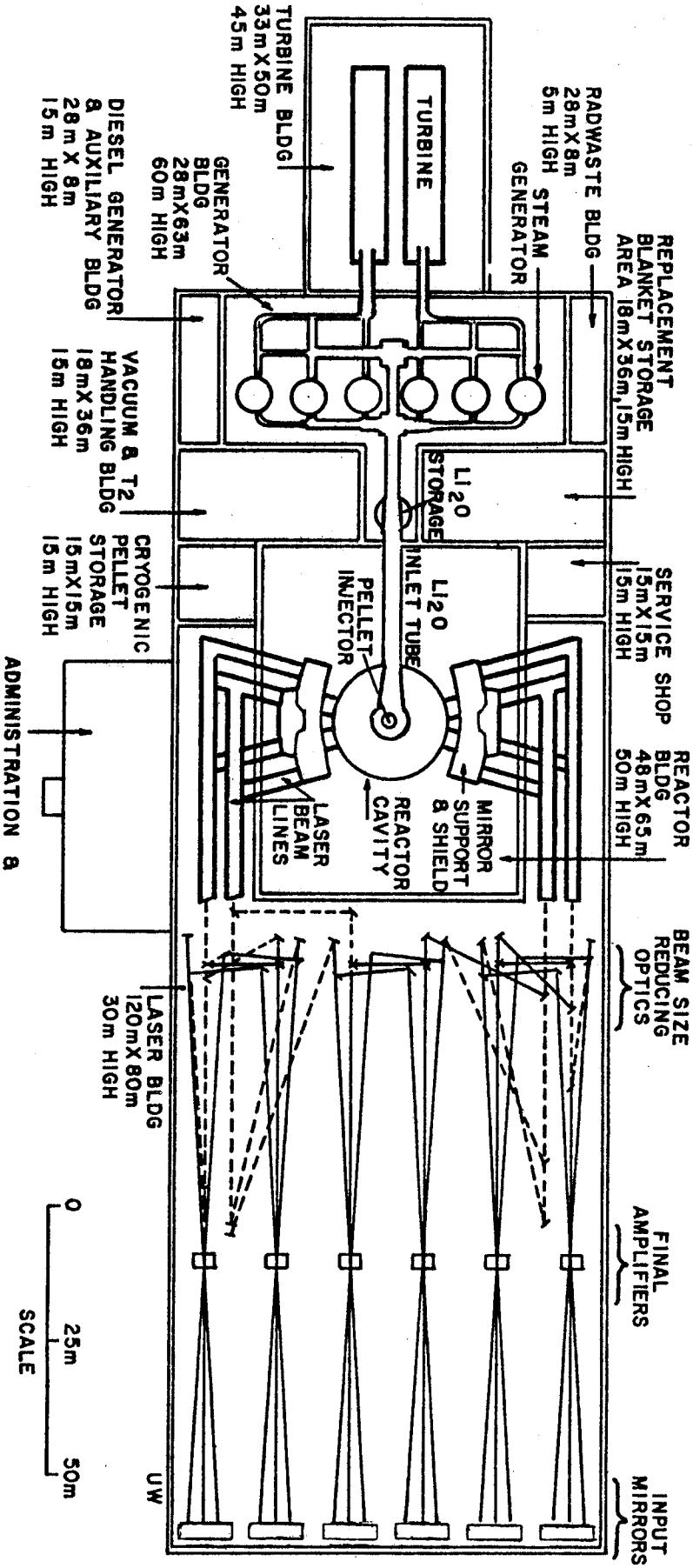
TOP VIEW OF SOLASE
A CONCEPTUAL LASER FUSION REACTOR POWER PLANT
RADWASTE BLDG
28m X 8m
5m HIGH
STEAM GENERATOR
TURBINE
TURBINE BLDG
33m X 50m
45m HIGH
GENERATOR BLDG
28m X 63m
60m HIGH
DIESEL GENERATOR & AUXILIARY BLDG
28m X 8m
15m HIGH
REPLACEMENT BLANKET STORAGE AREA 18m X 36m, 15m HIGH
VACUUM & T2 HANDLING BLDG
18m X 36m
15m HIGH
CRYOGENIC PELLET STORAGE
15m X 15m
15m HIGH
ADMINISTRATION & CONTROL BLDG
20m X 50m
15m HIGH
Li2O STORAGE
Li2O INLET TUBE
PELLET INJECTOR
SERVICE SHOP
15m X 15m
15m HIGH
REACTOR BLDG
48m X 65m
50m HIGH
LASER BEAM LINES
REACTOR CAVITY
MIRROR SUPPORT & SHIELD
BEAM SIZE REDUCING OPTICS
FINAL AMPLIFIERS
INPUT MIRRORS
LASER BLDG
120m X 80m
30m HIGH
UW
0
25m
50m
SCALE

16 spokes. The spokes are the junctions between adjacent blanket segments and the axle represents the location of the pellet injector.

Figure XIV-B-1 is a midplane cross section of a reactor quadrant without beam ports and Fig. XIV-B-2 is a similar view of a quadrant with beam ports. The first 60cm constitute the six 10cm zones of the blanket. Each circumferential zone will have progressively slower flowing breeding material. The flow rate is tailored to match the nuclear heat deposition in order to maintain a relatively constant temperature at the blanket exit (Section XII). The last zone will have slow moving Li_2O in order to preferentially heat it higher than the rest of the breeding material. This zone is separately ducted into a tritium extraction facility.

The blanket segments are made of chopped graphite fibers which are compressed together at elevated temperature and pressure to make panels. These panels are then shaped and joined together to form the structured blanket segments. The first wall and the internal partitions are 0.64 cm thick and the side and back panels are 1.0cm thick. If one assumes a density of 1.8gm/cc for this type of graphite, the weight of each segment will be 3.3 tonnes.

Figures XIV-B-1 and XIV-B-2 show four blanket segments attached to aluminum back structures. The back structures are quadrants of a spherical shell each weighing 14 tonnes and will be made of 1100-H14 aluminum alloy. This alloy was selected on the basis of its relatively low residual activity, an important consideration when it comes to maintaining and replacing blanket segments. Ceramic insulators and spacers are used between the graphite blanket segments and the cooled back structure in order to thermally

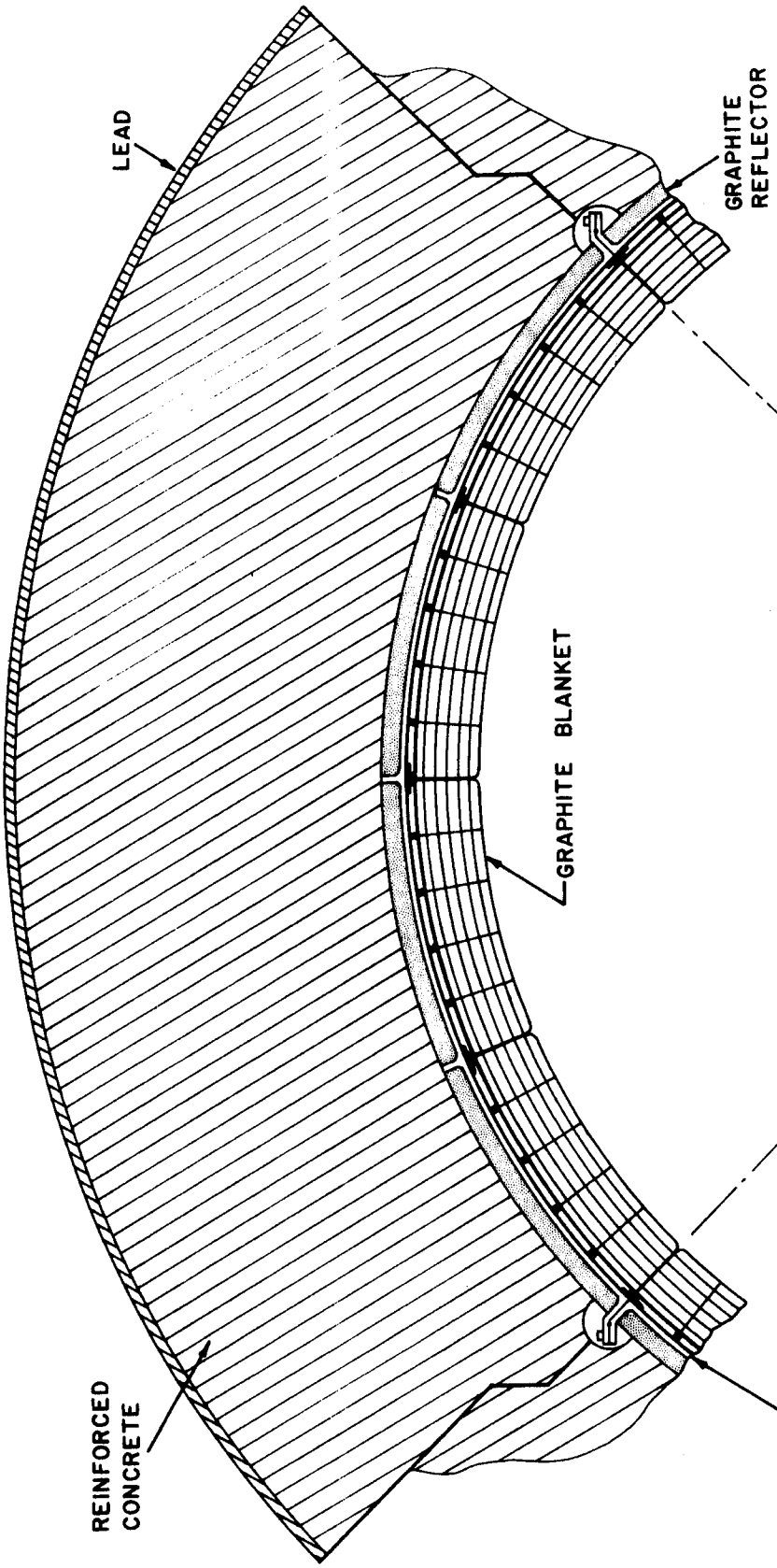

Fig. XIV-B-1.

Mid-plane Cross-section of a Reactor Cavity Quadrant Without Beam Ports.

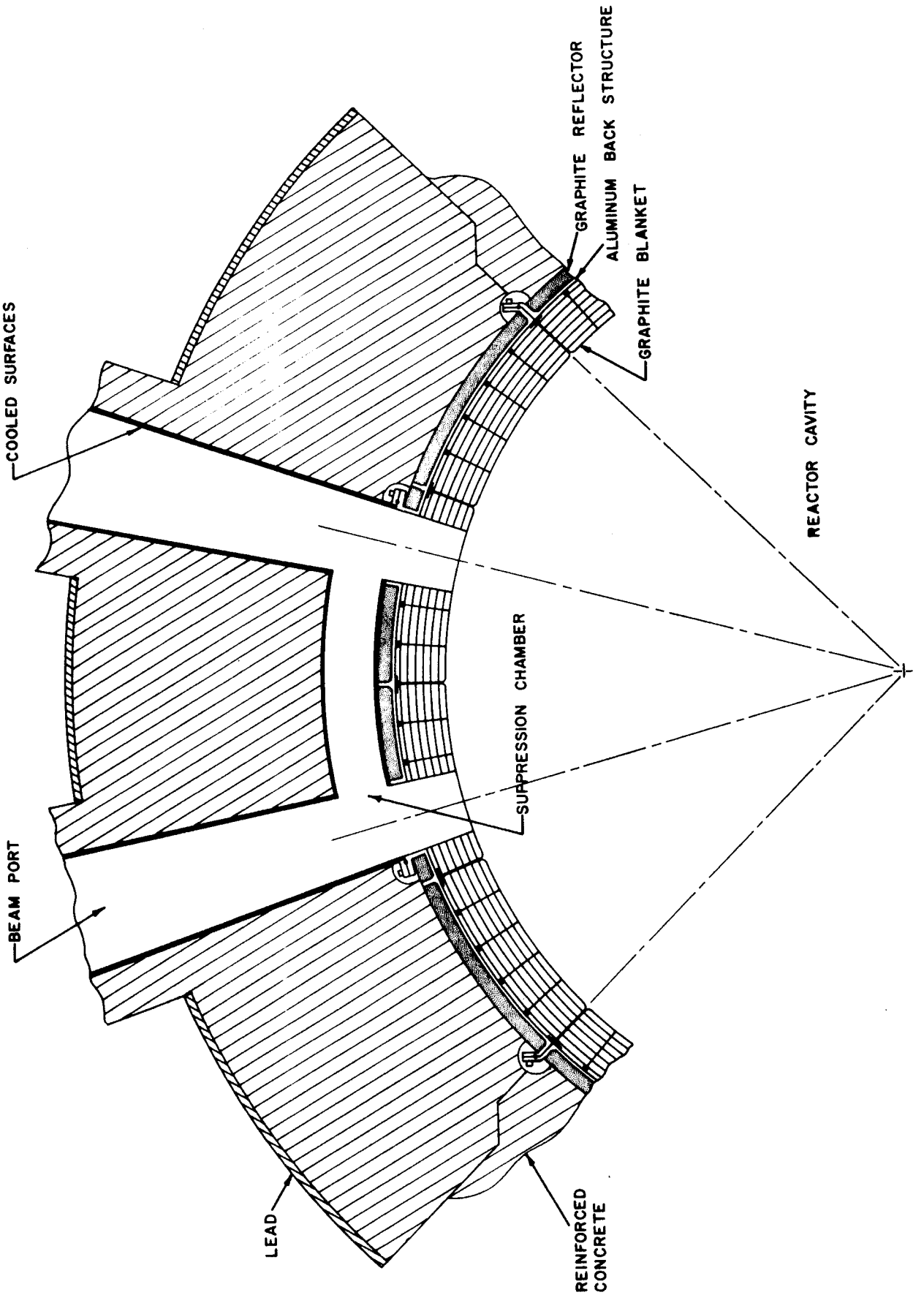

Fig. XIV-B-2.

Mid-plane Cross-section of a Reactor Cavity Quadrant With Beam Ports.

isolate them. The graphite is less susceptible to neutron-induced swelling when operating at a high temperature.

Figures XIV-B-3 and XIV-B-4 show a possible scheme for attaching the blanket segments to the back structure. Figure XIV-B-3 is a cross section of an end attachment where the lug is bolted to the back structure. The lugs at intermediate blanket segment junctions are inserted from the side to engage the attachement lip on the back of the blanket segment and then are slid down into a captive groove to engage with the back structure as shown in Fig. XIV-B-4. An adjacent blanket segment is then slid into place to engage the lugs already fixed to the back structure, and another set of lugs installed on the other side of the blanket segment. This scheme provides for a non-rigid attachment which will allow some degree of movement and shifting. It is estimated that the lugs will have to be 85cm apart which means that about 100 lugs will be needed for each quadrant. They will be made of 6061-T6 aluminum alloy. The ceramic spacers will be fixed to the blanket segments at the appropriate locations. The back side of the blanket segments will bear against the back structure through ceramic spacers permanently fixed to the aluminum. They will be located to coincide with the radial rib structure of the blanket.

Four blanket segments will have beam ports built into them. The two central blanket segments of the quadrants with the beam ports each will have three ports. Figure XIV-B-2 shows the two midplane ports, one in each of the two central blanket segments. Aside from the beam ports, these quadrants will also have suppression chambers designed to attenuate the shock waves from the micro-explosions before they reach the first mirrors. Another function of the suppression chambers is to serve as the plenums for the vacuum

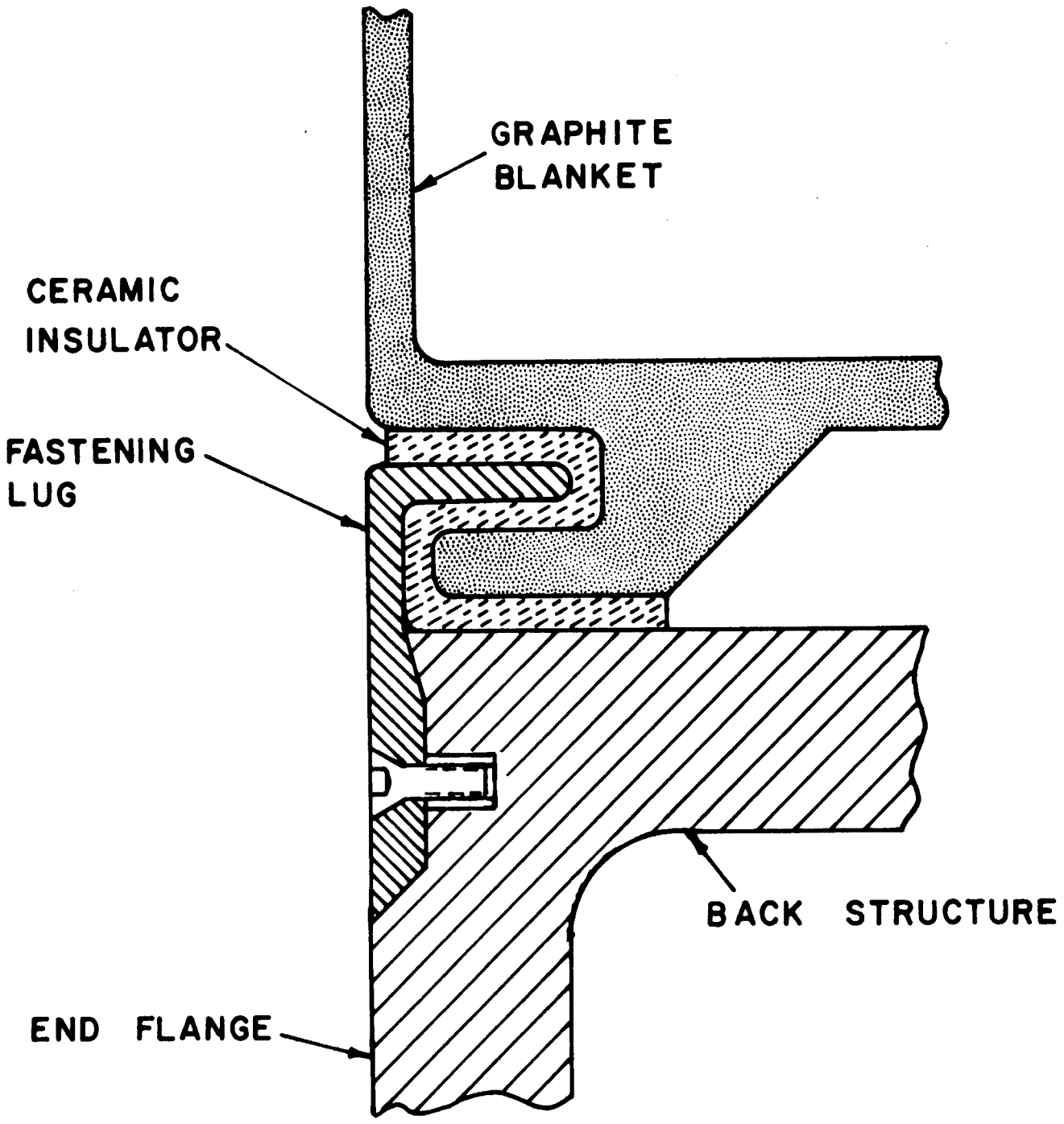

Fig. XIV-B-3.

Mode of Attachment between Blanket and Back Structure for End Blanket Segments.

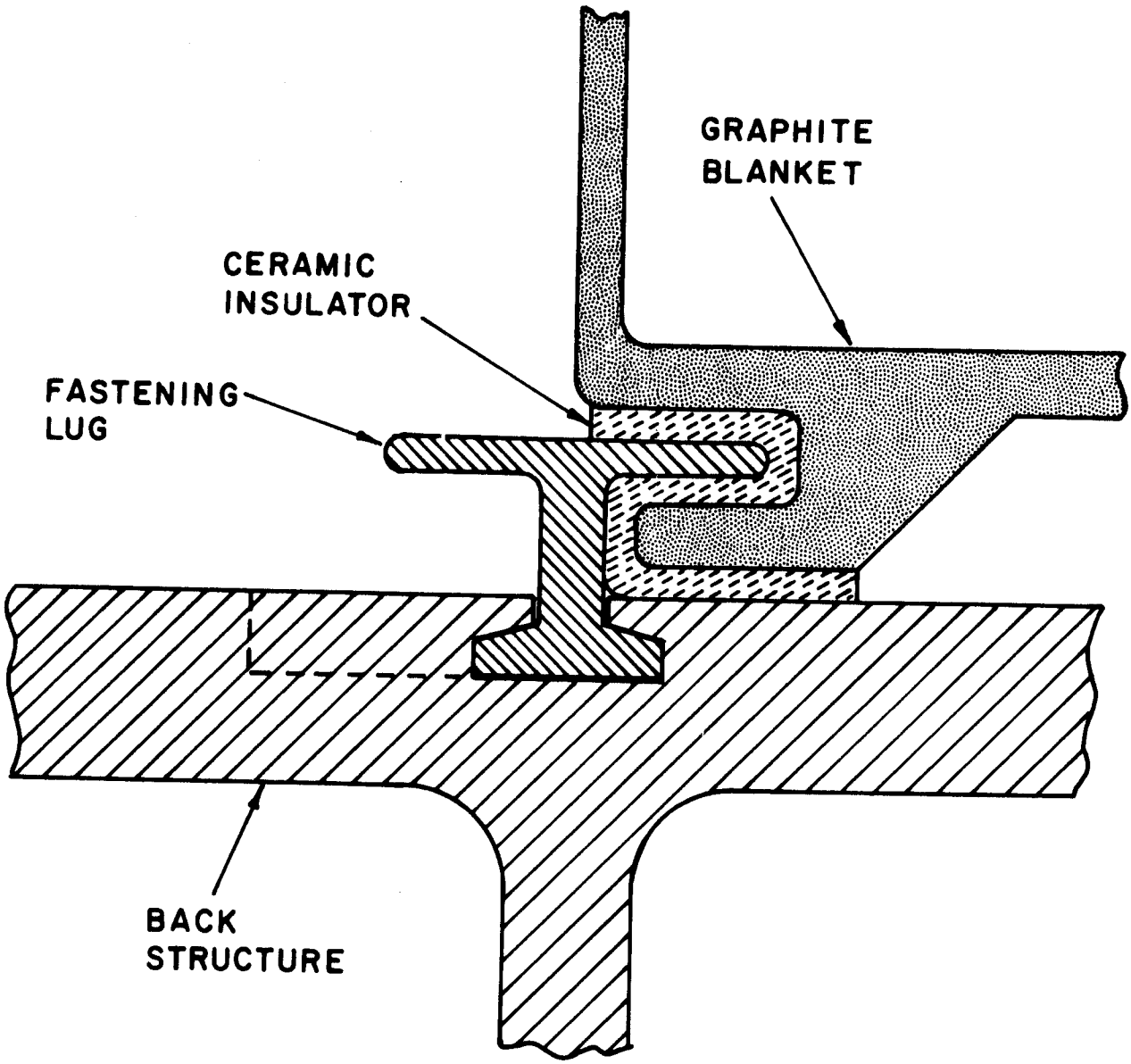

Fig. XIV-B-4.

Mode of Attachment between Blanket and Back Structure
for Intermediate Blanket Segments.

pumping system. Cooled surfaces within the suppression chamber will reduce the temperature of the pumped gases and condense out any materials coming from the reactor cavity to prevent them from being ingested in the vacuum pumps. Each port will have a graphite liner cemented to the blanket segment and sealed to the back structure. A flange on the back structure surrounding all six beam ports will mate with a similar flange on the suppression chamber. Bolting the two flanges together with a soft aluminum wire in between will seal the suppression chamber from the reactor building.

Figures XIV-B-1 and XIV-B-2 show how quadrants of back structure are bolted together. The flanges are bent at an appropriate angle to make the bolts accessible by impact wrenches extended through the shield. Captive bolts will be used to alleviate the problem of handling them during assembly and disassembly. A captive soft aluminum wire will be used to seal the quadrants together as well as any other place where seals will be required. Since the vacuum requirements of the reactor cavity are modest, reliance on mechanical seals will be made in order to avoid welding, which is both time comsuming and difficult to do by remote control (should it be necessary).

XIV-C. Shield

The shield is a free standing thick walled spherical shell made of concrete reinforced with 10% aluminum alloy structure. It is divided into four quadrants each weighing ~2200 tonnes, two of which will contain the suppression chambers and the beam ports. The quadrants with the beam ports will be stationary while the other two quadrants will be equipped with gas bearings to allow them to be retracted radially outward from the reactor

cavity. This provides accessibility to the blanket segements which will have to be replaced annually.

The back structure of the blanket is bolted to the shield with captive bolts. These bolts can be accessed by impact wrenches extended through holes in the shield. During normal operation, these holes are plugged with shielding material. Since the shield is designed for hands on maintenance even when the reactor is operating, the problems of making and breaking bolted joints will be minimal. The last 10 cm of the shield consists of a layer of lead. The lead will be canned in aluminum structure and bolted to the shield.

Gas bearings have been used extensively for moving heavy objects. There are two problems associated with them, one is the possibility of dispersing radioactive dust which will settle on internal reactor components and the other is that they require relatively flat surfaces to move over. The first problem is not really applicable here, since the area beyond the shield will receive very little activation and any dust can be effectively vacuum cleaned prior to opening of the shield quadrants. Since the excursion of the movable shield quadrants is rather short, it can be assumed that the floor in that area can be made uniformly flat for gas bearings to operate over.

Removable shield segments will be used above the reactor cavity to shield the Li_2O inlet tube. It is assumed that a 50 tonne overhead crane will be available in the reactor building. On the average, twenty 40 tonne shield segments will have to be removed from the top of the reactor to expose the inlet

tube for dissassembly prior to blanket segment replacement. These shield segments will be made to interlock with each other and bolts will be used to fasten them together.

Wherever threaded connections are made, 2219-T87 Aluminum alloy threaded inserts will be used in conjunction with stainless steel bolts. It is unfortunate that stainless steel bolts have to be used because of the long term activity problems associated with them. However, it is believed that when hands on operations will be performed on spent blanket segments, the bolts can be removed and stored in shielded containers. New unirradiated bolts will be used in assemblying new blanket segments.

XIV-D. Assembly and Disassembly

Power plant availability and consequently the price of electric power is greatly dependent on the amount of down time needed for routine maintenance. A primary maintenance requirement for SOLASE is the periodic replacement of the graphite blanket. The design of the reactor cavity and reactor building has been oriented toward a rapid blanket changeout scheme. This scheme is dependent on the premise that many of the difficult and time-consuming functions can be performed prior to the actual shutdown of the reactor for blanket replacement.

It will be assumed that two sets of back structure will be available, such that one set can be in use in the reactor while the other is being outfitted with new graphite blanket segments in a special maintenance shop adjacent to the reactor building. At the time of blanket replacement, each quadrant consisting of the back structure and four blanket segments

is uncoupled from its shield quadrant and taken out of the reactor building on motorized flat bed carriages. This will entail lifting the blanket quadrants, each weighing in the neighborhood of 28 tonnes, with the overhead crane and then laying them flat on the transport carriage as shown in Fig. XIV-D-1. The reverse procedure is used in bringing new blanket quadrants. A crude sequence of functions needed for blanket replacement is outlined in the next section. Table XIV-D-1 gives the masses in the blanket and shield.

- Reactor Shutdown
  - Lasers, pellet injectors, gas injectors and vacuum pumps are turned off.
  - The breeding material is drained into a storage vessel and valves close off the inlet and outlet lines at the point where they penetrate the reactor building.
  - Coolants are turned off.
  - The reactor cavity and reactor building are brought to an atmosphere of pressure.
- Shield Disassembly and Preparation for Reactor Opening
  - Main hatch in reactor building is opened.
  - One by one the twenty shield segments on the top of the cavity are disconnected, lifted by the overhead crane and stacked in a special area in the reactor building.
  - Pellet injector tube is retracted and removed.

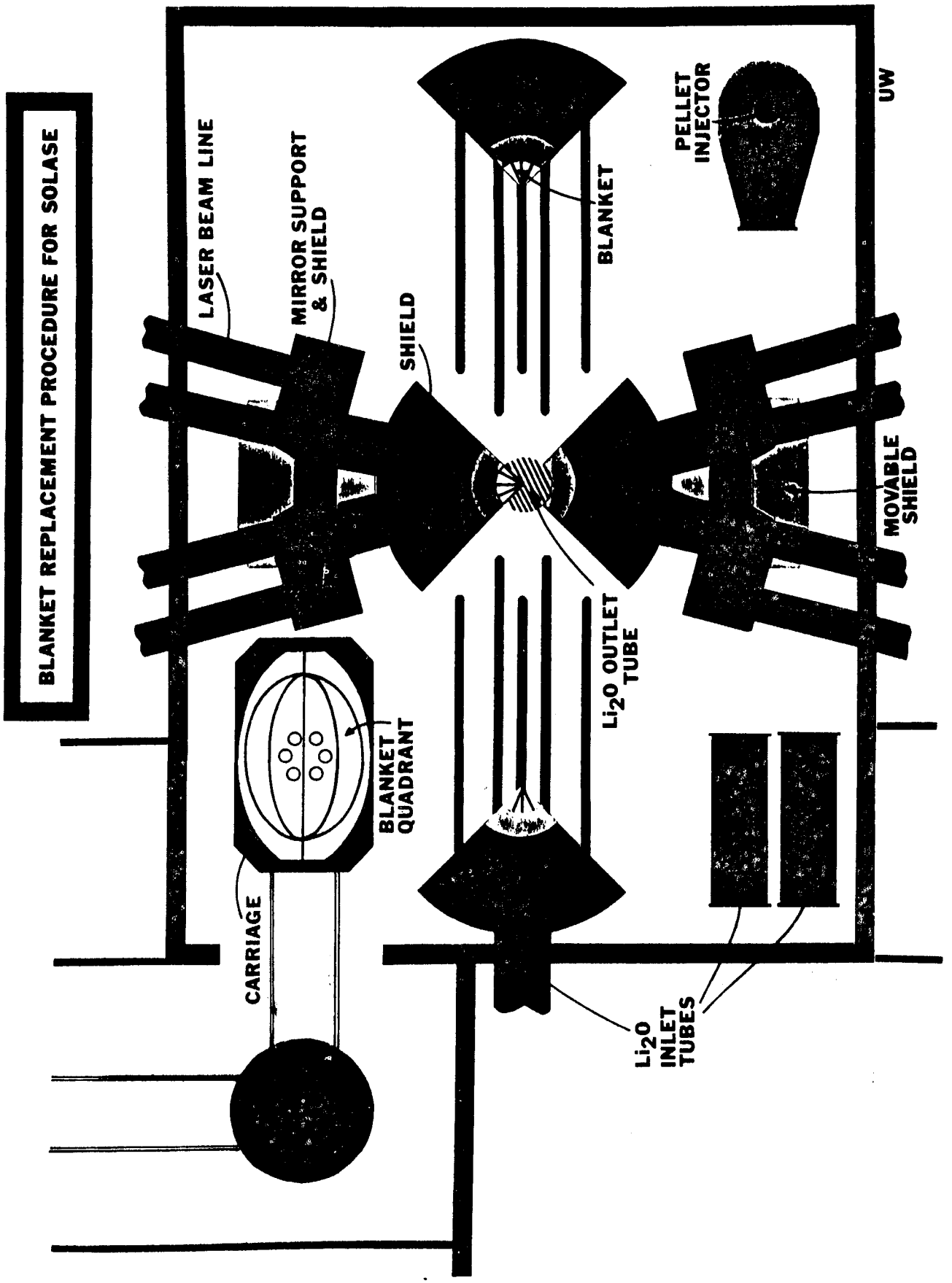
BLANKET REPLACEMENT PROCEDURE FOR SOLASE
LASER BEAM LINE
MIRROR SUPPORT & SHIELD
SHIELD
BLANKET
PELLET INJECTOR
UW
MOVABLE SHIELD
Li2O OUTLET TUBE
BLANKET QUADRANT
CARRIAGE
Li2O INLET TUBES

Fig. XIV-D-1.

Table XIV-D-1

Masses of Blanket & Shield	Tonnes
Weight of blanket segment	3.34
Total weight of blanket	53.4
Weight of back structure quadrant	14.4
Total weight of back structure	57.5
Weight of a shield quadrant	2200
Weight of Li_2O inlet tube shield	800
Total weight of shield	9580
Weight of removable section of Li_2O tube	15.0
Mass of graphite in shield	163
Mass of concrete in shield	6920
Mass of aluminum alloy in shield	950
Mass of lead in shield	1550

- Flanges connecting the breeding material inlet tube to the reactor cavity and to the extension leading out of the reactor building are disconnected and the section of tube immediately above the reactor lifted out and stored.
- The flange at the breeding material outlet tube connecting it to the reactor cavity is unbolted and freed.
- The seals at the junction between adjacent quadrant blanket segments are broken. There are four at the top and four on the bottom of the reactor.
- The bolts which hold the back structure flanges together are unscrewed.
- Coolant connections to the back structure and the suppression chambers are disconnected and the headers removed.
- The gas bearings under the movable shield quadrants are energized and the shield quadrants retracted.

- <u>Blanket Removal and Replacement</u>
  - All the bolts which attach the back structure to the shield are disconnected.
  - In the case of the quadrants with beam ports, the bolts sealing the back structure to the suppression chamber are disconnected.
  - Each quadrant of blanket is lifted out one by one and placed flat on a flat bed motorized carriage.
  - Blanket quadrants are transported through the main reactor building hatch into the maintenance shop.
  - Newly assembled blanket quadrants are transported into the reactor building from the maintenance shop.

- One by one the blanket quadrants are lifted from the transport carriage and placed on the shield quadrants. Provision is made to latch the blanket quadrant to the shield until the bolts can be installed.
- All the bolts needed to attach the blanket quadrants to the shield are installed.

- Shield Assembly and Reactor Preparation
  - Gas bearings are energized and the shield quadrants are assembled together.
  - Bolts which seal the back structures to each other are installed.
  - Coolant connections to the back structure and the suppression chamber are made.
  - Seals between blanket quadrant segments are made at the top and the bottom of the reactor.
  - The connection between the (breeding material) outlet tube flange and the reactor cavity is made.
  - The inlet tube is lifted into place and the flanges connected.
  - The pellet injector tube is inserted and sealed to the blanket segments.
  - Top shield sections are lifted into place one by one and bolted together.
  - Reactor building main hatch is closed and sealed.

- Reactor Startup
  - Mechanical transport systems which move the breeding material are started up, the valves opened and the blanket filled with Li_2O.

- Vacuum pumps are turned on to simultaneously evacuate the blanket system, the reactor building and the reactor cavity to the prescribed operating pressures.
- Dummy pellets are injected to test the alignment of the chamber with respect to the laser beams and corrections are made.
- Cooling is initiated for the back structure and the suppression chamber.
- Complete check of all systems is performed prior to initiation of reactor operation.

XV. Radiation Damage and Materials Considerations

XV-A. Radiation Effects in Graphite

XV-A-1. Behavior of Point Defects in Graphite

The crystalline structure of graphite, shown in Fig. XV-A-1, is highly anisotropic, and for this reason, the radiation-induced property changes are strongly related to this structure. This is particularly reflected in the migration of interstitials and vacancies. The interstitial, occupying a position between basal planes, has a very low activation energy of 0.45 eV for motion parallel to the basal planes, but a large energy of 2.8 eV for migration in the c-axis direction.[1] Likewise, the vacancy requires an activation energy of about 3 eV to move in the basal plane, but it takes 5.45 eV for motion along the c-axis. The addition of interstitials between basal planes results in a large increase of the lattice parameter "c" relative to the change in the other parameter "a". Contrary, the vacancies do not appreciably alter the c- spacing but give rise to a decrease in the a - spacing according to[2]

$\Delta a/a = -0.14\ n_v$, where n_v is the number density of vacancies.

Since in the production of interstitial-vacancy pairs by energetic recoil atoms the point defect pair is spacially separated, a correlated recovery is very unlikely unless the point defects are situated on the same basal plane. Consequently, the predominant reaction at high temperatures will be the formation of separate interstitial and vacancy clusters. As a result, the growing interstitial loops produce additional basal planes, whereas the old basal planes contract. Hence, each single-crystal region

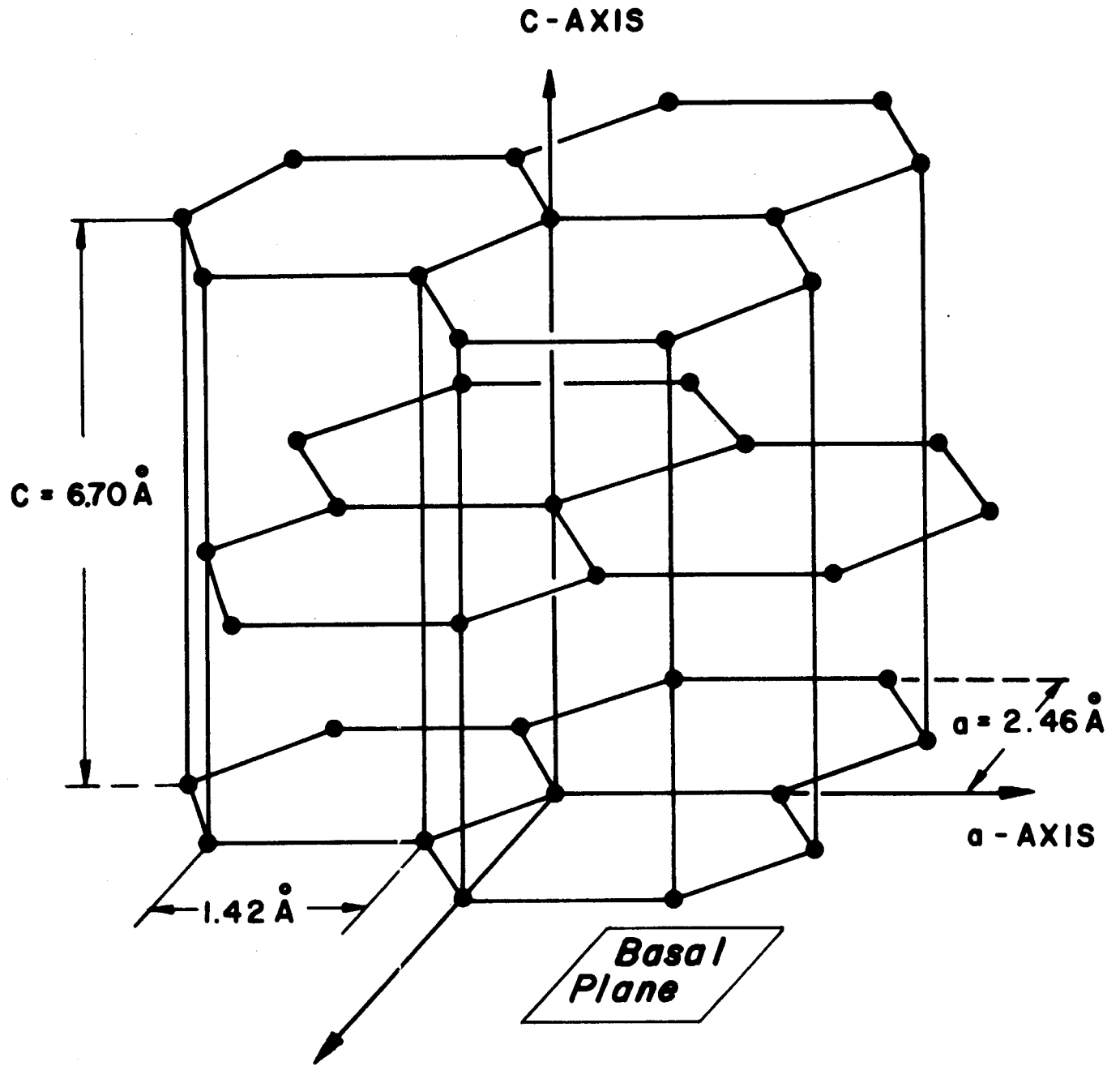

Fig. XV-A-1 Crystalline Structure of Graphite

in a graphite solid under irradiation will expand in the c-direction and contracts in the a-direction.

XV-A-2. Dimensional Changes of Polycrystalline Graphites

Polycrystalline graphites exhibit large dimensional changes after irradiation. These dimensional changes depend strongly on the raw material and the fabrication process used. As illustrated in Figs. XV-A-2 and 3, these changes are characterized by an initial densification followed by an expansion at higher radiation doses.

This phenomenon can be explained by the dimensional changes of the graphite crystallites that make up the graphite particles and by the closure and expansion of pores and microcracks. Following the notation of Engle[3], there are three different types of pores (see Fig. XV-A-4). The crystallites themselves contain micropores which contribute the volume ΔV_{p_1} to the total porosity. Many crystallites are contained in a single graphite particle, and transgranular microcracks between the crystallites occupy a volume ΔV_{p_2}. In turn, the particles are held together by a graphite binder, produced from coal-tar pitch, and they may enclose intergranular microcracks which take up the volume ΔV_{p_3}.

During irradiation the individual crystallites expand in the c-direction, i.e. perpendicular to the basal planes, but contract parallel to the basal planes (or in the a-direction). As a result, the different pore volumina change with time. Initially, the dimensional changes are produced by a partial closure of all three pore types. However, as the crystallites continue to expand in the c-directions, new and old microcracks open up, causing ΔV_{p_2} and ΔV_{p_3} to increase.

Fig. XV-A-2 Volume Change of Graphite with 20% Initial Porosity Irradiated at Temperatures between 400°C and 1000°C

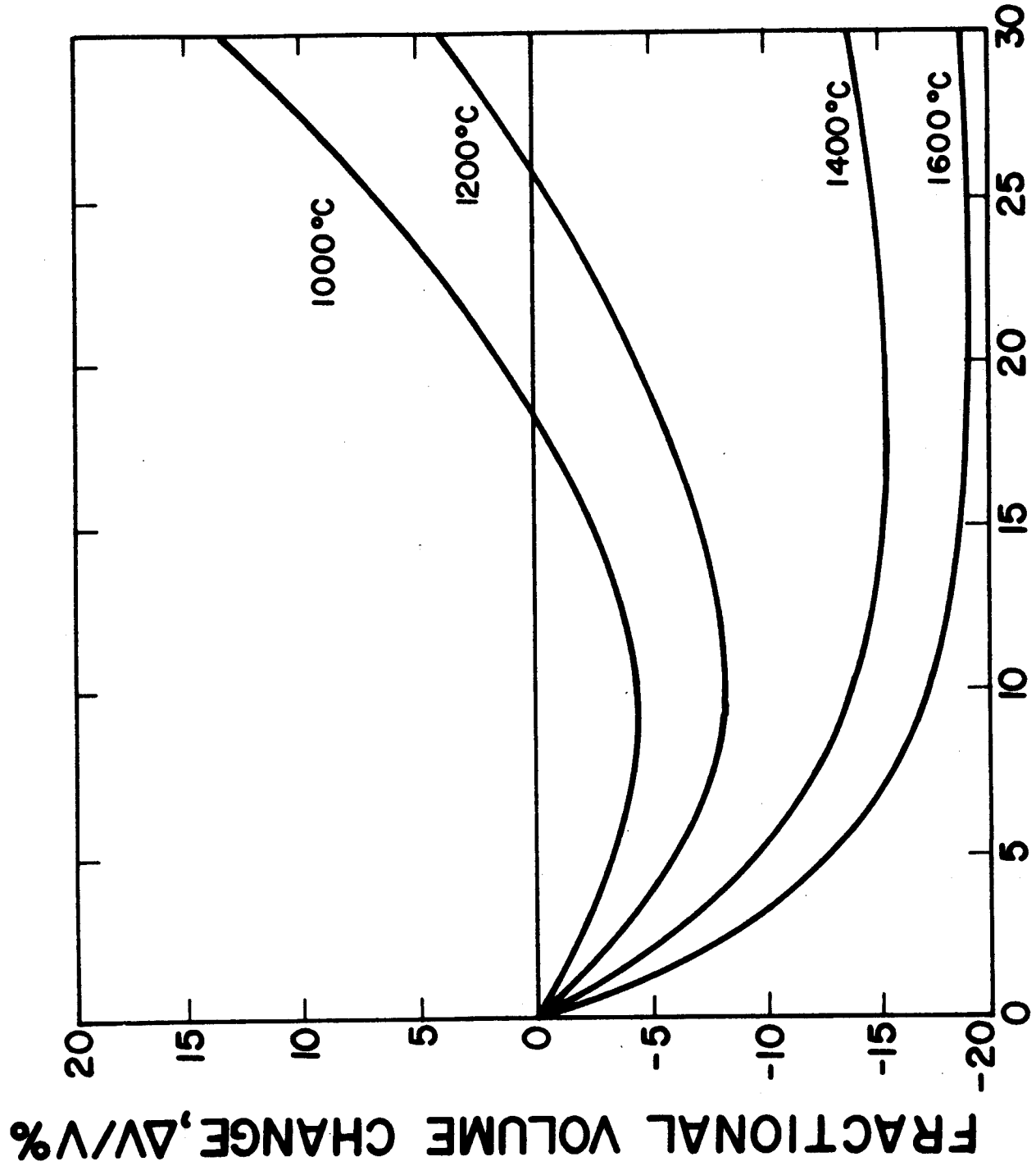

Fig. XV-A-3 Volume Change of Graphite with 20% Initial Porosity Irradiated at Temperatures between 1000°C and 1600°C

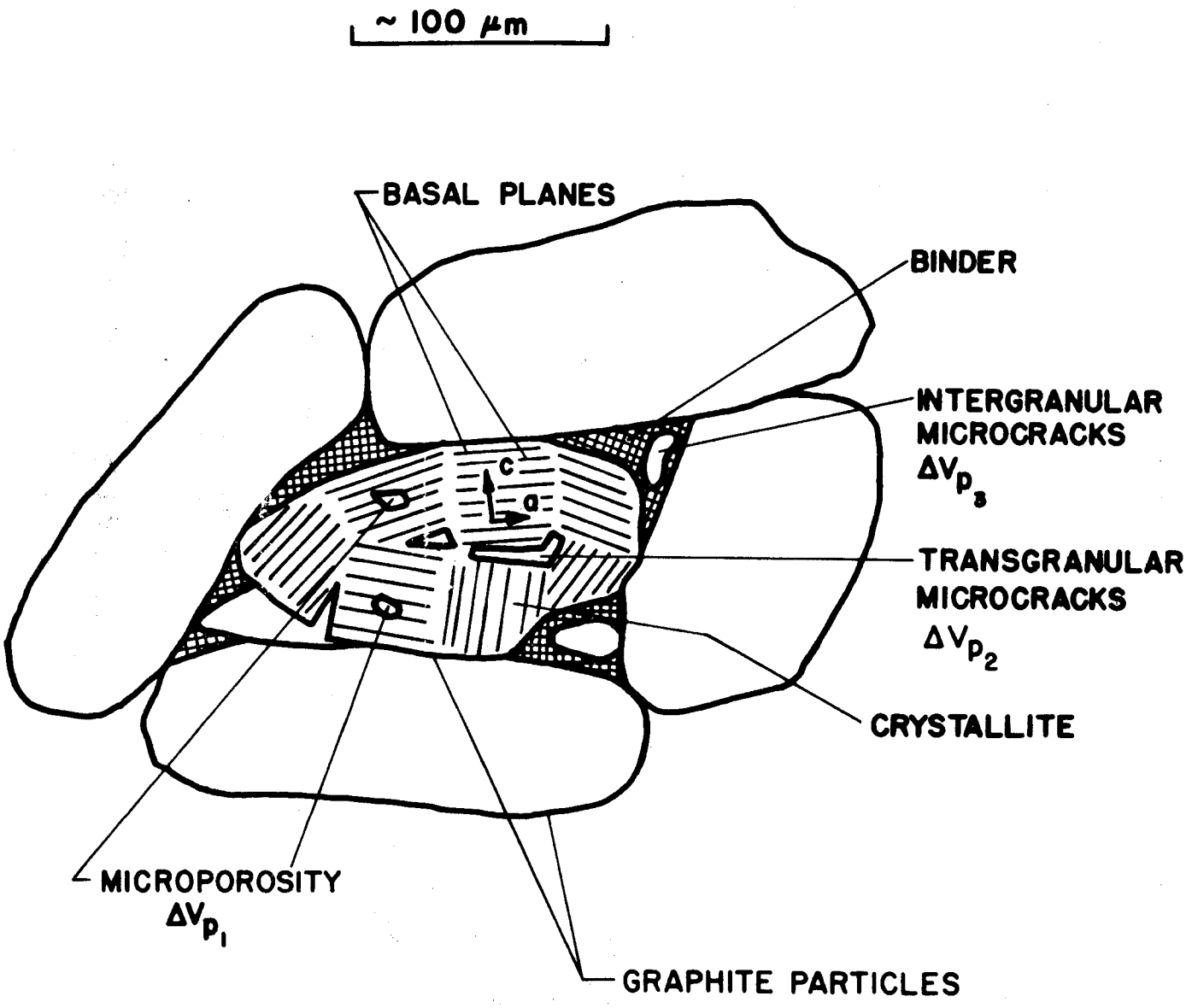

Fig. XV-A-4 Microstructure of Polycrystalline Graphite

The contribution of the three different types of pores has been measured as a function of irradiation dose by Engle.[3] This was accomplished in the following way. First, the total volume change

$$\Delta V = \Delta V_{p_1} + \Delta V_{p_2} + \Delta V_{p_3} \qquad (1)$$

was determined by length change measurements. After that the specimens were immersed in a liquid thereby filling the porosity ΔV_{p_3}. The measurement gave then $\Delta V_{p_1} + \Delta V_{p_2}$. Finally, the graphite was crushed into its particles, and the powder was again immersed in a liquid. Because the liquid penetrated the pore volume ΔV_{p_2}, the volume ΔV_{p_1} could then be found.

In summary, Engle was able to describe dose dependence of the three porosity contributions. He found that ΔV_{p_1} increases slightly initially and changes little thereafter. However, ΔV_{p_2} decreases initially, contributing mostly to the initial densification phase, and then increases moderately at higher doses. The pore volume ΔV_{p_3} changes little during the densification phase but then increases dramatically. Therefore, ΔV_{p_3} is the major contributor to the final expansion rate of graphite under irradiation.

In the manufacture of graphite components, the selected coke particles are combined with the binder material, and the components are formed at high temperatures either by extrusion or by molding. In the extrusion process, the particles and crystallites arrange themselves in such a fashion that there results a preferential orientation of the c-axis perpendicular to the extrusion direction. If the component is molded, the c-axis aligns itself parallel to the pressure direction.

The resulting composite exhibits anisotropic behavior. The direction which is predominantly influenced by the c-axis properties suffers an initial contraction followed by expansion at high exposures. On the other hand, the directions predominantly aligned with the a-axis of the crystallites continue to contract up to much higher exposures before the expansion begins. By proper selection of raw material and processing steps, it is possible to produce graphites with macroscopically isotropic properties.

The change of porosity in graphite as a function of irradiation is accompanied by corresponding changes in the strength, elastic properties, thermal expansivities, thermal conductivity and most other physical properties. Hence, it was important to develop a quantitative model for the dimensional changes of graphites which are used for structural purposes. As discussed above, one can rationalize the dimensional changes by a two-step process. Initially, the densification is mainly due to a partial closure of the fabricated porosity which accomodates the dimensional changes of the crystallites. After exhaustion of this process, further accomodation can only be accomplished by creation of new enlargement of existing micro-cracks between the particles and crystallites. It is then reasonable to assume that the initial densification rate is proportional to the initial porosity, P_o, but the final expansion rate should not depend on P_o. However, the onset of expansion is delayed with increasing initial porosity P_o.

A phenomenological equation, reflecting this behavior, is given by

$$P - P_o = \frac{\Delta V}{V_o} = \frac{A F^{n+1}}{BP + F^n} - P_o[1 - \exp(- CF)] \qquad (2)$$

where F is the radiation dose, and A, B, C and n are materials parameters which must be determined by fitting Eq. (2) to the experimental data. The particular dose dependence chosen for the first term in Eq. (2) is based on the assumption that the volumetric expansion will eventually become linear with dose. At present, there are no data at high doses available that either contradict or confirm this conjecture. However, it appears reasonable to assume that the expansion of the crystallites along their c-axis must eventually be linear with dose.

It has already been mentioned that the different graphites vary as far as their dimensional changes are concerned. Therefore, no attempt was made to fit Eq. (2) to any particular graphite. Instead, we strived for a description that is generic rather than specific. Accordingly, by inspection of available data and various equations of the form of Eq. (2) it was determined that the following equation is most compatible with the entire body of data utilized. This equation is

$$P - P_o = \frac{\Delta V}{V_o} = \frac{A F^3}{P_o/C + F^2} - P_o[1 - \exp(- CF)] \qquad (3)$$

It contains now only two parameters, A and C, which must be determined from experimental data. The most convenient way to accomplish this is to compare the initial shrinkage rate and the final growth rate with the data. Since

$$dP/dF = AF^2 \frac{3P_o/C + F^2}{(P_o/C + F^2)^2} - P_o C \exp(- CF) \qquad (4)$$

the initial shrinkage rate is given by

$$\dot{P}_i = (dP/dF)|_{F=0} = -P_o C \tag{5}$$

and the final growth rate is

$$\dot{P}_f = (dP/dF)|_{F\to\infty} = A. \tag{6}$$

The data that were used to determine A and C were length changes of anisotropic graphites. Therefore, the volume changes $\Delta V/V_o$ were computed from the length changes $(\Delta L/L)_{\parallel}$ parallel and the length changes $(\Delta L/L)_{\perp}$ perpendicular to the extrusion direction according to the formula

$$P - P_o = \frac{\Delta V}{V_o} = \left(\frac{\Delta L}{L}\right)_{\parallel} + 2\left(\frac{\Delta L}{L}\right)_{\perp} . \tag{7}$$

Conversion from fluence units to displacement units (dpa) were made according to correlations of Morgan.[4] The final growth rates for the length changes were estimated from the curves reported in the literature, and the volumetric growth rates were then computed with Eq. (7). These values are listed in Table XV-A-1 and plotted in Fig. XV-A-5. The same procedure was followed for obtaining the initial shrinkage rates. The corresponding values are given in Table XV-A-2 and plotted in Fig. XV-A-6.

According to Fig. XV-A-5, it appears that one can divide the different graphites into two groups. The group comprising the majority of the data in Fig. XV-A-5 has a modest final growth rate with a maximum of about $1.5(\frac{\Delta V}{V_o}\%)$/dpa at 1000°C. Both data groups were fitted to simple analytical expressions. For the low-growth graphites

$$A = \dot{P}_f = \{(\frac{800}{T})^2 + (\frac{T}{1250})^{12}\}^{-1} \quad [\frac{\Delta V}{V_o}\%/\text{dpa}] \tag{8}$$

where T is the temperature in °C, and for the high growth graphites

Table XV-A-1

Final Volumetric Growth Rates of Graphites

Graphite	Ref.	Temp. (°C)	$\dot{P}_f$ [%/dpa]	Symbol
Gilso	5	1125	1.03	●
		1150	1.44	
		1300-1500	0.20	
Petro-coke	5	1125-1150	1.32	○
		1175-1200	1.14	
		1300-1350	0.26	
		1400-1425	0.16	
Nuclear Grade	6	400-475	0.14	■
		650-750	1.42	
		950-1050	6.78	
		1200-1300	0.68	
Improved Isotropic	6	715	0.68	x
		950-1060	1.36	
Extruded Gilso	7	1400	1.25	▲
Pitch-coke	7	1400	3.90	✦

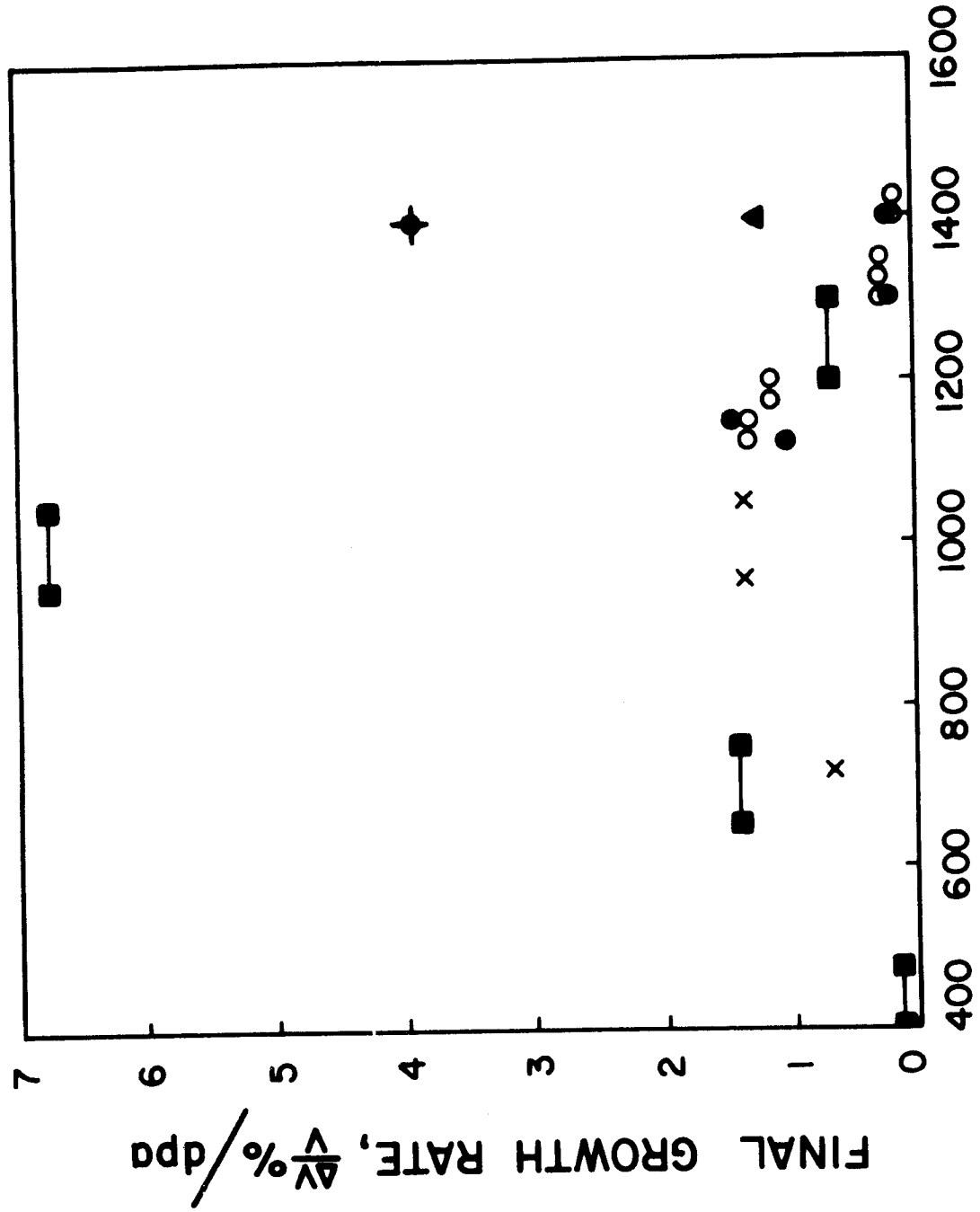

Fig. XV-A-5 Final Volumetric Growth Rate of Graphites as a Function of Irradiation Temperature. (For Meaning of Symbols see Table XV-A-1)

Table XV-A-2

Initial Volumetric Shrinkage Rates of Graphites

Graphite	Ref.	Temp. Range (°C)	$-\dot{P}_i/P_o$ [dpa^{-1}]	Symbol
Gilso	5	1125-1400	$0.096^{+0.031}_{-0.020}$	●
Petro-coke	5	1125-1425	$0.105^{+0.035}_{-0.024}$	o
Nuclear Grade	6	400-475	$0.036^{+0.012}_{-0.007}$	■
		650-750	$0.024^{+6.008}_{-0.005}$	
		950-1050	$0.045^{+0.025}_{-0.009}$	
		1200-1300	$0.068^{+0.032}_{-0.014}$	
Improved Isotropic	6	715	$0.0024^{+0.0008}_{-0.0004}$	X
		950-1300	$0.0068^{+0.0022}_{-0.0014}$	
Extruded Gilso	7	500	0.028	▲
		600	0.026	
		700	0.024	
		800	0.031	
		900	0.059	
		1000	0.074	
		1100	0.039	
		1200	0.067	
		1300	0.120	
		1400	0.170	
		1500	0.215	

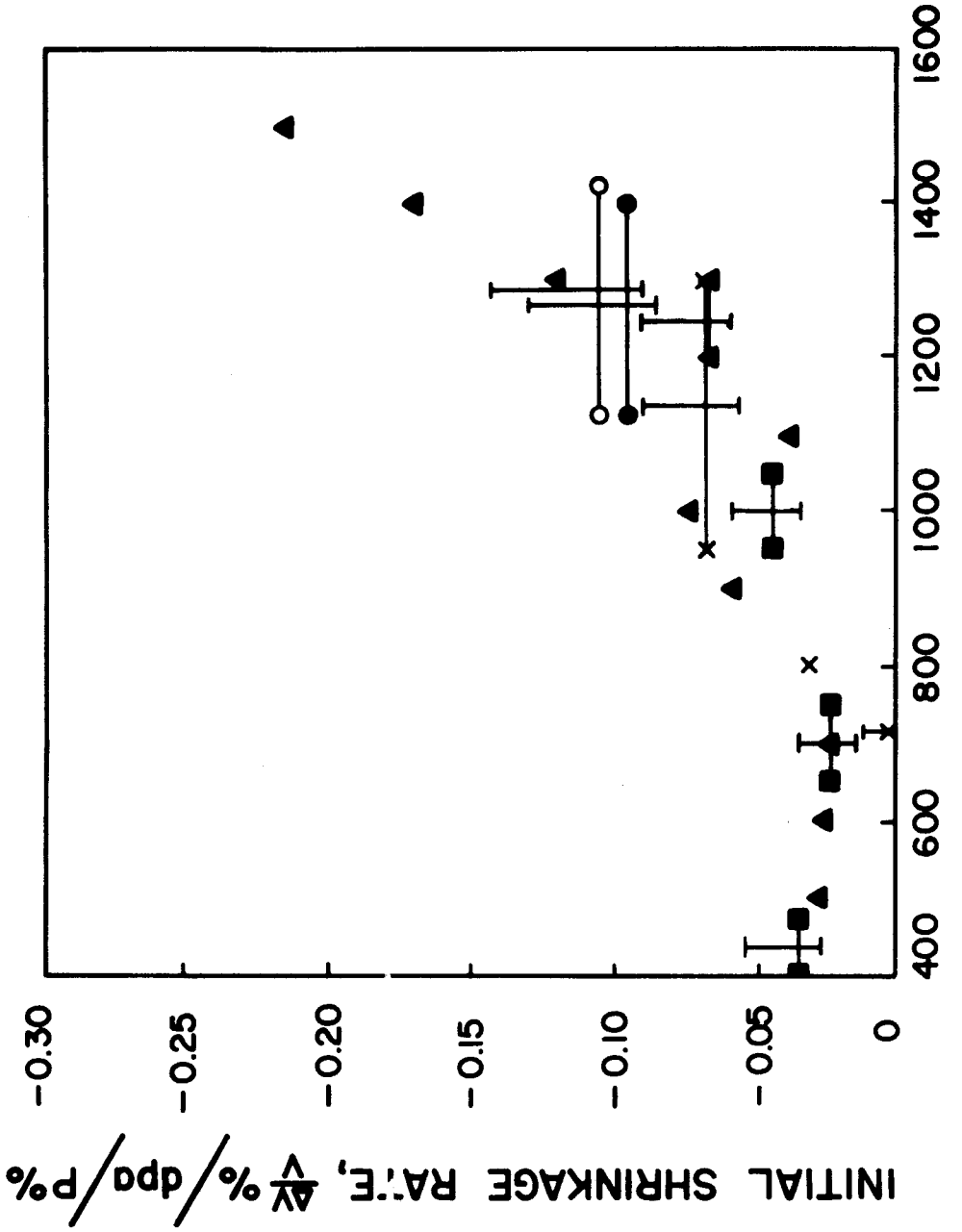

Fig. XV-A-6 Initial Volumetric Shrinkage Rate of Graphites as a Function of Irradiation Temperature. (For Meaning of Symbols see Table XV-A-2)

$$A = \dot{P}_f = 9.4 \left\{\left(\frac{900}{T}\right) + \left(\frac{T}{1050}\right)^4\right\}^{-1} \left[\frac{\Delta V}{V_o} \% \text{ /dpa}\right] \quad (9)$$

Plots of Eqs. (8) and (9) are shown in Figs. XV-A-7 and 8, respectively.

In contrast to the distinction in the final growth rate, the graphites considered for this study do not differ in their initial shrinkage rates, as can be clearly seen from Fig. XV-A-6. Therefore, all the data can be fitted to one expression. The nominal or average fit is simply given by

$$C = -\dot{P}_i/P_o = 0.01 \left(\frac{T-700}{210}\right)^2 + 0.02 \quad (9a)$$

A lower bound can be obtained from

$$C = \dot{P}_i/P_o = 0.01 \left(\frac{T-700}{230}\right)^2 \quad (9b)$$

And an upper bound from

$$C = -P_i/P_o = 0.01 \left(\frac{T-700}{170}\right)^2 + 0.04 \quad (9c)$$

All three expressions are plotted in Fig. XV-A-9. The volumetric changes for the model graphite, as given by Eq. (3), are shown in Figs. XV-A-2 and 3 for the low-growth graphite (A given by Eq. (8) and C given by Eq. (9)).

XV-A-3. Irradiation Creep of Graphite

Concurrent with the dimensional changes, graphite also exhibits radiation-enhanced creep when subject to either external loads or self-generated stresses due to non-uniform dimensional changes. A recent review and discussion of the data has been given by Blackstone.[8] The creep rate $d\varepsilon/dF$ of graphite under irradiation is a linear function of the stress σ, i.e.

$$\frac{d\varepsilon}{dF} = K\sigma \quad (10)$$

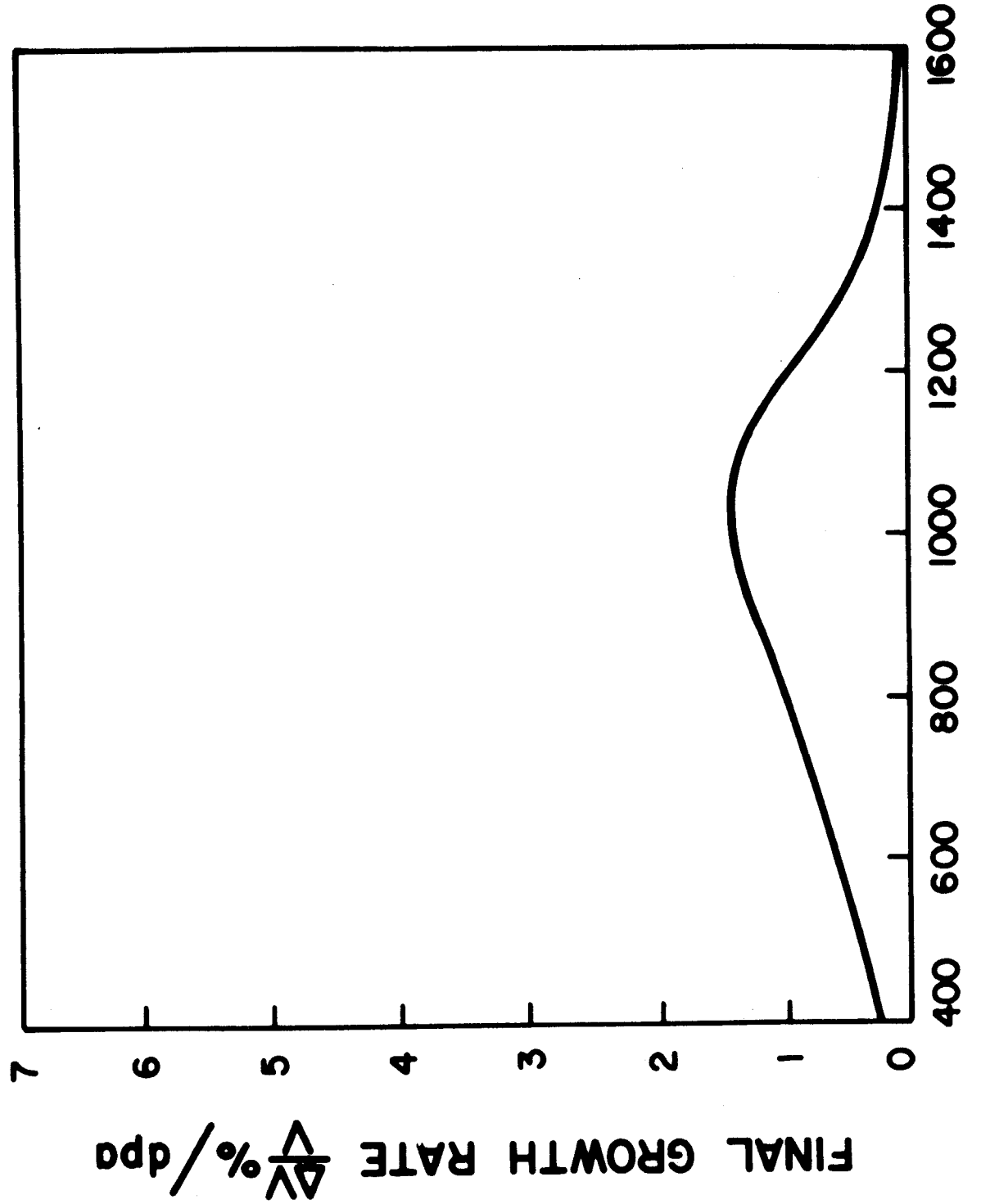

Fig. XV-A-7 Final Volumetric Growth Rate according to Eq. (8)

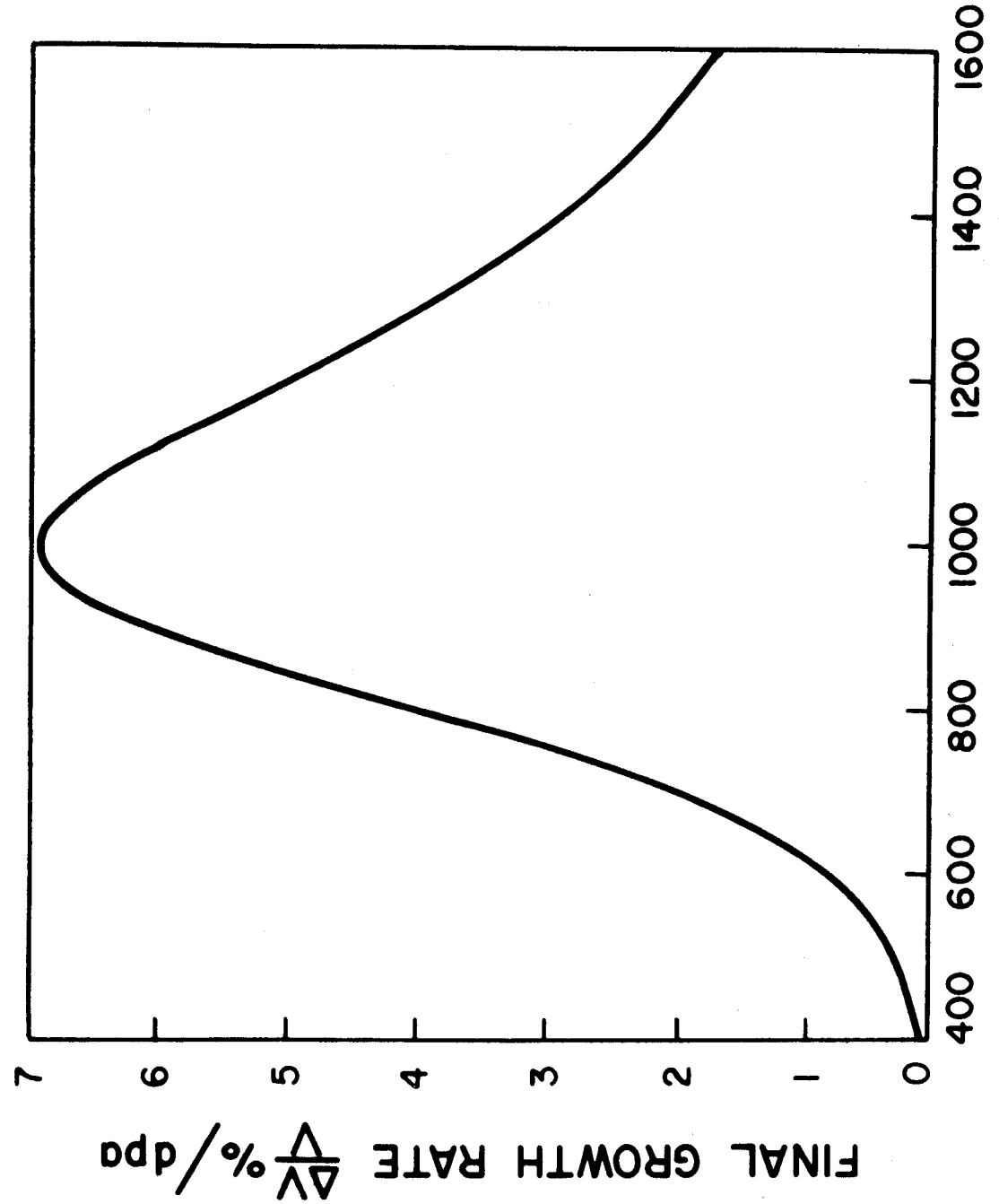

Fig. XV-A-8 Final Volumetric Growth Rate according to Eq. (9)

Fig. XV-A-9 Initial Volumetric Shrinkage Rates of Graphites according to Eqs. (9), (9a), and (9b).

where F is the dose. Veringa and Blackstone[9] have shown that a satisfactory correlation of most irradiation creep data can be obtained when the product of the creep coefficient K and the initial Young's modulus E_0 is plotted as a function of the irradiation temperature T, as shown in XV-A-10. The data can then be correlated with the expression

$$KE_0 = \frac{f(T)}{\dot{F}} + g(T) \tag{11}$$

where f(T) and g(T) are linear functions of the temperature and are given by

$$f(T) = (1.775 + 0.0185*T) \times 10^{-8} \text{ sec}^{-1} \tag{12}$$

and

$$g(T) = (-0.544 + 0.00403*T) \text{ dpa}^{-1} \tag{13}$$

Even though the creep correlation of Eq. (11) is based on the initial elastic modulus, E_0, the data can be equally well correlated with the final elastic modulus after the irradiation. In fact, since the elastic modulus changes as a function of the porosity, we presume that Eq. (11) should actually read

$$KE = \frac{f(T)}{\dot{F}} + g(T) \tag{14}$$

where E is the instantaneous elastic modulus. It should be noted that the transient or primary part of the irradiation creep has been neglected

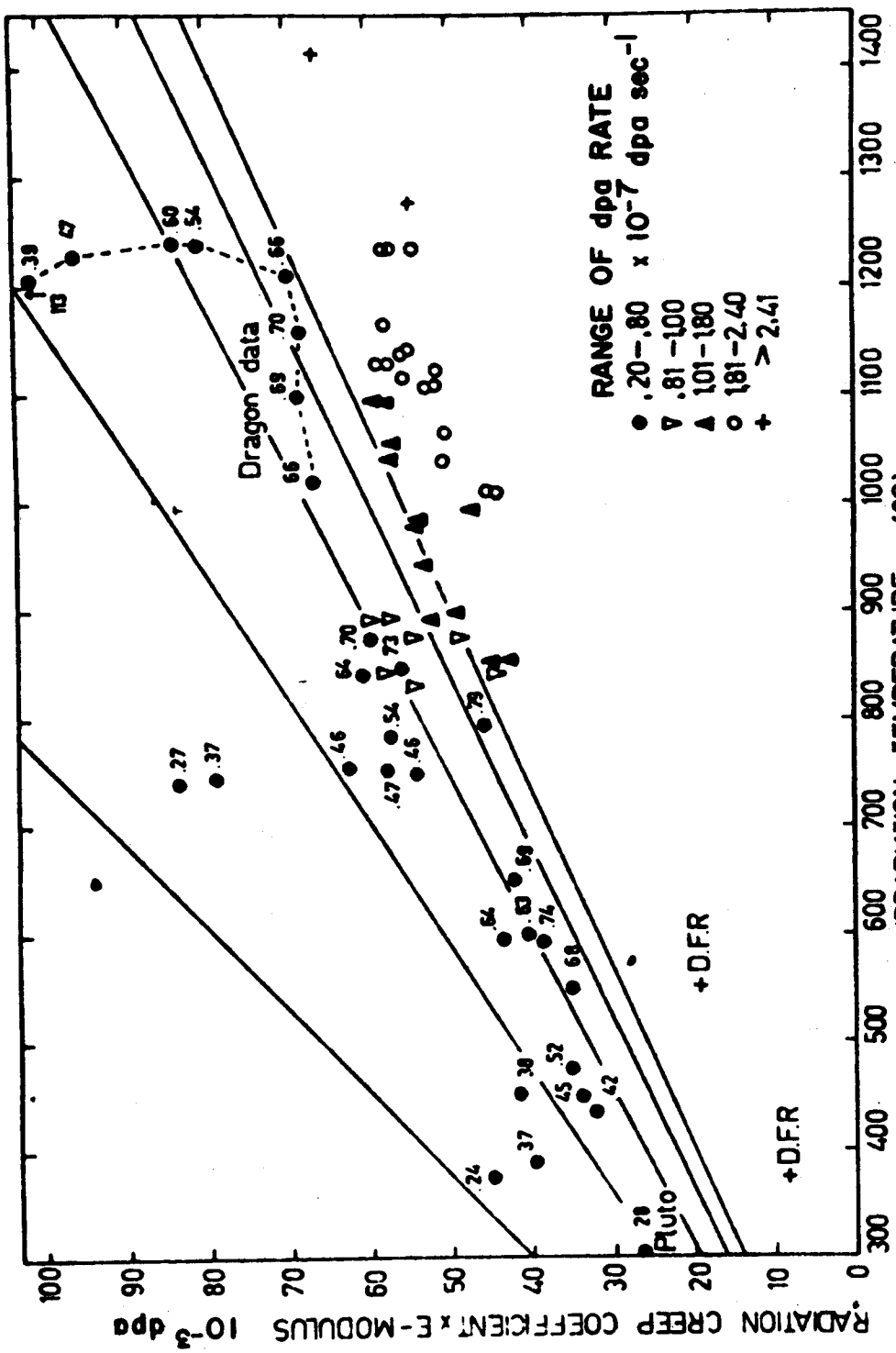

Fig. XV-A-10 The Product of Irradiation Creep Constant and Young's Modulus for Different Dose Rates and Different Irradiation Temperatures.

in Eq. (10) since it is of little consequence in the forthcoming analysis.

XV-A-4. Changes of Elastic Properties and Strength

Fast neutron irradiation produces changes in both elastic modulus and ultimate strength. Initially, both increase rapidly but then level off after a dose of about 1 dpa. Further changes take place more slowly, and they are accompanied by the corresponding dimensional changes. The initial rapid rise of the elastic modulus is commonly attributed to dislocation pinning by defect clusters within the crystallites, whereas the latter changes appear to be related to the changes in the porosity volumes of ΔV_{p_2} and ΔV_{p_3}. Fig. XV-A-11 shows the change of Young's modulus as a function of the fast neutron dose.[10]

The change in the tensile fracture stress is depicted[10] in Fig. XV-A-12 together with empirical fit of the form

$$\frac{\sigma}{\sigma_o} = \left(\frac{E}{E_o}\right)^n \tag{14}$$

It can be seen that a satisfactory correlation exists between σ and E for n = 1/2. This square-root relationship follows also from the Griffith fracture formula

$$\sigma = \sqrt{2E\gamma/\pi C} \tag{15}$$

where γ is the effective surface energy for fracture, and 2C is the length of the largest crack. This length can be expected to be of the order of the grain or graphite particle diameter. Hence, if we assume that 2C as

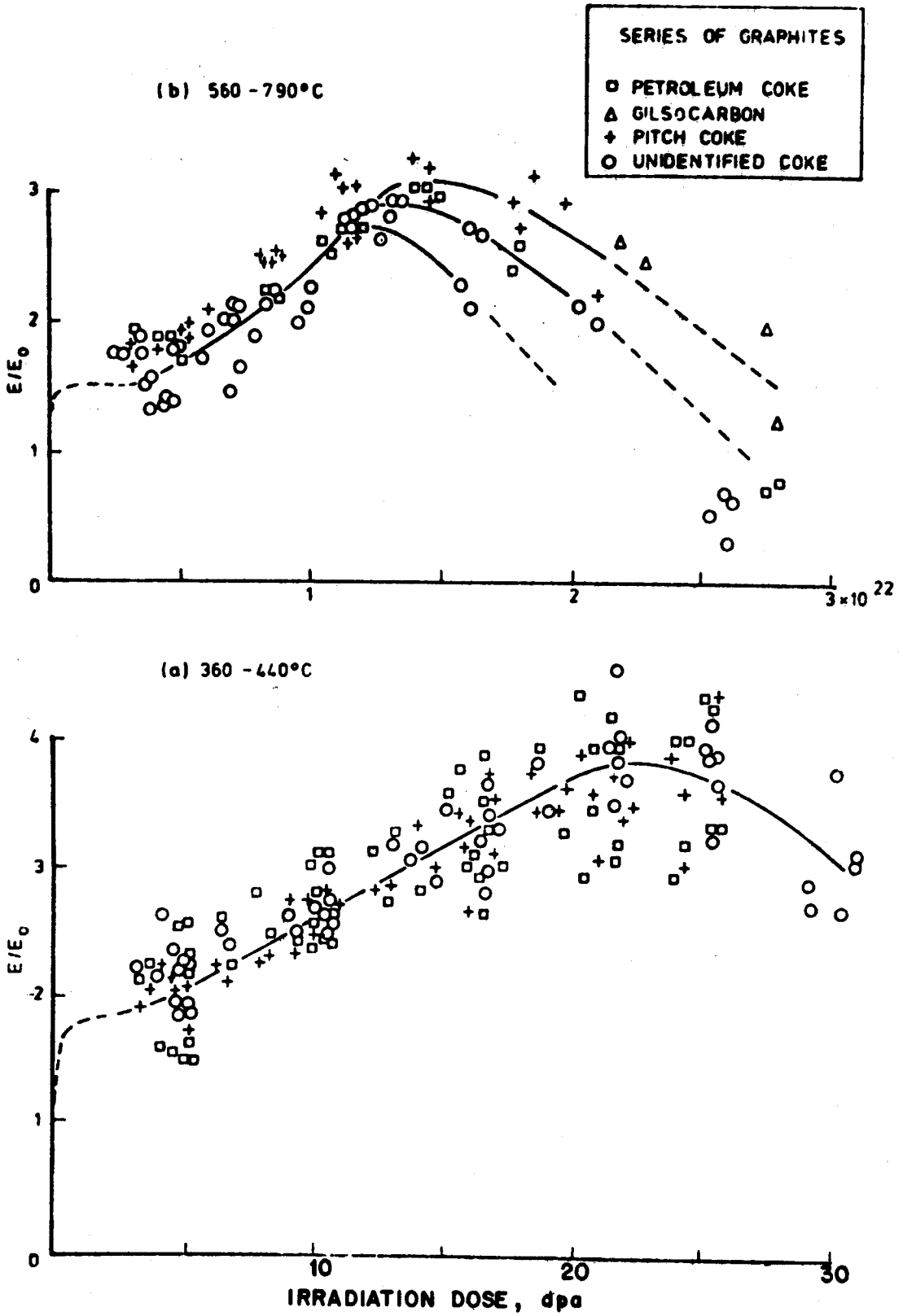

Fig. XV-A-11 Young's Modulus Changes with Fast-Neutron Dose for Different Near-Isotropic Graphites Irradiated in DFR (a) at Irradiation Temperature from 360 to 440°C and (b) from 560 to 790°C

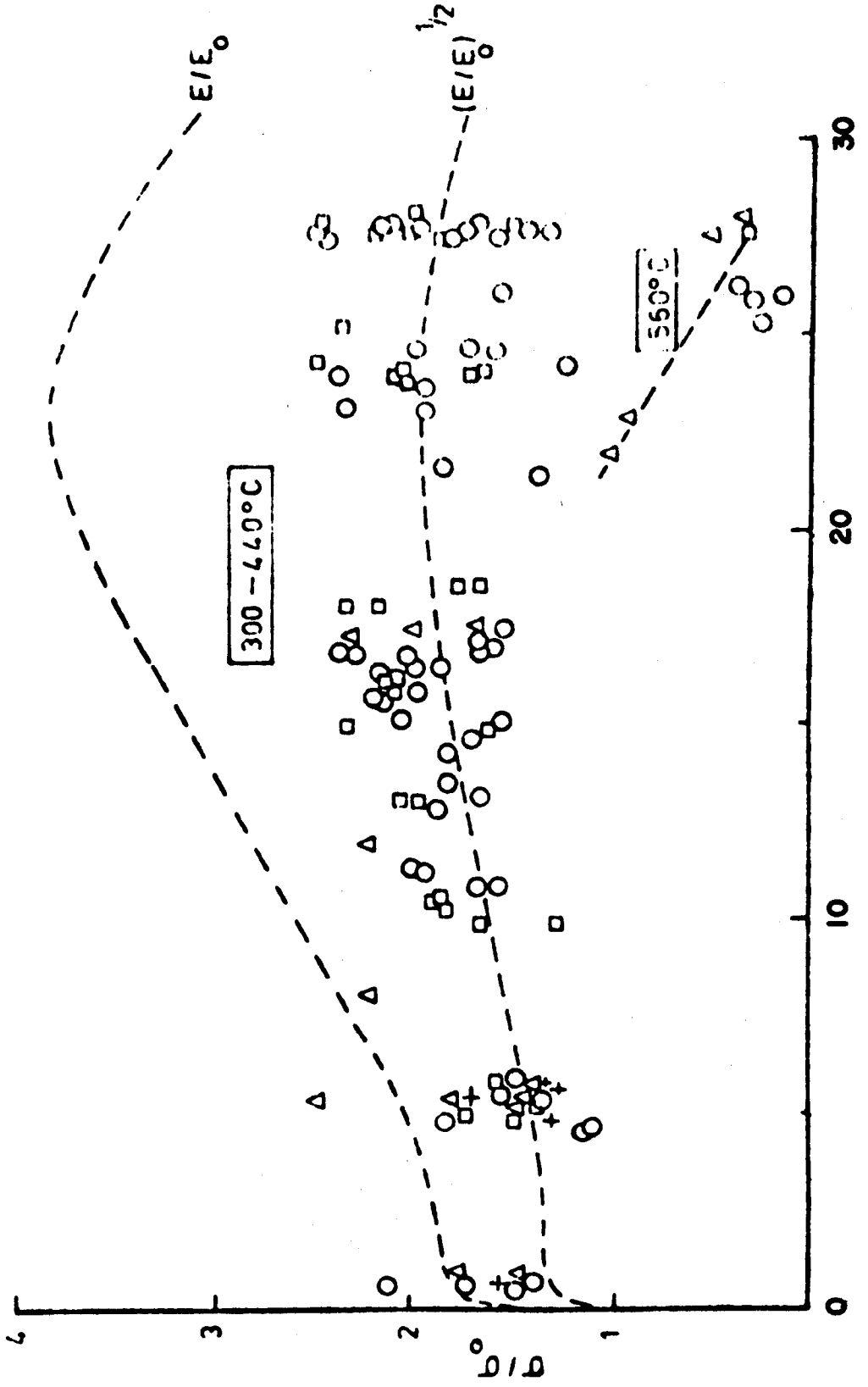

Fig. XV-A-12 Tensile Strength Changes with Fast-Neutron Dose for different Near-Isotropic Graphite Irradiated in DFR at 300 to 400°C and at 560°C.

well as γ are independent of the changes produced by radiation damage, then Eq. (15) reduces to

$$\sigma/\sigma_0 = \sqrt{E/E_0} \tag{16}$$

where σ_0 and E_0 are the tensile stength and elastic modulus, respectively, before irradiation.

By using this relationship (16), the tensile strength can be computed, knowing the elastic modulus. The latter, in turn, can be related to the porosity of the graphite. Although an exact relationship between elastic properties and porosity can only be established if the porosity is characterized in great detail, approximate relationships have been derived by many authors. These relationships give both upper and lower bounds for the elastic moduli as a function of the volume fraction of the porosity. In our analysis, we have used the results of Christensen,[11] who gives as a lower bound for the shear modulus the expression

$$\frac{G}{G^*} = \left\{1 + \frac{15(1-\nu)(7+5\nu)(p^{7/3}-1)p^{1/3}}{(7-5\nu)(7+5\nu)(1-p)(p^{7/3}-1)+126p(1-p^{2/3})^2}\right\}^{-1} \tag{17}$$

Here, ν is Poisson's ratio, G^* the shear modulus of the theoretically dense material, and p is the volume fraction of the pores, i.e. $p = P/100$. In order to compute a lower bound for E/E^*, it would be necessary to utilize the lower bound for the ratio K/K^* for the bulk modulus, which was also given by Christensen.[11] However, since G is much more affected by the porosity than K, we use the approximation

$$\frac{E}{E^*} \cong \frac{G}{G^*} ,$$

and we replace the relationship in Eq. (16) by

$$\frac{\sigma}{\sigma_o} \cong \sqrt{\frac{G}{G_o}} = \sqrt{\frac{G}{G^*}\frac{G^*}{G_o}} , \tag{18}$$

where G_o/G^* is given by Eq. (17) for $p = P_o/100$. The degradation of the tensile strength of graphite can now be computed with the help of Eqs. (18), (17), and Eq. (3).

XV-A-5. Fatigue Strength of Graphite

When graphite is subjected to alternating loads, fatigue fracture occurs at stress levels below the static strength of the material. In general, the lower the stress amplitude produced by the alternating load, the greater is the number of load cycles the material can endure before fracture.

Due to the heterogeneous structure of graphite, static as well as fatigue strengths show large statistical variations from sample to sample. As an example, Fig. XV-A-13 shows[10] the data for tensile fatigue (i.e. the alternating stress varies between zero and $\sigma_a > 0$). The data points represent the homologous stress $s_h = \sigma_a/\bar{\sigma}_s$, where $\bar{\sigma}_s$ is the average value of the static tensile strength. A substantial reduction of the data scatter can be achieved if the homologous stress is defined as $\sigma_h = \sigma_a/\sigma_s$, where σ_s is now a statistically defined value of the fracture strength during the first cycle which is analyzed according to a Weibull distribution.

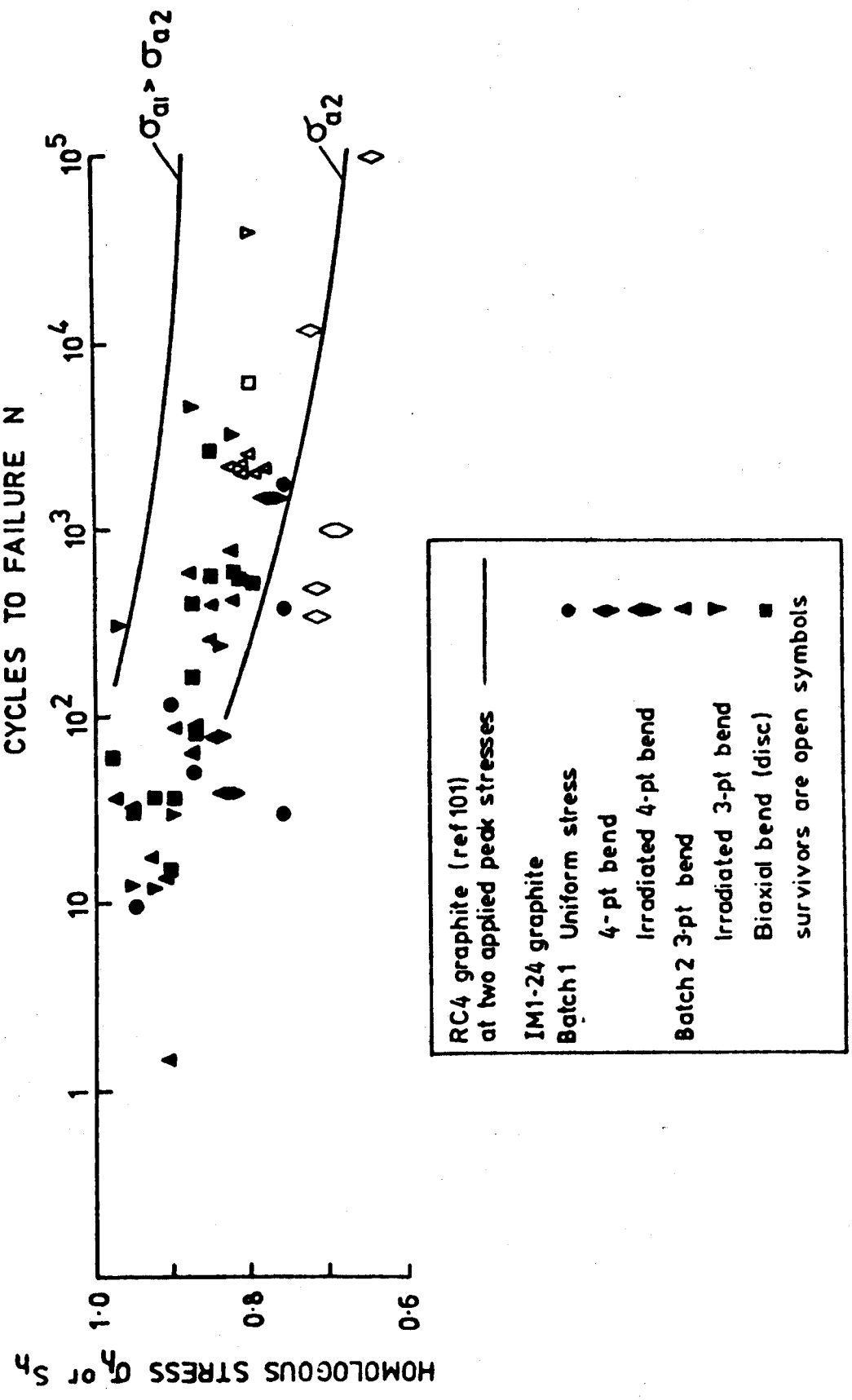

Fig. XV-A-13 Fatigue Endurance Data for Various Graphites under Tensile Fatigue Loading

Fatigue curves based on σ_h are shown in Fig. XV-A-13 as solid curves.

Regardless of the definition of the homologous stress, however, it is seen that a long fatigue life can be obtained if the stress amplitude does not exceed 65% of the static strength.

It is necessary to modify this rule somewhat since the fatigue life depends also on the mean stress. This is demonstrated by Fig. XV-A-14 which shows the fatigue curves for a mean stress of $\sigma_a/2$ (tensile fatigue) and for zero mean stress (loading between $+\sigma_a/2$ and $-\sigma_a/2$). Accordingly, it appears to be prudent to adopt the conservative rule that the tensile stress level for fatigue loading should not exceed one-half of the static tensile strength. This rule has been employed in the following stress analysis of the blanket structure as a design criterion.

XV-B. Stress and Failure Analysis of the Blanket

XV-B-1. Procedure for Lifetime Analysis

A lifetime analysis of the blanket structure was carried out according to the following guidelines, illustrated by the flow-diagram in Fig. XV-B-1.

The central criterion for determining the lifetime was that the stress at any location in the blanket structure must be lower than one-half of the tensile strength at that location. This must be true for the stress distribution during reactor operation as well as during a shutdown.

To implement this procedure, it is necessary to first specify the boundary conditions and the distribution of temperature and atomic displacement rates. Next, the thermal stress distribution is computed, and

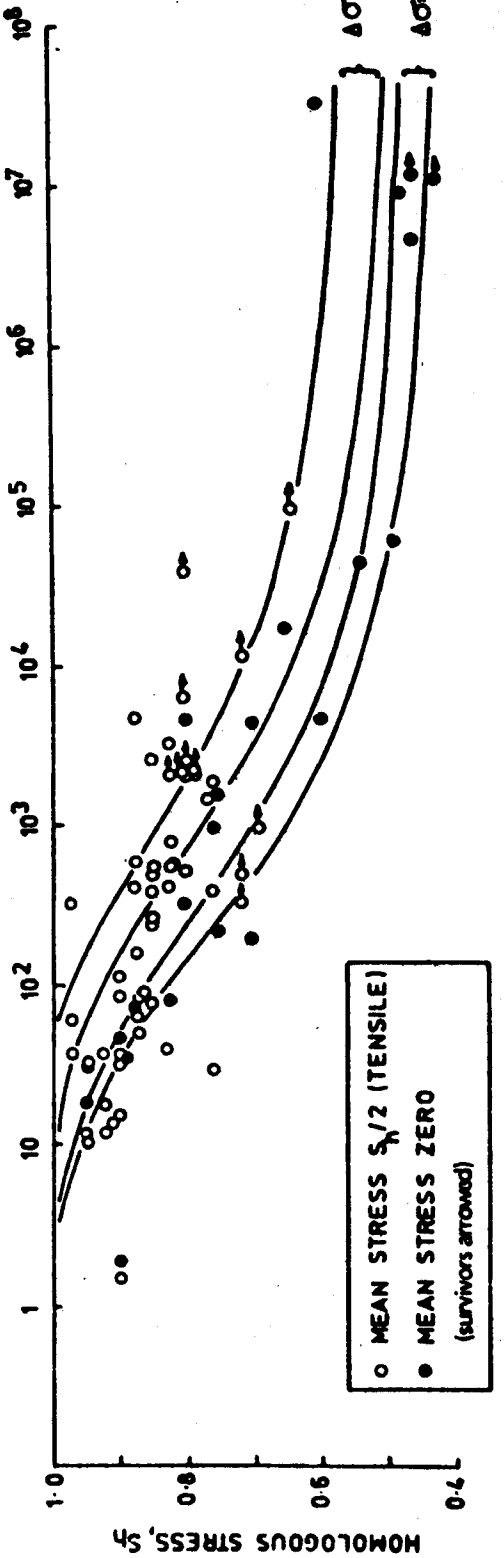

Fig. XV-A-14 Comparison of Fatigue Endurance Data for Tensile Fatigue (open symbols) and for Fatigue with zero mean stress (solid symbols)

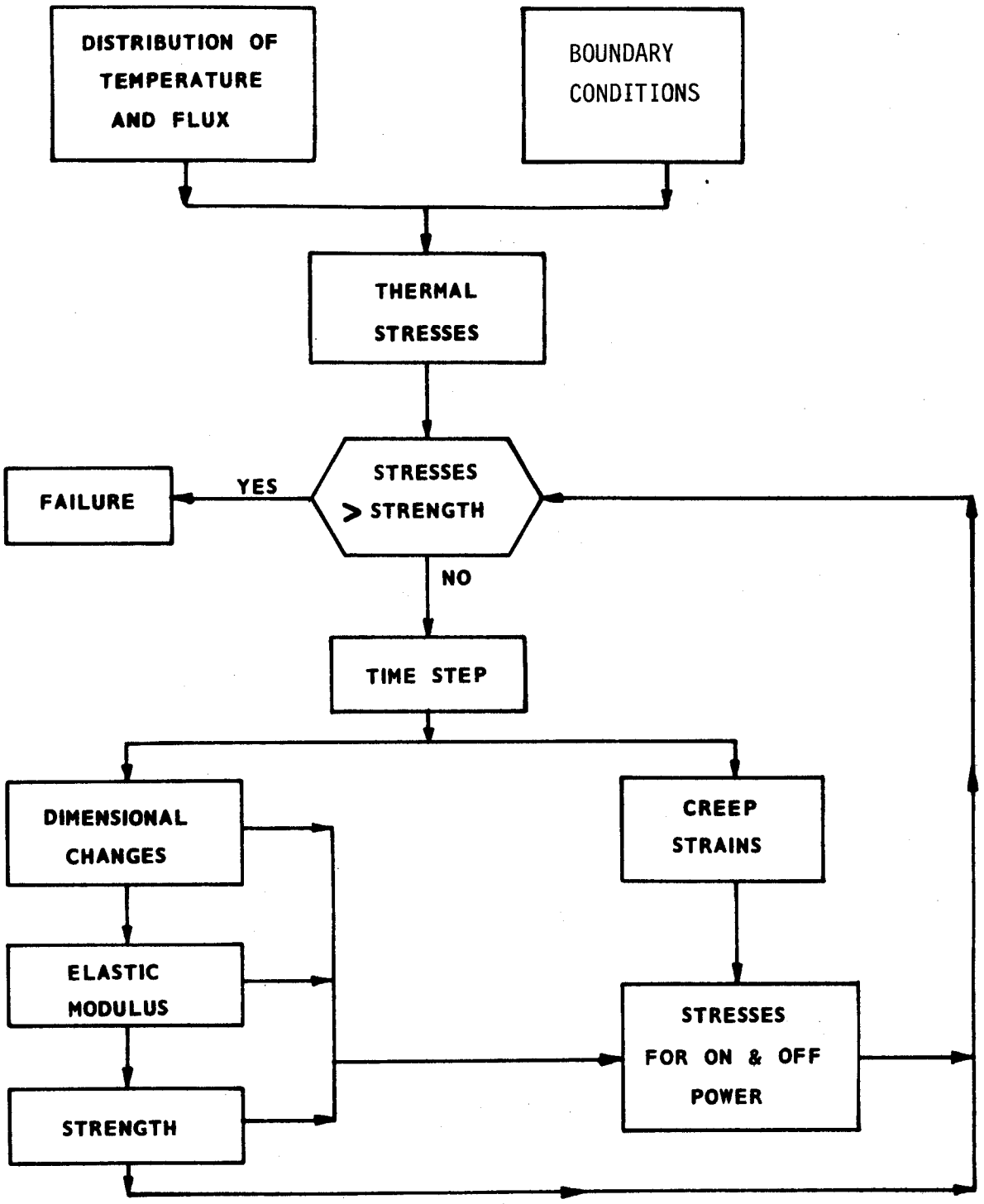

Fig. XV-B-1 Flow Diagram for the Lifetime Analysis Code

it is tested whether the strength is exceeded. Then, for a short time step, the change of the porosity, elastic modulus, and static strength is calculated. In addition, the irradiation creep strains are computed for this time interval, and the new stress distributions for on and off power are evaluated. Comparison between stresses and strength is made again. This cycle is repeated until the failure criterion is satisfied at some location in the blanket structure.

This procedure represents a general, self-consistent approach to the determination of the lifetime of fusion reactor components. However, to carry it out in detail would have required an inelastic finite-element analysis which was judged to be beyond the scope of this design study. Therefore, we selected a part of the blanket structure for the analysis which is subject to the largest temperature and neutron flux gradients. Clearly, this part is one of the radial dividers in a blanket module. To further simplify the analysis the radial divider was modelled as a thin, annular disk as illustrated in Fig. XV-B-2. This simulated in an approximate fashion the circumferential constraints imposed on the blanket sections when they are connected to form the entire reactor cavity.

XV-B-2. Inelastic Stress Analysis

In this section, we describe briefly the inelastic analysis of the blanket radial divider modelled as an annular disk.[12] The reader interested only in the final results may wish to proceed to the next section.

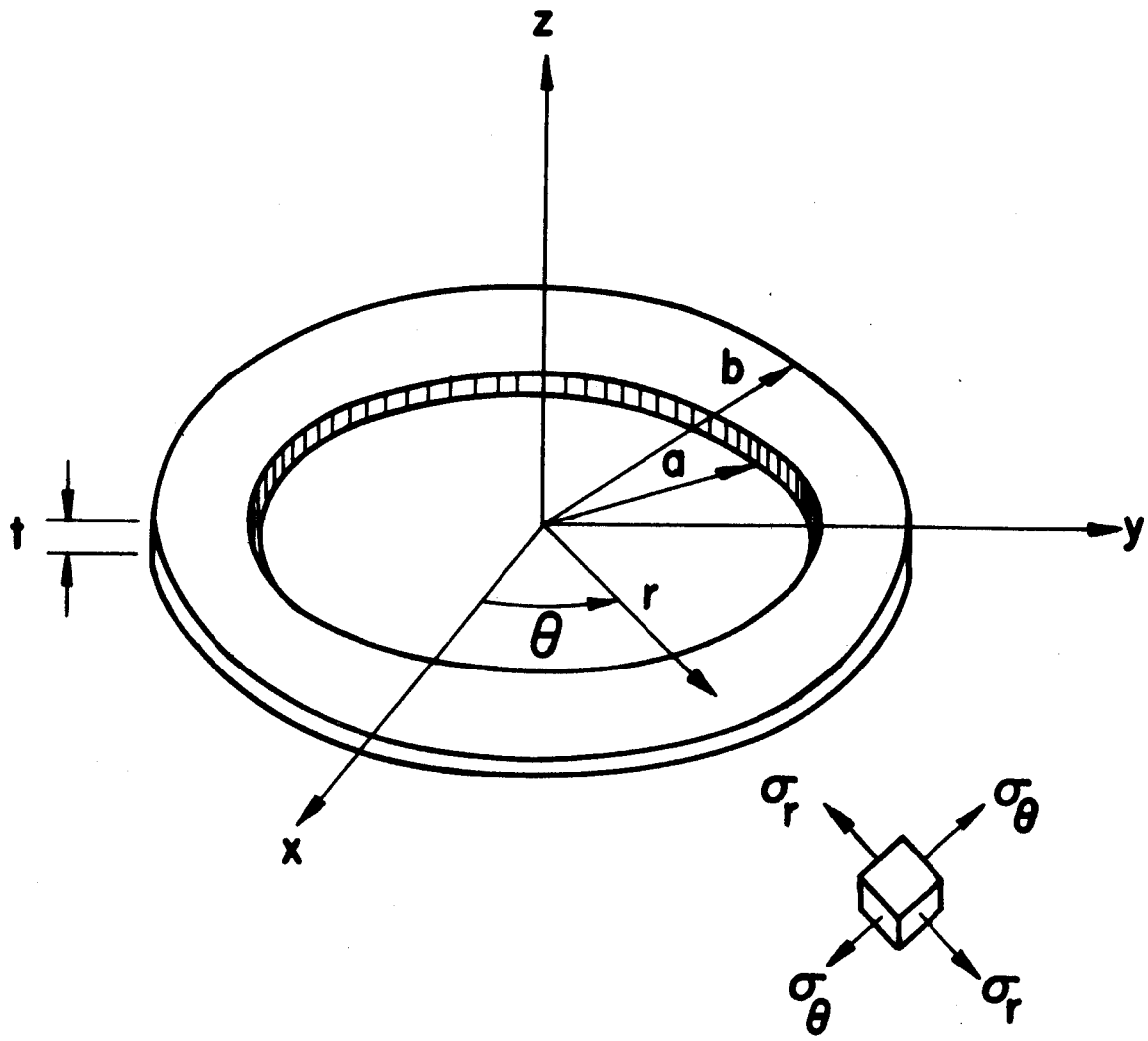

a = 6.0 meters
b = 6.6 meters
t = 0.64 centimeters

Fig. XV-B-2 Blanket Radial Divider Modelled as an Annular Disk, and Loaded in Plane Stress

If we neglect the circumferential variation of the temperature, i.e. assume axial symmetry, then the radial stress, σ_r, and the hoop stress, σ_θ, satisfy the equilibrium equation[12]

$$\frac{d\sigma_r}{dr} + \frac{\sigma_r - \sigma_\theta}{r} = 0 \tag{19}$$

The stress component normal to the disk can be neglected, i.e. $\sigma_z = 0$. If ε denotes a total and e an inelastic strain component, then Hooke's law is given by

$$\sigma_r = \frac{E}{1-\nu^2} \{(\varepsilon_r - e_r) + \nu (\varepsilon_\theta - e_\theta)\} \tag{20}$$

$$\sigma_\theta = \frac{E}{1-\nu^2} \{(\varepsilon_\theta - e_\theta) + \nu (\varepsilon_r - e_r)\} \tag{21}$$

The total strain components can be derived from a radial displacement function u(r) according to

$$\varepsilon_r = \frac{du}{dr}, \quad \varepsilon_\theta = \frac{u}{r} \tag{22}$$

If these equations are used in Eqs. (20) and (21), then Eq. (19) gives

$$\frac{d}{dr}\left(\frac{1}{r}\frac{d(ru)}{dr}\right) = \frac{d}{dr}(e_r + \nu e_\theta) + (1 - \nu)\frac{(e_r - e_\theta)}{r} \tag{23}$$

Integrating this equation twice we obtain after some manipulation the result

$$u(r) = \frac{1}{2} C_1 r + \frac{C_2}{r} + \frac{(1+\nu)}{2r} A(r) + \frac{(1-\nu)}{2} rB(r) \tag{24}$$

where

$$A(r) = \int_a^r r'dr' \ (e_r + e_\theta) \tag{25}$$

$$B(r) = \int_a^r \frac{dr'}{r'} \ (e_r - e_\theta) \tag{26}$$

The constants C_1 and C_2 must be determined from the boundary conditions. On the inner boundary, at r = a = 6 meters,

$$\sigma_r(a) = 0 \tag{27}$$

From Eqs. (24), (22), (20), and (21) one can derive the following expressions:

$$\frac{\sigma_r}{E} = \frac{C_1}{2(1-\nu)} - \frac{C_2}{(1+\nu)r^2} - \frac{A(r)}{2r^2} + \frac{1}{2} B(r) \tag{28}$$

$$\frac{\sigma_\theta}{E} = \frac{C_1}{2(1-\nu)} + \frac{C_2}{(1+\nu)r^2} + \frac{A(r)}{2r^2} + \frac{1}{2} B(r) - e_\theta \tag{29}$$

Hence, $\sigma_r(a) = 0$ implies that

$$\frac{C_1}{2(1-\nu)} = \frac{C_2}{(1+\nu)a^2} = C$$

and

$$\frac{\sigma_r}{E} = C \left(1 - \frac{a^2}{r^2}\right) - \frac{A(r)}{2r^2} + \frac{1}{2} B(r) \tag{30}$$

$$\frac{\sigma_\theta}{E} = C\left(1 + \frac{a^2}{r^2}\right) + \frac{A(r)}{2r^2} + \frac{1}{2}B(r) = e_\theta \tag{31}$$

For the condition at the outer boundary, namely at r = b = 6.6 m, we can consider either a stress-free situation, i.e.

$$\sigma_r(b) = 0$$

or a rigid constraint, i.e.

$$u(b) = 0$$

For the stress-free case,

$$C = \frac{A(b)}{2(b^2-a^2)} - \frac{b^2B(b)}{2(b^2-a^2)} \tag{32}$$

and for the rigid boundary,

$$C = \frac{-(1+\nu)A(b)+(1-\nu)b^2B(b)}{2[(1-\nu)b^2+(1+\nu)a^2]} \tag{33}$$

If the inelastic strains e_r and e_θ are known, the functions A(r) and B(r) can be computed, C be determined from either Eq. (32) or (33), and the stresses can then be found from Eqs. (30) and (31). For the initial thermal stresses, $e_r = e_\theta = \alpha(r)T(r)$ where α is the linear thermal expansion coefficient. To compute the time dependence of the stresses as a consequence of irradiation creep we differentiate Eqs. (30) and (31) with respect to time, holding a and b constant. The differentiation of A(r)

and B(r) results in the appearance of the inelastic strain rates $\dot{e}_r$ and $\dot{e}_\theta$. For isotropic graphite these strain rates are given by

$$\frac{de_r}{dt} = \dot{e}_r = \frac{1}{3}\dot{P} + (KE\dot{F})\left[\sigma_r - \frac{1}{2}\sigma_\theta\right]\frac{1}{E} \tag{34}$$

$$\frac{de_\theta}{dt} = \dot{e}_\theta = \frac{1}{3}\dot{P} + (KE\dot{F})\left[\sigma_\theta - \frac{1}{2}\sigma_r\right]\frac{1}{E} \tag{35}$$

where $\dot{P}$ can be obtained from Eq. (3). The irradiation creep coefficient KE is given by Eq. (14). Substituting these equations into the expressions for $\dot{A}$ and $\dot{B}$ we obtain

$$\dot{A}(r) = \frac{2}{3}\int_a^r r dr \dot{P} + \frac{1}{2}\int_a^r r dr\, KE\dot{F}\left(\frac{\sigma_r}{E} + \frac{\sigma_\theta}{E}\right) \tag{36}$$

$$\dot{B}(r) = \frac{3}{2}\int_a^r \frac{dr}{r} KE\dot{F}\left(\frac{\sigma_r}{E} - \frac{\sigma_\theta}{E}\right) \tag{37}$$

The rate of change for the stresses is given by

$$\frac{d}{dt}\left(\frac{\sigma_r}{E}\right) = \dot{C}\left(1 - \frac{a^2}{r^2}\right) - \frac{\dot{A}(r)}{2r^2} + \frac{1}{2}\dot{B}(r) \tag{38}$$

$$\frac{d}{dt}\left(\frac{\sigma_\theta}{E}\right) = \dot{C}\left(1 + \frac{a^2}{r^2}\right) + \frac{\dot{A}(r)}{2r^2} + \frac{1}{2}\dot{B}(r) - \frac{1}{3}\dot{P} - KE\dot{F}\left(\frac{\sigma_r}{E} - \frac{\sigma_\theta}{2E}\right) \tag{39}$$

We note that by making the assumption that the irradiation creep constant (KE) is independent of the dose, the changing modulus can be easily accommodated in the stress analysis. In view of the large scatter of the irradiation creep data this assumption is just as good as the original one (namely a constant coefficient KE_o, where E_o is the initial Young's modulus).

The two equations (38) and (39) represents a coupled set of integro-differential equations. The integral expressions for $\dot{A}$ and $\dot{B}$ were evaluated with the trapezoidal rule, and the Eqs. (38) and (39) are then replaced by a set of first order ordinary differential equations for the stresses at the nodal points, r_i. This set of equations was then intregated numerically by using a finite difference scheme with respect to time.

Although the numerical integration as outlined at the beginning of this section is straightforward, it was found that numerical errors accumulated rapidly unless the following corrections were applied after each time step. Integration of the equation (19) yields

$$\int_a^b \sigma_\theta(r)dr = b\sigma_r(b) \tag{40}$$

which is applicable for both free or fixed outer boundary conditions. Because the stresses are computed only at a finite number of points, the corresponding relationship

$$\sum_i \sigma_\theta(r_i)\Delta r_i - b\sigma_r(b) = R \tag{41}$$

will yield equilibrium only when the residual R = 0. It was found that this residual R is quite small for each individual time step, but can accumulate quite rapidly. Therefore, after each time step, the nodal stresses $\sigma_\theta(r_i)$ were corrected by addition of the term R/(b-a). The values for σ_θ and σ_r are forced to satisfy Eq. (40), so that R = 0.

Because of the large strains that accumulate over the entire lifetime, the radial positions, r_i, were corrected after each time step by adding the incremental displacement $\dot{u}(r_i)\Delta t$ of each nodal point to the previous nodal radius r_i. Here, $\dot{u}\Delta t$ was computed with Eq. (24). A finite strain analysis was accomplished in this fashion, and the radial motion of the disk could be followed.

XV-B-3. Results of the Stress Analysis

The inelastic stress analysis was carried out with 14 nodal points, whose position was selected to closely match the temperature profile. Table XV-B-1 lists the location of these nodal points together with the corresponding temperatures and radiation damage rates. It is seen that the temperature drops off precipitously over the first two centimeters and remains essentially constant for the remainder of the divider in the radial direction. The dose rate, on the other hand, decreases more uniformly across the blanket thickness, as illustrated in Fig. XV-B-3.

The computations of all stresses were carried out in the dimensionless units (σ/E_0), where E_0 is the Young's modulus of the unirradiated graphite. For the purpose of representation, however, the nodal stresses and strength are given in units of ksi which were obtained from the dimensionless values by multiplying them with $E_0 = 10^6$ psi. It should be noted that the comparison of strength and stress is independent of the values chosen for E_0.

The other materials parameters that were selected as input data for the computation were Poisson's ratio $\nu = 0.2$ and the linear thermal expansion coefficient of $\alpha = 4 \times 10^{-6}/^{o}K$.

Table XV-B-1

Initial Nodal Points with Corresponding Temperatures and Damage Rates

Nodal Points (m)	Temperature (°C)	Damage Rate (dpa/yr)
6.000	1500	32.50
6.003	1220	32.28
6.006	1050	32.10
6.01	886	31.75
6.02	688	31.00
6.03	625	30.25
6.04	607	29.50
6.06	602	28.00
6.10	600	25.00
6.20	600	17.50
6.30	600	12.00
6.40	600	6.5
6.50	600	3.93
6.60	600	1.35

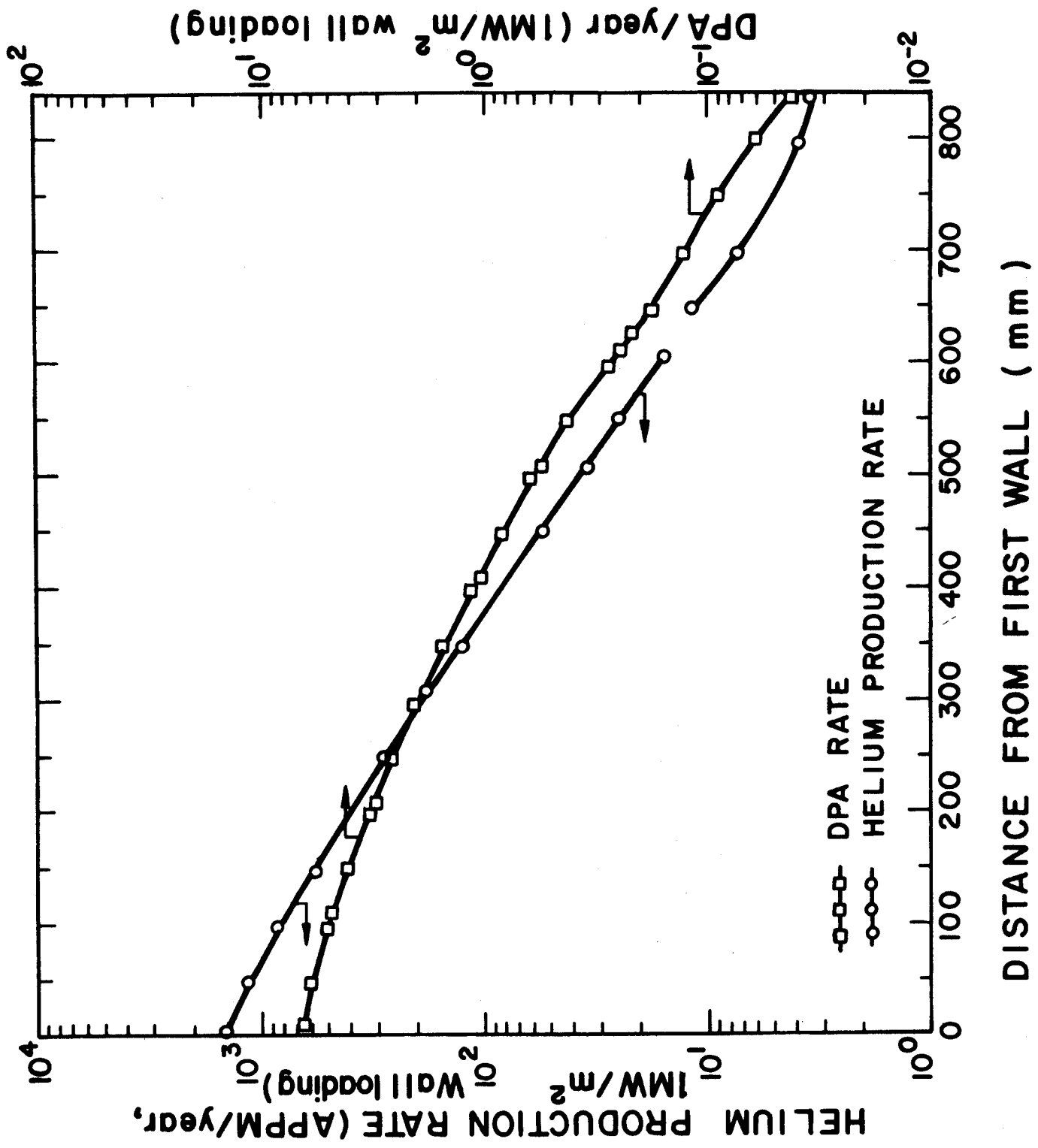

Fig. XV-B-3 Radial Dependence of Displacement Rates and Helium Production Rates in the Blanket Graphite Structure

The sequence of Figs. XV-B-4a to 4i shows the radial distribution of the hoop stress σ_θ for on and off power together with the distribution of one-half of the tensile strength for a graphite with 5% initial porosity.

It was assumed that the densification is described by the nominal case of Eq. (9), and that the final growth rate is the one given by Eq. (8) for low-growth graphites. Furthermore, the stress-free boundary condition was selected for this example. Beginning with Fig. XV-B-4a, the initial thermal stress distribution is shown. Because of irradiation creep, the thermal stresses relax rapidly, as can be seen from Figs. XV-B-4b and 4c. After about a month of operation, densification of the graphite commences where the temperature and neutron flux is high. This gives rise to a small tensile stress on power at the inside of the disk, as seen in Fig. XV-B-4d. Further irradiation leads then to expansion, particularly at the radial location $r \cong 6.01$ m, where the temperature is around $1000^{\circ}C$, the range of maximum expansion. At this location, compressive stresses build up, as seen in Fig. XV-B-4e.

The increase in porosity at this location is reflected in the reduction of the strength. This degradation of the strength becomes more pronounced with irradiation, as illustrated by Figs. XV-B-4f to 4i. It is seen that after about one year of operation the hoop stress for the off-power case approaches the value of 1/2 of the tensile strength near the inner boundary. It is important to emphasize that the analysis presented here shows that the stresses during shutdown are the controlling factor rather than the stresses during operation.

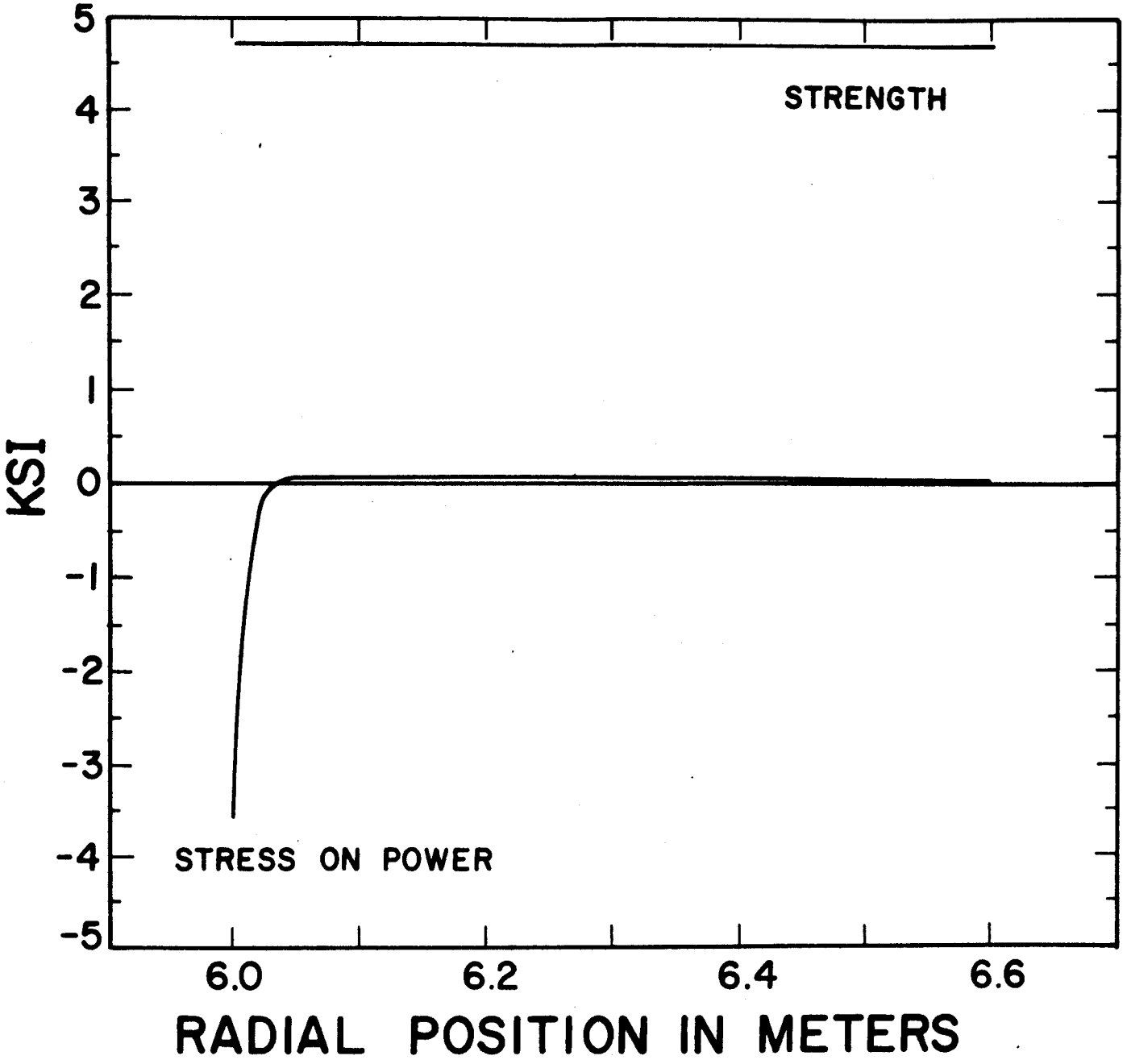

Fig. XV-B-4a Hoop Stress and Tensile Strength Distribution in the Radial Divider made of Low-Growth Graphite with 5% Initial Porosity; After Start-up

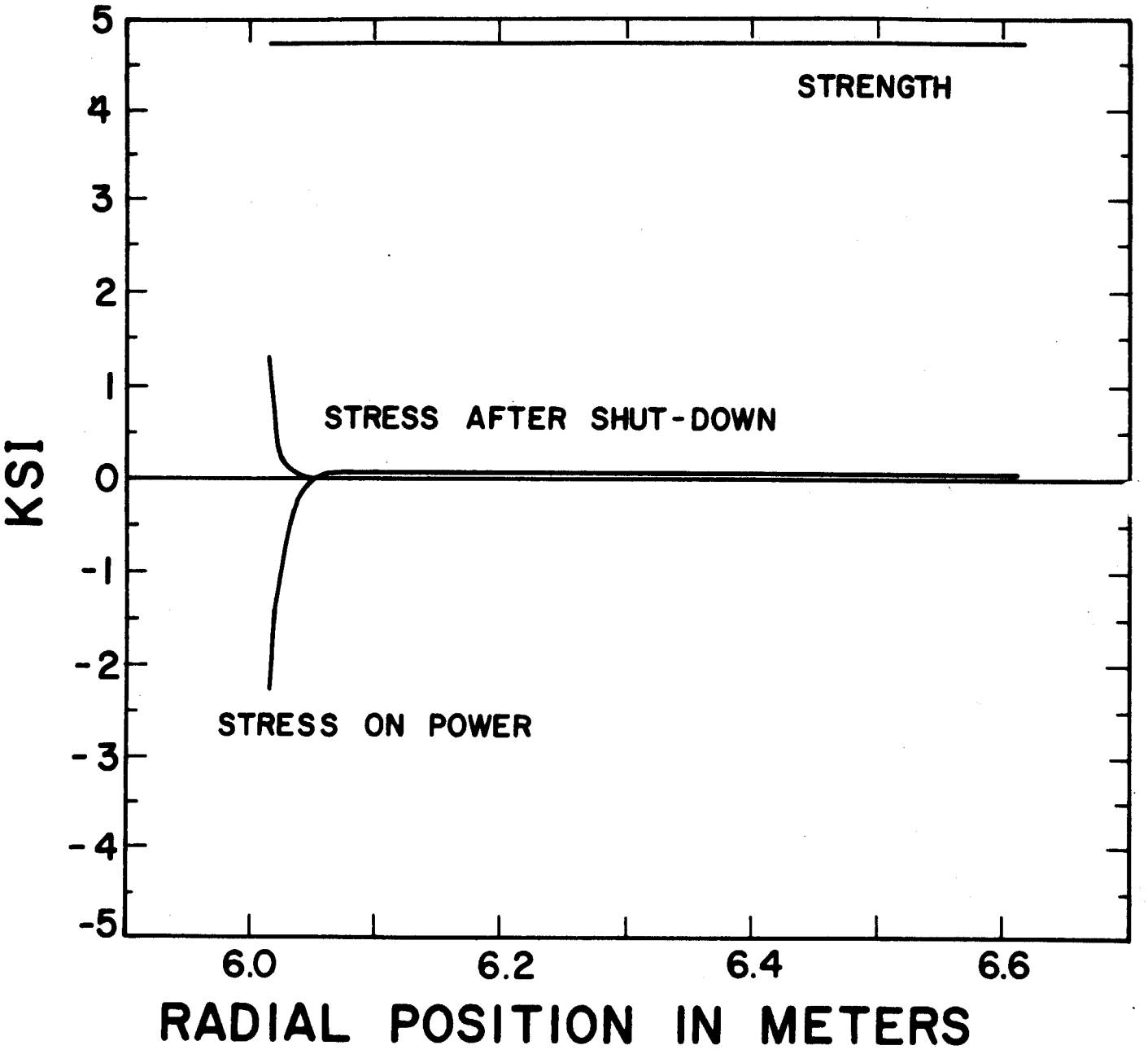

Fig. XV-B-4b After 17.5 Hours of Irradiation

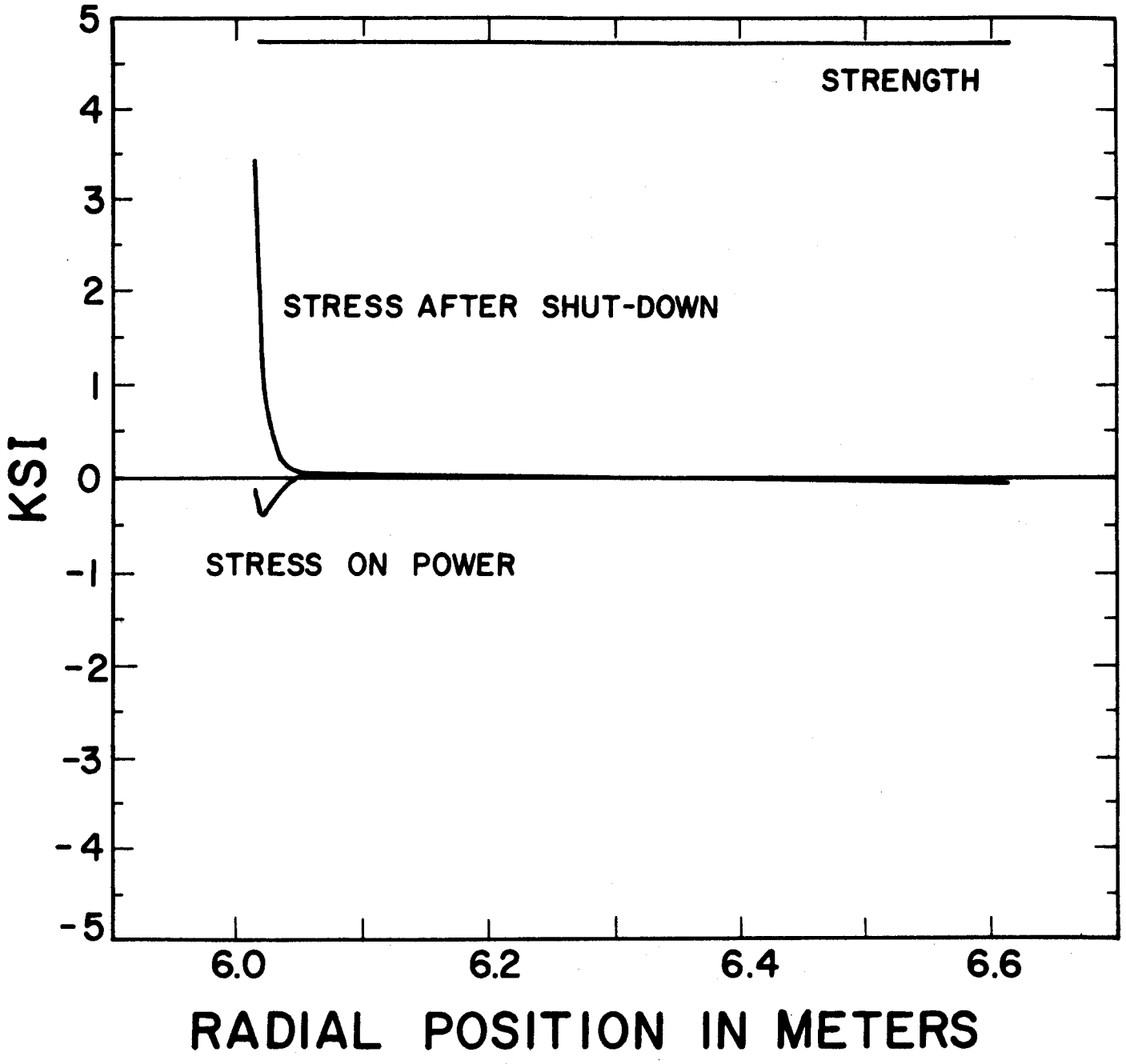

Fig. XV-B-4c After 3.6 Days of Irradiation

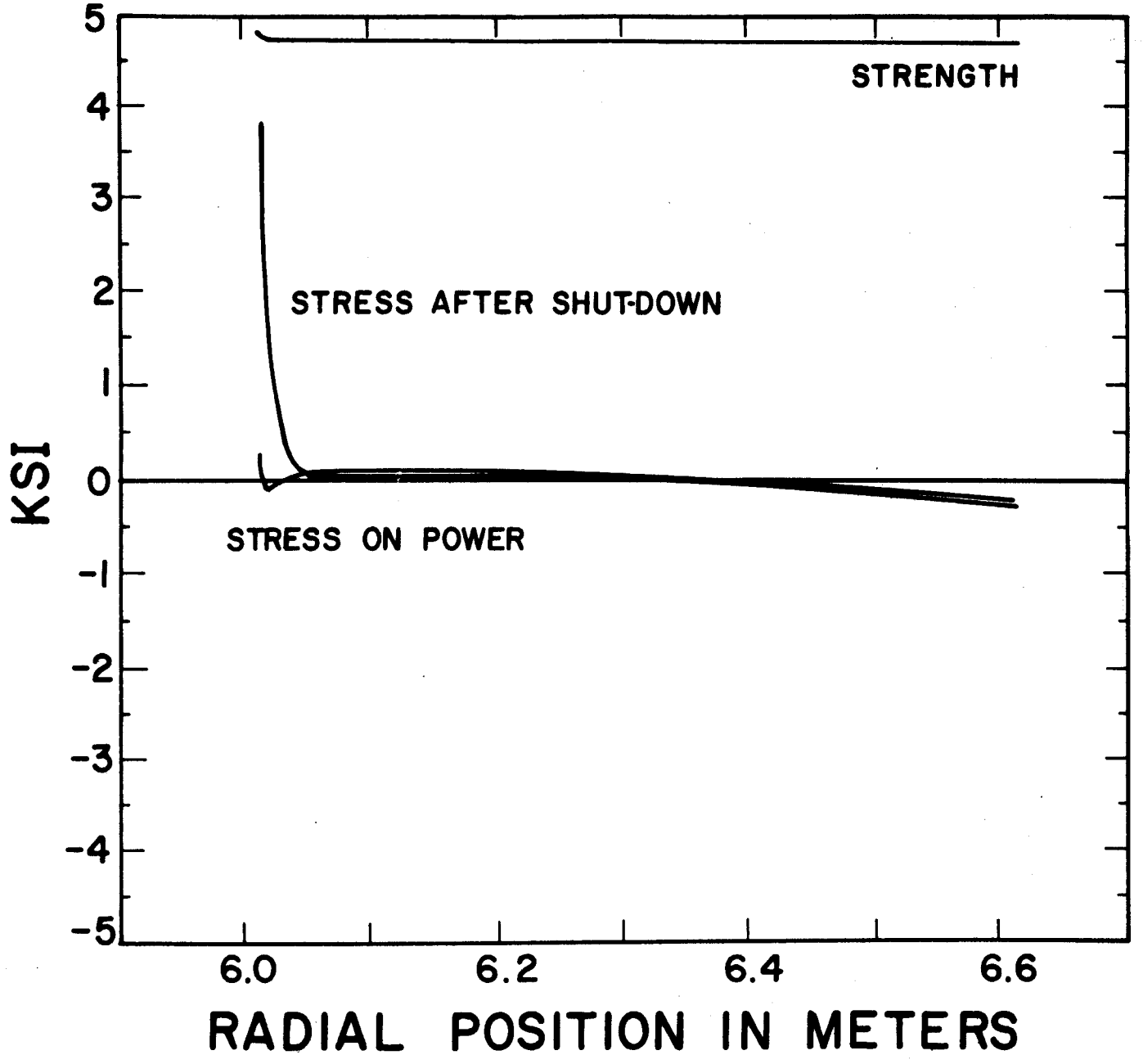

Fig. XV-B-4d After 36.5 Days of Irradiation

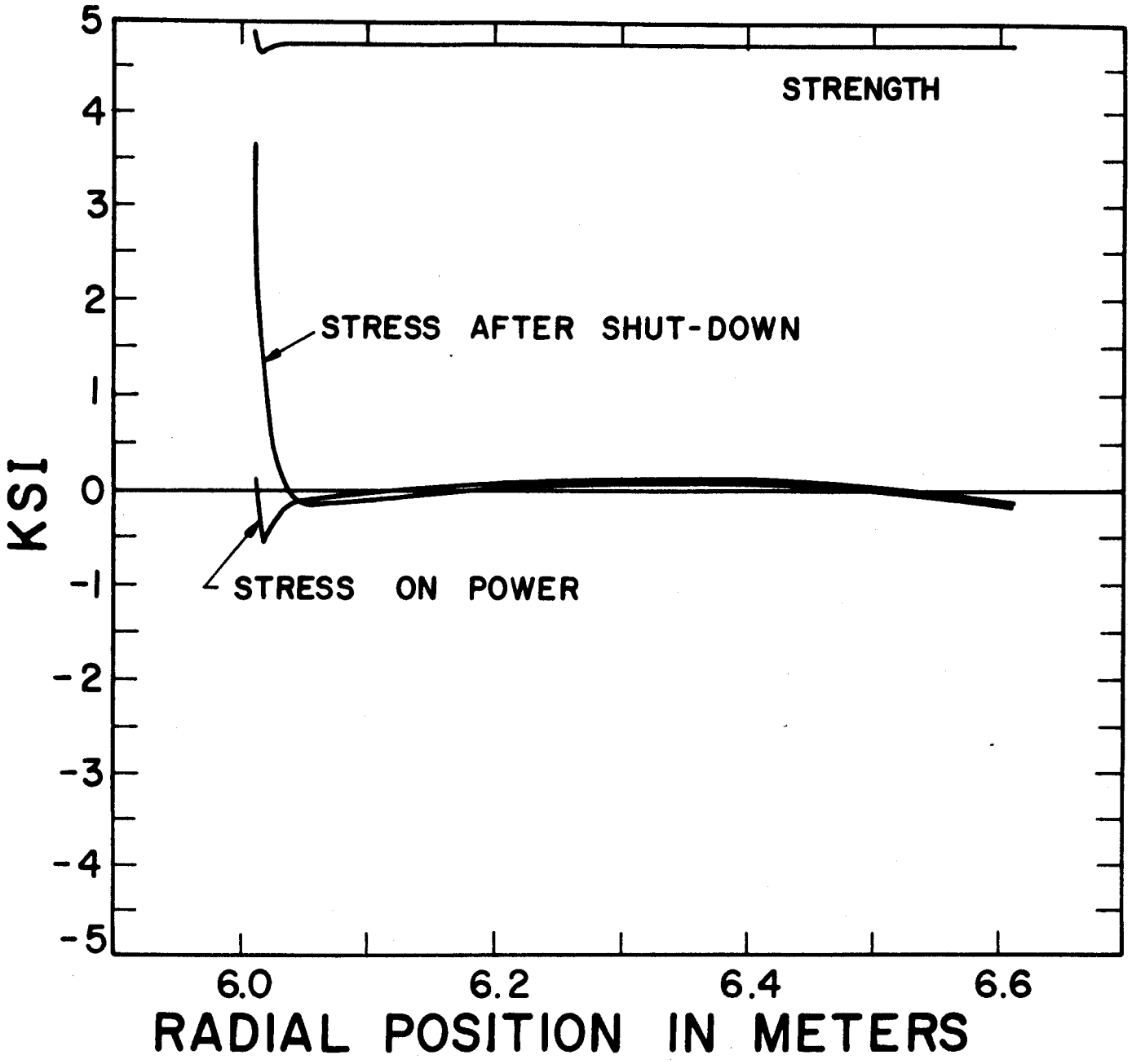

Fig. XV-B-4e After 0.2 Years of Irradiation

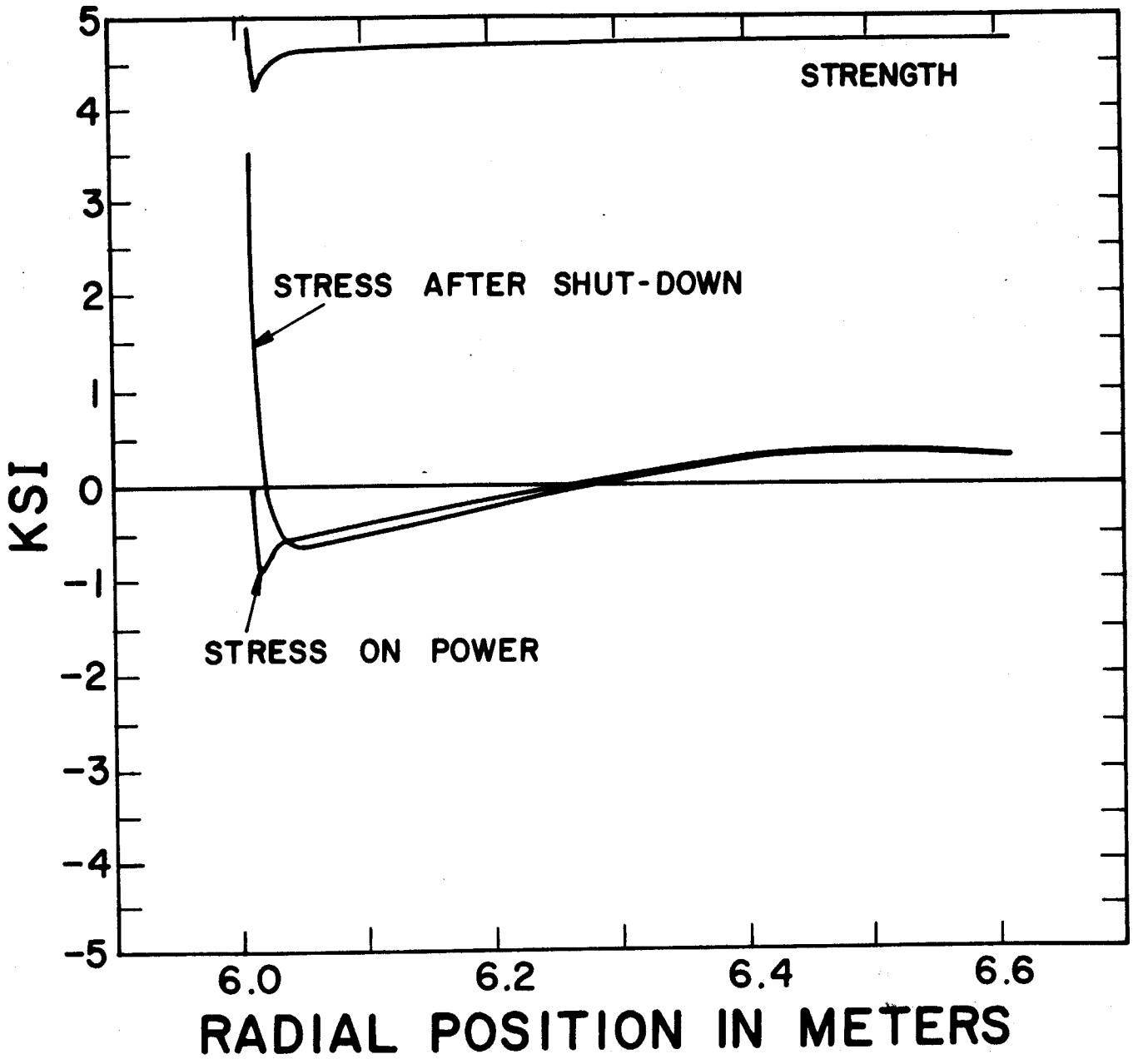

Fig. XV-B-4f After 0.4 Years of Irradiation

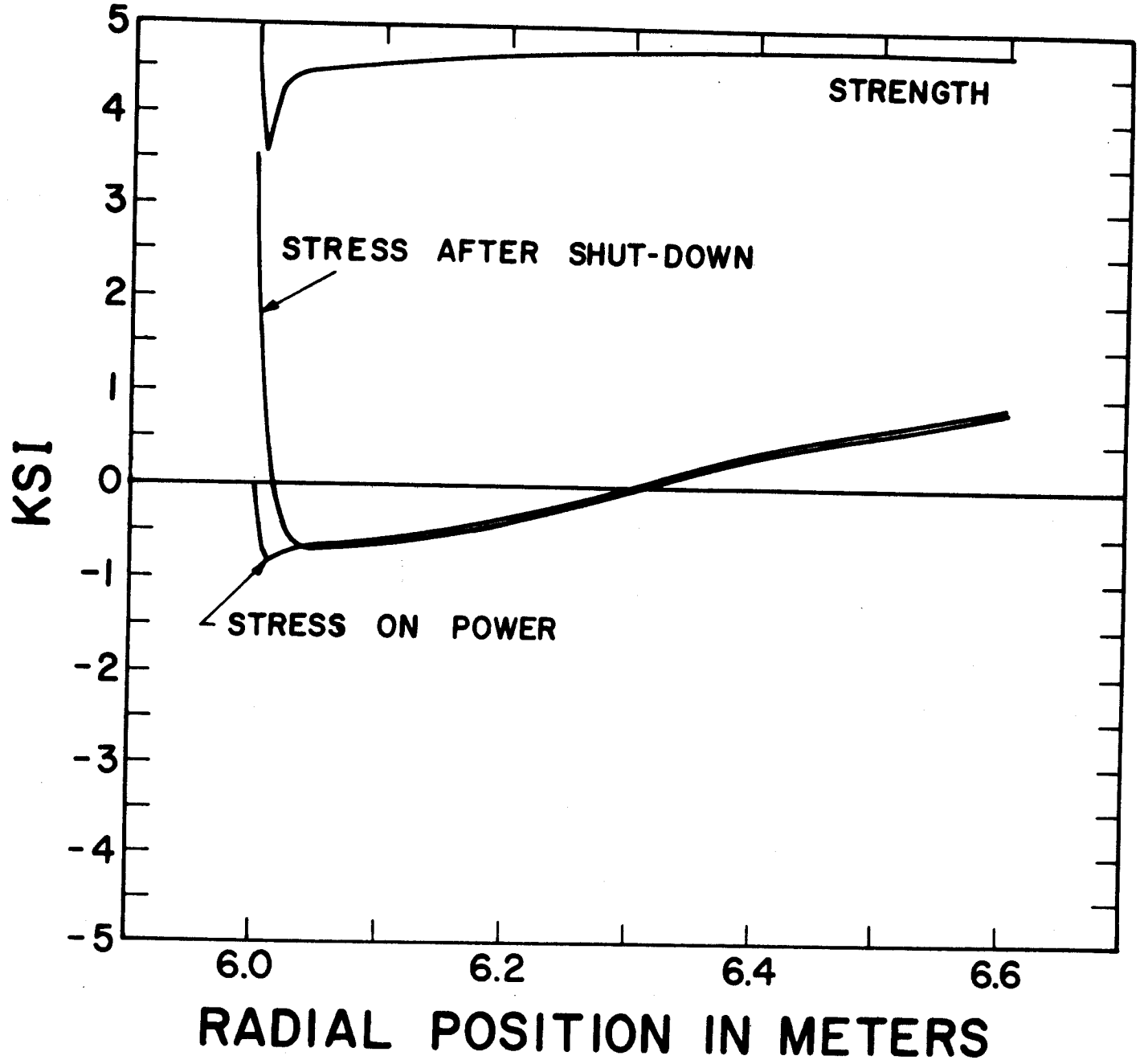

Fig. XV-B-4g After 0.6 Years of Irradiation

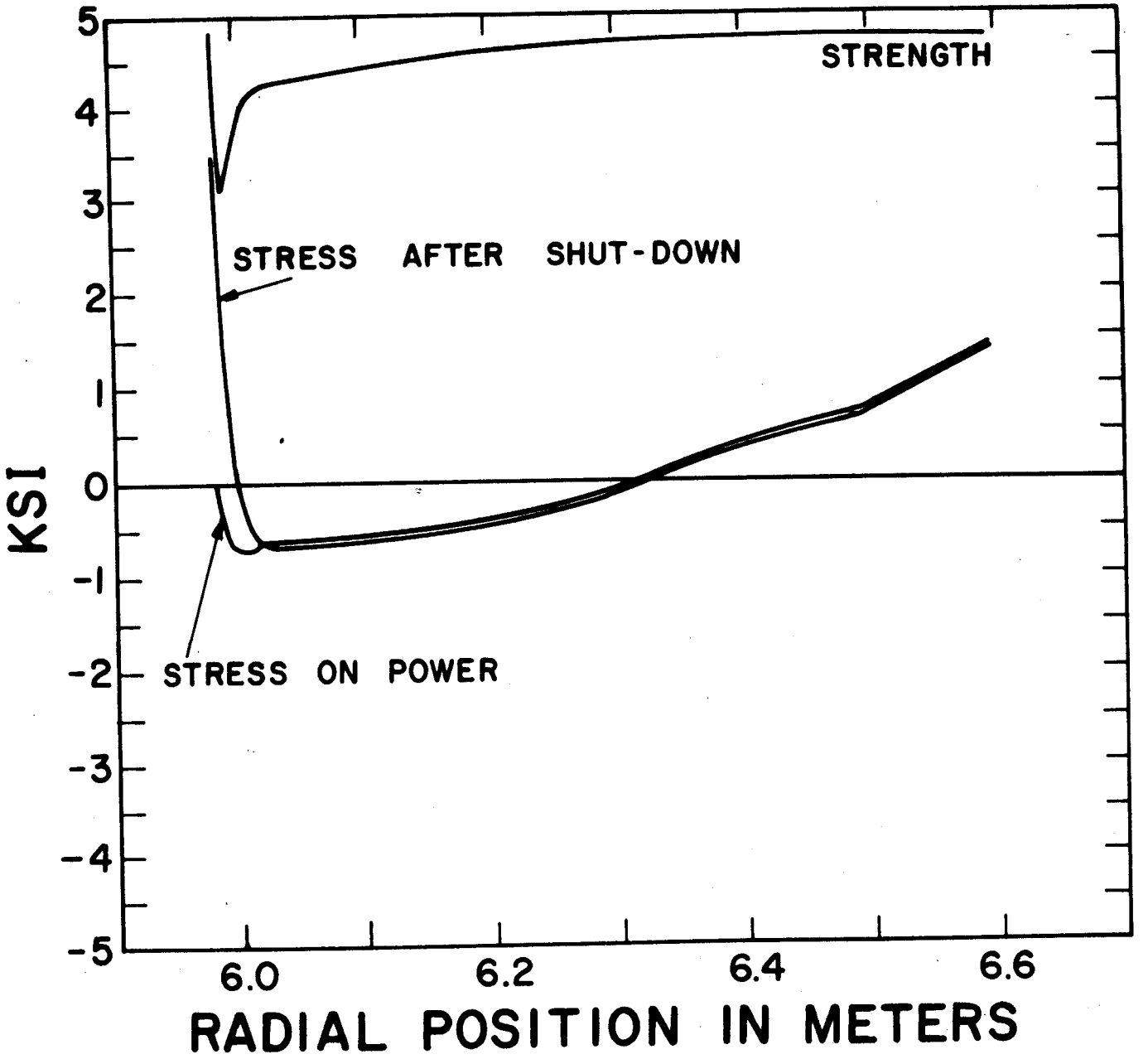

Fig. XV-B-4h After 0.8 Years of Irradiation

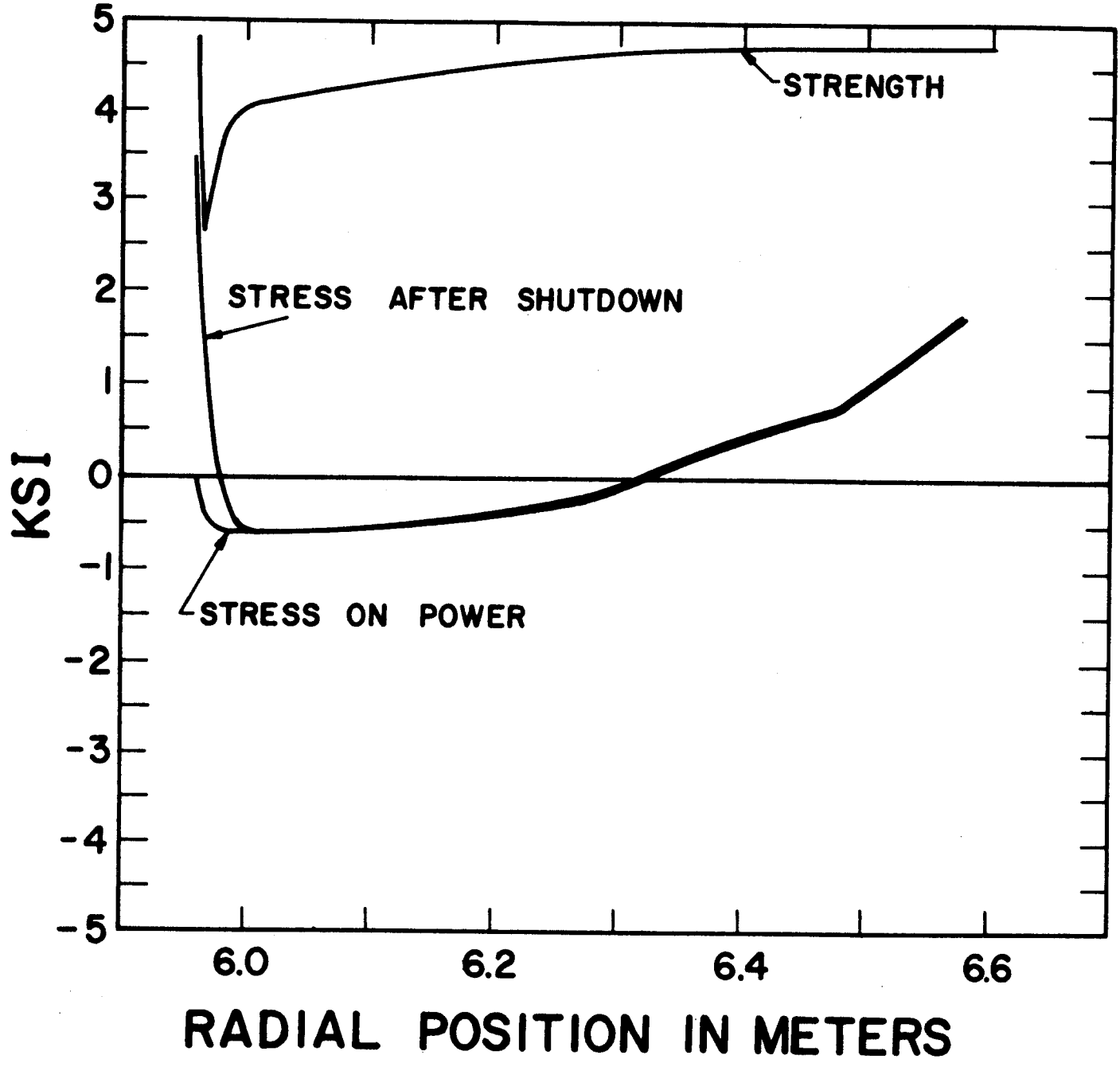

Fig. XV-B-4i After 1.0 Year of Irradiation

The case illustrated by the Figs. XV-B-4a to 4i is for a rather dense graphite with only 5% initial porosity. Present-day nuclear graphites have typically an initial porosity of 20%. For such a graphite material, the stress-distribution upon shutdown exceeds one-half of the strength after a short irradiation period of only 3.6 days. The reason for this situation, illustrated in Fig. XV-B-5a is that thermal stress relaxation and densification have produced a tensile hoop stress on the inner radius of the disk in excess of the safe limit. This problem persists up to an irradiation time of 36.5 days. At this time, the stresses are those shown in Fig. XV-B-5b, and further irradiation removes the problem, as can be seen from Fig. XV-B-5c. After about one year, the hoop stress near the inner boundary of the disk approaches again the value of 1/2 of the tensile strength, as shown in Fig. XV-B-5d.

A similar calculation with a graphite of 10% initial porosity also showed that the stresses on shutdown after 3.6 days exceed the safe limit. However, in this case, the problem persisted only for an irradiation time of about 15 days.

If the computations were made with a dense high-growth graphite whose final volumetric expansion rate is given by Eq. (9), the lifetime was reduced to 0.4 years. Fig. XV-B-6 shows the stress and strength distribution for this case, assuming again a stress-free outer boundary.

Finally, we note that the stress-distribution in a graphite disk with fixed outer boundary, the thermal stresses already reach intolerable values at start-up. Therefore, it is important that the blanket structure is allowed to expand freely.

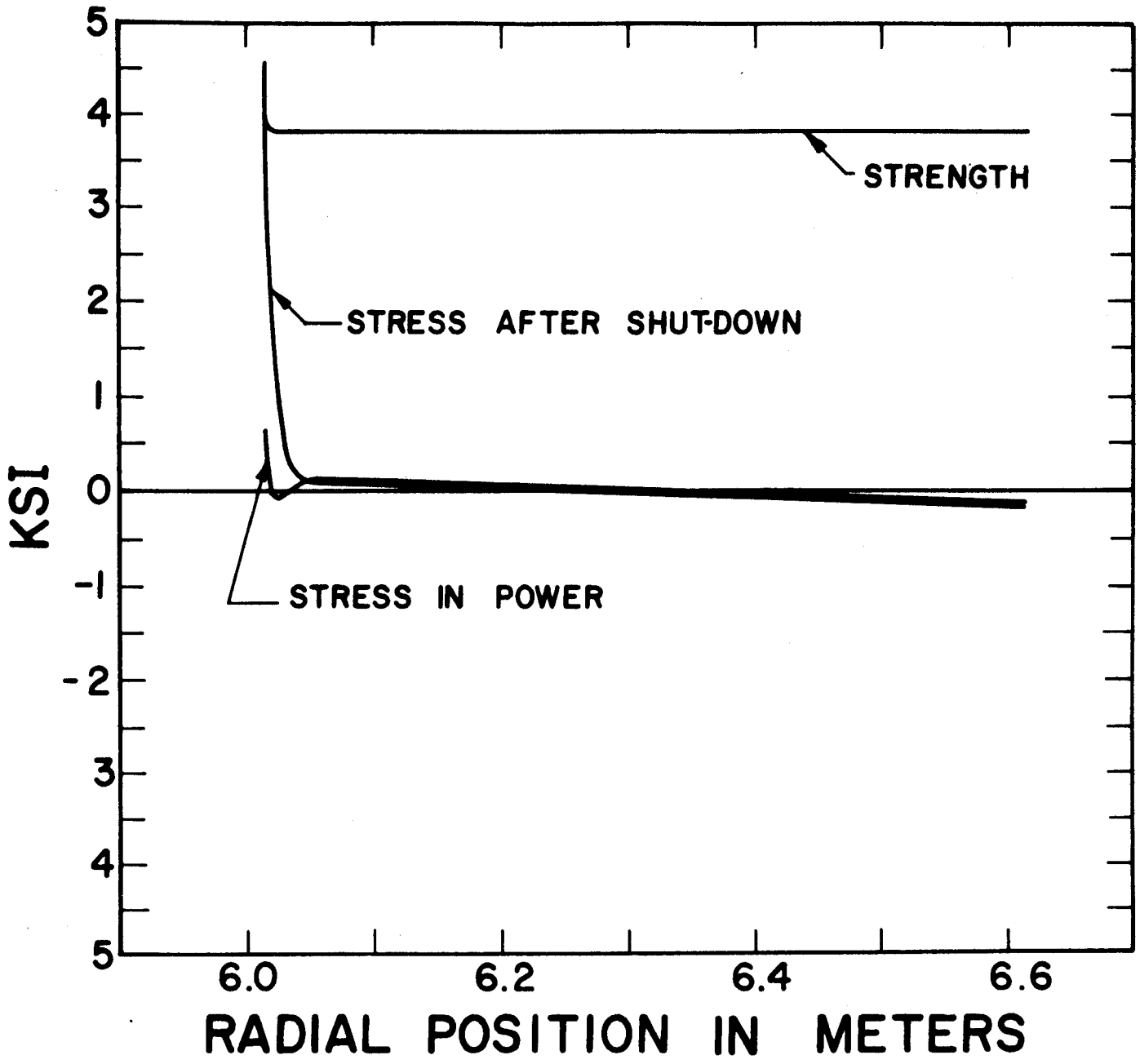

Fig. XV-B-5a Hoop Stress and Tensile Strength Distribution in the Radial Divider made of Low-Growth Graphite with 20% Initial Porosity; After 3.6 Days of Irradiation.

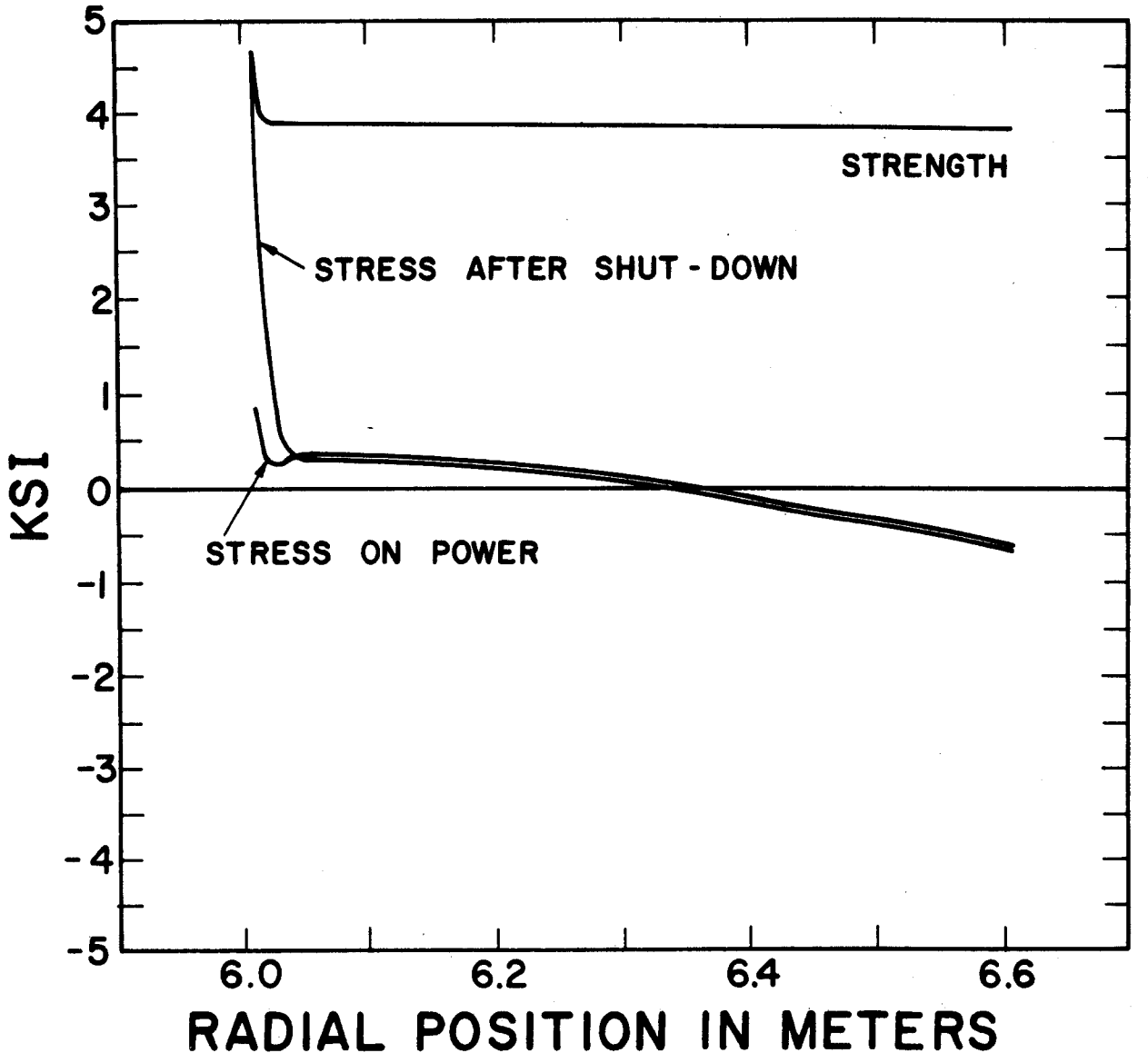

Fig. XV-B-5b After 36.5 Days of Irradiation

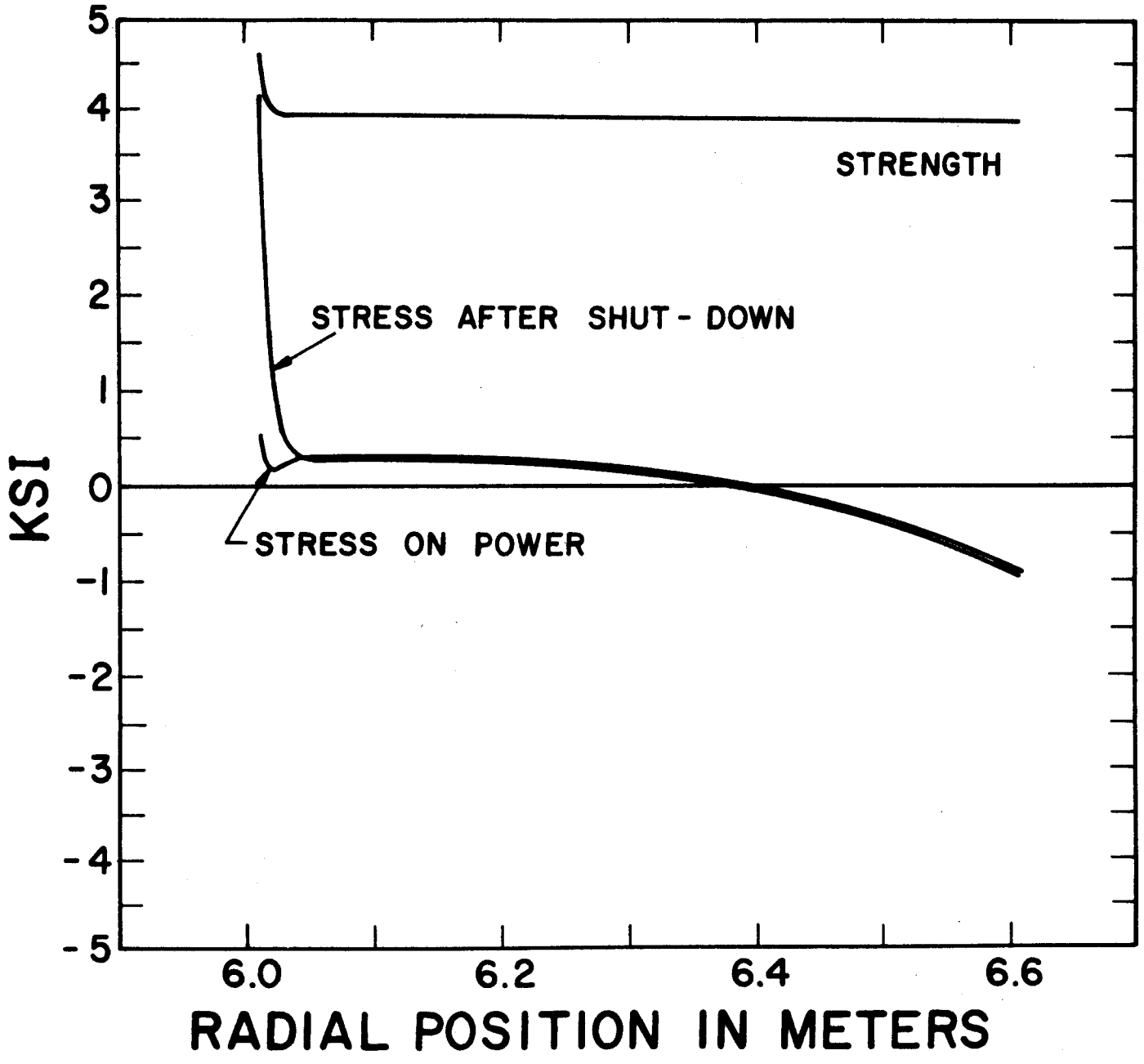

Fig. XV-B-5c After 73 Days of Irradiation

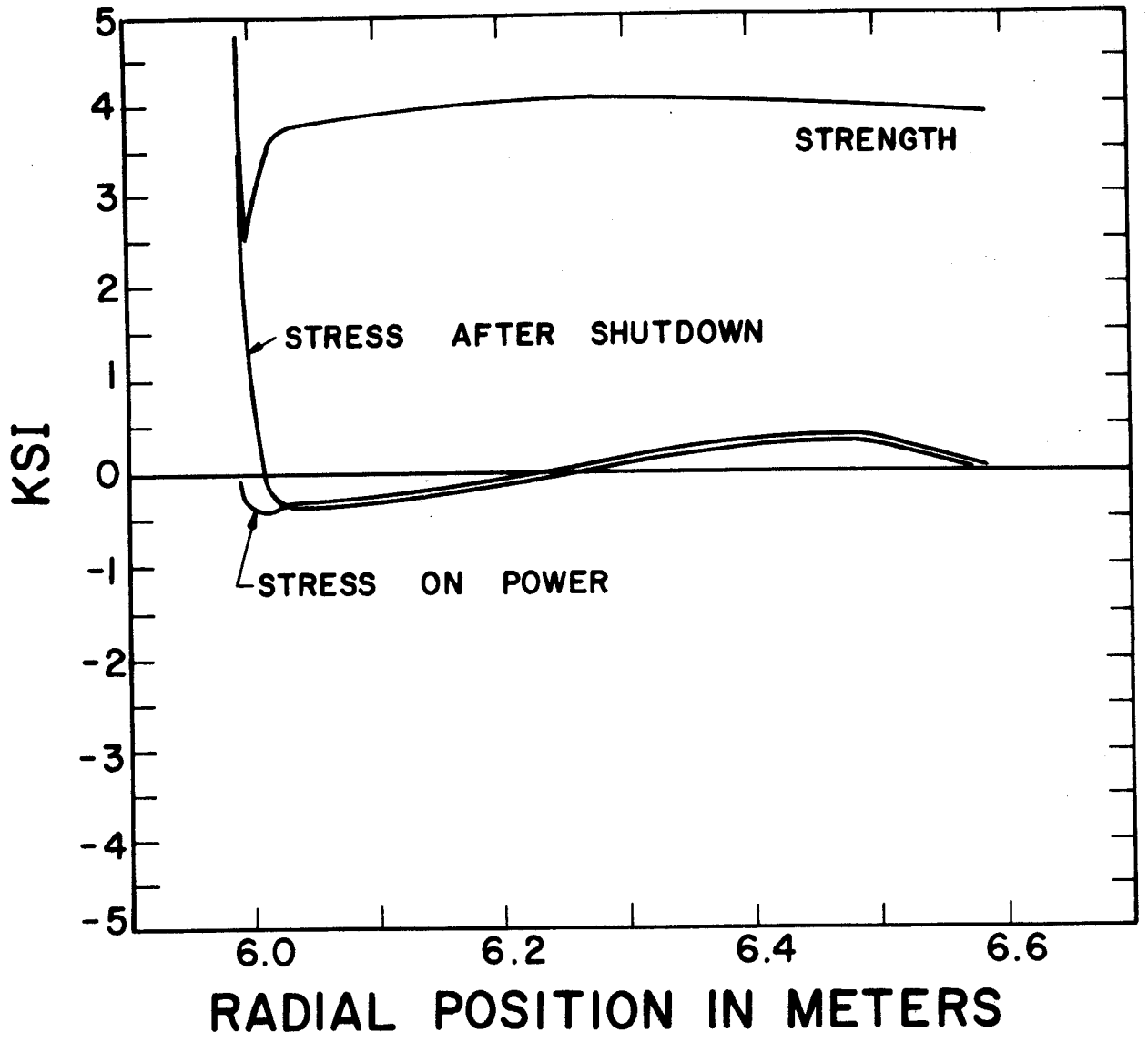

Fig. XV-B-5d After 1.2 Years of Irradiation

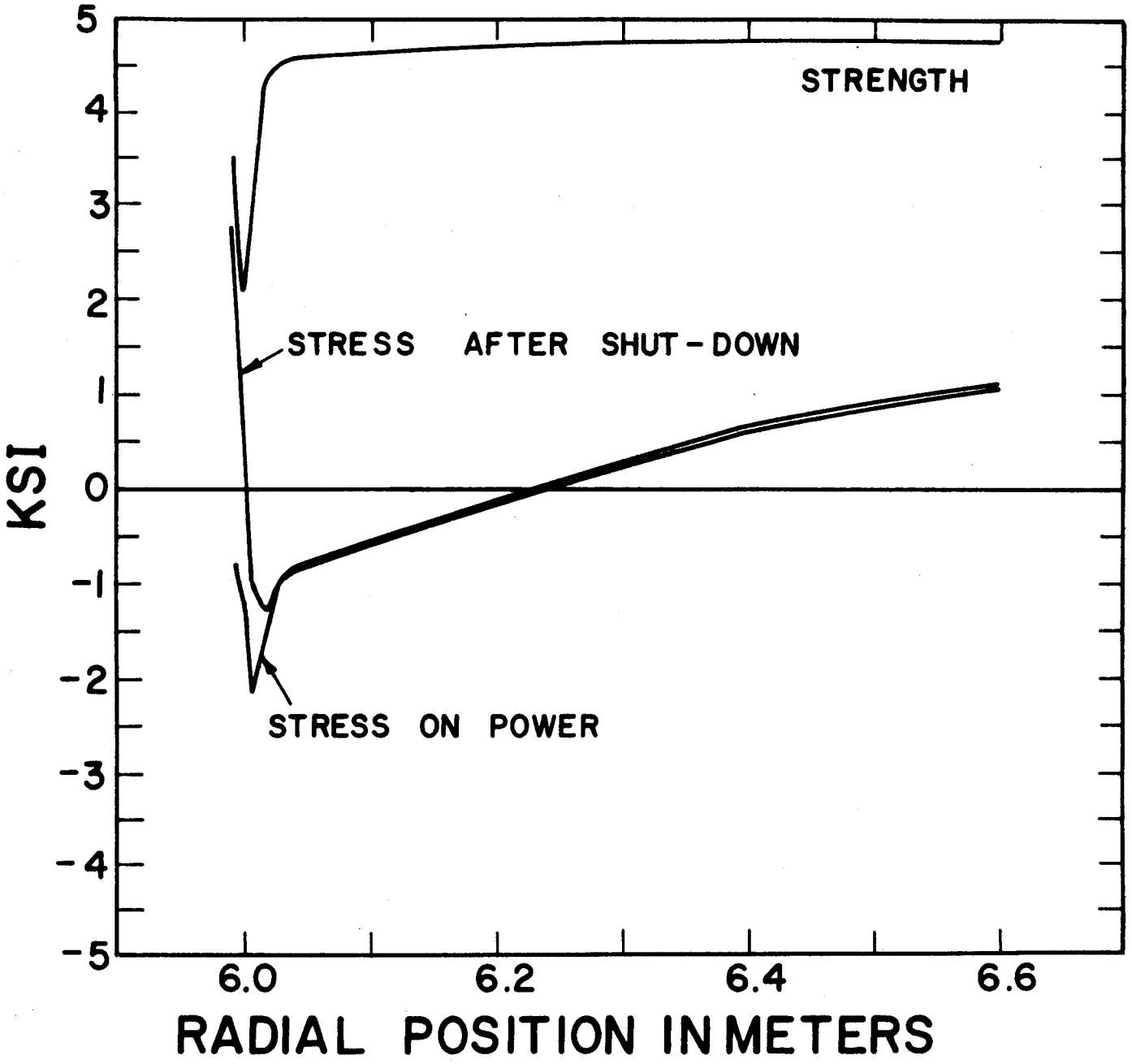

Fig. XV-B-6 Hoop Stress and Tensile Strength Distribution in the Radial Divider made of High-Growth Graphite with 5% Initial Porosity; After 0.4 Years of Irradiation.

The extent of the radial motion of an unrestrained divider can be seen from Fig. XV-B-7. Due to thermal expansion the outer boundary of the divider moves out about 2 cm during startup. In the course of the irradiation the graphite shrinks, and both boundaries start to reduce their radii. Since most of the graphite is never irradiated past the densification phase, the radial displacement of the boundaries is inward. After about one year the outer boundary radius is reduced by about 2 cm measured from the original radius of the cold structure. Therefore, the cold structure has a final radius of about 6.56 m on the outside and 5.94 on the inside.

XV-B-4. Discussion of the Results

The major results of the inelastic analysis on a graphite structure in SOLASE can be summarized as follows:

1. The structure must not be rigidly restrained at its boundaries in order to avoid excessive thermal and swelling stresses.
2. Stresses generated internally by differential shrinkage and growth are sufficiently relieved during operation.
3. However, stresses on shutdown, mainly due to the reversal of thermal stresses, are life limiting.
4. The safe limit of the tensile strength reduces with increasing growth of the graphite porosity. This represents the other life-limiting factor.
5. Low-density graphite develops tensile stresses due to excessive shrinkage which when added to the reversed thermal stresses exceed the allowable tensile strength very early in life.

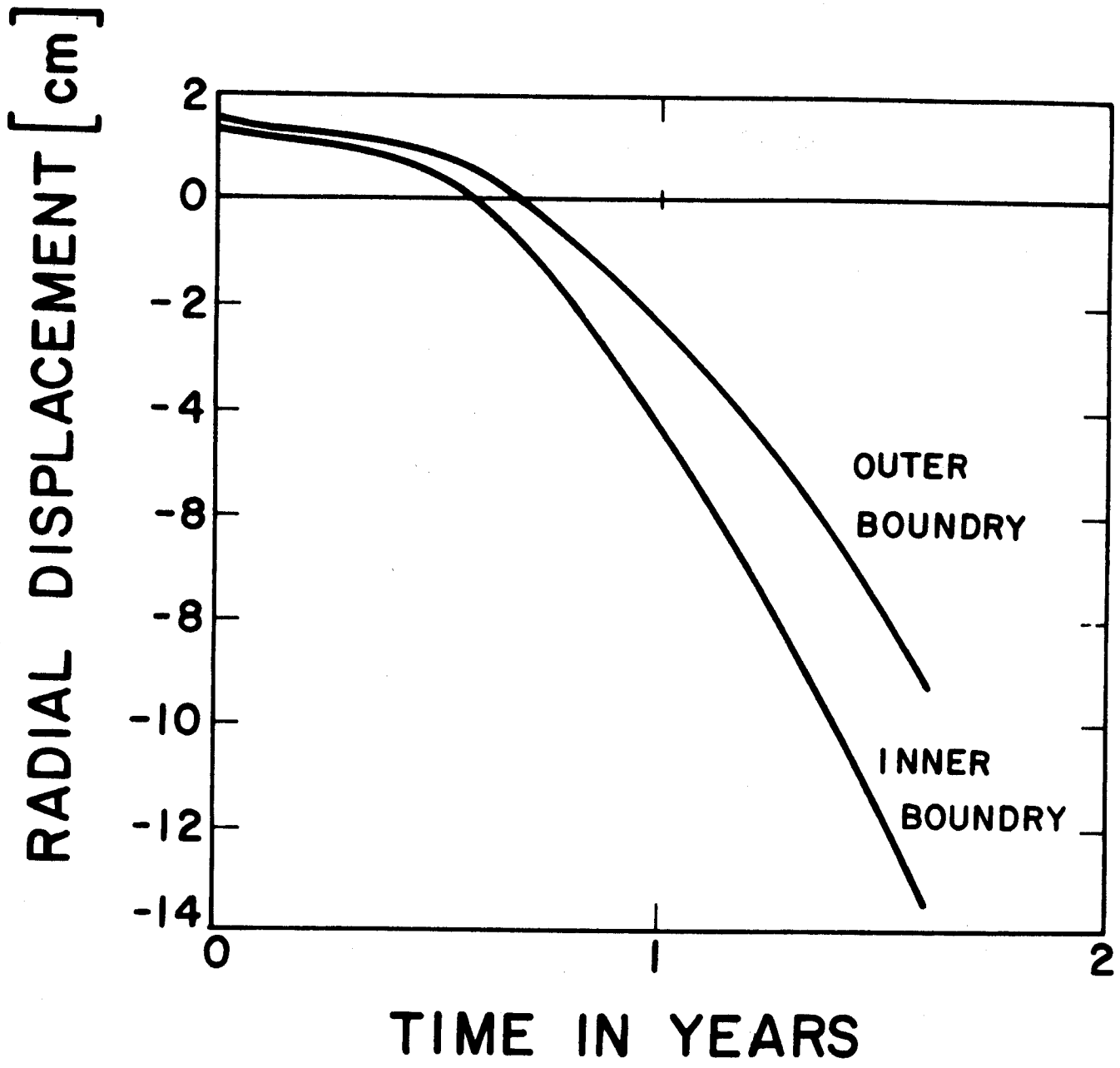

Fig. XV-B-7 The Radial Displacement of the Inner and Outer Boundaries of the Radial Divider made of Low-Growth Graphite with 5% Initial Porosity.

From these results we can draw a number of important conclusions.

The graphite structure must either be manufactured from a high-density-material (~ 5% initial porosity) or, possibly, a tailored density distribution must be designed so that the dense graphite is in the high-flux and medium-temperature region (~ 1000°C). The mechanical connections between the blanket structure and its surrounding support structure must be flexible. These two basic requirements are well within the range of present-day technology. Nevertheless, the behavior of graphite under irradiation was based on models which need further experimental verification, in particular with regard to irradiation at high temperatures (> 1200°C) and high fluences (> 10 dpa). Since the extrapolation of graphite behavior under irradiation was rather modest in this study, the results presented indicate that graphite is a suitable structural material for the blanket of fusion reactors, and lifetimes of about one year or more are realistic.

Within the scope of this study it was not possible to extend the analysis to the actual structure. Hence, the above conclusions are of a general nature.

It should be noted that more restrictive materials limitations often show up only after a more detailed structural analysis has been performed. Therefore, we recommend that future studies be directed towards a more comprehensive structural analysis and that they be performed in the same self-consistent fashion which was developed for this study. The inelastic analysis should, however, be generalized to anisotropic graphites. The need for such an analysis was perhaps best

demonstrated by the peculiar problem we encountered with low-density graphite. Problems of this kind can only be identified by detailed structural analysis.

XV-C. Effects of Radiation on Lithium Oxide

XV-C-1. An Assessment of Radiation-Enhanced Densification

The lithium oxide, Li_2O, used as a coolant and breeding material is in the form of small porous particles. In order to extract the tritium bred in these particles at a sufficient rate, the average diffusion distance should be of the order of 0.1 μm. This implies that the particles contain a network of interconnected pores formed by the agglomeration of 0.1 μ grains. Radiation-enhanced sintering, if it were to take place, would eliminate part of the pores, and the average diffusion distance for tritium release would be too large for efficient extraction.

For the assessment of this problem, the same model was used that describes successfully the densification of uranium oxide fuel in LWRs. Our analysis shows that radiation-enhanced densification in Li_2O will not occur because the stopping power of the recoiling atoms is too small to result in localized melting. The detailed account of this result is presented in the following section.

XV-C-2. The Densification Model

In a porous material, the slowing-down path of energetic ions (fission products in UO_2, primary recoil atoms in Li_2O) may intersect

the surfaces of pores. If the stopping power of the ion is low as it approaches a free surface, it will break through alone and strike the opposite surface of the pore. If, on the other hand, the stopping power is high, a temperature and pressure pulse is formed in the material surrounding the ion path, and material can be ejected from one side of the pore and be deposited on the other side in individual chunks. The deposited material contains many vacancies as well as cavities trapped under the chunks when they stick to the opposite pore surface. The vacancies in this region migrate subsequently, and they are in part annihilated at dislocations and grain boundaries, in the process of which densification occurs. The crucial parameter in this model is the value of the stopping power required for melting the material along the ion path.

In applying this model to the densification of UO_2, Whapham and Makin[13] have examined the temperature distribution along a fission fragment track as a function of time. They concluded that the heat will be conducted away from the track too quickly for this mechanism to operate, unless grain boundaries are present to inhibit rapid heat conduction. Hence, small grain material is more susceptible to densification than large grain material.

If we assume that the grain boundaries have a very large thermal resistance, then the energy deposition required for ejection is approximately equal to the energy required to melt a grain. Hence, the average stopping

power $(dE/dx)_{av.}$ of the energetic ion to cause melting is given by

$$\left(\frac{dE}{dx}\right)_{av.} 2r_o = \frac{4}{3}\pi r_o^3 \left[(\Delta H_f + C_p \Delta T)\frac{\rho}{M}\right] \qquad (41)$$

where $2r_o$ is the grain diameter, ΔH_f is the enthalpy of fusion, C_p the specific heat, ρ the density, and M the molar weight. ΔT is the difference between melting and operating temperature, i.e. $\Delta T = T_m - T_o$.

Table XV-C-1 Parameter for Li_2O Used in Equation (41)

Parameter	Symbol	Value
Grain radius	r_o	0.1 μm
Enthalpy of fusion	ΔH_f	14 kcal/mole
Specific heat	C_p	12.9 cal/mole,^oK
Density	ρ	2.013 g/cm^3
Molar weight	M	29.88 g/mole
Melting point	T_m	1900^oK
Operating temperature	T_o	1100^oK

Using the values given in Table XV-C-1, one finds that the stopping power necessary for melting of a Li_2O grain is

$$\left(\frac{dE}{dx}\right)_{av.} \cong 900 \frac{MeV}{\mu m} . \qquad (42)$$

Table XV-C-2 Maximum Energies of Energetic Ions in Li_2O, and Their Maximum Stopping Powers

Ion	^{7}Li	O	T	α
Max. Energy (MeV)	6.17	3.10	13.3	0.8
Max. Stopping Power (MeV/μm)	2.025	1.838	0.106	0.383

This must now be compared with the stopping power of energetic ions produced in Li_2O. Elastic collisions of fusion neutrons of 14.1 MeV energy produces recoil atoms, and the (n,α) reaction in ^6Li produces energetic reaction products. The maximum kinetic energies of these ions are listed in Table XV-C-2 together with their maximum stopping power in Li_2O. By comparing it with the value in Eq. (42) it is obvious that the stopping power of the ions produced in Li_2O is much too low to cause melting of a grain. Hence, radiation-induced densification will not occur in the Li_2O particles.

References for Chapter XV

1. W. N. Reynolds, "Physical Properties of Graphite", Elsevier Publ. Co. LTD., Amsterdam, 1968, Ch. VI.

2. B. T. Kelly, Nature 207, 257 (1965).

3. G. B. Engle, Carbon 9, 539 (1971).

4. W. C. Morgan, Nucl. Techn. 21, 50 (1974).

5. W. C. Morgan, E. M. Woodruff, and W. J. Gray in "Techn. of Controlled Nuclear Fusion",Vol. 1, CONF-760935-P1, p. 189 (1976).

6. W. J. Gray, W. C. Morgan in "Techn. of Controlled Thermonuclear Fusion Experiments and Eng. Aspects of Fusion Reactors", CONF-721111, p. 983.

7. M. Van den Berg, M. R. Everett, and A. Kingsbury, Proc. of the 12th Biennial Conf. on Carbon, Pittsburgh, 1975, p. 307.

8. R. Blackstone, J. Nucl. Matls. 65, 72 (1977).

9. H. J. Veringa and R. Blackstone, Carbon 14, 279 (1976).

10. J. E. Broklehurst, "Fracture in Polycrystalline Graphite" in Chemistry and Physics of Carbon, Vol. 13, Ed. by P. L. Walker, P. Tower, and M. Dekker, New York, 1977, p. 145.

11. R. M. Christensen, J. Mech. Phys. Solids 17, 23 (1969).

12. A similar, but less concise derivation of this problem can be found in the book of T. H. Lin, "Theory of Inelastic Structures", Wiley and Sons, New York, 1968, Chapter 7.

13. A. D. Whapham and M. J. Makin, Phil. Mag. 7, 1441 (1962).

XVI. The Fuel Cycle and Tritium Processing

XVI-A. Introduction

In this section we shall describe the tritium pathways for SOLASE. Our aim is to identify potential problems related to the tritium cycle in laser fusion reactors, and offer solutions to these problems. The areas investigated include: (1) Reactor fueling and pellet materials constraints, (2) Tritium breeding and blanket design, (3) Tritium extraction from the breeding material and reactor exhaust, (4) Tritium leakage to the environment, and (5) Building atmosphere control. The relationship between these different areas is shown schematically in Fig. XVI-A-1. Special attention will be given to the problem of first wall and pellet materials compatibility inasmuch as it affects the tritium extraction system.

The major parameters characterizing SOLASE are given in Chapter II. The pellet yield is 150 MJ at a gain of 150, a repetition rate of 20 sec^{-1}, and a total energy per fusion event of 18.6 MeV, so that the total thermal power for the reactor is 3190 MWt; the net electrical output is 1000 MWe. The daily D-T fuel requirements for SOLASE are given in Table XVI-A-1. These values are based on a pellet core fractional burnup of 45% (Chapter IV), The repetition rate is increased by 10% to allow for misfirings (22 sec^{-1}) so that the effective fractional burnup is 41% A plant factor of 70% is assumed and a five-day emergency fuel supply is maintained to allow for continued plant operation in case of tritium system failure.

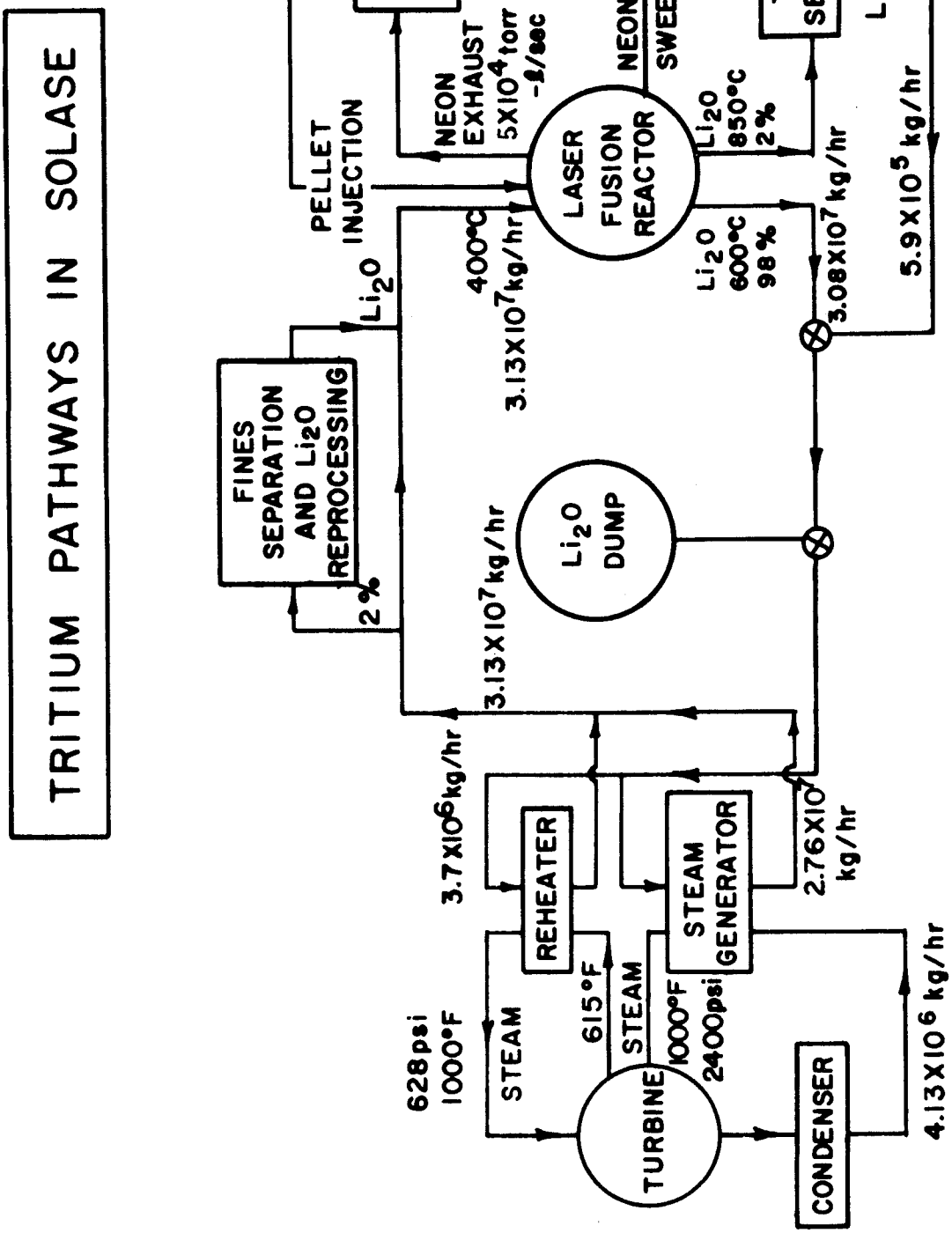
TRITIUM PATHWAYS IN SOLASE
FINES SEPARATION AND Li2O REPROCESSING
2%
Li2O
PELLET INJECTION
NEON PURIFICATION SYSTEM
T
0.67 kg/day
TRITIUM PREPARATION PELLET MAKER STORAGE
T
0.63 kg/day
NEON EXHAUST 5X10^4 torr -l/sec
NEON SWEEP
LASER FUSION REACTOR
400°C
3.13X10^7 kg/hr
Li2O 850°C 2%
TRITIUM SEPARATOR
Li2O
Li2O 600°C 98%
3.08X10^7 kg/hr
5.9X10^5 kg/hr
Li2O DUMP
3.13X10^7 kg/hr
3.7X10^6 kg/hr
REHEATER
STEAM GENERATOR
2.76X10^7 kg/hr
628psi 1000°F
STEAM
615°F
STEAM
1000°F 2400psi
TURBINE
CONDENSER
4.13X10^6 kg/hr

Fig. XVI-A-1.

Table XVI-A-1

Daily D-T Fuel Requirements for SOLASE

	D	T
Daily Consumption (moles/day)	156	156
Daily Consumption (kg/day)	0.31	0.47
Recycled Amount (kg/day)	0.45	0.67
Fabricated Amount (kg/day)	0.76	1.14

XVI-B. Reactor Fueling Cycle

XVI-B-1. Compatibility of Wall and Pellet Materials

XVI-B-1-a. General Description and Pellet Composition

Design of laser fusion pellets is in its infancy and a wide range of pellet materials and output characteristics is possible. In addition to implosion and burn dynamics requirements, pellet designs will be affected by other factors such as: manufacturing techniques and expected tolerances, method of delivery, and compatibility with wall materials. Pellet manufacturing and delivering problems have been discussed in Chapter IX. Here, we shall deal with the materialscompatibility problem. This problem is particularly important for dry-wall type reactors with graphite walls or liners such as SOLASE. The graphite front wall in SOLASE will reach a temperature of ~1750°C after each microexplosion. At these temperatures, a number of possible pellet constituents will react with the wall. This will result in wall erosion and the formation of products which must be continually removed from the chamber. In order to analyze this problem quantitatively, several pellet compositions have been considered (Table XVI-B-1).

XVI-B-1-b. Exhaust Gas Compositions

The composition of pellet debris and chamber exhaust for pellets I and II of Table XVI-B-1 are given in Table XVI-B-2.
The values given in this table correspond to a fill gas pressure of 0.5 torr at 1750°C. (The reactor cavity in SOLASE is filled with neon gas at less than 1 torr pressure in order to protect the front wall from the ions and soft X-rays produced by the microexplosion (Chapter XI).

Table XVI-B-1

Pellet Compositions Considered in this Investigation*

Material	Pellet #			
	I	II	III	IV
Fuel (D-T)	1 mg	1 mg	1 mg	1 mg
Low-Z				
Container	Glass^{+} (2.5 mg)	Polyvinyl alcohol (0.92 mg)	Glass (2.5 mg)	Glass (2.5 mg)
Ablator	CH_2 (1.75-3 mg)	CH_2 (1.75-3 mg)	CH_2 (1.75-3 mg)	CH_2 (1.75-3 mg)
High-Z**	Xe	Xe	Pb	Hg

*About 30 mg of neon are frozen on the outside surface of the pellet in order to insure cryogenic conditions in the pellet during its flight to the cavity center. All the neon will evaporate prior to laser-pellet interactions.

+Borosilicate glass is used.

**Hot electron shield and fuel tamper. A frozen layer of xenon on the inside surface will protect the plastic shell during pellet storage from the betas produced by the tritium decay (Chapter IX).

Table XVI-B-2

Composition of Chamber Exhaust

	Component	Pellet Debris (mg/shot)	Chamber Exhaust (moles/day)
Pellet I	H	0.250	263
	D	0.236	124
	T	0.354	124
	$C_2(H,D,T)_2$	-----	207
	Xe	?	?
	Ne	-----	220,000
	He	-----	156
	C	1.50	238
	SiO_2, B_2O_3	2.35	---
	SiC, B_4C	-----	68.9
	CO	-----	155
	Na_2O, Al_2O_3	0.15	4.0
Pellet II			
	H	0.334	392
	D	0.236	139
	T	0.354	139
	$C_2(H,D,T)_2$	-----	207
	Xe	?	?
	Ne	-----	288,000
	He	-----	156
	O	0.333	---
	CO	-----	39.6
	C	2.00	317